

**2018 International Conference on Computer Science, Electronics and
Communication Engineering**

CSECE2018

February 7-8, 2018, Wuhan, China

Preface

The 2018 International Conference on Computer Science, Electronics and Communication Engineering (CSECE 2018), co-sponsored by Science and Engineering Research Center, Hong Kong and Advanced Science and Industry Research Center, Hong Kong, China will be held in Wuhan from February 7-8, 2018, which is an international event that continues to attract attendees, academics, practitioners and junior researchers from all over the world, enjoying the friendly atmosphere conducive to free exchange of innovative ideas.

The theme of CSECE 2018 reflects the vital role of computer science, electronics and communication engineering in many evolving areas of basic and applied research. We sincerely hope it will be a helpful guide for scientists and researchers working or planning to work in the domains of computer science, electronics and communication engineering.

The Proceedings of CSECE 2018 is now ready, thanks to the sincere efforts of all the esteemed members of the Technical Program Committee, whose extensive preparations eventually culminated in the success of this conference. We also thank the Atlantis Press for publishing the Proceedings, the participants and authors. It is your active participation and encouragement that has instilled a sense of pride and achievement in us and has propelled us to strive in this edition.

CSECE 2018 has adopted a precise and strict reviewing process. All the submissions are divided into several chapters according to the topics, and removed the information of the authors, including name, affiliation, and email. Then the submissions are sent to reviewers according to their research interests. We use a double-blind system for peer review. Contributions will be reviewed by several invited reviewers at the same time, and the reviewers are asked to evaluate and give suggestions on revising based on its originality, research, relevance to conference, contributions and presentation etc. The review process may take about one month.

We received a large number of high-quality papers from all over the world and our TPC had a very tough time selecting the best papers. Eventually, we have selected 119 papers from 396 submissions with the assistance of members of TPC. We regret that we could not include more papers due to a variety of constraints and mandates of quality control. In this volume, the accepted submissions are included in 5 chapters.

Chapter 1: Communication Technology and Network Security
Chapter 2: Artificial Intelligence and Recognition Technology
Chapter 3: Power, Electrical and Electronic Engineering
Chapter 4: Applied Mathematics and Data Analysis
Chapter 5: Applied Information Technologies and Computational Methods

It is a great honor to become colleagues with so many excellent people. We hope all of you have a very pleasant stay in Wuhan and we look forward to having you as an active member in our future endeavors.

CSECE 2018 Organization Committees

Organization Committee

General Chairs

- Prof. V. Gurumurthy Iyer, Jawaharlal Nehru Technological University, India
Prof. S. Balakrishnan, Anna University, India
Prof. M. Bhardwaj, SRM University, India

International Scientific Committee

- Dr. T. G. Tan, University Malaysia Kelantan, Malaysia
Dr. Z. Ghemari, Electrical engineering department University Mohamed Boudiaf- M'sila, Algeria
Dr. M. K. Marichelvam, Mepco Schlenk Engineering College, India
Prof. R. H. Wong, Hwa-Hsia University of Technology, Taiwan, R.O.C.
Prof. A. Nekrasov, Southern Federal University, Russia
Dr. K. Ostad-Ali-Askari, Islamic Azad University, Iran
Dr. Z. Y. Jiang, University of Chinese Academy of Sciences, China
Dr. S. Ali, China University of Petroleum, Beijing, China
Dr. A. S. A. Alzubaydi, University of Babylon, Iraq
Prof. Z. Chen, University of Technology, China
Prof. K. Balakrishnan, Karpaga Vinayaga College of Engineering and Technology, India
Dr. S. A. Alavi, Islamic Azad University, Iran
Dr. I. Memon, Zhejiang University, China
Dr. W. C. Lai, National Taiwan University of Science and Technology, Taiwan
Prof. O. M. Lecian, KTFDF Comenius University in Bratislava, Slovakia
Prof. I. L. Popa, University of Alba Iulia, Romania
Prof. R. Szewczyk, Industrial Research Institute for Automation and Measurements PIAP, Poland
Prof. L. A. Abdillah, Universitas Bina Darma, Indonesia
Dr. M. A. CHUNG, Department of BU1, Quanta Computer Inc., Taiwan
Dr. P. M. K. Prasad, GVP College of Engineering for Women, Visakhapatnam, India
Prof. W. T. Sung, National Chin-Yi University of Technology, Taiwan
Dr. G. Ilewicz, University of Bielsko-Biała, Poland
Prof. S. Sharma, A P Goyal Shimla University, Shimla (H.P.), India
Dr. A. Zhauyt, Institute of Industrial Engineering, Satbayev University, Almaty 050013, Kazakhstan
Dr. Y. Polat, Research Center, Nevşehir Hacı Bektaş Veli University, Nevşehir, Turkey
Dr. H. N. Feng, Signal and Communication Research Institute, China Academy of Railway Sciences, China
Prof. Ş. Țălu, The Technical University of Cluj-Napoca, Romania
Dr. I. Izonin, Lviv Polytechnic National University, Lviv, Ukraine

CSECE2018 Contents

Chapter 1: Communication Technology and Network Security	
A New Method for Sorting Radar Signal Based on Entropy Features	
<i>Jun Han, Xiaofei Lu, Minghao He and Xiaojie Tang</i>	1
A Spectrum Analysis Algorithm Based on GPU	
<i>Kunyuan Xu, Yanhua Jin, Fangyuan Zhao and Haoran Ma</i>	5
Research on Access Control Model Based on User Trust Degree and Resource Life Cycle under Mobile Environment	
<i>Xiaoyan Zhang and Kai Kang</i>	10
A Probe into the Key Parameter Monitor of V2G System on Electric Vehicle Based on Wireless Power Transmission Technology	
<i>Wangcheng Zhu, Zhenchao Xie and Xinshu Wan</i>	14
An Air Bearing Facility for Antenna Pointing Mechanism	
<i>Guoyong Yang, Hongguang Wang, Lie Ling and Feng Gao</i>	21
Research on Multi-Hop Routing Protocol of Wireless Sensor Networks Based on Gradients	
<i>Chenglong Hu and Yongzhen Li</i>	26
Observation-based Clock Synchronization in Wireless Sensor Networks	
<i>Ayako Arao and Hiroaki Higaki</i>	31
Properties of a Self - gain Optical Fiber Differential Pressure Sensor Based on Damping Piston	
<i>Hao Hu and Liqiong Zhong</i>	36
Identifying Route Preferences over Origin-Destination Using Cellular Network Data	
<i>Zhichao Guo and Tongyu Zhu</i>	40
Two New Closed Form Approximate Maximum Likelihood Location Methods Based on Time Difference of Arrival Measurements	
<i>Wanchun Li, Qiu Tang, Yingxiang Li and Guobin Qian</i>	45
A Dynamic Symmetric Fully Homomorphic Encryption Mechanism for Privacy Protection of Cooperative Precision Positioning Cloud Service	
<i>Dibin Shan, Xuehui Du, Wenjuan Wang and Nan Wang</i>	50
Research on Temperature Control System Based on WeChat Remote Operation	
<i>Xuchen Guan, Yingqing Guo and Xinghuai Huang</i>	54
Anti-sunlight Jamming Technology of Laser Fuze	
<i>Xiangjin Zhang, Ruoyu Wu, Chengfang Shen and Wei Dai</i>	59
Elevation Angle Estimation by Time Reversal Method in Homogeneous Shallow Sea Environment	
<i>Haixia Jing, Haiyan Wang, Zhengguo Liu, Xiaohong Shen and Tianyi Jia</i>	64
An Improved TLD Tracking Algorithm for Fast-moving Object	
<i>Shijie Zhou, Yuanxi Peng, Kecheng Gong and Leizhi Shu</i>	69
Multiple Centroid-Based Multi-Object Tracking by Decision Making	
<i>Hao Zhou, Jian He and Zhangqin Huang</i>	74

Characterizing the Impact of DDoS Attack on Inter-domain Routing System: A Case Study of the Dyn Cyberattack	79
<i>Yujing Liu, Zhilin Wang and Nan Li</i>	
IoT Node Trust Authorization Model	83
<i>Ruizhong Du, Chong Liu and Fanming Liu</i>	
A Network System Security Assessment Method Based on Penetration Testing	88
<i>Yue Li, Xiaolin Zhao, Chonghan Zeng, Yu Fu and Ning Wang</i>	
A Novel Weak Deduction Password Strength Meter of Chinese Websites	96
<i>Yu Wu</i>	
A Novel Video Encryption Method Based on Faster R-CNN	100
<i>Lijuan Duan, Dongkui Zhang, Fan Xu and Guoqin Cui</i>	
Common-Key Cryptosystem with Mixture of Fake Plaintexts	105
<i>Masayoshi Hayashi and Hiroaki Higaki</i>	
Modeling Confrontations in Complex Networks Based on Game Theory	109
<i>Yapeng Li and Jun Wu</i>	
Complex Project Schedule Risk Simulation Based on Multi-agent	113
<i>Haolin Wen, Tao Hu and Gongda Yan</i>	
Research on Risk of Online Supply Chain Finance	118
<i>Daozhi Zhao, Di Wang and Baosen Wang</i>	
Supply Chain Financial Ecology Model Design and Risk Management Research	124
<i>Baosen Wang, Wenzhao Lan and Chunming Fan</i>	
The Effect of Behavior Conformity on Prisoner's Dilemma Game	131
<i>Zidong Chai, Yanbo Zhang, Xinyu Zhang and Xiaobo Liu</i>	
Chapter 2: Artificial Intelligence and Recognition Technology	
The Application of Real-Time Object Detection on Aerial HD Videos Based on Deep CNN	
<i>Guanghui Xu, Shuai Xie, Jun Wang and Guodong Wu</i>	134
Design of the UAV Digital Actuator Automatic Test System Based on Dual-core Microcontroller TMS320F28377D	
<i>Tao Yang, Liren Chai and Gang Wang</i>	139
A Load Identification Technology for Wireless Smart Home Systems	
<i>Zhenchao Xie, Daohong Lin, Yufeng Chen and Xinshu Wan</i>	142
A Feasible Control Method for Incomplete Symmetrical Marine Robot	
<i>Lei Zhang, Zaopeng Dong, Yongsuo Yan and Yuyin Cao</i>	147
Develop the AI Literacy of Infants by Deeply Integrated English Learning and Robot Education	
<i>Zhongyu Zhang</i>	154
A Hybrid Fusion Algorithm for Integrated INS/UWB Navigation and Its Application in Vehicle Platoon Formation Control	
<i>Yingmao Lu, Jianjun Yi, Liang He, Xiaomin Zhu and Pengfei Liu</i>	157

The Research of Internet Identity Authentication System Based on Fingerprint Information	162
<i>Feng Xiao, Yue Zhang, Fei Zhang and Yongzhen Li</i>		
Multi-Network Fusion Based on CNN For Facial Expression Recognition	166
<i>Chao Li, Ning Ma and Yalin Deng</i>		
Human Face Age Recognition Based on Convolutional Neural Networks	170
<i>Zijiang Zhu, Yi Hu, Dong Liu, Xiaoguang Deng and Junshan Li</i>		
Face Recognition Based on LBP(2D)²PCA+SVM	174
<i>Yanmei Jiang, Wei Wei, Xue Liu and Ying Shi</i>		
The Colony Count Based on Image Processing Using Matlab and Photoshop	179
<i>Xiaoming Chen, Shufang Li, Zhijun Zhang and Jun Gao</i>		
CT Image Segmentation Algorithm Based on Merging of Similar Adjacent Components	183
<i>Xueguang Sun and Weigen Qiu</i>		
BDS Common-View Method Based on CGTTS V2E Standard	187
<i>Xu Liu, Dangli Zhao and Junliang Liu</i>		
An Adaptive Bitrate Algorithm Based on Estimation and Video Adaptation for Improving QoE in DASH	191
<i>Saba Qasim Jabbar, Dheyaa Jasim Kadhim and Yu Li</i>		
Vehicle Target Detection Based on Improved Mixed Gaussian Modeling	196
<i>Caiyun Xie, Ruxia Hong, Jing Wang and Hong Yu</i>		
A Precision Evaluating Method of DEM Using Map Spots Generated by Contour Superposition	200
<i>Zechun Huang, Zhu Xu, Qianning Zhang, Min Xiao, Zipu Liu, Yongyou Qian and Tianting He</i>		
Sight Spot Buffer Model Based on Tourists' Interests	204
<i>Xiao Zhou, Shun He, Shixiang Zhang, Wei Chen, Yu Chen and Youwei Ma</i>		
Research on Creation and Technology to Make Large-scale Production of Vertical Greening Wall	207
<i>Wanlu Luo and Jianwu Ma</i>		
Chapter 3: Power, Electrical and Electronic Engineering		
Research on Assessment Method of Grid Frequency Fluctuation Characteristics and Optimization of Speed-governor Parameters	210
<i>Daohong Lin, Qiang Wu, Xinshu Wan, Yunqian Li, Lei Shao and Hongjun Zhou</i>		
Research on Control Strategies for Performance Optimization of Wireless Powering System for Smart Home Appliances	216
<i>Zhenchao Xie, Daohong Lin and Wangcheng Zhu</i>		
Design of Intelligent Charging Access System for Home Appliances	224
<i>Wangcheng Zhu, Xinshu Wan, Taobei Lin and Yun Liu</i>		
Coupling Characteristics and Optimization of the Resonators Applied to the Power Supply System of Tail-free Household Appliances	230
<i>Daohong Lin, Wangcheng Zhu and Zhenchao Xie</i>		

Research on Networked Sliding Mode Predictive Controller Based on Particle Swarm Optimization <i>Yang Yin, Hongke Li and Zhengying Ren</i>	237
Automated Detecting System for Elevator Guide Rails Based on Tilt Sensors and Acceleration Sensors <i>Yifeng Yang, Wei Guo, Yujun Wang and Wenxiu Lu</i>	242
An EMC Study on Intentional Transmitter of Railway Train Base on Poynting Vector <i>Ping Sun</i>	245
Teeth Classification Based on Haar Wavelet Transform and Support Vector Machine <i>Fangyuan Liu, Zhi Li and Wagner Quinn</i>	249
Online Algorithm for Velocity Estimation in Ultrasonic Doppler Measurement <i>Enyao Shang, Jinchun Hu and Shengwu Du</i>	253
Experimental Research and Analysis on a Vibration Model of Stator of L1B2 Linear Ultrasonic Motor <i>Xingyu Yi, Gang Zhao and Wenlei Xiao</i>	258
Control Modeling of a New Type Electric Mechanical Continuously Variable Transmission and Realization of the Control Objectives <i>Xiumin Yang, Song Zhang, Zeqi Wang and Lei Zhang</i>	261
Improved Rigid Cable Method for Prestress Optimization of Suspen-dome Structure <i>Wenfeng Du, Shuailiang Zhang, Longxuan Wang and Pengfei He</i>	265
Technology of Sound Velocity Correction for Multi-beam Bathymetry Sounding <i>Weiming Xu and Kai Ma</i>	269
Power Efficiency Optimization of Hydro-pneumatic Transformer of Air-powered Automobile <i>Xiangheng Fu</i>	274
Research on the Mathematical Modeling of Damping Controlled Oil Gas Spring <i>Yijie Chen, Yafeng Zhang, Mengyan Xu, Fu Du and Peng Gui</i>	279
Development of a Hydraulic Energy Harvester for Shock Absorber <i>Longhan Xie, Jiehong Li, Siqi Cai and Xiaodong Li</i>	282
Analysis on Transient Temperature Field of the Rod Fastening Rotor Based on Fractal Contact Theory <i>Yiping Li</i>	287
Study on Rules for Spiral Groove of Swirl Nozzle to Performance of Inside Flow <i>Yong Guo, Lili Guo and Longyan Zhang</i>	291
Research on Random Flow Simulation Model of Bridges <i>Li Cao and Limin Sun</i>	295
A Test Process Model and Optimization Framework Based on Network Schedule <i>Litian Xiao, Mengyuan Li and Nan Xiao</i>	298
Chapter 4: Applied Mathematics and Data Analysis Coefficient Distribution Method for Minimum Weight Design of Large-span Statically Determinate Trusses under the Constraint of Allowable Displacement <i>Wenfeng Du, Qi Liu, Kang Yuan and Jiyuan Ma</i>	302

Sieve Method: Sieve the Forward and Reverse In One Time <i>Sai Chuen Hui</i>	308
The Application of Vector Lyapunov Functions in Iterative Learning Control <i>Qunli Zhang</i>	315
Dynamic Data Modeling of SCR Denitrification System Based on Mutual Information <i>Wenjie Zhao and Luyao Zhang</i>	321
Research on Hierarchical Interactive Teaching Model Based on Naive Bayesian Classification <i>Dongyan Fan</i>	325
A Probability Model of Calculating L2 Cache Misses <i>Kecheng Ji, Ming Ling and Li Liu</i>	329
Deflection Analysis and Iterative Solution Method of Slender Telescopic Booms <i>Xuyang Cao, Zhenhua Gu and Haojie Yu</i>	333
The Reciprocal Sums of the Pell Numbers <i>Fuling Zhang</i>	337
Tests for Spatial Correlation of Dependent Variables in Spatial Dynamic Panel Data Models <i>Rong Sun</i>	345
MOOC Course Evaluation Based on Big Data Analysis <i>Yong Luo, Jianping Li, Zheng Xie, Guochang Zhou and Xiao Xiao</i>	349
The Application of Data Mining Techniques in College Students Information System <i>Yang Liu, Jingwei Chen, Jun Liu, Wei He and Tingting Li</i>	353
Design and Implementation of Database Centralized Access Control and Audit System <i>Ying Zheng and Qinghai Bai</i>	358
A Simple Fusion Method for Trajectory Data of Aerocraft <i>Dingxin Yang, Peng Du and Jinwei Sun</i>	361
Empirical Test of Arbitrage Pricing Model for the SSE 50 Index Stocks <i>Mingyue Ding, Yumei Pan and Yanqiang Ding</i>	364
The Results of the General Traffic Measurements Analysis on the Example of Łódź Voivodeship (in Poland) <i>Elżbieta Macioszek, Grzegorz Sierpiński, Marcin Staniek and Damian Lach</i>	372
Estimation of the Average Treatment Effect with Missing Outcome Data <i>Feng Han</i>	377
Parametric Design on Stubble-cutting Disc with Oblique Ripples Based on Reverse Engineering Methods <i>Ping Zhao, Xuewei Bai, Yongkui Li, Yue Tian and Changyi Lv</i>	383
The Mathematical Model of the Natural Evolution Law of Cosmic Material Organisms <i>Sai Chuen Hui</i>	389

Research on Filter Rod Loose Quality of Double Channel Forming Machine Based on Apriori Algorithm of Interestingness	396
<i>Min Zhang, Liming Zhu and Yumin Wang</i>	
Research on Process -Resources Dynamic Configuration Model of Digital Inspection Management System	399
<i>Jian Yao and Guijiang Duan</i>	
Two-step Gaussian Process Regression Improving Performance of Training and Prediction	403
<i>Wei Wang, Santong Zhang, Wei Yang and Xiangbin Liu</i>	
Research on Configuration Optimization of Multi-echelon Inventory Based on Component Commonality	408
<i>Lijun Qiu, Linyu Fu, Qi Dong, Chongyi Liu, Kun Xian and Xinhua Weng</i>	
Theoretical Research on Concentric Circular Selection of Sample Points for Flatness Error Measurement of Revolving Body End-face	413
<i>Lei Zhang, Wenying Wang, Peng Guan and Jun Cheng</i>	
An Improved Differential Evolution for Constrained Optimization Problems	417
<i>Liechao Zhang and Lin Shang</i>	
Effect of Workload Characteristics on Similarity Analysis	423
<i>Jiang Sha and Wenjuan Xu</i>	
Markov-Based Forecasting Model for Enterprise Human Resources Internal Supply	427
<i>Pu Li, Fengming Liu and Chengcheng Li</i>	
The Coordinated Replenishment Policy in a decentralized Assembly System	431
<i>Jianhong Yu</i>	
Hardware Design of SUAV Flight Control System Based on STM32F427	435
<i>Tao Yang, Liren Chai and Gang Wang</i>	
Chapter 5: Applied Information Technologies and Computational Methods	
The Current Status of Informatization and Information Literacy in Advanced Medical Institutions	
<i>Na Wang and Jinguo Wang</i>	439
Research and Realization for Information System of Shenhua Ningxia Coal Integration Based on XML	442
<i>Xiaoyan Zhang, Huan Li and Shiheng Liu</i>	
Designing of IoT Platform Based on Functional Reactive Pattern	445
<i>Haidong Lv, Xiaolong Ge, Hongzhi Zhu, Zhiwei Yuan, Zhen Wang and Yongkang Zhu</i>	
Networking Mechanism of Fire Monitoring System Based on Internet of Things	449
<i>Fangwen Xu, Jianjun Yi, Liang He, Xiaomin Zhu and Zhuoran Wang</i>	
Developing a smart Energy Monitoring Terminal Based on Internet of Things	453
<i>Shaoru Zhang, Jianjun Yi, Liang He and Fangwen Xu</i>	
A Cloud Platform for Smart Firefighting Facilities Maintenance Based Internet of Things	457
<i>Wenchao Guan, Jianjun Yi, Liang He, Yajun Zhang and Pengfei Liu</i>	

K-out-of-n Model to Calculate the Availability of a Business System <i>Huan Xu, Ruihong Yan and Xiaoling Wang</i>	461
Research on Implementation of Knowledge Convergence Based on Apache Jena3 <i>Xiabai Yang, Ming Yang, Deqiang Yang and Yu Huang</i>	464
The Semantic Retrieval System for Learning Resources Based on Subject Knowledge Ontology <i>Bei Wu</i>	467
A QoS-based User Reputation Measurement Method for Web Services <i>Jianlong Xu, Yindong Chen and Changsheng Zhu</i>	470
Prolong Lifespan of Wireless Sensor Network with Optimized Information Compression Algorithm and Magnetic Resonant Concept <i>Manish Bhardwaj and Anil Ahlawat</i>	474
Analysis of Topic Influence and Post Features of Sina-Weibo <i>Borong Lyu, Xinhui Shao, Yinbo Huang and Yuyang Xie</i>	479
Sentiment Analysis of Emergencies Based on Microblogging <i>Changjin Liu, Xin Ye, Hongxia Dai, Fan Chen and Luan Dong</i>	487
Research on the Similarity of Microblog Rumors Based on Bayesian Network <i>Chengcheng Li, Fengming Liu and Pu Li</i>	491
Attention-based ResNet for Chinese Text Sentiment Classification <i>Hu Han, Xuxu Bai and Jin Liu</i>	495
Speech Enhancement Based on Sparse Representation Using Joint Dictionary <i>Ming Wei, Zheng Liu, Xueqin Chen and Heming Zhao</i>	500
Research on Estimation Method of Mileage Power Consumption for Electric Vehicles <i>Yang Xu and Kaiyu Wang</i>	504
Coordinated Electric Vehicle Charging Based on Real-Time Pricing <i>Xinshu Wan, Wangcheng Zhu, Ning Su and Jiahong Wu</i>	509
Analysis and Research on the Task Pricing of “Making Photos and Making Money” <i>Leyuan Zhao, Bo Zhang, Juntian Bo and Wenfei Zhao</i>	514
Research on Task Pricing of Crowdsourcing Platform <i>Senrong Ma, Lei Wang, Jiaen Guo and Gang Zhou</i>	518
An Approach Assessing Software Trustworthiness <i>Xinglong Xie and Weixian Xue</i>	522
Study on Scientific Location Level Classification and Optimization Methods of Military Equipment Maintenance Support Sites Network <i>Gongda Yan, Peng Dong, Wei Lu and Peng Yu</i>	527
The Application of Circular Collision Detection and Target Tracking to Improve the Collision Accuracy in 2D Games <i>Jungyoon Kim, Jiyong Ge, Zhixiao Wang and Wonhyung Lee</i>	532

Research on the Protection and Reconstruction of the Landscape Heritage Based on Digital Reduction Technology	
—Taking AD1837 as an Example of the Huangci Bridge in Qing Dynasty in Nanning, Guangxi	
<i>Chongen Wang and Shaojie Wang</i>	536
Research on the Developing Approach of Digital Humanities in the Field of Library Science in China	
<i>Panpan He and Ya Chen</i>	541
Total Quality Management (TQM) or Continuous Improvement System (CIS) in Education Sector and Its Implementation Framework towards Sustainable International Development	
<i>Vijayan Gurumurthy Iyer</i>	546

A New Method for Sorting Radar Signal Based on Entropy Features

Jun Han, Xiaofei Lu, Minghao He and Xiaojie Tang*

Air Force Early Warning Academy, Wuhan 430019, China

*Corresponding author

Abstract—In order to figure out shortcomings of the existing method, such as the accuracy is not high and the method is sensitive to noise, we firstly Obtain the Wigner distribution space and bispectrum space for the received radar signal, then divide the space into subspace. Under the subspace distribution probability, the information entropy features of radar signals are constructed into two-dimensional eigenvectors, which reflects the energy distribution of the signal in these two spaces. Through the simulation results, it shows that extracted characteristic parameters have good separation and stability in the range of wide signal to noise ratio, verifying the validity of the method in this passage.

Keywords—component: sort; entropy feature; subspace; the Wigner distribution; bispectrum

I. INTRODUCTION

Radar source signal sorting is one of the key technologies of EW system [1], referring to the separation of impulses belonging to different sources of impulses from the intercepted dense radar pulse stream. With the increasing proportion of new complex radar, the sort of unknown radar's source signal plays an increasingly important role. Current radar's source signal sort uses features mainly based on the analysis of diverse general parameters of the intercepted signal, such as t_{TOA} , θ_{AOA} , f_{RF} , τ_{pw} and so on^[2-6]. But these general parameters of sort features all have their drawbacks. When the f_{RF} , τ_{pw} and other parameters of the signal change fast and variously, the usability of these general sorting features will be greatly reduced. Intra-pulse characteristics are one of the most characteristic parameters of radar signals. Although some of the current radar signals vary widely in their conventional parameters, the characteristic parameters in the pulse have certain stability. At present, many scholars have applied the intra-pulse characteristic parameters such as wavelet features and complexity features to the classification and recognition of radar source signals, and achieved some success^[7-9].

Radar source signals can be viewed as a superposition of certain useful signals and random noise, which have a certain degree of uncertainty. This uncertainty is related to the signal-to-noise ratio and the parameters of the signal received. In informatics, entropy represents the system's average uncertainty^[10]. The information entropy in the signal refers to the average amount of information contained in the signal. It decreases as the prior probability increases, but increases with the posterior probability, reflecting the complexity of the

information contained in the signal. When modulation form of radar source signal is certain, after a certain noise superimposed, its information entropy maintain a certain level. When the signal structure and transmission environment changes, the complexity of the information changes, uncertainty changes, and its entropy changes as well for detection and reception system. Therefore, the information entropy can be used for radar radiation source signal sorting.

This paper starts from the Wigner distribution and double spectrum of radar source signal and extract the features of information entropy and a high accuracy sorting of unknown complex radar signals with low signal-to-noise ratio is achieved.

II. INFORMATION ENTROPY

Information entropy represents the measure of the overall information of the signal in an average sense. The formula is:

$$H(S) = -\sum_{i=1}^N P_i \ln P_i \quad (1)$$

In the formula, $X = \{x_1, x_2, \dots, x_N\}$ is the discrete signal after sampling. From a wide area, it can be a signal on any domain, the probability of its magnitude is $P_i = P(x_i), i = 1, 2, \dots, N$, and $\sum_{i=1}^N P_i = 1$.

Radar radiation source signal amplitude is usually within a certain range of continuous distribution, and the amount of discrete signal after AD sampling is very large. According to the conventional method of obtaining information entropy, it is impossible to calculate the probability of the radar source signal according to the amplitude points one by one. Therefore, it is necessary to convert the radar source signal in the time domain to other domains in order to better obtain the entropy feature.

Information entropy can be established using a method of subspace distribution probabilities. Let S be the signal X 's feature space, S_1, S_2, \dots, S_N is its characteristic subspace, a complete division of S . Then the distribution probability of signal X under the feature subspace S_N can be expressed as follows:

$$P_{S_i} = \frac{\sum_{S_i} E(x_i)}{\sum_S E(x_i)}, i=1,2,\dots,N \quad (2)$$

Where $E(\cdot)$ is the energy function, N is the number of subspaces. From the formula we can see that P_{S_i} is characterized by the proportion of the energy of the signal subspace S_i occupied by the entire signal feature space.

According to the definition of information entropy, the information entropy of the signal under the probability of subspace distribution can be obtained:

$$H_s(X) = -\sum_{i=1}^N P_{S_i} \ln P_{S_i} \quad (3)$$

$H_s(X)$ characterizes the distribution of signal energy among subspaces of each feature. If the signal in a feature subspace mutation, the corresponding subspace probability will change, resulting in changes in information entropy. When each subspace energy is equal, the information entropy gets the maximum value, which is $H_s(X) = \ln N$, therefore, the standardization of information entropy can be expressed as:

$$H_s(X) = \frac{-\sum_{i=1}^N P_{S_i} \ln P_{S_i}}{\ln N} \quad (4)$$

III. WIGNER DISTRIBUTION ENTROPY CHARACTERISTICS

According to the definition in the previous section, the radar source signal can be converted to the corresponding spatial domain. The method of subspace distribution probability is used to establish the feature of information entropy.

For different modulation methods of radar signals, they have different time-domain distribution. Time domain analysis is a typical method of frequency domain feature analysis, which can establish the signal energy distribution status, widely used in the field of signal processing.

Wigner distribution is often used in time-frequency analysis of the method is a typical Cohen class time-frequency analysis. The Wigner distribution is defined as the Fourier transform of the central covariance function of the signal, which can fully reflect the instantaneous power spectral density characteristics of the signal in the energy space.

The Wigner distribution of the signal $s(t)$ is defined as:

$$W_x(t, f) = \frac{1}{2\pi} \int_{-\infty}^{\infty} x(t + \frac{1}{2}\tau) x^*(t - \frac{1}{2}\tau) e^{-j2\pi f\tau} d\tau \quad (5)$$

Where, $x(t)$ is the analytical signal of $s(t)$, τ is the time difference variable, f is the frequency. The total integral of Wigner distribution in time-frequency and two-axis is equal to the signal energy E , that is:

$$\frac{1}{2\pi} \int_{-\infty}^{\infty} \int_{-\infty}^{\infty} W_x(t, f) dt df = \frac{1}{2\pi} \int_{-\infty}^{\infty} |X(f)|^2 df = E \quad (6)$$

$$\frac{1}{2\pi} \int_{-\infty}^{\infty} \int_{-\infty}^{\infty} W_x(t, f) dt df = \frac{1}{2\pi} \int_{-\infty}^{\infty} |x(t)|^2 dt = E \quad (7)$$

From (5) to (7), we can see that the Wigner distribution has a clear physical meaning, which reflects the signal energy distribution in the time and frequency domains, and can fully describe the signal energy density distribution.

It can be seen from the above analysis that the different modulation forms of radar source signals have different energy distributions in each subspace of the Wigner distribution space, and the characteristics of the information entropy represented by them are also different.

Extraction of the Wigner distribution of signal characteristics of the signal entropy algorithm steps are as follows:

Step1 pre-process the received radar signal;

Step2 Find the Wigner spatial distribution of the radar signal according to formula (5)

Step3 subdivide the Wigner distribution space along the time axis and the frequency axis;

Step4 according to equation (2) to find the signal distribution probability in subspace;

Step5 obtains the information entropy feature of signal Wigner distribution according to formula (4);

IV. BISPECTRUM ENTROPY FEATURES

Reconnaissance receiver receives the radar radiation source signal, after the pre-processing, the noise included includes various clutters, receiving system thermal noise and so on. Research shows that such as the weather by a large number of scattered .The spot-induced clutter and receive system thermal noise tend to Gaussian distribution. As a tool of time series analysis, high order spectrum can effectively suppress the influence of Gaussian noise. Therefore, the use of bispectrum analysis, can effectively suppress the purpose of Gaussian noise.

The power spectrum characterizes the distribution of signal energy over frequency and the bispectrum is the decomposition of signal skew in the frequency domain. The bispectrum defined by the high order cumulant is as follows: If the higher-order cumulants $c_{kx}(\tau_1, \dots, \tau_{k-1})$ of random sequences $\{x(n), x(n+\tau_1), \dots, x(n+\tau_{k-1})\}$ satisfy [9]:

$$\sum_{\tau_1=-\infty}^{\infty} \dots \sum_{\tau_{k-1}=-\infty}^{\infty} |c_{kx}(\tau_1, \dots, \tau_{k-1})| < \infty \quad (8)$$

Then the k-order spectrum is defined as the k-1 dimensional discrete Fourier transform of the k-order cumulant, that is:

$$S_{kx}(\omega_1, \dots, \omega_{k-1}) = \sum_{\tau_1=-\infty}^{\infty} \dots \sum_{\tau_{k-1}=-\infty}^{\infty} c_{kx}(\tau_1, \dots, \tau_{k-1}) e^{-j(\omega_1 \tau_1 + \dots + \omega_{k-1} \tau_{k-1})} \quad (9)$$

$$|\omega_i| \leq \pi, \quad i=1, \dots, k-1, \quad |\omega_1 + \omega_2 + \dots + \omega_{k-1}| \leq \pi$$

Bispectrum is third order spectrum, defined as:

$$B_x(\omega_1, \omega_2) = \sum_{\tau_1=-\infty}^{\infty} \sum_{\tau_2=-\infty}^{\infty} c_{3x}(\tau_1, \tau_2) e^{-j(\omega_1 \tau_1 + \omega_2 \tau_2)} \quad (10)$$

From the definition of bispectrum, the bispectrum reflects the energy distribution of the signal on the two-dimensional frequency axis. The energy distribution of the bispectrum space in different modulation signals is different, and the information entropy features are also different.

Extraction of radar signal bispectrum information entropy feature algorithm steps are as follows:

Step1 pre-process the received radar signal;

Step2 Find the bispectrum function space of radar signal according to (10);

Step3 subdivide the two frequency axes in the bispectrum function space;

Step4 according to equation (2) to find the signal distribution probability in subspace;

Step5 obtains the information entropy features of the signal spectral function space according to formula (4);

V. SORTING STEPS

Based on the above analysis, the received radar source signal is processed as follows to achieve sorting.

Step1 pre-process the received radar signal;

Step2 separately obtain the information entropy features of the Wigner distribution space of the radar signal, the information entropy features of the bispectrum function space;

Step3 using the extracted characteristic parameters based on KFCM algorithm to achieve sorting;

VI. SIMULATION TEST

A. Simulation Conditions

Eight types of radar source signals are simulated, with conventional modulated radar signal(CW), linear Frequency Modulated Radar Signal (LFM), frequency diversity radar signal (FD), frequency Coded Radar Signal (FSK), binary

phase shift keying signal (BPSK), quadrature phase shift keying signal (QPSK), nonlinear FM radar signals (NLFM) and two-phase encoded hybrid chirp signal (BPSK + LFM) as an example. The frequencies of the frequency diversity radar signals are 10MHz and 50MHz. The frequencies of the frequency-coded radar signals are 20MHz and 40MHz. The other types of radar signals have a carrier frequency of 30MHz. The pulse width of all the signals is 10μs and the sampling frequency is 120MHz. The frequency bandwidth of LFM and NLFM signals are 2MHz and 5MHz respectively. The phase encoding rule of BPSK signal is [1001011001], and the phase encoding rule of QPSK signal is [0123031311]. When the signal-to-noise ratios are 5dB, 10dB, 15dB and 20dB, each type of signal produces 200 samples and 1024 samples for each sample.

B. Experimental Analysis

When the signal-to-noise ratios are 5dB, 10dB, 15dB and 20dB, each type of signal produces 200 samples and 1024 samples for each sample. The information entropy features of the Wigner distribution space and the information entropy features of the bispectrum function space of each type of signal at the corresponding signal-to-noise ratio are respectively obtained respectively, denoted by C_{wv} and C_{sp} respectively. The average and variance of C_{wv} and C_{sp} for each type of signal for each signal-to-noise ratio are averaged and the results are shown in Figure 1 and Figure 2.

1 ~ 8 in the figure are the above-mentioned 8 kinds of signals respectively. As can be seen from Figure 1, the C_{wv} and C_{sp} eigenvalues of Type 2 and Type 8 signals are relatively close at 5 dB signal-to-noise ratio. As can be seen from the detail diagram in the figure, there is a partial overlap between the two types of signals. The other types of signals do not have the two eigenvalues that are close to each other, so combining these two types of features can separate the remaining six types signal. When the signal to noise ratio reaches 20dB, 8 types of signals can be well separated.

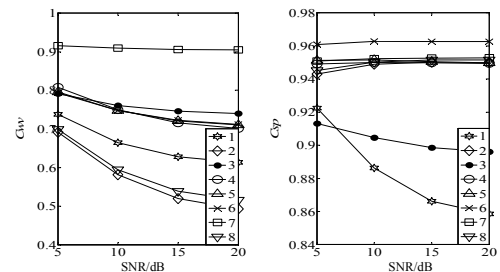


FIGURE I. MEANS OF C_{wv} AND C_{sp} AT DIFFERENT SNR

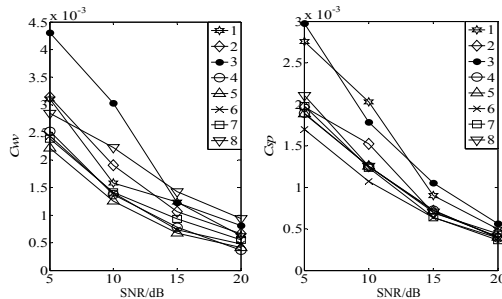


FIGURE II. VARIANCES OF C_{wv} AND C_{sp} AT DIFFERENT SNR

KFCM algorithm is used to sort 8 types of radar source signals. The characteristic parameters used for sorting are C_{wv} and C_{sp} , the initial clustering number $c = 2$, the maximum possible number of categories $c_{max} = 8$, the iteration number T

is set as 100, the stopping condition $\varepsilon \leq 0.00001$, the kernel function is Gaussian radial basis nuclear.

Under different signal-to-noise ratios, each 100 monte-carlo experiments were performed. The average sorting accuracy of 8 types of radar source signals is shown in Table 1. It can be seen from the table that in a wide range of signal-to-noise ratio, the sorting accuracy of C_{wv} and C_{sp} characteristic parameters is very high. When the signal-to-noise ratio reaches 15dB, the accuracy of sorting the signal of 8 types of radar source is 100%. As the SNR decreases, the accuracy of sorting decreases slightly. When SNR is 5dB, the characteristic parameters of LFM radar and BPSK + LFM radar partially overlap, so the accuracy of sorting fails to reach 100%, but the average sorting accuracy is above 98%; The remaining six types of radar source signal does not overlap, sorting accuracy rate of 100%.

TABLE I. SORT RATES OF 8 CLASSES RADARS

SNR	CW	LFM	FD	FSK	BPSK	QPSK	NLFM	BPSK+ LFM	General Sorting Accuracy
5dB	100	94.7	100	100	100	100	100	96.3	98.875
10dB	100	98.6	100	100	100	100	100	99	99.7
15dB	100	100	100	100	100	100	100	100	100
20dB	100	100	100	100	100	100	100	100	100

In this paper, the signal of radar source is preprocessed firstly, the Wigner distribution space and bispectrum space of the signal are obtained, then the subspace is divided, the information entropy characteristics of the signal in these two feature spaces are obtained, Radiation source signal sorting. Through the comparison of simulation experiment and method, this characteristic parameter reflects the good inter-class separation and stability under the condition of wide signal-to-noise ratio, which is of certain reference value.

ACKNOWLEDGEMENT

This work is supported by natural of Hubei province (no.2016CFB288)

REFERENCES

- [1] Wiley R G. ELINT: The Interception and Analysis of Radar Signals [M]. Second Edition, Boston, MA: Artech House, 2006: 317-334.
- [2] NELSON D J . Special purpose correlation functions for Improved signal detection and parameter estimation[C]/ICASSP , 1993 , 4 : 73276.
- [3] Li He-Sheng, Han Yu, Cai Ying-wu. Overview of the crucial technology research for radar signal sorting [J]. Systems Engineering and Electronics,2005,27(12):2035-2040.
- [4] Chen Sheng, Wang Xing, Chu Wei, Zhang Guan-rong. Research on recognition of phased-array radar based on analysis of pulses amplitude [J]. Computer Engineering and Applications, 2012,48(23):120-124.
- [5] Wang Shi-qiang, Zhang Deng-fu. Novel radar signal sorting method with low complexity [J]. Journal of XIDIAN University,2011,38(4):148-153.
- [6] Gee, Wesley A. Radar warning receiver (RWR)time-coincident pulse data extraction and processing[C]. IEEE National Radar Conference – Proceedings, Atlanta, United states.2012: 752-757.
- [7] Ren Ming-qiu, Huo Jin-yan. Radar emitter recognition based on wavelet ridge and FSVM [J]. Chinese Journal of Scientific Instrument, 2010,31(6):1424-1428.
- [8] Chen Tao-wei,Xin Ming. Feature extraction based on wavelet transform for radar emitter signals [J]. Information and Electronic Engineering, 2010 , 8(4) : 436-440.
- [9] ZHANG Gexiang , JIN Weidong , HU Laizhao. Radaremitter signal recognition based on complexity features[J] . Journal of Southwest Jiaotong University(EnglishEdition) , 2004 , 12 (2) : 1162122.
- [10] Shannon C E. A mathematical theory of communications [J]. Bell System Technical Journal, 1948, 27:379-42.
- [11] Havens, Timothy C. Cluster validity for kernel fuzzy clustering[C]. IEEE International Conference on Fuzzy Systems, Brisbane, Australia.2012: 124-127.
- [12] Miyamoto, Sadaaki. Different objective functions in fuzzyc-means algorithms and kernel-based clustering [J]. International Journal of FuzzySystems, 2011,13(2):89-97.

A Spectrum Analysis Algorithm Based on GPU

Kunyuan Xu, Yanhua Jin*, Fangyuan Zhao and Haoran Ma

School of Aeronautics & Astronautics, University Of Electronic Science and Technology Of China, Chengdu, 611731, China

*Corresponding author

Abstract—Considering the requirement of spectrum analysis, the parallel spectrum analysis algorithm is designed for a software radio platform built on the spectrum analyzer, where CPU is the controller and GPU is the baseband processor. The software platform is combined with the GPU processor, making it possible that the data required massive calculation in the RF collector is transferred to the GPU to process, which has the ability of powerful parallel computing. The key part of this paper is the parallel optimization of mixed-radix FFT algorithm and STFT algorithm, in which the data memory and memory allocation are also improved. Results show that the simulation via CUDA programming is superior than CPU processing.

Keywords—GPU spectrum analysis; parallel computing; mixed base FFT;STFT

I. INTRODUCTION

Spectrum analysis is one method that FFT is used to convert the baseband IQ data from the time domain to the frequency domain for correlation operations, requiring a more powerful processor when the data needs real-time processing with higher bandwidth demand.

In 1963, Cooley wrote the first FFT algorithm program. The algorithm uses divide and conquer strategy to make DFT computation from $O(N^2)$ to $O(N \log_2 N)$, in which computational efficiency improved significantly. In addition to the Cultrueki algorithm [1], there are many efficient algorithms, including split-base algorithm, radix-2 FFT algorithm, radix-4 FFT algorithm and hybrid algorithm [2,3].

About the parallel implementation of FFT algorithm, MIT has developed the CPU-based FFT algorithm library FFTW, which has good portability and adaptability. In 2003, Kenneth Moreland and Edward Angel used the GPU's shader compiler to transplant the FFT algorithm to the GPU platform [4]. In 2007, NVIDIA introduced the CUDA parallel development environment and published the CUDA-based FFT library function CUFFT. To a certain extent, its speed has increased when compared with the same period of the CPU FFT [5]. However, it leaves a lot to be desired in the implementation of small-power 2-power FFT. In order to solve this problem, this paper discusses the implementation of the hybrid-based FFT on the GPU. Since the global memory is accessed every time one-dimensional FFT is performed, it can not take full advantage of high storage bandwidth efficiency of GPU [6]. However, the progressive strategy can be used to solve the matching problem between computing power and storage bandwidth effectively [7].

As for non-stationary signals, the STFT algorithm is mainly studied in this paper, which is according to the theory that the sections of windowed signals can be optimized in parallel

computation. It is obvious that GPU has fast speed than CPU [8].

II. GPU SPECTRUM ANALYSIS FRAMEWORK AND COMPUTING FLOW

The applications of spectrum analyzers can make the IQ baseband signal converted from the time domain to the frequency domain, and the use of GPU processing can speed up this procedure. Common spectrum analysis system mainly consists of the underlying hardware, intermediate driver and upper software. As shown in Figure 1, in which the hardware is responsible to original input signal for attenuation / amplification, acquisition, analog / digital conversion, access to time-domain data, and finally the signal is transmitted to the host. The sampled data is transmitted from the host computer to the GPU memory, and the result is transmitted to the binary file after the spectrum analysis operation. These analyzed data contain information such as spectral series and energy spectra. The upper software is responsible for receiving, processing and analyzing the input signal to get the test result. The main content of this paper is the GPU spectrum analysis.

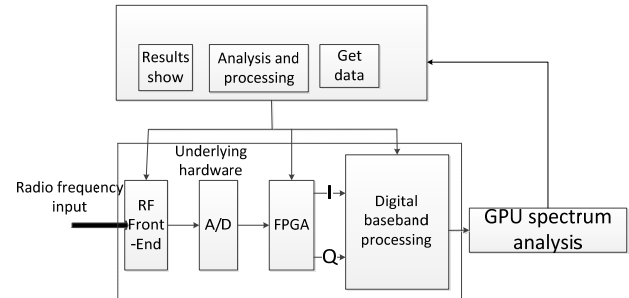


FIGURE I. GPU SPECTRUM ANALYSIS SYSTEM FRAMEWORK

There are five steps in the GPU spectrum analysis operation, looping in the case of constant input from the source signal. Usually, reading and writing global memory data is needed in each step of GPU computing, hence the design of parallel algorithms is introduced to reduce the global memory read and write operation times. The entire operation flow is shown as Figure 2.

The specific steps are as follows:

- (1) The Host side receives and buffers data, and copies data to the Device side memory through the PCI-E bus.
- (2) The format of the data to be transmitted is changed, and the character data passed in on the Device side is converted into floating-point data.

(3) Spectrum analysis algorithm including hybrid-based FFT algorithm and STFT algorithm is carried out on the GPU.

(4) The data is copied from the memory on the Device side to the Host side, and the parallel optimized spectrum is transmitted to the memory on the Host side.

(5) Spectrogram is output to the Host and displayed in the PC.

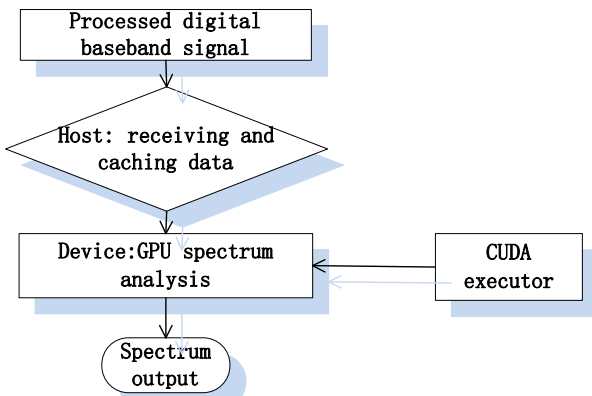


FIGURE II. COMPUTING FLOW CHART

III. MIXED-RADIX FFT PARALLEL ALGORITHM OPTIMIZATION

Spectral analysis of stationary signals based on GPU processor architecture, which is mainly based on the Cooley-Tukey algorithm framework of FFT, focuses on the optimization of mixed-radix FFT algorithms. When FFT operation is performed on one-dimensional signals, it is found that the computational efficiency is too low, and the optimized FFT can greatly improve the computational efficiency [9].

Assume $x(n)$ is a real sequence of $2N$ points, then its one-dimensional DFT calculation is formed as:

$$X(k) = \text{DFT}[x(n)] = \sum_{n=0}^{N-1} x(n)W_N^{nk} \quad k = 0, 1, 2, \dots, N-1 \quad (1)$$

where $W_N^{nk} = e^{-j\pi\frac{nk}{N}}$ ($n = 0, 1, 2, \dots, N-1$) represents the rotation factor and N is the DFT calculated length. The data length N is decomposed into the product of two factors: $N = N_1 \times N_2$, and then the DFT calculation based on the Cooley-Tukey algorithm is obtained as follows:

$$X(k_1, k_2) = \sum_{n_2=0}^{N_2-1} W_{N_2}^{n_2k_2} W_N^{n_2k_1} \sum_{n_1=0}^{N_1-1} x(n_1, n_2) W_{N_1}^{n_1k_1} \begin{cases} 0 \leq k_1 \leq N_1 - 1 \\ 0 \leq k_2 \leq N_2 - 1 \end{cases} \quad (2)$$

The Cooley-Tukey algorithm includes two index transformations and two one-dimensional DFTs, which is divided into the following five steps.

Step1: According to the column direction, N -point length data is stored in a two-dimensional matrix, the size of which is $N_1 * N_2$.

Step2: FFT calculation of each column of data is calculated, which means the N_1 -point one-dimensional FFT is calculated N_2 times (first-level transform).

Step3: Multiply the first-level transform result by the twiddle factor $W_N^{n_2k_1}$.

Step4: Do FFT calculation on each row of data, which means the N_2 -point one-dimensional FFT is calculated N_1 times (second-level transform).

Step5: Transpose the matrix into a matrix of $N_2 * N_1$, and read the data in the direction of the column.

The above formula contains two dimensions of the FFT calculation. In this paper, we use Cooley-Tukey FFT algorithm to realize FFT based on mixed-matrix. The basic theory is to convert long-sequence discrete Fourier transform to short-sequence FFT. After multi-basis decomposition, matrix transform is used to obtain the spectrum. GPU parallel processing architecture can improve efficiency. The 2^m FFT can be implemented by medium -2, medium -4, medium -8, medium -16 and other base combination. In reality, the higher the cardinality is, the less the number of data rearrangement is, and the greater the demand of register is. With the limited resources of register, the higher the cardinality is, the less the parallel threads is, but it also reduces the occupancy rate. Above all, 2^m can be preferentially decomposed into a combination of a base group of -16, -8, -4, and -2 in sequence.

In this parallel algorithm, how to choose the size of N_1 and N_2 should be modest, requiring that it can fully calculate the value of the FFT only using the on-chip shared memory and registers without revisiting the global memory to load onto the GPU when it is read from the global memory. While N_1 or N_2 is too large to be fully integrated into the on-chip memory for computing, the five steps above need executing to decompose each value until it is brought up to the required standard. The flow chart based on mixed-radix FFT algorithm is shown as Figure 3:

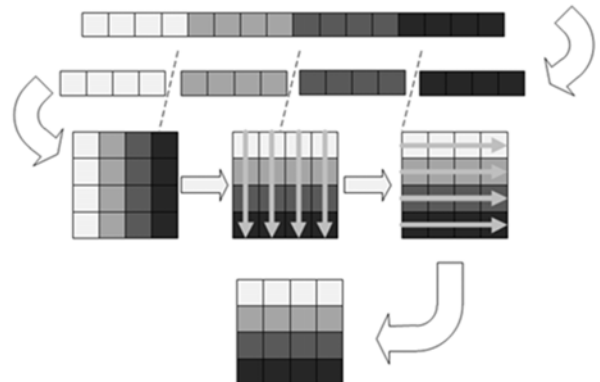


FIGURE III. FFT ALGORITHM FLOW CHART BASED ON HYBRID

Taking $N = 1024$ as an example, firstly, 1024 can be decomposed into 128×8 to make 128 rows of 8-point one-dimensional FFT; Secondly, perform data transposition in shared memory; Thirdly, considering that the 128-point FFT is hard, it can be further broken down into 16×8 . Usually there are many kinds of N decompositions such as 512 which can be also decomposed into $4 \times 16 \times 16$ or $8 \times 8 \times 16$. Different decomposition leads to different efficiency, and the smaller the base is, the greater the amount of computation is, so try to avoid radical decomposition of -2 or -4. As the level of decomposition increase, synchronous operation becomes more complex, therefore, try chose a base as large as possible in the case of meeting the requirements of shared storage. According to the above principle, the optimal decomposition of $N = 256$ is 16×16 instead of $4 \times 8 \times 8$, and the optimal decomposition of $N = 128$ is 16×8 instead of $8 \times 8 \times 2$.

In the CUDA programming model, parallel computing increases the thread to improve computing performance, but reduces the resource utilization and the computational efficiency. Therefore, there is a trade-off between occupancy and resource usage.

(1) Global memory optimization

The largest memory on the GPU is the global memory. Only the global memory can be read and written by both the host and the device, so it is necessary to optimize its access. Global memory efficiency can be increased by consolidating load accesses to data. Each warp can be global memory accessed with 32 or 64 or an integer multiple of 128 bytes. Real hardware access is based on half-warp, which is 16. In Figure 4 below, the thread accesses consecutively aligned 32-byte fields to satisfy the merge push condition. If not satisfied, the system will convert the 1 merge transmission to 16 transmissions, and the difference of their speed is 16 times.

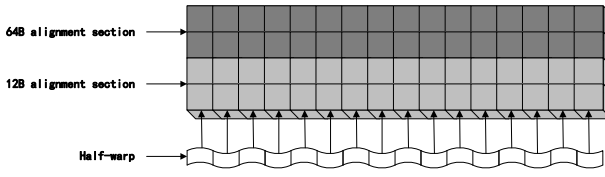


FIGURE IV. 32BIT MERGE ACCESS

According to the above access conditions we know that in order to use the global memory efficiently, the data need processing to be integer times of 32,64,128 bytes as much as possible, and writing into global memory when the amount of data to merge the length of the data.

(2) Shared memory optimization

Shared memory is high-speed memory in the GPU. If two or more threads are accessing the same bank, bank conflict occurs, as shown in Figure 5. This delay in access conflicts grows linearly with the increase of number of threads accessing the same address, which means there are n delays when there are n bank-conflicts. But in shared memory, when all threads in the same half-warp access read the same address, things change again. Because there is a mechanism in its access mechanism called broadcast, when the broadcast delivery conditions are met, the hardware sends the data to all the

required threads at once rather than becoming a multiple serial transfer, as shown in Figure 6.

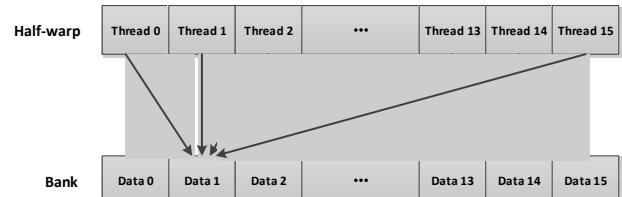


FIGURE V. BANK CONFLICT SHARED MEMORY ACCESS EXAMPLE

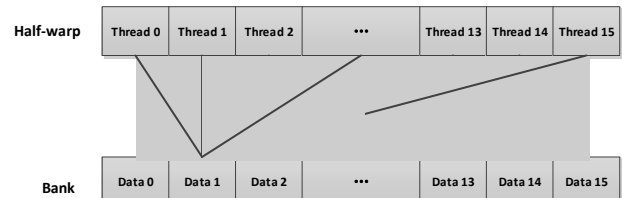


FIGURE VI. SHARED MEMORY BROADCAST MODE EXAMPLE

(3) Parallel optimization of matrix transpose

Matrix transposition is to transform the position of the data in the matrix, and finally did not change the data in the matrix. During the conversion, the position of data is independent, so that you can use different threads parallel computing.

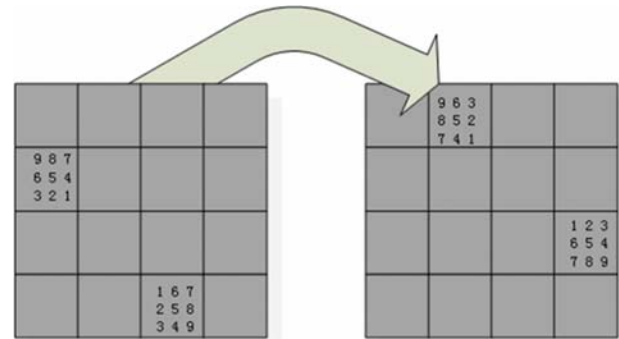


FIGURE VII. ARRAY BLOCK TRANSPOSE

In Figure 7, the original $12 * 12$ matrix is divided into a $4 * 4$ matrix according to $3 * 3$ blocks, so that the combined blocks (1,0), (3,2) transpose corresponds to the block (0,1), (2,3) after transpose. Using this method of merging and dividing, we can map $3 * 3$ blocks to concurrent data operations in different blocks in the GPU, so as to take full advantage of the parallelism of the GPU and speed up the operation of matrix transposition. When the matrix size is larger, the acceleration will be more obvious.

IV. STFT PARALLEL ALGORITHM OPTIMIZATION

The non-stationary signal spectrum analysis is mainly for short-time Fourier transform algorithm-STFT algorithm optimization, because of STFT small amount of computation, real-time, and achievement based on FFT. Analyzing the parallelism of STFT algorithm can be based on CUDA algorithm library CUFFT, not only improving the speed of operation, but also taking advantage of GPU parallelism to improve the operating efficiency.

Joint time-domain spectral analysis puts the traditional one-dimensional signal into two-dimensional time-frequency plane analysis in order to better reflect the variation of the signal frequency with time so as to fully understand the signal time-frequency characteristics and the energy accumulation at a specific time. The basic idea is that based on the traditional Fourier transform, the non-stationary signal is seen as a series of short-term stationary signal superposition.

Based on the basic principle of STFT described above, it can be known that STFT is a function of time moving to meet the condition, and then do FFT segmentally, which can finally analyze the changes of frequency in different time periods more clearly. For segmented FFTs, each piece of data is FFT operation independent of each other, therefore, can be processed in parallel, based on GPU time-frequency analysis.

The following two ways are to analyze the parallelism of STFT:

(1) The use of CUFFT to achieve serial STFT

Figure 8 is a N-point STFT flow chart, each time a single point to do a separate FFT in time, each segment to do in turn.

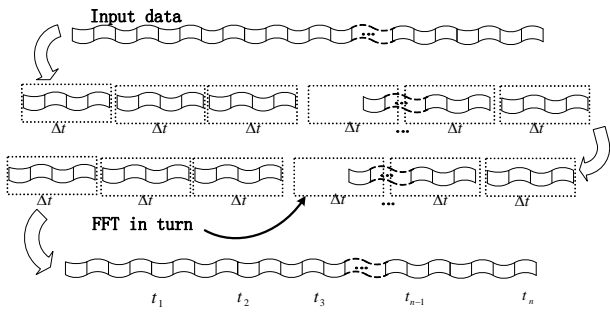


FIGURE VIII. STFT SERIAL

(2) the use of CUFFT parallel STFT

Figure 9 is a flow chart of STFT parallel processing with N points plus four time window functions. By time segmenting and combining into a time-sequential matrix, FFTs are performed on each row to reduce the number of stages one by one.

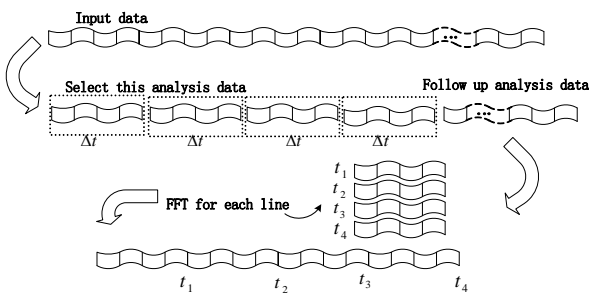


FIGURE IX. STFT PARALLEL

V. SIMULATION RESULTS

In this paper, the experimental hardware configuration: Intel (R) core (i7-7700k) clocked at 4.2GHz CPU, memory 32G, NVIDIA GeForce GTX 1070 GPU.

Hard disk: (KINGSTON SUV400S37240G (240G))
(ST2000DM006-2DM164 (2.0TB))

Software Configuration: Windows 10 64-bit operating system, VS2010 + CUDA7.5 programming environment.

(1) GPU-based parallel algorithm for mixed-radix FFT implementation

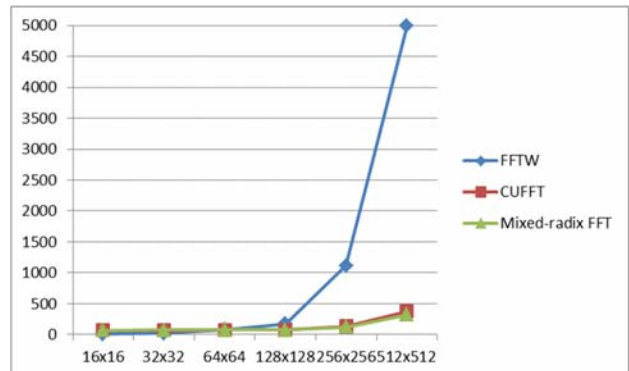


FIGURE X. EFFECT COMPARISON CHART

It can be seen from Figure 10 that GPU-based algorithm does not increase the speed with the small number of points, and the CPU and GPU communication bandwidth is small, resulting in data latency. Compared with the FFT speed on the CPU, the performance improvement on 128x128, 256x256, 512x512 points of the mixed-based FFT can be clearly seen on the GPU FFT algorithm, but the speed of mixed-radix FFT algorithm compared to the CUFFT library is not obvious at 512x512 points which can reach 1.2 times.

(2) parallel implementation of STFT algorithm

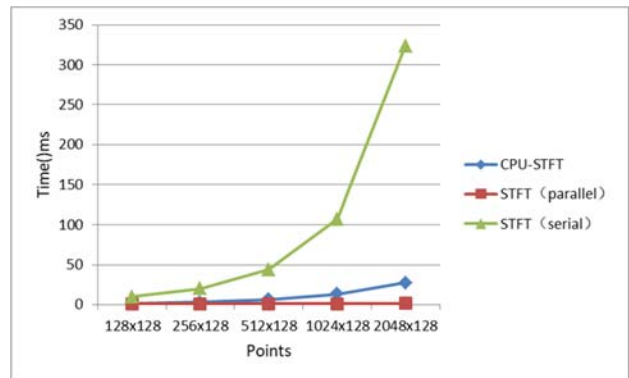


FIGURE XI. CPU-STFT, SERIAL STFT, PARALLEL STFT COMPUTING SPEED COMPARISON CHART

As can be seen from Figure 11, since GPU parallel computing for the point of less data speed calculation of the original operation has not been reflected, if the STFT in the GPU is serial computing, the time will be more when Serial STFT is carried out in the CPU, which did not reflect the advantages of speed.

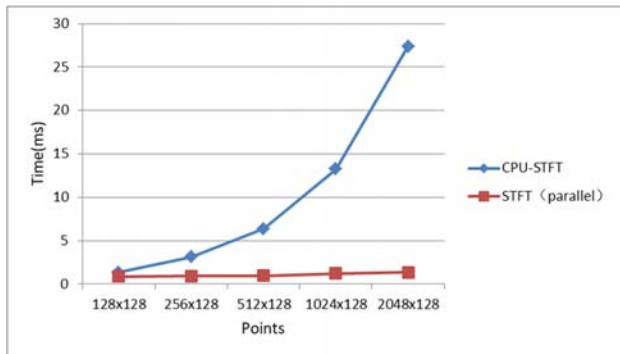


FIGURE XII. CPU-STFT, PARALLEL STFT COMPUTING SPEED COMPARISON CHART

It can be seen in Figure 12 CPU-STFT and parallel STFT images, with the use of parallel computing, the speed advantage quickly reflected in the data points for the 2048x128 when the speed up to 20.6 times, which is an obvious speed advantage.

VI. CONCLUSION

In this paper, according to the demand of spectrum analysis algorithm for spectrum analysis instrument, a parallel processing algorithm suitable for spectrum analysis system is designed based on GPU. The algorithm mainly optimizes the parallel algorithm of the mixed-radix FFT algorithm and the short-time Fourier transform algorithm. Experimentally collected results show that the speedup of the mixed-radix FFT algorithm at 512X512 compared with the FFTW library is 14.5 and the speedup of the parallel STFT algorithm at 2048X128 compared with Serial algorithm is 20.6, illustrating that both the mixed-radix FFT algorithm and the parallel STFT algorithm are advantageous.

REFERENCES

- [1] ZHANG Quan, BAO Hua, RAO Hua, Realization and Application of Two-dimensional Fast Fourier Transform Algorithm Based on GPU[J]. Opto-Electronic Engineering, 2016, 43(02): 69-75.
- [2] SUN Yingxia, LI Yali, NING Yupeng. The principle of spectrum analysis and using skills of spectrum analyzer[J]. Foreign Electronic Measurement Technology, 2014, 33(7):76-80.
- [3] LUO Dongjia, ZHANG Libiao. The research based on FFT spectrum analysis[J]. Practical Electronics, 2015(5):34.)
- [4] Moreland K, Angel E. The FFT on a GPU[C]// Proceedings of the ACM Siggraph/Eurographics Conference on Graphics Hardware, San Diego, California, July 26-27, 2003: 112-119.
- [5] ZHAO Lili, ZHANG Shengbing, ZHANG Meng, et al. High performance FFT computation based on CUDA[J]. Application Research of Computers, 2011, 28(4): 1556-1559.
- [6] HE Tao, ZHU Daiyin. Design and implementation of large-point 1D FFT on GPU[J]. Computer Engineering & Science, 2013, 35(11):34-41
- [7] Naga K Govindaraju, Brandon Lloyd, Yuri Dotsenko, et al. High performance discrete Fourier transforms on graphics processors [C]// Proceedings of the 2008 ACM/IEEE conference on Supercomputing, Austin, Texas, November 15-21, 2008: 1-12.
- [8] PanerasDE, MainR, NawabSH. STFT computation using pruned FFT algorithms[J]. IEEE Trans. On Signal Processing, 1994, 42(1):61- 63.
- [9] YANG Lijuan, ZHANG Baihua, YE Xuzhen. Fast Fourier transform and its applications[J]. Opto-Electronic Engineering, 2004, 31(Suppl): 21-23.
- [10] PING Zhaoqi, LI Yunhuan, ZHANG Liwei. The research of mixed-radix FFT programming algorithm based on two and third[J]. Science &Technology Association Forum, 2013(12):149-150.

Research on Access Control Model Based on User Trust Degree and Resource Life Cycle under Mobile Environment

Xiaoyan Zhang* and Kai Kang

Xi'an University of Science and Technology, China

*Corresponding author

Abstract—Traditional role-based access control models cannot meet the changing requirements of the roles and users under the mobile Internet environment due to their static attributes. To address such issue, this paper proposes an access control model, which is based on the user trust degree and the resource life cycle. From the perspective of subject, the proposed model takes the trust degree's impact factor and the trust degree's fading factor into consideration. From the perspective of object, it takes life cycle of resources into consideration. By using factors given above together, the model accomplishes the function of switching constraints dynamically in the mobile environment. At last, this paper analyzes the main characteristics of the proposed model and other traditional models, the results of analysis show that the proposed access control model has more advantages than other models in the mobile environment.

Keywords—access control model; mobile environment; user trust degree; resource life cycle

I. INTRODUCTION

With the development of mobile networks, mobile applications have become one of the indispensable parts in modern life, which contribute conveniences as well as unsafe elements towards networks. On the one hand, more and more private information is exposed to the mobile networks. On the other hand, the resources available to the mobile networks may be attacked by unauthorized users. Under such circumstances, it is worthy to research the access control model, especially the model working under mobile environment. Traditional RBAC models have acted as a bridge between the subject and the object, which realized mapping users into the fixed roles. In other words, the constraints between subject and object are unchanged. Obviously, it is difficult for the traditional RBAC models to meet the needs of unremitting changes of users and roles under mobile environment.

To solve the above problem, this paper presents an access control model, which is appropriate for mobile Internet environment. The model meets the requirements of mapping users into different roles automatically by adjusting the synthesized users' trust degree and the life cycle of resources under mobile environment.

II. RELATED WORKS

In 1994, the SANDHU's group came up with the principles of access control [1]. In 1996, they proposed the concept called RBAC96 [2]. This model was based on the previous RBAC

model and could be spitted into four nested models with the change of environments. After that, formal definition of access control models was put forward by SANDHU [3]. In 2008, Kulkarni e with other researchers came up with the context-aware role-based access control (CA-RBAC) model [4] basing on the SANDHU' works. CA-RBAC model could activate corresponding sessions and roles if contexts match the constraints.

In recent years, TOAHCHOODEE M [5] proposed the Spatial-temporal Role-based Access Control (STRBAC) model to deal with the access constraints of specific scenarios. In these usage scenarios, roles, space-time positions and access time are all restricted by constraints. The reference [6] devised a workflow-based access control model worked in a specific mobile scenario, and completing the mechanism of access control through a workflow manager. The reference [7] introduced Ebbinghaus's forgetting curve, and further proposed a trust-based access control model working under mobile environment. However, the final conclusion of the reference [7] does not consider the impacts of users' location in time and space as well as their behaviors. The reference [8] put forward another type of access control model, which was based on the evaluation of trust degree. Unlike reference [7], this model calculated the synthesized trust degree by adopting the combination of ANP theory and the super decision-making software. However, the model does not take resources into account. Therefore, the paper overlooked the dynamic change of resources in real mobile networks.

In summary, the existing access control models cannot meet the requirements between the diversified access control conditions under the mobile environment and the resource access control strategies needs to be dynamically and adaptively adjusted. Thus, the study of putting forward a feasible model which is suitable for the mobile environment is urgent.

III. MODEL DESCRIPTION

A. Mechanisms of Altering User Trust Degree

1) Impact factors

Impact factors in access control models refer to the factors that affect the change of user's trust degree under the mobile environment. As shown in Figure I, the impact factors include access time, users' location and user's behaviors.

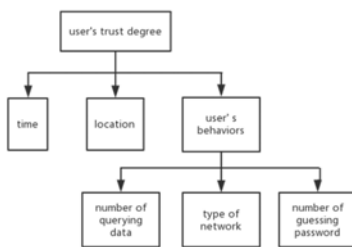


FIGURE I. IMPACT FACTORS OF USER TRUST DEGREE

To handle the time factor, we divided the discrete access time into a set of time periods. The lasting time of period is 2 hours during the daytime, and 4 hours during the nighttime results from the frequency of users' accesses to mobile Internet. In such cases, the time factor can be expressed as $T=\{t_1, t_2, \dots, t_9, t_{10}\}$. What's more, we denoted the user i 's trust degree in period j as $D(u_{i,j})$, the duration of access time as $L(u_{i,j})$, and the duration threshold as S_{t_j} . The calculating formula of $D(u_{i,j})$ is as belows if the time factor works alone.

$$D(u_{i,j}) = \begin{cases} D(u_{i,j-1}) - 1, & L(u_{i,j}) = 0 \\ D(u_{i,j-1}), & 0 < L(u_{i,j}) \leq S_{t_j} \\ D(u_{i,j-1}) + 1, & L(u_{i,j}) > S_{t_j} \end{cases} \quad (1)$$

To handle location factor, we adopted two-dimension coordinate. Within the coordinate, we considered the sites where time period is longer than 2 hours as safe point (SP), and the rest locations called relative point (RP) are calculated as the relative distance from SP to their real coordinates. Furthermore, we

represented user i 's trust degree in location RP_j as $D(u_{i,RP_j})$, the threshold of RP as S_{RP_j} . It means the $D(u_{i,RP_j})$ decrease when RP_j is greater than S_{RP_j} , and the $D(u_{i,RP_j})$ remains unchanged when the RP is within a certain range.

To handle user's behavior factor, we regulated the model from three aspects, including the number of querying data, the types of networks and the number of guessing passwords. The detailed regulations as bellow.

a) When the number of access times within a certain time period less than the threshold, the trust degree presents positive correlation with the number of access times; when the number of access times within a certain time period greater than the threshold, the trust degree presents negative correlation with the number of access times; when the number of the user access times within a certain range in a time period, trust degree remains unchanged.

b) When the network connected to the user is not a frequently used network, the trust degree presents negative correlation with the number of access times with in a certain time period.

c) When the number of guessing password greater than the threshold in a certain time period, the trust degree presents negative with the number of guessing time.

2) Fading factors and synthesized user trust degree

According to the trust theory, the trust degree would gradually reduce as time went on [8]. Let t_i indicates the time interval between the last access and the i -th access. We recalculate the trust degree at the beginning of each time period based on the Table 1., and the calculation formula as in [10] as follow.

TABLE I. COMPARISON OF DIFFERENT ACCESS CONTROL MODELS

Type	Time	Location	User behavior	User Trust degree	Resource Life Cycle	Confidentiality	Integrity	Flexibility
RBAC	✗	✗	✗	✗	✗	✗	✓	low
STRBAC	✓	✓	✗	✗	✗	✓	✓	medium
CA-RBAC	✗	✗	✓	✗	✗	✓	✓	medium
Mobi-CosWAC	✓	✓	✓	✗	✗	✓	✓	medium
DTDAC	✓	✓	✓	✓	✗	✓	✓	medium
reference[7]	✗	✗	✓	✓	✗	✓	✓	medium
Proposed model in this study	✓	✓	✓	✓	✓	✓	✓	medium

$$\alpha(t_i) = \begin{cases} 1 & t = 0 \\ \frac{1}{e^{t_i}} & t \neq 0 \end{cases} \quad (2)$$

The value of $\alpha(t_i)$ keeps reduced with the time increasing, and it will approach zero when t_i increases to a certain value. Therefore, This trend is consistent with the trust theory mentioned previously.

With regard to the synthesized user's trust degree, which is based on the impact factors of user's trust degree and further takes fading factor into account. That is, we calculate the sum of user's trust degree, after that, multiplying the sum by the fading factor $\alpha(t_i)$. The calculation fumula of the synthesized user's trust degree (D_{Syn}) is

$$D_{Syn} = \sum_{i=0}^n \alpha(t_i) = \sum_{i=0}^n \frac{1}{e^{t_i}} \quad (3)$$

B. Mechanisms of Altering Resource Life Cycle

Users can join and leave at any time under the mobile Internet environment, so the network nodes are generally uncertain, the state of the resources are also uncertain in the same way. As shown in Figure II, taking the activity diagram of publishing documents in a certain company as an example. The states of resources at different stages are distinctive. Therefore, the access control model requires to dynamically update the access control strategies for different stages according to the environment in which the object is located.

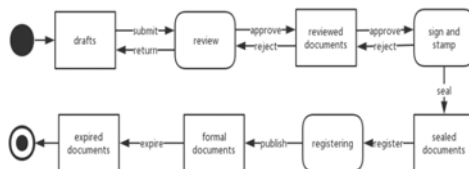


FIGURE II. ACTIVITY DIAGRAM OF PUBLISHING DOCUMENTS IN A COMPANY

C. Description of the Access Control Model

Based on the part C and part D discussed above, this paper proposes an access control model for mobile environment as shown in Figure III. This model is different from the traditional RBAC model due to the model has two modules – user's synthesized trust degree manager and the resource's life cycle manager.

The two modules are not independent of each other, the synthesized user trust degree is the basis of the model, and the life cycle manager work on it. The two together make mobile access control policies more flexible and secure.

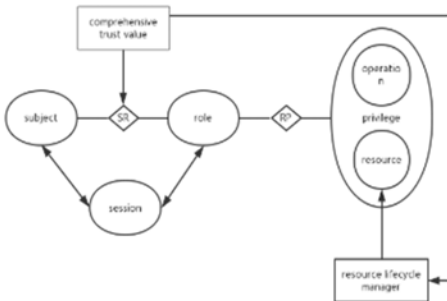


FIGURE III. THE DESCRIPTION OF ACCESS CONTROL MODEL UNDER MOBILE ENVIRONMENT

Specifically, the model uses the following strategy to alter the policies of access control model.

Step1: reading the user set $\{u_1, u_2, \dots, u_n\}$;

Step2: judging the value of $D(u_i)$, if $D(u_i) \geq D$, turn to step3; otherwise, stopping the accessing;

Step3: initializing the policies of access control;

Step4: reading the stage of resource's life cycle;

Step5: judging whether stepping into another stage, if the answer is yes, turn to step6; otherwise, stopping the accessing;

Step6: updating the policies of access control.

The following figure shows the process of updating access control policies.

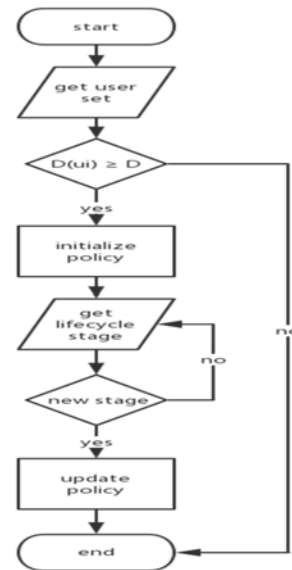


FIGURE IV.FLOWCHART OF DYNAMICALLY UPDATING ACCESS CONTROL POLICIES

IV. MODEL ANALYSIS

In this study, we refined the attributes of the subject and object by considering the synthesized user trust degree and resource life cycle respectively. The RBAC models can control the security of assigning rights, and the proposed model can satisfy the further requirements of the flexibility of the mobile environments.

In the subject aspect, the factors that could influence user trust degree are obtained by combining the user's temporal state, position state and concrete behaviors. Based on this, the trust degree's fading factor is introduced, and a relatively objective synthesized trust degree could be obtained. In the object aspect, the correlation and dynamic of resource's life cycle stage and access control strategy are considered, so that the access control strategy can change with the resource's life cycle, and the access control flexibility and adaptability in a mobile network environment is improved. Table I shows the main characteristics of traditional models and the proposed model.

V. CONCLUSION

In this work, we have proposed an access control model suitable for mobile environment. This model was based on the traditional RBAC model, and further explored the concept of resource life cycle and the synthesized user trust degree. It included the structure of the model, the process of access control and the mechanism of updating policy. Finally, we have compared it with other access control models. The results showed that the proposed model is more suitable for the mobile

network environment. The next work plan is to consider putting forward a more accurate formula for calculating the fading factor as well as the classification of the trust level, so as to further improve the reliability of the model.

VI. ACKNOWLEDGMENT

This research was supported by Industrial Project of Science and Technology Department of Shaanxi Province, the project number is 2014K05-37. Besides it, the research was also supported by Serving Local Project of Education Department of Shaanxi Province, the project number is 14JF016.

REFERENCES

- [1] SANDHUR S, SAMARATI P. Access Control: Principle and Practice[J]. IEEE Communications Magazine, 1994, 32(9): 40-48.
- [2] SANDHU R. Rationale for the RBAC96 Family of Access Control Models[C]. ACM. The First ACM Workshop on Role-based Access Control, November 30-December 1, 1995, Gaithersburg, MD, USA. New York: ACM, 1996: 9.
- [3] R. Sandhu. Role-based access control models. IEEE Computer, February 1996.
- [4] Devdatta Kulkarni, Anand Tripathi. Context-aware role-based access control in pervasive computing systems. In SACMAT'08 Proceedings of the 13th ACM symposium on Access control models and technologies, pp. 113-122, 2008.
- [5] TOAHCHOODEE M, RAY I. On the formalization and analysis of a spatio-temporal role-based access control model[C]. IFIP Wg 11.3 Working Conference on Data and Applications Security. Springer-Verlag, 2008:399-452.
- [6] Shaocan Chen. Research and application of access control of scientific workflow in mobile environment [D]. Fudan University, 2014.
- [7] Jianyu Shao, Fuzhen Chen, Pengyu Qin, Jiujun Cheng. Research on access control method based on dynamic trust degree in mobile Internet environment. [J]. Netinfo Security, 2016(08):46-53.
- [8] Yundong Fan, Xiaoping Wu, Xiong Shi. Research on cloud computing access control model based on trust degree evaluation. [J]. Netinfo Security, 2016(07):71-77.
- [9] Yuyu Bie. Research on trust - based access control technology in cloud computing environment. [D]. China University of Mining and Technology, 2014
- [10] Saizhe Zuo. Trust value Update Model Based on the Memory Theory [J]. The Journey of Southeast University (Natural Science Edition), Nov.2016

A Probe into the Key Parameter Monitor of V2G System on Electric Vehicle Based on Wireless Power Transmission Technology

Wangcheng Zhu*, Zhenchao Xie and Xinshu Wan

Electric Power Research Institute of Hainan Power Grid Co., Ltd., Haikou 570125, Hainan Province, China

*Corresponding author

Abstract—As it is both significant and practical to study how the bidirectional wireless power transmission system can be applied to the monitor control of electric vehicle under V2G environment, this paper analyzes how the bidirectional wireless power transmission system works, based on which, probes into the phase difference θ , which will influence the energy transmission direction, and ratio-voltage σ , which will influence transmission efficiency. It also promotes that coaxial installation of detection coil on secondary side and main power coil can monitor the 2 parameters in real time, and it also provides how to access the parameter. By simulation and experiments, it proved the feasibility of this method, providing a reference research approach on related studies.

Keywords—bidirectional wireless power transmission; V2G; parameter monitor

I. INTRODUCTION

In the traditional power supply and distribution system, power is mainly supplied in the one-way method, that is, terminal equipment consuming energy from beginning to end. As the electrical vehicle can store energy, the Vehicle to Grid technique (hereinafter known as V2G in short) has been given wide attention and research, which changes the traditional one-way power consuming idea. By controlling the power interface of the electric vehicle, the bidirectional interaction and exchange can be achieved between the vehicle itself and the grid. The surplus power can be returned to grid, being part of the energy which can be adjusted and distributed. In this way, the distribution flexibility, reliability, and power utilization can all be improved. Tracing back to the 1990s, some researchers have shown their great interest in the V2G technology. And as early as 1995, Amory Lovins, the chief scientist from the Rocky Mountain Institute (hereinafter short for RMI) has proposed the concept of V2G. Later, Prof. William Kempton from University of Delaware led his team and further promoted this technology [1-5].

Currently V2G technology is still wired, however, if the wireless transmission method can be adopted, the power utilization efficiency can be greatly improved. As the new energy has got higher penetration rate in grid, this technology will no doubt enhance the interactivity between electric vehicle and grid. In addition, as charging piles occupy too much land, the application of wireless power transmission will relieve the land use pressure. Meanwhile, the charging timing of electric

vehicle can be less concentrated by rational planning and scheduling, thus to lessen the shock on the grid causing by charging and discharging of large scale. At the moment, the mathematical modeling and key technology of bidirectional power transmission are both under exploration stage, with some fruit coming out. And the “one-to-one” [6-8] as well as the “one-to-many” [9-11] topological research on bidirectional wireless power transmission technology have been relatively mature. How to control the energy flow direction through the phase difference in the transducer outlet voltage has been verified in an effective way, yet how to apply the wireless power transmission to the V2G system of electric vehicle still has an uphill battle to fight. As the existing technique mainly relies on additional detection and communication system to monitor the primary and secondary outlet voltage, this thesis will analyze the phase difference θ , which will influence the energy transmission direction, and ratio-voltage σ , which will influence transmission efficiency, based on which, it promotes to coaxially install detection coil on secondary side and main power coil, thus to monitor and access the two parameters. By simulation and tests, it proved the feasibility of this method, providing a reference research approach on related studies.

II. THEORETICAL MODELING ANALYSIS

A. Working Principle Analysis on Bidirectional Wireless Power Transmission System

As shown in Figure I, this system can be divided into 2 parts: the primary side and the secondary side, which are a symmetric topology structure. Both the primary and secondary side span a DC source, an H-shape inverter composed of 4 MOSFETs and related controller, resonator and resonance compensation mechanism. By adjusting the MOSFET gate driver signal, the power bidirectional transmission under the topology structure can be achieved. When power is transferred from the primary side to the secondary side, which means, the primary side serving as “the source” while the secondary serving as “the charged”, the primary side H-shape inverter will act as high-frequency inverter, and the secondary H-shape inverter will be the controlled rectifier, and vice versa.

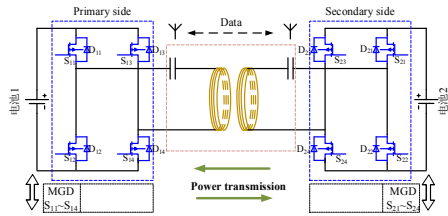


FIGURE I. THE BIDIRECTIONAL WIRELESS POWER TRANSMISSION SYSTEM STRUCTURE

As for the transitional wireless power transmission system, both the series LC fundamental type and the LCL composite type meet the resonant topology requirement, see Figure II about details of the two topology structures. To focus on the BD-WPT system energy transmission control technology, this paper only researches in the LCL composite resonant topology instead of analyzing on two different types of topology.

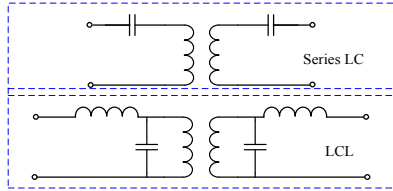


FIGURE II. THE LC AND LCL TOPOLOGY STRUCTURE DIAGRAM

The LCL bidirectional wireless power transmission system main circuit topology is as shown in the Figure III. As the BD-WPT system boasts an equivalent topology structure, we can just take the transmission from primary side to secondary side as an example to analyze its working principle. In the primary side circuit, the dc voltage source V_1 supplies power for BD-WPT system. The LCL resonant circuit is composed of L_m , C_1 and L_p , and the high frequency inverter is composed of MOSFET tube $S_{11}\sim S_{14}$ and anti-parallel diode $D_{11}\sim D_{14}$. In the secondary primary circuit, the controllable rectifier is composed of MOSFET tube $S_{21}\sim S_{24}$ and anti-parallel diode $D_{21}\sim D_{24}$, and the secondary side LCL resonant circuit is composed of L_n , C_2 and L_s , with the battery V_2 as the active load. M serves as the mutual inductance between the coupling coil L_p and L_s .

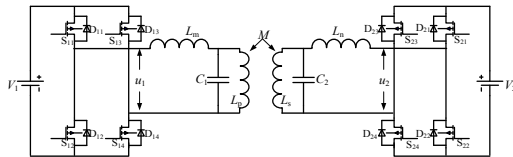


FIGURE III. LCL BIDIRECTIONAL WIRELESS POWER TRANSMISSION SYSTEM MAIN CIRCUIT TOPOLOGY

As for the LCL type BD-WPT system, if the H-shape trigger pulses in the two sides are controlled as shown in Figure IV, the power will be transmitted from the primary side to the secondary side. To be specific, when the control pulses of each MOS tube in the primary side are all 90° ahead of its counterpart in the secondary side, u_1 , the outlet voltage of the H-shape inverter in the primary side, will be 90° ahead of u_2 , the counterpart in the secondary side. Take $u_{gs11,14}$ opening at the moment of $t_0\sim t_1$ as an example, L_n , the current through the secondary series inductance generated by u_1 positive semicircle,

will be 90° lagging behind u_1 , and meanwhile u_2 will be 90° lagging behind u_1 , too. At this moment, if S_{21} and S_{24} in the MOS tube of secondary side are opened simultaneously, the current through L_n will have access to V_2 , which means, supplying power to V_2 , that is, transmitting power from the primary side to secondary side, and vice versa, similarly.

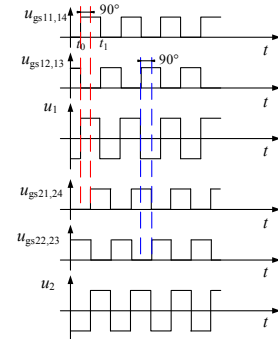


FIGURE IV. THE PULSE CONTROL WAVEFORM DIAGRAM AND OUTLET VOLTAGE WAVEFORM DIAGRAM WHEN POWER BEING TRANSMITTED FROM THE PRIMARY SIDE TO THE SECONDARY SIDE

The analysis above will lead to what is shown in the Figure V, the LCL type BD-WPT equivalent circuit Diagram, of which, L_p , L_s , R_p , and R_s represents the the coupling inductance and its Equivalent Series Resistance (hereinafter short for ESR) in the primary and secondary side correspondingly; C_1 and C_2 the resonant compensation capacitance of the primary and secondary side respectively; L_m , L_n , R_m , and R_n the series filter inductance and ESR of two sides respectively. At the meanwhile, $L_p=L_m=L_1$, $L_s=L_n=L_2$, $R_p=R_m=R_1$, and $R_s=R_n=R_2$, to keep the circular frequency of the inverter switch being consistent with the resonator in the primary side and secondary side, that is, $\omega_0=1/\sqrt{L_1C_1}=1/\sqrt{L_2C_2}$. U_p and U_s represents the fundamental harmonic voltage phasor of the H-shape inverter in the primary and secondary side respectively, assuming U_p as the reference phasor, i.e. $U_p=U_p<0^\circ$, the phase angle of U_s as θ , i.e. $U_s=U_s<\theta$, I as the current phasor, M as the mutual inductance between coil L_p and coil L_s , $M=k\sqrt{L_1L_2}$, of which, k being the coupling factor.

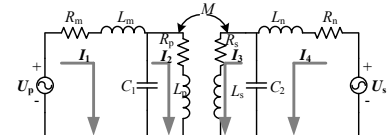


FIGURE V. THE LCL TYPE BD-WPT EQUIVALENT CIRCUIT DIAGRAM

According to the law of KCL, we obtain the voltage equation of LCL-type BD-WPT as:

$$\begin{bmatrix} R_1 & j/\omega C_1 & 0 & 0 \\ j/\omega C_1 & R_1 & j\omega M & 0 \\ 0 & j\omega M & R_2 & j/\omega C_2 \\ 0 & 0 & j/\omega C_2 & R_2 \end{bmatrix} \begin{bmatrix} I_1 \\ I_2 \\ I_3 \\ I_4 \end{bmatrix} = \begin{bmatrix} U_p \\ 0 \\ 0 \\ U_s \end{bmatrix}. \quad (1)$$

Solving equation (1),

$$\begin{aligned} \mathbf{I}_1 &= (a_{lcl}\mathbf{U}_p + j b_{lcl}\mathbf{U}_s)/\lambda_0 \\ \mathbf{I}_4 &= (c_{lcl}\mathbf{U}_s + j b_{lcl}\mathbf{U}_p)/\lambda_0 \end{aligned} \quad (2)$$

In this connection, in LCL-type BD-WPT, the active and reactive power of the primary and secondary side can be expressed as:

$$\begin{aligned} P_p^{lcl} &= \frac{1}{2} \operatorname{Re}[\mathbf{U}_p \mathbf{I}_1^*] = \frac{1}{2} \frac{a_{lcl} U_p^2 - b_{lcl} U_p U_s \sin \theta}{\lambda_0} \\ P_s^{lcl} &= \frac{1}{2} \operatorname{Re}[\mathbf{U}_s \mathbf{I}_4^*] = \frac{1}{2} \frac{c_{lcl} U_s^2 + b_{lcl} U_p U_s \sin \theta}{\lambda_0} \end{aligned} \quad (3a)$$

$$\begin{aligned} Q_p^{lcl} &= \frac{1}{2} \operatorname{Im}[\mathbf{U}_p \mathbf{I}_1^*] = -\frac{1}{2} \frac{b_{lcl} U_p U_s \cos \theta}{\lambda_0} \\ Q_s^{lcl} &= \frac{1}{2} \operatorname{Im}[\mathbf{U}_s \mathbf{I}_4^*] = -\frac{1}{2} \frac{b_{lcl} U_p U_s \cos \theta}{\lambda_0} \end{aligned} \quad (3b)$$

When $\theta=-90^\circ$, the power will transmit from the primary side to the secondary side, and we will obtain a positive efficiency as:

$$\eta_{for}^{lcl} = \frac{|P_s^{lcl}|}{P_p^{lcl}} = \frac{b_{lcl}\sigma - c_{lcl}\sigma^2}{a_{lcl} + b_{lcl}\sigma} \quad (4)$$

When $\theta=90^\circ$, the power will transmit from the secondary side to the primary side, and we will obtain a negative efficiency as:

$$\eta_{inv}^{lcl} = \frac{|P_p^{lcl}|}{P_s^{lcl}} = \frac{b_{lcl}\sigma - a_{lcl}}{c_{lcl}\sigma^2 + b_{lcl}\sigma} \quad (5)$$

In the equation, σ represents the ratio of U_p and U_s , i.e. $\sigma=U_s/U_p$,

and the parameter a_{lcl} , b_{lcl} , c_{lcl} are as shown in the Table I.

TABLE I. BD-WPT TRANSMISSION PARAMETER TABLE OF THE LCL TOPOLOGY STRUCTURE

	LCL-type
λ_0	$\omega_0^6 C_1^2 C_2^2 M^2 R_1 R_2 + \omega_0^4 C_1^2 C_2^2 R_1^2 R_2^2 + \omega_0^2 C_1^2 R_1^2 + \omega_0^2 C_2^2 R_2^2 + 1$
a	$\omega_0^6 C_1^2 C_2^2 M^2 R_2 + \omega_0^4 C_1^2 C_2^2 R_1 R_2^2 + \omega_0^2 C_1^2 R_1$
b	$\omega_0^4 C_1 C_2 M$
c	$\omega_0^6 C_1^2 C_2^2 M^2 R_1 + \omega_0^4 C_1^2 C_2^2 R_1^2 R_2 + \omega_0^2 C_2^2 R_2$

Take the derivative of formula (4) and (5) with respect of σ , we can get the optimal ratio-voltage with LCL compensation structure bi-direction power transmission system under the forward and reverse transmission condition respectively as:

$$\sigma_{for}^{optlcl} = \sqrt{\left(a_{lcl}/b_{lcl}\right)^2 + a_{lcl}/c_{lcl}} - a_{lcl}/b_{lcl} \quad (6)$$

$$\sigma_{inv}^{optlcl} = \sqrt{\left(a_{lcl}/b_{lcl}\right)^2 + a_{lcl}/c_{lcl}} + a_{lcl}/b_{lcl} \quad (7)$$

As analyzed above, the bidirectional wireless power transmission can be achieved by controlling the phase difference of primary and secondary side outlet voltage phasor.

As for BD-WPT system with the LCL compensation structure, the phase difference between the primary and secondary side of outlet voltage phasor is usually set to be -90° or 90° to achieve the forward or reverse direction transmission respectively. In the meantime, the system will boast different optimal ratio-voltage when working under forward or reverse transmission.

B. Key Parameter Monitor of the Bidirectional Wireless Power Transmission System

As for the LCL type BD-WPT system, θ , the phase-angle difference of the H-shape inverter outlet voltage, and σ , the ratio between the voltage of two sides, are both key parameters to measure indicators like the system transmission power and efficiency. In this connection, these parameters need to be monitored during the whole transmission process for the sake of better control.

Figure VI shows the LCL type BD-WPT Equivalent Circuit Diagram after detective coil is introduced, and the parameters in the system is as what we have introduced in the section 2.1. In addition, M_{pb1} and M_{pb2} represent the mutual inductance between the detective coil and the primary and secondary coil.

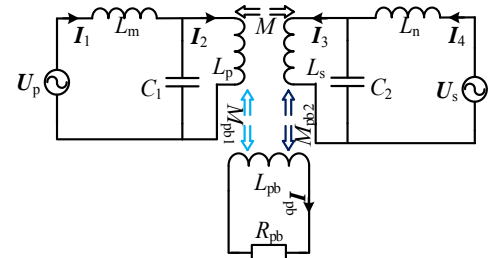


FIGURE VI. THE LCL TYPE BD-WPT EQUIVALENT CIRCUIT DIAGRAM WITH DETECTIVE COIL BEING INTRODUCED

The current equation in the circuit can be obtained based on Figure VI, as shown in Equation (8),

$$\begin{cases} \mathbf{I}_1 = k_1 (\mathbf{k}_1 \mathbf{U}_p + \mathbf{k}_2 \mathbf{U}_s) / Z_{pb} + j M \mathbf{U}_s / (\omega_0 L_1 L_2) \\ \mathbf{I}_4 = k_1 (\mathbf{k}_1 \mathbf{U}_p + \mathbf{k}_2 \mathbf{U}_s) / Z_{pb} + j M \mathbf{U}_p / (\omega_0 L_1 L_2) \\ \mathbf{I}_{pb} = (\mathbf{k}_1 \mathbf{U}_p + \mathbf{k}_2 \mathbf{U}_s) / Z_{pb} \end{cases} \quad (8)$$

of which, $k_1 = \omega_0^2 M_{pb1} C_1$, $k_2 = \omega_0^2 M_{pb2} C_2$, $Z_{pb} = R_{pb} + j \omega_0 L_{pb}$.

And the voltage on the detective resistance R_{pb} can be obtained as shown in Equation (9).

$$U_{pb} = -R_{pb}/|Z_{pb}| \angle -\alpha(k_1 U_p \angle \theta + k_2 U_s \angle 0) \quad (9)$$

In Equation (9), α represents the impedance angle between the detective coil and angle, i.e. $\alpha = \arctan(\omega_0 L_{pb}/R_{pb})$. Considering R_{pb} , Z_{pb} and α are given, we can define $B = k_1 U_p \angle \theta + k_2 U_s \angle 0$ as the proper phasor of U_{pb} , writing it as the form of “amplitude-phase angle”, as shown in Equation (10),

$$B = B \angle \delta \quad (10)$$

of which, amplitude B and the phase angle δ shown in Equation (11)and(12).

$$B = \sqrt{(k_1 U_p \cos(\theta) + k_2 U_s)^2 + (k_1 U_p \sin(\theta))^2} \quad (11)$$

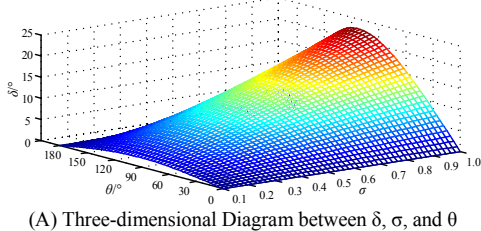
$$\delta = \arctan[k_1 U_p \sin(\theta)/(k_1 U_p \cos(\theta) + k_2 U_s)] \quad (12)$$

As we have assumed to install the detective coil and the secondary coil coaxially, we'd like to further assume that U_s , the outlet voltage in the secondary side inverter is given, in this way we can evolve the Equation (11) and (12) to (13) and (14), of which, $k_3 = k_1/k_2$, and the key parameters will be monitored based on Equation (13) and (14).

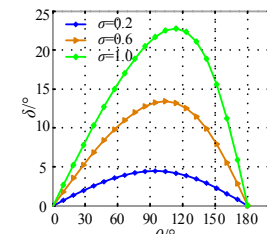
$$B' = B/(k_2 U_s) = \sqrt{(k_3 \sigma \cos(\theta) + 1)^2 + (k_3 \sigma \sin(\theta))^2} \quad (13)$$

$$\delta = \arctan[k_3 \sigma \sin \theta / (k_3 \sigma \cos \theta + 1)] \quad (14)$$

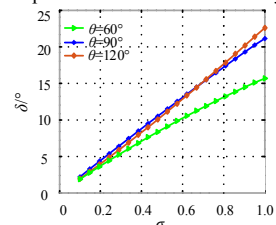
Figure VII shows the relations between δ and σ as well as θ , and Figure (A) is their three-dimensional diagram. For the convenience of analysis, we have given the relation curve between δ and σ under the typical θ value, as well as the relation curve between δ and θ under the typical σ value, shown in Figure VII (B) and (C). From (B), we can see that, when θ is some determined value, δ and σ keep a monotonic relation, that is, with the diminishing of the value σ , δ decreases too. And from (C), we can see that no matter what value σ is, there is always a θ that makes a maximum δ , which magnifies with the increasing of σ , deviating more from the 90° angle.



(A) Three-dimensional Diagram between δ , σ , and θ



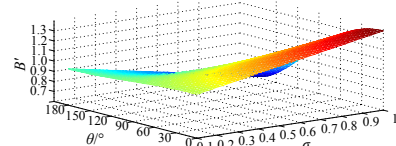
(B) Relationship between δ and σ under the typical θ value



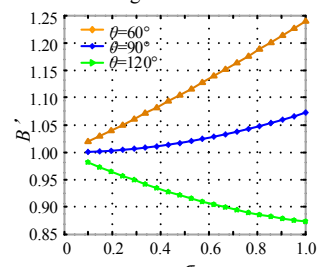
(C) Relationship between δ and θ under the typical σ value

FIGURE VII. THREE-DIMENSIONAL DIAGRAM BETWEEN Δ AND Σ AS WELL AS Θ AND THE RELATION CURVE UNDER TYPICAL VALUES

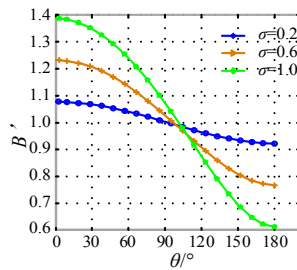
In addition, Figure VIII shows a set of typical relation curves between B' and σ as well as θ , and Figure (A) is their three-dimensional diagram. For the convenience of analysis, we have given the relation curve between B' and σ under the typical θ value, as well as the relation curve between B' and θ under the typical σ value, shown in Figure VIII (B) and (C). From (B), we can see that, the relationship between σ and B' will be affected and restricted by θ . with some θ values, B' decreases with the diminishing of σ , while under some other θ values, B' increases with the diminishing of σ . And from (C), we can see that B' decreases with the raising of θ . Therefore, the value of θ and σ can be uniquely indicated under a precise moment of B' and δ value. That is to say, the detected B' and δ value can be used to monitor the value of θ and σ in real time, so as to keep the system efficiently working.



(A) Three-dimensional Diagram between B' and σ as well as θ



(B) the Relation Curve between B' and σ under the typical θ value



(C) the Relation Curve between B' and θ under the typical σ value

FIGURE VIII. THREE-DIMENSIONAL DIAGRAM BETWEEN B' AND Σ AS WELL AS θ AND THE RELATION CURVE UNDER TYPICAL VALUES

III. SIMULATION AND EXPERIMENT VERIFICATION

Above we have analyzed the feasibility of how to use detective coil to monitor θ and σ in theory, and what follows in the passage will be a related experiment, which will further prove and verify the accuracy of the designed results. We have established a simulation platform based on Matlab/Simulink, and the related hardware platform is designed as shown in Figure IX. See the system parameter allocation in TABLE II.

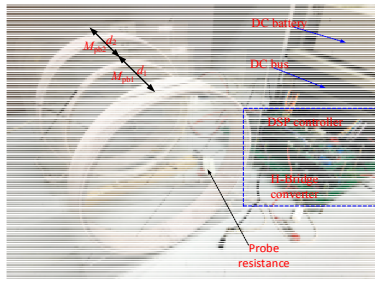


FIGURE IX. ARRANGEMENT PLAN OF THE DETECTIVE COIL

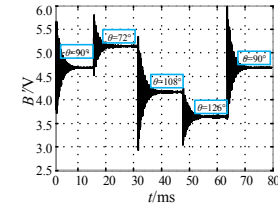
TABLE II. 2 SYSTEM PARAMETER ALLOCATION

Parameter	Values
L_1	$39\mu\text{H}$
L_2	$69\mu\text{H}$
L_{pb}	$1.9\mu\text{H}$
R_{pb}	200Ω
M_{12}	$4.8\mu\text{H}$
M_{pb1}	$0.65\mu\text{H}$
M_{pb2}	$0.94\mu\text{H}$
k_3	0.3866

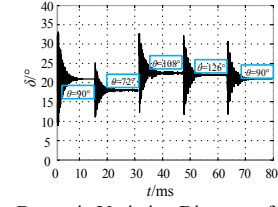
A. Analysis of Phase Angle Monitoring Results of Primary Side Power Supply U_p

Let's assume the battery is being charged when the system functions well, that is to say, power is transmitted from the primary side to secondary side, i.e. the phase position of U_p is $0 \sim 180^\circ$ ahead of U_s . In order to prove that the method proposed in this thesis is both correct and feasible to monitor θ in real time, U_p is being changed from time to time, so as to observe the U_{pb} changes (the amplitude), and the result is shown in Figure X. (A) shows the voltage amplitude changes in both sides of the detective resistance; (B) shows the voltage phase

angle changes. When the system functions well under $\theta=90^\circ$, if $t=16\text{ms}$, θ will vary to be 72° , and both amplitude and phase angle will rise to be a new steady value after a fleeting 5ms of oscillation. And similarly, if $t=16\text{ms}$, θ varies to be 108° , and oscillation will last about 7ms; when $t=48\text{ms}$, θ varies to be 126° ; and $t=64\text{ms}$, θ varies to be 90° again, both amplitude and phase angle can go after the change in a prompt manner. These data fully prove that the detective device can follow the θ changes in a timely and dynamic way.



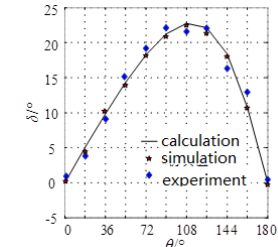
(A) The Dynamic Variation Diagram of δ with θ



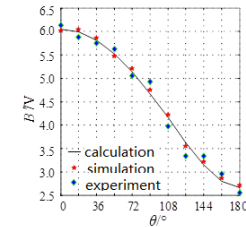
(B) The Dynamic Variation Diagram of B' with θ

FIGURE X. THE DYNAMIC VARIATION DIAGRAM OF Δ AND B' WITH Θ

Furthermore, when θ changes from 0° to 180° consecutively, the changing curve of the voltage amplitude and phase angel is as shown in Diagram 11. Results derived from simulation and experiments match the calculation basically. That means, even when θ varies in a larger range, the detective coil can do an accurate monitor.



(A) the Changing Curve of δ with θ



(B) the Changing Curve of B' with θ

FIGURE XI. THE CHANGING CURVE OF Δ AND B' WITH Θ

B. Analysis of the Amplitude Monitoring Results of the Primary Side Power Supply U_p

Similarly, Figure XII can prove that the method proposed in this thesis is both correct and feasible to monitor σ in real time.(A) shows the dynamic change of voltage amplitude of the detective resistance; (B) shows the dynamic change on the voltage phase angle. When the system functions well under $\sigma=1$, if $t=20ms$, σ will vary to be 0.75, and both amplitude and phase angle will rise to be a new steady value after a fleeting moment of oscillation. And similarly, if $t=40ms$, σ varies to be 0.25, and $t=60ms$, σ varies to be 0.5; and $t=80ms$, σ varies to be 1. we can see from the dynamic diagram, both amplitude and phase angle can go after the change in a prompt manner. These data fully prove that the detective device can follow the θ changes in a timely and dynamic way.

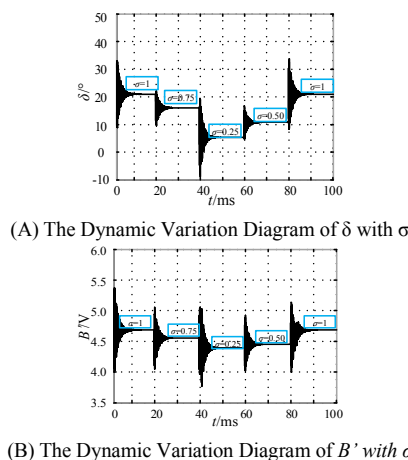


FIGURE XII. THE DYNAMIC VARIATION DIAGRAM OF Δ AND B' WITH Σ

Furthermore, when σ changes from 0.2 to 1 consecutively, the changing curve of the voltage amplitude and phase angel is as shown in Diagram 13. Results derived from simulation and experiments match the calculation basically. That means, even when σ varies in a larger range, the detective coil can do an accurate monitor. And it provides enough evidence that σ can be monitored by using the voltage amplitude and phase angel of detective resistance.

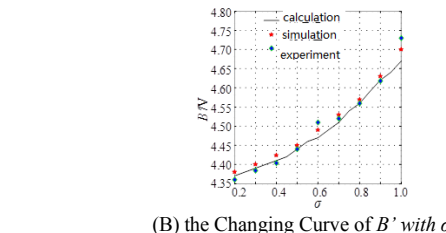
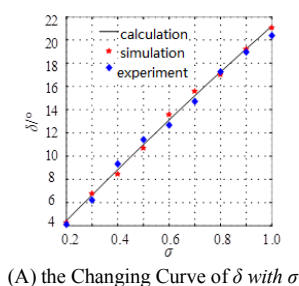


FIGURE XIII. THE CHANGING CURVE OF Δ AND B' WITH Θ

IV. CONCLUSION

By analyzing the phase difference θ , which will influence the energy transmission direction, and ratio-voltage σ , which will influence transmission efficiency, this paper verifies that, the bidirectional wireless power transmission can be achieved by controlling the phase difference of primary and secondary side outlet voltage phasor. In the meantime, the system will boast different optimal ratio-voltage when working under forward or reverse transmission. Based on the conclusion, it promotes that coaxial installation of detection coil on secondary side and main power coil can monitor the 2 parameters in real time. It not only provides how to access the parameter, but proves the feasibility by simulation and experiments, providing a reference research on how to apply the bidirectional power transmission system to V2G monitor control, on optimizing the control strategy of bidirectional wireless feeding system, and on the rational load allocation.

ACKNOWLEDGEMENT

This research is supported by China Southern Power Grid Corporation (Research and Application of Key Technologies of Intelligent Cloud Service in Hainan Power Grid).

REFERENCES

- [1] LIU Xiaofei, ZHANG Qianfan, CUI Shuhai. Review of electric vehicle V2G technology. *Transactions of China Electrotechnical Society*, 2012, 27(2): 121-127.
- [2] Kempton W, Tomić J. Vehicle-to-grid power fundamentals: Calculating capacity and net revenue. *Journal of Power Sources*, 2005, 144(1): 268-279.
- [3] Kempton W, Tomić J. Vehicle-to-grid power implementation: From stabilizing the grid to supporting large-scale renewable energy. *Journal of Power Sources*, 2005, 144(1): 280-294.
- [4] Madawala U K, Schweizer P, Haerri V V. "Living and mo-bility"- a novel multipurpose in-house grid interface with plug in hybrid BlueAngle// IEEE International Conference on Sustainable Energy Technologies. 2008: 531 - 536.
- [5] Iga Y, Omori H, Morizane T, et al. New IPT-wireless EV charger using single-ended quasi-resonant converter with power factor correction// International Conference on Renewable Energy Research and Applications. 2012: 1-6.
- [6] Madawala U K, Thrimawithana D J. A Bidirectional Inductive Power Interface for Electric Vehicles in V2G Systems. *IEEE Transactions on Industrial Electronics*, 2011, 58(10): 4789-4796.
- [7] Voglitsis D, Tsengenes G, Bauer P. Inductive power transfer system with improved characteristics// Transportation Electrification Conference and Expo. IEEE, 2014: 1-8.
- [8] LI Yanling, SUN Yue, DAI Xin, et al. Modeling and control of an LCL bi-directional inductive power transfer system. *Journal of Chongqing University*: 2012, 35(10): 117-123.

- [9] Swain A K, Devarakonda S, Madawala U K. Modeling, Sensitivity Analysis, and Controller Synthesis of Multipickup Bidirectional Inductive Power Transfer Systems. *IEEE Transactions on Industrial Informatics*, 2014, 10(2): 1372-1380.
- [10] Swain A K, Devarakonda S, Madawala U K. Modelling of multi-pick-up bi-directional Inductive Power Transfer systems// IEEE Third International Conference on Sustainable Energy Technologies. IEEE, 2012: 30-35.
- [11] Thrimawithana D J, Madawala U K, Neath M. A P&Q based synchronization technique for Bi-directional IPT pick-ups// IEEE Ninth International Conference on Power Electronics and Drive Systems. IEEE, 2011: 40-45.

An Air Bearing Facility for Antenna Pointing Mechanism

Guoyong Yang^{1,2,*}, Hongguang Wang¹, Lie Ling¹ and Feng Gao³

¹Shenyang Institute of Automation Chinese Academy of Sciences, Shenyang 110016, China

²University of Chinese Academy of Sciences, Beijing 100049, China

³Beijing Institute of Control Engineering, Beijing 100080, China

*Corresponding author

Abstract—An air bearing facility is built to test the antenna pointing mechanism of track and data relay satellite. A hierarchical and simultaneous gravity unloading method is proposed to unload the gravity on the ground. The air bearing facility is a two layers structure. Planar air bearings and air spindle are used to unload the gravity of antenna pointing mechanism. An artificial load is designed to replace the antenna. Two joints of antenna pointing mechanism can rotate separately or together freely without the influence of gravity on the ground. The artificial load not only matches the mass, moment of inertial and basic frequency of the antenna, but also solves the coupling problem of moment of both axes. The air bearing facility is designed and established based on the proposed method and analysis. The effectiveness of this facility is proved with the simulation and the experiments and test results.

Keywords—air bearing facility; planar air bearing; air spindle; unload gravity; antenna pointing mechanism

I INTRODUCTION

Air bearing simulator is designed to simulate the micro-gravity environment on the ground. It is used to test the performance of aircraft [1, 2]. Traditional air bearing simulators can unload the gravity of whole aircraft such as a satellite. The control, rotation or formation flight performance can be tested on the simulator [3, 4]. Traditional simulator can also unload the gravity of each link of robot arm. MIT has built several 3-DOF (degree of freedom) air bearing simulators to test the control method of small satellites formation flight [5-7]. Those simulators can move on the horizontal plane and rotate around the vertical axis. German company EDAS Astrium also develops 5-DOF air bearing simulator to verify software and software-hardware test for multi-purpose satellites [8]. Beijing Institute of Control Engineering designs a single-axis kinematic simulator for antenna pointing mechanism [9, 10]. Satellite technology institute of Harbin Institute of Technology develops a 5-DOF air bearing simulator [2, 11]. Stanford Aerospace Lab has built an air bearing simulator for a two-link arm [12, 13], which can only unload gravity while floating on horizontal plane. This simulator uses a planar air bearing to unload the gravity on the end of the arm. Because of the mechanical structure, all the above simulators can either unload the gravity of whole aircraft or unload the gravity of parallel joints.

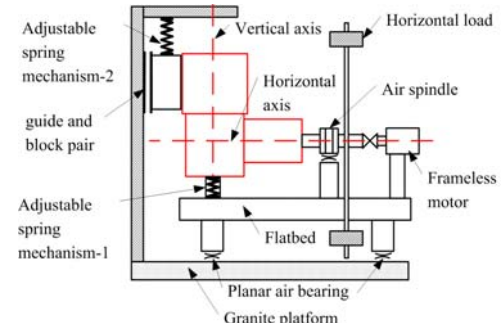
The objects can only float on the horizontal plane or rotate around vertical joint.

Tracking and data relay satellites (TSRD) can provide data relaying, continuous tracking and orbit monitoring services [14] between spacecraft (in low and medium orbit), spacecraft and ground stations [14]. Two large antennas are mounted on the TDRS to capture target vehicle [15]. The antenna is driven by the antenna pointing mechanism (APM), so the performance of the APM is a key part of the performance of the whole satellite. The APM consists of two joints which are orthogonal and traditional simulator cannot unload its gravity, then a new facility is needed to test the performance of the APM while the load is mounted [16].

II HIERARCHICAL AND SIMULTANEOUS GRAVITY UNLOADING METHOD

The APM consists of two orthogonal joints. The APM can be divided into three parts: vertical joint stator, vertical joint rotor and horizontal joint stator, horizontal joint rotor. Vertical joint stator is mounted on the satellite while the antenna is mounted on the horizontal joint rotor. Vertical joint rotor and horizontal joint stator is one piece. The goal is to unload the influence of gravity on two joint.

The facility should offer two rotational DOF. Planar air bearing, spherical air bearing and air spindle are used to unload gravity. Planar air bearing and air spindle are used to build the facility (shown in Figure I) based on the analysis of APM structure and characteristics of three kinds of air bearings. Planar air bearing is used to unload the gravity of vertical joint, while air spindle is used to unload the gravity of horizontal joint.



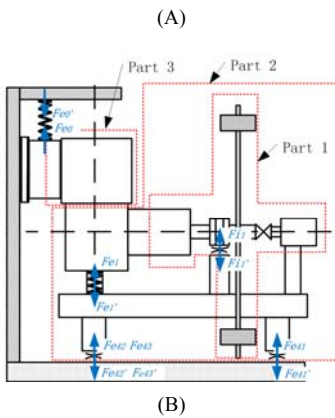


FIGURE I. SCHEME OF GRAVITY UNLOADING METHOD

Hierarchical and simultaneous gravity unloading method means that the air bearing facility is a two-layer structure (air spindle is used to unload the gravity of horizontal joint on the upper layer, planar air bearing is used to unload the gravity of vertical joint on the lower layer) and unload the gravity while both axes rotate one after another or together. This configuration uncouples two joints during the gravity unloading, thus the APM can rotate two joints freely without the influence of gravity. As shown in the figure, the main frame is mounted on the granite platform, vertical joint stator of APM is mounted on the main frame by the guide and block pair. Adjustable spring mechanism-2 is used to hold the position of APM vertical joint stator. Artificial load (to replace the antenna) is fixed onto the horizontal joint rotor through the air spindle rotor. Air spindle stator is fixed on the support flatbed. A frameless motor is equipped to simulate the influence of signal cable of antenna. Rotor of frameless motor is fixed coaxially with the rotor of air spindle. Stator of frameless motor and stator of air spindle are mounted on the support flatbed. Adjustable spring mechanism-1 is mounted between the support flatbed and vertical joint rotor of APM. Three planar air bearings are mounted under the support flatbed. Those air bearings can float on the granite platform.

Figure I (B) shows the hierarchical and simultaneous gravity unloading method. Firstly, the air spindle unloads the gravity of part 1. Horizontal joint rotor of APM, air spindle rotor, horizontal load and frameless motor rotor are fixed coaxially. The gravity center of part 1 coincides with the center of air spindle. The gap between the rotor and stator of air spindle is full of high-pressure air when the facility is working. So there is only viscous resistance while the horizontal joint of APM is rotating, just as rotates in space. Secondly, the gravity of vertical joint rotor of APM is unloaded by the adjustable spring mechanism-1 and planar air bearings. The adjustable spring mechanism-1 unloads the gravity of vertical joint rotor of APM precisely by adjusting the force of spring. The adjustable spring mechanism-1 can be fixed on the support flatbed stably because the contact area between the adjustable spring mechanism-1 and vertical joint rotor is a square plane. Three planar air bearings are placed as a triangle to support part 2 and offer the rotational DOF for vertical joint. There will be establish and disappear process

during the initiate and power off of the air bearing facility, so the APM may move vertically in a small range during those two steps. Guide and block pair and adjustable spring mechanism-2 are applied to free the vertical movement and hold the APM at the same time.

III HORIZONTAL LOAD DESIGN

A payload is necessary to test the performance of APM, but the actual antenna is unavailable. An artificial payload is designed to simulate the moment of inertia and frequency. The constraints are as follow taken the capacity of the granite platform, rotation angle of two joint and the mass of artificial payload into consideration:

$$\left\{ \begin{array}{l} J_{\min} \leq J_h \leq J_{\max} \\ J_{\min} \leq J_v \leq J_{\max} \\ freq_{\min} \leq freq \leq freq_{\max} \\ s.t. \quad \theta_h \geq \theta_1 \\ \quad \theta_v \geq \theta_2 \\ \sum_H m_i \leq m_{\max H} \\ \sum_V m_i \leq m_{\max V} \end{array} \right. \quad (1)$$

$$\sum_H m_i \quad \sum_V m_i$$

Where, $\sum_H m_i$ and $\sum_V m_i$ are payload mass of horizontal and vertical joint respectively. θ_h and θ_v are angle range of horizontal and vertical joint. J_h and J_v are moment of inertia of horizontal and vertical joint respectively. Moment of inertia is the function of mass distribution, $J_h = \int_h \Delta m_i r_i^2$, $J_v = \int_v \Delta m_i r_i^2$. $freq$ is the basic model of horizontal load. Hierarchical analysis method is applied to design the artificial load because there is not a structure with parameters to be optimized.

The configuration of horizontal load is analyzed firstly. The load should be either dumbbell or triangular star with the constraint of rotational angle range, as shown in the figure.

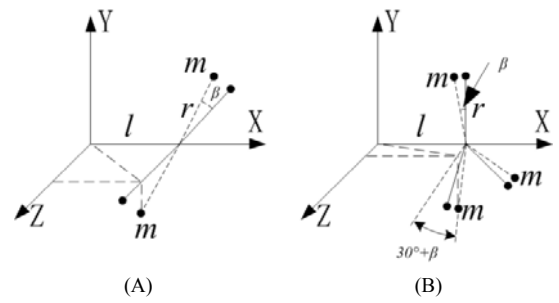


FIGURE II. STRUCTURE OF HORIZONTAL LOAD

In Figure II (A), the moment of inertia around vertical axis is:

$$J_{ya} = 2 \times m \left(\sqrt{(r \cos \beta)^2 + l^2} \right)^2 = 2ml^2 + 2mr^2 \cos^2 \beta \quad (2)$$

The moment of inertia changes with the angle of horizontal joint. In Figure II (B), the moment of inertia around vertical axis is:

$$J_{yb} = m \left(\sqrt{(r \cdot \sin \beta)^2 + l^2} \right)^2 + m \left(\sqrt{(r \cdot \cos(30^\circ + \beta))^2 + l^2} \right)^2 + m \left(\sqrt{(r \cdot \cos(30^\circ - \beta))^2 + l^2} \right)^2 = 3ml^2 + \frac{3}{2}mr^2 \quad (3)$$

The moment of inertia remains constant while horizontal joint is rotating. So the horizontal load is designed with the triangular star configuration which uncouples the moment of inertia of two joint.

Then the horizontal load should satisfy the requirement of frequency. The free vibration differential equation of n-DOF structure is:

$$[M]\{X\} + [K]\{X\} = \{0\} \quad (4)$$

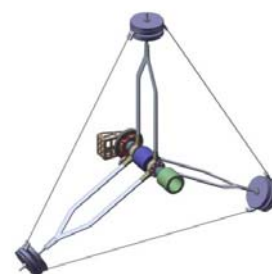
Where, $[M]$ is the n rank mass matrix of structure. $[K]$ is the n rank stiffness matrix. $\{X\}$ and $\{\dot{X}\}$ are the acceleration and displacement in the reference coordinate. The following equation is got after derivation:

$$\det(-\omega^2 [M] + [K]) = 0 \quad (5)$$

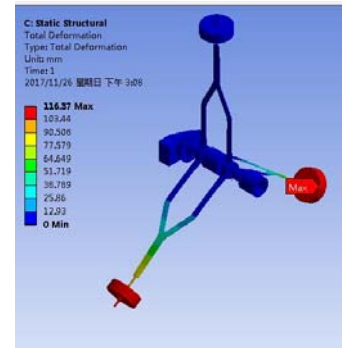
Natural frequencies are calculated: $\omega_1, \omega_2, \dots, \omega_n$. Each frequency is a function of stiffness matrix and mass matrix. So the mass and stiffness are adjusted after the initial design and frequencies calculation, then the frequencies are calculated again. Repeat this process until the basic frequency of final structure satisfies the requirement. The deformation and stress concentration are reduced after final optimization. The final design is shown in the following:



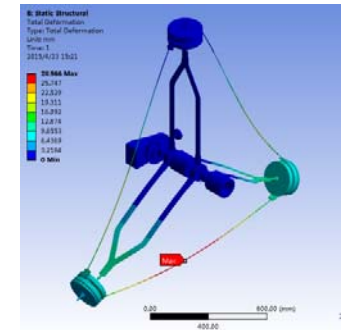
(A) STRUCTURE 1



(B) STRUCTURE 2



(C) DEFORMATION OF STRUCTURE 1



(D) DEFORMATION OF STRUCTURE 2

FIGURE III. HORIZONTAL LOAD

IV AIR BEARING FACILITY TEST

The air bearing facility is designed and established based on the analysis, shown in Figure IV.

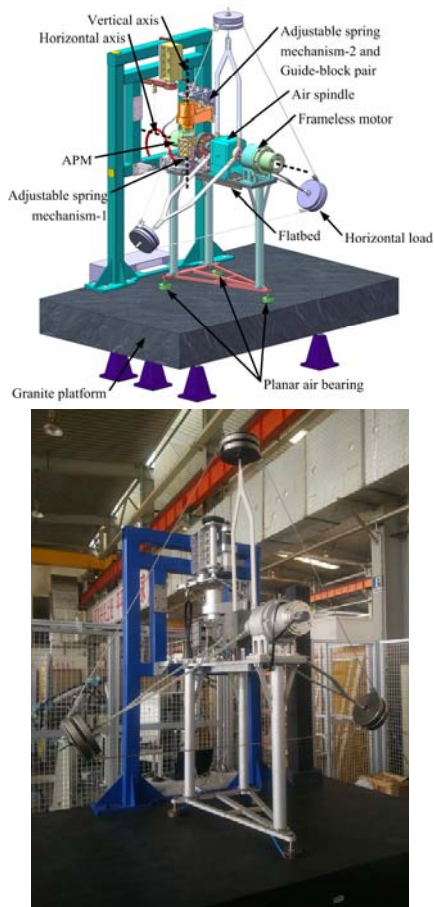
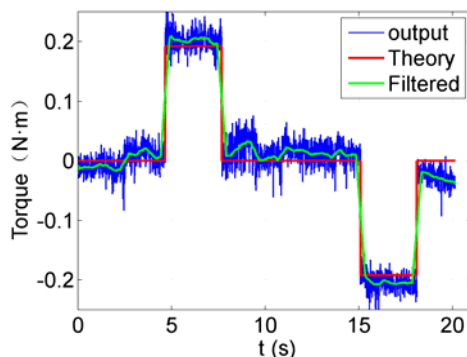
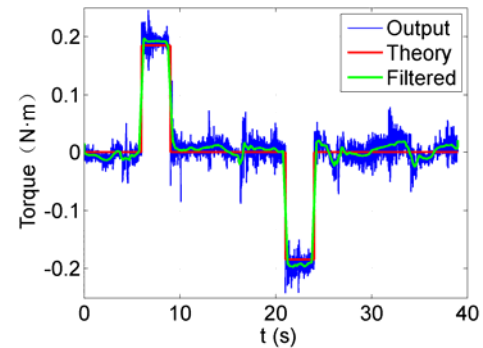


FIGURE IV. AIR BEARING FACILITY

Gravity unloading precision is tested on the facility. The precision is calculated with the output of torque sensor on the facility and theory calculation. After the initiate of the facility, both joint rotate with the process of Static-Acceleration-Uniform-Deceleration-Static. Acceleration is $\pm 0.1^\circ/\text{s}^2$



(A) TORQUE OF VERTICAL JOINT



(B) TORQUE OF HORIZONTAL JOINT

FIGURE V. TORQUE OF SENSOR AND THEORY CALCULATION

There are deviations between sensor output curve and theory calculation especially during the acceleration and deceleration. Compare the filtered curve and theory curve, the precision of gravity unloading is 90%. The precision reduce is caused by the tolerance of manufacture, assembly, viscous resistance, etc. which are inevitable.

V SUMMARY

A hierarchical and simultaneous gravity unloading method is proposed based on the analysis of antenna pointing mechanism. This method can unload the gravity of two orthogonal joint with air spindle and planar air bearings. The artificial load is designed and satisfies the constraints of moment of inertia and basic frequency. The artificial load also uncouples the moment of two joint. An air bearing facility is designed and established based on the method and analysis of load. The test results show that the precision of gravity unloading is 90%.

ACKNOWLEDGEMENT

This research was supported by the State Key Laboratory of Robotics.

REFERENCES

- [1] XU Jian, YANG Qingjun, BAO Gang, et al. Research on lateral Disturbance Force of the 5-DOF Air-bearing Spacecraft Simulator. *Journal of Astronautics*, 2009. 30(5):p.1823-1828
- [2] XU Jian. Prototype Development and Research on Key Thchnology of the Five Degrees of Freedom Air bearing Spacecraft Simulator. Harbin Instuite of Technology.
- [3] LI Jisu, Mu Xiaogang, ZHANG Jinjiang. Physical Simulation for Satellite Control System. *Aerospace Contorl*, 2004. 22(2): p. 37-41, 45.
- [4] Schwartz, J.L., M.A. PeckC.D. Hall, Historical review of air-bearing spacecraft simulators. *Journal of Guidance, Control, and Dynamics*, 2003. 26(4): p. 513-522.
- [5] Chung, S.-J., Nonlinear control and synchronization of multiple Lagrangian systems with application to tethered formation flight spacecraft. 2007, Massachusetts Institute of Technology.
- [6] Chung, S.-J., et al. Multidisciplinary control of a sparse interferometric array satellite test-bed. in Proc. AIAA Guidance, Navigation and Control Conf. 2003.
- [7] Saenz-Otero,A.,et al. SPHERES: Development of an ISS laboratory for formation flight and docking research. in IEEE Aerospace Conference. 2002.

- [8] ZHANG Shijie, CAO Xibin. Physical Simulation System for Spacecraft Rendezvous and Docking Based on MicroSim. Aerospace Control, 2006(02): p. 63-67+96.
- [9] LI Jisu, ZENG Haibo, LI Tieshou, et al. Ground Physical Simulation Experiment System for Combined Control of Multibody Satellite. Control Engineering, 2002(06): p. 14-18.
- [10] LI Jisu, ZENG Haibo, LI Tieshou. Physical Simulation Test System for Combined Control of Multibody Satellite. Aerospace Control, 2003. 21(2): p. 27-32.
- [11] XU Jian, YANG Qingjun, BAO Gang, et al. Research and Development of Air Bearing Spacecraft Simulator on the Multiple Degree of Freedom. Aerospace Control, 2009. 27(6): p. 96-101.
- [12] Schubert, H.C.J.P. How, Space construction: an experimental testbed to develop enabling technologies, in Telemanipulator and Telepresence Technologies IV, M.R. Stein, Editor. 1997, Spie-Int Soc Optical Engineering: Bellingham. p. 179-188.
- [13] Aeronautics, S.U.D.o., et al., Manipulation of a Free-floating Object Using a Macro/mimi-manipulator with Structural Flexibility. 1997.
- [14] LI Weidong, HOU Lihong. Research on High-speed Train Position Technology Based on Satellite Navigation System. Information and Control, 2016(04): p. 479-486.
- [15] ZHAO Yanzhi, ZHAO Fei, YANG Jiantao, et al. Modeling and Analysis of 6-RUS Parallel Mechanism of Image Compensation of Satellite Camera. China Mechanical Engineering, 2016(03): p. 369-375.
- [16] CHEN Yuhang, ZHAO Tieshi, SONG Xiaoxin, et al. Analysis of DOF Properties and Kinematics for Variable Configuration Parallel Multi-dimensional Vibration Platform. ROBOT, 2016(02): p. 135-143.

Research on Multi-Hop Routing Protocol of Wireless Sensor Networks Based on Gradients

Chenglong Hu and Yongzhen Li*

Department of Computer Science & Technology YanBian University YanJi, China

*Corresponding author

Abstract—The purposes of this paper are to lower the energy consumption in the wireless sensor network and to prolong network life cycle. Based on the maximum power a node can transmit, a multi-hop routing algorithm is proposed in this paper on the basis of gradients. We conducted a simulative experiment on the improved algorithm we proposed through MATLAB, and the results indicate that compared with LEACH algorithm and HEED algorithm, algorithm proposed in this paper is greatly improved in terms of energy consumption in the network and network life cycle.

Keywords—Wireless sensor network; broadcast radius; gradient; multi-hop transmission; network lifetime

I. INTRODUCTION

At present, studies of wireless sensor routing protocol have aroused many scholars' attention, yet the results are not remarkable. Except for classical routing algorithms about a decade ago, there has not been an improved routing protocol in recent years which is able to obtain support and affirmation at home and abroad [1], [2]. Therefore, there is still much to study in wireless sensor routing protocol.

Since battery energy in wireless sensor network is limited and cannot be charged [3], [4], and hardware resources and node computing abilities are all restrained, we can only seek improvements in algorithm under the circumstance that it is impossible to improve the sensor node from hardware.

Transmission distance of classical network protocol sensor nodes is limited, hindering it from transmitting at any distance. Based on this drawback, multi-hop transmission research method with gradients is proposed in this paper for the transmission distance between the nodes, so as to lower the energy consumption in the network and prolong the failure round of the first network node.

II. RELATED WORK

Routing protocols are divided into the following types: the plane protocol, the position-based protocol and the hierarchical protocol.

Nodes in the plane routing play the same role and each node shares the same status in the network. Flooding and Gossiping [5] are two classical algorithms in plane routing of wireless sensor network. Flooding is easy to operate, and there is no need to consume additional energy to maintain invariant topology and to achieve routing; in Gossiping, nodes are

selected randomly during data transmission for relay data transmission, which avoids the information internal explosion. Yet this method takes more time for information transmission.

In routing network based on position, nodes are distinguished according to their position. Distance between the nodes is calculated according to the signal length; the longer the signal, the shorter the distance between the nodes. In some protocols, nodes are allowed to sleep when there is no operation; for instance, GEAR and GPSR [6], [7].

In hierarchical protocol, nodes are divided into clusters and the node with highest energy is selected as the cluster head. Classical algorithms of mainstream protocols in hierarchical protocol include: LEACH, LEACH-C [8], LEACH-M [9], HEED [10], PEGASIS, etc.

LEACH is a cluster protocol whose main purpose is to realize the balanced load among sensor nodes so as to prolong network life cycle. Yet there are still several problems in LEACH algorithm, which are as follows [11], [12], [13], [14], [15], [16]:

1 In LEACH, cluster head has to be selected in each round, which consumes plenty of energies. Besides, head selection doesn't take remaining energy and node position into consideration. As a result, cluster head may gather in a certain region or at the marginal zone in the area.

2 In LEACH algorithm, data are transmitted in single-hop way from member nodes to cluster head nodes, and then to the base station. When in a large-scale network, nodes away from the sink node use up their energy early due to different distances between the sink node, which is harmful to data collection. This method is unsuitable for large-scale network due to its poor expansibility.

3 Cluster head nodes transmit data to the base station directly, and therefore, these nodes consume more energies than other common nodes and lose efficiency when their energies are used up, invalidating the network too early.

LEACH-M [9] adopts the same algorithm and mechanism as those of LEACH to form clusters; at the same time, cluster head nodes record all the locations and energy information of cluster head nodes in the network.

In HEED [10] algorithm, energy consumed by the average communication in clusters is taken as the criterion to evaluate the communication cost in clusters. Key of HEED algorithm is

that nodes decide the cluster head node through comparison of cost values between themselves and surrounding nodes.

PEGASIS algorithm organizes the nodes in the network into a chain. Its drawback is that each node must know the location information of other nodes in the network, which leads to too much expenditure and excessive routing table waiting to be maintained; when the network scale is too large, chain structure in the algorithm is too long and time delay of data transmission is relatively large, which fail to guarantee the timely data update, and chain structure cost is too large.

In a large-scale network, hierarchical routing protocol consumes less energy than plane routing protocol, and is thus more efficient. Circumstance of the research in this paper was large-scale network, so hierarchical routing protocol was selected. Algorithm realization was improved to prolong network life cycle.

III. OUR PROPOSED METHOD

Wireless sensor routing algorithm, which is designed in this paper based on gradients, improves the algorithm mainly in terms of cluster stage and data transmission stage.

A. Cluster Stage

1) Gradient partition

Different from the concentric circle division method of “ring-section”, gradient division method which improves the algorithm was proposed based on the concentric circle division method in this paper. It recorded the number of neighboring nodes in gradient division stage, and selected intermediate nodes to forward data within the broadcast radius.

We divided the gradients in the area under the circumstance where area dimension and node number were fixed. Detailed steps of gradient division are listed as follows:

a) Initialized the gradient value of each node into 0. Firstly, the base station delivered broadcast signal with a radius of R , and the message was *Broadcast_message(level:1)*. Nodes receiving the message from base station set their gradient as 1;

b) Nodes whose gradients were 1 in the last step continued to deliver broadcast signal with a radius of R , and the message was *Broadcast_message(level:2)*. Nodes who received this message and whose gradient values were 0 set their gradient as 2;

c) Circulated Step 2; divided the gradients; when each node in the network had a gradient value other than 0, the division was finished.

d) Gradient division was over. Each node recorded number of other nodes within its broadcast radius. This figure was the neighboring node number of each node, N_i .

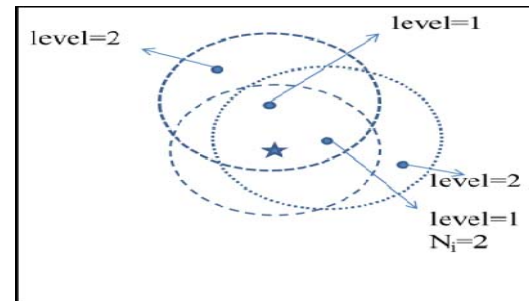


FIGURE I. SKETCH MAP OF LEVEL DIVISION

Figure 1 shows how to determine the gradient. Asterisk represents base station nodes, located in the middle of the area. In the circle which takes the base station as the center and the broadcast radius R as the radius, the circle is the range which the broadcast signal can reach. Divide all the regions in the whole network into different gradients according to the steps above, and each node has a gradient.

2) Cluster head selection:

In order to reduce the energy consumption, it is necessary to choose nodes with high remaining energy and suitable position as the cluster head nodes.

In classical LEACH algorithm, nodes select a random figure ranging from 0 to 1 when choosing the cluster head node, and compare it with the threshold. If the selected figure ranging from 0 to 1 is smaller than the threshold, it will be the cluster head node. This is the drawback of LEACH algorithm, and improvements on it are made in this paper. Steps of cluster head selection algorithm in this paper are as follows:

a) In each round of cluster head selection, each node selected a random figure from 0 to 1, and compared it with the threshold $T(n)$ in formula (1). Nodes smaller than the threshold were selected as cluster head nodes;

b) Selected cluster head nodes according to the method in Step 1. Cluster head nodes delivered the broadcast message that they had become the cluster head nodes with a radius of R , including their identifying ID value and gradient: *CH_MES(M_y_ID, M_y_Level)*. Other nodes which were not selected as cluster heads entered Step 3;

c) Nodes failing to be the cluster heads in Step 2 could decide which cluster to join according to the signal strength of broadcast message. They entered the cluster head nodes close to themselves, and became member nodes of the cluster head node;

d) Member nodes sent the message that they had become member nodes of the cluster head nodes to them, including identifying ID value of the cluster head and their own ID values: *Join_REQ(CH_ID, M_y_ID)*;

e) Member nodes in the cluster waited for the cluster node head to receive the information ACK, as well as the time slot TDMA the cluster head nodes distribute. Then one round of cluster head selection is over.

Threshold formula $T(n)$ is as follows:

$$T(n) = \begin{cases} \frac{p}{1-p(r \bmod(1/p))} (\alpha * \frac{E(i)_{res}}{E_{ave}} + \beta * \frac{S(i).n}{S(i).\ln}), & n \in G \\ 0, & \text{else} \end{cases} \quad (1)$$

P is the percentage of cluster head node number in the number of all the sensor nodes in the network (normally 5%); α and β are energy influence factor and density influence factor, and their sum is 1. E_n is the remaining energy of node n ; E_{ave} is the mean remaining energy of node n 's neighboring nodes; N_n is the neighboring node number of node n ; N_{avg} is the ideal neighboring node number.

Common nodes decided which cluster to join according to the signal strength, and they joined the closest cluster head node.

After member nodes joined the clusters, cluster head nodes distributed TDMA time slot towards member nodes, and broadcast the time slot of each node to member nodes in the cluster, including: TDMA(CH_ID, M₁:slot₁, M₂:slot₂, ..., M_n:slot_n). As is shown in Figure 2, the unit of wireless sensor in network routing stage is round. Each round is composed of set-up and steady state of data transmission. For a particular cluster, each round is composed of its data frames, in which each cluster member corresponds to a frame slot; and the cluster head node uses the last slot in each frame to communicate with base station.

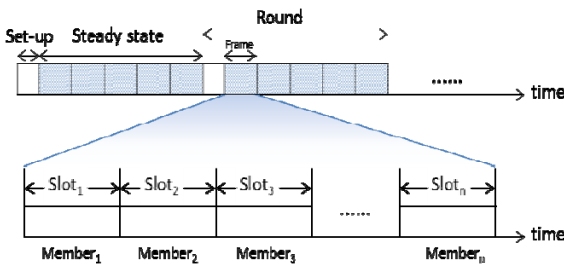


FIGURE II. SKETCH MAP OF TDMA ALLOCATION PROCESS

After the cluster head node received the message monitored by its member nodes, it integrated the information and removed the redundant message to avoid energy consumption caused by transmitting repeated message.

B. Data Transmission Stage

1) Intra-cluster transmission:

Figure 3 shows the diagram of intra-cluster transmission in data transmission. The black block is a cluster head node; the dotted circle is the assumed cluster range of this cluster head node, which is not necessarily the actual radius of this cluster head node. Cluster range of each cluster head node is not fixed, and it is only assumed here that the dotted circle is the cluster range. Each cluster transmits according to the diagram in Figure 3, after receiving member node messages, cluster head nodes integrate the data and intra-cluster transmission is over.

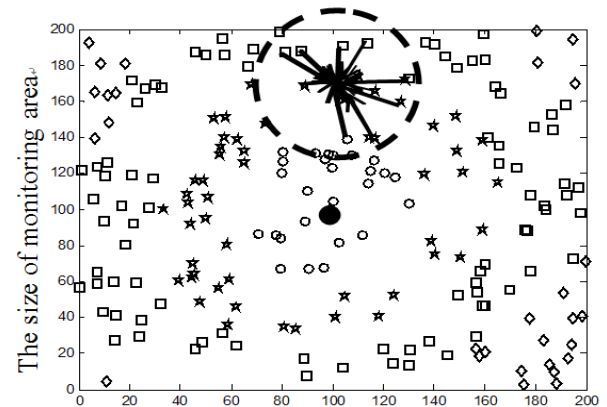


FIGURE III. SKETCH MAP OF TRANSMIT WITHIN THE CLUSTER

Figure 3 shows the diagram of intra-cluster transmission in data transmission. The black block is a cluster head node; the dotted circle is the assumed cluster range of this cluster head node, which is not necessarily the actual radius of this cluster head node. Cluster range of each cluster head node is not fixed, and it is only assumed here that the dotted circle is the cluster range. Each cluster transmits according to the diagram in Figure 3, after receiving member node messages, cluster head nodes integrate the data and intra-cluster transmission is over.

2) Transmission outside the cluster

In this paper, intermediate forwarding node was selected in the transmission outside the cluster, to forward the information from areas with large gradients into those with small ones, and eventually to the base station. Transmission algorithm outside the cluster is described as follows:

a) After intra-cluster transmission, member nodes had already sent the data to the cluster head. Now cluster head nodes needed to transmit the integrated information to sink nodes through transmission outside the cluster. Cluster head nodes whose gradients were 1 deliver the integrated information directly to sink nodes;

b) Cluster head nodes whose gradient was not 1 selected close nodes which were smaller than themselves within the broadcast radius as intermediate nodes to forward data;

c) Circulated Step 2. Selected intermediate nodes to forward the data until information was transmitted to the intermediate nodes whose gradient was 1. Transmited the message to sink nodes directly in the end;

d) All cluster head nodes forwarded data in multi-hop according to steps above until monitored information was all transmitted to sink nodes. The transmission outside the cluster in a round of data transmission was over.

IV. SIMULATION AND ANALYSIS

A. Initialization

In this paper, we used MATLAB to simulate the proposed algorithm and make comparisons between the proposed

algorithm with LEACH and HEED algorithms, and verified the efficiency and rationality through study result analyses. Parameters used in the improved algorithm experiment are as follows:

TABLE I. PARAMETERS OF EXPERIMENT

Parameter	Value
Area size	200*200m
Sink position	(100m,100m)
Number of sensor nodes	200
Ration of cluster head nodes in the total number p	0.05
Data package length	4000 bit
Control package length	200 bit
Node initial energy	1.0J
Energy consumption of sending and receiving circuits	50 nJ/bit
Free magnification	10 pJ/bit.m-2
Multi-path magnification	0.0013 pJ/bit.m-2
Energy consumption of data integration	5 nJ/bit.signal-1

B. Comparison of Network Survival Time

According to the parameters in TABLE 1, as well as the certain broadcast radius $R=41$, energy influence factor $\alpha=0.5$ and node density influence factor $\beta=0.5$, comparison experiment of network survival time of the algorithm in this paper, LEACH algorithm and HEED algorithm.

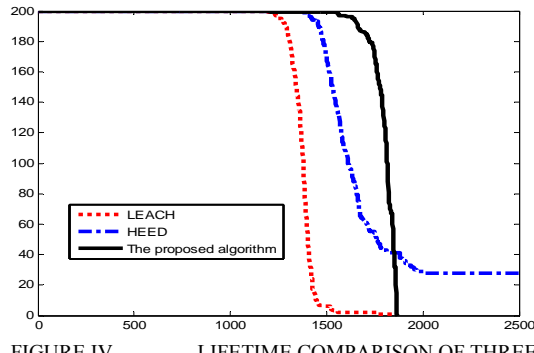


FIGURE IV. LIFETIME COMPARISON OF THREE ALGORITHMS

TABLE 2 shows the rounds in which the first node is invalidated of the three algorithms.

TABLE II. THE COMPARISON RESULTS OF NETWORK LIFETIME

Routing Algorithm	Lifetime(round n)
LEACH	1219
HEED	1473
The proposed algorithm	1711

From the slopes of the curves in Figure 4, that of the algorithm in this paper is steeper than those of LEACH and HEED. With the increase of round number, the full consumption speed of node energy is slower. Advantages of the algorithm in this paper over LEACH and HEED in terms of life

circle can be seen more directly from Table 2. Analyzed from the perspective of network life circle index, that of the improved algorithm raises 40.4% and 16.2% respectively, compared with LEACH and HEED. Therefore, algorithm in this paper is better than the two whether in curve slope or in detailed network life circle.

C. Comparison of Energy Consumption in the Network

Figure 5 is the comparison between the improved algorithm we proposed and the classic Routing Algorithm in the network energy consumption.

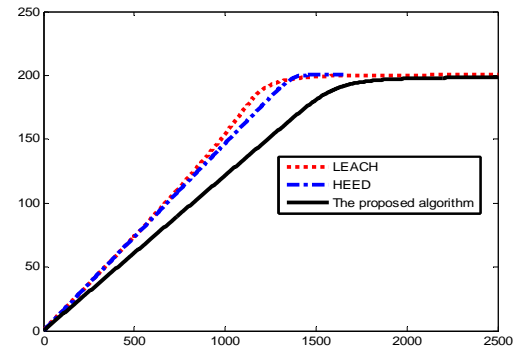


FIGURE V. ENERGY CONSUMPTION COMPARISON OF THREE ALGORITHMS

From Figure 5, curve change of this algorithm is the smoothest, that is, it has the lowest network energy consumption after the same rounds. Algorithm in this paper is more advantageous than LEACH and HEED from the round number, since with the increase of round number, cluster head nodes in LEACH have too little energy to transmit information; or cluster head nodes are distributed in areas with small or large density, which fastens the consumption of cluster head energy. When selecting cluster head nodes, this algorithm considers both the node remaining energy density among the nodes, balancing the cluster head node location distribution and cluster head node number.

V. CONCLUSION

In this paper, improvements are made on routing algorithm in cluster selection stage and data transmission stage, and a cluster multi-hop routing algorithm is proposed based on gradients. On the basis of simulative experiments, we analyzed property comparison of this algorithm, LEACH and HEED algorithms. In the end, we drew the conclusion that the proposed algorithm lowers the energy consumption and increases network survival time.

There are following drawbacks in the algorithm proposed in this paper and the next research plan is as follows:

1) In cluster head selection stage, that different gradients have different chances to become cluster head nodes can be considered. If we give nodes closer to the base station, that is, nodes with smaller gradients, higher possibility to become cluster heads, shorter distance to the base station leads to shorter transmission distance, which can balance the energy consumption in the network.

2) Next step in this paper is to conduct simulative experiments closer to the real network scale. In different network scales, we study on the relationship between the parameter and network scale.

REFERENCES

- [1] M. Sharma, K. Sharma, "An Energy Efficient Extended LEACH (EEE LEACH)," 2012 International Conference on Communication System and Network Technologies, Rajkot, India. pp.377~382, 2012.
- [2] S. Ning, J. Yoon-su, L. Sang-ho, Energy Efficient Mechanism Using Flexible Medium Access Control Protocol for Hybrid Wireless Sensor Networks. Central South University Press and Springer-Verlag. Berlin, Heridelberg. pp.2165~2174, 2013.
- [3] Shang Fengjun, Communication protocol for wireless sensor networks [M].Beijing: Publishing House of Electronics Industry.2011:1~30.
- [4] Sun Limin, Li Jianzhong, Wireless sensor networks [M].Beijing: Tsinghua University Press.2010:4~21.
- [5] Q. X. Xiong, C. H. Chen, "A Novel Application Semantics Based Routing Algorithm in Wireless Sensor Networks," 2014 Fourth International Conference Communication Systems and Network Technologies, Bhopal, India. pp.143~146, 2014.
- [6] S. Tyagi, N. Kumar, "A Systematic Review on Clustering and Routing Techniques Based Upon Leach Protocol for Wireless Sensor Networks," Journal of Network and Computer Applications,Vol.36 No.2 pp.623~645, 2013.
- [7] He Yongqiang, Gu Chunying, Wang Junpeng.,Flow divided-based uniform clustering for WSN routing algorithm [J] Application Research of Computers,2015,32(10):3075~3077.
- [8] Hu Yanhua, Zhang Jianjun, Improved algorithm of cluster head multi-hops based on LEACH [J] Computer Engineering and Applications, 2009, 45(34):107-109.
- [9] Li Yan, Zhang Xihuang, Li Yanzhong, Algorithm of cluster head multi-hops based on LEACH [J] Computer Engineering and Design, 2007,28(17):4158~4160.
- [10] O. Younis, S. Fahmy. Heed: a Hybrid, Energy-Efficient, Distributed Clustering Approach for Ad Hoc Sensor Networks [J]. IEEE Transactions On Mobile Computing. 2004, 3(4): 366~379.
- [11] A. Manjeshwar, D. Agrawal, "APTEEN: A Hybrid Protocol for Efficient Routing and Comprehensive Information Retrieval in Wireless Sensor Networks," Proceedings International on Parallel and Distributed Processing Symposium. Ft, Lauderdale, America. 2008.195~202.
- [12] Lang Lili, Design and Implementation of Dijkstra Shortest Path Clustering Wireless Network Based on nRF24L01[D].BeiJing: Northeastern University,2013:37~41.
- [13] J. B. Liang, J. X. Wang, "An Efficient Algorithm for Constructing Maximum Lifetime Tree for Data Gathering Without Aggregation in Wireless Sensor Networks," 2010 Proceedings IEEE INFOCOM, San Diego, America. 2010: 1~5.
- [14] H. J. Liao, C. H. R. Lin, Y. C. Lin, et al, "Inntrusion Detection System: a Comprehensive Review," Journal of Network and Computer Applications, Vol.36 No.1 pp.16~24, 2013.
- [15] Zhou Chong, Yu Zhenhong, Wang Nana, Research on data fusion based on clustering routing for wireless sensor network [J] Modern Electronics Technique,2012,35(7):43~46.
- [16] S. Ning, C. Young-bok, L Sang-ho, "A Distributed Energy Efficient and Reliable Routing Protocol for Wireless Sensor Networks," Proceeding of the 14th IEEE International Conference on Computational Science and Engineering, Dalian, Liaoning. 2011: 273~278.

Observation-based Clock Synchronization in Wireless Sensor Networks

Ayako Arao and Hiroaki Higaki*

Department of Robotics and Mechatronics, Tokyo Denki University, Japan

*Corresponding author

Abstract—In wireless sensor networks, each wireless sensor node records events occurred in its observation area with their observation time. Each wireless sensor node possesses its own local clock whose drift and offset are generally different from the others. By using observation records of the commonly observed events by neighbor wireless sensor nodes, this paper proposes a novel method to estimate the relative drift and offset between local clocks of the neighbor wireless sensor nodes. Here, each sensor node only detects the occurrences of events and cannot achieve the locations where the events occur. Hence, commonly observed events between neighbor wireless sensor nodes are required to be detected. Our proposed method applies a heuristic that multiple observation records in neighbor wireless sensor nodes whose intervals are the same are estimated to be commonly observed events.

Keywords—wireless sensor networks; observation time; local clock synchronization; relative drift estimation; relative offset estimation

I. INTRODUCTION

A wireless sensor network consists of numerous number of wireless sensor nodes with their sensor modules for achieving environmental data and wireless communication modules for transmission of data messages containing the environmental data to one of stationary sink nodes by using wireless multi-hop communication based on wireless ad-hoc communication. Each wireless sensor node possesses its local clock and the sensor node records observed events with the clock value at that time. Since the wireless sensor nodes work autonomously and their local clocks have individual differences, it is almost impossible for the local clocks in the wireless sensor nodes to be completely synchronized [3]. Especially due to individual differences in their crystal oscillators, incremented clock values in the same time duration are generally different one by one and networks with numerous number of nodes with their local clocks should be designed and managed on the assumption of the asynchronous local clocks [7]. Same as [9], this paper assumes that a local clock value $C_i(t)$ of a wireless sensor node S_i is represented with its offset O_i and drift dt_i/dt as $C_i(t) = (dt_i/dt)t + O_i$. Since each local clock of S_i has its own offset and drift, it is expected that a clock value difference $|C_i(t) - C_j(t)|$ between local clocks of S_i and S_j is required to be kept small by a certain clock synchronization procedure with a certain short interval.

II. RELATED WORKS

The problem of synchronization among local clocks in a network has been discussed and various synchronization

methods have been proposed. The most fundamental approach to solve the problem is the algorithm discussed in [1]. Here, between two computers, local clock value request and reply control messages are exchanged where these control messages carry local clock values of sender computers. However, since the receiver computer cannot achieve its local clock values when the received control message is transmitted, the transmission delay of the received control message is required to be estimated. Therefore, the methods for clock synchronization by exchange of local clock values require more precise estimation of transmission delay of control messages. Even with variation of transmission delay of control messages, it may be practically applicable for proposed methods to wired networks whose variation of transmission delay is not so large.

For synchronization of local clocks of wireless nodes in wireless ad-hoc networks, RBS [2], FTSP [4] and TSPN [6] have been proposed. All these methods are based on the transmissions of control messages carrying local clock values as discussed before. Hence, for achieving highly precise synchronization among local clocks in wireless nodes, more precise estimation of transmission delay of control messages carrying local clock values are required. However, due to collision avoidance methods such as CSMA/CA and RTS/CTS control, it becomes much more difficult to estimate transmission delay of control messages for clock synchronization as shown in Figure 1.

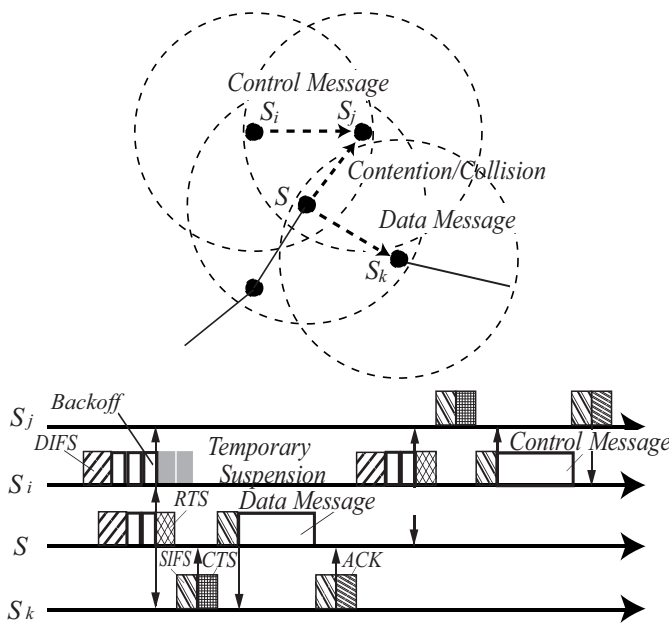


FIGURE I. UNPREDICTABLE TRANSMISSION DELAY OF CONTROL MESSAGES FOR CLOCK SYNCHRONIZATION IN WIRELESS AD-HOC NETWORKS.

III. PROPOSAL

A. Commonly Observed Events

Each wireless sensor node consists of a sensor module which detects events occurred within its observation area and a wireless communication module which transmits / receives wireless signals from / to its neighbor wireless nodes within its wireless signal transition area. A wireless sensor node S_i which detects an occurrence of an event within its observation area records kinds of the events with some additional related attributes including the clock value $C_i(t)$ of its local clock at the instance t when S_i observes the event. For simplicity, this paper assumes that each event is detected by all the wireless sensor nodes whose observation areas include the location of the event at that instance, i.e. without any observation delay. In reality, each sensor device requires its specific response time for an event observation and the effect of the delay is discussed in our future work. In addition, all events are assumed to be the same kind. Hence, in accordance with the event observation records by a wireless sensor node S_i , a sequence $ESeq_i := \langle C_i(t_0), C_i(t_1), \dots, C_i(t_{N_i}) \rangle$ of the clock values at the instances when S_i observes the events is induced. Here, $C_i(t_j)$ is the value of the local clock of S_i at the instance t_j when S_i observes an occurrence of an event $e_i(t_j)$ in its observation area. On the other hand, each wireless sensor node S_i communicates with its neighbor wireless sensor nodes within its wireless signal transmission area. Thus, it is possible for S_i to exchange its clock value sequence $ESeq_i$ at occurrences of locally observed events with its neighbor wireless sensor nodes. Generally, the observation area of a wireless sensor node is included in its wireless signal transmission area. In addition, in a wireless sensor network, an observation area where all the event occurred are surely observed and recorded by at least one wireless sensor node is required to be covered by observation areas of multiple

wireless sensor nodes [5,8]. Hence, observation areas of neighbor wireless sensor nodes usually overlap and the wireless sensor nodes whose observation area overlap can communicate directly by using wireless ad-hoc communication. Suppose the case where observation areas of wireless sensor nodes S_i and S_j overlap as shown in Figure 2.

[Commonly / Solely Observed Events]

An event which occurs at a certain instance t in an overlapped area of observation areas OA_i and OA_j of wireless sensor nodes S_i and S_j respectively and is observed and recorded with local clock values $C_i(t)$ and $C_j(t)$ into clock value sequences $ESeq_i$ and $ESeq_j$ by S_i and S_j respectively is called a commonly observed event of S_i and S_j . On the other hand, an event which occurs at a certain instance t in an area included by OA_i and excluded by OA_j and is observed and recorded with a clock value $C_i(t)$ into only a clock value sequences $ESeq_i$ by S_i is called a solely observed event of S_i against S_j .

Each wireless sensor node S_i assumes to observe all the events occur within an observation area OA_i of S_i . As various widely available sensor modules, S_i only identifies the occurrence of the events and gets the clock values of its local clock at the instance of the occurrence of the events; however, it cannot identify the precise locations of the events in its observation area. Hence, it is impossible for S_i to identify whether an observed event is a commonly observed event with a neighbor wireless sensor node S_j or a solely observed event against S_j . Even though clock values at an instance when an event occurs are recorded by wireless sensor nodes which observe the event, since clock values $C_i(t)$ and $C_j(t)$ of wireless sensor nodes S_i and S_j at any instance t are generally different, it is impossible for a wireless sensor node to identify its commonly observed events with a specified neighbor wireless sensor nodes only by comparison of local clock values in their clock value sequences as shown in Figure 2. Since clock values $C_i(t)$ and $C_j(t)$ of S_i and S_j for a commonly observed event at an instance t are different and it is impossible to identify commonly observed events of S_i and S_j only by simply comparing the sequences of clock values.

B. Relative Offset Estimation

By using commonly observed events defined in the previous subsection, this paper proposes a method to estimate a relative drift $dt_j/dt_i = (dt_j/dt)/(dt_i/dt)$ and a relative offset $O_j - O_i$ under an assumption that local clock values $C_i(t)$ and $C_j(t)$ of wireless sensor nodes S_i and S_j are given as $C_i(t) = (dt_i/dt)t + O_i$ and $C_j(t) = (dt_j/dt)t + O_j$, respectively. This subsection discusses a method to estimate only a relative offset where a relative drift is assumed to be 1. The method to estimate both a relative drift and a relative offset is discussed in the next subsection.

In case that a relative drift of $C_i(t)$ and $C_j(t)$ is 1, i.e. $dt_j/dt_i = 1$, $C_j(t) - C_i(t) = O_j - O_i$, i.e. a difference between clock values at any instance equals to their relative offset. Hence, if one of pairs of clock values of commonly observed events is identified, the difference between the clock

values is their relative offset. However, it is difficult to identify a pair of clock values of a commonly observed event from local clock value sequences of neighbor wireless sensor node. This is because, as discussed in the previous section, even if wireless sensor nodes S_i and S_j observe the same event, i.e. their commonly observed event, at an instance t , their local clock values $C_i(t)$ and $C_j(t)$ at t are usually different, i.e.

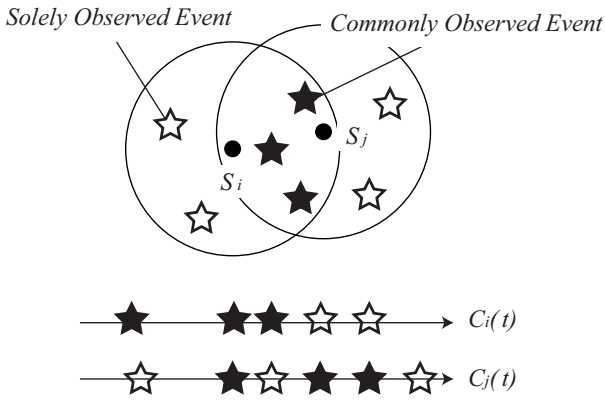


FIGURE II. LOCAL CLOCK VALUES OF OBSERVATION TIME IN S_i AND S_j .

$C_i(t) \neq C_j(t)$. In addition, even if the instances t and t' of solely observed events observed by S_i and S_j respectively are different, i.e. $t \neq t'$, their local clock values $C_i(t)$ and $C_j(t')$ might be the same, i.e. $C_i(t) = C_j(t')$. Hence, the simple comparison between individual clock values $C_i(t)$ and $C_j(t')$ recorded in sequences $ESeq_i$ and $ESeq_j$ of local clock values of S_i and S_j does not result in correct estimation of the relative offset between their local clocks.

In order to solve this problem, this paper proposes a novel method to estimate the relative offset and drift between the local clocks of neighbor wireless sensor nodes by using multiple pairs of clock values recorded in the sequences of local clock values. As discussed, a clock value sequence $ESeq_i$ of local clock values of a wireless sensor node S_i when it observes events in its observation area OA_i includes local clock values of commonly observed events with its neighbor wireless node S_j . Though local clock values of S_j for the same commonly observed events are surely included in a clock value sequence $ESeq_j$ of local clock values of S_j when it observes them, it is impossible to detect the commonly observed events by simple comparison of local clock values in $ESeq_i$ and $ESeq_j$. However, since the commonly observed events, i.e. events which occurs in the overlapped area of observation areas OA_i and OA_j of S_i and S_j , are observed at the same instance t by S_i and S_j even though $C_i(t)$ and $C_j(t)$ may be different, intervals between the same pair of commonly observed events in S_i and S_j are the same. That is, suppose that clock values of S_i and S_j when they observe two commonly observed events occur at instances t and t' are $C_i(t)$, $C_i(t')$, $C_j(t)$, $C_j(t')$, respectively. Even if $C_i(t) \neq C_j(t)$ and $C_i(t') \neq C_j(t')$, $C_i(t) - C_i(t') = C_j(t) - C_j(t')$ is surely satisfied.

Since both locations where events occur and intervals between successive events contain a certain randomness, i.e. a certain unpredictability, this paper introduces a heuristic based on a reversed proposition of the above one into estimation of commonly observed events. Thus, if there exist local clock values $C_i(t_1)$ and $C_i(t_2)$ in $ESeq_i$ of S_i and $C_j(t_3)$ and $C_j(t_4)$ in $ESeq_j$ of S_j and $C_i(t_2) - C_i(t_1) = C_j(t_4) - C_j(t_3)$ is satisfied though $C_i(t_1) \neq C_j(t_3)$ and $C_i(t_2) \neq C_j(t_4)$, it is highly possible for S_i and S_j to have been observed two same events, i.e. there are two commonly observed events occurred at $t_1 = t_3$ and $t_2 = t_4$ respectively in the overlapped area of their observation areas. Needless to say, it might be possible for solely observed events whose recorded clock values are $C_i(t_1)$, $C_i(t_2)$, $C_j(t_3)$ and $C_j(t_4)$ to satisfy $C_i(t_2) - C_i(t_1) = C_j(t_4) - C_j(t_3)$ on accident. Hence, our heuristical method regards the possible relative offset that provides the maximum number of estimated commonly observed events which satisfies the above condition as an estimated relative offset.

[Estimation of Relative Offset]

Let $ESeq_i$ and $ESeq_j$ be sequences of local clock values $C_i(t)$ and $C_j(t)$ at instances when wireless sensor nodes S_i and S_j observe events. An estimated relative offset is what provides the maximum number of estimated commonly observed events where the transformed clock values with the estimated relative offset are the same. That is, with the estimated relative offset O , if the number of pairs of local clock values satisfying $C_i(t) + O = C_j(t')$ where $C_i(t) \in ESeq_i$ and $C_j(t') \in ESeq_j$ is the maximum for all possible relative offsets, O is regarded as the estimated relative offset for S_i and S_j .

For example, Figure 3(a) shows two sequences of local clock values $ESeq_i$ and $ESeq_j$. Figures 3(b), 3(c) and 3(d) show the results of parallel translation of $ESeq_j$ with possible relative offsets, i.e. where a pair of a local clock value $C_i(t)$ and a transformed local clock value with a possible relative offset $C_j(t') + O$ become the same value. There are 1, 2 and 3 estimated commonly observed events with the same transformed local clock values. If the maximum number of estimated commonly observed events is 3, the relative offset in Figure 3(c) is the estimation result in our method.

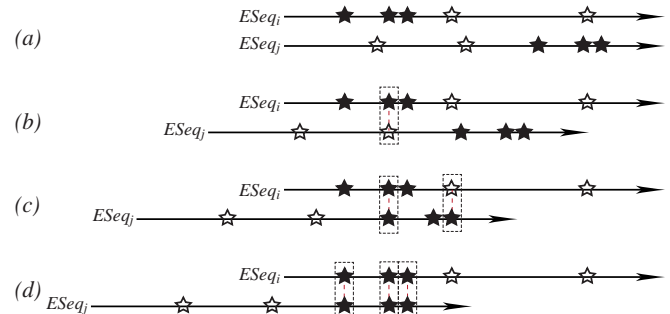


FIGURE III. ESTIMATION OF RELATIVE OFFSET.

C. Relative Drift Estimation

This subsection proposes an extended algorithm for estimation of both the relative offset and the relative drift for recorded local clock values in two neighbor wireless sensor

nodes whose observation areas overlap. Figure 4 shows the overview of our proposed method. Same as the method proposed in the previous subsection which supports only the cases with 1 relative drift, the number of estimated commonly observed events between local clock value sequences ESeq_i and ESeq_j for every possible relative offset $C_i(t_k^i) - C_j(t_l^j)$. In addition, for estimation of the relative drift, another pair of local clock values $C_i(t_{k'}^i) \in ESeq_i$ and $C_j(t_{l'}^j) \in ESeq_j$ ($k \neq k'$ and $l \neq l'$) is needed. Here, an estimated relative drift is $(C_i(t_{k'}^i) - C_i(t_k^i)) / (C_j(t_{l'}^j) - C_j(t_l^j))$. After applying the transformation of local clock values with the estimated relative offset and the estimated relative drift, the number of estimated commonly observed events whose local clock values are the same is evaluated. Same as the previous subsection, according to a heuristic that the correct pair of relative offset and relative drift provides the maximum number of estimated commonly observed events, our proposed method estimate them. In order to apply our proposed method, for neighbor wireless sensor nodes to estimate relative offset and drifts to transform the local clock values for synchronization, there should be more than 3 commonly observed events. Hence, enough observation period to record local clock values are required.

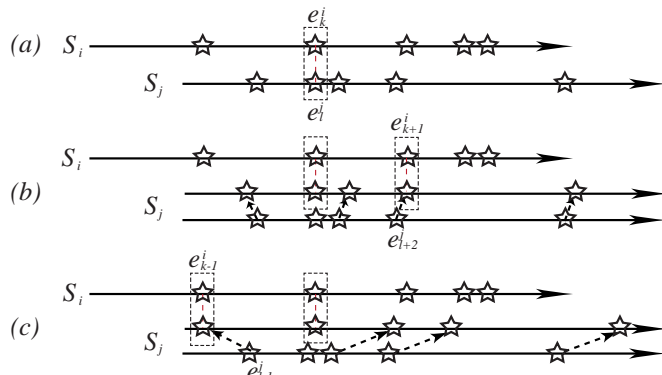


FIGURE IV. ESTIMATION OF RELATIVE DRIFT.

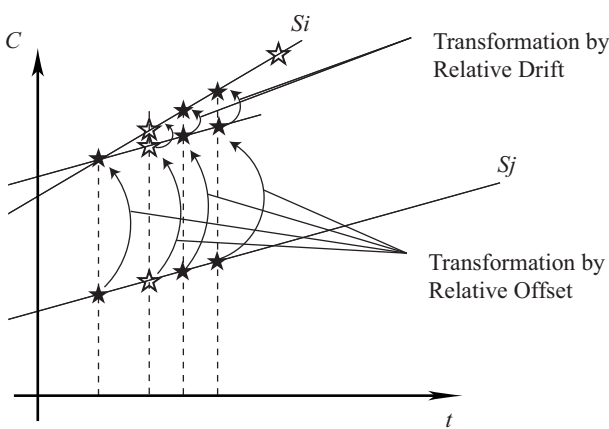


FIGURE V. ESTIMATION OF COMMONLY OBSERVED EVENTS BY OFFSET AND DRIFT ESTIMATION (CORRECT).

Figure 5 shows a case of correct estimation of commonly observed events with correct estimation of a relative drift dt_j/dt_i and a relative offset $O_j - O_i$. Here, pairs of local clock

values $C_i(t_1^i)$ and $C_j(t_1^j)$, $C_i(t_2^i)$ and $C_j(t_3^j)$, and $C_i(t_3^i)$ and $C_j(t_4^j)$ are those for commonly observed events, i.e., $t_1^i = t_1^j$, $t_2^i = t_3^j$ and $t_3^i = t_4^j$, respectively, and the rest $C_i(t_4^i)$ and $C_j(t_2^j)$ are local clock values for solely observed events in \$S_i\$ and \$S_j\$, respectively. By consideration that $C_i(t_1^i)$ and $C_j(t_1^j)$ are local clock values in \$S_i\$ and \$S_j\$ when a commonly observed events of \$S_i\$ and \$S_j\$ occurs, the relative offset is estimated as $O_j - O_i = C_j(t_1^j) - C_i(t_1^i)$ and the line representing the local clock value in \$S_j\$ is parallelly displaced as the points representing the local clock values $C_i(t_1^i)$ and $C_j(t_1^j)$ of the commonly observed event are overlapped. Then, by consideration that $C_i(t_2^i)$ and $C_j(t_3^j)$ are local clock values in \$S_i\$ and \$S_j\$ when a commonly observed events of \$S_i\$ and \$S_j\$ occurs, the relative drift is estimated as $dt_j/dt_i = (C_j(t_3^j) - C_i(t_1^i)) / (C_i(t_2^i) - C_i(t_1^i))$ and the line representing the local clock value in \$S_j\$ is rotated around the point representing the local clock value $C_i(t_1^i)$ as the points representing the local clock values $C_i(t_2^i)$ and $C_j(t_3^j)$ of the commonly observed event are overlapped. Now, the lines representing the local clock values of \$S_i\$ and \$S_j\$ are overlapped and all the commonly observed events including that for $C_i(t_3^i)$ and $C_j(t_4^j)$ are correctly estimated.

IV. CONCLUSION

This paper has proposed a novel clock synchronization method for wireless sensor networks. Different from the conventional methods by exchanging control messages with current local clock values and by estimation of transmission delay of the control messages, the proposed method estimates the relative offset and drift between two local clocks of neighbor wireless sensor nodes based on records of local clock values of event observations and estimation of commonly observed events of them. This paper has also designed estimation algorithms of relative offset and drift and evaluated their performance.

REFERENCES

- [1] Cristian, F., "Probabilistic Clock Synchronization," *Distributed Computing*, Springer, vol. 3, no. 3, pp. 146–158 (1989).
- [2] Jeremy, E., Lewis, G. and Deborah, E., "Fine-Grained Network Time Synchronization using Reference Broadcasts," *Proceedings of the 5th Symposium on Operating Systems Design and Implementation*, pp. 147–163 (2002).
- [3] Kopetz, H. and Ochsenreiter, W., "Clock Synchronization in Distributed Real-Time Systems," *ICE Transactions on Computers*, vol. C-36, no. 8, pp. 933–940 (1987).
- [4] Miklos, M., Branislav, K. and Kayla, S., "The Flooding Time Synchronization Protocol," *Proceedings of the 2AD International Conference on Embedded Networked Sensor Systems*, pp. 39–49 (2004).
- [5] Qu, Y., and Georgakopoulos, S.V., "A Distributed Area Coverage Algorithm for Maintenance of Randomly Distributed Sensors with Adjustable Sensing Range," *ICE Global Communications Conference*, pp. 286–291 (2013).
- [6] Saurabh, G., Ram, K. and Mani, B.S., "Timing-Sync Protocol for Sensor Networks," *Proceedings of the 1st International Conference on Embedded Networked Sensor Systems*, pp. 138–149 (2003).
- [7] Tanenbaum, A.S. and Steen, M., "Distributed Systems Principles and Paradigms," Prentice Hall (2002).

- [8] Tuba, E., Tuba, M., and Simian, D., "Wireless Sensor Network Coverage Problem Using Modified Fireworks Algorithm," Wireless Communications and Mobile Computing Conference, pp. 696–701 (2016).
- [9] Wu, Y-C., Chaudhari, Q. and Serpedin, E., "Clock Synchronization of Wireless Sensor Networks," ICE Signal Processing Magazine, vol. 28, no. 1, pp. 124–138 (2011).

Properties of a Self - gain Optical Fiber Differential Pressure Sensor Based on Damping Piston

Hao Hu and Liqiong Zhong*

College of Mechanical engineering, Guiyang college, Guiyang 550003,China

College of Mechanical engineering, Guizhou university, Guiyang 550025,China

*Corresponding author

Abstract—In this paper, the performance of a self-gain optical fiber differential pressure sensor based on damping piston is studied. Firstly, proposes the structure of mechanical packaging sensor probe based on the damping piston, and designs the sensor system; then, it carries out the theoretical research on the sensor and builds the intensity compensation modulation of the sensor. Finally, the experimental model machine is used for the strength compensation test and the differential pressure test. The experiment results show that after the intensity compensation of sensor, the output value can be maintained at a constant value, which is not affected by the fluctuation of light source power, and the output value can achieve the gain; the sensor of damping spring in different designed sizes has different detection range. When the detection range is [-80KPa, 80KPa], the sensitivity is about 0.024/KPa and the linearity is about 6%, with a good sensitivity and linearity. The research shows that the optical fiber differential pressure sensor has better detection performance and can meet the needs of different detection occasions.

Keywords—properties; damping piston; self-gain; geometric optics; optical fiber; differential pressure sensor

I. INTRODUCTION

With the advance and development of modern industrial technology, the differential pressure sensor has been applied in many high-precision detection occasions. From the micro-flow measurement, leakage test, clean room monitoring and environmental sealing test to the measurement of pressure field distribution, air quantity measurement, measurement of artificial respirator's respiratory capacity and measurement of micro-pressure difference between the rooms, all need a stable and reliable differential pressure sensor. Besides, with the development of modern detection technology, the application of differential pressure sensor will be further expanded, and the requirements for the differential pressure sensor technology will be increasingly high. Because of this, many scholars are committed to the improvement of differential pressure sensor's structure and advance of its performance in order to make it better serve the field of modern industrial detection [1-5].

Nowadays, the differential pressure sensor is mainly two kinds, respectively pressure resistance type and capacitance type. There are more prominent contradictions between sensitivity and frequency response of pressure resistance type, and the temperature has larger effect on the performance of this kind of sensor; for capacitance type, the parasitic capacitance and distributed capacitance have effect on sensitivity and

measuring accuracy, and there is complex circuit connected with the sensor and other deficiencies. It is because of so many shortcomings of traditional pressure sensor, the scholars both at home and abroad started to study some new differential pressure sensors, for example Dong Guoqiang et al conducts research on the micro-differential pressure sensor with the use of magnetic liquid [6], depending on the displacement process of magnetic fluid under pressure to generate an electrical signal to realize the detection of the pressure, and it has limitations in application; Hao-Jan Sheng of Taiwan and Jose.L.A.V of America et al each put forward a kind of optical fiber differential pressure sensor structure based on bragg grating [7-8]. The differential pressure sensor with such optical fiber grating has high degree of sensitivity but the structure is complex and the cost is very high, so it is not conducive to the promotion. But the intensity modulation as a widely used modulation method in optical fiber sensor technology has been studied by some scholars [9-10], but the research literature on optical fiber differential pressure sensor based on intensity modulation is very few. The Japanese Seiichiro Kinugasa proposes a conception of reflective optical fiber differential pressure sensor using the change of the reflector and the distance of the optical fiber to detect external differential pressure; Tong Chengguo designs the optical fiber differential pressure sensor with a double C-type spring tube, and based on the principle of intensity modulation, the differential pressure is detected in two double C-type spring tubes.

Under this background, this paper proposes a self gain-boosted differential pressure sensor based on the damping piston, and studies its structure and performance, in order to make the research on the differential pressure sensor further expanded and push the development of the design and promotion of new differential pressure sensor.

II. SENSOR STRUCTURE

As shown in Figure 1, the sensor comprises a probe part and the structure of self-compensating double light path of single light source. The light emitted by the light source S through the Y coupler is divided into two paths. The one enters the probe M_1 , and after reflection reaches the photoelectric detector D_1 ; the other enters the probe M_2 , and after reflection reaches the photoelectric detector D_2 .

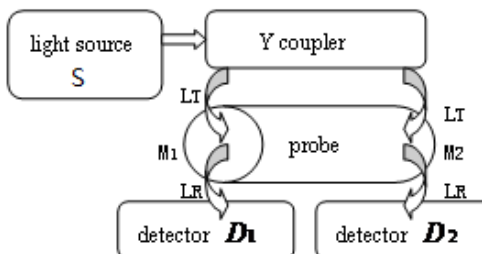
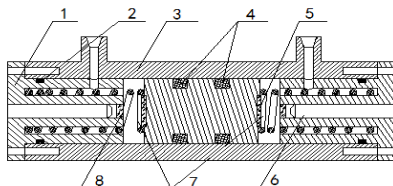


FIGURE I. SENSOR INTENSITY COMPENSATION PRINCIPLE DIAGRAM

As shown in Figure 2 below, the structure of sensor probe is made up of the end cover, cylinder, piston, spring, high light transmission layer, reflective layer and other parts. When the sensor is working, if there is differential pressure for the fluid on the detection cavities of both sides of the piston, the piston is out of balance and slides towards one side. The damping spring is compressed in this side, and the damping spring of the other side is stretched. With the damping spring compressed, the distance between optical fiber bundle and the reflector of piston surface decreases, and the signal intensity of the output light receiving optical fiber is weakened. With the damping spring stretched, the distance between optical fiber bundle and the reflector of piston surface increases, and the signal intensity of the output light receiving optical fiber is enhanced. After the photoelectric conversion and signal processing, the output value will increase exponentially, thus detection sensitivity is improved and the self-gain effect is achieved. Through the change of the output value, it is realized that the fluid differential pressure between two detection cavities can be judged, and the detection of differential pressure in different positions is realized; if the fluid pressure in the two detection cavities is equal and the piston does not produce axial displacement, then the signal intensity of output light of the fiber received by two fiber bundles is equal, and after the calculation of the photoelectric conversion and signal processing, the output value is 1.



1 end cap 2 sealing ring 3 cylinder 4 sealing ring 5 reflector 6 optical fiber probe 7 damping spring 8 high transmission film

FIGURE II. PROBE STRUCTURE

III. TEST RESULTS AND ANALYSIS

The damping piston optical fiber differential pressure sensor is used for the intensity compensation test. In the test, the light intensity detection system is used to detect the output electrical signal of the probe of two sensors. The light source adopts a semiconductor laser LD, with 1310nm of output peak wavelength. The photoelectric detector uses PIN photodiode, with the working wavelength range from 1100nm to 1650nm, the maximum dark current as 1nA, the minimum optical

response degree as 0.85A/W, and the response time as 0.1ns. Through the alternate control of circuits, the output power of light source is changed constantly, the output power of light source are respectively 100%, 70% and 40%. When the differential pressure between the two sides of sensor are 0KPa, 20KPa and 40KPa, the size of output signal of photoelectric detector D1 and D2 is recorded. The experimental results are shown in Figure 3, Figure 4 and Figure 5:

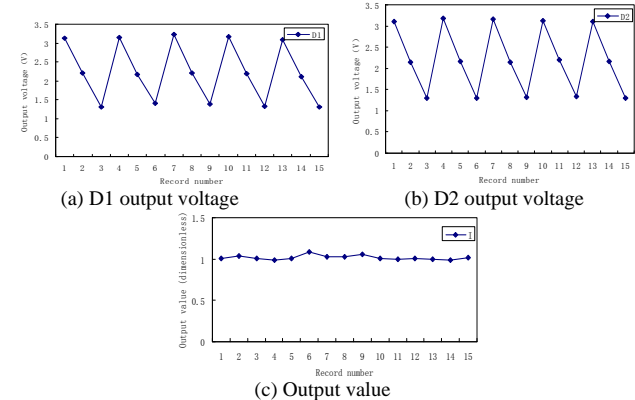


FIGURE III. IN THE DIFFERENTIAL PRESSURE 0KPa, D1 AND D2 OUTPUT VOLTAGE AND COMPENSATION OUTPUT VALUE I

From the above Figure 3 (a) and (b), it is not difficult to see that when the differential pressure of sensor is detect as 0KPa, the output power of light source changes and output voltage value of photoelectric detector D1 and D2 will have greater fluctuation. When the output power of light source is 100%, the output voltage is about 3.1—3.2V. When the output power of light source is 70%, the output voltage is about 2.1—2.2V. When the output power of light source is 40%, the output voltage is about 1.3—1.4V. If the intensity compensation is not carried out on it, the final detection value will not be correct. From the above Figure 3 (c), is not difficult to see that after the intensity compensation of sensor in the process of the change of the light source output power, the output value is maintained at constant value near 1, which will not fluctuate with the power fluctuation of the light source, that is when the differential pressure on both sides of sensor is 0KPa, the detection value of sensor is 1.

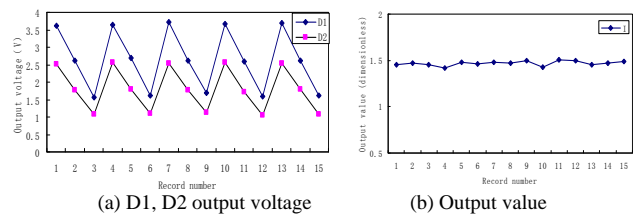


FIGURE IV. IN THE DIFFERENTIAL PRESSURE 20KPa, D1 AND D2 OUTPUT VOLTAGE AND COMPENSATION OUTPUT VALUE I

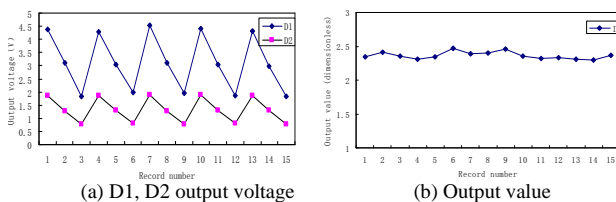


FIGURE V. IN THE DIFFERENTIAL PRESSURE 40KPa, D1 AND D2 OUTPUT VOLTAGE AND COMPENSATION OUTPUT VALUE I

From Figure 4(a) and Figure 5 (a), it is not difficult to see that when the differential pressure of sensor are detected are respectively 20KPa, 40KPa, the output power of light source changes and the output voltage value of photoelectric detector D1 and D2 also has large fluctuations. In the Figure 4 (a) and Figure 5 (a), the above toothed curve is the output voltage of photoelectric detector D1, and the below toothed curve is the output voltage of photoelectric detector D2. It is not difficult to see that in light of the same output power of light source, the output voltage of D1 increases with the increase of detected differential pressure and the output voltage of D2 decreases with the decrease of detected differential pressure. This is because the initial working state of the sensor is in the middle position of the curve of the intensity modulation curve. When the differential pressure effect is received, the output voltage of the low voltage side decreases and the output voltage of the high voltage side increases. From above Figure 4(b) and Figure 5 (b), it is not difficult to see that after the intensity compensation of the sensor, when the output power of light source changes, the output value is maintained about from 1.5 to 2.4, which will not fluctuate with the power fluctuation of the light source, that is when the differential pressure of the sensor on both sides is respectively 20KPa and 40KPa, the detection value of sensor is 1.5 and 2.4, reaching the intensity compensation effect. The increase rate of the output value in the three kinds of differential pressure is 50% and 60% respectively, and it will increase greatly with the increase of differential pressure and thus the gain effect can be achieved.

According to the above design and theoretical analysis, the experimental prototype of optical fiber differential pressure sensor based on damping piston is developed. The prototype is composed of the following key components: stabilized voltage supply, a light source of semiconductor laser, the optical fiber probe (multimode optical fiber) integrated with a incident optical fiber and a receiving optical fiber, mechanical packaged sensor probe, damping spring with certain rigidity and the photodiode. The photodiode is connected with the signal detection module of light intensity, and then connected with the A/D conversion module. After the pre-processing of photoelectric signal, then it is input to the computer for the calculation of the data at the later stage. Through the detection experiment of differential pressure, the results are obtained as following Figure 6.

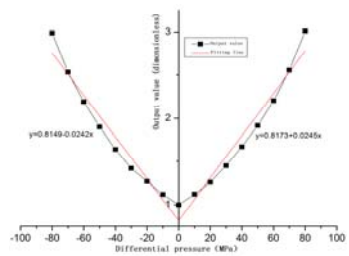


FIGURE VI. EXPERIMENTAL RESULT

The Figure 6 above shows the output value changes of the sensor when the differential pressure between the two detection cavities of sensor are respectively -80KPa, -70KPa, -60KPa, -50KPa, -40KPa, -30KPa, -20KPa, -10KPa, 0KPa, 10KPa, 20KPa, 30KPa, 40KPa, 50KPa, 60KPa, 70KPa and 80KPa. It is not difficult to see from the figure that in the damping spring with the current rigidity, the sensor's detection range is [-80KPa, 80KPa] and the change of the rigidity of the damping spring is used to change the sensor's detection range.

Then, the sensitivity of the sensor is about 0.024/KPa and the linearity is about 6%, which has high sensitivity and good linearity, and is consistent with the theoretical analysis.

Before you begin to format your paper, first write and save the content as a separate text file. Keep your text and graphic files separate until after the text has been formatted and styled. Do not use hard tabs, and limit use of hard returns to only one return at the end of a paragraph. Do not add any kind of pagination anywhere in the paper. Do not number text heads-the template will do that for you.

Finally, complete content and organizational editing before formatting. Please take note of the following items when proofreading spelling and grammar:

IV. CONCLUSIONS

This paper presents a new type of damping piston self-gain optical fiber differential pressure sensor. First, the probe structure of the differential pressure sensor and the light path structure of the sensor are designed. The probe of sensor is a mechanical packaged structure based on damping piston, and the light path of the sensor is the self-compensating double light path structure of single source, so as to realize the new type of optical fiber differential pressure sensor; then the paper analyzes the intensity compensation model of the sensor theoretically. the output signal after the intensity compensation of the sensor can effectively eliminate the power fluctuation of light source and the error of coupler, and then the ratio operation is conducted on the output value of two detection cavities of the sensor, which can better realize the self gain and self compensation of the sensor; Finally, the damping piston optical fiber differential pressure sensor is used for the intensity compensation test and differential pressure test. Through the intensity compensation test, it can be known that when the changes occur in the power of light source, the output voltage of photoelectric detector will have larger fluctuation, and that after intensity compensation, the output value can be maintained at a constant value, which will not fluctuate with the power fluctuation of the light source, that is the sensor

achieves better intensity compensation effect. Through the detection experiment of differential pressure, it can be known that for the damping spring with certain rigidity and the sensor with certain detection range, the detection range of the sensor can be changed by changing the rigidity of damping spring, and that the sensor has high sensitivity and good linearity, consistent with experimental results and theoretical analysis.

ACKNOWLEDGMENT

Science and technology cooperation plan of Guizhou Province (LH[2015]7660); The introduction of talent fund of Guizhou University ((2014)43).

REFERENCES

- [1] M. Shanmugavalli, G. Uma, M. Umapathy. Uncertainty Analysis Of Micro Differential Pressure Sensor Using Interval Analysis, J. International Journal On Smart Sensing And Intelligent Systems.2(2009)463-476.
- [2] J. Albert Chiou, Steven Chen. Thermal hysteresis and voltage shift analysis for differential pressure sensors, J. Sensors and Actuators. 135(2007)107-112.
- [3] Meenatchisundaram .S, Simha. Ashwin, Menon. Mukund Kumar, et al. Lumped parameter modeling of absolute and differential micro pressure sensors, J. Sensors and Transducers. 144(2012)76-91.
- [4] Takahashi Hidetoshi, Dung Nguyen Minh, Matsumoto Kiyoshi1, et al. Differential pressure sensor using a piezoresistive cantilever, J. Journal of Micromechanics and Microengineering. 22(2012).
- [5] Pavlik Michal, Haze Jiri, Vrba Radimir. Smart differential pressure sensor. International Conference on Informatics in Control, Automation and Robotics, Volume SPSMC,2007, pp: 244-248.
- [6] DONG Guo qiang, LI De cai, HAO Rui can. Study on Micro Differential Pressure Sensor Based on Ferrofluid, J. CHINESE JOURNAL OF SENSORS AND ACTUATORS. 22(2009)50-53.
- [7] Hao-Jan Sheng, Wen-Fung Liu,Kuei-Ru Lin,et al. High-sensitivity temperature-independent differential pressure sensor using fiber Bragg gratings, J. OPTICS EXPRESS. 16(2008)16014-16018.
- [8] Jose L.A.V, Riode J.R.J, Manoel F da S, et al. U.S. Patent 2006/0062510 A1, (2006).
- [9] Lars Rindorf, Poul Erik Hoiby, Jesper Bo Jensen,et al. Towards biochips using microstructured optical fiber sensors, J. Anal Bioanal Chem. 385(2006)1370-1375.
- [10] TANG Yu, LIU Chuanju. Study on Optical Fiber Sensor and its Application, J. Science & Technology Information. 7(2009)17-18.

Identifying Route Preferences over Origin-Destination Using Cellular Network Data

Zhichao Guo and Tongyu Zhu*

State Key Laboratory of Software Development Environment, Beihang University

*Corresponding author

Abstract—Current research on studying people's routing behavior focus on how to provide the minimum cost routes while ignore users' preference. Therefore, to analyze user's routing preference, identifying routes they actually choose is a crucial task. Cellular network data contains sufficient spatio-temporal information, which is widely used for trajectory analysis nowadays. However, it is a big challenge to extract precise trajectory from the cellular network data due to its low positioning accuracy. Compared to Density-Based Spatial Clustering of Applications with Noise algorithm, we present a Spatio-Temporal Density Clustering algorithm considering the timing sequence of the points to promote the precision of the trajectories, which aims to filter users' most probable routes with the map matching algorithm. Our approach could find out those most probable routes and the probability of each route. Finally, we experimented with real data. The results show that our approach is efficient for both extracting the probable trajectories and identifying multi-routes that users would prefer to route.

Keywords—cellular network data; spatio-temporal data; trajectory data mining; origin-destination

I. INTRODUCTION

Analyzing millions of urban inhabitants' mobility pattern is an important research field of urban computing. Many research on urban computing, such as transportation, urban planning and energy, are based on the analysis of people's moving regulations. Extracting people's trajectories and knowing how they move between key locations are fundamental to enhance our understanding of people's daily mobility pattern. Analysis of routing behavior could promote the performance of route recommender systems, help improve transportation infrastructure and reduce traffic congestion. Traditional route recommender systems are based on the assumption that individuals would choose the route that minimizes a cost, usually distance or time. However, some research has shown that many users choose some other routes, rather than the minimum cost path [1]. In fact, a user would choose different route with different purpose even with the same origination and destination. This shows results obtained by traditional optimal road selection theories are not credible when applied to route recommender systems which would try to learn users' preferences, and provide the most probable routes based on the analysis of users' real travel data. However, identifying the routes people really choose and analyzing their routing preference is not an easy task since it's hard to collect those privacy data from users since they are not willing to provide.

Some kinds of data have been used for Origin-Destination analysis, like volunteers' GPS data, probe vehicle data and bus

IC card data. But all of them have a fatal limitation: They all only provide the sample dataset which is too small to represent all people's preferences. Fortunately, the widespread use of mobile phone made it possible to capture everyone's trace [2]. Cellular network data which collected by telecom operators provides rich spatio-temporal information about all the phones accessed to the cellular network. Whereas cellular network data has two defects. One defect is its bad positional accuracy. The location of mobile phone is estimated of the cell tower's signal coverage, thereby the accuracy is much lower than GPS system. According to the statistical data from CMCC(China Mobile Communication Corp), the positioning accuracy of mobile phone is about 50-100 meters. The other one is its poor sampling rate. In most cellular infrastructures today, mobile phones leave a record of their connected cell tower only when some specific event occurs. These two characteristics of cellular network data present a great challenge to extract individual's fine-grained trajectory.

However, we can still extract those probable routes from cellular network data since routes can be regulated as points in a trajectory which can be matched to several real paths with map matching method. In this paper, we extract individual trajectory from cellular network data and acquire different routes over Origin-Destination matching to real paths, such as roads, subway. We define user's daily trajectory with a sequence of stay points and pass-by points. We propose a modified density-based spatial clustering algorithm, named Spatio-Temporal Density Clustering (STDC), to identify stay points. Compared to traditional spatial density clustering (i.e. DBSCAN), the expanding of cluster of STDC not only considers the ϵ -neighborhood in space, but also considers the adjacency in timing sequence. Therefore, STDC could distinguish clusters in the same location with different times. Then, an approach mining different routes over given Origin-Destination is presented. This approach uses Dynamic Time Warping algorithm to measure the similarity of two trajectories, and uses OPTICS clustering and map matching algorithms to find out the routes. Finally, experiments were conducted with real cellular network data in the city of Beijing to validate our methods. The results show that both STDC algorithm and routes mining method are effective.

II. RELATED WORK

Methods of extracting trajectories from GPS are widely developed nowadays. On the contrary, how to use cellular network data is quite a challenge due to its low positioning accuracy and unstable sampling rate. For this reason, a large number of institutions have made beneficial explorations.

Leontiadis developed an algorithm to parse the continuous sector observations and identify the stationary and mobility segments [3]. This algorithm mainly focuses on the preprocessing of sectors, additional information are needed. Isaacman proposed a technique based on clustering and regression for analyzing anonymized cellular network data to identify generally important locations, such as home and work [4,5]. However, this method didn't generate user's daily trajectory. Although many researchers are trying to extract trajectory from cellular network data, there is still a great challenge to find stay points with a high spatial and temporal accuracy. Therefore, we present a modified density-based spatial clustering algorithm named Spatio-Temporal Density Clustering (STDC) to find stay points, which considers the temporality of the sequence and could distinguish the multiple clusters in the same spatial location with different time.

Recently, some institutes focus on Origin-Destination analysis using users' trajectories. Iqbal proposed a methodology to develop OD matrices using cellular network data [6]. They combined the cellular network data and traffic counts data and generated a node-to-node transient OD matrix and they calculated the traffic flow in origin nodes and destination nodes. Alexander presented a method to produce OD trips by purpose and time of day [7]. They calculated the distribution of trip length and flows between home and work locations using mobile phone data. However, their research is mainly focusing on the origin and destination, didn't pay attention to people's moving pattern and routing behavior between origin and destination. Lima used GPS traces generated by 526 private cars to explore their routing behavior [8]. They extracted significant locations, firstly. Then they deployed a clustering algorithm to detect routes. However, the stability of this method relies on the accuracy of GPS data and the clustering algorithm is sensitive to the setting of ϵ . Therefore, we adopt a clustering algorithm that is not sensitive to the position accuracy in order to adapt for cellular network data.

III. DATASET DESCRIPTION AND PRE-PROCESSING

In this paper, we use a dataset consisting of anonymous cellular network data collected by telecom operator during a month in the area of Beijing. General information of the dataset is summarized in Table 1. Each record contains an anonymous user ID, timestamp, longitude, latitude, cell type, event ID, etc.

TABLE I. CELLULAR NETWORK DATASET INFORMATION

Dataset information	value
Number of calls	750.5 million per day
Number of users	14.9 million
Average update cycle	21.7 min
Population of beijing	21.15 million
Area of data coverage	16410.54 km ²

A. User Filtration

Cellular network data are generated when a phone connects to the cellular network including making or receiving calls, sending or receiving text messages, crossing Location Area

Codes (LACs), routinely collected by the network due to stale data that exceeds a pre-configured duration.

Therefore, due to the difference of users' uptime and activeness, the frequency of different users generating records varies greatly. Some users generate just a few records a day, which is not enough for extracting daily trajectory. After analysis, we filtered out about 70% users who generate records at least every 3 hours for the following analysis.

IV. INDIVIDUAL TRAJECTORY EXTRACTING

Identifying stay points from raw records is the core task of extracting trajectory. A stay point is generated from a series of raw records which are clustered in space and continuous in time. Density-based spatial clustering, like DBSCAN, is one of the best ways to identify clusters from the sequence of raw records. However, DBSCAN doesn't consider the temporality of the sequence, therefore it couldn't distinguish the multiple clusters in the same spatial location with different time. As shown in Figure 1.

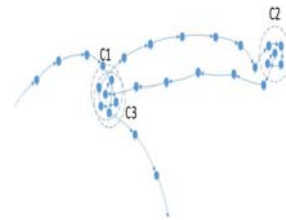


FIGURE I. EXAMPLE OF MULTIPLE CLUSTERS IN THE SAME LOCATION AT DIFFERENT TIME

We present a modified density-based spatial clustering algorithm named Spatio-Temporal Density Clustering (STDC). STDC considers the temporality, and optimizes for the low positioning accuracy and unstable sampling rate of the cellular network data. STDC inherits and modifies the definition of DBSCAN. In addition, it changes the clustering process and adds an input parameter compared to DBSCAN.

A. Definitions for Trajectory

- **Definition 1.** Raw record is pre-processed cellular network data, ignore the field of no use. We represent a raw record as:

$$\text{RawRecord: } R(\text{id}, t, \text{lon}, \text{lat}) \quad (1)$$

Which means a user appeared in the location of (lon,lat) at the time of t.

- **Definition 2.** Stay point is a part of trajectory, which indicates a user keep in a certain space (i.e. office building) for a certain time interval. A stay point SP is generated by a raw record cluster RC:

$$\text{StayPoint: } SP(RC_{(lon,lat)}, RC_{(ts,te)}) \quad (2)$$

Where $RC_{(lon,lat)}$ represents the geometric center of RC and $RC_{(ts,te)}$ represents the starting and ending time of RC:

$$RC_{(lon,lat)} = (\frac{1}{n} \sum_{i=1}^n R_{(i,lon)}, \frac{1}{n} \sum_{i=1}^n R_{(i,lat)}), R \in RC \quad (3)$$

$$RC_{(ts,te)} = (\min(R_{i,t}), \max(R_{i,t})), R \in RC \quad (4)$$

- **Definition 3.** Pass-by point is a part of trajectory, which indicates a passed place when a user move from a stay point to another one. A pass-by point is generated by a raw record which unable to gather into a cluster.

$$\text{PassbyPoint: } PP(R_{(lon,lat)}, R_t) \quad (5)$$

- **Definition 4.** Trajectory is defined as a sequence of stay points and pass-by points to represent a user's trace during one day:

$$\text{Trajectory: } TR(SP_1, SP_2, SP_3, \dots, SP_n) \quad (6)$$

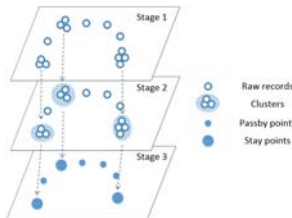


FIGURE II. DEFINITIONS FOR TRAJECTORY

B. Definitions for STDC

- **Definition 5. ϵ -neighborhood:** The ϵ -neighborhood of a point p is the region with the radius of ϵ by the center of p.
- **Definition 6. Directly timing density reachable:** A point q is directly timing density reachable from p if q in the ϵ -neighborhood of p and q is the following point of p in the sequence of time.
- **Definition 7. Timing density reachable:** A point q is timing density reachable from p if there is a path p_1, \dots, p_n with $p_1=p$ and $p_n=q$, where each p_{i+1} is directly timing density reachable from p_i .
- **Definition 8. Core point:** A point p is a core point if the time span of all the points timing density reachable from it (including p) is more than MinTimeSpan.

C. STDC Approach

STDC algorithm works as follows to visit all points:

- 1) In order to find clusters, STDC firstly marks all points in the dataset for unvisited, and sorts the points by timestamp.
- 2) STDC selects the first unvisited point p from the sorted sequence and marks it for visited. If p is a core point, STDC will create a new cluster C and add p into C. Then it will create a set N for points reachable from p.
- 3) For each unvisited q in N, if q is a core point, then add its' all reachable points to N; if q does not belong to any cluster, then add q to C. Until all points in N are visited output C. Otherwise output p as a pass-by point.
- 4) Repeat the above steps until all points are visited.

V. MULTI-ROUTES MINING

Routes mining is divided into three steps:

1) Quantitative description of the difference between two trajectories is critical. We propose a method based on dynamic time warping (DTW) algorithm to calculate the distance between trajectories.

2) We use clustering approach to distribute them into different clusters. Because the number of clusters cannot be known in advance, so we use density-based clustering, OPTICS, rather than the algorithms which need to specify cluster numbers, such as K-means.

3) We implement a map matching process to match the trajectory cluster with the road.

A. Measure Distance between Trips

Dynamic Time Warping (DTW) uses a dynamic programming approach to align the time series and a specific word template so that some distance measure is minimized. The pattern detection task involves searching two time series P with the length of n, and Q with the length of m.

$$P = p_1, p_2, p_3, \dots, p_n \quad (7)$$

$$Q = q_1, q_2, q_3, \dots, q_n \quad (8)$$

The first step is to define a n-by-m distance matrix, where each grid point (i,j) corresponds to an alignment between elements p_i and q_j .

$$D_{\text{Matrix}} = \begin{bmatrix} d(p_1, q_1) & \cdots & d(p_1, q_m) \\ \vdots & \ddots & \vdots \\ d(p_n, q_1) & \cdots & d(p_n, q_m) \end{bmatrix} \quad (9)$$

Where $d(p_i, q_j)$ is the distance between two time series. The definition of distance is the foundation of clustering.

The next step is to define a sequence of matrix element to represent the warping path.

$$W = w_1, w_2, w_3, \dots, w_k \quad (10)$$

According to the analysis of the distance matrix, warping path may have more than one solution. In this paper, we only concern the minimum one for simplicity. In logically, the maximum of similarity between the two time series as the criterion of the similarity search.

$$DTW(P, Q) = \min\left(\frac{1}{K} \sum_{k=1}^K w_k\right) \quad (11)$$

We use the average of w_k rather than the maximum value because the maximum value may affected by the noisy data which would lead to a wrong result.

B. Trajectories Clustering

Trajectories clustering is dividing trajectories into different clusters according to the similarity measure. The objects in the same cluster have a higher similarity, while the objects in different clusters have greater differences. Meanwhile,

clustering analysis for trajectories can also be used as a pre-processing step for other algorithms, like classification and pattern extracting.

In this paper, we use OPTICS algorithm for trajectories clustering, which based on the distance calculated by DTW. We would not use DBSCAN here because DBSCAN is sensitive to the value of ϵ and minPts, meanwhile the similarity distance of trajectories is sensitive to the distance between origin and destination. Although ϵ and minPts are also needed in OPTICS, they only play an assistant role in this algorithm.

C. Map Matching

Map matching is the process of matching trajectory with the road in a digital map, which could find the user's real route in the road network. After that, we analyze the means of transportation the user actually choose in this route. The research for map matching algorithm has mature results in the field of floating car data processing. We adopt a heuristic map matching algorithm in this research [9].

VI. EXPERIMENT AND RESULT

We implement three experiments to validate the effectiveness of our methods. Firstly, we choose the suitable parameters for STDC algorithm. Secondly, we selected user's trajectory to compare their raw records and stay points extracted by STDC algorithm. Finally, we implement the routes mining process for several Origin-Destination pairs.

A. STDC Parameters Setting

In order to select appropriate parameter of ϵ , we draw a scatter diagram for the distribution of distances between adjacent records. As shown in Figure 3, there is a peak in the interval of (500, 600). This indicates that most adjacent stay points have a distance about 500m, so the ϵ we choose must bigger than it. Hence, we set 800 meters as the value of ϵ and 30 minutes as the value of MinTimeSpan in this paper.

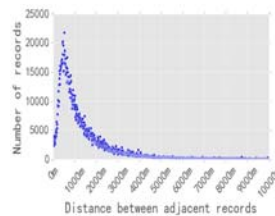


FIGURE III. DISTRIBUTION OF DISTANCE BETWEEN ADJACENT RECORDS

B. Stay Point and Trajectory

This experiment verified the effectiveness of the STDC algorithm through comparing user's raw records and stay points. We selected a user, as shown in Figure 4, he/she has three stay points in his/her one-day trajectory. The first stay point (01:22-06:54) and the third stay point (19:16-23:55) at the same location. The results show that STDC algorithm could correctly distinguish the stay points at the same location with different times.

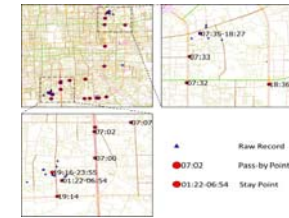


FIGURE IV. EXTRACTED USER'S STAY POINTS

C. Multi-routes over Origin-Destination

In this section, we choose 2 typical commuting OD pairs, OD1: Tiantongyuan-Guomao and OD2: Tongzhou-Zhongguancun. Firstly, we extract all trajectories over the Origin-Destination pair and use our method to cluster them. We compared the clustering results got by OPTICS and DBSCAN, we set $\epsilon = 800$ meters and minPts = 10 for both OPTICS and DBSCAN, the results are shown in Figure 5. For both OD1 and OD2, OPTICS could effectively distribute the trajectories into different clusters and discard the noisy data which could not be used. On the contrary, the DBSCAN's results are not obvious. It is because DBSCAN is sensitive to the parameters setting so that many trajectories are improperly divided into one cluster and many noisy data couldn't be filtered. It shows that OPTICS performs better in this scenario.

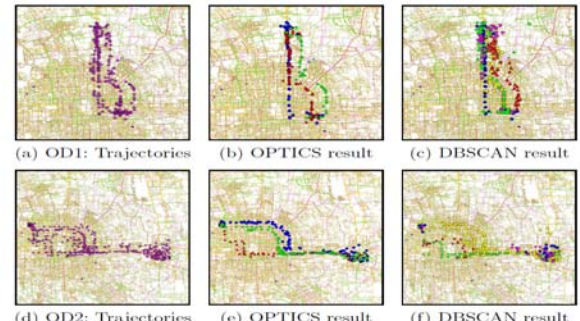


FIGURE V. TRAJECTORIES CLUSTERING RESULTS

Next, we matched the trajectory clusters with the digital map(in this paper, we use Baidu map). Combined with the subway data and bus data, each cluster is matched with a route, as shown in Figure 6. For OD1, the route 1 matched with a bus route, the route 2 matched with a subway route and the route 3 matched with a self-driving route. The ratio of the users who choose these three kinds of routes is about 5:3:2. For OD2, the route 1 and route 2 matched with subway routes and the route 3 matched with a bus route or self-driving route. The corresponding ratio is about 2:4:4. The map matching results show that that the trajectories we extracted are appropriate and the routes we identified are reliable.

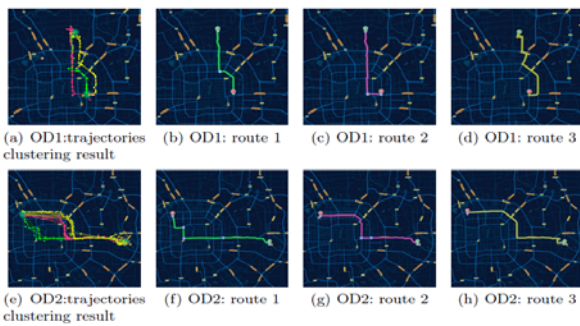


FIGURE VI. MAP MATCHING RESULTS

VII. CONCLUSIONS

How to analyze user's routing preference using cellular network data with low positioning accuracy is a challenge task. Compare with other approaches, we try to present those most probable routes with their probability between Origin-Destination through a novel algorithm named as STDC that extracts user's trajectory from cellular network data and mines multi-routes between Origin-Destination. First of all, we pre-processed the raw data to filter out noisy data. Then we defined the user's daily trajectory and present a new algorithm to identify stay points. This algorithm considered the temporality of points sequence. Then a new approach was presented for mining routes between Origin-Destination. This method used DTW algorithm to measure the similarity between trajectories and used OPTICS divided them into different clusters. Each cluster matched with a route between this Origin-Destination. Finally, we conducted a series experiments to validate our method is effective and practicable. The experimental results show that cellular network data could be used for identifying the different routes between Origin-Destination and count how many people choose the routes.

Our approach and experimental results could be used for urban traffic planning, and even avoid traffic congestion since we know users preferences and change traffic condition in advance. Our future work will focus on trajectory filling techniques, which uses user's a number of days of incomplete trajectories to generate a complete trajectory. This could help us to improve the precision of the method.

ACKNOWLEDGMENT

This research is supported by the National High Technology Research and Development Program of China (863 Program) No.2015AA124103.

REFERENCES

- [1] Lima, A., Stanojevic, R., Papagiannaki, D., Rodriguez, P., & González, M. C. (2016). Understanding individual routing behaviour. *Journal of the Royal Society Interface*, 13(116), 20160021.
- [2] Lane, N. D., Miluzzo, E., Lu, H., & Peebles, D. (2010). A survey of mobile phone sensing. *IEEE Communications Magazine*, 48(9), 140-150.
- [3] Leontiadis, I., Lima, A., Kwak, H., Stanojevic, R., Wetherall, D., & Papagiannaki, K. (2014). From Cells to Streets: Estimating Mobile Paths with Cellular-Side Data. *ACM International Conference on Emerging NETWORKING Experiments and Technologies* (pp.121-132). ACM.
- [4] Isaacman, S., Becker, R., Cáceres, R., Kobourov, S., Martonosi, M., & Rowland, J., et al. (2011). Identifying Important Places in People's Lives from Cellular Network Data. *International Conference on Pervasive Computing* (Vol.6696, pp.133-151). Springer Berlin Heidelberg.
- [5] Isaacman, S., Becker, R., Martonosi, M., Rowland, J., Varshavsky, A., & Willinger, W. (2012). Human mobility modeling at metropolitan scales. *Proceedings of the 10th international conference on Mobile systems, applications, and services* (pp.239-252). ACM.
- [6] Iqbal, M. S., Choudhury, C. F., Wang, P., & González, M. C. (2014). Development of origin-destination matrices using mobile phone call data. *Transportation Research Part C Emerging Technologies*, 40(1), 63-74.
- [7] Alexander, L., Jiang, S., Murga, M., & González, M. C. (2015). Origin-destination trips by purpose and time of day inferred from mobile phone data. *Transportation Research Part C Emerging Technologies*, 58, 240-250.
- [8] Lima, A., Stanojevic, R., Papagiannaki, D., Rodriguez, P., & González, M. C. (2016). Understanding individual routing behaviour. *Journal of the Royal Society Interface*, 13(116), 20160021.
- [9] Wu, D., Zhu, T., Lv, W., & Gao, X. (2007). A Heuristic Map-Matching Algorithm by Using Vector-Based Recognition. *International Multi-conference on Computing in the Global Information Technology* (pp.18). IEEE Computer Society.

Two New Closed Form Approximate Maximum Likelihood Location Methods Based on Time Difference of Arrival Measurements

Wanchun Li^{1,2}, Qiu Tang¹, Yingxiang Li² and Guobin Qian¹

¹School of Electronic Engineering, University of Electronic Science and Technology of China, Chengdu 611731

²School of Communication Engineering, Chengdu University of Information Technology, Meteorological information and Signal Processing Key Laboratory of Sichuan Higher Education Institutes Chengdu 611731

Abstract—In this paper, we propose two new closed form approximate maximum likelihood location methods via time difference of arrival (TDOA) measurements to determine the location of a target. For both two methods, an initial estimation is acquired by least square method in the first step. Then, supposing that the statistical structure of measurement noise are already known, the maximum likelihood function is derived. At last, for method one, we use first order Taylor expand at the initial point to approximate the residual error for nonlinear measurement equation and substitute it into the maximum likelihood function. While for method two, we use second order Taylor expand at the initial point to approximate the maximum likelihood function. At last, we derive the closed-form solution to both of the methods respectively. The computational complexity of our methods and AML method is derived and we analyze the performance of our two methods. The simulation results show that our methods are more accurate because our methods based on maximum likelihood function and have low computational complexity because we iterate only once.

Keywords—TDOA location; maximum likelihood; closed form solution; performance analysis

I. INTRODUCTION

The past few decades, the problem of determining the position of moving or static object(s) by measuring time difference of arrival (TDOA) of received signals has drawn considerable attention, and research on TDOA technologies has made great progress. Now, TDOA technologies are widely used in many areas, including radar, mobile communications, GPS and wireless sensor networks [1-8].

TDOA technologies have been used for target location for a long time, and many algorithms have been proposed. In [9], in order to handle nonlinear location equations, author employs Taylor series expansion so as to linearize it. Unlike [9], we apply Taylor expansion to approach the maximum likelihood equation rather than the location equations. Our methods also have less computational complexity because they need iteration procedure only once. In [10], authors use least-square solution, named as spherical-interpolation (SI). In [11], authors relax the cost function as minimum and maximum function and use two different SDR methods [11-14] for relaxation. In [15], authors propose a bi-iterative method to determine the location or speed of a moving target alternately. Authors derive a closed-form solution through the WLS

expression and employ Gauss-Newton method for a better solution. While our methods derive the closed-form solution through maximum likelihood equation.

In [16], Chan proposed a classical method to manage TDOA problem. When the error of TDOA is small enough, it can attain to CRLB, but when error is large, the performance of the algorithm is not guaranteed. In [6], in order to deal with the non-linear equation, authors apply the Levenberg-Marquardt algorithm and meet great balance between accuracy and computational complexity. Since the Chan method is biased when the measurement noise is large, authors of [17] propose two methods to reduce the bias considerably and achieve the CRLB for distant source location problem.

In [18], authors first change the maximum likelihood equations into two linear equations which coefficients are about unknowns target coordinates (x, y) , with some initial values of (x, y) , the approximate maximum likelihood (AML) solves the linear equations for new (x, y) and updates their coefficients. After five updates, AML selects the (x, y) that minimize the cost function as the solution.

Our method also starts from a maximum likelihood function, unlike [18], we do not need to iterate, which reduces the computation load. Applying the initial guess derived from the least squares method and final results can be derived through a maximum likelihood based closed form solution.

The arrangement of this paper lies follows: section II gives the derivation of our methods, The computer simulation results are shown in section III and our conclusion is drawn in section IV. At last, we analyze the bias and variance for least square location method in section VII.

II. PROPOSED METHOD

In this section, the model and the derivation of our two methods are presented. In this paper, we propose our two methods to determine an individual target position. The measurements we use are the time difference of target-receiver distance. Since the parameter extraction procedure is not considered in our paper, we do not care whether the target itself transmits signal or is illuminated by other kinds of

signals. As for receivers, we have their priori knowledge and know their position precisely.

In TDOA location, we have the measurement equations:

$$\tau_{k1} = \frac{1}{c}(R_k - R_i) \quad k = 2, 3, \dots, M \quad (1)$$

Where:

$$R_k = \sqrt{(\boldsymbol{\theta} - \mathbf{x}_k)^T (\boldsymbol{\theta} - \mathbf{x}_k)} \quad (2)$$

Here $\boldsymbol{\theta}$ is the target position to be determined and its dimension is K . Suppose $K=2$, our problem is based on the 2D plane, and when $K=3$, we locate a target in 3D space. For TDOA hyperbolic location, $K=M$ may cause fake focal point, we assume that $M \geq K+1$ to ensure a unique position solution. \mathbf{x}_k here is the k th receiver position and R_k represents the distance between target and k th receiver. For simplicity, we define:

$$\rho_k = c\tau_{k1} \quad k = 2, 3, \dots, M \quad (3)$$

Thus:

$$\rho_k + R_i = R_k \quad (4)$$

Squaring both sides of the equation (4) and get:

$$\rho_k^2 + 2R_i\rho_k + R_i^2 = R_k^2 \quad (5)$$

Substitute (2) into (5) and obtain:

$$\rho_k^2 + 2R_i\rho_k + 2(\mathbf{x}_k - \mathbf{x}_i)^T \boldsymbol{\theta} + \mathbf{x}_i^T \mathbf{x}_i - \mathbf{x}_k^T \mathbf{x}_k = 0 \quad (6)$$

Where $\boldsymbol{\theta}$ and R_i are unknowns. Note that equation (6) is a series of equations related to subscript from 2 to M. We can rewrite it in the form of matrix as:

$$\mathbf{Au} = \mathbf{b} \quad (7)$$

Where

$$\mathbf{A} = 2 \begin{bmatrix} \mathbf{x}_2^T - \mathbf{x}_1^T & \rho_2 \\ \mathbf{x}_3^T - \mathbf{x}_1^T & \rho_3 \\ \vdots & \vdots \\ \mathbf{x}_M^T - \mathbf{x}_1^T & \rho_M \end{bmatrix} \quad \mathbf{b} = \begin{bmatrix} \rho_2^2 + \mathbf{x}_1^T \mathbf{x}_1 - \mathbf{x}_2^T \mathbf{x}_2 \\ \rho_3^2 + \mathbf{x}_1^T \mathbf{x}_1 - \mathbf{x}_3^T \mathbf{x}_3 \\ \vdots \\ \rho_M^2 + \mathbf{x}_1^T \mathbf{x}_1 - \mathbf{x}_M^T \mathbf{x}_M \end{bmatrix} \quad \mathbf{u} = \begin{bmatrix} \boldsymbol{\theta} \\ R_i \end{bmatrix} \quad (8)$$

Notice that $\boldsymbol{\theta}$ and R_i are related to each other. Thus, a better solution requires decorrelation later, such as literature [16].

In receiver, measurements noise is inevitable. We model noisy TDOA measurements as:

$$\hat{\mathbf{p}} = \mathbf{p} + \mathbf{n} \quad (9)$$

Where

$$\hat{\mathbf{p}} = [\hat{\rho}_2 \ \cdots \ \hat{\rho}_M]^T; \quad \mathbf{p} = [\rho_2 \ \cdots \ \rho_M]^T \quad (10)$$

$$\mathbf{n} = [n_2 \ \cdots \ n_M]^T$$

Normally, measurements noise \mathbf{n} is zero mean Gaussian noise and its covariance matrix is \mathbf{Q} . Therefore, its probability density function is written as:

$$p(n | \boldsymbol{\theta}) = \frac{1}{(2\pi)^{\frac{M}{2}} |\mathbf{Q}|^{\frac{1}{2}}} \exp \left\{ -\frac{1}{2} [\hat{\mathbf{p}} - \mathbf{p}(\boldsymbol{\theta})]^T \mathbf{Q}^{-1} [\hat{\mathbf{p}} - \mathbf{p}(\boldsymbol{\theta})] \right\} \quad (11)$$

The likelihood function of (11) is represented as:

$$L(n | \boldsymbol{\theta}) = \ln p(n | \boldsymbol{\theta}) = -\frac{M}{2} \ln(2\pi) - \frac{1}{2} \ln |\mathbf{Q}| - \frac{1}{2} [\hat{\mathbf{p}} - \mathbf{p}(\boldsymbol{\theta})]^T \mathbf{Q}^{-1} [\hat{\mathbf{p}} - \mathbf{p}(\boldsymbol{\theta})] \quad (12)$$

Omit the constant term and obtain the maximum likelihood solution to it as:

$$\hat{\boldsymbol{\theta}}_{ML} = \min_{\boldsymbol{\theta}} l(\boldsymbol{\theta}) \quad (13)$$

Where

$$l(\boldsymbol{\theta}) = [\hat{\mathbf{p}} - \mathbf{p}(\boldsymbol{\theta})]^T \mathbf{Q}^{-1} [\hat{\mathbf{p}} - \mathbf{p}(\boldsymbol{\theta})] \quad (14)$$

For the sake of solving (14), we make use of the Taylor series location method [9,15] and iterate for the final solution. But the iteration needs a good initial value to void divergence, so we apply least square method to (7) so as to get the initial guess:

$$\hat{\mathbf{u}}_{LS} = (\hat{\mathbf{A}}^T \hat{\mathbf{A}})^{-1} \hat{\mathbf{A}}^T \hat{\mathbf{b}} \quad (15)$$

Where the first two row of $\hat{\mathbf{u}}_{LS}$ is the original value

$$\hat{\boldsymbol{\theta}}_{LS} = \hat{\mathbf{u}}_{LS} (1:2) \quad (16)$$

After we acquire the initial value, we propose two methods for the final determination of target location.

A. Proposed Method 1

Taylor expand $\mathbf{p}(\boldsymbol{\theta})$ at $\hat{\boldsymbol{\theta}}_{LS}$ and ignore terms more than second order and obtain:

$$\mathbf{p}(\boldsymbol{\theta}) = \mathbf{p}(\hat{\boldsymbol{\theta}}_{LS}) + \mathbf{F}(\boldsymbol{\theta} - \hat{\boldsymbol{\theta}}_{LS}) \quad (17)$$

Where

$$\mathbf{F} = \frac{\partial \mathbf{p}}{\partial \boldsymbol{\theta}^T} \Big|_{\boldsymbol{\theta} = \hat{\boldsymbol{\theta}}_{LS}} \quad (18)$$

Substituting (17) into (13), yields:

$$\hat{\boldsymbol{\theta}}_{ML} = \min_{\boldsymbol{\theta}} \left[\tilde{\mathbf{p}} - \mathbf{F}(\boldsymbol{\theta} - \hat{\boldsymbol{\theta}}_{LS}) \right]^T \mathbf{Q}^{-1} \left[\tilde{\mathbf{p}} - \mathbf{F}(\boldsymbol{\theta} - \hat{\boldsymbol{\theta}}_{LS}) \right] \quad (19)$$

Where

$$\tilde{\mathbf{p}} = \hat{\mathbf{p}} - \mathbf{p}(\hat{\boldsymbol{\theta}}_{LS}) \quad (20)$$

Solving (19) and obtain the closed-form solution as:

$$\hat{\boldsymbol{\theta}}_{ML} = \hat{\boldsymbol{\theta}}_{LS} + (\mathbf{F}^T \mathbf{Q}^{-1} \mathbf{F})^{-1} \mathbf{F}^T \mathbf{Q}^{-1} \tilde{\mathbf{p}} \quad (21)$$

B. Proposed Method 2

Taylor expand likelihood function (14) at $\boldsymbol{\theta} = \hat{\boldsymbol{\theta}}_{LS}$ and omit high-order terms more than third order and get:

$$l(\boldsymbol{\theta}) = l(\hat{\boldsymbol{\theta}}_{LS}) + \mathbf{p}^T \left[\hat{\mathbf{p}} - \mathbf{p}(\hat{\boldsymbol{\theta}}_{LS}) \right] + \frac{1}{2} \left[\hat{\mathbf{p}} - \mathbf{p}(\hat{\boldsymbol{\theta}}_{LS}) \right]^T \boldsymbol{\Omega} \left[\hat{\mathbf{p}} - \mathbf{p}(\hat{\boldsymbol{\theta}}_{LS}) \right] \quad (22)$$

Where

$$\begin{aligned} \mathbf{p} &= \frac{\partial l(\boldsymbol{\theta})}{\partial \boldsymbol{\theta}} \Big|_{\boldsymbol{\theta} = \hat{\boldsymbol{\theta}}_{LS}} = \mathbf{F}^T \mathbf{Q}^{-1} \left[\hat{\mathbf{p}} - \mathbf{p}(\hat{\boldsymbol{\theta}}_{LS}) \right] \\ \boldsymbol{\Omega} &= \frac{\partial^2 l(\boldsymbol{\theta})}{\partial \boldsymbol{\theta} \partial \boldsymbol{\theta}^T} \Big|_{\boldsymbol{\theta} = \hat{\boldsymbol{\theta}}_{LS}} = \mathbf{J} + \mathbf{S} \end{aligned} \quad (23)$$

Where

$$\mathbf{S} = \sum_{i=2}^M \sum_{j=2}^M \left(\phi_{ij} r_j \frac{\partial^2 r_i}{\partial \boldsymbol{\theta} \partial \boldsymbol{\theta}^T} + r_i \phi_{ij} \frac{\partial^2 r_j}{\partial \boldsymbol{\theta} \partial \boldsymbol{\theta}^T} \right) \quad (24)$$

$$\mathbf{J} = \sum_{i=2}^M \sum_{j=2}^M \left(\phi_{ij} \frac{\partial r_j}{\partial \boldsymbol{\theta}} \frac{\partial r_i}{\partial \boldsymbol{\theta}^T} + r_i \phi_{ij} \frac{\partial r_i}{\partial \boldsymbol{\theta}} \frac{\partial r_j}{\partial \boldsymbol{\theta}^T} \right) = 2 \mathbf{F}^T \mathbf{Q}^{-1} \mathbf{F} \quad (25)$$

$$\frac{\partial r_i}{\partial \boldsymbol{\theta}} = \begin{bmatrix} \frac{x - x_1}{\sqrt{(x - x_1)^2 + (y - y_1)^2}} & \frac{x - x_i}{\sqrt{(x - x_i)^2 + (y - y_i)^2}} \\ \frac{y - y_1}{\sqrt{(x - x_1)^2 + (y - y_1)^2}} & \frac{y - y_i}{\sqrt{(x - x_i)^2 + (y - y_i)^2}} \end{bmatrix}_{x=\hat{x}_{LS}, y=\hat{y}_{LS}} \quad (26)$$

$$\phi_{ij} = (\mathbf{Q}^{-1})_{ij} \quad (27)$$

$$\frac{\partial^2 r_i}{\partial \boldsymbol{\theta} \partial \boldsymbol{\theta}^T} = \begin{bmatrix} r_{i\theta 11} & r_{i\theta 12} \\ r_{i\theta 21} & r_{i\theta 22} \end{bmatrix}_{x=\hat{x}_{LS}, y=\hat{y}_{LS}} \quad (28)$$

And:

$$\begin{aligned} r_{i\theta 11} &= \frac{(y - y_i)^2}{\left[(x - x_1)^2 + (y - y_1)^2 \right]^{\frac{3}{2}}} - \frac{(y - y_i)^2}{\left[(x - x_i)^2 + (y - y_i)^2 \right]^{\frac{3}{2}}} \\ r_{i\theta 12} &= r_{i\theta 21} = \frac{-(x - x_1)(y - y_i)}{\left[(x - x_1)^2 + (y - y_1)^2 \right]^{\frac{3}{2}}} + \frac{(x - x_i)(y - y_i)}{\left[(x - x_i)^2 + (y - y_i)^2 \right]^{\frac{3}{2}}} \\ r_{i\theta 22} &= \frac{(x - x_1)^2}{\left[(x - x_1)^2 + (y - y_1)^2 \right]^{\frac{3}{2}}} - \frac{(x - x_i)^2}{\left[(x - x_i)^2 + (y - y_i)^2 \right]^{\frac{3}{2}}} \end{aligned}$$

The newton iteration solution thus can be represented as:

$$\boldsymbol{\theta}_{ML_Newton} = \hat{\boldsymbol{\theta}}_{LS} - \boldsymbol{\Omega}^{-1} \mathbf{p} \quad (29)$$

C. Steps for Proposed Method

The main steps of our two methods are presented in the Table 1 and Table 2 below.

TABLE I. THE CALCULATION PROCEDURE FOR PROPOSED LOCATION METHOD 1

Step 1	Acquire initial guess using (15), where \mathbf{A} and \mathbf{b} are calculated by (8)
Step 2	obtain the maximum likelihood using (14)
Step 3	Taylor expand $\mathbf{p}(\boldsymbol{\theta})$ at $\hat{\boldsymbol{\theta}}_{LS}$ and ignore terms more than second order and obtain (17)
Step 4	Using the closed-form expression in (21) to get the final location results

TABLE II. THE CALCULATION PROCEDURE FOR PROPOSED LOCATION METHOD 2

Step 1	Acquire initial guess using (15), where \mathbf{A} and \mathbf{b} are calculated by (8)
Step 2	obtain the maximum likelihood using (14)
Step 3	Taylor expand likelihood function (14) at $\boldsymbol{\theta} = \hat{\boldsymbol{\theta}}_{LS}$ and omit high-order terms more than third order and get (22)
Step 4	Using the closed-form expression in (29) to get the final location results

III. SIMULATION RESULTS

Monte Carlo simulations had been performed in this section to testify the performance of AML and our method comparing with CRLB.

A. Performance of Different TDOA Measurement Noise Variance

In this part, eight sensors are located at $xr(k) = R \times [\cos(k\pi/4), \sin(k\pi/4)]$, $k = 1, 2, \dots, 8$. where R is the radius of the circle and $R = 3000m$. The emitter is fixed at $(1000, 500)m$. The TDOA measurement noises are zero-mean Gaussian white noise, and the variance of the noise

varies from 10^{-10} m to $10^{3.2}$ m.

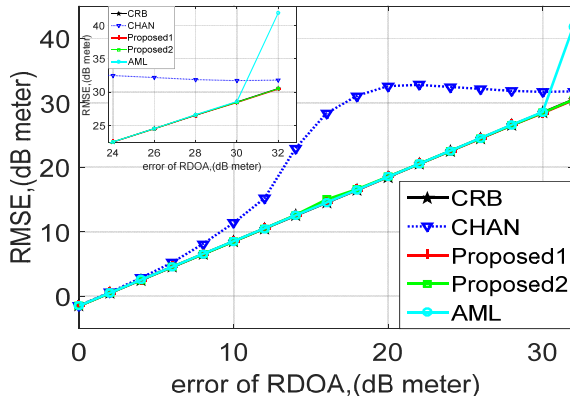


FIGURE I. THE POSITION ERROR OF DIFFERENT TDOA NOISE VARIANCE

Figure I compare the position error of different TDOA noise variance, where $RDOA = 10 \times \log_{10}(c \times TDOA)$. The RMSE used in Figure I is defined as $10 \times \log_{10} E\{[(\hat{x} - x)^2 + (\hat{y} - y)^2]\}$. We run Monte-Carlo simulation 10000 times to draw Figure I. As we can see from the figure, CHAN method is able to achieve CRLB at moderate SNR, and it starts to derivate CRLB at around 10dB. Our methods, however, start to derivate at around 30 dB and are little better than AML method.

B. Performance of Different Algorithm for Different Number of Sensors

In this section, receivers are located at

$x_m = R \times [\cos(m\pi/4), \sin(m\pi/4)]$, $m = 1, 2, \dots, M$. TDOA variance are fixed and set M from 4 to 10 to obtain table 3.

TABLE III. THE RMSE OF DIFFERENT RECEIVERS WHEN $\delta_{TDOA}^2 = 5$

$\delta_{TDOA}^2 = 5$	4	5	6	7	8	9	10
Proposed 1	5.16 73	4.59 04	4.11 15	3.84 26	3.58 30	3.39 88	3.23 78
Proposed 2	5.18 21	4.58 95	4.11 15	3.84 28	3.58 18	3.39 79	3.23 80
AML	5.28 61	4.67 15	4.18 33	3.89 80	3.63 21	3.45 47	3.29 50
CRLB	5.15 21	4.57 20	4.16 55	3.85 37	3.60 39	3.39 75	3.22 30

TABLE IV. THE RMSE OF DIFFERENT RECEIVERS WHEN $\delta_{TDOA}^2 = 10$

$\delta_{TDOA}^2 = 10$	4	5	6	7	8	9	10
Proposed1	10.2 782	9.222 7	8.361 1	7.773 2	7.207 5	6.815 0	6.487 2
Proposed2	10.6 849	9.230 5	8.336 3	7.766 0	7.206 7	6.809 2	6.482 4
AML	10.4 198	9.388 7	8.464 8	7.910 7	7.291 0	6.930 6	6.607 1
CRLB	10.3 034	9.144 1	8.330 9	7.707 5	7.207 8	6.794 9	6.446 1

Table 3 and table 4 show the RMSE versus the number of sensors for different TDOA noise levels when the noise variances were identical. As can be seen from tables, our proposed method slightly outperformed AML method, and is also able to attain to CRLB.

C. Performance of Different Algorithm for Near Field Situation (Target-receiver Distance Being Not Too Far).

The coordinates of the ten measuring sensors are $[-42, -12]$, $[-26, 30]$, $[-8, 40]$, $[16, 18]$, $[36, 6]$, $[24, -36]$, $[-12, 24]$, $[-20, 0]$, $[15, -15]$, $[-30, -40]$ m and the emitter is fixe at $[0, 0]$ m. And the noise variance ranges from -10dB to 14dB so as to draw fig.

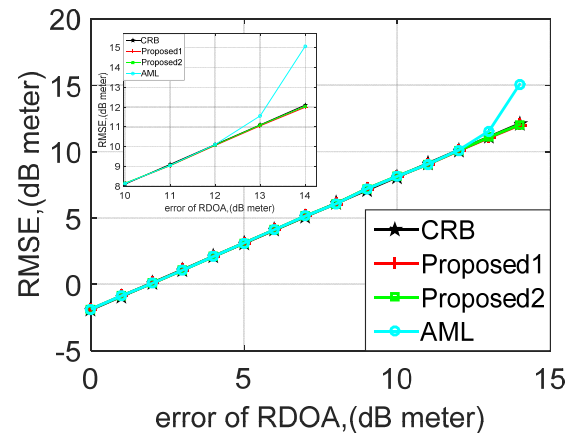


FIGURE II. RMSE OF PROPOSED TWO METHODS AND AML METHOD IN NEAR FIELD CONTEXT

Figure II compares the performance of our two methods and AML method under the near filed context. Our methods are slightly better than AML method, and proposed 1 functions even better than proposed method 2.

IV. CONCLUSION

In this paper, we proposed two closed-form approximate likelihood location method meant for TDOA location systems. Derivation and simulation both verify that our methods performance better than CHAN and AML method. Moreover, our methods apply Gauss-Newton iterate method only once for a better solution, which reduce the computation complexity and have less calculation load than AML method.

ACKNOWLEDGMENT

Manuscript December 13, 2017, this work was supported the Funds for the Meteorological information and Signal Processing Key Laboratory of Sichuan Higher Education Institutes, PRC.

Li WanChun, Tang Qiu and Qian GuoBin are with School of Electronic Engineering, University of Electronic Science and Technology of China, Chengdu 611731, PRC..

Li YingXiang is with School of Communication Engineering, Chengdu University of Information Technology, Meteorological information and Signal Processing Key

Laboratory of Sichuan Higher Education Institutes Chengdu, PRC..

This work was supported by Meteorological information and Signal Processing Key Laboratory of Sichuan Higher Education Institutes (No. QXXCSYS201702).

REFERENCES

- [1] Misra, P., and Enge, P.: 'Global Positioning System: Signal, measurements and performance' (Ganga-Jamuna Press, Lincoln, MA, 2006, 2nd edn)
- [2] Caffery, J.J.: 'Wireless location in CDMA cellular radio systems' (Springer, Massachusetts, USA, 2000)
- [3] Patwari, N., et al.: 'Locating the nodes: cooperative localisation in wireless sensor networks', *IEEE Signal Process. Mag.*, 2005, 22, (4), pp. 54–69
- [4] Zekavat, R., and Buehrer, R.M.: 'Handbook of position location: Theory, practice and advances' (Wiley, Natick, MA, USA, 2012, 27th edn)
- [5] Huang, Y., Benesty, J., Elko, G.W., and Mersereau, R.M.: 'Real-time passive source localization a practical linear-correction least-squares approach', *IEEE Trans. Speech Audio Process.*, 2001, 9, (8), pp. 943–956
- [6] Mensing, C., and Plass, S.: 'Positioning algorithms for cellular networks using TDOA'. Proc. IEEE Int. Conf. on Acoustics, Speech and Signal Processing, Toulouse, France, May 2006, Vol. 4, pp. 513–516
- [7] Coraluppi S.: 'Multistatic sonar localization', *IEEE J. Ocean. Eng.*, 2006, 31, (4), pp. 964-974
- [8] P. C. Chestnut, "Emitter location accuracy using TDOA and differential doppler," *IEEE Trans. Aerosp. Electron. Syst.*, vol. AES-18, no. 2, pp. 214–218, Mar. 1982.
- [9] Wade H Foy. Position-Location Solutions by Taylor-Series Estimation [J]. IEEE Transactions on Aerospace and Electronic Systems. VOL. AES-12, NO.2 MARCH 1976.
- [10] J. O. Smith and J. S. Abel, "Closed-form least-squares source location estimation from range-difference measurements," *IEEE Trans. Acoust., Speech, Signal Process.*, vol. ASSP-35, pp. 1661–1669, Dec. 1987.
- [11] ENYANG X, ZHI D, DASGUPTA S. Reduced Complexity Semidefinite Relaxation Algorithms for Source Localization Based on Time Difference of Arrival [J]. Mobile Computing, IEEE Transactions on, 2011, 10(9): 1276-82.
- [12] LUI K, CHAN F, SO H C. Semidefinite Programming Approach for Range-Difference Based Source Localization [J]. Signal Processing, IEEE Transactions on, 2009, 57(4): 1630-3.
- [13] LUO Z, MA W, SO A M C, et al. Semidefinite relaxation of quadratic optimization problems [J]. Signal Processing Magazine, IEEE, 2010, 27(3): 20-34.
- [14] BISWAS P, LIAN T C, WANG T C, et al. Semidefinite programming based algorithms for sensor network localization [J]. ACM Transactions on Sensor Networks (TOSN), 2006, 2(2): 188-220.
- [15] Guo Hui Zhu, Da Zheng Feng. Bi-iterative method for moving source localization using TDOA and FDOA measurements [J]. ELECTRONICS LETTERS, January 2015 Vol.51 No.1 pp. 8-10
- [16] Chan, Y.T., and Ho, K.C.: 'A simple and efficient estimator for hyperbolic location', *IEEE Trans. Signal Process.*, 1994, 42, (8), pp. 1905–1915.
- [17] Ho, K.C.: 'Bias reduction for an explicit solution of source localization using TDOA', *IEEE Trans. Signal Process.*, 2012, 60, (5), pp. 2101–2114
- [18] Chan, Y.T., and Huang, H.Y.C.: 'Exact and approximate maximum likelihood localisation algorithms', *IEEE Trans. Veh. Technol.*, 2006, 55, pp. 10–16.

A Dynamic Symmetric Fully Homomorphic Encryption Mechanism for Privacy Protection of Cooperative Precision Positioning Cloud Service

Dibin Shan^{1,2,*}, Xuehui Du^{1,2}, Wenjuan Wang^{1,2} and Nan Wang¹

¹Zhengzhou Institute of Information Science and Technology, Zhengzhou, China

²National Digital Switching System Engineering and Technological Research Center, China

*Corresponding author

Abstract—With the increasingly serious threat of privacy protect, the collaborative precision positioning cloud service urgently needs to be carried out homomorphic encryption protection for sensitive data. But the existing asymmetrical approaches are inefficient and are not practical for applications, while the symmetric approaches has low security. In this paper, based on the MORE and Enhanced MORE symmetric homomorphic encryption algorithms, we proposes a fully homomorphic encryption mechanism called DSFHE, with dynamic key generation, symmetric encryption and random encryption. Analysis and experimental results show that the proposed mechanism reduces the cipher-text storage overhead and execution time, which also can prevent the strong attacks.

Keywords—cooperative precise positioning; fully homomorphic encryption; symmetric encryption; cloud computing; cipher-text computation

I. INTRODUCTION

Collaborative precision positioning service cloud have a large amount of data and users, which is accessed frequently. Users' privacy data stored in cloud platform are easy to reveal, which need to be encrypted for privacy protection. But it is difficult to calculate for the data after encryption. The data on the cloud platform are facing security risks, such as external attacks to steal and leakage of internal operations staff. Traditional encryption technology can protect the confidentiality of the data processing. But data query, statistics, analysis and calculation are operated in the cloud data center, data cannot be treated under encryption. Data decryption reprocessing efficiency is quite low, and Sensitive data and privacy data are easy to leak to the attackers.

Existing cipher-text computation can perform computation on encrypted data, as encryption of computation on plaintext in theory. But asymmetric homomorphic encryption technology is faced with low calculation efficiency and serious problem with enforcing cloud platform to adjust to algorithms requirement, while the symmetric homomorphic encryption is not enough secure. Homomorphic encryption technology is difficult to get practical application in cloud computing. Therefore, it is time to put forward a kind of secure and efficient new homomorphic encryption algorithm, which can break through the bottleneck

of homomorphic encryption on the efficiency, safety and practical, achieving its application in the cloud data resource security protection.

The rest of this paper is organized as follows, Section 2 describes the Related Work of homomorphic encryption algorithm. Section 3 construct a dynamic symmetric fully homomorphic encryption mechanism. Security analysis and performances of DSFHE mechanism are given in Section 4. Conclusions are drawn in Section 5.

II. RELATED WORK

In 1978, the problem of homomorphic encryption [1] (privacy) was introduced by Rivest. According to its development stage [2], it can be divided into Partial Homomorphic Encryption, class Homomorphic Encryption, and Fully Homomorphic Encryption. Partial homomorphic encryption (PHE) only supports a single type of cipher domain homomorphism (add or multiply homomorphism). For example, the RSA algorithm only supports multiplicative homomorphism, and the GM algorithm only supports additive homomorphism. The class homomorphic encryption (SHE) can support the addition and multiplication of the finite number of cipher-text fields. Fully homomorphic encryption (FHE) can achieve arbitrary cipher-text addition and multiplication. In 2009, Gentry firstly proposed fully homomorphic encryption based on the Ideal case [3]. However, the fully homomorphic encryption algorithms are confronted with problems such as complex operation process, low operation efficiency and large cost of key generation.

The homomorphic encryption algorithms with symmetric key are also proposed. The MORE [4] algorithm supports the fully homomorphic encryption calculation, but whose security is not high. It is vulnerable to the chosen plaintext attack. The multi-user homomorphic encryption scheme [5] is designed, which also faces the chosen plaintext attack threat [6]. The enhanced MORE algorithm [7] supports key dynamic generation randomly, which needs both sides to negotiate synchronous secret keys beforehand. Adoption of different symmetric key may affect the results of cipher-text computation. Homomorphic encryption algorithm based on threshold scheme [9] was proposed, whose shared keys r remains unchanged, protected by threshold function.

In conclusion, homomorphic encryptions with asymmetric key are inefficient and not practical for applications. While the confidentiality and randomness of K in the symmetric homomorphic encryption mechanism need to be improved.

III. HYBRID FULLY HOMOMORPHIC ENCRYPTION MECHANISM

A. Design Concept

We propose a dynamic symmetric fully homomorphic encryption mechanism for cloud computing data security protection. Considering the advantage of symmetric scheme, the scheme takes homomorphic encryption with symmetrical keys on plaintext encryption in order to improve the calculation efficiency, which also improves the randomness of symmetric key and changes the simple linear relations by comprehensively utilizing of the displacement, the random number, dynamic key, which prevent chosen plain text attacks.

A Fully homomorphic encryption consists of four algorithms [2]:

(1) $Gen: U \rightarrow key$, is a randomized algorithm that takes a security parameter U as input, and outputs a secret key.

(2) $Enc: (key, P) \rightarrow C$, Enc is an Encryption algorithm that takes key and a plaintext P as input, and outputs a cipher text C .

(3) $Dec: (key, C) \rightarrow P$, Dec is a Decryption algorithm that takes key and a cipher text C

P as input, and outputs a plaintext.

(4) $Cal: (P, F) \rightarrow (C, F)$, $f \in F$, $(p_1, p_2, \dots, p_n) \in P$, F is a set of P on operation, for $f \in F$, $(p_1, p_2, \dots, p_n) \in P$. The operation on the P can be converted to the operation on the C by Cal, whose results are equivalent.

Definition 1, Homomorphic [2]: The encryption algorithm ε and operation on plaintext P satisfy Eq. 1, if $\forall p_1, p_2, \dots, p_n \in P$.

$$Dec: (key, Cal: ((c_1, c_2, \dots, c_n), f)) = (p_1, p_2, \dots, p_n). \quad (1)$$

B. Key Generation and Protection

In order to overcome the security problem of key in the MORE algorithm, the key sequence is generated and randomly selected by the stream cipher algorithm, and the public key algorithm is used to encrypt the protection of K , which is a $n \times n$ matrix.

The key stream sequence S is generated by stream cipher algorithm. A new sequence S' consists of $n^2/4$ elements (n is an even number) which are randomly selected from the S , as a child of a key matrix SK . A non-zero invertible matrix K is comprised of matrix SK and the identity matrix I . The inverse matrix [7] of the K is the K^{-1} . The S' , SK , K and K^{-1} is shown as Eq. 2, 3, 4 and 5.

Public key cryptography algorithm (RSA) are used to encrypt the key sequence S' , which is deleted after encryption of plaintext and random sequence.

$$S' = \{s_{11}, s_{12}, \dots, s_{1j}, s_{21}, s_{22}, \dots, s_{2j}, \dots, s_{j1}, s_{j2}, \dots, s_{jj}\}, \left(j = \frac{n}{2}\right), \quad (2)$$

$$SK = \begin{bmatrix} s_{11} & s_{12} & \cdots & s_{1j} \\ s_{21} & s_{22} & \cdots & s_{2j} \\ \cdots & \cdots & \cdots & \cdots \\ s_{j1} & s_{j2} & \cdots & s_{jj} \end{bmatrix}, \left(j = \frac{n}{2}\right), \quad (3)$$

$$K = \begin{bmatrix} SK & SK + I \\ SK - I & SK \end{bmatrix}, \quad (4)$$

$$K^{-1} = \begin{bmatrix} SK & -(SK + I) \\ -(SK - I) & SK \end{bmatrix}. \quad (5)$$

C. Encryption Operation

The permutation sequence $Q = \{q_1, q_2, \dots, q_L\}$ is generated by the stream cipher algorithm. After the permutation, the permuted plaintexts of P is divided into H blocks, where L is plaintext length, $H = 2L/n$. Each blocks M_i is a diagonal matrix which contains $n^2/4$ elements, whose $n/2$ elements belong to P . The random sequence $R = \{r_1, r_2, \dots, r_L\}$ is generated by the stream cipher algorithm. Each blocks R_i is a diagonal matrix which contains $n^2/4$ elements, whose $n/2$ elements belong to R . Matrix MR_i is constructed with M_i and R_i , which is $n \times n$ matrix. M_i , R_i and MR_i are shown as Eq. 6, 7, and 8.

$$M_i = \begin{bmatrix} m_{i1} & 0 & \cdots & 0 \\ 0 & m_{i2} & \cdots & 0 \\ \cdots & \cdots & \cdots & \cdots \\ 0 & 0 & \cdots & m_{ij} \end{bmatrix}, \left(1 \leq i \leq \left\lceil \frac{2L}{n} \right\rceil, j = \frac{n}{2}\right). \quad (6)$$

$$R_i = \begin{bmatrix} r_{i1} & 0 & \cdots & 0 \\ 0 & r_{i2} & \cdots & 0 \\ \cdots & \cdots & \cdots & \cdots \\ 0 & 0 & \cdots & r_{ij} \end{bmatrix}, \left(1 \leq i \leq \left\lceil \frac{2L}{n} \right\rceil, j = \frac{n}{2}\right). \quad (7)$$

$$MR_i = \begin{bmatrix} M_i & 0 \\ 0 & R_i \end{bmatrix}. \quad (8)$$

For each plaintext matrix, the corresponding cipher-text matrix $C_i = K^{-1} * MR_i * K$.

With symmetric encryption algorithm, Q and R are encrypted by the randomly generated keys T , which is encrypted with asymmetric encryption. After encryption, Q , R , and T can be eliminated.

D. Decryption

The replacement sequence Q , random number sequence R and key matrix K are decrypted by using the private key of

legitimate users. The plaintext MR_i is decrypted from the received cipher text C_i . $MR_i = K * C_i * K^{-1}$. M_i is reproduced from MR_i by permutation sequence Q and random sequence R .

E. Homomorphic Calculation

Addition and Multiplication calculation are shown as Eq. 9 and Eq. 10.

$$\begin{aligned} E(M1) + E(M2) &= K^{-1} \begin{bmatrix} M1 & 0 \\ 0 & R1 \end{bmatrix} K + K^{-1} \begin{bmatrix} M2 & 0 \\ 0 & R2 \end{bmatrix} K \\ &= K^{-1} \begin{bmatrix} M1 + M2 & 0 \\ 0 & R1 + R2 \end{bmatrix} K \\ &= E(M1 + M2) \end{aligned} \quad (9)$$

$$\begin{aligned} E(M1) * E(M2) &= K^{-1} \begin{bmatrix} M1 & 0 \\ 0 & R1 \end{bmatrix} K * K^{-1} \begin{bmatrix} M2 & 0 \\ 0 & R2 \end{bmatrix} K \\ &= K^{-1} \begin{bmatrix} M1 * M2 & 0 \\ 0 & R1 * R2 \end{bmatrix} K \\ &= E(M1 * M2). \end{aligned} \quad (10)$$

Obviously, the DSFHE scheme is FHE because it satisfies the both homomorphic properties.

F. Application Example

For individual users of collaborative precision positioning cloud service system, the client generate dynamic key, permutation sequence, and random sequence, who take advantage of DSFHE algorithm to encrypt plaintext data and the key. The cipher-text data are sent to the data center. The users submit the computation instructions to the data center. After the data center computes the cipher-text, the calculation results are fed back to the users. Only legitimate users can decrypt and restore the calculated result in plain text by using their private key.

IV. SECURITY AND PERFORMANCE ANALYSIS

A. Privacy and Key Security

The plaintext encryption key K is randomly selected and dynamically generated from the key stream, which ensures the randomness and dynamic of the key. The key is protected by the public key algorithm, which guarantees the confidentiality of the key. Hybrid fully homomorphic encryption mechanism can be immune to choose plaintext attack. On the one hand, the permutation of plaintext sequence and participation calculation of random grouping R_i , have changed the simple linear relationship between plaintext and cipher-text. On the other hand, the dynamic random key has increased the complexity of the relationship between plaintext and cipher-text.

B. Execution Time

DSFHE, Enhanced MORE and MORE are done in ThinkPad X230 laptop with specifications of Processor Intel Core i5 CPU, 2.5GHZ, quad-core processor, 4GB of memory. The execution time is studied for different plaintexts size, and for each plaintext size the mean execution time is measured for 200 iterations. Because each M_i encryption increased with random matrix R_i and K encryption compared with Enhanced MORE algorithm, the execution time of DSFHE is between Enhanced MORE and MORE, as shown in figure1. Compared with MORE algorithm, the increase of random number group is smaller, and the computation time cost is reduced.

C. Cipher-text Storage Overhead

In DSFHE mechanism, every plaintext data block M_i ($n/2^2$ valid elements) is encrypted to cipher-texts group C_i (n^2 elements). In addition to storage cipher-texts of the permutation sequence Q and the random number sequence R , the whole storage overhead of cipher-texts needs $2*m*n$ bytes per m bytes of plaintext. The storage overhead of cipher-texts is $m*n*n$ per m bytes plaintext in MORE algorithm. Enhanced MORE algorithm needs $m * n$ bytes of the cipher-texts to storage for m bytes of plaintexts, as shown in figure 2. But the store overhead for random number Matrix R makes sense for improving data security of symmetric encryption.

V. SUMMARY

In this paper, we proposed a dynamic symmetric fully homomorphic encryption mechanism. Based on the comprehensive MORE and Enhance MORE algorithm, the scheme encrypt plaintext with symmetric key, with encrypting symmetric key, permutation sequence and random number sequence by asymmetric encryption schemes. This scheme reduces the cipher storage overhead, which improved the security key and ability against the attacks. However, the algorithm proposed in this paper have not solve the problem of realizing homomorphic computation and security sharing of multi-user cipher text with different keys, which needs further study.

ACKNOWLEDGEMENTS

This work is supported by National Key R&D Plan of China (Grant No.2016YFB0501901).



FIGURE I. EXECUTION TIME

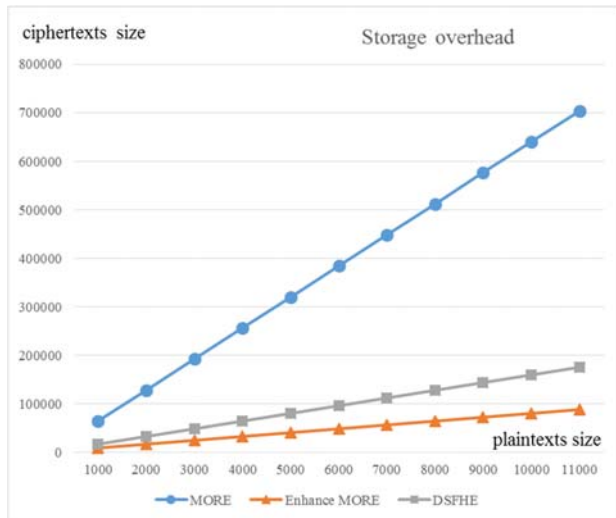


FIGURE II. STORAGE OVERHEAD

REFERENCES

- [1] Rivest R, Shamir A, Adleman L, A method for obtaining digital signatures and public-key cryptosystems, *Commun ACM* 1978, 21(2):120-126.
- [2] LI Zong-Yu, GUI Xiao-Lin, GU Ying-Jie, A Survey on Homomorphic Encryption Algorithm and Its Application in the Privacy preserving for Cloud Computing, *Journal of Software*, <http://kns.cnki.net/kcms/detail/11.2560.TP.20171017.1337.001.html>.
- [3] Gentry C, A fully homomorphic encryption scheme, Phd thesis, Stanford University, 2009.
- [4] Kipnis A., Hibshoosh E, Efficient methods for practical fully homomorphic symmetric-key encryption, randomization and verification, *IACR Cryptology ePrint Archive* 2012:1-20.
- [5] Xiao L., Bastani O., Yen I.-L, An efficient homomorphic encryption protocol for multi-user systems, *Citeseer, IACR Cryptology ePrint Archive* 2012:193-212.
- [6] Vizár D, Vaudenay S, Cryptanalysis of chosen symmetric homomorphic schemes, *Studia Scientiarum Mathematicarum Hungarica* 2015, 52(2):288-306.
- [7] Khalil Hariss, Hassan Noura, Abed Ellatif Samhat, Fully Enhanced Homomorphic Encryption algorithm of MORE approach for real world applications. *Journal of Information Security and Applications* 34 (2017):233-242.
- [8] Zhou Jun, Cao Zhenfu, Dong Xiaolei, etal, Security and privacy in cloud-assisted wireless wearable communications: challenges, solutions and future directions [J].*IEEE Wireless Communications*, 2015, 22(2):136-144.

Research on Temperature Control System Based on WeChat Remote Operation

Xuchen Guan¹, Yingqing Guo^{1,*} and Xinghuai Huang²
 Mechanical and Electronic Engineering College, Nanjing Forestry University, Nanjing, China
 Nanjing Dongrui Damping Control Technology Co., Ltd, Nanjing, China
 *Corresponding author

Abstract—In this paper, a temperature control system using WeChat remote operation is designed, including a design of the connection method, circuit and improved PID control algorithm. Besides, the STM32f103 control board with ENC28J60 Ethernet transceiver chip, WeChat server, connection and data exchange mode of WeChat official account are introduced. At the same time, the usage of WeChat open interface will be introduced. The control instructions can be sent to the temperature control motherboard by users or researchers through WeChat official account, and the current temperature and historical temperature of the temperature control box can be inquired by accessing the device server.

Keywords—WeChat remote operation; integral separation; anti-integration saturation; ZigBee

I. INTRODUCTION

In the field of modern scientific research, ambient temperature is often an important test point that need to take into consideration, which is also an important factor that affects the experimental results. In many experimental environments, the ambient temperature can be more sensitive to the experimental requirements in a long time. Under the condition of dangerous test environments and long test period, the need emerges that temperature control system can be intelligent and can be controlled. In addition, the system can record the test temperature anytime and anywhere makes the system more usable [1-2].

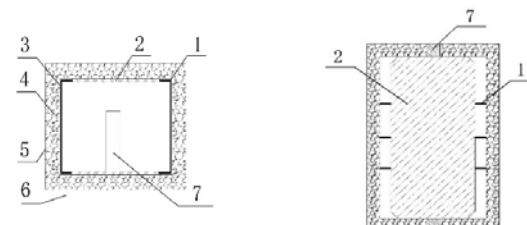
With the development of the ZigBee[3-7], this concept is introduced to the field of instrument science gradually. S. Amendola used RFID for remote temperature control[8]. Genuine remote control is not realized because of the limited operating distance of RFID. X. X. Zheng proposed a remote temperature control system based on GSM[9]. The amount of data to transmiss by GSM is limited, and it is difficult to realize cloud processing. WeChat platform itself has three very friendly basic conditions: the first is the mature platform technology, the second is the huge user group, and the third is the open user platform. These three conditions make WeChat become the ideal control terminal of the intelligent device system for users[10].

In this design, the APP is not a necessity while the user only need to subscribe to the WeChat official account and input device number, temperature value in the official account. WeChat official account sends the data to the WeChat server. Then WeChat server sends the data to the ENC28J60 Ethernet transceiver chip through the URL interface. ENC28J60

Ethernet transceiver chip send data to the STM32f103 through the serial port. After that, STM32f103 adjust the temperature by operating silicon rubber heating plate or refrigeration compressor with modified PID algorithm. In this process, the control instructions can be sent to the temperature control motherboard by users or researchers through WeChat official account, and the current temperature and historical temperature of the temperature control box can be inquired by accessing the device server.

II. SYSTEM COMPOSITION

The temperature control box containing silicone rubber plate for heating, refrigeration compressor for refrigeration whose type is Kangpu QD35, a small AC compressor. The box is made of two layers of iron - nickel alloy steel plate, and the steel plate is filled with adiabatic material, the size of the box is 30mm*25mm*45mm. The door of box can be opened in the front of box, with hinges linked between them, and the installation of the handle on the door is convenient for the installation of the test device. The Silicone rubber heating plate is installed in the front and back of the wall of the box, and compressor heat pipe is wined around inner layer of box. The compressor is installed on the rear side of the box to ensure that the radiator is well ventilated. The lower wall slotting on the box to the front wall is easy for the temperature control box to install on the stress loader. (The appearance of the temperature control box is shown in FIGURE I.)



(a)THE MAIN VIEW PROFILE (b) THE LEFT VIEW PROFILE
 1. Condensing copper pipe of compressor; 2. Silicone rubber heating plate; 3. Inner layer iron nickel alloy steel plate; 4. Aerogel felt; 5. Outer layer iron nickel alloy steel plate; 6. Handle; 7. Mounting hole of stress loader.

FIGURE I. STURCTURE OF TEMPERATURE CONTROL BOX

The circuit connection of the system is shown in FIGURE II. Among them, the solid-state relay whose type is SSR-D3805HK-E will be isolated by optical coupled isolator to prevent electromagnetic interference generated by AC 220V to STM32f103ZET6, and to prevent damaging motherboard due to the improper insulation. The temperature heated by the

silicon rubber heating plate is controlled through the opening and closing process of the solid-state relay at a certain frequency. The digital potentiometer whose type is X9C103S controls the rotating speed of the compressor by controlling the

conduction angle of the Silicon controlled voltage regulator whose type is BTA16-600B, through changing of the resistance, in which case, the low temperature can be adjusted accordingly.

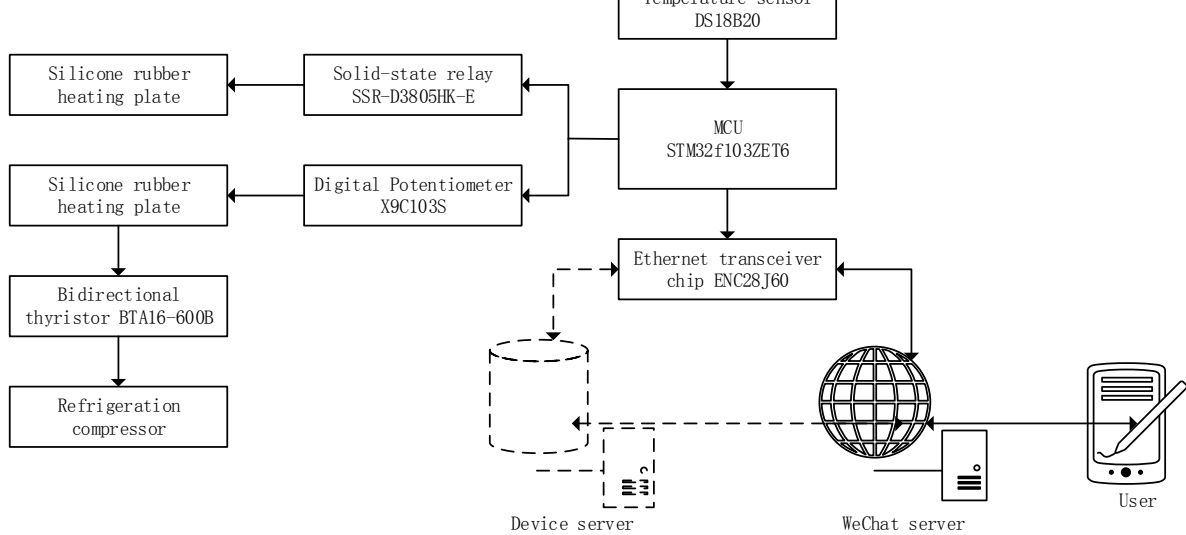


FIGURE II. CIRCUIT CONNECTION BLOCK DIAGRAM

The device server, whose role is to restore data for cloud operations is optional, and ENC28J60 can communicate directly with the WeChat server or communicate with the WeChat server through a device server. If the device server is required to provide data storage and query functions, it can be implemented by Linux on PC virtual machines or embedded devices such as ARM series. The Ethernet module can be replaced with a WIFI module to achieve good mobility

The WeChat server is a relay between the user and the device, and the WeChat public provides a good man-machine interface and a good operating experience. Users can send messages to WeChat official account conveniently through mobile devices such as mobile phones and pad. Messages of WeChat official account sent by users will be transmitted to the MCU by WeChat server, thus remote control and state query for devices can be realized. However the WeChat open platform only provides message forwarding services, and customized service system is required for a variety of custom function, in this case, equipment server or very be necessary to realize efficient remote control.

III. CONTROL ALGORITHM

Traditional PID is a simple and efficient way to control which will have some defects through, one of which is that the integral link makes the dynamic characteristics of the system worse. This section will give a modified PID algorithm based on the system model. The control block diagram of the whole system is illustrated in FIGURE III.

Traditional PID expression is:

$$T_u(t) = K_p(T_{err}(t) + \frac{1}{T_i} \int_0^t T_{err}(\zeta) d\zeta + T_d \frac{dT_{err}(t)}{dt}) \quad (1)$$

Where, $T_{err}(t) = T_{set} - T_{now}(t)$ that means the dynamic error, $T_u(t)$ is the set value of the temperature, K_p , T_i and T_d are proportionality constants.

While d_t is initialized as 20ms which is produced by TIM3 of STM32f103ZET6, the formula can be discretized as:

$$T_u(k) = K_p T_{err}(k) + K_i \sum_{n=0}^k T_{err}(n) + K_d (T_{err}(k) - T_{err}(k-1)) \quad (2)$$

Where, $K_i = 1/T_i$, $K_d = T_d$.

The purpose of introducing integral in PID control is to eliminate static error and improve control precision. However, in the process of setting the start and end or greatly increase or decrease, great deviation of output system within a short period of time will cause the integral accumulation of PID operation. For that reason, the ultima control volume exceeds the limit control corresponding to the maximum range of operation permitted by the executing agency, which results in larger overshoot and even greater oscillation.

Considering the integral separation, this formula can be rewritten as:

$$T_u(k) = K_p T_{err}(k) + K_i \sum_{n=0}^k T_{err}(n) \cdot \varepsilon(e_{max} - |T_{err}(k)|) + K_d (T_{err}(k) - T_{err}(k-1)) \quad (3)$$

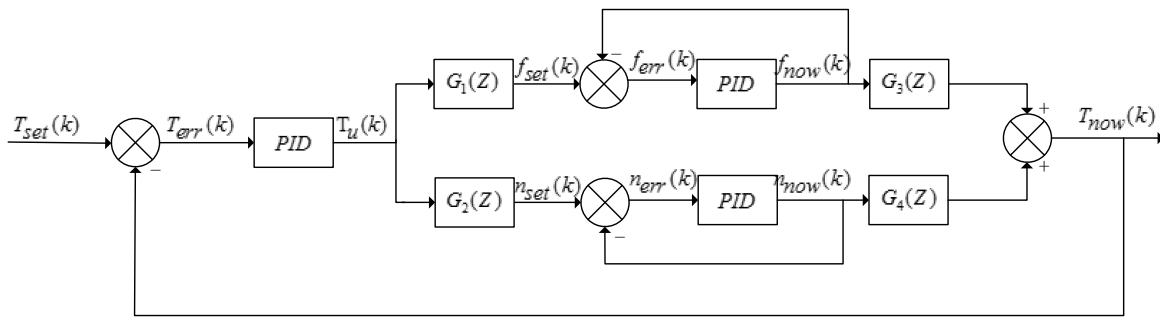


FIGURE III. THE CONTROL BLOCK DIAGRAM OF THE WHOLE SYSTEM

Where, $\varepsilon = (e_{\max} - |T_{err}(k)|)$ is the step function, e_{\max} is a constant that is related to the system.

The heating and cooling processes of the temperature control system are all highly time-dependent control processes; especially the nonlinearity of the relationship between motor speed and voltage is particularly evident in low voltage and high voltage areas.

In order to solve this problem, anti-integral saturation is needed. The cooling inner ring is designed as:

$$n_u(k) = K_p n_{err}(k) + K_i \left(\sum_{n=0}^{k-1} n_{err}(n) + \Delta'(k) \right) + K_d (n_{err}(k) - n_{err}(k-1)) \quad (4)$$

$$\Delta'(k) = n_{err}(k) \cdot (\varepsilon(n_{\min} - n_{err}(k)) - \varepsilon(n_u(k) - n_{\max})) \cdot \varepsilon(n_{\max} - |n_{err}(k)|) \quad (5)$$

Where, $n_u(k)$ is expected speed, $n_{err}(k)$ is the speed error, n_{\max} is the maximum speed of approximate linear region, n_{\min} is the minimum speed of approximate linear region.

When the temperature T_{now} is lower than $T_{set} - \Delta T$, the solid-state relay is enabled and the silicon rubber heating plate begins to work. The difference in temperature is converted to the frequency of the opening and closing of the solid-state relay. Here, a cycle is composed of Opening and closing time, and the opening time occupies 50% of the entire cycle. The trigger frequency of the solid-state relay can be described as:

$$f_{relay} = T_u(k) \cdot \mu \quad (6)$$

Where, μ is a frequency product constant set before which depends on the thermal efficiency of the silicon rubber heating plate and the maximum allowable trigger frequency of the solid state relay, f_{relay} is usually limited between the range that $0 < f_{relay} < 100\text{Hz}$. (High f_{relay} will exceed the allowable frequency of the solid-state relay and cause damage.)

ΔT is set up to prevent overshoot caused by rapid oscillation considering that an inert interval can slow down the oscillation. When the temperature T_{now} is higher than $T_{set} + \Delta T$, the refrigeration compressor start working. The rotational speed n of the refrigeration compressor can be described as:

$$n_u(k) = \frac{9550P}{T} = \frac{9550P \times \omega_1 [(R_s + \frac{R_r}{S})^2 + \omega_1^2 (L_{ls} + L'_{lr})^2]}{\frac{3n_p U_s^2 R_r}{S}} = \frac{9550P \times \omega_1 [(R_s + \frac{R_r}{S})^2 + \omega_1^2 (L_{ls} + L'_{lr})^2]}{\frac{3n_p \times \sum_{n=0}^k (\sqrt{2U_i} \sin \frac{\delta T_u(k)}{R_{sum}}) \times R_r}{S}} \quad (7)$$

Where, δ is the product constant for calculating the setting resistance of the digital potentiometer whose type is X9C103, P is power supplied, U_i is the effective value of the input voltage, ω_1 is the circumferential frequency of power supply, s is the transfer rate, n_p is rated speed, T_{sum} is the total resistance of the digital potentiometer, R_s , R_r , L_{ls} , L'_{lr} are structural parameters of the motor.

Cascade PID control is adopted in the system both in heating and refrigeration link. The integral separation and integral saturation theory are used for each PID controller. The outer ring is a temperature ring and the inner ring is the ring of the solid-state relay and the speed ring of the compressor. $T_u(k) \cdot G_i(Z)$ obtained by the outer ring is the target value of the inner ring. $f_{now}(k)$, $n_{now}(k)$ are the feedback of the inner ring, respectively.

In this model, $G_1(Z) = \mu$ as described above. $G_2(Z)$ can be described as:

$$G_2(Z) = \frac{\mathcal{L}[Q(k)]}{\mathcal{L}[T_u(k)]} \quad (8)$$

$$Q(k) = \frac{(9550P \cdot \omega_1 [(R_s + \frac{R_r}{S})^2 + \omega_1^2 (L_{ls} + L_{lr})^2])}{3n_p \cdot \sum_{n=0}^k (\sqrt{2U_i} \sin \frac{\delta T_u(k)}{R_{sum}})^2 \cdot R_r} \quad (9)$$

The transfer function $G_3(Z)$ and $G_4(Z)$ are related to many factors such as the performance of the equipment, the heat transfer rate and the temperature outside the box. The accurate transfer function of $G_3(Z)$ and $G_4(Z)$ can not be calculated, and specific analysis is not given here due to their complexity and uncertainty.

In this system, the feedback for calculation $T_{err}(k)$ is realized by the temperature sensor DS18B20. The sensor will send data to MCU through the one-wire bus directly, in which case the system does not need to spend too much resources and time on the AD conversion. The accuracy of the system is determined by the accuracy of $T_{err}(k)$, so the system uses 3 sensors for median filtering and mean filtering to obtain accurate errors. As temperature measured is the ambient temperature simulated by equipment, three sensors must be effectively suspended in the air.

IV. IMPLEMENTATION OF REMOTE OPERATION

The device server consists of STM32f103 and ENC28J60 Ethernet transceiver chips. The device server provides an interface URL to exchange data with the WeChat server. When accessing the WeChat platform API, URL, Token, and EncodingAESKey generated randomly are needed[11] (as shown in TABLE I).

TABLE I. MEANINGS OF NOUNS

Name	Meaning
URL	for receiving data from the server
Token	for the generation of a signature
Encoding	as a message body to decrypt the key
AESKey	

After providing the message, WeChat server will send GET request to the URL address to fill in, checking the signature sent by WeChat server to verify whether the message comes from WeChat server.

Access_token is the global unique interface call credential for the official account, and access_token is used when the WeChat official account call each interface. Developers need to be properly preserved. The storage of access_token must retain at least 512 character spaces.

When sending the request, three parameters required are grant_type, access_token and appid. The parameter grant_type is to obtain access_token to complete client_credential. The parameter appid is applied for third party certification and the parameter secret certificate is required for third party user key, i.e. appsecret. Normally, WeChat server will return the JSON packet to the official account.

After verification, the connection between WeChat server and user device server is effective. Users can realize remote control and status query indirectly through the communication

between WeChat official account and devices. What the user needs is just a mobile device to realize this process.

When setting the temperature, users can choose the device and set the temperature through the menu bar at the bottom of the WeChat official account, which is visualized. After receiving the data sent by WeChat server, the message will be packed into a string, for example, "Device: 001, Temp: 20", and execute it strictly. When STM32f103ZET6 receives the data package, it will get the device number of temperature control box that is 001, and it needs to reach a constant temperature of 20 degrees. When the user need to query the current temperature of the temperature control box, a request is sent to the WeChat official account, such as "Device: 001, Query". After receiving a string send by the WeChat server, the device server saves the string firstly and then use the regular expression regular expression syntax to detect that whether the word "Query" is involved in the string. If the word does exists, the corresponding value will be find with key "001". The temperature values sent to the device server by STM32f103ZET6 will be saved in the device server in the form of a dictionary in advance.

V.CONCLUSION

Combined with the example of this design, the improved PID algorithm is given based on the mechanical characteristic model of the motor and the heating model of the silicone rubber. The error of the temperature control box can be limited to 0.5°C through the three loop cascade PID algorithm with integral separation and anti-integral saturation. Integral separation ensures the fast response of the system. The anti-integral saturation theory avoids the delay caused by the defect of asynchronous motor.

The development of the Internet of things and the use of the open platform of WeChat make the remote control and state query of the equipment be realized. A solution to the remote operation is given with a good use of the platform. Under the condition of dangerous test environment and the test which is long distance away or needs long period, users can control and monitor the temperature control box through the WeChat official account.

Besides, the cloud interfaces (such as the GIZWITS, <http://www.gizwits.com/>) provided by many vendors have also made the development of the Internet of things develop rapidly which can be an alternative to the device server. Cloud providers provide storage space for data, and of course, the interface of HTML control involved. With these cloud service platforms, users can query the previous temperature state and analyze the previous data. With these tools, MCU only needs to send data to a fixed URL to control and manage the device.

ACKNOWLEDGMENT

This research is financially supported by the National Key Research and Development Program of China (2016YFE0119700), Jiangsu Training Programs of Innovation and Entrepreneurship for Undergraduates of China (201710298123H). These supports are gratefully acknowledged.

REFERENCES

- [1] C. Jiang, Z. Li, Y. Zhou, X. Qin and Z. Zhao, "Design of constant temperature boiler system with fuzzy control and remote monitoring function", IEEE International Conference on Communication Problem-Solving. pp. 38-42, 2016.
- [2] F. Hong, "Design of Remote Monitoring System based on Fuzzy Control of Furnace Temperature," Advanced Materials Research. vol. 630, pp.241-244, 2012.
- [3] D. Kyriazis and T. Varvarigou, "Smart, Autonomous and Reliable Internet of Things," Procedia Computer Science. vol.21, pp. 442-448, 2013.
- [4] L. K. Wadhwa, R. S. Deshpande and V. Priye, "Extended shortcut tree routing for zigbee based wireless sensor network," Ad Hoc Networks, vol. 37(P2), pp. 295-300, 2016.
- [5] M. Nitti, R. Girau, L. Atzori, Trustworthiness management in the social Internet of things. IEEE Transactions on Knowledge and Data Engineering, 2014.
- [6] R. Wang, L. Yang and D. Tang, Research and implementation of video monitoring system based on android and embedded web server. Electronic Design Engineering. 2016.
- [7] D. W. Zhang and X. J. Xie, Research on network virtual instrument. Applied Mechanics & Materials, vol. 432, pp. 603-608. 2013.
- [8] S. Amendola, G. Boveseccchi, A. Palombi, P. Coppa and G. Marrocco, "Design, calibration and experimentation of an epidermal rfid sensor for remote temperature monitoring," IEEE Sensors Journal. vol. 16(19), pp.7250-7257,2016.
- [9] X. X. Zheng, L. R. Li and Y.J, A GSM-Based Remote Temperature and Humidity Monitoring System for Granary, vol.44, pp.01060.
- [10] W. An, J. Li, B. Li, J. Qi and F. Liao, F, Design and implementation of intelligent control system based on wechat. Electronic Test,2017
- [11] Open platform. <https://open.weixin.qq.com>. (2017, Oct 20)

Anti-sunlight Jamming Technology of Laser Fuze

Xiangjin Zhang^{1,*}, Ruoyu Wu¹, Chengfang Shen¹ and Wei Dai²

¹ZNDY of Ministerial Key Laboratory, Nanjing University of Science and Technology, Nanjing 210094, China

²63963 army, China

*Corresponding author

Abstract—Environmental elements, especially sunny weather, can easily interfere with the operation of a pulsed laser fuze. The solar radiation entering the detection system causes the fuze to produce a “false alarm.” Consequently, the bomb may not work accurately. On the basis of the traditional theory of spectral radiation and the detection principle, this study establishes a transmission model of the solar radiation with loss medium damage to analyze the characteristics of sunlight interference. This work studies and simulates anti-sunlight methods, from the receipt of echo signals entering the receiving system to the reduction of the sunlight entering the system. Finally, on the basis of the small impact of laser detection systems, this study builds a test platform to verify the anti-sunlight measures.

Keywords—laser fuze; anti-sunlight; detection technology

I INTRODUCTION

A pulsed laser fuze is a laser detection system whose operation requires high accuracy and is affected by unavoidable external disturbances. The sun, as the largest source of radiation, covers a wide range of wavelengths [1,2]. The spectral response range of several common laser detectors at present is within this range of wavelength coverage. When sunlight enters the receiving field and is received with the target echo signal, the judgment of the target echo signal by the system is affected and the detection capability of the system is seriously reduced. Conventional ammunition is currently widely used, but its general size is small and the occupancy of the fuze is restricted. Meanwhile, the components of conventional ammunition are often loaded with tens of thousands of g because of the limit of their launching environment. Currently, the solar radiation interference of laser imaging systems and space borne laser detection systems and alarm technologies have been studied in depth [3]. The research on the anti-sunlight interference of ammunitions in low-load emission environments, such as missiles, has developed but is not suitable for conventional ammunition in low-load environments. Reducing or eliminating sunlight interference has become a primary research subject related to improving the detection performance of the miniaturized impact laser near fry fuze. According to the research requirements of the pulsed laser fuze against sunlight interference, this work establishes a transmission model that is based on classical optical radiation theory for the corresponding carrier and proposes schemes for resisting sunlight interference. Experimental results from simulation and verification tests are also provided.

II ANALYSIS OF CHARACTERISTICS OF SUNLIGHT INTERFERENCE

According to relevant tests, strong laser detection systems in environments with solar radiation are prone to false alarms and unstable detection distance. Therefore, a solar radiation transmission model needs to be established, and the characteristics of sun interference have to be analyzed. This study establishes an atmospheric transmittance model for miniaturized impact laser detection systems to address the uncertainty of target location and the influence of environmental factors by combining the advantages of the calculation method of two atmospheric transmittances [4], an empirical formula, and table lookup.

Factors affecting atmospheric transmittance include atmospheric absorption and scattering. According to Lambert Bill's law, the expression of atmospheric transmittance is as follows:

$$\tau_d(\lambda) = \tau_s(\lambda)\tau_a(\lambda) \quad (1)$$

$\tau_a(\lambda)$, $\tau_s(\lambda)$ indicate the transmittances associated with absorption and scattering, respectively, and $\tau_d(\lambda)$ is a function of wavelength lambda λ , atmospheric thickness, and medium density ρ .

In this study, a pulsed laser with a detection band of 905 nm is used, and the spectral response range of the typical photo detector is 400–1100 nm. The main absorption component in the atmosphere is water vapor, and the absorption of carbon dioxide and ozone is not apparent to the aforementioned band[5]. When atmospheric transmittance is calculated, the absorption of water vapor by the solar radiation is mainly considered, and the atmospheric transmittance formula can be simplified as

$$\tau_a(\lambda) = \tau_{a_{H_2O}}(\lambda)\tau_s(\lambda) \quad (2)$$

The absorption of water vapor is generally expressed as precipitation ω and expressed as

$$w = 10^{-3} H_r H_a / d \quad (3)$$

By using the engineering water vapor spectral transmittance formula proposed by Leckner et al. in McClatchey [5],

$$\tau_a(\lambda) = \tau_{a_{H_2O}}(\lambda) = \exp\left[-0.2358k_{a_{H_2O}} \cdot w \cdot \frac{m_r}{(1+20.27k_{a_{H_2O}} \cdot w \cdot m_r)^{0.45}}\right] \quad (4)$$

$k_{a_{H_2O}}$ is the spectral absorption coefficient of water vapor.

This coefficient can be found in the table [5]. m_r is the relative mass of the atmosphere at standard atmospheric pressure. In a cloudless atmosphere, atmospheric scattering is mainly Rayleigh scattering of solar radiation in air. Spectral transmittance is expressed by using the coefficient proposed by Leckner for the scattering of air to the solar radiation in the atmosphere in response to the Rayleigh scattering of atmospheric air molecules.

$$\tau_{y\lambda} = \exp(-0.00835\lambda^{-4.08})m_a \quad (5)$$

Solar spectral radiance is expressed according to Planck's radiation law and the definition of radiation emittance and by using the earth orbit eccentricity correction factor g by Daffie and Backman [6] as

$$L(\lambda T_s) = M(\lambda T_s) \cdot g = \frac{c_1}{\lambda^5} \frac{1}{e^{\frac{c_2}{\lambda T_s}} - 1} \cdot (1 + 0.033 \cos \frac{2\pi n}{365}) \quad (6)$$

A laser detector is coaxial with the projectile and the surface of the detector changes with the change in the spatial attitude of the projectile. Conventional artillery, especially for such low-extension ballistic guns as tank guns, is not vertically incident to the surface of the laser detection and receiving optical system. To thoroughly study the interference of sunlight to the laser detection system and the subsequent anti-interference technology, the solar radiation power model of the tilting surface is established. In this study, the solar radiation transmission model is created at a given time, and the inclined sun radiation is as shown in Figure I.

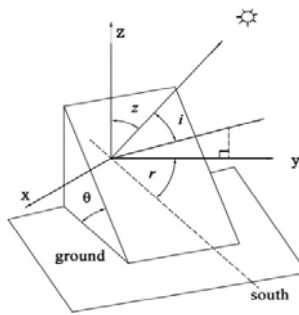


FIGURE I. SOLAR RADIATION ON INCLINED PLANE

In Figure I, θ is the angle between the inclined and horizontal planes of the detecting device, h is the sun height angle, r is the azimuth of the slope, and z is the zenith angle.

The expression of the incident angle i of the sun [7] is

$$\cos i = \cos \theta \sinh + \sin \theta \cosh \cos(a - r) \quad (7)$$

According to Formulas (6) and (7), the expression of the solar direct spectral irradiance on the inclined plane $E_\lambda(\theta, r)$ is

$$E_\lambda(\theta, r) = \varepsilon_\lambda L(\lambda T_s) \tau_d(\lambda) \Delta\Omega \cos i = \frac{\pi \varepsilon_\lambda L(\lambda T_s) \tau_d(\lambda) R_s^2 \cos i}{R_{se}^2} \quad (8)$$

$\Delta\Omega$ denotes the stereoscopic angle of the sun relative to the earth.

The expression of the full-band solar radiation illuminance on the inclined plane is

$$E(\theta, r) = \int_0^\infty [E_\lambda(\theta, r)] d\lambda \quad (9)$$

This research focuses on studies related to the maximum influence time of solar radiation on the receiving system during summer afternoons.

Forward detection is generally used for laser detection systems in conventional ammunition. Direct, reflected, and scattered sunlight enter the receiving field. The photo detector produces the random fluctuating noise voltage through photoelectric conversion, thereby decreasing the signal-to-noise ratio (SNR) of the detection system. Given the basic characteristics of sun interference, the filter and the adjustment of the bandwidth of the receiving circuit are considered to improve the SNR of the system to achieve the effect of anti-interference.

III SIMULATION OF ANTI-SUNLIGHT INTERFERENCE

The model of the space position of the detection target and the typical detection device are established as shown in Figure II.

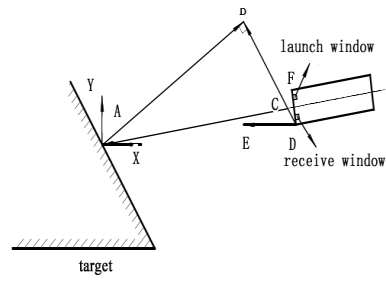


FIGURE II. DETECTING DEVICE AND SPACE POSITION OF DETECTION TARGET

$\angle EDF = \theta$ is the angle between the surface of the detector and the horizontal plane. $\angle BAC = \beta$ is the angle between the optical axis of the detection device and the surface of the detection target. $\angle BDE = \gamma$ is the angle between the target surface and the horizontal plane. The relationship among the three is denoted as $\beta + \gamma = \theta$.

The typical parameters of the system are as follows: laser power $P_t = 75W$, photosensitive diameter $d = 5mm$, emission efficiency of optical system $k_e = 0.8$, optical receiving system efficiency $k_r = \tau_t$, receiver aperture optical system $A_r = 2 \times 10^{-4} m^2$, target reflectivity $\rho = 0.3$, atmospheric attenuation coefficient at a given distance from laser $\alpha(r) = 0.1956$, $\lambda = 905nm$, quantum efficiency $\eta = 0.9$, average quantum efficiency $\bar{\eta} = 0.58$, and inclination of target surface $\beta = 68^\circ$.

By using the typical expression of echo power [8,9], the following is obtained:

$$P_r = \frac{P_t K_e K_r A_r \rho \bar{\eta} \cos \beta}{\pi S^2} e^{-2\alpha r} \quad (10)$$

A. Simulation of Filter Light Interference Suppression

Under intense sunlight, the echo energy of the system decreases with the increase in detection distance and the SNR of the system cannot meet the detection requirements. To suppress the solar radiation entering the receiving field of view, a certain measure of spectral filtering must be implemented.

A spectral filter is used to restrain the solar radiation energy that enters the receiving system. A 905 nm narrowband filter with bandwidths of 100, 80, 60, 40, and 20 nm is obtained for numerical simulation. The number of sunlight photons entering the receiving system is shown in Figure III.

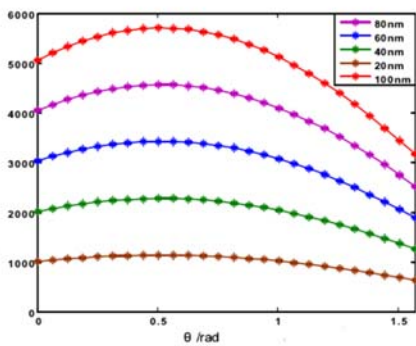


FIGURE III. FILTERING EFFECT OF DIFFERENT BANDWIDTH FILTERS

After the filter is added to the spectrum detection system, the solar radiation entering the receiving system can be effectively suppressed. The narrower the bandwidth of the filter, the better the filter effect. In the suppression of the filter bandwidth of 20 nm, the number of solar radiation entering the sub-receiving system is only approximately 1000. Therefore, the selected spectrum filter is suitable for solar radiation suppression and produces a good effect.

B. Simulation of Circuit Bandwidth Interference Suppression

Limiting the bandwidth of the receiving system reduces the amplitude of the target echo signal, shortens the rising time,

and decreases the SNR of the system. Meanwhile, limiting the bandwidth of the system can effectively reduce the equivalent noise of the receiving system and improve the SNR. Therefore, an appropriate bandwidth should be selected for the receiving circuit to suppress sunlight interference.

The bandwidth of the system directly affects the mean square value of the circuit noise. Figure IV shows the effect of the receiving system bandwidth on the SNR at various detection distances.

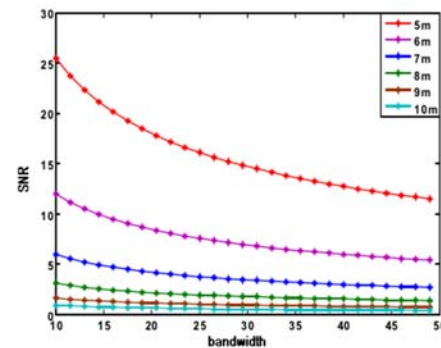


FIGURE IV. RELATIONSHIP CURVES BETWEEN SYSTEM EQUIVALENT BANDWIDTH AND SYSTEM SNR

When the detection distance is certain, the bandwidth has a great influence on the receiving system. The smaller the bandwidth, the higher the SNR. Furthermore, the bandwidth has a nonlinear relationship with the detection distance. However, when the system bandwidth is too narrow, the receiving system does not match the echo pulse signal. Consequently, the echo signal is distorted and the performance of the detection system is affected. Therefore, selecting the appropriate bandwidth of the receiving system plays an important role in laser fuze operation against sunlight interference and signal reception.

IV EXPERIMENT

A. Spectral Filtering Experiment

On the basis of the small-impact laser detection system, an acquisition experiment of the echo waveform of the detection target is conducted. The waveform acquisition device adopts a Tektronix MD04106-6 oscilloscope; the sampling rate is 5 GS/s, and bandwidth is 1 GHz. The system uses a pulse laser emission frequency of 3 KHz, and the gain of the receiving system is approximately 69 dB.

The noise size of the system without sunlight radiation is measured. Then, the collected echo signals are introduced into the data processing software, and the root mean square is calculated. The size of the system noise without sunlight is measured; the weak light in the room is negligible relative to the sunlight. An outdoor test platform is then constructed for the outdoor verification experiment of sunlight interference suppression.

The sunlight irradiance shown by the sun power meter is $1235 W \cdot m^{-2}$ under cloudless outdoor conditions (without considering the tiny floating). The receiving system does not

add spectral filters. A data acquisition device is used to collect echo signal waveforms from different detection distances. These data are imported into a data processing software to obtain the waveforms shown in Figure V.

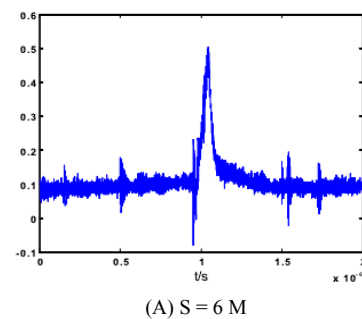
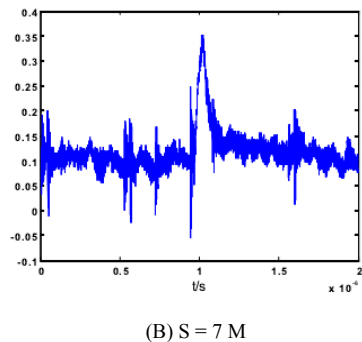
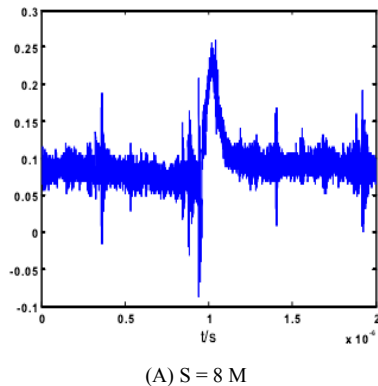


FIGURE V. WAVEFORMS OF TARGET ECHO SIGNAL WITHOUT FILTER AT DIFFERENT DETECTION DISTANCES

The echo signal is undulating, and a partial noise signal is processed. The root mean square of the system noise is 51.7 mV. The SNRs at detection distances of 6, 7, and 8 m are approximately 9, 6.3, and 4.5, respectively.

When the test environment and system parameters are constant, the irradiance of the sun is $1201 \text{W} \cdot \text{m}^{-2}$. The echo waveforms of the detection target at distances of 6, 7, and 8 m with the 905 nm filter are shown in Figure VI.

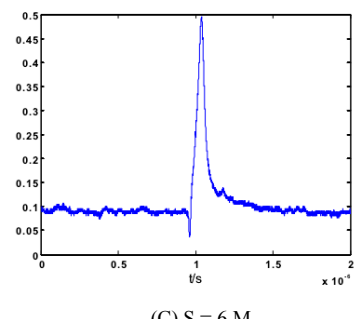
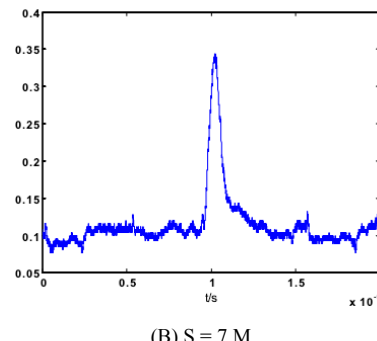
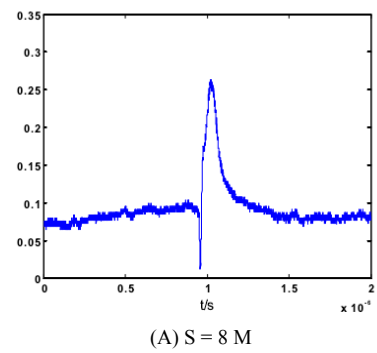


FIGURE VI. WAVEFORMS OF TARGET ECHO SIGNAL WITH FILTER AT DIFFERENT DETECTION DISTANCES

According to the abovementioned method, the system SNRs at distances of 6, 7, and 8 m are approximately 31, 21.8, and 15, respectively. Thus, the SNR of the system is noticeably improved. These experimental results show that adding the matching spectral filter to the front end of the detector can largely reduce the influence of the external solar radiation on the echo signal and improve the SNR of the receiving system.

B. Circuit Bandwidth Experiment

The bandwidth of the receiving circuit of the laser detection system directly affects the SNR.

The effect of sunlight interference is verified under the same environment and the same system parameters by setting the equivalent bandwidth Δf of different circuit by using the oscilloscope of the experimental platform to acquire the noise signal size with solar radiation in the background. The circuit

bandwidth used in this work is established by the bandwidth selection of the oscilloscope.

Figure VII shows the waveforms collected under the system bandwidths of 60, 40, and 20 MHz.

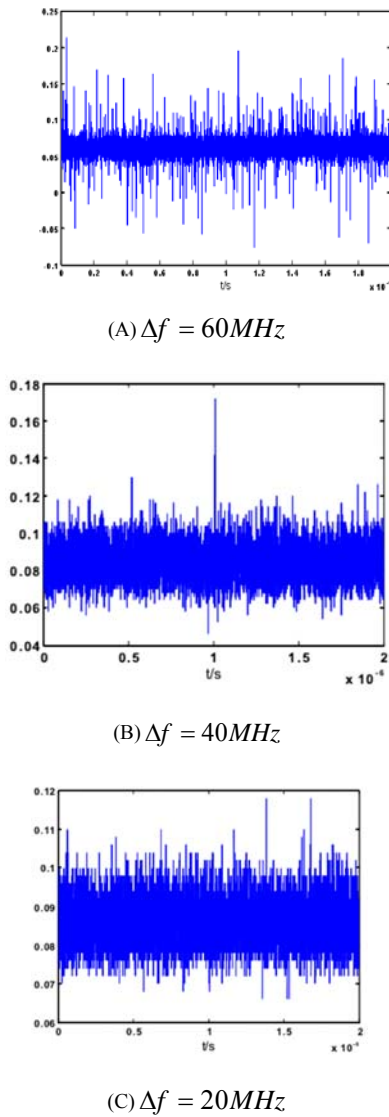


FIGURE VII. WAVEFORMS COLLECTED UNDER DIFFERENT BANDWIDTHS

The root mean squares of the noise are 53, 25, and 15 mV under receiving system bandwidths of 60, 40, and 20 MHz, respectively. Therefore, selecting the appropriate system bandwidth has a certain effect on the suppression of sunlight interference. When designing the receiving circuit, a reasonable selection of circuit bandwidth can effectively restrain the system noise caused by solar radiation and other interferences and improve the detection accuracy of the system.

V CONCLUSION

This study explores the operation of the laser fuze while overcoming solar radiation interference using interference

suppression theory and experimental research about improving system detection accuracy and reducing the false alarm phenomenon. Moreover, inhibition technology theory is applied to simulate the laser detection of sunlight interference from the echo signals entering the receiving system to inhibit solar radiation. Results show that the spectral filter suppresses sunlight interference well and selecting the appropriate system bandwidth reduces the solar radiation caused by the noise to a certain extent. Furthermore, the use of a small laser detection system to build a test platform for the verification of the sunlight interference suppression effect serves as reference for further research on anti-sunlight interference systems for the laser fuze. For the condition with no sun disturbances, this system can also work correctly because the solution listed in this passage will not influence the transmission of laser. However, such environment is ideal. Actually when the sun's interference is small, it is often accompanied by clouds and rain. These background climates can have a significant impact on laser detection, which is not discussed in detail here.

ACKNOWLEDGEMENT

This research was financially supported by the National Defense Program Foundation of Science and Technology, China (Grant No. 0106001) and the Weapons and equipment Pre-Research Project of China (Grant No. 41419050202).

REFERENCES

- [1] Wei Weidong, Sun Xiaoquan, Li Honghin, Zhang Yujun. Correlation detection of dual-wavelength laser pulse suppressing background light interference [J]. Infrared and Laser Engineering, 2012, 41(7):1777-1783.
- [2] Wang P Y. Beam-shaping optics deliver high-power beams[J]. Laser Focus World, 2001, 37(12):115-118.
- [3] Zhou G, Liu X, Xu J. A math model of calculate the atmospheric transmittance of infrared radiation[J]. Infrared Technology, 2008, 30(6):331-334.
- [4] Ping W H. Research into Theoretical Calculation Method on Engineering of Transmittance of Infrared Radiation Through Atmosphere[J]. Optics & Precision Engineering, 1998.
- [5] Bo L. The spectral distribution of solar radiation at the earth's surface—elements of a model[J]. Solar Energy, 1978, 20(2):143-150.
- [6] J. Duffie and W. Beckman, *Solar Engineering of Thermal Processes*, Wiley, New York, NY, USA, 1980
- [7] Cornelius J. Willers. *Electro-Optical System Analysis and Design: A Radiometry Perspective*[M].2013.
- [8] Xu Xiaobin, Zhang He. Optimal Pulsed Frequency and Scanning Speed of Laser Circumferential Detection System[J]. Chinese Laser, 2016(5):195-201.
- [9] Zhanghe. *Detection And Identification Technology*[M].Beijing Institute of Technology press.

Elevation Angle Estimation by Time Reversal Method in Homogeneous Shallow Sea Environment

Haixia Jing^{1,2}, Haiyan Wang^{1,*}, Zhenguo Liu³, Xiaohong Shen¹ and Tianyi Jia¹

¹School of Marine Science and Technology, Northwestern Polytechnic University, Xi'an Shaanxi 710072, China

²College of Engineering, Xi'an International University, Xi'an Shaanxi 710077, China

³China Shipbuilding Industry Corporation, Beijing, 100097, China

*Corresponding author

Abstract—This article discusses the problem of active detection and estimation for the elevation angle of a target in a homogeneous shallow sea environment, where a method using active detection on virtual time reversal (ADVTR) is proposed to solve the estimator performance decline problem caused by multipath and clutter. Unlike the conventional passive target estimation method ignoring the multipath effect, the ADVTR method will take full account of the multipath which exploits active detection (AD) to estimate channel, and virtual time reversal (VTR) to realize focusing in a computer to increase the signal-to-noise ratio (SNR) after the source-receive array (SRA) receives the reflected signal of the target. Furthermore, the Capon algorithm is adopted to compare the performance of ADVTR estimator and conventional one. Numerical simulations demonstrate its superior performance than the conventional estimators.

Keywords—active detection on virtual time reversal (ADVTR); elevation angle estimation; multipath effects; ULA; Capon algorithm

I. INTRODUCTION

To locate the position of a target, the range, azimuth and elevation angle need to be calculated simultaneously. Direction of arrival (DOA) estimation (including the horizontal and vertical plane) plays an important role in array signal processing with wide applications in communication, sonar and radar systems [1]. In this paper, we will focus on the DOA estimation of vertical plane (or the elevation angle estimation) in homogeneous shallow sea environment.

One of the important features in homogeneous shallow sea environment is the multipath effect of the channel. The conventional array signal processing DOA estimation method is based on the direct-path-only assumption; in which multipath is ignored or treated as a negative influence so as to be eliminated [2].

Time reversal [3] (TR) signal processing method raised in recent years, on the contrary, is to take full advantage of the multipath effect and the adaptive focusing characteristics to eliminate the problem of signal propagation channel caused by the multipath, which provides a new idea and method for high-precision DOA estimation.

TR can be divided into active time reversal (ATR) and passive time reversal (PTR) according to the implementation mode. The main difference is that it is necessary to re-emit the received signal with the noise to the real channel to complete

the focusing for ATR after time reversal mirror (TRM) receiving the reflected signal from the target, but for the PTR, TR operation and focusing are completed in the virtual channel established by simulation software in computers [4]. PTR is also referred as to virtual time reversal (VTR) in [5]. Combining the advantages of ATR with PTR, the first process of ADVTR will realize the detection and channel estimation in the real channel and the second process will complete TR focusing virtually in the computer. Compared with ATR, there is no real re-emitting process so that the second receiving process has no noise in ADVTR and the signal-to-noise ratio (SNR) of the array received signal are higher. Compared with PTR, the characteristics of ocean channel can be estimated ideally according to the active detection while avoiding the PTR approximation process on the basis of the same processing gain with PTR. Based on this idea, the ADVTR method can be applied to DOA estimation in active acoustic array to achieve better performance.

There are some literatures on the DOA estimation using ATR and PTR. For example, Publication [6] employs ATR for the DOA estimation of a passive target in radar system, and combines the TR/range estimator to realize the active array source location. Publication [7] proposes a VTR method for passive direction of arrival estimation of electromagnetic signal emitted from a single communication station. Publication [8] addresses a DOA estimation method with PTR in a low angle target parameter estimation and antenna array scenario. Publication [9] utilizes PTR to study the orientation estimation performance of underwater targets, which proposes a PTR super-directional element distribution model based on non-uniform linear array (NLA). Above methods have verified the validness of TR methods in improving the performance of DOA estimator under multipath conditions.

Relative to [6-9], the target DOA estimation method in vertical plane based on ADVTR is introduced from array signal processing DOA estimation in this paper. The ADVTR multipath model based on uniform line array (ULA) is established, and Capon algorithm is applied to achieve target DOA estimation. Armed with the acoustic field simulation tool Bellhop, the experimental data are obtained and the model is simulated. The performances of the estimation algorithm with and without ADVTR are compared.

II. MULTIPATH DOA ESTIMATION MODEL FOR ULA BASED ON ADVTR

A. Multipath Model Diagram for ULA

The multipath DOA estimation model diagram for ULA based on the ray theory is shown in Figure 1.

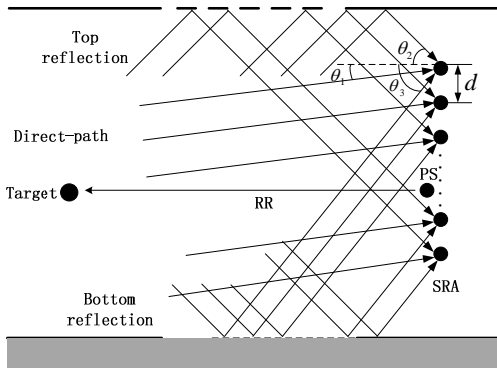


FIGURE I. MULTIPATH DOA ESTIMATION DIAGRAM FOR ULA

SRA in the Figure 1 is the vertical ULA, whose element number is P and interelement spacing is d . For convenience, only three propagation paths between the target and SRA are drawn: the direct-path, the top-reflection-path and the bottom-reflection-path, whose incident angle (i.e. DOA of backscatter from target propagating via various paths) is as follows: θ_1 , θ_2 and θ_3 . To be more general, the acoustic propagation paths deduced subsequently are not confined to these three paths, but N or M .

B. Conventional Multipath DOA Model for ULA

PS located in element k of SRA will transmit the signal $f(t)$. According to the ray theory, the channel transfer function between the transmitting acoustic source and the target can be expressed as

$$h_k(t) = \sum_{n=1}^N c_{kn} \delta(t - \tau_{kn}) \quad (1)$$

Where N is the total number of sound ray; c_{kn} is the amplitudes (or attenuation) of n-th eigen ray (also regarded as the propagation path) from element k to target; and τ_{kn} is the travel time (or delay) of n-th eigen ray from element k to target.

Ignoring the effect of the target reflection, the signal received by the element j is:

$$\begin{aligned} y_j(t) &= (f(t) \otimes h_k(t)) \otimes h_j(t) + v_j(t) \\ &= \sum_{m=1}^M \sum_{n=1}^N c_{jm} c_{kn} f(t - \tau_{jm} - \tau_{kn}) + v_j(t) \end{aligned} \quad (2)$$

Where $h_j(t)$ represents the channel function between the target and element j ; $v_j(t)$ is the noise between the element j and the target; c_{jm} and τ_{jm} represent amplitudes and travel time of the m-th propagation path from target to element j separately.

Suppose the transmitter signal as $f(t) = s(t)e^{j\omega_c t}$. Combining far field and narrow band model theory of array signal processing, Equation (2) can be expressed as:

$$\begin{aligned} y_j(t) &= \sum_{m=1}^M \sum_{n=1}^N c_{jm} c_{kn} f(t - \tau_{kn} - \tau_{1m} - \Delta\tau_{jm}) + v_j(t) \\ &\approx \sum_{m=1}^M \sum_{n=1}^N c_{jm} c_{kn} s(t) e^{j\omega_c (t - \tau_{kn} - \tau_{1m} - \Delta\tau_{jm})} + v_j(t) \\ &= \sum_{m=1}^M c_{jm} e^{-j\omega_c \Delta\tau_{jm}} e^{-j\omega_c \tau_{1m}} \cdot \sum_{n=1}^N c_{kn} e^{-j\omega_c \tau_{kn}} \cdot s(t) e^{j\omega_c t} + v_j(t) \end{aligned} \quad (3)$$

where τ_{1m} represents the reference delay associated with backscatter from target traveling via path m to element 1(the reference element); and $\Delta\tau_{lm}$ is the interelement delay associated with path m originating from target in excess of τ_{1m} with respect to the receiving element j .

The received signals of element j is generalized to other array elements and expressed in the matrix form as

$$Y(t) = (C \odot A)DX_k F(t) + V(t) \quad (4)$$

where the symbol “ \odot ” is Hadamard Product or Basic Product.; $Y(t) = [y_1(t), \dots, y_P(t)]^T$ is defined as the received signal matrix received by the element 1- P of the SRA; C is a ($P \times M$) matrix representing the attenuation matrix with respect to the channel response function between the target and SRA elements, whose element c_{jm} indicates the attenuation associated with backscatter from target traveling via path m to element j ; $A = [a(\theta_1), a(\theta_2), \dots, a(\theta_M)]$ is a ($P \times M$) matrix representing a relative delay matrix to the reference element (element 1), and is referred as the array steering matrix as shown by (5); $D = [e^{-j\omega_c \tau_{11}}, e^{-j\omega_c \tau_{12}}, \dots, e^{-j\omega_c \tau_{1M}}]^T$ is the reference delay matrix including interrelated delay from target traveling via all M paths to element 1; $F(t) = s(t)e^{j\omega_c t}$ is called the transmitting matrix; $V(t)$ indicates the noise matrix; and $X_k = \sum_{n=1}^N c_{kn} e^{-j\omega_c \tau_{kn}} = (C(k,:)) \odot (A(k,:)) D$ can be considered as a target-received signal matrix which is transmitted from the element j through the channel to the target.

$$\begin{aligned}
 A &= [a(\theta_1), a(\theta_2), \dots, a(\theta_M)] \\
 &= \begin{bmatrix} e^{-j\omega_c \Delta \tau_{11}} & e^{-j\omega_c \Delta \tau_{12}} & \dots & e^{-j\omega_c \Delta \tau_{1M}} \\ e^{-j\omega_c \Delta \tau_{21}} & e^{-j\omega_c \Delta \tau_{22}} & \dots & e^{-j\omega_c \Delta \tau_{2M}} \\ \vdots & \vdots & \vdots & \vdots \\ e^{-j\omega_c \Delta \tau_{P1}} & e^{-j\omega_c \Delta \tau_{P2}} & \dots & e^{-j\omega_c \Delta \tau_{PM}} \end{bmatrix} \\
 &= \begin{bmatrix} 1 & 1 & \dots & 1 \\ e^{-j\frac{2\pi}{\lambda} d \sin \theta_1} & e^{-j\frac{2\pi}{\lambda} d \sin \theta_2} & \dots & e^{-j\frac{2\pi}{\lambda} d \sin \theta_M} \\ \vdots & \vdots & \vdots & \vdots \\ e^{-j\frac{2\pi}{\lambda} (P-1) d \sin \theta_1} & e^{-j\frac{2\pi}{\lambda} (P-1) d \sin \theta_2} & \dots & e^{-j\frac{2\pi}{\lambda} (P-1) d \sin \theta_M} \end{bmatrix} \quad (5)
 \end{aligned}$$

C. ADVTR Multipath DOA Model for ULA

According to the idea of ADVTR, the first process of ADVTR is active detection, so the frequency of the transmitted signal has been known when the array receives the signal. Then the filter can be introduced to eliminate the impact of noise before TR operation. Subsequently VTR is performed virtually for the received signals of each SRA in the computer, and taking element j as an example:

$$y_j(-t) = B \cdot s(-t) e^{-j\omega_c t} = B f(-t) \quad (6)$$

Where B is expressed as equation (7), whose value is independent of time t and can be considered as a coefficient.

$$B = \left(\sum_{m=1}^M c_{jm} e^{-j\omega_c \Delta \tau_{jm}} e^{-j\omega_c \tau_{1m}} \right) \cdot \sum_{n=1}^N c_{kn} e^{-j\omega_c \tau_{kn}} \quad (7)$$

The signal is energy normalized and then re-transmitted virtually into the channel as a secondary transmission signal in the computer, which still satisfies the far field and narrow band model theory. Repeat the above first procedure, refer to (1) - (3), and suppose the signal received by element l is $z_l(t)$:

$$\begin{aligned}
 z_l(t) &\approx \sum_{m=1}^M \sum_{n=1}^N c_{lm} c_{jn} g_j B s(-t) e^{-j\omega_c (t - \tau_{jn} - \tau_{1m} - \Delta \tau_{lm})} \\
 &= \sum_{m=1}^M c_{lm} e^{j\omega_c \Delta \tau_{lm}} e^{j\omega_c \tau_{1m}} \cdot \sum_{n=1}^N c_{jn} e^{j\omega_c \tau_{jn}} \cdot g_j B s(-t) e^{-j\omega_c t}
 \end{aligned} \quad (8)$$

Where g_j is the normalized coefficient of element j obtained with reference to the transmitted signal power, and owing to the principle of virtual time reversal, the secondary process has no noise.

Referring to (4) - (5), the received signal of all of elements of SRA on the second time with element j probing virtually is

$$Z_j(t) = (C \odot A^*) D^* X_j^* g_j y_j(-t) \quad (9)$$

where A, C, D are the same as the parameters of (4), and X_j is the same as X_k of (4) except that X_k is the received signal

matrix with element k probing, X_j is the received signal matrix with element j probing.

The received signals element j probing is generalized to other array elements and the sum of received signals of SRA after TR can be obtained:

$$\begin{aligned}
 Z_{tr} &= \sum_{j=1}^P Z_j(t) \\
 &= \sum_{j=1}^P (C \odot A^*) D^* X_j^* g_j y_j(-t) \\
 &= (C \odot A^*) D^* \sum_{j=1}^P X_j^* g_j y_j(-t)
 \end{aligned} \quad (10)$$

III. DOA ESTIMATION ALGORITHM

A. Conventional Multipath Capon Algorithm

According to the array signal processing theory, the purpose of the Capon algorithm is attempting to minimize the power by noise and other interference signal except the desired signal, while maintaining a fixed gain in the direction from which the signal originated [6]. Combining the model established by (4), the Capon algorithm can be represented as the following minimum problem:

$$\begin{aligned}
 \min w^H(\theta) \hat{R}_Y w(\theta) \\
 \text{S.T.: } w^H(\theta) a(\theta_1) = 1
 \end{aligned} \quad (11)$$

Where $\hat{R}_Y = \frac{1}{N} E\{Y(t)Y(t)^H\}$ is the sample covariance matrix of the array output signal with the multipath; θ_1 is desired angle information and w is the weight value.

The Lagrange multiplier method can be used to obtain the solution of the above problem:

$$w = \frac{\hat{R}_Y^{-1} a(\theta_1)}{a^H(\theta_1) \hat{R}_Y^{-1} a(\theta_1)} \quad (12)$$

Equation (13) can be obtained by taking (12) into (11), which means the largest power in the desired direction while the power except the desired direction is the smallest:

$$P = \frac{1}{a^H(\theta_1) \hat{R}_Y^{-1} a(\theta_1)} \quad (13)$$

Thus the spatial spectrum of the Capon algorithm can be defined as:

$$P = \frac{1}{a^H(\theta) \hat{R}_Y^{-1} a(\theta)} \quad (14)$$

Where $a(\theta)$ is the steering vector and defined previously in (5) as:

$$a(\theta) = \left[1, e^{-j\frac{2\pi}{\lambda}d\sin\theta}, \dots, e^{-j\frac{2\pi}{\lambda}(P-1)d\sin\theta} \right]^T \quad (15)$$

B. ADVTR Capon Algorithm

According to (10), follow the same steps as the above conventional DOA estimation:

$$\begin{aligned} & \min w_{tr}^H(\theta) \hat{R}_{Ztr} w_{tr}(\theta) \\ & \text{subject to: } w_{tr}^H(\theta) a_{tr}(\theta_1) = 1 \end{aligned} \quad (16)$$

Where $\hat{R}_{Ztr} = \frac{1}{N} E\{Ztr(t)Ztr(t)^H\}$ is the sample covariance matrix after virtual time reversal output signal and the other values are the same as above. At this time, the spatial spectrum of the ADVTR Capon algorithm is:

$$P_{tr} = \frac{1}{a_{tr}^H(\theta) \hat{R}_{Ztr}^{-1} a_{tr}(\theta)} \quad (17)$$

Where $a_{tr}(\theta)$ is:

$$a_{tr}(\theta) = \left[1, e^{j\frac{2\pi}{\lambda}d\sin\theta}, \dots, e^{j\frac{2\pi}{\lambda}(P-1)d\sin\theta} \right]^T \quad (18)$$

IV. SIMULATION RESULTS

The simulation environment is as follows: shallow sea waveguide, uniform sound speed environment, regardless of the impact of ocean additive noise, and the case of single objective. The simulation model is shown in Figure 1, where the number of TRM (SRA) is 9, the interelement spacing is 0.75m, the element 1 is 75m from the sea surface, the depth of bottom is 500m, the sound speed is 1.5km/s and the range between PS and the target is 2km. The target is located in 253m, that is the DOA is -5° . PS transmits 1 kHz continuous wave (CW) signal. The simulation environment is shown in Table 1.

TABLE I. SIMULATION ENVIRONMENT

Simulation Condition	Parameter
Number of elements	9
Interelement spacing	0.75m
The depth of element 1	75m
The depth of bottom	500m
The source depth	78m
Target depth(-5°)	253m
The range	2km
Number of multipath	3

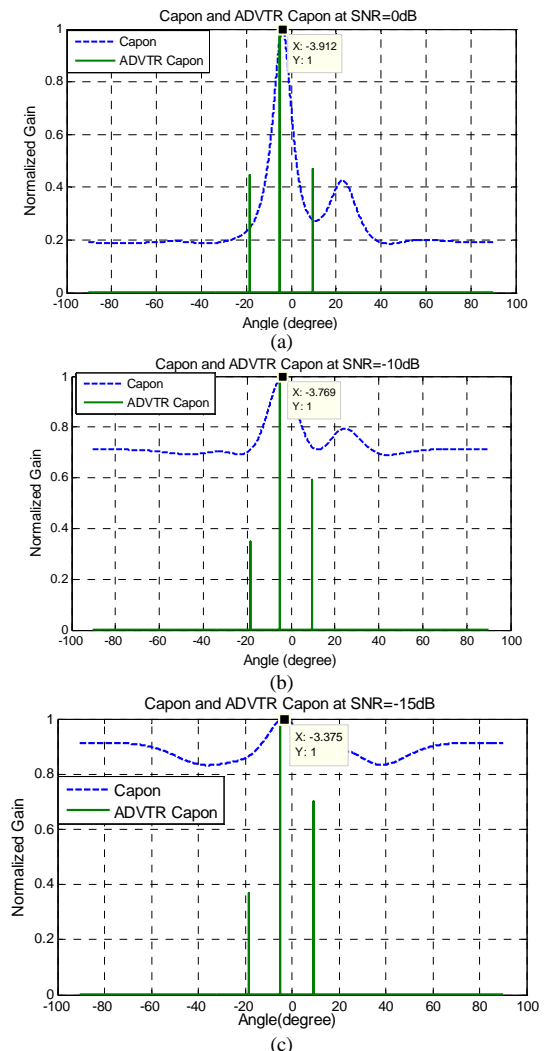
Bellhop special acoustic field simulation toolbox under MATLAB simulation environment is used to simulate the ocean sound field environment. The multiple reflection paths by sea surface or bottom are ignored, and only the three paths illustrated in Figure 1 are considered. Then the various parameters used for simulation are obtained, as shown in Table 2. Because through the simulation, we can discover that the amplitudes of the same paths from the target to each element (i.e. the amplitude from the target to each element via the top-reflection) are very closer. Then for convenience, the amplitude information between PS and the target expressed in

the table is the corresponding direct-path, top-reflection-path and bottom-reflection-path successively.

TABLE II. SIMULATION PARAMETERS TARGET AT -5°

Simulation Parameter	Value
Direction of arrival	{4.458°, 0°, -22.884°}
Amplitude	{4.99e-4, 5.0e-4, 2.92e-4}
Delay of element 1	{1.3372291, 1.3333348, 1.4479731}s

Figure 2 (a)-(d) shows the DOA estimation performance comparison with Capon estimator and ADVTR Capon estimator for target at -5° when the SNR is 0dB, -10dB, -15dB and -20dB.



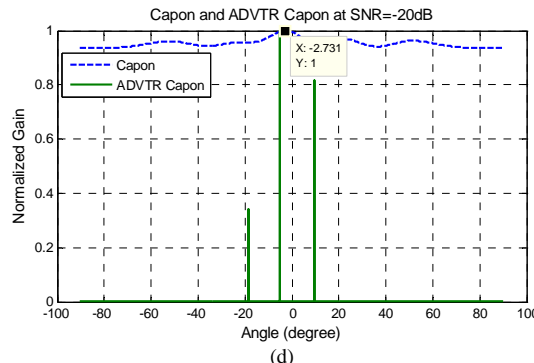


FIGURE II. CAPON ESTIMATOR AND ADVTR CAPON ESTIMATOR AT $\theta = -5^\circ$: (a) SNR=0dB; (b) SNR=-10dB; (c) SNR=-15dB; (d) SNR=-20dB

It can be seen from Figure 2 that:

(1) Relative to Capon algorithm, ADVTR Capon algorithm can estimate accurately the expected value of the target, whose energy of the main lobe is far higher than its corresponding sidelobes and resolution is higher.

(2) With the changes of SNR from 0dB to -20dB, the relations between main lobe and sidelobes for both Capon and ADVTR Capon algorithm are the same that the energy of the sidelobes is higher and higher, and is getting closer to the main lobe. The difference is that the resolution for Capon algorithm is getting lower and lower, and the estimation deviation is more and more great. However, the resolution for ADVTR Capon is almost not affected, and the target angle can be estimated without bias.

V. CONCLUSION

In this paper, we use the ADVTR method to study the performance of underwater target DOA in the presence of multipath, and a DOA estimation algorithm based on ADVTR Capon is proposed. Firstly, based on the ray theory, a conventional multipath DOA estimation model and an ADVTR DOA estimation model for ULA are established, and then the model is estimated by Capon algorithm. The simulation results show that the DOA estimator with ADVTR, compared with the conventional method without TR, has a more accurately estimated value, a higher resolution and a stronger ability to suppress sidelobes, so that the target DOA estimation can be achieved in the case of low SNR and multipath.

ACKNOWLEDGMENT

This work was supported by National Natural Science Foundation of China (61571365, 61571367, and 61671386), National Key R&D Program of China (2016YFC1400200), and Scientific Research Project of Shaanxi Provincial Education Department (16JK2173).

REFERENCES

- [1] H. Krim and M. Viberg, "Two decades of array signal processing research: the parametric approach," *IEEE Signal Processing Magazine*, vol. 13, no. 4, pp. 67–94, July 1996.
- [2] E. Daeipour, W. D. Blair, and Y. Bar-Shalom, "Bias compensation and tracking with monopulse radars in the presence of multipath," *IEEE Trans. Aerosp. Electron. Syst.*, vol. 33, no. 3, pp. 863–882, July 1997.
- [3] Mathias Fink, "Time reversal of ultrasonic fields-Part I: Basic principles," *IEEE Trans. Ultras., Ferroelec., Freq. Contr.*, vol. 3, no. 5, pp. 555–566, September 1992.
- [4] Hee-Chun Song, "An Overview of Underwater Time-Reversal Communication," *IEEE Journal of oceanic engineering*, vol. 41, no. 3, July 2016.
- [5] A. Silva, S. Jesus, J. Gomes, and V. Barroso, "Underwater acoustic communication using a virtual electronic time-reversal mirror approach," in Proc. 5th Eur. Conf. Underwater Acoust., Lyon, France, Jun. 2000, vol. V.
- [6] Foroohar Foroozan, Amir Asif, "Time Reversal Based Active Array Source localization," *IEEE Trans. SP*, vol. 59, no. 6, pp. 2655–2668, June 2011.
- [7] Yongqing Fu, Wei Liu, Ruijie Bai, Jingrui Li, and Jinlin Wang, "A Novel Virtual Time Reversal Method for Passive Direction of Arrival Estimation," *Mathematical Problems in Engineering*, Volume 2015, Article ID 613692, 12 pages, <http://dx.doi.org/10.1155/2015/613692>.
- [8] Xiaolu Zeng, Minglei Yang, Baixiao Chen and Yuanwei Jin, "Low Angle Direction of Arrival Estimation by Time Reversal," *2017 IEEE International Conference on Acoustics, Speech and Signal Processing (ICASSP)*, pp. 3161–3165, New Orleans, LA, USA, March 2017.
- [9] Fouzhou Yang, Haiyan Wang, Xiaohong Shen and Haixia Jing, "Super-direction element distribution model of NLA based on TR," *Journal of Shanghai Jiao Tong University*, vol. 47, no. 12, pp. 1907–1910, December 2013.

An Improved TLD Tracking Algorithm for Fast-moving Object

Shijie Zhou, Yuanxi Peng*, Kecheng Gong and Leizhi Shu

College of Computer, National University of Defense Technology, Changsha, Hunan, 410073, China

*Corresponding author

Abstract—Traditional object tracking is easily affected by deformation, scale changes, illumination changes, partial occlusions and so on. TLD(Tracking-Learning-Detection) is a classic effective algorithm in long-term tracking which can solve these problems well. Meanwhile, the real-time performance of the system should be taken into account while in the actual situation. An improved fast-moving object tracking algorithm based on TLD is proposed in this paper. In the paper, a method of narrowing the region of detection is proposed to effectively minimize the consumption of time, the method is combined with self-prediction of motion direction to ensure the accuracy of detection. To compensate for the possible missing and false detections caused by the reduction of detection region and the changing background, the variance threshold is updated dynamically to let more possible correct bounding boxes pass the variance classifier. Experiments have been conducted to verify the improved TLD algorithm, the results show that our algorithm ensures the accuracy of object tracking and has a good performance on the real-time.

Keywords—object tracking; TLD, real-time; narrowing region; variance threshold

I. INTRODUCTION

Visual based object tracking has been one of the core content in the field of computer vision, which is defined as estimating the trajectory of a moving object in an image sequence or a video with fixed or changing background. As the vision-based object tracking technology has been widely used in military and civil fields such as military guidance, visual navigation, automated security monitoring, artificial intelligence and so on, it is also faced with a lot of challenges as a practical matter such as deformation, scale changes, illumination changes, partial occlusions and so on. Especially in terms of real-time performance[1] for fast-moving object, due to the tremendous computing workload, the object can't be tracked timely and effectively. Meanwhile, the precision and robustness in the process of long-term tracking can't be guaranteed all the time. Thus, researchers from all over the world have done a lot of research work and proposed a series of objects tracking algorithms.

Unlike traditional object tracking algorithm, the latest object tracking algorithm tend to adopt an online learning mechanism to improve the tracking effect. The online learning mechanism means that the tracker needs to collect a variety of samples of the object to learn and train constantly, besides, the samples should cover various kinds of deformations, rotations, scales, attitudes and illumination, in other words, the sample selection is quite considerable for the performance of the tracker. Among the long-term tracking algorithms based on online learning and

detection for single object, TLD proposed by Zdenek Kalal[2] is an adaptive and reliable tracking technique which combines traditional tracking algorithm and traditional detection algorithm. And it updates the key feature points of tracking module and the object model and relevant parameters constantly by using an improved online learning mechanism[3,4] thus it can enhance the stability and reliability of tracking and basically achieves the goal of long-term tracking. However, there is still a defect when it comes to real-time capability. Because of the enormous computation burden, the running speed is less than ideal. In order to improve the efficiency of the tracking algorithm and track the fast-moving object accurately and timely, an improved algorithm based on TLD is proposed in this paper. On the basis of the original TLD, the paper makes improvements from two aspects. Firstly, we narrow the region of detection by predicting the position of the object which proves to improve real-time performance, and secondly, the reduction of detection area and the changing background will inevitably incur missing and false detections. Thus, we update the variance threshold[5] of variance classifier dynamically so that it suits the actual situation well.

II. ANALYSIS OF TLD ALGORITHM

A. Introduction of TLD Algorithm

In simple terms, TLD algorithm is made up of three modules: tracking module, learning module and detection module. The three capital letters: T, L and D represent the three modules and they are grouped together according to a certain formula so that detection module and tracking module can work in parallel with each other under the supervision of the learning module. The structure of TLD is shown in Figure 1.

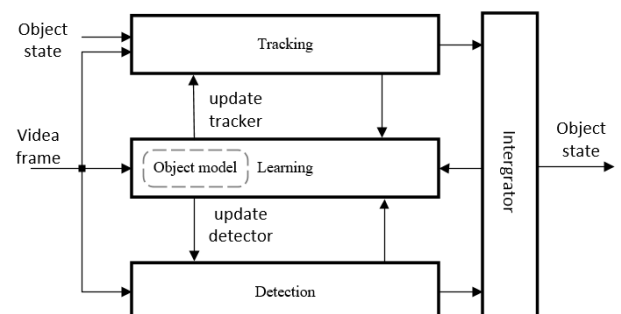


FIGURE I. THE STRUCTURE OF TLD ALGORITHM

Each module plays an indispensable role in the whole process of object tracking. They work like this: the tracker and detector execute in parallel. When the tracker fails to track the target in the previous frame, the tracking result in the current frame should take the result of the detector in the current frame. Otherwise, the tracker executes in the current frame, if the target fails to be tracked, the result of the current frame should also take the result of the detector. But if the target is tracked, we should compare the results of the tracker and the detector. When the overlap of the tracking result and the clustering result of the detector is less than 0.5 and the detector has higher confidence, the result is classified as trusted detections, if there is only one result, as before, the result depends on the detector. We should initialize the tracker with new position relocated by the detector. However, if the overlap of the tracking result and the clustering result of the detector is higher than 0.5 or the tracker has higher confidence, the tracking result is up to both the tracker and the detector. In this case, if the result of the tracker is credible, the learning module starts to work and the online learning model is updated. But we only take the detecting results of detector of which the overlap of the tracker and the detector is higher than 0.7. To get the final tracking result, take the abscissa as an example, a weighted mechanism is adopted here and the formula is as follows.

$$bbnextrx = \frac{10*tbbx + \sum_{i=1}^{close_detections} dbbx_i}{10+close_detections} \quad (1)$$

Where $bbnextrx$, $tbbx$ and $dbbx$ represent the abscissa of the final result, the tracking result and the satisfied detection result. Similarly, the ordinate, width and height can be computed by the mechanism.

Here are the core principles of each module:

1) Tracking Module

TLD adopts the strategy of overlapping blocks and detection is added to it based on median flow tracker algorithm[6] if tracking fails. Before tracking, the target is marked by the rectangle. In the rectangle, points are generated evenly with an equal interval. And then we estimate the forward and backward motion trajectory of the target between the previous frame and the current frame, the two frames are consecutive. For instance, we select a point A within the rectangle in the previous frame, according to A, a point B is tracked in the current frame. After that, a new point C is tracked in the previous frame according to the point B. Finally, we calculate the displacement from A to B, if the displacement is below a certain threshold, we regard the forward tracking as correct. In this way, we select all the eligible points within the rectangle but only half of them displacements of which are lower than the median are retained as final feature points. Meanwhile, d_i stands for the displacement of the i th feature point while d_m stands for the mean value of all the displacements, $|d_i - d_m|$ stands for the residual, if the residual is higher than 10 pixels, we regard the tracking as a failure. Otherwise, the tracking is successful and we select the minimum rectangle that can contain all the feature points in the current frame as final tracking result.

2) Detection Module

The detection module adopts scanning windows of 21 different scales. Based on the size of target rectangle box, we

take 10 incrementing scales and 10 diminishing scales using a fixed scaling factor. The size of window is limited by a minimum of 15*15 pixels and those that don't meet the criteria would be removed. Then each scanning window will scan the whole frame, the step lengths along the x-axis and y-axis of scanning are ten percent of the width and the height of the window. In this way, we get about 50 thousand image patches for each picture. Then all the patches would be put in the cascade classifier which is comprised of Variance classifier, Random Forest classifier and Nearest Neighbor classifier. The structure of cascade classifier is shown in Figure 2.

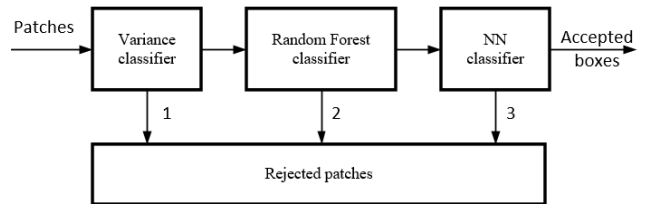


FIGURE II. THE STRUCTURE OF CASCADE CLASSIFIER

After screening by the three classifiers, the patches that fully satisfy the judgment of the three classifiers would be retained as the final result of detection. Otherwise, they would be filtered out. The mechanism of cascade classifier enhances the detection accuracy.

● Variance Classifier

This classifier needs to calculate the variance of gray value of each image patch. The formula of calculating is as follows.

$$D(p) = E(p^2) - E^2(P) \quad (2)$$

Where $D(p)$ is the variance of gray value of image patch p , $E(p)$ is the mean value of gray value of image patch p , $E(p^2)$ is the mean value of gray value in the square of image patch p . The image patch p is considered to contain the target if $D(p)$ is above a certain threshold. Usually we take $\text{var} = 0.5 * D_1$ as the threshold and D_1 is the variance of the initial patch.

● Random Forest Classifier

This classifier is essentially an ensemble classifier consists of 10 base classifiers[7]. Each classifier is like a tree and ten trees make up the forest. Each tree contains 13 nodes and each node performs a comparison of a pair of pixels, besides, each tree's 13 pairs of pixels are different from each other but for each tree, 13 pairs of pixels are fixed and arranged in fixed order so that each tree will generate a 13-bit binary code x for each patch. Then, the posterior probability of $p_i(y|x)$ is tallied, where $y \in (0,1)$ that indicate whether the i th patch contains the target. To ensure the accuracy, we need to calculate the mean value of p_1, p_2, \dots, p_9 and p_{10} . If the mean value is over 50%, the patch can be classified as the target or non-target.

● Nearest Neighbor Classifier

This classifier is the final stage of the detector. The process is like online Template Matching Algorithm. The classifier selects the image patch with the highest similarity compared with the original target model as the final test results. Meanwhile,

the online template is updated dynamically and the threshold that is used to train the NN classifier[8] is constantly corrected. The similarity between image patch p_i and p_j is as follows.

$$S(p_i, p_j) = \frac{1}{2}(NCC(p_i, p_j) + 1) \quad (3)$$

Where $NCC \in [-1, 1]$ is a normalized correlation coefficient.

3) Learning Module

The learning module is based on an online model and the function of the module is to synthesize the results of the tracker and the detector. In addition, it is in charge of the growth and pruning of the online model of the NN classifier and the updating of the posterior probability of $p_i(y|x)$. In other words, learning module reorganizes positive and negative samples to retrain the random forest classifier and the NN classifier.

B. Existing Defects and Possible Solutions

As mentioned in the previous section, for each frame, about 50 thousand image patches would be generated to be judged by the variance classifier. However most of them don't contain the target. Thus, it will take much time unnecessarily and lead to low efficiency of the algorithm. When tracking a fast-moving target, the processing speed of the algorithm is particularly important. To improve real-time performance, a concept of ROI is proposed in [9] which means that detection is only executed within the region of interest. For instance, [10] use Calman filter to predict the next region of detection, [11] adopts Pyramid LK optical flow method and [12] adds Meanshift algorithm to TLD to get the region of interest. All the method above can accelerate the process of the tracker.

III. IMPROVED TLD ALGORITHM

According to the above analysis, the processing time of each frame is greatly reduced. However, due to some potential defects and problems of the method of predicting the next region of detection, some correct samples will be inevitably missed. With the accumulation of error, the online model will be more and more inaccurate and the tracking accuracy will be significantly reduced which will ultimately lead to the failure of tracking. For the purpose of giving attention to both the real-time performance and the precision of tracking, we proposed an improved algorithm based on TLD.

A. Narrowing the Region of Detection

The main purpose is to reduce the number of image patches waiting to be detected so that the computation is eased and the running speed can be raised obviously. The specific method is as follows.

- (1) According to the target box in the last frame, the tracker predicts a new box in the current frame.
- (2) Compare the positions of the two boxes and we will get four possible directions of motion: the top left, the top right, the lower left and the lower right. Here we take the top left as an example and continue with the following steps.
- (3) Based on the lower right corner of the target box, we will get a point after a displacement. The displacement

vector is (X, Y) where the value of X is half of the value of the width of the target box and the value of Y is half of the value of the height of the target box.

- (4) Via (3), we get a point. Based on the point, we take the whole upper left area as the final region of interest. All patches that overlap with the region should be send to the detector.

It should be noted that not every frame is processed in this way, if the tracking of the last frame is a failure, then we should detect the whole image. The diagram of narrowing the region of detection is shown in Figure 3.

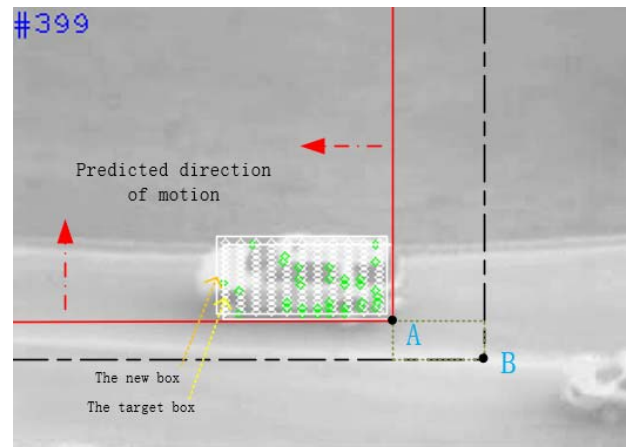


FIGURE III. THE DIAGRAM OF NARROWING THE REGION OF DETECTION

Most of the time, the results of the tracking module are credible if the target is not obscured and therefore the region near the location of the box predicted by the tracker is likely to contain the target in the current frame. As is shown in Figure 3, the region at the top left of point B is finally what we want.

B. Updating the Variance Threshold Dynamically

In the detection module, the variance classifier is the first to screen all the patches and it's particularly important for the accuracy. We already know from the previous text that the variance threshold is a fixed value which equals half of the initial target variance. Only the image patches of which the variance is greater than the threshold can pass through the classifier, and thus it's rather important to select a suitable threshold.

With the increase of video sequences, the shape and size of the object will change inevitably and the image information would be affected by the similar color, occlusion, light and other factors. As a result, the variance of the target will change more or less. If we still use the original fixed threshold, the correct patches will probably be filtered out and the subsequent tracking will fail.

To solve this problem, we adopt a mechanism of updating the variance dynamically. Under this mechanism, we give full consideration to the information of correct patches of all processed frames. With the increase of video frames, the new characteristics of the target tracked are obtained continuously and the variances of every target tracked are stored which can reflect the changes. D_i is the variance of the i th target tracked.

Each time the variance classifier executes, we take the minimum value of the existing top N variances as D_{min} and the threshold $var = 0.5 * D_{min}$. In this way, any possible correct patch won't be missed.

IV. EXPERIMENTAL RESULTS

Our experimental platform is Ubuntu14.04 and OpenCV 2.4.9. The processor is Intel(R) Core(TM) i5-4590 CPU @3.30GHz with 8GB RAM. The original version of TLD is C++ version by Alan Torres.

This paper selects different datasets from a benchmark and evaluates the proposed improved TLD by comparing it with the original TLD.

A. Datasets Introduction

The video sequences for testing the algorithm are from a benchmark. We compare the improved TLD with the original TLD under different scenes. There are ten open testing video sequences, the effect of tracking is as follows.

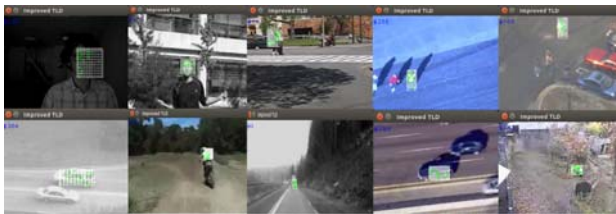


FIGURE IV. THE EFFECT OF TRACKING

The video sequences are named as David, Jumping, Pedestrian1, Pedestrian2, Pedestrian3, Car, Motocross, Volkswagen, Carchase and Panda. Among them, Jumping, Car, Motocross, Volkswagen and Carchase reflect a situation of fast motion.

B. Results and Analysis

In theory, the cost of time is greatly reduced benefited from the decreasing numbers of the image patches of most of the frames. Take the Car as an example, the comparison of the numbers of image patches of the two algorithm is shown in Figure 5.

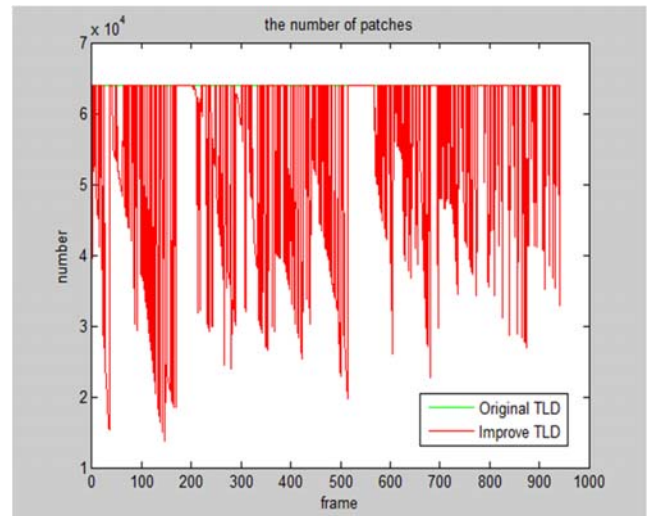


FIGURE V. THE COMPARISON OF ORIGINAL TLD AND IMPROVED TLD

From Figure 5, we know that for original TLD, all of the image patches generated by the sliding windows will be sent to the detection module. As a result, the detecting time for each frame is more than that of improved TLD.

The comparison of the time of detection each frame between the original TLD algorithm and the improved TLD algorithm is shown in Figure 6.

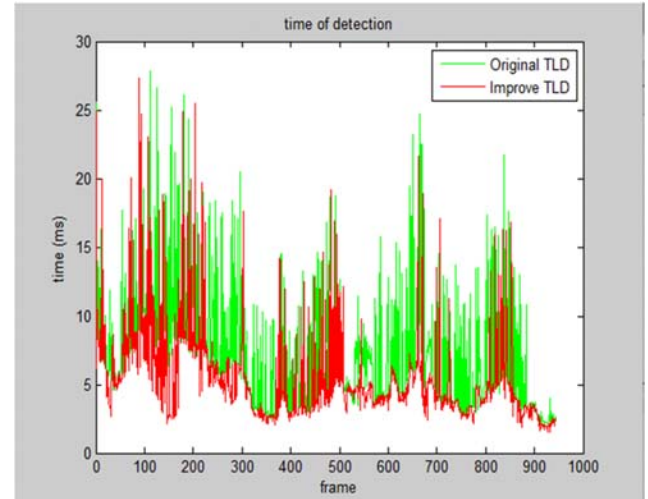


FIGURE VI. THE COMPARISON OF DETECTING TIME

We can know from the above figure that the detecting time for each frame of our improved TLD algorithm is obviously shorter than that of the original TLD. Though the time saved is negligible, with the accumulation of them, the final improvement is significant.

Next, let's have a look at the overall running time for each video sequence. Here is a comparison of the original TLD and the improved TLD shown in Table I.

TABLE I. THE OVERALL RUNNING TIMES

Name	Frames	Running time of original TLD/ms	Running time of improved TLD/ms
1.david	761	49316.7	46601
2.jumping	313	20284.8	19167
3.pedestrian1	140	11620.8	10147
4.pedestrian2	338	17257	17201.6
5.pedestrian3	184	15273.2	12433.5
6.car	945	57808.8	51669.5
7.motocross	2665	166372	147924
8.volkswagen	8576	660542	640314
9.carchase	9928	665135	563881
10.panda	3000	184243	179393

From the table, we can draw a conclusion that the improved algorithm can improve the real-time performance of tracking.

But a good performance in real time does not mean that our algorithm is better, we should also take its accuracy into consideration. Here we select Jumping, Car, Motocross, Volkswagen and Carchase which reflect the situation of fast motion to test our algorithm. Here we adopt the evaluation of Precision, Recall and F-measure. The result of the evaluation is shown in Table II.

TABLE II. THE RESULT OF THE EVALUATION

Name	Original TLD			Improved TLD		
	P	R	F	P	R	F
Jumping	1.000	0.613	0.760	1.000	0.732	0.845
Car	0.962	0.982	0.972	0.978	0.990	0.984
Motocross	0.704	0.470	0.564	0.935	0.493	0.646
Volkswagen	0.865	0.245	0.381	0.916	0.365	0.513
Carchase	0.981	0.147	0.263	0.997	0.159	0.274

As the is shown in the Table II, the precision, recall and f-measure are improved. A P-value indicates the proportion of tracked precise bounding boxes to tracked bounding boxes, an R-value indicates the proportion of tracked precise bounding boxes to all precise bounding boxes, and a F-value is the harmonic mean of P and R.

V. CONCLUSION

As the real-time performance of traditional tracking for fast-moving object is not ideal enough. This paper has presented an improved object tracking algorithm based on TLD to achieve long-term target tracking with ideal real-time performance. Based on TLD, we have introduced a new mechanism of generating the region of interest. The experimental results show that the proposed algorithm has faster running speed and higher tracking accuracy for fast-moving object.

The main direction of future work is to further speed up the operation of the system. Some modules such as the time-consuming NN classifier have much room for improvement.

REFERENCES

- [1] H. Grabner, M. Grabner, and H. Bischof, "Real-time tracking via on-line boosting," *Br. Mach. Vis. Conf.*, vol. 1, pp. 47–56, 2006.
- [2] Z. Kalal, K. Mikolajczyk, and J. Matas, "Tracking-Learning-Detection," vol. 34, no. 7, pp. 1409–1422, 2012.
- [3] Z. Kalal, J. Matas, and K. Mikolajczyk, "Online learning of robust object detectors during unstable tracking," *2009 IEEE 12th Int. Conf. Comput. Vis. Work. ICCV Work.* 2009, pp. 1417–1424, 2009.
- [4] Z. Kalal, J. Matas, and K. Mikolajczyk, "P-N learning: Bootstrapping binary classifiers by structural constraints," *Proc. IEEE Comput. Soc. Conf. Comput. Vis. Pattern Recognit.*, pp. 49–56, 2010.
- [5] T. Xu, C. Huang, Q. He, G. Guan, and Y. Zhang, "An improved TLD target tracking algorithm," *2016 IEEE Int. Conf. Inf. Autom. IEEE ICIA 2016*, no. August, pp. 2051–2055, 2017.
- [6] Z. Kalal, K. Mikolajczyk, and J. Matas, "Forward-backward error: Automatic detection of tracking failures," *Proc. - Int. Conf. Pattern Recognit.*, pp. 2756–2759, 2010.
- [7] B. L., "Random forest," *Mach. Learn.*, vol. 45, no. 1, pp. 5–32, 2001.
- [8] Y. Liao and V. R. Vemuri, "Use of k-nearest neighbor classifier for intrusion detection," *Comput. Secur.*, vol. 21, no. 5, pp. 439–448, 2002.
- [9] B. Nemade and V. A. Bharadi, "Adaptive automatic tracking, learning and detection of any real time object in the video stream," *Proc. 5th Int. Conf. Conflu. 2014 Next Gener. Inf. Technol. Summit*, pp. 569–575, 2014.
- [10] C. Sun, S. Zhu, and J. Liu, "Fusing Kalman filter with TLD algorithm for target tracking," *Chinese Control Conf. CCC*, vol. 2015–Septe., pp. 3736–3741, 2015.
- [11] B. Ahn, Y. Han, and I. S. Kweon, "Real-time facial landmarks tracking using active shape model and LK optical flow," *2012 9th Int. Conf. Ubiquitous Robot. Ambient Intell. URAI 2012*, no. Urai, pp. 541–543, 2012.
- [12] N. Fan, N. Huang, F. Yu, Y. Song, S. Zhao, and Z. Tan, "An Improved Target Tracking Scheme via Integrating Mean-shift with TLD Algorithm," pp. 7877–7882, 2017.

Multiple Centroid-Based Multi-Object Tracking by Decision Making

Hao Zhou^{1,*}, Jian He² and Zhangqin Huang²

¹Beijing University of Technology, China

²Xi'an Jiaotong University, China

*Corresponding author

Abstract—Multiple object tracking(MOT) has many applications in different life scenes, such as autonomous driving and traffic management. A novel approach to object predictive tracking, which is based on the Multiple centroid, is proposed in this paper to overcome the problems of occlusion, scale changes and shape, which cause the situation to lose object. Firstly, we formulate the MOT problem as decision making in Markov Decision Processes, where the lifetime of an object is modeled with a Markov Decision Process. Secondly, the object region is selected as the tracking region in the video to initialize the tracking process. Several image sampling segments are made ready for counting the initial pixels with the gray of a continuous gradient features pixels, which have the same gray-scale changes in intensity, and the discrete pixel group centroid(center centroid and edge centroid) coordinate is fitting for a time-domain trajectory curve. Edges of spectrum and track of spectrum are calculated by the time-domain trajectory curve. thirdly, we also model the lifetime of every centroid of every object with a Markov Decision Process. Finally, we compare both states and spectrum of each centroid and find the best trajectory. We conduct experiments on the MOT Benchmark[1] to verify the effectiveness of our method.

Keywords—multiple object tracking; multiple centroid; edges of spectrum; track of spectrum

I. INTRODUCTION

Multiple object tracking is one of the hot topics in the field of computer vision. It is a technology used to object identification, object location information extraction and analysis, object motion tracking from the image signal in real time. It has a very wide range of application in military industrial, security, and other fields; the development prospects are bright. Object motion randomness and complexity exist in the real environment, so its theoretical and applied research has some challenging. At present, there are still many problems to be resolved[2,3]. In order to resolve ambiguities in associating object detections and to overcome detection failures, most of these recent works [4, 5, 6, 7] process video sequences in a batch mode in which video frames from future time steps are also utilized to solve the data association problem.

Recently, there is a trend on learning to track that advocates the concept of injecting learning capabilities to MOT [8, 9]. Based on their learning schemes, we can categorize these methods into offline-learning methods and online-learning methods. In offline-learning, learning is performed before the actual tracking takes place. For instance, use super-vision from ground truth trajectories offline to learn a similarity function between detections and tracking for data association. As a result,

offline learning is static: it cannot take into account the dynamic status and the history of the target in data association, which is important to resolve ambiguities, especially when it needs to reassign missed or occluded objects when they appear again. In contrast, online-learning conducts learning during tracking. In multiple object tracking, problems are found such as too much time consuming in data processing and track loss of complex background. To elevate these problems, the multiple centroid theory of moving object was proposed in this work, concepts and definitions are given, and object tracking process based on multiple centroid is described.

II. MULTIPLE CENTROID

The first concern is tailing problem of object motion in space. Assuming that the moving object is expressed by rectangle template, denoted as M , the lengths of the template are $2a$ and $2b$. In three-dimensional coordinate system (x, y, z) , the tailing trajectory of rectangle template centroid is calibrated at time t the time-domain function of centroid trajectory ε is defined as $\varepsilon = \tau(x, y, z, t)$, and also at time-domain function $l = v(x, y, z, t)$ represents the edge centroid trajectory l . The rectangle template is described by $M_{x,y,z,t}$, after a moving time of Δt , the template is $M_{x,y,z,t+\Delta t}$. Centroid during time Δt moves along the function ε from template $M_{x,y,z,t+\Delta t}$ to $M_{x,y,z,t+2\Delta t}$. After the moving, the left vertical lines of two templates are overlap. The relevant definitions and concepts are given as follows. The model diagram is shown in Figure 1.

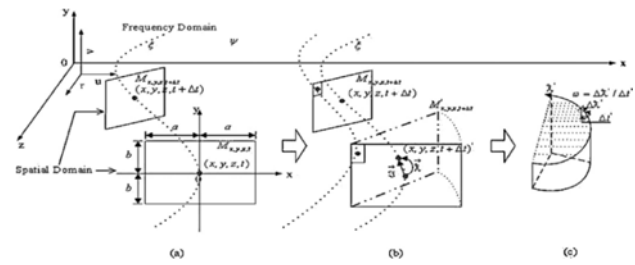


FIGURE I. MODEL CHART

A. Definition 1

In spatial domain, the vector between two centers of mass is defined as spatial vector, denoted as 3 , the modulus of spatial vector is 3 .

B. Definition 2

In frequency domain ξ , the vector between two centers of mass is defined as frequency vector, denoted as λ , and the modulus of it is $|\lambda|$.

C. Definition 3

Precedent impact strength of moving target is assumed as ω , where $\omega = \Delta\lambda/\Delta t$.

D. Definition 4

Centroid motion of the center of gravity formed the periodic tailing trajectory spectrum, it is defined as space spectrum, denoted by ξ . By Fourier transform time-domain orbit ε of centroid obtains frequency domain spectrum, it can be used to represent ξ :

$$\xi(u, v, r) = \int_0^{2a} \int_0^{2b} \int_0^{|\lambda|} \varepsilon(x, y, z) e^{-2\pi j(\frac{ux}{2a} + \frac{vy}{2b} + \frac{rz}{|\lambda|})} dx dy dz \quad (1)$$

E. Definition 5

Centroid motion of each edge formed the periodic (uniform or non-uniform) tailing trajectory spectrum, it is defined as edge spectrum, denoted by ψ . By Fourier transform time-domain orbit l of edge centroid obtains frequency domain spectrum, it can be used to represent ψ :

$$\psi^i(u, v, r) = \int_0^{2a} \int_0^{2b} \int_0^{|\lambda|} l^i(x, y, z) e^{-2\pi j(\frac{ux}{2a} + \frac{vy}{2b} + \frac{rz}{|\lambda|})} dx dy dz \quad (2)$$

Where i represents the number of edge center of mass, and $i \in [0, 4ab]$, $j = \sqrt{-1}$, and u, v, r are spectrum vectors, among them $u \in [0, 2a]$, $v \in [0, 2b]$, $r \in [0, |\lambda|]$.

F. Definition 6

The frequency which changes continuously and flexibly in space spectrum and edge spectrum is defined as soft feature, denoted by T . The value range of T is the differentiable range of space spectrum $\xi(u, v, r)$ and edge spectrum $\psi^i(u, v, r)$:

$$T = \begin{bmatrix} (u_{1,1}, v_{1,1}, r_{1,1}) & \dots & (u_{m,1}, v_{m,1}, r_{m,1}) \\ \vdots & \ddots & \vdots \\ (u_{1,n}, v_{1,n}, r_{1,n}) & \dots & (u_{m,n}, v_{m,n}, r_{m,n}) \end{bmatrix} \times U \sum_{i=1}^q \begin{bmatrix} (u_{1,1}^i, v_{1,1}^i, r_{1,1}^i) & \dots & (u_{q,1}^i, v_{q,1}^i, r_{q,1}^i) \\ \vdots & \ddots & \vdots \\ (u_{1,p}^i, v_{1,p}^i, r_{1,p}^i) & \dots & (u_{q,p}^i, v_{q,p}^i, r_{q,p}^i) \end{bmatrix}, \quad i \in [0, 4ab] \quad (3)$$

III. MARKOV DECISION PROCESS

In our framework, the lifetime of a target is modeled with a Markov Decision Process (MDP). The MDP consists of the tuple $(S, A, T(\cdot), R(\cdot))$:

- The target state $s \in S$ encodes the status of the target.
- The action $a \in A$ which can be performed to a target.
- The state transition function $T : S \times A \rightarrow S$ describes the effect of each action in each state.

- The real-valued reward function $R : S \times A \rightarrow R$ defines the immediate reward received after executing action a to state s .

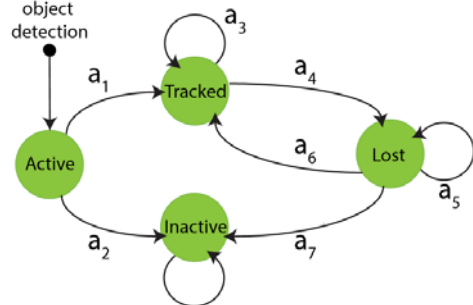


FIGURE II. THE TARGET MDP IN OUR FRAMEWORK

A. States

We partition the state space in the target MDP into four subspaces, i.e., $S = S_{\text{Active}} \cup S_{\text{Tracked}} \cup S_{\text{Lost}} \cup S_{\text{Inactive}}$, where each subspace contains infinity number of states which encode the information of the target depending on the feature representation, such as appearance, location, size and history of the target. Figure 2 illustrates the transitions between the four subspaces. “Active” is the initial state for any target. Whenever an object is detected by the object detector, it enters an “Active” state. An active target can transition to “Tracked” or “Inactive”. Ideally, a true positive from object detector should transition to a “Tracked” state, while a false alarm should enter an “Inactive” state. A tracked target can keep tracked, or transition to “Lost” if the target is lost due to some reason, such as occlusion, or disappearance from the field of view of the camera. Likewise, a lost target can stay as lost, or go back to “Tracked” if it appears again, or transition to “Inactive” if it has been lost for a sufficiently long time. Finally, “Inactive” is the terminal state for any target, i.e., an inactive target stays as inactive forever.

B. Actions and Transition Function

Seven possible transitions are designed between the states of a target, which correspond to seven actions in our target MDP. Figure 2 illustrate these transitions and actions. In the MDP, all the actions are deterministic, i.e., given the current state and an action, we specify a new state for the target. For example, executing action $a4$ on a tracked target would transfer the target into a lost state, i.e., $T(s_{\text{Tracked}}, a4) = s_{\text{Lost}}$.

C. Reward Function

In our MDP, the reward function is not given but needs to be learned from training data, i.e., an inverse reinforcement learning problem [10], where we use ground truth trajectories of the targets as supervision.

IV. POLICY

In MDP, a policy π is a mapping from the state space S to the action space A , i.e., $\pi : S \rightarrow A$. Given the current state of the target, a policy determines which action to take. Equivalently, the decision making in MDP is performed by following a policy. The goal of policy learning is to find a policy which maximizes the total rewards obtained. In this section, we first describe our policies designed for the Active subspace and the Tracked

subspace, then we present a novel reinforcement learning algorithm to learn a good policy for data association in the Lost subspace.

A. Policy in an Active State

In an Active state s , the MDP makes the decision between transferring an object detection into a tracked or inactive target to deal with noisy detections. This decision making can be considered to be a preprocessing step before tracking. Strategies such as non-maximum suppression or thresholding detection scores are usually used. In our implementation, we train a binary Support Vector Machine (SVM) [11] offline to classify a detection into tracked or inactive using a normalized 5D feature vector $\Phi_{Active}(s)$, i.e., 2D coordinates, width, height and score of the detection, where training examples are collected from training video sequences. This is equivalent to learning the reward function in Active:

$$R_{Active}(s, a) = y(a)(w^T_{Active}\phi_{Active}(s) + b_{Active}) \quad (4)$$

B. Policy in a Tracked State

In a Tracked state, the MDP needs to decide whether to keep tracking the target or to transfer it into a lost state. As long as the target is not occluded and is in the camera's field of view, we should keep tracking it. Otherwise, it should be marked as lost. This decision making is related to the goal of single object tracking in the literature [12, 13, 14, 15]. Inspired by these works, we build an appearance model for the target online and use it to track the target. If the appearance model is able to successfully track the target in the next video frame, the MDP leaves the target in a tracked state. Otherwise, the target is transferred to a lost state. Our framework is general to utilize different approaches in building the appearance model. We describe our implementation based on the TLD tracker [14] in this work. This is equivalent to learning the reward function in Tracked:

$$R_{Tracked}(s, a) = \begin{cases} y(a), & \text{if } e_{medFB} < e_0 \text{ and } o_{mean} > o_0 \\ -y(a), & \text{otherwise} \end{cases} \quad (5)$$

C. Policy in a Lost State

In a Lost state, the MDP needs to decide whether to keep the target as lost, transition it to a tracked state, or mark it as inactive. We simply mark a lost target as inactive and terminate the tracking if the target has been lost for more than T_{Lost} frames. The challenging case is to make the decision between tracking the target and keeping it as lost. We treat it as a data association problem: in order to transfer a lost target into a tracked state, the target needs to be associated with one of the detections from the object detector, otherwise, the target is kept as lost. This is equivalent to learning the reward function in Lost:

$$R_{Lost}(s, a) = y(a) \left(\max_{k=1}^M \phi(t, d_k) + b \right) \quad (6)$$

V. REVISE AND COMBINE

The flow-process diagram is shown in Figure 3.

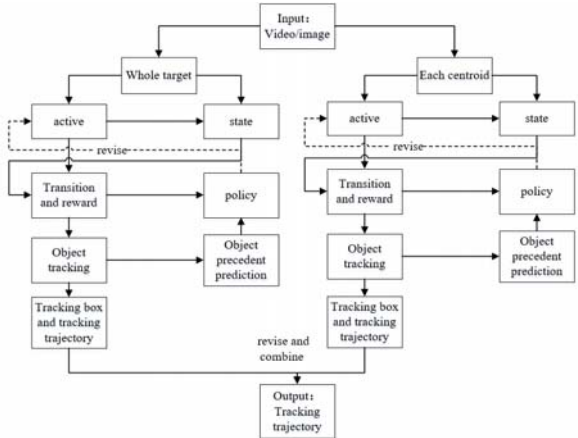


FIGURE III. THE FLOW-PROCESS DIAGRAM IN OUR FRAMEWORK.

VI. EXPERIMENT AND ANALYSIS

Figure 4 shows the tracing effect of three moving persons. In this figure, there are some illustrations with representative results of continuous video tests. With different shooting angles, feather occlusion is produced when three objects in the test (NO.187, NO.295). As the three moving objects merge a whole object visually, when edge separating of objects appears, High-dimensional Statistical Measure (HSM) and Probabilistic Fusion (PF) tracking algorithm of object occlusion proposed in [16, 17] lose the objects. With the algorithm of precedent predication tracking based on soft feature put forward in this paper, discrete convolution effect of precedent impact strength is considered in the process of tracking, so locations of the moving objects are tracked and predicted accurately in the case of object occlusion (NO.179, NO.306).

Table 1 shows our tracking performance on the test set, where we compare our tracker (MDP REinforcement Learning, MDP REL) with the state-of-the-art methods tested on the MOT benchmark. As we can see from the table, our tracker improves 7% in MOTA compared with the second best published tracker, and achieves the best performance in terms of mostly tracked and mostly lost targets even though it works in the online mode. The superior performance demonstrates the advantage so four learning to track strategy with MDPs. Figure 5 shows sampled tracking results on the 11 sequences in the test set.

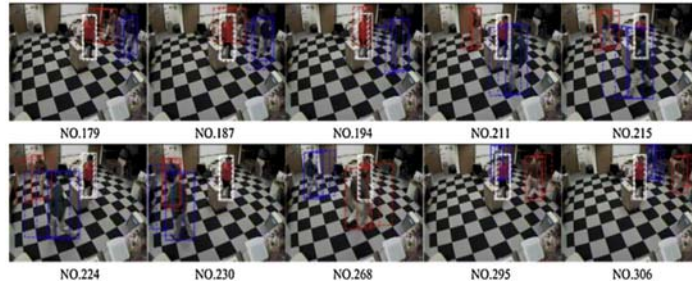


FIGURE IV. EXPERIMENT RESULTS OF THREE OBJECT TRACKING THROUGH SIMILAR BACKGROUND.

TABLE I. TRACKING PERFORMANCE ON THE TEST SET OF THE MOT BENCHMARK. MORE COMPARISONS ARE AVAILABLE AT [1]

Tracker	Tracking Mode	Learning Mode	MOTA	MOTP	MT	ML	FP	FN	IDS	Frag	Hz
DP.NMS [18]	Batch	N/A	14.5	70.8	6.0%	40.8%	13,171	34,814	4,537	3,090	444.8
TC.ODAL [19]	Online	Online	15.1	70.5	3.2%	55.8%	12,970	38,538	637	1,716	1.7
TBD [20]	Batch	Offline	15.9	70.9	6.4%	47.9%	14,943	34,777	1,939	1,963	0.7
SMOT [21]	Batch	N/A	18.2	71.2	2.8%	54.8%	8,780	40,310	1,148	2,132	2.7
RMOT [22]	Online	N/A	18.6	69.6	5.3%	53.3%	12,473	36,835	684	1,282	7.9
CEM [6]	Batch	N/A	19.3	70.7	8.5%	46.5%	14,180	34,591	813	1,023	1.1
SegTrack [23]	Batch	Offline	22.5	71.7	5.8%	63.9%	7,890	39,020	697	737	0.2
MotiCon [7]	Batch	Offline	23.1	70.9	4.7%	52.0%	10,404	35,844	1,018	1,061	1.4
MCMDP OFL	Online	Offline	30.1	71.6	10.4%	41.3%	8,789	33,479	690	1,301	0.8
MCMDP REL	Online	Online	30.7	71.3	13.2%	38.4%	9,717	32,424	681	1,500	1.1



FIGURE V. TRACKING RESULTS ON THE TEST SEQUENCES IN THE MOT BENCHMARK.

ACKNOWLEDGMENT

We thank Xiaohan Du for helpful discussions.

REFERENCES

- [1] Multiple object tracking benchmark. <http://motchallenge.net>. 8
- [2] M. Rezaeian, B.N. Vo, Error bounds for joint detection and estimation of a single object with random finite set observatio, IEEE Trans: Signal Process. 58(3) (2010)1493–1506.
- [3] D. Clark, B. Ristic, B.N. Vo, B.T. Vo, Bayesian multi-object filtering with amplitude feature likelihood for unknown object SNR, IEEE Trans. Signal Process. 58 (1) (2010) 26-37.
- [4] J. Berclaz, F. Fleuret, E. Turetken, and P. Fua. Multiple object tracking using k-shortest paths optimization. TPAMI, 33(9):1806–1819, 2011.1, 2
- [5] A. A. Butt and R. T. Collins. Multi-target tracking by lagrangian relaxation to min-cost network flow. In CVPR, pages 186–183, 2013. 1.
- [6] A. Milan, S. Roth, and K. Schindler. Continuous energy minimization for multitarget tracking. TPAMI, 36(1):58–72, 2014. 1, 2, 8.
- [7] L. Leal-Taix'e, M. Fenzi, A. Kuznetsova, B. Rosenhahn, and S. Savarese. Learning an image-based motion context for multiple people tracking. In CVPR, pages 3542–3549, 2014. 1, 8
- [8] X.Song, J.Cui, H.Zha, and H.Zhao. Vision-basedmultipleinteracting targets tracking via on-line supervised learning. In ECCV, pages 642–655. 2008. 1, 2.
- [9] Y. Li, C. Huang, and R. Nevatia. Learning to associate: Hybridboosted multi-target tracker for crowded scene. In CVPR, pages 2953–2960, 2009. 1, 2.
- [10] A. Y. Ng and S. J. Russell. Algorithms for inverse reinforcement learning. In ICML, pages 663–670, 2000. 3.
- [11] B. E. Boser, I. M. Guyon, and V. N. Vapnik. A training algorithm for optimal margin classifiers. In Proceedings of the fifth annual workshop on Computational learning theory, pages 144–152, 1992. 3.
- [12] B. Babenko, M.-H. Yang, and S. Belongie. Robust object tracking with online multiple instance learning. TPAMI, 33(8):1619–1632, 2011. 2, 3.
- [13] S.Hare, A.Saffari, and P.H.Torr. Struck: Structuredoutputtracking with kernels. In ICCV, pages 263–270, 2011. 2, 3, 4.
- [14] Z.Kalal, K.Mikolajczyk, and J.Matas. Tracking-learning-detection. TPAMI, 34(7):1409–1422, 2012. 2, 3, 4.
- [15] C. Bao, Y. Wu, H. Ling, and H. Ji. Real time robust l1 tracker using acceleratedproximalgradientapproach. In CVPR, pages 1830–1837, 2012. 2, 3, 4.
- [16] S. Boltz, E. Debreuve, M. Barlaud, High-dimensional statistical measure for region-of-interest tracking, IEEE Trans. Image Process. 18 (6) (2009) 1266–1283.
- [17] B.H. Han, L.S. Davis, Probabilistic fusion-based parameter estimation for visual tracking, Comput. Vision Image Und. 113 (2009) 435–445.
- [18] H. Pirsiavash, D. Ramanan, and C. C. Fowlkes. Globally-optimal greedy algorithms for tracking a variable number of objects. In CVPR, pages 1201–1208, 2011. 2, 8.
- [19] S.-H.Baeand K.-J.Yoon. Robustonlinemulti-object tracking based on tracklet confidence and online discriminative appearance learning. In CVPR, pages 1218–1225, 2014. 1, 2, 8.
- [20] A. Geiger, M. Lauer, C. Wojek, C. Stiller, and R. Urtasun. 3d traffic scene understanding from movable platforms. TPAMI, 36(5):1012–1025, 2014. 8.
- [21] C.Dicle, O.I.Camps, and M.Sznaier. Thewaytheymove: Tracking multiple targets with similar appearance. In ICCV, pages 2304–2311, 2013. 8.

- [22] J. H. Yoon, M.-H. Yang, J. Lim, and K.-J. Yoon. Bayesian multiobject tracking using motion context from multiple objects. In WACV, pages 33–40, 2015. 8.
- [23] A.Milan, L.Leal-Taix'e, K.Schindler, and I.Reid. Joint tracking and segmentation of multiple targets. In CVPR, pages 5397–5406, 2015. 8.

Characterizing the Impact of DDoS Attack on Inter-domain Routing System: A Case Study of the Dyn Cyberattack

Yujing Liu^{1,*}, Zhilin Wang² and Nan Li¹

¹College of Computer, National University of Defense Technology, Changsha, China

²Education Department, National University of Defense Technology, Changsha, China

*Corresponding author

Abstract—The inter-domain routing protocol BGP is sensitive to severe network congestion. In order to study the reliability of BGP under stress, we take the Dyn cyberattack on October 21st, 2016 as a study case to characterize the impact of DDoS attack on inter-domain routing system. We propose several metrics including number of BGP updates, reachability, and variance of AS link betweenness centrality to measure the reachability and stability of the Internet. After performing a thorough analysis based on publicly available BGP data, we obtain key insights about the event. Firstly, the attack affects the reachability from the inter-domain routing perspective, but the effect is very small. Secondly, during the attack, the Internet experiences an unstable routing state in terms of a surge of BGP updates and changes of AS links' betweenness centrality. Finally, route flapping doesn't happen, probably because of anycast routing technique employed by Dyn, balancing high volume of traffic among multiple data centers instead of converging in one single link.

Keywords—Internet; inter-domain routing system; DDoS; BGP

I. INTRODUCTION

The inter-domain routing system of the Internet consists of thousands of autonomous systems (ASes). Border Gateway Protocol (BGP) is the de facto protocol for inter-domain routing system, transmitting routing information among ASes. Reliability of BGP is very important to achieve stable communications in the Internet. Currently, the routing control packets of BGP, such as keepalive packets, share bandwidth and buffer space with normal data traffic. This co-location of control plane and data plane makes BGP sensitive to severe network congestion [1-3]. Therefore, the distributed denial-of-service (DDoS) attack which generates high volume of traffic will affect the inter-domain routing system. Previous researches about this subject haven't provided thorough analysis, especially in the real Internet environment.

On October 21st, 2016, a series of large-scale DDoS attacks were launched against a DNS provider - Dyn. The cyberattack caused major Internet platforms and services, such as Twitter, Paypal, Github, Amazon, to be unavailable to plenty of users in Europe and North America. These critical services are customers of Dyn [4]. In this paper, we take this event as a study case to characterize the impact of DDoS attack on inter-domain routing system, in order to answer the following

questions: Does the attack affect the reachability and stability of inter-domain routing system? Does route flapping happen as mentioned by related work [1]?

We propose several metrics including number of BGP updates, reachability, and variance of AS link betweenness centrality to characterize the reachability and stability of inter-domain routing system under this DDoS attack. By analyzing publicly available BGP data, we find that (1) the attack affects the reachability, but the effect is very small; (2) during the attack, the inter-domain routing system experiences an unstable routing state in terms of a surge of BGP updates and changes of AS links' betweenness centrality; (3) but route flapping doesn't happen, probably because of anycast routing technique among multiple data centers by Dyn, preventing high volume of traffic from converging in one single link.

II. RELATED WORK

Reference [1] introduces the Coordinated Cross Plane Session Termination, or CXPST, attack, a distributed denial of service attack that attacks the control plane of the Internet by using data plane traffic. By carefully choosing BGP sessions to terminate, CXPST induces targeted route flapping, moreover, generates a surge of BGP updates that are seen by nearly all core routers on the Internet. The CXPST attack can be considered as a kind of DDoS attack. The conclusion of their work is based on simulation results. In our paper, we are going to examine whether the conclusions are founded in the real Internet under real DDoS attack.

Reference [5] provides the first evaluation of several IP anycast services under DDoS attack with public data. They employ BGP data to evaluate whether there are route changes during the attack. The metric is simply the amount of BGP route changes over time. However, in order to characterize different perspectives of the Internet, more well defined metrics and characteristics should be proposed and evaluated.

Generally speaking, there is few related work about analyzing impact of DDoS attack on inter-domain routing system. In this paper, we propose several new metrics to characterize the impact by analyzing a real attack in the real environment.

III. METHODOLOGY

The key function of inter-domain routing system is to find a route for a peer of source and destination. Therefore, we define several metrics to characterize how a DDoS attack affects the routing process of the Internet.

A. BGP Routing Data Source

We explore the inter-domain routing data by analyzing BGP RIBs (Routing Information Bases) and updates collected by RIPE RIS [6] and Route Views [7]. These two projects employ multiple Remote Route Collectors (RRCs) to establish BGP peering sessions with many ASes around the world, collect their routing information to all the other destination ASes, and periodically dump their BGP routing tables and updates. Therefore, we can get routes from those monitors to routable IP prefixes in the Internet at a certain period of time. The available data from multiple vantage points reveals a broad and global though necessarily incomplete view of inter-domain routing over time. We use this data to sample the Internet's behavior after DDoS attacks.

B. Number of BGP Updates

BGP is a routing protocol driven by route changes. In other words, routing information carried by BGP update messages are exchanged among routers only when there are some changes in the inter-domain routing system, such as changes of topology and routing policy. Therefore, large amounts of updates indicate an unstable routing state of the Internet. In this paper, we calculate the number of BGP updates associated with particular IP prefixes in every 10 minutes for a period of time T . The BGP updates which we concern about consist of announcements and withdrawals. Announcement means appearance of route, whereas withdrawal means disappearance of route.

C. Reachability

Reachability measures whether there is an available route between source and destination in the inter-domain routing system. In this paper, we measure the reachability from monitors to certain IP prefixes. M is the set of monitors. It is formally defined as follows:

$$R_{mp} = \begin{cases} 1, & \text{if there is a route from } m \text{ to } p \\ 0, & \text{if there isn't a route from } m \text{ to } p \end{cases} \quad (1)$$

$$R_p = \sum_{m \in M} R_{mp} \quad (2)$$

The reachability from monitor m to prefix p is equal to 1 if there is an available route from m to p . It is equal to 0 if there is not. The reachability of prefix p is the summation of reachability from all the monitors in M . We measure the reachability for a period of time T and then obtain a sequence of reachability changes during that time.

D. Variance of AS Link Betweenness Centrality

Not all the BGP updates reflect inter-domain routing changes. Some of them are duplicated from the perspective of inter-domain routing because of intra-domain routing changes or just pathological duplicates. In this paper, we propose a metric named *variance of AS link betweenness centrality* to characterize inter-domain routing changes.

We model the Internet as a graph $G = (V, E)$ where V is the set of all ASes, and E is the set of AS links. Let e be an AS link in E , then its betweenness centrality associated with prefix p is defined as:

$$BC_p(e) = \sum_{m \in M} \sigma_{mp}(e) \quad (3)$$

where $\sigma_{mp}(e)$ denotes the total number of AS paths between monitor m and prefix p that pass through link e . Inter-domain routing changes will result in the changes of some AS links' betweenness centrality. Accordingly, we define the variance of AS link betweenness centrality to measure the difference of it at time $t-1$ and t as follows:

$$\Delta BC_{pt}(e) = BC_{pt}(e) - BC_{p(t-1)}(e) \quad (4)$$

We measure the variance of AS link betweenness centrality of every link in E for a period of time T to construct a variance matrix ΔBC_p , where every row represents a sequence of betweenness centrality changes associated with each AS link.

Analysis results from different dimensions of the variance matrix reveal useful characteristics such as the aggregated time of routing changes and the dominant routing patterns.

1) *Aggregated time of routing changes*: Each column of ΔBC_p contains every AS link's betweenness centrality change at time slot t . We calculate the mean value of all links' absolute variation at time t , denoted as μ_{pt} . Large value of μ_{pt} indicates aggregated time of routing changes.

2) *Dominant routing patterns*: Each row of ΔBC_p consists of betweenness centrality changes over time associated with a certain AS link e . We split all rows into two clusters using K-Means algorithm according to their absolute value. Because the variance of AS link betweenness centrality often demonstrates a 'power-law' distribution, the smaller cluster contains the dominant routing patterns. Moreover, routing patterns in the smaller cluster often show synchronization of route changes. Further analysis with the value of variation enable us to differentiate the correlative and backup relations.

IV. CHARACTERIZING THE IMPACT OF DYN DDoS ATTACK

The Dyn DNS network consists of four IP routing prefixes – 204.13.250.0/24, 204.13.251.0/24, 208.78.70.0/24 and 208.78.71.0/24. These prefixes are in AS33517. Many critical services, such as Twitter, Paypal, Github, Amazon and so on, employ Dyn DNS servers to be publicly available. As shown in Table 1, the DNS IPs of one customer are dispersed in four

prefixes, ensuring redundancy when a catastrophic failure happens. Unfortunately, the targets of this DDoS attack include all the four prefixes. Therefore, all the critical customers are affected. In this paper, we take these four prefixes as analyzing targets to characterize the impact of this attack.

TABLE I. EXAMPLES OF DYN DNS SERVER IP

Customer	DNS Server	DNS Server IP
twitter.com	ns1.p34.dynect.net	208.78.70.34
	ns2.p34.dynect.net	208.78.71.34
	ns3.p34.dynect.net	204.13.250.34
	ns4.p34.dynect.net	204.13.251.34
paypal.com	ns1.p57.dynect.net	208.78.70.57
	ns2.p57.dynect.net	208.78.71.57
	ns3.p57.dynect.net	204.13.250.57
	ns4.p57.dynect.net	204.13.251.57

A. Number of BGP Updates

According to technical report [4], the DDoS attack starts at 11:15 UTC on October 21st, 2016. We calculate the number of BGP updates associated with the four IP prefixes in every 10 minutes from 00:00 to 24:00 on that day. From the results shown in Figure 1, we can see that the amount of announcement updates increases dramatically after the attack starts. Moreover, the increasing patterns associated with the four prefixes indicate that 204.13.250.0/24 and 204.13.251.0/24 are in the same constellation, whereas 208.78.70.0/24 and 208.78.71.0/24 are in the same constellation. The emergence of updates is an indication that the inter-domain routing system experiences an unstable routing state.

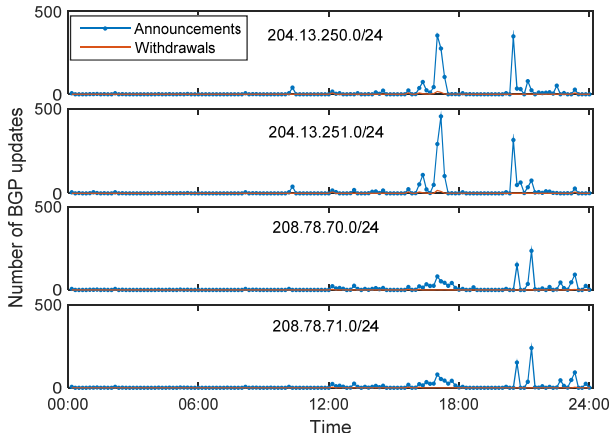


FIGURE I. NUMBER OF BGP UPDATES

B. Reachability

Along with the high volume of DDoS traffic toward the DNS sever, many services become unavailable. In this paper, we examine whether the DDoS affect the reachability from multiple monitors to DNS server prefixes. The measurement results in Figure 2 show that the attack indeed affects the reachability from the inter-domain routing perspective, but the effect is small, which is less than 5% averagely.

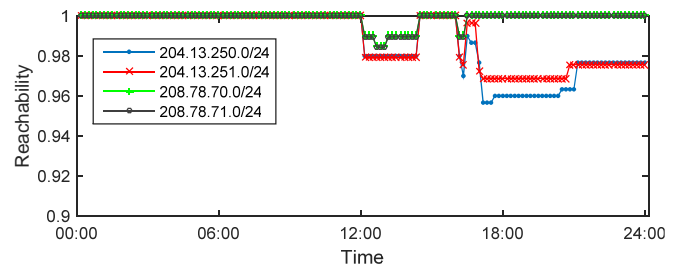


FIGURE II. CHANGES OF REACHABILITY

C. Aggregated Time of Routing Changes

By parsing the BGP RIB and update data associated with the four prefixes during one day, we maintain four variance matrixes of AS link betweenness centrality. These matrixes reflect non-redundant inter-domain routing changes. The values of μ_{pt} associated with the four prefixes are shown in Figure 3. Comparing with Figure 1, we find that routing changes and the emergences of BGP updates appear almost at the same time, but with different changing patterns. Updates of 204.13.250.0/24 and 204.13.251.0/24 contain more duplicated messages from the perspective of inter-domain routing. The aggregated time of routing changes include 16:50-17:20 and 20:20-20:30. We denote the first period as $T1$, and the second period as $T2$.

D. Dominant Routing Patterns

The variance matrix ΔBC_p of prefix 204.13.250.0/24 contains 458 rows, representing there are 458 AS links change at least once during that day in terms of inter-domain rerouting. In addition, matrix of 204.13.251.0/24 has 444 rows; matrix of 208.78.70.0/24 has 167 rows; and matrix of 208.78.71.0/24 has 161 rows. We divide the rows of variance values according to our clustering method mentioned before. The dominant routing patterns associated with four prefixes are shown in Figure 4. We infer that because of the high volume of DDoS traffic, BGP keepalive messages may be dropped by neighbor routers, making BGP sessions disconnect. Then routers will choose alternative routes to reach destinations. Therefore, the betweenness centrality of AS links will change accordingly.

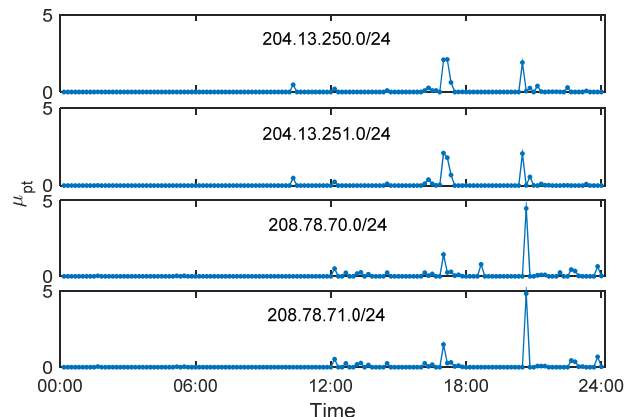


FIGURE III. AGGREGATED TIME OF ROUTING CHANGES

Take the first figure as an example. During period $T1$, paths from AS3356 to AS33517 are rerouted to paths through AS1299. Number of paths from AS174 to AS33517 increases first, and then decreases in the next 10 minutes. During period $T2$, paths from AS1299 to AS33517 are rerouted back to paths through AS174 and AS3356. From the dominant routing patterns we infer that AS1299, AS174 and AS3356 are multi-home providers of AS33517. Disconnection in one neighbor will result in routing changes to another neighbor, making the inter-domain routing system more reliable. Comprehensive analysis of the four figures reveals the fact that during DDoS attack, the Internet experiences more routing changes than usual time, but route flapping mentioned in related work [1] doesn't happen. We infer it is a consequence of anycast routing technique among 20 data centers by Dyn [4], preventing high volume of traffic from converging in one single link.

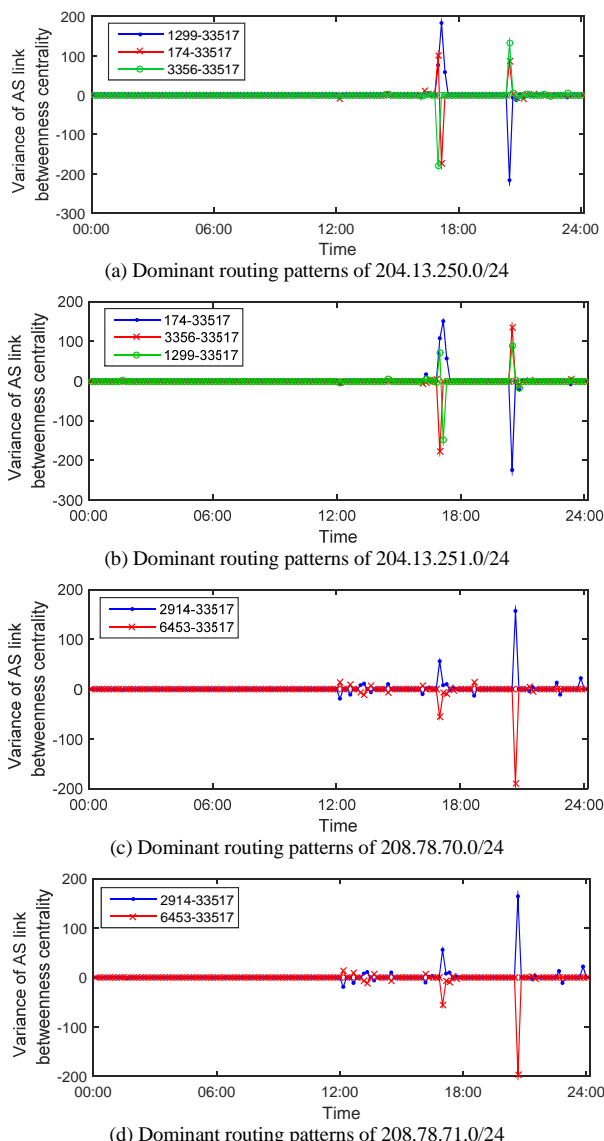


FIGURE IV. DOMINANT ROUTING PATTERNS

V. CONCLUSION

In this paper, we take the Dyn cyberattack event as a study case to characterize the impact of DDoS attack on inter-domain routing system. We propose several metrics to measure the characteristics of the impact including number of BGP updates, reachability, aggregated time of routing changes and dominant routing patterns. After performing a thorough analysis, we find that (1) the attack affects the reachability from the inter-domain routing perspective, but the effect is very small; (2) during the attack, the inter-domain routing system experiences an unstable routing state in terms of a surge of BGP updates and changes of AS links' betweenness centrality; (3) but route flapping doesn't happen, because of anycast routing technique among multiple data centers by Dyn, preventing high volume of traffic from converging in one single link.

ACKNOWLEDGMENT

This work is supported by the National Natural Science Foundation of China, under Grant No. 61602503 and No. 61472437.

REFERENCES

- [1] M. Schuchard, A. Mohaisen, D. Kune, N. Hopper, Y. Kim, and E. Vasserman, "Losing Control of the Internet: Using the Data Plane to Attack the Control Plane," in Proc. of CCS '10, pp. 726–728, 2010.
- [2] W. Deng, P. Zhu, X. Lu and B. Plattner, "On evaluating BGP routing stress attack," Journal of Communications, vol. 5, no. 1, pp. 13-22, 2010.
- [3] H. Liu, X. Hu, D. Zhao and X. Lu, "Failure Isolation based Defense against Internet CXPST-like Attack," International Journal of Hybrid Information Technology, vol. 5, no. 2, pp. 175–180, 2012.
- [4] N. Kephart, "The DDoS Attack on Dyn's DNS Infrastructure," <https://blog.thousandeyes.com/dyn-dns-ddos-attack/>, 2018.
- [5] G. Moura, R. Schmidt, J. Heidemann, W. Vries, M. Muller, L. Wei, and C. Hesselman, "Anycast vs. DDoS: evaluating the November 2015 root DNS event," In Proceedings of the 2016 ACM on Internet Measurement Conference, pp. 255-270, 2016.
- [6] RIPE Routing Information Service (RIS), <http://www.ripe.net/ris>, 2018.
- [7] University of Oregon Route Views Project, <http://www.routeviews.org>, 2018.

IoT Node Trust Authorization Model

Ruizhong Du, Chong Liu* and Fanming Liu

Cyberspace Security and Computer College, Baoding 071002, China

Key Laboratory on High Trusted Information System in Hebei Province, Baoding 071002, China

*Corresponding author

Abstract—Aiming at the characteristics of strong heterogeneity and limited computing ability of IoT nodes, this dissertation proposes a Trust Authorization Model based on detection feedback in IoT, combined with the current trust model of IoT and implement storage and other tasks by calculating and storing the cluster head node with strong ability to facilitate the data transmission and search for energy consumption, and help the local network be not limited by the computing power of the device. In terms of trust calculation, the threshold value is based on the recommendation. Simulation results show that this model has lower energy consumption than other similar models, has good coping ability for attacks such as malicious recommendation and malicious slander, and has a higher detection rate and response rate to attack nodes.

Keywords—Internet of things; trust evaluation; cluster

I. INTRODUCTION

Internet of Things is an important stage in the development of information age. With the continuous improvement of the level of social information, individuals and even countries pay more attention to them. Because of huge market demand and broad prospects for its development, the Internet of Things is regarded as the next trillion-level market opportunity. At present, many countries in the world also attach great importance to the Internet of Things such as the Japan's "wisdom earth" American's "IJPN" and EU's "Internet of Things Action According to expert estimates, billions of devices will be connected to the Internet over the next few years [1].

The Internet of Things is an open, intelligent system where most nodes are unmanaged and vulnerable to malicious attacks, In another way, the external environment will damage the IoT devices as well as , the IoT nodes with single function and limited computing resources are easily invaded and become malicious nodes, which are hidden inside the IoT network ,launch internal attacks with legal status and cause serious security risks. In the Internet of Things, network attacks will not only cause property damage, but also threaten life. Therefore, it is particularly urgent and important to formulate a security strategy in favor of the IoT environment.

At present, there are two main methods to ensure the security of perceived information: one is used by the similarity of perceptual nodes to deal with multiple data so that it eliminates false information sent by malicious nodes. The other is to ensure the authenticity of raw data, and using data encryption authentication to guarantee data security[2,3]. Traditional secure authentication methods and commonly used

encryption calculation are too complicated for limited resources and large-scale deployment of IoT devices [4]. In addition, these complex encryption methods considerIoT as a heterogeneous network with the feature of multiple fusion.

The model adopts the idea of trust model. And the trusted computing and storage functions are given to edge devices or devices with higher computational capabilities, reducing the overall energy consumption; the threshold dynamic adjustment reduces manual intervention and the network structure is more intelligent and automatic.

II. RELATED WORK

At present, there has been some research on the trust evaluation mechanism under the Internet of Things. Chen [5] and his colleagues proposed a trust management protocol for IoT devices, and conducted trust evaluation using the trustworthiness, interaction and domain preferences as parameters. Nitti et al. [6] put up a trust model that took into account the subjectivity and objectivity of SIoT (Social Internet of Tings), using the historical record of itself and neighboring nodes to calculate the trust of the trustee This model used global feedback records to calculate trustworthiness reflects the objectivity of the model. However, it neglected the reliability of the recommended data of neighboring nodes and was prone to malicious recommendation. [7] It proposed a distributed dynamic trust management model considered trust reliability. The use of reliability to assess the degree of trust, to a certain extent, reduces the impact of malicious recommendation data. However, a large number of nodes with weak computing power in the Internet of Things environment are not suitable for P2P trust calculation, transmission and storage mode, and some devices may not operate normally. Xu Huan [8] conducted his research on the structure characteristics of IOT, adopted the clustering structure in the IoT perception layer, evaluated the trustworthiness of nodes by predicting the interaction possibility of nodes, reduced the energy consumption and solved the problem of weaker Node, but he didn't settle down the corresponding resistance for malicious nodes. Liu Wenmao et al. [9] proposed a hierarchical trust structure of the perception layer under the Internet of Things (IoT) environment. Based on the evidence theory, the trust of dynamic motion readers was deduced, which has the ability to detect the malicious nodes. The detection process does not consider the IoT node computing power requirements and low energy consumption, these complex algorithms for the introduction of new equipment are not friendly.

III. TRUST AUTHORIZATION MODEL

A. Model Design

Nodes in the IoT environment are quite different from the nodes in the previous distributed system. IOT nodes contain a wide range of sensor devices. Different device nodes generally have different computing, storage and communication capabilities. Those intelligence nodes and man-hours nodes are small. For these reasons, some of these nodes need to be satisfied with some additional requirements. It is particularly important to propose a more specific trust evaluation model for the Internet of Things.

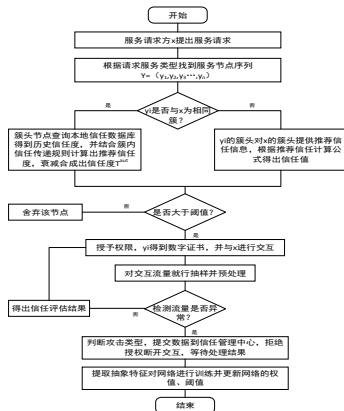


FIGURE I. SYSTEM FLOW CHART

(1)Cluster nodes: IoT composed of intelligent devices node with weak computing power .

(2)Cluster head nodes: Through the cluster head election algorithm, the nodes with strong computing power selected among cluster member nodes, Store and calculate the trust information of nodes in the cluster.

(3)Domain Trust management Center: comprehensive management and record of trust data in this domain. The domain trust management center is a trusted anchor. The trust management center includes the global trust storage module, which keeps trust information of network nodes in the entire domain.

In this paper, we present a model of IoT based on trusted authoritative choice of nodes and mutual trustworthiness detection. According to historical mutual trust and recommendation trust, dynamic selection of authorization is carried out by periodically checking the behavior of authorized nodes. If the node behavior exceeds the specified threshold, the abnormal response measures will be executed in time.

B. Trust Authorization

When the core information management center of the Internet of Things receives the service request sent by the user, it sends the request data to the subordinate management node, and then subordinate proxy node selects and authorizes the sensor node according to the personality of the service type. For the purpose of this article Trust management module, the basis of authorization is the assessment of trust. These include two types of trust factors - historical statistics trust value,

recommended trust value. Through the weighted synthesis of two types of trust factors, the static trustworthiness of this interaction is calculated and compared with the threshold to decide whether to authorize or not.

- Historical statistics trust calculation.

The historical trust calculation is to directly evaluate the direct trust of the target node according to the historical interaction record stored by the local database of the trust management node. Each trust management node maintains a history table that holds the history of trusts. The parameters include Flag, time, the corresponding historical trust and the address information of the interaction node (such as IPv6, EPC, etc.). For each time a node is selected, the local storage information is measured first, and if the flag in the latest interaction record is 0, the node is discarded directly. If 1 then continue to read the following information, its trust calculation. The time parameter is used to reflect the time decay of the data. The further the data is stored, the lower the reliability is. In the mathematical expression of this model, the time decay function is used as the weight of the historical interaction trust. The trustworthiness value for the node after the previous interaction is recorded by the composite trust record. The address information of the interaction node is used to provide an addressing basis for the second phase of the trust evaluation - the response scheme of the node behavior evaluation. The trusted behavior detection module will be described in detail.

Step1: Read the history trust sequence stored locally in cluster head Q_{all} . Here, it is assumed that Q_b is the trust history of the target node B. $Q_b = \{q_1, q_2, q_3, \dots, q_{dn}\}$, n is the number of historical interactions. One of the elements q_i ($i > n$) contains the Flag, time, comprehensive trust and address information of the interactive node.

Step2: Attenuate and synthesize for each node. Decay degree by the time function $\theta(t) = Q_t + e^{-N_t(t-t_i)}$ to represent, where Q_t and N_t is greater than 0 parameters, according to the degree of the specific application to determine. t is the current time, t_i is the time when hi is recorded.

In conclusion, the historical comprehensive trust of node A to node B is:

$$T^{his}(A \rightarrow B) = \sum_{i=1}^n \frac{\theta(t_i)}{\sum_{j=1}^n \theta(t_j)} hist_i \quad n>0 \quad (1)$$

Where $hist_i$ represents the history of the first i stored time trust. When there is no interaction between the local record, that $n = 0, hist_i = 0.5$ the default value. It means that they trust and distrust the unfamiliar node. To a certain extent, this is similar to that of human society.

- recommendation trust.

Similar to the transmission of trust in human society, there also exists trust transfer and exchange between nodes in the Internet of Things, namely, recommendation trust. The model in this paper is based on the clustering trust model. All cluster heads form the upper nodes, and the cluster heads store the

reputation values and related parameters of the nodes in the cluster. As a reference data of authorized trust evaluation, recommendation trust can reflect the reputation of nodes more comprehensively and makes the assessment results to be more reliable. However, there are some safety issues in recommending trust, such as collaborative deception and malicious evaluation.

According to the cluster of the mutual nodes of both parties, it can be divided into a cluster recommendation and a cluster recommendation:

(1)The recommended trust in the cluster: the subject node and the target node belong to the same cluster, and the subject node A records in the cluster head that there is too much or no interaction with the target node B. In this case, the cluster head node selects the nodes with higher credibility value to form the sequence $H_{rec} = \{h_1, h_2, h_3, \dots, h_m\}$, and H_{rec} satisfies the condition that there are many interaction records with the target node B. Trust record in H_{rec} sequence as recommended trust data as $T^{rec}(A \rightarrow B)$.

(2) Recommended trust among the clusters: the subject node and the target node are in different clusters. The nodes in different clusters need to communicate with each other through the cluster head node. Therefore, compared with the recommended trust relationship in the cluster, the recommended trust relationship among the clusters has a more relationship, that is, the mutual evaluation between the cluster heads of the two clusters.

From the above description, the recommended trust includes the following two cases:

Step1: The cluster head node chooses the recommended node in the cluster, and the recommended node C satisfies the following conditions: it has interacted with the main node A and has a high degree of trust, and interacts with the target node B to record it.

Step 2: Determine whether the target node B is in the same cluster as the principal node A.If you skip step 2 for the same cluster, if you add the cluster trust value to the cluster node as the data for the recommended trust calculation. The trust transfer mode between clusters with the main body of cluster nodes of the node in the cluster nodes as a new subject, target node in the cluster of cluster head nodes as recommended, the corresponding data generation into the calculation formula of recommendation trust, formula 2 in step 3.

Step3: According to the record, the recommendation sequence $H_{rt} = \{m_1, m_2, m_3, \dots, m_{rn}\}$ of the recommended node C for the target node B is selected, where r_n is the recommended node number, where m_i is the corresponding recommended node to the target node. The recommended trust, $0 < i < r_n$. Taking the recommended node C as an example in the cluster, the formula for calculating the m_i corresponding to the recommended node C is as follows:

$$m_i = T_i^{his}(A \rightarrow C) \times T_i^{his}(C \rightarrow B), \quad 0 < i < r_n \quad (2)$$

Step4: Weightedly aggregate the recommended trust values provided by each recommended node initially to obtain a recommended trust value. Because T^{rec} is formed by aggregating multiple recommended nodes, deliberately raising or degrading the target node in consideration of existence of a malicious node forms a collaborative fraud. This model reduces the influence of outlier nodes on trust evaluation by using the expectation of actual trustworthiness and the dispersion of actual value as the weight of the recommendation trust. It is almost impossible for most recommended nodes to be malicious nodes. The formula is as follows:

$$T^{rec}(A \rightarrow B) = \sum_{i=1}^m \omega_i \times m_i, \quad 1 < i < r_n \quad (3)$$

Where ω_i is the lazy degree of the recommended trust provided by the i -th recommendation node and the expected overall recommendation trust, and as the weight in the formula (3), the weight of the outlier data in the recommendation trust can be reduced to a certain extent so as to reduce the malicious recommendation Impact.

$$\omega_i = \frac{|E_r(m_i) - m_i|}{\sum_{i=1}^m |E_r(m_i) - m_i|}, \quad 0 < i < r_n \quad (4)$$

$E_r(m_i)$ is the mathematical expectation of overall recommendation trust.

$$E_r(m_i) = \frac{m_1 + m_2 + \dots + m_m}{r_n} \quad (5)$$

- authorization response

The weight of the historical statistical trust value T^{his} and the recommended trust value T^{rec} can be combined to obtain the authorized trust value T^{aut} , which is compared with the preset threshold value to obtain the decision whether to grant authorization to the target node B for interaction.

$$T^{aut} = \alpha T^{his} + (1 - \alpha) T^{rec} \quad (6)$$

The ∂ represents the historical statistical trust weight, which is obtained by the following formula:

$$\alpha = \frac{\frac{1}{D_h(his)}}{\frac{1}{D_h(his)} + \frac{1}{D_r(m)}} = \frac{D_r(m)}{D_h(his) + D_r(m)} \quad (7)$$

$D(x)$ is the variance function, used to represent the degree of dispersion of the data. Weights α , the general trust model

often rely on expert experience, simulation results and other means to determine the results of this often lack the scientific, agile and adaptive. In this paper, the variance function of historical statistics trust and recommended trust reflects its degree of dispersion as the reliability of data to dynamically adjust the weight factor. If the historical statistical trust dispersion to be large, then the recommended trust occupies a greater proportion. If the recommended trust dispersion to be larger, then there is a greater share of historical trust.

IV. SIMULATION

The experimental environment is as follows: Inter (R) Core (TM) i5-2400 @ 3.10GHz, 4GB RAM, 500GB hard drive.

In this paper, we design five sets of experiments to verify the relationship between trustworthiness and interaction rate, the relationship between mutual success rate and the proportion of three types of nodes.

C. Simulation of Trust Authorization Module

According to the clustering-based hierarchical framework, the nodes in IoT are abstractly processed. To verify this model, four clusters, Cluster1 ~ Cluster4, are set up. Each cluster has 25 nodes, including cluster head nodes. Cluster interaction and trust assessment. According to the behavior characteristics of nodes, it is divided into two categories: normal node, malicious node. Normal node classes provide normal services, and malicious serving nodes are generally Refers to the cluster of malicious nodes, including cluster heads, raising the trust of nodes in their own clusters and devaluating the trust of other cluster nodes. According to the function of nodes, it is divided into two categories: IntraClusterNode and ClusterHeadNode, in which the clusterhead node is responsible for maintaining a trust list including the trust between nodes and the nodes in the cluster.

The initial trust of nodes are all 0.5, the normal node is used to initiate the service request, the service nodes are selected in four clusters, and the interactive process is analyzed experimentally.

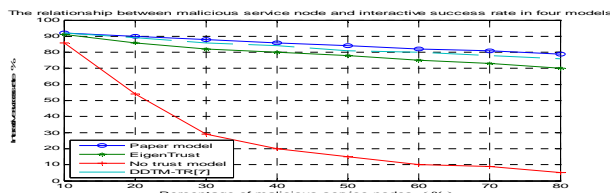


FIGURE II. THE RELATIONSHIP BETWEEN MALICIOUS SERVICE NODE AND INTERACTIVE SUCCESS RATE IN FOUR MODELS

Figure 2 describes the growth of malicious service nodes, interactive success rate changes. In contrast to the DDTM-TR model of the Eigentrust model and the literature [7], it is evident that the trust model has considerable advantages for the prevention of malicious service nodes. The interaction success rate of this model is higher than EigenTrust model, slightly higher than that of DDTM-TR. This is because the EigenTrust model relies excessively on subjective evaluation, and subjectivity is often not as accurate as expected. In addition, for over-dependent trust nodes, not only is there a

risk of single point of failure but also for IoT nodes with limited computing power. There will be additional recommended trust overhead resulting in overloading. The model emphasizes the objectivity of the evaluation and avoids the selection of malicious service nodes by dynamically adjusting the weighting factors.

The main source of energy consumption for a typical trust assessment model is finding recommended trust data. Figure 6 shows the energy consumption of the model. The Beth model does not take into account the heterogeneity of the IoT network and the limited resources of most nodes, so that the nodes uniformly store and recommend the recommended information. For some computing devices with low computing capabilities (such as cameras and thermometers) May cause node overload or even paralysis. Although the TMA model in [11] reduced the computational complexity compared with the Bath model, the common node is also regarded as the main body of the recommended trust, resulting in high overall energy consumption and is unfriendly to some IoT nodes with low computational capabilities . The goal of the Internet of Things is the Internet of Everything, which is bound to develop into an unprecedently large network. For iterative methods, the consumption of computing resources will increase exponentially. In this paper, we transfer the trust storage and delivery tasks to the cluster head nodes with powerful computing ability. And the number of cluster nodes can be dynamically allocated according to the different computing capabilities of cluster heads, which greatly reduces the computational overhead and enhances the robustness of the model.

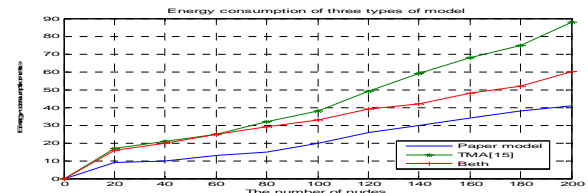


FIGURE III. ENERGY CONSUMPTION OF THREE TYPES OF MODEL

V. SUMMARY

Based on the classic theory of IoT, this paper regards trust as the basis of authorization and based on interaction records as the basis of trust evaluation to achieve a safe and reliable network. In view of the heterogeneity and low power consumption of IoT nodes, the computational tasks are concentrated on cluster head nodes, which not only avoids the risk of single point of failure but also improves the scalability of the network. Dynamic evaluation algorithms facilitate the management of a large number of IoT nodes and resist malicious recommendation attacks. The next research direction is for the characteristics of IoT nodes, combined with the development trend of attack means, customized custom parameters and higher trust evaluation algorithm.

REFERENCES:

- [1] K. Bloede, G. Mischou, A. Senan, and R. Koontz, "The Internet of Things,"<http://www.woodsidecap.com/wp->

- content/uploads/2015/03/WCP- IOT- M and A- REPORT- 2015-3.pdf, Woodside Capital Partners,2015,accessed:2016-10-27.
- [2] Liu yanbing, Hu Wenping. Internet of Things security model and key technologies [J]. Digital Communications, 010, 37 (4): 28-33,2010.
 - [3] Gong Xue Hong. Research on secure clustering mechanism of IoT-aware nodes based on trust [D]. Chongqing: Chongqing University of Posts and Telecommunications, 2014.
 - [4] ROMANA R, ZHOUA J, LOPEZB J. On the features and challenges of security & privacy in distributed Internet of Things[J]. Computer Networks, 2013, 57 (10):2266-2279.
 - [5] I.-R.Chen,F.Bao, and J.Guo, "Trust-based Service Management for Social Internet of Things Systems," IEEE Trans. Dependable Secur. Dependable Secur. Comput., vol. 5971, no. c, pp. 1-1, 2015.
 - [6] M. Nitti, R. Girau, and L. Atzori, "Trustworthiness management in the social internet of things," IEEE Trans. Knowl. Data Eng., vol. 26, no. 5, pp. 1253–1266, 2014.
 - [7] You Jing, Shangguan by Lun, Xu Shoukun and so on. A Distributed Dynamic Trust Management Model Considering Trust Reliability [J]. Journal of Software, 2017.
 - [8] Xu Huan. Research on the Trust Model of Internet of Things Based on Clustering [D]. Lanzhou Jiaotong University, 2017.
 - [9] Liu Wenmao, Yin Lihua, Fang Binxing and so on. Study on the trust mechanism under the Internet of things [J]. Chinese Journal of Computers, 2012,35 (5): 847-855.
 - [10] CROSBY G.V, HESTERL, PISSION N. Location-aware, trust-based detection and isolation of compromised nodes in wireless sensor networks[J]. International Journal Network Security, 2011, 12(2): 107-117.

A Network System Security Assessment Method Based on Penetration Testing

Yue Li¹, Xiaolin Zhao^{1,*}, Chonghan Zeng¹, Yu Fu¹ and Ning Wang²

¹School of Software, Beijing Institute of Technology, Beijing 100081, China

²Academy of Intelligent Collaborative Cloud System, China Aerospace Science and Industry Corporation Limited, Beijing 100081, China

*Corresponding author

Abstract—As the development of the information technology, people show strong interest to the emergence of all sorts of convenient and new technologies. However, there will be vulnerability in these technologies and bad attackers may be attack it to break it down. So, if we want to protect a system in detail, we must build a network system security assessment standard or method that can evaluate the security of network systems precisely. In recently years we are paying attention to problems of cyberspace security developing badly. Therefore, we attempt to establish the method of network system security evaluation based on penetration test to safeguard the improve of new technologies, the network system can defense the penetration and work well after the bad attacks.

Keywords—assessment; network system security; penetration test

I. INTRODUCTION

This paper standing on the penetration testing will research and analyze the key technologies in network system security evaluation, and design a network system security assessment method based on penetration test. We hope to make some improvements to our current security environment and get an effective system safety assessment method.

The main contents of this paper include:(1)Analyzing the current network system assessment methods.(2)Building a model of network system security assessment based on AHP, and confirm the weight of indication in the evaluation.(3)Designing a network system security assessment method based on penetration test and the coordinate of functions, architecture and models in detail.(4)Proving the effectiveness of this method by evaluate a entity system. From the above, we can weigh the pros and cons to choose the most effective and appropriate evaluation method. After penetration testing, the effectiveness of the evaluation method can be determined.

II. CURRENT SITUATION OF NETWORK SYSTEM SECURITY ASSESSMENT AND TECHNICAL ANALYSIS

A. Current Situation of Network System Security Assessment

Network security assessment is the basic premise and foundation for ensuring information security. Network security assessment is of great significance to information security. But there are less research achievements in our daily research life, and many in foreign have not been open because of the security and privacy. Since the 1990s, the researchers raised the demand

of implementing the security classified protection to the information system of computer, and then came up with a series of standard and management specification of it. After that, the awareness of network security began to form and increased it gradually. Nowadays, the main work pay attention to the building of the business architecture, and the standard and technology architecture are still in a researching stage.

B. The Current System Security Assessment Method and Its Shortcomings

As the development of information network systems, there have been raised a series methods of system security assessment. The building of indications, confirm of the weight of indications, the methods of evaluating the results are all the heart technologies. Every methods all have its advantages to address issues, but on the whole, there are all sorts of flaws in the table 1 that need to fix. Some methods and some disadvantages of these includes:

TABLE I. COMPARISON

method	defects
a Requirement Engineering-based Evaluation Approach[2]	<i>It is to note that this article mainly focuses on the derivation of evaluation criteria and not to perform a comparative study. [2].</i>
An Information Security Evaluation Method Based on Entropy Theory and Improved TOPSIS[3]	<i>Because the calculated amount of the maximum entropy model is huge, the use of models depend on the quality of the method in a project.</i>
Information security evaluation of system based on Bayesian network[1]	<i>Bayesian model needs to refer to available information when assessing a result of test, but these information may be not authoritative and queried by some exerts. So we can not prove the accuracy of result.</i>

III. THE ADVANTAGE OF PENETRATION TESTING MODEL

If we want to improve the method of network system security assessment, these aspects must be carried out:(1)Improve the technology when assessing a system. For example, some of the methods mentioned above, we must exploit the new technologies for these methods.(2)If we have chose a technology, we need to choose a method of result evaluation what is the most suitable for this technology to increase the effectiveness and

accuracy. According to the contrast described in above section, we have summarized the flows of each method. So, we decide to choose the penetration testing model to test the security of system and improve the security assessment methods to increase the accuracy.

A. The Choose of Assessment Technology

At first, Penetration testing is a simulation of an attack to verify the security of a system or environment to be analyzed. The objective of this test is to examine, under extreme circumstances the behavior of systems, networks, or personnel devices, in order to identify their weaknesses and vulnerabilities[4].

The reason why most network system being attacked is the vulnerability of it. For addressing the problem, we must find bugs by test. But if we want to seek out these bugs, penetration test can perfectly meet the demand. In recently years, the research on penetration test is deepening. In terms of building the standard of penetration test, NIST had raised the process of penetration test in Technical Guide to Information Security Testing and Assessment(NIST SP 800-115) including stages of planning, exploiting, attacking and reporting, and raises a dynamic feedback attack mining process through excavating .Contacting the excavating with attacking through this process adopt perfectly to the penetration test, and finally, through these four stages, we hope to achieve the test results.

PTES (The Penetration Testing Execution Standard)is a new standard that developing in area of penetration technology in security. This standard divides the penetration test process into seven stages: interaction, collecting intelligence, modeling threat, vulnerability analysis, penetration attack, After penetration attack, report. Penetration testing can help security assessment to repair some uncertain weights and parameter very good[10].

All in all, a network system security assessment based on penetration test is critical to protect the network security. From the characteristics of penetration testing, this paper also believes that the system security evaluation should be carried out from within the system. Analyzing the vulnerability of system by penetration test can improve the veracity and security of assessment of system safety.

B. The Choose of Result of Penetration Testing Assessment Method

Evaluation method for an object or event, said in general can be divided into two categories, one is individual evaluation, namely the application of certain criteria for evaluation of some aspect of the object to make quantitative evaluation, its purpose is to reveal the merits of the individual performance index of the evaluation objects. Another kind is a comprehensive evaluation, that is, according to different evaluation purposes, choose corresponding evaluation form, build a mathematical model of converting multiple evaluation factors or indicators to reflect the process of overall quality evaluation objects. Comprehensive evaluation from several aspects to meet the demand of evaluation subject degree of evaluation object quantitative test method, is to be objective, fair and reasonable evaluation object. The comprehensive evaluation method, therefore, the comprehensive evaluation method is also called multiple

attribute or multi-attribute evaluation method, which is one of the most effective evaluation method for complex systems.

Now, the common evaluation method includes fuzz comprehensive method, analysis hierarchy process, data envelopment analysis, grey relational analysis and so on. However, every methods all have its advantages and disadvantages. For example: Fuzzy comprehensive evaluation method is applicable to uncertain parameter values ,because network penetration testing results will be affected by the various factors. Otherwise, test results need to review with experts to be more objectively reflect the performance of these indicators. Therefore, the attack test results are uncertain. The fuzzy evaluation can be combined with other evaluation methods, and the fuzzy evaluation method is applicable to the evaluation of network penetration test results. Principal Component Analysis is a classic method of statistics analysis. This method adopt to issue that exist large sample of quantitative indexes. Although it can be used to assess a result of network penetration test, gaining a sample is so hard. So, this method can be used for evaluation under conditions of permit.

Data envelopment analysis needs a large of data when assessing a system. That applies only to quantitative discussion between each unit with the same industry background with the evaluation index, so this method is not adopt to the assessment. Grey relational analysis demands effective information from large data, and this method applies not to the evaluation of results of attack test.

Through the above comparative analysis, the paper choose AHP and fuzz comprehensive analysis to assess the result of network penetration test. Evaluate all levels by fuzz comprehensive analysis.

C. The Choose of Method of Determination of Weight

The methods of determining weights are usually determined by experts grading method, factor analysis weight method, information degree, dependence weight, RSR and AHP.

According to the analysis of 2.2, this paper determines the weight of test indicators by using hierarchical analytic hierarchy process. The reasons are as follows:

The analytic hierarchy process (AHP) was proposed by the famous American operations research scholar Sadie in the 1970s, which is a multi-objective decision analysis method combining qualitative and quantitative analysis. The analytic hierarchy process can be applied to the combination of quantitative and qualitative indicators, and can be used to reduce the complexity of evaluation by its layers' recursion. Therefore, the evaluation of the attack test results is more applicable, but the evaluation itself has greater subjectivity, so it should be corrected when used. The core of this method is to make quantitative analysis of the decision-maker's experience judgment, and provide decision basis in way of quantity for decision makers. As a result, in this paper, the analytic hierarchy process is used to determine the weight of test index system, and the weight of each layer is determined by the method.

IV. COMPUTATIONAL MODEL DESIGN

This section will conduct experimental design based on the improved methods and techniques mentioned in section 2.

A. Confirming the Weight

Weight is the relative importance of indicators relative to the previous level, and the determination of weight is based on the importance of each test index to the test target. Determining the weight of the index to make the importance of each index to form a rational and scientific proportion is an important link in the final scientific evaluation of test results.

The Delphi method is usually used to determine the judgment matrix of each evaluation expert and then synthesize it when we calculate the weight of each layer because experts from different professional backgrounds have different relative importance to different levels of elements.

The procedures of weight determination are as follows:

In the hierarchical substructure of the index system, We set the upper indicators of criterion A to be the criterion of its lower indicators. Weight is the importance of relative to the criterion A, b₁, b₂, ..., b_n. For these indicators, We can't directly quantify comparisons in normal condition, and the importance of each other can only be determined by qualitative evaluation. Its specific judgment comparison rule is: for criterion A, What is the importance of the indicator of the subordinate index, we usually ensure it in 1~9 scale. The specific meaning of the scale of 1 ~ 9 scale is shown in the table2 below:

TABLE II. SCALE OF IMPORTANCE SCALE

Scales	Meaning of scale
1	<i>It is of equal importance to represent two elements.</i>
3	<i>The former is slightly more important than the latter.</i>
5	<i>The former is obviously more important than the latter.</i>
7	<i>The former is more important than the latter.</i>
9	<i>The former is very more important than the latter.</i>
2,4,6,8	<i>Represents the intermediate value of the above adjacent judgment reciprocal</i>
	<i>If the ratio of the importance of element i to j is C_{ij}, the ratio of element j to element i is C_{ij}=1/C_{ji}.</i>

Therefore, according to the scale method of the above table, any expert can obtain a comparison judgment matrix C after comparing the underlying indicators of criterion A based on his own views:

$$C = (C_{ij})_{n \times n} \quad (1)$$

Among them, C_{ij} represents proportional scale of importance

TABLE III. THE VALUES OF AVERAGE RANDOM CONSISTENCY INDEX

Order	1	2	3	4	5	6	7	8	9	10	11	12
R.I.	0.00	0.00	0.52	0.89	1.12	1.25	1.35	1.42	1.46	1.49	1.52	1.54

Finally, calculating the consistency ratio C.R., The formula that it uses is: C.R. = C.I./R.I. , After calculate the value of C.R., For more than three orders of judgment matrix, If the value is less than or equal to 0.1, and it is considered that the consistency test is passed, otherwise the judgment matrix needs to be modified and adjusted. We refer to methods proved feasible in the past in the research and application of several problems in

of bi index relative to bj index.

Step 2: Integrated the judgment matrix

Since each of the experts gives a relative weight ratio matrix of multiple indicators under the same criterion, and in order to get a reasonable weight, the opinions of various experts should be integrated and the judgment matrix given by them should be integrated treatment. In this paper, we adopt the integrative approach to the eigenvector and then the consistency test method to determine the weight. The specific implementation steps are as follows:

a: Establishment of judgment matrix: Assuming that there are n indicators under the same criterion A, there are m experts, and the judgment matrix given by the 9th expert is C_k = (C_{ij})_{n × n}, k=1,2,...,m, At the same time, the judgment matrix given by any expert can satisfy the consistency test.

b: Calculate the average value of the matrix: There are many ways to calculate the mean of the matrix, and we use the geometric mean. Let C = (C_{ij})_{n × n}, Because there are m experts, there are m judgment matrices. The of the corresponding elements in these matrices defined the value of C_{ij}. According to previous proof, matrix C meets the consistency check.

c: The round numbers of geometric mean: In the last step, the geometric average method was used to find the value of each element of the matrix, but the number of results was more than one, so the results should be rounded.

Step 3: Consistency check of matrix

The consistency test here is mainly to overcome the complexity of things and the differences of people's understanding. When the expert constructs the judgment matrix, the matrix is only constructed from a mathematical point of view, but the non-transitive paradox of the importance of relative weights between indicators is not strictly required. It may appear that "a is more important than b, and b is more important than c, which is more important than a". Therefore, the consistency of the matrix should be tested again. The method is as follows: First, calculate the largest characteristic root λ_{max} of matrix, The matrix consistency index C.I. is also calculated. The formula(2) using is:

$$C.I. = (\lambda_{max} - n)/(n - 1) \quad (2)$$

Checked the average random consistency index R.I. of the matrix ,specific reference values are as follows:

analytic hierarchy process, Its core idea is to get new matrix after judgment matrix normalized. Use "sum-product method" for the new ordering vector matrix, at the same time, based on the original judgment matrix and the new matrix sequencing vector to construct the original matrix of the induced matrix. By using the induced matrix of the various elements of the original matrix adjustment, in order to make the new matrix to achieve

consistency. The aim is to obtain a judgment matrix that is not reconfirmed by experts, while maintaining the views of multiple experts at the same time.

Step 4: Calculating the relative weight vector between the indices under the same criterion ω

In the first three steps, the judgment matrix of each expert is combined and the consistency test is carried out, and the relative weight of each index is calculated by using the comprehensive judgment matrix C. There are many ways to calculate weight. For example: geometric mean; method of characteristic roots and so on. For simplicity and convenience, the geometric mean is used here. The method is as follows: Multiply the elements of the matrix C by column, then get a new vector by square-root. Then the vector of weight $\omega = (\omega_1, \omega_2, \dots, \omega_n)$ is obtained by the following formula(3):

$$\omega_i = \frac{\left(\prod_{j=1}^n c_{ij}\right)^{\frac{1}{n}}}{\sum_{h=1}^n \left(\prod_{j=1}^n c_{hi}\right)^{\frac{1}{n}}} \quad (3)$$

$i=1,2,\dots,n$. After ensure the relative weight, it needs to be tested for consistency, the exact method is the same as the third step, this paper is not going to describe it anymore.

Each indicator of the same criterion can be used to assign value to the weights.

B. Establishing a Multilevel Fuzzy Comprehensive Evaluation Model

The specific steps of multi-level fuzzy comprehensive evaluation are mainly divided into the following two steps:

Step 1: Determine the minimum limitation of system security. Its specific calculation method is: Suppose there are n experts, and statistics for each minimum value of experts, noted $S_{imin}, i=1,2,\dots,n$. The values of S_{imin} are integers between 0 and 10. Set a Comment set $D = \{\text{Excellent, good, general, unqualified}\}$, and then take statistics for each minimum value of experts, Count the frequency: $m_{it}, t=1,2,3,4$ of S_{imin} of each class belong to comment set.

Using the formula(4):

$$e_{min}^t = \frac{m_{it}}{n} \quad (4)$$

Calculated the minimum limitation of fuzzy evaluation value of S_{min} , and the fuzzy evaluation value of the minimum limitation of system security $E_{S_{min}} = (e_{min}^1, e_{min}^2, e_{min}^3, e_{min}^4)$.

According to the principle of maximum membership and entropy property, we use formula(5):

$$S_{min} = \left(1 + \sum_{i=1}^4 (\alpha_i e_{min}^i) \ln e_{min}^i \right) \times 100\% \quad (5)$$

The value of S_{min} is calculated, which is the minimum value to measure the system's security. It is considered that the system is safe if the result is greater than that value, whereas it is

considered unsafe. The α_i represents the relative weight of each security class importance ($\alpha_i = 0.25$).

Step 2: Implementing multilevel fuzzy comprehensive evaluation

Because of the hierarchy of the index system, the fuzzy comprehensive evaluation should be carried out from the lowest level index to the fuzzy comprehensive evaluation, until the comprehensive evaluation results of the highest level are obtained. First to network penetration testing various test data can be obtained by using normalized processing, obtains a bottom index fuzzy evaluation value relative to the evaluation set, second, we should calculate the index fuzzy evaluation value of calculation between the layers. Assuming that the system safety index system is divided into m layers, the lower indices of each index reflect the security features of the upper index relative to the whole system. The ith index x_i in the upper index is assumed to have n, and set jth index of the lower class x_{ij} . Its fuzzy evaluation value is $E_{x_{ij}} = (e_{ij}^1, e_{ij}^2, e_{ij}^3, e_{ij}^4)$, $(i,j=1,2,3, \dots, n)$.

The weight vector of the lower index of the index X_{ij} is $\omega_i = (\omega_{i1}, \omega_{i2}, \dots, \omega_{in})$. Then, representation of Matrix M_i of fuzzy evaluation values of the upper index X_i relative to the lower index is :

$$M_i = \begin{vmatrix} e_{i1}^1 & e_{i1}^2 & e_{i1}^3 & e_{i1}^4 \\ \dots & \dots & \dots & \dots \\ e_{in}^1 & e_{in}^2 & e_{in}^3 & e_{in}^4 \end{vmatrix}$$

The fuzzy evaluation value of upper index X_i can be calculated by formula(6):

$$E_{xi} = \bar{\omega} \bullet M_i \quad (6)$$

L is the ordinal number of upper index; \bullet is fuzzy operator. The current fuzzy operator usually adopts the Chad operator. The test indicator system is divided into four layers. The fuzzy evaluation value E of each criterion is calculated by using this method from the bottom level to the top level, until we have calculated the fuzzy evaluation value corresponding to the target $E_s = (e_s^1, e_s^2, e_s^3, e_s^4)$. Finally, the overall objective evaluation of system security is calculated. Using this formula(7) to calculate the result by the principle of maximum membership and the properties of entropy:

$$S = \left(1 + \sum_{i=1}^4 \alpha_i e_s^i \ln e_s^i \right) \quad (7)$$

We should get the system security values. The α_i expresses the importance of the relative weight of each grade in the comments set, e_i is the fuzzy evaluation result of the judgement layer relative to target layer. The calculated results are compared with the minimum system security value S_{min} calculated in the first step. If $S > S_{min}$, in the background of network penetration testing, the system is safe and can be used in practice. Otherwise, it is deemed that the system is unsafe and the system security personnel need to be reformed.

C. The Acquisition and Processing of Data of Penetration Test

Step 1: Acquisition of network penetration test results data. Using the network penetration test to test the system security, the result is to obtain the test result values of the underlying indexes in the test index system, which we call the raw data. Not only determine the relative scientific test results, but also will attack test data acquisition form submitted review committee of experts, based on the set of test scenarios and test data to obtain a list of comprehensive analysis, combined with own work experience, making evaluation and score to each kind of ability. The score is within 0-10 range.

Step 2: Processing of network penetration test results data. The result of data processing is the evaluation of single performance index, and the process of data processing is as follows:

Experts discuss the selection of evaluation methods->Experts discuss the determining of the evaluation criteria->Experts rate the raw data based on criteria->Score statistics->The evaluation of raw data of test results.

In order to make fuzzy evaluation, we need to set up a set of comments. This paper divided evaluation into collection of comments from high to low d_i ($i=1,2,3,4$) is: $D = \{\text{Excellent, good, general, unqualified}\} = \{d_1, d_2, d_3, d_4\}$. After consulting relevant experts, experts believe that if the score is within 9-10 range, the ability is excellent; In a 7-8 range, the ability is good; In the 4-6 range, the ability is general; Below 3 points, this ability is not qualified.

Suppose the experts in the evaluation group of network infiltration test results have n bits. And the fuzzy statistic is to let these experts classify the results according to the above comments. Calculate the results of each test index gradually, which is the frequency of each grade m_{ijt} ($t=1,2,3,4$). Then the calculation formula(8) for the fuzzy evaluation value $E_{zzi} = (e_{ij1}, e_{ij2}, e_{ij3}, e_{ij4})$ of the capability is as follows:

$$e_{ijt} = \frac{m_{ijt}}{n} \quad (8)$$

The e_{ij1} in the fuzzy evaluation E_{zzi} expression indicates the degree of excellence; e_{ij2} indicates the degree of good; e_{ij3} indicates general degree; e_{ij4} indicates disqualification.

V. EXPERIMENT

A. Overview of the System to be Tested

To verify the usability of the network system security assessment method based on penetration testing, this paper selects a system that is validated as security by other security assessment methods for penetration testing. This object system had established a set of security system index based on AHP, which is divided into target layer, criterion layer, sub-criterion layer and indicative layer according to the analytic hierarchy process.

The target layer S is the information system security based on osmotic testing. The criterion was named Z_1, Z_2, Z_3, Z_4 . Where Z_1 is divided into ZZ_1 and ZZ_2 . The rest of the sub-criteria layer

will not described in this articles in detail, and there are nine criterion sub-criterion layers and 29 indicators in indicative layer .In this safety indicator system, there are only 3 indicators in the sub-criteria except ZZ_1 and ZZ_2 .The index layer is named ZZ_{ij} ,($i=1,2,\dots,9,j=1,2,3,4$).

B. The Acquisition of Fuzzy Comprehensive Evaluation Values

According to the method in above, we set up 20 experts to make fuzzy evaluation of 29 indicators to get the fuzzy assessment value : E_{zzij} of each indicator.

The method of acquiring fuzzy evaluation value is taken as an example of ZZ_{11} .After giving results of test values to the experts, the grade giving by them are(9,9,8,9,10,7,6,5,6,9,7,7,8,9,10,10,10,8,9,6,5).According to the standard of the evaluation set in the preceding article, there are nine best evaluations, six good evaluations, five normal evaluations. Therefore, we can calculate the degree of excellence is 0.45,good is 0.3,normal is 0.25,disqualification is 0 by the formula (8).After the same calculation, the fuzzy evaluation value of 29 indexes is shown below:

$$\begin{aligned} E_{zz11} &= (0.45, 0.3, 0.25, 0) \\ E_{zz13} &= (0.7, 0.15, 0.15, 0) \\ E_{zz21} &= (0.5, 0.3, 0.2, 0) \\ E_{zz23} &= (0.75, 0.25, 0, 0) \\ E_{zz31} &= (0.05, 0.95, 0, 0) \\ E_{zz33} &= (0, 0.25, 0.75, 0) \\ E_{zz42} &= (0.25, 0.75, 0, 0) \\ E_{zz51} &= (0, 0.7, 0.25, 0.05) \\ E_{zz53} &= (0.05, 0.75, 0.15, 0.05) \\ E_{zz61} &= (0.35, 0.5, 0.1, 0.05) \\ E_{zz63} &= (0, 0.5, 0.45, 0.05) \\ E_{zz71} &= (1, 0, 0, 0) \\ E_{zz73} &= (0, 0.05, 0.75, 0.2) \\ E_{zz81} &= (0, 0.05, 0.45, 0.5) \\ E_{zz83} &= (0, 0.4, 0.5, 0.1) \\ E_{zz91} &= (0.85, 0.15, 0, 0) \\ E_{zz93} &= (0.05, 0.65, 0.15, 0.15) \end{aligned}$$

C. Confirming the Critical Point of This System Security

According to the qualitative description and the system security level of the system security, and the organization of the network penetration test, the experts of the group of security evaluation ensure the critical point of this system security S_{min} . During an attack test, the score of 20 experts was (9,8,6,7,5,10,9,7,8,6,8,8,7,9,10,6,9,10,8,7).In summary, the time of excellence is 7,good is 9,normal is 4,disqualification is 0.So E_{smi} equals to (0.35,0.45,0.2,0).Using formula(5),we can calculate the S_{min} is 72.7%.As a result, the critical point of this system security is 72.7%.

D. Giving Values to the Weight

According to the method of calculation of index weight, the relative importance of each indicator relative to the superior indicator is evaluated by experts. This paper set six experts to evaluate the weight of indicators. After we get the six judgment matrices, we set geometric mean on scale values. Then we can get the initial comprehensive judgment matrix, and examine its conformity. If the result is not met the conformity, the adjustment method of the judgment matrix will be adjusted until the matrix meets the consistency check.

Step 1: Calculate the weight of the sub-criterion layer relative of the index layer. Because of the large amount of calculation, we take ZZ_1 as an example to calculate the weight. The specific methods are follows:

There are four indicators: $ZZ_{11}, ZZ_{12}, ZZ_{13}, ZZ_{14}$ below ZZ_1 . According to the assessment of experts, the judgment matrix are follows:

$$C_{ZZ_1}^{(1)} = \begin{vmatrix} 1 & 1 & 1 & 1 \\ 1 & 1 & 1 & 1 \\ 1 & 1 & 1 & 1 \\ 1 & 1 & 1 & 1 \end{vmatrix} \quad C_{ZZ_1}^{(2)} = \begin{vmatrix} 1 & 1/2 & 1/2 & 1/2 \\ 1 & 2 & 2 & 2 \\ 1 & 2 & 2 & 2 \\ 1 & 2 & 2 & 2 \end{vmatrix}$$

$$C_{ZZ_1}^{(3)} = \begin{vmatrix} 1 & 1/3 & 1/3 & 1/2 \\ 1 & 1 & 3/2 & 3/2 \\ 1 & 3/2 & 1 & 3/2 \\ 1 & 3/2 & 3/2 & 1 \end{vmatrix} \quad C_{ZZ_1}^{(4)} = \begin{vmatrix} 1 & 1/2 & 1 & 1 \\ 1 & 2 & 2 & 2 \\ 1 & 2 & 2 & 2 \\ 1 & 2 & 2 & 2 \end{vmatrix}$$

$$C_{ZZ_1}^{(5)} = \begin{vmatrix} 1 & 1 & 1 & 1 \\ 1 & 1 & 1 & 1 \\ 1 & 1 & 1 & 1 \\ 1 & 1 & 1 & 1 \end{vmatrix} \quad C_{ZZ_1}^{(6)} = \begin{vmatrix} 1 & 1 & 1 & 1 \\ 1 & 1 & 1 & 1 \\ 1 & 1 & 1 & 1 \\ 1 & 1 & 1 & 1 \end{vmatrix}$$

After using the consistency test method, we affirm the matrices are consistent. Skip the process of calculation. After the roundness of geometric equalization of these matrices, the initial comprehensive judgment matrix is obtained:

$$C_{ZZ_1} = \begin{vmatrix} 1 & 1/2 & 1 & 1 \\ 2 & 1 & 1 & 1 \\ 1 & 1 & 1 & 1 \\ 1 & 1 & 1 & 1 \end{vmatrix}$$

The $\omega_{ZZ_1}^k$ ($k=1, 2, 3, 4$) of the matrix C_{ZZ_1} is obtained through the root method: $\omega_{ZZ_1}^1 = 0.841$; $\omega_{ZZ_1}^2 = 1.189$; $\omega_{ZZ_1}^3 = 1$; $\omega_{ZZ_1}^4 = 1$; After normalization, the relative weight value of the four underlying indexes relative to the sub-criterion layer index ZZ_1 is obtained: $\omega_{ZZ_1} = (0.2087, 0.2951, 0.2481, 0.2481)$;

Performing a consistency check, According to the formula(9):

$$\lambda_i = \frac{\sum_{j=1}^4 C_{ZZ_1j} \cdot \omega_{ZZ_1}^j}{\omega_{ZZ_1}^j} \quad (9)$$

we can calculate the $\lambda_1=4.085, \lambda_2=4.096, \lambda_3=4.031, \lambda_4=4.031$.

Using formula(10) :

$$\lambda_{\max} = \frac{1}{4} \sum_{i=1}^4 \lambda_i \quad (10)$$

to determine the $\lambda_{\max} = 4.061$. According to the formula(2),

$$C.I. = \frac{\lambda_{\max} - n}{n - 4} = 0.0203 \quad C.R. = \frac{C.I.}{R.I.} = 0.023 < 0.1$$

The above calculation indicates that the judgment matrix can be accepted and the relative weight can be applied.

Therefore, $\omega_{ZZ_1} = (0.2087, 0.2951, 0.2481, 0.2481)$.

According to the method above, the judgment matrix and weight of other underlying indexes relative to sub-standard layer indexes can also be obtained.

Step2: Calculate the judgment matrix and weight value of the relative criterion layer of sub-criterion. The exact step is the same as the first step, and this is just the result:

$$C_{Z_1} = \begin{vmatrix} 1 & 4/3 \\ 3/4 & 1 \end{vmatrix} \quad \omega_{Z_1} = (0.57, 0.43) \quad C.R. = 0$$

$$C_{Z_2} = \begin{vmatrix} 1 & 9/8 \\ 8/9 & 1 \end{vmatrix} \quad \omega_{Z_2} = (0.5294, 0.4706) \quad C.R. = 0$$

$$C_{Z_3} = \begin{vmatrix} 1 & 6/5 \\ 5/6 & 1 \end{vmatrix} \quad \omega_{Z_3} = (0.5455, 0.4545)$$

$$C_{Z_4} = \begin{vmatrix} 1 & 1/2 & 1/3 \\ 2 & 1 & 2/3 \\ 3 & 3/2 & 1 \end{vmatrix} \quad \omega_{Z_4} = (0.1667, 0.3333, 0.5)$$

Step3: Calculate the judgment matrix and weight value of the relative target layer of the criterion layer. The exact step is the same as the first step, and this is just the result:

$$C_s = \begin{vmatrix} 1 & 2 & 1 & 10/9 \\ 1/2 & 1 & 1/2 & 5/9 \\ 1 & 2 & 1 & 10/9 \\ 9/10 & 5/9 & 9/10 & 1 \end{vmatrix}$$

$$\omega_s = (0.3154, 0.1577, 0.3154, 0.2115) \quad C.R. = -0.0555 \approx 0$$

E. Fuzzy Comprehensive Evaluation

After calculation of the weight of various indicators, can make a comprehensive fuzzy evaluation, the purpose is the values of fuzzy evaluation of target layer, to ensure the degree of excellence, good, the proportion of qualified and unqualified degree. The specific calculation steps are as follows:

Step 1: to evaluate fuzzily the sub-criteria. Take ZZ_1 as an example to make a simple evaluation. The fuzzy evaluation value (the performance evaluation value of the single index) test results of the four indexes of ZZ_1 , ZZ_{11} , ZZ_{12} , ZZ_{13} and ZZ_{14} are represented by matrix representation as follows:

$$M_{ZZ_1} = \begin{vmatrix} 0.45 & 0.3 & 0.25 & 0 \\ 0.65 & 0.3 & 0.15 & 0 \\ 0.7 & 0.15 & 0.15 & 0 \\ 0.6 & 0.3 & 0.05 & 0.05 \end{vmatrix}$$

The result of evaluation of ZZ_1 is follow:

$$\begin{aligned} E_{ZZ_1} &= \omega_{ZZ_1} \bullet R_{ZZ_1} \\ &= (0.2087 \quad 0.2951 \quad 0.2481 \quad 0.2481) \bullet \begin{vmatrix} 0.45 & 0.3 & 0.25 & 0 \\ 0.65 & 0.3 & 0.15 & 0 \\ 0.7 & 0.15 & 0.15 & 0 \\ 0.6 & 0.3 & 0.05 & 0.05 \end{vmatrix} \\ &= (0.609, 0.263, 0.166, 0.013) \end{aligned}$$

The result after normalization is :

$$E_{ZZ_1} = (0.579, 0.25, 0.158, 0.013).$$

In the same way, the fuzzy evaluation value of indexes of other sub-criterion layer are:

$$\begin{aligned} E_{ZZ_2} &= (0.605, 0.223, 0.172, 0); E_{ZZ_3} = (0.02, 0.62, 0.35, 0.01); \\ E_{ZZ_4} &= (0.3, 0.675, 0.025, 0); E_{ZZ_5} = (0.219, 0.593, 0.15, 0.038); \\ E_{ZZ_6} &= (0.28, 0.467, 0.216, 0.037); \\ E_{ZZ_7} &= (0.415, 0.029, 0.478, 0.078); \\ E_{ZZ_8} &= (0, 0.1375, 0.5625, 0.3); \\ E_{ZZ_9} &= (0.389, 0.455, 0.089, 0.067). \end{aligned}$$

Step 2: set a fuzzy evaluation of each index of criterion layer. The results are as follows:

$$\begin{aligned} E_{z1} &= (0.59, 0.238, 0.164, 0.008); \\ E_{z2} &= (0.137, 0.584, 0.274, 0.005); \\ E_{z3} &= (0.248, 0.535, 0.179, 0.038); \\ E_{z4} &= (0.263, 0.278, 0.312, 0.147); \end{aligned}$$

Step 3: fuzzy evaluation of target layer can obtain the fuzzy evaluation value of this system security relative to the evaluation set:

$$E_s = (e_{s1}^1, e_{s1}^2, e_{s1}^3, e_{s1}^4) = (0.279, 0.507, 0.176, 0.038);$$

The formula(7) is used to calculate $S = 74.5\%$.

Comparing S with S_{min} , we get the result $S > S_{min}$, which can be determined that the system is in line with security objectives under the network penetration test, so the system is safe.

VI. CONCLUSION

This paper introduced a network system security assessment method based on penetration test by analyzing the current assessment methods and the flaws of these methods.

The main tasks includes: Introduction and analysis to the current system safety assessment method, building and using of penetration test model. The penetration test is designed to test the security of the information system and evaluate the system after expert evaluation and fuzzy evaluation. By using analytic hierarchy process and multilevel fuzzy evaluation method, carries out a relatively scientific and safe result of evaluation of test. Given the previous security assessment of the object system, the evaluation of the system was basically consistent with the evaluation of the system using a security assessment based on penetration testing. Therefore, it is reasonable and feasible to evaluate the security evaluation of network system based on osmotic testing, and also greatly improve the accuracy of the system security assessment from the aspect of simulated attack.

ACKNOWLEDGMENT

This work was supported the National Key R&D Program of China (No. 2016YFB0800700)

REFERENCES

- [1] Z. Q. Cai; J. B. Zhao; Y. Li; S. B. Si; M. N. Ni,Information security evaluation of system based on Bayesian network,2015 IEEE International Conference on Industrial Engineering and Engineering Management (IEEM),Pages: 315 - 319,2015.
- [2] Sravani Teja Bulusu, Romain Laborde, Ahmad Samer Wazan, François Barrère, Abdelmalek Benzekri; Which Security Requirements Engineering Methodology Should I Choose?: Towards a Requirement Engineering-based Evaluation Approach,ARES 2017: 29:1-29:6,2017.
- [3] Dongqing Wang,Yueming Lu,Jiefu Gan.An Information Security Evaluation Method Based on Entropy Theory and Improved TOPSIS,2017 IEEE Second International Conference on Data Science in Cyberspace (DSC),Pages:595-600,2017.
- [4] Arianit Maraj, Genc Jakupi, Ermir Rogova, Xheladin Grajqevci, "Testing of network security systems through DoS attacks", Embedded Computing (MECO) 2017 6th Mediterranean Conference on, pp. 1-6, 2017.
- [5] US Department of Commerce, NIST. Guide to Information Security Testing and Assessment[J]. Itlb.
- [6] Marri Rami Reddy, Prashanth Yalla, "Mathematical analysis of Penetration Testing and vulnerability countermeasures", Engineering and Technology (ICETECH) 2016 IEEE International Conference on, pp. 26-30, 2016.
- [7] Jinsoo Shin,Hanseong Son,Gyunyoung Heo. Cyber Security Risk Evaluation of a Nuclear Instrumentation and Control System Using Bayesian Networks and Event Trees[J]. Nuclear Engineering and Technology,2016.
- [8] William G J Halfond, Shauvik Roy Choudhary, Alessandro Orso, "Improving penetration testing through static and dynamic analysis[J]", Software Testing Verification & Reliability, vol. 21, no. 3, pp. 195-214, 2011.
- [9] Microsoft (2016) Common types of network attacks, [online] Available: <https://technet.microsoft.com/en-us/library/cc959354.aspx>.
- [10] M. Saindane, "Penetration Testing-A systematic Approach", 2012.
- [11] Gary McGraw, Software Security. Datenschutz und Datensicherheit - DuD, vol. 9, no. 36, pp. 662-665, 2012.

- [12] P. K. Manadhata, J. M. Wing, "An Attack Surface Metric", Software Engineering IEEE Transactions on, pp. 371-386, 2011.
- [13] Xue Qiu. An automated method of penetration testing[A]. IEEE Beijing Section.Proceedings of 2014 IEEE Computers, Communications and IT Applications Conference (ComComAp)[C].IEEE Beijing Section:,2014:6.
- [14] Patrick Engebretson. What Is Penetration Testing?[M].Elsevier Inc.:2011.
- [15] Sanjay Bavisi. Penetration Testing[M].Elsevier Inc.:2013.
- [16] Yu Jiao Wang,Hai Yun Lin. A Kind of Network Security Evaluation Method Based on Local Variable Weight[J]. Key Engineering Materials,2011,1244(474):..

A Novel Weak Deduction Password Strength Meter of Chinese Websites

Yu Wu*

Shanghai Key Laboratory of Trustworthy Computing, East China Normal University, Shanghai 200062, China

*Corresponding author

Abstract—With the increasing situation of passwords datasets disclosure, the security of user's account faces rising risks under various kinds of password attack. To protect the security of user authentication system, password strength meter (PSM), which is used to measure user's password strength is widely accepted by Internet service institution. However, traditional PSMs in use today are rarely consider about user's cross-site vulnerable behaviors. In this paper, we first conduct a large scale of password reuse behaviors from 200 million Chinese websites' passwords. Then we propose our new weak-deduction PSM (WDPSM) that inherits the advantage of traditional probabilistic context free methods. Also, our WDPSM is good at model users' cross-site behaviors. Specifically, we perform a series of experiments to show that our weak-deduction PSM outperforms traditional PSMs in gauging weak passwords.

Keywords—password strength meter; probabilistic context free grammar; weak deduction; rank correlation

I. INTRODUCTION

The password authentication system is regarded as the important method to protect system security and is widely used in various kinds of online service. In the past few years, a large-scale of password information have been leaked leading to serious threats to user's accounts security. In order to solve this problem, most of the majority of websites provide PSM to evaluate the user's password security. The password selected by the user cannot be received by the system unless it reaches a certain threshold. Hence, enhancing the accuracy becomes an important indicator in designing a PSM.

Burr et al. proposed a rule-based PSM so called NIST in 2006 [1]. After that, in nearly decades, a mass of PSM have been proposed which follow the spirit of NIST such as Google, Microsoft PSM [2]. NIST PSM suggest evaluating password strength in terms of guessing space (e.g., 6 bits entropy added if passwords have both uppercase letter and non-alphabetic characters, 1.5 bits each added for characters 9 through 20). Later, Carnavalet et al. [3] found that most of these PSM are simple and estimate password based on some heuristic rules by studying a large scale of popular websites' password strength meter.

Kelley et al. [4] suggest that the rule-based PSMs are difficult to provide accurate measurement of password strength for reason of lacking analysis on empirical data. To improve the accuracy of the PSM, Kelley et al. presented a new concept, namely: 'guessability' as the password strength metric. 'Guessability' is a metric that characterizes the guess number

needed for an efficient password-cracking algorithm to discover a password.

Most research on 'guessability' is based on Markov [5] and Probabilistic Context Free Grammar (PCFG) [6] cracking algorithm which are proposed by Narayanan et al. and Weir et al. respectively. Houshmand and Aggarwal [7] used probabilistic context free techniques [6] to analyze password strength (passwords probability). They first developed an analyze-modify system to estimate the probability of password. After that, they modifies the password slightly if it is weak enough. Castelluccia et al. [8] first proposed an adaptive PSM based on the Markov chain probabilistic guessing model, and their PSM is much better than NIST, Google and Microsoft PSM.

Das et al. [9] first conduct a user survey to study user's password reuse behaviors, and they developed the first cross-site password-guessing algorithm so called DBCBW algorithm which is better than the standard guessing algorithm presented by John the Ripper [10]. However, their password reuse study does not based on real-world password datasets and their guessing algorithm has not compared with other academic algorithm.

A. Our Contribution

In our work, we first analyze a large scale of password reuse behaviors based on 9 disclosure Chinese password datasets which contains 200 million passwords in total. By analyzing user's cross-site reuse or slightly modify passwords behaviors, we propose our new WDPSM. We first uses a weak password set collecting from leaked password sets to construct a password bk-tree. Then, we learns how to apply mangle rule and transformation rule in generating new password from similar original password. Finally, we extended traditional probabilistic context free method [5] to model user's password reuse behavior and gives rise to WDPSM.

We conduct a series of experiments to compare our new PSM with traditional PSMs, e.g. NIST and PCFG PSM. The result show that our WDPSM performs better in judge weak passwords.

B. Paper Organization

We introduce our password datasets with basic data analysis in section 2. Our WDPSM is proposed in section 3. In section 4 we present the comparison between various existing PSMs with WDPSM and we conclude our work in section 5.

II. PASSWORD DATASET ANALYSIS

In this section, we analyze nine representative Chinese password databases in two patterns: basic password statistics analysis and password reuse analysis. We collected nine famous Chinese password datasets which contains 203 million valid password in total. Table I shows their basic information Maintaining the Integrity of the Specifications

The template is used to format your paper and style the text. All margins, column widths, line spaces, and text fonts are prescribed; please do not alter them. You may note peculiarities. For example, the head margin in this template measures proportionately more than is customary. This measurement and others are deliberate, using specifications that anticipate your paper as one part of the entire proceedings, and not as an independent document. Please do not revise any of the current designations.

TABLE I. NINE CHINESE PASSWORD DATASETS

Datasets	Total PWs	Unique PWs	When Leaked
CSDN	6,414,425	4,026,595	2011.1
163	117,602,494	21,730,096	2011, 2014
Dodonew	16,020,739	9,989,007	2011
Tianya	29,010,375	12,817,411	2011.12
Renren	4,681,142	2,800,426	2014
Zhenai	5,236,113	3,503,765	2014
17173	9,956,882	3,629,363	2011.12
7k7k	9,435,506	4,887,257	2011
Weibo	4,942,426	2,825,096	2011.12
Total	203,300,102	66,326,824	

A. Basic Password Statistics Analysis

1) The most popular passwords: We analyze the nine datasets of Chinese websites and find that the most popular password is '123456' in most of the datasets. In addition, the most popular password is '123456789' in CSDN.

2) Length distribution: We analyze the nine datasets of Chinese websites and find that the most common used password length are among 6 ~ 11. Dodonew, weibo and renren have some password length less than 6.

3) Structure distribution: To understand the constitution of password in various website. We separate the character consist of passwords into four classes: L represent lower case letter, U represent upper case letter, D represent digits, S represent special symbol. Specially, for example, LD means a password with letter and digits. We analyze the nine datasets of Chinese websites and find that the top three most popular password structure is D-only, LD and L-only. Surprisingly, about half of users around most website use D-only password.

B. Password Reuse Analysis

In this section, we start to learn user's password reuse. We define the behavior that one user use identical password or

similar password from different websites as password reuse. In our work, we perform the first systematic assessment on password reuse based on a large-quantity of Chinese passwords datasets.

Before we describe the password reuse analysis, we split password reuse into 7 rules as follow. **Identical rule:** this rule means one password is same with another. **Substring rule:** this rule means one password is a substring of another one (e.g., wuyu and wuyu123). **Longest Common Substring (LCS) rule:** LCS rule implies the majority of two passwords are same, but one is not another one's substring. (e.g., wuyu123 and wuyu@123). **Uppercase rules:** this rules means the pair of two password is not same but upper case is. **Leet rule:** this rule uses some alphabetic character to replace the similar-looking character. (e.g., 0↔o, a↔@, 1↔I, e↔3, 5↔s, s↔\$, password ↔p@sword). **Reverse rule:** this rule means one password is the reverse form of another password. **Other rule:** the rest of passwords are classified as the other rule.

We analyze the password reuse by following steps:

- Removing invalid password from our datasets to avoid disturbing.
- Intersecting a dataset with another dataset by matching account name or email. This step produces a new datasets with two brother passwords for each account or user.
- Using above mentioned 7 rules to learn how do user use one password of brother pair to produce another one.

We use our password reuse analyze method to analyze the nine datasets and the result of the analysis is demonstrated in Table II.

In total, about 62% password pair is same with each other, this result show highly rate than the investigation result Das et al. [8] have done. About 11% password pair is similar to each other. Only 27% password is unmatched.

TABLE II. PASSWORD REUSE ANALYSIS

Transformatin rule	Ratio (%)
Uppercase	0.14%
Identical	62.09%
LCS	2.66%
Leet	0.00%
Substring	7.39%
Reversal	0.00%
Other	27.72%

III. OUR WEAK-DEDUCTION PSM

In this section, we propose our WDPSM which outperforms traditional PSMs in gauging weak passwords. First we give the formal definition of PSM and ideal PSM.

Definition 1 (PSM). A PSM is a function $F(\cdot)$ that take a password as an input over an alphabet Σ and outputs a probability p (as a number) in range of $[0,1]$. The probability p of a password is inversely proportional to the weakness of it.

Definition 2 (Ideal PSM). An ideal PSM is a function $F(\cdot)$ that $F(pw) = P(pw)$ where pw is a password and $P(pw)$ is a real probability of pw in an authentication system.

Through the password reuse analysis of previous section, we find that users have a very high probability of reusing password. This fact is in vast contrast with PCFG-based PSM assumes that users construct new passwords from scratch. To model user's password reuse behavior, we propose our WDPMS to measure passwords strength. The whole process can divide into three phases: **Training, Measuring and Updating**.

First we uses a set of leaked weak passwords as "Weak set" W to construct a weak password parsing bk-tree [11]; while using another target website or target website similarity website leaked passwords set as training set T . Then we parse password in T and automatically derive password-mangling rules.

Training: we measure the frequencies of certain patterns associated to the training passwords in T . First we assume weak password set $W = \{w_1, w_2, \dots, w_N\}$, a password of length n will be labeled as W_n . n is no longer than the maximum length accepted by target system. Each password in the training set T is parsed by the bk-tree using a new algorithm so called optimal longest common subsequence matching algorithm (OLCS). We will describe OLCS algorithm in **Algorithm 1**. If there exists some parts of pw which is unmatchable, we match the unmatchable part in the original PCFG method.

Algorithm 1 Optimal longest common subsequence matching algorithm (OLCS)

Input: pw, W, D (the distance threshold), S (the similarity threshold).

Output: omv (the optimal match value).

- 1) $optimal = \{\}$
- 2) $substring(pw) = \{\text{all substring of } pw\}$
- 3) for w in W
- 4) for sub in $substring(pw)$
- 5) $lcs = LCS(sub, pw)$
- 6) $dist = distance(w, pw)$
- 7) $smil = similarity(w, pw)$
- 8) $optimal.add((w, lcs) \text{ if } length \leq D \text{ and } score < S)$
- 9) $optimal = optimal.select(w \text{ if } min(dist))$
- 10) $optimal = optimal.select(w \text{ if } max(smil))$
- 11) $omv = optimal.select_one(w \text{ if } max(P[w]))$
- 12) return omv

Step 1 to 7 will get calculate all possible string pair with their distance score, similarity score and longest common subsequence. Step 8 will get a minimum distance score string pair set. Step 9 will get all string pair with maximum similarity score. Step 10 to 11 return the optimal match with high probability. Specifically, we choose select Levenshtein-distance as distance function, choose Levenshtein-smilarity as similarity function in **Algorithm 1**.

Our context free grammar is defined as $G=(V, \Sigma, S, P)$ where $V=\{S, L, D, S, insert, delete, replace, W_1, W_2, \dots, W_n\}$ is a finite set of variables, S is the start variable, $\Sigma=\{95\text{printable ASCII characters}\}$ is a finite set of terminals and P is finite set of productions of the form $\alpha \rightarrow \beta$, with $\alpha \in V$ and $\beta \in V \cup \Sigma$.

For example, $123.456abc \in T$, $123456 \in W$, OLCS would return $(123.456, 123456)$. The result tell us 123.456 is mostly similar with Weak password 123456 , so 123.456 would be parsed into W_6 and the remain part 'abc' is matched by original PCFG match. As a result, 'abc' will be parsed into L_3 . Then the whole password pattern is represented as W_6L_3 . In total, the whole parsing phase is similar with PCFG approach.

From our training set T , we derive a set of productions that generate the base structures, base segments (including weak passwords and other segments) with their associated probabilities of occurrence. Note that, G is a probabilistic context-free grammar because for a specific LHS variable all the associated productions add up to 1.

TABLE III. EXAMPLE OF EXTENDED GRAMMAR

LHS	RHS	probability
S	W6	1
W6	no	0.7
W6	insert	0.3
insert	D1	0.8
insert	S1	0.2
D1	0	1
S1	.	0.75
S1	+	0.25

TABLE IV. EXAMPLE OF PROBABILISTIC CONTEXT FREE GRAMMAR

LHS	RHS	probability
S	W6	1
W6	123456	0.7
W6	000000	0.3

Measuring: The Grammar G would be used to measure passwords probability in measuring phase. An example grammar is show in Table III~IV. The $P("123.456")=P(W_6)*P(W_6>insert)*P(insert>S_1)*P(S_1->.)=0.7*0.3*0.2*0.75=0.0315$.

Updating: The updating phase can dynamic modifies the grammar with the time go by. For example, while $123.456abc$ is accepted by the system, all probabilities that related to the base structure W_6 and L_3 , transformation rule $W_6>insert$ and $insert>S_1$, and terminals 123456 , abc shall be updated. This process is similar with The PSM in [7]. While the probability measured by meter of a valid password is higher than the threshold probability, that password will be add to weak password set. We named the above process that an original weak password deduce a new weak password as Weak

Deduction. Our WDPSM can associate one password with the similar password through weak deduction, which is in vast contrast with the PCFG-based PSM. So we claim that our context free grammar is a weak deduction one.

IV. EXPERIMENT ANALYSIS

A. Experiment Prepare

To model user's password reuse behavior, we use Houshmand and Aggarwal [7] method to collect weak passwords from the weakest dataset as weak password. Tianya datasets is the weakest one [12], so we use it in our experiments. Then we randomly split each dataset into equally four parts, the training set uses part-1 and testing set uses part-2, as [8,13] has done. Table V show how we choose training and testing set for experiment.

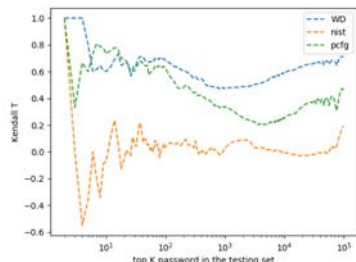
To compare with different password strength meter, we use Kendall coefficient. We will use it in our experimental evaluation.

TABLE V. TRAINING SET AND TESTING SET

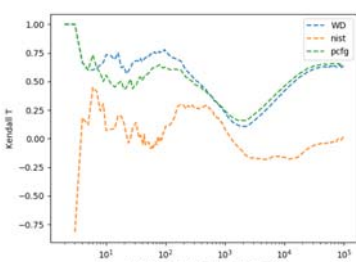
Weak password set	Traning set	Testing set
tianya	1/4 weibo	1/4 weibo
tianya	1/4 7k7k	1/4 7k7k
tianya	1/4 tianya	1/4 tianya

B. Result Evaluation.

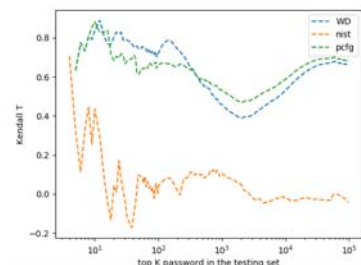
In this section, we compare the performance of our WDPSM with NIST PSM [1] and PCFG-based PSM [7]. The result is show in Figure I. All the tested password meters are measured by computing the Kendall rank correlation scores against with ideal meter. In most cases, DBPSM outperforms other PSMs.



(a) 1/4 weibo training with 1/4 weibo testing



(b) 1/4 7k7k training with 1/4 7k7k testing



(c) 1/4 tianya traning with 1/4 tianya testing

FIGURE I. EXPERIMENT RESULTS OF PSMS ACCURACY ANALYSIS

CONCLUSION

In this paper, we have analyzed 200 millions of passwords and millions of password pairs of Chinese password data. A high percentage (72.29%) of passwords are reused or slightly modified by user for different services. To defense the cross-site password attacking, we proposed a new password strength meter which can characterize user's password creation policy. Experiments show that our WDPSM performs higher accuracy than existing wildly used password strength meter. Although the data used in experiment is from Chinese passwords dataset, the measure method can be used to other language environment either.

REFERENCES

- [1] W. E. Burr, D. F. Dodson, and W. T. Polk. Electronic authentication guideline: NIST special publication 800-63, 2006.
- [2] D. Wang and P. Wang, "The emperor's new password creation policies," in Proc. ESORICS 2015, pp. 456–477.
- [3] X. Carnavalet and M. Mannan, "A large-scale evaluation of high-impact password strength meters," ACM Trans. Inform. Syst. Secur., vol. 18, no. 1, pp. 1–32, 2015.
- [4] P. G. Kelley, S. Komanduri, M. L. Mazurek, R. Shay, T. Vidas, L. Bauer, N. Christin, L. F. Cranor, and J. Lopez, "Guess again (and again and again): Measuring password strength by simulating password-cracking algorithms," in Proc. IEEE S&P 2012, pp. 523–537.
- [5] A. Narayanan and V. Shmatikov. Fast dictionary attacks on passwords using time-space tradeoff. In Proc. ACM CCS 2005, pp. 364–372.
- [6] M. Weir, S. Aggarwal, B. de Medeiros, and B. Glodek. Password cracking using probabilistic context-free grammars. In Proc. IEEE S&P 2009, pp. 391–405.
- [7] S. Houshmand and S. Aggarwal, "Building better passwords using probabilistic techniques," in Proc. ACSAC 2012, pp. 109–118.
- [8] C. Castelluccia, M. D'urmuth, and D. Perito, "Adaptive password strength meters from markov models," in Proc. NDSS 2012, pp. 1–15.
- [9] A. Das, J. Bonneau, M. Caesar, N. Borisov, and X. Wang. The tangled web of password reuse. In Proc. NDSS 2014, pp. 1–15.
- [10] John the ripper password cracking toolkit. <http://www.openwall.com/john/>.
- [11] BK-tree - Wikipedia. <https://en.wikipedia.org/wiki/BK-tree>.
- [12] J. Ma, W. Yang, M. Luo, and N. Li, "A study of probabilistic password models," in Proc. IEEE S&P 2014, pp. 689–704.
- [13] M. Weir, S. Aggarwal, M. Collins, and H. Stern, "Testing metrics for password creation policies by attacking large sets of revealed passwords," in Proc. ACM CCS 2010, pp. 162–175.

A Novel Video Encryption Method Based on Faster R-CNN

Lijuan Duan^{1,2,3,*}, Dongkui Zhang^{1,2,3}, Fan Xu^{1,2,3} and Guoqin Cui⁴

¹Faculty of Information Technology, Beijing University of Technology, Beijing 100124, China

²Beijing Key Laboratory of Trusted Computing, Beijing 100124, China

³National Engineering Laboratory for Critical Technologies of Information Security Classified Protection, Beijing 100124

⁴State Key Laboratory of Digital Multi-media Chip Technology, Vimicro Corporation, Beijing, 100191, China

*Corresponding author

Abstract—In order to improve the generalization performance of video encryption and reduce the amount of data in video encryption, this paper proposes a video encryption on regions of interest (ROI) method based on Faster R-CNN by combining machine learning with information security. The method trains a Faster R-CNN model using the ROI dataset firstly, and then uses the model to extract ROI in the video. Different encryption algorithms are used to encrypt ROI and non-ROI in the video respectively. To overcome the shortcomings of encryption algorithms that can only be used for a specific coded video, a special video encryption method is proposed to encrypt the video with different video coding structure and has better generalization performance. Compared with the encryption method in the video coding process, this method considers the content information of the video fully and has better performance. It can be concluded through experiments that the encryption method in this paper has the characteristics of higher security and less calculation.

Keywords—video encryption; faster R-CNN; the ROI of video

I. INTRODUCTION

In the age of information, with the rapid development of computer and Internet technologies, people can post messages and obtain information on the Internet anytime, anywhere. Large amounts of data are transmitted through the network and more than 50 million servers work on the network over the world. Zettabytes of data are produced each year, which contain a large amount of video data [5][7]. Video in the national defense, education, monitoring, entertainment and other fields have been widely used, so data security on the internet cannot be ignored. Unauthorized access and the openness of the network lead to more and more serious data security problems. Especially, video security issues have become more serious and aroused more attentions [10]. Video encryption is an effective data encryption strategy to improve video security. Video encryption protects the original video information and improves the security of video information. Researchers have done a lot of research on video encryption and put forward a lot of video encryption methods. Video encryption methods are mainly divided into complete encryption and partial encryption algorithm.

Video complete encryption algorithm is to encrypt the whole video data with encryption algorithm in order to achieve the purpose of protecting video information. Think of video data as a series of data streams and then encrypt the video data streams

with traditional encryption algorithms. However, traditional encryption algorithms such as AES and RSA can achieve good encryption effect on text data and unformatted data [13]. In [7], the author proposed a video encryption algorithm based on RSA. Because of the large quantity and strong correlation of video data, the information redundancy leads to too high complexity of video encryption and too long time consuming to meet real time encryption Request. Using image encryption algorithm to encrypt the video fully, the video is divided into a series of video frames, and then use the image encryption algorithm to encrypt every frame of video. It can reduce the amount of data to be encrypted in the video, but does not take the information redundancy between video frames into account, which results in higher encryption complexity [10]. Video complete encryption method does not consider the video data format and ignores the correlation between video frames, resulting in higher video encryption complexity, large amount of data to be encrypted and long time consuming. So it cannot meet the demands of real time encryption.

The video partial encryption algorithm encrypts the video in the coding process [6][11][13]. Encrypting video in the process of video encoding can reduce the amount of data to be encrypted and reduce the complexity of encryption. In [5], the author combines the stream cipher and the video cipher to encrypt the DCT transform coefficients. This method only encrypts the DCT transform coefficients, so it is not safe enough. In [10], the author encrypts motion vector difference (MVD), luma residual coefficients and chroma residual coefficients in the process of HEVC encoding. It can improve encrypted security to some extent. In [15], in order to protect the video data, the author proposed a video encryption method based on logistic chaos mapping, which encrypts the motion vector (MVD) and DCT variation coefficient the chaotic mapping in the process of HEVC encoding. In [13], the author proposed a video encryption method based on RGB three channel MPEG encoding, which achieved wonderful encryption effect on MPEG videos, but it has a weak generalization ability. In [14], Mamoon et al. proposed a video encryption method based on CABAC entropy coding and it has some limitations and can only encrypt H.264 and HEVC encoded video. The existing video encryption methods combined with video coding can reduce the complexity of encryption and increase the speed of encryption. However, they also have some limitations, and can only encrypt video in a specific encoding format, and have a weak generalization ability.

In order to overcome the shortcomings of existing video encryption algorithms, this paper proposed a region based video encryption method, which uses the Faster R-CNN to extract ROI in video frames. It can help to reduce the amount of video encrypted data. The video encryption method can encode a variety of video encoding and has a high generalization ability.

This article is organized as follows: Section 2 introduces the Faster-R-CNN network structure, training of ROI model, and extraction of ROI. Section 3 describes the encryption algorithm and the steps to encrypt the ROI. Section 4 is mainly to analyze the effect of video encryption through experiments.

II. PROPOSED METHOD

Video data often contains a lot of information, but people tend to focus only on some of the information they are interested in and ignore some of the background information. In order to meet this demand, a video encryption method based on Faster R-CNN and ROI is proposed in this paper. Faster R-CNN is a multi-layer convolution neural network that achieves good results in the field of object detection and recognition. In this method, the Faster R-CNN is used to extract ROI in the video. The framework of video encryption system is shown in Fig. I. It is mainly divided into three parts: the training of the ROI model, the extraction of the ROI in the video and the encryption of the ROI. The detailed ideas of this method is as follows: Firstly, a ROI model is trained with the Faster R-CNN by using the data set of the ROI, and then the ROI in the video is extracted with the trained ROI model. Finally, the ROI is encrypted.

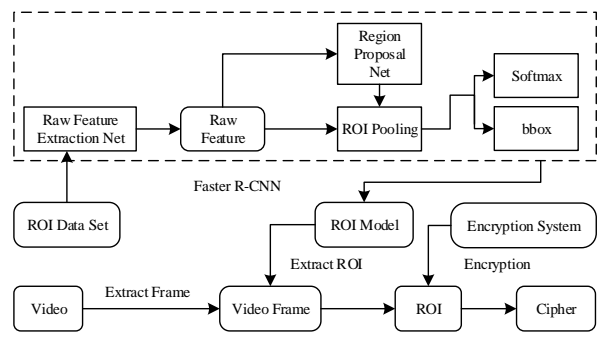


FIGURE I. THE FRAMEWORK OF VIDEO ENCRYPTION SYSTEM

A. Extraction of ROI

This section mainly introduces the extraction of the ROI in a video. In this paper, we used Faster R-CNN to extract the ROI in a video. The Faster R-CNN combines convolutional neural networks and machine learning [2]. It uses the region proposal network instead of the selective search algorithm to generate a suggestion window, and the region proposal network and the target detection network share the convolution layer features [3].

The structure of Faster R-CNN is shown in Figure II. Faster R-CNN consists of the convolutional neural network, ROI Pooling, Softmax, Bounding box regression and others. Convolution neural network is mainly used for the extraction of image feature[2][3]. In this paper, VGG16 is used to extract image features. Compared with other convolutional neural networks, VGG16 has simpler structure and superior performance. The Faster R-CNN with the region proposal network has better performance

than the Faster R-CNN and R-CNN with the selective search algorithm in generation of the candidate box. The ROI pooling layer mainly performs the pooling operation on the candidate boxes generated by the RPN and generates a fixed-size feature map for each ROI.

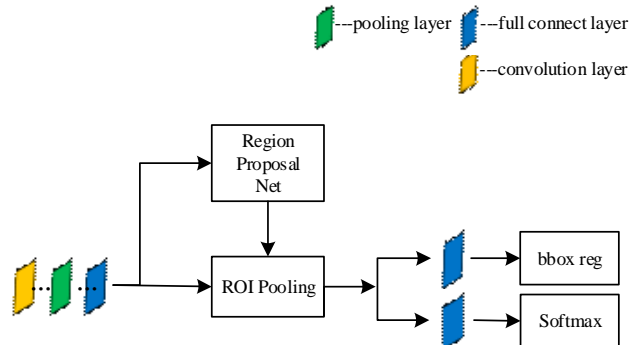


FIGURE II. THE STRUCTURE OF FASTER R-CNN

The dataset training the Faster R-CNN to generate the ROI model is from the WIDER FACE. More than 20,000 images were used to train and generate a ROI model on the GPU spending more than 10 hours. The effect of extraction of the ROI is shown in Fig. III. The model extracted the ROI in a) and extracted 5 ROI in b) accurately. It can be concluded that the ROI model in this paper is not only applicable to images containing a single ROI, but also to images containing multiple ROI.



FIGURE III. EXTRAC ROI

B. Encryption Algorithms

After the ROI of the video is extracted using the ROI model trained, the videos are divided into the ROI and the non-ROI. In this paper, different encryption algorithms are used respectively to encrypt the non-ROI and the ROI in the video. The non-ROI of the video is encrypted by $GF(17)$ domain diffusion encryption algorithm based on plaintext [8], while the ROI of the video is encrypted by the encryption algorithm based on hyperchaos system and pixel information, which is more secure and complex. Using different encryption algorithms according to different contents of the video can improve the security of encryption and increase the difficulty of cracking and speed up encryption.

The finite field, also known as the galois field, is a field that contains only a limited number of elements. If $GF(p)$ is a finite field, where p is a prime number, the addition is as shown in Equation 1, and the multiplication is as shown in Equation 2,

where x and y are the elements in the finite field. For the multiplication in $GF(p)$, only when p is a prime number, have the other elements in the finite field except 0 an inverse multiplication.

$$(x + y) \bmod p \quad (1)$$

$$(x \cdot y) \bmod p \quad (2)$$

TABLE I. MULTIPLICATION OPERATION OF GF(17) [8]

x	0	1	2	3	4	5	6	7	8	9	10	11	12	13	14	15	16
0	0	0	0	0	0	0	0	0	0	0	0	0	0	0	0	0	0
1	0	1	2	3	4	5	6	7	8	9	10	11	12	13	14	15	16
2	0	2	4	6	8	10	12	14	16	1	3	5	7	9	11	13	15
3	0	3	6	9	12	15	1	4	7	10	13	16	2	5	8	11	14
4	0	4	8	12	16	3	7	11	15	2	6	10	14	1	5	9	13
5	0	5	10	15	3	8	13	1	6	11	16	4	9	14	2	7	12
6	0	6	12	1	7	13	2	8	14	3	9	15	4	10	16	5	11
7	0	7	14	4	11	1	8	15	5	12	2	9	16	6	13	3	10
8	0	8	16	7	15	6	14	5	13	4	12	3	11	2	10	1	9
9	0	9	1	10	2	11	3	12	4	13	5	14	6	15	7	16	8
10	0	10	3	13	6	16	9	2	12	5	15	8	1	11	4	14	7
11	0	11	5	16	10	4	15	9	3	14	8	2	13	7	1	12	6
12	0	12	7	2	14	9	4	16	11	6	1	13	8	3	15	10	5
13	0	13	9	5	1	14	10	6	2	15	11	7	3	16	12	8	4
14	0	14	11	8	5	2	16	13	10	7	4	1	15	12	9	6	3
15	0	15	13	11	9	7	5	3	1	16	14	12	10	8	6	4	2
16	0	16	15	14	13	12	11	10	9	8	7	6	5	4	3	2	1

In this paper, $GF(17)$ domain multiplication is used as operation of diffusion encryption [8]. In order to prevent 0 element from appearing in multiplication in $GF(17)$ domain during encryption, the multiplication Operation of $GF(17)$ is shown in Table 1. For the first two pixels, the data is encrypted with equation 3, where c and the subscript i denotes the position of the data and the subscript h denotes the upper four bits of the data and the subscript l denotes the lower four bits of the data and the operator \times is a multiplication on the $GF(17)$ field. The encryption key k is generated with the overall information of the image and the data information of the pixel. Firstly, use the upper four bits of the encryption key to encrypt the upper four bits of the data. Secondly, use the lower four bits of the encryption key to encrypt the lower four bits of the data. Finally, generate the ultima encrypted ciphertext with the previous results.

$$\begin{cases} c_{i,h} = p_{i,h} \times k_{i,h} \\ c_{i,l} = p_{i,l} \times k_{i,l} \\ c_i = c_{i,h} \cdot 16 + c_{i,l} \quad i < 3 \end{cases} \quad (3)$$

When $i \geq 3$, the data is encrypted with equation 4, and the upper four bits and the lower four bits of data are encrypted respectively. Then the first two ciphertexts adjacent to the data are diffused into the encrypted ciphertext of the data. Finally, the final ciphertext is generated with the upper four digit ciphertext and the lower four digit ciphertext.

$$\begin{cases} c_{i,h} = p_{i,h} \times k_{i,h} \times c_{i-1,h} \times c_{i-2,h} \\ c_{i,l} = p_{i,l} \times k_{i,l} \times c_{i-1,l} \times c_{i-2,l} \\ c_i = c_{i,h} \cdot 16 + c_{i,l} \quad i \geq 3 \end{cases} \quad (4)$$

The detailed procedure of decryption in this paper is as follows: Firstly, decrypt the plaintext of the first two data and then decrypt the remaining data using equation (5).

$$\begin{cases} p_{i,h} = c_{i,h} \div k_{i,h} \div p_{i-1,h} \div p_{i-2,h} \\ p_{i,l} = c_{i,l} \div k_{i,l} \div p_{i-1,l} \div p_{i-2,l} \\ p_i = p_{i,h} \cdot 16 + p_{i,l} \quad i < 3 \end{cases} \quad (5)$$

III. RESULT

This section introduces the experimental results and analysis of the results. The experimental program ran on the Tesla K40c GPU platform. In order to analyze the security and effect of the video encryption method proposed in this paper, we use three groups of videos to experiment. It can be seen from the experimental results that the ROI model in this paper can accurately extract the ROI in the video. Encrypting the ROI and non-ROI of the video with different encryption algorithms can reduce the amount of data encrypted and reduce the complexity of encryption.

A. The Extraction of ROI

The ROI in the three groups of videos are extracted with the trained ROI model. The experimental results are shown in the Fig. IV. It is the results of the extraction of the ROI in the first, 50th, 100th and 150th frames of the video. And the ROI in the three groups of video were extracted accurately.

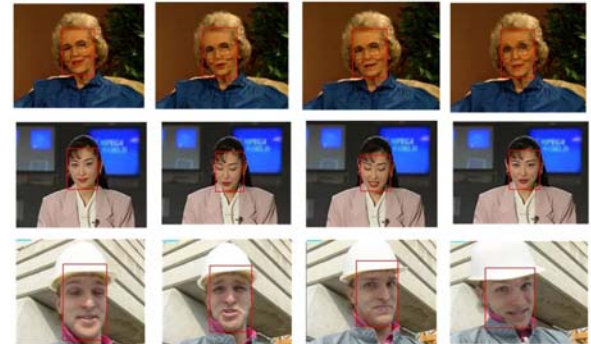


FIGURE IV. RESULT OF EXTRACTION OF ROI

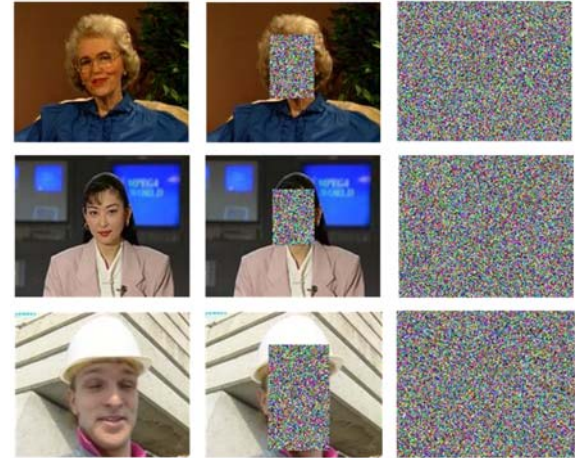


FIGURE V. ENCRYPTION OF THE VIDEO

The results of video encryption are shown in Fig. V. The ROI and non-ROI of the video are encrypted with different encryption algorithms. Both the ciphertext of the ROI and the non-ROI are noise-like and any information about images cannot be read from the ciphertext.

Figure VI shows the proportion of the ROI in every video frame. It can be seen that the ROI in every frame accounts for about 20%. So only encrypting the ROI in the video can almost reduce the amount of encrypted data by 80%, which can help to reduce the complexity of video encryption.

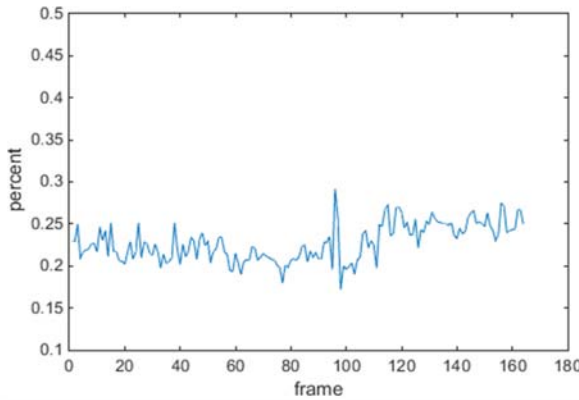


FIGURE VI. THE PERCENT OF ROI

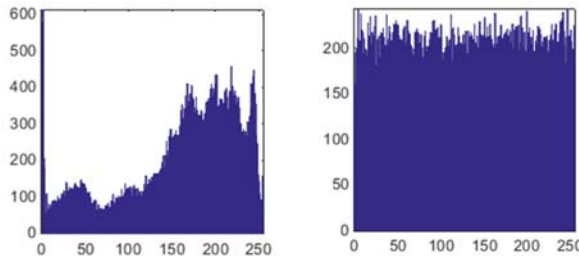


FIGURE VII. HISTOGRAMS OF THE PLAINTEXT AND THE CIPHERTEXT

B. Histogram Analysis

The histogram of the plaintext and the ciphertext is shown in Figure VII. It can be seen from the histogram of the plaintext that the pixel values are unevenly distributed, so some of image information can be read from it. But from the histogram of the ciphertext, it can be seen that the pixel values are evenly distributed, so any useful information cannot be read from it.

C. Correlation Analysis

The results of the correlation between adjacent pixels are shown in Figure VIII. It can be seen that there is a strong correlation between the adjacent pixels in the plaintext, while there is no correlation between adjacent pixels in the ciphertext because of the evenly distribution of pixel grey value.

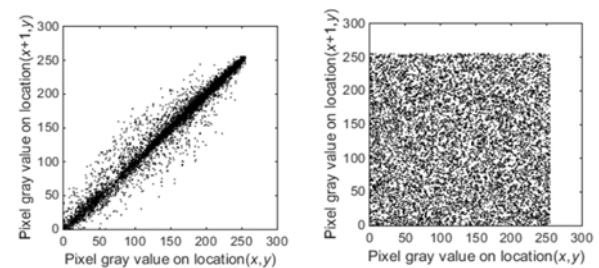


FIGURE VIII. CORRELATION BETWEEN ADJACENT PIXELS

The correlation coefficient is shown in Table II, the plaintext has a large correlation coefficient in three directions and the adjacent pixels have strong correlation. The correlation coefficient of ciphertexts in three directions is close to 0, which indicates that ciphertexts are not related between adjacent pixels.

TABLE II. CORRELATION COEFFICIENT

Image	Horizontal	Vertical	Diagonal
Plain	0.9862	0.9782	0.9623
Cipher	-0.0016	-0.0034	-0.0129

D. Key Sensitivity Analysis

This article make a small change to the key and then test the key's sensitivity. Table III shows the key sensitivity results. It can be seen that the NPCR and UACI of the three groups of test data are close to the theoretical value, so the encryption method has high key sensitivity.

TABLE III. KEY SENSITIVITY ANALYSIS

	grandma	akiyo	foreman	Theoretical
NPCR	99.6100	99.6452	99.6927	99.6094
UACI	33.4000	33.3395	33.3135	33.4635

E. Differential Attack Analysis

Differential attack is also called the choice of plaintext attack, the differential attack analysis results in Table IV, the three sets of data differential analysis of NPCR and UACI values are close to the theoretical value, indicating that the encryption method has high security, which can resist Differential attack.

TABLE IV. DIFFERENTIAL ATTACK ANALYSIS

	grandma	akiyo	foreman	Theoretical
NPCR	99.6633	99.7339	99.6756	99.6094
UACI	33.4409	33.7439	33.4504	33.4635

F. Encryption time Analysis

The analysis results of the encryption time are shown in Table V, T1 is the time of extracting the video region of interest. T2 is the time of encrypting the video region of interest. The region of interest in the video is encrypted by a fast scrambling encryption algorithm. T3 is the time of encrypting the non-ROI and T4 is the time of encrypting a video frame. It can be seen from Table 4 that the encryption method in this paper is less time consuming and faster than the video frame complete encryption.

TABLE V. DIFFERENTIAL ATTACK ANALYSIS

	T1(s)	T2(s)	T3(s)	Our(s)	T4(s)
grandma	0.2307	0.0470	0.0150	0.2927	0.3750
akiyo	0.2374	0.0460	0.0160	0.2994	0.6380
foreman	0.2267	0.1530	0.0050	0.3847	0.6500

IV. CONCLUSION

This paper presented a video encryption method on ROI of a video based on Faster R-CNN. We combined machine learning with video encryption and trained an extraction of ROI model with the dataset of ROI and Faster R-CNN. The ROI in the video was extracted effectively with the trained ROI model, then the ROI and non-ROI in the video were encrypted with different encryption algorithms. The method proposed in this paper can reduce the complexity of encryption and improve the encryption speed. And it can also deal with a variety of video encoding format, so it has a high generalization performance. And the encrypted video has the advantages of low correlation, high encryption sensitivity and high security.

ACKNOWLEDGMENT

This paper is partly supported by National Natural Science Foundation of China [grant numbers 61572004], the Beijing Municipal Natural Science Foundation [grant numbers 4152005], the Science and Technology Program of Tianjin [grant number 15YFXQGX0050], and the Science and Technology Planning Project of Qinghai Province [grant number 2016-ZJ-Y04].

REFERENCES

- [1] X.Y. Wang, K. Guo. A new image alternate encryption method based on chaotic map. *Nonlinear Dyn*,2014(76),pp.1943–1950.
- [2] J. Dai, K. He, and J. Sun. Convolutional feature masking for joint object and stuff segmentation. In *CVPR*,2015.
- [3] D. Erhan, C. Szegedy, A. Toshev, and D. Anguelov. Scalable object detection using deep neural networks. In *CVPR*,2014.
- [4] Siu-Kei Bing Zeng,Shuyuan Zhu. Perceptual encryption of H.264 videos:embedding sign-Flips into the integer-based transforms. *IEE Trans. Inf. Forensics Secur*,2014(9),9,pp 309-320.
- [5] Saeed Bahrami,Majid Naderi, Encryption of Video Main Frames in the Field of DCT Transform Using A5/1 and W7 Stream Encryption Algorithms, *Arabian Journal for Science and Engineering*,2014(39),pp 4077-4088.
- [6] S Mumthas,A Lijiya, Transform Domain Video Steganography Using RSA, Random DNA Encryption and Huffman Encoding, *Procedia Computer Science*,2017(115),pp 660-666.
- [7] M.Garcia-Martinez, E.Campos-Canton. Pseudo-random bit generator based on multi-modal maps. *Nonlinear Dyn*,2015(82),pp 2119-2131.
- [8] Zhang Yong. Chaotic digital image encryption[M]. BeiJing: tsinghua university press,2016.
- [9] Jovanovic B,Gajin S. An efficient mechanism of cryptographic synchronization within selectively encrypted H.265/HEVC video stream. *Multimed Tools Appl*,2017,pp 1-17.
- [10] A.Alfalou,C.Brosseau,N.Abdallah, Simultaneous compression and encryption of color video images. *Optics communications*,2015(338),pp 371-379.
- [11] Juan Chen,Fei Peng,Min Long, A Perceptual Encryption Scheme for HEVC Video with Lossless Compression, *International Conference on Cloud Computing and Security*,2017,pp 396-407.
- [12] Xiaoyu Li,Chen Tang,Xinjun Zhu. Image/video encryption using single shot digital holography. *Optics communications*,2015(342),pp 218-223.
- [13] Quist-Aphetsi Kester,Laurent NanaAnca,Christine Pascu, A Cryptographic Encryption Technique of MPEG Digital Video Images Based on RGB Layer Pixel Values, *Advances in Intelligent Systems and Computing*,2016,355.
- [14] Mamoonah N.Asghar,Rukhsana Kousar, Transparent encryption with scalable video communication: Lower-latency, CABAC-based schemes, *Journal of Visual Communication and Image Representation*,2017(45),pp 122-136.
- [15] Sallam, A.I., El-Rabaie, ES.M. Faragallah, Efficient HEVC selective stream encryption using chaotic logistic map,O.S. *Multimedia Systems*,2017,pp 1-19.
- [16] Tew Yiqi,Wong KokSheik,Phan Raphael C. Region-of-interest encryption in HEVC compressed video. *IEEE international conference on consumer electronics*,2016.
- [17] Xiao Di,Fu Qingqing,Xiang Tao. Chaotic image encryption of ROI. *International journal of bifurcation and chaos*,2016(26).
- [18] Liu Yuling,Qu Xinxin,Guojiang. A ROI-based reversible data hiding scheme in encrypted medical images. *Journal of visual communication and image representation*,2016(39),pp 51-57.

Common-Key Cryptosystem with Mixture of Fake Plaintexts

Masayoshi Hayashi and Hiroaki Higaki*

Department of Robotics and Mechatronics, Tokyo Denki University, Japan

*Corresponding author

Abstract—One of the fundamental methods for eavesdroppers to achieve a plaintext from a cryptogram is the brute force attack where possible candidates of decryption keys are exhaustively applied to the decryption algorithm. Here the only reason why the eavesdroppers believe to find the common-key and to achieve the plaintext is that the output of the decryption algorithm is contextually acceptable. According to this fact, this paper proposes a novel common-key cryptosystem where fake plaintexts which are also contextually acceptable are mixed into a cryptogram with the legal plaintext. If an eavesdropper applies a fake common-key to the decryption algorithm, it outputs the fake plaintexts which the eavesdroppers might believe legal. This paper also proposes concrete encryption/decryption algorithm which can be combined with any conventional common-key cryptosystem.

Keywords—*cryptography; common key cryptosystem; fake plaintexts; brute force attack*

I. INTRODUCTION

For support enough security in recent network environments, especially including wireless networks where wireless signals are easily overheard by any other wireless nodes including eavesdroppers, cryptography is widely applied. There are two classes of currently available cryptography; common-key and asymmetry-key cryptosystems. For eavesdroppers, wiretapping of cryptogram and estimation of the decryption key is essential for achieving the plaintext illegally since the encryption/decryption algorithms are usually public in these internetworking era. With help of cheaper high-performance computers, widely available encryption/decryption algorithms face the crisis of the brute force attack. Here, a contextually acceptable output of the decryption algorithm is believed to be the original plaintext. Hence, this paper proposes a novel common-key cryptosystem to solve the problem of the brute force attack by making possible for a decryption algorithm to output not only the legitimate plaintext but also fake plaintext to deceive the eavesdroppers.

II. RELATED WORKS

In cryptography for secure transmissions of valuable information called plaintexts from a source computer to a destination one, a source computer translates each plaintext into a cryptogram, the cryptogram is transmitted through networks and a destination computer extracts the plaintext from the cryptogram. Here, a pair of an encryption and a decryption algorithms for translation between a plaintext and a cryptogram provides enough security to make difficult for eavesdroppers to illegally achieve the plaintext from the wiretapped cryptogram.

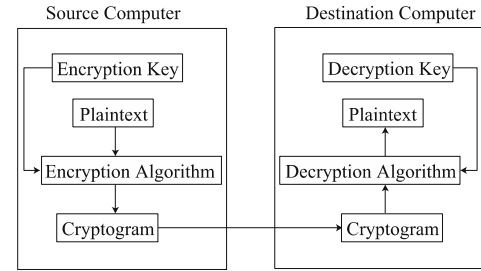


FIGURE I. CRYPTOGRAPHY WITH ENCRYPTION/DECRIPTION KEYS

The encryption and decryption algorithms are usually implemented as software products in currently available various computers connected to open networks such as the Internet. That is, not only the encryption algorithm for translation from a plaintext to a cryptogram but also the decryption algorithm for reverse translation from a cryptogram to a plaintext are public as open software for all possible users including the eavesdroppers. Hence, the provision of enough security currently depends on secret parameters for the algorithms, i.e., most of widely available encryption/decryption algorithms require encryption and decryption keys as their inputs (Figure 1).

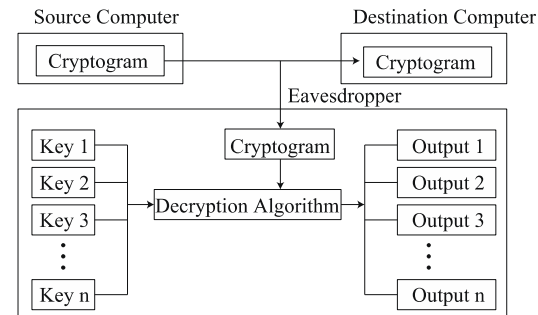


FIGURE II. BRUTE FORCE ATTACK

One of the methods for eavesdroppers to achieve a plaintext from a cryptogram is the brute-force attack. An eavesdropper tries to extract the plaintext by from the cryptogram by applying a decryption algorithm with all possible decryption key candidates (Figure 2). Theoretically, the eavesdropper should try too large number of candidate decryption keys to detect the legal decryption key and achieve the plaintext illegally. Thus, various methods for estimation of the legal decryption key have been developed. By gathering huge numbers of cryptograms transmitted through networks and analyzing them by using cheap but high-performance computers, decryption keys might

be estimated depending on some statistical deviation and the currently widely-available cryptosystems might fall into crisis in near future.

Now, consider a case that an eavesdropper tries to achieve the plaintext from a wiretapped cryptogram by the brute force attack. The eavesdropper applies the decryption algorithm to the cryptogram with candidate decryption keys one by one and regards the candidate as the legal decryption key if the output of the decryption algorithm {it seems contextually acceptable}. This criterion is usually too vague; however, it is inevitable since the eavesdropper has only the cryptogram and is impossible to refer the original plaintext. Hence, even if the eavesdropper achieves a contextually acceptable output from the decryption algorithm, it is not always the same as the legitimate plaintext. In addition, if the eavesdropper achieves multiple contextually acceptable output from the decryption algorithm by using different decryption key candidates, it is also impossible to surely select one of them as the legitimate plaintext as shown in Figure 3.

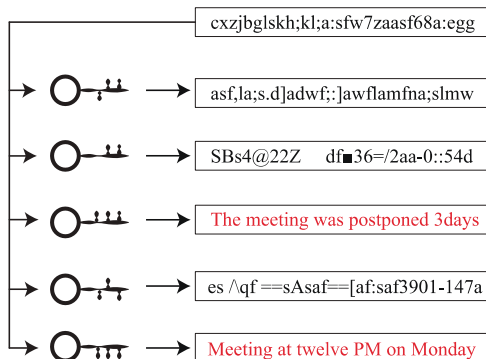


FIGURE III. MULTIPLE CONTEXTUALLY ACCEPTABLE OUTPUTS OF DECRYPTION ALGORITHM.

In [2], the one time pad whose decryption algorithm can generate multiple contextually acceptable outputs from a cryptogram has proposed. In its encryption algorithm, a cryptogram ET is generated by bit-by-bit exclusive-OR calculation between a plaintext PT and a same size common-key K . In its decryption algorithm, the plaintext PT is achieved by bit-by-bit exclusive-OR calculation between the cryptogram ET and K . Here, number of possible candidate's decryption keys is $2^{|K|}$ and all possible $|PT|$ bit-length outputs is generated by applying the decryption algorithm with all the possible decryption candidates. Hence, numerous numbers of contextually acceptable outputs are surely expected to be generated. For example, all the possible $|PT|$ bit-length text files are generated by the decryption algorithm and it is impossible for the eavesdroppers to determine which is the legitimate plaintext. However, since the outputs of the encryption algorithm take over the statistical deviation of the plaintexts, it may be possible to estimate the encryption key by analyzing numbers of outputs. In cryptography for secure transmissions of valuable information called plaintexts from a source computer to a destination one, a source computer translates each plaintext into a cryptogram, the cryptogram is transmitted through networks and a destination computer extracts the plaintext from the cryptogram. Here, a pair of an encryption and a decryption

algorithms for translation between a plaintext and a cryptogram provides enough security to make difficult for eavesdroppers to illegally achieve the plaintext from the wiretapped cryptogram. The encryption and decryption algorithms are usually implemented as software products in currently available various computers connected to open networks such as the Internet. That is, not only the encryption algorithm for translation from a plaintext to a cryptogram but also the decryption algorithm for reverse translation from a cryptogram to a plaintext are public as open software for all possible users including the eavesdroppers. Hence, the provision of enough security currently depends on secret parameters for the translation from a cryptogram to a plaintext are public as open software for all possible users including the eavesdroppers. Hence, the provision of enough security currently depends on secret parameters for the algorithms, i.e., most of widely available encryption/decryption algorithms require encryption and decryption keys as their inputs (Figure 1).

One of the methods for eavesdroppers to achieve a plaintext from a cryptogram is the brute-force attack. An eavesdropper tries to extract the plaintext by from the cryptogram by applying a decryption algorithm with all possible decryption key candidates (Figure 2). Theoretically, the eavesdropper should try too large number of candidate decryption keys to detect the legal decryption key and achieve the plaintext illegally. Thus, various methods for estimation of the legal decryption key have been developed. By gathering huge numbers of cryptograms transmitted through networks and analyzing them by using cheap but high-performance computers, decryption keys might be estimated depending on some statistical deviation and the currently widely-available cryptosystems might fall into crisis in near future.

III. PROPOSAL

This paper proposes a pair of algorithms for a common-key cryptosystem with mixture of a legitimate plaintext and a fake plaintext in order for more secure communication. In a source computer, an encryption algorithm translates a legitimate and a fake plaintext with a common-key shared with a destination computer into a cryptogram. On the other hand, in the destination computer, a decryption algorithm extracts the legitimate plaintext from the cryptogram by using the same common-key. The decryption algorithm also extracts the fake plaintext from the cryptogram by using a certain available key (Figure 4). Hereafter, we call it a fake common-key.

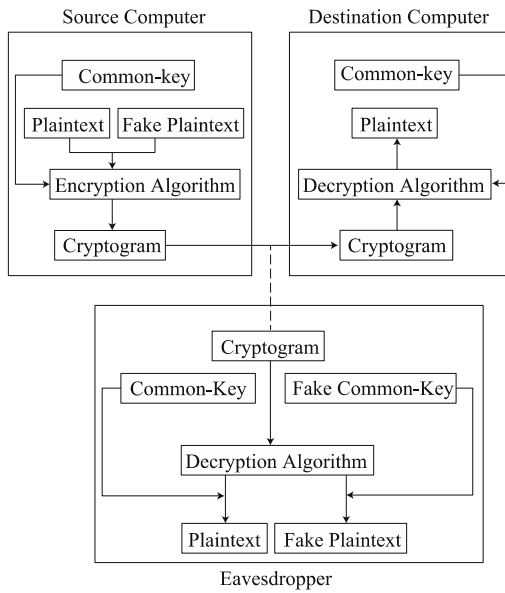


FIGURE IV. OUR PROPOSAL COMMON-KEY CRYPTOSYSTEM WITH MIXTURE OF FAKE PLAINTEXTS.

Same as most of widely available common-key and asymmetric-key cryptosystems, encryption and decryption algorithms are assumed to be open. Hence, an eavesdropper who tries to apply the decryption algorithm to the wiretapped cryptogram with the common-key by accident gets the legitimate plaintext. However, the eavesdropper gets the fake plaintext by applying the decryption algorithm to the cryptogram with the fake common-key. The eavesdropper may believe the achieved fake plaintext to be legitimate and terminate the trials decrypting the cryptogram without achieving the legitimate plaintext. Even though the eavesdropper continues the trials and achieves both the fake and the legitimate plaintexts, it is impossible for the eavesdropper to distinguish them. As a result, our proposal makes difficult for the eavesdropper to achieve the legitimate plaintext (Figure 5).

[Cryptosystem with Mixture of Fake Plaintexts]

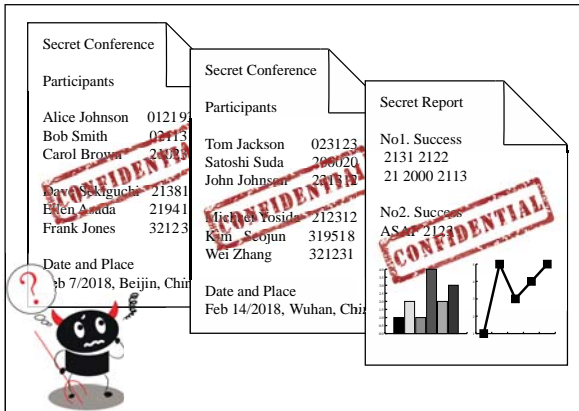


FIGURE V. EFFECTS OF MIXTURE OF FAKE PLAINTEXTS

Let PT , FPT , K_e and K_d be a legitimate plaintext, a fake plaintext, an encryption key and a decryption key. The following pair of an encryption E and a decryption D algorithms are called

algorithms for a cryptosystem with mixture of fake plaintext. Here, FK_e and FK_d are fake encryption and decryption keys, respectively.

$$D(ET, K_d) = PT \text{ and } D(ET, K_d) = FPT \text{ where } ET := E(PT, FPT, K_e)$$

Same as other widely available conventional common-key cryptosystems, it is assumed that a common-key $K := K_e = K_d$ is safely delivered in advance to both the source and the destination computers. Or, same as other widely available conventional asymmetric-key cryptosystems, it is assumed that a decryption-key K_d is strictly kept secret by the destination computer while an encryption-key K_e is publicly delivered possibly through networks. On the other hand, the fake encryption-key FK_e is implicitly generated in the encryption algorithm E . That is, FK_e is generated and used for encrypting the fake plaintext FPT in E ; however, an explicit output of E is only an encrypted-text (cryptogram) ET . FK_e is never used out of E and is never transmitted through any network. In addition, only the existence of FK_d is important for deceiving eavesdroppers by extraction of the fake plaintext FPT from ET in the decryption algorithm D . Since FK_d is expected to be applied by the eavesdroppers by accident, is never transmitted through any network either. Therefore, the fake common-key $FK := FK_e = FK_d$ in common-key cryptosystems and the fake encryption FK_e and decryption FK_d keys in asymmetric-key cryptosystems never become security flaws. As a concrete encryption and decryption algorithms for common-key cryptosystems with mixture of a fake plaintext, this paper proposes a method concatenating {it sub-cryptograms} which are outputs of a conventional encryption algorithm E with inputs PT and FPT . The concatenation order is determined only by the common-key K in order to conceal the concatenation order from eavesdroppers. At this time, since a fake common-key FK generated in the encryption algorithm E never contradicts the concatenation order, the fake plaintext FPT is surely extracted in the decryption algorithm D by using FK . The proposed encryption and decryption algorithms are as follows where E' and D' are an encryption and a decryption algorithms of any conventional common-key cryptosystem, respectively.

[Encryption Algorithm E] (Figures 6 and 7)

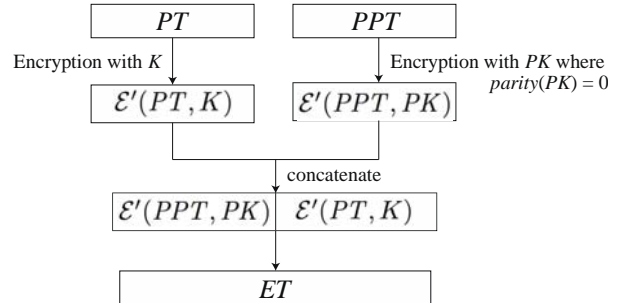


FIGURE VI. ENCRYPTION ALGORITHM (IN CASE OF $\text{parity}(K) = 0$).

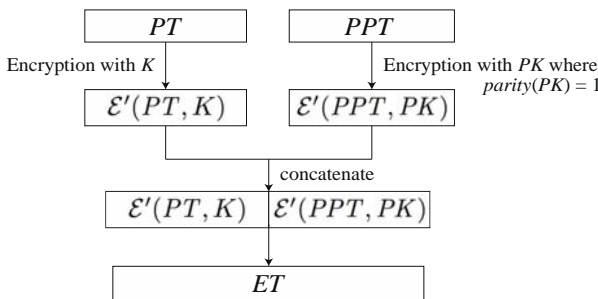


FIGURE VII. ENCRYPTION ALGORITHM (IN CASE OF $\text{parity}(K) = 1$)

- 1) A source computer C_s calculates a binary-parity $\text{parity}(K)$ of a common-key K .
- 2) C_s translates a legitimate plaintext PT to a sub-cryptogram $E'(PT, K)$ by applying E' with K .
- 3) C_s generates a fake common-key FK satisfying $\text{parity}(FK) = \text{parity}(K)$
- 4) C_s translates a fake plaintext FPT to another sub-cryptogram $E'(FPT, FK)$ by applying E' with FK .
- 5) C_s generates a encrypted-text (cryptogram) ET by concatenation of $E'(PT, K)$ and $E'(FPT, FK)$. The concatenation order is determined by $\text{parity}(K)$ as follows where $+$ is a concatenation operator:
 - a) $ET := E'(PT, K) + E'(FPT, FK)$ if $\text{parity}(K) = 0$.
 - b) $ET := E'(FPT, FK) + E'(PT, K)$ if $\text{parity}(K) = 1$.

[Decryption Algorithm D] (Figure 8)

- 1) A destination computer C_d calculates a binary-parity $\text{parity}(K)$ of a common-key K .
- 2) C_d divides ET into the same size $ET[0]$ and $ET[1]$.
- 3) C_d extracts the legitimate plaintext $D'(ET[\text{parity}(K)], K)$ from $ET[\text{parity}(K)]$ by applying D' with K .

[Property]

If the decryption algorithm D is applied to the encrypted-text ET with the fake common-key FK , the fake plaintext FPT is extracted instead of PT .

That is, $D'(ET[\text{parity}(FK)], FK) = FPT$ is satisfied.

Hence, an eavesdropper under a brute-force attack extracts the fake plaintext by accidentally using the fake common-key as discussed in this section.

IV. CONCLUDING REMARKS

This paper proposes a novel common-key cryptosystem with mixture of fake plaintexts. In order to support enough security even against the brute force attack, the proposed decryption algorithm generates not only the legitimate plaintext but also fake plaintexts which are contextually acceptable and the eavesdroppers cannot determine which output is legal. The proposed algorithm can combine with any conventional common-key cryptosystem providing enough statistical difficulty and computational complexity for common-key estimation.

In future work, we evaluate the proposed method by possibility of illegal achievement of legitimate plaintext in comparison with the conventional common-key cryptosystems.

REFERENCES

- [1] Daemen, J., Rijnmen, V., "The Rijndael Block Cipher," AES proposal, First AES Candidate Conference (AES1), (1998).
- [2] Shannon, C.E., "Communication Theory of Secrecy Systems," IEEE Press, p. 84--143 (1949).

Modeling Confrontations in Complex Networks Based on Game Theory

Yapeng Li¹ and Jun Wu^{1,*}

¹College of Systems Engineering, National University of Defense Technology,
Changsha, Hunan 410073, China

*Corresponding author

Abstract—To fully understand the structure robustness of complex networks where confrontations of attackers and defenders happen, we build a game model which is a zero-sum game in simultaneous form. We assume that the attack and defense are only against the top-n vital nodes and evaluate the payoffs using the full information of the network. A mapping process is introduced which maps the probabilities of pure strategies onto nodes. The experimental results in random scale-free networks reveals that the attacker pay more emphasis on attacking the nodes with relatively small degrees while the defender allocates more resource to nodes which play a more important role in maintaining the connectivity of the network.

Keywords—complex networks; game theory; nash equilibriums; scale-free networks

I. INTRODUCTION

Complex networks describe a myriad of systems in real-world, such as the Internet, electric power grids, urban road networks, the world trade web, among many others. In the last decades, a great deal of interest in studying complex networks has been stimulated since the discovery of small-world [1] and scale-free [2]. As we know, the structures of networked systems have a significant influence on their functions and behaviors, making the structural robustness, as one of the critical structural features, become a central topic in complex networks and receive growing attention. [3-5]

To enhance the structural robustness of a networked system, many studies have proposed a wide range of methods, i.e., designing robust networks [6, 7] and optimizing the existing networks [8-10]. Besides, many studies investigate the attack or defense strategies in existing networks. These researches measure the structural robustness of a network by some explicit measure functions and investigate how these measure functions will change when a set of nodes are removed. The original work is done by Albert et al, where they introduced two typical strategies, i.e., random failure and intentional attack, and suggested that scale-free networks are robust against random failure but very fragile against intentional attack. [11] This “robust yet fragile” feature of scale-free networks leads to a lot of interests in finding the optimal attack or defense strategies.[12,13] However, most of these studies have an implicit assumption that there exists only one decision maker, either the attacker or the defender, and this process is static. So, these problems are actually identifying vital nodes. [14] But in

many real-world scenarios, the activities of attack and defense probably occur simultaneously in many confrontations of networked systems such as transportation networks. The attacker or the defender can predict the other’s probable actions and make his/her best decisions. In this dynamic case where the attacker considers the probable defense strategy when plotting an attack, and vice versa, attacking or defending the vital nodes may no longer be the best choice for them.

To investigate the behaviors of attackers and defenders in confrontations of complex networks, we will build a game model in this paper, using the framework and methods of game theory which provides useful mathematical tools to model conflicts between intelligent decision-makers.

II. THE GAME MODEL

Firstly, we make some basic assumptions of the game. We only consider one attacker and one defender in our game model, which are the players. Besides, it’s assumed that both players can obtain the complete information of the network and they fully understand the other’s preference and possible strategies. So, they are perfectly informed of the opponent’s payoff for all possible strategy profiles. We also assume that this game is a simultaneous-move game, which means they don’t know each other’s decisions before they move.

III. BUDGET CONSTRAINTS AND STRATEGIES

We consider a complex network described by a simple undirected graph $G(V, E)$, where V is the set of nodes and $E \subseteq V \times V$ is the set of edges. Let $N = |V|$ be the number of nodes. Denote $A(G) = (a_{ij})_{N \times N}$ as the adjacency matrix of G , where $a_{ij} = a_{ji} = 1$ if nodes v_i and v_j are adjacent, and $a_{ij} = a_{ji} = 0$ otherwise. Let k_i be the degree of node v_i , which is the number of edges connected to it. In real-world networks, the costs of attacking different targets for the attacker as well as the defender are different. In this game, the attack and defense approaches are both against nodes and it’s assumed that the attached edges are removed if one node is removed. Thus, we assume that the cost c_i^A or c_i^D of node v_i is a function of its degree k_i with the following forms:

$$c_i^A = k_i^{\alpha_A}, \quad c_i^D = k_i^{\alpha_D} \quad (1)$$

In eq. 1, $\alpha_A \geq 0$ is called the attack-cost-sensitivity and $\alpha_D \geq 0$ is the defense-cost-sensitivity. A larger α_A means the attacker is more sensitive to the costs among different nodes. In the extreme case where $\alpha_A = 0$, the attack costs of all targets are equal. The parameter α_D has similar meaning for the defender. As we know, many real-world networks are heterogeneous, which means there are a few hub nodes which play a significant role in maintaining the connectivity of the network. These nodes are called vital nodes where both the attacker and the defender pay a lot of attention because the removal of these nodes can collapse the network. There are many methods to identify vital nodes in complex networks [14]. But in this paper, what we focus is not the methods about vital nodes identification but exploring what the attacker and the defender will do when they consider the opponent's probable action. So, we assume that both the attacker and the defender only consider the attack or defense toward top-n hub nodes with the largest degrees. In the extreme case that $n = N$, all the nodes are considered. Although only n hub targets are considered, the costs of different targets and the connectivity should be measured in the whole network. So, we sort the nodes in descending order of their degree and the budgets of the two players which are often limited are defined as

$$\hat{C}^A = \beta_A \sum_{i=1}^n c_i^A = \beta_A \sum_{i=1}^n k_i^{\alpha_A} \quad (2)$$

And

$$\hat{C}^D = \beta_D \sum_{i=1}^n c_i^D = \beta_D \sum_{i=1}^n k_i^{\alpha_D}, \quad (3)$$

Where $\beta_A \in [0,1]$ and $\beta_D \in [0,1]$ are the cost-constraint parameter of the attacker and the defender, respectively. Denote by $V^A \subseteq V$ the attack set. We define an attack strategy as $X = [x_1, x_2, \dots, x_n]$, where $x_i = 1$ if $v_i \in V^A$, otherwise $x_i = 0$. Let $C_X = \sum_{v_i \in V^A} c_i^A$ be the total cost of an attack strategy X . So,

$$C_X = \sum_{v_i \in V^A} c_i^A = \sum_{i=1}^n x_i c_i^A = \sum_{i=1}^n x_i k_i^{\alpha_A} \quad (4)$$

To satisfy the budget constraint of the attacker, we have

$$C_X = \sum_{i=1}^n x_i k_i^{\alpha_A} \leq \hat{C}^A = \beta_A \sum_{i=1}^N k_i^{\alpha_A}. \quad (5)$$

Any solution X that satisfies Eq. 5 is a feasible attack strategy. But it is easy to know that the attacker will get higher payoff when he/she attacks more nodes. So, we only consider the attack strategies where the addition of any nodes into the attack set violates the budget constraint. Similarly, defense set V^D , defense budget \hat{C}^D and defense strategy $Y = [y_1, y_2, \dots, y_n]$ are defined in the same way. We now use a simple example to illustrate the attack and defense strategies of the game model. If $n = 4$, $\alpha_A = \alpha_D = 0$ and $\beta_A = \beta_D = 0.5$, which means the costs of each target are equal for both players, there are 6 attack strategies totally which are $x_1 = \{v_1, v_2\}$, $x_2 = \{v_1, v_3\}$, $x_3 = \{v_1, v_4\}$, $x_4 = \{v_2, v_3\}$, $x_5 = \{v_2, v_4\}$, $x_6 = \{v_3, v_4\}$ and the defense strategies are the same.

IV. DEFINITION OF PAYOFFS

In the confrontations of the attacker and the defender, we assume that the attacker successfully attacks a node v_i if it is attacked but not defended, namely, $x_i = 1$ and $y_i = 0$. Denote by Γ the measure function of network performance which decreases monotonically when a set of nodes are removed. The common measure functions include the size of largest connected component, the efficiency and so on. Denote by \hat{G} the network when a set of nodes are removed from the initial network G , the payoff functions of the attacker are defined as

$$U^A(X, Y) = \frac{\Gamma(G) - \Gamma(\hat{G})}{\Gamma(G)} \in [0, 1], \quad (6)$$

And the payoff of the defender is

$$U^D(X, Y) = \frac{\Gamma(\hat{G}) - \Gamma(G)}{\Gamma(G)} \in [-1, 0]. \quad (7)$$

		defender			
		Y_1	Y_2	...	Y_t
attacker	X_1	$u_{11}, -u_{11}$	$u_{12}, -u_{12}$...	$u_{1t}, -u_{1t}$
	X_2	$u_{21}, -u_{21}$	$u_{22}, -u_{22}$...	$u_{2t}, -u_{2t}$
	\vdots	\vdots	\vdots	...	\vdots
	X_s	$u_{s1}, -u_{s1}$	$u_{s2}, -u_{s2}$...	$u_{st}, -u_{st}$

FIGURE I. PAYOFF MATRIX OF THE ATTACKER-DEFENDER GAME IN ALL STRATEGY PROFILES WHERE THE ATTACKER HAS s POSSIBLE ATTACK STRATEGIES TOTALLY AND THE DEFENDER HAS t DEFENSE STRATEGIES IN ALL

Noting that $U^A(X, Y) + U^D(X, Y) = 0$, our game is a zero-sum game. The payoff matrix under all strategy profiles is showed in Fig. 1 where the row player is the attacker and the column is the defender. Nash equilibrium is calculated using the following linear programming.

$$\begin{aligned} & \min z \\ \text{s.t. } & \sum_{j \in S_D} u_{ij} \cdot y_j \leq z \quad \forall i \in S_A \\ & \sum_{j \in S_D} y_j = 1 \\ & y_j \geq 0 \quad \forall j \in S_D \\ & S_D = \{Y_1, Y_2, \dots, Y_t\} \end{aligned} \quad (8)$$

$$\begin{aligned} & \max z \\ \text{s.t. } & \sum_{i \in S_A} u_{ij} \cdot x_i \geq z \quad \forall j \in S_D \\ & \sum_{i \in S_A} x_i = 1 \\ & x_i \geq 0 \quad \forall i \in S_A \\ & S_A = \{X_1, X_2, \dots, X_s\} \end{aligned} \quad (9)$$

Nash equilibrium (x^*, y^*) is obtained and the equilibrium payoff of the attacker is $z = x^{*T} \cdot U \cdot y^*$.

Denote the probabilities of each pure attack strategy in Nash equilibrium by $P_S^A = [p_1^A, p_2^A, \dots, p_s^A]$ and that of each pure defense strategy by $P_S^D = [p_1^D, p_2^D, \dots, p_t^D]$. Then, we use a mapping mechanism to distribute the probabilities toward each node, which shows the probabilities of attacking or defending each node. The probabilities toward each node is obtained by

$$P_N^A = \sum_{i=1}^s p_i^A \cdot X_i, P_N^D = \sum_{i=1}^t p_i^D \cdot Y_i. \quad (10)$$

According to this probability distributions, the attacker and defender can determine the proportion of their resource toward the top-n nodes. For example, if $X_1 = [1 1 0]$, $X_2 = [1 0 1]$, $X_3 = [0 1 1]$, $P_S^A = [0.5, 0.3, 0.2]$, $P_S^D = [0.2, 0.3, 0.5]$, so, $P_N^A = [0.8, 0.7, 0.5]$ and $P_N^D = [0.5, 0.7, 0.8]$.

V. EXPERIMENTAL RESULTS

Because of the ubiquity of scale-free networks in most natural and man-made systems, we execute the experiments in random scale-free networks whose degree distributions follow $P(k) : k^{-\lambda}$. In this paper, we use the efficiency as measure function Γ and set that $\alpha_A = \alpha_D \equiv 0$ and $\beta_A = \beta_D \equiv \beta$. In this case, the size of the attack set V^A and V^D are both equal to $n \cdot \beta$. For the convenience of calculation and analysis, we set $n = 10$. We use the configuration model[15] to get the random scale-free network and the computations of Nash equilibriums are done in MATLAB R2015b using CPLEX 12.5.

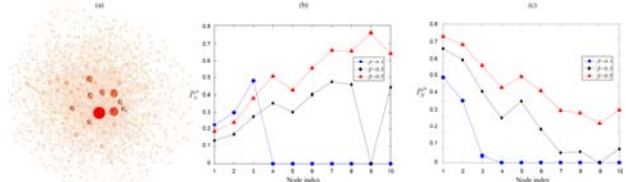


FIGURE II. TOPOLOGY STRUCTURE OF A RANDOM SCALE-FREE NETWORK (A) AND THE PROBABILITIES TOWARD EACH NODE IN EQUILIBRIUMS FOR THE ATTACKER (B) AND THE DEFENDER (C). THE DEGREE DISTRIBUTION FOLLOWS $p(k) = (\lambda - 1)m^{\lambda-1}k^{-\lambda}$, WHERE $N = 1000$, $\lambda = 3$ AND $m = 2$. THE NODE INDEX OF (B) AND (C) ARE IN THE DESCENDING ORDER OF THEIR DEGREES AND THESE 10 NODES ARE SHOWED IN (A)

We play the game in a random scale-free network and map the mixed strategy of pure strategies onto the nodes. The results are showed in Fig. 2 which shows the topology structure of the network and probabilities toward each node of the attacker and defender. It's easy to see that both the attacker and the defender allocate all probabilities onto only 3 nodes with the largest degree when $\beta = 0.1$. When β is larger, the probabilities are mixed in all the top-10 nodes. Moreover, the attacker pays more attention to the nodes with relatively small degrees while the defender allocates larger probabilities onto the nodes with largest degrees regardless of β . This result means that the attacker is less concentrated on attacking the most important nodes with largest degrees while the defender allocates more resource to these nodes. It can be understood by the interactive

process of the two players, where the defender can't afford the loss of abandoning the vital nodes and thus the attacker attacks the nodes with relatively lower importance to dodge the defense. We also do the experiments in other scale-free networks with different degree exponent and average degree and get similar results.

VI. SUMMARY

The study of structural robustness of complex networks is a hot topic in the past decades. However, most researches neglect the confrontations in complex networks where the attacker and defender exist simultaneously. To model this situation and explore the behaviors of them in equilibriums, we first proposed a two-player game model and define the strategies and payoffs. Because the attacker and defender in real-world always focus vital nodes, we assumed that the attack and defense are only against the top-n vital nodes while the payoffs are evaluated through the whole network. We then introduced the mapping mechanism which mapped the mixed strategy of pure strategies onto the nodes. The experimental results in random scale-free networks revealed that the attacker was less concentrated on attacking the most important nodes with the largest degrees while the defender allocated more resource to these nodes.

ACKNOWLEDGEMENT

This research was financially supported by the National Science Foundation of China under Grant No. 71371185 and the Program for New Century Excellent Talents in University under Grant No. NCET-12-0141.

REFERENCES

- [1] Watts D J, Strogatz S H. Collective dynamics of 'small-world' networks, *Nature*, 393(1998): 440.
- [2] Barabási A, Albert R. Emergence of Scaling in Random Networks, *Science*, 286(1999): 509.
- [3] Jun Wu, S-Y T, Zhong Liu, Yue-Jin Tan, Xin Lu. Enhancing structural robustness of scale-free networks by information disturbance, *Sci. Rep.*, 7(2017).
- [4] Carlson J, Doyle J. Complexity and robustness, *Proc. Natl. Acad. Sci. USA*, 99(2002): 2538-45.
- [5] Gao J, Barzel B, Barabási A L. Universal resilience patterns in complex networks, *Nature*, 530(2016): 307-12.
- [6] Valente A X C N, Sarkar A, Stone H A. Two-peak and three-peak optimal complex networks, *Phys. Rev. Lett.* 92(2004): 118702.
- [7] Peng G-S, Tan S-Y, Wu J, et al. Trade-offs between robustness and small-world effect in complex networks, *Sci. Rep.*, 6(2016)
- [8] Hayashi Y, Matsukubo J. Improvement of the robustness on geographical networks by adding shortcuts, *Physica A*, 380(2007): 552-62.
- [9] Li Y, Wu J, Zou A Q. Effect of Eliminating Edges on Robustness of Scale-Free Networks under Intentional Attack, *Chin. Phys. Lett.*, 27(2010): 068901.
- [10] Ash J, Newth D. Optimizing complex networks for resilience against cascading failure, *Physica A*, 380(2007)673-83.
- [11] Albert R, Jeong H, Barabási A L. Error and attack tolerance of complex networks, *Nature*, 406(2000): 378-82.
- [12] Deng Y, Wu J, Tan Y J. Optimal attack strategy of complex networks based on tabu search, *Physica A*, 442(2016): 74-81.
- [13] Tan S Y, Wu J, Lü L, et al. Efficient network disintegration under incomplete information: the comic effect of link prediction, *Sci. Rep.*, 6(2016)22916
- [14] Lü L Y, Chen D, Ren X-L, et al. Vital nodes identification in complex networks, *Phys. Rep.*, 650(2016)1-63.
- [15] Newman M E J. The structure and function of complex networks, *SIAM Rev.*, 45(2003): 167-256.

Complex Project Schedule Risk Simulation Based on Multi-agent

Haolin Wen, Tao Hu¹ and Gongda Yan

Department of management engineering and equipment economic of the Naval Engineering University, China

Abstract—In order to solve the problems of complex projects schedule risk assessment, a project schedule risk assessment model based on the multi-agent was established by the Anylogic software in this paper. In this model, a “process” agent, a “process flow”, a “risk factor” and a “control” agent were designed by taking into account the process state, transformation conditions and the internal processing behavior of the state. Multiple nested relations between the process flow and the process were formed, which was caused by the risk factors. The model presented in this paper can analyze the equipment risk and order the importance of risk control, the experiment result shows that the model for complex projects schedule risk assessment has a certain reference value.

Keywords—*multi-agent; complex project; schedule risk; risk assessment*

I. INTRODUCTION

The characteristics of complex project include a wide range, many contents, long period and strong correlation of processes. In the process of implementation, the risk factors of technology, resources and environment are of high uncertainty and the project schedule is difficult to control. Therefore, identifying and assessing the risk factors affecting the progress are crucial for the successful management of the project [1]. The existing evaluation methods are network planning technology [2], discrete event system simulation [3], system dynamics model [4] and so on. But network planning plans and discrete events can not achieve good assessment results. In this paper, we use the message components and state transition components of multi-agent to model complex projects, and divide the process, process flow and risk factor into different object types so that the complex problems are classified as a single object, so that each object achieve good independence and autonomy, and better solve the complexity of process logic in the rework path, and verify the applicability and practicability of the model by simulating specific problems.

II. MODELING ANALYSIS

Multi-agent system is a collection of multiple agents, which is autonomous, distributed and coordinated, and has self-organizing ability, learning ability and reasoning ability [5]. The goal of using multi-agent modeling techniques is to build large, complex systems into small, easily managed systems that communicate and coordinate with each other, and therefore it has great robustness and reliability to use this method to solve complex project risk assessments, and has higher problem solving efficiency [6]. Each agent in the model is independent and autonomous, modular, scalable and flexible in design. It overcomes the difficulty of management and expansion caused

by building a huge system. It can effectively reduce the total system cost and complexity, it also reduces the complexity of solving each agent problem and effectively improves the ability of solving problems [7].

The research establishes three named types of agents by dividing the objects in the schedule risk assessment of construction projects into processes, risk factors and process flows, and establish "control" to control the simulation and record the simulation data.

(1) "Process" Agent: each process is considered as the same type of object independently. The "Process" agent only needs to consider the relevant parameters of process status and the existing risk factors.

(2) "Risk factor" agents: take the risk factors as a kind of object, and the occurrence of the risk leads to the rework, so the risk is in one-to-one correspondence with the "process flow" of the rework.

(3) "Process Flow" Agent: the process sequence is regarded as a kind of object, among which "Process Flow" can be divided into main "process flow" and rework "process flow". The main "process flow" is controlled by the "control" agent, and the rework "process flow" is guided by the "risk factor" agent.

(4) "Control" Agent: control the progress of simulation experiment and coordinate other agent.

Among them, the relationship between agents as shown in Figure 1.

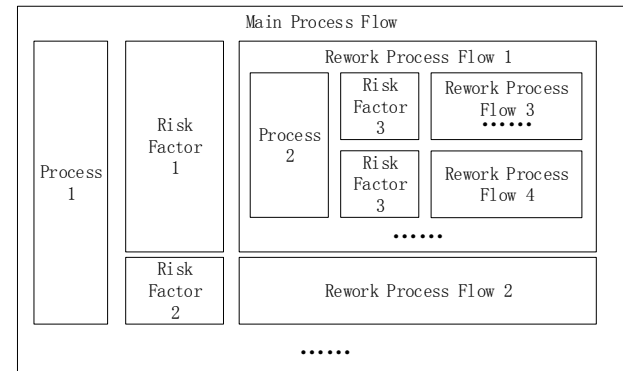


FIGURE I. AGENT RELATIONSHIP BETWEEN THE OBJECT DIAGRAM

The main "process flow" includes several "processes" that constitute the construction sequence under the sequential process. There are several different "risk factors" corresponding

to the "process", and the "risk factors" trigger different rework "process flows", rework "process flow" contains a number of different "processes". If the "process" in the main "process flow" is the same as the "process" in the rework "process flow", then the structure of the rework cycle is formed. The nested relational model can better reflect the rework of the project in the actual situation.

III. MODELING BASED ON MULTI-AGENT

According to the requirements of process modeling and simulation, "Process" agent, "Process Flow" agent, "Risk factor" agent and "Control" agent are established. The specific modeling elements are as follows:

A. Process

Process is the main part of the project. The following describes the logical behavior of "process" agents from the three aspects: status, branches, and transitions.

1. According to the four states of the process, set the status as follows: "waiting", "proceeding", "rework" and "fulfillment".

2. There is a branch in the "process" agent, used to determine whether the risk is generated.

① Branch: Used to judge whether the defect occurs or not, provided that the risk occurrence rate of each "risk factor" agent existing in the process is compared with the random generation factor to generate an array structure and sequentially trigger the corresponding rework "process flow" and transfer to the "rework flow" state. If the risk factor in the process is not triggered, then transferred to the "fulfilment" state.

3. According to the transfer process conditions and simulation requirements, designing a process state diagram shown in Figure 2.

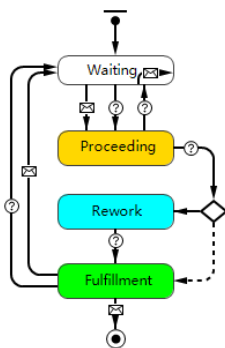


FIGURE II. PROCESS STATE DIAGRAM

The following figure shows the role of the changes.

(1) Reset the completion status of the process in the database when the "process" agent is generated.

Execute Statement ("UPDATE completion status table SET completion status = 0 WHERE name = " + get Name () + "");

(2) Message transition from the "waiting" state to the "proceeding" state is the start of this process instruction issued by the "control" or "process flow" agent.

(3) Conditions transition from "waiting" to "proceeding", with the condition that the number of pre-processes equals the pre-process completion and the status is adjusted when all the pre-processes are "completed".

(4) Condition transition from "proceeding" to "waiting", with the condition that the number of pre-process is not equal to the completion of pre-process. The change does not exist in practice. However, considering that the transmission of messages between agents is asynchronous, the order of transmission is not controlled by programming, it may happen that some agents are triggered by the pre-process conditions, while the multi-process rework instruction has been "proceeding" state, then the pre-process of the agent has not been completed. So we need to add further changes from the "proceeding" state to the "waiting" state.

(5) Condition transition from "proceeding" to branch ①, with the condition that the remaining construction period is less than or equal to 0, and the condition of less than 0 is to solve the problem of simulation accuracy defects. When calculating the remaining period, it has become a number less than zero. Transferred to the judgment of the occurrence of the risk after the procedure is finished.

(6) Condition transition from "proceeding" to "rework" state, provided that the risk in the risk factor does occur.

(7) Conditions transition from branch ① to the "fulfillment" state are as follows: the probability of the random generation factor being greater than the risk factor.

(8) Conditions transition from "rework" state to "fulfilment" state, conditions for the process corresponding to the risk factor "process flow" all completed.

(9) Message transition from "fulfillment" to "waiting", which is a "reset" command sent to other agents to receive commands issued by "control" agents or other agents and then transferred to initial state.

(10) Conditions transition from "fulfillment" to "waiting", provided that the number of pre-process is not equal to the pre-process completion. Through this transition, we can form a state transition chain structure, and finally enable the multi-process rework in the main simulation environment to form a sequential rework loop from the rework point.

(11) Message transition from "Fulfillment" state to "Final" state, the message is received "simulation end" command, then the agent's operation is forced to end.

B. Process Flow

Process flow is the environment of process operation. The "process" in the same "process flow" can interact with each other through the message components. Therefore, the main function of the "process flow" is to isolate the influence of "process" messages in different "process flows". The parameters include the process start sequence number, process termination sequence number and the "process" agent connection structure. "Process Flow" state transition diagram shown in Figure 3:

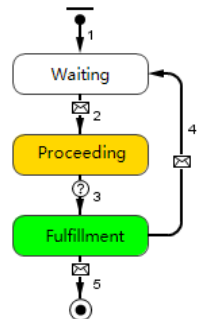


FIGURE III. PROCESS FLOW" AGENT STATE DIAGRAM

The effect of the transitions indicated by the numbers in Figure 3 are as follows:

- (1) Create a "process flow" agent.
- (2) When receiving the process flow start instruction issued by a "risk factor" agent, the "process flow" transitions from the "waiting" state to the "proceeding" state and the "starting" instruction is sent to the internal initial "process", then it started working.
- (3) When the "process" in the "process flow" is completed, the completion status of the final process is triggered. When the conditions are satisfied, the "process flow" is switched from the "proceeding" status to the "fulfillment" status.
- (4) When the "process flow" receives the "reset" command, it will be transferred from the "fulfillment" status to the "waiting" status.
- (5) "Process Flow" becomes the final state when "Simulation Fulfill" command is received.

C. Risk Factor

The risk factor of each process has different numbers and different types, each of the risk factors as a "risk factor" agent. The "risk factor" agent connects "process" and "process flow" as a parameter object throughout the simulation. Its parameters should include the corresponding rework "process flow" serial number and risk distribution.

Therefore, the "risk factor" agent parameters include:

- (1) The risk occurrence rate: the type is "double".
- (2) Rework process flow: the type is "Process Flow".

D. Control

The role of the "control" in this simulation is to control the main process flow, the number of simulations, recording the simulation results and send "reset" instructions to coordinate the

operation of the process agent. The state diagram of the "control" agent is shown in Figure 4:

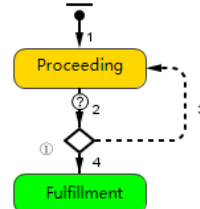


FIGURE IV. CONTROL" STATE DIAGRAM

The effects of transitions in the diagram are illustrated as follows:

- (1) Empty the database time table:

Execute Statement ("TRUNCATE TABLE time table");

- (2) Condition transition from "Proceeding" state to branch ①. The condition is whether the final procedure completion state is completed or not.

- (3) Condition transition from branch ① to "Fulfillment" state. The conditions for the current number of simulations and the total number of simulations equal.

- (4) Default transition from branch ① to "Proceeding" state.

IV. CASE SIMULATION AND RESULTS ANALYSIS

At present, there is a common phenomenon of budget overruns and a delay in progress in warship maintenance projects, resulting in warships failing to complete training tasks expectedly and equipment funding has not been used reasonably and effectively [8]. Therefore, this paper selected a type of marine diesel engine minor repair projects for the case of simulation and analysis, with the key consideration of duration, through the gap between the actual average total duration and the average duration after control to reflect the influence level of complex project risk factors, and then analyze the major risk factors that have an important impact on the duration of maintenance and need to take priority measures to control, so as to provide a reliable basis for the schedule risk management of complex projects.

Combined with the characteristics of diesel engine maintenance and learn from relevant experts' experience in the field to take the initial parameters of each process shown in Table 1.

TABLE I. INITIAL PARAMETERS OF DIESEL ENGINE MAINTENANCE PROCESS

ID	R_{init}	ID_{pre}	Risk	$Flow_{re}$	P_{re}	ID	R_{init}	ID_{pre}	Risk	$Flow_i$	P_{re}
S1	8		0.02	S1	6	S14	5	S12	0.01	S14	1
S2	9	S1	0.03	S2	7	S15	6	S12	0.02	S15	3
S3	10	S2	0.02	S3	9	S16	6	S12	0.01	S16	1
S4	5	S2	0.03	S4	3	S17	7	S5;S9;S10	0.03	S17	3
S5	6	S2	0.03	S5	3	S18	8	S13;S14;S15;S16;	0.02	S18	5
S6	12	S3	0.05	S6	10	S19	7	S18	0.04	S19	5
S7	11	S3	0.01	S2;S3;S7;		S20	8	S18	0.02	S20	4
S8	10	S3	0.01	S8	8	S21	4	S11;S17;S19;S20;	0.001	S21	1
S9	15	S3	0.02	S9	5	S22	4	S21	0.01	S22	3
S10	10	S4	0.02	S10	6	S23	3	S21	0.01	S23	2
S11	3	S1	0.01	S11	1	S24	5	S21	0.01	S24	2
S12	3	S6;S7;S8;	0.01	S12	1	S25	0	S22;S23;S24;	0	S25	0
S13	7	S12	0.02	S13	3						

Take the parameters of each process as shown in Table 1 to establish “process”, “risk factor”, “rework process flow” agent, set the initial process and process parameters in the main process flow interface, and output the process status diagram, the process remaining time line chart, the average duration line chart and the average time, simulation interface shown in Figure 5.

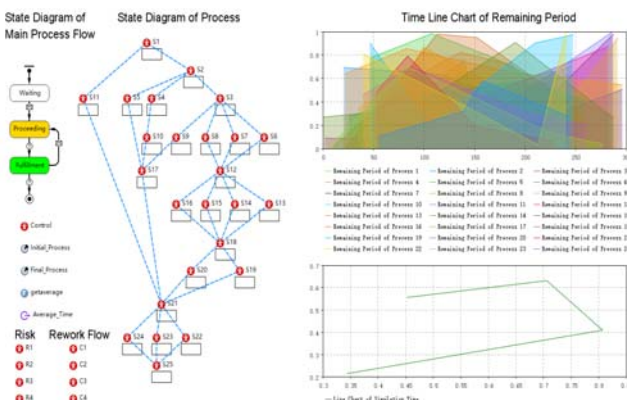


FIGURE V. MAIN PROCESS FLOW INTERFACE DIAGRAM

According to the characteristics of the maintenance process of the diesel engine, the process parameters in Table 1 are obtained, a diesel engine schedule risk assessment model based on multi-agent is established and simulated 100000 times to get the average total duration under risk control, which is 75.565d. Then, the average total duration is obtained by adjusting the defect rate of a single process, and the average total duration is compared with the average total duration without controlling the risk to obtain the variation of the total duration, and then the degree of influence of each process defect rate on the total maintenance schedule is analyzed. Finally, the order of importance of maintenance processes that require prioritized control is obtained. Suppose the cost of reducing the same rate

of each process of diesel engine maintenance’ defect rate is the same, thus the average duration of the simulation is shown in Table 2 by artificially adjusting the defect rate of each process to reduce by 30%.

TABLE II. DURATION CHANGES UNDER THE DEFECT CONTROL

ID	$R_{control}$	P_{aver}	P_{change}	ID	$R_{control}$	P_{aver}	P_{change}
S1	0.014	75.492	0.073	S13	0.014	75.495	0.07
S2	0.021	75.502	0.063	S14	0.007	75.558	0.007
S3	0.014	75.361	0.204	S15	0.014	75.541	0.024
S4	0.021	75.539	0.026	S16	0.007	75.539	0.026
S5	0.021	75.554	0.011	S17	0.021	75.545	0.02
S6	0.035	75.329	0.236	S18	0.014	75.463	0.102
S7	0.007	75.531	0.034	S19	0.028	75.486	0.079
S8	0.007	75.484	0.081	S20	0.014	75.349	0.216
S9	0.014	75.565	0	S21	0.0007	75.477	0.088
S10	0.014	75.517	0.048	S22	0.007	75.471	0.094
S11	0.007	75.545	0.02	S23	0.007	75.538	0.027
S12	0.007	75.441	0.124	S24	0.007	75.471	0.094

According to the above simulation results, it can be concluded that the change of total duration caused by the detect rate reduction of process S6 is the highest, followed by the process S20, process S3, process S12 and process S18, indicating that the adjustment of defect rate of process S6 has the greatest impact on the total duration of the diesel engine maintenance. Therefore, it is more effective to control the defect rate of process S6, S20, S3, S12 and S18 for the average duration of the project, it is feasible to adopt certain control measures to control these processes in priority. In addition, the rework period of each process can be adjusted, and the average timetable under the control of rework period of different processes can be obtained.

V. CONCLUSION

The schedule risk assessment is directly related to the execution efficiency and quality of complex projects. Based on the analysis of the logic conditions of warship diesel engine

maintenance process status transition, a method for assessing the schedule risk of complex projects based on multi-agent is proposed. By using this method, we have got the influence of the parameters of each process on the complex project duration, and have completed the schedule risk importance analysis of a type of warship diesel engine maintenance project, which is general network plan can not reach. What's more, the model has some expansibility, it can introduce the hybrid modeling method based on system dynamics, and consider the resource, cost and other factors to make the simulation more practical. In addition, it is more vaguer to consider the defect rate response to the risk and can be studied in a "proceeding" state considering a certain distribution of defect occurrence rules.

REFERENCES

- [1] Muhammed Mufazzal Hossen, Sunkoo Kang, Jonghyun Kim. Construction schedule delay risk assessment by using combined ahp-rii methodology for an international npp project. Nuclear engineering and technology, 47(2015):362-379.
- [2] GUO Qi, HE Jin-jing, HU Miao. Project network planning schedule risk analysis based on monte-carlo simulation. J. Project Management Technology, 2013, 11(11):66-70.
- [3] MAN Qing-peng. Research on modeling and controller method of schedule planning in building construction. D. Harbin Engineering University, 2008.
- [4] LI Cun-bing, LU Gong-shu, LI Peng, LI Shang. System dynamics model for grid construction project schedule risk management. J. East China Electric Power, 2012, 40(02):178-182.
- [5] B C Draa, B M oulin. Trends in distributed artificial intelligence [J]. Artificial Intelligence, 1992, 56(6):3566.
- [6] LIU Jin-kun, ER Lian-jie. Overview of application of multi-agent technology. J. Control and Decision, 2001(02):133-140+180.
- [7] Singh M P. Multi-Agent System: A Theoretical Framework for Intentions, Know-how, and Communications. Berlin: Springer-Verlag KG, 1994.
- [8] LIU Zhi-qiang. The research of schedule control on the project of ZB vessels middle lever maintenance. D. South China University of Technology, 2011.

Research on Risk of Online Supply Chain Finance

Daozhi Zhao¹, Di Wang¹ and Baosen Wang^{2,*}

¹College of Management and Economics TianJin University, Tianjin China

²School of Economic of Beijing Wuzi University, Beijing China

*Corresponding author

Abstract—In recent years, with the deeply combine of "Internet + finance", traditional supply chain finance has also accelerated the pace of online operation, and its risks have gradually been exposed. Therefore, it is necessary to study the risk of the online supply chain finance in order to clarify its characteristics, classification, identification and evaluation and make it better serve the end-customers of the online supply chain finance.

Keywords—online supply chain finance; credit risk; operational risk; market risk

I. INTRODUCTION

A. The Definition of Online Supply Chain Finance

Online supply chain finance (OSCF) is an entity based on supply chain finance. It forms a new form of supply chain finance through Internet and informationization, and becomes a complex financial innovation product. The nature of Internet supply chain finance is to regard the core enterprises in the supply chain and their upstream and downstream SMEs as a entity, the industrial chain as the base, focusing on the transaction, the funds allocate as the line, ensuring the risk management, Win-win cooperation as the goal, with the help of internet technology comprehensively develop the financial services throughout the entire financial supply chain[16].

online supply chain finance include the e-commerce transactions, online payment, online financing and logistics management. Financing platform is the core of the online supply chain finance, it can link with e-commerce platform, logistics platform, and payment platform. Linking with e-commerce platform realize the online business and transactions between the enterprises[20]. Linking with logistics management platform achieve the goal of online goods management of enterprise. In addition, linking with payment platform realize the real-time monitoring of bank funds. Therefore, the online supply chain finance has realized the connection between the supply chain enterprises and the financial entities, and the data real-time sharing of enterprises' business activities. As a result, banks can provide supply chain enterprises with great online financial services, and the resources will be optimally allocated[17].

The advantages of online supply chain finance lie in the unification of logistics, business flow, capital flow and information flow, and named "four flows convergence"[24]. Making the core enterprises with upstream and downstream enterprises in the supply chain as an entity, and provide the financial service and financing project, so as to transform the uncontrollable risks of a single enterprise into the risks that can be controlled by the whole supply chain. Moreover, with the real

trade background, supply chain finance reduces the demand for commercial banks as a credit intermediary.

B. Sources and Categories of Risk in Online Supply Chain Finance

The risk comes from the uncertainty, and there are many factors that lead to the uncertainty of supply chain financial eco-mode, mainly from the uncertainty of financial eco-environment. External uncertainties in the financial eco-environment include policy uncertainty, economic uncertainty, natural uncertainty and social uncertainty[27]. The uncertainty of the internal environment of the financial environment mainly refers to the immaturity of the Internet technology and the uncertainty of the real data[18].

In addition, the supply chain financial eco-mode has two attributes of industry and finance, so it also has the dual risks from the industrial chain and the financial sector. Due to the large number of participants in the supply chain finance with the long industrial chain, the vertical segmented industrial chains have different attributes and characteristics, the operational procedures are also complicated, and the various factors in the supply chain financial ecology are interdependent and interlocking. Any part of the problem will endanger the normal operation of the entire supply chain[26].

This article roughly divid the online supply chain financial risks into: credit risk, operational risk and market risk.

II. CREDIT RISK

A. The Definition of Credit Risk

Credit risk as the most traditional bank risk is born at the same time with its loan business. Customer loans are the source of the most fundamental credit risk for all banks. Credit risk, also known as the borrower's default risk, mainly refers to the risk that the borrower's debt or bank loans may not be able to repay to the bank and cause some losses due to various reasons. When a default occurs, creditors or banks will certainly bear some financial losses because they have not obtained the expected benefits.

In order to solve the major problem of SME financing more effectively, banks are facing the credit risk existing in the new business model through the online supply chain finance . The credit risk of online supply chain financing model, as the name implies, is the credit risk arising from issuing loans under the mode of online supply chain finance. It is a special case of credit risk.

B. The Characteristics of Credit Risk

Several basic characteristics of credit risk are summarized as follows[1]:

- Endogenesis of credit risk. Endogenesis is the most characteristic of credit risk. Endogeneity is the debt default or not directly related with the lender itself. Therefore, the lender's creditworthiness and repayment willingness and ability to the bank must be accurately tracked from time to time and understand the detail[21]. Bank tracking SME credit status changes are mainly through: First, access to financial information of SMEs, such as financial reports; the second is to use the bank establish the credit rating system. However, both channels for information need banks to spend a certain amount of manpower material and financial resources and lack of timeliness reliability and effectiveness. Due to the small size of SMEs[19], not listed and other characteristics of their own limitations, we can not though the authoritative credit rating agencies to obtain effective credit information; we also can not use the secondary market price information to understand the financial status and default possibility of enterprises. If only a little of information obtained through the above two methods, we will not find potential SME clients[25]. The construct of online supply chain financing platform has made the bank access the credit information more easily. The provision of credit information of e-commerce by third-party B2B e-commerce enterprises can more fully capture the credit information of SMEs. Establish a credit risk assessment system that is more suitable for this new type of business.
- Asymmetry of risk and return. In the past, scholars assumed that the market risk showed a normal distribution. This is because it is almost impossible for the market price to stay away from the expected value, probably on the opposite side of the expected value. However, in reality, the market risk not obey the standard normal distribution, and it is likely to be the form of spikes and thick tails. Therefore, the basic characteristics of credit risk in the market can not be fully reflected in this assumption. The distribution of credit risk is biased. Because they are inherently asymmetric: a small probability of a small gain for a bank, and a small probability of a greater loss for a loan business.
- Obvious non-systematic features. Not only systemic risks such as economic crisis but also macroeconomic cycle affect credit risk, under normal circumstances, some non-systematic micro-factors such as the financial status of the lender, operating ability, repayment ability and repayment willingness will affect the credit risk extently. However, when banks in the business practice, the credibility of old customers more easily obtain bank loans, and SMEs are indeed impossible to obtain financing through bank loans.
- Credit risk data is difficult to obtain. In the assessment of credit risk, the more difficult part is the objective evaluation of credit risk. The main reason is that banks'

lones do not have a secondary market. Therefore, their poor liquidity in the secondary market makes it difficult to obtain data because fewer transactions can be made available to the lending business database.

C. Credit Risk Evaluation Method

1) Traditional credit risk evaluation model.

Before analyzing the modern credit risk management model, we need to briefly review the traditional credit risk management model. Because some of the ideas in the traditional credit risk assessment model also include in the modern credit risk assessment model partly, and almost all the credit risks are more or less linked, and even some new methods and models comes from the improvement of the traditional method. However, in the credit decision-making process the traditional credit risk assessment method the decisive factor is the intuitive qualitative analysis[28].

a) Credit risk evaluation method based on subjective analysis and traditional proportional analysis:

The characteristics of this stage assessment method are: Experienced credit experts hold the bank's credit decision-making power. A representative assessment method is the "5C" factor analysis method, which includes five factors: the borrower's character, capacity, capital, collateral and operating environment condition ,through this five qualities analysis the borrower's repayment willingness and repayment ability. Except the typical "5C" factor analysis, the more famous financial ratio comprehensive analysis are the DuPont analysis system and Wall Weight Grading. They are focus on the financial status of the company. But these can not meet the current banking business needs[2] . Although the credit risk evaluation method based on subjective analysis and traditional proportional analysis studies on some financial accounting indicators by calculating financial accounting data, it always uses a single variable to evaluate credit risk. This method has a serious flaw that is it does not rank and analyze the financial accounting indicators. It is not allow an accurate analysis of the strong and weak ratios of SMEs.

b) Credit risk evaluation method based on statistical analysis :

With the development of the social, new science and technology are gradually applied in the credit risk assessment and the multivariable method is also used to evaluate the credit risk. For example, Z-Score model and ZETA scoring model.The multivariate statistical analysis method is the basis of the Z-Score model by selecting multiple financial ratios of enterprises and assigning weights according to the size of the role and finally calculating the total discriminant score to predict the enterprise risk, we can judge the severity of the financial crisis [3]. The ZETA scoring model is based on the Z-Score model with seven variables, more variables and a wider range of scalability, greatly improving the accuracy of credit ratings for companies. But also based on the analysis of corporate financial ratios.

c) Credit risk evaluation method based on mathematical model of credit rating:

Because a simple analysis of the financial ratio has been unable to meet the needs of practice. Therefore, scholars

combined qualitative analysis and quantitative analysis, and introduced the mathematical model in credit evaluation that will be more scientific and can more systematically and comprehensively evaluate the credit risk of enterprises. The fuzzy comprehensive evaluation method that the basic principle are that there are many ambiguous phenomena in the economy and the fuzzy membership function can be constructed to transform the qualitative analysis into the quantitative analysis to make a comprehensive evaluation of the corporate credit. Gray analytic hierarchy process, which combines gray system theory and analytic hierarchy process, based on analytic hierarchy process, calculates the appraisal value according to gray system theory and gets the comprehensive credit score of the enterprise.

2) Modern credit risk evaluation model:

In recent years, financial institutions are experiencing various exponentially increasing risks, thus putting higher technical requirements for credit rating models. At present, the credit risk evaluation models that are widely used are: the Risk Metrics is the risk control model used by JPMorgan to calculate VaR, the KMV's Credit Monitor Model, the JPMorgan credit scale model Credit Metrics. These models are based on a large number of market and bank credit data for analysis.

a) VaR model:

In 1993, the G30 Group proposed a VaR[22] (Value at Risk) method for measuring market risk. Based on this, the Risk Metrics risk control model introduced by J. P. Morgan to calculate VaR is widely adopted by many financial institutions[23]. VaR (Value at Risk) refers to the maximum possible loss of the value of a financial asset or portfolio under a certain probability level (confidence level) in a specific period of time in the future [4].

b) KMV model:

In 1997, the KMV Company in the United States San Francisco established the KMV model used to estimate the probability of default of borrowing companies [5]. The KMV model is a model for default forecast established by using modern option pricing theory, and it is a remedy to the deficiency of traditional credit risk assessment methods [6].

c) Credit metrics model:

The Credit Metrics model is a risk management product introduced by J.P. Morgan in 1997 to quantify credit risk. The most important feature of this model is the risk-value measurement model used to evaluate the assets of an enterprise. It proposes to use the mark-to-market system of futures to evaluate the risk changes of enterprises.

D. Analysis of Factors Influencing the Credit Risk

Therefore, based on the characteristics of online supply chain finance and the actual conditions of SMEs, we will analyze the credit risk evaluation index system from four aspects: industrial factors, the strength of SMEs, credit records and supply Chain strength to analyze its credit risk factors.

1) Industrial factors:

SMEs may have two kinds of risks of non-systemic risk and systematic risk in their business operation. Systematic risk is caused by changes in the macroeconomic cycle or industry

development. When recognize the credit risk based on third-party B2B supply chain finance, industrial risk is serious one aspect.,therefore, we can examine the industrial risk from the following aspects [8].

a) Macro environment:

For a business, the macro environment is important where we can get relevant information about the company's growth, such as macroeconomic policies. If the macroeconomic is not good, the risk of SME loans will rise, banks need to pay attention and take appropriate risk control measures.

b) Pledge property:

Throughout the industry, the price stability and passage of the pledged property can also clearly characterize the stability and development of the entire industry.

2) SME strength:

In the third-party B2B supply chain finance, SMEs can enhance their credit rating by using of the strength of core enterprises and supply chains. However, SMEs, as the recipients of loan funds, have their own indicators and overall power, which affect SMEs' repayment willingness and repayment ability. Therefore, in the bank credit rating, various risk factors of SMEs has becomed even more important. Among them, the factors affecting the credit rating of SMEs include: basic qualifications, operational capacity, profitability, innovation, development capability, solvency and credit quality and so on [9].

3) Credit history:

a) Financial credit:

The status of corporate credit is generally the focus of bank review, reflecting the repayment ability and willingness of enterprises. Due to the imperfect credit evaluation system in our country and the low default cost of small and medium-sized enterprises, it may cause the intentional default of the enterprises and bring losses to the banks. Therefore, when reviewing the credit, the credit records of the enterprises will be mainly investigated.

b) E-commerce credit level:

The biggest difference in Internet + Supply Chain Finance and supply chain finance is the use of Internet technology that is the electricity supplier companies to build third-party B2B supply chain financing platform based on e-commerce business and use the e-commerce credit system credit information to add the bank inadequate financial credit data to better identify potential high-quality SME clients. Indicators measured mainly include online application time, online transactions, online trading volume, online credit rating and SME customer evaluation.

c) Financing platform credit record:

There are also many data that can be tapped on the Internet supply chain financing platform. Combining with different business models, the indicators reflecting solvency mainly include the following: the financing amount of the member enterprises on the platform, the number of financing, the amount of credit Percentage and so on.

4) Supply chain strength:

Based on the third party's B2B supply chain finance, the core idea is to examine the overall operation and trading status of the supply chain of the enterprise instead of separately examining the financial risk of SMEs, combined with several other factors comprehensively evaluate the credit rating of SMEs and determining the credit rank [10]. According to the content we will mainly study from the following aspects.

a) Core business strength:

The core enterprise strength plays an invisible guarantee role for small and medium-sized enterprises. The production level and management ability of SMEs can be reflected by this factor. The strength of core enterprises can be measured by the following indexes: status of core enterprises, assets and liabilities of core enterprises Rate, the core business profit margins.

b) Supply chain competitiveness:

Mainly through the overall strength of the supply chain to determine the level of competitiveness of SMEs, if the competitiveness of enterprises is strong, you can maintain a long-term cooperation with the core business, which is easier to obtain credit and you can evaluate from two aspects of the consumer products Satisfaction and product quality competitiveness.

c) Supply chain cooperation:

The cooperation between upstream and downstream firms in the supply chain will affect the bank's credit rating. If the relationship between firms is closer and there will be more cooperation, they will establish long-term and stable supply and demand relations. The closer this relationship, more the less sufficient for SMEs will be diluted.

Information sharing not only directly reflects the smooth communication between enterprises in the supply chain, but also reflects the extent of enterprise information sharing it have a direct impact on every aspect of the supply chain and business, and its measurement indicators mainly include sustainable transactions, close cooperation between upstream and downstream enterprises, upstream and downstream information sharing and so on.

III. OPERATIONAL RISK

A. Definition of Operational Risk

The expression of operational risk at home and abroad are also different. Different meanings and subjects determine different management modes. According to the definition of operational risk in the most authoritative Basel Capital Accord and the online supply chain finance, this paper considers that the operational risk refers to the risk that in the financial activities of Internet supply chain, due to procedural defects, personnel errors, technical failures, failure of financial institutions and failure caused by external factors and cause the loss to financial institutions.

B. Classification of Operational RIisk

As can be seen from the foregoing, the synergic operational framework of online supply chain finance realizes the unification of business flow, capital flow, information flow and

logistics, which is referred to as "four-flow unification." Operational risk is also hidden in the four major trading stages, the four major transactions are often intertwined to interact with each other, may lead to operational risk events. In view of this situation, according to the specific aspects of risk can be classified as online financing risk, e-commerce risk, logistics risk and online payment risk, as follows:

- **Online financing risk.** Online financing risk is mainly generated in the online financing process, several major steps of online financing also lurk operational risk. In this regard, in credit, not only to adhere to the legal rigor of the contract and the strict credit process, but also pay attention to the scientific method [11]. In terms of financing approval, we must uphold the authenticity of the object of approval and the compliance and rigor of the procedure. In the subsequent management phase, we must uphold the management's non-slackness and pay attention to the possibility of parties' default. In addition, system stability and hardware security are also important aspects of online financing risk.
- **E-commerce risk.** In the e-commerce transaction phase, the main transaction happened in the core supply chain companies and other upstream and downstream enterprises, the authenticity of the transaction is the basis of the financial activities of the Internet supply chain. The operational risk at this stage is also mainly from the transaction, it should pay attention to the authenticity of the transaction management and effectively prevent false transactions.
- **Logistics risk.** In the logistics trading stage, with higher operational risk occurrence probability are mainly in the logistics warehouse supervision and logistics delivery and delivery, and the commercial banks need to strengthen the monitoring of the credit supporting assets. In the logistics phase of the risks are mainly non-compliance operations, credit losses cause the loss.
- **Online payment risk.** Online payment transaction stage, bank account payment and corporate payment back is the risk point of operation risk. The risk in this phase is mainly caused by personnel and system, for example, mistakes of accounts due to personnel errors, or due to system-induced payment errors .

C. Operation Risk Identification Method and Selection

- **Questionnaire method.** The method of questionnaire survey refers to the method that investigators do not enter the site but through the issuance of audit forms or other forms of questionnaires to identify the operational risk of online supply chain financial operations. The method mainly focuses on the questionnaire prepared by the risk management department of financial institutions and analyzes the current situation of financial operational risk management in supply chain by collecting the questionnaires and evaluating them. When preparing the questionnaire, the respondents may refer to the internal and external historical loss database and consider about the knowledge, literacy and attitudes that the respondents have. Survey method

used correctly depends mainly on the scientific, rational, limited and applicability of the questionnaire, so the method of questionnaire quality requirements are relatively high.

- Flow chart method. Flow charts analysis is a flow chart drawn from the business operations and product operations processes in the online supply chain finance. Based on past history, experts and others then identify the risk points that may cause losses during the operation [13]. The flowchart can explain relevant information in the business operations and product operation flow to show the movement in the system. Flow chart can help decision-making, so that business managers more clearly find the problem will appear in a probable area, so as to formulate a program that can avoid operational risk. The flowchart method is a kind of identification method applied by many Internet supply chain finance at present.
- Expert investigation method. The method of specialist investigation is a method of identifying financial risks using the collective wisdom of experts. This method consists of working groups of experts in the fields of risk management department and business department to make judgment on the operational risk of online supply chain finance. The expert investigation method mainly includes expert conference method, brainstorming method and Delphi method.
- Scenario Analysis. Method of scenarios analysis is a scenario simulation of the environment in which the research subject is located. Each scenario describes a future state of the research subject and simulates and analyzes changes in the impact factor and predicts the likelihood of future scenarios, in order to examine the important factors that cause the associated risks and their impact size. In financial risk management, the most commonly used scenario analysis method that can measure the risk of extreme events is stress experiment. The method of scenario analysis is generally applicable to the analysis of financial products newly developed and can be used to identify the subject to be researched in advance.
- Fuzzy Set Analysis. The method of fuzzy set analysis is an analytical tool based on fuzzy mathematics that can solve the problem of fuzzy events. Fuzzy set analysis includes fuzzy pattern recognition, fuzzy clustering analysis and fuzzy comprehensive evaluation. Evaluation method for a fuzzy event analysis need to consider the impact of many factors, and according to the degree of different factors' impact on the evaluation, using different weights and measures to evaluate the study, the qualitative evaluation transform into the quantitative evaluation [14].
- Fault Tree Analysis. The Fault Tree Analysis (FTA) is a method of resolving possible faults into different levels of glitches in the form of logical diagrams [15]. The FTA method can not only qualitatively analyze failure risks, but also conduct quantitative analysis.

Fault tree analysis can describe the risk of complex systems and identify risk, and based on objective facts have great reliability. Graphical interpretation of fault tree analysis can be a specific operational risk failure layer by layer to study and reflect the different events and the logical relationship between system failures.

The above six risk identification methods can identify the operational risk of online supply chain finance, but there are still some shortcomings in the practical application. The research is not very clear many of the identification method is only classified in different categories of operational risk, not from the deep logic of the online supply chain financial operational risk. The advantages and disadvantages of various operational risk identification methods are shown in Table 1.

TABLE I. IDENTIFICATION METHODS ANALYSIS

	advantages	disadvantages
Questionnaire method	Small input costs, the survey results to collect and organize conveniently	The requirements of the questionnaire designer is relatively high
Flow chart method	Conducive to optimizing the process	Higher initial investment costs
Expert investigation method	The evaluation result is more accurate	A longer time, higher input costs
Scenario Analysis	Prior to the risk before	Accuracy is low
Fuzzy Set Analysis	More scientific, realistic assessment of the quantitative	Computational complexity, the index weight more subjective
Fault Tree Analysis	Logically strong	Spend more time

By comparing different operational risk identification methods in Table 1, it is found that the fault tree analysis method with its unique image deduction, can make further research on the operational risk of the target one by one. The fault tree analysis not only reflects the relationship of online supply chain financial system operational risk within the different risk factors, but also reflects the logic relationship of basic events intermediate events and top events in the operational risk. It is more suitable for identifying Internet supply chain financial operational risk.

IV. MARKET RISK

Market risk refers to the risk of uncertain value or return of financial products due to the fluctuation of interest rate, exchange rate, stock market, price and other factors. Market risk mainly includes interest rate risk, exchange rate risk, stock market risk and price risk.

The marketization of interest in our country is not yet mature or not fully mature. The pricing of bank supply chain financing products still adopts the fixed interest rate as the traditional working capital loans. Once the interest rate changes, the bank can't adjust the interest rate in time and can't make any adjustment until the beginning of the next benchmark year. This also exposes banks to the risks of interest rates. In addition, there is a lot of business in supply chain finance that is international trade. In international trade, whether single import or export business or back-to-back letter of credit transactions, if not using the same currency will have exchange rate risk. In the free-market economy, the volatility of commodity prices is a normal phenomenon. It is also more likely that the prices will fluctuate within a certain period of time. Therefore, there is also a price risk in the supply chain finance business.

REFERENCES

- [1] Li Yixue, Supply chain financial risk assessment [J], Central University of Finance and Economics, 2011 , pp.36-41.
- [2] Xia Liming, et al. Study on the construction of SME credit risk assessment model [J], Journal of Economics and Management, 2011 , pp.103-105.
- [3] Zhu Xiaodong, Zhang Zongyi, Geng Huadan. Analysis and Comprehensive Comparative Analysis of Modern Credit Risk Measurement Models [D]. Finance and Economics Research, 2010 , pp.34-46.
- [4] Jin Zhibo, Wang Hongjuan. Comparison of Modern Credit Risk Measurement Models [J], Contemporary Economy, 2009 , pp.142-143.
- [5] Matthew Kurbat, Methodology for Testing the Level of the EDF credit Measure [J], Moodys KMV Corporation 2002, pp.26-28.
- [6] Darrell Duffle, David Land, Term Structures of Credit Spreads with Incomplete Accounting Information, Econometrics, Econometrics, 2001, pp.633-664.
- [7] Yuan Lili, China's small and medium commercial banks credit risk management research [D], Chengdu: Southwest University of Finance and Economics, 2013.
- [8] Liu Xiuying, Research on credit risk evaluation of GEM listed companies based on gray system theory [D] , Anhui: University of Science and Technology of China, 2010.
- [9] Bian Ning , SME supply chain financing model machine credit risk assessment [D], Wuhan: Wuhan University of Technology, 2008.
- [10] Fan Xinmin, Study on the Risk of Default in Financial Supply Chain [D], Shanghai: Donghua University, 2011.
- [11] Zhou Hui, Online Supply Chain Finance [D], Hunan University, 2014.
- [12] Zhang Jinqing, Financial Risk Management (Second Edition) [M], Shanghai: Fudan University Press, 2012, pp.63-69.
- [13] Pan Biao, A clever use of component animation complex interactive interactive tree branch flow chart [J], Hefei: Computer Knowledge and Technology, 2013 , pp.61-63.
- [14] Yang Junqi, Hou Xiaokang, Yang Yijie. Studies on the performance evaluation system of party building based on fuzzy comprehensive evaluation model [J] , Anzhou University, 2012, pp.64-72.
- [15] Wei Xuanping, Fault tree analysis and its application [J], Computer Science and Technology, 2004 , pp. 43-47.
- [16] Leon Busch., Supply Chain Finance: The Next Big Opportunity[J], Supply Chain Management Review. 2014, pp.57~60
- [17] Gupta, S, Dutta, K. Modeling of Financial Supply Chain[J], European Journal of Operational Research, 2011, pp.47~56.
- [18] Chopra S, Sodhi M. Managing risk to avoid supply chain break-down.[J], MIT Sloan Management Review, 2004, pp.53~61.
- [19] Dunham A, UDELLGF. A More Complete Conceptual Framework for SME Finance[J], Journal of Banking & Financing, 2004, pp.2945~2966.
- [20] Michael Lamoureux. A supply chain finance prime[J], Supply Chain Finance, 2007, pp.34~48.
- [21] Basu P, Nair S K. Supply chain finance enabled early pay: unlocking trapped value in B2B logistics[J], International Journal of Logistics Systems and Management, 2015, pp.334~353.
- [22] Bouchard, A VAR analysis informed by a DSGE model[J], Journal of Hydraulic Engineering, 2015, pp.12~22.
- [23] Sentana, VaR as the CVaR sensitivity: Applications in risk optimization[J], Journal of Computational and Applied Mathematics, 2010, pp.43~51.
- [24] Hawnee K. Vickery, Roland. Managing the Finance Supply Chain [J], Supply Chain Management Review, 2003, pp.190~196.
- [25] Cressy, R. Olofsson Christer. "The financial conditions for Swedish SMEs: Survey and Research Agenda ". Small Business Economics, 1997, pp.179-194.
- [26] Badr Y., Stephan J.. Security and Risk Management in Supply Chains [J], Journal of Information Assurance Security, 2007, pp.287-296.
- [27] Barsky N-P, Catanach A-H. Evaluating business risks in the commercial lending decision[J], Commercial Lending Review, 2005, pp.3-10.
- [28] Demoulin, Embrechts, Value and risk assessment of supply chain management improvement projects[J], Int.J.Production Economics 2006, pp.186-201.

Supply Chain Financial Ecology Model Design and Risk Management Research

Baosen Wang, Wenjiao Lan* and Chunming Fan

1st Fuhe Street, Tongzhou District, Beijing, China

*Corresponding author

Abstract—Supply chain finance is an emerging model, which treats the core enterprises in the supply chain and the upstream and downstream SMEs as a whole. The commercial banks provide financial services to the entire supply chain. According to the natural ecosystem structure model, this paper summarized the composition of the supply chain financial ecosystem, designed the financial eco-mode of the supply chain, cleverly integrated the financial tree theory, and vividly linked the relationship among the environment, big data platform and enterprises. Through the use of VaR model for operational risk analysis and research, then used Matlab software to get VaR value. This paper used historical data to prove that banks and factoring companies and financial leasing companies strengthen cooperation to reduce operational risk, which also proved the scientific nature of supply chain financial eco-mode design.

Keywords—*supply chain finance; financial ecology; operational risk; VaR model*

I. COMPOSITION OF SUPPLY CHAIN FINANCIAL ECOSYSTEM

Supply chain financial ecology is a concept with Chinese characteristics, so a lot of foreign researches on ecology are about risk. Keynes believed that the inevitable factors that caused financial instability were the asymmetric information and irrational investment[1]. Michael Lamoureux pointed out that supply chain finance should be placed on the ecosystem to get better research so that core and upstream and downstream enterprises can get optimization of capital and supply chain models[2]. Parker emphasized that different functional departments in the ecosystem should work together and plan together to stabilize the development of the ecosystem[3]. Russell pointed out that in order to develop a stable ecosystem and get a long-term development, a more comprehensive sales system and a corresponding operation management system should be established[4].

Supply chain financial ecosystem is a complete ecosystem, which takes into account the different industries, different regions, different companies. Different businesses, businesses and government will be linked to the Internet of things and the big data, cloud computing and other advanced technology. Dewei Zhu's[5] research showed the improvement of financial ecology, first, it is conducive to preventing and resolving financial risks, making its non-performing loans decline. The second is to help optimize the geographical environment and better promote the local economic development. Third, it helps to raise the awareness of honesty and risk and the awareness of risk in all walks of life and speed up the construction of a

social credit system.

Supply chain financial ecology has a large number of data support, relying on the real trade and industrial chain as the background, is committed to combining production and financial[6]. Good financial environment is beneficial to optimize the internal structure of commercial banks and earnings management, thereby reducing operational risk[7]. Supply chain financial ecosystem consists of three parts: ecological environment, ecological interests and supply chain finance platform. Supply chain finance ecological interests, including the core business, upstream and downstream small and medium enterprises, logistics companies and financial institutions. Supply chain finance platform includes information processing platform (online, information flow), operating platform (offline, logistics), service platform (capital flow) and risk management platform. A complete integrated supply chain finance service platform integrates information flow, logistics, capital flow, business flow and risk system. In this paper, the supply chain finance integrated service platform is divided into four parts, which are supply chain financial information processing platform, supply chain financial operation platform, supply chain financial service platform, supply chain financial risk management platform[8].

II. SUPPLY CHAIN FINANCIAL ECOLOGY MODEL DESIGN

According to the principle of adaptability and diversity, the principle of stability and sustainable development and the principle of science in supply chain financial eco-mode design, this paper designs a mutually beneficial symbiotic supply chain financial eco-mode based on the traditional supply chain financial eco-mode. The financial eco-environment is like a tree root. The big data platform is like a trunk. Branches are used to represent different industries in different regions, commercial banks, factoring companies, financial leasing companies, core enterprises, upstream and downstream SMEs and logistics enterprises. Big data platform from the ecological environment and financial institutions to get sufficient information, funds, and then all of this information quickly and effectively passed out, companies can accept these "nutrients." Due to the effectiveness of these nutrients and the full service of big data platform, these enterprises are no longer restricted by the regions and industries. Therefore, the tree of financial ecology is the fruit of different fields, different industries and different regions, Which also reflects the characteristics of the financial ecology across industries and regions. In this model, commercial banks and factoring

companies and financial leasing companies step up their cooperation to jointly provide financial services for the supply chain. To build a good financial environment, the government should reduce its intervention in the local economy and financial markets, improve laws and regulations so that the political, cultural, economic and legal harmonizations will develop in line with the local economic development trend. The full application of big data platform enables it to serve all aspects of the entire supply chain in all aspects and accelerate the real-time tracking and sharing of information transmission, information sharing, information exchange and logistics information.

One of the most notable features of supply chain financial eco-mode is the establishment of integrated supply chain finance service platform. It brings together the big data, information flow, capital flow, logistics, business flow and wind control management platform, a full range of control supply chain from the procurement of raw materials to the final sale of the entire process of payment, at the same time rely on Internet technology and data analysis technology, It make the formation of an interactive regulatory and risk control mechanism, information sharing and cooperation win-win situation. At the same time, the supply chain finance integrated service platform records the real data of the past SMEs in the upstream and downstream. Under the circumstance that the data supports the ecological environment, commercial banks and other financial institutions can directly fund upstream suppliers and downstream distributors. After the upstream suppliers of goods sent to the core enterprise funds received and then return to a financial institution. Similarly, downstream distributors to the flow of funds to the core business, the core business delivery to the downstream distributors, dealers will sell to consumers to get the funds received and then flow to financial institutions. That creates a closed flow of funds. On the other hand, the closed capital flow reflects that the ecological model is a self-compensating trade model, thus avoiding the risks of external use of funds, ensuring the efficient recycling of funds and ensuring the stable development of the financial eco-mode of the supply chain.

Due to the constantly changing ecological environment and the external pressure of competition, the ecosystem status will also change. Supply chain finance service platform should be updated in a timely manner to maintain data and technical personnel, along with members of the ecological body time to adjust their own evolution, feedback to the consumer. In this way, consumers' consumption behavior can positively affect the ecological environment and make its supply chain financial ecology develop towards healthy development. Positive healthy competition and ecological environment can make its financial subjects rationalize and control all kinds of costs, which is low cost and high efficiency, so as to bring a positive effect on the ecosystem and promote the evolution of the entire ecosystem, so that supply chain finance ecological model tends to be stable.

In the supply chain financial eco-mode, the establishment of big data platform has solved the problem of information asymmetry. Logistics, information flow, capital flow and past trade data for small and medium-sized enterprises will be

presented in the data platform, which reduce credit risk. For their own survival and development, all enterprises have formed a reasonable division of labor and cooperation with other enterprises, forming a relationship that is interrelated, interdependent, interactive and competing with each other. Financial institutions will also make business innovations and product innovations that will make their ecological entities and their ecological environment more cohesive. The diversity of supply chain financial eco-mode also determines that its ecological main body will find its own foothold with the constant changes of ecological environment, and also makes the supply chain financial eco-mode more stable and sustainable development.

III. THE MAIN RISKS OF SUPPLY CHAIN FINANCIAL ECO-MODE

Supply chain financial ecology based on real transactions, with relatively good returns, but the details of the risk control is still the focus of research[9]. There are many factors leading to the uncertainty of supply chain financial eco-mode, which mainly comes from the uncertainty of financial eco-environment. This article roughly divided the risks involved in the supply chain financial ecology into: operational risk, credit risk and market risk.

A. Operational Risk

The most important of supply chain financial eco-mode is big data platform integration, every aspect of data processing is crucial. The quality of personnel, the level of business information, the stability of the network system and the level of resource sharing among the main financial operations all directly affect the operational risk of the supply chain financial eco-mode. This article classifies operational risk into six broad categories: resource sharing, staffing, external fraud, internal fraud, business informatics and network system vulnerabilities.

B. Credit Risk

Core enterprises play a crucial role in information flow, logistics and capital flow. Once the credit problems arise in the core enterprises, it will inevitably endanger the upstream and downstream enterprises in the supply chain, affect the safety of the entire supply chain finance and also undermine the stability of the supply chain financial ecology.

In the supply chain financial eco-mode, small and medium-sized enterprises as direct lending entities, unsuitable corporate governance structure, imperfect system, non-transparent information, unstable management, anti-risk ability and other unstable factors will make the whole supply chain bear a greater credit risk.

C. Market Risk

The interest rate liberalization of China is not yet mature. Pricing of bank supply chain financing products still takes the fixed interest rates as the same to traditional working-capital loans. Once the interest rate changes, the bank can not adjust the interest rate in time and only can make adjustments until the beginning of the next benchmark year when the benchmark interest rate changes. This makes banks take the risks posed by

changes in interest rates. In addition, there is a lot of business in supply chain finance that is international trade. In international trade, whether single import or export business or back-to-back letter of credit transactions, if not using the same currency will be subject to exchange rate risk. In a market economy, the volatility of commodity prices is a normal phenomenon, and there is a greater possibility of price changes in a given period of time. Therefore, there is also price risk in the supply chain finance business.

IV. VAR MEASUREMENT OF OPERATIONAL RISK IN SUPPLY CHAIN FINANCIAL ECOLOGY MODEL

A. Construction of VaR Model in Supply Chain Financial Ecology Model

In recent years, the VaR model is simple and easy to operate and analyze. It is widely used in various fields such as risk analysis. Therefore, the VaR model is one of the main financial risk measurement methods. Experts and scholars have done a great deal of work to study the VaR model, but also make different out to optimize the improved model to make the result more accurate. Gaivoronski and Pflug expected to eliminate local irregularities in the model to obtain similar VaR values, thus obtaining the mean-VaR effective frontier in the study[10]. Berkowitz proposed a new evaluation of VaR[11]. Despite the high level of confidence, there is still the possibility of unpredictable loss[12]. Generally speaking, there are three kinds of measurement methods of operational risk: basic index method, standard method and advanced measurement method. Advanced measurement methods include internal measurement, scorecard method and loss distribution method. In this paper, loss distribution method is used to measure the operational risk in the supply chain financial model.

1) Loss distribution model

This article draws on Philippe Jorion's method of calculating operational risk VaR in Value at Risk that the loss caused by operational risk in the supply chain financial eco-mode can be explained by two independent random variables, namely, the frequency N and severity of the loss X. The frequency of loss is the number of times a certain type of supply chain financial operation risk occurs during a fixed period of time. The severity of the loss is the operational risk loss, generally measured in monetary units, such as yuan.

a) The distribution of loss frequency

Binomial distribution, geometric distribution, Poisson distribution, etc. are suitable for the frequency model. It is assumed that the loss frequency obeys the geometric distribution in this paper, the probability density function when loss frequency is n

$$f(n) = P(1-P)^{n-1} \quad n = 1, 2, \dots,$$

P indicates the probability of a risk event occurring once, and $0 < P < 1$, $f(n)$ decrease by the geometric

progression, the expected loss frequency $E(N) = \frac{1}{P}$, variance $D(N) = (1-P)P^2$.

b) Distribution of severity of loss

Operating loss data does not obey normal distribution at almost any time. This paper assumes that the severity of the loss X follows an exponential distribution. The probability density function of X is

$$g(x) = \lambda e^{-\lambda x} \quad x \neq 0$$

2) Data collection and preliminary analysis of loss distribution

There are many main participants in the supply chain financial eco-mode. Based on the historical data of commercial banks, factoring companies and financial leasing companies in our country and the loss distribution of the traditional supply chain financial model, this article makes a comprehensive statistical analysis of these data and summarizes the classification of operational risk according to the financial eco-mode of the supply chain, as shown in Table I, Table II, Table III

TABLE I. DISTRIBUTION OF OPERATIONAL RISK IN CHINA'S COMMERCIAL BANKS FROM 2004 TO 2014

Category	Number of samples
<i>Internal fraud</i>	15
<i>External fraud</i>	15
<i>Personnel operation</i>	25
<i>Network system vulnerabilities</i>	33
<i>Business information level</i>	30
<i>Resource sharing</i>	10

TABLE II. DISTRIBUTION OF OPERATIONAL RISK IN IMPORT FACTOR FROM 2010 TO 2014

Category	Number of samples
<i>Internal fraud</i>	3
<i>External fraud</i>	2
<i>Personnel operation</i>	7
<i>Network system vulnerabilities</i>	6
<i>Business information level</i>	5
<i>Resource sharing</i>	1

TABLE III. DISTRIBUTION OF OPERATIONAL RISK IN FINANCIAL LEASING COMPANY FROM 2010 TO 2014

Category	Number of samples
<i>Internal fraud</i>	1
<i>External fraud</i>	8
<i>Personnel operation</i>	5
<i>Network system vulnerabilities</i>	5
<i>Business information level</i>	4
<i>Resource sharing</i>	0

We can see from the above table that after the reclassification of operational risk in the supply chain financial eco-mode, there are more operational risk events caused by network system vulnerabilities and business informationalized level. This reflects the maintenance of the data platform in supply chain financial eco-mode is a key issue on the other hand.

According to the requirements of loss distribution method, this paper classifies the collected samples according to the types of loss events in the financial eco-mode of supply chain and conducts statistical analysis, as shown in Table IV

TABLE IV. DISTRIBUTION OF OPERATING RISK LOSSES IN SUPPLY CHAIN FINANCE ECOLOGY MODEL (MILLION)

Category	Commercial banks	Factoring company	financial leasing company
<i>Stock pledge</i>	175	8	67
<i>receivables</i>	56	40	6
<i>Prepayments</i>	48	2	3

It can be seen from Table 4 that stock pledge has the largest loss of operational risk. This may be because stock pledges generally pledged to the logistics company goods to achieve the transfer of possession of the material. However, because of different logistics company scales in China and no unified standard in warehousing, it is easy to make mistakes in terms of regulation, personnel operation and network system. The article will be from the stock pledge / commercial bank, inventory pledge / factoring company, inventory pledge / financing leasing company, accounts receivable / commercial bank, accounts receivable / factoring companies, accounts receivable / financing leasing company, prepayments / commercial banks, prepayments / factoring companies, prepayments / leasing companies these nine categories of operational risk have tested in the generalized Pareto distribution.

B. Operational Risk Analysis in Supply Chain Financial Ecology Model

1) Empirical analysis of loss distribution

a) Empirical analysis of inventory pledge / commercial banks case

Use SPSS software to analyze the amount of inventory pledging / commercial bank losses, sample averages=42257.56,standard deviation of samples=145563.53, Skewness=4.34,Kurtosis=40.31,Data's from the intuitive degree of dispersion is high and does not meet the normal distribution, in addition, kurtosis is larger, so the distribution has a larger fat tail phenomenon.

The generalized Pareto distribution has a thick tail characteristic. Therefore, the text assumes that the Pareto distribution follows the generalized Pareto distribution in the financial eco-supply chain model, and then tests. In this paper, Kolmogorov test for non-parametric fitting test. The likelihood function can be derived from the generalized Pareto distribution function.

$$L(\varepsilon, \beta, y) = n \ln \varepsilon - n \ln \beta - \left(\frac{1}{\varepsilon} + 1 \right) \sum_{i=1}^n \ln \left(1 + \frac{\varepsilon}{\beta} y_i \right)$$

The likelihood function is used to derive the likelihood equation and using the maximum likelihood method to get the maximum likelihood estimation $\hat{\varepsilon} = 481, \hat{\beta} = 0.78$.

At a confidence level of 0.05, $D_n^*(a) = D_n^*(0.05) = 0.4 > D_n^* = 0.3525$, so can not reject the null hypothesis. That is, the amount of loss of inventory pledging / business information can not be rejected subject to generalized Pareto distribution.

b) Empirical analysis of stock pledge / factoring company cases

Using the SPSS to make statistical analysis on the amount of losses of inventory pledge / factoring companies, the result is as follows sample averages=43247.91,standard deviation of samples=134563.53, Skewness=4.56,Kurtosis=24.84. The amount of such events does not fall within the normal distribution. Using Kolmogorov test, at a confidence level of

$D_n^*(a) = D_n^*(0.05) = 0.4 > D_n^* = 0.2833$. Can not refuse the assumption that the amount of loss in corporate finance / infraction enforcement cases obeys the generalized Pareto distribution. Use the maximum likelihood method to estimate the parameters $\hat{\varepsilon} = 459, \hat{\beta} = 0.65$.

c) Empirical analysis of stock pledge / financing lease cases

Using the SPSS to make statistical analysis on the amount of losses of inventory pledge / financing leasing companies, sample averages=42257.56,standard deviation of samples=145563.53,Skewness=4.34,Kurtosis=25.31. The amount of such events does not fall within the normal distribution. Using Kolmogorov test, at a confidence level of

$D_n^*(a) = D_n^*(0.05) = 0.4 > D_n^* = 0.2901$. Therefore, we can not reject the null hypothesis that we can not refuse corporate financial / system vulnerabilities losses under the generalized Pareto distribution. Use the maximum likelihood method to estimate the parameters $\hat{\varepsilon} = 501, \hat{\beta} = 0.59$.

d) Empirical analysis of accounts receivable / commercial bank cases

Using the SPSS to make statistical analysis on the amount of losses of accounts receivable / commercial banks, sample averages=412357.76,standard deviation of samples=137653.12, Skewness=4.14,Kurtosis=24.68. The amount of such events does not fall within the normal distribution. Using Kolmogorov test, at a confidence level of 0.05, $D_n^*(a) = D_n^*(0.05) = 0.4 > D_n^* = 0.2793$. Therefore, we can not reject the null hypothesis that we can not refuse corporate financial / system vulnerabilities losses under the

generalized Pareto distribution. Use the maximum likelihood method to estimate the parameters $\hat{\varepsilon} = 490$, $\hat{\beta} = 0.43$.

e) Empirical analysis of accounts receivable / factoring company cases

Using the SPSS to make statistical analysis on the amount of losses of accounts receivable / factoring companies, sample averages=404337.12, standard deviation of samples=132833.09, Skewness=4.33, Kurtosis=22.98. The amount of such events does not fall within the normal distribution. Using Kolmogorov test, at a confidence level of 0.05, $D_n^*(a) = D_n^*(0.05) = 0.4 > D_n^* = 0.2832$. Therefore, we can not reject the null hypothesis that we can not refuse corporate financial / system vulnerabilities losses under the generalized Pareto distribution. Use the maximum likelihood method to estimate the parameters $\hat{\varepsilon} = 487$, $\hat{\beta} = 0.42$.

f) Empirical analysis of accounts receivable / financing leasing companies

Using the SPSS to make statistical analysis on the amount of losses of accounts receivable / financing leasing companies, sample averages=432661.56, standard deviation of samples=134522.54, Skewness=4.26, Kurtosis=21.99. The amount of such events does not fall within the normal distribution. Using Kolmogorov test, at a confidence level of 0.05, $D_n^*(a) = D_n^*(0.05) = 0.4 > D_n^* = 0.2901$. Therefore, we can not reject the null hypothesis that we can not refuse corporate financial / system vulnerabilities losses under the generalized Pareto distribution. Use the maximum likelihood method to estimate the parameters $\hat{\varepsilon} = 472$, $\hat{\beta} = 0.41$.

g) Empirical analysis of prepayments / commercial banks cases

Using the SPSS to make statistical analysis on the amount of losses of prepayments / commercial banks, sample averages=409876.12, standard deviation of samples=136594.12, Skewness=4.19, Kurtosis=23.91. The amount of such events does not fall within the normal distribution. Using Kolmogorov test, at a confidence level of 0.05, $D_n^*(a) = D_n^*(0.05) = 0.4 > D_n^* = 0.2787$. Therefore, we can not reject the null hypothesis that we can not refuse corporate financial / system vulnerabilities losses under the generalized Pareto distribution. Use the maximum likelihood method to estimate the parameters $\hat{\varepsilon} = 484$, $\hat{\beta} = 0.44$.

h) Empirical analysis of prepayments / factoring company cases

Using the SPSS to make statistical analysis on the amount of losses of prepayments / factoring companies, sample averages=412300.67, standard deviation of samples=137620.23, Skewness=4.08, Kurtosis=22.99. The amount of such events does not fall within the normal distribution. Using Kolmogorov test, at a confidence level of 0.05, $D_n^*(a) = D_n^*(0.05) = 0.4 > D_n^* = 0.2692$. Therefore, we can not reject the null hypothesis that we can not refuse

corporate financial / system vulnerabilities losses under the generalized Pareto distribution. Use the maximum likelihood method to estimate the parameters $\hat{\varepsilon} = 472$, $\hat{\beta} = 0.40$.

i) Empirical analysis of prepayments / financing Leasing company cases

Using the SPSS to make statistical analysis on the amount of losses of prepayments / financing leasing companies, sample averages=419862.31, standard deviation of samples=136281.68, Skewness=4.11, Kurtosis=23.19. The amount of such events does not fall within the normal distribution. Using Kolmogorov test, at a confidence level of 0.05, $D_n^*(a) = D_n^*(0.05) = 0.4 > D_n^* = 0.2693$. Therefore, we can not reject the null hypothesis that we can not refuse corporate financial / system vulnerabilities losses under the generalized Pareto distribution. Use the maximum likelihood method to estimate the parameters $\hat{\varepsilon} = 474$, $\hat{\beta} = 0.41$.

As can be seen from the above results, stock pledge / commercial bank, inventory pledge / factoring company, inventory pledge / finance lease company, accounts receivable / commercial bank, accounts receivable / factoring company, accounts receivable / finance leasing company, prepayments / commercial banks, prepay accounts / factoring companies, prepayments / finance leasing companies all follow the generalized Pareto distribution. The above empirical results have two aspects of the policy implications: 1. In the supply chain financial eco-mode, the loss distribution method is more accurate than other methods of operational risk measurement. 2. When applying the loss distribution method, it is possible that most subclasses satisfy the generalized Pareto distribution and some subclasses conform to other distributions, such as Weibull distribution, normal distribution, etc. Although the empirical results in this paper are shown to be subject to the generalized Pareto distribution, it can not be ruled out that there may exist other generalized Pareto distributions in other subclasses. Then this time need to make the calculate separately and then add up. Based on the above generalized Pareto distributions, the operational risk capital is calculated using the loss distribution method.

2) Calculate operational risk capital

Before calculating the capital, we analyze the loss frequency data of commercial banks, factoring companies and financial leasing companies first, as shown in the following table V, VI, VII

TABLE V. ANALYSIS ON THE LOSS FREQUENCY DATA OF CHINESE COMMERCIAL BANKS

<i>average value</i>	17.01	<i>kurtosis</i>	0.40
<i>median</i>	13.00	<i>skewness</i>	1.01
<i>mode</i>	9.00	<i>minimum</i>	3.00
<i>Standard deviation</i>	11.12	<i>maximum</i>	33.00
<i>variance</i>	126.21	<i>summation</i>	355.00

TABLE VI. ANALYSIS ON THE LOSS FREQUENCY DATA OF CHINESE IMPORT FACTOR

<i>average value</i>	12.34	<i>kurtosis</i>	0.30
<i>median</i>	9.00	<i>skewness</i>	0.91
<i>mode</i>	6.00	<i>minimum</i>	2.00
<i>standard deviation</i>	8.05	<i>maximum</i>	21.00
<i>variance</i>	98.76	<i>summation</i>	201.00

TABLE VII. ANALYSIS ON THE LOSS FREQUENCY DATA OF FINANCIAL LEASING COMPANY

<i>average value</i>	11.34	<i>kurtosis</i>	0.30
<i>median</i>	7.00	<i>skewness</i>	0.87
<i>mode</i>	5.00	<i>minimum</i>	2.00
<i>standard deviation</i>	8.05	<i>maximum</i>	19.00
<i>variance</i>	96.14	<i>summation</i>	196.00

The article used matlab software to fit the collected loss frequency data, the results shown in Table VIII. The negative binomial distribution and the geometric distribution can fit the data better from the table.

TABLE VIII. FITTING RESULTS OF LOSS FREQUENCY DISTRIBUTION OF OPERATIONAL RISK

frequency distribution	Chi-square	P
<i>Negative binomial distribution</i>	1.98	0.161
<i>Geometric distribution</i>	3.58	0.060
<i>Poisson distribution</i>	8.72	0.003
<i>Binomial distribution</i>	9.92	0.000

The above has given the loss distribution model and the loss frequency, the following apply the Matlab software to Monte Carlo simulation to get VaR value. Confidence level is 95%.

TABLE IX. THE SUMMARY OF OPERATIONAL RISK CAPITAL

	Commercial Bank	Factoring Company	Finance Leasing Company
<i>95% confidence level operating risk VaR (yuan)</i>	8.76×10^7	0.73×10^7	0.69×10^7

C. Result analysis

From the above operation results we can see, in supply chain financial eco-mode, whether it is commercial banks, factoring companies or financial leasing companies, there are operational risks in inventory pledge, accounts receivable and prepayments which all subject to generalized Pareto distribution. Operating risk capital calculated by loss distribution method. At the confidence level of 95%, the VaR values of commercial banks, factoring companies and finance leasing companies are quite different. The VaR of commercial banks is the largest, and the VaR of finance leasing companies is the smallest. It suggests that financial leasing companies have relatively good operational risk management. The

combination of commercial banks and factoring companies and the combination of commercial banks and financial leasing companies can reduce the reserved capital of commercial banks and at the same time reduce the operational risks of the supply chain financial eco-mode.

In addition, good financial environment can make the financial internal and external operating mechanism more efficient, and can maximize the interests of financial institutions, thereby helping to improve the quality of earnings, inhibit the loss of operational losses, thereby reducing the reserve capital and reduce the operation risk.

The construction of big data platform in supply chain financial eco-mode and the multi-faceted participation and data application of supply chain financial eco-service platform can also effectively restrain the internal fraud, external fraud and personnel operations in the traditional supply chain financial model Problems, thereby reducing the operational risk.

V. CONCLUSION

This article designed the supply chain financial eco-mode, in which the main is interdependent and mutually beneficial. These companies constitute the value chain or value network business ecosystem. Compared with the traditional model, all the subjects in the supply chain financial eco-system have a higher degree of cohesion and a more stable and sustainable development.

The article used the VaR model to analyze the operation risk and used the generalized Pareto distribution to test the data. Then using the loss distribution method to calculate the VaR of operational risk, the result is that the VaR of commercial bank is the largest and the VaR of finance leasing company is the smallest. The final result showed that commercial banks provide financial services to upstream and downstream enterprises need larger amounts of capital, whereas factoring companies and financial leasing companies have a much smaller VaR. Therefore, this paper suggests that banks should strengthen cooperation with factoring companies and financial leasing companies to reduce operational risk. Finally, the article also analyzed that the financial eco-environment and big data platform can effectively reduce operational risk. The research of supply chain finance in our country can be considered from the ecological point of view. The supply chain finance ecological mode that the article designed and the operation risk research hope can provide the reference for the future research.

REFERENCES

- [1] Keynes. Enterprise systems and the supply chain[J]. Journal of Enterprise Information Management,2005,17(1):44~46
- [2] Michael Lamoureux. A supply chain finance prime[J]. Supply Chain Finance, 2007, (5): 34~48
- [3] C. Parker,N.S. Hawkins.Sharing of Information Across Studies to Inform Choice of Functional Form When Conducting Parametric Survival Analysis[J]. Value in Health . 2014 (7)
- [4] Russell Davis. Heart failure: key points and recent developments in management[J]. Prescriber . 2015 (6)
- [5] Dewei Zhu. Optimize Financial Structure: Another Perspective to Improve Financial Ecology[J].Shanghai Finance,2006,(01):19-23.

- [6] Xiangjun He,Ding Zhou. Innovative Exploration of the Operation Mode of Supply Chain Finance Business[J].Manufacturing automation,2012,(34):72~81
- [7] Ming Zhang,Lu Xie,Lijun Ma.Financial Ecology Environment and Earnings Quality of Commercial Banks[J].Finance Research,2015,(05):117~131
- [8] Xuefeng Xu,Jianxin Xia. Some Problems in Innovative Development of Supply Chain Finance in China[J].Shanghai Finance,2014,(3):23~26
- [9] Xinyu Huang,Supply Chain Finance New Ecological Picture[J].CFO,2016,(16):32~43
- [10] Lingyun Tang.Research on Supply Chain Financial Operational Risk Measurement Based on VaR[J].Chinese Market,2010,(15):12~14
- [11] Berkowitz. Kalman Filter or VAR Models to Predict Unemployment Rate in Romania[J].Computational and Mathematical Methods in Medicine, 2015, (6): 64~72
- [12] JDanielsson. Examining Eurozone Crisis and Unemployment Relationship Using Var Models[J].Supply Chain Finance, 2016, (2): 34~48

The Effect of Behavior Conformity on Prisoner's Dilemma Game

Zidong Chai, Yanbo Zhang*, Xinyu Zhang and Xiaobo Liu

School of Physics and Electronics, Henan University, Kaifeng, China

*Corresponding author

Abstract—Explaining the evolution of cooperative behavior is one of the most important and interesting problems in a myriad of disciplines. Game players on complex networks usually change their strategies by copying special rules. In this research, we combine the prisoner's dilemma game player's behavior conformity with the Fermi process. The game player changes the strategy by choosing a Fermi process or behavior consistency by a certain probability. And we have researched the evolutionary process of game players' cooperative behavior on a regular network of different sizes. The analysis of the data shows that the demand for behavior conformity is conducive to the emergence of the cooperative behavior of the game groups in prisoner's dilemma. Cooperative phenomenon is of great significance for intelligent machine collaboration.

Keywords—prisoner's dilemma; behavior conformity; network.

I. INTRODUCTION

In social group, cooperation is one of the important factors of group survival and reproduction. Human sometimes give support to help others without any feedback[1]. These actions will consume personal assets some. Mutual cooperation among members of the group, human and social species have achieve success of evolutionary success. Cooperation makes our lives better[2]. However, the formation of scope cooperation in the group is still difficult, and the prisoner's dilemma reveals the relationship of cooperation and betrayal among individuals. In the basic model, each player must simultaneously choose one strategy between cooperation (**C**) and defection (**D**). If both of them choose cooperation (or defection), they will get the reward **R**(or defection **P**). However, if one cooperator meets one defector, the former gets sucker's payoff **S**, while the later gets Temptation **T**. If the payoff ranking satisfy $T > R > P > S$ and $2R > T + S$, it will be the prisoner's dilemma game; It is obvious that, mutual defection and cooperation-defection pair optimizes the individuals' payoff in prisoner's dilemma, although mutual cooperation could yield a higher collective benefit. Thus, the survival of cooperation seems to be still difficult[3].

When choosing a kind of behavior, the actual individual not only considers the objective income that the behavior brings to himself, but also collects the relevant information of the people around them[4]. The communication of this information is one of the most important ways to achieve competition or cooperation. If the individuals around are the same as their own behavior, the individual would gets a greater sense of satisfaction. Otherwise, the experience feels

that he is incompatible with the environment and produces subjective uncomfortable. This psychology makes the individual prefer to choose the strategy of most people around[5]. The ways of the individual's own behavior strategies are complex and diverse, conformance, namely, behavior conformity is one of the most common kind ways[6]. Based on this, the main research of this paper: In the regular network model, The effect of behavior consistency and replication dynamics (Fermi rules) on the evolution of group behavior. Through experimental simulation, The evolution of group cooperative behavior on a homogeneous small world network based on grid networks is studied.

II. STRUCTURE

We consider the evolutionary prisoner's dilemma game in this study. The payoff matrices for both games are shown in the following Table.1:

TABLE I. GAIN MATRIX		
strateg ies	C	D
C	R	S
D	T	P

Table.1: The evolutionary prisoner's dilemma game is assigned as follows: the temptation **T** = 2 if one player defects while his opponent cooperates, reward **R** = 1 if both cooperate, and both the punishment **P** = 0 for mutual defection as well as the sucker's payoff **S** = -2.

Players are located in lattices with $L * L$ units. Each player adjusts or maintains strategy by comparing with the gain of neighborhood after each round of game[7]. Self-interest maximization is the rational player's pursuit in game, this is determined by player's need for development. Otherwise some rational players may occasionally make a certain degree of error when they change strategy, through statistics and analysis of the vast data, at present, most researchers use Fermi rules to express irrational imitation of players[8]. The game player *i* selects a neighbor *j* randomly from four neighbors, then the probability of the player *i* takes the strategy of neighbor *j* in the next game is:

$$P_{(i \leftarrow j)} = \frac{I}{1 + e^{[(u_i - u_j)/k]}} \quad (1)$$

u_i and u_j represent gain of player i and j respectively. K quantifies the uncertainty by strategy adoption, which indicates that the player chooses irrationally. The probability of irrational selection increases with the increasing of value K [8,9]. In the $K \rightarrow 0$ limit, player i copies the strategy of player j only when $u_j > u_i$. Conversely, in the $K \rightarrow \infty$ limit, payoffs cease to matter and strategies change as per flip of a coin[10].

In the evolutionary mechanism proposed in this paper: Game players in each round of game, there is a probability of $p\theta$ for selecting behavior conformity strategy, and a probability of $(1 - p\theta)$ for selecting Fermi rules to replace the probability of choosing their own strategies. The formula of behavior consistency are described as follows:

$$\frac{(kc - kd)}{ki^2} >= cmp \quad (2)$$

In the above formula, cmp is the degree of demand for individual behavior conformity. The number of individual neighbors choosing C strategy is kc , and kd is the number of D chooser number, ki is the number of neighbors besides individual. When players use behavioral conformity to change strategies, the formula (2) is established, and the game player will choose the C strategy. Otherwise, game player will choose D strategy. When $L = 10$ (**number of player** = $L * L$), and the density of the cooperator at initialization is 0.5, $R = 1$, $S = -2$, $T = 2$, $P = 0$, $cmp = 0.1$, $p\theta = 0$. The statistical results of the game players' strategy ratio in each game are shown as below Figure 1:

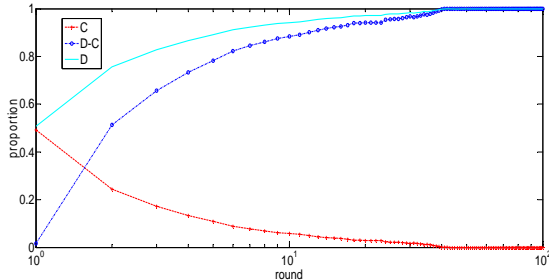


FIGURE I. THE GAME PLAYERS' STRATEGY RATIO IN EACH GAME

Figure 1. For everyone in our game selects their strategies obey the Fermi rules. When $p\theta = 0$, in the range of (0 - 80) rounds, the proportion of D (blue) selector is waved in 50 to 100%, and reached the peak in round 80, the selectors of C (red) will disappeared in (0 - 80) rounds. That means to pursue profit maximization inflexibly would evolve the betrayal of the whole because of the use in Fermi.

To analyze the useful of $p\theta$, we paid attention to the cooperative evolution in the network when $p\theta$ means different figure, $(N_D - N_C)/L^2$ means the selectors who choose betrayal subtracts the selectors of cooperation.

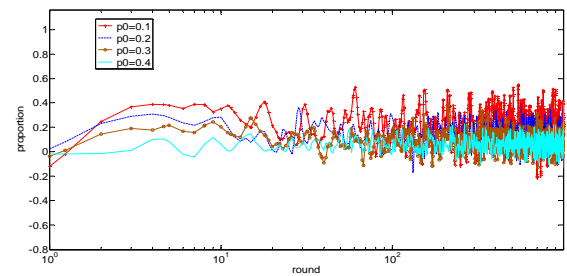


FIGURE II. CHANGING SITUATION OF $(N_D - N_C)/L^2$ IN DIFFERENT $p\theta$

Figure 2. When $p\theta = 0.1$ (red), the average of $(N_D - N_C)/L^2$ is 0.2257 in $0 < \text{round} < 1000$ and the variance is 0.0202; when $\text{round} > 18$, the value of $(N_D - N_C)/L^2$ is between -0.24 (round = 701) and 0.58 (round = 544). When $p\theta = 0.2$ (blue), the average is 0.1356, the variance is 0.011 and the $(N_D - N_C)/L^2$ is between -0.2 (round = 132) and 0.48 (round = 390). When $p\theta = 0.3$ (brown), the value of $(N_D - N_C)/L^2$ has arrived at the top of 0.44 (round = 212) and has reached the peak valley of -0.2 (round = 711), at this time, the average is 0.0870 and the variance is 0.0088. When $p\theta = 0.4$ (cyan), the top value of $(N_D - N_C)/L^2$ is 0.34 (round = 264) and the bottom is -0.16, the average is 0.0594 and the variance is 0.0061. Along with the increasing of $p\theta$, the top value of $(N_D - N_C)/L^2$ has decreased from 0.58 to 0.34 and the bottom has increased from -0.24 to -0.16, the average and the variance has let up. That all means when the range of cooperation has increased, the wave of $(N_D - N_C)/L^2$ has decreased.

When $L = 20$, the proportion of strategies distribution $(N_D - N_C)/L^2$ after fitting is shown as followed:

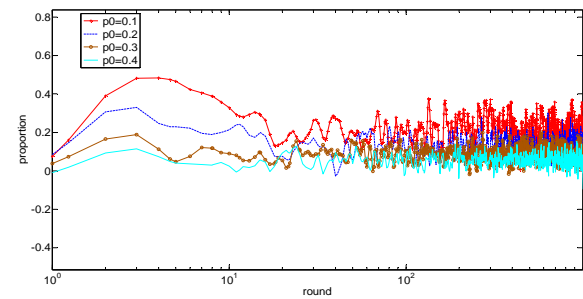


FIGURE III. CHANGING SITUATION OF $(N_D - N_C)/L^2$ IN DIFFERENT $p\theta$

Figure 3. When $p\theta = 0.1$ (red), the value of $(N_D - N_C)/L^2$ has arrived at the top of 0.485 (round = 5) and then it decreased at the bottom of 0.281 (round = 12); it raised again to 0.3 (round = 14) and then it has fluctuate within the region of -0.01 (round = 443) to 0.37 (round = 134). The average of $(N_D - N_C)/L^2$ is 0.214 between 1000 rounds and the variance is 0.0055. When $p\theta = 0.2$ (blue), the value of $(N_D - N_C)/L^2$ has arrived at the top of 0.3550 (round = 2) and then it decreased at the bottom of -0.05 (round = 40), the average is 0.1314 and the variance is 0.0031. When $p\theta = 0.3$ (brown), the value of $(N_D - N_C)/L^2$ has arrived at the top of 0.215 (round = 668) and then it decreased at the bottom of -0.04 (round = 381), the average is 0.0893 and the variance is 0.0021. When $p\theta = 0.4$ (cyan), the value of $(N_D - N_C)/L^2$ has arrived at the top of

0.185 (round = 935) and then it decreased at the bottom of -0.08 (round = 199), the average is 0.0564 and the variance is 0.0017.

Along with the increasing of $p\theta$, the value of $(N_D - N_C)/L^2$ will decrease within limits, and the bottom of it is decreasing of the whole except when $p\theta = 0.2$ and $p\theta = 0.3$. We could see the wave range of $(N_D - N_C)/L^2$ in Figure 3, it is decreasing when $p\theta$ is increasing. That means the range of cooperation is also enlarged while $p\theta$ is increasing. When $L = 50$, the proportion of strategies distribution of game players simulation $(N_D - N_C)/L^2$ after fitting is shown as followed:

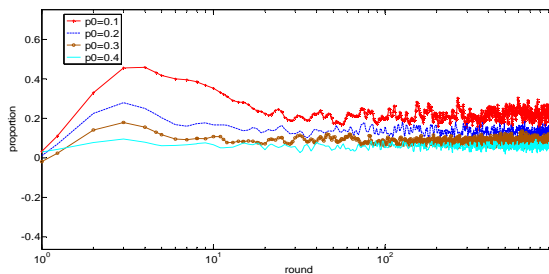


FIGURE IV. CHANGING SITUATION OF $(N_D - N_C)/L^2$ IN DIFFERENT $p\theta$

From Figure 4, when $p\theta = 0.1$ (red), the value of $(N_D - N_C)/L^2$ has arrived at the top of 0.4632 (round = 4), and then, within the increasing of the round, it has reached 0.21 (round = 21). From then it has fluctuate within the region of 0.14 (round = 345) to 0.30 (round = 265), the average of it is 0.2213 between 1000 rounds and the variance is 0.0012. When $p\theta = 0.2$ (blue), the value of $(N_D - N_C)/L^2$ has arrived at the top of 0.2688 (round = 3), within the increasing of the round, it has reached 0.1647 (round = 25). From then it has fluctuate within the region of 0.1031 (round = 35) to 0.1714 (round = 984), the average of it is 0.1351 and the variance is 5.5196×10^{-4} . When $p\theta = 0.3$ (brown), the top of it is 0.1736 (round = 2) and the average is 0.0876, the variance is 3.6431×10^{-4} . When $p\theta = 0.4$, the top of it is 0.1144 (round = 757) and the bottom of it is -0.0048 (round = 502), the average is 0.0579 and the variance is 2.4668×10^{-4} . Within the increasing of $p\theta$, the value of $(N_D - N_C)/L^2$ has decreased. The bottom is also decreasing except when $p\theta = 0.3$ (brown) and $p\theta = 0.4$ (cyan). That means the range of cooperation is also enlarged while $p\theta$ is increasing. With the increasing of L , for example, when $p\theta = 0.1$:

TABLE II. THE DIFFERENT PARAMETER OF $(N_D - N_C)/L^2$ IN DIFFERENT VALUE OF L

L	Max	Min	Mean	Var
10	0.58	-0.24	0.2257	0.0202
20	0.485	-0.01	0.214	0.0055
50	0.4632	0.0088	0.2213	0.0012

Table 2 We can know from Table 2 that with the increasing of L , the top value of $(N_D - N_C)/L^2$ is decreasing from 0.58 to 0.4632. It means the cooperation range has

enlarged but the degree of it is lesser. The average of $(N_D - N_C)/L^2$ is about 0.21 and the variance of it is decreasing from 0.0202 to 0.0012. From Figure 2, Figure 3 and Figure 4, we could see that the volatility of $(N_D - N_C)/L^2$ is reducing when the value of L is increasing, it means the stability of game players is strengthened.

III. CONCLUSION

In the state of the constant density of initial cooperator, the introduction of behavior conformity in the prisoner's dilemma game structure is helpful to the cooperative evolution of the group on the lattices. And to a certain extent resists the invasion of the betrayer. With the expansion of the network scale, the volatility of formula $(N_D - N_C)/L^2$ becomes smaller after the evolution of stability. It means that the strategy stability is strengthened, and it can promote group cooperation.

ACKNOWLEDGMENTS

This paper is supported by educational technology equipment and practice education in Henan (GZS029); key project of science and technology research of Henan Provincial Education Department (16A140004); teaching reform project of Henan University.

REFERENCES

- [1] Dreber A, Rand D G, Rand D G, et al. Winners don't punish[J]. Nature, 2008, 452(7185):348-351.
- [2] Perc M. Phase transitions in models of human cooperation[J]. Physics Letters A, 2016, 380(36):2803-2808.
- [3] Ma Y, Lu J, Shi L. Diversity of neighborhoods promotes cooperation in evolutionary social dilemmas[J]. Physica A Statistical Mechanics & Its Applications, 2017, 468:212-218.
- [4] Coulas J C. When in Rome. An Evolutionary Perspective on Conformity[J]. Group Processes & Intergroup Relations, 2004, 7(4):317-331.
- [5] Effersonabd C, Richerson P J, McElreath R, et al. Conformists and mavericks: the empirics of frequency-dependent cultural transmission [J]. Evolution & Human Behavior, 2008, 29(1):56-64.
- [6] Goyal, Sanjeev, Vega-Redondo, et al. Network Formation and Social Coordination[J]. Working Papers, 2003, 50(2):178-207.
- [7] Liu C, Li R. Power-law distributed temporal heterogeneity of human activities promotes cooperation on complex networks[J]. Physica A Statistical Mechanics & Its Applications, 2016, 457:93-100.
- [8] Perc M, Gómez-Gardeñes J, Szolnoki A, et al. Evolutionary dynamics of group interactions on structured populations: a review[J]. Journal of the Royal Society Interface, 2013, 10(80):20120997.
- [9] Szolnoki A, Perc M, Szabó G. Topology-independent impact of noise on cooperation in spatial public goods games[J]. Phys Rev E Stat Nonlin Soft Matter Phys, 2009, 80(2):056109.
- [10] Kurzban R, Houser D. Individual differences in cooperation in a circular public goods game[J]. European Journal of Personality, 2001, 15(S1):S37-S52.

The Application of Real-Time Object Detection on Aerial HD Videos Based on Deep CNN

Guanghui Xu, Shuai Xie*, Jun Wang and Guodong Wu

College of Communication Engineering, Army Engineering University of PLA, Nanjing, Jiangsu 210007, P.R. China

*Corresponding author

Abstract—Efficient real-time object detection in aerial HD videos is an urgent need, with the increasing use of UAV(unmanned aerial vehicles) in various fields. But it is still challenging to detect objects accurately and timely due to its large pixel size and relatively small objects. We use the popular SSD to detect people, cars, boats and so on from real-time HD videos which behave better than traditional methods. Moreover, we improve the deep learning algorithm by tailoring its networks and enlarging its size. We apply this algorithm to the real time detection of UAV aerial HD video and experiments show that our method can realize the organic combination of detection efficiency and detection effect.

Keywords—real-time object detection; SSD; HD videos; UAV

I. INTRODUCTION

High resolution cameras is being used in areas of video surveillance like security of public places, traffic monitoring, military and satellite imaging. This leads to a demand for computational algorithms for real time processing of high resolution videos. Recently, detection methods based on deep learning, such as Faster R-CNN, YOLO and SSD [1-4], have rapidly advanced. However, they require numerous samples to train the detection model and cannot be directly used to efficiently handle large-area remote sensing HD videos.

Simonyan et al. began to pay attention to the application of deep convolutional networks in high resolution remote sensing images [5]. Bin Pan et al. proposed a cascade convolutional neural network based on transfer-learning for aircraft detection on high-resolution remote sensing images [6]. Chongyuan Tao et al. proposed a pedestrian detection in a down-looking perspective using deep learning [7]. Nevertheless, all the algorithms mentioned can not accurately detect relatively small targets on high-resolution remote sensing images. To address this problem, we propose an algorithm that performs better in this respect by tailoring and enlarging SSD. Then we apply this algorithm to the real time detection of UAV aerial video.

This paper is organized as follows. Section II presents the idea, model architecture and training details about the improved networks. Section III gives experimental results from comparisons. Conclusions are drawn in Section IV.

II. APPROACH

Our approach is based on SSD which is a particular successful method for general object detection. And we tailor the last two feat layers and enlarge the model size to detect

small objects and get higher detection efficiency, as introduced in the following.

A. Enlarged the Input Layer and Tailored the Last Two Feat Layers

The original SSD with a 300×300 input size is not suitable for aerial HD videos, because it is hard to detect relatively small object from a high altitude perspective when the HD videos which is resized to a size of 300×300 was inputted to original SSD. As shown in Figure *, the input size of SSD is enlarged from 300×300 to 1280×720 , which leads to the decline of detection speeds accompanying with the increase of anchors. However, it is concerned a lot in real-time object detection, so that we tailored the last two feat layers whose receptive field is relatively larger to improve detection efficiency. As a reason of that the targets in aerial videos, such as people, cars and boats, are small, the accuracy of object detection is almost not affected.

B. Model Architecture

This is implemented using TensorFlow. The framework is shown in Figure 1. The SSD approach is based on a feed-forward convolutional network that produces a fixed-size collection of bounding boxes and scores for the presence of object class instances in those boxes, followed by a non-maximum suppression step to produce the final detections.

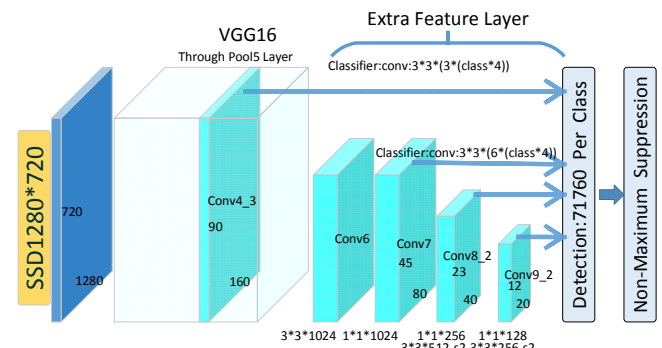


FIGURE I.

OUR SINGLE SHOT DETECTION MODELS WITH A SIZE OF 1280x720

Figure I shows that the first layer is input layer with a size of 1280×720 . The early network layers are based on a standard architecture, a part of VGG16 [3], used for high quality image classification (truncated before any classification layers), which consists of five max-pooling layers and thirteen convolutional

layers where we use filters with a very small receptive field: 3×3 (which is the smallest size to capture the notion of left/right, up/down, center). As the fifth max-pooling layer uses kernels of size 3×3 with a stride of 1, its output size is 80×45 . Then we add auxiliary structure to the network to produce detections. The layer named conv6 uses 1024 kernels of size 3×3 , but the layer named conv7 uses 1024 kernels of size 1×1 . The layer named conv8_1 uses 256 kernels of size 1×1 . The layer named conv8_2 uses 512 kernels of size 3×3 . A max-pooling layer is between conv8_1 and conv8_2, which is the same as conv9_1 and conv9_2. These layers decrease in size progressively and allow predictions of detections at multiple scales. Next a multiple boxes detection layer is followed, which is also a convolution layer where we use k filters with a size of 3×3 . We choose conv4_3, conv7, conv8_2 and conv9_2 as features to be sent to multiple boxes layer. Finally non-maximum suppression layer eliminate the boxes whose IoU [4] values greater than 4.5. Equations

C. Parameters Interoperability

The model architecture except non-maximum suppression layer is a fully convolutional network. And all the parameters are convolution kernels with a size of 3×3 , which is the same as original SSD. On the one hand, the number and size of the convolution kernels is not changed, although we enlarge the size of the input layers so that the size of the feature map [8] layers are correspondingly increased. On the other hand, the abstract levels of the convolution kernels is not changed. Our model with a size of 1280×720 can reuse the relative parameters of the original SSD when we adjustment the number and position of default boxes [3]. As a result, our model with a size of 1280×720 reuse the parameters which is trained beforehand on a model with a size of 300×300 , instead of being trained directly on itself.

D. Training Details

Primarily, the popular datasets can not include all the categories, while we are usually required to discover specially designated objects in the target detection task. In order to test the practicability of the model better, we make part of our datasets through collecting 200 images of tank which we have chosen as a target category. Then we chose the three other categories, person, car and boat (646 images), which are part of the popular datasets, PASCAL VOC2012. We resized all the images to 300×300 before training. At last, we fine-tune the model which is based on pre-trained VGG16 network, with 10^{-3} learning rate for 60k iterations, then 10^{-4} for 20k iterations.

III. EXPERIMENT

A. Difference in Speed of Different Model Sizes

The difference in speed is obvious when we apply the trained parameters to different size models. We use a system Windows 10 with a CPU Inter Core i7-7700k(4.2GHz), memory 16 GB, and a graphics card NVIDIA GeForce GTX 1080Ti.

TABLE I. THE DETECTION SPEED SLOWS DOWN WITH THE INCREASE OF THE MODEL SIZES

Input Resolution	Items		
	Default boxes	FPS	mAP
300×300	8732	53	78.3
512×512	24564	29	82.2
1280×720	71760	11	76.6
1920×1080	193860	53	75.9

Table II shows that the detection speed slows down with the increase of the model sizes. Especially, the detection speed drops from 11FPS to less than 1FPS when size changes from 1280×720 to 1920×1080 . It is more than theoretical expectations. In fact, the total variable of the model with a size of 1920×1080 outnumbers the memory of our GPU so that a part of the calculation is put on the CPU. However, the calculation speed of CPU is much slower than that of GPU, which conduct that the real-time performance of 1920×1080 model is far worse than that expected. Our application use the model with a size of 1280×720 which is a little bit visually discontinuous with a speed of 11FPS, but it is enough for searching.

B. Application

The application as shown in figure II intends to use unmanned aerial vehicles to patrol independently, in order to find specially designated objects. When the targets is detected, the drone sends out an alarm and then returns home automatically. Figure 2 shows the block diagram of the system. We use a UAV DJI Phantom4 Pro with a remote control, a HDMI-to-USB3.0 acquisition card, an android mobile phone and a notebook computer.

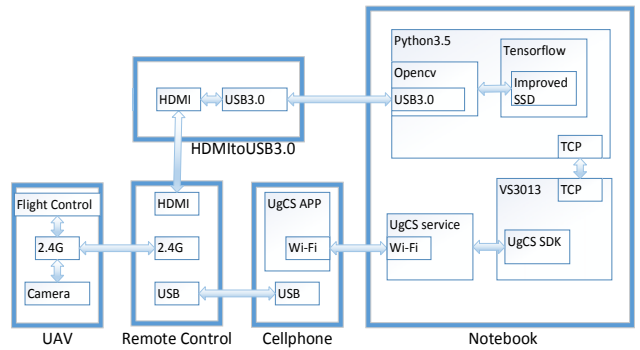


FIGURE II. SYSTEM BLOCK DIAGRAM OF THE APPLICATION

UgCS is a complete software to plan and fly drone survey missions, supporting most popular UAV platform, providing convenient tools for areal and linear surveys and enabling direct drone control. The preplanned path is introduced into the UAV through UgCS, and the UAV can completely patrol independently. At the same time, the real-time videos with a pixel size of 1280×720 captured by the UAV camera is transmitted to the remote control by the graphic transmission module. Through the HDMI interface on the remote control, the acquisition card converts the video into the UVC format and sends it into the notebook, which shows excellent real-time

performance. There are two main parts in the notebook, which are completed by Python and C#, respectively. The former completes the detection of video frames (not frame by frame but only real-time frames), and the latter uses UgCS SDK to control the UAV. The communication between the two depends on the socket. Once the target is found, it sends a voice alarm and controls the automatic return of the UAV. In the mission, the UAV is completely separated from human surveillance and control after taking off. The system delay is 0.24 seconds (Detection Processing + Transmission Delay). That is to say, the UAV finds the target and reacts accordingly when it flies to the target area for 0.24 seconds.

IV. CONCLUSION

Efficient real-time object detection in aerial HD videos is an urgent need, with the increasing use of UAV(Unmanned arm'd force:0 car:2 person:29 boat:6



Aerial Vehicles) in various fields. But it is still challenging to detect objects accurately and timely due to its large pixel size and relatively small objects. Recently, detection methods based on deep learning have rapidly advanced. However, they require numerous samples to train the detection model and cannot be directly used to efficiently handle large-area remote sensing HD videos. We use the popular SSD to detect people, cars, boats and so on from real-time HD videos which behave better than traditional methods. Moreover, we improve the deep learning algorithm by tailoring its networks and enlarging its size. We apply this algorithm to the real time detection of UAV aerial HD video and experiments show that our method can realize the organic combination of detection efficiency and detection effect. The detection results of some video frames is shown in Figure III.



FIGURE III.

EXAMPLES OF EXPERIMENTAL RESULTS

REFERENCES

- [1] Girshick, R.: Fast R-CNN. In: ICCV,2015.
- [2] Ren, S., He, K., Girshick, R., Sun, J.: Faster R-CNN: Towards real-time object detection with region proposal networks. In: NIPS,2015.
- [3] Redmon, J., Divvala, S., Girshick, R., Farhadi, A.: You only look once: Unified, real-time object detection. In: CVPR,2016.

- [4] Wei Liu. SSD: Single Shot MultiBox Detector[J]. ECCV16, 2016.
- [5] Simonyan, K., Zisserman, A.: Very deep convolutional networks for large-scale image recognition. In: NIPS,2015.
- [6] Bin Pan,Jianhao Tai,Qi Zheng,Shanshan Zhao,María Guijarro. Cascade Convolutional Neural Network Based on Transfer-Learning for Aircraft Detection on High-Resolution Remote Sensing Images[J]. Journal of Sensors,2017.

- [7] Chongyuan Tao. Pedestrian Detection in A Down-Looking Perspective Using Deep Learning[A]. Proceeding of The 2nd Asia-Pacific Computational Intelligence and Information Technology Conference (APCIIT2017)[C],2017.
- [8] Zhang, L., Lin, L., Liang, X., He, K.: Is faster r-cnn doing well for pedestrian detection. In:ECCV,2016.

Design of the UAV Digital Actuator Automatic Test System Based on Dual-core Microcontroller TMS320F28377D

Tao Yang*, Liren Chai and Gang Wang

China Academy of Aerospace Aerodynamics, Beijing, 100074, China

*Corresponding author

Abstract—For purpose of UAV digital actuator test, one of UAV's key components, whose static and dynamic performance impacts on the UAV maneuvering performance, this paper studies an automatic digital actuator test system, introduces its hardware and software design scheme, and demonstrates its application. The TI dual-core microcontroller TMS28377D serves as its core with abundant communication interfaces widely used in digital actuators such as RS422, RS485, RS232, and CAN Bus. Besides, there are rotary incremental encoders connected to the test system, providing the actual position information of digital actuator, as well as a SD card for data record in real time. Via Ethernet communication, the test system communicates with the upper computer which sends command and receives feedback. The advantages of automatic digital actuator designed in this paper are high reliability and easy upgrading. The automatic test system has great potential in the development, production and storage of the UAV digital actuator.

Keywords—UAV; digital actuator; automatic test system; TMS320F28377D

I INTRODUCTION

UAV, short for Unmanned Aerial Vehicle, is a reusable and controllable unmanned aircraft, carrying different payloads and executing different tasks. Thanks to its low cost, great reusability and high maneuver, UAV is widely used in military field, civilian area and scientific research [1]. As one of its key components, the actuator receives command from UAV flight control computer. The actuator is a typical servo system and it works as the control computer tells it to [2]. Its performance impacts on the UAV maneuvering performance severely. If not working properly, the UAV turns uncontrollable and stands a big possibility of crash on the ground, leading to heavy economic loss or even innocent casualty [3, 4]. As a prevailing trend, the digital actuator is now replacing the old-fashioned analog actuator. And this is what our research group is doing now. Although there are analog and PWM signal as the command and feedback signal for the current actuator, the newly developed actuator adopts digital signal for higher precision and better anti-interference ability. As a result, the corresponding automatic test system has to be designed. The automatic test system, which is pretty important in digital actuator debug, error detection and status indication during the whole process of development, production, storage and maintenance, provides the test support for the digital actuator

and offers footstone of actuator reliable performance [5, 6]. As long as the digital actuator can pass all the tests, it can be mounted in the UAV for flight mission. What's more, with the advance of the UAV technology, high stability, high precision, fast response and long life are the essential qualities of the digital actuator. The test system had better be updated easily just by software modification without any change of the hardware.

II DIGITAL ACTUATOR AUTOMATIC TEST SYSTEM

The controller and the electric actuator comprise the digital actuator. The controller is made up of different circuit with different functions, namely, communication interface, motor drive, power supply and digital control, while the electric actuator includes DC motor, drive reducer, output mechanism and potentiometer. As the core of the digital actuator, the controller communicates with the automatic test system via various digital communication interfaces. In the meanwhile, the automatic test system is linked to the upper computer for command transmission and data interaction. As shown in Figure I, the block scheme of system connection is presented. The digital interfaces between the digital actuator and automatic test system are RS422, RS485, RS232, and CAN Bus. There is the rotary incremental encoder mounted on the same axis of actuator output mechanism, and the reference of actual actuator position is given and sent back to the test system for the convenience of data analysis. Fast Ethernet communication circuit is the bridge of the automatic test system and the upper computer. The exclusive software developed in the upper computer sends command, receives data, and draws curves.

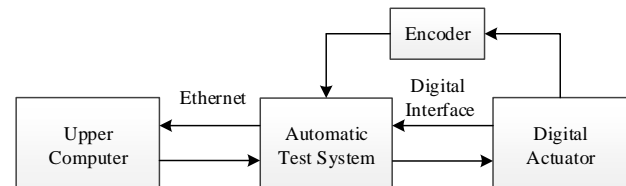


FIGURE I. SYSTEM CONNECTING BLOCK SCHEME

III THE HARDWARE DESIGN

As for the hardware design, it is introduced in the form of modular design. The digital control core is the TI microcontroller TMS320F28377D with dual-core architecture.

Power circuit offers power supply for different circuits in the system. The RS422/RS485/RS232 and CAN communication circuit conduct communication between the test system and the digital actuator. The Ethernet communication circuit connects the test system and the upper computer. The encoder circuit obtains position, direction and speed information from the rotary incremental. And the data storage circuit records the data online in real time via a SD card.

A. Digital Control Core

TMS320F28377D is a fast-speed and high-precision control chip with great reliability, in which two 32-Bit CPUs can cooperate together to provide 200 MHz of signal processing performance in each one. It supports up to 1MB of onboard flash memory with error correction code and up to 204KB of SRAM. The circuit design is simplified by its rich communication and control peripherals, among which the SCI, eCAN, SPI, and eQEP modules are used. As shown in Figure 2, the SPI modules are connected to the Ethernet circuit and the SD card; the SCI modules are connected to RS422, RS485 and RS232 transceivers; the eCAN module is connected to the CAN transceiver; the eQEP module is connected to the rotary incremental encoder.

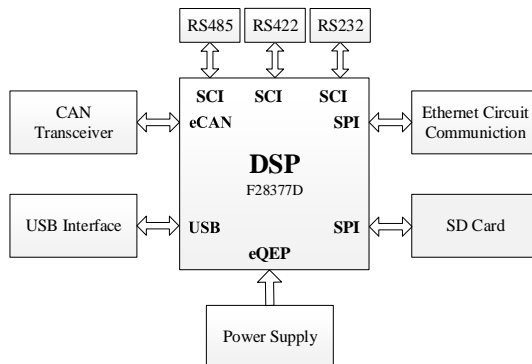


FIGURE II. BLOCK DIAGRAM OF THE DIGITAL CONTROL CORE

B. Power Circuit

The EMI filter helps eliminate the electromagnetic interference of DC power and then cleaner power supply +5V is obtained. As shown in Figure III, +5V is used to power up the CAN transceiver and the rotary encoder; the step down DC/DC converter TPS54331 is selected to transform +5V into +3.3V and +1.2V respectively to power up the control chip TMS320F28377D. And also +3.3V acts as the power source of the Ethernet controller and the RS422/RS485/RS232 transceiver.

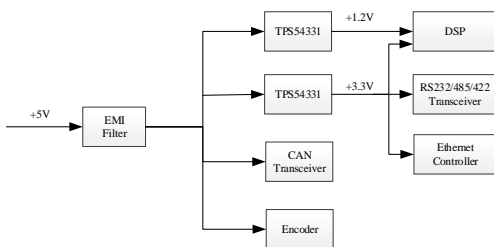


FIGURE III. SYSTEM POWER SUPPLY

C. RS422/RS485/RS232 Communication Circuit

Serial communication is used for all long-haul communication and it is becoming more and more common even at shorter distances because of improved signal integrity and transmission speed. The RS422, RS485 and RS422 are the typical standards for serial communication, which can be used in the digital actuator communication. So for high extensibility, the test system designs all these communication interfaces. As shown in Figure IV, MAX3490 serves as the RS422 transceiver in the communication circuit; MAX3485 serves as the RS485 transceiver in the communication circuit; MAX3232 serves as the RS232 transceiver in the communication circuit. For the simple reason that the three transceivers are able to operate from a single +3.3V supply, the SCITXD pin and SCIRXD pin of the F28377D SCI modules can directly connect to the transceivers' driver input and receiver output respectively.

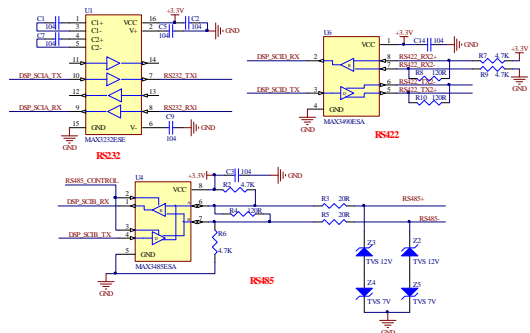


FIGURE IV. RS422/RS485/RS232 COMMUNICATION CIRCUIT

D. CAN Communication Circuit

The CAN bus is a robust message-based protocol, designed originally for multiplex electrical wiring within automobiles to save on cooper, but recently it is also used in many other contexts. The digital actuator is one of its application areas. As for TMS320F28377D, the CAN module is a serial communications protocol which efficiently supports distributed real-time control with a high level of reliability. The CAN module supports bit-rates up to 1 Mbit/s and is compliant with the ISO11898-1 (CAN 2.0B) protocol specification. In Figure V, it can be seen that fast CTM1050T with isolation is selected as the CAN transceiver. Despite the fact that it is powered by +5V, the electrical level of its driver and receiver are compatible with +3.3V, namely, the I/O level of TMS320F28377D. The CTM1050T can be connected to the CAN module directly via CAN_TX and CAN_RX.

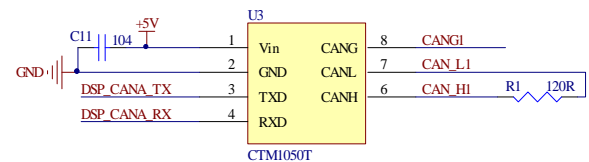


FIGURE V. CAN COMMUNICATION CIRCUIT

E. Ethernet Communication Circuit

The communication between the test system and the upper computer has to be fast and stable. In this case, the Ethernet communication is a perfect choice and W5500 is selected as the Ethernet controller. The W5500 chip is a hardwired TCP/IP embedded Ethernet controller that provides easier Internet connection to the digital control core by SPI peripheral. W5500's SPI supports 80 MHz speed and new efficient SPI protocol for the high speed network communication. W5500 embeds the 32Kbyte internal memory buffer for the Ethernet packet processing. It is fast and easy to implement the Ethernet application just by adding the simple socket program. As shown in Figure VI, the W5500's SPI works in the slave mode, and connects to TMS320F28377D SPI module via SCS, SCLK, MOSI and MISO. The TXN/TXP and RXN/RXP differential signals are linked to the HR91105A, a RJ45 connector with integrated magnetics.

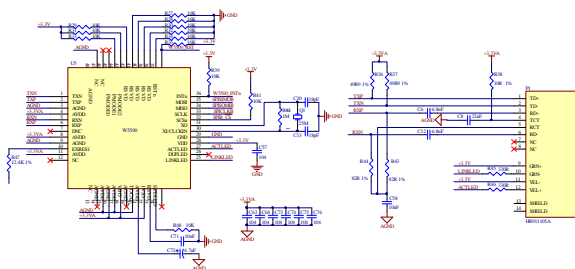


FIGURE VI. ETHERNET COMMUNICATION CIRCUIT

IV THE SOFTWARE DESIGN

The software design is made up of two parts, the DSP embedded software and the upper computer software. The embedded software refers to software of the digital control core TMS320F28377D, while the upper computer software offers the human-machine interaction. The embedded software conducts digital communication control, whose flow is as follows. At first, after power up, the control core is reset. And then it initiates the whole system control, SCI module, eCAN module, SPI module, eQEP module and the Cputimer0. The relevant vector table of peripheral interrupt controller and the interrupt function is initiated. Enable the global interrupt and then enter the while (1) infinite loop. The transmission of different communication peripherals with different intervals are triggered in Cputimer0 interrupt. The digital data acquisition is conducted by the communication peripheral receiver interrupts. In this way, the reliability and real-time performance of the digital data acquisition is ensured. Different digital actuators have different communication protocol. In order to meet the requirement of universality and easy upgrading, the communication protocol analysis is conducted in while (1) function. The test system sends data to the upper computer via the Ethernet controller with a period of 1ms and data length 40 bytes. As for the upper computer software shown in Figure VII, it transmits all kinds of commands to the automatic test system. After analyzing the commands, the test system sends corresponding commands to the digital actuator to perform automatic test. Also, it can accomplish data storage and draw curves of the data received in real time.

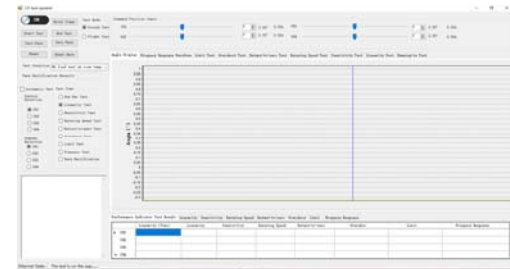


FIGURE VII. THE UPPER COMPUTER SOFTWARE

V CONCLUSION

As UAV's key component, the digital actuator is a determinant factor for UAV performance. To find out whether the digital actuator works well or not before flight, the automatic test system is needed. In this paper, the automatic digital actuator test system is developed with the dual-core TMS28377D with high reliability as its control core. The automatic system facilitates digital actuator debug, error detection and status indication with rich communication interfaces in the whole life span of the digital actuator from development and production to storage and maintenance. Taking different factors into consideration when the automatic test system is designed, its advantages such as fast response, high reliability and easy upgrading are not hard to figure out, which is also verified by a recent digital actuator test with CAN communication interface. As more and more digital actuators designed in our research group, the application prospect of the automatic test system is apparently promising. Time will tell and prove its superiority in the digital actuator test field.

References

- [1] Di Bin, Zhou Rui, Ding Quanxin, Distributed Coordinated Heterogeneous Task Allocation for Unmanned Aerial Vehicles, *Control and Decision*. 2 (2013) 274-278.
- [2] Li Saihui, Lei Jinkui, Design and Implementation of Digital Rudder Control System Based on DSP, *Computer Measurement and Control*. 3 (2009) 484-486.
- [3] Zhou Xiaoqing, Design and Implement of Electrical Actuator Control System of High Speed Unmanned Aerial Vehicle, Hangzhou: Zhejiang University, 2010.
- [4] Kong Xiangji, Hou Wen, Chen Chunxi, Digital Rudder Control System Based on DSP, *Electronic Test*. 13 (2013) 31-32.
- [5] Zhao Qiang, Liu Songfeng, Cheng Peng, Development and Key Technology in General Purpose Automatic Test System, *Electronic Design and Engineering*. 5 (2011) 160-162.
- [6] Huang Shenglin, Shen Conghui, Sun Weichao, Core of NxTest: Synthetic Instrument System, *Electronic Measurement Technology*. 5 (2011) 64-67.

A Load Identification Technology for Wireless Smart Home Systems

Zhenchao Xie^{1,*}, Daohong Lin¹, Yufeng Chen² and Xinshu Wan¹

¹Electric Power Research Institute of Hainan Power Grid Co., Ltd., Haikou 570125, Hainan Province, China

² Nanjing Sifang E-power Automation Co., Ltd., Nanjing 211111, China

*Corresponding author

Abstract—Aiming at the applications in wireless smart homes, a wireless charging system based on LCL topology is designed. Moreover, the constant-current (CC) output of the system is realized according to the charging characteristics of lithium batteries. On this basis, a charging strategy is proposed, which is able to identify load characteristics and take corresponding actions after the access of loads in smart homes to the system, and can guarantee the safety of the loads in power supply process. Finally, an experimental prototype of the system was established to wirelessly charge the lithium battery with a nominal voltage of 7.4 V and verify the validity of the proposed charging strategy for protecting the system when illegal loads were connected in the system.

Keywords—wireless power transfer; load identification; lithium battery; charging strategy

I. INTRODUCTION

Research on the wireless power transfer (WPT) technology has never stopped ever since the proposal of the technology. Compared with traditional wire power transfer approaches, WPT has many advantages, such as being more flexible, safe, and reliable. It avoids potential safety hazards such as electric sparks of wired connection [1-4]. Characterized by these advantages, the WPT technology has been widely used in smart homes. At present, many smart homes are powered by lithium batteries, the whole charging process of which has two phases: CC charging and constant-voltage (CV) charging processes [5].

In general, to realize the control over the CC and CV charging of lithium batteries, a specific direct current (DC) CV/CC conversion circuit needs to be designed [6-7]. For example, CV power supply is provided for handheld devices by adding DC converters in the secondary side of the wireless charging system in previous research [6]. Existing studies also found that resonant WPT systems have inherent CC characteristics under specific topological structures and frequencies. If the topological structures of WPT systems can be used to realize the CC charging of lithium batteries, it is of great significance for reducing the complexity of the back-end circuits of the systems.

Meanwhile, to guarantee the operation safety of wireless smart home systems, corresponding protections need to be designed for the systems. As the transmission characteristics of WPT systems are related to the system loads (batteries), the random access of batteries of different voltage classes is disadvantage for the safe operation of wireless systems with

given parameters. If we can detect the properties and sizes of loads after the loads are connected to the system and then control the system on this basis, the safety of the system can be improved. Aiming at the problem, an effective identification method for loads was put forward in previous study [8]. The method allows one to detect the sizes and properties of loads connected to the systems by means of the energy injection mode and the free harmonic vibration mode.

Based on wireless smart home systems, the research designs a wireless charging system. The LCL compensation network is always in the primary side of the system. By reasonably designing the compensation network in the primary side, the LCL-LCL wireless system is formed, which is used for controlling the CC charging of lithium batteries. Then, a charging strategy of the system is proposed based on the reflection and impedance characteristics of the system. The charging strategy enables the system to identify illegal loads and improves the safety of the system. Finally, an experimental prototype of the system was built to carry out wireless charging of the lithium battery with a nominal voltage of 7.4 V and verify the validity of the proposed charging strategy after the access of illegal loads to the system.

II. DESIGN OF THE WIRELESS CHARGING SYSTEM

When factors including the internal resistance are ignored, the schematic diagram of the ideal LCL circuit is illustrated in Figure I, where U_{in} represents the input power, L_X and L_p denote inductances, C_P refers to compensating capacitor, and Z represents equivalent load. Let the parameters $L_X=L_p$ and $\omega_0=\sqrt{1/L_p C_p}$, the current i_{Lp} flowing through the load Z is $U_{in}/(j\omega_0 L_p)$ when the system works at the resonant angular frequency ω_0 .

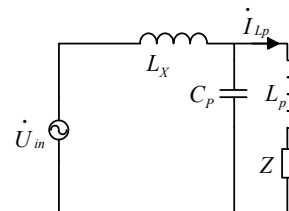


FIGURE I. SCHEMATIC DIAGRAM OF THE CIRCUIT BASED ON LCL TOPOLOGY

Under the condition, the current i_{Lp} of the load is irrelevant to Z but only related to the power source U_{in} , inductance L_p ,

and the resonant angular frequency ω_0 . That is, the branch current in the LCL circuit where the inductance has CC characteristics. Suppose that the CC characteristics of LCL topology are combined with WPT systems, LCL topology is taken as the topological structure of the wireless energy transmit side, and the inductance L_p is assumed as the equivalent inductance of the transmit coil. Under the condition, it is equivalent to add a voltage source with the voltage of $j\omega M I_{Lp}$ in the branch of the receiving coil (inductance) L_s in the receiving side according to the M model. The value of the voltage source is merely influenced by the power source in the transmit side but not impacted by the circuit parameters in the receiving side.

To endow the loads in the receiving side with the CC output characteristics, it is necessary to further design the topological structure in the receiving side. According to the connection mode of coils and capacitors, the authors design the LCL topology for the receiving side, as illustrated in Figure II. In the figure, U_{in} represents a high-frequency alternating current (AC) power source, L_x and L_y are the inductances of the compensating inductor, C_p and C_s denote the capacitances of the compensating capacitor, L_p and L_s represent the inductances of the transmit and the receiving coils, M refers to the mutual inductance between the transmit and receiving coils. A microprocessor MCU1 is placed in the primary side of the system to control the value of the input voltage U_{in} by detecting the effective value of the voltages of the compensating capacitor in the primary side. A switch S_4 is set in the secondary side to protect the system and controlled by the microprocessor MCU2.

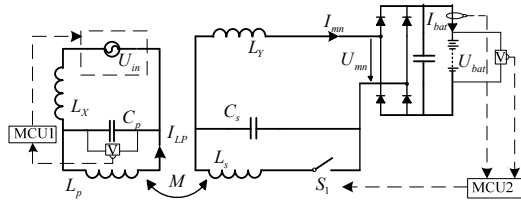


FIGURE II. EQUIVALENT CIRCUIT DIAGRAM OF THE WIRELESS CHARGING SYSTEM

Let the inductances be $L_x=L_y=L_p=L_s=L$, the capacitances be $C_p=C_s=C$, and the working angular frequency be $\omega=\sqrt{1/LC}$ in the system. While analyzing the output characteristics of the system in the section, it is assumed that the system works normally and the switch S_4 is closed. In this way, a connection mode based on LCL-LCL topology is formed in the primary and secondary sides of the system. Then, the current I_{Lp} flowing through the transmit coil is

$$I_{Lp} = U_{in}/j\omega L \quad (1)$$

Obviously, the value of I_{Lp} is merely related to the parameters in the primary side. According to the theory of mutual inductance, it is equivalent to introduce a constant controlled voltage source $j\omega M I_{Lp}$ in the primary side of the system. In accordance with the calculation, it can be found that the current I_{mn} flowing before the rectifier is

$$\mathbf{I}_{mn} = M \mathbf{U}_{in} / (j\omega L^2) \quad (2)$$

It can be seen that the current before the rectifier is not related to the size and properties of the loads. The following current relation before and after the rectifier can be obtained:

$$I_{bat} = 2\sqrt{2} |\mathbf{I}_{mn}| / \pi. \quad (3)$$

Then, it can be learnt from Formulae (2) and (3) that based on the LCL-LCL topology, the current flowing through the battery is

$$I_{bat} = 2\sqrt{2} M |\mathbf{U}_{in}| / (\pi \omega L^2) \quad (4)$$

Apparently, the charging current of the battery does not change after the parameters of the system are set. It means that the system achieves CC output in the connection mode based on LCL-LCL topology.

III. CHARGING STRATEGY OF THE SYSTEM

While WPT technology is applied to charge batteries, WPT systems need to be designed with different parameters for different batteries. In other words, a designed WPT system can merely charge specific type of batteries. Other types of batteries cannot enter the system optionally. It is stipulated that in the wireless charging system in Figure II built according to the actual charging demand of batteries, the corresponding batteries are legal loads while other loads whose nominal voltages are different with the legal loads are illegal loads. As the nominal voltage of illegal loads has disparities with that of the legal loads and different batteries have dissimilar bearable charging currents, the access of illegal loads can probably damage the batteries. Therefore, it is necessary to analyze the protection of the loads after illegal loads enter a WPT system.

Suppose that for a lithium battery, its nominal voltage is $U_{bat,n}$, the voltage of the fully charged battery is $U_{bat,s}$, the minimum voltage in under-voltage state is $U_{bat,u}$, and the charging current of the battery during CC charging is $I_{bat,p}$. The external circuit of the lithium battery can be regarded as linking a DC power source in the two sides of the battery at any moment during the charging, and its voltage is the voltage U_{bat} of the battery and the charging current is I_{bat} . Therefore, the external circuit of the battery can be equivalent to a varying resistance $R_{bat,eq}=U_{bat}/I_{bat}$.

As shown in Figure II, the voltage of the power source in the primary side of the system is controlled by MCU1 which controls the switch of the power source between two working conditions: one is the normal working state, in which the output voltage of the inverter is U_{in} ; and the other is standby state, in which the output voltage of the inverter is $U_{in,s}$, and $U_{in,s} \ll U_{in}$. According to Formula (4), as the power source in the two states has different voltages, the charging current of the battery also changes in the system based on LCL-LCL topology. Therein, the charging current of the battery in normal working state is $I_{bat,p}$.

$$I_{bat,p} = 2\sqrt{2}M|\mathbf{U}_{in}|/(\pi\omega L^2) \quad (5)$$

In the standby state, the charging current is $I_{bat,s}$.

$$I_{bat,s} = 2\sqrt{2}M|\mathbf{U}_{in,s}|/(\pi\omega L^2) \quad (6)$$

On the basis of the above analysis, the identification of illegal loads and the protection measures for the system are shown as follows:

1) When no battery enters the system, the system is in the standby state and the output of the inverter is $\mathbf{U}_{in,s}$. Under the condition, all of the switches in Figure I are turned off and the voltage in two sides of the compensating capacitor C_p is $U_{in,s}$.

2) When there is battery connected to the system, the secondary side of the system detects the voltage U_{bat} in two sides of the battery. If the voltage satisfies

$$U_{bat,u} < U_{bat} < U_{bat,s} \quad (7)$$

then the secondary side believes that the battery entering the system is a legal load and the S_1 is turned on under the control of MCU2. Under the condition, the system forms a LCL-LCL topology. The information of the primary side is independent to that of the secondary side, and the primary side identifies the load in the system by detecting the voltage in the two sides of the compensating capacitor C_p in real time. Then the relation between the equivalent resistances before and after the known rectifier is

$$R_{mn} = 8R_{bat,eq}/\pi^2 \quad (8)$$

Where $R_{mn} = \mathbf{U}_{mn}/\mathbf{I}_{mn}$. Based on this, it is obtained that the voltage in the two sides of the compensating capacitor C_p and the load has the following relation in the LCL-LCL topology:

$$\dot{\mathbf{U}}_{Cp} = \dot{\mathbf{U}}_{in}(1 + \omega M^2 CR_{mn} / (jL^2)) \quad (9)$$

Then, the relation between the effective value of the voltage in the two sides of the compensating capacitor C_p and the load is

$$|U_{Cp}| = |U_{in}| \sqrt{(1 + M^4 R_{mn}^2 / (\omega^2 L^6))} \quad (10)$$

Formula (8) reveals that if the battery in the system is a legal load, then the equivalent resistance of the battery meets

$$U_{bat,u} / I_{bat,s} \leq R_{bat,eq} \leq U_{bat,s} / I_{bat,s} \quad (11)$$

It is deduced that the equivalent resistance before rectification satisfies

$$\frac{8U_{bat,u}}{\pi^2 I_{bat,s}} \leq R_{mn} \leq \frac{8U_{bat,s}}{\pi^2 I_{bat,s}} \quad (12)$$

By substituting Formula (12) into (10), it is observed that if the primary side finds that $|\mathbf{U}_{Cp}|$ meets the following condition

$$|\mathbf{U}_{in,s}| \sqrt{(1 + \frac{64M^4 U_{bat,u}^2}{\pi^4 \omega^2 L^6 I_{bat,s}^2})} \leq |\mathbf{U}_{Cp}| \leq |\mathbf{U}_{in,s}| \sqrt{(1 + \frac{64M^4 U_{bat,s}^2}{\pi^4 \omega^2 L^6 I_{bat,s}^2})}, \quad (13)$$

then the primary side regards the battery as a legal load. Afterwards, the power source is switched to the normal working voltage \mathbf{U}_{in} under the control of MCU1, turning the system to the normal working state.

3) If the battery entering the system is detected as an illegal load, the voltage in the two sides of the battery detected by the primary side of the system does not meet Formula (7), then the switch in the secondary side is turned off under the control of the MCU2. Under the condition, the capacitor voltage detected by the primary side of the system is still

$$|\mathbf{U}_{Cp}| = |\mathbf{U}_{in,s}|. \quad (14)$$

Under the control of MCU1, the output voltage of the inverter is still the standby voltage $U_{in,s}$, that is, the system is still in the standby state.

IV. EXPERIMENTAL VERIFICATION

To verify the validity of the proposed charging strategy for batteries, the research took a lithium battery with a nominal voltage of $U_{bat,n}=7.4$ V as the charging object. After being fully charged, the battery has an open-circuit voltage of $U_{bat,s}=8.4$ V. Let the charging current of the lithium battery in CC charging mode be $I_{bat,p}=1$ A. Based on the above charging parameters of the battery, the authors established the experimental prototype, and the parameters of the system are displayed in Table I. After building the system, the lithium battery became a legal load of the system. In the experimental prototype, the transmit and receiving coils of 12 turns were wound using Litz wires of 1.5 mm wide, and the spacing between them was 3 cm. The bridge inverter circuit was taken for the inverter and the bridge driving chip UCC3895 was used to drive four IRFP460 MOS tubes. In the standby state, the input voltage $U_{in,s}$ of the system was 1 V, while the input voltage U_{in} in the normal working state was 36.5 V.

TABLE I. SYSTEM PARAMETERS

Parameters	Value	Parameters	Value
$L_p=L_s=L_x=L_y=L$	12μH	$U_{in,s}$	1V
M	2.5μH	f	90kHz
U_{in}	36.5V	$C_p=C_s=C$	0.26μF

After the accesses of the legal load to the system, the S_1 was turned on under the control of MCU2. In this way, the

system formed a LCL-LCL topology allowing the CC output and the MCU1 adjusted the input voltage of the system to 36.5 V, so that the system can normally charge the lithium battery. Figure III shows the changes of the charging current and voltage of the battery when the system charges the legal load.

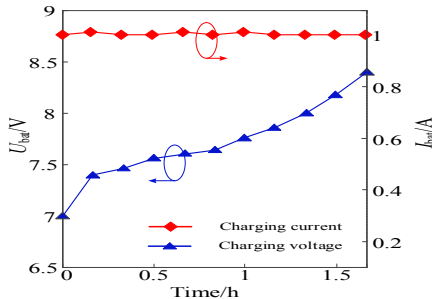


FIGURE III. CHANGES OF THE CHARGING VOLTAGE AND CURRENT OF THE BATTERY WITH TIME

It can be seen that in the CC mode, the charging current of the battery maintained at 1 A while the voltage of the battery gradually enlarged with time, till reaching $U_{\text{bat},s}$, that is, 8.4 V. According to the above analysis relating the charging strategy of the system, all of the switches in the system were turned off before the access of the battery, the voltage of the power source was the standby voltage, and the voltage of the compensating capacitor U_{Cp} was equal to that of the power source. After the access of the legal load to the system, the switch S_1 was turned on, and U_{Cp} should meet Formula (13). If the battery connected to the system was an illegal load, the switch in the secondary side was still turned off and U_{Cp} still equaled the standby voltage of the power source. To verify whether Formula (13) is able to identify illegal loads in the system, four groups of lithium batteries of different voltage classes were used in the experiment. The switch S_1 was turned on to measure the voltage U_{Cp} in the two sides of the compensating capacitor C_p after the access of different batteries to the system with same parameters.

The nominal voltages of the batteries connected to the system were 7.4 V, 3.7 V, 11.1 V, and 14.8 V in the A, B, C, and D groups of experiments, respectively. Among them, the battery in the A group was the legal load corresponding to the system. For a lithium battery with a nominal voltage of 7.4 V, its voltage changes in the range of 7~8.4 V, that is, $U_{\text{bat},u}=7$ V and $U_{\text{bat},s}=8.4$ V. According to Formula (10), when the voltage of the power source of the system was the standby voltage $U_{\text{in},s}$, the output current of the system in CC mode was $I_{\text{bat},s}=0.028$ A. Then, the authors defined the detection range of legal loads based on Formula (13). That is, when the voltage U_{Cp} of the compensating capacitor in the primary side of the system was detected to satisfy Formula (13), the primary side judged that the battery was a legal load. According to the data in Table I, the voltages of the compensating capacitor need to meet $1.65 < U_{\text{Cp}} < 1.87$ when the battery entering the system is a legal load through calculation. Figure IV displays the detected voltages of the compensating capacitor after the access of the four groups of batteries to the system when the S_1 was switched on.

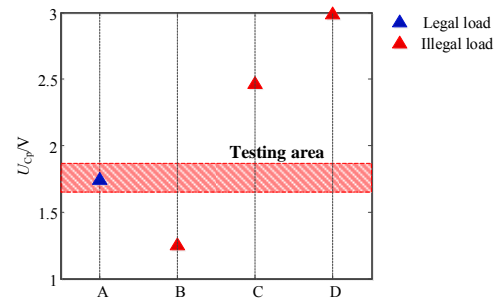


FIGURE IV. DETECTION PROCESS OF LEGAL LOADS

In the A group of experiment, the battery connected to the system had an open-circuit voltage of 7.2 V, and it was detected that $U_{\text{Cp}}=1.69$ V, which fell into the detection range of legal loads. Therefore, the battery was judged as a legal load. In the B group of experiment, the open-circuit voltage of the battery was 4 V and $U_{\text{Cp}}=1.25$ V, which did not satisfy Formula (13), so the system judged that the battery was an illegal load. Similarly, in the C and D groups of experiment, the voltages of the compensating capacitor were measured to be 2.46 V and 2.98 V, also not meeting Formula (13). Therefore, the system judged that the two batteries were also illegal loads. The comparison between the judgment results of the system and the real conditions of the batteries shows that the designed charging strategy can accurately identify the properties of batteries in the system and thereby improves the safety of the system.

V. CONCLUSIONS

The research put forwards the LCL-LCL topology that can realize the CC output by investigating the output characteristics of the WPT systems with different compensation topological structures. Then, the above topology is applied to the wireless charging of lithium batteries. Based on the above analysis, the authors design the wireless charging system allowing CC charging and propose the charging strategy of wireless charging systems combining the charging characteristics of lithium batteries. The charging strategy not only can guarantee the CC charging of lithium batteries, but also can identify illegal loads in the system and make corresponding responses, thus improving the safety of the system. Finally, the experimental prototype of the system was built to charge the lithium battery with a nominal voltage of 7.4 V wirelessly. Meanwhile, it is verified that the system can accurately identify illegal loads when they enter the system.

ACKNOWLEDGEMENT

This research is supported by China Southern Power Grid Corporation (Research and Application of Key Technologies of Intelligent Cloud Service in Hainan Power Grid).

REFERENCES

- [1] X. Huang, W. Wang, L. Tan, "Fast non-intrusive load identification algorithm for resident load based on template filtering," in *Automation of Electric Power Systems*, vol. 41, no. 2, pp. 2-14, 2017.
- [2] Y. Zhai, Y. Sun, X. Dai, et al, "Modeling and analysis of magnetic resonance wireless power transmission systems," in *Proceedings of the CSEE*, vol. 32, no. 12, pp. 155-160, 2012.

- [3] Q. Yang, P. Zhang, L. Zhu, et al, "Key fundamental problems and technical bottlenecks of the wireless power transmission technology," in Transactions of China Electrotechnical Society, vol. 30, no. 5, pp. 1-8, 2015.
- [4] A. Kurs, A. Karalis, Moffatt R, et al, "Wireless power transfer via strongly coupled magnetic resonances," in Science, vol. 317, no.5834, pp. 83-86, 2007.
- [5] A. Khaligh, Z. Li, "Battery, Ultracapacitor, Fuel Cell, and Hybrid Energy Storage Systems for Electric, Hybrid Electric, Fuel Cell, and Plug-In Hybrid Electric Vehicles: State of the Art," in IEEE Transactions on Vehicular Technology, vol. 59, no. 6, pp. 2806-2814, 2010.
- [6] J. T. Boys, G. A. Covic, Y. Xu, "DC analysis technique for inductive power transfer pick-ups," in IEEE Power Electronics Letters, vol. 99, no. 2, pp. 51-53, 2003.
- [7] H. H. Wu, A. Gilchrist, K. D. Sealy ,et al, "A High Efficiency 5 kW Inductive Charger for EVs Using Dual Side Control," in IEEE Transactions on Industrial Informatics, vol. 8, no. 3, pp. 585-595, 2012.
- [8] Z. H. Wang, Y. P. Li, Y. Sun, et al. "Load Detection Model of Voltage-Fed Inductive Power Transfer System," in IEEE Transactions on Power Electronics, vol. 28, no.11, pp. 5233-5243.

A Feasible Control Method for Incomplete Symmetrical Marine Robot

Lei Zhang^{1,*}, Zaopeng Dong², Yongsuo Yan¹ and Yuyin Cao¹

¹Harbin Engineering University, College of Shipbuilding Engineering, Harbin City, HeilongJiang Province, China

²Wuhan University of Technology, School of Transportation, Wuhan City, Hubei Province, China

*Corresponding author

Abstract—For the incomplete symmetrical underactuated USV (unmanned surface vehicle), this paper proposed a global asymptotic stabilization control method. The global diffeomorphism transformation for the USV model was performed twice in order to obtain the form of nonlinear cascade systems, so the stabilization problem of the original USV system was simplified to the stabilization of the cascade systems. Then the cascade system stabilization controller was designed based on Backstepping, realize the global asymptotic stabilization control of the incomplete symmetrical underactuated USV. Effectiveness and reliability of the research methods and the controller designed was verified by simulation results.

Keywords—USV; global asymptotic stabilization; underactuated control; cascade systems; backstepping

I INTRODUCTION

Surface robots, also called USV (unmanned surface vehicle), was a kind of small ships, which can autonomous navigate in the actual ocean and complete corresponding mission. Because of the superiority in intelligence, surveillance, reconnaissance, naval protection, demining, antisubmarine, precision, search and rescue, navigation and hydrographic investigation, USV had been paid much attention by the world navy, USV was developing rapidly in recent decades. The motion control technology was a key technology to realize unmanned autonomous control of USV, and the stabilization control was a key link. About the stabilization control of USV, many researchers had conducted relative study, and published a number of research results.

M.Reyhanoglu (1996) discussed the stabilization of USV control. In this work, transformation method was used to design the time invariant continuous feedback control law, make the system to achieve global exponential stability. Base on differential geometry theory, J.Ghomman et al. studied the stabilization control of underactuated USV and designed time-varying discrete feedback control law using differential homeomorphism transform. Through adding index convergence item to the state feedback control of underactuated ships, Liao et al. designed the time-varying smooth stabilization control law, and make the system to achieve global exponential stability. Ma Baoli got the exponential stability variable switching control law of underactuated USV using discontinuous coordinate transformation and Lyapunov like switching function, but because of the switching, the control law is discontinuous. LIU et al. proposed an algorithm using diffeomorphism

transformation and control input transformation, transformed the motion model of ship into a cascade system, designed feedback control law based on Backstepping, and demonstrate the stability. Kristin and Thor proposed the feedback control law about time function using combined back-to-back method and homogenous method, accelerated the speed of system stabilization, and verified the system clam in a field near the equilibrium point by experimental, but there was an ineradicable oscillations at the equilibrium point. Mazenc et al. designed a time-varying smooth state feedback controller using Backstepping, made the USV can achieve uniform global asymptotic stability.

Except for some special limitations and defects, all of the stabilization controllers of USV designed by the scholars, were assume that the motion model of USV was fore-aft and bilateral symmetry (because just study the USV motion in the horizontal plane, the up-down symmetry was not considered). This did not tally with the actual model of USV, USV was only bilateral symmetrical, but not fore-aft symmetrical. This paper studied the incomplete symmetrical USV, the USV was bilateral symmetrical, but not fore-aft symmetrical, in this case, nonzero terms existed in the off-diagonal elements of the USV added mass coefficient, the inertia coefficient matrix and the damping coefficient matrix of the USV motion were no longer the diagonal line of the standard, not all the off-diagonal elements were zero.

II INCOMPLETE SYMMETRICAL USV MODEL

A. Kinematics and Dynamics Model

This paper mainly study the motion of USV in surge, sway and yaw, the kinematic model of the system can be written as follows[8]:

$$\dot{\eta} = R(\varphi)\nu \quad (1)$$

where, η is the state vector of systems, and $\eta = [x, y, \varphi]^T$. x is the surge displacement, y is the sway displacement, φ is the yaw angle, the reference direction is north. R is Rotation Matrix of yaw, defined as: $R(\varphi) = \begin{pmatrix} \cos \varphi & -\sin \varphi & 0 \\ \sin \varphi & \cos \varphi & 0 \\ 0 & 0 & 1 \end{pmatrix}$.

where, v is the velocity vector, and $v = [u, v, r]^T$. u is the surge velocity of the USV, v is the sway velocity, r is the yaw palstance.

The nonlinear dynamical model of the USV in horizontal plane is as follow[8]:

$$M(v)\dot{v} + C(v)v + D(v)v = \tau. \quad (2)$$

where, M is the inertia coefficient matrix, C is the centripetal force matrix, D is the damping coefficient matrix. They are respectively defined as:

$$\begin{aligned} M &= \begin{bmatrix} m_{11} & 0 & 0 \\ 0 & m_{22} & m_{23} \\ 0 & m_{32} & m_{33} \end{bmatrix}, \quad C = \begin{bmatrix} 0 & 0 & C_{13} \\ 0 & 0 & C_{23} \\ C_{31} & C_{32} & 0 \end{bmatrix}, \quad D = \begin{bmatrix} d_{11} & 0 & 0 \\ 0 & d_{22} & d_{23} \\ 0 & d_{32} & d_{33} \end{bmatrix}, \\ C_{13} &= -C_{13} = -m_{22}v - \frac{1}{2}(m_{23} + m_{32})r, \quad C_{23} = -C_{32} = m_{11}u. \end{aligned}$$

where, τ is control force, the USV system is underactuated, so just consider the input in surge and yaw, and $\tau = [\tau_u \ 0 \ \tau_r]^T$.

B. Global Diffeomorphism Transformation

Due to the off-diagonal elements of the matrix (the inertia coefficient matrix and the damping coefficient matrix) of the USV system are not all zero, the analysis and design of the USV system are more difficult. In order to overcome this problem, the global diffeomorphism transformation for the USV model was performed twice, and obtained the form of cascade systems.

1) Diffeomorphism transformation-A

$$\begin{cases} z_1^* = x + \frac{m_{23}}{m_{22}}(\cos\varphi - 1) \\ z_2^* = y + \frac{m_{23}}{m_{22}}\sin\varphi \\ z_3^* = \varphi \\ z_4^* = u \\ z_5^* = v + \frac{m_{23}}{m_{22}}r \\ z_6^* = r \end{cases}, \text{ it can be described as:}$$

$$\begin{cases} \dot{z}_1^* = z_4^* \cos(z_3^*) - z_5^* \sin(z_3^*) \\ \dot{z}_2^* = z_4^* \sin(z_3^*) + z_5^* \cos(z_3^*) \\ \dot{z}_3^* = z_6^* \\ \dot{z}_4^* = f_1^* \\ \dot{z}_5^* = -\alpha z_4^* z_6^* - \beta z_5^* + \gamma z_6^* \\ \dot{z}_6^* = f_2^* \end{cases}. \quad (3)$$

If the control input by feedback can be changed as:

$$\begin{cases} f_1^* = \frac{1}{m_{11}} \left(\tau_u + m_{22}vr + \frac{(m_{23} + m_{32})}{2}r^2 - d_{11}u \right) \\ f_2^* = \frac{m_{22}}{m_{22}m_{33} - m_{32}m_{23}} \left\{ \tau_r + \frac{(m_{11}m_{22} - m_{22}^2)uv + [m_{11}m_{32} - \frac{m_{22}(m_{23} + m_{32})}{2}]ur}{m_{22}} \right. \\ \left. + \frac{(m_{32}d_{22} - m_{22}d_{32})v - (m_{22}d_{33} - m_{32}d_{23})r}{m_{22}} \right\} \end{cases}$$

$$\text{where, } \alpha = \frac{m_{11}}{m_{22}}, \quad \beta = \frac{d_{22}}{m_{22}}, \quad \gamma = \frac{d_{22}m_{23}}{m_{22}^2} - \frac{d_{23}}{m_{22}}.$$

The stabilization target of the original USV system is: design suitable control input τ_u, τ_r , make u, v, r, x, y, φ of the USV system global asymptotic stabilization. After the diffeomorphism transformation, the target is: design suitable control input f_1^*, f_2^* , make $z_1^*, z_2^*, z_3^*, z_4^*, z_5^*, z_6^*$ global asymptotic stabilization. Because the system is still complex after transformation, not suitable for the stability analysis of stabilization control and the design of controller directly, the global diffeomorphism transformation for System(3) was performed again.

2) Diffeomorphism transformation-B

$$\begin{cases} z_1 = z_1^* \cos(z_3^*) + z_2^* \sin(z_3^*) \\ z_2 = -z_1^* \sin(z_3^*) + z_2^* \cos(z_3^*) + \frac{1}{\beta}z_5^* - \frac{\gamma}{\beta}z_3^* \\ z_3 = z_3^* \\ z_4 = -\frac{\alpha}{\beta}z_4^* - z_1^* \cos(z_3^*) - z_2^* \sin(z_3^*) \\ z_5 = z_5^* \\ z_6 = z_6^* \end{cases}.$$

Transform the control input by feedback change as:

$$\begin{cases} f_1 = -\frac{\alpha}{\beta}f_1^* + \frac{\beta}{\alpha}(z_1 + z_4) - z_2z_6 + \frac{1}{\beta}z_5z_6 - \frac{\gamma}{\beta}z_3z_6 \\ f_2 = f_2^* \end{cases}$$

Then, obtain the new system as follow:

$$\begin{cases} \dot{z}_1 = -\frac{\beta}{\alpha}z_1 - \frac{\beta}{\alpha}z_4 + z_2z_6 - \frac{1}{\beta}z_5z_6 + \frac{\gamma}{\beta}z_3z_6 \\ \dot{z}_2 = z_4z_6 \\ \dot{z}_3 = z_6 \\ \dot{z}_4 = f_1 \\ \dot{z}_5 = -\beta z_5 + \beta(z_4 + z_1)z_6 + \gamma z_6 \\ \dot{z}_6 = f_2 \end{cases}. \quad (4)$$

So far, system (3) is transformed to the form as system (4) by homeomorphic transformation, corresponding stabilization target is transformed as: design suitable control input f_1, f_2 ,

make $z_1, z_2, z_3, z_4, z_5, z_6$ global asymptotic stabilization. To facilitate the analysis of system (4), it is written in the form of a cascade system:

$$\begin{cases} \dot{z}_1 = -\frac{\beta}{\alpha}z_1 - \frac{\beta}{\alpha}z_4 + z_2z_6 - \frac{1}{\beta}z_5z_6 + \frac{\gamma}{\beta}z_3z_6 \\ \dot{z}_5 = -\beta z_5 + \beta(z_4 + z_1)z_6 + \gamma z_6 \end{cases} . \quad (5)$$

$$\begin{cases} \dot{z}_2 = z_4z_6 \\ \dot{z}_3 = z_6 \\ \dot{z}_4 = f_1 \\ \dot{z}_6 = f_2 \end{cases} . \quad (6)$$

III GLOBAL ASYMPTOTIC STABILIZATION ANALYZE

First, here is the three lemmas required in the process of stabilization analysis:

Lemma 1[9]: the nonlinear cascade system is the following form:

$$\begin{aligned} \sum_1: \dot{x}_1 &= f_1(t, x_1) + G(t, x)x_2 \\ \sum_2: \dot{x}_2 &= f_2(t, x_2, u) \end{aligned} .$$

where, $x = [x_1, x_2]^T$, function $f_1(t, x_1)$ is continuously differentiable on (t, x_1) , $f_2(t, x_2, u)$, $G(t, x)$ are local Lipschitz continuous in the interval. If meet the following conditions:

(1)system $\dot{x}_1 = f_1(t, x_1)$ is global uniform asymptotic stabilized;

(2)exist control law u , make system $\sum_2: \dot{x}_2 = f_2(t, x_2, u)$ global asymptotic stabilized;

(3)exist continuous function $\theta_1(\cdot): \mathbb{R}_+ \rightarrow \mathbb{R}$ and $\theta_2(\cdot): \mathbb{R}_+ \rightarrow \mathbb{R}$, make function $G(t, x)$ meet the conditions:

$$\|G(t, x)\|_2 \leq \theta_1(\|x_2\|_2) + \theta_2(\|x_2\|_2)\|x_1\|_2$$

Then, the nonlinear cascade system is global uniform asymptotic stabilized.

Lemma 2[10]: if within a domain $D \subset R^n$, $f(t, x)$ and $\frac{\partial f}{\partial x}(t, x)$ is continuous in $[a, b] \times D$, then for x , f is local Lipschitz continuous in $[a, b] \times D$.

Lemma 3(Barbalat Lemma): assume $x: [0, \infty) \rightarrow R$ is first order continuous derivative, when $t \rightarrow \infty$, exist finite limit, if $\dot{x}(t), t \in [0, \infty)$ is uniformly continuous, $\lim_{t \rightarrow \infty} \dot{x}(t) = 0$.

This paper demonstrates the global asymptotic stability of system (4), by demonstrating system (4) (asymptotic system (5) and (6)) meet the conditions of lemma 1. First, setting $x_1 = [z_1, z_5]^T$, $x_2 = [z_2, z_3, z_4, z_6]^T$, $x = [x_1, x_2]^T$, so equation (5) can be transformed as follow:

$$\dot{x}_1 = \begin{bmatrix} -\frac{\beta}{\alpha} & 0 \\ 0 & -\beta \end{bmatrix} x_1 + \begin{bmatrix} z_6 & \frac{\gamma}{\beta}z_6 & -\frac{\beta}{\alpha} & -\frac{z_5}{\beta} \\ 0 & 0 & \beta z_6 & \beta z_1 + \gamma \end{bmatrix} x_2$$

Setting

$$\begin{aligned} f_1(t, x_1) &= \begin{bmatrix} -\frac{\beta}{\alpha}z_1 \\ -\beta z_5 \end{bmatrix} = \begin{bmatrix} -\frac{\beta}{\alpha} & 0 \\ 0 & -\beta \end{bmatrix} x_1 \\ G(t, x) &= \begin{bmatrix} z_6 & \frac{\gamma}{\beta}z_6 & -\frac{\beta}{\alpha} & -\frac{z_5}{\beta} \\ 0 & 0 & \beta z_6 & \beta z_1 + \gamma \end{bmatrix} \\ f_2(t, x_2, u) &= \begin{bmatrix} z_4z_6 \\ z_6 \\ f_1 \\ f_2 \end{bmatrix} \end{aligned} . \quad (7)$$

The First step: demonstrate system (5) meet the condition (1) of Lemma 1.

It can be known from the first equation of formula (7):

$$\dot{x}_1 = f_1(t, x_1) = \begin{bmatrix} -\frac{\beta}{\alpha} & 0 \\ 0 & -\beta \end{bmatrix} x_1$$

Obviously function $f_1(t, x_1)$ is continuously differentiable on (t, x_1) , and the system is linear time-invariant system, eigenvalues are $\lambda_1 = -\frac{\beta}{\alpha}$ and $\lambda_2 = -\beta$. By the definition of α and β , α and β are all positive number, so, the two eigenvalues of system are strictly negative, system $\dot{x}_1 = f_1(t, x_1)$ is global uniform asymptotic stabilized. Meet the condition (1) of Lemma 1. Next, demonstrate the system meet the condition (3) of Lemma 1.

The second step: demonstrate system (5) meet the condition (3) of Lemma 1.

It can be known from the second equation of formula (7):

$$G(t, x) = \begin{bmatrix} z_6 & \frac{\gamma}{\beta} z_6 & -\frac{\beta}{\alpha} & -\frac{z_5}{\beta} \\ 0 & 0 & \beta z_6 & \beta z_1 + \gamma \end{bmatrix}$$

$$G_1(t, x) = \begin{bmatrix} z_6 & \frac{\gamma}{\beta} z_6 & -\frac{\beta}{\alpha} & 0 \\ 0 & 0 & \beta z_6 & \gamma \end{bmatrix}.$$

By the Lemma 2, obviously can see that $G(t, x)$ is local Lipschitz continuous in the interval. The above formula can be broken into:

$$G(t, x) = \begin{bmatrix} z_6 & \frac{\gamma}{\beta} z_6 & -\frac{\beta}{\alpha} & -\frac{z_5}{\beta} \\ 0 & 0 & \beta z_6 & \beta z_1 + \gamma \end{bmatrix}$$

$$= \begin{bmatrix} z_6 & \frac{\gamma}{\beta} z_6 & -\frac{\beta}{\alpha} & 0 \\ 0 & 0 & \beta z_6 & \gamma \end{bmatrix} + \begin{bmatrix} 0 & 0 & 0 & -\frac{z_5}{\beta} \\ 0 & 0 & 0 & \beta z_1 \end{bmatrix}$$

according to the property of norm, it can be known:

$$\|G_1(t, x)\|_2 \leq \left(\beta + 1 + \left| \frac{\gamma}{\beta} \right| \right) \|z_6\|_2 + \frac{\beta}{\alpha} + |\gamma|. \quad (8)$$

And because of $\|z_6\|_2 \leq \|x_2\|_2$, inequation (8) can be transformed into:

$$\|G_1(t, x)\|_2 \leq \left(\beta + 1 + \left| \frac{\gamma}{\beta} \right| \right) \|x_2\|_2 + \frac{\beta}{\alpha} + |\gamma| = \theta_1(\|x_2\|_2). \quad (9)$$

where, θ_1 is a function of $\|x_2\|_2$.

Similarly, define: $G_2(t, x) = \begin{bmatrix} 0 & 0 & 0 & -\frac{z_5}{\beta} \\ 0 & 0 & 0 & \beta z_1 \end{bmatrix}$

According to the property of norm, it can be known:

$$\|G_2(t, x)\|_2 \leq \left(\frac{1}{\beta} + \beta \right) \sqrt{z_1^2 + z_5^2} = \left(\frac{1}{\beta} + \beta \right) \|x_1\|_2 = \theta_2(\|x_2\|_2) \|x_1\|_2. \quad (10)$$

where, θ_2 is a function of $\|x_2\|_2$.

So, according to the property of norm and formula (9) and (10), obtain:

$$\|G(t, x)\|_2 \leq \|G_1(t, x)\|_2 + \|G_2(t, x)\|_2 \leq \theta_1(\|x_2\|_2) + \theta_2(\|x_2\|_2) \|x_1\|_2$$

Therefore, meet the condition (3) of Lemma 1. In order to illustrate the system meet the condition (2) of Lemma 1 better, design the stabilization controller of system (6) firstly.

Where:

First, system (6) can be divided into two subsystems as follow:

$$\sum_{21} \begin{bmatrix} \dot{z}_2 \\ \dot{z}_3 \\ \dot{z}_4 \end{bmatrix} = \begin{bmatrix} z_4 z_6 \\ z_6 \\ f_1 \end{bmatrix}. \quad (11)$$

$$\sum_{22} \begin{bmatrix} \dot{z}_6 \end{bmatrix} = \begin{bmatrix} f_2 \end{bmatrix}. \quad (12)$$

The first part: in this part, design the control input f_1 by subsystem (11) of the USV stabilization system.

Assume virtual input $z_6 = \Gamma$, and subsystem (11) is transformed into the following type:

$$\sum_{21} \begin{bmatrix} \dot{z}_2 \\ \dot{z}_3 \\ \dot{z}_4 \end{bmatrix} = \begin{bmatrix} z_4 \Gamma \\ \Gamma \\ f_1 \end{bmatrix}. \quad (13)$$

where, z_2, z_3, z_4 are state variable, f_1 and Γ are input variable. For system (13), select Lyapunov function as follow:

$$V_1 = \frac{1}{2} k_2 z_2^2 + \frac{1}{2} z_4^2 \geq 0. \quad (14)$$

Calculate the derivative of (14), and bring the formulas of (13) in, obtain:

$$\dot{V}_1 = k_2 z_2 \dot{z}_2 + z_4 \dot{z}_4 = k_2 z_2 z_4 \Gamma + z_4 f_1 = z_4 (k_2 z_2 \Gamma + f_1). \quad (15)$$

For formula (15), select the control law as follow:

$$f_1 = -k_4 z_4 - k_2 z_2 \Gamma. \quad (16)$$

Therefore

$$\dot{V}_1 = z_4 (k_2 z_2 \Gamma + f_1) = -k_4 z_4^2 \leq 0. \quad (17)$$

Formula (14) and (17) show that V_1 is nonincremental, and V_1 will converge to a limit $V_{1\lim} (\geq 0)$, so get that $\lim_{t \rightarrow \infty} z_4 = 0$, and z_2 is bounded.

In order to ensure z_2 converges to zero, this paper select

$$\Gamma = \dot{z}_3 = -k_3 z_3 + \lambda z_2 . \quad (18)$$

where, λ is bounded.

Demonstrate Γ converges to zero by paradox: assume Γ does not converge to zero, it has been demonstrated z_4 converges to zero already, and obtain that $z_2 \Gamma$ converges to zero by Lemma 3, thus deduced z_2 converges to zero, combining with (18) know that z_3 converges to zero too, then obtain that Γ converges to zero, it is inconsistent with the assumed condition. Thus demonstrate that Γ converges to zero.

Select $\lambda = -\sin t$, then

$$\begin{aligned} \Gamma &= -k_3 z_3 + \lambda z_2 = -k_3 z_3 - z_2 \sin t \\ \dot{\Gamma} &= -k_3 \dot{z}_3 - \dot{z}_2 \sin t - z_2 \cos t = -k_3 \Gamma - z_4 \Gamma \sin t - z_2 \cos t \end{aligned}$$

Where, $k_3 \Gamma$ and $z_4 \Gamma \sin t$ converge to zero, $z_2 \cos t$ is uniformly continuous, combining with Lemma 3, $z_2 \cos t$ converges to zero, so $z_2 \cos^2 t$ converges to zero too. Calculate the derivative of $z_2 \cos t$, and combine with Lemma 3, $z_2 \sin t$ converges to zero in the same way, so $z_2 \sin^2 t$ converges to zero, and $z_2 = z_2 \cos^2 t + z_2 \sin^2 t$ converges to zero. Through $\Gamma = -k_3 z_3 + \lambda z_2 = -k_3 z_3 - z_2 \sin t$, z_3 converges to zero too. Similar situation, when $\lambda = \pm \sin t$ or $\lambda = \pm \cos t$, the control law in the follow can make system (13) global asymptotic stabilized.

$$\begin{cases} \Gamma = \dot{z}_3 = -k_3 z_3 + \lambda z_2 \\ f_1 = -k_4 z_4 - k_2 z_2 \Gamma \end{cases} . \quad (19)$$

The first part: in this part, design the control input f_2 by stabilizing the USV system (6), then obtain the global stabilization control law of USV.

Assume $\Theta = z_6 - \Gamma$, then $z_6 = \Theta + \Gamma$. System (6) can be written as follow:

$$\begin{cases} \dot{z}_2 = z_4(\Theta + \Gamma) \\ \dot{z}_3 = \Theta + \Gamma \\ \dot{z}_4 = -k_2 z_2 \Gamma - k_4 z_4 \\ \dot{z}_6 = f_2 \end{cases} . \quad (20)$$

Select the Lyapunov function of system (20) as follow:

$$V_2 = \frac{1}{2} k_2 z_2^2 + \frac{1}{2} z_4^2 + \frac{1}{2} \Theta^2 \geq 0 . \quad (21)$$

Calculate the derivative of formula (21), get

$$\begin{aligned} \dot{V}_2 &= k_2 z_2 \dot{z}_2 + z_4 \dot{z}_4 + \Theta \dot{\Theta} \\ &= k_2 z_2 z_4 (\Theta + \Gamma) + z_4 (-k_2 z_2 \Gamma - k_4 z_4) + \Theta (\dot{z}_6 - \dot{\Gamma}) \\ &= -k_4 z_4^2 + k_2 z_2 z_4 \Theta + \Theta (f_2 - \dot{\Gamma}) \\ &= -k_4 z_4^2 + \Theta (f_2 - \dot{\Gamma} + k_2 z_2 z_4) \end{aligned} . \quad (22)$$

Based on formula (22), select the control law as follow:

$$f_2 = \dot{\Gamma} - k_2 z_2 z_4 - k_6 \Theta = \dot{\Gamma} - k_2 z_2 z_4 - k_6 (z_6 - \Gamma) . \quad (23)$$

bring the formulas of (23) in formula (22), get:

$$\dot{V}_2 = -k_4 z_4^2 + \Theta (-k_6 \Theta) = -k_4 z_4^2 - k_6 \Theta^2 \leq 0 . \quad (24)$$

Formula (21) and (24) show that V_2 is nonincremental, and V_2 will converge to a limit $V_{2,\lim} (\geq 0)$, get that $\lim_{t \rightarrow \infty} \Theta = 0$, and due $\lim_{t \rightarrow \infty} \Gamma = 0$, so $\lim_{t \rightarrow \infty} z_6 = 0$.

Comprehensive the above contents, for system (6), the control law in the follow is able to make z_2, z_3, z_4, z_6 global uniform asymptotic stabilized.

Now back to the third step of the global asymptotic stabilization analyze in the third section: demonstrate system (6) meet condition (2) of Lemma 1.

Through the process of design system (6) stabilization controller, obviously show that the system meet condition (2) of Lemma 1. Through Lemma 2, obviously $f_2(t, x_2, u)$ is locally Lipschitz continuous.

Through a set of demonstrating process above, it can be seen that the underactuated USV system (4), that is system (5) and system (6), meet all the conditions of Lemma 1, so system (4) is global uniform asymptotic stabilized, and the control law is formula (33).

V SIMULATION RESULTS

Using the control law designed above doing USV stabilization control simulation experiment, the model parameters of the USV is[11]: $m_{11} = 1.1274$, $m_{22} = 1.8902$, $m_{33} = 0.1278$, $m_{23} = -0.0744$, $m_{32} = -0.0744$, $d_{11} = 0.0358$, $d_{22} = 0.1183$, $d_{33} = 0.0308$, $d_{23} = -0.0124$, $d_{32} = -0.0041$. The initial state of USV is set to: $x(0) = -1$, $y(0) = -1$, $\varphi(0) = \frac{\pi}{2}$, $u(0) = 0$, $v(0) = 0$, $r(0) = 0$. Parameter selection

for the control: $k_2 = 1.5$, $k_3 = 0.8$, $k_4 = 1.12$, $k_6 = 1$, $\lambda = \sin t$. The simulation results are shown in the figure below:

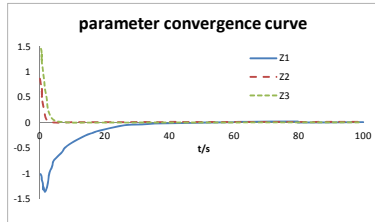


FIGURE I. CONVERGENCE CURVE OF z_1, z_2, z_3

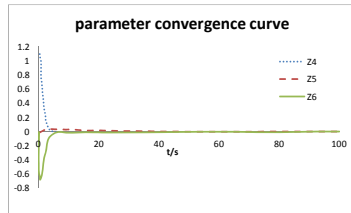


FIGURE II. CONVERGENCE CURVE OF z_4, z_5, z_6

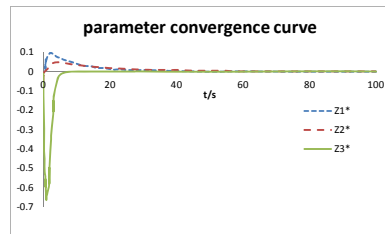


FIGURE III. CONVERGENCE CURVE OF z_1^*, z_2^*, z_3^*

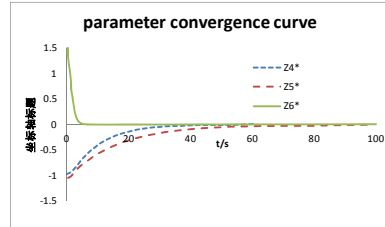


FIGURE IV. CONVERGENCE CURVE OF z_4^*, z_5^*, z_6^*

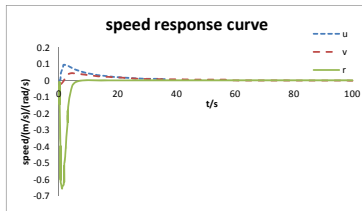


FIGURE V. CONVERGENCE CURVE OF u, v, r

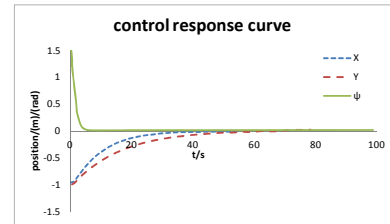


FIGURE VI. CONVERGENCE CURVE OF x, y, φ

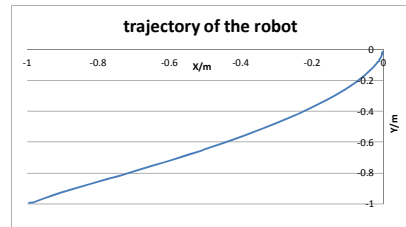


FIGURE VII. TRAJECTORY CURVE OF USVFIG.

In the figure above, Figure I and Figure II show convergence curves of state variables $z_1, z_2, z_3, z_4, z_5, z_6$ of system (4) in the simulation process, Figure III and Figure IV show convergence curves of state variables $z_1^*, z_2^*, z_3^*, z_4^*, z_5^*, z_6^*$ of system (3) in the simulation process. Figure V and Figure VI show convergence curves of the speed variables u, v, r and position variables x, y, φ of original system (1) and (2) in the USV stabilization control simulation process, Figure VII show the trajectory curve of USV in the stabilization process. Through a series of simulation results above, it can be seen the original incomplete symmetrical underactuated USV system (1) and (2), and the transformed system (3) and (4), all the state variables of them converge to zero uniformly, this means that these three systems are all global uniform asymptotic stabilized. The simulation results demonstrate the effectiveness of the twice global diffeomorphism transformation and the control law designed in this article.

VI CONCLUSIONS

This paper study the stabilization control of underactuated USV, while the USV model is incomplete symmetrical, through performing global diffeomorphism transformation twice, obtain the form of cascade systems, design the control law based on Backstepping, make the system achieve global asymptotic stabilized, and analyze the stability of the stabilization control. Finally, demonstrate the method proposed and controller designed in this paper can make the incomplete symmetrical underactuated USV realize global asymptotic stabilization.

ACKNOWLEDGEMENT

We gratefully acknowledge the support of the National Natural Science Foundation of China (51609054).

REFERENCE

- [1] Reyanoglu M. Control and stabilization of an underactuated surface vessel[C]. Proceedings of the 35th IEEE Conference on Decision and Control, Kobe, Japan, 1996: 2371-2376
- [2] Ghommam J, Mnif F, Benali A, Derbel N. Asymptotic backstepping stabilization of an underactuated surface vessel[J]. IEEE Transactions on Control Systems Technology. 2006, 14(6): 1150-1157

- [3] LIAO Yulei, PANG Yongjie, ZHANG Tiedong. Global K-exponential stabilization of underactuated autonomous surface vessels by a smooth time-varying feedback control [J]. Journal of Harbin Engineering University, 2011, 32(4): 417-422.)
- [4] Ma Baoli. Global k-exponential asymptotic stabilization of underactuated surface vessels [J]. Systems & Control Letters. 2009, 58: 191-201P
- [5] LIU Yang, GUO Chen, LIU Yu. Discontinuous varying parameters stabilization control for underactuated surface vessel motion [J]. Journal of Dalian Maritime University, 2009, 35(1): 9-12.)
- [6] Kristin Y Pettersen, Thor I Fossen. Underactuated dynamic positioning of a ship-experimental results [J]. IEEE Transactions on Control Systems Technology, 2000, 8(5): 856-863
- [7] Frdric Mazenc, Kristin Pettersen, Henk Nijmeijer. Global uniform asymptotic stabilization of an underactuated surface vessel [J]. IEEE Transactions on Automatic Control, 2002, 47(10): 1759-1762.
- [8] Thor I. Fossen. Guidance and Control of Ocean Vehicles [M]. University of Trondheim, Norway, 1994.
- [9] E. Lefeber. Tracking control of nonlinear mechanical systems. Universiteit Twente Ph.D. thesis. 2000
- [10] Hassan K. Khalil. Nonlinear Systems, Third Edition [M]. Beijing: Publishing House of Electronics Industry. 2011
- [11] Do K D, Pan J. Global tracking control of underactuated ships with off-diagonal terms[C]. Proceeding of 42nd IEEE Conference on Decision and Control. Hawaii, 2003: 1250-1255.

Develop the AI Literacy of Infants by Deeply Integrated English Learning and Robot Education

Zhongyu Zhang

Modern Educational technology institute of Qujing Normal University, Qujing, Yunnan , China 655000

Abstract—In this paper, a new learning model which integrate the English Learning and Robot Education for infants was proposed. According to this model, a textbook of using robot to teach English was designed. A corresponding course which matched with the textbook was developed. An experiment of using this course was done in a training institution. The result illustrate that this model is apparently effective for the kindergarten school students to learn English and robot.

Keywords—integrate; English learning; robot education; language skill, intelligent; information literacy; science and technology literacy

I. INTRODUCTION

Artificial Intelligent (AI) is becoming more and more important whether in research field or industry. Chinese government had given out a plan which named *about the new generation AI industry development plan*, in which the AI industry had been put the most important place [1]. According to this plan, The GDP will reach 1,000 billion Yan in directly AI industry and 10,000 billion Yan in indirectly related industry in 2030. With the rapid progress of this plan, the AI personnel training is much necessary. As Deng Xiaoping, a great Chinese president, had put it that the computer education must begin from the babies [2]. An Excellent AI personnel must also begin to be trained from a baby. As our viewpoint, An Excellent AI personnel must have not only higher science and technology literacy but also better foreign language skills.

However, in many primary schools or kindergartens, no matter the English learning or the AI education is very poor. Robot is the best media for children to learning AI knowledge. In a survey about the English learning and robot education to the Kindergartens in Qujing. Almost all the public kindergarten have not English and robot course. More than 90 percent private kindergartens have not English and robot courses. Early childhood is the key time to learn a language. The adage that “it is never too early to begin reading to infants and toddlers” appears throughout both the professional and popular literatures [3]. The information, science and technology literacy should be developed in Children’s early childhood. So perhaps integrating the English learning and robot education will be a very good method to develop the AI literacy of early children. In this paper, a new learning model which integrate the English Learning and Robot Education for the infants was proposed. According to this model, an experiment of deeply integrated the English learning and robot education was done in a training institution. The result illustrate that the effects of learning English and robot is very good. So we can conclusion that the deeply integration model is

apparently effective for the kindergarten school students to learn English and robot.

II. WHY IS IT IMPORTANT FOR INFANTS TO LEARN ENGLISH AND ROBOT

With the development of AI industry. The requirement of AI professionals will grow more and more rapidly. The problem of lack of AI professionals will exist for a long time. During the past a few years, the high, elementary and secondary school had spent more time in raising the student test scores and less time in developing the AI literacy of them. The social training organization didn’t also focus on the AI field but more and more on the physical exercise and art. The college and university have planned to found the AI-related majors or subjects. Where will the students come from? The students which enter into these AI-related majors will not be the high quality source if they are not good at electronics, information and programming. Most of the advanced country pay high attention to develop the AI literacy of the high, elementary and secondary school students, or even kindergarten infants. It is related for students to develop their literacy during the time they learn from kindergarten to the college or university. So developing the AI literacy of infants is also very important. Robot, as a kind of hardware product of AI industry, is the most suitable tool to develop the AI literacy of infants. Jigsaw robot is a very good product. According to the related research, the benefits of learning robots are as follows [4]:

- (1) For the left brain, it is beneficial to:
 - Instill math and science interest
 - Improve memory power
 - Increase concentration
 - Critical thinking skills
 - Logical and analytical skills
 - Communication skills
- (2) For the right brain, it is beneficial to:
 - Reduce study stress
 - Spatial reasoning
 - Imaginative skills
 - Creative thinking skills
 - Problem solving skills
 - Innovation skills

In our training practice, we also found most of the kindergarten infants or the primary school students can't master English as a second language. As we think, English is very important for students to be taught to become the leaders in the future AI times. Early childhood is the key time to develop the language skills of children.

Here we try to explore the path of integrated the English learning and robot education for the infants.

III. HOW TO INTEGRATE THE ENGLISH LEARNING AND ROBOT EDUCATION

How to integrate the English learning and robot education. The aims of English g and robot learning for the infants are what the educator should think firstly. Generally speaking, the aims of English learning often include the listening, speaking, reading and writing. But to infants, listening and speaking is probably more suitable and reading and writing is probably not. As for the robot education, building up, operating and program thinking excising is the main point for infants.

According to the describing above, a model for developing the AI literacy of infants by integrating English learning and robot education together was proposed. A textbook was designed. A corresponding course match with this text book can be developed. In this course, the basic teaching and learning equipment include the Lego jigsaw robot and Zhongming Weier robot suit products. Weier is a jigsaw robot with an intelligent pen to control the robot. When the infants use the intelligent pen to point the special chart in the textbook, the robot can display the corresponding action. This equipment can be use as the programming excising.

Teachers can design a lot of activities to teach English and robot by using these equipment. The robot learning focus on the building up, operating and controlling and programming. The jigsaws are the most suitable for the English teaching and learning. For example, the teaching of *colors, shapes, size, letters, numbers and so on* can be done by using of Lego jigsaws. During the process of building up the robots, some simple operating actions can be express by English. For example, *Put the two squares together. Put the triangle on the top of the robot. etc.*, Zhongming Weier robot also provide a program thinking excising textbook. Infants can be taught and master the basic program ideas and logics. The benefits of this model is that infants can master not only the English skills but also robot professional knowledge. The most important feature is that the infants can be immersed in the English and robot learning activities all the long time.

IV. AN EXPERIMENT OF INTEGRATING ENGLISH LEARNING AND ROBOT EDUCATION FOR INFANTS

In order to verify the effects of the above model, an experiment of using this mode to teach infants to learn English and robot knowledge was held in a training institution. The experiment method is the pretest and posttest of a single group. The treatments is ten infants whose ages are between 4 – 6 years old. There are five boys and five girls in this 10 infants. They didn't all have learnt English before. The learning content include concepts, operating sentences and programing thinking.

Task 1: English concept learning activity.

Content of English concept learning activity is the nine kinds of colors in our life. They are *red, blue, yellow, green, orange, purple, brown, black and white*.

Task 2: English sentences learning activity.

The content of English sentences learning activity included the seven English sentences of operating the Weier jigsaw robot:

- Programming starts.
- Go forward 1 second.
- Take backwards 2seconds
- Turn left 3seconds.
- Turn right 4seconds.
- Stop.
- Programming is over.

The aim of this learning activity includes:

- (1) The pronouncing of all the words in these sentences.
- (2) The meaning of all the words in these sentences.
- (3) The fluently reading of all these sentences.
- (4) The translating of all these sentences.

In task 1, teacher guided the boys and girls when she built up the same robot as what the infants did. Boys and girls looked the teacher as their partner. So they felt very naturally and didn't feel to be learning English. They naturally followed the teacher saying English words. Parents can also play the role of teacher. It is also effective to do the shared parent-infant book reading on early language acquisition [5].

The result of task 1 illustrate the time to master the nine kinds of colors is less than in the traditional classroom. When they play the Weier robot.

In task 2, teacher guided the boys and girls operating the intelligent pen to control the Zhongming Weier robot. At the same time, teacher teach the boys and girls to say out the English sentences corresponding to the operating. Infants looked saying English as a part of the game or the story [6]. So they can easily speak out all the sentences.

The result of task 1 and 2 also illustrated that all the boys and girls were interested in the learning process. In the traditional teaching process, the time of infants concentrate on a learning activity is less than 10 minutes. But in this experiment, the time of infants concentrating on a learning activity is more than half an hour. Infants seemed to be no tired when they build up and operating the robot.

V. CONCLUSIONS AND FUTURE WORK

In this paper, a new learning model which integrate the English Learning and Robot Education for infants was proposed. According to this model, a textbook by using of robots to teach English was designed. A corresponding course which matched with this textbook was developed. In order to verify the effects of this model, an experiment of using this course was done in a training institution. The result illustrate that this model is

apparently effective for the kindergarten school students to learn English and robot. Infants can easily complete the learning task and master the English skills. In addition to the better learning effectiveness, the nonintellectual factors of infants, such as interest, attention, and willpower, are also developed to some extent.

Certainly, the above model pointed out only the basic path to integrate the English learning and robot education. The experiment used also only a basic English learning materials. How to design more and more learning materials? Whether this model is suitable to the students of other ages? These are our future research work.

REFERENCES

- [1] The state concil issued *the informs of the development plan about new generation of AI industry*. State issued [2017]No. 35. http://www.gov.cn/zhengce/content/2017-07/20/content_5211996.htm
- [2] Dengxiaopinginspected Shanghai: Computer education must begin from the babies. <http://www.chinanews.com/gn/2014/08-22/6522779.shtml>
- [3] Dunst, C. J., Simkus, A., & Hamby, D. W. Relationship between age of onset and frequency of reading to infants and toddlers and later language and literacy development. *CELLreviews*, 5(3), 1-10. Available at http://www.earlyliteracylearning.org/cellreviews/cellreviews_v5_n3.pdf
- [4] Benefits of Robotics Learning. <http://www.robots2u.com/benefits/benefits.php>
- [5] Karrass, J., & Braungart-Ricker, J. M. (2005). Effects of shared parent-infant book reading on early language acquisition. *Journal of Applied Developmental Psychology*, 26, 133-148.
- [6] Zeece, P. D., & Churchill, S. L. (2001). First stories: Emergent literacy in infants and toddlers. *Early Childhood Education Journal*, 29, 101-104. doi:10.1023/A:1012572812166

A Hybrid Fusion Algorithm for Integrated INS/UWB Navigation and Its Application in Vehicle Platoon Formation Control

Yingmao Lu¹, Jianjun Yi^{1,*}, Liang He^{2,3}, Xiaomin Zhu¹ and Pengfei Liu^{2,3}

¹Department of Mechanical Engineering, East China University of Science and Technology, Shanghai 200237, China

²Shanghai Aerospace Control Technology Institute, Shanghai 201109, China

³Shanghai Key Laboratory of Aerospace Intelligent Control Technology, Shanghai 201109, China

*Corresponding author

Abstract—The vehicle positioning technology is playing an important role in Cooperative Vehicle Infrastructure System (CVIS). In those single positioning modes, the precision of wireless positioning is greatly affected by the environment. However, the accumulative errors of inertial navigation system (INS) and positioning can not be eliminated. In this paper, a hybrid fusion algorithm based on UWB (Ultra Wide Band) and INS is proposed and applied to the vehicle platoon formation control system. The hybrid fusion algorithm can overcome the shortcomings of non-line-of-sight (NLOS) problem in UWB positioning algorithm and accumulative errors of INS. This algorithm can also significantly enhance positioning accuracy in vehicle platoon formation control. The application scene consists of three types: road scene, junction scene and parking lot scene. The hybrid fusion algorithm can be used in combination with different scenarios to ensure the smooth operation of the vehicle platoon.

Keywords—UWB (Ultra Wide Band); INS (inertial navigation system); hybrid fusion algorithm; vehicle platoon formation control

I. INTRODUCTION

Vehicle location technology is the key to Cooperative Vehicle Infrastructure System (CVIS). The vehicle positioning technology mainly uses Dead Reckoning (DR), subgrade positioning and Global Navigation Satellite System (GNSS).

DR can maintain high accuracy in a short time, but will bring an accumulative error [1]. The main advantage of subgrade positioning technology is its efficiency and reliability. But it also can be affected by the environment dramatically. Especially when non-line-of-sight (NLOS), multipath or other circumstances exist. In these cases, the subgrade positioning error is huge [2]. GNSS has all-weather service, high efficiency and other functional advantages. Due to the multipath effect, the current GNSS positioning error is huge and significantly influenced by environmental factors. GNSS can not meet the requirements of positioning accuracy in CVIS [3].

As each single means of positioning has its own inevitable shortcomings which can not be overcome. In practical applications, we usually use the combination of these positioning methods, which also combined with Map Matching (MM) method to improve the positioning accuracy. Integrated

positioning algorithms such as GPS/MM, GPS/DR, GPS/DR/MM are wildly used.^[4]

The vehicle platoon formation control is mainly divided into longitudinal control, lateral control and integrated control. Longitudinal control mainly includes adaptive cruise control system, obstacle avoidance system and autonomous vehicle platoon formation control system. Lateral control includes lane change warning system, lane keeping system, vehicle tracking system and so on. Integrated control is a combination of longitudinal and lateral control. In vehicle platoon formation control, there is a very high demand on the vehicle's distance in the vehicle platoon formation, which includes the front-to-back and left-right distances. So it requires higher positioning accuracy.

In this paper, the hybrid fusion algorithm is a combination of UWB positioning and INS technology which is a new form of the above multiple combined positioning methods. The hybrid fusion algorithm combines the advantages of overall high accuracy in UWB positioning and high accuracy within a short time in INS positioning. It can supply a high-precision positioning and communication, collision warning and so on in the vehicle platoon formation control. This is a new exploration and new application of this combination of positioning methods^[5-8].

The UWB positioning technology, UWB module selection, embedded hardware and software design and system integration program are introduced in first section. Then, the UWB and INS data fusion localization algorithm based on Federated Kalman Filter is proposed. And the algorithm is applied to vehicle distance estimation and collision pre-warning algorithm in vehicle platoon formation control. Finally, this paper analyzes the application of hybrid fusion algorithm in different scenarios of vehicle platoon formation control.

II. OVERALL PROGRAM DESIGN

A. Overview of the UWB Positioning Technology

UWB (Ultra Wide Band) is a carrierless communication technology that uses nanoseconds to microseconds non-sinusoidal narrow pulses to transmit data (Figure 1). UWB has other incomparable communication system features include:

High rate and large channel capacity; Suitable for short distance communication; Good coexistence and confidentiality; Strong multipath resolution and high positioning accuracy; Small size, low power consumption; etc [9]. UWB was used in the near-field high-speed data transmission early. In recent years began to use its sub-nanosecond ultra-narrow pulse in close-range accurate positioning. Precise Positioning is an applications of UWB in the field of IEEE802.15.4a. It is a low-speed low-power transmission for precise positioning of the technology. The rise of UWB technology has a great promotive effect for the WSN positioning. Compared with other WSN positioning methods, the positioning accuracy of UWB technology has been greatly improved, and the cost is much less than expensive positioning methods such as laser positioning. UWB has the advantages of low cost, anti-multipath interference and penetrating ability in positioning. So it can be applied to the positioning and tracking of stationary or moving objects and personnel, and can provide very accurate positioning accuracy. Currently UWB technology is mainly used in indoor positioning, less application in vehicle positioning. The United States PAL650 system using UWB system successfully solved the problem of container transport vehicles positioning. Ubisense UK's UWB positioning system has been able to complete the precise positioning of 20 ~ 50m range of 15cm, so that it can be applied in the parking lot, logistics and other vehicle related aspects.

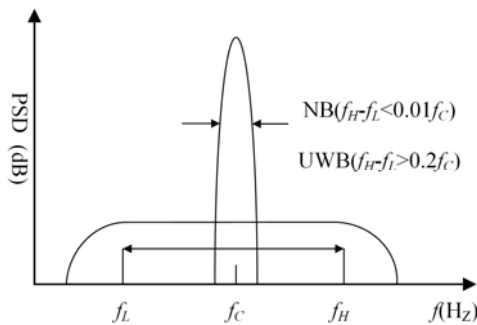


FIGURE I. SIGNAL IN ACCORDANCE WITH THE BANDWIDTH CLASSIFICATION

B. UWB Selection, Hardware Design, Integration and Embedded Software Development

In this paper, the overall scheme of UWB vehicle positioning is shown in Figure 2, in which each vehicle is equipped with UWB positioning nodes. And it is arranged with fixed UWB anchor nodes in the whole space. The positioning node sends data to the anchor node according to a certain frequency. After receiving the data, the anchor node gives a response and calculates the ranging.

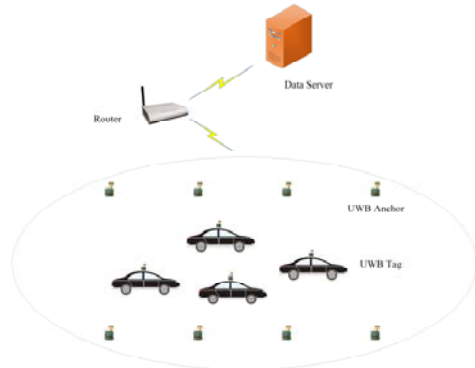


FIGURE II. SYSTEM OVERALL PROGRAM

After receiving the signal and calculating the distance value with each positioning node, the UWB anchor node sends the positioning result information to the dedicated router through the TCP/IP communication module. And the dedicated router collects information and sends it to the data center uniformly through the network. The high-performance computer in the

data center performs the uniform processing on the ranging data of each UWB node and quickly locates each UWB node.

UWB positioning nodes fall into two categories, of which the onboard control system serves as a mobile node or a label node, and which is fixed in an indoor environment as a reference node or anchor node. Anchor nodes and tag nodes can have the same hardware design. Different positioning roles can be performed by changing the configuration on the software.

UWB transceiver is the core of UWB communication and positioning among the positioning nodes. Take DecaWave DW1000 for example. The UWB transceiver chip can communicate with the host through the SPI interface. Its internal structure is shown in Figure 3. At the same time the UWB transceiver chip has the following excellent features: Supports the highest 6.8Mbps communication rate; Farthest communication distance up to 290m under 110kbps; High anti-multipath ability; Excellent NLOS communication ability; Low-power control strategy.

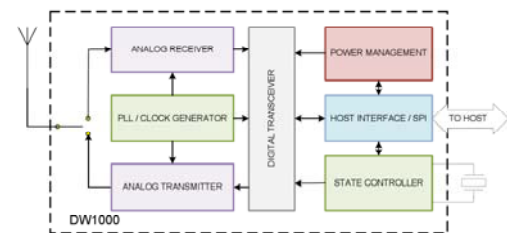


FIGURE III. DW1000 INTERNAL STRUCTURE

In addition to transceiver chip, UWB positioning node also need a host to configure its state and transmit data. In this paper, a STM32F105RCT6 chip is used as a controller to communicate with the UWB transceiver through the SPI interface. At the same time, the host chip communicates with other hosts through TCP / IP or USB interface and transmits the ranging data to other nodes. The main structure of UWB positioning node shown in Figure 4.

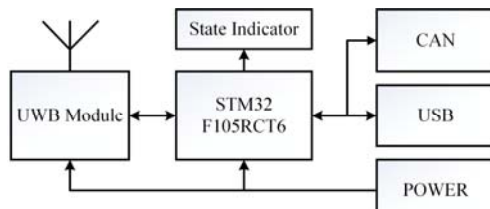


FIGURE IV. HARDWARE STRUCTURE OF UWB NODE

In this paper, the host controller of vehicle which needs to be integrated with the UWB as tag node connects to the UWB node via CAN. And the vehicle's controller obtain the information such as the wireless connection status and the ranging result from the UWB node. At the same time, the vehicle controller supplies power to the UWB node through the power interface. In combination with the software design and switch module, the node can be used as the label or anchor node, which greatly increases the universality of the UWB node.

In this paper as a dedicated router for information transfer, the hardware structure is shown in Figure 5. The MCU module is developed using TI's Cortex-A8-based AM335X core chip. The chip has a wealth of industrial interfaces and is able to run Linux operating system, which provide a reliable guarantee to the development of hardware and software for the router. Dedicated router includes a power module. When the power module can not supply power, the backup power will be enabled to ensure the reliable operation of the system. The LCD module provides the working status display of the current router, such as the information of the number of each UWB node currently connected, the information of the death node, the connection status of the node, and so on.

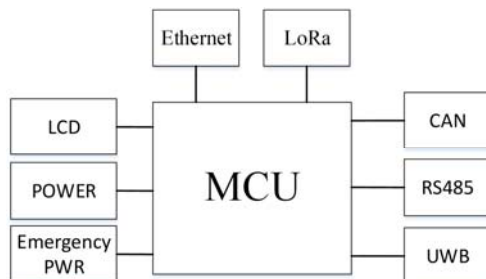


FIGURE V. HARDWARE STRUCTURE OF ROUTER

As a dedicated router, it has a wealth of peripheral interfaces. First of all, it has UWB module to communicate with other UWB nodes in the system. RS485 and CAN are the mainstream industrial application interfaces that ensure reliable data communication between this dedicated router and other nodes. The Ethernet interface is a communication interface for uploading UWB positioning data. When the router is in an environment that does not have reliable Ethernet access, data is communicated over an extra LoRa wireless network. As a long-distance wireless communication technology, LoRa can guarantee reliable data communication within 5Km. Therefore, LoRa can greatly expand the use range of the router and reduce its dependence on the Internet.

C. UWB Localization Algorithm and Its Data Fusion Algorithm with Inertial Positioning

The basis of UWB positioning is to model the current environment effectively to express its environmental characteristics. UWB positioning is also a relative positioning method in the map model. So map creation is an important step in UWB positioning. There are two main ways of modeling the environment of the map: net/graph modeling method and grid-based modeling method. The former mainly includes modeling methods such as free space method and visual method. The latter grid-based modeling method is the grid map method. Because grid map modeling method is relatively simple to implement, and can be well applied to the modeling of the rule environment. Therefore, this paper intends to use the modeling method of grid map to model the vehicle operating environment. Although grid maps are easy to implement, the size of the grid directly affects the efficiency of path planning. Therefore, how to divide the environment, the precision of the grid needs to be further studied according to the specific environment so that the vehicle can achieve a better balance between the positioning accuracy and the efficiency, so as to meet the optimal posture determination of the vehicle under dynamic conditions. At the same time, in grid maps, the expression of irregular obstacles is also an important aspect that affects their accuracy and efficiency^[10,11].

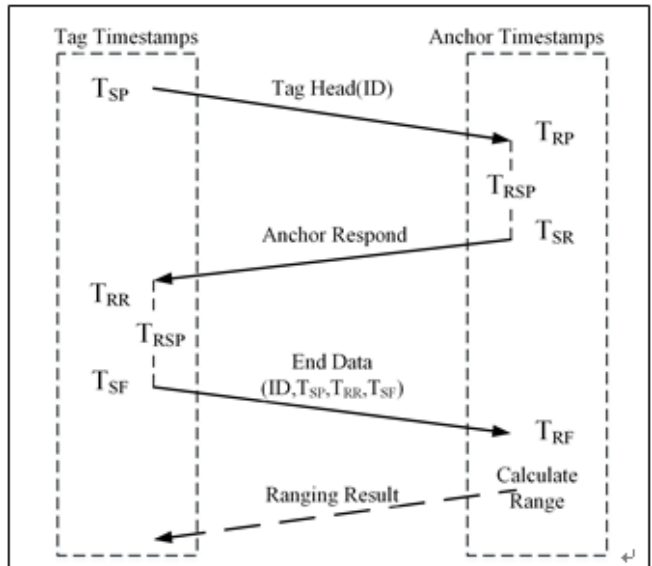


FIGURE VI. TAO-WAY RANG

In order to solve the wireless positioning of the time synchronization problem, this paper uses a Two-Way Rang (TWR) method based on time of flight. The one-way flight time is calculated by passing the signal's timestamps when two nodes communicate bi-directionally, thereby being immune to clock synchronization. The principle of TWR method is shown in Figure 6. In Figure 6, the left side represents the label node and the right side is the anchor node. The tag node starts the ranging process at a certain time interval. The anchor node will always keep listening state and respond to the ranging signal and calculate the distance between nodes. A complete ranging process is as follows:

For tag nodes, the signal transmission delay T_{TRT} can be used ($T_{RR}-T_{SP}$) to represent. For anchor nodes, the round trip delay T_{ART} can be expressed as ($T_{RF}-T_{SR}$). Obviously in addition to the flight time of the signal round trip delay time, there is a response time from the received transmission of a node. Therefore, removing the response time ($T_{RSP}=T_{SR}-T_{RP}$) of the anchor node from T_{TRT} and removing the response time ($T_{RSP}=T_{SF}-T_{RR}$) of the label node from T_{ART} can obtain the net time for the signal to travel back and forth between two nodes. In order to eliminate the impact caused by the clock discrepancy of the terminal equipment on both sides, the time of the round trip on both ends is averaged, and then divided by 2 to obtain the one-way time. That is, the one-way flight time can be calculated by equation (1):

$$TOF=((T_{RR}-T_{SP})-(T_{SR}-T_{RP})+(T_{RF}-T_{SR})-(T_{SF}-T_{RR}))/4. \quad (1)$$

Multiplying the calculated flight time TOF by the transmission speed of the radio waves (the speed of light c), we obtain the distance L between the two nodes. Through the above method, the requirement of extremely high time synchronization in UWB positioning can be avoided, and the difficulty and cost of implementation are greatly reduced.

Based on the UWB ranging above, accurate positioning can be achieved by ranging projection and trilateral positioning algorithm. Based on the UWB positioning data and the INS data of the vehicle, the data fusion of the two positioning algorithms is realized. In this paper, the Federated Kalman Filter is used to fuse the above two positioning methods.

Kalman filter is a class of optimal filters for Gaussian noise in linear systems. And it is a mainstream technology in the field of information fusion. Federated Kalman filter is the most widely used distributed Kalman filter. It is designed into different structures according to system requirements. And it can distribute system information among subsystems through the principle of information distribution.

In federated Kalman filter-based fusion localization, UWB positioning and inertial positioning are used as subsystems. The structure of it is shown in Figure 7. Firstly, each subsystem inputs data Z_i to a respective local filter. Each local filter predicts and updates the data. Then input the local estimated value \hat{X}_i and the covariance matrix P_i to the main filter. The main filter does the time update and data fusion to obtain the global optimum estimate. After that the main filter returns the global estimate X_g and the covariance matrix P_g to the sub-filter through the information distribution principle, and resets the estimated value of the sub-filter and the covariance matrix. Then the main filter can output the optimal positioning estimation.

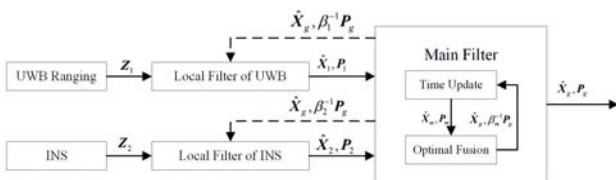


FIGURE VII. HYBRID FUSION ALGORITHM BASED ON FEDERATED KALMAN FILTER

D. Vehicle Distance Estimation and Collision Warning Algorithm in Vehicle Platoon Formation Control

In addition to the vehicle location, the system also needs to obtain the current pose information of the vehicle, speed information, and so on. When the vehicle gets into the positioning area, the collision warning system starts to work. The vehicle on-board unit acquires vehicle status information such as vehicle speed, position, acceleration, angular velocity and course angle through UWB and INS. Then send these information to the router so that it can upload to the server via UWB anchor node. The server performs data processing of the vehicle collision algorithm to detect whether the vehicle collision exists. If there is no vehicle collision, the vehicle can safely pass the area in its current state. If there is a vehicle collision, the severity of the collision is evaluated to calculate the safety interval of the vehicle speed. According to the collision of different security levels to the collision may be sent to vehicles warning information. Early warning information is transmitted to the vehicle control unit via UWB wireless communications. The vehicle will alert the driver to take the necessary measures to avoid the impending collision of vehicles.

E. Application of Hybrid Fusion Algorithm in Vehicle Platoon Formation Control

This application scene of the hybrid fusion algorithm in the Vehicle platoon formation control is divided into three types: roads, junctions and parking. Described below separately:

1) *Roads Scene*: In the road scene (Figure 8), the vehicles in the vehicle platoon formation realize the networking through UWB communication, and make use of the hybrid fusion algorithm of UWB and INS to locate the relative position. Based on this, the vehicle distance is estimated, and the vehicle distance information is sent to the moving vehicles in real time. Then the system realizes the precise control of the distance of the vehicle platoon formation and the complete vehicle platoon formation early warning system.



FIGURE VIII. ROADS SCENE APPLICATION OF HYBRID FUSION ALGORITHM

2) *Junctions*: In the intersection scene, the vehicles in the vehicle platoon formation communicate with the UWB anchor nodes at the intersection. The hybrid fusion algorithm can calculate the real-time position and driving direction of the vehicle and combine with the electronic map to achieve collision warning and lane keeping in the vehicle platoon formation. Lane change warning function.

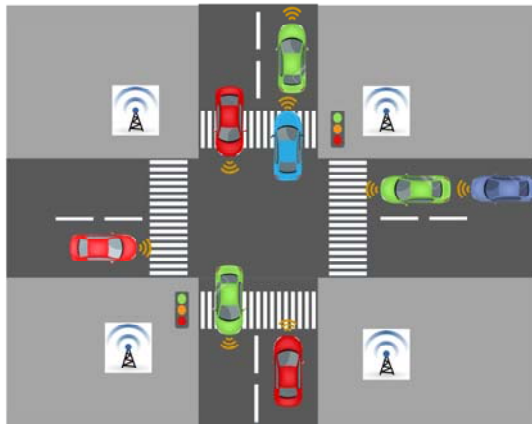


FIGURE IX. JUNCTIONS SCENE APPLICATION OF HYBRID FUSION ALGORITHM

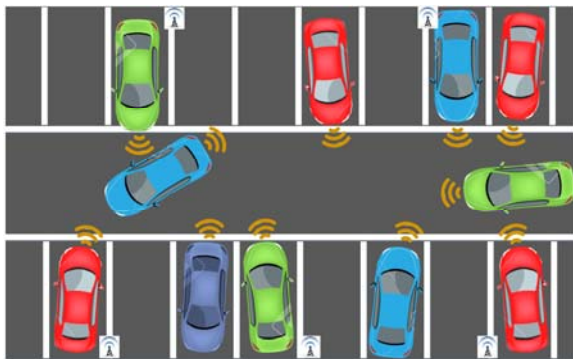


FIGURE X. PARKING SCENE APPLICATION OF HYBRID FUSION ALGORITHM

3) *Parking:* In the parking lot scene (Figure 10), vehicles in the vehicle platoon formation communicate with UWB anchor nodes, and the hybrid fusion algorithm can be used to calculate the real-time location and area information of the vehicle. In combination with the electronic map, the vehicle distance prediction in the parking lot (including the longitudinal and horizontal car), to ensure that the vehicle entering the collision prevention process early warning.

III. CONCLUSION

In this paper, a completed vehicle platoon formation control system is proposed which mainly contains a hybrid fusion algorithm for integrated INS/UWB navigation and its application in this system. First of all, the INS and UWB

positioning data is collected, including final location data and intermediate data. The TWR (Two-Way Range) method based on time of flight can solve the time synchronization problem in UWB positioning algorithm. Moreover, the hybrid fusion algorithm uses Federated Kalman Filter integrate INS/UWB positioning data to get an accuracy location. The UWB model selection, location scheme confirmation, hardware and software design, and so on are also put forward among them in this paper. At last, the hybrid fusion application in vehicle platoon formation control is analyzed which includes

vehicle distance estimation, collision warning algorithm and vehicle platoon formation control in different scenarios.

ACKNOWLEDGMENT

This paper was supported by the Research Foundation of Science and Technology Commission of Shanghai under Grant No. 10DZ1500200, the Natural Science Fund of China (NSFC) under Grant Nos. 51575186, 51275173, and 50975088, the Fundamental Research Funds for the Central Universities under Grant No. WH0913009, Shanghai Pujiang Program under Grant No. PJ201000353, and Shanghai Software and IC industry Development Special Fund under Grant No. 120493.

REFERENCES

- [1] Hye Ri Park, Dong Jun Hyun, Hyun Seok Yang, et al. A Dead Reckoning Sensor System and a Tracking Algorithm for Mobile Robot. Japan: ICROS-SICE International Joint Conference, 2009.
- [2] Tim, Tau, Hsieh. Using sensor networks for highway and traffic application. IEEE Potentials Apprial, 2004, (24): 13-16.
- [3] Vicent Pereira, Audrey Giremus, and Eric Grivel. Modeling of Multipath Environment Using Copulas for Partical Filtering Based GPS Navigation. IEEE Signal Processing Letters. 2012, 19(6): 360-363.
- [4] Seong Yun Cho, Wan Sik Choi. Robust Positioning Technique in Low-cost DR/GPS for Land Navigation. IEEE Transaction on Instrumentation and Measurement. 2006, 55(4): 1132-1142.
- [5] Ghasemzadeh H, Behrangi E, Azgomi M A. Conflict-free scheduling and routing of automated guided vehicles in mesh topologies. Robotics & Autonomous Systems, 2009, 57(6): 738-748.
- [6] Qigao Fan, Yaheng Wu, Jing Hui, Lei Wu, Zhenzhong Yu, Lijuan Zhou, Chingiz Hajiyev. Integrated Navigation Fusion Strategy of INS/UWB for Indoor Carrier Attitude Angle and Position Synchronous Tracking. The Scientific World Journal, 2014(2014).
- [7] KOK M, HOL J D, SCHON T B. Indoor positioning using ultrawideband and inertial measurements. IEEE Transactions on Vehicular Technology, 2015, 64(4):1293-1303.
- [8] Accurate pedestrian indoor navigation by tightly coupling foot-mounted IMU and RFID measurements. IEEE Transactions on Instrumentation and Measurement, 2012, 61(1):178-188.
- [9] FCC 02-48, FIRST REPORT AND ORDER. Adopted: 2002, February 14, Released: 2002.
- [10] Cui Bing-bo, Chen Xi-yuan, Xu Yuan, et al. Performance analysis of improved iterated cubature Kalman filter fand its application to GNSS/INS. ISA Transactions, 2017, 66:460-468.
- [11] Xu Yuan, Chen Xi-yuan, Wang Yi-min, et al. Improving indoor pedestrian navigation method using low cost foot-mounted AHRS and shoulder-mounted compass. Journal of Chinese Inertial Technology, 2016, 24(3):325-329.

The Research of Internet Identity Authentication System Based on Fingerprint Information

Feng Xiao, Yue Zhang, Fei Zhang and Yongzhen Li*

Department of Computer Science & Technology YanBian University YanJi, China

*Corresponding author

Abstract—With the Internet stepping into thousands of households, human beings really come into in the age of the Internet. When people are cheering for their achievements, however, information security has gradually become our incubus. And how to ensure the security of information is the most urgent problem to be solved. Because of the advantages of biometric identification, it has become a new trend in the Internet authentication. Among numerous biological characteristics, fingerprint has the characteristics of uniqueness, stability, and being collected easily. What's more, researches of identification based on fingerprint are more mature than others. Therefore, we chose the fingerprint identification as the authentication methods of our Internet authentication system. In the process of the research, we used for reference some mature fingerprint identification algorithms, and carried out a series of operations on fingerprint information which including preprocessing, feature extraction, matching and so on. After many tests and modifications, the certification system basically achieved the expectant results.

Keywords—information security; biological characteristic; fingerprint identification; identify authentication

I. INTRODUCTION

Human beings have only spent decades entering the information age from the Atomic age. The advent of the information age, so that our lives are filled with the color of science and technology, and the most obvious is the development of the network. In the virtual world of network, in order to set up personalized scenes, maintain order and ensure security, we need to distinguish and locate each individual. With the further development of the information age, the traditional authentication method has not satisfied the requirement of user identification in today's society. A variety of ways to crack the user's password, coupled with a growing human and network links, a variety of confidential information, property, as well as private information is transmitted and stored in the network. Using the traditional authentication method, once the user password is cracked, the loss can be disastrous, people need a more secure and reliable way to authenticate the Internet.

Biometric features have become a new trend in internet identity recognition. In many biometric features, fingerprints have long existed as a tool for identity authentication. As early as the 7000 to the first 6000 BC, fingerprints have been used as identification tools in ancient China and ancient Syria [1]. For the first time in 1880, the characteristics of fingerprint were expounded; in the same year, Henry Fonde first made a

scientific exposition of the uniqueness of human biological characteristics of fingerprints, which laid the foundation for the development of modern fingerprint authentication technology. In 1974, Osterburg passed the argument that the probability of two fingerprints appearing at 12 of the same character but not of the same person was about one in ten trillion [1], for the fingerprint identification of the "12 feature points" rule provides a theoretical basis, and fingerprint recognition has been recognized by the vast number of users, which shows a very broad market and prospects. In recent years, the research on fingerprint identification has been more mature. Therefore, this paper chooses fingerprint information as the focus of the research, and focuses on the research of Internet identity authentication based on biological feature.

II. COMPARISON AND SCREENING OF FINGERPRINT RECOGNITION ALGORITHMS

A. Basic Steps of Fingerprint Identification

A complete fingerprint identification process, roughly including four steps: fingerprint image acquisition, fingerprint image preprocessing, fingerprint feature value extraction and fingerprint information matching (Figure 1.). By reference to some existing fingerprint recognition algorithms, two algorithms are selected to compare.

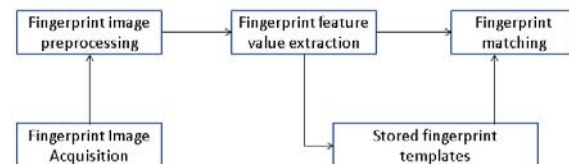


FIGURE I. AUTOMATIC FINGERPRINT IDENTIFICATION PROCESS

B. Fingerprint Recognition Algorithm Based on Point Pattern Matching

The human finger usually has 80-120 detail feature points, of which the most commonly used detail features are both vertebrae and branch points. The most commonly used feature point matching method is to use the fingerprint minutiae model proposed by the FBI to make the detail matching [2,3]. The specific algorithm is as follows:

- Normalization: The purpose is to eliminate the noise caused by the acquisition equipment and the change of the intensity of the finger, and the normalization can solve the problem so as to follow.

- Directional filtering: The algorithm uses the average separating filter based on the spatial domain directional filter to enhance the fingerprint t image.
- Banalization: The gray information needs to be removed and only the black and white color information is saved to reduce the information amount of the image.
- Thinning: Delete the edge pixels of the lines on the basis of the line's connectivity, until the line is single pixel wide, and the main purpose is to reduce the amount of computation.
- Detail feature extraction: The detailed extraction method of the algorithm is to extract the ridge tip and the fulcrum in the thinning graph of the fingerprint.

The key technical difficulty of this method is how to extract the detail features effectively and accurately, and avoid mixing pseudo features as far as possible. So it uses the 8 neighborhood codes commonly used in image processing to track the image, thus the effective extraction of the true detail feature is completed.

C. Fingerprint Recognition Algorithm Based on Texture Feature

Different from the previous algorithm, the algorithm is based on texture characteristics. The object is the characteristics of the whole stripe line, such as the curvature of the lines. In addition, the algorithm is very different from the first algorithm in the processing of directional filtering[4].

The specific algorithm is as follows:

- Direction diagram: The algorithm is used to calculate the directional graph by using Multi window method. The fingerprint direction graph is divided into several 4x4 blocks, in order to calculate the direction of each block area, it is necessary to consider the 8 neighboring blocks of the neighborhood . A direction D which has the most occurrences among the four peak directions is selected as the area direction of the 4×4 sub-block. The direction of the area of each sub-block is sequentially obtained to obtain the block pattern of the fingerprint.
- Seek the center point: The center point is defined as the maximum curvature of the ridge curve of fingerprint. In the matching algorithm based on point pattern, the center point as a matching reference point has strong consistency. The algorithm is based on the fingerprint direction map, and the algorithm is simple and adaptable to the type.
- Gabor filtering: Since the extracted fingerprints are the local structure of the fingerprint texture, the grid scheme of the fingerprint sub blocks chosen in this algorithm is a circular grid. Therefore, before the Gabor filter is filtered, the image should be fanned and then the ridge frequency estimated.

By carefully comparing the advantages and disadvantages of the two algorithms, and according to the problems we

encounter in the concrete practice, we use the fingerprint recognition algorithm based on the point pattern matching to carry on our design research.

III. FINGERPRINT IMAGE PROCESSING

A. Fingerprint Information Collection

We use optical fingerprint collector. The fingerprint samples collected are as follows:



FIGURE II. SAMPLE

B. Fingerprint Image Preprocessing

1) Normalization of fingerprint images

The normalization of an image is an operation on each pixel point on the original grayscale image, which changes its gray value artificially. The purpose of normalization is to adjust the contrast and average grayscale of different original images to a fixed level, to reduce the influence of different contrasts of different fingerprint images, to eliminate the noise caused by the collector itself and to be caused by the difference of finger pressure. The difference of the gray level, the average separation filter based on spatial domain directional filtering is used to filter the fingerprint image, which is more effective for filling holes and broken lines, providing a more uniform image specification for subsequent processing. Calculating the gray mean and variance of the whole image [5]:

$$M(I) = \frac{1}{N^2} \sum_{i=0}^{N-1} \sum_{j=0}^{N-1} I(i, j), (i, j) \in I$$

$$VAR(I) = \frac{1}{N^2} \sum_{i=0}^{N-1} \sum_{j=0}^{N-1} (I(i, j) - M(I))^2, (i, j) \in I$$

Normalize the fingerprint image:

$$G(i, j) = \begin{cases} M_0 + \sqrt{VAR_0 * (I(i, j) - M(I)^2) / VAR(I)}, & I(i, j) \geq M(I) \\ M_0 - \sqrt{VAR_0 * (I(i, j) - M(I)^2) / VAR(I)}, & I(i, j) < M(I) \end{cases}$$

Let the fingerprint image I be the size of $N \times N$, and $I(i, j)$ be the gray level of the pixel point (i, j) . M and VAR are the mean and variance of the fingerprint image respectively.

$G(j)$ is the original gray value of the input pixel. M_0 is the expected average gray value of the image. VAR_0 is the difference of the expected image. M represents the estimated mean gray level of the real input image. Var represents the estimated gray variance of the real input image, and $G(j)$ represents the normalized image gray value. Subsequent fingerprint images are processed on this basis.

Most of the research on the enhancement of grain lines has been done, and most of the lines are used as the parameters of the enhancement algorithm. For example, Hong proposed a Gabor function filter to improve the quality of low-quality fingerprint images, the effect is better, but the algorithm is quite complicated and time-consuming, it is difficult to meet the real-time requirements. Sherlock [6] and others designed to achieve the fingerprint image enhancement, but the algorithm does not use the frequency domain information of the ridge. O 'Gorman and others[7]proposed a method of designing a set of directional filters to improve the quality of the fingerprint image, which is faster and more accurate when the direction information of the fingerprint is more accurate. Because the fingerprint direction of the paper is more accurate, we use o 'Gorman and other people's methods.

2) Fingerprint image filtering

Because the fingerprint is directional and special image of alternating ridges, in the filter design must consider its particularity, according to the different direction of pixels using the principle of design of different filter templates are as follows [5]:

- The filter template size should be appropriate. The size of the filter template requires one or a half cycle of the ridge.
- The size of the template must be odd so that the template can be symmetrical about the x-axis and y-axis through the center.
- In order to improve the contrast between ridges and valleys and achieve the effect of edge sharpening, the template should be designed such that the coefficients of the central part are positive and the coefficients of both sides are negative perpendicular to the direction of the ridge.
- The filtering result should be independent of the average gray level of the original image, so the algebraic sum of all the coefficients in the filter template should be zero.

A basic directional filter (shown as c in Figure 3.) is composed of the averaging filter (a in Figure 3.) and the decoupling filter (b in Figure 3.). The average filter coefficients satisfy: $X \geq Y \geq Z \geq 0$, if there is a breakpoint in the image, that is, the gray value of this point is much smaller than the surrounding points, and its average gray value is close to the average after the filter processing Point of the gray value. So the average filter has the effect of connecting breakpoints. The coefficients of separation filtering satisfy: $P + 2Q + 2R = 0$. In the image, the connecting point of the fork is the point connecting the adjacent two ridge lines. Therefore, the gray value of the upper and lower rows of the connecting point of the fork is larger while the gray value of the neighboring point on the same row is smaller. Through the processing of the separation filter, the gray value of the fork will be significantly reduced, so the separation filter has the effect of removing the fork connection point.

Z Z Z Z Z	R R R R R	M M M M M
Y Y Y Y Y	Q Q Q Q Q	L L L L L
X X X X X	P P P P P	K K K K K
Y Y Y Y Y	Q Q Q Q Q	L L L L L
Z Z Z Z Z	R R R R R	M M M M M

a. averaging filter b. decoupling filter c. directional filter

FIGURE III. FILTER

The filtered image is processed by two valued fingerprint images, and the gray image is transformed into two gray level images, which can be used to reduce the amount of information of the image. We combine the advantages of the two algorithms to improve the refinement effect. First of all, the fast thinning algorithm is used to make a preliminary refinement, the thinning fingerprint is wider, and then the improved OPTA algorithm is further refined [8].

C. Feature Value Extraction of Fingerprint Image

The detail extraction method of the fingerprinting algorithm based on the point pattern is to extract the tip of the ridge and the branch point on the thinning map of the fingerprint. The accuracy of this method is relatively high, and the complexity of the algorithm is also relatively low, easy to implement.

At present, most systems use the method of extracting features from the thinned binary image. This method is relatively simple. Only a 3×3 template can be used to extract the tip and bifurcation points after a reliable thinned binary image is obtained come out. For the refinement of binary images, there are only two kinds of gray values of pixels (assume that 0 represents the gray level of the background point and is represented by the white dot; 1 represents the gray level of the dark line dotted line). N is the number of pixels Point, X1, X2 ... X8 is its 8 neighborhood points, R (1), R (2) ... R (8) are the gray values of X1, X2 ... X8. If N is a vertex, then its 8 neighborhoods satisfy [9]:

$$C_N = \sum_{k=1}^8 |R(k+1) - R(k)| = 2, R(9) = R(1)$$

If N is a bifurcation point, then its 8 neighborhood points are satisfied:

$$C_N = \sum_{k=1}^8 |R(k+1) - R(k)| = 6, R(9) = R(1)$$

Using ridge tracking technology, the number of its 8-neighborhood documents is defined as:

$$S_N = \sum_{k=1}^8 R(k)$$

$$\begin{matrix} \mathbf{x}_4 & \mathbf{x}_1 & \mathbf{x}_2 \\ \mathbf{x}_7 & \mathbf{N} & \mathbf{x}_3 \\ \mathbf{x}_6 & \mathbf{x}_5 & \mathbf{x}_4 \end{matrix}$$

FIGURE IV. N POINT 8 NEIGHBORHOOD

For the tip point, the neighborhood of 8 ridge points $SN = 1$, that is, there is only one ridge point 8 neighborhood. This point is the next point of the line tracking. For the middle point of the ridge, the number of adjacent ridge points in 8 is $SN = 2$, that is, there are two ridge points in the neighborhood of 8, and the last point to be tracked is removed, and the remaining point is the next point to be tracked. For the bifurcation point, 8 neighborhood ridge points $SN = 3$, that is, there are three ridge points in 8 neighborhoods. For the bifurcation point tracking, we can start from these three ridge points separately, tracking along three different ridge lines respectively. Combined with the distribution of the detail feature points in the thinned fingerprint, the pseudo-feature points of the fingerprint details are filtered out and the false feature structures such as burrs, triangles and broken lines are identified and filtered, and finally the true feature points are obtained.

IV. THE SPECIFIC REALIZATION OF FINGERPRINT MATCHING

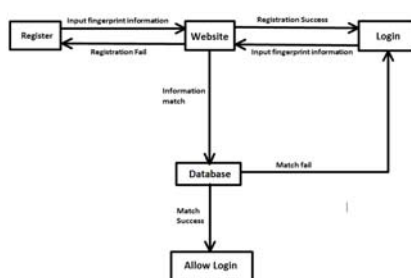


FIGURE V. FINGERPRINT MATCHING FLOW CHART

Through the fingerprint image processing, we will get the fingerprint information into the database. In order to simulate user login and better complete the related research, we made a simple login website. At this point, all the preparatory work is completed. Next, the identity authentication of the user is the most important step in our entire study. Among the main problems to be solved are:

- Real-time processing efficiency of user fingerprint information.
- Threshold setting of matching algorithm.

Through the actual testing of the data obtained from some of the relevant algorithms and experience threshold, we have made the authentication system threshold as follows: For users whose fingerprinting matching rate is higher than 90%, they are regarded as legal users and pass the authentication. Match rate higher than 75% lower than 90% of users, give hints for the second authentication; For users whose matching rate is less than 75%, they are regarded as illegal users. Authentication fails and login is denied. Based on the above settings, we have done a lot of tests on the system. After statistics, we found that

the passing rate of user authentication of the system is 89%, which achieves the expected result basically.

V. CONCLUSION

Through this study and related confirmatory experiments, we have a deeper understanding of the importance of the security of Internet identity authentication and the tendency of biological features to replace the traditional login methods. The work we do is far from enough and we hope to get more results in the future. Here, thank our guidance teacher, thank all in these months to help our predecessors and classmates.

REFERENCES

- [1] Hao Li, Xi Fu, Proficient in Visual C++ And Algorithms Implement of Fingerprint Pattern Recognition System [M]. Posts & Telecom Press, BeiJing,2008
- [2] LI Chen-Dan, XU Jin. Facilities Implementation of Fingerprint Image Preprocessing and Feature Extraction [J] .Computer Science and Engineering, 2002,31 (7)
- [3] Wang Chong wen, Li Jian Wei, Zheng Zhiwei. A fingerprint identification method based on model [J]. Journal of Chongqing University, 2002,25 (6): 27-31
- [4] Zhu Lingyun, Chen Shao Chun. Fingerprint recognition algorithm based on texture features [J]. automation and instrumentation, 2009, (2)
- [5] Zhang Ming. Fingerprint image enhancement algorithm based on directional filtering, [J]. microcomputer development, 2005, 15 (33): 86
- [6] Sherlock D, Momro D M, Millard K. Fingerprint enhancement by directional Fourierfilter[J]. IEEEProceedings of Vi-sion Image and Signal Processing, 1994,141(2):87-94.
- [7] O'Gorman L, Nickerson J V.An approach to fingerprint fil-ter design[J]. Pattern Recognition, 1989,22(1):29-38.
- [8] Wang Lixiang. Research on fingerprint thinning algorithm [J]. Heilongjiang science and technology information, 2009, 15-42
- [9] Liu Ling li. Fingerprint image preprocessing and feature extraction [D].2005.11-33

Multi-Network Fusion Based on CNN for Facial Expression Recognition

Chao Li^{1,2}, Ning Ma^{3,*} and Yalin Deng³

¹Beijing Engineering Laboratory of IOT content security, School of Computer Science and Engineering, Beihang University, Beijing 100191, China

²Shenzhen Key Laboratory of Data Vitalization, Research Institute in Shenzhen, Beihang University, Shenzhen 518057, China

³School of Computer Science and Engineering, Beihang University, Beijing, China

*Corresponding author

Abstract—We propose a method which is multi-network fusion (MNF) based on CNN to recognize facial expressions. Our experimental data adopts the ICML2013 facial expression recognition contest's dataset (FER-2013) and JAFFE dataset. Based on the classic Tang's network structure and Caffe-ImageNet structure, we perform pre-training separately to extract the optimal initialization parameters which are applied for the MNF. We adjust the MNF's parameters through fine-tuning and use L2-SVM for classification. Our experiment has achieved a high accuracy, and the result shows that the effect of the MNF is more obvious than a single network on the facial expression recognition. In this paper, we will describe the specific MNF structure and our training process, as well as the accuracy on the test set.

Keywords—facial expression recognition; fusion; multi-network; CNN; SVM

I. INTRODUCTION

Facial expression recognition (FER) technology is an emerging research area of artificial intelligence, which has broad application prospects in intelligent interpersonal interaction. At the same time, the technology is also widely used in transportation, healthcare and public safety. In recent years, FER technology has attracted more scholars' attention and become a hot topic in the field of artificial intelligence. Therefore, the research on FER technology has typically much value on theoretical research and practical applications. The technology of FER focuses on seven basic categories: neutrality, anger, disgust, fear, happiness, sadness and surprise, which is widely accepted by the public [1]. The seven expression samples in FER-2013 dataset are shown in Figure 1. The experiment on the FER-2013 facial expression dataset is challenging, because the expressions are the real expressions of people in the natural environment, rather than the human expressions making a gesture over against a camera, just like JAFFE dataset. Furthermore, the low image resolution of the dataset and different slope angel increase the difficulty of recognition. In addition, the relatively small dataset makes the training process difficult and the model prone to over-fit [1, 2]. Still, there are many researchers conduct experiments on the FER-2013 and JAFFE datasets, the two datasets have become accepted datasets.



FIGURE I. SEVEN EXPRESSION SAMPLES IN FER-2013 DATASET

In recent year, CNN has become the most popular structure to solve the problem of FER. Theoretically, the more convolution layers are, the more complex features of the active mapping will be obtained [3, 4]. However, deep network is not suitable for small datasets, which can lead to inadequate training. In order to extract discriminative and convincing features of the facial expression, we adopt the technology of MNF. The method is different from the existing methods of FER which are usually trained by single CNN [3], and the performance is better than those. It is not appropriate to apply network structures directly to FER-2013 and JAFFE datasets. The main reason is that the datasets are too small, and too many network parameters make it easy to over-fit in the training process. Therefore, we use the data augmentation in our experiments, after all, collecting more facial expression data is a time-consuming project [5].

In this paper, we use the MNF based on classic Tang's network structure [6] and the Caffe-ImageNet structure [7] to train the dataset respectively. However, the original Softmax classification at the end of the Caffe-ImageNet is replaced by the L2-SVM to classify the expression features. Then we select the most competitive network model from the learning task which can represent the face expression features well as the initialization parameters of MNF, training data through fine-tuning. L2-SVM classifier is used to achieve better effect on the face expression classification. Finally, the recognition accuracy is 68.7% on the FER-2013 validation set, 70.3% on the FER-2013 test set, and 95.7% on the JAFFE dataset (the JAFFE dataset doesn't distinguish between validation set and test set).

II. RELATED WORK

In the various kinds of classification methods which are widely used at present, the method based on CNN is outstanding. CNN can fuse feature extraction and classification in a framework, reducing the large workload of manual design features. In addition, there are many levels and parameters in deep learning models, it can obtain good effect on image and video.

CNN structure is widely used in the recognition and classification of facial expressions. Based on CNN, many researchers have made new changes and innovations to make FER effect better. For example, Tang, the winner of the ICML contest, trained with a CNN structure on the face expression images, and used L2-SVM instead of Softmax to classify facial expression features [6]. In our experiment, L2-SVM classification will also be used. This classification method is suitable for multi-classification tasks, and the result really has slightly improvement. The Caffe-ImageNet structure is designed to classify ImageNet datasets into 1000 categories [7], the number of final output nodes is reduced to seven in [8], but the classification accuracy of Caffe-ImageNet is generally higher than those of other CNN-based methods, such as [9, 10].

Many researchers fused different training networks to train in the latter study. For example, in [5], the extracted appearance features of the image sequence and the extracted geometric features of the temporary facial landmark were merged to enhance the FER effect. Besides, the author in [3] fused different images to extract respective features cross-transformations, and the results showed the effectiveness of the method. In [11], Kim proposed a method which constructed a hierarchical architecture of the committee with exponentially-weighted decision fusion in order to form a better committee in structural and decisional aspects. Our approach is to train two single network model first, and then extract the best network model parameters from them for the MNF's initialization parameters, which is followed with fine-tuning fusion network's parameters. What's more, the MNF structure can be dynamically adjusted, we can try different combinations of the fusion network structure as long as it has a good extraction of the face expression features.

In the process of training, due to the small amount of FER-2013 dataset and JAFFE dataset, it is easy to over-fit when using complex CNN models. In order to solve the problem, researchers in [2] randomly mirror the images, remove 3 pixels in every direction, rotate 45 degrees and magnified to 1.2 times, and finally the transformed image was crop into the size of 42×42 . There are many predecessors in this field who also use transfer learning between different tasks. Before fine-tuning on the target dataset, the network parameters of CNN are initialized by training on the related tasks [1, 12, 13]. These methods are all better performed than training directly on the original small dataset, and the method we adopt is data augmentation.

III. OUR APPROACH

A. Dataset Preparation

Since the FER-2013 image is naturally-obtained, there may be a problem with uneven lighting, and the illumination or contrast greatly affects the accuracy of the result. Therefore, the original image usually needs to be processed to reduce the illumination effect. Histogram equalization (Hist-eq) is a good way to normalize the image grey-scale value and enhance the discrimination of brightness between the foreground and background in face images [8]. As shown in Figure 2, the contrast of the image enhanced after Hist-eq, and the image details become clearer.



FIGURE II. COMPARISON BETWEEN THE RAW IMAGE AND THE PROCESSED IMAGE WITH HIST-EQ

The image of FER-2013 has low resolution, not aligned, that means in early training of the facial expression classification models, quantity is more important than quality to improve experiment results [1]. Moreover, stochastic disturbances through cropping images can essentially generate additional invisible training samples, thus making the network more robust [9]. In this article, images are cropped and rotated for data augmentation and promoting data diversification. We first rotate each image with fixed angle in $\{-10, -5, 5, 10\}$ (the experiment proves that the rotation of 15 degrees will decrease the recognition rate, because rotating a large angle will destroy the original features of the image), and this makes the model robust to slight rotation variation of the input images. Figure 3 shows the original image and the rotated image. Then, we proceed with image normalization, decentralized (subtract the mean value), and mirroring image. Finally, we cut the original 48×48 face images into five 42×42 images (center, top left, top right, bottom left and bottom right), and we get the augmented data.



FIGURE III. THE ROTATED FACE IMAGES (THE NUMBERS UNDER THE IMAGES REPRESENT THE ROTATED ANGLES)

B. Network Architecture

Our proposed MNF structure is based on Tang's network structure [6] and Caffe-ImageNet's structure [7], both of them are based on CNN, and the two networks are chosen because they have very good effect on FER problem. Tang's structure using SVM instead of Softmax classification has improved the classification results and won the champion of FER in ICML2013 competition. Caffe-ImageNet structure is a deep level network, which has better ability to extract facial expression features. We use the augmented training set to train the network model, the validation set to tune the learned models, and the test set to test the trained model's ability of distinguishing facial expressions.

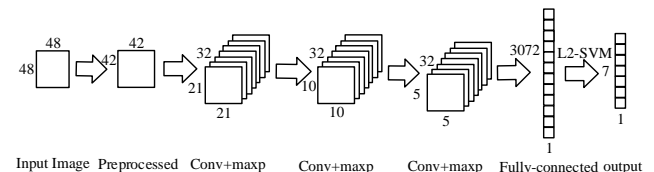


FIGURE IV. TANG'S NETWORK STRUCTURE

The first CNN structure based on Tang's structure consists of three convolutional neural network and max pooling layers,

followed by a fully connected layer, and finally using L2-SVM to classify facial expressions into 7 types, as shown in Figure 4. The second network based on Caffe-ImageNet structure consists of two convolutional neural network, max pooling and LRN layers, then two convolutional neural networks, a convolutional network and max pooling layer, followed by a convolutional layer and a fully connected layer. Finally, the original classifier is changed to L2-SVM classifier, as shown in Figure 5. We select the best model parameters from each of the two trained neural network models, regarded as the

initialization parameter of the MNF. Then two based network structures are fused. Similarly, L2-SVM classifier is adopted at the end. We keep the parameters before the two networks fuse unchanged. The MNF parameters after fully connected layer are fine-tuned. This process is illustrated in Figure 6. In the network models, rectified linear units (ReLU) are used between the fully connected layer and the output layer, so that the convolutional neural networks can approximate any function, which a linear combination of inputs can't.

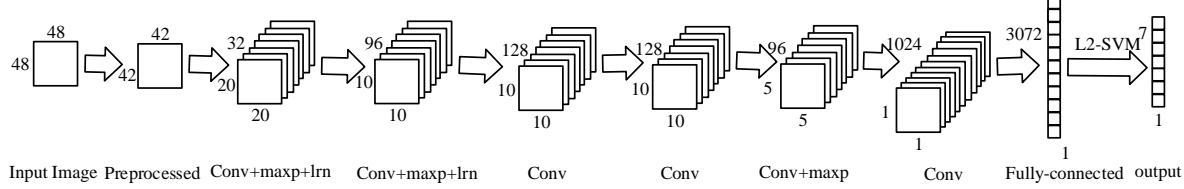


FIGURE V. CAFFE-IMAGENET STRUCTURE

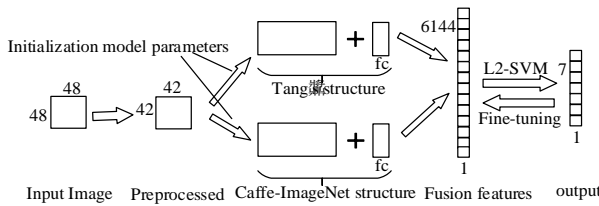


FIGURE VI. THE MNF STRUCTURE

IV. EXPERIMENT

A. Image Database and Experimental Setup

MNF experiments based on CNN are implemented on the FER-2013 dataset and JAFFE dataset. Our experiments are conducted on the NVIDIA GeForce GTX TITAN X GPU using Caffe framework.

The experiment input is a 42×42 size of facial expression image, which is preprocessed by clipping, mirror transformation, and reduction of the average value to normalize the image. We use different test methods to evaluate the experiment results on the two datasets. In order to improve the accuracy of classification, the performance between Softmax and L2-SVM classification is compared. It was found that the model effect will be enhanced using the L2-SVM, so we adopt L2-SVM to classify the facial expressions.

B. Experiments on the FER-2013 Database

FER-2013 dataset comes from the ICML 2013 PERL workshop's facial expression recognition contest, which includes 28709 images in training set, 3589 images in validation set, and 3589 images in test set. Each sample is a 48×48 face image with an expression label.

As we can see from Figure 7, the best method is Tang's, which achieves accuracy of 71.2%. We reproduce Tang's method, but we achieve accuracy of 64.2% which differs by 5% from Tang's result, maybe we have different initialization parameters. We use Tang's method as one part of the MNF structure, and find that the recognition accuracy of MNF is 70.3% which is higher than that of the individual training network.

Therefore, the MNF structure is effective for the improvement on the FER accuracy.

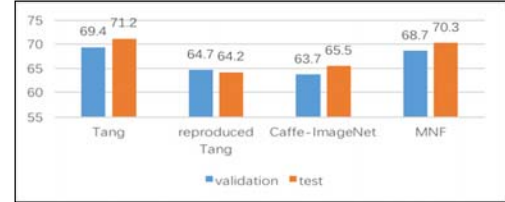


FIGURE VII. THE COMPARISON OF OUR METHOD WITH SOME CLASSIC APPROACHES ON FER-2013 DATASET (%)

TABLE I. CONFUSION MATRIX OF OUR PROPOSED METHOD ON FER-2013 VALIDATION DATASET (%)

	AN	DI	FE	HA	SA	SU	NE
AN	56.1	0.4	9.2	6	9.9	1.9	16.5
DI	19.6	60.7	0	3.6	10.7	0	5.4
FE	7.5	0	46.6	3.4	17.9	8.9	15.7
HA	1.5	0	1.1	85.9	1.5	1.6	8.5
SA	7.5	0	8.0	4.9	58.0	1.7	19.9
SU	1.5	0	3.4	4.6	2.7	84.6	3.4
NE	5.3	0	2.3	7.4	12.5	1.0	71.5

TABLE II. CONFUSION MATRIX OF OUR PROPOSED METHOD ON FER-2013 TEST DATASET (%)

	AN	DI	FE	HA	SA	SU	NE
AN	57.2	0.4	7.7	5.3	14.5	1.4	13.4
DI	23.6	63.6	3.6	1.8	3.6	0	3.6
FE	9.7	0.2	52.1	4.0	15.2	6.8	12.1
HA	1.8	0	1.5	86.9	3.0	1.9	4.9
SA	6.9	0	11.3	5.2	55.9	0.7	20.0
SU	0.5	0.2	4.8	4.8	1.7	84.9	3.1
NE	3.5	0.2	2.6	5.8	10.9	1.0	76.2

Table 1 and Table 2 are confusion matrix of our method, we can find that the accuracy is high in classifying happiness, surprise and neutrality expressions, this is because it's obvious

to distinguish the three types of expression images from other types in test set, so as the human eyes. Other expressions, especially fear, have low recognition accuracy because the human eyes can't categorize them well either.

C. Experiments on the JAFFE Database

The JAFFE dataset contains 213 images (resolution: 256×256 pixels per image) of Japanese women's faces. There are 10 people in the expression database, and each person has seven expressions. JAFFE database is all frontal face, the face size is basically the same, the illumination is frontal light source, but the illumination intensity is different. Since the expression database is completely open and the expressions are indexed very standardly, it is now used in most studies of expression recognition.

There are no specific training and testing samples in JAFFE dataset, so we use the ten-fold cross-validation method to evaluate the recognition effect. In the experiment, the dataset is randomly divided into ten folds, and each contains about 21 face images. We take nine out of ten for training network models and the remaining one for testing in turn, and finally get an average accuracy of 95.7%. The accuracy rates of ten experiments are shown in Table 3, we can see that nine out of ten of the experimental recognition accuracies is over 90%, and three of them reach 100%. Recognition rate's comparison of our proposed method with the state-of-art methods is shown in Table 4, it shows that the MNF structure we design is more effective.

TABLE III. THE ACCURACY OF OUR EXPERIMENTS ON JAFFE DATASET

Ten times experiment on different folds of the dataset			
Fold number	Accuracy (%)	Fold number	Accuracy (%)
1	95.2	6	100
2	85.7	7	100
3	95.2	8	95.2
4	100	9	90.9
5	95.2	10	100

TABLE IV. THE COMPARISON OF OUR METHOD WITH SOME CLASSICAL APPROACHES ON JAFFE DATASET

Method	Accuracy (%)
Zhao X, et al [16]	91.0
Mlakar, et al [17]	86.7
MNF	95.7

V. CONCLUSION

In this paper, we introduce a new method which is MNF based on CNN to recognize facial expressions. We first train two network structures in the experiment, one based on Tang's network structure, the other based on Caffe-ImageNet, and then use L2-SVM for classification. The best network model parameters are extracted from the two previous trained networks as the initialization parameters of MNF structure, and then the MNF structure is fine-tuned. Our experiment is conducted on the FER-2013 dataset and JAFFE dataset. The results demonstrate

that the recognition effect of MNF is better than that of each single network, and MNF structure is competitive with other state-of-the-art recognition networks. What's more, MNF structure is extensible, we can find possible combinations of other different models for further research.

ACKNOWLEDGMENT

This work was supported by the National Natural Science Foundation of China (No.61370122).

REFERENCES

- [1] Winkler, Stefan, et al. "Deep Learning for Emotion Recognition on Small Datasets using Transfer Learning." ACM on International Conference on Multimodal Interaction ACM, 2015:443-449.
- [2] Shin, Minchul, M. Kim, and D. S. Kwon. "Baseline CNN structure analysis for facial expression recognition." IEEE International Symposium on Robot and Human Interactive Communication IEEE, 2016:724-729.
- [3] Xie, Siyue, and H. Hu. "Facial expression recognition with FRR-CNN." Electronics Letters 53.4(2017):235-237.
- [4] Matthew D. Zeiler, and Rob Fergus. "Visualizing and Understanding Convolutional Networks." 8689(2013):818-833.
- [5] Jung, Heechul, et al. "Joint Fine-Tuning in Deep Neural Networks for Facial Expression Recognition." IEEE International Conference on Computer Vision IEEE, 2016:2983-2991.
- [6] Tang, Yichuan. "Deep Learning using Support Vector Machines." Eprint Arxiv (2013).
- [7] Jia, Yangqing, et al. "Caffe: Convolutional Architecture for Fast Feature Embedding." Acm International Conference on Multimedia ACM, 2014:675-678.
- [8] Devries, Terrance, K. Biswaranjan, and G. W. Taylor. "Multi-task Learning of Facial Landmarks and Expression." Computer and Robot Vision IEEE, 2014:98-103.
- [9] Yu, Zhiding, and C. Zhang. "Image based Static Facial Expression Recognition with Multiple Deep Network Learning." ACM on International Conference on Multimodal Interaction ACM, 2015:435-442.
- [10] Kahou, Samira Ebrahimi, et al. "Combining modality specific deep neural networks for emotion recognition in video." ACM on International Conference on Multimodal Interaction ACM, 2013:543-550.
- [11] Kim, Bo Kyeong, et al. "Hierarchical committee of deep convolutional neural networks for robust facial expression recognition." Journal on Multimodal User Interfaces 10.2(2016):1-17.
- [12] Ross Girshick, et al. "Rich Feature Hierarchies for Accurate Object Detection and Semantic Segmentation." (2013):580-587.
- [13] Yosinski, Jason, et al. "How transferable are features in deep neural networks?" International Conference on Neural Information Processing Systems MIT Press, 2014:3320-3328.
- [14] Mayya, Veena, R. M. Pai, and M. M. M. Pai. "Automatic Facial Expression Recognition Using DCNN ☆." Procedia Computer Science93(2016):453-461.
- [15] Mollahosseini, Ali, D. Chan, and M. H. Mahoor. "Going deeper in facial expression recognition using deep neural networks." Applications of Computer Vision IEEE, 2016:1-10.
- [16] Yadan Lv, Zhiyong Feng, and Chao Xu. "Facial expression recognition via deep learning." IETE Technical Review 32.5(2015):347-355.
- [17] Lopes, André Teixeira, et al. "Facial expression recognition with Convolutional Neural Networks: Coping with few data and the training sample order." Pattern Recognition 61(2017):610-628.

Human Face Age Recognition Based on Convolutional Neural Networks

Zijiang Zhu*, Yi Hu, Dong Liu, Xiaoguang Deng and Junshan Li

South China Business College of Guangdong University of Foreign Studies , Guangzhou 510545, China

*Corresponding author

Abstract—In the field of image recognition, the issue of face age recognition has attracted the attention of many scholars, and a lot of outstanding algorithms have been proposed, but the correctness rate of age recognition is not high. To improve the AGE identification accuracy, this paper proposes a face AGE recognition based on convolutional neural network (CNN) -- the AGE model, the IMDB - WIKI database and Caffe framework for training and testing, and the AGE recognition has the highest accuracy of 52%. Through experiments, this model is proved to be scientific and provides new ideas and methods for the study of face age recognition.

Keywords—human face age recognition; convolutional neural networks; CNN-AGE; caffe

I. INTRODUCTION

In the field of machine vision and image processing, age recognition based on face image is an important research subject, which has attracted the attention of scientific researchers at home and abroad in recent years [1]. The issue of age recognition has broad application prospects in academic researches and business applications. For example, it has important application value in security monitoring, personalized human-computer interaction, image retrieval and criminal investigation, etc. [2] But it is relatively difficult to identify age from face image, mainly because of the following three reasons [3][4]: 1) The positioning of age recognition is fuzzy because it can be either classification issue or regression issue; 2) It is difficult to gather data of human face image ages; 3) Facial image features of the same age are significantly different.

The key of extracting age feature through face image is facial feature model. At present, there are corresponding studies on the features of the local appearance and the global appearance. J. Ylioinas et al. [5] used the improved Local Binary Patterns (LBP) to extract features and carried out the test in Gallagher database, getting an accuracy rate of 51.7%. Yan S et al. [6] divided the age into 0-2 categories, namely, 3-7, 8-12, 13-19, 20-36, 37-65, >66, 7, and the improved LBP feature extraction method was used. Finally, the accuracy rate in Gallagher database was 50.3%. Eidinger et al. [7] used FPLBP feature extraction method to extract the age characteristics of face images, and achieved a 66.6% accuracy rate on Gallagher database, and achieved 45.1% accuracy on Adience data base. F. Gao et al. [8] proved that the method of extracting the age feature of the face image by Gabor feature extraction is better than the Local Binary Patterns (LBP). Ueki et al. [9] used the Expectation Maximization (EM) algorithm to

build 11 kinds of Gauss models in the low dimensional 2DLDA+LDA feature space and achieved good results. In the research of Ueki et al, the accuracy rate reached 50% when the age classification interval was 5 years old, and the accuracy rate reached 82% when the age interval was 10 years old. However, the face image test set they used were all males or females.

It can be seen that it is very difficult to carry out the research of face age recognition. The accuracy of age recognition is affected by objective factors such as the time span of face image (age classification interval), sex and individual senescence speed. Based on convolution neural network, a neural network model of face age recognition is constructed in this paper in a bid to contribute to the research of face age recognition.

II. CONVOLUTIONAL NEURAL NETWORKS (CNN)

Convolutional Neural Networks (CNN) is an improved algorithm based on Back Propagation (BP). The common point between CNN and BP neural network is that during the training process, the output value of the network is calculated in the forward propagation phase of the signal, and the weights and biases between the neurons are adjusted in the reverse propagation stage of the error. The main difference between CNN and BP neural networks is that the neuron nodes between the adjacent layers of the BP neural network are all connected, while the CNN is partially connected [10]. As shown in Figure 1, CNN mainly includes three parts: the convolution layer, the pool layer and the full connection layer.

In CNN, there are three basic concepts: local receptive fields, shared weights and pooling.

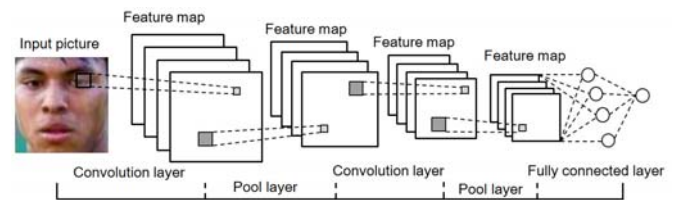


FIGURE I.

BASIC STRUCTURE OF CONVOLUTIONAL NEURAL NETWORKS

- 1) Local Receptive Fields.

The local sensing domain of CNN is not connected to all neuron nodes while connecting the neurons at the input layer to the hidden layer. It only connects some neuron nodes, that is, the local sense. Taking 8 * 8 gray level image as an example,

the number of neurons in the input layer is 64, and the window of the local receptive field is set to $4 * 4$. Each neuron node in the hidden layer connects only part of the neuron nodes in the input layer, that is, the local $4 * 4=16$ connected to the input layer, as shown in Figure 2. Through mobile local receptive field window (from top to bottom, left to right), all input layer neurons are covered, and each neuron node with local receptive field is connected to different neuron nodes of hidden layer, respectively. This is the learning process of the convolution neural network from the local feature of the input layer to the global feature.

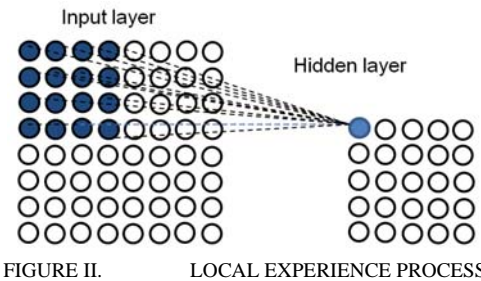


FIGURE II. LOCAL EXPERIENCE PROCESS

Assume that the receptive field is only connected to the 1 neuron nodes of the hidden layer, and the mobile step length is 1. From Figure 2, it can be seen that if the field moves down 4 times to the right direction, it can reach the edge of the image, and the hidden layer has $5 * 5=25$ neuron nodes. For $8 * 8$ images, the receptive field is $4 * 4=16$, the first hidden layer has 25 neurons, and the number of neurons is 16, and the total weight is $25 * 16=400$. Compared with the BP neural network, this method greatly reduces the number of parameters of the weights, that is, the number of parameters of the training weight is reduced.

- 2) Shared Weight.

It is known from the above 1) that the $8 * 8$ image requires 400 weight parameters. If each neuron corresponds to the 16-weight parameter is equal, the total weight parameter is only 16, 25 neurons share 16 weights, which reduces the number of weight parameters, i.e., the concept of shared weight. Suppose that the neurons are located in the hidden layer (i, j) , its $O_{i,j}$ output can be expressed as follows:

$$O_{i,j} = f\left(\sum_{k=0}^3 \sum_{m=0}^3 w_{k,m} a_{i+k, j+m} + b\right) \quad (1)$$

In equation (1), f is a neuron activation function, $w_{k,m}$ is $4 * 4$ weight sharing matrix, $a_{i,j}$ is the input value of the neuron in the hidden layer (i, j) , and b is a shared bias parameter. It can be seen that the feature extraction method of CNN is convolution operation, and the neuron extracts the characteristics of the same statistical characteristics at different positions in the image. The feature map is the input and output of the hidden layer. The weights and biases on the feature map are shared weights and biases. All the shared weights and biases are called convolution kernels, also known as filters. In practical applications, there are often multiple convolution

cores in CNN, indicating that there are multiple feature graphs. The more the feature maps, the more the content of the image is expressed.

- 3) Pooling.

CNN classifies sample instances through feature graphs, but because of too many feature maps, the classifier has a large amount of computation. When a large number of feature graphs are input, the training of the classifier is difficult, and it will lead to the over fitting (over-fitting) phenomenon of CNN. To solve this problem, the feature graph is put into the pool layer for pooling and aggregate the statistics of different regions, calculate the maximum or average value of a region's characteristics, reduce the dimension of statistical features and prevent the over fitting phenomenon.

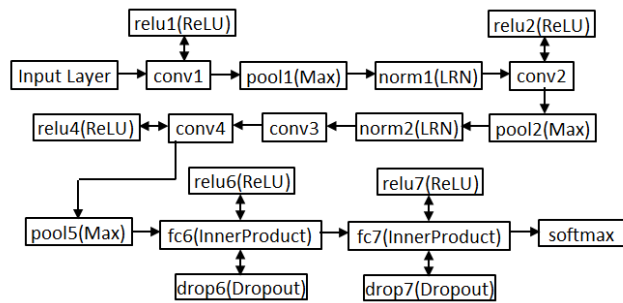


FIGURE III. CNN-AGE MODEL STRUCTURE

In Figure 3, Input Layer is the input layer. Conv1, conv2, conv3 and conv4 are 4 volumes. Pool1, pool2 and pool5 are 3 pools. fc6 and fc7 are 2 full link layers, and pool5 is classifier. In CNN, because the ReLU function has a fast convergence property [11], the ReLU function is used as the activation function of the convolution layer and the fully connected layer. In the pool layer, in order to achieve the purpose of local normalization, the LRN (Local Response Normalization) function is proposed by Krizhevsky et al. In order to prevent training over fitting, the Dropout processing is added to the entire connection layer, and dropout sets the output neuron to zero [12, 13] according to a certain probability. After convolution layer conv3 is convoluted, considering that the feature graph is very small, then pooling is meaningless, but it increases resource consumption. Therefore, the pool layer is canceled, and the next volume layer is directly connected to extract the deep features of the image. Softmax is a classifier that classifies and outputs the age category.

III. TRAINING PROCESS

A. Experiment Environment

The experiment in this paper is carried out using the depth learning framework (Caffe) of BVLC. The training data set is a IMDB-WIKI database, because the data is too big, just select 62 thousand pictures from Wikipedia. Face detection is done for each picture. Only face images are selected for training and testing. The face images are pre-processed (aligned and clipped) before the experiment. The experimental environment is shown in Table 1 as follows.

TABLE I. EXPERIMENT ENVIRONMENT OF HUMAN FACE AGE RECOGNITION

System	Ubuntu 16.04 Beta
Memory	DDR4 16G
CPU	NVIDIA Ge Force GT 4G
CPU	inter(R) Xeon(R) CPU E5-2620 v2 @ 2.10GHz

B. Data Set Division and Age Classification

The pictures provided in the IMDB-WIKI database contain detailed information files, and two Matlab codes written by the author can be used to realize data partition and age classification. Because the data in different age groups of IMDB-WIKI dataset are not balanced, it is possible to get less than 5 years old or more than 85 years old. There are relatively few sample photos. So we use 5-84 year old age photos, and configuration information is like Figure 4. The age division of 10 years is divided into 8 categories, and the span of each class is 10 years. The log information of the age classification is shown in Figure 5.

```

ratio = 8;
sel = 1;
class = 10;
min = 5;
max = 84;
maxsel = 84;
minsel = 5;

```

FIGURE IV. DATA SET DIVISION

```

train.list and val.list created by age_div_train_test.m
dataset:35699
sel: 1.00000, ratio:8:1
selected:35699 (about 31732 train(88.89%), 3967 test(11.11%))
class capacity: 10, class num: 8 (about 4462 per class)
guaranteed num of every class:
    235 4462 4462 4462 3078 1786 867
min:5, max:84
minsel:5, maxsel:84

```

FIGURE V. AGE CLASSIFICATION LOG

TABLE II. HUMAN FACE RECOGNITION EXPERIMENT RESULTS OF ALL AGES

No.	Physical age	Experiment results of all ages							
		5-14	15-24	25-34	35-44	45-54	55-64	65-74	75-84
1	11	0.273	0.255	0.194	0.067	0.053	0.076	0.059	0.023
2	8	0.297	0.306	0.254	0.073	0.021	0.022	0.027	0
3	19	0.172	0.369	0.31	0.094	0.043	0.008	0.004	0
4	21	0.091	0.471	0.325	0.111	0.001	0.001	0	0
5	26	0.006	0.232	0.512	0.200	0.043	0.007	0	0
6	34	0.011	0.148	0.479	0.321	0.019	0.019	0.003	0
7	38	0.006	0.093	0.247	0.465	0.173	0.015	0.001	0
8	39	0.003	0.122	0.191	0.517	0.161	0.007	0	0
9	49	0.004	0.003	0.122	0.277	0.296	0.205	0.089	0.004
10	53	0.004	0.018	0.016	0.013	0.310	0.323	0.193	0.123
11	55	0.003	0.011	0.009	0.026	0.293	0.307	0.257	0.094
12	61	0	0	0	0.013	0.301	0.298	0.255	0.133
13	73	0	0.001	0.001	0.021	0.243	0.305	0.233	0.196
14	70	0	0.001	0.003	0.016	0.221	0.363	0.240	0.156
15	81	0	0	0.002	0.038	0.090	0.265	0.379	0.226
16	79	0	0	0.009	0.032	0.230	0.239	0.286	0.204

C. Training Results

Through repeated experiments and repeated adjustment of the relevant parameters, the best accuracy rate of face age recognition is 9000 iterations, and the accuracy rate is 52% as shown in Figure 6. The experiment was carried out with random initialization of Gauss distribution function, the volume weight average layer is set to 0, the random drop rate is set to 0.5 fully connected layer Dropout, the number of training samples set Batchsize to 256, on a gradient weight momentum is set to 0.9, the initial learning rate of base_lr is set to 0.0001.

```

d_solver.cpp:106] Iteration 9009, lr = 0.0001
lver.cpp:337] Iteration 9010, Testing net (#0)
lver.cpp:404]   Test net output #0: accuracy_test_top01 = 0.519
lver.cpp:404]   Test net output #1: accuracy_test_top02 = 0.635
lver.cpp:404]   Test net output #2: loss = 1.35133 (* 1 = 1.35133 loss)
lver.cpp:228] Iteration 9010, loss = 1.31241
lver.cpp:244]   Test net output #0: loss = 1.31241 (* 1 = 1.31241 loss)
d_solver.cpp:106] Iteration 9010, lr = 0.0001
lver.cpp:228] Iteration 9011, loss = 1.21332

```

FIGURE VI. TRAINING RESULTS

IV. ANALYSIS OF EXPERIMENT RESULTS

A. Scientificity of CNN-AGE Model

According to the above training results, select two pictures from 8 age groups at random for human face age identification experiment, and the experiment results are as shown in the following Table 2.

From the experimental results of the last table 2, it can be seen that the accuracy of the test at the age of 15-44 is higher and the maximum is 52%. The accuracy of the tests at the age of 5-14 and 55-64 is generally close to 30%, and the accuracy of the test at the age of 65-84 is low, and the maximum is only 24%. The accuracy of the tests at all ages is shown in Figure 7.

As can be seen from Figure 7, with the change of age, the CNN-AGE model has a larger age recognition rate for facial features. Figure 7 shows that the changes in the facial features at the age of 15-44 are relatively slow, and the changes in other age groups are relatively large. This is consistent with the natural law of human being from maturity to maturity, from maturity to aging. It also proves the scientificity of the face recognition model based on convolutional neural network.

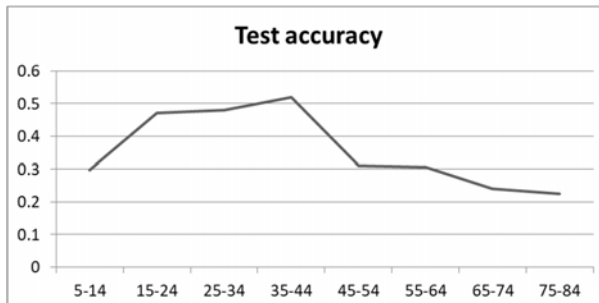


FIGURE VII. CORRECT RATE OF TESTING FOR ALL AGES

B. Summary of the Experiment

In the process of using Caffe to realize the CNN-AGE model, there are many problems, and the main problems are summarized as follows:

- 1) When the training set is converted into LevelDB or LMDB, shuffle treatment is necessary, otherwise train loss will quickly return to 0, leading to the failure of network training.
- 2) Corresponding pre-treatment must be carried out on the data set, particularly the human face data. After the human face testing, aligning and cutting, the training speed and accuracy will be greatly improved.
- 3) The mean value of the image data must be deduced, or the accuracy may reduce.
- 4) Learning rate and momentum cannot be set too large, otherwise, it may lead to the rapid and infinite trend of the weight of some point. Normalization of scale may improve this problem.
- 5) A deep network will consume a lot of computing resources and memory resources, and it takes a very long training time if the situation allows for a smaller network. Too simple networks may be difficult to extract the appropriate classification features, and the appropriate network should be built or selected according to the situation.
- 6) The number of samples in the data set must be enough, otherwise it is easy to fall into the case of fitting.

V. CONCLUSION

Many scholars have carried out research on the age prediction of face information, and many more successful cases have been put forward. According to different methods, the data set, age classification, prediction accuracy rate of high and low, but were not used in the actual production. The main reason is that the accuracy of age identification is not high, and it cannot meet the needs of practical application. But this does not mean that the research is of no value, but it means a better way has not been found to solve the problem. The face age recognition model based on the convolution neural network, which is proposed in this paper with the highest accuracy of 52%. Although it has not reached the standard of practical application, it provides new ideas and methods for the research

of face age recognition, and provides an important reference for future research.

ACKNOWLEDGEMENTS

This article has received the support of the Characteristics innovation project of colleges and universities of Guangdong Province (Natural Science), 2016, No.2016KTSCX182; and also received the support of the Youth Innovation Talent Project of colleges and universities of Guangdong Province,2016, No. 2016KQNCX230.

REFERENCES

- [1] Savvides, Marios, Seshadri, Keshav, Luu, Khoa. Face age-estimation and methods, systems, and software therefor[J]. 2016.
- [2] Wang Xianmei, Liang Lingyan, Wang Zhiliang, et al. On the Technology to Estimate Ages from the Image of Human Face [J]. Journal of Image and Graphics, 2012,17(6):603-618.
- [3] Fu Y, Guo G, Huang T S. Age synthesis and estimation via faces: A survey[J]. PatternAnalysis and Machine Intelligence, IEEE Transactions on, 2010, 32(11): 1955-1976.
- [4] Zhou Feng, Li Deqiang, Huang Danyi, et al. Design of a Face-age Decision Method [J]. Software, 2015(7):46-52.
- [5] Ylioinas J, Hadid A, Pietikainen M. Age Classification in Unconstrained Conditions Using LBP Variants[C]// Pattern Recognition (ICPR), 2012 21st International Conference on. IEEE, 2012:1257-1260.
- [6] Shan C. Learning local features for age estimation on real-life faces[C]// Proceedings of the 1st ACM international workshop on Multimodal pervasive video analysis. ACM,2010:23-28.
- [7] Eiderer E, Enbar R, Hassner T. Age and gender estimation of unfiltered faces[J]. Information Forensics and Security, IEEE Transactions on, 2014, 9(12): 2170-2179.
- [8] Gao F, Ai H. Face age classification on consumer images with gabor feature and fuzzy lda method[M]. Advances in biometrics. Springer Berlin Heidelberg, 2009: 132-141.
- [9] Ueki K, Hayashida T, Kobayashi T. Subspace-based Age-group Classification Using Facial Images under Various Lighting Conditions[C]// International Conference on Automatic Face and Gesture Recognition. 2006:13-18.
- [10] Le Cun Y, Bengio Y. Convolutional networks for images, speech, and time series[J]. The handbook of brain theory and neural networks, 1995, 3361(10): 1995.
- [11] Bartlett M S, Littlewort G, Frank M, et al. Recognizing Facial Expression: Machine Learning and Application to Spontaneous Behavior[C]// 2005:568-573.
- [12] Srivastava N, Hinton G, Krizhevsky A, et al. Dropout: A Simple Way to Prevent Neural Networks from Overfitting[J]. Journal of Machine Learning Research, 2014,15(1):1929-1958.
- [13] Hinton G E, Srivastava N, Krizhevsky A, et al. Improving neural networks by preventing co-adaptation of feature detectors[J]. Computer Science, 2012, 3(4): 212-223.

Face Recognition Based on LBP(2D)²PCA+SVM

Yanmei Jiang, Wei Wei, Xue Liu and Ying Shi

LMIB and School of Mathematics and Systems Science Beihang University Beijing, China

Abstract—In this work, we present a novel approach of face recognition which considers local binary pattern (LBP), principal component analysis (PCA) and support vector machine (SVM) algorithms, which is named as LBP(2D)²PCA+SVM. This method firstly extracts facial texture features, then uses (2D)²PCA algorithm to reduce its dimensions, and finally employs SVM algorithm to classify and recognize the images. Our consideration is that LBP algorithm has a characteristic of rotation invariance, which is robust to illumination change and pose variation; (2D)²PCA is an improvement of PCA, using this method the image can reach the maximum degree of dimension reduction; SVM has the advantages of global optimization, simple structure, strong generalization ability and so on. By synthesizing the advantages of the algorithms, our proposed LBP(2D)²PCA +SVM algorithm performs higher recognition rate than other algorithms, and the effective combination of different strategies can greatly help us to improve the recognition rate.

Keywords—face recognition; (2D)²PCA; LBP; SVM

I. INTRODUCTION

Face recognition is an important biometric identification technology, detects the human face image and compares the face images from a static image or video image in the database, and finds matching face process in order to achieve the purpose of identification and appraisal [1]. Face recognition is important in both theory and application. On one hand, it can deepen persons' understanding of human visual system. On the other hand, it can meet the requirements of artificial intelligence in practical applications [2]. To improve the efficiency, many researchers have developed the method of the geometric characteristics, the method of template matching, the method of characteristics of face, hidden Markov model [3], neural network [4], the method of elastic graph matching and so on. At present, most mainstream face recognition algorithms are based on statistical characteristics, such as principal component analysis [5] and linear discriminant analysis [6]. The basic idea of these methods is to use the algebraic tools to reduce the face image to a linear subspace, and then performs classification and identification. The two-dimensional principal component analysis (2DPCA) [8] was proposed for face representation and recognition. The main idea behind 2DPCA is that it is based on 2D matrices as opposed to the standard PCA [7], which is based on 1D vectors. By simultaneously considering the row and column directions, Daoqiang ZHANG, Zhi-Hua ZHOU developed the two-directional 2DPCA, i.e. (2D)²PCA [9]. The (2D)²PCA algorithm reduces the dimension of the image feature matrix from two directions, and the computation time and memory space are reduced. The availability of numerous commercial face recognition systems attests to the significant progress in the research field. Despite these achievements have achieved, face recognition continues to be an active topic in computer vision research. The current

system works well in a relatively controlled environment, but it tends to be affected when different factors (such as posture, lighting, etc.) change. Timo Ahonen, Abdenour Hadid, Matti Pietikainen et al. presented a new approach for face recognition with local binary pattern (LBP) [10]. The goal of the research is to increase the robustness of the systems against different factors. Support Vector Machines (SVMs) have been recently proposed by Vapnik and his co-workers as a very effective method for general purpose pattern recognition.

On the basis of previous work, we introduce a new approach LBP(2D)²PCA+SVM which adopts the LBP algorithm to extract the face image texture information, reduces the influence of illumination change of face image, then uses (2D)²PCA dimension reduction to decrease the computer storage cost and save time for subsequent classification recognition, and finally utilizes support vector machine for classification and identification. The experimental results show that this method combines the advantage of the main component analysis, the robustness of LBP algorithm, the efficiency of support vector machine's classification ability, which improves the face recognition rate.

II. ALGORITHM DESCRIPTION

As the local binary pattern has illumination invariant and the advantage of rotation invariance, and can effectively describe the image of the local characteristics, we make use of the local binary pattern for feature extraction [11, 12]. The process is stated as follows.

LBP operator is used to calculate the LBP value of each pixel in the image, and the LBP value is used to replace the gray value of corresponding pixel, and get a new image $f_{LBP}(x, y)$. Then we calculate the histogram of the image $f_{LBP}(x, y)$:

$$H = (H_0, H_1, \dots, H_{n-1}),$$

Where $H_i = \sum_{x,y} I\{f_{LBP}(x, y) = i\}$ $i = 0, 1, \dots, n - 1$,

$$I\{A\} = \begin{cases} 1 & A \text{ true} \\ 0 & A \text{ false} \end{cases}$$

Then we show an example which deals with images using the LBP algorithm, and the image size of ORL face library [15] is 92x112, and the face image and LBP image are obtained respectively, and their histograms are given.

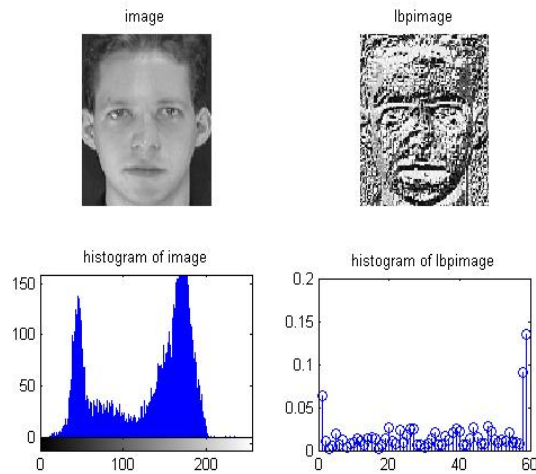


FIGURE I. THE LEFT TOP IS THE ORIGINAL IMAGE WITH THE LEFT BOTTOM ITS HISTOGRAM, AND THE RIGHT TOP IS THE CORRESPONDING LBP IMAGE WITH THE RIGHT BOTTOM ITS HISTOGRAM.

In order to present spatial location information of the small image pattern, we perform the image block to divide the image into several non-overlapping rectangle areas R_0, R_1, \dots, R_{m-1} , then calculate the histograms of each block area:

$$H_{i,j} = \sum_{(x,y) \in R_j} I\{f_{LPB}(x,y) = i\},$$

$$i = 0, 1, \dots, n - 1; j = 0, 1, \dots, m - 1.$$

For example, we divide the above image into 16 subdomain, and their histograms are given.

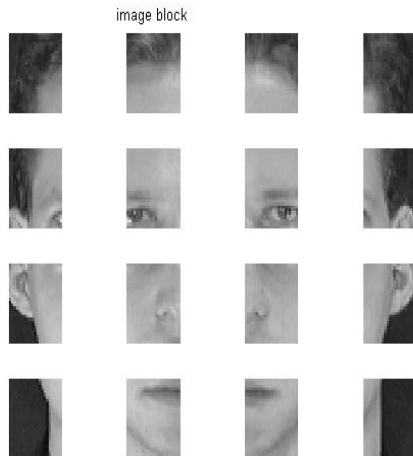


FIGURE II. THE BLOCK IMAGE OF FOUR ROWS AND FOUR COLUMNS.

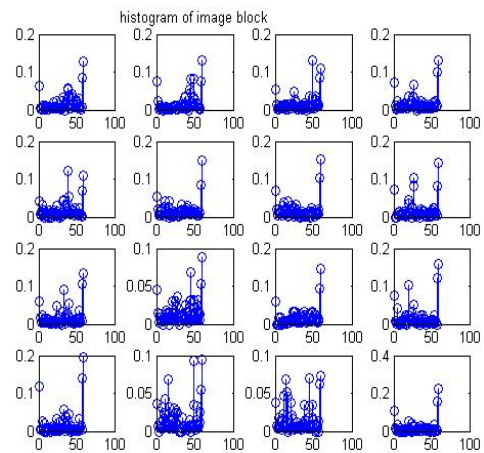


FIGURE III. HISTOGRAMS OF BLOCK IMAGE OF FOUR ROWS AND FOUR COLUMNS.

Because the (2D)²PCA algorithm lowers down the dimension of the image feature matrix from two directions, the computation time and memory space are saved, and we use (2D)²PCA algorithm for feature reduction. The process is as follows.

The characteristic vector of the face image is generated by connecting these histogram of image blocks,

$$H = (H_{0,0}, \dots, H_{0,m-1}, \dots, H_{n-1,0}, \dots, H_{n-1,m-1}).$$

The characteristic vector can be rearranged, and the rearrangement is expressed by H' ,

$$H' = \begin{bmatrix} H_{0,0} & H_{0,1} & \dots & H_{0,m-1} \\ H_{1,0} & H_{1,1} & \dots & H_{1,m-1} \\ \vdots & \vdots & \ddots & \vdots \\ H_{n-1,0} & \dots & \dots & H_{n-1,m-1} \end{bmatrix}.$$

By the (2D)²PCA algorithm, the row and column of the matrix are reduced in two directions. Then the covariance matrix in the direction of the row is obtained:

$$G_t = \sum_{p=1}^n (H'^p - \bar{H}'^p)^T (H'^p - \bar{H}'^p).$$

Similarly, in the direction of column, the covariance matrix can be expressed as:

$$G_t' = \sum_{p=1}^n (H'^p - \bar{H}'^p)^T (H'^p - \bar{H}'^p).$$

The eigenvalues and eigenvectors of the covariance matrix are calculated. The eigenvectors corresponding to the eigenvalues of about 90% rate of contribution are selected as the optimal projection matrix. Therefore, by this way we can gain the row direction of projection matrix X and column

direction of projection matrix Z , and the image matrix A of size $m \times n$ can be projected onto X and Z respectively. The projection of A on X and Z is denoted by a matrix C with size $q \times d : C = Z^T A X$ in face recognition, and matrix C is called the characteristic matrix.

Because the support vector machine [13] has the advantages of global optimal, simple structure and strong promotion ability, we can use support vector machine to solve the multi-classification problem of face recognition.

The SVM have been recently proposed by Vapnik and his co-workers [14] as a very effective method for general purpose pattern recognition. Intuitively, given a set of points belonging to two classes, a SVM finds the hyperplane that separates the largest possible fraction of points of the same class on the same side, while maximizing the distance from either class to the hyperplane. According to Vapnik [14], this hyperplane is called Optimal Separating Hyperplane (OSH) which minimizes the risk of misclassifying not only the examples in the training set but also the unseen examples of the test set.

We put the corresponding labels on the feature matrix, select a part of the data as a training set with the rest as a test set, and then use the test set to predict identification and recognition rate.

The main steps of general facial recognition process include: face detection, feature extraction, feature dimensionality reduction and classification and recognition. Our LBP(2D)²PCA+SVM algorithm flow is as follows:

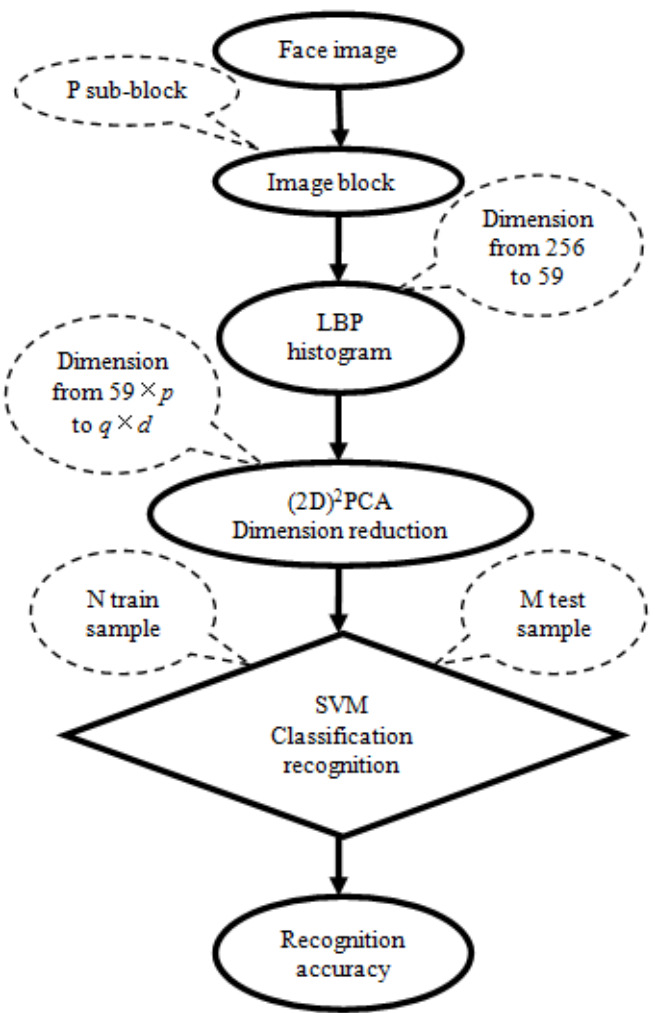


FIGURE IV. THE LBP(2D)²PCA+SVM ALGORITHM FLOW.

III. EXPERIMENTAL RESULTS AND ANALYSIS

We program the algorithm into MATLAB language and conduct experiments in MATALB2014A platform. In order to verify the superiority of the LBP(2D)²PCA+SVM algorithm in face recognition, use ORL face image database for face recognition rate experiment.

The ORL databases[15] contains 400 images of 40 people with a 92x112 grayscale image, and each person is collected with 10 different images. All images have similar dark background, and different images are from the same person at different times, different illumination and different head posture, facial expression and facial details under sub-Saturn hemisphere, but the above several changes usually will not appear in the same 10 images at the same time.

In the experiments, we use 1-8 training samples separately to fulfill recognition process of LBP(2D)²PCA +SVM algorithm and other algorithms. The face recognition rate data and line graph are gained with different algorithms in different training samples.

FIGURE I. THE TABLE IS THE FACE RECOGNITION RATE FOR DIFFERENT ALGORITHMS

Train sample	1	2	3	4	5	6	7	8
SVM	51	64	71	77	76	82	84	84
PCASV M	48	63	74	80	83	91	90	93
PCA2DS VM	70	70	75	81	84	94	94	95
PCA2D2 SVM	63	78	83	87	89	92	95	95
LBPSV M	59	67	69	77	82	85	92	93
LBPPC ASVM	46	58	58	67	75	79	85	86
LBP4X4 PCA2D2 SVM	54	62	79	93	98	99	98	96
LBP8X4 PCA2D2 SVM	61	78	82	92	93	98	97	96

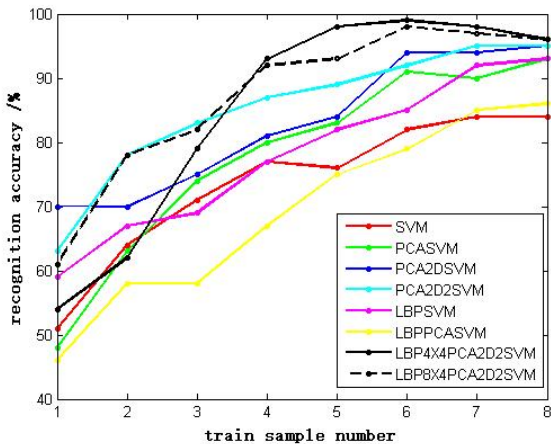


FIGURE V. THIS DIAGRAM SHOWS THE LINE DRAWING OF DIFFERENT ALGORITHMS UNDER DIFFERENT TRAINING SAMPLES.

By the experiment results, the LBP(2D)²PCA+SVM algorithm includes the principal component analysis (PCA) dimensionality reduction effect and the local binary pattern texture illumination invariant and rotation invariance, and the fast and efficient classification of support vector machine (SVM) algorithm. Therefore, it has a good effect on face recognition. When the number of training samples is low, the recognition effect is not very good which compared with other algorithms. When the number of training samples is large, the recognition effect is obvious. When the training sample is over half, the recognition rate was over 95%. When the training sample is six, the recognition rate is up to 99%. The LBP(2D)²PCA+SVM algorithm uses the statistical characteristics of the face information effectively, and has the light robustness and rotation invariance of LBP algorithm to extract image texture information of the face effectively. In changes of the light, attitude and expression, the recognition rate has improved obviously, so the overall recognition rate has improved.

IV. CONCLUSION

In this article, we mainly studied the face recognition method LBP(2D)²PCA+SVM. First, the face image is partitioned, then we calculate each sub-block face image texture image and their statistics histograms, and connect each sub-block histogram into a histogram vector. The blocks are too many, and the dimension of the histogram vector is too high, which make us use (2D)²PCA algorithm for the histogram dimension reduction. Finally, the algorithm of support vector machine is used to classify the test images. The method takes the advantages of dimension maximization reduction of the principal component analysis (PCA) and combines it with the rotation invariance of LBP operator and merits of illumination invariance. Therefore, it can effectively utilize the statistical features of face images and make full use of the texture features of face images, thus reduces the influence of light changes on face recognition and improves the recognition rate. Comparing the LBP(2D)²PCA+SVM algorithm with other algorithm, we conduct our algorithm is better for face recognition.

ACKNOWLEDGMENT

This work was supported by the Major Program of National Natural Science Foundation of China (11290141), National Natural Science Foundation of China (11401017, 11571028 and 11671025) and Fundamental Research of Civil Aircraft No. MJ-F-2012-04.

REFERENCES

- [1] Zhou Ji-Liu, Zhang Ye. Research advances on the theory of face recognition [J]. Journal of Computer-Aided Design & Computer Graphics. 1999, 11(2): 180-184.
- [2] A.K. Jain, R.P.W. Duin, J. Mao, Statistical pattern recognition: a review, IEEE Trans. Pattern Anal. Mach. In tell. 22 (1) (2000) 4-37.
- [3] Samaria F. Face Recognition Using Hidden Markov Models [D]. PhD Thesis. Cambridge, University of Cambridge, 1994.
- [4] Lawrence S, Giles C L, Tsoi A C, et al. Face recognition: A convolutional neural network approach[R]. IEEE Trans. PAMI, 1997, 8: 98-113.
- [5] I.T. Jolliffe, Principal Component Analysis, Springer, New York, 1986.
- [6] W.J.Krzanowski, P.Jonathan, W.V Mc Carthy, and M.R. Thomas. Discriminant analysis with singular covariance matrices: methods and applications to spectroscopic data. Applied Statistics, 44: 101–115, 1995.
- [7] Agarwal M, Jain N, Kumar M, et al. Face recognition Using Principle Component Analysis, Eigen face and Neural Network [C]. Signal Acquisition and Processing, 2010: 310-314.
- [8] J. Yang, D. Zhang, A.F. Frangi, J.Y. Yang, two-dimensional PCA: a new approach to appearance based face representation and recognition, IEEE Trans. Pattern Anal. Mach. In tell. 26 (1) (2004)131–137.
- [9] Daoqiang Zhang, Zhi-Hua Zhou. (2D)²PCA: Two-directional two-dimensional PCA for efficient face representation and recognition [J]. Neuro, computing, 2005, 69(1/3): 224-231.
- [10] Timo Ahonen, Abdenour Hadid, Matti Pietikainen et al. Face Recognition with Local Binary Patterns[C]. //8th European Conference on Computer Vision (ECCV 2004), part I.2004: 469-481.
- [11] Ojala, Pietikäinen, Mäenpää, Multiresolution gray-scale and rotation invariant texture classification with local binary patterns[C]. IEEE Transactions on Pattern Analysis and Machine Intelligence, 2002, 24, 971-987.
- [12] Timo Ahonen, Abdenour Hadid, Matti Pietikainen et al. Face Description with Local Binary Patterns: Application to Face Recognition[J].IEEE Transactions on Pattern Analysis and Machine Intelligence, 2006,28(12): 2037-2041.

- [13] G. Guodong, S. Li, and C. Kapluk. Face recognition by support vector machines. In Proc. IEEE International Conference on Automatic Face and Gesture Recognition, pages196–201, 2000.
- [14] V. N. Vapnik. Statistical learning theory. John Wiley & Sons, New York, 1998.
- [15] http://cobweb.ecn.purdue.edu/~aleix/aleix_face_DB.html

The Colony Count Based on Image Processing Using Matlab and Photoshop

Xiaoming Chen, Shufang Li*, Zhijun Zhang and Jun Gao

TianJin Institute of Forestry and Pomology, Tianjin, China

*Corresponding author

Abstract—Using two conventional software programs to do a counting method on the colony image from a normal photograph, and the comparison between the methods.

Keywords—colony counting; image processing; Matlab; Photoshop

I. INTRODUCTION

Although modern and automated advanced instruments can do well of counting the colony count, the simple image processing and counting of the colony images, especially from ordinary digital cameras and mobile phone cameras, is still significant.

In this paper, we used two common software, Matlab and Photoshop, to experiment and compare three simple methods of colony counting with simple image processing.

II. MATERIAL

A. Subject

The colony is from Lactobacillus spp. and Saccharomyces cerevisiae by drop plate methods [1,2] in PDA culture mediums. The PDA plate culture medium at 25°C was cultured after 48h.

B. Software

Using three software, mathematic software as Matlab R2014a 32-bit; image processing software as Adobe Photoshop CC 2017 32-bit for colony counting

Results data was processed and statistics Microsoft Office EXCEL 2013 32-bit.

C. Instrument

Canon 450d digital camera for image taken.

III. METHODS

A. Image Acquisition and Pretreatment

For simplicity and convenience this experiment uses a Canon digital camera 450D to photograph the colonies which is formed by drop plate methods on a petri dish.

The camera using the attached 28-70mm zoom lens during the shoot. The lens parameters are set to the focal length =70

mm; Aperture F=5.6. Camera body parameter are set to: sensitivity =200 ISO; Shutter speed S= 1/150s. camera manual mode to "Macro mode" and "Auto focus". All other parameters are camera default.

During shooting, the culture dish containing colonies was lined with black background and illuminated with natural light.

After the photo is exported from the camera, it is loaded into Adobe Photoshop. Using the "select" tool in the software, the image of the colony was intercepted to square as the side length of about 13.34cm, and the resolution was about 72ppi. The captured photos are stored in.jpg format. The original image is shown in figure I.



FIGURE I. TWO KINDS OF TYPICAL ORIGINAL IMAGE PROCESSED BY PHOTOSHOP

B. Image Processing and Counting Methods Using Adobe Photoshop

Select the "color range" option in the "select" menu bar in Photoshop. When the dialog box pops up, the cursor of the shape of the dropper is directly selected for any single colony sampling in the center of the image. When the dialog box pops up, the cursor in the shape of the "dropper" selects any single colony sample in the center of the image.

After sampling, click "ok" and the colony will be surrounded by a dotted line. At this point, click the "measurement record" tab in the "window" menu bar, and you will see the "measurement record" window. Records at this time click the interface "measure" button, you can record in "measurement" window displays the number of colonies surrounded by a dashed line (selected by the dotted line not colonies cannot be count and display). The operation diagram is shown in figure II. This method is abbreviated to M1.

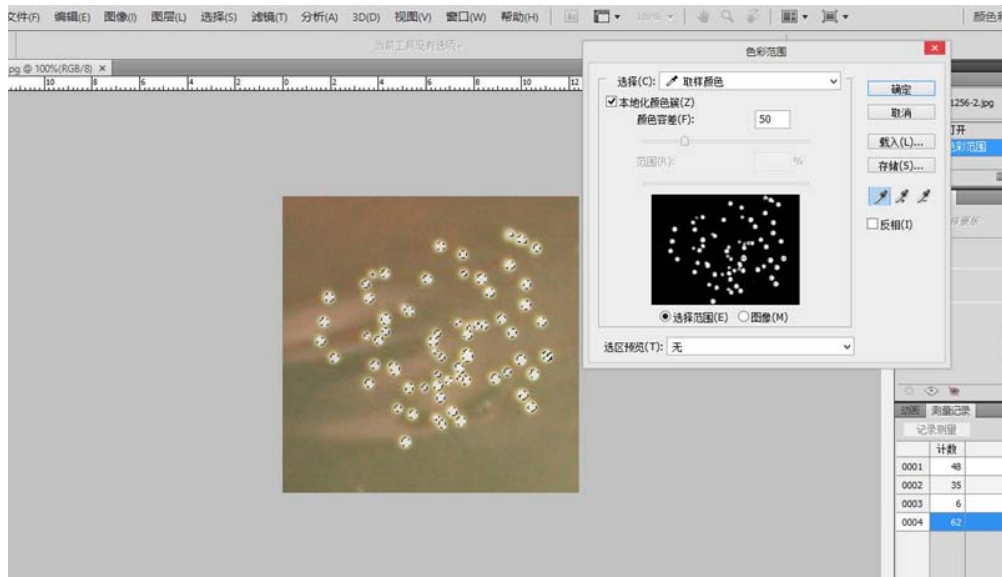


FIGURE II. SHOWS THE OPERATION SCHEMATIC DIAGRAM USING THE COLOR RANGE COUNT OF PHOTOSHOP

C. Another Method of Image Processing and Counting Using Adobe Photoshop

Using the "image" menu under the Photoshop menu, "adjust" the "black and white" button in the menu of the "adjust" submenu to transform the image into a black-and-white image. Adjust the image threshold to the current half through the "threshold" menu in the same submenu. Select the "color range" option in the "select" menu bar in Photoshop. When the dialog box pops up, the cursor of the shape of the dropper is directly selected for any single colony sampling in the center of the image. When the dialog box pops up, the

cursor in the shape of the "dropper" selects any single colony sample in the center of the image.

After sampling, click "ok" and the colony will be surrounded by a dotted line. At this point, click the "measurement record" TAB in the "window" menu bar, and you will see the "measurement record" window. Records at this time click the interface "measure" button, you can record in "measurement" window displays the number of colonies surrounded by a dashed line (selected by the dotted line not colonies cannot be count and display). The operation diagram is shown in figure III. This method is abbreviated to M2.

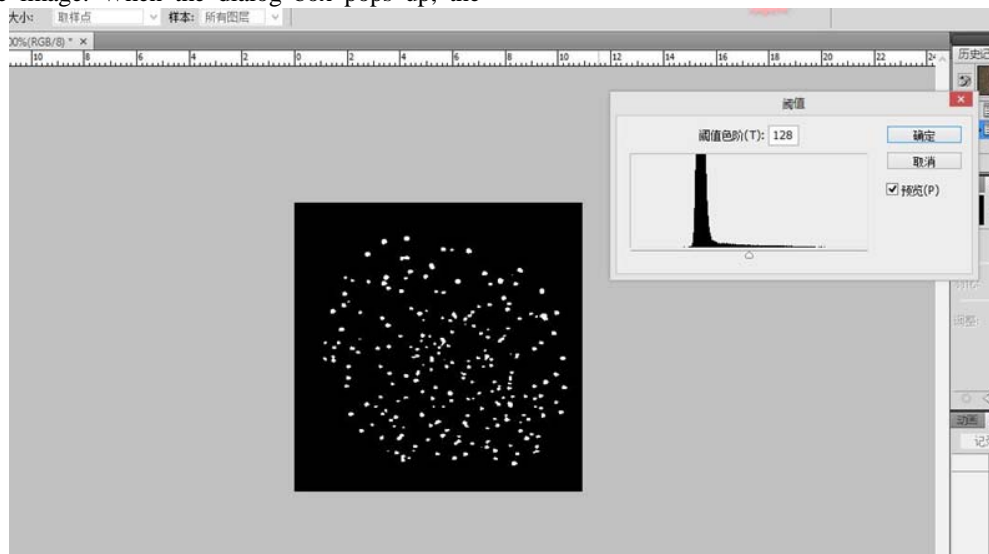


FIGURE III. USING PHOTOSHOP GRayscale COLOR RANGE COUNTING OPERATION SCHEMATIC.

D. Image Processing and Counting Methods Through Software Matlab

The collected image import Matlab folders in the Matlab software, the image converted to black and white image

binarization, the ash filtering, through top-hat transform and bottom hat transformations, Unicom area count, this method shorthand for M3[3,5].

The operation steps of the above method are as follows: enter the following five sets of program codes in the Matlab command input box:

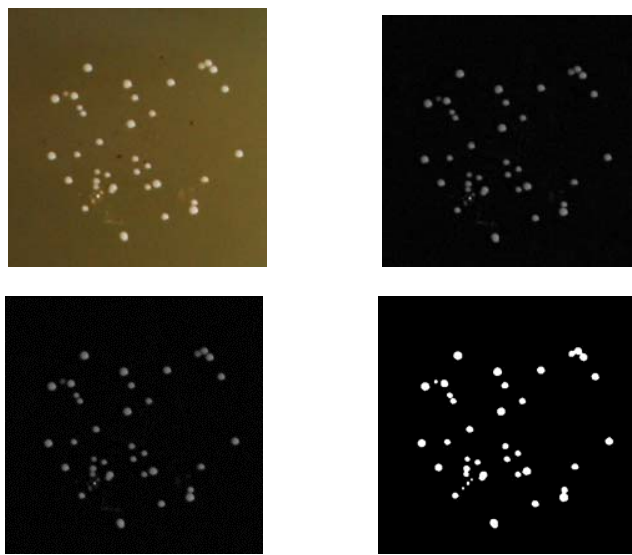


FIGURE IV. TWO KINDS OF ORIGINAL IMAGE(A) ORIGINAL IMAGE PARTS OF A FIGURE. (B) IMAGE BY TOP-HAT FILTERING CONVENT (C) GARY IMAGE BY 2-D MEDIAN FILTERING CONVENT (D) IMAGE BY BINARY CONVENT USING LEVEL THRESHOLD

- Import Image. The program code is as follows, The original image is shown in figure IV (A):
 - clear
 - filename='filename.jpg';
 - imfinfo (filename);
 - f=imread (filename);
 - subplot (221),imshow (f);
 - title ('Original image');
- Using Top-hat Filtering to correct uneven illumination or flash Spot. The program code is this, By Top-hat Filtering convert, the image is transformed into a form as shown in figure IV (B).
 - se=strel ('disk',10);

- f1=imtophat (f,se);
- subplot (222), imshow (f1);
- title ('Image by imtophat filtering');
- Convert the Top-hat filtering image to grayscale image. The program code is this:
 - A2 = rgb2gray (f1);
 - imwrite (A2,'A2=gray.jpg');
- Using the 2-D median filtering to Remove Salt and Pepper Noise from Image. The program code is as follows, Removing Salt and Pepper Noise, the image is transformed into a form as shown in figure IV (D).
 - A3 = medfilt2 (A2);
 - subplot (223), imshow (A3);
 - title ('Gary image by medfilt2 Filtering');
- Convert an Indexed Intensity Image to Binary Image Using Level Threshold. The program code is this, Removing Salt and Pepper Noise, the image is transformed into a form as shown in figure IV (D).
 - Level = graythresh (A3);
 - imwrite (A3,'A3=medfilt2gray.jpg');
 - A4 = im2bw (A3,level);
 - subplot (224), imshow (A4);
 - title ('Image by BW Filtering');
- 6. Label Components Using 4-connected Objects, and print out the number of components. The program code is as follows, label Components, the software input result of colony counting by command window.
 - imwrite (A4,'A4=bwmedfilt2gray.jpg');
 - [l,n] = bwlabel (A4,4);
 - display (n);

IV. RESULT

Taking the results of the colony count of 10 pictures as an example, the results of the colony count produced by each image processing method are shown in figure V.

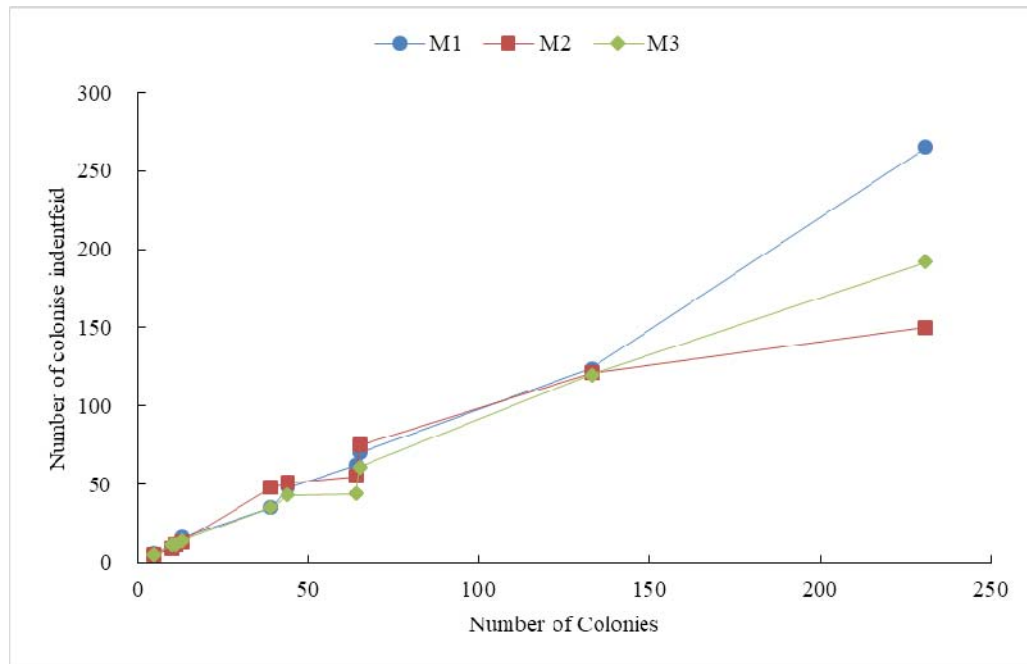


FIGURE V. RESULTS OF COLONY COUNT OF EACH METHOD

It can be seen that all three methods have good accuracy when the number of colonies is less than 50, and when the number of colonies is greater more than 100, the recognition result of the method M1 is closer to the actual number of colonies.

ACKNOWLEDGEMENT

This research was financially supported by the National Public Welfare Vector (agriculture) research and special Foundation of China (201503142-09).

REFERENCES

- [1] Hoben HJ, Somasegaran P. Comparison of the pour, spread, and drop plate methods for enumeration of Rhizobium spp. In inoculants made from presterilized peat [J]. Applied and Environmental Microbiology, 1982, 44(5): 1246-1247.
- [2] Herigstad B, Hamilton M, Heersink J. How to optimize the drop plate method for enumerating bacteria [J]. Journal Microbiology Method, 2001, 44 (2): 1212-1291.
- [3] Marotz J. Effective object recognition for automated counting of colonies in Petri dishes (automated colony counting). Computer Methods and Programs in Biomedicine 66 (2001).
- [4] Wu D Y, Wei P. Measuring The Condition of Parking Lot by Image Processing [J]. Journal of Beijing Institute of Technology, 1999, 8(3): 232-237.
- [5] Hieu T, Marcel M, Rein V. Water snakes: Energy driven watershed segmentation [J]. IEEE Transaction on Pattern Analysis and Machine Intelligence, 2003, 25(3): 330-342.

CT Image Segmentation Algorithm Based on Merging of Similar Adjacent Components

Xueguang Sun and Weigen Qiu

Guangdong University of Technology, Guangzhou, 510006, Guangdong, China

Abstract—CT is one of the most widely used medical imaging techniques. Image segmentation is of great significance to medical image aided clinical diagnosis. Due to the complexity of structure and shape of CT image, and the inhomogeneity of organization, the commonly used image segmentation algorithm can not meet the requirements. Therefore, a CT image segmentation algorithm based on similarity criterion of adjacent components is proposed in this paper. The component tree is built quickly for the CT image, and the component tree protocol is carried out according to the attribute similarity criterion of adjacent components to complete the segmentation target. The experimental results show that the segmentation results are more accurate and more efficient.

Keywords—*CT images; adjacent components; image segmentation*

I INTRODUCTION

Image segmentation is to separate the subregion of the target image from the complex background, and it is the basis of the higher level image analysis. In recent years, scholars have proposed a large number of excellent segmentation algorithms[1]. These algorithms can be roughly divided into the following: voxel based image segmentation, region based image segmentation, local priori based image segmentation, image segmentation based on global character priori and artificial intelligence based segmentation. [2,3] Medical image segmentation has been a hot research field in medical image processing. Frank et al. [4] successfully segmented the gray matter, white matter and cerebrospinal fluid fluid in the T1 weighted brain MR images by using the optimal threshold. In document [5], Wang H and so on use region based segmentation method to synthesize pixel information and local relationship between pixels, and have been applied to hippocampus segmentation successfully. The Snake method [6] is based on the priori of the local shape, and is suitable for the segmentation of various shape targets, and is widely used in two-dimensional image segmentation.

Compared with ordinary image segmentation, medical image segmentation has higher requirements for the precision of image segmentation and the speed of segmentation because of its special domain. In this paper, the CT image segmentation method based on component tree is studied. In this paper, we first use the algorithm of [7] to set up the component tree of the image, and insert the gray and area dual attributes in its component nodes. Then we merge the similar components with the adjacent components' gray similarity decision rule to complete the segmentation of CT images. Finally, the experimental results show that the segmentation method has low time complexity and high algorithm efficiency, which not only

can effectively remove the noise in the image, but also suppress the over segmentation phenomenon, and achieves the desired segmentation effect. The algorithm flow of this article is shown in Figure I.

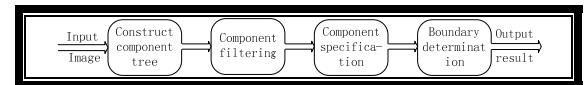


FIGURE I. THE FLOW CHART OF THE ALGORITHM IN THIS PAPER

II BASIC NOTIONS

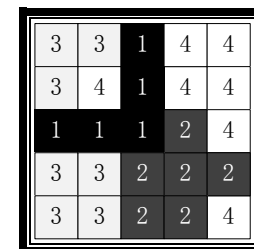
Let Ω is a nonempty finite set, V is a non empty finite poset, which is supposed to have the minimum value of \perp . An image is the function $f: \Omega \rightarrow V$, the set Ω and the V are called the support set and the value space of the image f , respectively.

The following is a part of the definition about the concept of the component tree.

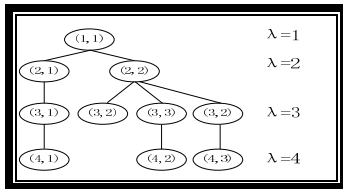
Definition 1: Let $X \subseteq \Omega$ and $v \in V$, threshold function $\lambda v: V\Omega \rightarrow 2^\Omega$, for any $f: \Omega \rightarrow V$, $\lambda v(f) = \{x \in \Omega | f(x) \geq v\}$. for any $v \in V$, all of the Connected branches in the threshold set $\lambda v(f)$ noted $C[\lambda v(f)]$.

Definition 2: Let $X \subseteq \Omega$ and $v \in V$, barrel function $C(X, v): \Omega \rightarrow V$, for any $x \in X$, $C(X, v)(x) = v$; or else $C(X, v)(x) = \perp$. Using the threshold function λv , the f can be decomposed into some bucket functions. On the contrary, the image f can also be reconstructed by these bucket functions, $f = \bigvee_{v \in V} \bigvee_{x \in C[\lambda v(f)]} C(X, v)$ \vee notes that supremum function of the points set function. The Connected branch X may belong to more than one $C[\lambda v(f)]$, noted that $m(X) = \max\{v \in V | X \in C[\lambda v(f)]\}$, generally, $m(X) = \min\{x \in X | f(x)\}$.

We note that $\Psi = \{(X, m(X)) | X \in V, v \in VC[\lambda v(f)]\}$, The definition of partial order relation in Ψ : $(X_1, m(X_1)) \leq (X_2, m(X_2)) \Leftrightarrow X_1 \subseteq X_2$. As shown in Figure II, a schematic diagram of the image f component tree is constructed.



(A) F



(B) COMPONENT TREE OF F

FIGURE II. (A) THE IMAGE F AND THE COMPONENT TREE OF F .

III ALGORITHM OF MERGING OF SIMILAR ADJACENT COMPONENTS

L.Najman and M.courprié, Bertrend and others propose to use component tree structure to represent images, which lays a deep theoretical foundation for the establishment of component tree. Generally, in constructing the component tree, every node has qualitative or quantitative statistical information such as shape, area and so on. This information provides a basis for further image manipulation, such as the pruning of a tree, that is, the so-called image filtering. Set pruning function F_p , which is based on a p test predicates on the attribute set. This pruning function can remove the nodes that does not meet the test of the P, the pixel reduction to other nodes nearby, so the triplet (Ψ, L, R) called component tree of f evolved into (Ψ', L', R) , note that $F_p(\Psi, L, R) = (\Psi', L', R)$. This process is called the reduction of the component tree.

This algorithm includes four processes, such as image preprocessing, image component tree construction, component specification and boundary determination.

A. Image Preprocessing

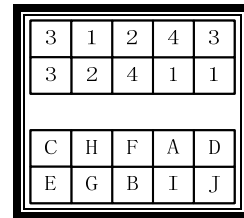
The image preprocessing method adopted in this paper is Gauss Laplasse (LoG) transformation. Experimental results are shown in Figure 4. After LoG transformation, the image noise is effectively suppressed, and the image details are significantly enhanced. The Gauss Laplasse operator is:

$$\text{LoG} = \frac{x^2 + y^2 - 2\sigma^2}{\sigma^4} e^{-(x^2 + y^2)/2\sigma^2} \quad (1)$$

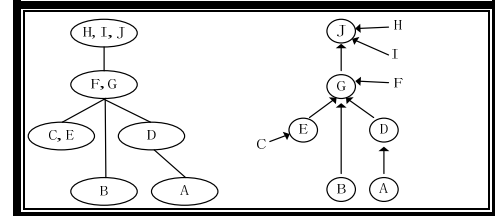
The smaller the sigma, the better the enhancement, and on the contrary, the better the smoothness. The proper Sigma value should be selected during the enhancement process. The value of the sigma in the experiment, shown in Figure IV, is 0.8.

B. The Construction of Component Tree

We use the immersion algorithm to construct the component tree quickly. In the process of constructing the component tree, using find-union algorithm aimed to implement path compression. As shown in Figure III (A), a simple graph f is a four connection, and all the pixels of the image f are the full order relation on the R , and are descended in descending order by the gray value.



(A) SAMPLE IMAGE F (TOP) AND THE ORDERING BETWEEN PIXELS (BOTTOM)



(B) COMPONENT TREE OF F

BEFORE PATH COMPRESSION

(C) COMPONENT TREE OF F

AFTER PATH COMPRESSION

FIGURE III COMPONENT TREE CONSTRUCTION PROCESS

C. Component Reduction and Boundary Determination

The first constructed component tree contains a large number of similar constructs. The component reduction should be based on two basic principles: (1) the gray difference between the two components; (2) the difference between the pixels in the component.

- 1) The calculation of the node area;
- 2) Find the gray value of the node;
- 3) component tree reduction;

The area change rate between two components C_1 and C_2 is defined, and the rate of gray change is respectively:

$$D_{\text{Area}} = \frac{|\text{Area}(C_1) - \text{Area}(C_2)|}{\max(\text{Area}(C_1), \text{Area}(C_2))} \quad (2)$$

$$D_{\text{Level}} = \frac{|L(C_1) - L(C_2)|}{\max(L(C_1), L(C_2))} \quad (3)$$

Considering the difference of area and gray level, the noise can be avoided as an independent component, so the image segmentation can be realized.

$$\text{diff}(C_1, C_2) = \begin{cases} 1 & \text{if } D_{\text{Level}} \geq T_L \text{ and } D_{\text{Area}} < T_A \\ 0 & \text{else} \end{cases} \quad (4)$$

Among them, "1" indicates the existence of boundary, and "0" indicates that there is no boundary. T_L and T_A represent the gray change rate and the threshold of area change rate respectively. In the experiment, the segmented images are different, and the values of the two are also changed.

D. This Algorithm Flow is Described in This Paper

After the image component tree is set up, the algorithm description of the component merging based on the dual

attributes of the gray and area is given.

(1) According to the input image component tree T , the area of each component in all grayscale levels is calculated.

(2) According to the merging criteria, the components are merged according to the order of gray level decreasing.

(3) According to the new component tree T' , output the segmented image f .

IV ANALYSIS OF EXPERIMENTAL RESULTS

In this paper, two groups of experiments were designed. The first group was divided by a patient's liver CT (this patient has Liver pseudotumor), and the second group was divided by a Budd Chiari syndrome patient's liver CT. The value range of the selected TA is (0.15~0.25), and the range of TL is (0.50~0.60).The segmentation method of this paper is compared with the fuzzy clustering algorithm [8] and the Canny operator [9].

TABLE I THIS ALGORITHM AND OTHER RUNNING TIME COMPARISON UNIT: S

Image	Fuzzy clustering algorithm	Canny operator	Algorithm in this paper
Figure 4	4.56	3.65	1.36
Figure 5	4.68	3.89	0.98



(A) ORIGINAL



(B) LOG ENHANCEMENT



(C) FUZZY CLUSTERING ALGORITHM



(D) CANNY OPERATOR



(E) ALGORITHM IN THIS PAPER

FIGURE IV. COMPARISON OF FIRST GROUP EXPERIMENTAL RESULTS



(A) ORIGINAL



(B) LOG ENHANCEMENT



(C) FUZZY CLUSTERING ALGORITHM



(D) CANNY OPERATOR



(E) ALGORITHM IN THIS PAPER

FIGURE V. COMPARISON OF SECOND GROUP EXPERIMENTAL RESULTS

In conclusion, compared with fuzzy C mean algorithm and Canny operator, it can be seen from segmentation results that the algorithm achieves ideal segmentation results. The running time of the algorithm is shorter.

V CONCLUSION

In this paper, we study the CT image segmentation algorithm based on the similarity judgment of the adjacent component's regional attributes. Aiming at the uneven and fuzzy features of the image itself, the LOG is enhanced in the

image preprocessing stage, so that the details of the image are enhanced while reducing the noise. Then, we use the immersion algorithm to build the component tree, and calculate the grayscale and area attribute data of tree nodes. According to the algorithm of adjacent component attribute similarity determination proposed in this paper, the nodes are specified. Finally, the purpose of image segmentation is achieved. The experimental results show that the algorithm proposed in this paper can achieve accurate image segmentation and the efficiency of the algorithm is higher. In this paper, the complex node attributes are designed in order to extend the image segmentation in the future.

ACKNOWLEDGEMENT

This research was financially supported by the National Science Foundation (No. 61572142).

REFERENCE

- [1] P Chinmayi, L Agilandeswari, M Prabukumar. Survey of Image Processing Techniques in Medical Image Analysis: Challenges and Methodologies, International Conference on Soft Computing & Pattern Recognition, 2016:460-471.
- [2] Guiping Jiang, Wenjian Qin, Shoujun Zhou, Changmiao Wang, State-of-the-art in Medical Image Segmentation, Chinese journal of computer,38(6),1222-1242,2015.
- [3] Aiju Li, Yujie Lie, Tingmei Wang, Wenliang. Medical Image Segmentation Based on Maximum Entropy Multi-threshold Segmentation Optimized by Improved Cuckoo Search Algorithm, 2015 8th International Congress on Image and Signal Processing (CISP 2015), 2015: 470-475.
- [4] Frank R J,Grabowski T J, Damasio H. Voxelwise percentagetissue segmentation of human brain Magnetic resonance images Proceedings of the 25th annual Meeting, Society for Neuro-science, Society for Neuroscience. Washington, DC, USA, 1995:694.
- [5] Wang H, Suh J W, Das S, et al. Hippocampus segmentation using a stable maximum likelihood classifier ensemble algorithm. IEEE International Symposium on Biomedical Imaging: From Nano to Macro. Rotterdam, Holland, 2011: 2036-2040.
- [6] Yuwei Wu, Jia Liang, Yuanquan Wang, A method for segmentation of the cardiac MR images based on GGVF Snake[J].Journal of image and Graphics, 2010,15(4):598-606.
- [7] Edwin Carlinet. A comppareative review of component tree computation algorithms, IEEE Trans. on Image Processing, 2014, 23(9): 3885-3895.
- [8] Sharma N, Ray A K, Sharma S, et al. Segmentation of medical images using simulated annealing based fuzzy C Means algorithm. Interntional Journal of Biomedical Engineering Technology, 2009, 2(3): 260-278.
- [9] Canny J, A computational approach to edge detection. IEEE Transactions on Pattern Analysis and Machine Intelligence, 1986, 8(6):679-698.

BDS Common-View Method Based on CGGTTS V2E Standard

Xu Liu^{1,2}, Dangli Zhao¹ and Junliang Liu¹

¹National Time Service Centre, Chinese Academy of Sciences, Xi'an 710600, China

²Graduate University of Chinese Academy of Sciences, Beijing 100039, China

Abstract—CCTF published CGGTTS for Common GNSS Generic Time Transfer Standard that is CGGTTS V2E. To support the standard in the BDS common-view, the paper refers to the standard and simulates corresponding algorithm in the standard realizing BDS common-view method based on CGGTTS V2E. The result show that the accuracy is about 1ns based on BDS in processing algorithm that is mentioned in the standard.

Keywords—BDS; CGGTTS V2E; common-view

I. INTRODUCTION

The common-view method is a main form that is used for time transfer. With the development of BDS, the common-view method based on BDS is becoming increasingly important in many fields of China. In addition, the CGGTTS V01 [1] only supports GPS and the CGGTTS V02 only covers GPS and GLONASS [2], but the CGGTTS V2E [3] provides extension for all GNSS system in development. Meanwhile, the CGGTTS V2E is fully compatible with the previous versions GGTTS V01 and CGGTTS V02 for the data progressing algorithm and data format. Taken together, common-view based BDS can be implemented and is available. Therefore, the paper simulates the computation algorithm raised by CGGTTS V2E providing supports to the development of time transfer receiver based on BDS.

II. THE PRINCIPLE OF COMMON-VIEW

The common-view is one of the ways being used for remote time transfer. As FIGURE 1, assume that user A and user B are located at two points on the earth. A and B observe the same satellite at the same time. Suppose the local time of A is τ_A and the local time of B is τ_B , the satellite clock is τ_S . The time delay of signal propagation is $\Delta\tau_A$ and $\Delta\tau_B$ respectively. So the offset between the local time of user A and the satellite clock is τ_{AS} and the offset between the local time of user B and the satellite clock is τ_{BS} [1]. The τ_{AS} and τ_{BS} will be obtained as:

$$\tau_{AS} = \tau_A - \tau_S - \Delta\tau_A \quad (1)$$

$$\tau_{BS} = \tau_B - \tau_S - \Delta\tau_B \quad (2)$$

The offset between local time of user A and local time of user

B is τ_{AB} that will be obtained as:

$$\begin{aligned} \tau_{AB} &= \tau_{AS} - \tau_{BS} \\ &= (\tau_A - \tau_B) - (\Delta\tau_A - \Delta\tau_B) \end{aligned} \quad (3)$$

Common-View method can remove the satellite clock, and partly eliminate the time delay of signal propagation.

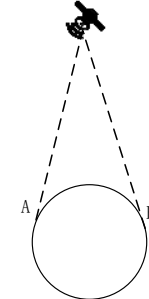


FIGURE I. THE PRINCIPLE OF COMMON-VIEW

III. DATA PROCESSING BASED CGGTTS V2E

The data to be used are the pseudorange measurements collected during 13 minutes. The original GGTTS directive asked for 1-second measurements grouped into blocks of 15 seconds. Then Defraigne et al. proposed a collection method that is a 30-second sampling rate. These authors verified that the differences between CGGTTS results based on either method is less than 0.1ns. The sampling rate of observation raw-data in this paper is a 30-seconds. In other words, give a total of 26 data per 13-minute track.

First, the pseudorange measurements collected are corrected for their frequency-dependent hardware delay as:

$$\bar{P}_i = P_i - c(t_{INTDLY}(f_i) + t_{CABDLY} - t_{REFDLY}) \quad (4)$$

where P_i is pseudorange measurement on the frequency f_i , c is the velocity of the light in the vacuum, $t_{INTDLY}(f_i)$ is the electric delay of the GNSS signal inside the antenna and the receiver, t_{CABDLY} is the signal group delay inside the antenna cable, t_{REFDLY} is the offset between the receiver internal clock and the local clock.

Second, for B1I signal frequency users the offset between

local clock and the satellite clock that is *REFSV* will be obtained as:

$$t_{\text{clock}} - t_{\text{sat}} = \frac{1}{c} \left[\overline{P}_1 - \left\| \overrightarrow{x_{\text{sat}}} - \overrightarrow{x_{\text{rec},l}} \right\| - S \right] + t_{\text{rel}} - t_{\text{iono},l} - t_{\text{tropo}} - t_{\text{GD}} \quad (5)$$

where $\overrightarrow{x_{\text{sat}}}$ is the satellite position at the emission time, $\overrightarrow{x_{\text{rec},l}}$ is the position of the phase center of antenna for frequency f_l that is B1I signal frequency for BDS, S is the Sagnac correction, Δt_{rel} is the relativistic clock correction, $\Delta t_{\text{iono},l}$ is the propagation delay caused by ionospheric refraction, Δt_{tropo} is the propagation delay caused by tropospheric refraction, t_{GD} is the broadcast group delay.

The $\Delta t_{\text{iono},l}$ will be obtained by Klobuchar model [4] and the Δt_{tropo} will be obtained by Saatamaninen model and GPT/GMF model [5].

The $\overrightarrow{x_{\text{sat}}}$ will be obtained based on ICD file on BDS [6]. Meanwhile, the Sagnac is corrected by a rotation matrix [7]. Assume that the satellite position is (x_k, y_k, z_k) in the ECEF at the emission time, and $(x^{(s)}, y^{(s)}, z^{(s)})$ in the ECEF at the reception time. The Sagnac correction will be obtained as:

$$\begin{bmatrix} x^{(s)} \\ y^{(s)} \\ z^{(s)} \end{bmatrix} = R \left(\dot{\Omega}_e \tau \right) \cdot \begin{bmatrix} x_k \\ y_k \\ z_k \end{bmatrix} \quad (6)$$

where the R is a rotation matrix:

$$R(\varphi) = \begin{bmatrix} \cos \varphi & \sin \varphi & 0 \\ -\sin \varphi & \cos \varphi & 0 \\ 0 & 0 & 1 \end{bmatrix} \quad (7)$$

The Δt_{rel} will be obtained as [6,7]:

$$\Delta t_k = -\frac{2}{c^2} \cdot e \cdot \sqrt{a\mu} \cdot \sin E_k \quad (8)$$

where a is the semimajor axis, e is the orbit eccentricity of the satellite orbit and E_k is the eccentric anomaly of the satellite, an angle relate to the position of the satellite on its orbit.

Third, for each of the 26 epochs, the broadcast satellite clock offset with respect to the reference time scale of the BDS is then added to the result of (5), which gives:

$$t_{\text{clock}} - t_{\text{ref}} = (t_{\text{clock}} - t_{\text{sat}}) + \Delta t_{\text{sat}} \quad (9)$$

where the Δt_{sat} will be obtained as:

$$\Delta t_{\text{sv}} = a_0 + a_1(t - t_{\text{oc}}) + a_2(t - t_{\text{oc}})^2 \quad (10)$$

where a_0, a_1, a_2 are the polynomial coefficients related to satellite clock, t_{oc} is the clock data reference time in seconds.

According to (5), the computation algorithm flow diagram as FIGURE 2

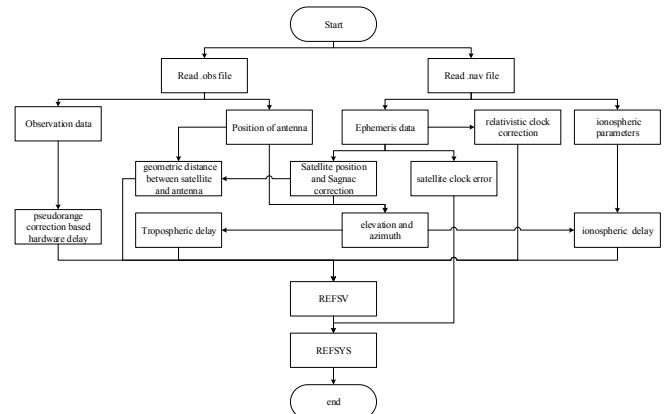


FIGURE II. THE COMPUTATION ALGORITHM FLOW DIAGRAM THE TESTING PLATFORM

The testing platform is comprised of two receivers using time and frequency transfer, two 10MHz references and two PPS signals and two antennas. The 10MHz reference and PPS signal originating from a local clock. The receivers supports standard inputs for time and frequency as well as incorporates a calibration circuit to measure and compensate for the delay between the PPS input and the internal time reference and outputs observation data and navigation data in RINEX format. The system diagram as FIGURE 3. The receiver at master station is marked as MASTER, and the receiver at remote station is marked as REMOTE.

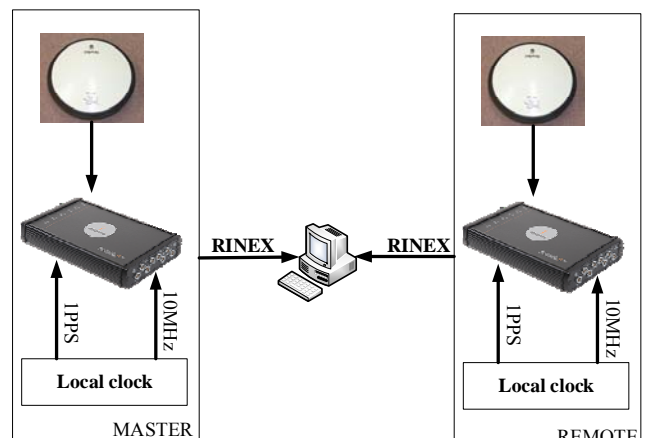


FIGURE III. SYSTEM DIAGRAM ALGORITHM SIMULATION

In this section, the paper will show some simulation results. There results contains three parts. First, the offset between the local clock and the satellite clock are represented REFSV. Second, the offset between the local clock and the reference time scale of the BDS are represented REFSYS. Third, the offset between the local clock at MASTR station and the local clock at REMOTE station.

To PRN13 of BDS as example, the paper demonstrates the simulation results including the REFSV, the REFSYS and the offset between the local clock at MASTR station and the local clock at REMOTE station. The results as in FIGURE 4~6:

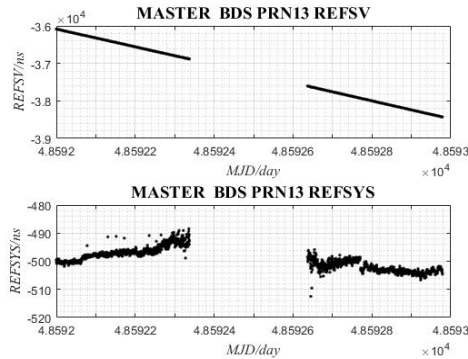


FIGURE IV. THE REFSV AND REFSYS AT MASTER STATION BASED PRN13 OF BDS

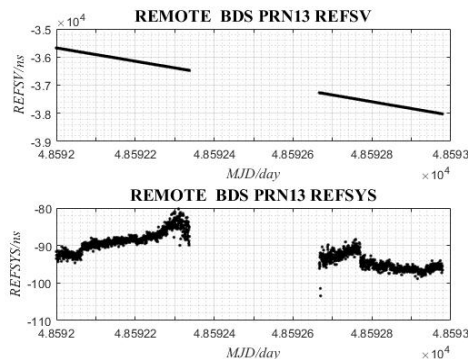


FIGURE V. THE REFSV AND REFSYS AT REMOTE STATION BASED PRN13 OF BDS

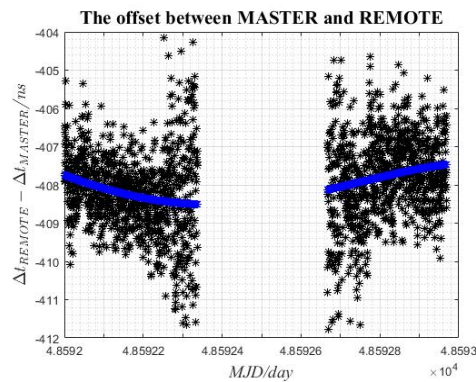


FIGURE VI. THE OFFSET BETWEEN THE LOCAL CLOCK AT MASTR STATION AND THE LOCAL CLOCK AT REMOTE STATION

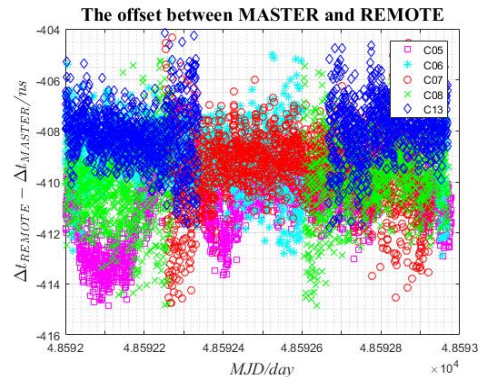


FIGURE VII. THE OFFSET BETWEEN THE LOCAL CLOCK AT MASTR STATION AND THE LOCAL CLOCK AT REMOTE STATION BASED ON MULTIPLE SATELLITES

TABLE I. THE OFFSET BETWEEN THE LOCAL CLOCK AT MASTR STATION AND THE LOCAL CLOCK AT REMOTE STATION BASED ON MULTIPLE SATELLITES

Satellite ID	std(ns) (least square fitting)	$\Delta t_{\text{REMOTE}} - \Delta t_{\text{MASTER}}$ (ns) (least square fitting)
PRN05	0.743	-410.598
PRN06	0.249	-408.951
PRN07	0.404	-409.520
PRN08	0.309	-410.007
PRN13	0.311	-408.008

As in FIGURE 7 and TABLE 1, there are five satellites in the data processing, including a GEO satellite identified PRN05. The difference of the local clock at REMOTE station and local clock at MASTER is about -409 ns, the standard deviation after least square fitting is less than 1 ns that is the accuracy less than 1 ns from TABLE 1. But the standard deviation of the PRN05 is greater than others, because the lower elevation of the PRN05, and the signals could therefore suffer from more noise and multipath.

IV. CONCLUSIONS

The paper has been realized the common-view based on BDS according to the standard of CGGTTS V2E. These results in very short baseline shows that the IGSO increases the BeiDou satellite availability, though it will bring a bit more noise into the result. However, the CV results obtained from GEO satellite are significantly noisier.

REFERENCES

- [1] Allan, Thomas. Technical Directives for Standardization of GPS Time Receiver Software [J]. Metrologia, 1994(31):69-79.
- [2] Lewandowski W, Azoubib J, Gevorkyan A G, et al. A Contribution to the Standardization of GPS and GLONASS Time Transfers: PTI, Virgiuia, 1996 [C].
- [3] Defraigne, Petit. CGGTTS-Version 2E: an extended standard for GNSS Time Transfer [J]. Metrologia, 2015.
- [4] Wei-Peng L I, Jian-Wen L I, Dai W. Study on the methods of updating Klobuchar ionospheric delay correction model [J]. Science of Surveying & Mapping, 2009, 34(5):49-51.
- [5] Boehm, Niell, Tregoning, et al. Global Mapping Function (GMF): A new empirical mapping function based on numerical weather model data [J]. Geophysical Research Letters, 2006.

- [6] BeiDou Navigation Satellite System Signal In Space Interface Control Document Open Service Signal (Version 2.1) [R].China Satellite Navigation Office, 2016.
- [7] Teunissen Peter.J.G, Montenbruck O. Handbook of Global Navigation Satellite Systems [M]. Springer, 2017.

An Adaptive Bitrate Algorithm Based on Estimation and Video Adaptation for Improving QoE in DASH

Saba Qasim Jabbar^{1,*}, Dheyaa Jasim Kadhim² and Yu Li¹

¹School of Electronics and Information, Huazhong University of Science and Technology, Wuhan National Laboratory for Optoelectronics, Division of Communication and Intelligent Networks, Wuhan, Hubei, 430074, P.R. China.

²Electrical Engineering Department, University of Baghdad, Baghdad, Iraq

*Corresponding author

Abstract—Dynamic Adaptive streaming over HTTP (DASH) is widely used by content providers for video delivery and dominates traffic on cellular networks. The variation in both video bitrate and network bandwidth badly impacts on the user Quality of Experience (QoE), so recent works is going to submitting better design of DASH adaptation algorithms. In this work, an adaptive bitrate algorithm is proposed which incorporates the network state, the application state and the video variety conditions to adapt video quality under time varying wireless system. The proposed algorithm consists of two main units: estimation unit and video adaptation unit. During the estimation unit, a new attribute is included that scales the buffer occupancy estimation and the throughput estimation based on the variations in the current buffer level and measured throughput of previous download segments. While during the video adaptation unit, the selection of video bitrate is done based on both the measurements at estimation unit and a target level. The simulation results show that the proposed algorithm significantly outperforms the other rate adaptation algorithms in terms of providing maximum download bit rates, minimum number of bitrates switches and the maximum utilization of available bandwidth while maintaining the playback buffer level within limits without any playback interruptions.

Keywords—video streaming; DASH, video buffer; adaptive rate algorithm; QoE

I. INTRODUCTION

Video content constitutes a dominant fraction of Internet traffic today. Furthermore to ride the Internet bandwidth requirements, current video streaming systems adopt some adaptive and scale-able video coding techniques to facilitate the transmission [1]. Dynamic adaptive streaming over HTTP (DASH) is an HTTP-based technique in which each video is divided into segments encoded at multiple rates [2]. Each segment is encoded into different quality levels that may vary in resolution, quality and bitrates. This approach provides TCP fairness in the network as well as ordered lossless delivery. However, the adaptive algorithm at client side does not be defined by DASH system for choosing which segment to request or how to adapt the video bitrates so as to get good Quality of Experience (QoE). One of the commercial solutions for adaptive streaming is the adaptive algorithm “Adobe Open Source Media Framework” (OSMF) [3], which considers the download time of last video segments and decides a suitable bitrate for the next segment to be fetched. The state-of-the-art

for adaptive bitrates algorithms can be generally divided as buffer-based [4], rate-based [5] and hybrid strategies [6][7].

One of the main features in wireless system is the time variations due to its multi-path nature, user mobility, and medium sharing. Moreover, the changing nature of the bitrates in video traffic contributes to the system's natural change. Such variable operating conditions may significantly affect the performance of different adaptation algorithms that degrade the QoE [8]. In this approach, there are some related works such as [9], which the authors utilized the physical layer information to enhance the available throughput estimation and then enhancing the streaming performance in cellular networks. In contrast, the proposed algorithm only bases on application level information and it can be used with any access technology. In [10], authors introduced an adaptation scheme based on a Markov Decision Process (MDP) framework. The authors suggested three heuristics that can use online or offline estimation for available bandwidth in statistic way to absorb MDP complexity. In [11] A. Zahran et al. proposed OSCAR algorithm which it is an optimized algorithm controlled by a probabilistic constraint on stalls using a detailed optimization framework to improve the quality of experience. In [12] the authors studied the problems of bitrate adaptation and determined the causes of many unwanted interactions that arise as a result of modifying the video bitrate over HTTP. In [13] the author investigates the delivery of on demand video streaming under variable bit rate (VBR) coding. The adaptation method is based on detailed instant bitrates of future segments in order to understand the fluctuation traits of the VBR video.

In this work, an adaptive bitrate algorithm is proposed which incorporates the network state, the application state and the video variety conditions to adapt video quality under time varying wireless system. Essentially, the proposed algorithm consists of two main units: estimation unit and video adaptation unit where the download throughput and the buffer occupancy are measured through estimating the available network bandwidth according to the current buffer occupancy of last downloaded segments. During the estimation step, a new attribute is included that scales the buffer occupancy estimation and the throughput estimation based on the variations in the current buffer level and measured throughput of previous download segments. The variation is taken at short term level. At video adaptation unit, the selection of video bitrate is done based on both the measurements at estimation unit and a target

level. The target level is defined for checking the new level if where it is near or far from the target in order to prevent buffer overflow/underflow situations and achieve high quality of experience at user aspect. During the simulation results, the proposed algorithm significantly outperforms the other rate adaptation algorithms in terms of providing maximum download bit rates, minimum number of bitrates switches and the maximum utilization of available bandwidth while maintaining the playback buffer level within limits without any playback interruptions.

The work of this paper is organized as follows: Section II describes our system design and construction of the video streaming model that we will consider in this work, also this section will explain the proposed algorithm which it consists mainly from two parts (estimation unit and video adaption unit). Section III presents our simulation results of experimental tests for our proposed approach in this work. Finally section IV gives the main conclusions that can be drawn from our work.

II. VIDEO STREAMING MODEL DESIGN

We consider a client streaming video divides into M segments each of which contains τ seconds of video. We assume a continuous HTTP connection over which segments are sequentially requested using HTTP GET requests. Each segment is encoded into L video quality representations Q_v with each representation having an average encoding rate V_{R_i} , where $Q_v \in \{1, 2, \dots, Q_{VL}\}$. For each i^{th} segment, the client selects the video bitrate V_{R_i} from $V = \{V_{R1}, V_{R2}, \dots, V_{RL}\}$. The main goal of the propose algorithm is to improve the quality of experience (QoE) by minimizing QoE metrics such as number of interrupts, duration of interrupts, average quality rate, average number of quality switches, and average level of quality switching. The streaming system which it is considered in this work is consisting from main two parts (estimation unit and video adaptation unit). Figure 1 below shows the client/ server system that it is considered for our work, where the network bandwidth represents the data producing rate and video content's bitrate represents the data consuming rate to the video buffer of the client. At the beginning of each download stage, an adaptation algorithm at client side will select the suitable bitrate of the next segment to be downloaded. The rates of the different video representation levels are transferred to the client by the server in the Media Presentation Data (MPD) file.

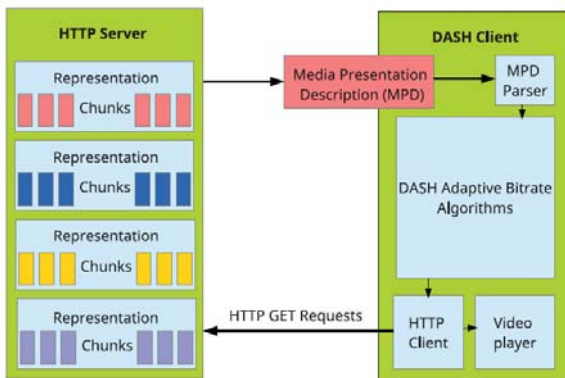


FIGURE I. HTTP STREAMING SYSTEM

A. Estimation Unit

The estimation unit includes the estimate for both buffer occupancy and download throughput for i^{th} segment. At t_i the video player starts downloading the i^{th} segment. The segment download time is $\tau V_{R_i} / T_i$ which is the ratio between the size of chosen segment i.e. τV_{R_i} according to quality level and the average download throughput T_i . Immediately after the download process is completed for i^{th} segment, the video player then starts download the $(i+1)^{th}$ segment, if the download throughput at time t is $T_i(t)$ hence:

$$t_{i+1} = t_i + \frac{\tau V_{R_i}}{T_i} \quad (1)$$

$$T_i = \frac{1}{t_{i+1} - t_i} \int_{t_i}^{t_{i+1}} T_i(t) dt \quad (2)$$

When segments are downloaded and video is being playback, the video buffer occupancy is developed. The buffer occupancy is changed by τ sec after i^{th} segment is downloaded and minimizes as the user watches the video. The dynamic changes for buffer occupancy could be formulated at time t as:

$$B_{i+1}(t) = \left(\left(B_i - \frac{\tau V_{R_i}}{T_i} \right)_+ + \tau \right) \quad (3)$$

Here, the notation $(x)_+ = \max\{x, 0\}$ to ensures that the term can never be negative as well as if $B_i < \tau V_{R_i} / T_i$, the buffer occupancy becomes empty while the video player is still downloading i^{th} segment, leading to stopping events. Now, let W_B be the weighted mean estimation of buffer occupancy which is based on an exponentially weighted changing estimation window that absorbs S_b samples with i be the index of the last downloaded segment then after i^{th} segment download the buffer occupancy would be assigned with a weight, denoted as s while the weight of previous segments in the buffer estimation window would be assigned as $s(1-s)^{i-j}$ where j is the segment index. Then these weights are normalized and the final weights are expressed as:

$$s_j = \frac{s(1-s)^{i-j}}{1 - (1-s)^{S_b}}, \forall j \in \{1, \dots, S_b\} \quad (4)$$

The weighted mean of buffer occupancy can be expressed as:

$$W_B = \sum_{j=1}^{S_b} s_j B_{i-j} \quad (5)$$

where B_i the measured buffer occupancy at the download of i^{th} segment and $s_j \in (0,1)$. The response of the estimation unit

would enhance the changes in buffer occupancy if s be with large value but at the same time might lead to frequent disturbing switches in video quality level. The proposed algorithm adapts the weighted mean of buffer occupancy based on information on network and application states. Usually when the buffer level is low it means a bad network condition that might lead to buffer underflow and impact on video quality of experience. While a high buffer level means the network condition is good and the buffer occupancy would reach the maximum level size B_{max} , the streaming client stops requesting new segments until there exists enough buffer space for one or more segments which leads to ON-OFF behavior and hence effects on QoE [14]. The OFF interval affects on the adaptation process for the bitrate algorithm since the client would not have an accurate estimate for the available network condition during OFF periods. The proposed algorithm uses a scaling factor for buffer level to avoid stalls and construct the video buffer. The scaling factor for buffer level f_B is given as:

$$f_B = f_B^L + (f_B^H - f_B^L) \frac{B_i}{B_{max}} \quad (6)$$

where f_B^H and f_B^L is the higher and lower bound of scaling factor and B_{max} is the maximum buffer size. The above equation scales up the rate of estimation to avoid OFF periods and improve the video. The estimation process also includes the network throughput since any fluctuation in the available bandwidth would impact on the buffer occupancy, so we use a smoothing factor ρ that reflects the changing in network conditions as:

$$\hat{T}_i = \rho T_{i-1} + (1-\rho) \hat{T}_{i-1} \quad (7)$$

A large value of ρ means the network conditions has changed abruptly and so the upcoming bandwidth is calculated by giving more weight to the last available throughput. Contrarily, bandwidth is calculated by giving more weight to the last estimated throughput. Finally, our adjusted throughput estimate T is calculated as:

$$\tilde{T}_i = f_B \times W_B \times \hat{T}_i \quad (8)$$

B. Video Adaption Unit

The last step of adaptive algorithm is to specify a suitable representation quality for $(i+1)^{th}$ segment such that $V_{Ri} \leq \tilde{T}_i$ and buffer level is at the steady region where $0 < B_L < B_i < B_H < B_{max}$. B_L and B_H are two operating thresholds for preventing buffer underflow/overflow, measured in seconds, B_i is the current buffer occupancy after download i^{th} segment and B_{max} is the buffer maximum size. Let B_{aim} represent the target for keeping the buffer level between these thresholds as:

$$B_{aim} = \frac{B_L + B_H}{2} \quad (9)$$

The HTTP adaptive streaming clients download the segments without any wait until the video buffer level reaches the target level B_{aim} .

The following steps represent our proposed adaptive algorithm procedure:

```

input :  $\hat{T}_{i+1}, s, S_b, f_B^L, f_B^H, B_{max}, B_i, L, V, \tau$ 
output :  $V_{Ri+1}$ 
estimate  $W_B, f_B, \tilde{T}_{i+1}$ 
I = J = k = c = e = x = 1;
while(I ≤ L) do
if( $V[I] \leq \tilde{T}_{i+1}$ ) then      A[J] = V[I];  J+ = 1; I+ = 1;
end;
if( $\tilde{T}_{i+1} = V_{Ri}$ ) then  $V_{Ri+1} = V_{Ri}$  ; else
while (k < J) do
 $B_{i+1}^{expected} = B_i + (\frac{\hat{T}_{i+1}-A[J]}{\hat{T}_{i+1}}) \times \tau$ ;  C[k] =  $B_{i+1}^{expected}$ ; k+ = 1; end;
while(c < k)      do
D[c] = |C[c] -  $B_{aim}$ |;  c+ = 1;  end;
Y = D[x];
while(e < c)  do
if(D[e] < Y)  then  Y = D[e]; x = e; e+ = 1;  end;
 $V_{Ri+1} = V[x]$ ;
if  $(\frac{B_L + B_{aim}}{2}) < Y < (\frac{B_H + B_{aim}}{2})$  then   $V_{Ri+1} = V_{Ri}$ ;
else  $V_{Ri+1} = V_{Ri+1}$ ;
```

III. SIMULATION RESULTS

The proposed adaptive algorithm is evaluated using ns-3 network simulator and the topology implemented in this work is shown in Figure 2 below. The topology consists of an HTTP server, HTTP clients and a network element. To achieve adaptive streaming, the HTTP server offers the client seven levels of representations to adapt the video rates these are $V = \{356, 500, 800, 1200, 1500, 2400 \text{ and } 4500 \text{ Kbit/s}\}$. The length of video segment and video buffer is chosen to be 4s and 40s respectively. The values of other parameters B_L , B_H are 15s, 35s respectively. The bandwidth traces is varied according to network traces [15]. The values for s , S_b , f_B^L, f_B^H and ρ are 0.4, 10, 0.5, 1.5 and 0.8 respectively. The proposed algorithm is compared with other algorithms such as: the smooth video adaptation algorithm (SVAA) [16] and Buffer-Based Approach algorithm [4].

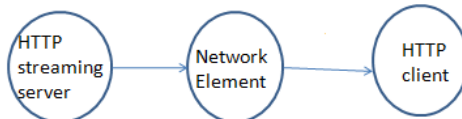


FIGURE II. NETWORK TOPOLOGY FOR SIMULATION

Figure 3 explains the video bitrate achieved by each of the rate adaptation algorithms, while Figure 4 indicates the corresponding client's buffer occupancy under a wireless network environment. In Figures 3 and 4, the aim of these algorithms (proposed , SVAA , BBA) is to improve the quality of experience (QoE) by minimizing the oscillations between the highest and lowest video qualities since the oscillation would increase the number of interruptions during the video playback. From these figures, SVAA has low number of bitrates switches with low average downloaded bit rates, because it follows a conservative approach in adapting the video bitrates under time varying condition in order to keep the client buffer occupancy away from underflow level. For BBA algorithm, the number of bitrates switches is moderate since the algorithm depends on the current playback buffer level in making the decision of rate adaptation. Finally, for our proposed algorithm, the number of quality switches is less than BBA with high average video bitrates because the bitrate adaptation process of the proposed algorithm is done according to the estimation of the available throughput and the current buffer occupancy. Also from Figure 4, the buffer level is kept away from underflow/overflow level because the selection for next bitrate is made according to the target level hence maintaining high video quality.

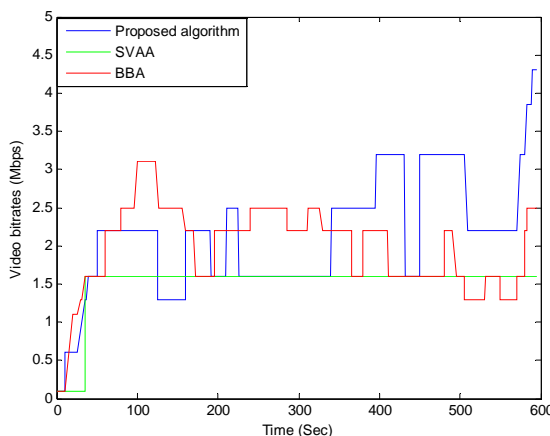


FIGURE III. VIDEO BITRATES VS. TIME

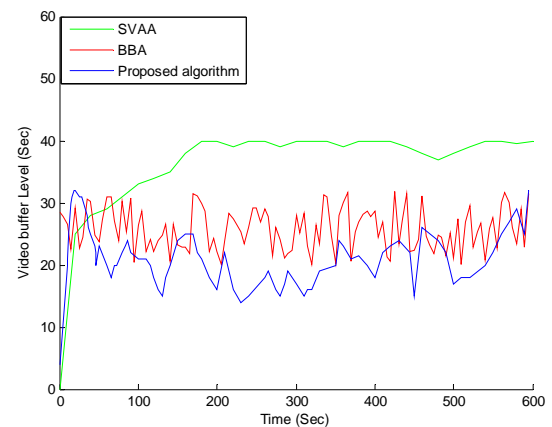


FIGURE IV. VIDEO BUFFER LEVEL VS. TIME

Figures 5 and 6 draw the cumulative distribution function (CDF) for the algorithms with different QoE metrics. In Figure 5, SVAA achieves low average bitrates because it selects lowest video quality compare with BBA and the proposed algorithm. With changing the buffer size, all algorithms tend to select the higher bitrates when minimize the video buffer size for many reason BBA select the higher bitrate to download the next segments because the buffer be full faster and hence the client starts to request higher video quality while the proposed algorithm tends to select higher bitrates because the scaling factor for buffer occupancy is activated earlier as the buffer occupancy increases. Figure 6 plots the CDF of number of interrupts encountered by different algorithms. This figure observes that doubling the buffer size from 60 sec to 120 sec helps increasing the number of interrupt free sessions from 85% to 95% for BBA, from 88% to 96.5% for the proposed and from 90% to 97% for SVAA. Increasing the buffer size also mitigates the maximum number of interrupts for all algorithms to 5 interrupts from 8, 13, and 17 interrupts for SVAA, proposed algorithm, and BBA, respectively.

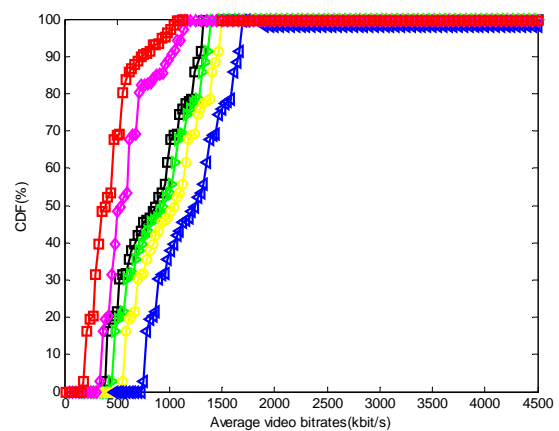


FIGURE V. THE CUMULATIVE DISTRIBUTION FUNCTION OF AVERAGE VIDEO BITRATES

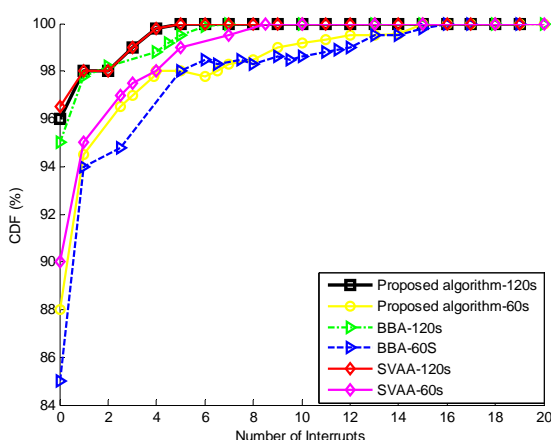


FIGURE VI. THE CUMULATIVE DISTRIBUTION FUNCTION FOR THE NUMBER OF INTERRUPTIONS

IV. CONCLUSION

In this work, adaptive algorithm for obtaining a smooth video bitrate and improve the QoE relies on estimating the available network throughput and current buffer occupancy. The simulation shows that the proposed algorithm outperform other algorithms in avoiding buffer underflow/overflow, high average bitrates and minimum number of interruptions due to use the scaling factor for buffer occupancy in that changing the buffer size effects on the video quality level i.e. minimizes the buffer size let's all the compared algorithms pick the high bitrates for avoiding the risk of playback interruption while increases the size improving the video quality with free number of interruptions.

REFERENCES

- [1] N. Pengpeng, R. Eg, A. Eichhorn, C. Griwodz, and P. Halvorsen. "Flicker effects in adaptive video streaming to handheld devices." In Proceedings of the 19th ACM international conference on Multimedia, pp. 463-472. ACM, 2011.
- [2] T. Stockhammer. "Dynamic adaptive streaming over HTTP—design principles and standards." In Proceedings of the Second Annual ACM Conference on Multimedia Systems, vol. 2014, pp. 2-4. New York, USA: ACM, 2011.
- [3] M. Ricky, X. Luo, E. Chan, and R. Chang. "QDASH: a QoE-aware DASH system." In Proceedings of the 3rd Multimedia Systems Conference, pp. 11-22. ACM, 2012.
- [4] H. Te-Yuan, R. Johari, N. McKeown, M. Trunnell, and M. Watson. "A buffer-based approach to rate adaptation: Evidence from a large video streaming service." ACM SIGCOMM Computer Communication Review 44, no. 4 (2015): 187-198.
- [5] J. Junchen, V. Sekar, and H. Zhang. "Improving fairness, efficiency, and stability in http-based adaptive video streaming with festive." IEEE/ACM Transactions on Networking (TON) 22, no. 1 (2014): 326-340.
- [6] S. Yi, X. Yin, J. Jiang, V. Sekar, F. Lin, N. Wang, T. Liu, and B. Sinopoli. "Cs2p: Improving video bitrate selection and adaptation with data-driven throughput prediction." In Proceedings of the 2016 conference on ACM SIGCOMM 2016 Conference, pp. 272-285. ACM, 2016.
- [7] D. Luca, V. Caldaralo, V. Palmisano, and S. Mascolo. "Elastic: a client-side controller for dynamic adaptive streaming over http (dash)." In Packet Video Workshop (PV), 2013 20th International, pp. 1-8. IEEE, 2013.
- [8] X. Renchao, F. Richard Yu, T. Huang, J. Liu, and Y. Liu. "Joint user association and rate allocation for HTTP adaptive streaming in heterogeneous cellular networks." In Communications (ICC), 2016 IEEE International Conference on, pp. 1-6. IEEE, 2016.
- [9] X. Xiufeng, X. Zhang, S. Kumar, and L. Erran Li. "pistream: Physical layer informed adaptive video streaming over lte." In Proceedings of the 21st Annual International Conference on Mobile Computing and Networking, pp. 413-425. ACM, 2015.
- [10] B. Ayub, M. Hassan, and S. Kanhere. "Http-based adaptive streaming for mobile clients using markov decision process." In Packet Video Workshop (PV), 2013 20th International, pp. 1-8. IEEE, 2013.
- [11] A. Zahran, J. Quinlan, D. Raca, C. J. Sreenan, E. Halepovic, R.K. Sinha, R. Jana, and V. Gopalakrishnan. "Oscar: an optimized stall-cautious adaptive bitrate streaming algorithm for mobile networks." In Proceedings of the 8th International Workshop on Mobile Video, p. 2. ACM, 2016.
- [12] Y. Xiaoqi, M. Bartulović, V. Sekar, and B. Sinopoli. "On the efficiency and fairness of multiplayer HTTP-based adaptive video streaming." In American Control Conference (ACC), 2017, pp. 4236-4241. IEEE, 2017.
- [13] Y. Li, T. Tillo, and J. Xiao. "QoE-Driven Dynamic Adaptive Video Streaming Strategy With Future Information." IEEE Transactions on Broadcasting (2017).
- [14] A. Saamer, L. Anantakrishnan, A. Begen, and C. Dovrolis. "What happens when HTTP adaptive streaming players compete for bandwidth?." In Proceedings of the 22nd international workshop on Network and Operating System Support for Digital Audio and Video, pp. 9-14. ACM, 2012.
- [15] R. Haakon, P. Vigmostad, C. Griwodz, and P. Halvorsen. "Commute path bandwidth traces from 3G networks: analysis and applications." In Proceedings of the 4th ACM Multimedia Systems Conference, pp. 114-118. ACM, 2013.
- [16] T. Guibin, and Y. Liu. "Towards agile and smooth video adaptation in dynamic HTTP streaming." In Proceedings of the 8th international conference on Emerging networking experiments and technologies, pp. 109-120. ACM, 2012

Vehicle Target Detection Based on Improved Mixed Gaussian Modeling

Caiyun Xie¹, Ruxia Hong^{1,*}, Jing Wang² and Hong Yu¹

¹YuZhang Normal University, Nanchang, Jiangxi, China

²Information Electromechanical Department, The Board of the Middle Route Project of South-to-North Water Diversion Project, Zhengzhou, Henan, China

*Corresponding author

Abstract—In the modern world, with the rapid development of science and technology, computer and related technologies have been used in many fields; of course, intelligent video surveillance system cannot do without computer technology. This system also cannot do without the core issue: the detection of the goal vehicle. Only the smooth detection of moving vehicles can complete the intelligent video surveillance system speed. This paper mainly introduces several methods of vehicle target detection, and provides the advantages and disadvantages of every method, and improves the traditional mixed Gaussian modeling method. The steps required to complete this method are introduced in detail.

Keywords—gaussian modeling; video speed; vehicle target detection component

I. INTRODUCTION

With the rapid economic growth, the number of vehicles in our country has risen sharply, which has also helped to gradually expand the scale of our country's highways. Therefore, the annual number of traffic accidents in our country also increases. In order to effectively reduce traffic accidents and improve traffic quality, it is necessary to introduce intelligent monitoring system to monitor the traffic and traffic conditions in real time through the intelligent traffic system so as to solve the problem of traffic disturbance in time and improve the processing efficiency of related parts and avoid unnecessary troubles. In the field of intelligent transportation, the term "video tachymeter" has also appeared frequently in recent years as a hot spot. Video tachometer is a very cost-effective technology that can keep abreast of traffic conditions only through the camera without installing radar and sensors. Therefore it is also widely used.

In the intelligent monitoring system, the most critical and foremost step is to detect the target of a moving vehicle. By detecting a series of images, dynamic pixels and static pixels are respectively obtained, and then the changed regions are extracted from the pixels. By judging the detected moving pixels to draw whether we need to deal with the unexpected situation. The accuracy vehicle target detection of the latter part of the video speed is crucial; it is the first step in the completion of video speed measurement.

II. INTRODUCTION OF VEHICLE TARGET DETECTION METHOD

The basic technology in the intelligent monitoring system is to track and identify the moving vehicles. This technology also occupy a large part of the field of computer vision, causing a large number of experts in related fields to study it, so the technology is developing more and more fast. Since only the monitoring system can mainly identify the vehicles in motion, the vehicle target detection is mainly to solve the problem that the moving objects can be identified and extracted from the static background, and the focus is on the moving targets.

For the quality of the entire monitoring system, the detection of moving targets has played a decisive role. External factors (road conditions of highway, heavy rain, cloudy, etc.) are brought different degree of impact to the vehicle detection, which requires the use of better vehicle target detection methods to try to avoid these external interference. In this way we call it robust to the external environment [1,2].

This section mainly introduces several traditional vehicle target detection methods, including four methods [3]: method based on feature(corner), method based on the difference between the frames, method based on the optical flow field and method based on the background difference. Here are the main ideas of these four methods.

A. Method Based on Feature

This method is also called corner-based method. Its idea is to find out its special corner from the appearance of things, and then perform the matching operation with the images in the system [4].

To complete the matching operation need to go through the following two steps.

- First, extract some representative corners or features from two or more consecutive images detected by the video and create a collection of images for later use.
- Then according to the feature image set obtained in the last step, the structures of the objects corresponding to the corresponding images are matched one by one to complete the calculation of the moving objects to obtain the motion parameters in the coordinate axes.

After completing these two steps, we can find the corresponding corner for the moving vehicle seen in the video detection, and finish the remaining steps according to the feature in the later target detection.

The feature-based approach sums up well the relevant features of the moving vehicle. However, this method also has limitations, because it is difficult to find the corner of the object and to complete the matching work. In particular, there are many vehicles on the highway, which make it difficult to distinguish between multiple targets.

B. Method Based on the Difference Between the Frames

The term difference between the frames which is also known as time-domain difference (DT) is a relatively simple method that quickly distinguishes moving objects. The method detects the foreground of the moving target by determining the gray value of the background pixel plus the decisive position.

Generally, the image detected by the video is not three-dimensional, but a projection on the two-dimensional plane. The projection changes as the three-dimensional image changes. The magnitude of the difference between consecutive frames of images depends on the transformation of successive scene images in the video. This difference is calculated by extracting the difference between two or more consecutive frames of image.

The point of this method is that the programming complexity is relatively low and the algorithm is easy to implement. It also can solve the influence caused by the external environment interference mentioned in the feature method and has good stability. The disadvantage is that the method is limited by the noise generated by the equipment during the shooting process and also influences the foreground area of the later picture due to the background being blocked so that the formed pixel becomes empty.

C. Method Based on Optical Flow Field

The optical flow field is generally due to the shooting movement, which produces an instantaneous velocity field in the movement of the target. In other words, it is the pixel point [5] generated on the surface of the photographed object during its movement. The method based on the optical flow field focuses on the simulation of the object's motion field, first proposed by Gibson [6]. This method can check the information of anything under any circumstances, and it is easy to realize the target detection in exercise. However, it cannot be avoided by external force majeure. At the same time, accurate data information cannot be calculated, and a requirement that most systems must meet is not satisfied: real-time.

D. Method Based on the Background Difference

The above three methods are typical target detection methods, method based on the background difference is also one of the common methods to achieve target detection [7]. The main idea of this method is to construct the background from the detected continuous multi-frame images to obtain the latest background image, and then subtract the background image from the video image to be detected in a certain frame. The larger one is the sport we need to look for.

The method based on background difference is mainly for obtaining efficient background image, so this method depends on the key step of background image extraction. Figure I is the background subtraction extraction prospects of the target out of the process.

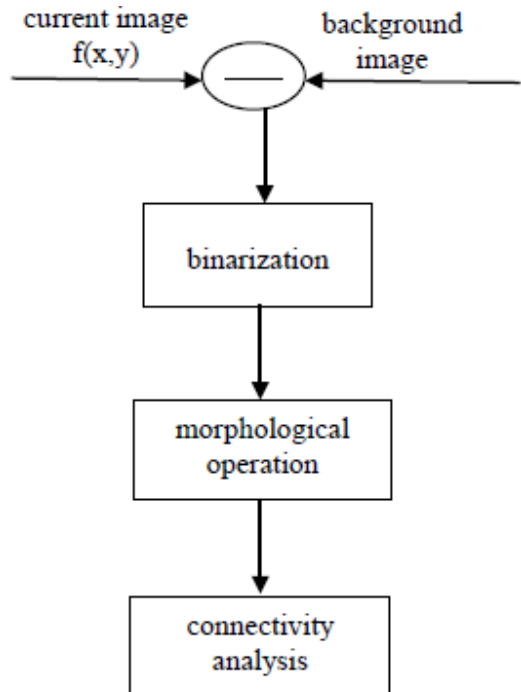


FIGURE I. BACKGROUND SUBTRACTION EXTRACTION PROSPECTS OF THE TARGET OUT OF THE PROCESS

The key to extracting the foreground object by the background subtraction method is how to get the better background image. If the background image is not accurately extracted, then it is impossible to get the accurate foreground object image.

There are basically three methods for background modeling: statistical averaging, filtering, and Gaussian modeling. The statistical averaging method is to perform statistical analysis on the data of the multiple video images and obtain the pixel average as the background pixel value. The more the images are used in this method, the better the effect will be, but at the same time, the higher demand the amount of calculation and the storage amount need. The filtering method is based on the statistical average method to introduce attenuation control factor to update the background image weighted method, this method for the selection of control factors depend greatly. Gaussian background modeling method is the most widely used method for the detection of moving targets and the background modeling algorithm is used in this paper, which is described in detail in the next section.

III. IMPROVED MIXED GAUSSIAN MODELING METHOD

Since there are some limitations on the above target detection methods, this section will introduce an improved mixed Gaussian modeling method. Based on the traditional Gaussian modeling, this paper gives an improved method.

A. Traditional Mixed Gaussian Modeling

Mono-Gaussian background modeling is based on the background of the pixel formed by the image, and the metric function $f(x, y)$ is formed according to the horizontal and vertical coordinates (x, y) where the pixel is located. The value that exceeds the set threshold is used as the background pixel in the model, while the pixels below the threshold will form the foreground pixel.

Mixed Gaussian modeling method is based on the Mono-Gaussian modeling method based on the completion of at different times, for each pixel to construct a number of measurement functions, such as the measurement function at t_1 time is $f_1(x, y)$, measurement function at t_i moment is $f_i(x, y)$. The average of all the metric functions at different moments is taken as the Gaussian distribution average and then compared with the threshold.

In all methods, the Gaussian modeling method best meets the background modeling of the highway environment.

B. The Main Drawbacks of Traditional Mixed Gaussian Modeling

The traditional mixed Gaussian modeling method mainly has the following shortcomings.

- The model requires Gaussian distribution model for each pixel in the image. The calculation of this model will increase as the number of objects used in modeling increases, which leads the hardware to keep up with the system request.
- In general, a vehicle traveling on an highway with a low vehicle density occupies a relatively small proportion of the entire monitoring picture, so that the relatively large occupying area of the vehicle occupies a smaller area. When a frame is Gaussian modeled and updated, the corresponding pixel must be selectively processed.

In view of the above shortcomings, this section will focus on the improved Gaussian modeling method.

C. Method and Steps of Improved Gaussian Modeling

In view of the above two points, we make improvements to the traditional mixed Gaussian modeling method, which is to simply optimize the Gaussian background model. Since the optimized model is for vehicles traveling in lane lines and not caring for anything else, we start off with lane lines and accurately lock the vehicles in the lane as long as the lane lines are accurately extracted. The following three steps give the lane line extraction process.

1) Extract lane line boundaries

Lanes on normal highway are some obvious edges from the direction of image processing. Therefore, in order to get the lane line image, we should first extract the edge of the original image. In addition, the video speed system for the highway shooting direction is either from front to back or from back to front, but not horizontal shooting, so reflected in the image is the lane line in the image is the direction of the vertical direction. Therefore, in the edge detection only need to detect

the vertical edge. In the related art of image processing, there are many algorithms for edge extraction, but some algorithms are computationally intensive, which is not good for system real-time, such as Canny algorithm. Some algorithms to extract the edge of the effect is not good, have a bad influence on the follow-up processing, such as Laplace algorithm. Considering the efficiency and complexity of the Sobel algorithm [8], it is more suitable for the system.

2) Binarization of Lane Boundary

In the previous step, we extracted the lane boundary, but the boundary picture of other objects (green belts and fence, etc.) in addition to the lane line will cause interference to us and we must eliminate this interference information to avoid occurrence. There is an error extracting the edge information. According to the pictures taken, we conclude that the gray value of the lane boundary line is higher than the gray value of other objects. Therefore, using the binarization formula, the gray value is calculated. If the gray value is below a given threshold, it is excluded. That is the boundary line of other objects.

3) Extracting the lane boundary line and highway traffic zone

After step 2), we get the boundary picture we need, but the line in the picture is a part of the original picture. Therefore, we need to use Hough transform algorithm to extract the straight line in front of the lane to complete the repair of the lane boundary line. Although the Hough algorithm has high time complexity and space complexity, this lane edge line only needs to be repaired once, which is negligible for the overall system complexity.

After all the above steps, we can get an edge line that can identify all the vehicle information. In this way, a model is built to track the vehicle's target.

For the practical application of this article, it is only a background of the lane inside the line modeling, so galloping branches on both sides or some other disturbing factors will not have an impact on the background update. Usually, there will be no other interference factors in addition to moving vehicles outside the lane line area, and because the interval time in the continuous between the two video images is too short, except where the vehicle pixel values will have a greater change, the rest of the background area usually does not change much (in the case of sudden changes in the weather), the general idea of updating the Gaussian background model proposed in this paper is as follows.

- According to the two adjacent frames of image difference image, the driving area in the lane line is divided into the moving area (the pixel value is quite different) and the non-moving area.
- For the non-moving region, since the pixel value of the background pixel changes very slowly, it is not necessary to perform a Gaussian model updating operation with a large amount of calculation. Instead, the Gaussian model matching the pixel in the previous frame is directly used for the current frame in.

- For the motion region, the traditional mixed Gaussian background model must be updated due to the large and irregular changes of pixel values.

According to the improved mixed Gaussian model method, the flow chart of vehicle detection is given as Figure II.

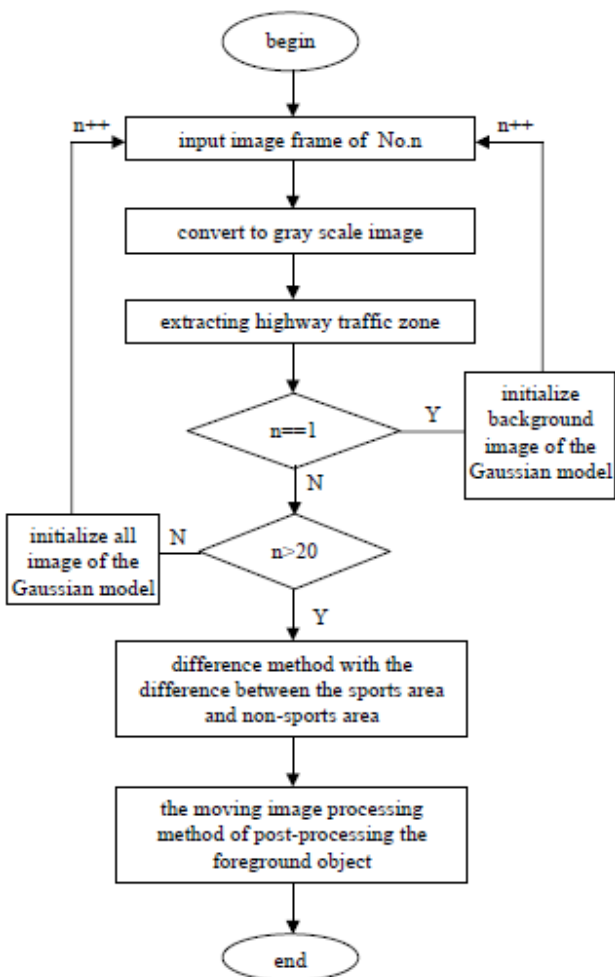


FIGURE II.

FLOW CHART OF IMPROVED MIXED GAUSSIAN MODEL METHOD

ACKNOWLEDGMENT

The project is supported by Foundation of Jiangxi Provincial Education Department (No.GJJ161309, No.GJJ161304 and No. GJJ151332).

REFERENCES

- [1] Cheng Juan. Motion Target Recognition Algorithm in Complex Background[D], Wuhan, Wuhan University of Technology, 2008.
- [2] Paulo A.C. Marques, Jose M.B. Dias, R. Conselheiro Emidio Navarro. Optimal Detection and Imaging of Moving Objects with Unknown Velocity[J]. In Pro. Of the 3rd European Conference on Synthetic Aperture Radar, 2000: 561-564.
- [3] Shi Zhiqiang. Motor vehicle speed target detection and tracking technology research and application[D]. Nanchang University, 2007.
- [4] Li Guodong, Liu Chunyang, Liu Chang'an. A Feature-based Dynamic Target Detection and Tracking Algorithm[J]. Journal of Harbin Institute of Technology, 2005,7: 927-929.
- [5] Fang Yuqiang, Dai Bin, Song Kanazawa, et al. A method of moving object segmentation based on optical flow and level set[C]. 2009 Automation Conference, 2009,3: 1541-1547.
- [6] Chen Wenjie. The Research of the Eliminate Shadow and the Tracking of Multi-objective in Video Speed Measuring System[D]. Nanchang University, 2012.
- [7] Gupta S. Modeling O. Martin RFK, et al. Detection and Classification for Vechicles[J]. IEEE Transcations on Intelligent Transporatation System. 2002, 3 (1): 37-47.
- [8] Tan Xiaojun, Shen Wei, Guo Zhihao. A video-based traffic monitoring method for road traffic[J]. Computer Applications, 2005 (5).

IV. CONCLUSION

Intelligent information processing for the highway is now very popular means; it is also a more mature technology, which can provide real-time and accurate access of all of the vehicle information for law enforcement and other relevant departments to give important judgments. The premise of accurate vehicle information acquisition is to track and detect the vehicle targets. In this paper, several popular vehicle target detection methods are introduced and the corresponding advantages and disadvantages are given. Then the method of traditional mixed Gaussian modeling method has been improved correspondingly, and the edge extraction of vehicles in the driving area of highway has been realized in three steps, which provides a solid foundation for vehicle target detection.

A Precision Evaluating Method of DEM Using Map Spots Generated by Contour Superposition

Zechun Huang*, Zhu Xu, Qianning Zhang, Min Xiao, Zipu Liu, Yongyou Qian and Tianting He

Faculty of Geosciences and Environmental Engineering, Southwest Jiaotong University, Chengdu, Sichuan, 611756, China

*Corresponding author

Abstract—Aiming at the shortcomings of traditional contour superposition analysis in quantitative evaluation of DEM error, the purpose of this paper is to propose a new method to measure the DEM accuracy by using the map spots of contour superposition. To begin with, the concepts of the difference rate and the matching rate for contour overlaying was described, and the calculating methods about the two indices were illustrated in accordance with the map spots generated by contour overlaying. Then, this paper comparatively illustrated the consistency between the terrain coincidence reflected by the matching rate of the same name contour lines and the mean elevation difference of the reconstructed DEM and the original DEM. Finally, this paper analyzed the influence of contour interval to the difference rate of the contour superposition. Meanwhile, taking slope as the complexity factor of terrain and selecting different experimental areas with different average slope, the correlation between the difference rate of contour superposition and the average slope of experimental area was quantitatively measured by regression analysis method. The experimental results show that map spots generated by contour superposition can be used to reflect the terrain coincidence between reconstructed DEM and original DEM, and the matching rate of contours is positively correlated with the total number of the map spots, but negatively correlated with the relevant indexes of the area of the map spots. The method proposed in this paper not only can reflect the statistical characteristics of DEM error, but also can describe the spatial distribution of error.

Keywords—DEM; contour superposition; map spot; error analysis; regression analysis

I. INTRODUCTION

DEM error affects the reliability and accuracy of digital terrain analysis results, so the study of DEM data quality has very important theoretical significance and application value [1]. In practical application, we should not only consider the elevation precision of DEM, but also study the coincidence between the terrain expressed by reconstructed DEM and natural terrain [2]. Usually the contour superposition method is used to evaluate the terrain coincidence [3]. But using this method can only qualitatively analyze the general situation of DEM precision and the terrain coincidence. Thus, the traditional contour superposition method lacks quantitative measurement criteria for evaluation of DEM error [3, 4].

To improve the effect of traditional contour superposition method which cannot quantitatively describe the accuracy of DEM, the academia has carried on the related exploration, and has obtained some research achievements. The concept of terrain description error was proposed to quantitatively describe

the terrain expression accuracy of DEM [5]. According to that the change of the terrain surface shape is necessary to change the contour shape, the method of evaluating the contour superposition error which reflect the accuracy of the terrain surface shape was presented [6]. Using the ratio of the area difference between reconstructed contour and original contour to the length of original contour as an index for DEM precision evaluation, scholars illustrated the overall deviation of before and after reconstructing contour and the coincidence degree between the reconstructed terrain and original terrain [7]. Based on two precision indexes of the maximum reconstructed offset and average maximum reconstructed offset, the coincidence degree between DEM and actual terrain was measured in the local area [8]. In addition, for the sake of evaluating the agreement degree of the river net, a quantitative description method was produced by using the ratio of the total area of small polygon generated by overlaying of two river networks and the area of the basin in experimental area [9].

Described as above, a comparative analysis of contour reconstructed by DEM is a visual quality evaluating method, and it can quantitatively analysis the coincidence degree between the reconstructed terrain surface and the original terrain surface, furthermore it can evaluate the quality of DEM [6]. However, these methods only use a single index to evaluate the overall accuracy of DEM. So, they can neither describe the statistical characteristics of contour superposition errors, nor describe its spatial distribution quantitatively. For this purpose, this paper aims to propose a new method to evaluate the accuracy of reconstructed DEM using map spots generated by contour superposition. We will build correlation indices of map spots, and then analyze the statistical characteristics of reconstructed DEM error by means of statistical description method. It is hoped that not only can quantitatively evaluate the coherence degree between the reconstructed terrain surface and the actual terrain surface, but also can describe the statistical characteristics and spatial distribution of the errors of the reconstructed DEM.

II. DEM ERROR MODEL BASED ON MAP SPOTS OF CONTOUR SUPERPOSITION

The basic idea of the DEM error model is to carry out the spatial overlaying operation based on the contour from reconstructed DEM and the original DEM, and then to generate a series of map spots as shown in Figure I, and to reflect quantitatively the difference degree of the two contours generated from reconstructed DEM and original contour according to the area of the map spots. The ratio of all the map

spots total area and the experimental region area is called the difference rate, which indicated the whole difference between the reconstructed contour and the original contour. The calculating formula of the indices is shown in equation (1). The calculating formula for matching ratio between the reconstructed contour and the original contour is shown in equation (2). In the equation (1) and (2), A represents the area of the experimental region, and α_i represents the area of the map spot i , and n indicates the number of map spots, and ε indicates the difference radio of contour superposition, and p stands for the matching ratio of contour superposition.

$$\varepsilon = \frac{\sum_{i=1}^n \alpha_i}{A} \quad (1)$$

$$p = 1 - \varepsilon \quad (2)$$

III. EXPERIMENTAL METHODS

For accessing DEM accuracy by using the map spots of contour superposition, this paper firstly takes the conversion of DEM from 30m resolution to 90m resolution as an example, then selects four kinds of method which are the nearest neighbor resampling, mode resampling, median aggregating, and mean aggregating to rebuild DEM; Secondly, the two contour lines generated according to the reconstructed DEM and the original DEM are overlapped to create map spots through spatial calculating of polygon, and moreover analyze the spatial distribution characteristics of map spots. Thirdly, the mean elevation difference index is taken as the reference object of the terrain coincidence degree, and the consistency of the coincidence rate between the contour difference rate and the mean elevation difference index will be analyzed. Based on the four kinds of scale transformation method, the statistical analysis of the indexes of the map spots will be carried out, and the relationship between the contour matching rate and the index variables of the map spots will be explored.

The density of contour lines can affect the number of map spots, which will lead to variety of DEM error distribution. For contour interval can affect the density of contour lines, it is necessary to analyze the influence of the contour interval on contour matching rate. To this end, firstly based on the data of one experimental area, we use the nearest neighbor resampling method to reconstruct DEM from 30m resolution into 90m resolution. Secondly, for the reconstructed DEM and the original DEM, the corresponding contour lines will be created

respectively by six kinds of contour interval of 50m, 100m, 200m, 300m, 400m, 500m. Meanwhile, the correlation index value of the map spots will be calculated successively by spatial overlapping operation of contour lines with the same name. Finally, the relationship between the contour lines and the number of map spots, the area index, the difference rate and the matching rate will be analyzed to find out the influence rule of the contour interval to the DEM error evaluated by map spots of contour overlapping.

The slope is chosen as the terrain feature factor to explore whether the method of evaluating the DEM error by map spots is affected by the terrain features. Firstly, this paper selects 16 experimental areas of different terrain complexity, using the nearest neighbor resampling method for DEM scale transformation, and calculate the indexes value of the average slope, contour difference rate and contour matching rate. Then, the correlation between the difference rate and the average slope will be analyzed by using the scatter plot, and the correlation coefficient will be used to analyze the correlation degree between them. Finally, the regression analysis method will be used to quantitatively describe the correlation between them, and the quantitative relationship between the contour difference rate and the slope of the experimental area will be measured with empirical regression equation.

IV. STATISTICAL ANALYSIS OF MAP SPOTS AND THE EFFECT OF CONTOUR INTERVAL

The mean elevation difference index reflects the terrain coincidence between the reconstructed DEM and the original DEM. The area of map spots can also be used to measure the deviation degree of the contour with the same altitude, and it can be used to quantitatively evaluate the matching degree between the two contour lines generated respectively by the reconstructed DEM and the original DEM. The statistical data of map spots are listed in Table I. Through the comparative analysis of the difference between height mean difference and the contour difference ratio, it could be seen that the smaller absolute value of the mean elevation difference is, the smaller the contour difference rate is, and vice versa. The statistical results showed that the map spots of contour superposition can be used to reflect the terrain coincidence degree of reconstructed DEM. Analyzing the statistical data of map spots, it showed that contour matching rate and the total number of map spots was positively correlated, and it was negatively correlated with the total area, mean area, area standard deviation.

TABLE I. STATISTICAL DATA OF MAP SPOTS GENERATED BY CONTOUR SUPERPOSITION USING DIFFERENT METHODS

Methods to reconstruct DEM		Nearest neighbor resampling	Median aggregating	Mean aggregating	Mode resampling
number of map spots		48276	44504	33456	18618
Area of map spots [m ²]	Sum	28628668.8	31956977.8	37806971.3	112994271.6
	Mean	593.0	718.1	1130.1	6069.1
	Standard deviation	1080.8	1329.2	1967.3	25908.4
Mean height difference [m]		0.8	1.1	1.2	-11.8
Difference rate [%]		3.2	3.5	4.2	12.5
Matching rate [%]		96.8	96.5	95.8	87.5

As shown in table II, with the increase of the contour interval, the number of the map spot reduced. At the same time, the difference rate decreased, and the matching rate increased. In the same experimental area, the smaller the contour interval is, the more the contour lines generated by DEM is, and the larger the total area of map spots is, and the greater the difference rate is, but the smaller the matching rate is. Further analysis results showed that the contour interval was negatively correlated with

the difference rate and the number of map spots, and the correlation between the contour interval and the contour matching rate was positively correlated. From the above analysis, contour interval has an influence on the evaluation of the DEM accuracy. Therefore, it is necessary to make a comparative analysis with the same contour interval when the method is used to measure the terrain surface coincidence.

TABLE II. STATISTICAL DATA OF THE CONTOUR INTERVAL INFLUENCE TO THE MAP SPOTS

contour interval(m)	number of map spots	Area of map spots(m ²)					Difference rate (%)	Matching rate (%)
		minimum	maximum	sum	mean	Std.		
50	88524	0.000005	22580.0	57265227.0	646.9	1170.7	6.4	93.6
100	42941	0.000005	24138.5	28858774.7	672.1	1219.6	3.2	96.8
200	21356	0.000034	27586.5	14381969.8	673.4	1236.0	1.6	98.4
300	14272	0.000007	21864.1	9436242.2	661.2	1229.1	1.0	99.0
400	10554	0.000034	21977.5	7135833.8	676.1	1207.1	0.8	99.2
500	8520	0.000041	13270.4	5752290.4	675.2	1230.3	0.6	99.4

V. CORRELATION BETWEEN THE CONTOUR DIFFERENCE RATE AND THE AVERAGE SLOPE

The sample data contain the average slope and the contour difference rate, which were calculated based on the DEM of 16 experimental areas. Results of statistical analysis shows that with the increase of the average slope, the difference rate increases, and the contour matching rate decreases. As shown in Figure II, it could be seen that approximate linear relationship between the difference rate and average slope is obvious. For quantitatively determining the correlation between them, the correlation analysis of the average slope and the difference rate were carried out. The correlation coefficient of the two variables was 0.96. The value of correlation coefficient showed that the difference rate was correlated with slope. To further determine the degree of influence between the two variables, the average slope was taken as the independent variable, and the difference rate was used as the dependent variable, and a linear regression model was established based on independent variables and dependent variables. On the base of the sample data, the model parameters were solved, and the empirical regression equation (3) is obtained. In the regression equation (3), *Slope* stand for the average slope of experiment area, and ε stand for difference rate of contour superposition.

$$\varepsilon = 0.094308 \times \text{Slope} + 0.244789 \quad (3)$$

R^2 is the deterministic coefficient of the regression equation, which represents the explanatory power of the independent variable in the equation. The R^2 value calculated by the regression model is 0.9139, which shows that the "average slope" explains the variation degree of the difference rate of 91.39%. From the empirical regression equation, when the average slope increased by 1 degree, the difference rate will increase by 9.4308 percentage points. The results showed that the influence of the average slope on the contour difference ratio was not significant.

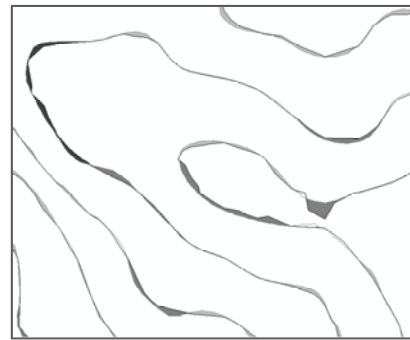


FIGURE I. MAP SPOTS OF CONTOURS SUPERPOSITION

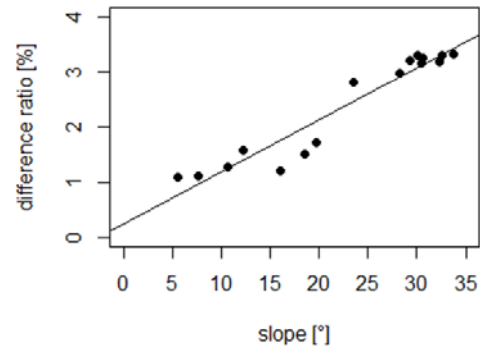


FIGURE II. CORRELATION BETWEEN THE DIFFERENCE RATE AND THE AVERAGE SLOPE

VI. SUMMARY

Aiming at shortcomings of the traditional contour matching in automatic interpretation and quantitative evaluation, this paper proposed a new method of evaluating DEM error, which was evaluated by using the ratio of the map spots and the total area of the experimentation area. This method overcame the shortcomings of the traditional contour superposition method which only carry out qualitative analysis. It can not only

quantitatively evaluate the DEM error, but also can describe its statistical characteristics. The experimental results showed that using contour matching rate to describe the terrain coincidence degree of the reconstructed DEM had the same effect compared with using the average elevation difference index. Under the condition of using the same contour interval to create contour lines, the contour matching rate was positively correlated with the number of the map spots, but negatively correlated with the area indexes of the map spots. There was a strong linear correlation between the difference rate of contour matching and the average slope of the experiment area. Compared with the traditional contour reconstruction method, this method proposed in this paper not only can access quantitatively the DEM error overall, but also can according to the area of map spots in different position analyze the spatial distribution of DEM error. Contour interval had a major influence on contour matching rate in the same experiment area. Therefore, it is necessary to compare and analyze terrain matching effect using map spots in the case of the same contour interval. But the selecting strategy of contour interval needs further study.

ACKNOWLEDGEMENT

This research was financially supported by Mapping Geographic Information Public Service Industry Research Funds (Grant No.201512028) and the Central Universities Fundamental Research Funds (Grant No.2682014CX017).

REFERENCES

- [1] ZHIWEI W. The study and application of DEM error model based on the reconstructed contours [D]; PLA Information Engineering University, 2007.
- [2] CHUN W, YANG T, DUN-XIN J, et al. Study on the accuracy of regular grid DEM topographical description morphology [J]. Geomatics World, 2008, (01): 46-52+72.
- [3] FEN Q, XUE-JUN J. Study on buffer superposition to quantitatively evaluate DEM precision completely [J]. Acta Agriculture Borealioccidentalis Sinica, 2008, 17(03): i336-42.
- [4] GUANG-XIA W, SHU-LI B, YIN-BAO Z. Evaluating DEM accuracy based on reconstructed contours [J]. Journal of Geomatics Science and Technology, 2010, 27(01): 9-13.
- [5] YONG Z, GUO-AN T, QI P. A mathematical simulation of DEM terrain representation error—a case study in the Loess hill-gully areas of China [J]. Journal of Mountain Science, 2003, 21(02): 252-6.
- [6] GUO-AN T, YANG T, CHUN W. Contour-matching-difference and Its application in DEM quality assessment [J]. Bulletin of Surveying and Mapping, 2007, (07): 65-7.
- [7] FAN J. Researches on the surface modeling and the accuracy evaluation of DEM [D]; PLA Information Engineering University, 2006.
- [8] CHANGQING Z, ZHIWEI W, HAIYAN L. Accuracy Evaluation Model of DEM Based on Reconstructed Contours [J]. Geomatics and Information Science of Wuhan University, 2008, 33(02): 153-6.
- [9] WEI-TAO L, CHUN W, PENG L, et al. Influences of DEM generalization methods on extracting accuracy of hydrological structure information [J]. Bulletin of Soil and Water Conservation, 2012, 32(04): 168-71.

Sight Spot Buffer Model Based on Tourists' Interests

Xiao Zhou*, Shun He, Shixiang Zhang, Wei Chen, Yu Chen and Youwei Ma

Information Engineering University, No.62 Kexue Avenue, High-tech Zone, Zhengzhou, China

*Corresponding author

Abstract—Aim at the current problems that tourism GIS cannot provide individual service to meet the needs of tourists, this paper brings forward sight spot buffer model based on tourists' interests and needs. Firstly, sight spot classification model is set up and all the sight spots are coded. According to tourists' needs, sight spot interest needs model is set up. Aim at specific needs, interest sight spot buffer model is set up and sight spot as well as service information around within the buffer is classified. Sight spot buffer maps in the sample example proves that this model can help tourists to rapidly know sight spots and service information around, which can provide tourism decision support and increase efficiency.

Keywords—Interest needs; sight spot; sight spot buffer; classification information

I. INTRODUCTION

Before tourists going to visit an unfamiliar city, they usually study the sight spots in the city and plan the proper route. According to the sight spot star and public comments, they mainly choose proper and interested ones to have a tour. Tourists usually get tourism information by purchasing books in the store, surfing Internet, turning to travel agency, etc., which is passive. The analysis and selecting on sight spots is subjective. As to current tourism GIS, they mainly provide sight spots' mass geographic information, which considers no individual needs and interests and cannot provide special service for single individuality. According to the age, tourists can be divided into several grades. Each grade has different needs and interests, and developing one kind of tourism GIS cannot meet the needs of all grades. In the mean time, mixing all kinds of service information and GIS information cannot provide individual service. Aim at these problems, based on the current tourism GIS, this paper brings forward sight spot buffer model based on tourists' interests and needs. This model can provide sight spot information and service information around within buffer relying on tourists' needs and interests, which can provide convenience for tourists to select sight spots and plan tour route.

II. TOURIST INTEREST NEEDS MODEL

A. Sight Spot Classification Model

Take Zhengzhou city for example. According to sight spot features, sight spots in Zhengzhou city can be classified into four sorts $S_i, i \in (0, 4] \in \mathbb{Z}^+$. Sort S_1 : Park and Greenland. Sort S_2 : Shopping. Sort S_3 : Venue. Sort S_4 : Entertainment.

In each sight spot sort, several sub-sorts are set as $S_i R_j$, $j \in (0, \max k_i] \in \mathbb{Z}^+$. k_i is the maximum sight spot number of a certain sort. TABLE I is the sight spots of each sort. Take sight spots as elements to set up sight spot classification database and store sight spot codes, as FIGURE I shows.

TABLE I. SIGHT SPOT CLASSIFICATION AND ELEMENTS

Sight spot	Sight spot code	Sight spot	Sight spot code
S_1	$S_1 R_1$ Renmin Park	S_3	$S_3 R_1$ HenanMuseum
	$S_1 R_2$ Bishagang Park		$S_3 R_2$ GeologyMuseum
	$S_1 R_3$ Zijingshan Park		$S_3 R_3$ ErqiMuseum
	$S_1 R_4$ Forest Park		$S_3 R_4$ Gallery
	$S_1 R_5$ Lvcheng Square		$S_3 R_5$ ZhengzhouMuseum
	$S_1 R_6$ Botanical garden		$S_3 R_6$ Science museum
	$S_1 R_7$ Zhengzhou zoo		$S_3 R_7$ Aquarium
	$S_1 R_8$ YellowRiver View		
S_2	$S_2 R_1$ Wangfujing	S_4	$S_4 R_1$ CenturyPark
	$S_2 R_2$ Department store		$S_4 R_2$ FountPark
	$S_2 R_3$ Erqi Uanda		$S_4 R_3$ WaterPark
	$S_2 R_4$ Zhongyuan Unada		$S_4 R_4$ ChildrenPark
	$S_2 R_5$ Dehua street		
	$S_2 R_6$ CC mall		

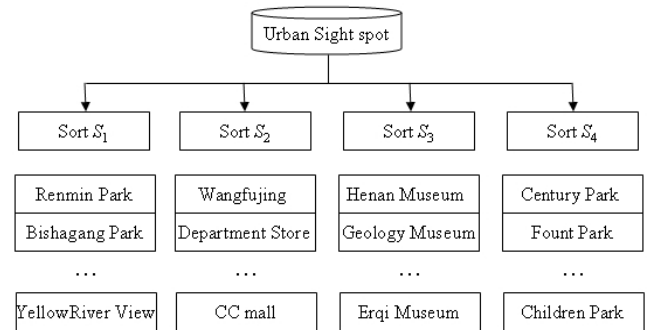


FIGURE I. URBAN SIGHT SPOT DATABASE

B. Interest Needs Model

According to the provided sight spots in the tourism GIS, tourists choose sight spots in two ways. One is selecting directly, the other is selecting randomly.

Method 1 Selecting directly. Under the condition of tourists being familiar with sight spots and having certain needs or interests on sight spots, they can directly load in selecting interface and select the interested sight spots in each sort, as FIGURE II shows.

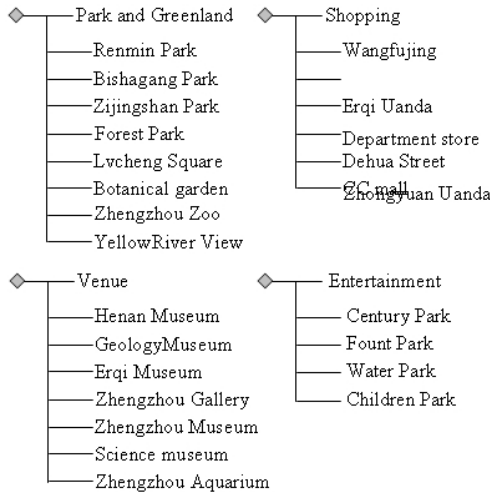


FIGURE II. SIGHT SPOT SELECTING IN THE SYSTEM

Method 2 Selecting randomly. When tourists are not familiar with the sight spots, they can turn to the system for help. Firstly, tourists provide the number of sight spots, and then system transfers random function to generate random numbers. Set the distribution function of continuous random variable X as:

$$F(x) = \frac{x-a}{b-a}, \quad x \in [a, b] \quad (1)$$

Continuous random variable X meets the uniform distribution on $[a, b]$, note as $X \sim U(a, b)$. Transfer uniform distribution function for one time on $[a, b]$ can get random numbers within the maximum value b . Select the uniform distribution function on $[0, k]$ to set up sight spot element random selecting model, in which k is the maximum sight spot number of one sight spot sort.

III. INTEREST SIGHT SPOT BUFFER MODEL

Buffer area is the obtained object neighborhood after the confirmation of the object, whose range is determined by neighborhood radius or buffer foundation conditions. Thus, as to a certain object K_t , its buffer area is defined as follows.

$$P = \{x \mid d(x, K_t) \leq r\} \quad (2)$$

The object K_t buffer area with neighborhood radius r is the collection of points whose distance d to object K_t are less

than r . Index d can be minimum Euclidean distance or other defined distance.

Set the sight spot as center to set up buffer model. Set the buffer radiiuses are(km):

- $r_1 = 0.5$
- $r_2 = 1.0$
- $r_3 = 1.5$
- $r_4 = 2.0$.

Draw sight spot service information within four radiiuses respectively, including λ_1 sight spot star, λ_2 bus station number, λ_3 subway station number, λ_4 hotel number, λ_5 shop number and λ_6 bank number. Take entertainment for example, Table II is sight spot service information and indexes within four radiiuses.

TABLE II. SIGHT SPOT SERVICE INFORMATION AND INDEXES $\lambda_1 \sim \lambda_6$

Sight spot	$r_1 = 0.5$	$r_2 = 1.0$	$r_3 = 1.5$	$r_4 = 2.0$
D1 Century Park	4,2,0,1,2,3	4,3,0,2,3,3	4,3,0,3,5,3	4,4,1,4,5,4
D2 Fount Park	5,1,0,0,2,0	5,2,0,0,1,0	5,3,0,0,2,1	5,4,0,1,3,1
D3 Water World	3,2,0,3,3,2	3,2,1,5,3,4	3,3,1,5,5,4	3,3,1,5,5,4
D4 Children Park	2,2,1,2,4,3	2,2,1,4,5,4	2,3,1,4,6,4	2,3,1,5,6,4

As to multi-level sight spot information, tourists can choose a certain level, such as bus station. Look up the name of bus station, location, bus number, time information and transfer information, etc. All the information is close to the sight spots, so it is critical for tourists to select sight spots and seize sight spot information, and it is important condition for tourists to meet the best motive benefits. After selecting sight spots, tourists can get sight spot buffer and information on the map.

IV. MODEL EXAMPLE

Model example is designed according to the model set up. A tourist requires visiting one Park and Greenland, one shopping mall and one venue. He is unfamiliar with Zhengzhou city and turns to system for help. System invokes distribution function to generate random numbers according to tourists' needs and draws one Park and Greenland, one shopping mall and one venue. TABLE III is the sight spot service information indexes within the three sight spot buffer.

TABLE III. SIGHT SPOT SERVICE INFORMATION AND INDEXES $\lambda_1 \sim \lambda_6$

Sight spot	$r_1 = 0.5$	$r_2 = 1.0$	$r_3 = 1.5$	$r_4 = 2.0$
A2 Bishagang Park	3,4,1,3,4,3	3,4,1,4,4,4	3,5,2,4,4,5	3,5,2,5,5,6
B6 CC mall	3,2,1,2,3,2	3,2,1,2,4,3	3,3,2,3,5,4	3,3,2,4,6,5
C5 Zhengzhou Museum	4,4,1,3,3,2	4,5,1,4,5,3	4,5,1,5,6,3	4,5,1,6,7,4

According to the selected sight spots and different service information within buffer, interest sight spot buffer model is

set up on the tourism map, as FIGURE III shows.

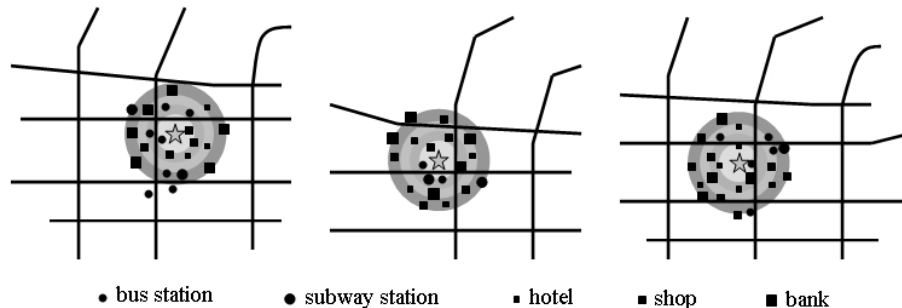


FIGURE III. SIGHT SPOT BUFFER INFORMATION MAPS

This model realizes the function of displaying interest sight spot and service information within buffer via different levels in mass data, which has relatively high pertinence. As to all the sight spot service information within buffer, it includes all the information tourists demand. The distribution location, service information integrity and convenience extent all meet the basic needs. Tourists can get best motive benefits by visiting the selected sight spots. Through the interest sight spot buffer service function in the tourism GIS, tourists can choose sight spots, look up information in different levels and know the sight spots rapidly to make a proper decision, which can raise the tourism efficiency.

V. CONCLUSION

Aim at the problems of current tourism GIS being lack of individuality service which can not meet tourists' interests and needs, this paper brings forward sight spot buffer model based on tourists' interests and needs. Through the interest sight spot buffer service function in the tourism GIS, tourists can choose sight spots, look up information in different levels and know the sight spots rapidly to make a proper decision, which can raise the tourism efficiency.

REFERENCES

- [1] Nicolau J L, Ma's F J. The influence of distance and prices on the choice of tourist destinations: the moderating role of motivations [J]. *Tourism Management*, 2006, 27: 982-996.
- [2] ZHAO X M, SUN Q X, DING Y. Passenger choice behavior for regional rail transit under express/local operation with overtaking[J]. *Journal of Transportation Systems Engineering and Information Technology*, 2016, 16(5): 104-109.
- [3] ZHAO X, GUAN H Z, WANG H. An analysis on choice behavior of tourist destination based on tourist motivation[J]. *Journal of Transportation Systems Engineering and Information Technology*, 2014, 14(5): 175-180.
- [4] LI X J, CUI S S, ZHANG K. Neural net method of best tourism route choice[J]. *Transportation and Computer*, 2006, 24(5): 103-106.
- [5] XU F, DU J P. Study on travel route planning based on improved ant colony algorithm[J]. *Computer Engineering and Applications*, 2009, 45(23): 193-195.
- [6] Nicolau J L, Ma's F J, Sequential choice behavior: Going on vacation and type of destination[J]. *Tourism Management*, 2008, 29:1023-1034.
- [7] LONG X Q, WANG J J, ZHOU B. Travelers dynamic decision making based on decision field theory[J]. *Journal of Transportation Systems Engineering and Information Technology*, 2016, 16(1): 12-18.
- [8] Bosque I R, Martin H S. Tourist satisfaction: A cognitive affective model [J]. *Annals of Tourism Research*, 2008, 35(2) : 551-573.
- [9] WANG C Y, QU H L. Tourist motive, destination image and tourism expectation[J]. *Tourism Tribune*, 2013, 28(6): 26-34.
- [10] LI M, CAI L A. The effects of personal values on travel motivation and behavioral intention[J]. *Journal of Travel Research*, 2011, 51(4) :473-487.

Research on Creation and Technology to Make Large-scale Production of Vertical Greening Wall

Wanlu Luo¹ and Jianwu Ma^{2,*}

¹Gold Mantis School of Architecture, Suzhou University. Suzhou, Jiangsu, China

²Gold Mantis School of Architecture, Suzhou University. Suzhou, Jiangsu, China

*Corresponding author

Abstract—This paper introduces a kind of vertical greening wall system on which climbing plants could grow. It emphasizes on illustrating that this system could be manufactured in large scale in factories in advance, and climbing plants can grow on a nursery-land-based structure to become a landscape. It has further discussed at scene installment approaches and post-maintenance management of the vertical greening wall system, which is manufactured in large scale in advance. At last, it has presented that the cost of production of this system is low, the manufacture is rapid, the greening effect is obvious, and the post-maintenance is simple and easy, so it has promoted the development of the vertical greening wall to a great extent.

Keywords—greening wall; large-scale; creation; technology

I. INTRODUCTION

With the rapid development of urbanization in our country, natural ecological environment has been gradually eroded by reinforced concrete. In order to improve the city's ecological environment and promote the development of vertical greening industry, the government has issued *Technical Specification for Vertical Greening Engineering CJJ/T236-2015* in 2015 as the industrial standard. Meanwhile, many scholars in our country has been working about researches on vertical greening technology. Besides the greening wall effect generated by original climbing plants directly clinging to the surface of the wall, there has emerged many new types of vertical greening walls. However, greening walls in the market are expensive and costly, having a high maintenance cost too, only some key cities are using it and it is hard to popularize it to a large scale. Now there has been a greening wall system which can be manufactured in the factory in large scale. Volume production can effectively save the cost of greening wall, and the post-maintenance is simple and easy, so this kind of greening wall is available to be popularized so as to beautify the city's environment and life people's living standard.

II. THE IMPORTANCE OF FACTORY-MANUFACTURED GREENING WALL

A. The Effect and Meaning of the Vertical Greening Wall

The vertical greening wall has all effects of greening plants, especially the landscape effect. It can use limited space to raise the green coverage ratio, fully express the comprehensive effects of plants, and improve the city's environmental aspect. What's more, the vertical greening system is playing an important role in energy-saving and ecological effect. According to statistics, the vertical greening wall can

effectively reduce indoor temperature in summer, which is 3.01°C on average. This means that it would reduce the consumption of air-conditioners indoor and save energy. It could also raise the indoor temperature of 2-3°C in winter, having warm-keeping effect to architectures to some extent, and effectively reducing the cost on heating. Researches have shown that every 0.5°C of temperature reducing in summer can save the load of air-conditioner for 8%. Hence, the vertical greening wall is a kind of low-carbon economic way. Greening plants preserve heat, meanwhile, they play fully roles in transpiration, which could increase air humidity. Some climbing plants like costustoot can increase 3.42% humidity within 1000m² air, and campsis grandiflora can increase 2.87% of that.

III. GENERAL SITUATION AND PROBLEMS OF THE VERTICAL GREENING WALL

In our country, the industry of vertical greening wall starts quite late, so there have been grand gaps between the industry of vertical greening wall of our country and that of foreign countries, although we have made many achievements in the form of greening, the application of plants, the innovation of material, and maintenance and management in recent years. In the year of 2010, many exhibition halls on the Shanghai EXPO were competing with each other for beauty of "green". Statistics said that among nearly 240 exhibition halls on the EXPO, over 80% of them made roof greening, vertical greening, and indoor greening. These exhibition halls had concentrated in displaying their latest vertical greening technology, which made the greening thinking step forward from two-dimensional to three-dimensional. By using new technology, new material, and new craft, the vertical greening had been shown a wide prospect. For the time being, there have been emerging many technically customized planting wall companies in China who manufacture the greening walls, which consist of the supporting system, irrigating system, cultivation medium, and plants materials, in small scales, based on the customers' needs. This kind of greening wall system rarely makes the common customers satisfied due to the long production phase and high production cost. Shanghai Hainer Company is the earliest technical company that set foot in roof greening and greening system in our country, and the cost budget is based on the area and height of the greening wall, whether or not it needs water-proof material and the category of plants, which is generally 2000 to 5000 yuan per square meter, and some of the greening walls would come to over 10000 yuan per square meter, shrinking back many greening wall amateurs and consumers because of the price.

IV. MANUFACTURING THE GREENING WALL IN FACTORIES IN A LARGE SCALE

In order to popularize the application of vertical greening walls, we should seek out a new technology and approach. In agriculture, our country vigorously promoted a standardized production way with high production efficiency, low labor intensity, and standard products based on the production experience from home and abroad so as to achieve the development target of modern “high-efficient agriculture”. Being the similar, it is the goal of all people in the industry of greening wall to achieve the standardization of the development of vertical greening wall, and to work out a low-cost greening wall with diversification of green plants, abundance of greening forms, simplification of high altitude operation, and generalization of post-maintenance.

V. GENERAL SITUATION OF FACTORY PRODUCTION

The vertical greening walls can be divided into the climbing type, the modular type, and the paving type greening wall system. Traditional climbing plants greening walls have the strong points of low cost, and easy to be maintained and managed, while their weak points are having the low speed in covering the wall; the modular type and water-cultivated type greening wall systems are abundant in the category of plants, which have a good landscape effect, but being difficult in manufacture and having a quite high death rate.

VI. A SYSTEM GREENING WALL

At present, AN System is an advanced vertical greening system at abroad, adopting a modular type of full-automatic irrigation system which could be installed simply and independently on any structure and size of architecture. When the production of every type of structural member is over, multiple items as follows should be installed, which include frames, mould layers, waterproof membranes, fixed tracks, 500mm×500mm×60mm ANS modules, irrigation pipes, drain pipes, etc. Using ANS modules to plant needs to base on the design made by Party A in advance before installment, and the landscape will show up forthwith. This way of cultivating seedlings several months before installment could made the death rate and landscape effect of the plants be affected by seasons, and all kinds of force majeures will directly influence the completion time; and being limited by standard base plate, it is quite difficult for manufacturing.

VII. PAVING TYPE GREENING WALL SYSTEM

The paving type vertical greening wall system represented by the “Vertical Garden” technology invented by a French botanist Patrick Blanc consists of supportive frame, PVC board, cloth felt, automatic spraying system and its accessory members. Without soil or other cultivation medium, the plant directly grows on the blanket of nutrient solution and moisture, the thickness of the whole green wall shrinks greatly, and the structure wall bearing decreases. PVC board is mainly made of polyester, lightweight and anti-impact, and a 10 mm thick PVC only weighs 7 kg/m². The cloth felt cloth of this kind of greening wall system is full of moisture and nutrient solution for a long time, it is easy to rot and go bad, and outdoor plants are difficult to survive in winter.

VIII. LARGE SCALE VERTICAL GREENING WALL SYSTEM

A. *The Structure of Large Scale Vertical Greening Wall System*

Based on traditional cheap climbing plants greening, it has been developed a greening wall system which can be put into large-scale factorial manufacture. This kind of greening wall retains the strong points of the traditional climbing plants greening walls such as low cost and easy to maintain and manage, what's more, it could grow rapidly and green the wall, which breaks the limitation of the material of walls to the categories of plants.

During the production in the factory in advance, the landscaping wall unit will be transferred to the site and can be assembled in the scene quickly to form a complete green wall system. The greening wall consists of many 1m×2m unit modules including the assembled frames, assembled frame of climbing vines, and string bags or cloth bags for delivering partial of nutrient soil from the root of climbing plants. The Figure 1 illustrates the greening wall landscape produced by factories.

IX. CHOICE OF PLANTS

There are many forms of vertical greening. When choosing plant materials, you should first make full use of local plant resources, not only because these plants are most suitable for local growth in terms of ecological adaptability, but also should people consider the light condition and the appearance of frame structure and color form, comprehensively based on above factors shall we choose suitable vines. Based on the characteristics of the frame, the adsorption type and support type of vines are selected as green plants.

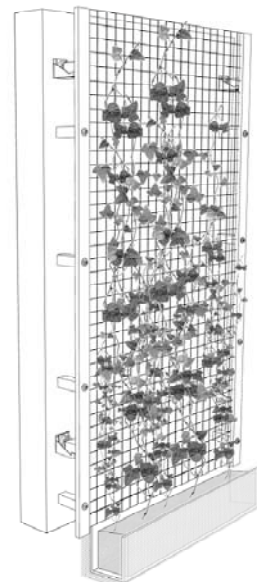


FIGURE I. A DIAGRAM OF THE GREENING WALL LANDSCAPE PRODUCED BY FACTORIES

The stem tendrils of the adsorbent vines of the vines form suction or air rooting, which adsorb on the surface of the supporting material or penetrate into the interior and attach to it

for growing. The climbing plants with the help of an acetabulum are optional as follows: *Parthenocissus tricuspidata*, *Parthenocissus quinquefolia* (L.) Planch, etc. If you choose these climbing plants, the assembled frame should be wrapped by string bags so as to make the absorbent plants climb up. Those plants with aerial roots can be chosen from *Hedera nepalensis Var. Sinensis*, *Campsis grandiflora* (Thunb.) Schum, *Campsis radicans* (L.) Seem, *Trachelospermum jasminoides* (Lindl.) Lem, *Trachelospermum jasminoides* 'Flame', *Trachelospermum asiaticum* Ougonnishiki, etc.

The supporting vines include tendrils, twining classes and thorns, which can be grown by the support of the grid. So the main choices include *Passiflora coerulea* L, *Lonicera japonica* Thunb, *Morden cvs.of Climbers and Ramblers*, etc.

In order to facilitate the maintenance and management of plants, the selected adsorption type and support type climbing plants should have good tolerance, drought resistance and good growth ability on the basis of fitness, and the common climbing plants such as *Hedera nepalensis* Var. *Sinensis*, *Trachelospermum jasminoides* (Lindl.) Lem, *Trachelospermum asiaticum* Ougonnishiki, and *Campsis radicans* (L.) Seem have strong drought resistance ability. Zhou Jun et al have made a comprehensive assessment on the drought resistance ability of above four vines and the result of which shows that the order of the drought resistance ability (from strong to weak) is *Hedera nepalensis* Var. *Sinensis*, *Trachelospermum jasminoides* 'Flame', *Trachelospermum asiaticum* Ougonnishiki, and *Campsis radicans* (L.) Seem.

X. TECHNOLOGICAL ANALYSIS

During the scene manufacture, the weight of landscape's frame and the material of wall surface are the key factors to influence the installment. The dead load of landscape frame include the weight of frame and the weight of plants. The unit weight of landscape frame is approximately $6\text{kg}/\text{m}^2$, so as to say, the dead load of the greening wall system with landscape frame is not large, and the requirement of wall structure is not strict. The architecture have different kinds of walls such as masonry walls, block walls, brick walls, cement walls, glass curtain walls, etc., and the installment of assembled frame is to use M12 expansion bolts to fix it into the walls. The allowable tension of M12 expansion bolt in M5 mortar brick walls and C10 cement is 10.30kN, and the allowable shearing force of which is 6.90kN, the minimum burial depth is 65mm. As it goes deeper, the intensity of the buried objects goes up, and the index of allowable tension lifts with it. So it is applicative in masonry walls, block walls, brick walls, and cement walls. The installment of vertical greening on glass curtain walls can depend on the wall adjoining to the curtain wall.

XI. SUMMARY

The vertical greening is the direction of the development of greening industry in the future, and it is the market's demand to produce the vertical greening industry to a large scale. Experts and scholars should work on the problems of creation and technology on large scale produced vertical greening walls. This paper has provided a kind of large scale rapid assembled vertical greening walls that keeps the strong points of traditional

vines greening walls like low cost and easy to be managed, and is able to rapidly climb up the greening wall, breaking the imitation of wall material to plant species, which is a kind of vertical greening wall can be processed in factories in a large scale.

ACKNOWLEDGEMENTS

Fund Program: Natural Science Foundation of China "Research on Multiple Targets Management Strategy for Park Green Space in Tropical Plateau Monsoon Climate Zone in Yunnan", Item Number: 51168043

"2016 Jiangsu Regular Institutions of Higher Learning Postgraduates Practical and Innovative Project Item", Item Number: SJLX16_0538

REFERENCES

- [1] Meng Tao. Practical Research on Vertical Greening's Energy-saving and Reformative Effect on Office Buildings in Shanghai [J]. Shanghai Energy Conservation, 2016, (05):252-255
- [2] Dunnett N, Kingsbury N. Planting green roofs and living walls [M]. Timber Press Portland, OR: 2004.
- [3] Yin Lifeng, Li Shuhua. The Features of Temperature Distribution of Ultra-low Energy Consumption Green Roofs in Tsinghua University [J]. Scientia Silvae Sinicae, 2007, 43(8):143-147
- [4] Shi Qi. Research on Cooling and Humidifying Effect on Different Vertical Greening Approaches in Zhengzhou [D]. Henan Agricultural University, 2006.DOI:10.7666/d.y962621.
- [5] Zhu Xiaofang. A New Form of Urban Vertical Greening— From the Perspective of Ecological Landscape [D]. Hebei University of Technology, 2010.DOI:10.7666/d.d113150
- [6] He Xiaobo. Research on the Evolution of Vertical Greening Technology and the Design and Practice of Planting Wall [D]. Zhejiang A&F University, 2013.
- [7] Zang Dekui, Zhou Shujun. Climbing Plants and Vertical Greening [J]. China Landscape Architecture, 2000, (05):79-81.
- [8] Chen Qing, Cai Yongli, Choice and Settlement of Vines in Urban Vertical Greening [J]. Urban Environment & Urban Ecology, 2006, (05):26-29.
- [9] Zhou Jun, Wu Jincui, Du Baoming, Li Pengli. Drought Resistance Comparison of Four Kinds of Vines [J]. Jiangsu Journal of Agricultural Sciences
- [10] Cai Zhiwen. Expansion Bolt and Fastener [J]. Builder's Monthly, 1992, (05):24-25
- [11] Tang Dengming. Application of Ornamental Vines in Landscape Architecture [J]. Jiangsu Agricultural Sciences, 2017, 45(08):127-129.

Research on Assessment Method of Grid Frequency Fluctuation Characteristics and Optimization of Speed-governor Parameters

Daohong Lin¹, Qiang Wu¹, Xinshu Wan¹, Yunqian Li², Lei Shao² and Hongjun Zhou³

¹Hainan Electric Power Company Research Institute, Haikou

²Southeast University, Nanjing

³Beijing Ponovo Power Co., Ltd, Beijing

Abstract—With the enlargement of power grid scale, connections between different power subsystems in interconnected network have been more-closely related and the analysis of power system dynamic behaviors becomes more complex. This paper selects 3 area indexes which comprehensively reflect frequency change through transient process based on transient frequency stability curve and frequency change ratio curve, and there out builds the quantitative assessment method of frequency fluctuation characteristics. Then a generator set speed governor magnification-targeted optimization model, which determines the optimum of frequency fluctuation characteristics as optimal objective with proposed indexes, is built and solved by multivariate optimization algorithm. At last, an optimal example of practical power grid verifies the feasibility and validity of the proposed assessment method and the optimization model.

Keywords—dynamic frequency responses; frequency fluctuation characteristics; frequency stability; multivariate optimization algorithm; speed governor

I. INTRODUCTION

With the formation of interconnection pattern of power grid in China, the problems of voltage stability, power angle stability and frequency stability caused by faults are becoming more significant [1]. There is a certain possibility that the interconnected power grid divides into several regional isolated island networks due to the tie line fault. Under these circumstances, the different operation characteristics of different isolated networks and the complexity would make the frequency problem more prominent [2]-[4].

Frequency is one of the important indicators of power grid operation, and it reflects the active power supply-demand balance between generation side and load side of power system [5]. Therefore, the domestic and international research on frequency stability control is widespread at present. In [6] and [7], the frequency characteristics of different regional power grids were discussed and the optimal schemes of under-frequency load-shedding and over-frequency generator-tripping strategies were put forward via time-domain simulation of transient stability; reference [8] analyzed the different influences of power system stabilizer (PSS) selection on frequency stability of islanded power grid. In [9], a preventive correction control system was developed for the frequency

control of an offshore island power system, which was used to effectively predict the lowest frequency, frequency changing rate and so on, and thus contributing to the arrangement of generator working schedule and the preparation for generator-tripping or load-shedding strategy; reference [10] proposed that the relay protection equipment based on frequency change ratio and the inertia simulation method could be adopted to reduce the frequency instability risk of power grid system; aiming to accurately identify the fault events which would result in isolated island network as early as possible and effectively avoid more losses, reference [11] proposed a hybrid islanding detection technique and a priority-based load-shedding scheme and guaranteed frequency stability by releasing weak current load in the island.

In the above references, it can be found that almost all kinds of research work mainly focus on the frequency control strategies of the risks faced by power grid and isolated island network in engineering practice, but the frequency characteristics optimization schemes were all determined by comparing the visual image of the transient frequency stability curves or comparing the minimum or maximum values of frequency. Nevertheless, the optimization depends not only on the optimization of the frequency value, but also on the time. So there exist some difficulties when selecting the optimal scheme through the above method because that the method is a qualitative method but not a quantitative method.

As is known to all, the frequency control of power system is closely related to the adjustment of governing system, and generator governor control is the key to the initial frequency control [12]-[13]. In [14], the influence of system frequency characteristics and governor parameters on frequency stability was analyzed; reference [15] analyzed the low frequency oscillation in the southeastern part of the European power system, which explored the influence of governor parameters, especially the dead zone of speed deviation, on oscillation damping. It is the consensus of the current research to optimize the dynamic frequency characteristics by adjusting governor parameters. Consequently, after establishing a quantitative assessment method for dynamic frequency fluctuation characteristics, the governor parameters could be adjusted to optimize the characteristics according to the method.

This paper is organized as follows. In Section II, three indexes related to the frequency curve are selected and the

quantitative assessment method of frequency fluctuation characteristics is constructed based on the indexes. In Section III, a generator set speed governor magnification-targeted optimization model, which determines the optimum of frequency fluctuation characteristics as optimal objective, is built. In Section IV, the proposed model is solved by multivariate optimization algorithm (MOA). In Section V, an optimal example of practical power grid verifies the feasibility and validity of the proposed method based on assessment indexes and the optimization model. Section VI concludes the paper and provides recommendations for further work.

II. ASSESSMENT INDEXES OF FREQUENCY FLUCTUATION CHARACTERISTICS

Frequency stability can be divided into short-term transient frequency stability and long-term frequency stability according to time scale. The former mainly evaluates whether the frequency of power system in the transient process satisfies the short-term security and stability constraints of system and equipment and whether the frequency will continue to decline and cause frequency collapse. The latter mainly assesses whether the stable frequency of new steady state meets the requirements of long-time operation of power system after transient process [16]. This paper considers the dynamic frequency response under the condition that the frequency of power grid system stays stable after a fault disturbance in a long term, and assesses the dynamic frequency fluctuation characteristics and further selects the evaluation indexes. If the energy generated by generation side is less than the energy consumed at load side of power system when the fault occurs ($W_{gen} < W_{load}$), there will be a substantial drop in frequency due to power imbalance. Conversely, if the energy generated by generation side is greater than the energy consumed at load side of power system when the fault occurs ($W_{gen} > W_{load}$), the system frequency will increase considerably. The greater the power difference between supply and demand sides is, the more serious the power imbalance is, and the frequency curve will fall or rise more sharply. Frequency stability problems occur mostly in isolated island networks, and generally speaking, low-frequency problems are more extensive and typical than high-frequency ones, so the following will exclusively consider the situation of frequency drop after failure. In this case, after the initial frequency dip, the frequency curve enters the oscillation regime and its oscillation amplitude will continue to reduce until it finally reaches the new frequency state and stabilizes.

In transient frequency stability curve $f(t)$, this paper defines f_0 as the original steady-state frequency, f_s as the new steady-state frequency, t_0 as the time node of fault beginning, t_1 as the time node when frequency fluctuates for the first time and returns to f_s in that process, t_2 as the time node when frequency enters into new steady-state tolerance range and no longer exceeds limit of the frequency tolerance range for the first time.

The area S_1 which reflects the frequency-dip situation is chosen as the first evaluation index, which is called frequency

dropping index. This index can describe the dropping amplitude and duration of transient frequency and it is mainly affected by synchronous generator and load dynamics and the fast control. The formula of S_1 is:

$$S_1 = \int_{t_0}^{t_1} |f - f_s| dt \quad (1)$$

The diagram of S_1 is shown in Figure I.

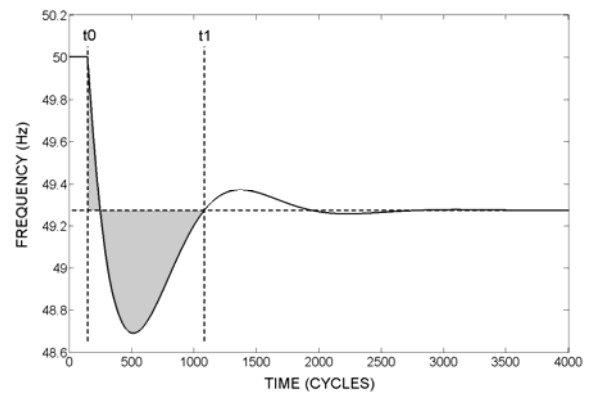


FIGURE I. DIAGRAM OF FREQUENCY DROPPING INDEX

The area S_2 which reflects the specific situation of frequency oscillation is chosen as the second evaluation index, which is called frequency fluctuation index. The index can describe the amplitude and decay rate of transient frequency oscillation and it is mainly affected by generator governor, load dynamics and the damping intensity of network. The formula of S_2 is:

$$S_2 = \int_{t_1}^{t_2} |f - f_s| dt \quad (2)$$

The diagram of S_2 is shown in Figure II.

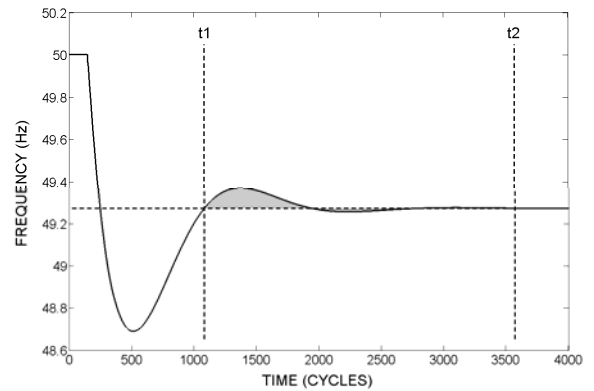


FIGURE II. DIAGRAM OF FREQUENCY FLUCTUATION INDEX

The area S_3 , which reflects the overall fluctuation situation of transient frequency relative to the steady-state frequency, is considered as the third evaluation index, which is called frequency global moving index. The index is selected from the transient frequency change ratio curve $K_f(t)$ and can describe the fluctuation amplitude, the recovery speed after failure and duration of the whole change process of transient frequency, which is mainly affected by the operation mode of power grid before and after the disturbance, the damping intensity of the network and the fast control. The formula of S_3 is:

$$\begin{cases} K_f = \frac{df}{dt} \\ S_3 = \int_{t_0}^{t_2} |K_f| dt \end{cases} \quad (3)$$

The diagram of S_3 is shown in Figure III.

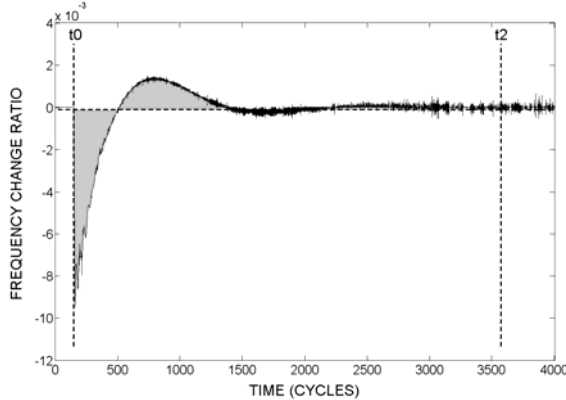


FIGURE III. DIAGRAM OF FREQUENCY GLOBAL MOVING INDEX

The third index is derived from the derivative curve and the derivatives are susceptible to be affected by noises. However, the index is area index and the spikes or glitches of the curve have little effect on index value. Hence, this index can meet the requirement of precision when the requirement of accuracy is not too harsh.

These three indexes are selected from transient frequency stability curve and its derived frequency change ratio curve. By reflecting the two characteristics which are duration and numerical value of frequency or frequency change rate, the whole process of transient frequency change is characterized and described comprehensively. And it is feasible to evaluate the dynamic frequency fluctuation characteristics by using the above indexes as the basic quantitative indicators. In power grid system, when the frequency remains stable, i.e., the frequency change ratio is always in a small range near 0 and there are neither dropping nor fluctuation of frequency, it can be regarded as an ideal state. In this case, the status of indexes above is $S_1 = S_2 = S_3 = 0$. According to the above analysis, in the engineering practice, if the assessment indexes of frequency fluctuation characteristics are small, the frequency will be more stable in dynamic process; if the assessment indexes are large,

there will be more risks of frequency instability in dynamic process.

III. OPTIMIZATION MODEL OF FREQUENCY FLUCTUATION CHARACTERISTICS

In this paper, optimization model is established, whose optimization target is the parameter selected from generator governor system and optimization objective is to optimize the dynamic frequency fluctuation characteristics.

A. Governor Parameters Selection

The governor system of generator sets plays an important role in regulating the frequency of power grid. At present, power system stability analysis mainly uses the standard model provided by IEEE to simulate the governor model, i.e., the model used in BPA which is the main power system simulation software. This paper focuses on the steam turbine governing system whose BPA model is shown in Figure IV.

Since the system is open-loop, the feedback coefficients such as K_p , K_i and K_d will be not considered. Among the remaining adjustable parameters, the speed deviation magnification of governor system is chosen to be optimization target of the model, which is the parameter K in Figure IV.

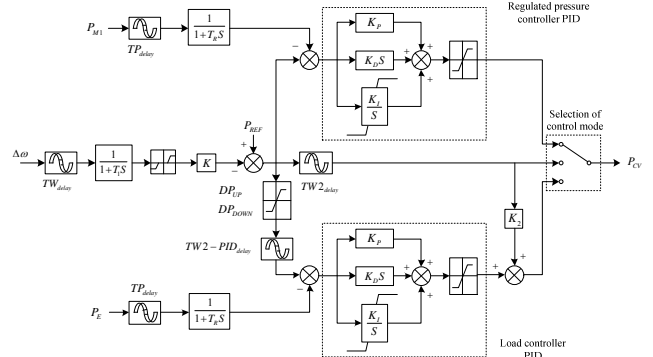


FIGURE IV. THE BPA MODEL OF STEAM TURBINE GOVERNING SYSTEM

B. Objective Function

According to the above discussion, the frequency curve could be affected by many factors in dynamic process. Without considering the secondary regulating strategy such as under-frequency load-shedding and over-frequency generator-tripping, frequency fluctuation characteristics are still related to the rapid adjustment measures such as governor system of generator sets, load dynamics, the operation mode of grid, damping intensity and so on. The appropriate adjustment of the above factors will have influence on the specific direction of transient frequency stability curve which is further reflected by the indexes. Therefore, in the process of optimizing frequency fluctuation characteristics, four indexes are all set as the optimization objectives. The multi-objective optimization function is constructed as:

$$F = \{\min S_1, \min S_2, \min S_3\} \quad (4)$$

There are various associated factors which could have effects on frequency fluctuation. And the index S_1 and S_2 are selected from the same curve and they have the same dimension, so they are transformed to one single objective by linear weighting method. According to the definition of linear weighting method [17], the multi-objective function is transformed into single objective function by:

$$\begin{cases} g = \sum_{i=1}^2 \omega_i \times S_i \\ \sum_{i=1}^2 \omega_i = 1 \end{cases} \quad (5)$$

The target weighting factors are discussed below. Index S_1 and S_2 reflect the transient frequency dropping and fluctuation of power grid system. The process of grid frequency fluctuation may bring a lot of harm. It not only threatens the safety of system and generator sets, but also affects power quality of load. Besides, it may also cause malfunction of some relay protection devices [18]. The frequency dropping can be regarded as frequency starting oscillating due to fault, after which the fluctuation amplitude gradually decreases and finally a new steady state will be reached at a certain frequency value. Therefore, frequency dropping and fluctuation can be regarded as homogeneous actions, and it can be defined that $\omega_1 = \omega_2$. According to the equations of weighting factors, the single objective function is calculated and the objective function of the multi-objective optimization model is:

$$F = \{\min g, \min S_3\} \quad (7)$$

C. Constraints

1) Governor speed deviation magnification constraint

$$K_{\min} \leq K \leq K_{\max} \quad (7)$$

In (7), K represents the speed deviation magnification of governor system, while K_{\min} and K_{\max} are respectively the upper and lower limits of the speed deviation magnification of governor system.

2) Speed deviation dead zone constraint

$$0 \leq \delta \leq \delta_{\max} \quad (8)$$

In (8), δ is the dead zone of speed deviation and δ_{\max} expresses the predefined maximum critical value of speed dead zone.

3) Generator set power constraint

$$\begin{cases} P_{\min} \leq P_{gen} \leq P_{\max} \\ Q_{\min} \leq Q_{gen} \leq Q_{\max} \end{cases} \quad (9)$$

In (9), P_{gen} and Q_{gen} are respectively active and reactive power of the generator set. P_{\min} and P_{\max} are upper and lower limits of active power output of generator. Q_{\min} and Q_{\max} are upper and lower limits of reactive power output of generator.

4) Power balance constraint

$$P_{gen,t} = P_{load,t} \quad (10)$$

In (10), $P_{gen,t}$ represents the active power generated by generator set at time t while $P_{load,t}$ represents the active power consumed by load side at time t . The power balance should be guaranteed when power grid operates at any time of original and new steady state.

IV. MULTIVARIATE OPTIMIZATION ALGORITHM

Multivariate optimization algorithm (MOA) is a diversified-search intelligent optimization algorithm based on data structure, which divides multiple search elements into global atoms G_a and local atoms L_a . In each iteration, G_a is first used to investigate the global situation. Once more potential solutions are found, the information is immediately shared, prompting a new local atom L_a to mine the area meticulously. Thus, the solution space is searched efficiently by the alternate global-local search and the global optimum is approached gradually [19]. MOA always maintains the global search field in the process of searching and will not fall into the trap of local convergence and premature, which has higher convergence success rate and higher precision compared with other mature population optimization algorithm, so this paper chooses MOA to solve the proposed optimization model.

A. Principles of Multivariate Optimization Algorithm

An iteration of MOA consists of two stages which are global search and local search. Define the number of global atoms in each iteration as m and the number of local atoms assigned in part i as m_i ($1 \leq i \leq m$). At the beginning of the algorithm, the empty stack is set up to store the global atoms and the potential optimal solutions. In addition, the maximum iteration number is set as I_{\max} . In the phase of global searching, global atoms G_a are randomly generated in the entire search space which also is the solution space according to the formula that is:

$$\begin{cases} G_a = [h_1, \dots, h_d] \\ h_i = unifrnd(\min_i, \max_i) \end{cases} \quad (11)$$

In (11), d is the dimension of solution variable; \min_i and \max_i are the upper and lower bounds of the i th dimension of solution space respectively; $unifrnd(\min_i, \max_i)$ indicates that the function returns a random number that is uniform distributed between \min_i and \max_i . Comparing the newly

generated global atom with global atoms in global stack, the one with better fitness value is chosen as the center of latent solution region to be recorded in global stack of the structure. In the stage of local searching, in order to realize the local search of each potential solution region, local atoms L_a are randomly generated in the local neighborhood with the center which is the global atom G_a and the radius which is r according to the formula that is:

$$L_a = G_a + r \times [l_1, \dots, l_d] \quad (12)$$

In (12), l_i ($1 \leq i \leq d$) is a random number between -1 and 1. Comparing the newly generated local atom with local atoms in local stack, the one with better fitness value is selected to retain as historical information.

B. Model Solving Process Based on MOA

The objective function of the optimization model of network frequency fluctuation characteristics is $F = \{\min g, \min S_3\}$, in which g and S_3 represent the objective functions derived from transient frequency stability curve and frequency change ratio curve respectively. Since S_3 can describe the whole change process of dynamic frequency fluctuation relative to the steady state and has unitary meaning, define it as the fitness for comparison in the process of global searching, that is, the indicator of rough searching. Conversely, define g as the fitness for comparison in the process of local searching, i.e., the indicator of meticulous searching.

To sum up, MOA-based solving process of the proposed optimization model of frequency fluctuation characteristics is summarized as follows:

a) Acquire the specific information of the power system lines, load nodes and generator sets, and input the original data of the system.

b) Define an empty global stack and a local stack and define the number of global atoms and local atoms. Define the maximum times of outer iteration and set the current iteration times as 0. Define the maximum times of inner iteration and set the current iteration times as 0.

c) Generate each global atom in the search space randomly and then it is plugged into transient stability simulation and calculation program. Determine whether system data meet the model constraints.

d) Select the global atom which has the minimum global fitness value to enter global stack and update global stack. If the fitness value of the new global atom is the minimum in existing global stack, move on to the next step. Otherwise, determine whether the times of inner iteration is up to the upper limit. If the upper limit has been reached, output the current top of local stack as the optimal solution and the program is finished. If not, go back to step c) and the number of inner iteration times is added by 1.

e) Centering on the newly input global atom, generate each local atom in the local neighborhood with certain radius. Then

it is plugged into transient stability simulation and calculation program. Determine whether system data meet the model constraints.

f) Select the local atom which has the minimum local fitness value to enter local stack and update local stack.

g) Determine whether the terminate condition of iterative process has been met, i.e., whether the number of outer iteration times has reached the presupposed maximum number. If so, output the current top of local stack as the optimal solution and the program is finished. If not, the number of outer iteration times is added by 1 and the number of inner iteration times is set as 0, and then go back to step c) to continue the iteration.

V. CALCULATING EXAMPLE ANALYSIS

The actual operation data from Z-S district power system in J regional grid are used as an example to verify the feasibility and correctness of the proposed assessment method and optimization model. After simulating the dynamic process in which the district grid is disconnected from the main network and come into islanded operation mode due to line-failure by software BPA, it is indicated that the district grid frequency can maintain long-term dynamic stability in winter valley-load operation scene. Therefore, this paper selects this scene to do research.

In the example of Z-S district grid, there are four 220kV power plants which are named plant 1 to plant 4 in turn. Among them, plant 1, plant 2 and plant 3 each have two generating sets, while plant 4 has four generating sets. The property and parameter configuration of each generator set in the same power plant are approximate, so the research parameters of each generator set in the same power plant are considered the same in this example and will be changed simultaneously in the optimization process. According to engineering experiences, the constraint of governor speed deviation magnification of each generator set is set as $5.0 \leq K \leq 55.0$.

Define the number of global atoms is 5 and the number of local atoms is 10. The maximum number of outer iteration times is set as 200 while the maximum number of inner iteration times is set as 30. The dimension of each searching atom is 4 according to the practical example. The optimization model is solved by MOA. The comparison between original and optimal data of governor speed deviation magnification is shown in Table 1 and the comparison between each evaluation index of frequency fluctuation characteristics calculated from original and optimal data is shown in Table 2. According to the original and optimal parameters of speed governor, the transient process is simulated respectively and the transient frequency stability curves are compared in Figure V.

TABLE I. THE ORIGINAL AND OPTIMAL DATA OF GOVERNOR SPEED DEVIATION MAGNIFICATION

	Plant 1	Plant 2	Plant 3	Plant 4
Origin	11.7	11.7	11.7	11.7
Optimization	32.8	34.23	34.86	33.1

TABLE II. THE COMPARISON OF FREQUENCY FLUCTUATION CHARACTERISTICS EVALUATION INDEXES

	S_1	S_2	S_3
Origin	184.707	22.3365	1.4507
Optimization	127.5887	7.7345	0.1753

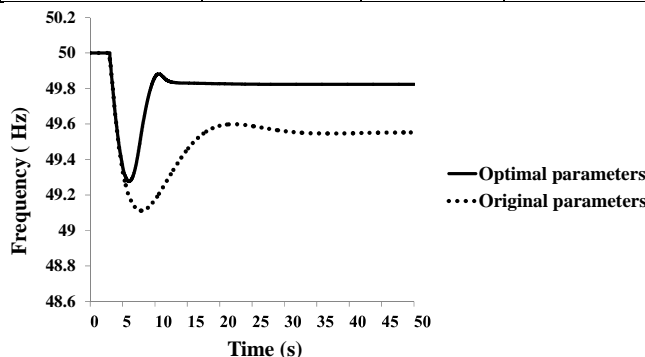


FIGURE V. THE COMPARISON OF TRANSIENT FREQUENCY STABILITY CURVES BASED ON ORIGINAL AND OPTIMAL PARAMETERS

VI. CONCLUSION

Base on the analysis of dynamic frequency response characteristics which maintains long-term frequency stability after large disturbance caused by fault in power grid, this paper selects 4 area indicators as assessment indexes from transient frequency stability curve and frequency change ratio curve and establishes the quantitative assessment method of frequency fluctuation characteristics, which makes up for the deficiency of intuitive judgment of frequency fluctuation characteristics. Then a generator set speed governor magnification-targeted optimization model, which determines the optimum of frequency fluctuation characteristics as optimal objective, is built and solved by MOA. Finally, in the practical calculating example of Z-S district power system in J regional grid, the feasibility and validity of the assessment method and the optimization model are verified by using MOA to solve the model. However, there still exists room for improvement and refinement in the field of frequency fluctuation characteristics evaluation method, which needs further study.

ACKNOWLEDGMENT

The authors gratefully acknowledge the support of the National Natural Science Foundation of China (Study of Regional Interconnected Power Grids Dynamic Stabilization Corrective Control Based on Network Control, No51277029) and the key project of smart grid technology and equipment of national key research and development plan of china (2016YFB0900602).

REFERENCES

- [1] Hou Yuqiang, Fang Yongjie and Yang Weidong, "A new method of UFLS/UVLS based on multi-agent technology," *Automation of Electric Power Systems*, vol. 35, no. 4, pp. 1-5, 2011.
- [2] Chang Haijun, Huo Chao and Li Wei, "Research on emergency control scheme of isolated power grid based on splitting information triggering," *Power System Protection and Control*, vol. 44, no. 2, pp. 27-35, 2016.
- [3] Zhang Peigao, Li Xingyuan and Li Zheng, "Research on frequency stability and control strategy in isolated power grid," *Power System Protection and Control*, vol. 40, no. 15, pp. 143-149, 2012.
- [4] J. Horne, D. Flynn and T. Littler, "Frequency stability issues for islanded power systems," *IEEE PES Power Systems Conference and Exposition*, vol. 1, pp. 299-306, 2004.
- [5] Zhang Zhen'an, Guo Jinpeng and Zhang Xuemin, "Blackout model and its application considering frequency stability," *Proceedings of the CSU-EPSA*, vol. 27, no. 4, pp. 26-32, 2015.
- [6] Zhao Qiang, Wang Limin and Liu Zhaoxu, "Study on dynamic frequency characteristics and coordinative under-frequency load shedding scheme for nationwide interconnected power grid of China," *Power System Technology*, vol. 33, no. 8, pp. 35-40(in Chinese), 2009.
- [7] Hu Jianchen, Hu Feixiong and Li Xian, "Frequency stability and control measures of Hainan power grid after interconnection with China Southern Power Grid," *Southern Power System Technology*, vol. 3, no. 5, pp. 31-35, 2009.
- [8] Zheng Chao, Chen Xiang, "Influence of Power System Stabilizer on Frequency Stability of Isolated Power Network," *Power System Technology*, vol. 1, pp. 214-219, 2016.
- [9] Y. K. Wu, "Frequency Stability for an Island Power System: Developing an Intelligent Preventive-Corrective Control Mechanism for an Offshore Location," in *IEEE Industry Applications Magazine*, vol. 23, no. 2, pp. 74-87, March-April 2017.
- [10] J. O'Sullivan, A. Rogers, D. Flynn, P. Smith, A. Mullane and M. O'Malley, "Studying the Maximum Instantaneous Non-Synchronous Generation in an Island System—Frequency Stability Challenges in Ireland," in *IEEE Transactions on Power Systems*, vol. 29, no. 6, pp. 2943-2951, Nov. 2014.
- [11] N. K., S. A. Siddiqui and M. Fozdar, "Hybrid islanding detection method and priority-based load shedding for distribution networks in the presence of DG units," in *IET Generation, Transmission & Distribution*, vol. 11, no. 3, pp. 586-595, 2017.
- [12] Zhu Jizhong, Xu Guoyu, "Study of governor dead-band and generator regulating speed limit in the decentralized load frequency control," *Proceedings of the CSEE*, vol. 11, no. 1, pp. 15-22, 1991.
- [13] Zhu Wei, Tang Ying-jie and Tan Xiyi, "Effect of additional control on frequency stabilization of generator governing system," *Electric Power Automation Equipment*, vol. 28, no. 12, pp. 21-24, 2008.
- [14] He Jingbo, Zhang Jianyun and Li Mingjie, "Frequency domain analysis and control for governor stability problem in islanded HVDC sending systems," *Proceedings of the CSEE*, vol. 33, no. 16, pp. 137-143(in Chinese), 2013.
- [15] J. C. Mantzaris, A. Metzios and C. D. Vournas, "Analysis of Interarea Oscillations Including Governor Effects and Stabilizer Design in South-Eastern Europe," in *IEEE Transactions on Power Systems*, vol. 28, no. 4, pp. 4948-4956, Nov. 2013.
- [16] Li Changgang, "Studies on assessment and control of power system transient frequency stability," Ph.D. dissertation, Dept. Electrical Engineering, Shandong University, 2012.
- [17] Wu Hongbin, Hou Xiaofan and Zhao Bo, "Economical dispatch of microgrid considering plug-in electric vehicles," *Automation of Electric Power Systems*, vol. 38, no. 9, pp. 77-85, 2014.
- [18] He Benteng, Jin Huafeng, "Real-time estimation of power system oscillation period," *Automation of Electric Power Systems*, vol. 24, no. 15, pp. 32-35(in Chinese), 2000.
- [19] Li Baolei, Shi Xinling and Gou Changxing, "Multivariant optimization algorithm and its convergence analysis," *Acta Automatica Sinica*, vol. 41, no. 5, pp. 949-959, 2015.

Research on Control Strategies for Performance Optimization of Wireless Powering System for Smart Home Appliances

Zhenchao Xie*, Daohong Lin and Wangcheng Zhu

Electric Power Research Institute of Hainan Power Grid Co., Ltd., Haikou 570125, Hainan Province, China

*Corresponding author

Abstract—With the development of smart technology and the improvement of living standard, the demand for a life with smart home appliance is increasing. The advancement of wireless power transfer technology has provided an opportunity to charge home appliance wirelessly. The combination of smart home appliance and wireless power transfer will make life more intelligent. The one-to-many wireless power supply system of smart home appliance and its control strategy optimization is studied. Firstly, the equivalent circuit model of one-to-many wireless power supply system of smart home appliance is set up and the influence of load on the output power and transfer efficiency is analyzed. Afterwards, the control strategy of power is studied, including power stability and emergency power supply. Finally, the experiment platform of one-to-many wireless power supply system is constructed, and the power transfer capacity and load property is tested, verifying the theoretic analysis.

Keywords—smart home appliance; wireless power transfer; multiple load; performance Introduction

I. INTRODUCTION

With the rapid development of science and technology, people continue to pursue higher quality of life. Therefore, the concept of smart home appliances was born. Smart home appliances have been widely used in nearly every country in the world, and in-depth study on the design of user interface and the collaborative working mechanism among smart home devices have been conducted. But now home appliances are still powered by traditional electricity supply system, which demands connectors to achieve electrical connection. In order to make home appliances more intelligent, the research on wireless power system for smart home appliances attracts more and more attentions. The application of wireless power transmission technology greatly improves the flexibility, convenience and reliability of smart home appliances. It is also of great significance to the further introduction of smart home appliances [1-5].

Wireless electricity transmission technology can be achieved through multiple means, such as electromagnetic induction, magnetic coupling resonance, microwave, etc. The technology is able to meet the demand of the smart home appliances system, with its transmission distance ranging from a few centimeters to several meters, and its transmission power reaching hundreds of kilowatts. As security is a major concern in the real application of the microwave radio transmission

technology, wireless power transmission is mostly materialized by electromagnetic induction and magnetic resonance coupling. In order to improve the transmitting efficiency of the system and reduce the sensitivity of the system performance to relevant parameters involved, this paper mainly studies the wireless power supply system for smart home appliances based on the magnetic coupling resonant technology [6-8].

At present, the research on wireless power transmission technology for smart home appliances has become a hot topic in academia and a popular destination for investment in the business world [9]. Great progress has been made in the field in terms of theoretical modeling, system control, resonator design, optimization of overall operating characteristics, and specific applications. However, most research at present still focuses on the "one-to-one" wireless power supply system. Research on the "one to many" system (one power transmitting coil supplies power to multiple loads) is still under exploration. Many key problems are yet to be resolved. There is still a long way to go before this system is put into real application.

II. ANALYSIS OF THE WIRELESS POWER SUPPLY SYSTEM FOR SMART HOME APPLIANCES

A. Modeling of the Wireless Power Supply System for Smart Home Appliances

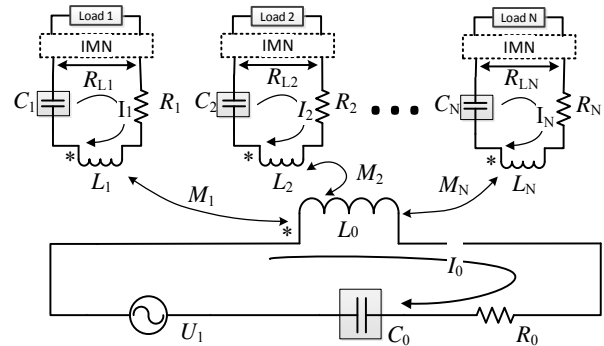


FIGURE I.
EQUIVALENT CIRCUIT OF WIRELESS POWER TRANSFER OF SMART HOME APPLIANCES

The wireless power supply system for smart home appliances mainly consists of the following parts: high frequency inverter, energy transmitting coil, energy receiving coil, rectifier and filter circuit, impedance matching network

and loads. Figure I is an equivalent circuit diagram for the wireless power supply system for smart home appliances.

The KVL circuit equation can be drawn accordingly:

$$\begin{cases} U_1 = Z_0 I_0 - j\omega M_1 I_1 - j\omega M_2 I_2 \\ j\omega M_i I_0 = Z_i I_i \quad (i=1, \dots, N) \end{cases}. \quad (1)$$

In equation (1), N is the number of loads of smart home appliances; Z_0 is the impedance of the transmitting end and $Z_0 = j\omega L_0 + 1/j\omega C_0 + R_0$ while Z_i is the impedance of the receiving end and $Z_i = j\omega L_i + 1/j\omega C_i + R_{Li} + R_i$; R_i and R_{Li} are the internal resistance of transmitting coils and receiving coils respectively; R_{Li} is the equivalent impedance of the rear end of the receiving coils, which can be adjusted by the Impedance Matching Network (IMN) on either side of loads; L_0 and L_i are the inductance for transmitting coils and receiving coils, respectively; C_0 and C_i are the compensation capacitance for transmitting and receiving ends, respectively [10-12].

When the loads are powered, there are certain distances among these loads. The mutual inductance among the receiving coils is neglected in this paper. When the size of the energy transmitting coils is relatively large, the mutual inductance between the transmitting coil and each receiving coil follows the rule: $M_1 = M_2 = \dots = M_i = \dots = M_N$. Then, according to equation (1), the currents in the transmitting coil and the receiving coils are

$$\begin{aligned} I_0 &= \frac{U_1}{Z_0 + \omega^2 M_1^2 \sum_{i=1}^N \frac{1}{Z_i}} \\ I_i &= \frac{j\omega M_1 U_1}{Z_i \left(Z_0 + \omega^2 M_1^2 \sum_{i=1}^N \frac{1}{Z_i} \right)}. \end{aligned} \quad (2)$$

Therefore, the power supply of a single load and the total loads can be expressed as

$$\begin{aligned} P_i &= I_i^2 R_{Li} = \frac{\omega^2 M_1^2 U_1^2 R_{Li}}{Z_i^2 \left(Z_0 + \omega^2 M_1^2 \sum_{i=1}^N \frac{1}{Z_i} \right)^2} \\ P_o &= NP_i = \frac{N\omega^2 M_1^2 U_1^2 R_{Li}}{Z_i^2 \left(Z_0 + \omega^2 M_1^2 \sum_{i=1}^N \frac{1}{Z_i} \right)^2}. \end{aligned} \quad (3)$$

According to formula (3) the transmitting efficiency of the system is

$$\eta = \frac{\sum_{i=1}^N P_i}{U_1 I_0} = \frac{\omega^2 M_1^2}{Z_0 + \omega^2 M_1^2 \sum_{i=1}^N \frac{1}{Z_i}} \sum_{i=1}^N \frac{R_{Li}}{Z_i^2}. \quad (4)$$

In order to simplify the research on power control and efficiency optimization of the multi-load wireless power supply system for smart home appliances and to make it easier to design and control such a system, and also with the feasibility of the system taken into account, the receiving coils can be designed with same specifications and the equivalent impedance of the rear end of the receiving coils can be adjusted to the same by the impedance matching network. These are two important prerequisites for the theoretical analysis in the paper. Based on that, $L_1 = L_i$, $C_1 = C_i$, $R_i = R_{Li}$, $R_{Li} = R_L$, $Z_1 = Z_i$ ($i=1, 2, \dots, N$).

By adjusting the power frequency and the size of the compensation capacitor to ensure $\omega L_0 = 1/\omega C_0$ and $\omega L_i = 1/\omega C_i$ when the system can operate in a resonant state, the equivalent impedance of the transmitting and receiving end can be expressed as $Z_0 = R_0$, $Z_i = R_{Li} + R_i$ ($i=1, 2, \dots, N$), respectively. Then equation (3) and (4) can be simplified as

$$P_o = \frac{N\omega^2 M_1^2 U_1^2 R_L}{(R_0(R_i + R_{Li}) + N\omega^2 M_1^2)^2}, \quad (5)$$

$$\eta = \frac{N\omega^2 M_1^2 R_L}{(R_0 + R_L)(R_0(R_i + R_{Li}) + N\omega^2 M_1^2)}. \quad (6)$$

B. Analysis on Load Characteristics of the Wireless Power Supply System for Smart Home Appliances

In real life, the parameters of energy transmitting and receiving coils in the wireless power supply system for smart home appliances are generally fixed, so the mutual inductance between the energy transmitting and receiving coils is also basically unchanged. In the following, the influence of the equivalent impedance of the rear end of the receiving coils on the output power and energy transfer efficiency will be studied.

The numerator and denominator of equation (5) can be multiplied by $1/R_L$ simultaneously, then we get

$$P_o = \frac{N\omega^2 M_1^2 U_1^2}{\frac{(N\omega^2 M_1^2 + R_0 R_L)^2}{R_L} + R_L R_0^2 + 2R_0(N\omega^2 M_1^2 + R_0 R_L)}. \quad (7)$$

When $\frac{(N\omega^2 M_1^2 + R_0 R_1)^2}{R_L} = R_L R_0^2$, namely $R_L = R_{LO1} =$

$\frac{N\omega^2 M_1^2 + R_0 R_1}{R_0}$, the output power of the system reaches its maximum value of

$$P_{o,\max} = \frac{N\omega^2 M_1^2 U_1^2}{4R_0(N\omega^2 M_1^2 + R_0 R_1)} \quad (8)$$

The numerator and denominator of equation (6) can be multiplied by $1/R_L$ simultaneously, then we get

$$\eta = \frac{N\omega^2 M_1^2}{N\omega^2 M_1^2 R_1 + R_0 R_1^2 + R_0 R_L + 2R_0 R_1 + N\omega^2 M_1^2} \quad (9)$$

When $\frac{N\omega^2 M_1^2 R_1 + R_0 R_1^2}{R_L} = R_0 R_L$, namely $R_L = R_{LO2} =$

$\sqrt{\frac{R_1}{R_0}(N\omega^2 M_1^2 + R_0 R_1)}$, the energy transmitting efficiency of the system reaches its maximum value of

$$\eta_{\max} = \frac{N\omega^2 M_1^2}{(\sqrt{R_0 R_1 + N\omega^2 M_1^2} + \sqrt{R_0 R_1})^2} \quad (10)$$

The quality factors of the transmitting and the receiving coils are defined as $Q_0 = \frac{\omega L_0}{R_0}$, $Q_1 = \frac{\omega L_1}{R_1}$ respectively, then equation (8) and equation (9) can be further expressed as

$$P_{o,\max} = \frac{U_1^2 N k^2 Q_0 Q_1}{4R_0(1 + N k^2 Q_0 Q_1)}, \quad (11)$$

$$\eta_{\max} = \frac{N k^2 Q_0 Q_1}{(\sqrt{1 + N k^2 Q_0 Q_1} + 1)^2} \quad (12)$$

Then, let $F = N k^2 Q_0 Q_1$, the maximum power and maximum efficiency values can also be approximated as

$$P_{o,\max} = \frac{F U_1^2}{4R_0(1 + F)} = \begin{cases} \frac{U_1^2}{4R_0} & F \gg 1 \\ \frac{U_1^2}{4R_0} \left(1 - \frac{1}{1 + F}\right) & \end{cases}, \quad (13)$$

$$\eta_{\max} = 1 - \frac{2}{\sqrt{1 + F} + 1}. \quad (14)$$

Figure II depicts the relationship between the maximum output power, the maximum transmitting efficiency and F . As can be seen from the figure: as F increases, the maximum output power will increase and then tend to reach a stable value: $U_1^2 / 4R_0$. The maximum transmitting efficiency will also increase correspondingly, then gradually approach 100%.

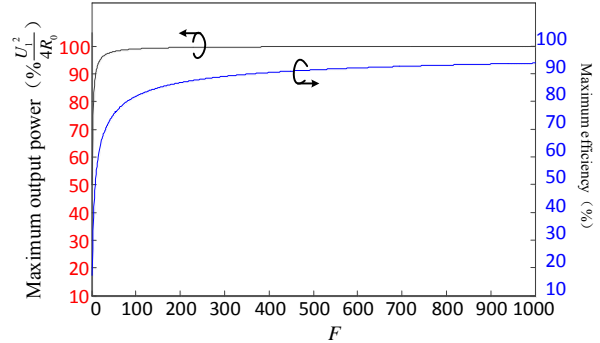


FIGURE II. THE RELATIONSHIP BETWEEN MAXIMUM POWER OUTPUT, MAXIMUM TRANSFER EFFICIENCY AND F

The above analysis shows that, in order to improve the maximum output power and maximum transmitting efficiency of the system, two measures can be taken:

1) Increase the coupling coefficient of coils. The tightness of the coupling between the coils is mainly determined by the size and structure of the coils. Under normal circumstances, the relative position of the energy dispatch coils also affects the coupling coefficient. In wireless power supply system for smart home appliances, the actual position of the load and the horizontal and vertical offset of transmitting coils are main factors that cause the coupling coefficient to decrease. In order to solve this problem, we can study energy dispatch coils with high capacity deviation ratio.

2) Design coils with high quality factor. The design of coils with high quality factor can effectively reduce the sensitivity of the system efficiency to the coupling coefficient. In practical applications, wires with low resistivity such as Litz wire can be used for coil winding. The high frequency of the system is also a trend. Note that, because of that, the overall design of the system will be more complex, and harsher electromagnetic environment will also be triggered. The quality factor of the coils should not be too high as well [13], since the offset of other parameters of the system will lead to huge fluctuations in the system when it is operating.

In addition, it can be found that R_{LO1} , the load value corresponding to the maximum output power is different from R_{LO2} , the load value corresponding to the maximum energy transmitting efficiency, and the relationship between the two can be expressed as

$$\frac{R_{LO1}}{R_{LO2}} = \sqrt{1+F}. \quad (15)$$

It is obvious that $R_{LO1} > R_{LO2}$, and the smaller F is, the closer R_{LO1} and R_{LO2} will be. To meet $R_{LO1} = R_{LO2}$, we must ensure that $F = 0$, but under such circumstances, the output power and transmitting efficiency will also be 0, which is obviously of no meaning, so the maximum power and the maximum efficiency of the system cannot be achieved simultaneously. That means we have to strike a balance between the two according to which objective we give priority to control.

III. CONTROL STRATEGIES FOR PERFORMANCE OPTIMIZATION OF WIRELESS CHARGING SYSTEM FOR SMART HOME APPLIANCES

A. Power Stability Control

Under the premise of constant output voltage of the power supply, as the numbers of loads increases, the change of the current at the receiving ends and the power supply of each single load can be seen in Figure III. As it can be seen, as the number of loads increases, the current at the transmitting end and the receiving ends will decline, which will lead to lack of power supply; as the number of loads decreases, the current at the transmitting end and the receiving ends will increase significantly, which may cause destructive damage to the system. Although using components with higher current rating can alleviate this problem, more system loss cannot be avoided. Therefore, to promote the "one-to-many" wireless power supply system for smart home appliances, the problem of instability caused by the varied number of loads to the system work must be addressed.

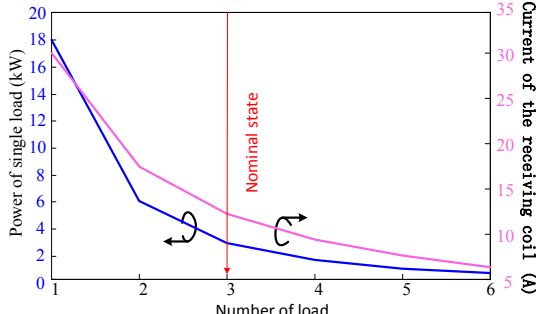


FIGURE III. RELATIONSHIP BETWEEN LOAD POWER AND RECEIVER CURRENT OF SINGLE LOAD

In order to solve the above problem and ensure the stability of power supply to the loads and the working state of the system, the power supply voltage needs to be controlled in real time according to the changing number of loads. A solution is to install a sensor to monitor the number of loads in real time and send the information back to the power control unit at the transmitting end. However, this solution cannot distinguish loads that have been powered from those that haven't, thus less feasible. Therefore, this paper will further research on how to control the power stability of the wireless power supply system

for smart home appliances. In this paper, the number of loads can be measured by detecting the current at the transmitting end in real-time terms. Based on that, the voltage of power supply can be regulated. Ultimately, the stability of power supply to each single load can be achieved even though the number of loads continues to change. The workflow of the power stability control program is shown in Figure IV, with more specific control steps as follows:

Step 1. According to $I_0 = U_{IN} / (Z_0 + N\omega^2 M_1^2 / Z_i)$, draw a look-up table of the current at the transmitting end, that is, the current at the transmitting end corresponding to different supply voltages and the number of loads. Here, U_{IN} refers to the supply voltage that can ensure that each single load can receive rated electric power when N loads are simultaneously powered. Drawing the look-up table of transmitting current in advance can avoid potential complicated calculations and reduce the time required for the control process.

Step 2. Initialize the power supply voltage: $U_1 = U_{IN}$. The purpose is to generate the current available for detection at the receiving ends. To avoid excessive current, U_{IN} , the minimum voltage are selected.

Step 3. Detect the size of I_0 , the current at the transmitting end.

Step 4. Identify the number of loads by referring to the look-up table according to the size of the current at the transmitting end.

Step 5. Set the voltage of power supply according to the number of loads to ensure stable power supply to each single load.

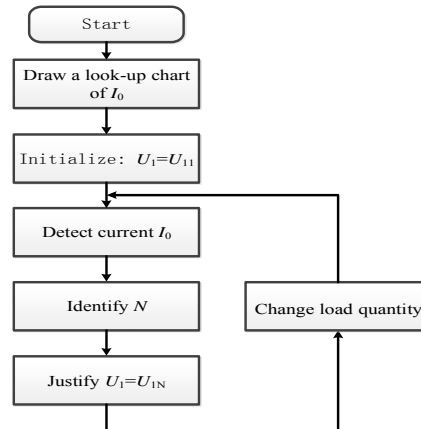


FIGURE IV. FLOW CHART OF CONTROL STRATEGY OF POWER STABILITY

B. Emergency Power Demand Control

When some loads need emergency power supply, the above control strategy is difficult to meet the corresponding powering demand. Therefore, based on the impedance matching network, a control strategy in times of emergency power supply is proposed in this paper. By controlling the load matching

network at the load sides, load characteristics can be adjusted and the distribution of received power can thus be changed.

Equivalent loads of home appliances can be set at a nominal value through the impedance matching. Assuming that the power demand of the n-th load is emergent, the power supply can be expressed as

$$P_n = \frac{\omega^2 M_1^2 U_1^2 R_{Ln}}{(R_{Ln} + R_i)^2 \left(R_0 + \omega^2 M_1^2 \sum_{i=1}^N 1/(R_{Li} + R_i) \right)^2}. \quad (16)$$

At this point, the power supply of loads with normal power demand can be expressed as

$$P_m = \frac{\omega^2 M_1^2 U_1^2 R_L}{(R_L + R_i)^2 \left(R_0 + \omega^2 M_1^2 \sum_{i=1}^N 1/(R_{Li} + R_i) \right)^2}. \quad (17)$$

Let $D = R_0 + \omega^2 M_1^2 \sum_{i=1, i \neq n}^N 1/(R_{Li} + R_i)$, then (16) can be simplified as

$$\begin{aligned} P_n &= \frac{\omega^2 M_1^2 U_1^2 R_{Ln}}{(R_{Ln} + R_i)^2 \left(D + \frac{\omega^2 M_1^2}{R_{Ln} + R_i} \right)^2} \\ &= \frac{\omega^2 M_1^2 U_1^2}{\left((\omega^2 M_1^2 + R_i D)^2 + R_{Ln} D^2 + 2R_i D^2 + 2D \omega^2 M_1^2 \right)} \end{aligned} \quad . \quad (18)$$

From the above equation, it can be obtained that: When the equivalent loads of other loads stay unchanged, P_n , the power supply of the n-th load increases first and then decreases as R_{Ln} increases, and reaches its maximum value when $R_{Ln,o} = (\omega^2 M_1^2 + R_i D)/D$:

$$P_{n,max} = \frac{\omega^2 M_1^2 U_1^2}{4D(R_i D + \omega^2 M_1^2)}. \quad (19)$$

Therefore, when individual loads are in urgent need of power supply, the characteristics of other loads can stay unchanged and more energy can be absorbed by optimizing characteristics of the former loads. In addition, (17) can be simplified as

$$P_m = \frac{\omega^2 M_1^2 U_1^2 R_L}{\left((R_L + R_i)D + \frac{\omega^2 M_1^2 (R_L + R_i)}{R_{Ln} + R_i} \right)^2}. \quad (20)$$

From the above equation, we can see that: the power supply to loads with normal power demand will increase as the variable load R_{Ln} increases, which means that to meet the emergency power demand of certain loads, the cost is power supply fluctuations suffered by other loads, so this control strategy is only applicable to the case of emergency power supply demand.

IV. EXPERIMENTAL RESEARCH ON THE WIRELESS POWER SUPPLY SYSTEM FOR SMART HOME APPLIANCES

A. The Overall Design of the System

In order to verify the characteristics of the loads in the system and the control strategy of power supply, a small-scale experimental platform was set up, as shown in Figure V. The current generated by the direct current source is converted by a high frequency inverter into an alternating current of 85 kHz and transmitted to the receiving ends through the electromagnetic coupling between the energy transmitting coil and the energy receiving coils. The receiving coils directly supply power to the resistive loads.

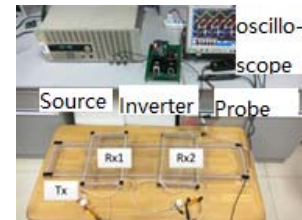


FIGURE V. EXPERIMENT PLATFORM OF WIRELESS POWER SUPPLY SYSTEM OF MULTIPLE LOAD

Transmitting and receiving coils are made from 2025 strands of Litz wires, each of which has a diameter of 0.05mm. Rx1, Rx2 stand for the spiral rectangular coil, with more specific parameters shown in Table 1. The transmission distance between the transmitting and the receiving coils is 5cm.

TABLE I. PARAMETERS OF ENERGY SENDING AND RECEIVING COIL

Coil	Size(m)	Resistance(Ω)	Inductance(μH)	Capacitance(nF)
Tx	1.00×0.20	0.080	71.2	49
Rx1	0.30×0.20	0.030	25.8	136
Rx2	0.30×0.20	0.030	25.9	136

B. Experiment on the Influence of Loads on Power Supply and Transmitting Efficiency

The above analysis shows that the number of loads with power supply and their equivalent impedances have a great impact on the power supply and transmitting efficiency. In this paper, power resistances are used to represent loads, and the fixed input voltage is 17.0V. The output power of the system is measured with the change of load resistances when N (the number of power loads) equals to 1, 2, and 3. The experimental results and Matlab results are shown in Figure VI (the curves in the figure below represent the results of Matlab calculation, and

the dots represent the experimental test results). As can be seen from the figure, with the increase of the load resistance, the total power supply of the system increases first and then decreases gradually. There is an optimal load resistance value that maximizes the total power supply of the system and the corresponding optimal load value are 2Ω , 5Ω and 7Ω , respectively. The maximum output power increases with the increase of the number of loads with power supply, which is consistent with the theoretical analysis.

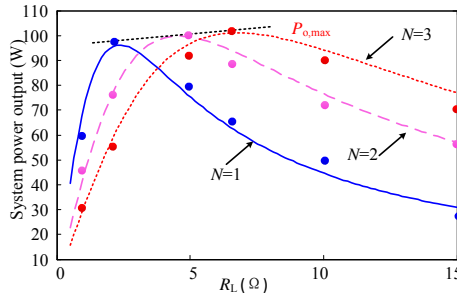


FIGURE VI. CHANGE OF SUPPLY POWER WITH LOAD

By measuring the input power of the system when N (the number of loads with power supply) equals to 1, 2, and 3, respectively, the change of the transmitting efficiency of the system is shown in Figure VII as the load resistance changes. As can be seen from the figure, the greater the number of loads is, the higher the transmitting efficiency of the system will be, which is consistent with the theoretical analysis. For a certain number of loads, the system transmitting efficiency increases first and then decreases as load resistance increases, and there is an optimal load resistance value that maximizes the system efficiency, with the corresponding optimal load value being 1Ω , 1.5Ω and 2Ω . The maximum transmitting efficiency increases as the number of loads grows, which is due to the increased mutual inductance.

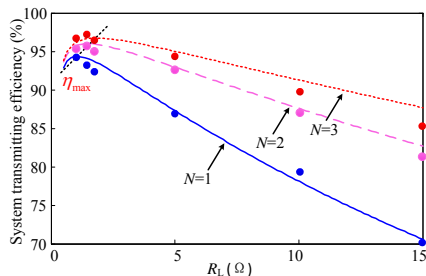


FIGURE VII. VARIATION OF TRANSFER EFFICIENCY WITH LOAD

When compared with the results calculated by theoretical formulas, the experimental values show a certain deviation. This is because the actual values of the inductance and the capacitance cannot reach the full resonance state. However, both the experimental results and the theoretical analysis show the same variation rule. In summary, the following conclusions can be drawn: 1) There is an optimal load value that maximizes the output power of the system and the maximum output power of the system remains unchanged even with different loads; 2) There is an optimal load value that maximizes the transmitting

efficiency of the system. As the number of loads increases, the maximum transmitting efficiency of the system will also increase, which is due to the improvement of the overall coupling coefficient. 3) The optimal load values corresponding to the maximum output power and the maximum transmitting efficiency are different.

C. Experiment on Power Supply Control

In order to avoid fluctuating power supply caused by the change of load quantity, this paper measures the change of current at the transmitting end when the number of load is changing. The rated supply power of the resistor load (with the resistance of 4Ω) is 50W. The rated current and the current at the transmitting end are 3.5A and 8.3A, respectively after calculation. Table 2 is a look-up table recording the current at the transmitting end gained from the above theoretical analysis of the system. The number of loads with power supply ranges from 1 to 4, with the corresponding rated input voltage being 13.0V, 17.0V and 22.0V, respectively. When the supply voltage is fixed, the quantity change of loads with power supply can be reflected in the change of the current at the transmitting end.

TABLE II. TAB.2 LOOK-UP TABLE OF CURRENT

I_0 (A)	N	1	2	3	4
13.0	8.3	8.3	6.4	4.9	4.0
17.0	10.9	10.9	8.3	6.5	5.2
22.0	14.1	14.1	10.8	8.3	6.7

When the input voltage is fixed at 17.0V, as the number of loads with power supply changes, the change of the currents at the transmitting and receiving end is shown in Figure VIII. It can be seen that the currents at the transmitting and receiving ends will increase as the number of loads decreases. For example, when the number of loads changes from 2 to 1, by adjusting the input voltage of the power supply according to the current look-up table, the change of the current at the transmitting end is shown in Figure IX. When the number of loads changes abruptly, the effective value of the emitter current changes from 8.14 A to 10.8 A, then after adjustment, the value returns to 8.14 A. The power supply is also stabilized.

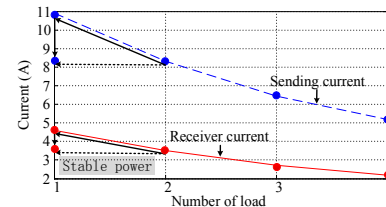


FIGURE VIII. INFLUENCE OF NUMBER OF LOAD ON SENDING AND RECEIVING CURRENT



FIGURE IX. CURRENT CHANGE OF SENDING COIL

When the input voltage is fixed at 17.0V, take the case when $N = 2$, $N = 3$, and $N = 4$, by changing the values of load resistances with emergent power demand and keeping the resistance of other loads unchanged, the relationship between power distribution and the load resistance with emergent power demand is shown in Figure X. Here, the working point when all the loads have the same resistance is defined as the average power point, as shown in Figure X, point 1, and the working point when the loads with emergent power demand reach their maximum receiving power is defined as the maximum receiving power point, as shown in Figure X, point 2.

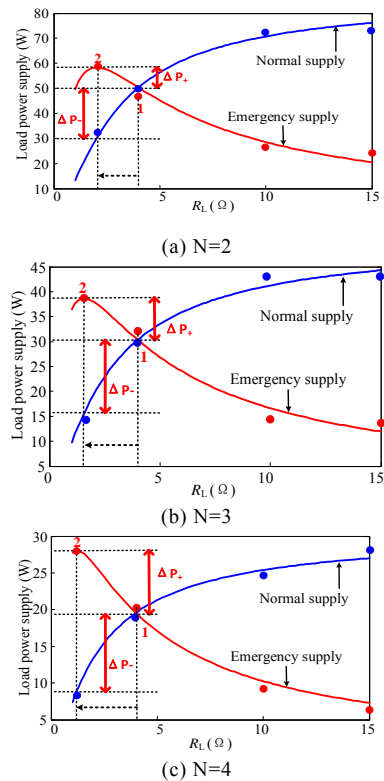


FIGURE X. INFLUENCE OF EMERGENCY POWER DEMAND LOAD ON POWER DISTRIBUTION

When $N = 2$, by adjusting the resistance of loads with emergent power demand along the direction of the dotted arrow in the figure, and shifting the operating point from point 1 to point 2, the power supply to the loads with emergent power demand increases from 50W to 58W, while the power supply to other loads decreases from 50W to 30W. When $N = 3$, by

adjusting the resistance of loads with emergent power demand along the direction of the dotted arrow in the figure, and shifting the operating point from point 1 to point 2, the power supply to the loads with emergent power demand increases from 30W to 40W, while the power supply to other loads decreases from 30W to 15W. When $N = 4$, by adjusting the resistance of loads with emergent power demand along the direction of the dotted arrow in the figure, and shifting the operating point from point 1 to point 2, the power supply to the loads with emergent power demand increases from 20W to 28W, while the power supply to other loads decreases from 20W to 9W. When we define the increased power of loads with emergent power demand as ΔP_+ , the reduced power of other fixed loads as ΔP_- , when $N = 2$, $N = 3$ and $N = 4$, the corresponding $\Delta P_+ / \Delta P_-$ is 0.4, 0.66 and 0.73, respectively. The greater the number of loads with power supply is, the less impact will be exerted on other fixed loads, and the more significant the effect of such power regulation means is.

V. CONCLUSIONS

This paper studies the working mechanism of the wireless power supply system for smart home appliances and the control strategies for performance optimization. The structure of the wireless power supply system for smart home appliances is introduced and the equivalent circuit model of "one-to-many" wireless power supply system for smart home appliances is established. On this basis, the load characteristics of the system are analyzed. The paper also studies how the number of loads will influence the charging power and transmitting efficiency of the system. An optimal load value, which can ensure the maximum of the charging power and maximum transmitting efficiency, was found. As for the instability of power supply caused by the change of load quantity in the wireless power supply system, a power stability control strategy based on current detection of the transmitting end is proposed. In the light of the situation when some loads require emergent power supply, a control strategy is also suggested. A hardware platform for the system was built and performance optimization experiment was carried out to verify the correctness of the theoretical derivation.

ACKNOWLEDGEMENT

This research is supported by China Southern Power Grid Corporation (Research and Application of Key Technologies of Intelligent Cloud Service in Hainan Power Grid).

REFERENCES

- [1] K Feng, S Tong, "Origin and trend of development of smart home appliances," in China New Technologies and Products, vol. 23, no. 6, pp. 1-7, 2010.
- [2] G Wang. "Practice and Prospect of China intelligent power utilization," in Electric Power, vol. 45, no. 1, pp. 1-5, 2012.
- [3] R Abhishek, K D B Soumya, B Amiya, et al. "Location Aware Resource Management in Smart Homes," Proceedings of the First IEEE International Conference on Pervasive Computing and Communications (PerCom'03). IEEE CS Press, 2003.
- [4] Q Wang, Y Zhu, G Ge, et al. "Application discussion of packet transfer technology for smart power distribution and utilization networks," in Power System Protection and Control, vol. 42, no. 9, pp. 139-146, 2014.

- [5] Q Tang, N Liu, J Zhang. "Theory and key problems for automated demand response of user side considering generalized demand side resources," in Power System Protection and Control, vol. 42, no. 24, pp. 138-147, 2014.
- [6] X Huang, L Tan, Z Chen, et al. "Review and research progress of wireless power transfer technology," in Transactions of China Electrotechnical Society, vol. 28, no. 10, pp. 1-11, 2013.
- [7] S Cheng, X Chen, J Wang, et al. "Key technologies and applications of wireless power transmission," in Transactions of China Electrotechnical Society, vol. 30, no. 19, pp. 68-84, 2015.
- [8] M Soljačić, A Kurs, A Karalis, et al. "Wireless power transfer via strongly coupled magnetic resonances," in Science Express, vol. 112, no. 6, pp. 1-10, 2007.
- [9] X Zhang, F Zhou. "Smart grid leads the journey to innovative smart home and energy consumption patterns," in Power System Protection and Control, vol. 42, no. 5, pp. 59-67, 2014.
- [10] B X Nguyen, D M Vilathgamuwa, G H B Foo, et al. "An Efficiency Optimization Scheme for Bidirectional Inductive Power Transfer Systems," in IEEE Transactions on Power Electronics, vol. 30, no. 11, pp. 6310-6319, 2015.
- [11] W Fu, B Zhang, D Qiu, et al. "Maximum efficiency analysis and design of self-resonance coupling coils for wireless power transmission system," in Proceedings of the CSEE, vol. 29, no. 18, pp. 21-26, 2009.
- [12] R L Steigerwald. "A comparison of half-bridge resonant converter topologies," in IEEE Transactions on Power Electronics, vol. 3, no. 2, pp. 174-182, 2002.
- [13] Z Pantic, S M Lukic. "Framework and Topology for Active Tuning of Parallel Compensated Receivers in Power Transfer Systems," in IEEE Transactions on Power Electronics, vol. 27, no. 11, pp. 4503-4513, 2012.

Design of Intelligent Charging Access System for Home Appliances

Wangcheng Zhu^{1,*}, Xinshu Wan¹, Taobei Lin¹ and Yun Liu²

¹Electric Power Research Institute of Hainan Power Grid Co., Ltd., Haikou 570125, Hainan Province, China

²Nanjing Sifang E-power Automation Co., Ltd., Nanjing 211111, Jiangsu Province, China

*Corresponding author

Abstract—In order to realize intelligent charging of electric equipment in the circumstances of Smart Grid, such as sweeping robots, inspection robots and automatic guided vehicles, this paper designs a new intelligent charging access system using intelligent outlet technology and wireless charging technology. Firstly, the paper illustrates the disadvantages of existing charging mode, including low-level automation and poor security. Then, this paper gives a general introduction of the new system for the above drawbacks and a detailed description of its hardware and software design. Furthermore, as for hardware facilities, the modular design is adopted, including intelligent outlet, high-frequency power supply, transmitter, receiver and on-board charger. Moreover, to realize intelligent real-time control, it takes advantage of the WiFi communication technology to reduce the difficulty and cost of intelligent access of terminal equipment. Meanwhile, with the adoption of the two-stage circuit status monitoring and abnormality judgment, the system security is improved effectively. In the last part, the paper focuses on the introduction to working flow of the system.

Keywords—smart grid; intelligent power; access; wireless power transmission

I. INTRODUCTION

Driven by the increasing demands of energy and electricity, the world's power grid which has experienced a leaping development from the traditional power grid to the modern power grid, from isolated urban power grids to large-scale cross-district, transnational interconnected power grid has entered a new phase marked by strong smart grid. Recently, China Southern Power Grid released The Report of Research on "the 13th Five Year" China Southern Power Grid Smart Grid (hereinafter referred to as "Report"). The Report aims to create a safe, reliable, green and efficient smart grid, which analyzes the new trend of energy transformation and development, and expounds the great strategic significance of developing smart grid. Besides, the Report constructs the development framework of the smart grid in China Southern Power Grid systematically and completely, making it clear that the significance and the future direction of smart grid, proposing a variety of interactive electricity links [1].

To build a strong smart grid smart grid, it is imperative to achieve intelligent service through mature intelligent power technology to meet the diversified needs of users, and to achieve the goal to build a steady, reliable, economic and secure power supply by constructing a new power supply-demand relationship. What's more, the new relationship can

achieve the real-time interaction of power flow, information flow, service flow between grid and customers [2]. At this stage, with the development of Smart Home level, average home users buy much more intelligent electrical equipment, such as cleaning robot, smart meters and so on. Meanwhile, the smart applications, like unattended substations, patrol robots for high voltage power lines and AGV (Automatic Guided Vehicle, AGV) at ports, are developing to a higher level and more advanced stage.

The foregoing intellectualized and movable electrical devices are all powered by batteries and are connected to the power grid through wired connections of cables, so they can exchange energy with the power grid. This direct cable access charge mode has various disadvantages like requiring manual plugs to check the charging status from time to time, low level of automation and intelligence, which seriously affects the efficiency of intelligent electrical devices and the interaction with smart grid. Therefore, in order to realize the expansion of smart grid from pure power transmission network to the integration infrastructure of intelligence, energy and information, it is necessary to study the problems existing in the charging process of the intellectualized and movable electrical devices above and to explore new types of power access technology. It is also necessary to design smart and efficient electrical systems to enhance the intelligence and automation of electrical devices and to promote the interaction between electrical devices and the smart grid and to enhance the intelligence of electrical energy applications in the fields like household, industrial and power supply.

Based upon the above analysis, taking AGV (Automatic Guided Vehicle) as an example, this paper conducts an overall design of the intelligent access system firstly, and then carries on a further research design of the technology involved in intelligent access system, including smart power plug, intelligent outlet technology [3], wireless power transfer technology [4], detection and recognition, as well as protection technology. Finally, merging the above-mentioned technology, this design is devoted to realize the charging detection and recognition, automatic charge, and intelligent switch functions of AGV (Automatic Guided Vehicle), which aims to improve the charging rate and reduce the charging time of electrical equipment.

II. OVERALL DESIGN OF THE INTELLIGENT ACCESS SYSTEM

A. Introduction to AGV and Its Charge Modes

AGV (Automatic Guided Vehicle), which is commonly used in industry, usually includes five parts: sensing unit, control unit (including communication), driving unit and power supply unit [5], as shown in Figure I. The sensing unit mainly consists of parts like road guide magnetic sensor, obstacle avoidance sensor and microwave photoelectric sensor, which is responsible for detecting the road information in the work area and transmitting the information to the control unit in real time. The control unit mainly consists of communication module, guidance module, route calculation and selection module. This unit is in charge of receiving the origination and destination information of the cargo handling sent by the server, and calculating the optimization route without influencing the routes of other AGVs. At the same time, the calculating results are turned into drive and detection signals and then being sent to the driving unit and sensing unit. The achievement of precise, speeding and convenient delivery relies on the coordinated control of the above two units. Driving unit is mainly composed of the drive motor, driver and controller module, guide wheel and power wheel. This unit takes charge of the real-time movement, precise handling, start-up and stop of AGV (Automatic Guided Vehicle). The power supply unit mainly has parts like battery, power management module and power information transmission module. It is obvious that this unit provides power supply, charging management and power information service for the AGV (Automatic Guided Vehicle).



FIGURE I. SYSTEM COMPOSITION OF LATENT AGV

There are three charge modes for the latent Automatic Guided Vehicles (AGVs) including battery replacement, contacting with the ground charging brush plate, and telescopic charging lever. AGV supports both manual and automatic way to replace the battery. The alternate use of a main and a backup battery can realize 24-hour non-stop operation of AGV (Automatic Guided Vehicle). However, because the equipment occupies large area, it will cause some unsafe phenomena easily when changing the battery, for example, poor contact during cable dismantling and connection, sparks flew. As for the second charging method, AGV is parked in a fixed position where the van's metallic brush can contact the ground charging brush plate, which makes the power transmission come true. This way also has its own shortcomings. There exists a certain voltage between the two brush plates, if any foreign metal bodies fall between two plates, it will cause short circuit, and even worse safety problems, like fire disaster. The third mode, telescopic charging rod, sets a ground telescopic charging lever in a fixed charge position, which can reach to the same height as the car chargers of AGV, therefore the power transmission is

realized when AGV arrives and contacts to the charging lever. This approach has disadvantages including inexactitude position and loose contact, which decreases charging efficiency and even causes short-circuit or electric leakage problems. Based upon the above analysis, it is necessary to bring the wireless power transmission in charging AGV in order to increase security greatly by avoiding accidents in contact charging.

B. Introduction to Wireless Power Transfer Technology

Historically, the development of wireless power transfer technology has undergone several stages includes sprout, initial exploration, continuous research, major breakthroughs and rapid development. So far, wireless power transfer can be achieved by ways like magnetic induction, magnetic coupling resonance, microwave, femtosecond laser, ultrasonic, electric field coupling [7-8].

C. System Overall Design

Based on the above introduction and research, an intelligent charging access system is designed in the paper, as shown in Figure II, which mainly consists of intelligent outlet, high-frequency power supply, transmitter, receiver, OBC (on-board charger), battery and server. Intelligent outlet can record and pass some parameters like voltage, current, and power of AGV transmitter to sever through communication module, so that the server can record the parameters and monitor the charging state of AGV. High-frequency power supply is responsible for changing the 220V power frequency supply into the high frequency AC (alternating current) through the rectifier-inversion way, and then transfers it to the transmitter. The transmitter transfers the high-frequency power to receiver by high-frequency alternating electromagnetic wave generated by the coil formation. Receiver is responsible for receiving the high-frequency power carried by the high-frequency electromagnetic wave and passes it to the OBC (on-board charger). OBC (on-board charger) is in charge of rectification, and filtering the received high-frequency energy rectification, as well as voltage conversion and voltage-stabilizing, and then it converts the current into steady DC (direct current) for battery charging. At the same time, it can monitor the charging voltage, current and power and then upload the data to the server. There is no doubt that the function of battery is receiving power. As for receiver, it not only has functions of AGV like vehicle routing, power control or charging schedule, but also has the functions including comparing parameters of voltage, current, and power, and monitoring charging behavior, so that it can detect anomalies in charging and send abnormal information to human control center without delay.

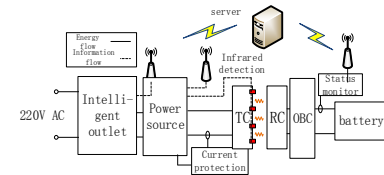


FIGURE II. OVERALL DESIGN OF INTELLIGENT CHARGING ACCESS SYSTEM

III. HARDWARE DESIGN

A. Intelligent Outlet Design

The existing movable electrical devices especially AGV(Automatic Guided Vehicle)have various charging modes, and the varying applications of these devices have different scenario demands. In order to combine the wireless power transmission charging modes with the existing charging modes better and minimize the problems of reconstruction caused by charging modes change, the paper aims to design an intelligent outlet in the front end of the wireless charging system which is compatible with existing charging modes, thus reducing construction difficulties of changing charging modes.

The overall structure of intelligent outlet design is shown in Figure III, which includes MCU processing unit, WiFi communication unit, electrical parameters measurement unit, intelligent outlet system power supply unit and extension units like clock and electric relay. Under the coordination and control of the MCU processing unit, the intelligent outlet transforms the electric energy information by potential transformer and current transformer firstly, and then performs operations like signal conditioning, sampling and A / D conversion to transfer the electric energy information to MCU via the electrical parameters measurement unit; MCU analyzes and calculates the collected power information of electrical devices and then transfers the information to the server through WiFi communication unit. Electric relay can cut off the main power circuit of electrical devices when it receives the cut-off charging command from the receiving server, which usually sends this command as soon as it detects anomalies. In this way, the back-end electrical devices can be protected. Besides, the Electric relay is normally closed.

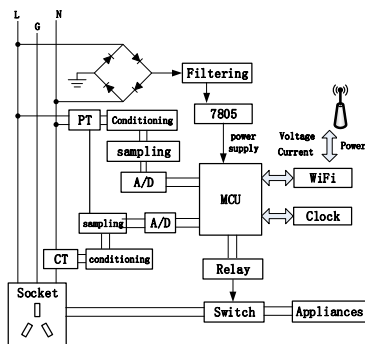


FIGURE III. THE OVERALL STRUCTURE OF INTELLIGENT OUTLET

B. High-Frequency Power Supply Design

The high-frequency power supply used in wireless power transmission can be divided into different types according to eight rules, which are introduced in detail in Table I.

TABLE I. STRUCTURE CLASSIFICATION OF HIGH-FREQUENCY POWER SUPPLY

Classification rules	Classifications		
usages of electric power after inverting	active inversion		Passive inversion
features of input DC power supply	voltage mode		current mode
adjustability of output frequency	constant frequency output		variable frequency output
load current waveform	sinusoidal wave		non-sinusoidal wave
output phase number	single-phase	three-phase	multi-phase
frequency of output DC	low frequency 50~60Hz	medium frequency 400Hz~100kHz	high frequency 100kHz~1MHz
structure form	one-terminal	push-pull	half-bridge
power device	SCR	GTO	BJT
	MOSFET	IGBT	hybrid

In the process of wireless charging of AGV, considering that the power transmission distance is short, the paper chooses the operating frequency of 50-100 kHz as the high-frequency power supply, which is a moderate frequency. Besides, the rectification and filtration design of high-frequency power supply is relatively simple, so the paper mainly focuses on the introduction to inverting design. Based on the above analysis and the classifications in the table, MOSFET is more suitable for half-bridge inversion circuit.

The half-bridge inversion circuit has two capacitors with the same capacitance value and two switching devices Q1 and Q2, which alternatively performs a turn-on operation in a half period. Because the capacitor will branch voltage, the maximum output voltage of the structure can only reach up to half of input DC voltage. Under the same conditions of constant rectified DC voltage and same load, compared with the full-bridge inversion circuit, the half-bridge inversion circuit has smaller volume and drives more simply, although its output power is lower. So, half-bridge type is more suitable for AGV wireless charging system with narrow space and precise location. The structure map of high-frequency power supply with both communication and detection functions is shown in Figure IV.

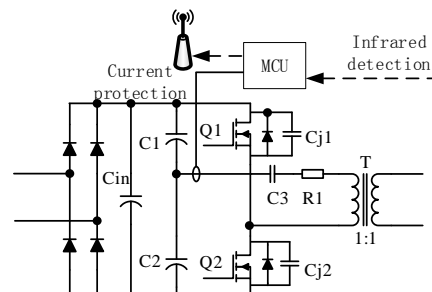


FIGURE IV. STRUCTURE OF HIGH-FREQUENCY POWER SUPPLY

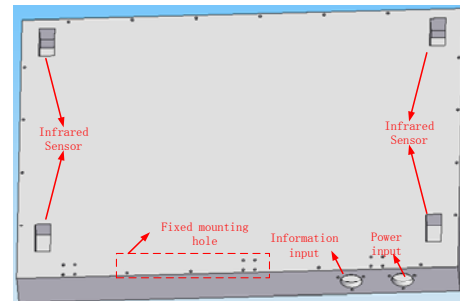
As shown in Figure IV, the high-frequency power supply is composed of rectifier, filter, inversion, control and protection module. Rectifier module adopts four diodes full-bridge rectification form, and equips with a large capacity electrolytic capacitor in the back end for filtering. After filtering, the half-bridge inversion circuit converts the DC into high-frequency AC to the isolation transformer, which drives the transmitter coil to generate high-frequency electromagnetic field and transfers power. At the same time, in high-frequency power supply, it sets up a MCU control and protection module. On the one hand, it can generate drive waveform by controlling the driver chip and switch the MOSFET on and off; on the other hand, the current detection module, designed in the main power loop, keeps the security of high-frequency power supply by comparing with the internal threshold of MCU. Moreover, MCU can detect whether the receiver is connected to wireless charging system through the infrared sensor installed in the transmitter, so that it can control the on and off state of high-frequency power supply.

C. Transmitter and Receiver Design

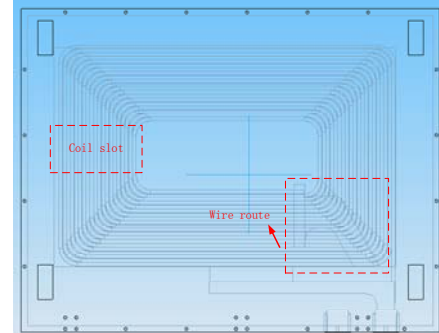
The transmitter and the receiver are collectively referred to as resonator of wireless power transmission system, which is used to change high-frequency power into high frequency electromagnetic field and transfer the power to the receiver. The structure is an important part of electrical devices' intelligent charging access system. The transmitter and the receiver are mainly composed of coils. The coils can be divided into different types according to the structure like disk spiral coil and solenoid coil. Disk spiral coil mainly includes ring coil, pancake coil and square coil. The basic structure of solenoid coil is cylindrical.

The solenoid coil is not suitable for AGV charging because AGV has small charging space, which leaves no room for solenoid coil. After comparing the three mentioned types of disk spiral coil, ring coil has lower coupling factor and quality factor, so it is unfit for wireless transmission system. Meanwhile, in order to make full use of the side charging area of AGV, it is more appropriate to adopt the square coil as the resonator part of the electrical devices' intelligent charging access system.

Based on the above analysis, the paper designs a transmitter coil shown in Figure V. The coil adopts non-metallic material with elaborate structures. The internal part of the coil carves coil slot and coil winding plate for looping metal wires. And the external part has structures including infrared sensor hole, power input interface, power output interface and mounting hole. Infrared sensor hole is used for fixing the infrared sensor; the power input hole is used for connecting the two-core aviation plug with the metal wire to realize the power input function; the information output hole is used for connecting the infrared sensor's signal line, power line with the high-frequency power MCU controller to achieve the transmission of power supply signal; mounting hole is used for the mounting and fixing of the transmitter bracket.



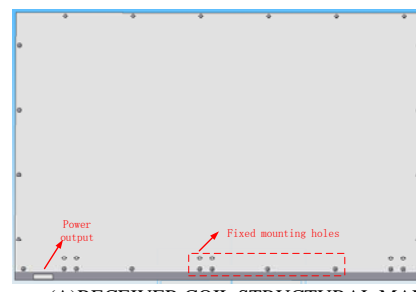
(A)TRANSMITTER COIL STRUCTURAL MAP



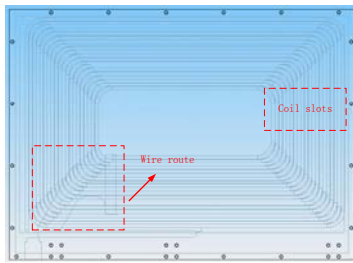
(B)TRANSMITTER COIL PERSPECTIVE IMAGE

FIGURE V. TRANSMITTER COIL STRUCTURE

Based upon the design of the transmitter coil, the receiver coil also adopts a similar structure, i.e. the square coil. Unlike the transmitter coil, there is no need to arrange the infrared sensor on the receiver coil and the energy output hole can adopt a simple rectangular copper-core interface. Therefore, the receiver coil is lighter and smaller than the transmitter coil, which paves the way for the convenient installation on the AGV, meanwhile, it also largely reduces the AGV's reconstruction difficulty. What's more, the size and turns of coils, the number of sensors, the diameter of the metal wire and other parameters can be further designed according to the power and distance requirements of AGV, patrol robot and other electrical devices.



(A)RECEIVER COIL STRUCTURAL MAP



(B) RECEIVER COIL PERSPECTIVE IMAGE

FIGURE VI. RECEIVER COIL STRUCTURE

D. OBC Design

The contact charging of AGV generally converts power frequency current into DC with constant voltage at first, and then transfers the DC to the receiving end of AGV for charging the AGV battery directly. Differing from contact charging, AGV wireless charging needs debugging high-frequency AC power to battery acceptable level through rectifier, filter and voltage regulation in vehicle terminal. Therefore, the intelligent charging intelligent charging access system needs to design the charger at the AGV vehicle end in order to realize the rectification, filtering and voltage regulation of the high-frequency alternating current. The circuit topology of OBC (on-board charger) designed in the paper is shown in Figure VII. The topology consists of rectifier module, filter module, chopper stabilizer module and batteries status monitoring module. What's more, the topology can realize real-time monitoring and scheduling in the process of charging and power consumption by connecting the vehicle controller with WiFi communication unit.

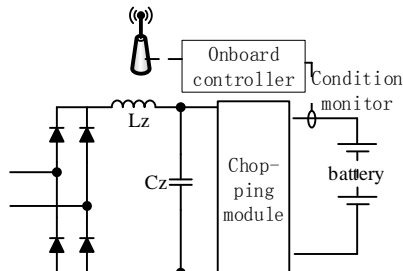


FIGURE VII. CIRCUIT TOPOLOGY OF OBC

E. Overall Structure Design

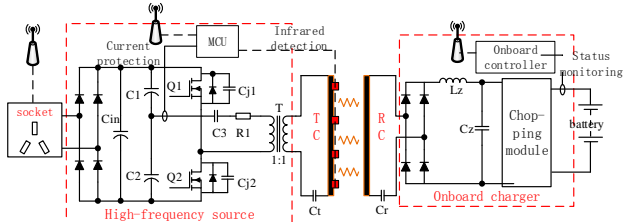


FIGURE VIII. CIRCUIT TOPOLOGY OF ELECTRICAL DEVICES' INTELLIGENT CHARGING ACCESS SYSTEM

Based on the above research and design, considering the structure and function of each part, the circuit topology of

electrical devices' intelligent charging access system is shown in Figure VIII. Owning to the coordination and cooperation of each part in circuit topology, many functions can be achieved, such as AGV intelligent charging, automatic switch and anomaly detection, which greatly improve efficiency of AGV.

IV. SOFTWARE DESIGN

A. Workflow of Intelligent Outlet

The workflow of intelligent outlet is shown in Figure IX. Firstly, the intelligent outlet connects with 220V power supply system, and then provides power supply for MCU and intelligent outlet system through internal rectifier and filer, meanwhile, MCU completes initialize settings. Then communication test with sever is carried out. If the communication fails, it will keep trying and turn on abnormal indicator. If the communication goes well, it will sample some signals, including voltage and current signals of outlets, besides, it will calculate power. If sampling process is unfinished, it shall check whether there are abnormalities. If so, the abnormalities shall be uploaded to sever which will send some operational orders. If the sampling is finished, it is time to check whether the voltage and current are within the normal range. If it is normal, the data shall be reported to the server, otherwise, the abnormalities shall be checked and sent to the server which will send some operation instructions, too. If the server instructs to cut off the circuit, the MCU will send a cut-off command to the electric relay to protect circuit. If the server indicates nothing, the signal sampling will continue, and the real-time monitoring of system status is realized.

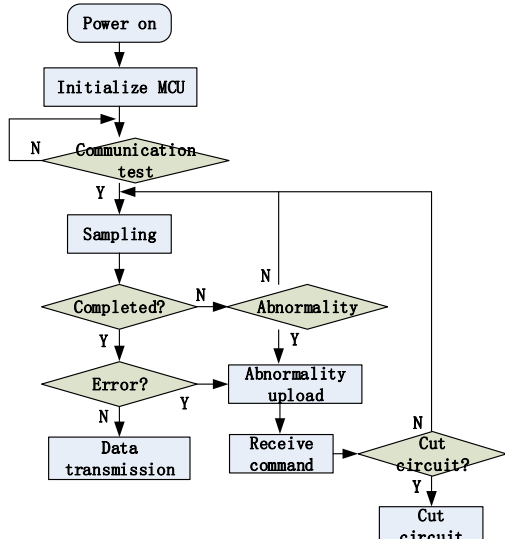


FIGURE IX. WORKFLOW OF INTELLIGENT OUTLET

Relying on the real-time docking of intelligent outlet and server, the system realizes the detection of the first-level working status and protects the first-level circuit.

B. Workflow of High-Frequency Power Supply

The workflow of high-frequency power supply is shown in Figure X. The high-frequency power supply connects to intelligent outlet through an external three-pin plug at first, and

it powers MCU and the whole system through the internal rectifier and filter, which helps power system complete initialization settings. Followed by the server communication test, if the communication fails, it will keep trying and turn on abnormal indicator; if the communication is successful, it will check the receiver devices by infrared sensor and judge whether the electrical devices is connected to the system. If the infrared detection does not identify the electrical devices, it will cut off the power and continue the detection. Provided that the electrical devices have been connected to the system, it will turn on the power, activate driver chip, and drive the MOSFET to produce high-frequency current and to send power to the receiver. In addition, after high-frequency power inversion, the current detection is started. This step mainly includes following operations: sampling the main power circuit's current and calculating the current RMS value which is compared with the threshold value set in the circuit. If the results are abnormal, the abnormalities shall be uploaded to sever which will send some operational orders. If the server instructs to cut off the circuit, the whole system will stop working; if the server indicates to work on, it shall come back to the infrared detection. If there is no abnormality in current detection, it still returns to the infrared detection to complete the workflow cycle. Intelligent outlet also controls the on-off statuses of high-frequency power supply, once the power outage happens, the whole system will stop work.

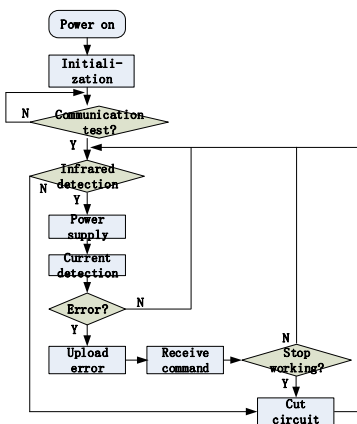


FIGURE X. WORKFLOW OF HIGH-FREQUENCY POWER SUPPLY

Through the real-time docking of high-frequency power supply and server, the system realizes the detection of the second-level working status and second-level protection, which further improves the security of electrical devices' intelligent charging access system. Meanwhile, adopting infrared photoelectric measurement helps achieve the intelligent detection of receiver and turn on or turn off the intelligent charging automatically.

C. Vehicle Terminal Workflow

The system design of the vehicle terminal mainly combines the charger with the car battery, so the communication and battery status monitoring of OBC terminal are basically similar to the existing AGV's communication and battery status monitoring [9]. The vehicle terminal workflow is also similar

to that of the existing AGV's vehicle terminal. So there is no more detailed description.

V. CONCLUSION

The paper designs a new intelligent charging access system taking intelligent outlet technology and wireless charging technology as the core. Under the circumstances of smart grid, the system can realize the electricity information acquisition, coordination and control and safety monitoring of movable electrical devices at the wide range. The system can not only be applied into the intelligent charging of AGV, but also applied into the intelligent charging of both industrial and domestic electrical devices like substation patrol robots and cleaning robots. Besides, the system has many advantages. On the one hand, it has higher convenience and security; on the other hand, it shows great advantages in the reconstruction of existing devices for its low reconstruction cost. In order to promote the application of intelligent charging in electrical devices, the further research shall be made to investigate the "one to multiple" intelligent charging and scheduling study on the basis of this system.

ACKNOWLEDGEMENT

This research is supported by China Southern Power Grid Corporation (Research and Application of Key Technologies of Intelligent Cloud Service in Hainan Power Grid).

REFERENCES

- [1] S. He. "China Southern Power Grid released the Report of Research on 'the 13th Five Year' China Southern Power Grid Smart Grid." Internet: www.csg.cn/xwzx/2017/gsyw/201708/t20170822_159482.html, [Aug. 22, 2017].
- [2] Z. Liu, Global energy internet. Beijing, China: China Electric Power Press, 2015.
- [3] W. Xiao, G. Su, Y. Lu, et al. "Smart Home Based on WiFi Intelligent Plug," in Microcontrollers & Embedded Systems, vol. 14, no. 5, pp. 46-48, 2014.
- [4] X. Huang, W. Wang, L. Tan, "Technical Progress and Application Development of Magnetic Coupling Resonant Wireless Power Transfer," in Automation of Electric Power Systems, vol. 41, no. 2, pp. 2-14, 2017.
- [5] T. Ganesharajah, N. Hall, C. Sriskandarajah, "Design and operational issues in AGV-served manufacturing systems," in Annals of Operations Research, vol. 76, no. 1, pp. 109-154, 1998.
- [6] W. Wu, "The overall scheme and key technology research of logistics transportation AGV," M.Eng thesis, Shenyang Ligong University, Shenyang, China, 2013.
- [7] A. Brecher, D. Arthur. "Review and Evaluation of Wireless Power Transfer (WPT) for Electric Transit Applications," in Human Factors & Ergonomics Society, vol. 49, no. 5, pp. 832-841, 2014.
- [8] X. Huang, L. Tan, Z. Chen, et al, "Review and research progress on wireless power transfer technology," in Transactions of China Electrotechnical Society, vol. 28, no. 10, pp. 1-11, 2013.
- [9] J. Zhong, "Design of an AGV System Combining Multiple Navigation Technologies," M.Eng thesis, Zhejiang University, Hangzhou, China, 2016.

Coupling Characteristics and Optimization of the Resonators Applied to the Power Supply System of Tail-free Household Appliances

Daohong Lin*, Wangcheng Zhu and Zhenchao Xie

Electric Power Research Institute of Hainan Power Grid Co., Ltd., Haikou 570125, Hainan Province, China

*Corresponding author

Abstract—As household appliances become more and more intelligent, increasingly strict demands are put forward for their power supply. Existing draw-out power supply mode of household appliances has many shortcomings including low waterproof grade, touch spark, and wire constraint. Considering this, a tail-free power supply system based on magnetically-coupled resonant wireless power transfer (MCRWPT) technology is investigated. Aiming at the coupling problems, such as frequency splitting, of the resonator during the design of the system, the analytic calculation is adopted to obtain the advisable domain values of mutual inductance that can evade frequency splitting. On this basis, the authors also carry out theoretical calculation on the combination modes of disc spiral coils and spatial spiral coils so as to attain the accurate mutual inductance between the resonators. In addition, a calculation method more accurate than the traditional Neumann formula is also proposed. The theoretical analysis is finally validated by conducting simulation and experiments and comparing the obtained results.

Keywords—tail-free household appliances; wireless power transfer; resonator; frequency splitting; mutual inductance calculation

I. INTRODUCTION

With the constant innovation of the technologies in emerging and manufacturing industries, household appliances are developed to be intelligent and somatosensory so as to have high user experience. However, the traditional draw-out power supply mode limits the flexibility, reliability, and safety in power utilization of household appliances [1]. Moreover, frequently drawing out and inserting plugs is likely to cause problems relating safety utilization of electricity such as aging of contact elements, loose contact, and sparks. For this reason, it is urgent for experts in the field of household appliances to develop a new power supply mode, so as to cast off the last “tail” of the household appliances—wires [2].

Wireless power transfer (WPT) technology, as a non-traditional power transmission mode emerging in recent years, adopts electromagnetic coupling to realize isolated power supply of electric equipments. The WPT technology was firstly investigated by Croatia American physicist Nikola Tesla, while the presence of relevant bottleneck technical issues restricts the development of the technology [3]. In 2007, Marin Soljacic and his research team in Massachusetts Institute of Technology put forward the magnetically-coupled resonant wireless power

transfer (MCRWPT) technology, which provides an opportunity for the development of high-power and mid-range WPT technology [4]. Since then, research teams in China and abroad have vigorously explored and solved key problems of MCRWPT, for example the increase in the transmission distance, the establishment of the accurate model of the system, and the further optimization of the efficiency and power. Meanwhile, great progress has been obtained [5-8]. The continuous development of the MCRWPT technology provides a new solution to the intelligent and green power supply for household appliances [9].

Through modeling analysis of the power supply system of tail-free household appliances, the coupling problems involving frequency splitting that need to be considered in the design of the system is studied using the KVL circuit analysis method converted by equivalent impedance. Moreover, the advisable domain values of the mutual inductance which can avoid the occurrence of frequency splitting of the power supply system are obtained. The value of mutual inductance is not only related to whether frequency splitting will occur or not, but also is associated with whether the system has optimal transmission performance or not. Therefore, it is very necessary to maintain the mutual inductance in the critical saturated state under conditions with a fixed transmission distance. However, the commonly-used analytic calculation methods at present are relatively rough, such that the theoretical mutual inductance cannot meet the requirement for maintaining in the critical saturated state. Therefore, an accurate calculation method is proposed for mutual inductance between resonance coils in the wireless power supply system for tail-free household appliances. Finally, the theoretical analysis of the research is validated through experimental measurement and comparison. The research result is of great practical significance for avoiding the occurrence of frequency splitting while improving the transmission performance of the system.

II. THEORETICAL MODELING AND COUPLING CHARACTERISTICS OF THE SYSTEM

From the perspective of power types, MCRWPT systems can be classified into voltage-source (V) and current-source (I) types. While according to the capacitance compensation approaches of transmit and receiving coils, the systems can be divided into four types: serial-serial (SS), serial-parallel (SP), parallel-serial (PS), and parallel-parallel (PP) ones. Therefore,

through permutation and combination, there are eight types of resonant topology of MCRWPT systems [10-11]. Taking a MCRWPT system with V-source power and SS compensation topology for an example, the structure of the power supply system is shown in Figure I.

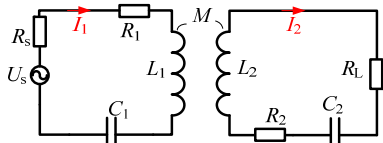


FIGURE I. WIRELESS POWER SUPPLY SYSTEM FOR HOUSEHOLD APPLIANCES

In Figure I, U_s represents the non-ideal voltage source, and its internal resistance is R_s . Moreover, L_1 , R_1 , and C_1 denote self-inductance, internal resistance, and resonant compensation capacitance of the transmit coil; while L_2 , R_2 , and C_2 are those of the receiving coil, respectively. By using the KVL circuit analysis method converted by equivalent impedance, the equivalent input impedance in the power source is

$$Z_{in} = R_s + R_1 + j \left(\omega L_1 - \frac{1}{\omega C_1} \right) + \frac{(\omega M)^2}{R_L + R_2 + j \left(\omega L_2 - \frac{1}{\omega C_2} \right)} \quad (1)$$

When the system is in the resonant state, the imaginary part of the input impedance should be 0, that is,

$$\left(\omega L_1 - \frac{1}{\omega C_1} \right) - \frac{(\omega M)^2 \left(\omega L_2 - \frac{1}{\omega C_2} \right)}{(R_L + R_2)^2 + \left(\omega L_2 - \frac{1}{\omega C_2} \right)} = 0 \quad (2)$$

Suppose that the transmit and receiving coils have same parameters and natural resonant frequency, namely,

$$\begin{cases} L_1 = L_2 = L \\ C_1 = C_2 = C \\ 1/\sqrt{L_1 C_1} = 1/\sqrt{L_2 C_2} = \omega \end{cases} \quad (3)$$

Therefore, Formula (2) can be further simplified as

$$\left(\omega L - \frac{1}{\omega C} \right) \left[(R_L + R_2)^2 + \left(\omega L - \frac{1}{\omega C} \right)^2 - (\omega M)^2 \right] = 0 \quad (4)$$

Two solutions to the resonant frequency can be obtained by solving Formula (4), i.e. making either the first or second part zero. There is a real solution in the solution set and the other one needs to undergo discrimination of the root according to the actual parameters. Therefore, the determined real solution, that is, $\omega = 1/\sqrt{LC}$ is the natural resonant frequency of the

wireless power supply system of household appliances. When the second part in Formula (4) is zero, the formula can be solved based on the quadratic equation of one variable as

$$\omega_{1,2} = \sqrt{\frac{-\left[(R_L + R_2)^2 - \frac{2L}{C} \right] \pm \sqrt{\Delta}}{2(L^2 - M^2)}}, \quad (5)$$

where $\Delta = \left[(R_L + R_2)^2 - \frac{2L}{C} \right]^2 - \frac{4(L^2 - M^2)}{C^2}$ is the discriminant of the root. In many cases, the self-inductance of coils is larger than the mutual inductance between coils. Therefore, if Formula (5) has a real solution, it needs to meet the following constraints:

$$\begin{cases} \Delta \geq 0 \\ (R_L + R_2)^2 - \frac{2L}{C} \leq 0 \end{cases} \quad (6)$$

The above analysis reveals that when the transmit and receiving coils of the MCRWPT system have a large distance, the mutual inductance is ignorable compared with the self-inductance, so $4(L^2 - M^2)/C^2 \approx 4L^2/C^2$. Therefore, the discriminant can be further rewritten as

$$\Delta \approx (R_L + R_2)^2 \left[(R_L + R_2)^2 - \frac{4L}{C} \right] \quad (7)$$

By combining Formulae (6) and (7), it is obtained that $4L/C \leq (R_L + R_2)^2 \leq 2L/C$. As the two inequalities do not exist at the same time, #2 in Formula (4) has no real solution. It means that when the transmit and receiving coils of the MCRWPT system have a large distance, there is one and only one resonant frequency, i.e. natural resonance frequency ω , to make the Equation (4) valid. Under the condition, the system will not have frequency splitting. When there is a short transmission distance, that is, the mutual inductance between coils cannot be ignored relative to the self-inductance of the coils, to avoid the occurrence of frequency splitting in the MCRWPT system, the following condition needs to be satisfied:

$$M < 0.5(R_L + R_2)\sqrt{4LC - C^2(R_L + R_2)^2} \quad (8)$$

With given system parameters including load impedance, self-inductance of coils, matching capacitance, and internal resistance, the condition of not having frequency splitting changes to the condition that the mutual inductance between coils is less than a constant under certain parameter combination of the system. In other words, when coils in the system have a short distance, there is definitely a mutual inductance which causes the occurrence of frequency splitting.

As the wireless power supply system of household appliances has a limited transmission distance, the mutual inductance needs to be effectively defined according to Formula (8) while designing the system, so as to avoid phenomena such as frequency splitting that difficult to deal with.

III. ACCURATE CALCULATION OF MUTUAL INDUCTANCE AND COUPLING OPTIMIZATION

The above analysis reveals that the mutual inductance between the coils is a significant factor determining whether frequency splitting occurs to the wireless power supply system of household appliances or not. Moreover, setting a proper mutual inductance is also an effect approach for guaranteeing the optimal transmission efficiency. To ensure that the theoretically designed mutual inductance matches with the actual inductance between coils, the mutual inductance between coils requires to be accurately calculated. An approximate calculation method for mutual inductance between spatial spiral coils was proposed in previous research [12], that is, the calculation formula for mutual inductance in multi-turn coil domains based on Neumann formula. The model of the coil is demonstrated in Figure II and the calculation expression is shown as Formula (9).

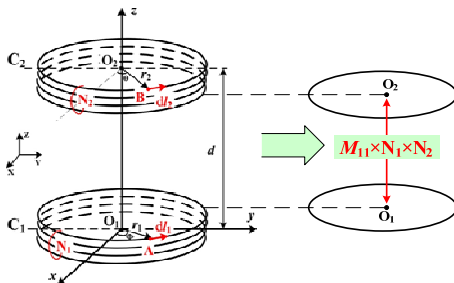


FIGURE II. CALCULATION MODEL FOR MUTUAL INDUCTANCE IN MULTI-TURN COIL DOMAINS BASED ON NEUMANN FORMULA

$$M = N_1 N_2 \frac{\mu_0}{4\pi} \oint_{C1} \oint_{C2} \frac{d\ell_1 d\ell_2}{|A - B|} \quad (9)$$

$$= N_1 N_2 \frac{\mu_0}{4\pi} \int_0^{2\pi} d\varphi \int_0^{2\pi} \frac{r_1 r_2 \cos(\theta - \varphi) d\varphi}{\sqrt{r_1^2 + r_2^2 - 2r_1 r_2 \cos(\varphi - \theta) + d^2}}$$

where C_1 and C_2 represent the serial numbers of the two coils, r_1 and r_2 are the radii of the two coils, Φ and θ denote the angles between arbitrary points on C_1 and C_2 coils with x axis, and $d\ell_1$ and $d\ell_2$ refer to the infinitesimal integral phasors of arbitrary points on the two coils. Moreover, d denotes the distance between the two coils, and N_1 and N_2 are the numbers of turns of the two coils.

As shown in Figure II and Formula (9), the approximate method of multiplying single-turn inductance by the number of turns of each coil is generally used to calculate the mutual inductance between multi-turn spatial spiral coils, while the winding height of the coils are ignored. The method has little calculation amounts and is easy to realize. However, the calculated results have great errors with the actual values.

Therefore, while designing a wireless power supply system, the coils need to be calibrated through experiments according to specific performance indexes. So the method has less theoretical guiding significance.

Aiming at the above problem, a more accurate calculation method for mutual inductance between coils is proposed based on the Neumann formula. Taking spatial spiral coils and disc spiral coils as examples, the detailed sketch map is illustrated in Figure III.

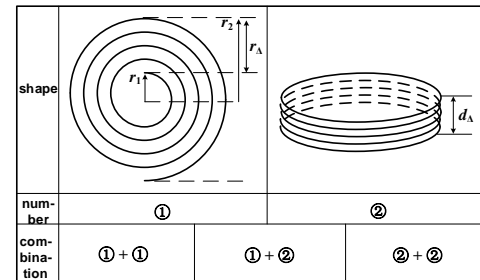


FIGURE III. CALCULATION MODEL FOR MUTUAL INDUCTANCE BETWEEN DIFFERENT COILS

There are two winding modes of wires in Figure III, where ① and ② represent the disc spiral coil and the spatial spiral coil, respectively, so there are three combination modes while designing the wireless power supply system for household appliances. In the figure, r_1 , r_2 , and r_Δ represent the inner radius, external radius, and their difference of the disc spiral coil, separately, and d_Δ denotes the height of the spatial spiral coil.

According to the Neumann formula, the coil radius and the transmission distance of wireless power supply systems are major variables determining the mutual inductance between coils. Taking spiral coils for an example, the actual mutual inductance between two spiral coils is less than the theoretical value calculated using Formula (9) due to the existence of the height of the coils. Therefore, the mutual inductance of power supply coils in different combination modes needs to be accurately calculated.

A. Combination Mode ①+①

Suppose that the transmit and receiving coils of a wireless power supply system are C_1 and C_2 which have N_1 and N_2 turns and an initial radius of r_1 . Moreover, the diameter of the winding wire is a , the space between turns is q , and the transmission distance is still d . Therefore, the mutual inductance between the coils can be represented as the cumulative sum of the mutual inductances of each turn of the coils, so

$$\sum_{j=1}^{N_2} M_{1j} = M_{11} + M_{12} + \dots + M_{1j} + \dots + M_{1N_2}$$

$$= M(r_1, r_1) + M(r_1, r_2) + \dots + M(r_1, r_j) + \dots + M(r_1, r_{N_2}) \quad (10)$$

$$= \sum_{j=1}^{N_2} M(r_1, r_j), \quad j \in [1, N_2]$$

where $r_j = r_1 + (j-1)(a+q)$. In this way, the mutual inductance between the two disc coils can be deduced as

$$\begin{aligned} M_{C_1 C_2} &= \sum_{j=1}^{N_2} M(r_1, r_j) + \cdots + \sum_{j=1}^{N_2} M(r_i, r_j) + \cdots + \sum_{j=1}^{N_2} M(r_{N_1}, r_j) \\ &= \sum_{i=1}^{N_1} \sum_{j=1}^{N_2} M(r_i, r_j), \quad i \in [1, N_1] \end{aligned} \quad (11)$$

where $r_i = r_1 + (i-1)(a+q)$.

B. Combination Mode ①+②

Suppose that C_1 and C_2 represent a disc spiral coil and a spatial spiral coil which have N_1 and N_2 turns, respectively. The disc spiral coil has an initial radius of r_1 and a space of q between turns. The initial radius and the space between turns of the spatial spiral coil are δ_1 and p . In addition, the diameter of the winding wire is a and the shortest distance between the two coils is d , so the mutual inductance between the two coils can be calculated using the following formula:

$$\begin{aligned} M_{C_1 C_2} &= \sum_{j=1}^{N_2} M(r_1, d_j) + \cdots + \sum_{j=1}^{N_2} M(r_i, d_j) + \cdots + \sum_{j=1}^{N_2} M(r_{N_1}, d_j) \\ &= \sum_{i=1}^{N_1} \sum_{j=1}^{N_2} M(r_i, d_j), \quad i \in [1, N_1], j \in [1, N_2] \end{aligned} \quad (12)$$

where $r_i = r_1 + (i-1)(a+q)$ and $d_j = d + (j-1)(a+p)$.

C. Combination Mode ②+②

Suppose that the spatial spiral coils in this combination mode have the same parameters with that in the combination mode of ①+②. Therefore, the calculation formula for the mutual inductance is

$$\begin{aligned} M_{C_1 C_2} &= \sum_{j=1}^{N_2} M(d_1, d_j) + \cdots + \sum_{j=1}^{N_2} M(d_i, d_j) + \cdots + \sum_{j=1}^{N_2} M(d_{N_1}, d_j) \\ &= \sum_{i=1}^{N_1} \sum_{j=1}^{N_2} M(d_i, d_j), \quad i \in [1, N_1], j \in [1, N_2] \end{aligned} \quad (13)$$

where $d_i = d + (i-1)(a+p)$ and $d_j = d + (j-1)(a+p)$.

IV. SIMULATION AND EXPERIMENTAL VERIFICATION

To verify the correctness of the theoretical analysis and the accuracy of the calculation for the mutual inductance, a wireless power supply device for tail-free household appliances was designed. In addition, a LCR tester was used to measure the actual mutual inductance between coils in different combination modes. On this basis, the authors discussed the relation between the optimal transmission performance of the power supply device for tail-free household appliances based on mutual inductance coupling and the mutual inductance.

Besides, the correctness and accuracy of the proposed accurate calculation method were verified as well.

To verify the accuracy of the proposed expression for calculating the mutual inductance, the values calculated using Formulae (9) and (11)~(13) were compared with the measured values. The experimental parameters are displayed in Table I.

TABLE I. PARAMETERS OF THE EXPERIMENTAL SYSTEM

	Number of turns	Inner radius (cm)	Wire diameter (mm)	Winding pattern
Coil mode ①	5~15	15	4	Close winding
Coil mode ②	5~15	20	4	Close winding
Input voltage (V)			10	
Transmission distance (cm)			15	
Load (DVD)			24 V/15 W	
Resonant frequency (kHz)			200	

Under conditions with the above coil parameters, the mutual inductances between coils with different numbers of turns were measured and compared with the theoretical value. In the experiment, the transmit and receiving coils always have same number of turns. The results are listed in Table II.

TABLE II. CALCULATED AND MEASURED MUTUAL INDUCTANCES IN DIFFERENT COIL MODES

Coil mode	Number of turns	Calculated value using Formula (9) (μH)	Accurately calculated value (μH)	Measured value (μH)	Error 1	Error 2
①+①	5	0.37	0.36	0.36	2.8%	0%
	10	2.05	2.04	2.03	1%	0.5%
	15	6.20	6.12	6.10	1.3%	0.3%
①+②	5	0.48	0.43	0.40	20%	7.5%
	10	2.28	1.85	1.83	24.6%	1.1%
	15	5.94	4.36	4.30	38.1%	1.4%
②+②	5	0.63	0.53	0.55	14.5%	3.6%
	10	2.53	1.69	1.77	42.9%	4.5%
	15	5.70	3.13	3.31	72.2%	5.4%

In Table II, error 1 represents the absolute error between the value calculated using Formula (9) and the measured value, and error 2 is that between the accurately calculated value with the measured value. The comparison between the values calculated using different formulae and the measured value reveals that the traditional calculation formula has a large error with the measured value and therefore cannot accurately guide the parameter design of the wireless power supply system. This is

because in the traditional calculation formula, the reference radius of coils and transmission distance are fixed when the coils have different numbers of turns. For this reason, the more the turns, the larger the error is. In comparison, all parameters of the proposed accurate calculation formula for mutual inductance are variables changing with the numbers of turns of coils, and therefore are more approximate to those of actual systems. Therefore, the calculated results using the proposed formula have a smaller error and can favorably guide the optimization design of the system, especially for the design of the mutual inductance in critical coupling involving the optimal transmission performance and the frequency splitting.

To more intuitively describe the changes of the mutual inductance with the numbers of turns of coils in wireless power supply systems, Figures VI(A), (B), and (C) show the changes of the mutual inductance in different combination modes of the coils.

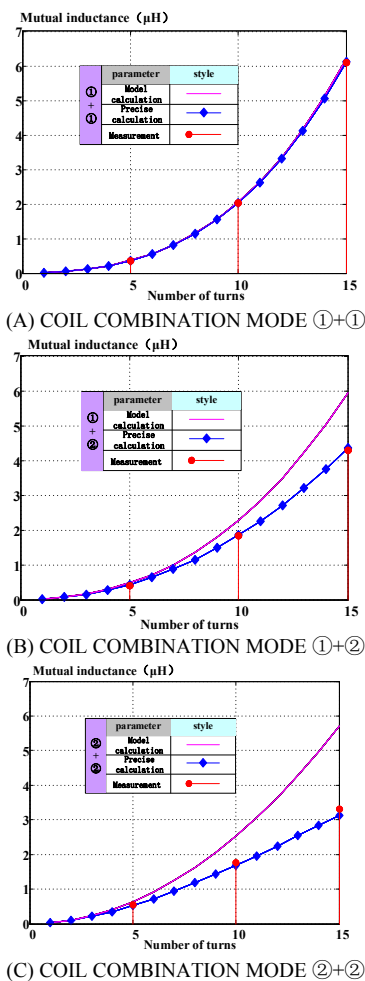


FIGURE IV. RELATIONS BETWEEN MUTUAL INDUCTANCE AND NUMBER OF TURNS IN DIFFERENT COMBINATION MODES OF COILS

By comparing the changes of mutual inductance in the three combination modes of coils in Figure IV, it is found that the mutual inductance between coils non-linearly augments with the increasing number of turns. In the combination mode of ①

+①, the calculated values using the traditional formula are well consistent with the accurate results calculated using the proposed formula and the measured values. While in the other two combination modes, the calculated value using the traditional formula cannot guide the parameter design of the wireless power supply system, which well agrees with the results in Table II.

According to Formula (8), when the wireless power supply system has the optimal transmission efficiency, the mutual inductance needs to be smaller than a constant under certain parameter combination of the system. Under the condition, no frequency splitting occurs to the wireless power supply system. Owing to the traditional calculation formula has large errors while guiding the design of the actual system, which leads to inaccurate and deviated optimal transmission performance, it calls for multiple calibrations in the actual system design according to experience. In comparison, the proposed accurate calculation formula can preferably guide practical system design. Figures V to VII show the curves of transmission performances of the system in different combination modes of coils with parameters in Table I.

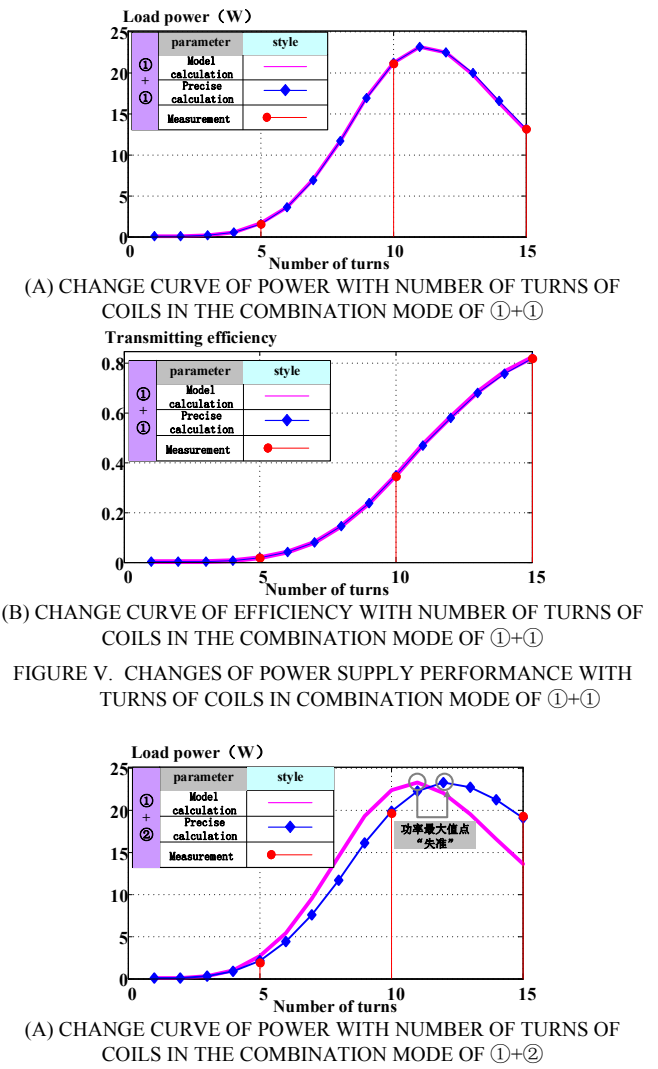
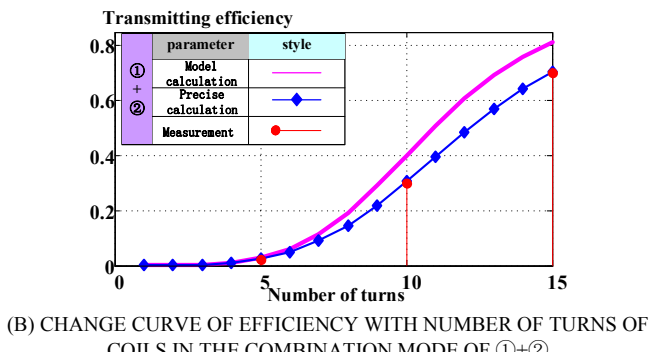
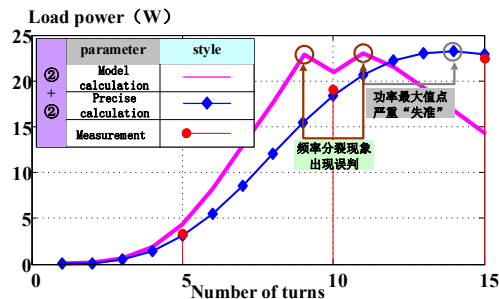


FIGURE V. CHANGES OF POWER SUPPLY PERFORMANCE WITH TURNS OF COILS IN COMBINATION MODE OF ①+①

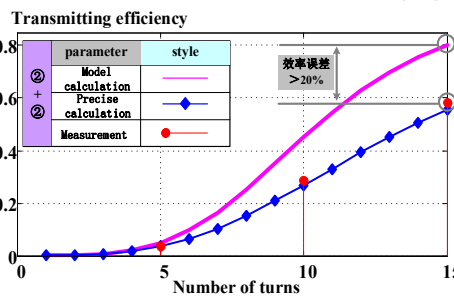


(B) CHANGE CURVE OF EFFICIENCY WITH NUMBER OF TURNS OF COILS IN THE COMBINATION MODE OF ①+②

FIGURE VI. CHANGES OF POWER SUPPLY PERFORMANCE WITH TURNS OF COILS IN COMBINATION MODE OF ①+②



(A) CHANGE CURVE OF POWER WITH NUMBER OF TURNS OF COILS IN THE COMBINATION MODE OF ①+②



(B) CHANGE CURVE OF EFFICIENCY WITH NUMBER OF TURNS OF COILS IN THE COMBINATION MODE OF ②+②

FIGURE VII. CHANGES OF POWER SUPPLY PERFORMANCE WITH TURNS OF COILS IN COMBINATION MODE OF ②+②

It can be seen from the above change curves that the transmission efficiency of the system grows with the increasing number of turns of coils. When one or two spatial spiral coils (coil ②) exist in the wireless power supply system, the theoretical values obtained using the traditional calculation formula differ greatly from the experimental results and exert certain disturbance to the system design. Meanwhile, the mutual inductance and the power-supply power of loads do not absolutely monotonously augment, as shown in Figure V(A). In Figures VI(A) and VII(A), the points of maximum power are inaccurate and deviated, which is caused by the inaccurate calculation of the mutual inductance. Moreover, frequency splitting occurs to the power-supply power of loads calculated using the traditional formula in Figure VII(A). If the resonators of the power supply system of tail-free household appliances are designed according to the change curve, the power-supply power with planned number of turns (9 turns for instance)

cannot meet the power demand for loads. Finally, experiments were carried out to verify the correctness of the theoretical analysis in the research and the experimental results were found to be basically consistent with the theoretical results obtained using the accurate calculation method proposed in the research.

V. CONCLUSIONS

Based on the significance of resonator design in elevating the performance of the power supply system of tail-free household appliances, the theoretical modeling method for circuits is adopted to analyze the coupling optimization of resonators. To get rid of the influences of the frequency splitting probably happening in the design process on the transmission performance of the power supply system, the analytic calculation is conducted to obtain the advisable domain value of mutual inductance that can avoid frequency splitting. On this basis, to obtain the accurate mutual inductance between resonators, the authors also carry out theoretical calculation in different combination modes of disc spiral coils and spatial spiral coils. The calculation method for mutual inductance more accurate than the traditional Neumann formula is proposed. Finally, the theoretical analysis in the research was verified through experimental measurement and comparison. The research is of great significance for improving the transmission performance of the power supply system of tail-free household appliances and avoiding the occurrence of frequency splitting.

ACKNOWLEDGEMENT

This research is supported by China Southern Power Grid Corporation (Research and Application of Key Technologies of Intelligent Cloud Service in Hainan Power Grid).

REFERENCES

- [1] Huang Huiqun, Dong Xiulan, Li Dan, et al. Research on wireless transmission technology in the application of home appliance. *China Appliance*, 2012, 14(S1): 644-648(in Chinese).
- [2] Huang Xueliang, Wang Wei, Tan Linlin, Technical progress and application development of magnetic coupling resonant wireless power transfer. *Automation of Power Systems*, 2017, 41(2): 2-14(in Chinese).
- [3] TESLA N. The transmission of electric energy without wires. *The Thirteenth Anniversary Number of the Electrical World and Engineer*, Mar. 5, 1904, New York, USA.
- [4] Kurs A, Karalis A, Moffatt R, et al. Wireless power transfer via strongly coupled magnetic resonances. *Science*, 2007, 317(5834): 83-86.
- [5] Abdolkhani A, Hu A P, Moridnejad M, et al. Wireless charging pad based on travelling magnetic field for portable consumer electronics. *2013*, 45(11): 1416-1421.
- [6] Li Changsheng, Zhang He, Cao Juan, et al. Analysis and optimal design for power and efficiency transmission characteristics of magnetic resonance coupling power transmission systems. *Automation of Electric Power Systems*, 2015, 39(8): 92-97(in Chinese).
- [7] Zhang Xian, Yang Qingxin, Cui Yulong, et al. Design optimization and verification on the power transmitting coil in the high-power wireless power transmission system. *Transactions of China Electrotechnical Society*, 2013, 28(10): 12-18(in Chinese).
- [8] Nguyen V T, Kang S H, Choi J H, et al. Magnetic resonance wireless power transfer using three-coil system with single planar receiver for laptop applications. *IEEE Transactions on Consumer Electronics*, 2015, 61(2): 160-166.

- [9] Wang W, Huang X L, Guo J P, et al. Power stabilization based on efficiency optimization for WPT systems with single relay by frequency configuration and distribution design of receivers. *IEEE Transactions on Power Electronics*, 2017, 32(9): 7011-7024.
- [10] Yeo T D, Kwon D S, Khang S T, et al. Design of maximum efficiency tracking control scheme for closed-loop wireless power charging system employing series resonant tank. *IEEE Transactions on Power Electronics*, 2017, 32(1): 471-478.
- [11] Zhao Zhengming, Zhang Yiming, Chen Kainan. New progress of magnetically-coupled resonant wireless power transfer technology. *Proceedings of the CSEE*, 2013, 33(3): 1-13(in Chinese).
- [12] Wang Wei, Huang Xueliang, Tan Linlin, et al. Effect analysis between resonator parameters and transmission performance of magnetic coupling resonant wireless power transmission system. *Transactions of China Electrotechnical Society*, 2015, 30(19): 1-6(in Chinese).

Research on Networked Sliding Mode Predictive Controller Based on Particle Swarm Optimization

Yang Yin*, Hongke Li and Zhengying Ren

College of Electrical Engineering, Naval University of Engineering, Wuhan, China

*Corresponding author

Abstract—Aiming at the development of ship information and intellectualization, this paper researched the control law design problems of the network control system under total ship computing environment (TSCE). Firstly, we analyzed and constructed the computing environment network architecture for the development of ship intelligent information technology. Then, the sliding mode predictive control law based on particle swarm optimization was designed for the delay and packet loss problem caused by information network. The control strategy and realization method were analyzed, and the actual control quantity selected at each moment was the optimal sliding mode prediction control signal provided by the actuator. The simulation results showed the effectiveness and robustness of the proposed algorithm.

Keywords—Total Ship Computing Environment (TSCE); Networked Control Systems (NCS); Sliding Mode Predictive Control; Particle Swarm Optimization Algorithm (PSO)

I INTRODUCTION

With the development of intelligent technology of new ship information technology, the research of integrated platform system with interconnection, intercommunication and interoperation is getting more and more attention. Intelligent ship total ship computing environment (TSCE) is a new generation of shipboard integrated system which is leading changes in design and integration mode of ship system [1]. Replacing the original independent control system with network control, make numerous such as sensors, actuators and controllers are connected through the network, can make the ship's architecture flattening and greatly improve the level of ship automatic control and intelligent management. However, problems such as the delay of the network itself, packet loss, communication constraints and multi-packet transmission will inevitably lead to the change of system control strategy, namely, Networked control systems (NCS) [2-5]. Therefore, it is of great practical significance to study the control technology under the TSCE network. This paper focuses on the ship TSCE system structure and its control network system optimization. Inspired by the discrete sliding mode predictive control method [6], we design the sliding mode predictive controller based on particle swarm optimization [7,8]. And then study the control strategy and the implementation method, in order to reduce the influence of network on the control system performance and guarantee system robustness under external disturbance.

II TSCE ARCHITECTURE AND NETWORK CONTROL MODELING

The TSCE has three tiers: Core, Adaptation, and Presentation. The Core Tier provides a common environment hosting the majority of the software applications on a redundant infrastructure whose targeted hardware location is designed to be transparent to the applications. The Adaptation Tier utilizes much more compact hardware to provide a means to integrate software into the TSCE. The Presentation Tier is that part of the TSCE responsible for rendering displays on the consoles. Its control hierarchy network configuration is shown in Figure I.

DCU is distributed control units. DAP is Distributed Adaptation Processors which perform function of controller and interface to other applications running in the TSCE infrastructure. RTU is remote terminal units that work as the interface to the engineering plant equipment, just like Soft PLC application and Ladder Logic to control and drive the remotely located I/O, and so on. HCI is Human Computer Interface.

Mainstream industrial Ethernet technologies include PNO Profinet, EPSG Powerlink, ODVA Ethernet/IP, ETG EtherCAT and EPA. EPA is the first field bus national standard with independent intellectual property rights in China. Regardless of which network technology is chosen, the network problem of delay packet loss is brought to the control system.

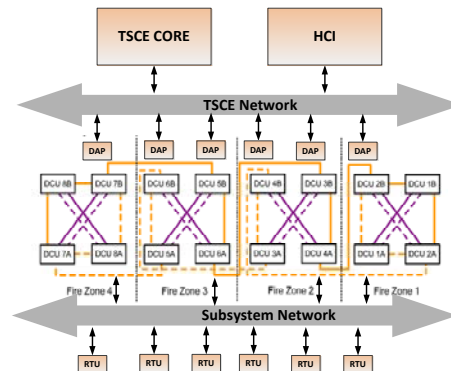


FIGURE I. TSCE CONTROL HIERARCHY NETWORK CONFIGURATION

Consider the discretization model of a class of network control systems under TSCE.

$$x(k+1) = Ax(k) + Bu_a(k) + G \cdot M(k) \quad (1)$$

Where $x(k)$ is the state, $M(k)$ is expressed as an external disturbance. U_a represents the input control amount of the system executor. Because the introduction of TSCE network, the controller and actuator information transmission may be time delay or packet loss. So some moments actuator may receive less information than the controller transmission. Thus cause control performance degradation and even lead to instability. This paper intends to use the sliding model predictive controller based on particle swarm to produce multi-step input predictive control values. And then set buffer zone in front of actuators, storing the predictive control values. According to the actual network conditions to select the latest optimizing control values control the controlled object. The typical network control system model block diagram is shown in Figure II.

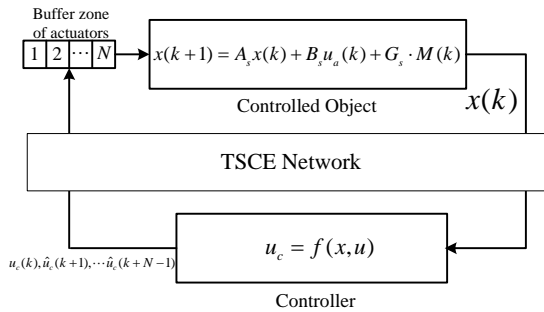


FIGURE II. BLOCK DIAGRAM OF TSCE NETWORKED SYSTEM

III PREDICTIVE CONTROL OF NETWORK SLIDING MODE BASED ON PARTICLE SWARM OPTIMIZATION

The traditional design of discrete variable structure control method usually use uncertain bound as the prerequisite to ensure the robust stability of closed-loop system. Due to consider condition is the worst, cause controller is too conservative and chattering. In order to solve this problem, a discrete sliding mode prediction controller based on particle swarm optimization is designed. After the controller receives the sensor signal at current moment, the discrete sliding mode prediction algorithm with particle swarm optimization is used to generate certain predictive steps control signal.

A. Discrete Sliding Mode Predictive Control

Firstly, we give the analysis and modeling of the control algorithm of sliding mode prediction function. Consider the system (1) and define the linear sliding mode function.

$$s(k) = Cx(k) \quad (2)$$

The ideal sliding mode must satisfy the motion equation of the following system:

$$\begin{cases} x(k+1) = A_s x(k) + B_s u_a(k) \\ Cx(k) = 0 \end{cases} \quad (3)$$

The sliding surface is determined by quadratic optimal control or pole assignment. Regardless the presence of parameter perturbation and external disturbance or not, the movement of the system starting from any initial state can be reached in neighborhood of the sliding mode surface within limited time and stability. Then act into a quasi sliding mode motion.

The nominal model of system (1) is used as the prediction model.

$$x(k+1) = A_s x(k) + B_s u_a(k) \quad (4)$$

The predicted time domain is N and the prediction value of the sliding mode function of the future P step is

$$s_y(k+p) = CA^p x(k) + \sum_{i=1}^p CA^{i-1} Bu(k+p-i) \quad (5)$$

Using the error between the current measured value and the predicted value, the predicted value of the future time is corrected as:

$$\begin{aligned} \hat{s}_y(k+p) &= s_y(k+p) + H_p [s(k) - s_y(k|k-p)] \\ &= CA^p x(k) + \sum_{i=1}^p CA^{i-1} Bu(k+p-i) + H_p [s(k) - s_y(k|k-p)] \end{aligned} \quad (6)$$

Where $s_y(k|k-p)$ Denotes the predicted k step value of the sliding mode at time $k-p$. The correction factor is $h_p \in R$, usually choose $h_1 = 1$.

$$s_y(k|k-p) = CA^p x(k-p) + \sum_{i=1}^p CA^{i-1} Bu(k-i) \quad (7)$$

Then we select the optimization index:

$$J_E = \sum_{p=1}^N q_p [\hat{s}_y(k+p) - s_r(k+p)]^2 + \sum_{p=1}^N r_p [u(k+p-1)]^2 \quad (8)$$

Where q_p, r_p are the weighted coefficients, $s_r(k+p)$ is sliding mode reference trajectory.

The reference trajectory is a desired trajectory. The selection of sliding mode reference trajectory determines the final form of the variable structure control law obtained. Therefore, we select the most commonly used index approach rate as the sliding mode reference trajectory.

$$\begin{cases} s_r(k+p) = (1-qT)s_r(k+p-1) - \varepsilon T \operatorname{sgn}(s_r(k+p)) \\ s_r(k) = s(k) \end{cases} \quad (9)$$

Where $\varepsilon > 0, q > 0, 1 - qT > 0$.

Control problem is transformed into search $u^*(k)$ to makes the performance index J_E optimum. According to the Eq.6, the input and state of the past and present time can pass out the input of the future time. Then rolling optimization, find out the optimal control input. In this paper, particle swarm optimization algorithm is proposed to solve this optimization problem.

B. Particle Swarm Optimization

Particle swarm optimization (pso) is an evolutionary algorithm based on group bionics, which mainly uses information sharing and group evolution mechanism in biological groups. In recent years, particle swarm algorithm has been developed rapidly and successfully applied to various optimization problems.

The basic idea of particle swarm algorithm is as follows: the solution of optimization problem is regarded as a point (d dimension particle) in the search space. Several particles constitute a group. The pros and cons of each particle performance depends on fitness value of objective function of optimization problem. The particle velocity determine the direction and speed of flight. All particles follow the current optimum particles search in the solution space. The algorithm firstly initializes a group of random particles (candidate solution) and then finds the optimal solution by gradual iteration. Each particle represents a candidate solution, and the position and velocity relation of the particle can be described as:

$$v_{ik}(t+1) = wv_{ik}(t) + c_1r_1(p_{ik}(t) - x_{ik}(t)) + c_2r_2(p_{gk}(t) - x_{ik}(t)) \quad (10)$$

$$x_{ik}(t+1) = x_{ik}(t) + v_{ik}(t+1) \quad (11)$$

Where k is Pointer of iterations, x_k is current position of particle at iteration k , v_k is the velocity of particle at iteration k , c_1, c_2 is acceleration constant, w is inertia weight factor. $P_i = (p_{i1}, p_{i2}, \dots, p_{id})$ represents the individual extreme value, $P_g = (p_{g1}, p_{g2}, \dots, p_{gd})$ represents the group global extreme value.

In the iterative process, the particle can update its own speed and position by tracking individual extremum and group global extreme values. Formula (10) mainly calculates the new velocity of the first particle through three parts. First part is the velocity of the first particle at the first moment. The second is the distance between the current position and its best position. The

third is the distance between the current position and the best position of the group. The particle swarm algorithm has less parameters, simple operation, and the initial convergence performance is excellent.

IV IMPLEMENTATION FOR PSO OPTIMIZATION SLIDING MODE PREDICTION CONTROL

Because the standard particle swarm algorithm is easy to get into local optimum, and combined with TSCE network characteristics, this paper selects the specific implementation steps of particle swarm prediction control algorithm.

Step 1: Particle swarms initialize. Identify TSCE network delay, set the population size. Then set the upper and lower limit of the search space, limit the maximum speed and minimum speed of the particle, and initialize the position and velocity of the particle;

Step 2: The fitness of the particle is calculated. The optimization objective function formula (9) of the particle is calculated so that the formula (8) is satisfied.

Step 3: Calculate individual extremum and global extremum. Initializes the initial individual extreme point P_i of each particle and sets it to the initial position. The best setting in P_i is set as the fitness value P_g of the initial global extreme point. Then the individual extremum and global extremum of each step are updated successively.

Step 4: The dynamic shrinkage factor method is selected to adjust the weight coefficient to avoid getting into local optimum.

$$w(k) = w_{\min} + \frac{k_{\max} - t}{k_{\max}}(w_{\max} - w_{\min}) \quad (12)$$

Where k_{\max} is maxima pointer of iterations, w_{\max} is maxima inertia weight factor, w_{\min} is minimum inertia weight factor, v_k is Velocity of particle at iteration k .

Step 5: According to Eq.9, Eq.10, Eq.10, adjust the position and velocity of the particle.

Step 6: Check the termination condition: when the maximum number of iterations is reached or the desired precision is reached, the iteration is terminated, otherwise the step 2 is returned. The optimal value $u^*(k)$, $u^*(k+1)$, ..., $u^*(k+N-1)$ of the group control quantity of the time is stored in the actuator end buffer after network transmission. According to the situation of network actual delay packet loss, the corresponding control actuator is selected to realize the control of TSCE control system.

V SIMULATION EXAMPLE

Suppose a ship TSCE network control system is modeled as equation (1). The nominal parameters are as follows:

$$\begin{cases} x(k+1) = \begin{bmatrix} 1 & 0.08198 & 0.0005247 \\ 0 & 0.6412 & 0.004486 \\ 0 & -3.068 & -0.02147 \end{bmatrix} x(k) + \begin{bmatrix} -0.449 \\ -8.943 \\ -76.46 \end{bmatrix} u_a(k) + M(k) \\ y(k) = [1 \ 0 \ 0]x(k) \end{cases} \quad (13)$$

Where the Uncertainty is

$$M(k) = \sigma\% \begin{bmatrix} 0 & 1 & 1 \end{bmatrix}^T [1 + \sin(3\pi k / 20)] \quad (14)$$

Take the sliding mode surface parameter as $C = [47 \ 12 \ 1]$ and approach the law parameter as $q = 5$, $\varepsilon = 1$, $Q, R, H = \text{diag}[1, 1, 1]$. $\sigma\%$ is the percentage of interference. The predicted number of steps is greater than or equal to the maximum time delay period of the actual network. Networked sliding mode predictive controller based on particle swarm optimization design is adopted, and the performance of the system is analyzed. The unit step response of the system is shown in the red real curve in Figure III when the system has five percent constant value disturbance and sinusoidal disturbance. The response curve of the system with fifteen percent constant value disturbance and sinusoidal perturbation is shown in Figure VI. In order to facilitate comparison, the virtual curve represents the step response curve of the system with the traditional pole assignment control algorithm and without PSO optimization.

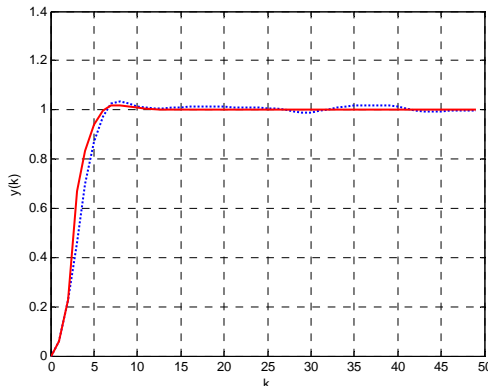


FIGURE III. SIMULATION RESULTS WITH FIVE PERCENT INTERFERENCE

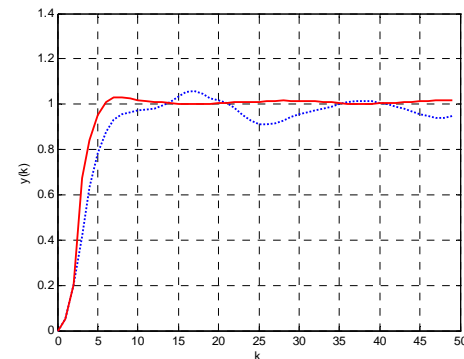


FIGURE IV. SIMULATION RESULTS WITH FIFTEEN PERCENT INTERFERENCE

The simulation results show that, when the system interference is less and due to the influence of the network, the traditional method has a slow response speed and a certain steady-state error. When the interference of the system increases, the traditional method can not track input effectively, and there is a possibility of large oscillation. In contrast, using networked sliding mode predictive controller based on particle swarm optimization, The system has good dynamic and steady state performance. And it has strong robustness against external disturbance and certain network delay.

VI SUMMARY

According to the trend of intellectualized development of ship information, this paper studied the network control problem of the system under ship's TSCE network. Based on particle swarm optimization, a sliding mode prediction control strategy was designed and its concrete realization steps were given. The simulation results showed that the proposed algorithm was reasonable and effective. Next, we will continue to study the method of combining the characteristics of TSCE network with the control theory to improve the performance of the ship control systems.

REFERENCES

- [1] DONG Xiao-ming, SHI Chao-ming, etc. Analysis on the Architecture of USN DDG-1000 Total Ship Computing Environment. Chinese Journal of Ship Research. 2012, 7(6), 7-15.
- [2] Liu, Y.-C & Liu, B & Zhang, Y & Li, W.-G. Stability analysis for networked control systems with bilateral random delay and packet dropout. Control and Decision. 2017, 32, 1565-1573.
- [3] Xie, R & Fan, W & Wang, C & Chen, Q. Dead band scheduling and control co-design method for uncertain networked control systems. 2016, 40, 643-652.
- [4] J.Baillieul and Panos J.Antsaklis. Control and communication challenges in networked real-time system. Proc. IEEE, vol.95, no.1, Jan.2007, 9-28.
- [5] Li Hong-bo, SUN Zeng-qi, SUN Fu-chun. Networked control systems: an overview of state-of-the-art and the prospect in future research. Control Theory & Applications, 2010, Vol. 27, No.2, pp.238-243.
- [6] Song lizhong, Chen shaochang, Yao qionghui. Predictive discrete variable structure control [J]. Control theory and application, 2004, 21(5), 826-829.
- [7] DAI Yong-bin. Analysis and Simulation Research on Nonlinear Predictive Control Based on Particle Swarm Optimization. Journal of

Liaoning University of Technology (Natural Science Edition). Vol.34, No.6, Dec.2014:360-363.

- [8] Gao peng, liu haoran, hao xiaochen, et al. Research on predictive control of hybrid model based on particle swarm optimization [J]. Mechanical and electrical engineering, 2012, 28(2): 231-234.

Automated Detecting System for Elevator Guide Rails Based on Tilt Sensors and Acceleration Sensors

Yifeng Yang¹, Wei Guo², Yujun Wang² and Wenxiu Lu^{3,*}

¹Department of Mechanical Engineering, Tsinghua University, Beijing, China

²Hubei Special Equipment Inspection and Testing Institute, Wuhan, China

³Department of Mechanical Engineering, Tsinghua University, Beijing, China

*Corresponding author

Abstract—Straightness, verticality and step height deviation are the main parameters to evaluate the safe and stable operation of the elevator. One kind of automated detecting system is devised to detect these multiple parameters of elevator guide rails at the same time exactly and efficiently. The detecting system, which is powered by a traction machine, is based on tilt sensors and acceleration sensors. The detecting system can verify the installation of elevator guide rails and the detection efficiency can be greatly improved.

Keywords—elevator guide rails; straightness; verticality; step deviation

I INTRODUCTION

The Straightness, verticality and step height deviation of the elevator guide are the most important parameters that affect the operation of the elevator. The verticality error of elevator guide rail is one of the main factors that cause vibration and acceleration wear of elevator cab, and straightness error directly affects the comfort of elevator operation. The step deviation affects the stability of elevator operation.

The traditional measurement techniques for elevator guide rails are based on hand tools. The inspectors use feeler and guide rule to measure the deviation between the guide rails and a plumb line. In recent years, with the rapid development of the elevator industry, new methods to detect elevator guide rails efficiently become increasingly concerned. Some methods are proposed by many researchers. Liu and Chen [1] designed a system combined by an automatic-climbing robot and a laser sensor to detecting the guide rails. Laser sensor is accurate enough, but the volume of the robot is too larger for some scenarios. Noguchi, Naoaki [2] used an acceleration sensor, which was installed on a platform connected to the elevator cabs, to analyze the step deviation. The data acquired by the sensor can be dealt with to figure out the deviation. The system cannot be used before the installation of elevator cab because of without the power system. Liu [3] used a tilt sensor to measure the verticality of the guide rail. The system used long time step to measure the verticality. Long time step method is more convenient than continuously sampling, but has lower accuracy at the same time. An [4] compared several methods and devices, then the limits of different methods are pointed out in the paper. In paper [5-6], a method based on vibration analysis is put forward; a model of platform was designed to describe vibration. Some technologies including neural

network and computer vision are applied to detect the elevator guide rails, some positive result has been gotten [7-8].

The single error of the elevator guide can be detected only by the methods above. If all the error of the elevator need to be detected, it is very difficult to replace the different measuring devices, which is time-consuming. This paper proposed an automated detecting system based on tilt sensors and acceleration sensors. The precision, sensitivity and stability in this automated detecting system are better than traditional measurement technique. The measurements of multiple parameters such as straightness, verticality and step height deviation of the elevator guide are fully automated one time.

II PRINCIPLE AND STRUCTURE

A. Structure of System

As shown in Figure I, the structure of the whole system consists of three parts: traction system, measurement platform and base station. The measurement platform is driven by a traction machine, which can avoid the vibration and noise of motor in the measurement platform. The control system receives the signal transmitted by the base station, and then controls the measure platform to complete the detecting task. The speed of the platform is on-line controllable, and the design improves the accuracy.

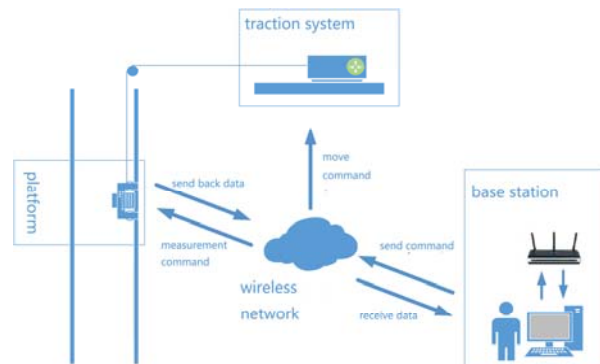


FIGURE I. STRUCTURE OF WHOLE SYSTEM

B. Measurement Platform

The measurement platform carries a SCM-based control system. One guide rail has three work surfaces, as shown in Figure II, including two side guiding surfaces and one top

surface. Two tilt sensors and one acceleration sensor are assigned to each work surface.

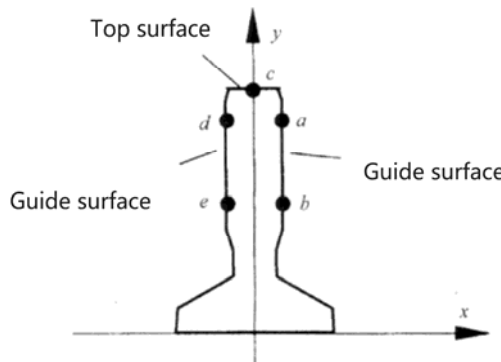


FIGURE II. WORK SURFACES OF GUIDE RAIL

Tilt sensors measure the angle in order to detecting the straightness and verticality of guide rails. Acceleration sensors measure the vibration of platform, the data can be processed to detect the step deviation at the joints. The system is shown in the Figure III.

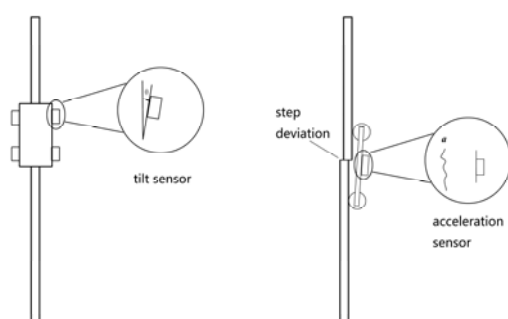


FIGURE III. WORK SURFACES OF GUIDE RAIL

The width of guide surface or guide rails is range from 10mm to 36mm. A adaptive platform is designed to apply to different types of guide rails. The electromagnetic wheels installed on the platform located the platform on the guide surface. The magnetic intensities can be controlled in order to adapt to different working conditions. If the guide surface is smooth, user can raise the magnetic force to prevent derailment. The platform is shown in Figure IV.

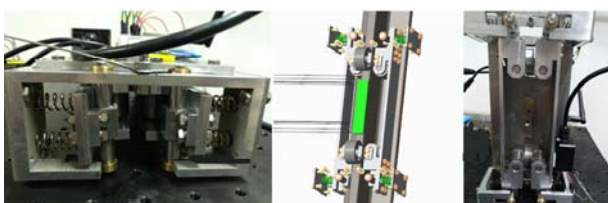


FIGURE IV. MEASUREMENT PLATFORM

There are three kind of acceleration sensor to be chosen, liquid tilt sensor, solid tilt sensor, mems acceleration sensor.

Liquid tilt sensor is chosen for the system because the liquid tilt sensor has damping so that it can filter high frequency noise. The sensor can measure the tilt angle of two axes. The accuracy of the sensor is 0.01°.

The data from the sensors is transmitted to the base station through the wireless transceiver system. The height of elevator guide rails can range from 10 m to 100 m. The commonly used wireless module is based on 2.4 Ghz. The transmission distance of 2.4 Ghz module is shorter than 433 Mhz module, when they work in same power. The 433 Mhz wireless module is chosen for the system. The transmission distance of the wireless transceiver system is 1000m.

C. Base Station System

Base station system consists of a computer and a wireless module. Relevant software is developed in the compute to control the traction system and to deal with the data measured by the sensors. Users can real-time monitor the state of the measurement platform, in case of colliding and derailment. The software will deal with the data to get the deviation of the three surfaces of guide rail, and then display the result as curve on the screen of the computer in real time. The data and the result will be stored in the disk for future reviewing.

Base station system is shown in Figure V.



FIGURE V. BASE STATION

D. Software System

The software system consists of three parts: control software, data processing software and the embedded software.

The control software is installed in the compute of the base station system. The function of the software is to control and monitor the platform. There are two interfaces in the software, the one is to monitor the platform, the other one is to control the traction system.

The data processing software is used to deal with the data submitted by the sensors. And the results will be shown on the interface as curve. A method based on wavelet analysis is applied in the software to eliminate the noise. The precision of the result is higher than traditional methods.

The embedded software is installed in the SCM-based control system. The software will communicate with the base station to control the platform.

Figure VI shows the interface of the software.

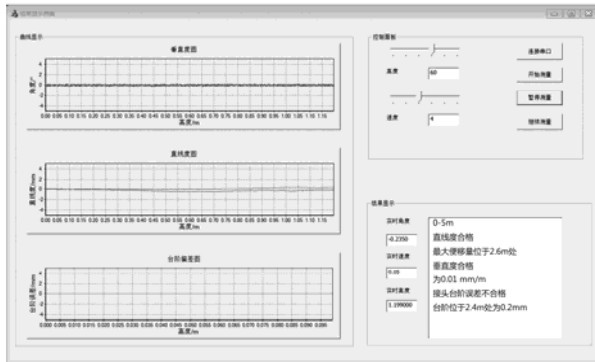


FIGURE VI. SOFTWARE INTERFACE

III EXPERIMENT

Several experiments were conducted to test the whole system. A self-leveling laser collimator is used to calibrate the system. And then the tools stipulated in the China standard including guiding rule and feeler are used to get result as control group. Our automated system has a higher accuracy than traditional methods. Figure VII shows the straightness measurement value of different methods.

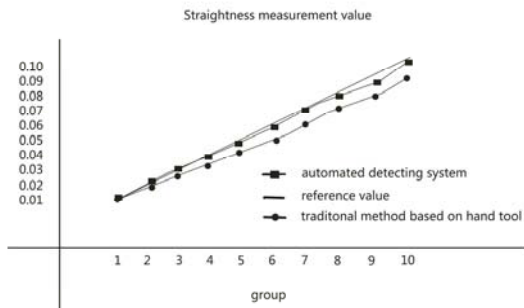


FIGURE VII. STRAIGHTNESS MEASUREMENT VALUE

IV SUMMARY

This system realized automated measurement of straightness, verticality, step deviation, of elevator guide rails. The accuracy of the result is better than previous methods. The system simplified the detecting process. In the future, more signal processing methods will be applied to improve the accuracy, and the platform will be redesigned to simplify structure and reduce the size. High-speed wireless module could possibly raise stability of the whole system.

ACKNOWLEDGEMENT

This research was financially supported by the National Science Foundation of China (Grant No. 51335006).

REFERENCES

- [1] Wenang Liu, Li Chen, Xu zhiliang, The design of automatic straightening machine system for high precision elevator guide rails, Proceedings of the 33rd Chinese Control Conference, 2014, pp.2964-2968.
- [2] Noguchi, Naoaki, Identification method of elevator rail deformation using operational acceleration data, Japan Society of Mechanical Engineers, 2012.
- [3] Liu zhidong, Research on the perpendicularity detection robot of elevator guide based on tilt angle detection, Hebei University of Technology, 2011.
- [4] Hongyun An, Study on the measurement method and experiment of the straightness of the elevator guide, Beijing Jiaotong University, 2008.
- [5] Qianyin Zhang, The development of the inspection system for the straightness and distortion of the elevator guide, China Plant Engineering, 2017, Vol 4.
- [6] Zhou Lei, Modeling, simulation and experiment for straightening lateral bending of elevator guide rail, Journal of Central South University, 2011, pp.1636-1642.
- [7] Yu Qin, Jingjing Wu, Wei An, Meijuan Zhang, Research on automatic measurement system of elevator guide rail based on binocular vision, Modern Manufacturing Engineering , 2017, No 6.
- [8] Kai Wang, Baoyu Wang, Chuancheng Yang, Calculation of elevator guide straightening based on Neural Network, Machinery Design & Manufacture, 2012.

An EMC Study on Intentional Transmitter of Railway Train Base on Poynting Vector

Ping Sun

National Engineering Research Center of Railway Vehicles, CRRC Changchun Railway Vehicles CO., LTD, Changchun, 130062, China.

Abstract—Base on Poynting Vector to determine the field strength sensitive boundary between the intentional transmitter antenna and the equipment or apparatus installed on railway train. A detail calculation is made to analyse radiation field strength. This paper focuses on how to determine the far field of the rod antenna. By analyzing the radiation field strength of the antenna, it is beneficial to determine the layout design of the antenna on the vehicle at the beginning of the design.

Keywords—EMC; intentional Transmitter; poynting vector

I. INTRODUCTION

This paper presents a way to determine the boundary of intentional transmitter, which is sensitive to the equipment or apparatus installed on railway train.

Equipment or apparatus installed on railway train complies with the EN 50121-3-2 EMC Standard. The Standard applies to emission and immunity aspects of EMC for electrical and electronic apparatus, and it states the radiated emission requirement in this standard is not intended to be applicable to the intentional transmission from a radio-transmitter as defined by the ITU.

Intentional transmitter is a high field strength source. Near it, the field strength may exceed the equipment's resistance. Base on Poynting Vector, the boundary can be calculated.

The field strength in the near field is complex and not easy to calculate. The field strength in the far field is easy to calculate. This paper focuses on how to determine the far field of the rod antenna.

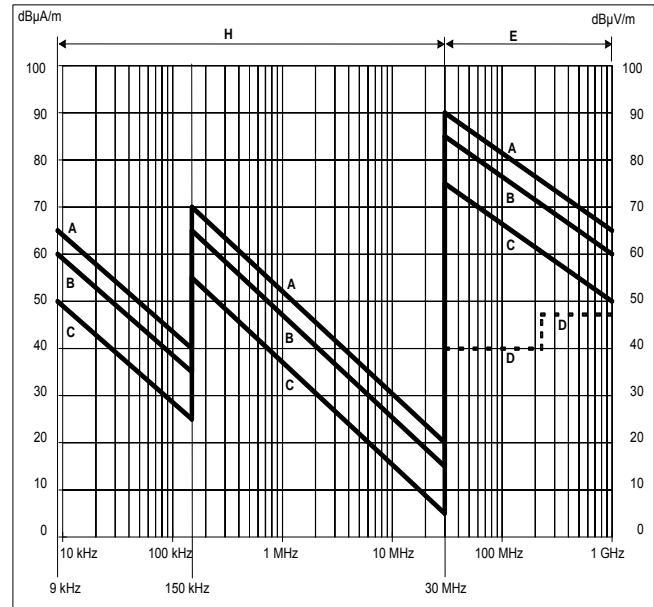
II. EN 50121 REQUIREMENTS

A. Train Unintentional Transmitters Emission Limit

The train has many electronic and power electronics switching devices which are capable of generating electromagnetic disturbances.

All of the systems on the train are designed and tested to satisfy the limits of EN50121-3-1 and EN50121-3-2:2006.

This limits the radiated emissions for the train and systems below 50kVA are shown in Figure 1.



NOTE 1. Emission limits
 A = 25 kV a.c.
 B = 15 kV a.c., 3 kV d.c. & 1.5 kV d.c.
 C = 750 V & 800 V d.c., including trams/trolleybuses for use in city streets
 Limits for slow moving test(Peak, 10m)
 D = Equipment limits (QP, 10m)

FIGURE I. UNINTENTIONAL RADIATED EMISSION LIMITS FOR EQUIPMENT AND TRAIN [1, 2]

B. Equipment or Apparatus Immunity Level

The Radiated Immunity Level of the equipment or apparatus installed on railway train refers to Table 1.

TABLE I. RADIATED IMMUNITY LEVEL OF THE EQUIPMENT OR APPARATUS [1]

	Environmental Phenomena	Test specification		Basic Standard	Test set-up	Applicability note	Remarks	Performance criteria
1	Radio-frequency electromagnetic field. Amplitude modulated	80 MHz to 800 MHz 20 V/m (rms) 80 % AM, 1 kHz	Unmodulated carrier	EN 61000-4-3	EN 61000-4-3	See a and b	The test level specified is the rms value of the unmodulated carrier	A
2	Radio-frequency electromagnetic field, from digital communication devices	800 MHz to 1000 MHz 20 V/m (rms) 80 % AM, 1 kHz	Unmodulated carrier	EN 61000-4-3	EN 61000-4-3	See b	The test level specified is the rms value of the unmodulated carrier	A
		1400 MHz to 2000 MHz 10 V/m (rms) 80 % AM, 1 kHz						
		2000 MHz to 2700 MHz 5 V/m (rms) 80 % AM, 1 kHz						
		5100 MHz to 6000 MHz 3 V/m (rms) 80 % AM, 1 kHz						
a This limit applies to equipment mounted in the passenger compartments, drivers cab or external to the rolling stock (roof, underframe). For equipment mounted in all other areas a severity level of 10 V/m may be used. b For large apparatus (e.g. traction drives, auxiliary converters) it is often not practical to perform the immunity test to radiated electromagnetic fields on the complete unit. In such cases the manufacturer should test susceptible sub-systems (e.g. control electronics). The test report should justify the selection or not of sub-systems and any assumptions made (e.g. reduction of field due to case shielding).								

The key characteristics are detail in Table 2 and Table 3.

III. INTENTIONAL TRANSMITTER

The Intentional Transmitter is called Train Radio, it is a Tetra system, which is Terrestrial Enhanced Trunked Radio [4].

TABLE II. TRAIN COMMUNICATION SYSTEM

System	Operating Characteristics		Additional Information
Train Radio System	Frequency bands	380 – 430 MHz, 407 – 473 MHz	Tetra system Located in Cab. Use of screened coax cable to antenna.
	Duplex spacing	5, 7, 8, and 10 MHz programmable	
	Channel	25 kHz	
	Time multiplexing	TDMA, 4 slots per port	
	Digital Modulation	$\pi/4$ DQPSK	
	RF Output Power	1 W	
	Output impedance	50 Ohms	
	Receiver class	Class A and B	
	Static Sensitivity	-112 dBm	
	Dynamic Sensitivity	-103 dBm	

TABLE III. TRAIN RADIO ANTENNA

System	Operating Characteristics		Additional Information
Train Radio Antenna	Frequency range	410 – 430 MHz	Located on Roof of Cab.
	Operational bands	S2	
	Bandwidth @ 2:1 VSWR	5%	
	Gain: Isotropic	2dBi	
	Compare with 1/4 wave	0dB	
	Polarisation	Vertical	
	Groundplane	Integrated baseplate Groundplane	
	Height	42mm	
	Diameter	160mm	
	Material	Engineering Plastic	

IV. TRAIN RADIO ANALYSIS

$$c = 2.997 \times 10^8 \text{ m / s} \quad \text{Speed of light in a vacuum}$$

$$f_1 = 410 \times 10^6 \text{ Hz} \quad f_2 = 430 \times 10^6 \text{ Hz} \quad \text{Upper and lower bounds antenna frequency Tetra range}$$

$$f = 410 \times 10^6 \text{ Hz} \quad \text{Lower bound of frequency in use antenna by Tetra system}$$

$$\lambda = c / f \quad \text{Calculation of wavelength}$$

$$\lambda = 0.731 \text{ m} \quad \text{and} \quad \lambda / 4 = 0.183 \text{ m}$$

The Transition Boundary between Reactive/Radiating Field is calculated from solution of the Raleigh function for practical antennas (ones with finite length) it is found to be $\lambda / 4$.

$$\lambda / 4 = 0.183 \text{ m} \quad \lambda / 2\pi = 0.116 \text{ m} \quad [3, 5]$$

The diameter of antenna shroud: diameter = 160mm
 radius = diameter/2 = 0.08m

From inspection of the antenna the maximum linear dimension of the antenna is the length $D = 42 \text{ mm} = 0.042 \text{ m}$

The transition between near field and far field for a practical (finite) antenna is found by $2D^2 / \lambda = 0.004826 \text{ m}$ Ref 3.4.5

As $2D^2 / \lambda < \lambda / 4$, for the antenna ,the far Field will use $\lambda / 2\pi = 0.116 \text{ m}$. [3, 5]

In order to calculate the Electric Field Strength versus distance a variable for distance must be defined.

$$n = 1 : 1000 \quad \text{Index for array variables}$$

$$r_n = (n / 100 + 0.1)m \quad \text{Distance variable } r_n \text{ for 0.11m to 10m in 10mm step}$$

$$Pwr = 1W \quad \text{Train Radio System RF Output Power}$$

The Poynting Vector can be used to find the radiated Power Density S of an infinitesimal isotropic antenna. It also holds true for any antenna when the distance is large compared to the antenna dimensions (in wavelength terms) and providing the directive/gain is taking into account.

A. The Poynting Vector

$S = \text{Power} / \text{Area}$ In the case of an isotropic antenna it radiates equally in all directions hence the area is the surface of a sphere $4 * \pi * \text{radius}^2$

$$\text{Gain} = 10^{(2 / 20)} \quad \text{Convert Gain from dB}$$

$$EIRP = Pwr * Duty * Gain \quad \text{Radiated Power}$$

$$S_n = EIRP / (4 * \pi * r_n^2) \quad \text{Radiated Power Density}$$

$$For \quad far \quad Field, \quad The \quad Poynting \quad Vector \\ S = E \wedge H = E^2 / \eta$$

$$In \quad Free \quad Space, \quad the \quad characteristic \quad impedance \\ \eta_0 = 120 * \pi \Omega$$

$$E_n = \sqrt{S_n * \eta_0} \quad \text{Electric Field Strength}$$

A SCILAB program is used to implement the above calculation.

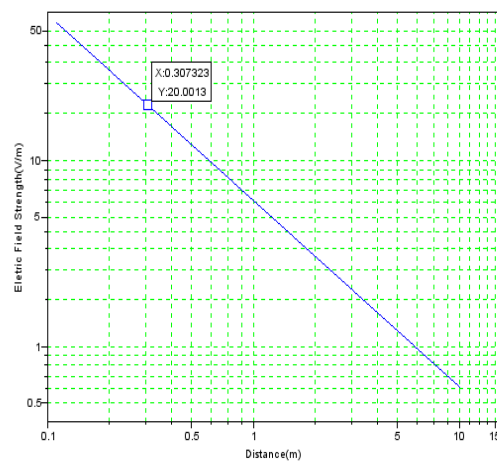


FIGURE II. ELECTRIC FIELD STRENGTH VERSUS DISTANCE FOR TRAIN RADIO ANTENNA

As the frequency is 410MHz, refer to Table 1, the Radiated Immunity Level of the equipment or apparatus is 20V/m.

Finding the Boundary at which 20V/m is exceeded using the Poynting vector from Figure 2.

$$r = 0.30732m = 307.32mm$$

An analysis of the trainborne radio installation shows that the 20V/m field strength threshold is reached at a distance of 0.307m from the centre of the antenna on the top surface of the train. Below top surface of the train radio antenna the field strength will be significant lower due to the antenna polarization. The electrical and electronic equipments on the train have been designed against 20V/m (146dB μ V/m) field strength in the train radio frequency range according to EN 50121-3-2, and it should also be noted that the peak field strength in EN50121-3-2 is actually 36V/m due to the 80% Amplitude Modulation. And the location of antenna is away from any emissive equipment on top surface of the train.

V. SUMMARY

By analyzing the radiation field strength of the antenna, it is beneficial to determine the layout design of the antenna on the vehicle at the beginning of the design.

REFERENCES

- [1] EN 50121-3-2:2015 Railway applications – Electromagnetic Compatibility Part 3-2 Rolling Stock Apparatus.
- [2] EN 50121-3-1:2006 Railway applications – Electromagnetic Compatibility Part 3-1 Train and complete vehicle.
- [3] BS EN 50383-2002 Basic standard for the calculation and measurement of electromagnetic field strength and SAR related to human exposure from radio base stations and fixed terminal stations for wireless telecommunications system (110 MHz 40-GHz)
- [4] ETSI TS 100 392-15 V1.5.1 (2011-02) Terrestrial Trunked Radio (TETRA); Voice plus Data (V+D); Part 15: TETRA frequency bands, duplex spacings and channel numbering.
- [5] Dipak L. Sengupta, Valdis V. Lipepa, *Applied Electromagnetics and Electromagnetic Compatibility* Hoboken, New Jersey, 2006

Teeth Classification Based on Haar Wavelet Transform and Support Vector Machine

Fangyuan Liu^{1,*}, Zhi Li² and Wagner Quinn³

¹Jiangsu Key Laboratory of 3D Printing Equipment and Manufacturing, Nanjing, Jiangsu 210042, China

²Department of Stomatology, Jinling Hospital, School of Medicine, Nanjing University, 210002, Nanjing, Jiangsu, China

³Department of Computer Science, University College Cork, Ireland

*Corresponding author

Abstract—To improve the efficiency of stomatology practitioners, this paper proposed a novel teeth type classification method. Our method was based on three successful components: Haar wavelet transform, principal component analysis, and support vector machine. We create a 120-image dataset, with 30 images for incisor, canine, premolar, and molar. The results showed our method achieved an overall classification accuracy of $81.83 \pm 1.79\%$, better than decision tree and multilayer perceptron methods.

Keyword—Haar wavelet transform; support vector machine; principal component analysis

I. INTRODUCTION

It is well known that teeth are one of the most important organs in the human body, which help chew food, control pronunciation and keep healthy. Learning and acquiring dental information is closely watched by researchers from the medical and academic fields. At present, dental information is collected and recorded by the staff through the oral head imaging equipment. In practical application, CT technique is most beneficial to identify, diagnose, and treat teeth. CT has the advantages of low ray volume, short scan time, high image clarity and simple operation, so as to provide accurate data recording and reduce the experimental cost.

In recent years, researchers have proposed various methods for tooth recognition and classification. Yoke-San, Xin [1] introduced a classification system based on the iterative closest point algorithm(ICP) to handle four types of teeth. The system used PCA extracted eigenteeth feature, projected datasets into the tooth geometric space and then classify tooth type by KNN. Ghodsi and Faez [2] created an automated dental identification system (AIDS) which applied Zernike moment(ZM) to extract feature and calculate Euclidian distance in the match phase. The method reduced search space, increased matching certainty by voting mechanism and ZM ensured the stability of experimental results. Al-sherif, Guo [3] established a method contains two stages for identifying bitewing dental images: (i) Orthogonal Locality Preserving Projection(OLPP) projected Laplacian teeth spaces to complete the initial classification; (ii) validate class and assign number based on teeth neighborhood rules, the classification accuracy reached 89%. Hosntalab, Zoroofi [4] combined the traditional segmentation techniques with wavelet-Fourier descriptors(WFDs) to select the most effective eigenvector, and then used feed-forward neural network to classify tooth images. Pushparaj, Gurunathan [5] utilized

support vector machine and universal numbering system to recognize teeth and number of teeth respectively. The key part of this approach is feature extraction which is aimed at individual teeth identification. PPED vectors, geometric features and regional descriptors are used in the process of feature extraction. The results show that the method is feasible and effective, and the average accuracy rate is 92.65%. Yeesarapat, Auephanwiriyakul [6] adapted fuzzy C-means clustering algorithm(FCM) based on multiple features(the pixel values of RGB and HIS) to classify dental fluorosis. FCM determines tooth status by cyclic updating membership values and prototypes until stable. Tangel, Faticahah [7] presented a fuzzy inference system to achieve four categories of dental images. This system used Mamdani type FIS with centroid defuzzification method which employed multiple fuzzy attributes and the selected threshold is 0.15. This approach can deal with blurred tooth images and guaranteed the robustness of the classification, the overall classification accuracy reaches 82.51%. Karthick and Harikumar [8] analyzed the performance of Naïve Bayes and SVM in the classification of five dental diseases. Before classifying the tooth images, they preprocessed through Median filter, segmented and extracted GLCM features by FCM algorithm. Veeraprasit and Phimoltares [9] described a model to recognize the tooth images by using the mixed feature. The researchers fused global features (singular values and color histogram) and local features (teeth width), and then applied MLP with Levenberg-Marquardt algorithm to determine the type of tooth effectively. Finally, the accuracy rate of the experiment is about 93.6%, which is superior to Naïve Bayes and k-Nearest Neighbor methods.

Based on the above studies on classification methods, the potential for various learning is getting better in various fields at the same time. In this paper, support vector machine is proposed to classify four kinds of dental images: central incisor, lateral incisor, canine and premolar. The methodology adopted in this study is described in Section 2. The material used in the experiment is shown in Section 3. In Section 4, we analyzed the experiments and results in detail, which is compared with the current methods. The last part is Section 5 which includes conclusion and the prospects we expect.

II. METHOD

Firstly, we utilize histogram equalization technique [10] to enhance the data of dental images. Histogram equalization method has the following advantages: (i) increased the contrast; (ii) improved the changes of gray tone; (iii) enhanced the

sharpness of the image, so that we can obtain high-quality sample data.

Next, Haar wavelet transform is one of the most popular wavelet transform in the field of wavelet analysis [11-14]. It can guarantee the integrity of image information because it gets the global information while recording the local information. The basic Haar wavelet function [15] is defined as Formula (1) and the scaling function is defined as Formula (2). In Formula (2), j is a scaling factor and i is a translation parameter. In the future, we shall test the performance of biorthogonal wavelet [16, 17].

After extracting the four-level wavelet features, we used PCA to decrease the feature dimension. This way can reduce the number of features, noise and redundancy, and the likelihood of excessive fitting.

$$x(a) = \begin{cases} 1, & 0 \leq a \leq 1/2 \\ -1, & 1/2 \leq a \leq 1 \\ 0, & \text{otherwise} \end{cases} \quad (1)$$

$$x^j(a) = x(2^j a - i), i = 0, \dots, (2^j - 1) \quad (2)$$

Finally, we employ an effective classification learning model, support vector machine (SVM), to classify four types of dental images.

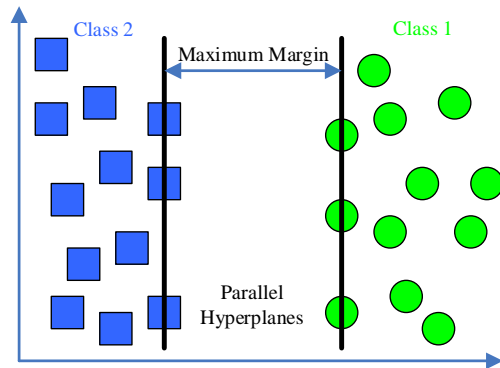


FIGURE I. ILLUSTRATION OF SVM

As far, SVM has been widely used in medical detection, text processing [18], speech recognition [19], and so on. SVM has been reported to be superior to the traditional classification method, such as BPNN [20], RBF network [21], k-Nearest Neighbors algorithm. Figure 1 gives an illustration of SVM, which finds several samples called “support vectors” [22-24] and created hyper-planes based on them [25-30].

III. DATASET

We used the ISO standard dental notation. Take upper right as an example, 11 and 12 are incisors; 13 is canine; 14 and 15 are premolars; 16, 17, and 18 are molars. Some samples of the dataset are listed in Figure 1. The images were obtained by participating hospitals. In total, we have a 120-image dataset, which contains 30 incisors, 30 canines, 30 premolars, and 30 molars. Figure 2 gives an example of each teeth type.

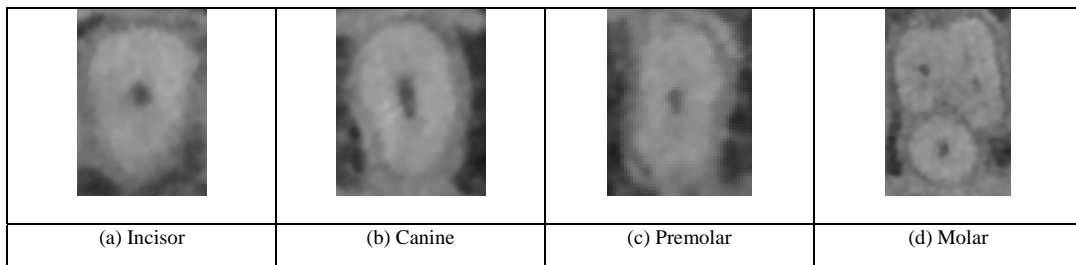


FIGURE II. SAMPLES OF DATASET

IV. EXPERIMENTS AND RESULTS

This proposed “HWT_PCA_SVM” method was implemented 10 times. Within each time, a 5-fold cross validation was used. That means there are 6 image for each tooth type within each fold. The classification results in terms of sensitivity were given in Tables 1. The whole accuracy of all four classes were given in Table 2.

TABLE I. SENSITIVITY OF EACH CLASS

	Incisor	Canine	Premolar	Molar
R1	76.67	86.67	73.33	90.00
R2	86.67	86.67	76.67	86.67
R3	83.33	76.67	90.00	86.67
R4	76.67	76.67	86.67	83.33
R5	83.33	83.33	80.00	83.33
R6	86.67	80.00	83.33	76.67
R7	80.00	80.00	86.67	86.67
R8	86.67	83.33	83.33	70.00
R9	80.00	80.00	80.00	83.33
R10	86.67	76.67	73.33	76.67
Average	82.67 ± 4.10	81.00 ± 3.87	81.33 ± 5.71	82.33 ± 6.10

TABLE II. ACCURACY OF ALL FOUR CLASSES

	F1	F2	F3	F4	F5	Total
R1	70.83	87.50	91.67	83.33	75.00	81.67
R2	87.50	83.33	87.50	83.33	79.17	84.17
R3	79.17	87.50	79.17	91.67	83.33	84.17
R4	75.00	66.67	91.67	75.00	95.83	80.83
R5	75.00	83.33	83.33	87.50	83.33	82.50
R6	79.17	79.17	83.33	79.17	87.50	81.67
R7	79.17	87.50	95.83	62.50	91.67	83.33
R8	75.00	66.67	95.83	75.00	91.67	80.83
R9	79.17	75.00	87.50	83.33	79.17	80.83
R10	70.83	70.83	91.67	83.33	75.00	78.33
Average						81.83 ± 1.79

We observe that the sensitivities of incisor, canine, premolar, and molar are $82.67 \pm 4.10\%$, $81.00 \pm 3.87\%$, $81.33 \pm 5.71\%$, and $82.33 \pm 6.10\%$, respectively. The whole accuracy was $81.83 \pm 1.79\%$. This demonstrates the effectiveness of HWT, PCA, and SVM. Except HWT, there are many other excellent feature descriptors, such as fractional Fourier transform [31], etc.

In addition, we compared our method with traditional decision tree (DT) [32], and multilayer perceptron (MLP) [33]. All the methods were implemented by 10 runs, and the results are shown in Table 3.

TABLE III. ALGORITHM COMPARISON

Method	Accuracy
DT [32]	73.83 ± 2.05
MLP [33]	76.25 ± 3.54
SVM (Proposed)	81.83 ± 1.79

The DT [32] obtained an overall accuracy of $73.83 \pm 2.05\%$. MLP [33] obtained an overall accuracy of $76.25 \pm 3.54\%$. The details of two basis algorithms were show in Table 4. Finally, the proposed SVM method could yield the greatest accuracy of $81.83 \pm 1.79\%$.

TABLE IV. ACCURACY OF DT [32] AND MLP [33]

DT [32]	F1	F2	F3	F4	F5	Total
R1	75.00	75.00	75.00	62.50	83.33	74.17
R2	66.67	70.83	70.83	83.33	66.67	71.67
R3	79.17	79.17	62.50	79.17	79.17	75.83
R4	83.33	70.83	70.83	83.33	70.83	75.83
R5	75.00	62.50	66.67	66.67	79.17	70.00
R6	66.67	70.83	70.83	79.17	79.17	73.33
R7	83.33	62.50	79.17	79.17	75.00	75.83
R8	58.33	91.67	75.00	87.50	66.67	75.83
R9	75.00	75.00	62.50	75.00	79.17	73.33
R10	75.00	66.67	79.17	83.33	58.33	72.50
Average						73.83 ± 2.05

MLP [33]	F1	F2	F3	F4	F5	Total
R1	91.67	95.83	75.00	70.83	62.50	79.17
R2	62.50	75.00	91.67	75.00	83.33	77.50
R3	70.83	79.17	87.50	79.17	75.00	78.33
R4	79.17	83.33	95.83	83.33	66.67	81.67
R5	70.83	75.00	75.00	62.50	62.50	69.17
R6	75.00	62.50	75.00	87.50	83.33	76.67
R7	87.50	62.50	83.33	62.50	66.67	72.50
R8	83.33	58.33	83.33	70.83	79.17	75.00
R9	79.17	79.17	75.00	79.17	75.00	77.50
R10	83.33	66.67	70.83	79.17	75.00	75.00
Average						76.25 ± 3.54

Although SVM obtained good results, we shall try to collect

more data than used in this study, and tested the effect of deep learning, such as convolutional neural network [34-36], deep belief network [37], and autoencoder [38, 39].

V.CONCLUSIONS

In this study, we proposed a novel method based on Haar wavelet transform, principal component analysis, and support vector machine. The simulation experiments validated the effectiveness of our method.

REFERENCES

- [1] Yoke-San, W., et al. *An approach for single tooth classification and identification*. in *2015 IEEE 10th Conference on Industrial Electronics and Applications (ICIEA)*. 2015. p. 1698-1702
- [2] Ghodsi, S.B. and K. Faez. *A novel approach for matching of dental radiograph image using Zernike moment*. in *2012 IEEE International Conference on Computer Science and Automation Engineering (CSAE)*. 2012. p. 303-306
- [3] Al-sherif, N., G. Guo, and H.H. Ammar. *Automatic Classification of Teeth in Bitewing Dental Images Using OLPP*. in *2012 IEEE International Symposium on Multimedia*. 2012. p. 92-95
- [4] Hosntalab, M., et al. *Automated Dental Recognition in MSCT Images for Human Identification*. in *2009 Fifth International Conference on Intelligent Information Hiding and Multimedia Signal Processing*. 2009. p. 1318-1321
- [5] Pushparaj, V., et al. *An effective numbering and classification system for dental panoramic radiographs*. in *2013 Fourth International Conference on Computing, Communications and Networking Technologies (ICCCNT)*. 2013. p. 1-8
- [6] Yeesarapat, U., et al. *Dental fluorosis classification using multi-prototypes from fuzzy C-means clustering*. in *2014 IEEE Conference on Computational Intelligence in Bioinformatics and Computational Biology*. 2014. p. 1-5
- [7] Tangel, M.L., et al. *Dental classification for periapical radiograph based on multiple fuzzy attribute*. in *2013 Joint IFSA World Congress and NAFIPS Annual Meeting (IFSA/NAFIPS)*. 2013. p. 304-309
- [8] Karthick, G. and R. Harikumar. *Comparative performance analysis of Naive Bayes and SVM classifier for oral X-ray images*. in *2017 4th International Conference on Electronics and Communication Systems (ICECS)*. 2017. p. 88-92
- [9] Veeraprasit, S. and S. Phimoltares. *Hybrid feature-based teeth recognition system*. in *2011 IEEE International Conference on Imaging Systems and Techniques*. 2011. p. 302-305
- [10] Wu, X., *Smart detection on abnormal breasts in digital mammography based on contrast-limited adaptive histogram equalization and chaotic adaptive real-coded biogeography-based optimization*. Simulation, 2016. **92**(9): p. 873-885
- [11] Phillips, P., *Intelligent facial emotion recognition based on stationary wavelet entropy and Jaya algorithm*. Neurocomputing, 2018. **272**: p. 668-676
- [12] Li, P. and G. Liu, *Pathological Brain Detection via Wavelet Packet Tsallis Entropy and Real-Coded Biogeography-based Optimization*. Fundamenta Informaticae, 2017. **151**(1-4): p. 275-291
- [13] Li, Y. and C. Cattani, *Detection of Dendritic Spines using Wavelet Packet Entropy and Fuzzy Support Vector Machine*. CNS & Neurological Disorders - Drug Targets, 2017. **16**(2): p. 116-121
- [14] Nayak, D.R., *Detection of unilateral hearing loss by Stationary Wavelet Entropy*. CNS & Neurological Disorders - Drug Targets, 2017. **16**(2): p. 15-24
- [15] Evans, F., *Haar wavelet transform based facial emotion recognition*. Advances in Computer Science Research, 2017. **61**: p. 342-346
- [16] Lu, H.M., *Facial Emotion Recognition Based on Biorthogonal Wavelet Entropy, Fuzzy Support Vector Machine, and Stratified Cross Validation*. IEEE Access, 2016. **4**: p. 8375-8385
- [17] Zhan, T.M. and Y. Chen, *Multiple Sclerosis Detection Based on Biorthogonal Wavelet Transform, RBF Kernel Principal Component*

- Analysis, and Logistic Regression.* IEEE Access, 2016. **4**: p. 7567-7576
- [18] Bouadjenek, N., H. Nemmour, and Y. Chibani, *Fuzzy integrals for combining multiple SVM and histogram features for writer's gender prediction.* IET Biometrics, 2017. **6**(6): p. 429-437
- [19] Chau, G. and G. Kemper, *One Channel Subvocal Speech Phrases Recognition Using Cumulative Residual Entropy and Support Vector Machines.* IEEE Latin America Transactions, 2015. **13**(7): p. 2135-2143
- [20] Rao, R.V., *Abnormal Breast Detection in Mammogram Images by Feed-forward Neural Network trained by Jaya Algorithm.* Fundamenta Informaticae, 2017. **151**: p. 191-211
- [21] Lu, Z., *A Pathological Brain Detection System Based on Radial Basis Function Neural Network.* Journal of Medical Imaging and Health Informatics, 2016. **6**(5): p. 1218-1222
- [22] Yang, J., *Identification of green, Oolong and black teas in China via wavelet packet entropy and fuzzy support vector machine.* Entropy, 2015. **17**(10): p. 6663-6682
- [23] Liu, A., *Magnetic resonance brain image classification via stationary wavelet transform and generalized eigenvalue proximal support vector machine.* Journal of Medical Imaging and Health Informatics, 2015. **5**(7): p. 1395-1403
- [24] Yang, J., *Preclinical diagnosis of magnetic resonance (MR) brain images via discrete wavelet packet transform with Tsallis entropy and generalized eigenvalue proximal support vector machine (GEPSVM).* Entropy, 2015. **17**(4): p. 1795-1813
- [25] Gorri, J.M. and J. Ramírez, *Wavelet entropy and directed acyclic graph support vector machine for detection of patients with unilateral hearing loss in MRI scanning.* Frontiers in Computational Neuroscience, 2016. **10**: Article ID. 160
- [26] Zhou, X.-X., *Comparison of machine learning methods for stationary wavelet entropy-based multiple sclerosis detection: decision tree, k-nearest neighbors, and support vector machine.* Simulation, 2016. **92**(9): p. 861-871
- [27] Chen, M., *Morphological analysis of dendrites and spines by hybridization of ridge detection with twin support vector machine.* PeerJ, 2016. **4**: Article ID. e2207
- [28] Yang, M., *Dual-Tree Complex Wavelet Transform and Twin Support Vector Machine for Pathological Brain Detection.* Applied Sciences, 2016. **6**(6): Article ID. 169
- [29] Chen, S., J.-F. Yang, and P. Phillips, *Magnetic resonance brain image classification based on weighted-type fractional Fourier transform and nonparallel support vector machine.* International Journal of Imaging Systems and Technology, 2015. **25**(4): p. 317-327
- [30] Liu, G., *Pathological brain detection in MRI scanning by wavelet packet Tsallis entropy and fuzzy support vector machine.* SpringerPlus, 2015. **4**(1): Article ID. 716
- [31] Phillips, P., *A Comprehensive Survey on Fractional Fourier Transform.* Fundamenta Informaticae, 2017. **151**(1-4): p. 1-48
- [32] Senanayaka, J.S.L., H.V. Khang, and K.G. Robbersmyr, *Towards online bearing fault detection using envelope analysis of vibration signal and decision tree classification algorithm.* in *20th International Conference on Electrical Machines and Systems (ICEMS).* 2017. Sydney, NSW, Australia: IEEE. p. 1-6
- [33] Chakraborty, S., S.K. Adhikary, and M. Roy, *Automatic land-cover classification using semi-supervised multilayer perceptron for analyzing remotely sensed images.* in *International Conference on Innovations in Electronics, Signal Processing and Communication (IESC).* 2017. Shillong, India: IEEE. p. 33-38
- [34] Zhao, G. *Polarimetric synthetic aperture radar image segmentation by convolutional neural network using graphical processing units.* Journal of Real-Time Image Processing, 2017, DOI: 10.1007/s11554-017-0717-0.
- [35] Lv, Y.-D., *Alcoholism detection by data augmentation and convolutional neural network with stochastic pooling.* Journal of Medical Systems, 2018. **42**(1): Article ID. 2
- [36] Muhammad, K. *Image based fruit category classification by 13-layer deep convolutional neural network and data augmentation.* Multimedia Tools and Applications, 2017, DOI: 10.1007/s11042-017-5243-3
- [37] Bibin, D., M.S. Nair, and P. Punitha, *Malaria Parasite Detection From Peripheral Blood Smear Images Using Deep Belief Networks.* IEEE Access, 2017. **5**: p. 9099-9108
- [38] Jia, W., *Three-Category Classification of Magnetic Resonance Hearing Loss Images Based on Deep Autoencoder.* Journal of Medical Systems, 2017. **41**(10): Article ID. 165
- [39] Hou, X.-X. *Seven-layer deep neural network based on sparse autoencoder for voxelwise detection of cerebral microbleed.* Multimedia Tools and Applications, 2017, DOI: 10.1007/s11042-017-4554-8.

Online Algorithm for Velocity Estimation in Ultrasonic Doppler Measurement

Enyao Shang, Jinchun Hu* and Shengwu Du

State Key Laboratory of Tribology, Department of Mechanical Engineering, Tsinghua University, Beijing 100084, China

*Corresponding author

Abstract—Ultrasonic Doppler technique is widely used for velocity estimation in medical electronic systems. This technique is signal-processing intensive with an increasing requirement on accuracy, real time and stability. The clutter caused by human tissues contains little information about blood flow velocity. Since conventional algorithms are based on an idealized signal model where the residual clutter is not fully considered, high-performance filters are required for clutter rejection in ultrasonic Doppler measurement. This paper focuses on how to extract the velocity information from ultrasonic echo signals without extra filters. We presented an online algorithm that identified the clutter as unknown parameters instead of filtering. The algorithm does not rely on the performance of extra clutter filters. Simulation results show that this algorithm is simpler and more stable than conventional correlation algorithms.

Keywords—online algorithm; velocity estimation; ultrasonic; Doppler; filter

I. INTRODUCTION

Ultrasonic Doppler technique is widely used in clinical diagnoses, such as cardiology, gynecology and obstetrics. The cardiovascular disease is the leading cause of death that threatens human health. A common symptom of the cardiovascular disease is blood flow abnormality. As one of the most suitable methods for measuring blood flow velocity, ultrasonic Doppler technique has advantages of low cost, no wound and large detection depth. With the rapid development of computer technology and electronic engineering, high-precision, real-time and stable processing has become possible. However, how to extract the velocity information from massive data effectively is still a difficult problem in ultrasonic Doppler measurement.

The conventional algorithms such as auto-correlation algorithm [1], cross-correlation algorithm [2] and maximum likelihood algorithm [3] are based on an idealized signal model. In this model, the residual clutter is not fully considered. The clutter caused by human tissues contains little information about blood flow velocity. High-performance filters are required for clutter rejection. Common examples of linear time-invariant filters were applied, such as finite impulse response filters [4], infinite impulse response filters [5] and auto-regression filters [6]. Besides these, many efforts have been made to improve the filtering. C. Demene *et al.* [7] presented a method for ultrafast ultrasonic imaging based on spatiotemporal singular value decomposition. The method significantly enhanced image contrast. Noting the different spatial characteristics of human tissues and blood flow, C. H.

Yu *et al.* [8] proposed an eigen-based filtering method using Hankel singular value decomposition formulation. The method provided less bias than auto-correlation algorithm. To remove the zero-frequency component, Y. Zhang *et al.* [9] presented a filter based on empirical mode decomposition. It was proved that the filter had little loss of low blood flow information. Z. Shen *et al.* [10] suggested a filtering method based on ridge ensemble empirical mode decomposition. The method achieved a high blood-to-clutter energy ratio. Considering the time-varying characteristics of the clutter, various adaptive strategies were proposed [11], [12]. G. Park *et al.* [13] provided an adaptive method for clutter rejection based on spectral decomposition and tissue acceleration. H. Takahashi *et al.* [14] presented an adaptive moving-target-indicator filter for clutter rejection. The filter could significantly improve automated identification of the heart wall. In these methods, the clutter was regarded as the interference that should be removed. However, even idealized filters cannot remove the clutter completely due to spectral similarities of the tissue motion and low blood flow. Furthermore, the phase and magnitude of the blood flow signal are changed by filter. The changes will inevitably affect the subsequent processing.

In this paper, we present an online algorithm that identifies the clutter as unknown parameters instead of filtering. The algorithm does not rely on the performance of extra clutter filters. There are three main sections in this paper. Firstly, a typical model of ultrasonic echo signals will be described. Then, we will detail the principle and implementation of the new algorithm. Finally, the algorithm will be evaluated by simulation.

II. SIGNAL MODEL

To extract the velocity information from ultrasonic echo signals, it is necessary to analyze the quantitative relation between them. In this section, we will describe a typical model of the received signal.

The blood flow signal of interest mainly results from the scattering of red blood cells. This signal is so weak that it is easily obscured by the clutter and observation noise. We model the received signal $x(t)$ as

$$x(t) = s_b(t) + s_c(t) + \varepsilon(t), \quad (1)$$

where $s_b(t)$ is the blood flow signal with a frequency shift due to Doppler effect, $s_c(t)$ is the clutter and $\varepsilon(t)$ is observation

noise. A common approach is assuming that the clutter is caused by static tissues [15]. Therefore, the clutter has the same frequency as the excitation. A typical excitation in ultrasonic Doppler measurement is periodic pulses. Due to the use of digital processing system, a discrete-time data set can be sampled. Let $x[n_s, n_{\text{prf}}]$, $s_b[n_s, n_{\text{prf}}]$, $s_c[n_s, n_{\text{prf}}]$ and $\varepsilon[n_s, n_{\text{prf}}]$ denote the values of $x(t)$, $s_b(t)$, $s_c(t)$ and $\varepsilon(t)$ at the n_s -th sampling moment in the n_{prf} -th period. If the excitation pulses are sinusoidal, then

$$s_b[n_s, n_{\text{prf}}] \approx A_b \sin(2\pi f_0 T_s n_s - 4\pi f_0 T_{\text{prf}} n_{\text{prf}} v / c + \varphi_b), \quad (2)$$

$$s_c[n_s, n_{\text{prf}}] \approx A_c \sin(2\pi f_0 T_s n_s + \varphi_c), \quad (3)$$

where A_b and A_c represent the amplitude attenuation due to propagation losses, φ_b and φ_c are the phase shifts that are related to the detection depths, f_0 is the center frequency of the transmitted pulses, T_s is the sampling interval, T_{prf} is the pulse repetition period, v is the blood flow velocity, and c is the speed of sound.

Finally, the sampling value could be expressed by

$$\begin{aligned} x[n_s, n_{\text{prf}}] &= s_b[n_s, n_{\text{prf}}] + s_c[n_s, n_{\text{prf}}] + \varepsilon[n_s, n_{\text{prf}}] \\ &\approx A_b \sin(2\pi f_0 T_s n_s - 4\pi f_0 T_{\text{prf}} n_{\text{prf}} v / c + \varphi_b) + A_c \sin(2\pi f_0 T_s n_s + \varphi_c) + \varepsilon[n_s, n_{\text{prf}}]. \end{aligned} \quad (4)$$

In summary, we model the sampling value as the summation of the blood flow signal, the clutter and observation noise. The blood flow signal has a frequency shift that is proportional to the velocity due to Doppler effect.

III. SIGNAL PROCESSING ALGORITHM

The previous section analyzed the quantitative relation between the blood flow velocity and the received signal. The problem now is how to estimate the velocity v based on 2-D data set $x[n_s, n_{\text{prf}}]$. This section will detail the principle and implementation of the new algorithm.

A. Algorithm Principle

We wish to maximize the probability density function $p(x; v)$ over v . Consider the velocity estimator

$$\hat{v} = \arg \max_v [p(x; v)]. \quad (5)$$

Assume that $\varepsilon[n_s, n_{\text{prf}}]$ is white Gaussian noise. Then,

$$\frac{1}{N_s} \sum_{n_s=0}^{N_s-1} \varepsilon[n_s, n_{\text{prf}}] \exp(i2\pi f_0 T_s n_s) \quad (6)$$

is also white Gaussian noise. Let σ^2 denote the variance of $\varepsilon[n_s, n_{\text{prf}}]$ and

$$J = \sum_{n_{\text{prf}}=0}^{N_{\text{prf}}-1} \left| \frac{1}{N_s} \sum_{n_s=0}^{N_s-1} \varepsilon[n_s, n_{\text{prf}}] \exp(i2\pi f_0 T_s n_s) \right|^2. \quad (7)$$

Thus, the probability density function can be written as

$$p(x; v) = (\pi \sigma^2 / N_s)^{-N_{\text{prf}}/2} \exp(-N_s J / \sigma^2). \quad (8)$$

Now we are equivalently minimizing J in maximizing $p(x; v)$. From (5),

$$\hat{v} = \arg \max_v [p(x; v)] = \arg \min_v (J). \quad (9)$$

Let $f = 2\pi f_0 T_{\text{prf}} / c$, $\theta_1 = 0.5 A_b \cos \varphi_b$, $\theta_2 = 0.5 A_b \sin \varphi_b$, $\theta_3 = 0.5 A_c \cos \varphi_c$, $\theta_4 = 0.5 A_c \sin \varphi_c$ and

$$y[n] = \frac{1}{N_s} \sum_{n_s=0}^{N_s-1} x[n_s, n] \exp(i2\pi f_0 T_s n_s). \quad (10)$$

The real part and imaginary part of $y[n]$ are denoted by $y_R[n]$ and $y_I[n]$ respectively. Then, we have

$$\begin{aligned} J &\approx \sum_{n_{\text{prf}}=0}^{N_{\text{prf}}-1} (y_R[n] - \theta_4 + \theta_1 \sin(2\pi f n) - \theta_2 \cos(2\pi f n))^2 + \\ &\quad \sum_{n=0}^{N_{\text{prf}}-1} (y_I[n] - \theta_3 - \theta_1 \cos(2\pi f n) - \theta_2 \sin(2\pi f n))^2. \end{aligned} \quad (11)$$

J is a function of f , θ_1 , θ_2 , θ_3 and θ_4 . f is proportional to the velocity. Since $J(f+1) = J(f)$, we only need to consider $-0.5 < f \leq 0.5$. Besides f of interest, θ_1 , θ_2 , θ_3 and θ_4 are all unknown parameters. Consider the parameters that minimize J , denoted by

$$\hat{\theta} = [\hat{\theta}_1 \ \hat{\theta}_2 \ \hat{\theta}_3 \ \hat{\theta}_4]^T. \quad (12)$$

The superscript T represents matrix transpose.

Setting the partial derivatives of J to zero, we have

$$\left. \frac{\partial J}{\partial \theta} \right|_{\hat{\theta}} = \mathbf{0}. \quad (13)$$

That is

$$\begin{pmatrix} N_{\text{prf}} & 0 & \sum \cos & -\sum \sin \\ 0 & N_{\text{prf}} & \sum \sin & \sum \cos \\ \sum \cos & \sum \sin & N_{\text{prf}} & 0 \\ -\sum \sin & \sum \cos & 0 & N_{\text{prf}} \end{pmatrix} \hat{\theta} = \begin{pmatrix} \sum y_I \cos - \sum y_R \sin \\ \sum y_I \sin + \sum y_R \cos \\ \sum y_I \\ \sum y_R \end{pmatrix}. \quad (14)$$

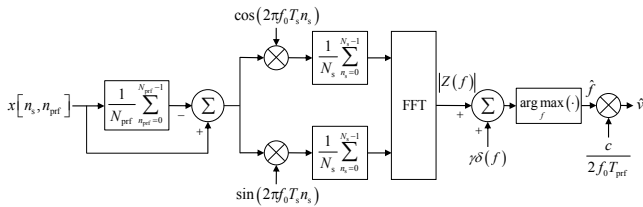


FIGURE I. SCHEMATIC DIAGRAM OF BATCH ALGORITHM.

If $f \neq 0$, then solving (14) yields $\hat{\theta}$. Substituting $\hat{\theta}$ in (11) and letting $z[n] = y[n] - \sum y[n]/N_{\text{prf}}$, we have

$$J|_{\hat{\theta}} = \sum |z[n]|^2 - \frac{1}{N_{\text{prf}}} \frac{|\sum z[n] \exp(-i2\pi f n)|^2}{1 - \left| \frac{1}{N_{\text{prf}}} \sum \exp(-i2\pi f n) \right|^2}. \quad (15)$$

Let $Z(f)$ denote the Fourier transformation of $z[n]$. If N_{prf} is large enough, then

$$J|_{\hat{\theta}} \approx \sum |z[n]|^2 - |Z(f)|^2 / N_{\text{prf}}. \quad (16)$$

From (9),

$$\begin{aligned} \hat{v} &= \arg \min_v (J) = \frac{c}{2f_0T_{\text{prf}}} \arg \min_f (J) \\ &= \frac{c}{2f_0T_{\text{prf}}} \arg \min_f (J|_{\hat{\theta}}) = \frac{c}{2f_0T_{\text{prf}}} \arg \max_f |Z(f)|. \end{aligned} \quad (17)$$

However, the estimator is not always feasible because (15) requires $f \neq 0$. Noting that $|Z(0)| = \sum z[n] = 0$, the estimator is invalid if $f \approx 0$. Hence, revise(17) as

$$\hat{v} = \frac{c}{2f_0T_{\text{prf}}} \arg \max_f (|Z(f)| + \gamma \delta(f)), \quad (18)$$

where γ is a constant selected by user and δ is the Dirac function.

In summary, the velocity estimator of the new algorithm is

$$\hat{v} = \frac{c}{2f_0T_{\text{prf}}} \arg \max_f (|Z(f)| + \gamma \delta(f)), \quad (19)$$

where c is the speed of sound, f_0 is the center frequency of transmitted pulses, T_{prf} is the pulse repetition period, γ is a constant selected by user, δ is the Dirac function, $Z(f)$ is the Fourier transform of $z[n]$ and

$$z[n] = \frac{1}{N_s} \sum_{n_s} \left[\left(x[n_s, n] - \frac{1}{N_{\text{prf}}} \sum_n x[n_s, n] \right) \exp(i2\pi f_0 T_s n_s) \right]. \quad (20)$$

B. Algorithm Implementation

The above batch algorithm processes all the data at once. It means that users have to wait for all the available data, or compute the preceding data repeatedly. To reduce time and calculation work, we process the samples sequentially in time.

If we received the data of the k -th period just now, then compute $y[k-1]$ based on the new data $x[n_s, k-1]$ by

$$y[k-1] = \frac{1}{N_s} \sum_{n_s=0}^{N_s-1} x[n_s, k-1] \exp(i2\pi f_0 T_s n_s). \quad (21)$$

Introduce intermediate variables $\bar{y}^{(k)}$ and $u^{(k)}$. Let

$$\bar{y}^{(k)} = \frac{1}{k} \sum_{n=0}^{k-1} y[n], \quad (22)$$

$$u^{(k)} = \frac{1}{k} \sum_{n=0}^{k-1} \exp(-i2\pi f n). \quad (23)$$

Then, their recursive formulas are

$$\begin{aligned} \bar{y}^{(k)} &= \frac{1}{k} \sum_{n=0}^{k-1} y[n] = \frac{1}{k} \left(\sum_{n=0}^{k-2} y[n] + y[k-1] \right) \\ &= \bar{y}^{(k-1)} + \frac{1}{k} (y[k-1] - \bar{y}^{(k-1)}), \end{aligned} \quad (24)$$

$$\begin{aligned} u^{(k)} &= \frac{1}{k} \sum_{n=0}^{k-1} \exp(-i2\pi f n) \\ &= u^{(k-1)} + \frac{1}{k} [\exp(-i2\pi f(k-1)) - u^{(k-1)}]. \end{aligned} \quad (25)$$

Letting $Z^{(k)}(f)$ denote $Z(f)$ obtained from the first k periods, we have

$$Z^{(k)}(f) = Z^{(k-1)}(f) + \frac{k-1}{k} [y[k-1] - \bar{y}^{(k-1)}] \left[\exp(-i2\pi f(k-1)) - u^{(k-1)} \right]. \quad (26)$$

Summarize the recursive procedures as follows:

Step 1. Initialize the variables: $k = 0$, $\bar{y}^{(0)} = 0$, $u^{(0)} = 0$, $Z^{(0)}(f) = 0$;

Step 2. Increase the index k by 1 and wait for new data;

- Step 3. Compute $y[k-1]$ based on the most recent data $x[n_s, k-1]$ by (21);
- Step 4. Update the variables $\bar{y}^{(k)}, u^{(k)}$ and $Z^{(k)}(f)$ by (24)(25)(26);
- Step 5. Compute $|Z^{(k)}(f)|$ and select a proper γ ;
- Step 6. Compute $\hat{v}^{(k)}$ by (19), and then return to Step 2 until no more data are sampled.

IV. SIMULATION RESULTS AND DISCUSSION

In this section, we will compare the new algorithm with conventional correlation algorithms by simulation. Simulate echo signals with the toolkit Field II, and then compute the velocity estimators separately.

Firstly, set sound field parameters. The speed of sound in human tissues is 1540m/s. The excitation is sinusoidal periodic pulses with the center frequency of 5MHz. There are 32 pulses with intervals of 100 μ s. The sampling interval is 25ns. The radius of the vessel is 4mm and the vessel is at the depth of 30mm with a 45° angle to the ultrasonic beam. A 128-element ultrasonic phased array probe is used. The elements are 0.15mm width and 5mm length with kerfs of 0.03mm. The intensity ratio of red blood cells to static tissues is 0.1. The given velocity v has a parabolic profile where the maximum is 0.8m/s. The algorithms are implemented in the MATLAB programs. 58,062 points are generated using the Monte Carlo method. The simulation results are shown in Figure 2.

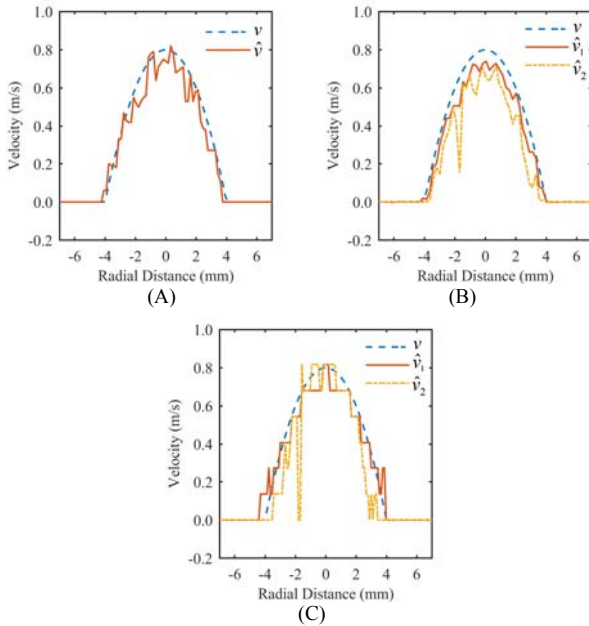


FIGURE II. VELOCITY ESTIMATORS OF (A) THE NEW ALGORITHM, (B) AUTO-CORRELATION ALGORITHM AND (C) CROSS-CORRELATION ALGORITHM.

In Figure 2, the x-axis shows the radial distance from the center of the vessel. In Figure 2(A), v represents the theoretical velocity and \hat{v} represents the velocity estimator of the new

algorithm. Although v is slightly smaller than \hat{v} , the new algorithm performs well. In Figure 2(B), a second-order low-pass filter and a second-order Chebyshev Type I high-pass filter are used. \hat{v}_1 and \hat{v}_2 represent the velocity estimators of auto-correlation algorithm. \hat{v}_1 is calculated with proper filter parameters, while \hat{v}_2 is calculated with improper filter parameters. Similarly, in Figure 2(C), a second-order Chebyshev Type I high-pass filter is used. \hat{v}_1 and \hat{v}_2 represent the velocity estimators of cross-correlation algorithm. From Figure 2(B) and Figure 2(C), both the correlation algorithms provide good performance with proper filters, but produce notable error when the filters are improper. In other words, correlation algorithms rely on the performance of clutter filters. Auto-correlation algorithm employs a low-pass filter to remove high-frequency noise and a high-pass filter to the clutter. Cross-correlation algorithm requires a high-pass filter that is essential in noisy environment. By contrast, the new algorithm is simpler because it does not involve the design of extra filters.

In summary, we compare the algorithms in three aspects.

- 1) *Accuracy.* All the algorithms work well.
- 2) *Stability.* Correlation algorithms are sensitive to the clutter. The new algorithm which does not rely on the performance of extra filters is the most stable one.
- 3) *Simplicity.* Compared with the conventional correlation algorithms, the new algorithm is easier to implement.

V. CONCLUSION

This paper focused on how to extract the velocity information from ultrasonic echo signals without extra filters.

An online algorithm was presented. Since the algorithm identifies the clutter as unknown parameters instead of filtering, it does not rely on the performance of extra clutter filters. To reduce time and calculation work, the sequential processing is recommended.

Compared with the conventional correlation algorithms, the new algorithm is simpler and more stable.

ACKNOWLEDGMENT

We thank Dr. Yu Zhu and Dr. Ming Zhang for helpful conversations, Dr. Kaiming Yang for excellent technical assistance, Zhongcheng Zhou and Peng Lei for assistance with the experiments.

REFERENCES

- [1] A. C. Chan, E. Y. Lam and V. J. Srinivasan, "Comparison of Kasai autocorrelation and maximum likelihood estimators for Doppler optical coherence tomography", *IEEE Trans. Med. Imag.*, vol. 32, no. 6, pp. 1033-1042, Jun. 2013.
- [2] J. A. Jensen, S. I. Nikolov, A. C. H. Yu and D. Garcia, "Ultrasound vector flow imaging—Part I: Sequential systems", *IEEE Trans. Ultrason. Ferroelectr. Freq. Control*, vol. 63, no. 11, pp. 1704-1721, Nov. 2016.
- [3] N. Thong-un, W. Wongsaroj, W. Treenuson, J. Chanwutitum and H. Kikura, "Doppler frequency estimation using maximum likelihood function for low ultrasonic velocity profile", *Acoust. Sci. & Tech.*, vol. 38, no. 5, pp. 268-271, 2017.
- [4] L. W. Chang, K. H. Hsu and P. C. Li, "Graphics processing unit-based high-frame-rate color doppler ultrasound processing," *IEEE Trans.*

- Ultrason. Ferroelect. Freq. Contr., vol. 56, no. 9, pp. 1856-1860, Sep. 2009.
- [5] S. Koçkanat, T. Koza and N. Karaboga, "IIR filter parameter estimation with ABC algorithm for mitral valve Doppler signal denoising," 2015 23nd Signal Processing and Communications Applications Conference (SIU), Malatya, 2015, pp. 1989-1992.
- [6] J. Kang, Y. Kim, W. Lee and Y. Yoo, "A new dynamic complex baseband pulse compression method for chirp-coded excitation in medical ultrasound imaging", IEEE Trans. Ultrason. Ferroelect. Freq. Contr., vol. 64, no. 11, pp. 1698-1710, Nov. 2017.
- [7] C. Demene, T. Deftieux, M. Pernot, B. F. Osmanski, V. Biran, J. L. Gennisson et al., "Spatiotemporal clutter filtering of ultrafast ultrasound data highly increases Doppler and fultrasound sensitivity", IEEE Transactions on Medical Imaging, vol. 34, no. 11, pp. 2271-2285, Nov. 2015.
- [8] C. H. Yu and R. S. C. Cobbold, "Single-ensemble-based eigen-processing methods for color flow imaging—Part I. The Hankel-SVD filter", IEEE Trans. Ultrason. Ferroelect. Freq. Contr., vol. 55, no. 3, pp. 559-572, Mar. 2008.
- [9] Y. Zhang, Y. Gao, L. Wang, J. Chen and X. Shi, "The removal of wall components in Doppler ultrasound signals by using the empirical mode decomposition algorithm", IEEE Trans. Biomed. Eng., vol. 54, no. 9, 2007, pp. 1631-1642.
- [10] Z. Shen, N. Feng, Y. Shen, and C. H Lee, "A ridge ensemble empirical mode decomposition approach to clutter rejection for ultrasound color flow imaging", IEEE Trans. Biomed. Eng., vol. 60, no. 6, pp. 1477-1487, 2013.
- [11] G. Park, S. Yeo, J. J. Lee, C. Yoon, H. Koh, H. Lim, Y. Kim, H. Shim and Y. Yoo, "New adaptive clutter rejection based on spectral analysis for ultrasound color Doppler imaging: Phantom and in vivo abdominal study", IEEE Trans. Biomed. Eng., vol. 61, no. 1, pp. 55-63, Jan. 2014.
- [12] C. H. Yu and L. Lovstakken, "Eigen-based clutter filter design for ultrasound color flow imaging: A review", IEEE Trans. Ultrason. Ferroelect. Freq. Contr., vol. 57, no. 5, pp. 1096-1111, May 2010.
- [13] G. Park, Y. Kim, H. Shim, H. W. Koh, H. Lim, J. J. Lee, S. Yeo, T. K. Song and Y. Yoo, "New adaptive clutter rejection based on spectral decomposition and tissue acceleration for ultrasound color Doppler imaging." IEEE Ultrason. Symp., 2014:1484-1487.
- [14] H. Takahashi, H. Hasegawa and H. Kanai, "Improvement of automated identification of the heart wall in echocardiography by suppressing clutter component", Japanese Journal of Applied Physics, vol. 52, no. 52, pp. 1044-1055, 2013.
- [15] D. H. Evans and W. N. McDicken, "Doppler Ultrasound: Physics Instrumentation and Signal Processing", New York, NY:Wiley, 2000.

Experimental Research and Analysis on a Vibration Model of Stator of L1B2 Linear Ultrasonic Motor

Xingyu Yi, Gang Zhao and Wenlei Xiao^{*}

School of Mechanical Engineering & Automation, Beihang University, China

^{*}Corresponding author

Abstract—The vibration of stator is an important part of the linear ultrasonic motor operating mechanism. Linear ultrasonic motor is driven by the interface force between stator and slider. Changes in vibration mode are not considered in the traditional motor vibration model which fails to reflect the vibration amplitude variations of LUSM during the process of running. In order to study the vibration of the ultrasonic motor stator, adequate experimental data of vibration of stator and the speed of the slider is necessary. This paper simply introduces the experimental system. According to the experimental results and its analysis, we propose a stator vibration model with variable vibration mode. The experiment is performed to verify the feasibility of this stator vibration model. The simulation results are validated by the measured vibration amplitude data. The paper points out some problems to be improved in future.

Keywords—linear ultrasonic motor; vibration model

I INTRODUCTION

Linear ultrasonic motor (LUSM) has been of interest in high precision motion control due to its unique characteristics such as high torque at low speed, fast response, accurate positioning, simple design, compact size, light weight, auto-locking on power, low electromagnetic interferences[1]. Many engineers are focusing on the research and development of LUSM since 1980s. The LUSM has been applied in high precision motion stage and other industrial fields. The piezoelectric stator of the motor is excited to produce bending and longitudinal vibrations, the two orthogonal vibrations generate an elliptical motion on the material points of the driving foot of stator. The slider is in contact with the driving wave crests by the preload, the dynamic contact force produce the linear motion. The piezoelectric linear ultrasonic motor is an electromechanical coupling system. It has two energy conversion stages [2]. In the first stage, the electrical energy converts into ultrasonic frequency mechanical oscillations. In the second stage, depending on the contact force between driving foot and slider the high-frequency vibration is rectified into macroscopic linear motion.

In order to predict the linear ultrasonic motor behavior, numerous of dynamic models of linear ultrasonic motor are proposed to predict the transient and steady-state responses of the LUSM [3, 4], but can't reflect the vibration amplitude variations phenomenon of the experiments. This paper a stator vibration model is proposed, it is found that the model can predict the vibration amplitude in a range of drive voltage.

II DESCRIPTION OF THE LUSM INVESTIGATED

The LUSM investigated in this paper is a double-mode L1B2 ultrasonic motor, the schematic of the motor is illustrated in Figure 1 (a). The structure of the motor consists of the stator with driving foot, a slider and a preload spring. The motor shell clamps the stator in the vibration nodes. The LUSM is driven by the asymmetry of the piezoelectric stator of the motor applying to the electrodes 1-4 or 2-3 at a time to produce the first longitudinal mode and the second bending mode to produce the elliptical motion in different directions [5].

III THE EXPERIMENT STUDY

A. Implement of Experimental System

The experimental system includes the LUSM motion platform, vibration measurement platform, motion control and drive platform. In order to get the vibration of stator in a running process, we design a special LUSM experimental motion platform, which opens a window on the measuring side of LUSM motor. So the laser Doppler vibrometer can measure the vibration. The vibration experiment based on the laser doppler vibrometer, we build a vibration measurement platform consists of the Polytec OFV laser doppler vibrometer, NI-DAQ device and DAQmx. In order to ensure the motion and vibration data of LUSM is accurate and synchronous, a 50nm linear grid ruler is used in the motion platform and a special EtherCAT driving controller is designed. The linear grid ruler makes sure the experiment can obtain the accurate location and speed data of slider. The EtherCAT driving controller which uses LC resonance voltage step-up circuit to provide the high-voltage at the operating frequency uses the EtherCAT as the motion data and control signal exchange protocol between the host computer and the driving controller. The host computer uses TwinCAT a real time automation PC controller with a multi-PLC system. The system architecture is illustrated in Figure I (B).

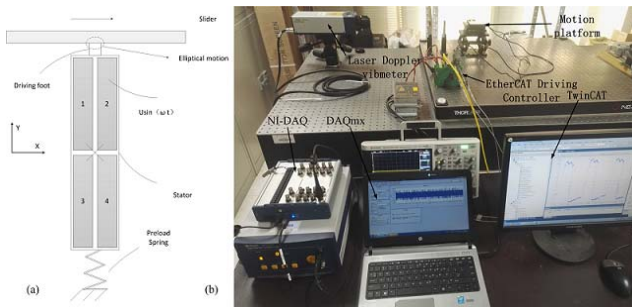


FIGURE I. LUSM SCHEMATIC (A) AND SYSTEM ARCHITECTURE (B)

B. Speed Experimental Results and Analysis

Figure II (A) shows the speed performance of the slider. The ideal steady-state speed of the slider in response to a step control signal is steady. But in the actual operation of the linear ultrasonic motor, the speed is not stable. In this paper, we adjust the voltage amplitude with the special ultrasonic frequency to adjust the speed of LUSM. Figure II (B) shows the relationship between speed in a special voltage and position of the slider in three experiments. In other speed experiments, the same phenomenon appears. The speed of the slider is changing during the process of running and the value of speed is related to the position where the slider is in contact with the stator.

C. Vibration Experimental Results and Analysis

The elliptical motion of the driving foot of the stator is the important key of linear ultrasonic motor motion. The elliptical directly decides the output performance of linear ultrasonic motor. Figure II (C) shows the relationship between vibration amplitude in the same voltage and position of the slider in three experiments. In other vibration experiments, the same phenomenon appears. The vibration amplitude of stator is changing during the process of running. The vibration experimental results show that the linear ultrasonic motor's vibration amplitude will be not stable after start up and the vibration amplitude is related to the position where the slider is in contact with the stator.

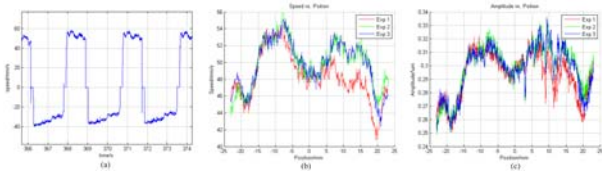


FIGURE II. SPEED PERFORMANCE (A), RELATIONSHIP BETWEEN SPEED IN A SPECIAL VOLTAGE AND POSITION (B) AND RELATIONSHIP BETWEEN VIBRATION AMPLITUDE AND POSITION (C)

D. Analyses of Speed and Vibration Experimental Results

The speed and vibration experimental results show that the relationship between the speed of the slider and the vibration amplitude of stator is proportional. That means the essence of LUSM speed adjustment is to adjust the vibration amplitude of the driving foot of the stator. A reasonable explanation the unstable of the speed is that the vibration amplitude of the stator is changing during the process of running.

IV THE VIBRATION MODEL

A. Analytical Model

According to the operating mechanism of LUSM, a vibration model of LUSM is derived. The bending vibration of the stator is treated as the bending of a beam [1]. Applying the method of separation of variables, the lateral vibration displacement is expressed as follows

$$w(x, t) = \phi(x)q(t). \quad (1)$$

The function $q(t)$ indicates harmonic motion, and the function $\phi(x)$ represents B2-mode shape. According to vibration experimental phenomenon that the bending vibration amplitude changed and is related to the position where the stator contact with the slider, the constant the free-free boundary B2-mode is not suitable. The function $\phi(x)$ considering the effect of axial force P on the bending vibration mode with a free-free boundary is written as

$$\phi(x) = \cos\beta_1 x + D \sin\beta_1 x + E \sinh\beta_2 x + F \cosh\beta_2 x. \quad (2)$$

$$\beta_1^2 = [(P/(2EI))^2 + \rho S/(EI) \omega^2] - P/(2EI). \quad (3)$$

$$\beta_2^2 = [(P/(2EI))^2 + \rho S/(EI) \omega^2] + P/(2EI). \quad (4)$$

According to the free-free boundary[1], Eq. 5, Eq. 6, Eq. 7 and Eq. 8 can be derived.

$$-\beta_1^2 + F\beta_2^2 = 0. \quad (5)$$

$$-D\beta_1^2 + E\beta_2^2 = 0. \quad (6)$$

$$-\beta_1^2 \cos\beta_1 l - D\beta_1^2 \sin\beta_1 l + E\beta_2^2 \sinh\beta_2 l + F\beta_2^2 \cosh\beta_2 l = 0. \quad (7)$$

$$\beta_1^2 \cos\beta_1 l - D\beta_1^2 \sin\beta_1 l + E\beta_2^2 \sinh\beta_2 l + F\beta_2^2 \cosh\beta_2 l = 0. \quad (8)$$

The l , S , E , ρ and ω are the length of the stator, the cross section area, elastic modulus of material, mass density and frequency of vibration, respectively. According to the energy method and Lagrange equation, the bending mode of the stator can be obtained [1, 6].

$$Mq''(t) + Cq'(t) + Kq(t) = A_v V_0 \sin(\omega_d t) + F_t(\phi(0) - \phi(l)). \quad (9)$$

The M , C and K are the mass, damping and stiffness for the B2-mode of stator, respectively. V_0 and ω_d are the amplitude of the driving voltage and the driving frequency, respectively. A_v is the force factor related to the electromechanical coupling effects. Subjected to the excitation of the piezoelectric stator,

the steady-state bending vibration response of the beam can be expressed as

$$w(x, t) = F_d \phi(x) / K [(1 - (\omega_d / \omega_n)^2)^2 + (2C/(2MK) (\omega_d / \omega_n))^2]^{1/2} \sin(\omega_d t - \phi). \quad (10)$$

$$\tan \phi = -2 C/(2MK) (\omega_d / \omega_n) / (1 - (\omega_d / \omega_n)^2). \quad (11)$$

This model focus on the steady-state of the vibration, the time-varying force F_t is simplified to constant generalized effect. The tangential force F_t is related to the force P . The force factor is A_p , so the effect of the generalized force simplified to

$$F_d = A_v V_0 + A_p P. \quad (12)$$

B. Identification and Simulation

According to the experimental results, it is obvious that the bending vibration amplitude is related to the position where the stator contact with the slider, so that the axial force P which affects the B2-mode is related to the position. The steady-state vibration amplitude is the function of position. The vibration experimental results reflect the relationship between vibration amplitude and position. And we obtain the relationship between the axial force P and vibration amplitude by the analytical model, so we can identify the relationship between the axial force P and position. Some parameter used for simulation list in Table I, the rest of the parameters are drove according to the energy method and Lagrange equation, and the driving voltage is obtained from experiments.

According to the identification of the axial force P . The identification results is shown in Figure III (a) and (b). It is found that the identification results can be divided into three parts according to the driving voltage: low voltage zone, medium voltage zone and high voltage zone. In low voltage zone ($0V \sim 353V$), the vibration amplitude is small, some axial force P can't be identified. In medium voltage zone ($361V \sim 410V$), there is no uniform rule in the identification results. In high voltage zone ($450V \sim 675V$), there are similar rules in the identification results.

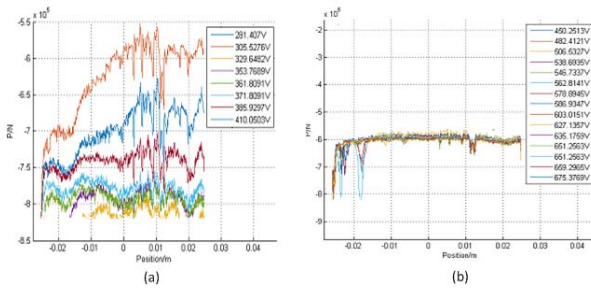


FIGURE III. IDENTIFICATION RESULTS IN LOW AND MEDIUM VOLTAGE ZONE (A) AND IDENTIFICATION RESULTS IN HIGH VOLTAGE ZONE (B)

According to the identification results, a stator vibration model with variable vibration mode suitable for the high voltage zone is proposed. The simulation results are shown in

Figure IV (a), and the relative error of the model is shown in Figure IV (b). The stator vibration model applied in the high voltage zone can predict the vibration amplitude for every position where the stator contacts with the slider effectively.

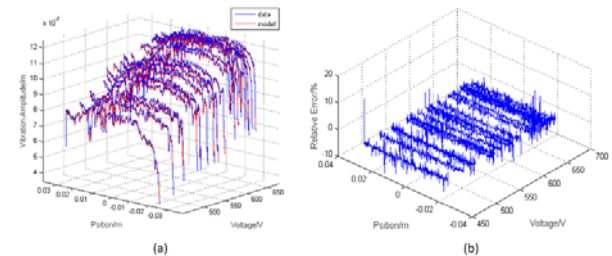


FIGURE IV. SIMULATION RESULTS OF THE VIBRATION MODEL

TABLE I. PARAMETERS

Parameter	Value	S	$2.25e-5m^2$
1	0.03m	C	$178Ns/m$
ω_d	$3.0473e+05rad/s$	I	$1.0544e-10m^4$
E	$8.6957e10N/m^2$	c_{66}^E	$3e10 N/m^2$
c_{11}^E	$5.1e10 N/m^2$	e_{31}	$24.8cl/m^2$

V SUMMARY

In this paper, a stator vibration model of LUSM is proposed to predict the stator vibration amplitude. This model differs from the previous reported model, the effect of axial force on the bending vibration mode is considered in the operation of the linear ultrasonic motor. The vibration experiments are designed to examine the feasibility and effectiveness of the proposed model. It is shown that the axial force in different position makes a significant impact on the bending vibration of the stator, which directly influence on the speed of the slider. In future research, the dynamic axial force and tangential force will be considered to make the model can be used for low and medium voltage zone.

ACKNOWLEDGEMENT

The authors would like to acknowledge the support of National Natural Science Foundation of China (No.51505020).

REFERENCES

- [1] Zhao, Ultrasonic Motor Technologies and Applications, Science Press, Beijing, 2007.
- [2] S. Ueha, Y. Tomikawa, Ultrasonic Motors: Theory and Applications, Clarendon Press, Oxford, 1993.
- [3] X. Li, Z. Yao, R. Wu, Modeling and analysis of stick-slip motion in a linear piezoelectric ultrasonic motor considering ultrasonic oscillation effect, J. International Journal of Mechanical Sciences 107(2016)215-224.
- [4] X. Li, Z. Yao, Q. Lv, Z. Liu, Modeling stick-slip-separation dynamics in a bimodal standing wave ultrasonic motor, J. Journal of Sound & Vibration 382(2016)140-157.
- [5] G. Peled, R. Yasinov, N. Karasikov, Performance and Applications of L1B2 Ultrasonic Motors, J. Actuators 5.2(2016) 15.
- [6] M. S. Tsai, C. H. Lee, S. H. Hwang, Dynamic modeling and analysis of a bimodal ultrasonic motor, J. IEEE Transactions on Ultrasonics Ferroelectrics & Frequency Control 50.3(2003) 245.

Control Modeling of a New Type Electric Mechanical Continuously Variable Transmission and Realization of the Control Objectives

Xiumin Yang^{1,*}, Song Zhang¹, Zeqi Wang² and Lei Zhang²

¹Department of Automatic Controls, Shenyang Institute of Engineering, Shenyang 110136, China

²Mechanical Engineering and Automation School, Northeastern University, Shenyang 110004, P. R. China

*Corresponding author

Abstract—A new electric mechanical metal belt (chain) continuously variable transmission (EMCVT) for vehicles was studied in this paper. With the use of direct-current (DC) motor controlling the rolling screw, the displacement of the taper disc pressed by the Belleville spring can be controlled, which achieves the function of speed governing. To make sure that the control objectives are realized, the taper disc clamp force control model of the Belleville spring was established by analyzing the speed ratio control model and studying the axial thrust ratio between the driving taper disc and the driven taper disc. So the association model between the CVT transmission ratio under the steady-state condition and the engine speed was proposed. The economic and driving force characteristic curve were determined by tests, and the EMCVT was controlled with the method of the incompleteness differential PID control. The validity of models and control strategies were proved by bench tests and road tests.

Keywords—electric -mechanical continuously variable transmission (EMCVT); control model; axial thrust ratio; clamp force control; speed ratio control

I. INTRODUCTION

The current vehicle metal belt (chain) continuously variable transmissions generally adopt the hydraulic pressure device or electric hydraulic pressure system as the control plan. However, using the pump, the valve and the hydraulic torque converter to control the clamp force and the transmission ratio makes the efficiency reduced and failure rate improved. Meanwhile, the vehicle actual fuel consumption is still very high. In this paper, the Electric-Mechanical Continuously Variable Transmission (EMCVT) works through the metal belt (chain), abandoning the low efficient pumps, valves and other hydraulic elements. Instead, motors, gears and Belleville springs are applied to the EMCVT, which not only reduces the energy consumption and the cost, but also improve the reliability.

As a result of using the speed governing method of the rolling screw drive, the Belleville spring preressing clamp and the taper disc displacement control, the speed ratio relation and the clamp force characteristic directly influence the control strategies and the control efficiency in this new EMCVT.

II. MECHANICAL SYSTEM STRUCTURE OF EMCVT

The new EMCVT is composed of the front case, the middle case, the rear case, the clutch control motor and the speed ratio control motor. The three cases mentioned above are all made of cast aluminum, ensuring the entire system much lighter in the premise of meeting the strength requirements. The clutch control motor consists of the permanent magnet DC motor, the self-locking worm gear reducer, the spring compensation mechanism, the position sensor, the mechanical position limitation mechanism, inhaul cables and so on. When the clutch motor is rotating forward or reversely, the straight reciprocating motion can be achieved by using the worm gear mechanism and lever mechanism. The power is transmitted by the inhaul cables.

The structure of the speed ratio control motor is shown in Figure 1. The permanent magnet DC motor that the rated voltage is 12V with the contracting brake device is chosen as the speed ratio control motor. Through the synchromesh toothed belt and the dual-range reduction gear, the clamp force used to control the speed ratio is applied on the driving taper disc by the ball screws and the Belleville springs. Then the pressure between the belts and the driven taper disc Belleville springs reaches a new state of equilibrium. Thus, the speed ratio of the transmission is controlled. The driving wheel and the driven wheel both consist of the fixed taper disc and the movable taper disc. The power between the fixed and movable taper discs is transmitted through the metal belt. During the operation of the mechanism, the movable taper discs of driving wheels and driven wheels produce the axial displacements under the Belleville springs force.

From the transmission principle of the EMCVT, we can know that EMCVT can continuously and arbitrarily change the transmission ratio in the entire design transmission ratio area. At the same time, with the motor and the deceleration system replaced by the traditional CVT that adopts the hydraulic system, the overall efficiency of the EMCVT has a significant improvement. Currently, this transmission has completed the bench tests and passed the tests from National Motor Vehicle Quality Supervision and Inspection Center (Chongqing, China). (Report NO. 10-WT-DBJ-N76). Meanwhile, it has also passed the technical appraisement from China Machinery Industry

Federation. Now, the transmission has installed on the vehicles, and carried out a series of other tests.

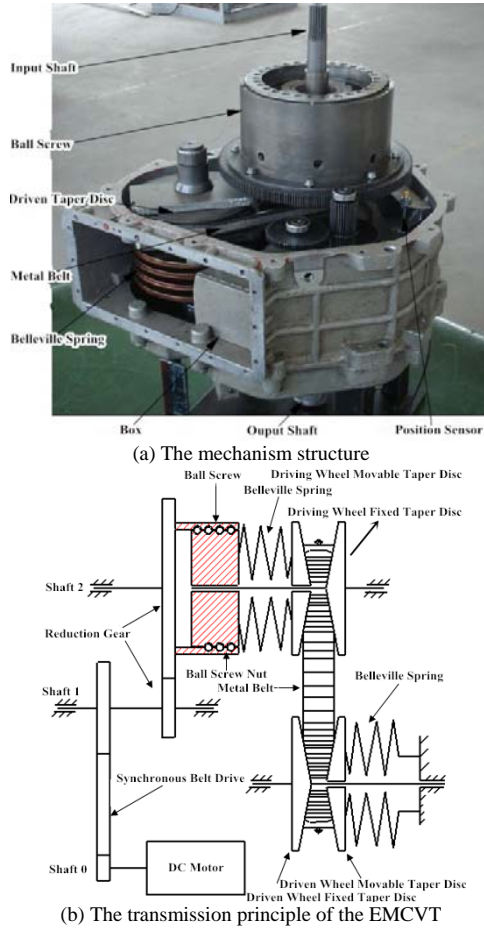


FIGURE I. THE MECHANISM STRUCTURE AND THE TRANSMISSION PRINCIPLE OF THE EMCVT

III. MODELING OF EMCVT SPEED RATIO CONTROL SYSTEM

As is shown in Fig.1, the transmission ratio of this EMCVT is changed by changing the radius of the metal belt powered by the taper disc. In turns, the movement of the taper disc is achieved by the movement of the nuts, and the nuts are driven by the screw rotation. The screw rotation is driven by the tri-range cylindrical gear reduction mechanism powered by the DC motor. Obviously, it's the DC motor that achieves the goal of speed governing.

IV. SPEED RATIO MODEL OF THE CVT

From the mechanical structure of the EMCVT, the transmission ratio can be determined by the driving wheel pitch radius (R_{DR}) and the driven wheel pitch radius (R_{DN}),

During the process of the transmission, because the length (L) of the metal belt can be regarded as a constant (the variation caused by the elastic deformation is very small), so we can know that,

$$L = (\pi + 2\alpha)R_{DR} + (\pi - 2\alpha)R_{DN} + 2d \cos \alpha \quad (1)$$

Where $\alpha \approx \sin \alpha = (R_{DR} - R_{DN})/d$, d is the center distance of the transmission shaft. From the equation (1), the approximate calculation equation of the speed ratio can be determined [1],

$$i = \frac{-B \pm \sqrt{B^2 - 4AC}}{2A} \quad (2)$$

In equation (2), $A = R_{DR}/d$, $B = \pi - 2R_{DR}/d$, $C = \pi + R_{DR}/d + 2d/R_{DR} - L/R_{DR}$. The speed ratio of the metal belt continuously variable transmission device ranges from 0.5 to 2.5.

V. AXIAL THRUST RATIO φ BETWEEN DRIVING TAPER DISC AND DRIVEN TAPER DISC

The axial thrust ratio φ is an important parameter in terms of the EMCVT design calculation and the entire control system, that is $\varphi = F_{aA}/F_{aB}$. The experiments show that the axial thrust ratio φ changes with the transmission ratio i and the torque ratio $\lambda = T_e/T_{e\max}$. After further experimental analysis, we can know that the axial thrust ratio φ is mainly determined by the transmission ratio i and the torque ratio λ . The maximum torque that the mechanism can transfer has a very little impact on the axial thrust ratio φ , especially under the condition that the torque ratio $\lambda > 0.5$, λ almost has no impact on the φ . However, when the CVT works normally, the actual torque ratio generally is higher than 0.5. Thus, the influence from the torque ratio λ can be ignored.

The relations among the axial thrust are calculated under the circumstance of not transferring torque. We use F_{asmall} to represent the axial thrust when the belt wheel meshed with the belt in the small working radius R_{small} . Thus, the radical force per unit arc length of the metal steel ring in the V-gutter is represented by P_T and the relation between the initial tension of the steel ring and the axial thrust of the belt wheel is

$$4T_0 \cos \lambda = 2 \int_0^{\frac{\pi}{2}-\lambda} P_T \times \cos \theta \times (R_{small} + \Delta h) d\theta$$

$$= \frac{4 \times F_{asmall} \times \tan \alpha}{(\pi - 2\lambda)} \times \cos \lambda \quad (3)$$

Where, α is the cone angle of the taper disc. Δh is the distance between the pendulum edge of the thrust sheet and the saddle surface. The relation between the belt wheel axial thrust is

$$\varphi = \frac{F_{asmall}}{F_{abig}} = \frac{(\pi - 2\lambda) \times \tan \alpha'}{(\pi + 2\lambda) \times \tan \alpha} \quad (4)$$

In terms of the actual control of the CVT, the most intuitive and effective method is to calibrate the relations among axial thrusts of driving wheels and driven wheels. Then, the experimental results are collected to make the data map.

VI. AXIAL CLAMP FORCE MODEL OF CVT DRIVING AND DRIVEN WHEELS

In the process of speed governing, the clamp force F_{diskR} , F_{diskN} of the driving and driven wheel both has the function relationship with the taper discs deformation. With an arbitrary ratio i , the distance between the driving shaft movable taper disc and its initial position is s_1 , similarly, the distance between the driving shaft movable taper disc and its initial position is s_2 . So we can acquire the value of the spring force of the driving and driven taper discs during the process of the speed governing.

$$\begin{cases} F_{diskR} = F_{diskR}(k - \frac{s_1}{8}) \\ F_{diskN} = F_{diskN}(k' + \frac{s_2}{8}) \end{cases} \quad (5)$$

Where,

$$\begin{aligned} s_1 &= 2(R_{DR} - R_{DR\min}) \tan \alpha, \\ s_2 &= 2(R_{DN\max} - R_{DN}) \tan \alpha. \end{aligned}$$

According to the relations among the driving taper disc, the driven taper disc and the transmission ratio, we can acquire that

$$s_2 = 2 \tan \alpha [R_{2\max} - i(\frac{s_1}{2 \tan \alpha} + R_{1\min})] \quad (6)$$

VII. ASSOCIATION MODEL OF THE CVT TRANSMISSION RATIO AND ENGINE SPEED UNDER STEADY-STATE CONDITIONS

The definition of the steady-state conditions: all parameters of the vehicle power transmission system are all constant, such as the throttle opening, the speed, the torque, the wheel speed, the frontal drag, the road gradient and so on. The control of the CVT is relatively easy under the steady-state conditions.

Assuming that the clutch is in a state of the lock-up, that is, there is no belt slip when the vehicle is running at the drive shift. Thus, the angular velocity of the engine crankshaft ω_e is equal to the angular velocity of the driving wheel ω_p . The ratio of the CVT is

$$i = \frac{\omega_p}{\omega_s} = \frac{T_s}{T_p \eta} \quad (7)$$

In the above equation, T_p represents the torque applied to the driving wheel from the metal belt. T_s represents the torque applied to the driven wheel from the metal belt. η is the transmission ratio of the CVT. Under the condition that the vehicle is running at a steady speed, we can acquire the power of the vehicle from the engine characteristics curve.

$$P = \omega_e \cdot T_e = \omega_d \cdot T_d \quad (8)$$

Where, P is the power of the vehicle. T_e is the engine output torque. T_d is the equivalent drag torque of the driving shaft.

Because we know that $T_p = T_e$, $T_s = T_e \eta_a$, $\omega_d = i_a \omega_s$, $\omega_e = \omega_p$, we can acquire the relation equation of the CVT transmission ratio and the engine speed in the steady-state working condition.

$$i \omega_e = \frac{P \eta_a}{T_p \eta} \quad (9)$$

In equation (9), i_a is the transmission ratio from the driven wheel to the driving shaft. η_a is the effectiveness from the driven wheel to the driving shaft. In the steady-state conditions, the engine optimizing dynamic performance and economic performance shift curve can be converted into the engine optimizing dynamic speed ratio performance and economic performance curve. That lays the foundation of controlling the speed ratio.

VIII. CONTROL STRATEGIES OF EMCVT

The economic gear shift is taken as the example to illustrate the control strategy. When the vehicle is driving under the economic gear shift, the signals of the current throttle and the engine speed will be read. Whether the current engine speed is equal to the optimizing economic speed corresponding to the current throttle is the basis for determining the gear shift is chosen as the economic gear shift. If the engine speed meets the above judgement, a new throttle signal will be detected to repeat the above process. If not, the signal will go back to the main procedure. According to the equation (9), we know that the engine speed is in inverse proportion of the transmission ratio. If the current engine speed is lower than the current throttle optimizing economic speed, we have to judge that the transmission ratio is whether in a state of the maximum position. At that time, the transmission ratio is supposed to reduce to increase the engine speed. If the transmission is in a state of the minimum position, the transmission ratio is supposed to remain unchanged. If the current engine speed is higher than the current throttle optimizing economic speed, we have to judge that the transmission ratio is whether in a state of the minimum position. At that time, we have to judge that the transmission ratio is whether in a state of the maximum position. If the transmission is in a state of the maximum position, the transmission ratio is supposed to remain unchanged. After detecting the transmission ratio, the engine speed will be detected in a new round. Similarly, the dynamic gear shift has almost the same control strategy. The only difference is that the engine speed has to compare with the optimizing dynamic speed.

During the process of the vehicle driving, all kinds of disturbances occur successively. Thereby, the traditional incremental PID is not suitable to choose. In order to solve this problem, the incomplete differential PID control is adopted, adding a first-order inertia process (the low-pass filter),

$G_f(s) = 1 / [1 + T_f(s)]$. Currently, there are two kinds of incomplete differential PID control methods. One is adding the first-order inertia process to the differential link, and the other one is adding the first-order inertia process to the PID controlling unit. Because of relying on the same principle, we will illustrate the first control method. For the first structure, the transfer function is

$$u_D(k) = \frac{T_f}{T_f + T} u_D(k-1) + \frac{K_p T_D}{T_f + T} [e(k) - e(k-1)] \quad (10)$$

From above equations, we can find that the height of the control pulsing signals from the differential output in the first sampling period all reduce in certain degree after introducing the incomplete differential. In the following periods, the height will gradually reduce according to the law of $d^k u_D(0)$. Thus, the problem of lacking in incremental PID control is solved, and now it has excellent control characteristics.

IX. CONCLUSION

EMCVT is a new vehicle continuously variable transmission. By adopting the DC motor to control the ball screws, the displacement of the taper disc compressed by the Belleville springs. Thus, the function of speed governing is realized. For this special structure, the speed ratio control model, the clamp force control model and the speed governing under the steady-state working conditions are all established. Meanwhile, all of the models are all verified by the comparison bench tests in the later stage. The control strategies of the EMCVT are also verified by bench tests and road tests. The experiments all indicate that the expected control objectives can be achieved and they have the strong stability and anti-interference.

ACKNOWLEDGEMENT

This research was supported by the Science and Technology Funds from Liaoning Education Department (No. L2015375).

REFERENCES

- [1] Lei Zhang, Xiaomei Cong, Huijian Pan, Zuge Cai, Xiumin Yang, The Control System Modeling and The Mechanical Structure Analysis For EMCVT, TELKOMNIKA, 2013, 11(7): 4159-4167
- [2] Toru Fujii, Takemasa Kurokawa and Shigeru Kanehara. A Study of a Metal Pushing V-Belt Type CVT--Part 1: Relation between Transmitted Torque and Pulley Thrust, SAE, Tech. Paper Series 930666(1993)
- [3] Naishi Cheng et al. Automotive metal V-belt Type CVT: CVT principles and design, Beijing: Machinery Industry Press, 2007

Improved Rigid Cable Method for Prestress Optimization of Suspen-dome Structure

Wenfeng Du*, Shuailiang Zhang, Longxuan Wang and Pengfei He

Institute of Steel and Spatial Structure in School Civil Engineering and Architecture, Henan University, Kaifeng 475004 China

*Corresponding author

Abstract—For considering the losses of prestress in suspen-dome structure after pre-stress optimization using rigid cable method, an improved rigid cable method was proposed. The temperature stress is applied to corresponding element to compensate the loss of prestress, and the relationship between temperature and prestress loss is deduced. An example and engineering application are discussed. Results show that the improved rigid cable method is effective and applicable.

Keywords—suspen-dome structure; losses of prestress; rigid cable method

I. INTRODUCTION

Stringed dome structure is a kind of self-balanced structure system composed of three elements of cable, rod and beam. Through the appropriate prestressing to the cable, the single-layer lattice shell of the strut generates the opposite displacement when using the load, which will achieve the effect of improving the structural rigidity and reducing the internal force of the grid shell rod, while the lower inclined cable can offset the horizontal thrust at the support. Pestress of cable is an externally-controlled assembly force whose size has a significant effect on the internal force distribution and displacement of the structure. If prestress of cable isn't properly applied, which will be counterproductive. Excessive prestress not only does not play the role of prestress, but also makes the cable exceed its ultimate tensile load under the action of damage, and too low prestress can't meet the structural requirements of the stiffness.

So it is reasonable determining the level of prestress, which is one of the key issues in the design of the suspen-dome structure.

II. PRESTRESSED OPTIMIZATION METHOD

A. Three Prestressed Optimization Methods

Prestressed cable is the most active and sensitive element in the suspen-dome structure. The value of prestress in practical engineering must be reasonable, and the value range should be the process of initial state to load state when the structure is formed as a whole. The axial force of the upper monolayer reticulated shell should be reduced as much as possible while taking into account the influence on structural stability and horizontal thrust.

At present, there are three main methods to optimize the cable prestress of the suspen-dome structure. The first is the geometric method. The method uses the vertical upward force generated by the struts at different locations of the cable to be

equal to the equivalent node load on the single-layer lattice shell. Based on the inner radial cable and the adjacent outer ring pole in the winding node and static load balance to determine the proportion of prestressed ring method [1]. The second is rigid cable method. This method refers to the method of prestress analysis in cable-stayed bridge, ie, magnifying the elastic modulus of the lower cable by several times, doing static analysis without prestressing, and then confirming each circle according to the calculation result Prestress ratio [2,3]. The third tangential balance method, so that the inner radial cable and the adjacent outer ring bar connected to the winding node in the outer force generated in the upper shell spherical tangential principle to determine the proportion of prestress the ring [4,5]. The case analysis and comparison study show that the stress and node displacement of the rod members are all uniform with the rigid cable method. However, the prestress applied by the geometric method and the tangential balance method changes the shape of the reticulated shell [4, 5].

B. Improve Rigid Rope Method

The concept of rigid cable method is clear and easy to operate. However, the rigid cable method applies prestress to the structural unit by applying the initial strain. If the prestress value is directly converted into the initial strain and applied to the corresponding cable, the cable structure will be rebalanced Deformation, leading to loss of cable prestress.

In order to accurately apply the equilibrium prestress, it is necessary to consider the prestress loss of the cable after structural rebalance. First of all, according to the rigid cable method, the section of each lap cable is estimated in advance. The elastic modulus of the cable is increased by 100 times and the initial strain is 0, and the tension force of each cable unit can be obtained by using the ANSYS software to calculate the tensile force of N_i .

Then the elastic modulus of the cable was changed back to the original value, and the initial strain was calculated according to N_i , which is applied to the corresponding cable element, and the static force calculation was performed again to obtain the pulling force of each cable element at this moment, which is denoted as \bar{N}_i .

There is a loss of prestress between the tension of each cable unit and the tension after rebalancing:

$$\Delta N_i = N_i - \bar{N}_i \quad (1)$$

Next, the prestress for these losses can be compensated for with temperature stress.

$$\Delta N_i = \Delta \sigma A_i \quad (2)$$

$$\Delta \sigma A_i = \Delta L E_i * A_i / L \quad (3)$$

$$\Delta L = T_i \alpha_i * L \quad (4)$$

Where σ is the stress, A is the cross-sectional area, L is the length, E is the modulus of elasticity and T is the temperature, α is the coefficient of linear thermal expansion of the material at temperature.

$$T_i = \Delta N_i / (E_i * A_i * \alpha_i) \quad (5)$$

Therefore, if the temperature T_i is applied to the corresponding cable unit, the temperature stress can be used to compensate for the loss of the prestress ΔN_i . At this time, the recalculation of the pulling force of each cable unit is the prestress that the equilibrium state is expected to be applied.

The above analysis method of improving rigid cable method adopts the method of applying temperature stress to make up for the loss of cable internal prestress caused by the deformation of cables after structural rebalance.

C. Examples

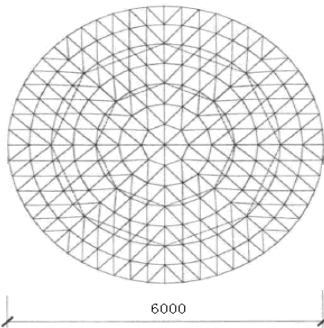


FIGURE I. STRING BRANCH DOME PLANE

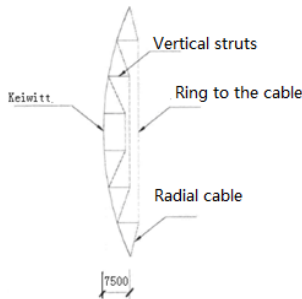


FIGURE II. STRING BRANCH DOME FAÇADE

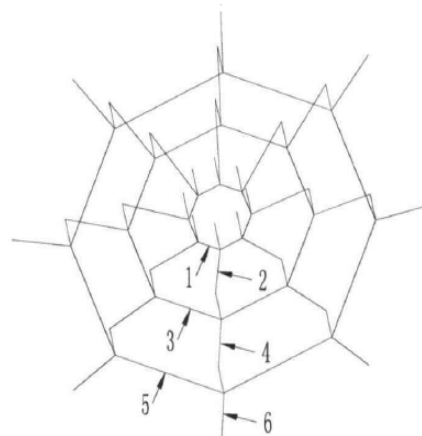


FIGURE III. CABLE NUMBERS

As shown in Figure 1, the chord support dome has a span of 60m and a height of 7.5m. Three rings of ring cables are arranged. The same cross-section of the radial cables and hoop cables of the same ring is used. The innermost cable is PES5-37 (726mm²). Ring cable is PES5-55 (1080mm²). Outer ring cable is PES5-109 (2139mm²). Tilting the cords along the eight radial ribs, Structure withstand vertical uniform load. Single-layer reticulated shell members use Ø 180 round bar and the bar use Ø 159 round tube. Steel elastic modulus is 2.06E11N/m² and cable elastic modulus is 1.9E11N/m² and steel linear expansion coefficient is 1.2e-5. The peak load is 14.1kN and the load of the outermost node is 5.7kN and the load of the other nodes is 11.55kN. The three lap ring cable, radial cable were numbered as 1, 2, 3, 4, 5, 6 group cable, shown in Figure 2. When using ANSYS for calculation, the winding rod adopts the BEAM4, and the nodes are just connected. Rod adopts LINK8 and cable adopts LINK10, and prestress is applied by applying the initial strain method.

Table 1 shows the structure of the example using the rigid cable method and the improved rigid cable method. Table 1 shows that the use of rigid cable method, the recalculated loss of prestress about 13%, which is not to be ignored. With the improved rigid cable method, the cooling compensation of each corresponding cable unit needs to be compensated. The error between recalculated prestress and expected prestress is up to about 1%. One reason for this error is that the choice of the decimal places in the calculation process is caused by the other reason that the structure has certain geometric nonlinearity.

TABLE I. PRESTRESSED OPTIMAL DESIGN VALUE (KN)

Cable number	1	2	3	4	5	6
Rigid cable method(KN)	41.760	36.296	196.499	162.702	700.00	558.016
recalculate(KN)	36.179	31.422	170.676	141.355	611.314	487.477
Prestress loss(KN)	5.581	4.874	25.823	21.347	88.686	70.539
Prestress loss percentage	13.364	13.428	13.142	13.120	12.669	12.641
Apply temperature(°C)	-3.372	-2.945	-10.4879	-8.669	-18.185	-14.464
Recalculate again(KN)	41.420	35.886	194.628	160.934	697.057	555.053
error	0.814	1.130	0.952	1.087	0.420	0.531

III. OPTIMUM EXAMPLE OF PRESTRESSING OF SLANTING DOME IN QINYANG GYMNASIUM

The roof adopts the chord dome structure, which is supported by 32 hinge supports on the concrete ring beam. Winding for the Kaweite form single-layer spherical reticular shell, the outermost edge of the ring is sunflower arrangement, the lower part of the arrangement of 4 rings, strut height from the inside to outside 4.5m, 5m, 5.5m, 6.0m. Single-layer reticulated shell members are used Q345B steel section, which is a total of 7 kinds of rod. The smallest is $\varnothing 219 \times 6$ and the largest is $\varnothing 500 \times 25$ and the strut is $\varnothing 245 \times 8$. Ring to the cable from the inside to the outside using high strength steel wire bundle (tensile strength 1670MPa), section is $\varnothing 7 \times 55$, $\varnothing 7 \times 55$, $\varnothing 7 \times 109$, $\varnothing 7 \times 109$. The outermost ring of radial cable is made of high strength steel rod with $\varnothing 60$ mm diameter (yield strength 550MPa). The second outer ring is made of high strength steel rod with $\varnothing 50$ mm diameter. The other inner rings are made of high strength steel rod with diameter of $\varnothing 50$ mm. The elastic modulus of the steel pipe is $2.06 \times E11 N/m^2$ and the elastic modulus of the cable is $1.9 \times E11 N/m^2$. The initial tension of the hoop cable is introduced through the initial strain of the application unit. The prestressing force controlled by the prestressing force of the hoop cable from the inside to the outside is obtained through the prestress optimization design. The initial pulling force of the radial cable is indirectly introduced through the hoop cable. Reticulated node is just connected, the connecting point between strut and reticulated shell and the connecting point between strut and cable are hinged. Roof single-layer reticulated shell and cable system as shown in Figure 4 and Figure 5.

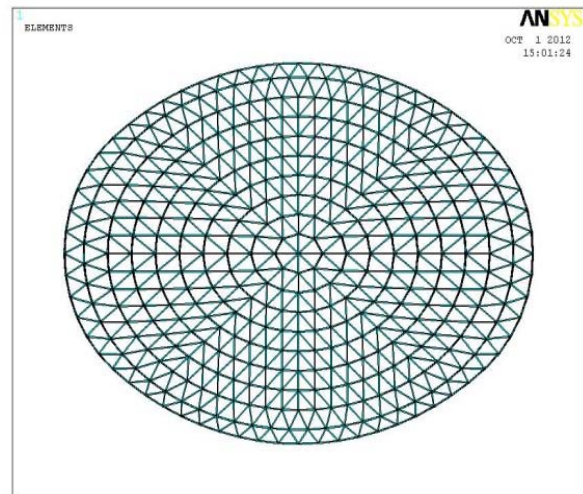


FIGURE IV. ROOF SINGLE-LAYER RETICULATED SHELL

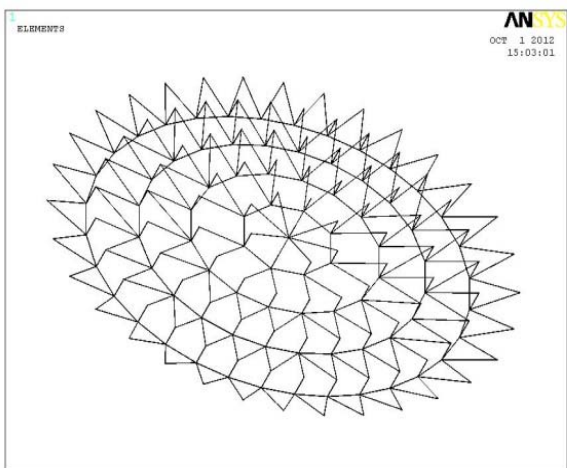


FIGURE V. ROOF CABLE SYSTEM

Table 2 shows the structure of the improved rigid method of calculation results. It can be seen that with the rigid cable method, the recalculated prestress loss is about 30%. However, with the improved rigid cable method, the cooling compensation for each cable unit needs to be compensated. The error between the recalculated prestress and the expected prestress is the largest Less than 5%.P

At the same time, the calculation results show that the maximum vertical displacement of the structure is 46.1mm, the maximum axial pressure of the top single-layer shell member is 596kN, the average radial displacement of the support joint is 0.7mm, and the optimization result of the cable prestress is ideal.

TABLE II. PRESTRESSED OPTIMAL DESIGN VALUE (KN)

Ring cable location	The innermost ring	The inner ring	Outer ring	The outermost ring
Rigid cable method(KN)	37.64	482.71	1677.96	2887.5
recalculate(KN)	23.56	356.38	1129.96	1947.9
Prestress loss percentage	37.4	26.2	32.6	32.5
Apply temperature(oC)	-2.92	-26.19	-57.3	-98.3
Recalculate again(KN)	35.84	475.22	1624.89	2736.81
error	4.78	1.55	3.16	5.22

IV. SUMMARY

(1) Of the three methods for cable prestress optimization of the suspen-dome structure, the rigid cable method is the most convenient and the stress and node displacement of the winding rod are relatively uniform. However, the defect is caused by applying the initial strain to the structural unit prestressing is applied. If the prestress value is directly converted into the initial strain and applied to the corresponding cable, the cable will be deformed after the structure is rebalanced, resulting in loss of prestressing force in the cable.

(2) It is a good attempt to make up for the loss of cable pre-stress caused by the deformation of the cable after the structure rebalance due to the application of thermal stress. The results of the calculation and the actual engineering proves the effectiveness of this method.

REFERENCES

- [1] Zhang Ming-Shan, Zhang Shi-Hong.Determination and Stability Analysis of Initial Prestressing Distribution of Slab Dome [J]. Spatial Structure, 2004, 10 (2): 8-12.
- [2] Zhang Xiaofeng. Research on overall stability and dynamic performance of suspend dome in Olympic badminton stadium [D]. Beijing: Beijing University of Technology, 2008.
- [3] Wang Bohui. Cable-stayed bridge structure development and China's experience. Transportation Press, 2004.
- [4] Fu Zhiqiang. Dynamic catastrophic dome structure of the disaster [D]. Hangzhou: Zhejiang University master's degree thesis, 2008.
- [5] Yang Bo, Dai Guoxin, Nie Shidong, and so on. ZHAO Jin-hua.Pre-optimization of Chamfered Triangular Dome Structures [J]. Construction Technology, 2010, 40 (5): 100-104.

Technology of Sound Velocity Correction for Multi-beam Bathymetry Sounding

Weiming Xu^{*}and Kai Ma

Department of Hydrography and Cartography, Dalian Naval Academy 116018, Dalian, Liaoning, P. R. China

^{*}Corresponding author

Abstract—The multi-beam echo sounding system was the most effective instrument to detect the seabed topography. In order to reduce the seafloor terrain distortion caused by the representative error of sound velocity profile (SVP), the indirection adjustment inversion method was introduced after analyzing the impact of the sound profile measuring error on the seabed terrain. To testify the proposed indirection adjustment technology, two group experiments were designed, in which Group 1 used the adjustment inversion method to correct the SVP data with the small error while Group 2 utilized the same method to correct the SVP data with the large error. The results of field experimental data are shown that: the standard deviation (STD) of the inverting SVP is reduced by 64.2% and that of the single Ping seabed topographic reduce 80.7%. The computational efficiency of adjustment inversion method is better than that of the substitute SVP method. Additionally, the presented approach, which can overcome many disadvantages of the manual approach to SVP correction, is superior to that of the substitution SVP and optimizing the structure of SVP.

Keywords—multi-beam bathymetry sounding; sound correction; seabed topography; indirection adjustment

I. INTRODUCTION

Acoustic is the best and often the solo mean to detect the water column and sea bottom efficiently and accurately [1]. A large variety of instruments now available, in these sonar mapping systems which can be divided into three categories, that is, single-beam echo-sounders, multi-beam echo-sounders, and side scan system. Nowadays, the multi-beam sounding system, which integrates the technologies of satellite navigation and positioning, computer science, and the digital sensor etc., is widely used in the domains such as the marine engineering, the underwater archaeology, and the marine national defense construction [2-3]. The velocity at which the acoustics waves travel is also varied with the temperature of the water, its salinity, and whether it contains heterogeneities (e.g., bubbles or suspended sediments). Because it is generally difficult to measure local sound velocity, it is most often derived from proxy measurements of temperature, salinity, and depth, using tools such as XBT (expendable - bath - thermograph) or CTD (conductivity – temperature - depth). When even these measurements are not available, approximate values can be derived from compilations such as the Levitus database [1]. Accordingly, the accuracy of multi-beam seabed topography measurement significantly depends on the measuring accuracy of the sound velocity profile (SVP) [3]. Due to the sound velocity would change in space and time as

the sea flow, different sound velocity profile structure could also lead to the changes of the acoustic wave propagation, which brings about the distortion terrain of the seabed. Three technologies of sound velocity correction are used to deal with the above-mention distortion [2-5]. The first is based on the substitution of sound velocity profile, namely, the principle of minimal distance or minimal time. However, the correction effect of this method is limited and hard to meet the actual requirement. The second is the artificial modification of some parameters during the data processing system. With the continually increasing volume of data from advanced multi-beam sonar systems, the manual editing process has become very time consuming, especially in shallow water surveys. The third is to optimize the structure of simulating a velocity profile based on the sound velocity formula, however, which requires more samples and parameters, and more complicated calculation. Therefore, based on the indirection adjustment theory, the inversion SVP is contrastive analyzed with the equivalent SVP in this paper.

II. THE IMPACT OF THE SOUND PROFILE ERROR ON THE SEABED TOPOGRAPHY

Using the multi-beam system (MBS) to detect the flat area shallow water would be affected by the complicated marine environment. Consequently, there would be certain errors between the measured sound profile data and the actual sound profile data. The measuring accuracy of sound velocity profile restricted the multi-beam measuring precision of the seafloor topography, which was affected by temperature, salinity, and pressure, etc [6-7].

As shown in FIGURE I, according to Snell's law [1], the entire water could be regarded as a composition of multiple uniform layers of water. Assuming that with $1, 2, \dots, n$ to index each water layer, in the surface of each layer, according to the law of refraction, which is given by

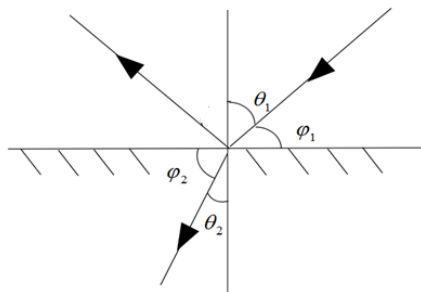


FIGURE I. THE GEOMETRY OF ACOUSTIC REFRACTION

$$\frac{\sin q_{1j}}{C_1} = \frac{\sin q_{2j}}{C_2} = \dots = \frac{\sin q_{nj}}{C_n} = p_j \quad (1)$$

where θ_{ij} is the grazing angle after beam pass through each water layer. C_{ij} is referred to as the velocity in each uniform water layer, $i = 1, 2, \dots, n$. p is the Snell constant. According to the Snell's law, after continuously propagating through each multiple layer, it appears that the sound ray turn to be bent. It's obviously that the sound velocity error may interfere with the multi-beam measuring precision due to the sound ray bending. On the edge of the beam, this interference phenomenon is particularly serious [8-10]. The seafloor topography appears as a curving shape on the transverse section, which is referred to as the "frown face", or its symmetric graph, namely, the "smiling face".

III. INDIRECTION ADJUSTMENT INVERSION METHOD

The actual seafloor terrain also be regarded as flat, and the aim of the adjustment inversion method is to seek for a set of model correction coefficients to ensure its correctional and actual displacement match optimally. In another words, the terrain distortions can be transform into the actual topography which be supposed to flat by nonlinear weighted least squares (NWLS) principle, and then the inversion SVP that close to the actual SVP is obtained [11-13].

Consider the acquired beam signal travel time T of unidirectional transmission beam in the process of the entire sounding without error. Using adjustment inversion method to correct the sound velocity error and the seabed distortion, assume the vertical displacement of a certain beam is Z_j , and the horizontal displacement is X_j . According to the stratification, we know the heights of layers $n-1$, the sound velocity of each layer, the Snell ray parameters, and the true value of the one-way spreading time T of sound wave. Without considering the errors of surface velocity, we obtain the observation equations by indirect adjustment as follows

$$X_j = F_j(C_1, C_2, \dots, C_n) = \sum_{i=1}^{n-1} \Delta t_{ij} \cdot C_i^2 p_j + \left(T_j - \sum_{i=1}^{n-1} \Delta t_{ij} \right) C_n^2 p_j \quad (2)$$

$$Z_j = H_j(C_1, C_2, \dots, C_n) = \sum_{i=1}^{n-1} \Delta Z_{ij} + \left(T_j - \sum_{i=1}^{n-1} \Delta t_{ij} \right) \cdot C_n \cos \theta_{nj} \quad (3)$$

where i is the number of layers, $i=1, 2, \dots, n$. j is the number of sound beams, $j=1, 2, \dots, m$. Δt_{ij} is beam travel time in the layer.

The number of observed beam m is often greater than the number of sound velocity parameters, so the equation system has a unique solution. But the observation equations is nonlinear, it needs to be linearized by Taylor series expansion method. Taking X_{ij}^o and Z_{ij}^o as the approximation of the vertical displacement true value and the horizontal displacement true value while the sound beam j passing through the layer i , dX_i and dZ_i as the correction of the approximation and the true value, therefore, the linear model of the indirect adjustment function is [14-15]

$$\hat{X}_j = X_j^o + dX_j = F_j(C_1^o, C_2^o, \dots, C_i^o) + \sum_{i=1}^n A_{ij} \hat{c}_i \quad (4)$$

$$\hat{Z}_j = Z_j^o + dZ_j = H_j(C_1^o, C_2^o, \dots, C_i^o) + \sum_{i=L}^n B_{ij} \hat{c}_i \quad (5)$$

where \hat{c} is the true value of sound velocity. C_o is the observed value of sound velocity. A_{ij} and B_{ij} are the coefficients of sound velocity correction for the adjustment inversion model, namely, the derivative of the vertical displacement and horizontal displacement on the sound velocity.

Solving simultaneous equations (4) and (5) would get a $m \times n$ Jacobi matrix of \mathbf{A} and \mathbf{B} . The sound velocity correction of partial derivative matrix \mathbf{A} and \mathbf{B} could get the total matrix $\mathbf{D} = [\mathbf{A} \ \mathbf{B}]^T$. The actual research indicates that some characteristic values of the coefficient of square $\mathbf{D}^T \mathbf{P} \mathbf{D}$ is small, and the condition number of equations is large, the inverse square matrix is singular, therefore, the solution tends to diverge. To solve this problem, the damping least-square method [13-15], which adds a damping term after the phalanx $\alpha \mathbf{I}$, is introduced. It is found that the co-factor matrix tends to singularity, and the reasonable damping coefficient value should be established. The method of design selection damping coefficient, currently, the damping coefficient of adaptive selection is still a subject of academic discussion, and the most widely used is ridge-tracing method. Apply the ridge-tracing method to determine a set of α value at the starting point 0.5, the greater the divergence of the co-factor array, the smaller the value. And the corresponding parameter values are listed, and α is the damping coefficient which makes the most stable parameter values.

Thus, the equations to get the sound velocity correction is attained as follows

$$\hat{c} = (\mathbf{D}^T \mathbf{P} \mathbf{D} + \alpha \mathbf{I})^{-1} \mathbf{D}^T \mathbf{P} \mathbf{L} \quad (6)$$

where \mathbf{P} is the weight matrix of the observed value. The setting of weight should be considered that the reliability of the edge beam signal data in the multi-beam system is lower than the central beam. According to the precision of the actual measurement for the various sound beams, the lower the accuracy is, the smaller the weight of the beam is. Where \mathbf{I} is the unit matrix, α is the damping factor, the size of which depends on the actual situation, that is, if the coefficient of square $\mathbf{D}^T \mathbf{P} \mathbf{D}$ has a relatively large singularity, then a larger damping coefficient is required. Otherwise, choosing a smaller coefficient, the matrix \mathbf{L} is written by [13]

$$\mathbf{L} = \begin{bmatrix} X^0 - F(C^0) \\ Z^0 - H(C^0) \end{bmatrix} \quad (7)$$

And the correction value of the underwater observation value matrix \mathbf{v} is [16]

$$\mathbf{v} = [\mathbf{x} \ \mathbf{z}] = \mathbf{D}\hat{\mathbf{c}} - \mathbf{L} \quad (8)$$

Add the distortion correction value to the seabed topography data, based on the central beam measurements to assess its correction accuracy, and assume the iteration threshold is 0.25% of the depth and central beam depth is actual depth. If the relative error of depth is greater than the iteration threshold, add the sound velocity correction to the original sound profile data again as the initial parameter to calculate, and iterative calculation will be constantly conducting to meet the requirements of International Hydrographic Organization (IHO) and National Oceanic and Atmospheric Administration (NOAA) [6-7].

IV. EXPERIMENTAL DATA AND ANALYSIS

In order to testify the effectiveness of the proposed technology, the multi-beam sounding data of China East Sea is chosen as the experimental model. In the experimental data the seabed topography appears the distortion caused by the sound velocity error.

The calculation example selects 6 main test lines and 1 inspection line in the sea area, and the depth variation is 49.2 ~63.1 m. The inspection line is mainly used to verify the effect of correction and does not participate in correction. Remove abnormal data and add correction (attitude, tide and time delay, etc.) as experimental preparation.

In this section, two groups of experiment are designed. Group 1 uses the adjustment inversion method to correct the SVP data with the small error and Group 2 uses the same method to correct the SVP data with the large error.

A. The Experimental Group 1

The number of sampling points for the actual seabed topography is 101. The obtained parameter C_0 is 1502 m/s and the g is -0.315. After 35.6 seconds equivalent SVP is

calculated. Set the depth of the inspection line to the actual depth.

As shown in FIGURE II, the inversing SVP is svp6 curve, the measuring SVP is svp1 curve, and the replaced SVP is svp2 curve. The single Ping depth correction is shown in FIGURE III, in which data1 is the actual depth, data2 is the correction depth, and data3 is error depth, respectively. The statistics of terrain correction is listed in TABLE II.

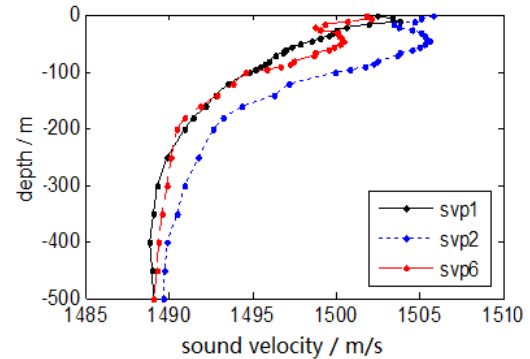


FIGURE II. THE SOUND VELOCITY PROFILE OF GROUP 1

TABLE I. THE ERROR STATISTICS OF GROUP 1 / (m/s)

Error value	Minimum	Maximum	STD
Error SVP	0.11	8.12	1.48
Inversion SVP	0.01	3.11	0.53

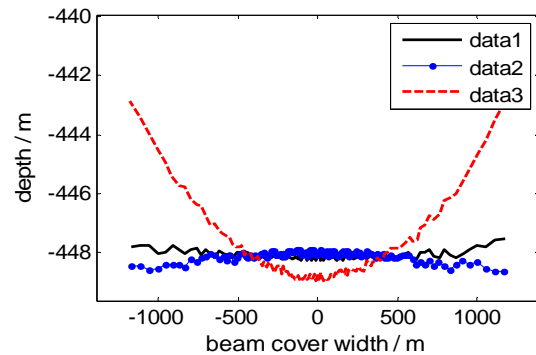


FIGURE III. SINGLE PING CORRECTION OF GROUP 1

TABLE II. TERRAIN CORRECTION STATISTICS OF GROUP 1 / (m)

Error value	Minimum	Maximum	STD
Error depth	0.01	3.41	0.90
Correction depth	0.01	0.46	0.37

As shown in TABLE I and TABLE II, The field data results show that the STD error of the inversing SVP is reduced by 64.2% and that of the single Ping seabed topographic reduce 66.7%. Obviously, the seabed terrain is significantly improved as shown in FIGURE III.

B. The Experimental Group 2

The water volume is designed by step, by which, 0m-100m each layer 5m, 100m-300m each layer 10m, and 300m-500m each layer 20m. When solving the normal equation, the co-factor matrix tends to singularity, and the singularity is larger. The parameter value diverges to 10^{-3} , therefore, to search for the damping coefficient in the range of $a=1\times 10^{-2}$ to $a=1\times 10^{-4}$, and get the optimal damping coefficient $a=2\times 10^{-3}$.

After iteration calculating, the inversion SVP is obtained, then, setting the depth of the inspection line to the actual depth.

As shown in FIGURE III, the inversing SVP is svp7 curve, the measuring SVP is svp3 curve, and the replaced SVP is svp1 curve. The single Ping depth correction is shown in FIGURE V, in which line1 is the actual depth, line2 is the correction depth, and line3 is error depth, respectively. The statistics of terrain correction is listed in TABLE IV.

The field data results show that the STD error of the inversing SVP is reduced by 64.2% and that of the single Ping seabed topographic reduce 80.7%.

TABLE III. THE ERROR STATISTICS OF GROUP 2 / (m/s)

Error value	Minimum	Maximum	STD
Error SVP	2.02	8.21	3.08
Inversion SVP	0.25	3.11	1.10

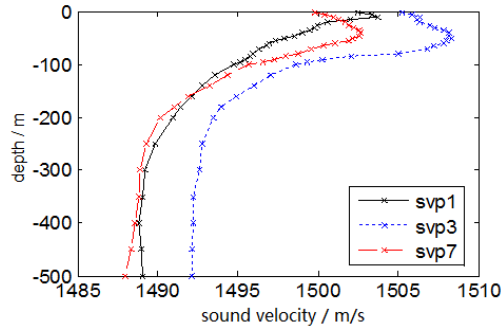


FIGURE IV. THE SOUND VELOCITY PROFILE OF GROUP 2

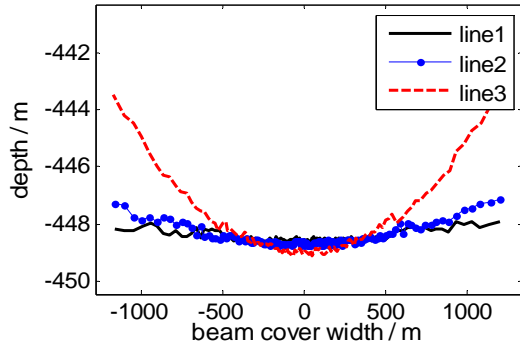


FIGURE V. SINGLE PING CORRECTION OF GROUP 2

TABLE IV. TERRAIN CORRECTION STATISTICS OF GROUP 2 / (m)

Error value	Minimum	Maximum	STD
Error depth	0.02	4.18	2.34
Correction depth	0.01	0.94	0.45

V. CONCLUSION

This paper first analyzed the main reason of the underwater terrain distortion due to the velocity error in the MBS for the flat area measurement. And then a sound velocity profile and the distortion correction technology of seabed topography are proposed based on indirection adjustment. The field experimental data show that: in the shallow sea water, the inversion sound velocity profile calculated by adjustment method is closer to the real profile compared to the error sound profile. Furthermore, the technology could effectively correct the distortion of the seafloor topography, reduce the depth error, which is satisfied the demand of high precision in the terrain measurement of the shallow sea. Additionally, the presented approach that can overcome many disadvantages of the manual approach to SVP correction, such as: time requirement, repeatability, and human error.

ACKNOWLEDGEMENT

This work was supported by the National Science Foundation under Grant 61071006, by the National Science Foundation for Post-doctoral Scientists of China (Grant No.2012T5087), by Open Fund of State Key Laboratory of Information Engineering in Surveying, Mapping and Remote Sensing under Grant 10P03.

REFERENCES

- [1] B. Philoppe, *The Handbook of Sidescan Sonar*. Chichester: Praxis Publishing Ltd, 2009.
- [2] R. Dashen, S. M. Flatte, W. H. Munk, *et al*, *Sound Transmission Through A Fluctuating Ocean*. UK: Cambridge University Press, 2010.
- [3] G. J. Zhan, Y. Z. Ouyang, X. P. Lu, *et al*, “Comments on the revision of the specifications for hydrographic survey”. *Hydrographic Surveying and Charting*, 2014, 34(1): pp.76-79.
- [4] X. P. Lu, S. F. Bian, M. T. Huang, *et al*, “An improved method for calculating average sound speed in constant gradient sound ray tracing technology”. *Geomatics and Information Science of Wuhan University*, 2012, 37(5) : pp. 590-593.
- [5] B. Calder and L. Mayer, *Robust Automatic Multi-beam Bathymetric Processing*. U.S. Hydrographic Conference. Norfolk, VA, USA, 2001.
- [6] NOAA, *Hydrographic Surveys Specification and Deliverables*. 2003
- [7] IHO, *IHO Standards for Hydrographic Surveys*, Special Publication No.44(4th). International Hydrographic Bureau, 1996.
- [8] X. Geng and A. Zielinski “Precise multi-beam acoustic bathymetry”. *Marine Geodesy*, 1999, 22(3) : pp. 157-167.
- [9] R. Hare, *Error Budget Analysis for US Naval Oceanographic Office Hydrographic Survey Systems*. Final Report for Task 2, FY 01, September 2001.
- [10] S. Dan, “On the least-squares adjustment of a straight line”. *Bulletin Géodésique* (1946-1975), 1972, 103(1) : pp.25-30.
- [11] J. J. Zhu, T. Y. Zuo, and Y. C. Song, *Error Theory and Foundation of Surveying Adjustment*. Beijing: Surveying and mapping press, 2013.
- [12] B. Schaffrin and Y. A. Felus, *On Total Least-Squares Adjustment with Constraints*. Berlin: Springer Heidelberg, 2005.

- [13] J. J. Moré, “The Levenberg-Marquardt algorithm: implementation and theory”. Lecture Notes in Mathematics, 1978, 630: pp.05-116.
- [14] C. L. Lawson and R. J. Hanson, “Solving least squares problems”. Siam Review, 2006(3) : pp.518-520.
- [15] G. I. Allen, L. Grosenick L, and J. Taylor, “A generalized least-square matrix decomposition”. Journal of the American Statistical Association, 2014, 109(505) : pp.145-159.
- [16] X. D. Yin, Y. Chen, J. Tang Jun, *et al*, “A comparison of international standards for hydrographic survey”. Hydrographic Surveying and Charting, 2011, 32(4) : pp. 35-38.

Power Efficiency Optimization of Hydro-pneumatic Transformer of Air-powered Automobile

Xiangheng Fu*

School of Automation Science and Electrical Engineering, Beihang University, Beijing 100191, PR China

*Corresponding author

Abstract—Hydro-pneumatic transform (short for HP transformer) wastes a lot of compressed air when working, and its power efficiency is low. To improve its efficiency, we carry on the parameter optimization which influences the power efficiency of HP transformer system. Firstly, we build up a mathematical model and use the MATLAB software to simulate. Next, we establish the test bench to experiment and verify the mathematical model. Through simulation we set different values to study the relationship between the efficiency and key parameters. We can get some conclusions that, when the input compressed air pressure ranges from 0.5MPa to 0.55MPa, or the area ratio of piston ranges from 4 to 6, the efficiency will exceed 30%. The efficiency nearly keeps constant when the stroke of the piston varies. What's more, with the increase of input pressure and effective piston area ratio, the output power will be rising. When the piston's stroke increases, the output power decreases a little bit. This paper can be a reference of researches on the design and optimizing of HP power system used on air-powered automobile.

Keywords—air-powered automobile; efficiency; HP transformer; optimization

I. INTRODUCTION

As hydro-pneumatic transform (short for HP transformer) has the advantages of smart size, simple structure and excellent performance, it is widely used to transmutation the power of the compressed air to the hydraulic power, such as air-powered automobile and pneumatic machinery [1-3]. However, it still has some disadvantages definitely: its efficiency is low because HP transformer wastes a lot of compressed air when working. Nowadays, studies about HP transformer are mainly refers to its structure and performance, while the efficiency is always ignored. Shen et al [4] research the dynamic performance of an air-powered pump during the air injecting process, and Takeuchi et al [5] design an expansion-type pump by using expansion energy, and they prove the efficiency of the new air booster structure. Shaw et al [6] design a hydraulic motor system which is driven by compressed air. He gets the relationship of speed and efficiency, but he doesn't research the method of parameter improvement. To solve the problem mentioned above, we explore the parameters influencing the efficiency.

In this paper, we introduce the working principle of the HP transformer firstly and then build up a mathematical model based on the principle. To verify the correctness of the mathematical model, we make the Physical object. And though the experiment, we can know that the results of simulation are similar to the experiments'. We also explore the key factors

that influence the power and efficiency. And we can make a conclusion that with the increase of the input compressed air pressure and the stroke of piston, the efficiency increase distinctly within the certain range. But with the effective area ratio of the piston increases, the efficiency decreases distinctly. In response to this situation, we analyzed the reasons in the paper. According to our study, a better choice we suggest is that the input compressed air is range from 0.5MPa to 0.55MPa and the area ratio of the piston floats between 4 and 6, the power efficiency will be optimized, and at this point, the power efficiency will exceed 30 percent. Also, the stroke of the piston can be decided by output power actually needs, because the efficiency keeps constant nearly when the stroke varies. This paper can be a reference of the performance to study and help designing optimization of the HP.

II. WORKING PRINCIPLES OF THE HP TRANSFORM

A typical HP transformer is shown in figure1, which is composed of two pneumatic chambers, two hydraulic chambers, one relief valve, eight check valves, piston, silencer, pressure regulator, solenoid directional valve and mechanical load.

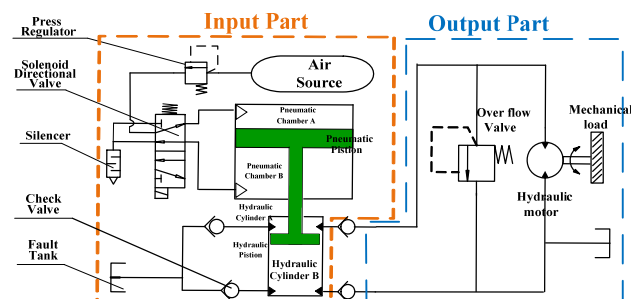


FIGURE I. HP TRANSFORMER STRUCTURE

At the moment that pneumatic chamber A is connected with air source and the pneumatic chamber B connects with atmosphere, low pressure oil will be injected into the hydraulic pumping chamber B. Because stress on the piston is not balance, the pressurized air in pneumatic driving chamber A will drive pistons moving to right. Fuel pressure will increase until it is equal to the output pressure. And then the compressed oil will flow out through the check valve.

When pistons reach the end of their strokes, they will impact the relief valve and lead to change its state. After that, the pneumatic chamber A is connected with the atmosphere and the compressed air flow into air. On the other hand, the pneumatic chamber B is connected to air source and

compressed air flows into it. Also, the low pressure oil flows into the hydraulic pumping A. The piston will move to left as the stress on it is not balance. The pressure of the oil in the hydraulic pumping A will increase until it is equal to the output pressure. Finally, the reversing valve will change its state at the time pistons reach the stroke ends. The high pressure oil will flow out continually by repeating the process mentioned above.

III. MATHEMATICAL MODEL

Through analyzing the working principles of the HP transformer, we have built a mathematical model, which is verified by the experiment study. The mathematical model of the pneumatic and hydraulic system as follows.

A. Pneumatic Energy Equations

We regard the air as ideal. Furthermore, there is no leakage in the chambers and no air comes in and goes out the chamber at the same time. So we can get the energy equation of pneumatic system as follows.

$$C_e M_a \frac{d\theta}{dt} = (A_h \cdot h_c + C \cdot q_e)(\theta_a - \theta_t) + R q_e \theta_a - p \quad (1)$$

$$C_e M_a \frac{d\theta}{dt} = A_h \cdot h_d(\theta_a - \theta_t) + R q_e \theta_a - pA \quad (2)$$

And in the equations, C_e : specific heat capacity of constant volume, 720J/(kg*K); M_a : mass of gas; A_h : the area of heat transfer; q_e : air mass flow; R : Gas constant, 287J/(kg K); θ_t : temperature; θ_a : the temperature of atmosphere; p : pressure; A : piston's area; u : piston's velocity; t : time.

B. Pneumatic Continuity Equations

The continuity equation of pneumatic system can be expressed as follows according to the ratio of p_b/p_d .

If $\frac{p_b}{p_d} > 0.528$, then:

$$q = \frac{A_e p_d}{\sqrt{\theta_t}} \sqrt{\frac{2k}{R(k-1)}} \left[\left(\frac{p_b}{p_d} \right)^{\frac{2}{k}} - \left(\frac{p_b}{p_d} \right)^{\frac{k+1}{k}} \right] \quad (3)$$

else if $\frac{p_b}{p_d} \leq 0.528$, then:

$$q = \frac{A_e p_h}{\sqrt{\theta_t}} \left(\frac{2}{k+1} \right)^{\frac{1}{k-1}} \sqrt{\frac{2k}{R(k-1)}} \quad (4)$$

And in the equations, A_e : the area of pneumatic intake and exhaust port; p_d : pressure of the upstream side; p_b : pressure of the downstream side; k : specific heat ratio; θ_t : temperature of the upstream side;

C. Pneumatic State Equations

The state equation of the compressed air in each pneumatic chamber can be written as follows:

$$\frac{dp}{dt} = \frac{1}{V} \left[\frac{pV}{\theta_t} \cdot \frac{d\theta_t}{dt} + R\theta_t q_e - pA_h u \right] \quad (5)$$

And in the equations, V : Volume.

D. Motion Equations

The total friction force F_f includes the viscous friction and Coulomb friction. According to the Newton's second law, we can get the motion equation of the piston as follows:

$$\frac{d^2x}{dt^2} = \frac{1}{M_p} (p_{dA} \cdot A_{dl} - p_{dB} \cdot A_{bl} - p_{bA} \cdot A_{bl} - p_{bB} \cdot A_{br} - F_f) \quad (6)$$

$$\frac{dx}{dt} = 0 \quad x = 0, L \quad (7)$$

$$F_f = \begin{cases} F_s & u = 0 \\ F_c + Cu & u \neq 0 \end{cases} \quad (8)$$

And in the equations, x : piston displace; p_{dA} : Pressure of pneumatic chamber A; p_{dB} : Pressure of pneumatic chamber B; p_{bA} : Pressure of hydraulic chamber A; p_{bB} : Pressure of hydraulic chamber B; F_f : Friction force; F_c : coulomb friction; F_s : maximum static friction; C : friction coefficient; L : stroke length; M_p : total mass of rod and pistons.

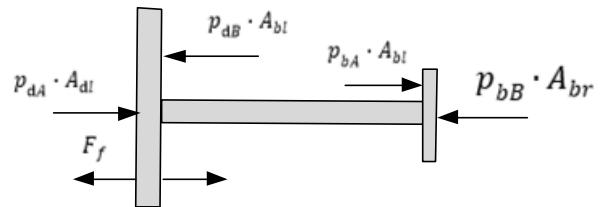


FIGURE II. THE FORCES ON THE PISTONS OF HP SYSTEM.

E. Hydraulic Pressure Equations

The pressure equation of the hydraulic pumping chambers can be written as follows:

$$\frac{dpdA}{dt} = \frac{\beta_t}{V} (Q_{A_in} - Q_{A_out} - A_{bh}u) \quad (9)$$

$$\frac{dpdB}{dt} = \frac{\beta_t}{V} (Q_{B_in} - Q_{B_out} - A_{bt}u) \quad (10)$$

And in the equations, β_t : bulk modulus; Q_{A_in} : input flow to hydraulic chamber A; Q_{A_out} : output flow from hydraulic chamber A; Q_{B_in} : input flow to hydraulic chamber B; Q_{B_out} : output flow from hydraulic chamber B.

F. Hydraulic Flow Equations

The flow equation of the oil can be written as follows:

$$Q_{out} = C_f A_h \sqrt{\frac{2(p_h - p_l)}{\rho_o}} \quad (11)$$

And in the equation, C_f : flow coefficient of the check valve orifice; ρ_o : oil's density; A_h : the area of hydraulic intake and exhaust port.

G. Hydraulic Motor Equations

$$q_{mo} = C_{Im}(p_{o1} - p_{o2}) + C_{Em}p_1 + D_{Em} \frac{d\theta_{om}}{dt} + \frac{V_0}{\beta} \cdot \frac{dp_1}{dt} \quad (12)$$

$$D_{Em}(p_{o1} - p_{o2}) = J_{Im} \frac{d^2\theta_m}{dt^2} + B_{Im} \frac{d\theta_{om}}{dt} + G\theta_{om} + T_{IL} \quad (13)$$

And in the equations, q_{mo} : hydraulic flow through the motor; C_{Im} , C_{Em} : hydraulic motor flow coefficient; D_{Em} : displacement of hydraulic motor; J_{Im} : inertia coefficient; B_{Im} : damp coefficient; G : stiffness coefficient; T_{IL} : extra load.

IV. SIMULATION AND EXPERIMENTAL STUDIES ON SYSTEM OPTIMIZATION

We use the mathematical software MATLAB/Simulation to analyze the system. The pressure of the input compressed air and the output oil is set at 0.6MPa and 2MPa. The figure 5a describes the output flow of experiments and simulation; figure 5b describes the rotated speed of the piston.

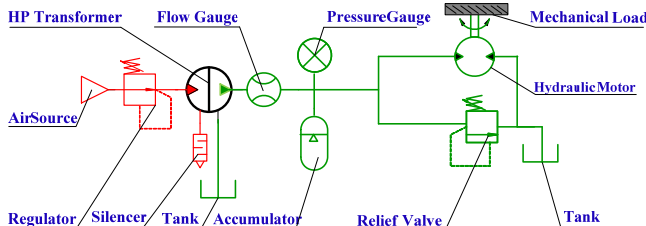


FIGURE III. GRAPHIC OF THE EXPERIMENT SYSTEM

As we can see from figure 5(a), the simulation's results of the output flow are consistent with the experiments', which verifies the mathematical model of the HP transformer is correct. The pressure of pneumatic chamber A increases to the input pressure and the pressure of chamber B decreases to the atmosphere when the reversing valve's state is changed. Once the pneumatic force is higher than resistance force towards left, the piston will move to right to build up the oil's pressure until it reaches its terminus. Then the pressure of the pneumatic chambers and hydraulic chambers changes with the reversing valve changing its state again.

One thing is clear that the amplitude of the experiments' result varies up and down compared with the simulation in the figure 5a and 5b, while the curves of the simulation are smoother. This is because the piston's stress is not evenness and the condition of the device is unstable.



FIGURE IV. EXPERIMENTAL STATION.

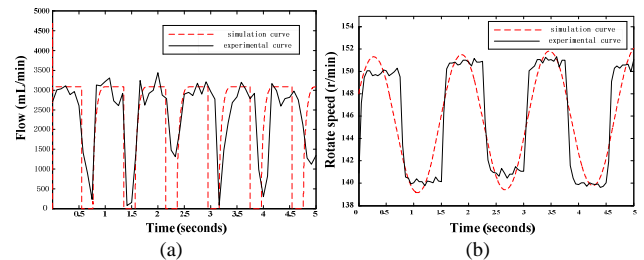


FIGURE V. SIMULATION AND EXPERIMENTAL COMPARISON CURVES. (A) FLOW (B) ROTATE SPEED

We set key parameters influencing the efficiency is input air pressure, including the stroke of the piston and the effective area ratio of the piston on the pneumatic chambers and hydraulic chambers. To explore the relationship between the each parameter and the efficiency, we take the control variable method that changes one variable while others keep constant.

A. Influence of Input Compressed Air's Pressure

The output pressure of the pumping chamber can be adjusted though the compressed air's pressure. The output oil's flow and efficiency is studied when the stroke of the piston and area ratio is set at 0.09 and 6, and the compressed air's pressure is set at 0.50MPa, 0.55MPa, 0.60MPa, 0.65MPa and 0.700MPa. Figure 5 describes the output power under the difference situation and the figure 6 shows the value of efficiency when input compressed air's pressure varies.

As we can see from the figure 6 and 7, the output power increases with the increase of the input air pressure, but it is also obviously that efficiency decreases in this process. This is because more expansion energy is wasted when the pneumatic chamber is connected with the atmosphere. And if the expansion energy of the compressed air can be reused, the efficiency of the HP transformer will be increase. Considering the output power and efficiency, we suggested that input pressure of compressed air is range from 0.5-0.55MPa.

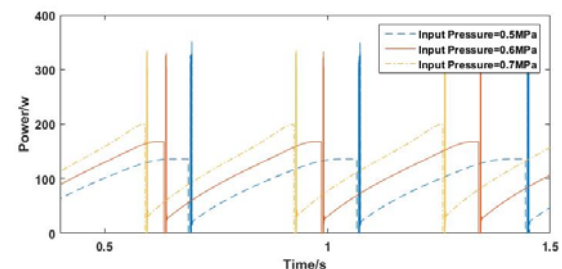


FIGURE VI. POWER-TIME CURVES.

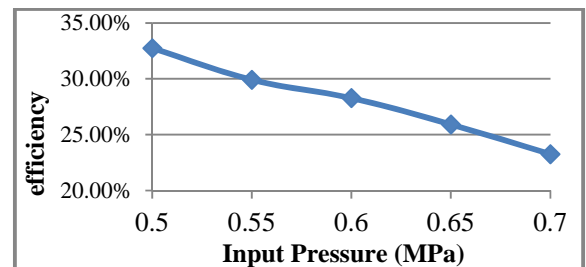


FIGURE VII. EFFICIENCY CURVES.

B. Influence of Piston's Stroke

Piston's stroke is up to chamber's size. The output power and efficiency is studied at the time input pressure and area ratio is set at 0.60MPa and 6, and the stroke of the piston is set at 600mm, 750mm, 900mm, 1050mm and 1200mm. Figure 8 describes the output power under the difference situation. Figure 9 shows relationship of efficiency and stroke of pistons.

As can be seen in figure 8 and 9, output power has a little bit decreasing with the increase of the piston's stroke, but the efficiency keeps the constant nearly in this process. This is because the speed of doing work is slowing down when the stroke of the piston increase. So the stroke of the piston is mainly up to output power, and we can select the value of the stroke according to the actual power needs. And during the process of our study, the value of the stroke floating around 0.09m is a better choice.

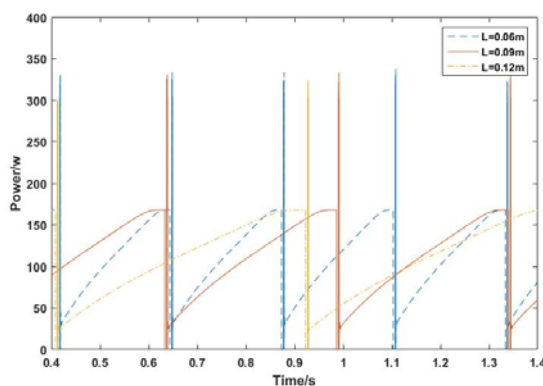


FIGURE VIII. POWER-TIME CURVES

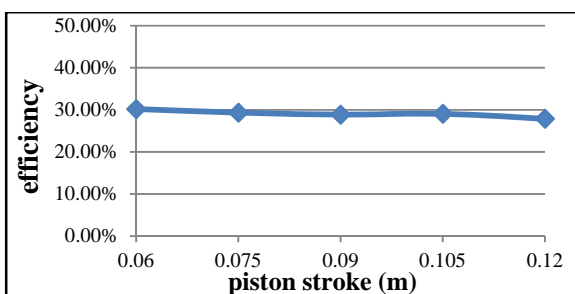


FIGURE IX. EFFICIENCY CURVES

C. Influence of Piston Area ratio

The area ratio of the piston is that the effective area of the piston in pneumatic chamber divided by the effective area of the piston in pneumatic chamber. The output power and efficiency is studied when the stroke of the piston and input pressure is set at 0.09m and 0.60MPa, and then piston area ratio is set 4.0, 5.0, 6.0, 7.0 and 8.0. Figure 10 describes the output power under the difference situation. Figure11 shows the value of efficiency when the area ratio of the piston varies.

From the picture 10 and 11, we would know that enlarging the area ratio will lead to output power increasing, but the efficiency decreases linear in this process. Because the driving chamber's area is bigger, the more expansion energy will be

wasted when the pneumatic chamber is connected with the atmosphere. In order to maximize efficiency and power at the same time, the area ratio of the piston can be range from 4 to 6, which assure that efficiency would exceed 30%.

v. CONCLUSION

We build up a mathematical model of the hydro-pneumatic transformer. To optimize the efficiency performance, we study the key parameters influencing the output power and power efficiency. And some conclusions can be draw as follows:

(1).Output power increases with the increase of the input air pressure, but efficiency decreases in this process. Considering the output power and efficiency, we suggested that input pressure of compressed air is range from 0.5-0.55MPa.

(2).The output power has a little bit decreasing with the increase of the piston's stroke, but the efficiency keeps the constant nearly in this process. So the stroke of the piston is mainly up to output power.

(3). Enlarging the area ratio will lead to output power increasing, but the efficiency decreases linear in this process. And the area ratio of the piston can be range from 4 to 6 in order to maximize efficiency and power at the same time, which assure that efficiency would exceed 30%.

This paper can be a reference in designing and optimizing of the HP transformer used on air-powered automobile.

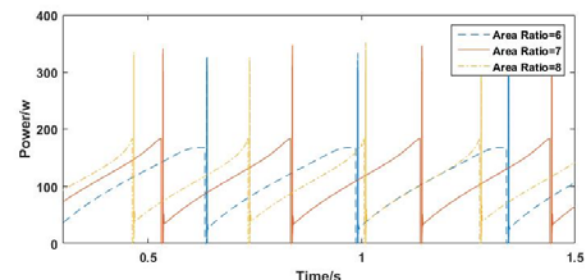


FIGURE X. POWER-TIME CURVES

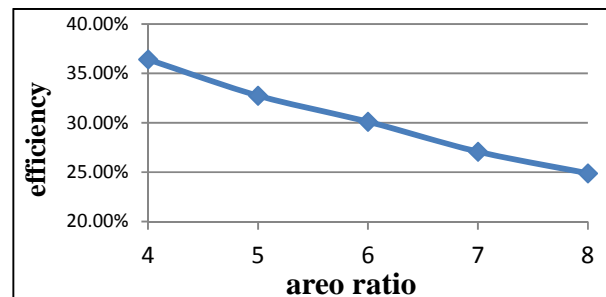


FIGURE XI. EFFICIENCY CURVES

REFERENCES

- [1] Li, J., Li, C. F., Zhang, Y. X., & Yue, H. G. (2014). Compressed Air Energy Storage System Exergy Analysis and its Combined Operation with Nuclear Power Plants. *Applied Mechanics and Materials*, 448, 2786-2789.
- [2] Cai, M., Wang, Y., Shi, Y., & Liang, H. (2016). Output dynamic control of a late model sustainable energy automobile system with nonlinearity. *Advances in Mechanical Engineering*, 8(11), 1687814016672784.

- [3] Shi, Y., Wang, Y., Liang, H., & Cai, M. (2016). Power characteristics of a new kind of air-powered vehicle. *International Journal of Energy Research*, 40(8), 1112-1121.
- [4] Shen, Y. T., & Hwang, Y. R. (2009). Design and implementation of an air-powered motorcycles. *Applied Energy*, 86(7), 1105-1110.
- [5] O. Takeuchi, et al., Characteristics Analysis of Expanding-type Booster. Proceedings of 1995 Autumn Symposium on Hydraulics and Pneumatics, Tokyo (Japan):1995 (in Japanese).
- [6] Shaw, D., Yu, J. J., & Chieh, C. (2013). Design of a Hydraulic Motor System Driven by Compressed Air. *Energies*, 6(7), 3149-3166

Research on the Mathematical Modeling of Damping Controlled Oil Gas Spring

Yijie Chen*, Yafeng Zhang, Mengyan Xu, Fu Du and Peng Gui

China North Vehicle Research Institute, Beijing, China

*Corresponding author

Abstract—In order to improve the vehicle performance, the mathematical model and experimental research of damping controlled oil gas spring were carried out in this paper, a proportional throttle valve was installed on the basis of the original damping valve system. The proportional valve adopted slide valve structure and had 15 gear adjustment positions, through regulating the current intensity to achieve the purpose of controlling valve opening and flow. After that, the flow coefficient was fitted by comparing the valve flow through the flow test, which could make the analytical calculation of damping characteristics realize conveniently. Compared with the experimental data, the maximum calculation error could be controlled to 5.6%.

Keywords—damping controlled; oil gas spring; proportional valve; mathematical modeling

I. INTRODUCTION

For the passive suspension, when the damping valve structure parameters was determined, the system output force cannot be adjusted in a large range, and the mobility and manipulation stability are difficult to achieve to the ideal condition on different road conditions and the vehicle speed^[1]. According to the semi-active suspension structure principle, the electromagnetic proportional control valve is mounted outside the oil gas spring for using the high pressure pipeline, and it connects parallel with damping valve. The control valve throttle area could be adjusted through changing the current intensity, and the damping force also could be changed following the current.

II. STRUCTURE AND WORKING PRINCIPLE

As shown in FIGURE I, it is oil gas spring structure diagram. Control valve connected to upper and lower chambers of the oil gas spring through pressure pipelines. The damping valve with throttle slice was mounted inside the piston, when the piston reciprocating movement, throttle slice will be deformed because differential pressure of upper and lower chamber. The oil and nitrogen were isolated by floating piston, and the gas chamber length was changed through the oil gas spring displacement.

As shown in FIGURE II, it is oil gas spring equivalent flow diagram. In which Q is oil gas spring flow, Q_k is the control valve flow, Q_f is damping valve flow, Q_g is passing oil orifice flow, and Q_{gk} is the high pressure pipeline flow.

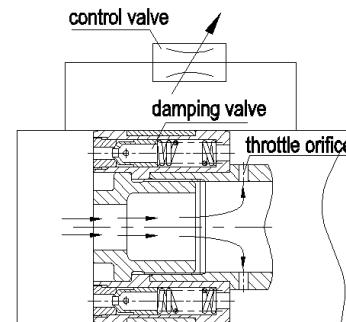


FIGURE I. OIL GAS SPRING STRUCTURE DIAGRAM

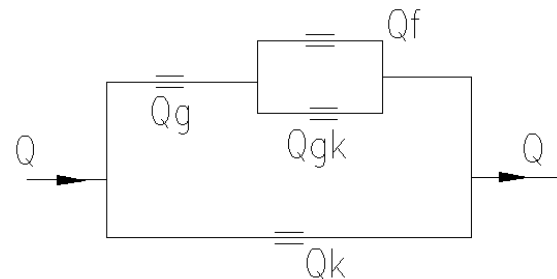


FIGURE II. OIL GAS SPRING EQUIVALENT FLOW DIAGRAM.

III. MATHMATICAL MODEL OF SEMI ACTIVE SUSPENSION

A. Flow and Differential Pressure of Control Valve

In FIGURE III, it is the structure of control valve, which mainly control the output force through changing the current, and the pressure difference is produced by the local resistance loss when oil flow the passage which is indicated by arrow in the figure. The regulating current accuracy of control valve is $I = 0.1A$. When $I = 0A$, the orifice area maximum, the output force minimum, it is suitable for vehicle traveling on a flat road, to improve the comfort. When $I = 1.5A$, the control valve is closed, and only the damping valve work normally, system output force maximum, it is suitable for vehicle running on the rough road, in order to ensure the driving safety.

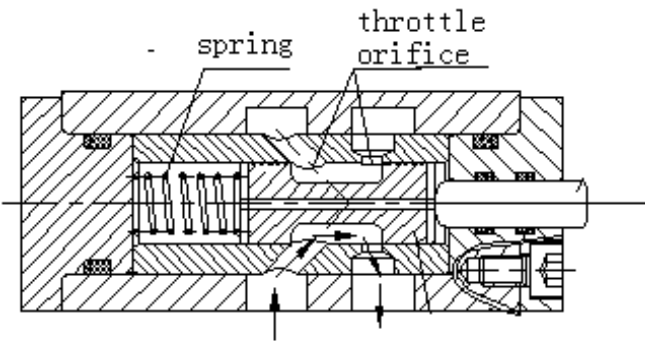


FIGURE III. STRUCTURE OF CONTROL VALVE

Because the control valve of oil flow passage is more complex, so it is difficult to accurate analyze the flow field structure using analytic method. In this article, the least square method is used to fit the test data curve of control valve, and the following function expression is selected for parameter approximation^[2-4]:

$$Q_k = C_k \sqrt{\frac{2\Delta p_k}{\rho}} \quad (1)$$

In which, C_k is control valve flow coefficient.

The flow residual error square expression is:

$$\Pi = \sum_{i=1}^n (Q_k - Q_{ki})^2 = \sum_{i=1}^n \left(C_k \sqrt{\frac{2\Delta p_{ki}}{\rho}} - Q_{ki} \right)^2 \quad (2)$$

In which, Q_{ki} is control valve flow test data, Δp_{ki} is the pressure difference of test data, $i(1, 2 \dots n)$ is a data group.

$$\frac{\partial \Pi}{\partial C_k} = 2 \sum_{i=1}^n \sqrt{\frac{2\Delta p_{ki}}{\rho}} \left(C_k \sqrt{\frac{2\Delta p_{ki}}{\rho}} - Q_{ki} \right) = 0 \quad (3)$$

The flow coefficient formula is:

$$C_k = \sqrt{\frac{\rho}{2}} \sum_{i=1}^n \frac{Q_{ki}}{\sqrt{\Delta p_{ki}}} \quad (4)$$

The test data curve fitting is shown in FIGURE IV, and control valve flow coefficient of different current is shown in TABLE I.

TABLE I. CONTROL VALVE FLOW COEFFICIENT OF DIFFERENT CURRENT

I / A	0	0.3	1.5
C_k / mm^2	12.69	9.92	0

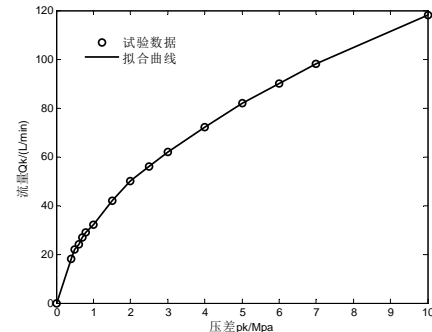


FIGURE IV. THE TEST FITTING CURVE OF CONTROL VALVE

B. Units Damping Force of Semi Active Oil Gas Spring

The gap flow formula is:

$$Q_f = \frac{\pi r_n \Delta p \delta^3}{6 \mu nh} \quad (5)$$

In which, μ is oil dynamic viscosity, n is the number of valve slice, h is the slice thickness, r_n is the outer radius, Δp is total pressure of oil gas spring, δ is annular gap width.

The total pressure of oil gas spring is:

$$\begin{cases} \Delta p = \Delta p_f = \Delta p_k \\ A_u V_d = \frac{\pi r_n \Delta p \delta^3}{6 \mu nh} + C_k \sqrt{\frac{2\Delta p}{\rho}} \end{cases} \quad (6)$$

In which, A_u is the piston area, V_d is the piston velocity, ρ is the oil liquid density.

And the differential pressure is:

$$\Delta p = \frac{6\mu nh}{\pi r_n \delta^3} (A_u V_d - Z_2) \quad (7)$$

In which,

$$Z_1 = \sqrt{18C_k^2 \mu^2 n^2 h^2 + 6\pi r_n \rho \delta^3 A_u V_d \mu nh}$$

$$Z_2 = \frac{C_k \left(-6\sqrt{2}C_k \mu nh + 2Z_1 \right)}{\sqrt{2\pi r_n \rho \delta^3}}$$

The slice turbulent flow formula:

$$Q_f = 2\pi r_n \left\{ -127.79v + \left[3 + 2.5 \ln \left(\sqrt{\frac{\Delta p \delta^3}{8v^2 nh \rho}} \right) \right] \sqrt{\frac{\Delta p \delta^3}{2nh \rho}} \right\} \quad (8)$$

The total pressure difference of semi active suspension is:

$$\begin{cases} Z_3 = 127.79v + \frac{A_g}{2\pi r_n} \sqrt{\frac{2\Delta p_g}{\xi_g \rho}} \\ Z_3 = \frac{A_u V_d - C_k \sqrt{\frac{2\Delta p_k}{\rho}}}{2\pi r_n} + 127.79v \\ \Delta p_k = \left(\frac{A_{gk}}{C_k} \right)^2 \frac{\Delta p_{gk}}{\xi_{gk}} \\ \Delta p = \Delta p_f + \Delta p_g = \Delta p_k + \Delta p_{gk} \end{cases} \quad (9)$$

In which, A_g is passing oil orifice cross-sectional area, A_{gk} is cross-sectional area of pressure pipeline, ξ_{gk} is the local resistance loss coefficient, ξ_g is the local resistance loss coefficient of passing oil orifice.

C. The Test And Simulation

TABLE II. KEY POINT FORCE WHEN CURRENT $I = 1.5A$

The force name	F_z max	F_z min	F_{zy0}	F_{zf0}
Test data (kN)	56.99	11.29	41.44	17.23
Simulation data (kN)	57.55	11.95	41.63	16.54
Data error (%)	0.97	5.52	0.46	5.6

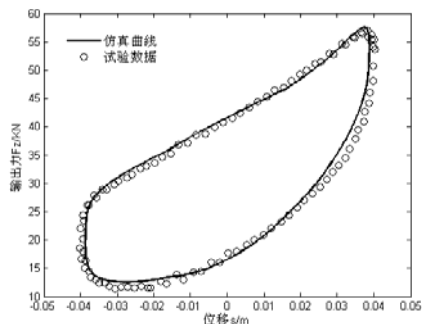


FIGURE V. THE TEST FITTING CURVE OF CONTROL VALVE

From the above chart can be seen, the deviation of simulation results and experimental data is very small, and it is verified that oil gas spring mathematical model and the control valve data fitting method are correct.

REFERENCES

- [1] Kwangjin Lee, "Numerical modelling for the hydraulic performance prediction of automotive monotube dampers", Vehicle System Dynamics, in press.
- [2] Chen Yijie, "Research on Analytical Computation of Valve Parameters and Design of Hydro-pneumatic Spring", Beijing Institute of Technology, in press.
- [3] ByungYoung Moona, Kawabata Showa, SungWon Chung, "Mechanical properties study and design of a suspension system by considering tension force", Materials Processing Technology, in press.
- [4] Chen Yijie, Gu Liang, Guan Jifu, "Research on the mathematical model and analysis the throttle aperture of hydro-pneumatic spring", Beijing Institute of Technology, in press.

Development of a Hydraulic Energy Harvester for Shock Absorber

Longhan Xie*, Jiehong Li, Siqi Cai and Xiaodong Li

School of Mechanical and Automotive Engineering, South China University of Technology, Guangzhou, China

*Corresponding author

Abstract—This project is to design and manufacture a novel shock absorber with energy harvesting to reclaim vibration energy from automotive suspension system during driving. In order to improve safety and comfort, shock absorbers are used in automotive to remove vibration energy during driving, who adopt hydraulic system to convert vibration energy into heat so that vibration can be removed from the automotive suspension system. Obviously, the vibration energy is wasted. In this project, on the basis of satisfying the function request of automotive shock absorber, a mechanism for harvesting vibration energy is added to shock absorber to reclaim the vibration energy and convert it to electricity. Analysis shows that all four shock absorbers in one car can generate 2~4kW electricity at 0.25~0.5 m/s RMS suspension velocity, which can power all electronics in car and reduce automotive emission.

Keywords—shock absorber; energy harvesting; hydraulic

I INTRODUCTION

Suspension is one of the most important parts of the vehicle, which connects the wheels to the car body. Recently, the research indicates that the suspension has a substantial influence on the fuel efficiency. Because of the roughness of the road, the vehicle will vibrate and this will not only lower the stability of the vehicle, but also waste the fuel. At this time, the conventional hydraulic shock absorber converts the vibration to heat, and dissipates it to air. Although this way can overcome the vibration rapidly, but the vibration energy is inevitably wasted. Due to there's a large quantity of vehicle in the world, we waste a huge amount of energy every day. In order to extract the vibration energy to drive the vehicle, the regenerative shock absorber has been suggested.

During the past decades, many researchers explored different principles and designs of regenerative shock absorber, which can be classified into two categories. The first category is based on conventional mechanism, which generate the power in hydraulic, pneumatic or magnetorheological way. Wang [1] et al proposed an idea of using the hydraulic motor to drive an electric generator in order to generate electric. Wendel [2] used a regenerative damp to extract the vibration energy of suspension. Noritsugu [3] investigated a pneumatic drive system, which store a part of the exhaust gas in order to reuse it in the air tank. Li and Tse[4] developed an energy-harvesting hydraulic damper to extract the vibration energy from suspension. Chen and Liao [5], as well as Sapinski [6] proposed to use MR damper to dismiss the vibration and extract the vibration energy. Beside the conventional mechanism, the second category is to generate the power in the electromagnetic

way. When the coil and magnet assemblies move relatively with each other, electricity will be produced. There three configurations to produce electricity, including a linear electromagnetic generator[7,8,9], rack-pinion[10,11,12] and ball-screw[13,14,15]. Although the linear electromagnetic generator has a simple construction and works steadily, its efficiency is relatively low. The rack-pinion and ball-screw convert the up-and-down motion to rotation and have a very high efficiency, but both of them can not adapt the load with high frequency.

This paper aims at designing, characterizing a regenerative shock absorber based on hydraulic mechanism that can recover the vibration energy of the suspension. With a hydromotor, the shock absorber can utilize the hydraulic pressure to drive an electric generator in order to convert the vibration energy to electric energy. Using hydraulic mechanism not only can extract the vibration energy, but also be active controlled easily. For the hydraulic technique is mature enough, so the hydraulic energy harvester system is stable. This paper is organized as follow. In section2, we introduce the design of the energy harvester. In section3, we describe the system modeling and theoretical analysis. Then the conclusion is given in section4.

II DESIGN OF THE ENERGY HARVESTER

In this section, we firstly describe the working principle of the active-control harvester. Then the test setup and experimental results of prototype will be given.

A. Working Principle

The harvester is shown as Figure I. This system can be clarified into two parts. The first part is a hydraulic damper, which connects the sprung mass to the wheel. The damper subassembly consists of two motion sensors, a spring, a piston, a cylinder and two valves. The damper is divided by the piston into two chambers. When the piston move up and down, it drives the hydraulic oil and convert the vibration energy to hydraulic energy. And due to the viscosity of hydraulic oil, vibration of the car body can be released. Besides the mechanism part, the second part is an energy harvester system. This energy recovery system consists of four check valves, a hydraulic motor, a generator with coupler, the active control system and an oil tank, etc. When the piston pushes the hydraulic oil, the oil can only pass through the check valve1 because the check valve1 and check valve4 are mounted relatively. The hydraulic oil with high kinetic energy will drive the hydraulic motor. Since the hydraulic motor and the electric generator are coupled by the coupler, the generator will rotate with the hydraulic motor and produce electricity. Then because

after the oil has driven the generator, its pressure is less than the oil behind the valve4, so it can only pass through the check valve2 and reach the oil tank. In this time, since the pressure of the tank's oil is lower than the oil in the left side of check valve3, it can not pass valves3. When the piston move up, the pressure of the oil in the left side of valve3 is lower than the pressure of the oil in the other side. Then the oil pass through the valve3 and drives the generator. It should be noted that the oil can not pass through the valve2 for the same reason, but the oil can go through the valve4 and get back to the chamber of the damper.

The four check valves work as the rectifiers of the electric circuit, which convert the bidirectional flow to unidirectional flow. For the flow is unidirectional, the electric generator rotates unidirectional, too. In addition, the flow of the chamber is higher than the channel among the system, so it can drive the generator rotates quickly. When the hydraulic motor is rotating, we can change its rotating velocity by changing its flow displacement. But the active control is not discussed in this paper.

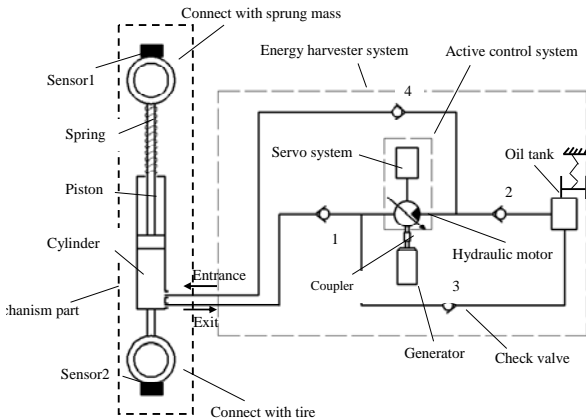


FIGURE I. THE SCHEMATIC OF THE HYDRAULIC ENERGY HARVESTER

B. Prototype Device and Experimental Approach

Following the working principle in section 2.1, a model of prototype is developed. The schematic of the model is shown as Figure II, which consists of the hydraulic damper and the energy harvester system. The configuration of the damper is similar to the conventional damper, so it is easily to be mounted on the suspension. The damper and the spring are mounted in parallel. In addition, the configuration of energy harvester system is compact, so it is also easy to mount on the car body. The two systems are connected to each other by the pipeline. The prototype mounted on the vehicle is shown in the Figure III and Figure IV.

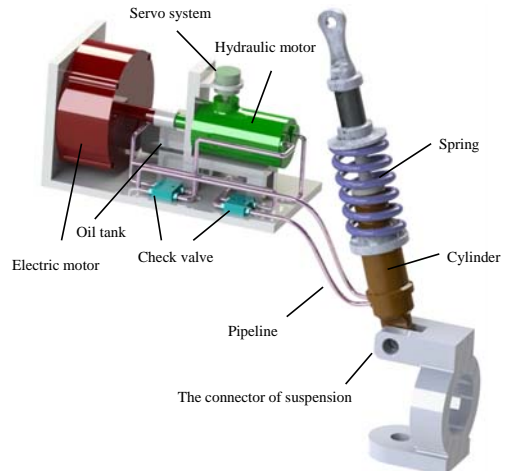


FIGURE II. THE MODEL OF THE HYDRAULIC ENERGY HARVESTER

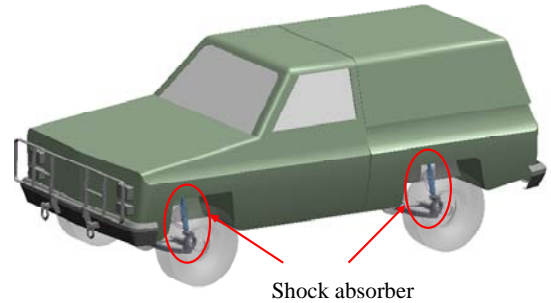


FIGURE III. THE EQUIPMENT IN THE VEHICLE

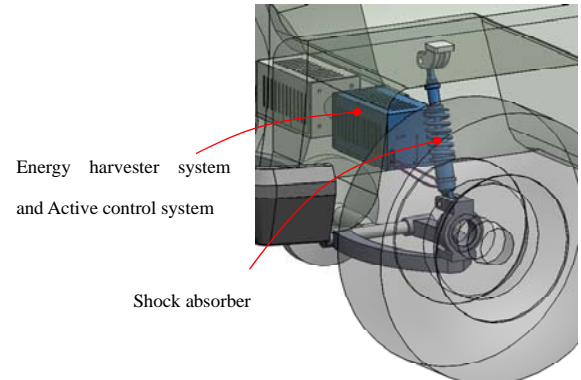


FIGURE IV. THE PROTOTYPE MOUNTED ON THE SUSPENSION

III SYSTEM MODELING AND THEORETICAL ANALYSIS

When vehicles travel on the road, it will receive excitation from road roughness, baking forces etc., which discomfort the drivers. Shock absorbers can reduce the vibration by dissipating the vibration energy into heat waste. Although conventional damper can reduce the vibration effectively, its damping force is a constant. The conventional damper can be modelled as Figure V (a). m_1 represents the unsprung mass and m_2 represents sprung mass. The input of the system is the road roughness y_0 . This system has two degree of freedom, the movement of unsprung mass y_1 and the movement of sprung mass y_2 . In addition, k_1 is stiffness of the tire and k_2 is stiffness

of the suspension's spring. Moreover, C_1 is a damping coefficient between the tire and the road, and C_2 is considered to be a damping coefficient of the shock absorber. When the vehicle leaves the factory, C_2 is set as a constant. So when the vehicle travels in different kind of road, its damping coefficient remains the same.

The model of hydraulic energy harvester is shown as Figure V (b), with a harvester system based on hydraulic damper. Its damping coefficient is C_2 . With the hydraulic energy harvester, the damper converts the vibration energy into electric energy. After the electricity is rectified by electric circuit, it can be stored in the battery.

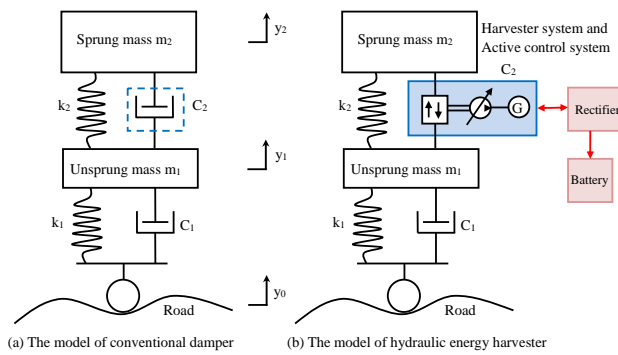


FIGURE V. QUARTER CAR MODEL

For this two-degree-freedom system of Figure V (b), we can get the following equation:

$$\begin{cases} m_2 \ddot{y}_2 + C_2 (\dot{y}_2 - \dot{y}_1) + k_2 (y_2 - y_1) = 0 \\ m_1 \ddot{y}_1 + C_1 (\dot{y}_1 - \dot{y}_0) + k_1 (y_1 - y_0) - C_2 (\dot{y}_2 - \dot{y}_1) - k_2 (y_2 - y_1) = 0 \end{cases} \quad (1)$$

where the coefficients including of m_1 , m_2 , C_1 , k_1 and k_2 are constant, only C_2 is a variable. The coefficient y_0 is the input of the system.

The relative displacement and velocity between the piston and the cylinder can be calculated by

$$\begin{cases} u = y_2 - y_1 \\ \dot{u} = \dot{y}_2 - \dot{y}_1 \end{cases} \quad (2)$$

which are the relative displacement between unsprung mass and sprung mass.

The damping force can be produced following the relationship:

$$F = C_2 \dot{u}^g \quad (3)$$

The damping force is proportional to the relative velocity. The coefficient C_2 is a variable which is controlled by changing

the flow of the hydraulic damper. But the controlling method is not included in this paper.

With four check valves composing a rectifying system, the hydraulic oil drives the hydraulic motor unidirectionally. With the inner diameter d of the cylinder, efficiency η_l and the displacement of hydraulic motor V , the rotational speed of the motor can be calculated by equation(4).

$$n = \frac{\pi d^2 |u|}{4V} \eta_l \times 60 \times 10^6 \quad (4)$$

With $a = \frac{\pi d^2}{4} \eta_l \times 60 \times 10^6$, the equation(4) can be produced as Eq.(5).

$$n = a \frac{|u|}{V} \quad (5)$$

where n is proportional to $|u|$ and inversely proportional to V . So the output power of the generator can be written as state equation:

$$P = P_0 \frac{a^2}{n_0^2} \left(\frac{u}{V} \right)^2 \quad (6)$$

where P_0 is the rated power of the generator and n_0 is the rotational speed under the rated power. For both P_0 and n_0 are constant, the output power of the generator is proportional to the velocity of piston and inversely proportional to V .

In the experimental test, we adopt a white noise as input of the harvester:

$$y_0 = -2\pi f_0 y_0 + 2\pi \sqrt{G_0 U_0} w \quad (7)$$

where y_0 is the excitation of the road, G_0 is the coefficient of the road surface roughness, U_0 is the velocity of vehicle, w is the Gaussian white noise with the mean value of zero, and f_0 is lower cutoff frequency with the range from 0.06 to 0.07Hz. Figure VI shows the input of the road with surface of Rank C at 72km/h.

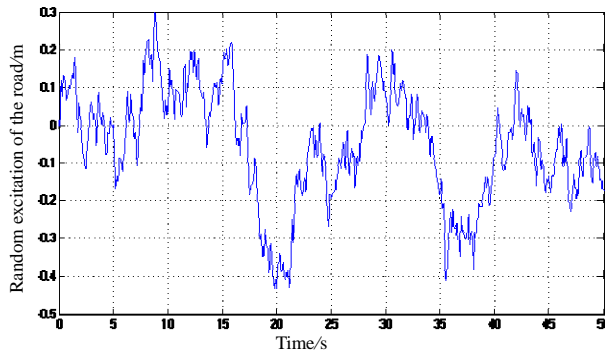


FIGURE VI. THE EXCITATION AT 72KM/H OF THE ROAD WITH SURFACE OF RANK C

In this test, the nominal parameters of hydraulic harvester system for the simulation are $m_1=40\text{kg}$, $m_2=363\text{kg}$, $k_1=182087\text{N/m}$, $k_2=20053\text{N/m}$, $C_1=200\text{NS/m}$, $C_2=1388\text{NS/m}$ and the input y_0 is the white noise which is shown in Figure VI. And the relative velocity of piston is shown in Figure VII. We can find that the velocity fluctuates greatly which indicates that the output power of the generator changes greatly, as shown in Figure VII.

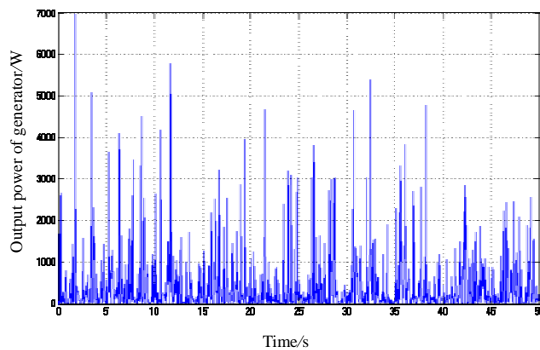


FIGURE VII. THE OUTPUT POWER OF THE GENERATOR

As you can see in Figure VIII, the output power is chaos, so it must be rectified before stored in the battery. Moreover, Figure VIII shows the different output power in different driving condition. When vehicle travelling on the road with surface of rank B at 60km/h, the harvester can extracts about 80W energy. When vehicle travelling on the road with surface of rank C at 60km/h, the harvester can extracts about 300W energy, as shown in Figure VIII. So we can find that the worse condition of road, the more power produced. When the vehicle travels on the different road, it needs different damper force to absorb the vibration. Obviously, the conventional shock absorber can not adapt the different conditions of the road.

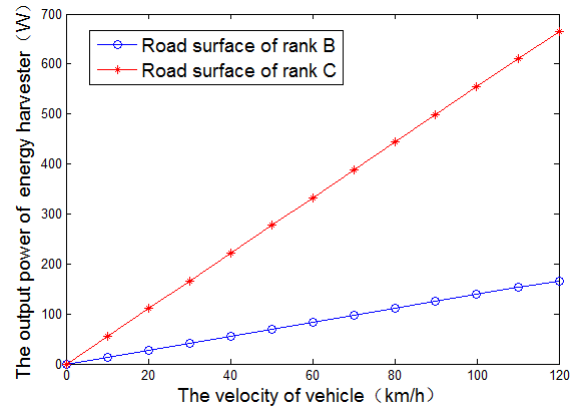


FIGURE VIII. THE OUTPUT POWER OF DIFFERENT VELOCITY AND DIFFERENT ROAD CONDITION

IV CONCLUSIONS

Since the conventional shock absorber's damping coefficient is a constant, so it can't adapt different condition of the road. In this paper, we proposed an innovative shock absorber, which based on the hydraulic mechanism. With the hydraulic motor drives the generator, the harvester can extract the vibration energy effectively. And for hydraulic system is easy to be controlled, the harvester's damper coefficient can be changed automatically and adapt the different road condition. The result of simulation indicates that with worse condition of the road, the output power is corresponding higher.

ACKNOWLEDGEMENT

This work was supported in part by the National Natural Science Foundation of China (Grant No. 51575188), Natural Science Foundation of Guangdong Province (Grant No. 2016A030313492), and Research Foundation of Guangdong Province (Grant No.2015A020214007).

REFERENCES

- [1] Ruichen Wang, Zhi Chen, Haijun Xu, Karsten Schmidt, Fengshou Gu and Andrew.D.Ball. Modelling and Validation of a Regenerative Shock Absorber System. Proceedings of the 20th International Conference on Automation & Computing, Cranfield University [C]. Bedfordshire, UK, 12-13 September 2014.
- [2] Fodor M, Redfield R. The variable linear transmission for regenerative damping in vehicle suspension control [J]. Vehicle System Dynamics, 1993, 22 (1) : 1~20.
- [3] Noritsugu T. Energy saving of a pneumatic system (2). Energy regenerative control of a pneumatic drive system. Application to active air suspension [J]. Hydraulics & Pneumatics, 1999, 38 (4) : 1~4.
- [4] Chuan Li and Peter W Tse. Fabrication and testing of an energy-harvesting hydraulic damper [J]. Smart Mater. Struct. 2013.
- [5] ChaoChen, Wei-Hsin Liao. A self-sensing magnetorheological damper with power generation [J]. Smart Mater. Struct. 2012.
- [6] Bogdan Sapinski. Energy-harvesting linear MR damper: prototyping and testing [J]. Smart Mater. Struct. 2014.
- [7] Lei Zuo, Design and characterization of an electromagnetic energy harvester for vehicle suspensions [J]. Smart Materials and Structures, 2010, 19.
- [8] Longxin Zhen: Structure and Magnetic Field Analysis of Regenerative Electromagnetic Shock Absorber, WASE International Conference on Information Engineerin, 2010.

- [9] J. H. Beno, D. A. Weeks, D. A. Bresie, A. M. Guenin, J. S. Wisecup, W. Bylsma. Experimental Comparison of Losses for Conventional Passive and Energy Efficient Active Suspension Systems[C]. SAE, 2002.
- [10] Weeks D. A., Beno J. H., Guenin A. M., Bresie D. A.. Electromechanical Active Suspension Demonstration for Off-Road Vehicles[C]. SAE, 2000.
- [11] Yasuhiro Uchiyama, Masayuki Fujita. Application of Two-Degree-of-Freedom Control to Multi-axis Electrodynamic Shaking System Using-Synthesis and Adaptive Filter [J]. JSME International Journal, c2003, 3:828-835.
- [12] Lei Zuo, Energy-harvesting shock absorber with a mechanical motion rectifier [J], Smart Materials and Structures, 2013, 22.
- [13] Ryuzo Hayashi, Yoshihiro Suda, Kimihiko Nakano. Anti-Rolling Suspension for an Automobile by Coupled Electromagnetic Devices [J]. Journal of Mechanical Systems for Transportation and Logistics, 2008, Vol. (I): 43-55.
- [14] Kimihiko Nakano, Yoshihiro Suda, Shigeyuki Nakadai, Yuji koike. Anti-Rolling System for Ships with Self-Power Active Control [J]. JSME International Journal, 2001, 3:587-594.
- [15] Chew Kuew Wai, Electric Vehicle Energy Harvesting System Regenerative Shock Absorber For Electric Vehicle, IEEE Conference on Sustainable Utilization and Development in Engineering and Technology, 2013.

Analysis on Transient Temperature Field of the Rod Fastening Rotor Based on Fractal Contact Theory

Yiping Li*

School of Chemical and Environmental Engineering Shanghai Institute of Technology, Shanghai 201418, China

*Corresponding author

Abstract—When the disks of the rod fastening rotor were contacted with each other, the contact thermal resistance between the contact surfaces would play a critical role in heat transfer and the distribution of temperature field. On the basis of the surface fractal characteristics, combining Mandelbrot - Tian (M - T) fractal network model and the classical conduction theory, the Cantor set, which was not dependent on the observation scale, was chosen to obtain the relationship between the pressure and the heat transfer coefficient of contact surfaces. The rotor transient temperature field distribution was obtained through determining the contact thermal resistance. It was found that the thermal conductivity caused by the pre-tightening force had a little influence on the transient temperature field. Therefore, when the rotor dynamic characteristics were analyzed, the influence of the transient temperature field could be ignored.

Keywords—transient temperature field; contact thermal resistance; rod fastening rotor; fractal contact theory

I INTRODUCTION

Rod fastening rotor was used by many heavy-duty gas turbine, which was consist of many discs compacted by a single central rod bolts or circumferential rod bolts. The contact interface between discs was either plane or terminal face tooth. The contact thermal resistance between the contact interfaces of discs would affect the rotor temperature distribution and impacted on the rotor dynamics[1]. Fractal theory described the rough surface morphology by using the fractal dimension which was nothing to do with the scale of roughness parameters. The heat conduction model was set up through the rough self-affine fractal surface, which was expected to further reveal the physical nature of heat conduction. In this paper, the heat transfer coefficient under different contact pressure was obtained by using the fractal Cantor set theory. The transient temperature field, which was affected by the contact thermal resistance, was studied.

II CONTACT THERMAL RESISTANCE AND HEAT TRANSFER COEFFICIENT

When two metal surfaces were contacted with other, the nominal surfaces seemed to contact entirely, but the real contact parts were dispersed convex body. The presence of these convex bodies would make contact plane not complete. Bowden[2] pointed out that under the condition of pressure up to 10 MPa, the actual contact area was only 1% ~ 2% of the nominal contact

area, which generated the contact thermal resistance R , expression was as follows:

$$R = \frac{\Delta T}{q} \quad (1)$$

Where ΔT was the temperature difference between the two contact surface, its dimension was °C; q was average heat flux density of the contact surface, its dimension was W/m². Contact element in ANSYS could simulate the contact thermal resistance between the surfaces. To take into account the conductive heat transfer between contact and target surfaces, it was need to specify the thermal contact conductance coefficient which was real constant TCC. The conductive heat transfer between two contact surfaces was defined by:

$$q = TCC \times \Delta T \quad (2)$$

Where q was the heat flux per area; TCC was the thermal contact conductance coefficient, having dimensions of W/m²·K; ΔT was the temperature difference between the two contact surfaces. TCC was a function of temperature, pressure, time and location. After the thermal contact conductance coefficient between plates were obtained by fractal Cantor set elastic-plastic deformation model, the model of the finite element calculation and analysis of transient temperature field could be established.

III FRACTAL THEORY BASED ON CANTOR SET

A. Morphology Characteristics Based on Cantor Set

By the conclusion of the literature [3]: The cantor set of contact surface and the surface generation process was: from down to up, each step after segmentation, the length of the line segment of the layer was $1/f_r$ ($f_r > 1$) of pre-layer. Vertically, each fractal depth was $1/f_z$ ($f_z > 1$) of pre-depth. f_r was level reduction ratio, f_z was vertical reduction ratio, s was each layer of the fractal repeat part. Based on the literature [3], the derivation of self affine fractal Cantor set surface profile fractal dimension was as follows:

$$D = 1 - \frac{\ln f_z}{\ln(sf_r)} + \frac{\ln s}{\ln(sf_r)} \quad 1 < D < 2. \quad (3)$$

Specific contact surface could be described by a particular Cantor set parameters s, fr and fz. The surface roughness Ra (its dimension was μm) could be measured, according to the experiments of literature [4]. The fractal roughness parameter G (its dimension was μm) and fractal dimension D of Cantor set were obtained through the surface roughness by approximate conversion formula:

$$D = 1.2996 / R_a^{0.2178} \quad (4)$$

$$G = 10^{8.2594} / R_a^{0.2183} \quad (5)$$

The measurement sampling contour length, which corresponding to Cantor set morphology parameters, were substituted by its related length[5]:

$$l_0 = [(4-2D)/G^{2D-2}]^{1/(4-2D)} \quad (6)$$

The level reduction ratio and the vertical reduction ratio could be achieved by the relation of Warren[5] normal displacement u and contact area (or cross-sectional area) Ar:

$$A_r = \frac{l_0^2}{k\varphi} \left(\frac{R_q - u}{f_z h_0} \right)^k, \quad k = \frac{\ln f_r^2}{\ln f_z}, \quad \varphi = \frac{f_z - 1}{f_r^2 - 1} \quad (7)$$

Where h_0 was 2 times as each contact surface root mean square roughness Rq . The cross-sectional area of the rough surface contour A_{r1} and A_{r2} could be obtained with different height ($Rq-u_1$) and ($Rq-u_2$) intercept and equation (7). The reduction ratio fr and fz could be obtained by solving nonlinear equations simultaneously, and s could be obtained by the formula (3).

B. Thermal Resistance Model

According to the literature [3], the real contact state could be equivalent to the contact state between the Cantor set fractal rough surface with elastic-plastic deformation and the ideal smooth rigid half infinite solid surface. Under the load F, the some materials of contact surface would begin to produce plastic deformation and flow into the groove between two convex bodies until the end of (n_c-1) generation. So for a given normal load, the rough surface in every generation of convex bodies could be divided into two categories: 1) the range of $[n_c, \infty]$, generation of the plastic deformation; 2) the range of $[0, n_c-1]$, generation of the elastic deformation. The value of Critical generation n_c was:

$$n_c = trnu \left[\frac{\ln \xi}{\ln(1/f_r^2)} \right], \quad \xi = \frac{F}{\sigma_y \cdot l_0^2}. \quad (8)$$

Supposing, when a given normal load F was applied on the surface of cantor set, plastic flow of the convex body of $[n_c, \infty]$ generation would occur and flow completely into the adjacent clearance gap. Based on the plastic deformation model of Warren t. L[5], the plastic displacement of n_c generation could be obtained. The height increment of (n_c-1) generation could be calculated at the case of volume conservation. Based on recursive generation process of fractal theory of contact surface, the total thermal resistance of the contact surface were consist of convex body contraction thermal resistance and heat conduction thermal resistance, the total contact thermal resistance was given by:

$$R_{t,0} = \frac{\sum_{i=1}^{n_c-1} s^{2i} (R_{b,(n_c-1-i)} + R_{c,(n_c-1-i)})}{s^{2n_c}}, \quad 0 \leq i \leq n_c - 1. \quad (9)$$

Where R_b was thermal resistance of the heat conduction of the convex body, R_c was contraction thermal resistance of the convex body.

IV TRANSIENT HEAT TRANSFER ANALYSIS OF THE TESTING ROTOR

A. Rotor Disc Model and Contact Heat Transfer Coefficient

The material of the testing rotor disc was steel 45, its structure size was shown in Figure I.

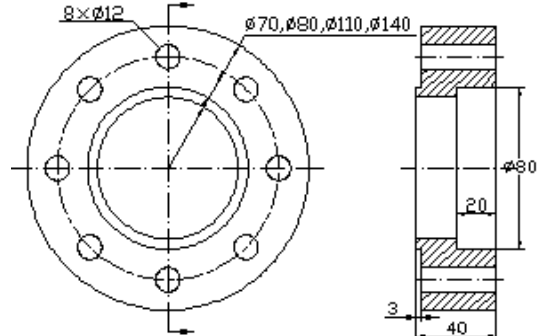


FIGURE I. THE STRUCTURE OF TESTING ROTOR DISC

In this paper, based on the size of the testing rotor disc, the 3D model and finite element model were established through ANSYS APDL programming. Because the structure of the rotor was symmetrical, 1/8 of testing rotor disc was established by using SOLID 90 elements for swept meshing. A total of 21522 elements and 91615 nodes were generated. Two-dimensional TARGE 170 and CONTA 174 were selected to simulate contact, testing rotor disc assembly and grid diagram were shown in Figure II.

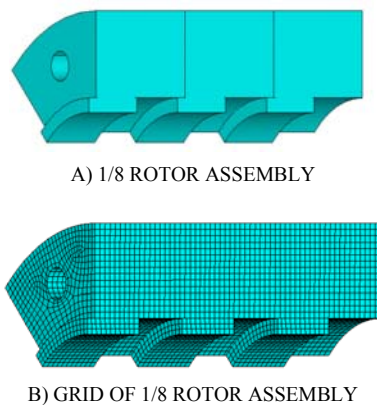


FIGURE II. 1/8 TESTING ROTOR DISC ASSEMBLY AND ITS GRID DRAWING

The section area A_r of a single rod was $7.85 \times 10^{-5} m^2$, yield strength σ_y of the steel 45 was 500 MPa, the safety factor could be set as 2, allowable stress $[\sigma] = \sigma_y/2 = 250$ MPa. In order to prevent the rod failure in the experiments, the pre-tightening load $FN < [\sigma] \times Ar = 19.6$ kN. The scope of pre-tightening force could be appropriately expanded by calculation of the theoretical value. The contact pressure under pre-tightening force 30 kN could be calculated:

$$P = \frac{F}{A_w} = \frac{30000N}{1.21 \times 10^{-3} m^2} = 24.8 \text{ MP}_a \quad (10)$$

Where, A_w was the disc area of 1/8 testing rotor. According to the theoretical analysis in second section, Cantor set elastic-plastic deformation and the calculation program of contact thermal resistance could be obtained based on Matlab. The fractal parameters of the contact surface could be obtained by the surface profiler. The parameters in table I were used in the Matlab program to calculate thermal resistance.

TABLE I. THE SURFACE FRACTAL PARAMETERS AND MATERIAL PARAMETERS OF STEEL 45

Roughness $R_a/\mu m$	Level reduction ratio f_r	Vertical reduction ratio f_z	Thermal conductivity y $k/W \cdot m \cdot K$	Yield strength σ_y/MP_a	Elastic modulus E/MP_a
0.8	1.26	1.21	44	500	2.1×10^5

According to the fractal parameters of the rough surface, the discrete relationship between the contact pressure and the heat transfer coefficient of the contact surface of a rod fastening rotor under 30 kN load could be obtained by the Matlab program, and furthermore, the linear relationship between the contact pressure and the heat transfer coefficient of the contact surface could be fitted. Based on the output image of the contact stress, the linear relationship between contact stress and the heat transfer coefficient of the contact surface was shown in Figure III.

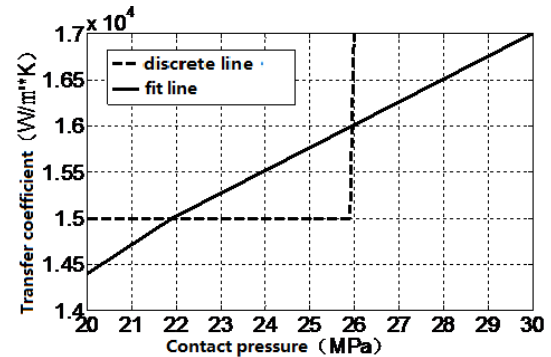


FIGURE III. CONTACT PRESSURE AND THE HEAT TRANSFER COEFFICIENT OF THE CONTACT SURFACE

According to Figure III, when the contact pressure was 24.8 MPa, the heat transfer coefficient of the contact surface was 15.6 kW/m²K. Therefore, the heat transfer coefficient of the contact surface under any contact pressure could be obtained.

B. Calculation of Transient Heat Transfer

In order to study the influence of heat transfer coefficient of the different contact surface on the transient heat transfer process, a simple example was designed. The contact area of the disks was set up contact pair; the heat transfer coefficient of the interface was 15.6 kW/m²K. Supposing the rotor surface was insulation and material coefficient of thermal conductivity was 44 kW/m²K. The material density was 7850 kg/m³, specific heat capacity was 560 J/kg.K. The initial temperature for the left disc was 500°C, the initial temperature for other two was 25°C, shown in Figure IV.

In order to execute transient analysis, the calculation time was 600s. The temperature distribution at 100s was shown in Figure V. The temperature distribution, which was shown by color, changed rapidly in contact surface, which meant that there was a larger temperature difference between the contact interfaces.

According to the same way, when rod pre-tightening force was 25, 20, 15, 10 and 5 kN respectively, the heat transfer coefficient of the interface was 14.6, 13.2, 12.5, 10.1 and 8.3 kW/m²K respectively. Settings the heat transfer coefficient of the interface respectively, the temperature of node 23646 on the third disc of the rotor model was extracted to draw curve with time, which were used to simulate respectively working conditions of rod pre-tightening force of 30, 25, 20, 15, 10 and 5 kN, the result was shown in Figure VI.

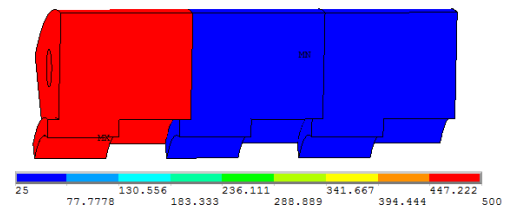


FIGURE IV. THE INITIAL CONDITIONS OF THE ROTOR DISC FOR TRANSIENT ANALYSIS

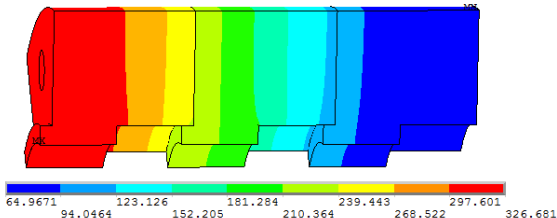


FIGURE V. TEMPERATURE DISTRIBUTION IN TESTING ROTOR AT 100S

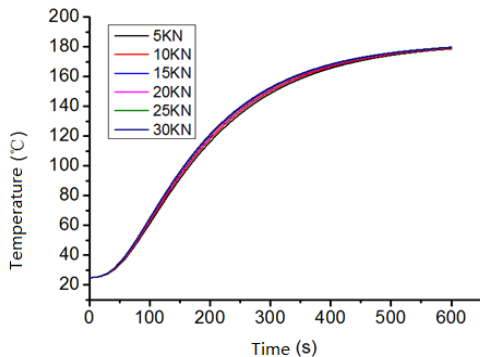


FIGURE VI. TEMPERATURE CHANGES OF NODE 23646

When the pre-tightening force was 20kN, a series of nodes in axial direction of the rotor discs were selected at the time 20, 60 and 100s, which revealed the temperature field distribution, and could be used to compare with the conditions without thermal resistance. The temperature distribution was shown in Figure VII.

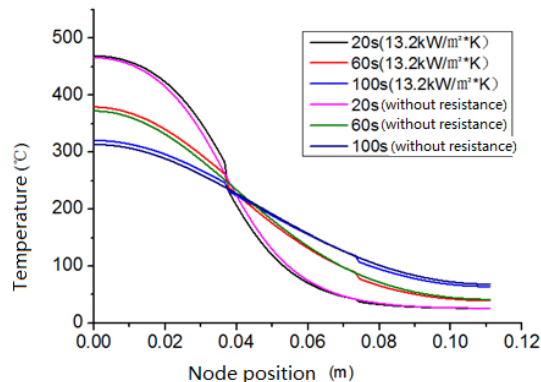


FIGURE VII. THE AXIS TEMPERATURE DISTRIBUTION UNDER 20kN AND WITHOUT THERMAL RESISTANCE

The simulation results showed that, when the pre-tightening force increased, the heat transfer distance of the contact interface decreased, and at the same time, the real contact area increased, which resulted in the increase of the heat transfer coefficient of the contact surface between the discs. Because the heat transfer process was prevented by contact thermal resistance, and temperature field distribution was also influenced, the influence of thermal contact resistance cannot be ignored.

V SUMMARY

Analysis on the transient heat transfer of testing rotor model was done by using ANSYS. When the influence of the contact pressure on the contact surface heat transfer coefficient was taken into account, the Cantor set of the fractal theory, which was not dependent on the observation scale, was chosen to obtain the relationship between the pressure and the heat transfer coefficient. The change regularity of temperature with time was analyzed under the different pre-tightening force. It was found that the pre-tightening force led to the change of contact pressure, and further led to the change of the heat transfer coefficient of the contact surface. Therefore, the transient temperature field distribution was influenced by the pre-tightening force. The distribution of temperature field was also influenced by the contact thermal resistance. The contact thermal resistance model could be used to determine the heat transfer coefficient of the contact surface. The influence of the thermal stress on the transient temperature field could be ignored.

ACKNOWLEDGEMENT

This project is supported by National Natural Science Foundation of China (Grant No. 51475311).

REFERENCES

- [1] He Peng, Research of the influences of elastic-plastic contact and temperature distribution on tie-bolted fastened rotor dynamics, Jilin: Harbin Institute of Technology, 2013 (in Chinese).
- [2] F.P Bowden, D. Tabor, The friction and lubrication of solids, Oxford University Press, London, 1950.
- [3] Xu Ruiping. Study on thermal contact resistance of solid interfaces Cantor set based on fractal theory, Shanghai: Shanghai Jiaotong University, 2005 (in Chinese).
- [4] Tian Hongliang. Dynamic modeling on fixed joint interface virtual material in mechanical structure, Wuhan: Huazhong University of Science and Technology, 2011 (in Chinese).
- [5] T.L. Warren, D. Krajcinovic, Random Cantor set models for the elastic-perfectly plastic contact of rough surface, Wear. (1996) 1-15.
- [6] R. P. Xu, L. Xu, An experimental investigation of thermal contact conductance of stainless steel at low temperatures, Cryogenics. (2005) 694-704.
- [7] Fu Shixin, Physical parameters characterization research of mechanical joint interface on thermo-mechanical coupled loads, Wuhan: University of Science and Technology, 2013 (in Chinese).
- [8] Gao Yaodong, Zhang Yubao, Ren Xueping, Finite Element Theory and ANSYS Application, Electronics industry press, Beijing, 2016 (in Chinese).

Study on Rules for Spiral Groove of Swirl Nozzle to Performance of Inside Flow

Yong Guo^{1*}, Lili Guo² and Longyan Zhang³

¹Hunan University of science and technology, HuNan Xiangtan, 411100, China

²Hunan Bilv EP industry development Co.,LTD, HuNan Xiangtan, 411100,China

* Corresponding author

Abstract—With the advantages of convenient processing, easy control for geometry size and adjustable parameters, single head spiral groove nozzle is widely applied in the field of environmental protection equipment. According to the lackage of rules on structure parameters of spiral groove to spray performance and supply power, spiral slot geometric model was set up, and three dimension numerical analysis was carried on using k-ε predominate turbulence model by fluent. The rules of spiral slot length, spiral groove depth, and groove pitch to flow velocity increasing ratio and frictional pressure loss were acquired. It supplies a theoretical guidance and basis for design of spiral groove of swirl nozzle.

Keywords—nozzle; spiral groove; velocity increasing ratio; pressure loss component

I. INTRODUCTION

The small particles generated by swirl atomizing nozzle are more stable. It can make cleaning effect of dust and industrial waste gas better with the increasing of the effective contact area of air purification. Owing to this virtue, it is a key component widely used in the field of environmental protection equipment, such as spray scrubber, flue gas desulphurization equipment, spray atomization device. The atomization effect of the swirling nozzle is enhanced by the speed increase with spiral structure. The main structure has two kinds [1-2]. One is done by setting a pipe with different angles of incidence, and the other is to set a spiral groove on the pipe. It is difficult to process and control the structure size by setting the swirling flow of the pipes with different incidence angles [3]. Spiral grooves on pipelines are easy to process. The geometric structure and size of spiral grooves are easy to control with some parameters easily adjustable, so that atomizing effect can be adjusted within a certain range. Therefore, the spiral groove structure of pipes has been widely applied in nozzles [4].

The geometric parameters of spiral groove directly affect the effect of speed increasing and the pressure loss along the pipeline, and can cause a change of water atomization degree and increase of the power supply of the water supply unit. Most of the existing studies on spiral grooved tubes are focused on heat transfer and resistance characteristics in a single tube with spiral grooved tubes [5-6]. The influence rules of structural parameters on heat transfer coefficient and drag coefficient are analyzed through the flow field analysis of pipe fluid. According to the spray performance requirements of the nozzle, the study on the effect of the spiral groove structure on the effect of speed

increasing and the pressure loss along the pipeline is still very short.

In this paper, a swirl spray nozzle with a spiral groove is proposed, and an analytical model of the flow field for spiral groove using the finite volume method is established. The influence law of spiral groove length, depth and slot to the effect of speed increasing and the pressure loss along the pipeline is acquired, which provide theoretical guidance and a basis for the design of a spiral groove swirl nozzle.

II. PHYSICAL MODEL OF FLOW FIELD ANALYSIS OF SINGLE HEAD SPIRAL GROOVE OF SWIRLING NOZZLE

The common spiral groove swirling nozzle structure, as shown in Figure I, is made up of a spiral speed increase catheter, a pitch nut, a locking nut and a nozzle. The water flows through the spiral tube growth by damping holes evenly distributed. The first time of atomization occurs in the cavity spiral growth. Then, the water flows through the valve nozzle and spiral growth between the nozzle and orifice catheter for second time atomization. The water atomization performance is enhanced by double atomization. At the same time, the adjustment of the pitch nut can change the ejection distance.

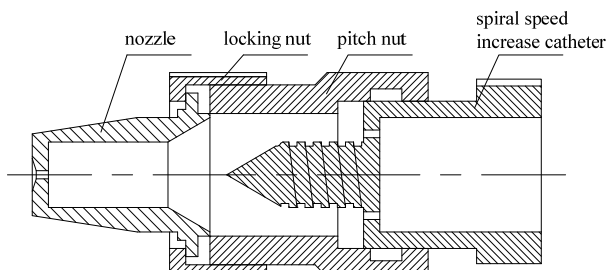


FIGURE I. SWIRLING NOZZLES WITH SPIRAL GROOVE

The spiral groove tube formed by spiral speed increase catheter and the pitch nut makes the flow speed increase, which is the guarantee of the atomization effect. The fluid pipe formed by the two components is represented by the spiral groove tube illustrated in Figure II. In the picture, the inner diameter of the spiral groove tube is 8mm, the outer diameter is 15mm, the effective spiral distance is 10mm, the pitch is 2mm, and the spiral groove depth is 1mm.

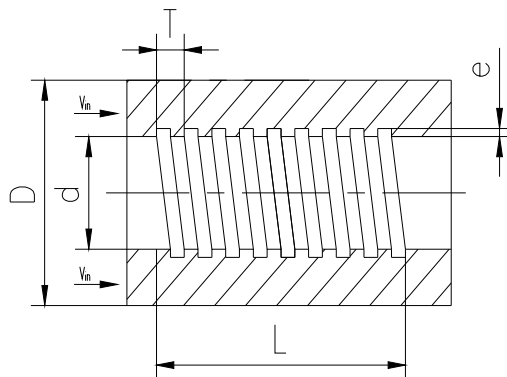


FIGURE II. FLOW FIELD MODEL OF SINGLE HEAD SPIRAL GROOVE OF SWIRLING NOZZLE

III. ESTABLISHMENT OF CFD SIMULATION MODEL FOR SPIRAL GROOVE

A three-dimensional model of a spiral groove tube is established using Gambit. The flow field is divided into two parts. One is the pipe fluid, and the other is the trough fluid. The inner surface of the fluid in the trough is meshed by nonstructural grid, and the hexahedral grid is used in fluid meshing. The fluid in the pipe is meshed by tetrahedral grid. The division of the fluid grid in the spiral groove is shown in Figure III. with hexahedral mesh in the surface area, and the rest with tetrahedral mesh, and the number of initialization grids is 9553.

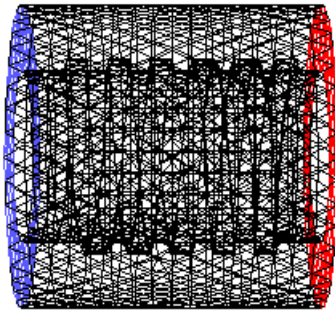


FIGURE III. MESH MODEL OF FLUID IN SPIRAL GROOVE

The boundary conditions of the calculated area are set according to the actual conditions as follows. The spiral conduit at the inlet of the nozzle is provided by the water pump for the velocity entrance boundary. According to the definition of various parameters in Fluent, the inlet speed of swirl nozzle spiral groove is 1m/s. The turbulence intensity is 1%, and the hydraulic diameter is 8mm. The outlet of the spiral groove is the pressure outflow boundary. The turbulence intensity is 1%, and the hydraulic diameter is 8mm. The rest of the surface is set to the wall, and the default settings are reserved.

A separate solver is set up in Fluent to solve the problem. The flow field in the spiral groove is a turbulence model. The Realize k-e model is adopted, the wave parameter Ce2is set to 1.9, the turbulent Prandtl number is set to 1, the TDR Prandtl number is set to 1.2, and the energy Prandtl number is set to 0.85. After the above parameters are set in Fluent, the initialization

iteration calculation is carried out. The convergence of the calculation is judged through the residual curve. If the residual difference reaches 10-6, it can be considered to be convergent. At the same time, the entry and exit quality monitoring curves are set up to monitor the convergence process of the equations solution. The relevant settings are adjusted according to the problems until the specified convergence accuracy is achieved. The simulation carried on 100 times, and the residual curve is shown in Figure IV. The residual curve fluctuation remains unchanged after iteration of 72 times, and the residuals of all indexes are all below 10-6.

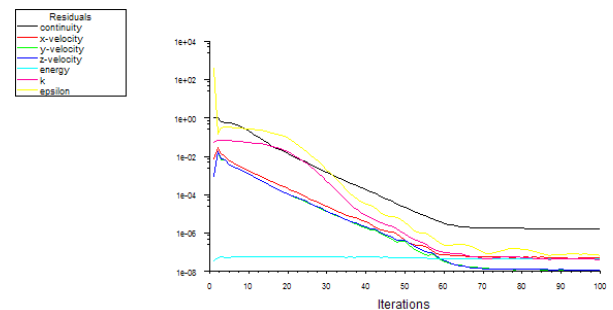


FIGURE IV. RESIDUAL MONITORING CURVE OF CALCULATION AND ANALYSIS

IV. SIMULATION RESULTS

The velocity curve at the center section obtained by simulation is shown in Figure V, and the pressure curve at the center section is shown in Figure VI. As you can see, the average pressure at the exit is 0.18Mpa, and the average speed at the exit is 1.128m/s, which increase by 0.13 time of the entrance. The pressure loss from the entrance to the exit is 0.08Mpa. Therefore, the setting of the spiral groove can increase the flow velocity of the fluid to improve the effect of fluid atomization, but it also increases the pressure loss at the same time.

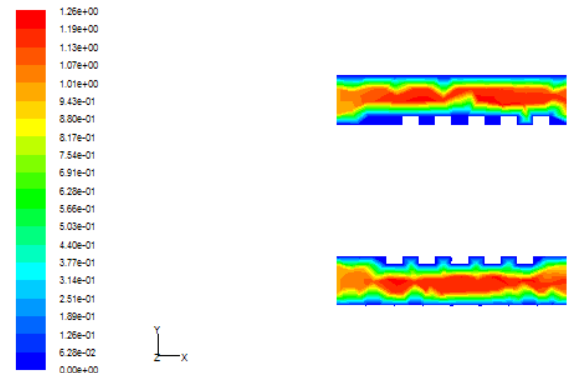


FIGURE V. VELOCITY DISTRIBUTION CLOUD MAP IN CENTER SECTION OF SPIRAL GROOVE TUBE

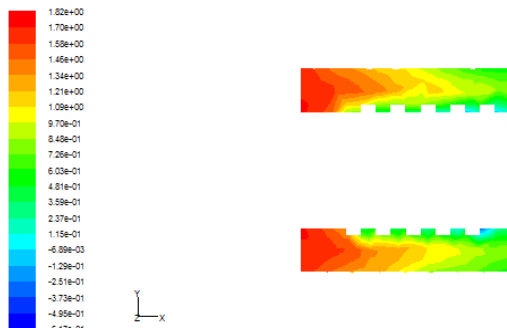
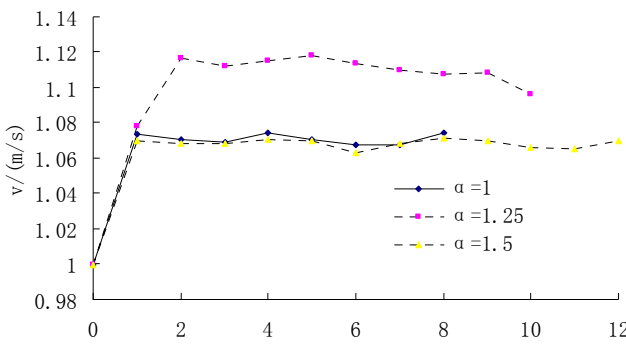
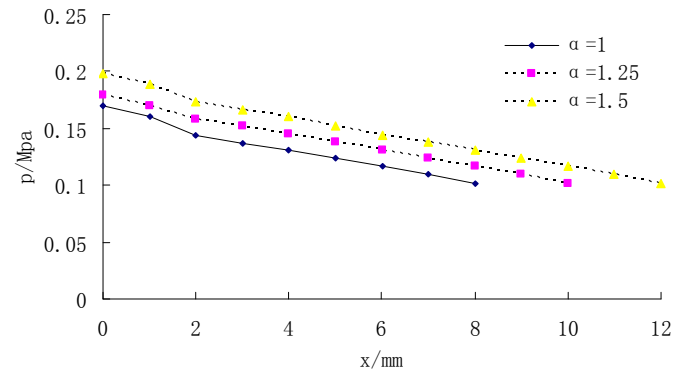


FIGURE VI. PRESSURE DISTRIBUTION CLOUD MAP IN CENTER SECTION OF SPIRAL GROOVE TUBE

The length of the spiral groove, groove depth and spiral slot structure parameters has a great effect on speed increasing and pressure loss. The length of the spiral groove is changed. L=8mm, 10mm and 12mm are taken respectively. The average velocity curve of the spiral groove pipe section is obtained by taking the ratio of spiral groove length to inner diameter ratio as the research object, as shown in Figure VII (a). The average pressure curve of spiral groove pipe section is shown in Figure VII (b). Figure VII shows that when the ratio of the length of the spiral groove to the inner diameter is 1.25, the speed-up effect is the most significant and the speedup ratio reaches to 1.09. Therefore, the ratio of the spiral groove length to the inner diameter value should be chosen within the range of 1~1.5 in order to make the speedup ratio approach to the maximum. At the same time, the greater the value of the alpha, the higher the pressure loss produced by the spiral groove. But when alpha is 1~1.5, the pressure loss is less than 0.09MPa. Therefore, when the alpha is in the 1~1.5 range, the pressure loss produced by the spiral groove is very small, which can be ignored.



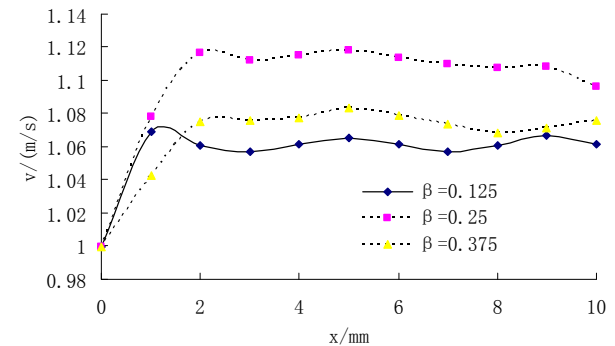
(a) Average velocity of cross section of spiral groove tube



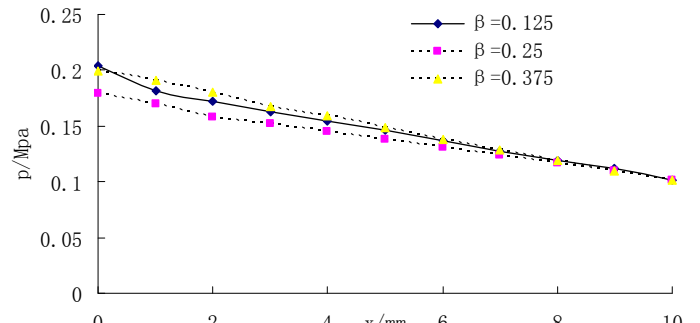
(b) Average pressure of cross section of spiral groove tube

FIGURE VII. EFFECT OF ATO FLOW VELOCITY AND PRESSURE IN SPIRAL GROOVED TUBE

The spiral slot of spiral groove is changed. T=1mm, 2mm and 3mm are taken respectively. The average velocity curve of spiral groove pipe section is obtained by taking the ratio of slot to inner diameter as the research object, as shown in Figure VIII (a). The average pressure curve of spiral groove pipe section is shown in Figure VIII (b). Figure VIII shows that the speed-up effect is the most significant when the ratio of slot to inner diameter is 0.25. At the same time, when the value of the ratio for slot and the inner diameter is 0.25, the pressure loss of the spiral groove is the least, only 0.06MPa.



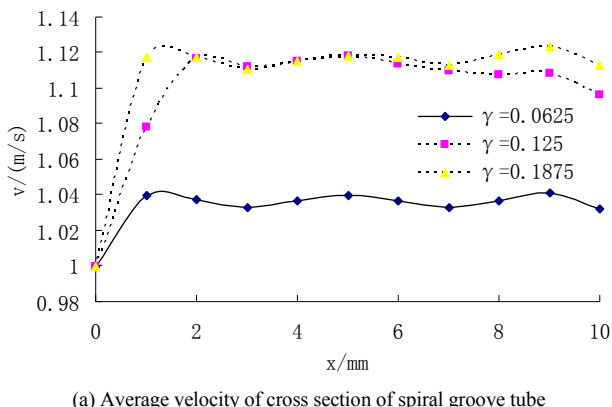
(a) Average velocity of cross section of spiral groove tube



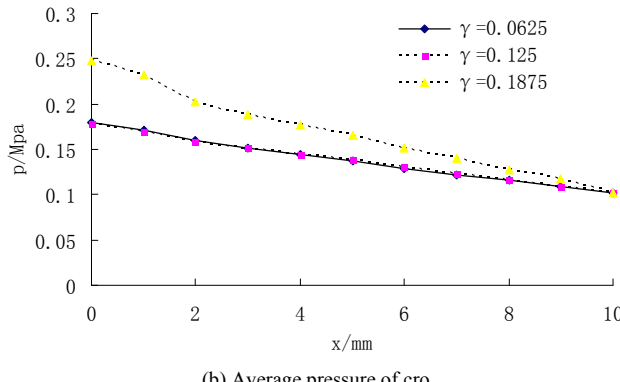
(b) Average pressure of cross section of spiral groove tube

FIGURE VIII. EFFECT OF β TO FLOW VELOCITY AND PRESSURE IN SPIRAL GROOVED TUBE

The depth of spiral grooves is changed. $e=0.5\text{mm}$, 1mm and 1.5mm are taken respectively. The ratio for depth of spiral groove to inner diameter is taken as the research object, and the average velocity curve of spiral groove section is obtained, which is shown in Figure IX (a). The average pressure curve of spiral groove section is shown in Figure IX (b). Figure IX shows that the speed-up effect is more significant when the ratio for depth of spiral groove to inner diameter increases. However, the pressure loss also increases with the increase of the ratio for depth of spiral groove to inner diameter, and the effect is very small when the ratio is in the range of $0.0625\sim0.125$.



(a) Average velocity of cross section of spiral groove tube



(b) Average pressure of cro

FIGURE IX. EFFECT OF FLOW VELOCITY AND PRESSURE IN SPIRAL GROOVED TUBE

V. CONCLUSION

The setting of the spiral groove has an obvious effect on the speed-up effect of the fluid, and also increases the pressure loss along the path. In order to acquire the maximum speed-up effect of the fluid, the ratio of spiral groove length to inner diameter should be chosen in the range of $1\sim1.5$, the ratio for slot of spiral groove to inner diameter should be chosen in $0.125\sim0.375$, and the ratio for depth of spiral groove to the inner diameter should be chosen as large as possible. The increase of the ratio for length of spiral groove to the inner diameter and the ratio for depth of spiral groove to inner diameter causes the increase of the pressure loss. However, the effect to pressure loss is very small when the ratio is in the range of $0.0625\sim0.125$. When the

value of the ratio for the slot and the inner diameter is 0.25, the pressure loss of the spiral groove is the least.

ACKNOWLEDGEMENT

This research was financially supported by the National Science Foundation 51705147, and Hunan Provincial Education Department Project 15C0542.

REFERENCES

- [1] L.J. Wang, D.W. Sun, P. Liang , et al. Heat transfer characteristics of carbon steel spirally fluted tube for high pressure pre heaters, *Energy Conversion and Management*. 41(2000) 993-1005.
- [2] D.P. Liu, S.D. Li. Contrast experiment of the spray characteristics of four atomizing nozzle, *Fluid Machinery*. 41(2013)1-6.
- [3] L.Q. Wang, S.D. Lin, Y.L. Tian, et al. Study on great flow nozzle performance with CFD method, *Fluid Machinery*. 36(2008)17-23.
- [4] M.Z. Li, G.R. Zhao. High pressure spray nozzle design and parameter optimization based on finite element simulation analysis, *Journal of China Coal Society*.40 (2015)509-514.
- [5] P.G. Vicente, A. Garcia, A. Viedma. Experimental investigation on heat transfer and frictional characteristics of spirally corrugated tubes in turbulent flow at different Peclet number, *International Journal of Heat and Mass Transfer*. 47(2000) 671-681.
- [6] Y.H. Wang, N. Sun, K.T. Gui. Numerical simulation of the convection-based heat exchange characteristics outside spirally grooved tube bundles, *Journal of Engineering for Thermal and Power*.29 (2014)509-514.

Research on Random Flow Simulation Model of Bridges

Li Cao and Limin Sun

Department of Bridge Engineering, Tongji University, Shanghai, China

Abstract—With the rapid development of automobile industry and economy, the randomness of traffic flow characteristics such as vehicle speed and vehicle weight acting on the bridge is more and more obvious. However, the previous studies are based on determination of traffic flow, so fatigue, deflection and other issues of bridges will be deviated from actual situations. Therefore, the model fitting the vehicle characteristics such as vehicle speed, vehicle weight, headway, model proportion and so on is found based on the statistical characteristics of the traffic flow on the actual bridge in this paper. The parameters of the model are statistically determined and the traffic flow program based on Monte-Carlo algorithm is established. Finally, the results show that the above theory can well simulate the actual traffic flow of the bridge through comparing the results of the program with the statistics of an actual bridge.

Keywords—traffic flow; MATLAB; time interval

I. INTRODUCTION

Because of the complexity of the traffic flow on the bridge, it is necessary for us to study the traffic flow characteristics of the bridge, to establish a scientific traffic flow model, to accurately describe and predict traffic flow on the bridge, and to provide science data support for subsequent bridge fatigue, deflection problems and so on. For the traffic flow model, there are mainly macroscopic continuous flow model [1], mesoscopic gas dynamics model and microscopic following model [2], and cellular automata model [3]. Some scholars have proposed that the distribution of expressway traffic capacity obeys lognormal distribution and Gamma distribution [4]. The literature [5] developed a set of traffic flow generating procedure based on Monte-Carlo algorithm, combined VIS-SIM simulation software, and realized real-time simulation of traffic flow in different states. In literature [6], the random traffic flow program of each lane through Monte-Carlo algorithm was established based on the traffic flow measured by toll and weighing system on the Nanjing Yangtze River Third Bridge. In literature [7], a traffic jam reconstruction model based on sequential Monte-Carlo method was proposed to evaluate current road conditions and reasonably estimate the congestion situations. The existing literature mainly studies traffic flow characteristics of the entire traffic line. In this paper, a traffic flow simulation model of the bridge is established according to the statistical characteristics of the traffic flow of the bridge.

II. THEORY

First of all, investigation and statistics on the traffic flow characteristics of specific bridges is conducted, which determines the distribution model that accurately reflects the characteristics of vehicle weight, lateral position, vehicle speed

and headway in a random traffic flow, and determines the parameters of the corresponding model. A bridge random flow simulation model based on Monte-Carlo algorithm [8] through MATLAB is developed. The flow chart is shown in Figure 1 below.

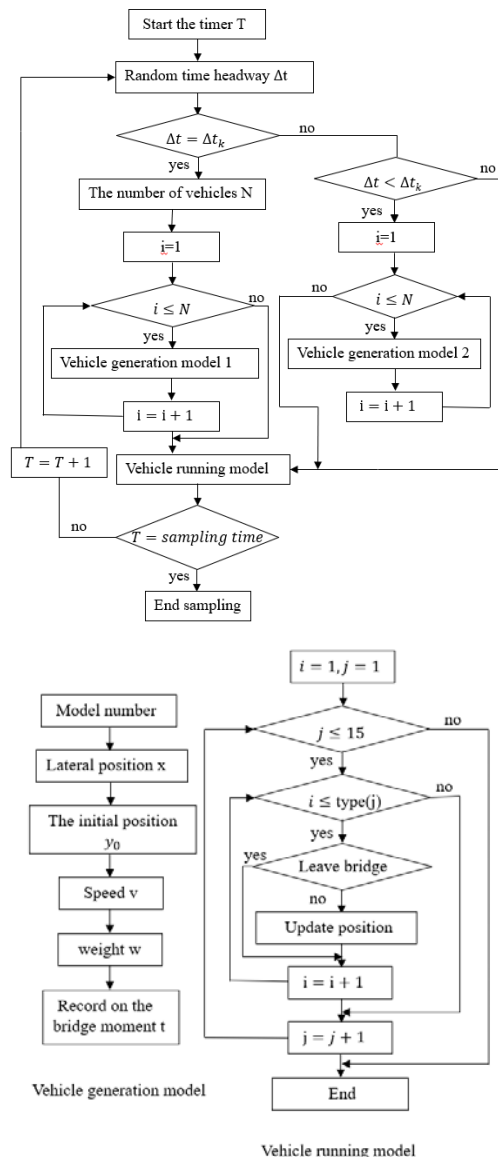


FIGURE I. FLOW CHART OF RANDOM FLOW SIMULATION MODEL

Among them, the random time interval is generated based on the Monte-Carlo algorithm, that is to produce a uniform random vector between 0 and 1, which is represented as the probability of the time interval, and then the time interval Δt is obtained through finding the inverse function of the probability distribution function. Suppose the time interval distribution function is:

$$F(x = k) = \begin{cases} 1 - e^{-\frac{(x-k)^m}{\eta}}, & x \geq 0 \\ 0, & x < 0 \end{cases} \quad (1)$$

Where, x represents the time interval of two adjacent cars, $F(x = k)$ represents the probability as the time interval x of two adjacent cars is k .

$$x = \eta^m \sqrt{-\ln(1 - F(x = k))} \quad (2)$$

A random variable x can be obtained by Eq (2) by assuming probability $F(x = k)$ as a uniform random vector within $(0, 1)$.

III. FINITE ELEMENT SIMULATION

The simulation of random vehicle is based on the parameters such as vehicle weight, lateral position, vehicle speed and time interval of vehicles in random traffic flow provided in reference [9], which reckons that the vehicle speed follows the normal distribution, the time intervals follows Wilbur distribution, vehicle weight obeys the logarithm normal distribution, the vehicle lateral position obeys the normal distribution. The vehicle weight, speed, lateral position and time interval and other data of the random traffic flow in one day are extracted through running random traffic simulation model, which is compared with the measured data.

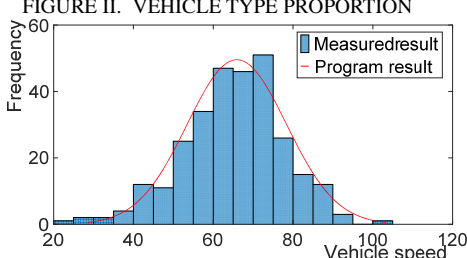
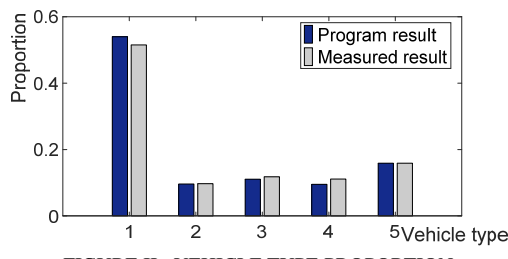


FIGURE III. FOURTH VEHICLE SPEED PROFILE

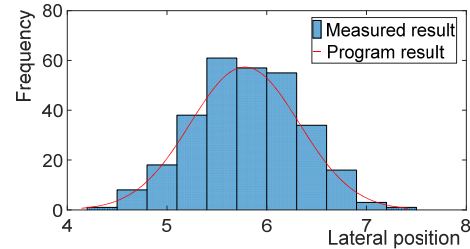


FIGURE IV. FOURTH VEHICLE LATERAL POSITION

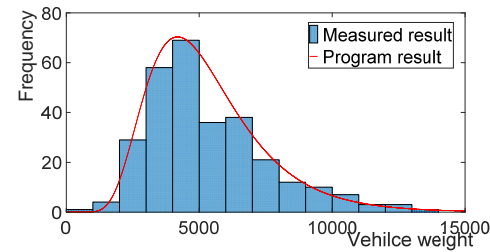


FIGURE V. FOURTH VEHICLE WEIGHT

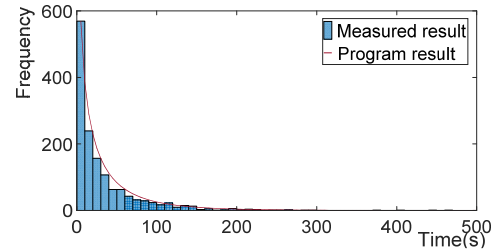


FIGURE VI. TIME INTERVAL DISTRIBUTION

IV. CONCLUSION

The traffic flow on the bridge is a stochastic process. The traffic flow characteristics such as vehicle model proportion, vehicle speed, lateral position, vehicle weight and time interval follow a certain probability distribution. The traffic flow data of the actual bridge are used to determine the traffic flow distribution types and parameters. Then the Monte-Carlo method is used to generate a uniform random number and the inverse function of the distribution function is used to simulate the traffic flow characteristics. It is known that the speed follows the normal distribution, the time interval follows the Wilbur distribution, the vehicle weight follows the logarithm normal distribution, the vehicle lateral position follows the normal distribution according to the bridge traffic flow survey data. As shown in the above Figure II to Figure VI, the adopted random traffic flow model can well reflect the actual vehicle model characteristics such as proportion, speed, lateral position, vehicle weight and time interval.

REFERENCES

- [1] Peng, G.H., et al., A new lattice model of traffic flow with the consideration of the traffic interruption probability. *Physica A Statistical Mechanics & Its Applications*, 2012. 391(3): p. 656-663.
- [2] Gazis, D.C., R. Herman, and R.W. Rothery, Nonlinear Follow-The-Leader Models of Traffic Flow. *Operations Research*, 1961. 9(4): p. 545-567.
- [3] Cremer, M. and J. Ludwig, A fast simulation model for traffic flow on the basis of Boolean operations. *Mathematics and Computers in Simulation*, 1986. 28(4): p. 297-303.

- [4] Xing, J., et al., Analysis of Bottleneck Capacity and Traffic Safety in Japanese Expressway Work Zones. in Transportation Research Board 89th Annual Meeting. 2010.
- [5] ZHENG Xiao-yan, et al., Traffic flow simulation based on Monte-Carlo algorithm. Journal of Hefei University of Technology: Natural Science Edition, 2009. 32(9): p. 1374-1377.
- [6] XU Han-jiang, et al., Vehicle Load Analysis of the Third Nanjing Yangtze River Bridge Based on Measured Traffic Flow. Journal of Disaster Prevention and Mitigation Engineering, 2011, 31(Supplement): p. 48-51.
- [7] Huang Yu-da, WEI Xia, and WANG Yi-ran, A Sequential Monte Carlo Method-based Event Reconstruction Method for Traffic Event Simulation. Computing Technology and Automation, 2017(1): p. 150-154.
- [8] HUANG Ling, The interval estimation of Multi-parameter distribution based on the Monte Carlo method. 2016, Central China Normal University.
- [9] GAO Wen-bo, Theory and Program Development of Highway Traffic Flow Simulation Based on Measured Data. 2010, Chang'an University.

A Test Process Model and Optimization Framework Based on Network Schedule

Litian Xiao^{1,2,*}, Mengyuan Li¹ and Nan Xiao³

¹Beijing Special Engineering Design and Research Institute, Beijing 10028, China

²School of Software, TNList, KLISS, Tsinghua University, Beijing 10084, China

³China Aerospace Academy of System Science and Engineering, Beijing 10048, China

*Corresponding author

Abstract—In order to shorten the test period of spaceflight articles at the launch site and improve facility utilization and launch rate, the paper proposes our research about test process model and optimization framework. The approach overlays test activity on activity-on-arrow for network schedule. The test process model is composed of the test network schedule. Based on the relativity of test items and input driving as well as output response, the test process optimization framework is formed. The test critical paths are dismantled and shortened as much as possible to shorten the entire test period. Through practice, our achievement effectively improves the test efficiency of flight articles at the launch site. It lays the foundation for constructing the integrated test system.

Keywords—aerospace test; network scheduling; test process model; critical path; optimization framework

I. INTRODUCTION

All mechatronics equipment such as cars, planes, train, launch vehicle, etc., need to be tested before they can be put into normal operation. Especially for the high risk and high-reliability systems of space articles, test verification is particularly critical. In general, the system units of space flight hardware are shipped separately and integrated at the launch site. Then full-system tests provide confidence that the system can accomplish the mission and launch technology states [1]. Test plan explicitly takes into account the dependencies of each test activity on other activities. Establishing a network schedule can determine test process definition and the test duration for test activities. A network schedule is a workflow diagram such as activity-on-arrow network diagram as shown in FIGURE I. At present, space launch missions are very intensive. As short as possible, test critical path is the key to shortening the entire test duration. It also is the key to enhancing the launch efficiency at the existing launch sites.

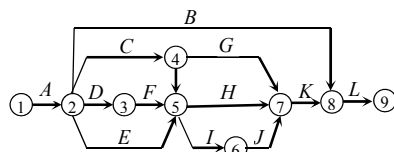


FIGURE I. ACTIVITY-ON-ARROW DIAGRAM FOR NETWORK SCHEDULES

II. RELATED WORK

A. On the Test Process Model

Test process model is a process model. Process description modeling is a hot research direction in process management system. According to their own needs and application, different scholars put forward different modeling methods [2][3]. The existing modeling methods are mainly based on interaction, activity, state transition, and relational capture. Its modeling methods do not take into account the impact of test schedule. It is not suitable for the actual physical test or simulation to improve the test schedule.

B. On Network Schedule

The activity-on-arrow diagrams for network schedule reflect the logical relation between the various activity processes of the project. It optimizes the durations, the costs and the resources of all activities by using the flexible time of each operation process. The activity-on-arrow diagrams for network schedule mainly adopt the ECRS' process optimization method (Eliminate, Combine, Rearrange, Simplify) [4][5]. The changes of test activity flow can involve the change of the technical states or configurations of the flight article and product or equipment. Mostly they are not acceptable to the flight projects.

C. On Aerospace Test

The research on aerospace test focuses on the planning resource construction and environment usage. The kinds of test resources continuously abundant at present, while the increased flexibility of a test system provides a greater number of choices of resources and routings [6][7]. The test activity schedule optimization of aerospace test system focuses the critical point to construct the resources and routings [8]–[10]. Planning resources is not involved in the schedule optimization of network schedule and related test items.

There are still some shortages of the related research in the field of aerospace testing. This paper presents an actual physical test perspective for test activity scheduling with shortening test critical paths. The research creates the test process model combined activity-on-arrow diagram with test activities and test items. We are working to break up the critical path of the test process, optimize the test process and shorten the test duration.

III. PRELIMINARY DEFINITIONS

A. Activity-on-Arrow Diagram for Test Networked Schedule

The tested system transforms the driving input into the response output according to the design state and configuration mapping. A test item needs to drive the tested system. Its result is the measurement data of the response output. A test system is composed of a tested system and test items.

Definition 1. According to the activity-on-arrow diagram, if test activity A , B and C are the serial test items labeled on the vector lines, LEN is defined as the time length, written as $\text{LEN}(\alpha_i)$, to complete a test item. $\alpha_i \in \{A, B, C\}$. The vector lines of unlabeled characters only represent the logical relationship, and the time length is zero. The time length to complete all the test activities is $T_L = \text{LEN}(A) + \text{LEN}(B) + \text{LEN}(C)$. If the test activities are parallel test items, $T_L = \text{MAX}(\text{LEN}(A), \text{LEN}(B), \text{LEN}(C))$. MAX is a maximum function. The test item of a test activity is the related subsystem testing.

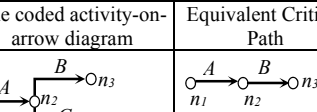
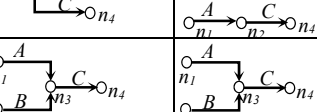
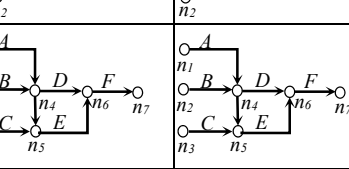
B. Test Process Model Based on Activity-on-Arrow Diagram

On the basis of activity-on-arrow diagram for network schedule, each activity is defined as a test item on the diagram. Each start node of the arrow line is test input driving. Each terminal node of that is output responses or data.

Definition 2. Activity-on-arrow diagram is coded to form the set of M nodes, $N = \{n_1, n_2, \dots, n_M\}$, according to the sequences from left to right and from top to bottom (showed in Table 1.). Each node represents the input/output interfaces related the test items of a subsystem. It is the output results of the previous node and the input driving of the latter one. The start node of the whole diagram is the input driving of the test items, and the terminal node is the output results.

The typical logical relationship of test items is shown in Table 1. And other logical relationship can be dismantled into them. The start node or the end node can be the same one.

TABLE I. TYPICAL LOGICAL RELATIONSHIP BETWEEN TEST ITEMS

	Logical relationship between test items	The coded activity-on-arrow diagram	Equivalent Critical Path
1	To complete testing A , then testing B and C .		$n_1 \xrightarrow{A} n_2 \xrightarrow{B} n_3 \xrightarrow{C} n_4$
2	To complete testing A and B , then testing C .		$n_1 \xrightarrow{A} n_2 \xrightarrow{B} n_3 \xrightarrow{C} n_4$
3	To complete testing A and B , then testing D . To complete testing A , B and C , then testing E . To complete testing D and E , then testing F .		$n_1 \xrightarrow{A} n_2 \xrightarrow{B} n_4 \xrightarrow{D} n_6 \xrightarrow{F} n_7$ $n_1 \xrightarrow{A} n_2 \xrightarrow{B} n_4 \xrightarrow{D} n_6 \xrightarrow{E} n_5 \xrightarrow{C} n_6 \xrightarrow{F} n_7$

Definition 3. The tested system features of a test item are decided by $\{PI, Tc, PO\}$, i.e. test items' action is controlled by input (PI), output (PO) and internal transition configuration (Tc) in a system. The description of test system can be defined as a tuple: $Tsys = \langle Tc, Tc_0, PI, PO, R_{PI} \rangle$, where Tc is the finite set of non-empty configuration function inside the tested system. With a test item, PI is the finite set of non-empty input, PO is the finite set of non-empty output, R_{PI} is the mapping transition set of an

input subset. $R_{PI} \subset \beta(PI) \ni \{r_i\}$, ($i=1, 2, \dots$), which β is the transition function set of confirmed generalized verification. β filters an input subset that is effective in handling. r_i is the set of R_{PI} .

P^M describes the incomplete mapping of the tested system, i.e. the testing input is transited to testing output. $P^M(a, b) : \beta(Tc) \times R_{PI} \rightarrow \beta(Tc) \times \beta(PO)$, where

$a \in \beta(Tc)$, $b \in \beta(Tc) \times \beta(PO)$. $Tc_0 \in \beta(Tc) \times \beta(PI)$, where Tc_0 is the initial state of the tested system.

C. The Relation of Test Systems

Definition 4. Test activities are connected by nodes. The relation R_{jl} of two test items can be represented as $(n_i \xrightarrow{\alpha_j} n_{i+1}) R_{jl} (n_k \xrightarrow{\alpha_l} n_{k+1})$, ($i, k \in (1, 2, \dots, N-1); j, l \in (1, 2, \dots, L)$), where R_{jl} is combinational operator $\{\rightarrow | \cup | \cap | \oplus | \neg | \emptyset\}$.

A node is preceded by $?$ as an input and by $!$ as an output. Then $?n_i(\alpha_j)$ denotes an input of α_j and $!n_i(\alpha_j)$ denotes an output of α_j at a node n_i . A test item is demonstrably described by $(?n_i \xrightarrow{\alpha_j} !n_{i+1})$ or a tuple (n, α, n') . It can be tagged with $P_j^M(?n_i, !n_{i+1})$ and briefly with P_j^M .

Definition 5. Let $P^M = [P_1^M, P_2^M, \dots, P_L^M]$, R_c is $L \times L$'s relation matrix $\begin{bmatrix} \emptyset & R_{21} & \dots & R_{L1} \\ R_{12} & \emptyset & \dots & R_{L2} \\ \dots & \dots & \dots & \dots \\ R_{1L} & R_{2L} & \dots & \emptyset \end{bmatrix}$. The test relation set can be briefly expressed as $P_j^M \circ R_c \circ (P^M)^T$. " \circ " is the relational composition operator.

IV. RELATIVITY IN TEST PROCESS MODEL

According to the definition of the relation R_{jl} associated nodes, the relativity of test item is divided into following four types.

(1) Independence, labeled R_{jl}^0 . There are no relation between two test items which can be performed separately. The input of a test item is only self-correlation.

$P_j^M(?v_i, !v_{i+1}) R_{jl}^0 P_l^M(?v_k, !v_{k+1}) \xrightarrow{?n_k \neq !n_{i+1}} (P_j^M(?v_i, !v_{i+1}), P_l^M(?v_k, !v_{k+1}))$

(2) Uncorrelated, labeled R_{jl}^- .

The latter test item is unaffected by the result of the previous one. Two test items can be performed independently. The input of a test item could be regarded as self-correlation. $P_j^M(?n_i, !n_{i+1}) R_{jl}^- P_l^M(?n_k, !n_{k+1}) \xrightarrow{?n_k \neq !n_{i+1}} (P_j^M(?n_i, !n_{i+1}), P_l^M(?n_k, !n_{k+1}))$

(3) Weak correlation, labeled R_{jl}^\sim .

The output result of the previous test item can exert influence on the result of the later one. However, as long as the output result of the previous test item is at normal or positive deviations (better than normal), it cannot influence on the result

of the later one. If it is a negative deviation, the result of the latter test item must be incorrect or uncertain.

$$\frac{P_j^M(\nu_i, \nu_{i+1}) R_{jl} P_l^M(\nu_k, \nu_{k+1})}{(\nu_k \neq \nu_{i+1}) \cup (\nu_k = \nu_{i+1})} \rightarrow P_j^M(\nu_i, \nu_{i+1}) \cup P_l^M(\nu_k, \nu_{k+1})$$

(4) Strong correlation, labeled R_{jl}^+ .

The output result of the previous test item determines the result of the later one. The next test item requires the actual values of the previous result as the input. Strong correlated path is consisted of continuous strong correlated test items.

$$P_j^M(\nu_i, \nu_{i+1}) R_{jl}^+ P_l^M(\nu_k, \nu_{k+1}) \xrightarrow{\nu_k \geq \nu_{i+1}} P_j^M(\nu_i, \nu_{i+1}) \times P_l^M(\nu_k, \nu_{k+1})$$

Therefore, according to the relativity, the critical paths can be dismantled into some strong correlated paths and separated test items. The shortest test period is determined by a maximum of the longest time length of the strong correlated critical path and max time length in the single tests.

Finally, the test process model can be abbreviated as

$$\cup P^M \circ R_c \circ (P^M)^T.$$

V. THE OPTIMIZATION FRAMEWORK FOR TEST PROCESS MODEL

A. The Transition of Strong Correlated Test Items

There are two cases of the relationship between two strong correlated test items. One case is that the response results are output at one-time after finishing the previous test item. The latter test item simultaneously receives the output as its input. We call this case synchronous testing.

Another case is that the previous test item output the grouping responses at different time intervals. The previous test item has not completed, the latter one start performance and testing after it receive the first group or several groups of the previous outputs. The subsequence groups of the previous outputs continue to be as the inputs of the latter test item until finishing the previous. We call this case asynchronous testing. FIGURE II shows the output of time progresses along from n_1 to n_2 which represents the testing process.

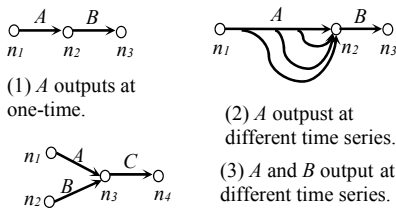


FIGURE II. THE INPUT/OUTPUT OF SYNCHRONOUS AND ASYNCHRONOUS TESTING

B. Synchronous Testing for Strong Correlated Test Items

Under synchronous testing of test items, an execution of the test items on strong correlated path is a finite sequence $\langle ?n_i, r_j \rangle$

$\langle ?n_2, r_2 \rangle, \dots, \langle ?n_i, r_j \rangle, \dots$, where $\langle ?n_i, r_j \rangle \in (P_I \times U, Tc)$ for each i and j . $\forall i & j, \exists$ a transition $(?n_i, \varphi, !n_{i+1}) \in R_{PI}$: $(r_i, r_{i+1}) \models \varphi$. A path is a finite sequence $\rho = (?n_1, \varphi_1, !n_2), (?n_2, \varphi_2, !n_3), \dots (?n_i, \varphi_j, !n_{i+1}) \dots$ of transitions from the initial node to the end of strong correlated path. A compound transition $(?n_1, \varphi, !n_k)$ can be defined by $(\sigma \circ \tau)(Tc, Tc') = \exists Tc''. \sigma(Tc, Tc'') \cap \tau(Tc'', Tc')$, where $\varphi = \varphi_1 \circ \varphi_2 \dots \circ \varphi_j$ and “ \circ ” is the relational composition operator. σ ’s definition is consistent with τ .

Therefore, the inputs of the start node on the strong correlated path are synchronously transformed to the inputs of each test item by mapping transition. Each test item can be synchronously performed by the transformed inputs. The strong correlated path can be cut into the single test items which are performed with the transformed inputs. In the case of sufficient test resources, the maximum of test time lengths in the single test items determines the shortest test period.

C. Asynchronous Testing for Strong Correlated Test Items

Under asynchronous testing of test items, test items may have the delayed inputs/outputs that are asynchronous input/output. The next test item is performed according to the previous outputs by triggering on a first-come and first-served basis. If the previous output sequences are discrete on time, the strong correlated test items can be disposed of according to the below definition and rules.

Definition 6. Under the condition of asynchronous input and output, $?n = !n(1)!n(2)\dots!n(t)$ is the relation between input and output at different time t on n . Given path ρ of the asynchronous testing path, $\Delta(\rho)$ is the smallest set of the path defined as the below rules.

There is $\rho \in \Delta(\rho)$. If $\rho_1 n^1 n^2 \rho_2 \in \Delta(\rho)$, $n^1 \in P_O$ and $n^2 \in P_I$, then $\rho_1 n^2 n^1 \rho_2 \in \Delta(\rho)$. Given set π of asynchronous testing path, let $\Delta(\pi) = \cup_{\rho \in \pi} \Delta(\rho)$.

Given node set Nd belonged to ρ , $\Delta_{Nd}(\rho)$ is the smallest set of the asynchronous testing path. Definition 6 can be extended by the following:

1) $\rho \in \Delta_{Nd}(\rho)$. 2) If $\rho_1 n^1 n^2 \rho_2 \in \Delta_{Nd}(\rho)$, $\rho_1 n^2 n^1 \rho_2 \in \Delta_{Nd}(\rho)$ when:

- (a) n^1 and n^2 are at the same node, also $n^1 \in PO$ and $n^2 \in PI$.
- (b) n^1 and n^2 are at different nodes and either $n^1 \in PO$ or $n^2 \in PI$.

Given set π of asynchronous testing path, let $\Delta_{Nd}(\pi) = \cup_{\rho \in \pi} \Delta_{Nd}(\rho)$.

This extended definition can adapt to the general situation that n^1 and n^2 are at different nodes. Then n^1 and n^2 can be swapped as shown in FIGURE III.

FIGURE III (1), n^1 and n^2 are inputted. Since there is C channel between node n_1 and n_3 , the input orders of $?n_3$ in which they were sent by the transitions of B ’s $?n_2$ and C ’s $?n_1$ may be different.

FIGURE III (2), n^1 and n^2 are outputted. Since there is C channel between node n_1 and n_3 , the output orders of $!n_3$ in which

they were sent by the transitions of B 's $!n_2$ and C 's $?n_1$ may be different.

FIGURE III (3), n^1 is an output and n^2 is an input. If the output of C 's $?n_1$ is produced before the output of B 's $!n_2$, it is possible that the input orders of $?n_3$ firstly receives C 's output after it sends the input.

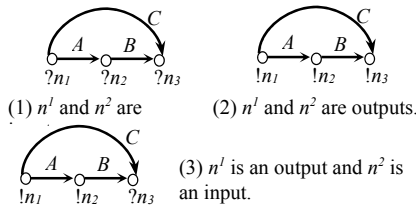


FIGURE III. n^1 AND n^2 HAVE THREE INTERCHANGEABLE TRANSFORMATION

If there is asynchronous testing path, a finite path $\Delta_{Nd}(\rho)$ has k items and an execution $\{<?n_i, r_j>\}$, a compound transition $(?n_1, \varphi, !n_k)$ can be defined by $\Delta_{Nd}(\sigma \circ \tau)(Tc, Tc') = \exists Tc''. \Delta_{Nd}(\sigma(Tc, Tc'')) \cap \Delta_{Nd}(\tau(Tc'', Tc'))$, where $\varphi = \varphi_1 \circ \varphi_2 \dots \circ \varphi_j$ and \circ is the relational composition operator.

So the strong correlated test items can be cut into the separated parallel test items. Thus the whole test period will be shortened. Synchronous testing can be considered as a special case of asynchronous testing. The optimized test process model can be described as $\cup \Delta_{Nd}(P^M) \circ R_c \circ \Delta_{Nd}((P^M)^T)$, i.e. $\cup \Delta_{Nd}(P^M \circ R_c \circ (P^M)^T)$. Shortening the length of the strong correlated path is the critical to further shorten the test activity duration.

VI. CONCLUSION

If the relationship between test items is independence or uncorrelated, based on the test relativity in the test process model, separately to test each test item is clearly feasible. In the case of weak correlation between the test items, each test item can be independently tested. Optimizing the test process model makes the strong correlated test items in test system dismantled into shorter strong correlated paths and separated test items. It's feasible to be proved on theory, which limited space not to be carried out here.

Although the research imperfections need to be studied continuously, the model and the optimization framework have achieved good results. We have effectively reduced the full-system test period for flight articles at launch sites. The period is 40-60 days or longer in past. Now it can be shortened by 20-30 days. The achievement improves the utilization rate and the launch rate at launch sites. There are some imperfections, we are also committed to further research for improving the approach. From the preliminary results and the practice, the technical route for improving imperfections is feasible.

Through practice, this model not only contributes to shortening the test period but also lays the foundation for constructing the integrated test system. It can provide the basis on the quantitative model for the configuration of test resources.

ACKNOWLEDGEMENT

This work was funded by the project of General Technology on Test and Launch partially sponsored by the 973 program. We would like to thank Tsinghua's Prof. Yu Liu who provided us with the helpful suggestions and some research resources in the research.

REFERENCES

- [1] H Dezfuli, et al., NASA Systems Engineering Handbook, NASA USA, June 2007
- [2] MA Ramos, et al., Extending statecharts to model system interactions, J. Journal of Software Engineering Research & Development, 3 (1) (2015) 1-25.
- [3] A Natarajan, User-oriented modeling of scientific workflows for high-frequency event data analysis, C. IEEE International Conference on Data Engineering Workshops, 8-12(2013) 306-309.
- [4] Tan et al. A business process intelligence system for enterprise process performance management, J. IEEE Transactions on systems, man and cybernetics - Part C: Applications and Reviews, Vol. 38, No. 6 (2008).
- [5] M Fathi, M Ghobakhloo, A technical comment on "a review on assembly sequence planning and assembly line balancing optimisation using soft computing approaches", J. International Journal of Advanced Manufacturing Technology, 71 (9-12) (2014) 2033-2042.
- [6] George Tsakalidis, Kostas Vergidis, Towards a Comprehensive Business Process Optimization Framework, C. 2017 IEEE 19th Conference on Business Informatics (CBI), Vol.01(2017) 129-134.
- [7] Janis Grabis, Charu Chandra. Joint optimization of process design and operational policies. IEEE Engineering Management Review, Volume: 44, Issue: 3(2016) 32-45.
- [8] J Tong, Y Cai, A Method of Aerospace Test Task Scheduling Based on Genetic Algorithm, C. 2012 Spring Congress on Engineering & Technology, (2012) 1-4
- [9] Derek J. Seibel, Eric A. Mehiel, Task Scheduling through a Hybrid Genetic Algorithm, C. AIAA Modeling and Simulation Technologies Conference, Chicago. (2009) 1-13
- [10] Anneliese Andrews, et al., Testing Proper Mitigation in Safety-Critical Systems: An Aerospace Launch Application, C. 2015 IEEE Aerospace Conference, (2015) 1-19

Coefficient Distribution Method for Minimum Weight Design of Large-Span Statically Determinate Trusses under the Constraint of Allowable Displacement

Wenfeng Du*, Qi Liu, Kang Yuan and Jiyuan Ma

Institute of Steel and Spatial Structure in School Civil Engineering and Architecture, Henan University, Kaifeng 475004 China

*Corresponding author

Abstract—To achieve the minimum weight design of large-span statically determinate trusses under displacement constraint, a method called the coefficient distribution method was proposed. The calculation formula of the displacement for statically determinate trusses was provided at first. Then the critical condition of minimum weight design satisfying the allowable displacement was deduced using Cauchy Inequality. At last, the distribution coefficient of material consumption, which was used to determine the proportional relationship of weight of each member in a truss, was defined. An example was analyzed using the coefficient distribution method. Study results show that the coefficient distribution method is correct, reliable and effective.

Keywords—the allowable displacement; the minimum weight design; the coefficient distribution method; large-span determinate truss

I. INTRODUCTION

The truss has been one of the most common used structures since ancient times in structural engineering history [1]. Using such a design is advantageous in that it can form a stable large system by assembling small members connected at their ends by hinges [2]. Under the action of joints loads members in a truss are subjected only to axial forces, so it is simple to design and construct trusses [3]. However, how to minimize the weight during designing a truss has been a resurgence of interest for past 30 years [4, 5].

The design optimization of trusses can be divided three levels. The first is the level of cross section. The weight of a truss member depends directly on its cross section. Optimization using sizing variables such as areas or thickness has been the most popular form [6]. The second is the level of members. Because of the problem of instability, choose of section shapes and length-width-ratio of compression members become complex [7]. The third is the level of the structure. The structural configuration and the layout of each member have important influences to the weight of a truss. Topology optimization has been studied and researched worldwide [8, 9].

Depending on the number of variables, such an iterative technique may require a large number of structural analyses that are generally costly and time consuming. Therefore, if the condition of the critical value corresponding to the minimize weight with displacement constraints can be found through the

theoretical analysis, it is meaningful to guide the design. A method called the coefficient distribution method was proposed by theoretical analysis in this paper to reach the minimum weight design of large-span statically determinate trusses under the displacement constraint.

II. COEFFICIENT DISTRIBUTION METHOD

A. Fundamental Assumption

(1)The joints of the large-span truss are regarded as ideal hinges. Most of the trusses in practical engineering conform to this assumption.

(2) The trusses are made of the linear elastic material. The common used material, such as steel, reinforced concrete, aluminum, and wood follow this assumption.

(3)Static loads are only applied on joints. Therefore, there are only axial forces in members. Most trusses usually can use this assumption.

B. Calculation Formula of Displacement

The calculation formula of displacement of the truss structure is:

$$\Delta = \sum_{i=1}^n \frac{\bar{N}_i \bar{N}_i L_i}{E_i A_i} \quad (1)$$

Where, Δ is the displacement of each joint, i is the number of each member, N_i is the axial force of member i under static loads, \bar{N}_i is the axial force of member i under the virtual unit load, L_i is the length of the member i , A_i is the cross section area of the member i , E_i is the modulus of elasticity.

C. Mathematical Optimization Model of Minimum Weight

The weight of each member can be calculated by the cross section area and the length. Therefore, the weight of a truss is:

$$W = \rho g \sum_{i=1}^n L_i A_i \quad (2)$$

Where, g is the acceleration of gravity, and ρ is the density of material. Due to the acceleration of gravity and the density of material are constant, ρg can be regarded as a constant C for simple, $C = 1$.

Then, the mathematical optimization model of minimum weight that need satisfy the requirement of allowable displacement is:

$$\left. \begin{array}{l} \text{Min}, W \\ \text{s.t. } \Delta = \sum_{i=1}^n \frac{N_i \bar{N}_i L_i}{EA_i} \leq [\Delta] \\ \text{var } 1 \leq i \leq n, i \in N \end{array} \right\} \quad (3)$$

Where, W is the objective function, $[\Delta]$ is allowable

$$\begin{aligned} W\Delta &\geq (\sqrt{L_1 A_1} * \sqrt{\frac{N_1 \bar{N}_1 L_1^2}{EA_1 L_1}} + \sqrt{L_2 A_2} * \sqrt{\frac{N_2 \bar{N}_2 L_2^2}{EA_2 L_2}} + \dots + \sqrt{L_i A_i} * \sqrt{\frac{N_i \bar{N}_i L_i^2}{EA_i L_i}} + \dots + \sqrt{L_n A_n} * \sqrt{\frac{N_n \bar{N}_n L_n^2}{EA_n L_n}})^2 \\ &= (\sqrt{\frac{N_1 \bar{N}_1 L_1^2}{E}} + \sqrt{\frac{N_2 \bar{N}_2 L_2^2}{E}} + \dots + \sqrt{\frac{N_i \bar{N}_i L_i^2}{E}} + \dots + \sqrt{\frac{N_n \bar{N}_n L_n^2}{E}})^2 \end{aligned} \quad (5)$$

The critical condition for equality is as following.

$$\sqrt{\frac{N_i \bar{N}_i L_i^2}{EA_i L_i}} / \sqrt{L_i A_i} = \sqrt{\frac{N_j \bar{N}_j L_j^2}{EA_j L_j}} / \sqrt{L_j A_j}, (i = j) \quad (6)$$

Then,

$$L_i A_i / L_j A_j = \sqrt{N_i \bar{N}_i L_i^2} / \sqrt{N_j \bar{N}_j L_j^2} = W_i / W_j \quad (7)$$

The formula (7) indicates that there exists a certain proportion among individual member weight for large-span determinate trusses to achieve the minimum weight design meeting the requirement of the allowable displacement. So, we can define a coefficient μ which is the ratio between the weight of each member and the structural total weight.

$$\mu_i = \sqrt{N_i \bar{N}_i L_i^2} / \sum_{i=1}^n \sqrt{N_i \bar{N}_i L_i^2} \quad (8)$$

Where, μ is the ratio between the weight of member i and the total weight. It denotes that when the total material usage

deflection.

D. Solution of Optimization Design Model

When the structural weight is lightest, the displacement of structure equals the allowable displacement theoretically, namely $\Delta = [\Delta]$.

After that, to find the minimum value of W , we can calculate the minimum value of $W \cdot \Delta$ equivalently.

$$W\Delta = (L_1 A_1 + L_2 A_2 + \dots + L_n A_n) \left(\frac{\bar{N}_1 \bar{N}_1 L_1^2}{EA_1 L_1} + \frac{\bar{N}_2 \bar{N}_2 L_2^2}{EA_2 L_2} + \dots + \frac{\bar{N}_i \bar{N}_i L_i^2}{EA_i L_i} + \dots + \frac{\bar{N}_n \bar{N}_n L_n^2}{EA_n L_n} \right) \quad (4)$$

According to the Cauchy Inequality.

are determined, if the amount of material of each member in a statically determinate truss is decided by the distribution coefficient, the maximum structural stiffness is obtained. In another word, under the constraint of allowable displacement, if the proportion of material usage of each member in a statically determinate truss is decided by this distribution coefficient, the material consumption of structure is lightest. Therefore, μ can be defined as the distribution coefficient.

Substitute formula (8) into formula (1) and formula (2), then we can obtain the minimum weight of a statically determinate truss:

$$W = \left(\sum \frac{N_i \bar{N}_i L_i^2}{Eu_i} \right) / [\Delta] \quad (9)$$

E. Calculation Process of Coefficient Distribution Method

According to the previous derivation, when the coefficient distribution method was used to design large-span statically determinate trusses, following steps can be used.

- (1) Applying a unit load at the joint where the maximum displacement may happen;
- (2) Calculating the axial force of each member i under the unit load;

(3) Calculating the axial force of each member i under external loads;

(4) Calculating the distribution coefficient μ according to formula (8);

(5) Calculating the minimum consumption of material using formula (9);

(6) Finally, the section area of each member i is calculated.

III. AN EXAMPLE OF APPLICATION

A. Project Introduction

The structural model of a statically determinate truss is shown in Fig.1. The span and height of the structural model is 24m and 4m respectively. There are 45 members in the structure and the number of each element is shown in Fig.1. The total number of joints is 24, and two ends of the structure are simply supported. The steel Q235B is used, whose elastic modulus, yield strength and density are 206KN/mm², 215MPa, and 7850kg/m³ respectively. The vertical load of 412kN is added on each joint. The allowable displacement [Δ] equals to 60 mm ($L/400$, L is the structural span).

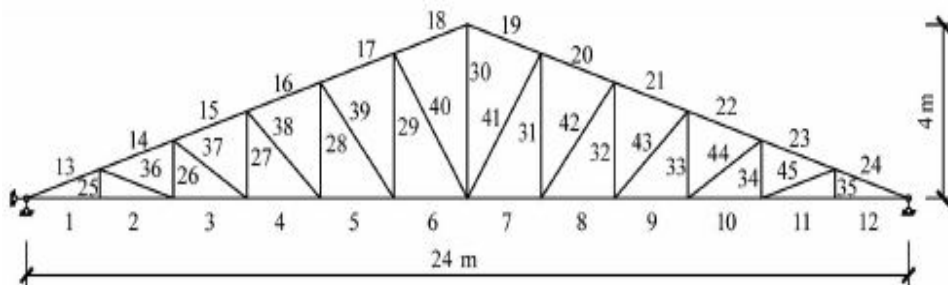


FIGURE I. STRUCTURAL MODEL AND THE NUMBER OF EACH MEMBER

B. Calculation and Comparison

At first, the structure was designed using the full stress design method and the steel consumption of each member was shown in the third column in Table 1. And according to the equation (1), the structural displacement was calculated to be 83.15mm which exceeds the allowable displacement (60mm). Then, to satisfy the requirement of the allowable displacement, the section area of each member was expanded by the proportion 83.15/60, and the structural displacement was recalculated, until it met the requirement of allowable displacement. Both the amount of steel used for each member of the structure and the total amount of the steel are shown in the fourth column of Table 1.

After that, the structure was designed according to the coefficient distribution method proposed in this paper. First, the

axial force of every element under the same load was calculated, as shown in the fifth column in Table 1. And a unit force was applied on the lower chord joint in the middle of the truss, as shown in the sixth column in Table 1. Then, formula (9) was applied to calculate the total amount of steel and the distribution coefficient of each member can be got from formula (8). The total amount of steel is assigned to each member according to its distribution coefficient, as shown in the 7th column in Table 1.

Then the displacement of the structure can be calculated according to the formula (1), which is equal to the allowed displacement [Δ].

The data in the 8th column is the amount of steel that meets the requirement of strength on the basis of the 7th column

TABLE I. THE CALCULATED RESULTS

element number (i)	length of each member (Li /m)	steel consumption using the Full Stress Design Method (W/kg)	steel consumption after adjustment (W/kg)	Axial forces under loads (Ni/kN)	Axial forces under the unit load. (Ni/kN)	steel consumption using the Coefficient Method (W/kg)	steel consumption after adjustment (W/kg)
1	2	5.290535	7.365394	72.45	1.5	6.663822	6.663822
2	2	5.290535	7.365394	72.45	1.5	6.663822	6.663822
3	2	4.830488	6.724925	66.15	1.5	6.367502	6.367502
4	2	4.370442	6.084456	59.85	1.5	6.056703	6.056703
5	2	3.910395	5.443987	53.55	1.5	5.729067	5.729067
6	2	3.450349	4.803518	47.25	1.5	5.381522	5.381522
7	2	3.542358	4.931612	48.51	1.5	5.452803	5.452803
8	2	4.140419	5.764222	56.7	1.5	5.895162	5.895162
9	2	4.830488	6.724925	66.15	1.5	6.367502	6.367502
10	2	5.290535	7.365394	72.45	1.5	6.663822	6.663822
11	2	5.750581	8.005864	78.75	1.5	6.947515	6.947515
12	2	5.750581	8.005864	78.75	1.5	6.947515	6.947515
13	2.11	5.883433	8.190817	-76.369	1.581139	7.410621	7.410621
14	2.11	5.37183	7.478572	-69.7282	1.581139	7.081093	7.081093
15	2.11	4.860227	6.766327	-63.0874	1.581139	6.735463	6.735463
16	2.11	4.348624	6.054082	-56.4467	1.581139	6.37111	6.37111
17	2.11	3.837021	5.341837	-49.8059	1.581139	5.984616	5.984616
18	2.11	3.325418	4.629592	-43.1651	1.581139	5.571374	5.571374
19	2.11	3.325418	4.629592	-43.1651	1.581139	5.571374	5.571374
20	2.11	3.939342	5.484286	-51.134	1.581139	6.063886	6.063886
21	2.11	4.604426	6.410205	-59.767	1.581139	6.555818	6.555818
22	2.11	5.37183	7.478572	-69.7282	1.581139	7.081093	7.081093
23	2.11	5.883433	8.190817	-76.369	1.581139	7.410621	7.410621
24	2.11	6.395035	8.903062	-83.0098	1.581139	7.726106	7.726106
25	0.67	0	0	0	0	0	0
26	1.33	0.101977	0.141971	2.1	0	0	0.101977
27	2	0.306698	0.426979	4.2	0	0	0.306698
28	2.67	0.614162	0.855026	6.3	0	0	0.614162
29	3.33	1.021303	1.421841	8.4	0	0	1.021303
30	4	3.373674	4.696773	23.1	1	6.144613	6.144613
31	3.33	1.327694	1.848394	10.92	0	0	1.327694
32	2.67	0.921243	1.282539	9.45	0	0	0.921243
33	2	0.306698	0.426979	4.2	0	0	0.306698
34	1.33	0.101977	0.141971	2.1	0	0	0.101977
35	0.67	0	0	0	0	0	0
36	2.11	0.511603	0.712245	-6.64078	0	0	0.511603
37	2.4	0.663489	0.923698	-7.57166	0	0	0.663489
38	2.83	0.920605	1.28165	-8.90955	0	0	0.920605
39	3.33	1.276629	1.777302	-10.5	0	0	1.276629
40	3.89	1.73916	2.42123	-12.245	0	0	1.73916
41	3.89	2.086992	2.905476	-14.694	0	0	2.086992
42	3.33	1.659618	2.310492	-13.65	0	0	1.659618
43	2.83	1.380907	1.922476	-13.3643	0	0	1.380907
44	2.4	0.663489	0.923698	-7.57166	0	0	0.663489
45	2.11	0.511603	0.712245	-6.64078	0	0	0.511603
sum	—	133.0833	185.2763	—	—	160.8445	176.9604

C. Analysis and Discussion

According to the results of this project, it can be known that when the strength requirement is met only, the minimum amount of steel calculated by full stress design method is 133.108kg. When stiffness requirement is met only, the minimum amount of steel calculated by the coefficient distribution method is 160.184kg.

When both the strength and stiffness requirements are met, the minimum amount of steel is 176.196kg, which is obtained using the coefficient distribution method. It is to meet the stiffness requirement at first and then to adjust the members who cannot meet the strength requirement to the values

calculated using the full stress design method. If the process above is reversed, the outcome will be 185.128kg. Table.1 shows that under the constraints of strength and stiffness, the results according to the coefficient distribution method can save the amount of steel by 4.5% compared with the results of the full stress design method. Fig.2 shows the situation of the distribution coefficient of each member.

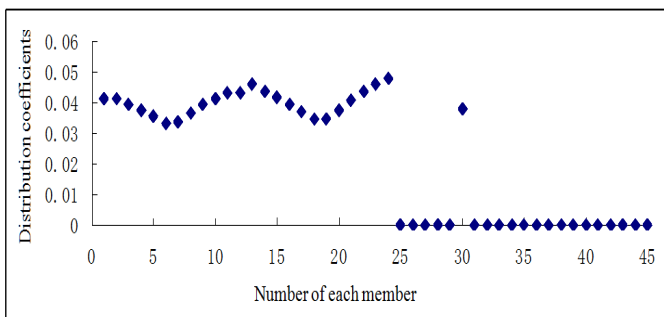


FIGURE II. DISTRIBUTION COEFFICIENT OF EACH MEMBER

The distribution coefficients of these members numbering from 1 to 24 and 30 are not zero (about 0.04), and the distribution coefficients of the rest members are all zero. That indicates these members did not affect the vertical displacement of the middle joint, because the internal forces of these members under the unit load are zero. These members whose distribution coefficients are not equal to zero are located at the top chord, the lower chord and the middle vertical web. The distribution coefficient demonstrates that the influence of each member to structural displacement, and the member numbering 24 and 13 have the largest influence on vertical displacement because their distribution coefficients are both the largest (about 0.048). They are located at the top chord connecting with supports. While, the other webs in the truss have no effect on the structural displacements because their distribution coefficients are zero.

Because there are many kinds of trusses applied in practical engineering, three common forms in Fig.3 were chosen to make a further analysis. Their spans were 4m, 8m, 12m, 16m, 20m, 24m, 28m, 32m, 36m separately, and the length of each lower chord member is 2 m.

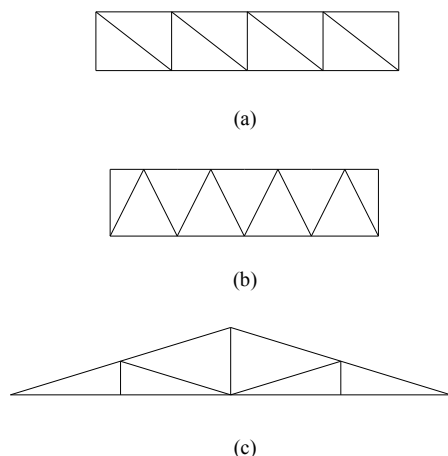


FIGURE III. THREE KINDS OF TYPICAL TRUSS STRUCTURE

Using the same process with the example in Fig.1, these three typical kinds of trusses were calculated respectively. The results show that these three trusses designed with the coefficient distribution method can save the amount of steel compared with the full stress design method, as shown in Fig.4.

It is obvious the effect of the coefficient distribution method depend on the structural spans. The larger the span is, the more amount of steel saved in the three kinds of trusses are from Fig.4.

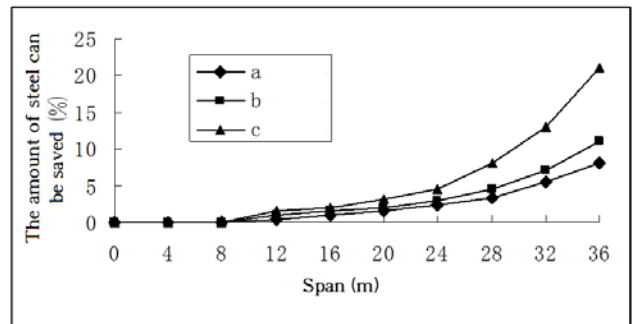


FIGURE IV. THE SAVED STEEL WITH THE STRUCTURAL SPAN OF THE THREE TYPICAL TRUSSES

Type C truss can save the most amount of steel obviously, when the span is 36m, the saved steel consumption can reach to 21%. It indicates the coefficient distribution method is very suitable for applying on triangle shape trusses obviously. When the span is small, the results of the full stress design method and those of the full displacement coefficient distribution method are the same, because the structural stiffness does not control the design of the structure.

IV. CONCLUSION

(1) This article proposed the coefficient distribution method to realize the minimum weight design of large-span statically determinate trusses under the constraint of allowable displacement. This is a design method of structural optimization to improve the structural stiffness meeting the requirement of displacements. The coefficient distribution method has theoretical and practical applications on the large span light steel trusses whose designs are decided by stiffness.

(2) The coefficient distribution method is based on the Cauchy Inequality. The critical condition shows that there exists a certain proportion relationship among individual member weight for statically determinate trusses to achieve the minimum weight design meeting the requirement of the allowable displacement.

(3) Results of comparison between the coefficient distribution method and the full stress method, the former is more economic than the latter for trusses. To the truss with triangle shape, 21% steel can be saved using the coefficient distribution method when the structural span is 36m.

REFERENCES

- [1] L. Gil, A. Andreu, Shape and cross-section optimization of a truss structure, *J. Computers & Structures*, 79(2001) 681-689.
- [2] L. Lamberti, An efficient simulated annealing algorithm for design optimization of truss structures, *J. Computers & Structures*, 86(2008)1936-1953.
- [3] V. Plevris, M. Papadrakakis, A hybrid particle swarm-gradient algorithm for global structural optimization, *J. Computer-Aided Civil and Infrastructure Engineering*, 26(2011)48-68.

- [4] K. Mela, Resolving issues with member buckling in truss topology optimization using a mixed variable approach, *J. Structural and Multidisciplinary Optimization*, 50(2014) 1037-1048.
- [5] A. Cerveira, A. Agra, F. Bastos, J. Gromicho, A new Branch and Bound method for a discrete truss topology design problem, *J. Computational Optimization and Applications*, 54(2013)163-168.
- [6] M. Jalalpour, T. Igusa, J.K. Guest, Optimal design of trusses with geometric imperfections: Accounting for global instability, *J. International Journal of Solids and Structures*, 48(2008)3011-3022.
- [7] R.J. Balling, R.R. Briggs, K. Gillman. Multiple optimum size/shape/topology designs for skeletal structures using a genetic algorithm, *J. Journal of Structural engineering*, 132(2006)1158-1165.
- [8] D. Wang, W.H Zhang, J.S Jiang, Truss shape optimization with multiple displacement constraints, *J. Computer Methods in Applied Mechanics and Engineering*, 191(2002)3597-3612.
- [9] A.R. Yildiz, A novel hybrid immune algorithm for global optimization in design and manufacturing, *J. Robotics and Computer-Integrated Manufacturing*, 25(2008)227-261.

Sieve Method: Sieve the Forward and Reverse In One Time

Sai Chuen Hui

Frontier Science Research Institute of Hong Kong Limited

Abstract—This article carries on "Sieve Method: Sieve the Forward and Reverse In One Time" through establishing the dual element set and forms a new fundamental mathematical theory to sieve odd prime number pairs. The conclusion verifies the formula that calculating the total number of pairs that any even number is the sum of two odd prime numbers, and the minimum is that when an even number is extacted of root, the total number of odd prime number pairs is never less than one, so the Goldbach Conjecture is solved.

Keywords—*sieve Method; sieve the forward and reverse in one time; prime number pairs; dual element set*

I. POSITIVE AND NEGATIVE SCREENING

The only assumption is that "prime" is the only element in the mathematics of mass energy (matter and energy).

Example: take a W=26 even after prescribing the prime number of prime sieve to 2, 3, 5 (red):

Positive subsets: +S = 0 1 ② ③ 4 ⑤ 6 7 8 9 10 11 12 13 14 15 16 17 18 19 20 21 22 23 24 25 26 (positive energy of superscript)

Reverse subsets: -S = 26 25 24 23 22 21 20 19 18 17 16 15 14 13 12 11 10 9 8 7 6 ⑤ 4 ③ ② 1 0 (subscript negative energy)

(1) [theorem 1] Goldbach's conjecture for the exact solution of the formula:

$$Z_w(w) = Z_{p,q}(w) + 2Z_a(w) \dots \dots \dots (1.1)$$

$$Z_{pq}(w) = w+1 + \sum_{\substack{l \leq n \leq m \\ l \neq 0}} (-1)^{l+m} \sum_{\substack{k \leq j_1 < j_2 \leq n \\ k \leq j_1 < j_2 \leq m \\ |j_1 - j_2| \geq 2}} \left[\frac{w - p_{j_1}^{k_1} \cdot p_{j_2}^{k_2}}{p_{j_1} \cdot p_{j_2} \cdot p_{j_3} \cdots p_{j_m}} + 1 \right] - 2A_{W-1} \dots \dots \dots (1.2)$$

(2) the theorem 2 any even W table as the sum of two odd primes p+q of odd prime number is at least W after prescribing an odd prime number, and a constant total of not less than 1.

$$Z'_w(w) \geq [\pi(\sqrt{w}) - 1] + A_{w-1}$$

$$A_{w-1} = \begin{cases} 1 & w-1 \text{ prime number } \binom{1}{w-1} \text{ Not sifted} \\ 0 & w-1 \text{ Is a factor } \binom{1}{w-1} \text{ To be sifted} \end{cases}$$

Checking calculation: Taking the minimum value =6 of the even number, the limit value.

Goldbach's conjecture

[theorem 1-2] is confirmed by the appraisal document of the United States intellectual property rights bureau and the certificate of authorization of the 2012.4.4.

After 51 years (1962-2012) and 17 Chinese University professor... Hong Kong has Qiwen professor Su Dazhu, Ph.D., Southern China Normal University clock set column number of tutors, Xiamen University mathematician Li Wenqing guiding the audit results. Opening an equation to solve two unknowns is an alternative mathematics.

If the formula (1.1) is used to calculate the "heavy prime" table, "double key lock password" "DNA sequence" "atomic energy meter"... All the "universe tables" can be accurately looked up! The realization of Ai Bernstein "... How to establish an aesthetic system that can be strictly expressed by a formula." A mathematical description of the lifetime of the universe!

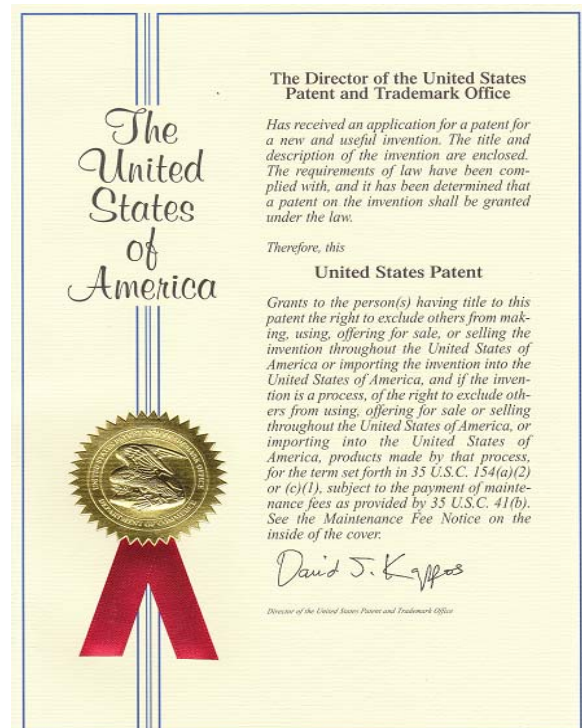


FIGURE I. US PATENT CERTIFICATE

It is easy to get w by adding to prime numbers p and q , but factoring w into p and q is difficult because it is a one-way function of uncertain solutions. It is difficult to factorize w when it is big because p and q are required to be odd prime numbers. Based on Goldbach's conjecture, the numbers of combination of (p, q) can be derived by:

$$Z_w(w) = Z_{pq}(w) + 2Z_a(w) \quad (1.1)$$

$$Z_{pq}(w) = w + 1 + \sum_{\substack{1 < p_1 < p_2 < \dots < p_n \\ p_1, p_2, \dots, p_n \text{ are odd}}} \left[\frac{w - r_{j_1, j_2}^{j_1-j_2}}{p_1 \cdots p_n} + 1 \right] - 2A_{n-1} \quad (1.2)$$

and here, $p_i (i=1,2,3,\dots,n, n=\pi\sqrt{w}, p_1=2)$. $Z_a(w)$ is the number of the combination pairs of (p, q) in the interval $[0, \sqrt{w}]$.

$$A_{n-1} = \begin{cases} 1, \text{if } w-1 \text{ is prime number} \\ 0, \text{if } w-1 \text{ is non-prime number} \end{cases} \quad r_{j_1, j_2}^{j_1-j_2} \text{ is the solution of the below equation between the interval } [0, w].$$

$$\begin{cases} x \equiv 0 \pmod{p_1 p_2 \cdots p_n} \\ x \equiv w \pmod{p_1 p_2 \cdots p_n} \end{cases} \dots \dots \dots \quad (1.3)$$

The lower boundary of $Z_w(w)$ is $Z_w'(w)$, which is defined as

$$Z_w'(w) = \lfloor \pi(\sqrt{w}) - 1 \rfloor + A_{w-x} \quad (1.4)$$

7. In view of the above, it is submitted that the claims are in condition for allowance. Reconsideration and withdrawal of the rejection are requested. Allowance of claims 21-26 and 29-37 at an early date is solicited.

App. Nr.: 11/881,299

Amendment B (contd)

10

8. Should the examiner believe that anything further is needed in order to place the application in condition for allowance, he is requested to contact the undersigned at the telephone number listed below.

Respectfully submitted,



Raymond Y. Chan
Reg. Nr.: 37,484
108 N. Ynez Ave.
Suite 128
Monterey Park, CA 91754
Tel.: 1-626-571-9812
Fax.: 1-626-571-9813

CERTIFICATE OF MAILING

I hereby certify that this correspondence is being deposited with the United States Postal Service with proper postage as first class mail in an envelope addressed to: "Commissioner for Patents, P.O. Box 1450, Alexandria, VA 22313-1450" or being facsimile transmitted to the USPTO on the date shown below.

Signature:  Date: 12/20/2011
Name in print: Raymond Y. Chan

FIGURE II. IDENTIFICATION DOCUMENTS OF THE UNITED STATES INTELLECTUAL PROPERTY OFFICE

Take any even number, $w = 26$ say.

We look at the set of its non-negative integers:

Forward Subset: $S^+ = 0, 1, 2, \dots, 24, 25, 26$

Backward Subset: $S^- = 26, 25, 24, \dots, 2, 1, 0$

The prime factors of the subsets S^+ and S^- are:

S^+ =	0	1	2	3	4	5	6	7	8	9	10	11	12	13	14	15	16	17	18	19	20	21	22	23	24	25	26
S^- =	26	25	24	23	22	21	20	19	18	17	16	15	14	13	12	11	10	9	8	7	6	5	4	3	2	1	0

By combining the two subsets, we can see that the sum of any arbitrary pair of numbers is equal $w = 26$.

S^+ =	x	1	2	3	x	5	x	7	x	x	x	11	x	13	x	x	x	17	x	19	x	x	x	23	x	x	x
S^- =	x	x	x	23	x	x	x	19	x	17	x	x	x	13	x	11	x	x	x	7	x	5	x	3	2	1	x

$\sqrt{w} = \sqrt{26} = 5.099$, which after rounding, the prime factors are 2, 3 and 5.

This gives us two pairs of odd primes of known elements: 3+23 and 23+3, along with three pairs of odd primes with

II. BACKGROUND

In a letter to Euler on June 7th 1742, Goldbach proposed the conjecture expressed this in two forms:

(A) Every even integer ≥ 6 can be written as the sum of two odd primes.

(B) Every odd integer ≥ 9 can be written as the sum of three odd primes.

We call (A) the strong conjecture and (B) the weak conjecture.

By sieving the numbers that can be divided exactly by 2, 3 and 5 in the subsets S^+ and S^- , we obtain the forward and reverse collection as follows:

unknown elements: 7+19, 13+13 $Z_{pq}(w)$ and 19+7.

III. THE THEORY

Mr. Hui uses his "Sieve Method: Sieve the Forward and Reverse In One Time" to analyze the strong form of Goldbach's Conjecture, i.e. given any even number $w > 5$, there exists two odd primes p, q such that $w = p + q$.

- Let $Z_w(w)$ be the number of pairs (p, q) that satisfies $w = p + q$.

- Let

$$A_{w-1} = \begin{cases} 1, & \text{if } w-1 \text{ is prime (i.e. } (1, w-1) \text{ hasn't been sieved)} \\ 0, & \text{if } w-1 \text{ is not a prime (i.e. } (1, w-1) \text{ has been sieved)} \end{cases}$$

- Let $Z_a(w)$ be the number of pairs $(p_i, w-p_i)$ and hence Mr. Hui proposes that:

where p_i is a prime between $[0, \sqrt{w}]$ and $w-p_i$ is also prime.

- Let $Z_{pq}(w)$ be the number of pairs (p, q) that satisfies $w=p+q$ but falls outside the categories of $Z_a(w)$ and A_{w-1} .

This covers all types of number pairs we will encounter,

$$Z_{pq}(w) = w+1 + \sum_{\substack{l+m \leq n \\ l, m \geq 0}} (-1)^{l+m} \sum_{\substack{1 \leq i_1 < \dots < i_l \leq n \\ 1 \leq j_1 < \dots < j_m \leq n \\ \{i_1 \dots i_l\} \sqcup \{j_1 \dots j_m\} = \emptyset}} \left[\frac{w - r_{j_1 \dots j_m}^{i_1 \dots i_l}}{p_{i_1} \dots p_{i_l} p_{j_1} \dots p_{j_m}} + 1 \right] - 2A_{w-1} \quad (2)$$

where $r_{j_1 \dots j_m}^{i_1 \dots i_l}$ is the initial value of $S_{j_1 \dots j_m}^{i_1 \dots i_l}$, and

$$S_{j_1 \dots j_m}^{i_1 \dots i_l} = S^{p^{i_1}} \cap \dots \cap S^{p^{i_l}} \cap S_{p_{j_1}} \cap \dots \cap S_{p_{j_m}}$$

with S^{p_i} and S_{p_j} being the resultant subsets that are obtained by sieving the top and bottom rows of S by p_i and p_j respectively.

The lower bound of $Z_w(w)$, called $Z'_w(w)$, is:

$$Z'_w(w) = [\pi(\sqrt{w}) - 1] + A_{w-1} \quad (3)$$

where $n = \pi(\sqrt{w})$ is the number of primes between $[0, \sqrt{w}]$.

It is easy to show that $[\pi(\sqrt{w}) - 1] + A_{w-1}$ is always

$$S = \left\{ \binom{0}{w}, \binom{1}{w-1}, \binom{2}{w-2}, \dots, \binom{p_i}{w-p_i}, \dots, \binom{x}{w-x}, \dots, \binom{w-p_i}{p_i}, \dots, \binom{w-2}{2}, \binom{w-1}{1}, \binom{w}{0} \right\}$$

A(0)

B(\sqrt{w})

C($w-\sqrt{w}$)

D(w)

And divide by \sqrt{w} into three segments: AB, BC and CD.

AB and CD are symmetrical. p_i is a prime between $[0, \sqrt{w}]$ which we use to sieve the top and bottom rows of S

greater than or equal to 1 (as there are infinitely many primes), and thus by combining (1) and (3), Goldbach's Conjecture can be verified. The author fully understands the implication of this statement and would like to clarify that the aims behind his theories are solely for the purpose of furthering any discussion in this field. This is because the basis of his proof is fundamentally based on his concept of a 2-Way Sieve, which he believes requires a much higher level of scrutiny than it currently receives. Otherwise, he is afraid that the concept would only be deemed worthy of ridicule by the worldwide community.

IV. PROOF

Here is how the proof roughly goes:

Take the set S

separately.

(a) Sieve the top row of S (i.e. the Forward Sieve)

using p_i , and call the resulting subset S^{p_i} (note we will express p_i as $p_{i_1} \dots p_{i_l}$, $l \leq n$):

$$S^{p_i} = \left\{ \binom{0}{w}, \binom{p_i}{w-p_i}, \binom{2p_i}{w-2p_i}, \dots, \binom{x}{w-x}, \dots \right\} \quad x \equiv 0 \pmod{p_i}$$

The smallest x could be 0, which we'll denote as $r^{p_i} = 0$, the initial value of S^{p_i} . Remove S^{p_i} from S and note that $\binom{p_i}{w-p_i}$ is also sieved.

(b) Take p_j and sieve the bottom row of S (the

$$S_{p_j} = \left\{ \dots, \binom{w-x}{x}, \dots, \binom{w-2p_j}{2p_j}, \binom{w-p_j}{p_j}, \binom{w}{0} \right\} \quad x \equiv w \pmod{p_j}$$

Since $w-x = \lambda p_j$ (with λ an integer), we get $w-x \equiv 0 \pmod{p_j}$, hence $x \equiv w \pmod{p_j}$. The

minimum value of x is $r_{p_j} = \langle w \rangle_{p_j}$, $\langle w \rangle_{p_j}$ being the remainder of w divided by p_j . As before this is the initial value

of S_{p_j} , which we remove from S and noting again that $\binom{w-p_j}{p_j}$ is also sieved.

By subtracting $S^{p_{j_1}}, S^{p_{j_2}}, \dots, S^{p_{j_l}}, S_{p_{j_1}}, S_{p_{j_2}}, \dots, S_{p_{j_m}}$ from

Backwards Sieve), expressing p_j as $p_{j_1} \dots p_{j_m}$, with $m \leq n$.

We obtain the subset S_{p_j} :

S , all elements of the form $\binom{\lambda p_i}{w-\lambda p_i}$ are sieved from segments AB, BC and CD. This leaves us with pairs of odd primes $\binom{p}{q}$ in the BC, which we will denote as $Z_{pq}(w)$.

Upon letting $2Z_a(w)$ be the number of pairs between AB and CD where p_i and $w-p_i$ are both prime, we get:

$$Z_w(w) = Z_{pq}(w) + 2Z_a(w)$$

We begin by looking at the size of the sets:

$$|S| = w+1, |S^{p_i}| = \left[\frac{w-r^{p_i}}{p_i} + 1 \right], |S_{p_j}| = \left[\frac{w-r_{p_j}}{p_j} + 1 \right]$$

Suppose we know what $\pi(\sqrt{w})$ is. If we now consider the number of primes between BD, we obtain the following:

$$\pi(w) - \pi(\sqrt{w}) = (w+1) - 1 - \sum_{i=1}^n \left[\frac{w-r^{p_i}}{p_i} + 1 \right] + \sum_{0 \leq I_1 < I_2 \leq N} \left[\frac{w-r^{p_1 p_2}}{p_1 \cdot p_2} + 1 \right] - L + (-1)^n \left[\frac{w-r^{p_1 L p_N}}{p_1 L p_N} + 1 \right]$$

Which simplifies to

$$\pi(w) - 1 = \left[\pi(\sqrt{w}) - 1 \right] + w + \sum_{1 \leq l \leq n} (-1)^l \sum_{1 \leq i_1 < \dots < i_l \leq n} \left[\frac{w - r^{i_1 \dots i_l}}{p_{i_1} \dots p_{i_l}} \right] \quad (2.1)$$

Now,

$$\begin{aligned}
Z_{pq}(w) &= \left| S - \bigcup_{\substack{i=1 \\ j=1}}^n S_{p_j}^{p_i} \right| = |S| + \sum_{\substack{l+m \leq n \\ l,m \geq 0}}^n (-1)^{l+m} \sum_{\substack{1 \leq i_1 < \dots < i_l \leq n \\ 1 \leq j_1 < \dots < j_m \leq n}} \left| S_{j_1 \dots j_m}^{i_1 \dots i_l} \right| \\
&= |S| + \sum_{\substack{0 \leq i \leq n \\ 0 \leq j \leq n}} (-1)^{i+j} \sum_{\substack{1 \leq i_1 < \dots < i_l \leq n \\ 1 \leq j_1 < \dots < j_m \leq n}} \left| S^{p_{i_1}} L S^{p_{i_2}} S_{p_{j_1}} L S_{p_{j_m}} \right| \\
&= |S| + \sum_{\substack{0 \leq i \leq n \\ 0 \leq j \leq n}} \left| S_{p_j}^{p_i} \right| + \sum_{\substack{0 \leq i_1 < i_2 \leq n \\ 0 \leq j_1 < j_2 \leq n}} \left| S^{p_{i_1}} S_{p_{j_2}} \right| - \sum_{\substack{0 \leq i_1 < i_2 < i_3 \leq n \\ 0 \leq j_1 < j_2 < j_3 \leq n}} \left| S^{p_{i_1}} S_{p_{j_2}}^{p_{i_2}} S_{p_{j_3}} \right| + L + (-1)^{l+m} \left| S^{p_{i_1}} \square S_{p_{j_m}} \right| \\
&= w + 1 - \sum_{\substack{0 \leq i \leq n \\ 0 \leq j \leq n}} \left[\frac{w - r_j^i}{p_{i,j}} + 1 \right] + \sum_{\substack{0 \leq i_1 < i_2 \leq n \\ 0 \leq j_1 < j_2 \leq n \\ \{i_1 i_2\} \neq \{j_1 j_2\}}} \left[\frac{w - r_{j_1 j_2}^{i_1 i_2}}{p_i p_j} + 1 \right] - \sum_{\substack{0 \leq i_1 < i_2 < i_3 \leq n \\ 0 \leq j_1 < j_2 < j_3 \leq n \\ \{i_1 i_2\} \neq \{j_1 j_2\}}} \left[\frac{w - r_{j_1 j_2 j_3}^{i_1 i_2 i_3}}{p_i \square p_j} + 1 \right] \\
&\quad + L + (-1)^{l+m} \left[\frac{w - r_{j_1 \dots j_m}^{i_1 \dots i_l}}{p_i \square p_j} + 1 \right] - 2A_{w-1} \\
&= w + 1 + \sum_{\substack{l+m \leq n \\ l,m \geq 0}} (-1)^{l+m} \sum_{\substack{1 \leq i_1 < \dots < i_l \leq n \\ 1 \leq j_1 < \dots < j_m \leq n \\ \{i_1 \dots i_l\} \neq \{j_1 \dots j_m\} = \emptyset}} \left[\frac{w - r_{j_1 \dots j_m}^{i_1 \dots i_l}}{p_{i_1} \dots p_{i_l} p_{j_1} \dots p_{j_m}} \right] - 2A_{w-1}
\end{aligned}$$

Where

$$r_{j_1 \dots j_m}^{i_1 \dots i_l} = \begin{cases} x \equiv 0 \pmod{p_{i_1}} \\ x \equiv 0 \pmod{p_{i_2}} \\ \dots \\ x \equiv 0 \pmod{p_{i_l}} \\ x \equiv w \pmod{p_{j_1}} \\ x \equiv w \pmod{p_{j_2}} \\ \dots \\ x \equiv w \pmod{p_{j_m}} \end{cases} = \begin{cases} x \equiv 0 \pmod{p_{i_1} \dots p_{i_l}} \\ x \equiv w \pmod{p_{j_1} \dots p_{j_m}} \end{cases}$$

Moving on, we now show

$$Z'_w(w) = [\pi(\sqrt{w}) - 1] + A_{w-1} \quad (3)$$

Prior to sieving, we can alter (2.1) slightly to express the sum of odd prime pairs $Z_w(w)$ and pairs that contain a

single odd prime $Z_p(w)$ as:

$$2Z_w(w) + Z_p(w) = 2 \left\{ \left[\pi(\sqrt{w}) - 1 \right] + w + \sum_{1 \leq l \leq n} (-1)^l \sum_{1 \leq i_1 < \dots < i_l \leq n} \left[\frac{w - r^{i_1 \dots i_l}}{p_{i_1} \dots p_{i_l}} + 1 \right] \right\} \quad (2.2)$$

After applying the 2-Way Sieve, segments AB and BD are

removed, leaving us with $Z_{pq}(w)$ in segment BC, i.e.

$$2Z_w(w) + 2Z_a(w) = 2 \left\{ \left[\pi(\sqrt{w}) - 1 \right] + w + \sum_{1 \leq l \leq n} (-1)^l \sum_{1 \leq i_1 < \dots < i_l \leq n} \left[\frac{w - r^{i_1 \dots i_l}}{p_{i_1} \dots p_{i_l}} + 1 \right] \right\} - Z_p(w) - 2 \left[\pi(\sqrt{w}) - 1 \right] - 2A_{w-1}$$

And substituting in equation (1), we get:

$$2Z_{pq}(w) + Z_p(w) = 2 \left\{ w + \sum_{1 \leq l \leq n} (-1)^l \sum_{1 \leq i_1 < \dots < i_l \leq n} \left[\frac{w - r^{i_1 \dots i_l}}{p_{i_1} \dots p_{i_l}} + 1 \right] \right\} - 2A_{w-1} \quad (2.3)$$

So equations (2.2) and (2.3) must be satisfied before and

after sieving. Thus we can solve these simultaneously to get:

$$\begin{aligned} 2Z_w(w) - 2Z_{pq}(w) &= 2[\pi(\sqrt{w}) - 1] + 2A_{w-1} \\ Z_w(w) &= [\pi(\sqrt{w}) - 1] + A_{w-1} + Z_{pq}(w) \end{aligned}$$

Now suppose that $Z_{pq}(w) = 0$, then we are left with the minimum value of $Z_w(w)$, which is:

$$Z'_w(w) = [\pi(\sqrt{w}) - 1] + A_{w-1} \quad (3)$$

V. SOME BRIEF EXAMPLES

1) Take $w = 10$.

$w - 1 = 10 - 1 = 9$ is not prime, so $A_{w-1} = 0$.

$$n = \pi(\sqrt{10}) = 2, \quad p_{i_1} = p_{j_1} = 2, \quad p_{i_2} = 3, \quad p_{j_m} = 3'$$

$$\begin{aligned} Z_{pq}(w) &= 10 + 1 - \left\{ \left[\frac{10-0}{2} + 1 \right] + \left[\frac{10-1}{3} + 1 \right] + \left[\frac{10-1}{3'} + 1 \right] \right\} + \left\{ \left[\frac{10-4}{3.2} + 1 \right] + \left[\frac{10-4}{2.3'} + 1 \right] \right\} - 0 \\ &= 11 - (6 + 4 + 4) + (2 + 2) = 11 - 14 + 4 = 1 \end{aligned}$$

and $2Z_a(w) = 2$ (since we have 7+3 and 3+7).

$$\therefore Z_w(w) = Z_{pq}(w) + 2Z_a(w) = 1 + 2 = 3 \quad (\text{the three pairs being } 3+7, 5+5 \text{ and } 7+3).$$

$w - 1 = 12 - 1 = 11$ is prime, so $A_{w-1} = 1$.

$$\begin{aligned} n &= 2 \quad p_{i_1} = 2, 3 \quad p_{j_m} = 2', 3' \quad r^{2,3} = r_{2',3'} = \langle 12 \rangle_{2',3'} = 0 \\ \text{and } Z_a(w) &= 0. \end{aligned}$$

$$Z'_w(w) = [\pi(\sqrt{w}) - 1] + A_{w-1} = 2 - 1 + 0 = 1$$

is also correct.

2) Take $w = 12$

$$\begin{aligned}
 Z_{pq}(w) &= 12 + 1 - \left\{ \left[\frac{12}{2} + 1 \right] + \left[\frac{12}{3} + 1 \right] \right\} + \left[\frac{12}{2.3} + 1 \right] - 2 \\
 &= 13 - (7 + 5) + 3 - 2 = 2 \\
 \therefore Z_w(w) &= Z_{pq}(w) + 2Z_a(w) = 2 + 0 = 2 \\
 &\quad (\text{the two pairs being } 5+7 \text{ and } 7+5)
 \end{aligned}$$

$$Z'_{w'}(w) = [\pi(\sqrt{w}) - 1] + A_{w-1} = 2 - 1 + 1 = 2 \quad \text{is also correct.}$$

Calculation :

$$Z'_w(w) = [\pi(\sqrt{w}) - 1] + A_{w+1} \quad (1.4)$$

REFERENCES

- [1] 2001-2004, the vice professor Song Fugao of Shen Zhen university calculated $w=6 \rightarrow 10^7$ comformed with (1.4)
- [2] 2002, professor Zhu Lie of Su Zhou university calculated $w < 20001$ comformed with (1.4)
- [3] 2006, professor Xu Zuoming of Liao Ning university calculated $w = 6 \rightarrow 10^{11}$ comformed with (1.4)

The Application of Vector Lyapunov Functions in Iterative Learning Control

Qunli Zhang*

College of Mathematics and Statistics, Heze University, Heze, Shandong 274015, China

*Corresponding author

Abstract—This paper presents iterative learning control of multiple state vector system, whose initial states are equal. By introducing the vector Lyapunov function, it involves interesting criteria to guarantee the robust convergence of the tracking error in the sense of the λ -norm. Finally, the validity of the proposed method is verified by an example.

Keywords—iterative learning control; convergence; vector lyapunov function; λ -norm

I INTRODUCTION

Since iterative learning control, which belongs to the intelligent control methodology, is proposed by Arimoto et al. in 1984(See[1]), this feed-forward control approach for fully utilizing the previous control information and improving the transient performance of studied systems that is suitable for repetitive movements has been a major research area and a hot issue in recent years. Its goal is to get full range of tracking tasks on finite interval (See [2-15]).

It is well known that the more complex the considered dynamical system is, the more difficult it is to find a Lyapunov function. This arouse us to employ several Lyapunov function, which is called to be a vector Lyapunov function, for each component provides information about a part of the dynamics. Hence, the corresponding theory, namely, the method of vector Lyapunov function, offers a very flexible process (see [16-22]).

There are few research results on iterative learning control for systems with time-varying coefficient as well as vector Lyapunov function. In this paper, using vector Lyapunov function and λ -norm, we obtain some sufficient conditions to guarantee the output states of the considered time-varying coefficient system to converge to the desired trajectories. It is shown that the proposed method can achieve the ILC convergence property significantly.

Before ending this section, it is worth pointing out the main contribution of this paper is the design of iterative controllers from vector Lyapunov function, which is different from the designed controllers by positive definite Lyapunov function, in past literature.

II PRELIMINARIES

Throughout this paper, the 2-norm for the n -dimensional vector $x = (x_1, x_2, \dots, x_n)^T$ is defined as $\|x\| = (\sum_{i=1}^n x_i)^{1/2}$, while the λ -norm for a function is defined as $\|\cdot\|_\lambda = \sup_{t \in [0, T]} \{e^{-\lambda t} \|\cdot\|\}$, where the superscript T represents the transpose and $\lambda > 0$. $|A| = (\|a_{ij}\|)_{n \times n}$, where $A = (a_{ij})_{n \times n} \in R^{n \times n}$ is a matrix.

Lemma 1[10,23]

$$\sup_{t \in [0, T]} \{e^{-\lambda t} \int_0^t \|x(\tau)\| d\tau\} \leq \frac{1}{\lambda} \|x(t)\|_\lambda.$$

Consider

III MAIN RESULTS

Consider the following multiple state vector system

$$\begin{aligned} \dot{x}_k &= F(t, x_k, y_k) + u_{x,k}(t), \\ z_{x,k}(t) &= Cx_k + Du_{x,k}(t), \\ u_{x,k+1}(t) &= u_{x,k}(t) + Me_{x,k}(t), \\ \dot{y}_k &= G(t, x_k, y_k) + u_{y,k}(t), \\ z_{y,k}(t) &= Cy_k + Du_{y,k}(t), \\ u_{y,k+1}(t) &= u_{y,k}(t) + Me_{y,k}(t), \end{aligned} \quad (1)$$

where $x_k, y_k \in R^n$ are the state vectors, $u_{x,k}, u_{y,k} \in R^n$ are input vectors of x_k, y_k , and $z_{x,k}, z_{y,k} \in R^n$ are output vectors of x_k, y_k , respectively. k is the number of iterations, $k \in \{1, 2, 3, \dots\}$ and $t \in [0, T]$, T is a constant.

Let

$e_{x,k}(t) = z_{x,d}(t) - z_{x,k}(t)$, $e_{y,k}(t) = z_{y,d}(t) - z_{y,k}(t)$, where $z_{x,d}(t)$, $z_{y,d}(t)$ are reference outputs of x_k , y_k , respectively. So we have

$$\begin{aligned} e_{x,k+1}(t) &= z_{x,d}(t) - z_{x,k+1}(t) = z_{x,d}(t) - z_{x,k}(t) + z_{x,k}(t) - z_{x,k+1}(t) \\ &= e_{x,k}(t) + z_{x,k}(t) - z_{x,k+1}(t), \end{aligned}$$

$$e_{y,k+1}(t) = e_{y,k}(t) + z_{y,k}(t) - z_{y,k+1}(t). \quad (2)$$

We define the operator $V : R^n \times R^n \rightarrow R^n$ such that

$$(1) \quad V(0, 0) = 0;$$

$$(2) \quad V(x+z, y+w) = V(x, y) + V(z, w) \quad \text{for any vectors } x, z, y, w \in R^n,$$

(3) there is a constant $\gamma > 0$ such that $V(Cx, Cy) = C^\gamma V(x, y)$ for any vectors $x, y \in R^n$ and matrix $C \in R^{n \times n}$;

(4) the derivative $\frac{\partial V}{\partial x}$ and $\frac{\partial V}{\partial y}$ of $V(x, y)$ exist, where $x, y \in R^n$.

For the sake of convenient, we denote that the set, whose elements are operators $V : R^n \times R^n \rightarrow R^n$ and satisfy the above four conditions, is \mathbb{N} .

For any operator $V \in \mathbb{N}$, the following conclusion can be gotten

$$\begin{aligned} V(e_{x,k+1}(t), e_{y,k+1}(t)) &= V(e_{x,k}(t) + z_{x,k}(t) - z_{x,k+1}(t), e_{y,k}(t) + z_{y,k}(t) - z_{y,k+1}(t)) \\ &= V(e_{x,k}(t), e_{y,k}(t)) + V(z_{x,k}(t) - z_{x,k+1}(t), z_{y,k}(t) - z_{y,k+1}(t)) \\ &= V(e_{x,k}(t), e_{y,k}(t)) + V(C(x_k(t) - x_{k+1}(t)) \\ &\quad + D(u_{x,k}(t) - u_{x,k+1}(t)), C(y_k(t) - y_{k+1}(t)) + D(u_{y,k}(t) - u_{y,k+1}(t))) \\ &= V(e_{x,k}(t), e_{y,k}(t)) + C^\gamma V(x_k(t) - x_{k+1}(t), y_k(t) - y_{k+1}(t)) \\ &\quad + D^\gamma V(u_{x,k}(t) - u_{x,k+1}(t), u_{y,k}(t) - u_{y,k+1}(t)) \\ &= V(e_{x,k}(t), e_{y,k}(t)) + C^\gamma V(x_k(t) - x_{k+1}(t), y_k(t) - y_{k+1}(t)) \\ &\quad - (DM)^\gamma V(e_{x,k}(t), e_{y,k}(t)) \\ &= (I - (DM)^\gamma)V(e_{x,k}(t), e_{y,k}(t)) + C^\gamma V(x_k(t) - x_{k+1}(t), y_k(t) - y_{k+1}(t)), \end{aligned} \quad (3)$$

where I is identical matrix. In fact:

$$\begin{aligned} z_{x,k}(t) - z_{x,k+1}(t) &= C(x_k(t) - x_{k+1}(t)) + D(u_{x,k}(t) - u_{x,k+1}(t)), \\ z_{y,k}(t) - z_{y,k+1}(t) &= C(y_k(t) - y_{k+1}(t)) + D(u_{y,k}(t) - u_{y,k+1}(t)), \end{aligned}$$

$$u_{x,k}(t) - u_{x,k+1}(t) = -Me_{x,k}(t), u_{y,k}(t) - u_{y,k+1}(t) = -Me_{y,k}(t).$$

Then from (3) we can obtain that

$$\|V(e_{x,k+1}(t), e_{y,k+1}(t))\| \leq \|I - (DM)^\gamma\| \cdot \|V(e_{x,k}(t), e_{y,k}(t))\| + \|C\| \cdot \|V(x_k(t) - x_{k+1}(t), y_k(t) - y_{k+1}(t))\|. \quad (4)$$

For $\|V(x_k(t) - x_{k+1}(t), y_k(t) - y_{k+1}(t))\|$ in (4), we have

$$\begin{aligned} \frac{d e^r V(x_k(t) - x_{k+1}(t), y_k(t) - y_{k+1}(t))}{dt} &= r e^r V(x_k(t) - x_{k+1}(t), y_k(t) - y_{k+1}(t)) \\ &\quad + e^r \left(\frac{\partial V}{\partial (x_k(t) - x_{k+1}(t))} \cdot \frac{d(x_k(t) - x_{k+1}(t))}{dt} \right) \\ &\quad + e^r \left(\frac{\partial V}{\partial (y_k(t) - y_{k+1}(t))} \cdot \frac{d(y_k(t) - y_{k+1}(t))}{dt} \right) \end{aligned}$$

$$\begin{aligned} &= r e^r V(x_k(t) - x_{k+1}(t), y_k(t) - y_{k+1}(t)) \\ &\quad + e^r \left(\frac{\partial V}{\partial (x_k(t) - x_{k+1}(t))} \cdot (F(t, x_k, y_k) - F(t, x_{k+1}, y_{k+1})) \right) \\ &\quad + e^r \left(\frac{\partial V}{\partial (y_k(t) - y_{k+1}(t))} \cdot (G(t, x_k, y_k) - G(t, x_{k+1}, y_{k+1})) \right) \end{aligned}$$

$$\begin{aligned} &\quad + e^r \left(\frac{\partial V}{\partial (x_k(t) - x_{k+1}(t))} \cdot (-Me_{x,k}) \right) \\ &\quad + e^r \left(\frac{\partial V}{\partial (y_k(t) - y_{k+1}(t))} \cdot (-Me_{y,k}) \right) \end{aligned}$$

$$\begin{aligned} &= r e^r V_k(t) + e^r (V_{x,k}(t) \cdot f_k(t) + V_{y,k}(t) \cdot g_k(t)) \\ &\quad - e^r (V_{x,k}(t) \cdot M e_{x,k} + V_{y,k}(t) \cdot M e_{y,k}). \end{aligned}$$

$$\begin{aligned} \text{where } V(x_k(t) - x_{k+1}(t), y_k(t) - y_{k+1}(t)) &= V_k(t), \\ \frac{\partial V_k}{\partial (x_k(t) - x_{k+1}(t))} &= V_{x,k}, \frac{\partial V_k}{\partial (y_k(t) - y_{k+1}(t))} = V_{y,k}, \\ F(t, x_k, y_k) - F(t, x_{k+1}, y_{k+1}) &= f_k(t), \\ G(t, x_k, y_k) - G(t, x_{k+1}, y_{k+1}) &= g_k(t). \end{aligned} \quad ,$$

we integrate $e^r V_k(t)$ with respect to t and obtain

$$\begin{aligned} e^r V_k(t) &= e^r V_k(s) + \int_s^t [r e^r \rho V_k(\rho) + e^r (V_{x,k}(\rho) \cdot f_k(\rho) + V_{y,k}(\rho) \cdot g_k(\rho))] d\rho \\ &\quad - \int_s^t e^r \rho (V_{x,k}(\rho) \cdot M e_{x,k} + V_{y,k}(\rho) \cdot M e_{y,k}) d\rho. \end{aligned}$$

$$\begin{aligned} e^r \|V_k(t)\| &= e^{rs} \|V_k(s)\| + \int_s^t e^{r\rho} \|rV_k(\rho) + (V_{x,k}(\rho) \cdot f_k(\rho) + V_{y,k}(\rho) \cdot g_k(\rho))\| d\rho \\ &\quad + \int_s^t e^{r\rho} \|V_{x,k}(\rho) \cdot Me_{x,k} + V_{y,k}(\rho) \cdot Me_{y,k}\| d\rho. \end{aligned}$$

$$\begin{aligned} re^r \|V_k(t)\| + e^r \|V_k(t)\|_r &= e^r \|rV_k(t) + (V_{x,k}(t) \cdot f_k(t) + V_{y,k}(t) \cdot g_k(t))\| \\ &\quad + e^r \|V_{x,k}(t) \cdot Me_{x,k} + V_{y,k}(t) \cdot Me_{y,k}\|. \end{aligned}$$

If there exists a constant ϖ such that

$$\|V_{x,k}(t) \cdot Me_{x,k} + V_{y,k}(t) \cdot Me_{y,k}\| \leq \varpi \|V(e_{x,k}(t), e_{y,k}(t))\|, \quad (5)$$

the following conclusion

$$\begin{aligned} \|V_k(t)\|_r &\leq \|rV_k(t) + (V_{x,k}(t) \cdot f_k(t) + V_{y,k}(t) \cdot g_k(t))\| - r \|V_k(t)\| \\ &\quad + \varpi \|V(e_{x,k}(t), e_{y,k}(t))\| \end{aligned} \quad (6)$$

is true.

It is easy to prove that $\|rV_k(t) + (V_{x,k}(t) \cdot f_k(t) + V_{y,k}(t) \cdot g_k(t))\| - r \|V_k(t)\|$ is monotonically

decreasing on r , thus the limit $\lim_{r \rightarrow +\infty} (\|rV_k(t) + (V_{x,k}(t) \cdot f_k(t) + V_{y,k}(t) \cdot g_k(t))\| - r \|V_k(t)\|)$ exists. From 2-norm of the n -dimensional vector, we obtain

$$\begin{aligned} \lim_{r \rightarrow +\infty} (\|rV_k(t) + (V_{x,k}(t) \cdot f_k(t) + V_{y,k}(t) \cdot g_k(t))\| - r \|V_k(t)\|) \\ = \frac{(V_{x,k}(t) \cdot f_k(t) + V_{y,k}(t) \cdot g_k(t))^T V_k(t)}{\|V_k(t)\|} = h_k(t). \end{aligned}$$

$$\|V_k(t)\|_r \leq h_k(t) + \varpi \|V(e_{x,k}(t), e_{y,k}(t))\|. \quad (7)$$

Based on the above calculation, the following theorem is obtained.

Theorem 1 If the system (1) and the operator $V \in \mathbb{N}$ satisfy the condition (5), then the conclusions (4) and (7) are true.

Corollary 1 when $x_k(t) \in R^n$, $y_k(t) \in R^m$, and $n > m$, let $y_k(t) \rightarrow \begin{pmatrix} y_k(t) \\ 0_{n-m} \end{pmatrix} = \tilde{y}_k(t)$,

$$G(t, x_k(t), y_k(t)) \rightarrow \begin{pmatrix} G(t, x_k(t), y_k(t)) \\ 0_{n-m} \end{pmatrix} = \tilde{G}(t, x_k(t), \tilde{y}_k(t)), \quad \text{then}$$

one obtains the similar result with above Theorem.

Remark When there are three parts x_k, y_k, z_k about the multiple state vector system (1), we can construct $V(e_{x,k}(t), e_{y,k}(t), e_{z,k}(t)) \in \mathbb{N}$ and imitate the above proof to get the similar conclusion with Theorem 1.

Corollary 2 For system (1), taking $V(e_{x,k}(t), e_{y,k}(t)) = \alpha e_{x,k}(t) + \beta e_{y,k}(t)$,

$$V(x_k(t) - x_{k+1}(t), y_k(t) - y_{k+1}(t))$$

$= \alpha(x_k(t) - x_{k+1}(t)) + \beta(y_k(t) - y_{k+1}(t))$, the following results are drawn:

$$\|\alpha e_{x,k+1}(t) + \beta e_{y,k+1}(t)\| \leq \|I - DM\| \|\alpha e_{x,k}(t) + \beta e_{y,k}(t)\| + \|C\| \|\alpha(x_k - x_{k+1}) + \beta(y_k - y_{k+1})\|. \quad (8)$$

$$\|p_k(t)\|_r \leq \frac{p_k^T(t) q_k(t)}{\|p_k(t)\|} + \|M\| \|\alpha e_{x,k}(t) + \beta e_{y,k}(t)\|, \quad (9)$$

where

$$\begin{aligned} p_k(t) &= \alpha(x_k - x_{k+1}) + \beta(y_k - y_{k+1}), \\ q_k(t) &= \alpha[F(t, x_k, y_k) - F(t, x_{k+1}, y_{k+1})] \\ &\quad + \beta[G(t, x_k, y_k) - G(t, x_{k+1}, y_{k+1})]. \end{aligned}$$

In fact,

$$\begin{aligned} \alpha e_{x,k+1}(t) + \beta e_{y,k+1}(t) &= \alpha e_{x,k}(t) + \beta e_{y,k}(t) + \alpha(z_{x,k} - z_{x,k+1}) \\ &\quad + \beta(z_{y,k} - z_{y,k+1}) \\ &= (\alpha e_{x,k}(t) + \beta e_{y,k}(t)) + \alpha[C(x_k - x_{k+1}) + D(u_{x,k} - u_{x,k+1})] \\ &\quad + \beta[C(y_k - y_{k+1}) + D(u_{y,k} - u_{y,k+1})] \\ &= (I - DM)(\alpha e_{x,k}(t) + \beta e_{y,k}(t)) \\ &\quad + C[\alpha(x_k - x_{k+1}) + \beta(y_k - y_{k+1})]. \end{aligned}$$

Imitating the inference of (7), we have

$$\frac{de^r p_k(t)}{dt} = re^r p_k(t) + e^r q_k(t) - e^r M [\alpha e_{x,k}(t) + \beta e_{y,k}(t)],$$

$$e^r p_k(t) = e^{rs} p_k(s) + \int_s^t e^{ru} [rp_k(u) + q_k(u) - M(\alpha e_{x,k}(u) + \beta e_{y,k}(u))] du,$$

$$e^r \|p_k(t)\| \leq e^{rs} \|p_k(s)\| + \int_s^t e^{ru} \|rp_k(u) + q_k(u)\| du + \int_s^t \|M\| \|\alpha e_{x,k}(u) + \beta e_{y,k}(u)\| du,$$

$$e^r \|p_k(t)\|_r \leq e^r [\|rp_k(t) + q_k(t)\| + \|M\| \|\alpha e_{x,k}(t) + \beta e_{y,k}(t)\|] - re^r \|p_k(t)\|.$$

Going on to the next item, we will infer the important

conclusion of this paper.

Conditions (A), (B) are satisfied if the following conditions hold:

- (A) The operator $V_{k,i}(t) \in \aleph, i=1,2$. There exist functions $p_{ji}(t), i, j=1,2$, and such that

$$\frac{(V_{x,k,i}(t) \cdot f_k(t) + V_{y,k,i}(t) \cdot g_k(t))^T V_{k,i}(t)}{\|V_{k,i}(t)\| \cdot \|V_{k,j}(t)\|} \leq p_{ji}(t).$$

$$\|V_{x,k,i}(t) \cdot M e_{x,k} + V_{y,k,i}(t) \cdot M e_{y,k}\| \leq \varpi_{i1} \|V_1(e_{x,k}(t), e_{y,k}(t))\| + \varpi_{i2} \|V_2(e_{x,k}(t), e_{y,k}(t))\|,$$

where ϖ_{ij} are constants.

Theorem 2 Suppose the operator F, G in system (1) satisfy $F(t, 0, 0) = G(t, 0, 0) = 0$. There are operators $V_{k,i}(t) \in \aleph, V_i(e_{x,k}(t), e_{y,k}(t)), i=1,2$, such that conditions (A),(B), and

$$V_i(e_{x,k}(t), e_{y,k}(t)) = 0 \text{ if and only if } e_{x,k}(t) = e_{y,k}(t) = 0. \quad (10)$$

If there exists a constant $\lambda > 0$ such that initial state vector $x_k(0) - x_{k+1}(0) = 0, y_k(0) - y_{k+1}(0) = 0$, and

$$\lim_{k \rightarrow +\infty} Q^k(t) = \begin{pmatrix} 0 & 0 \\ 0 & 0 \end{pmatrix}, \quad (11)$$

where

$Q(t) = \begin{pmatrix} \|I - (DM)^T\| & 0 \\ 0 & \|I - (DM)^T\| \end{pmatrix} + \begin{pmatrix} \|C'\| & 0 \\ 0 & \|C'\| \end{pmatrix} \cdot |\Phi(t)| \cdot \frac{B(t)}{\lambda}$, $\Phi(t)$ is a basic solution matrix of the system

$$\begin{pmatrix} \|V_{k,1}(t)\| \\ \|V_{k,2}(t)\| \end{pmatrix}' \leq \begin{pmatrix} p_{11}(t) & p_{12}(t) \\ p_{21}(t) & p_{22}(t) \end{pmatrix} \begin{pmatrix} \|V_{k,1}(t)\| \\ \|V_{k,2}(t)\| \end{pmatrix}, \quad B(t) = |\Phi(t)| \begin{pmatrix} \varpi_{11} & \varpi_{12} \\ \varpi_{21} & \varpi_{22} \end{pmatrix},$$

then the system (1) can guarantee that $z_{x,k}(t), z_{y,k}(t)$ can track $z_{x,d}(t), z_{y,d}(t)$, respectively.

Proof From conditions (A), (B) and the above inference, we can obtain

$$\begin{pmatrix} \|V_{k,1}(t)\| \\ \|V_{k,2}(t)\| \end{pmatrix}' \leq \begin{pmatrix} p_{11}(t) & p_{12}(t) \\ p_{21}(t) & p_{22}(t) \end{pmatrix} \begin{pmatrix} \|V_{k,1}(t)\| \\ \|V_{k,2}(t)\| \end{pmatrix} + \begin{pmatrix} \varpi_{11} & \varpi_{12} \\ \varpi_{21} & \varpi_{22} \end{pmatrix} \begin{pmatrix} \|V_1(e_{x,k}(t), e_{y,k}(t))\| \\ \|V_2(e_{x,k}(t), e_{y,k}(t))\| \end{pmatrix}. \quad (12)$$

From (1)-(7) and (12), the following conclusion

$$\begin{pmatrix} \|V_{k,1}(t)\| \\ \|V_{k,2}(t)\| \end{pmatrix} \leq \Phi(t) \cdot \int_0^t \Phi^{-1}(\rho) \begin{pmatrix} \varpi_{11} & \varpi_{12} \\ \varpi_{21} & \varpi_{22} \end{pmatrix} \begin{pmatrix} \|V_1(e_{x,k}(\rho), e_{y,k}(\rho))\| \\ \|V_2(e_{x,k}(\rho), e_{y,k}(\rho))\| \end{pmatrix} d\rho$$

$$\text{is true because } x_k(0) - x_{k+1}(0) = 0, \\ y_k(0) - y_{k+1}(0) = 0.$$

$$\begin{pmatrix} \|V_1(e_{x,k+1}(t), e_{y,k+1}(t))\| \\ \|V_2(e_{x,k+1}(t), e_{y,k+1}(t))\| \end{pmatrix} \leq \begin{pmatrix} \|I - (DM)^T\| & 0 \\ 0 & \|I - (DM)^T\| \end{pmatrix} \begin{pmatrix} \|V_1(e_{x,k}(t), e_{y,k}(t))\| \\ \|V_2(e_{x,k}(t), e_{y,k}(t))\| \end{pmatrix} \\ + \begin{pmatrix} \|C'\| & 0 \\ 0 & \|C'\| \end{pmatrix} \cdot \Phi(t) \cdot \int_0^t \Phi^{-1}(\rho) \begin{pmatrix} \varpi_{11} & \varpi_{12} \\ \varpi_{21} & \varpi_{22} \end{pmatrix} \begin{pmatrix} \|V_1(e_{x,k}(\rho), e_{y,k}(\rho))\| \\ \|V_2(e_{x,k}(\rho), e_{y,k}(\rho))\| \end{pmatrix} d\rho.$$

Taking λ -norm, we have

$$\begin{pmatrix} \|V_1(e_{x,k+1}(t), e_{y,k+1}(t))\|_\lambda \\ \|V_2(e_{x,k+1}(t), e_{y,k+1}(t))\|_\lambda \end{pmatrix} \leq \begin{pmatrix} \|E - (DM)^T\| & 0 \\ 0 & \|E - (DM)^T\| \end{pmatrix} \begin{pmatrix} \|V_1(e_{x,k}(t), e_{y,k}(t))\|_\lambda \\ \|V_2(e_{x,k}(t), e_{y,k}(t))\|_\lambda \end{pmatrix} \\ + \begin{pmatrix} \|C'\| & 0 \\ 0 & \|C'\| \end{pmatrix} \cdot |\Phi(t)| \cdot \frac{B(t)}{\lambda} \begin{pmatrix} \|V_1(e_{x,k}(t), e_{y,k}(t))\|_\lambda \\ \|V_2(e_{x,k}(t), e_{y,k}(t))\|_\lambda \end{pmatrix} \\ = Q(t) \cdot \begin{pmatrix} \|V_1(e_{x,k}(t), e_{y,k}(t))\|_\lambda \\ \|V_2(e_{x,k}(t), e_{y,k}(t))\|_\lambda \end{pmatrix}.$$

when the condition (11) holds, we have

$$\lim_{k \rightarrow +\infty} \begin{pmatrix} \|V_1(e_{x,k}(t), e_{y,k}(t))\|_\lambda \\ \|V_2(e_{x,k}(t), e_{y,k}(t))\|_\lambda \end{pmatrix} = \begin{pmatrix} 0 \\ 0 \end{pmatrix}. \quad \text{That implies}$$

$$\lim_{k \rightarrow +\infty} \|V_j(e_{x,k}(t), e_{y,k}(t))\|_\lambda = 0, j=1,2, \lim_{k \rightarrow +\infty} \|V_j(e_{x,k}(t), e_{y,k}(t))\| = 0, \quad \text{i.e.}$$

$\lim_{k \rightarrow +\infty} e_{x,k}(t) = 0, \lim_{k \rightarrow +\infty} e_{y,k}(t) = 0$ from the condition (10).

Corollary 3 Suppose the operator F, G in system (1) satisfy $F(t, 0, 0) = G(t, 0, 0) = 0$. There are operators $V_i(e_{x,k}(t), e_{y,k}(t)) = \alpha_i e_{x,k}(t) + \beta_i e_{y,k}(t), i=1,2$, such that conditions (A), and

$$\alpha_i e_{x,k}(t) + \beta_i e_{y,k}(t) = 0, \quad i=1,2, \quad \text{if and only if} \\ e_{x,k}(t) = e_{y,k}(t) = 0.$$

If there exists a constant $\lambda > 0$ such that initial state vector $x_k(t) - x_{k+1}(t) = 0, y_k(t) - y_{k+1}(t) = 0$, and

$$\lim_{k \rightarrow +\infty} Q^k(t) = \begin{pmatrix} 0 & 0 \\ 0 & 0 \end{pmatrix}, \quad (13)$$

where

$$Q(t) = \begin{pmatrix} \|I - (DM)^T\| & 0 \\ 0 & \|I - (DM)^T\| \end{pmatrix} + \begin{pmatrix} \|C'\| & 0 \\ 0 & \|C'\| \end{pmatrix} \cdot |\Phi(t)| \cdot \frac{B(t)}{\lambda},$$

$\Phi(t)$ is a basic solution matrix of the system

$$\begin{pmatrix} \|V_{k,1}(t)\| \\ \|V_{k,2}(t)\| \end{pmatrix}' \leq \begin{pmatrix} p_{11}(t) & p_{12}(t) \\ p_{21}(t) & p_{22}(t) \end{pmatrix} \begin{pmatrix} \|V_{k,1}(t)\| \\ \|V_{k,2}(t)\| \end{pmatrix},$$

$B(t) = |\Phi^{-1}(t)|$, then the system (1) can guarantee that $z_{x,k}(t), z_{y,k}(t)$ can track $z_{x,d}(t), z_{y,d}(t)$, respectively.

IV EXAMPLE

Considering the system

$$\begin{aligned} \dot{x}_k &= 0.2e^{-t}x_k + 0.3y_k \sin t + u_{x,k}, \\ z_{x,k} &= 0.03x_k + 0.3u_{x,k}, \\ u_{x,k+1} &= u_{x,k} + 3e_{x,k}, \\ \dot{y}_k &= 0.3x_k \sin t + 0.2e^{-t}y_k + u_{y,k}, \\ z_{y,k} &= 0.03y_k + 0.3u_{y,k}, \\ u_{y,k+1} &= u_{y,k} + 3e_{y,k}. \end{aligned}$$

We take $T=3$, that is $t \in [0, 3]$, and $z_{x,d}(t) = \sin t, z_{y,d}(t) = \cos t$. It is easy to verify this example satisfies the conditions of Theorem 2 when $V_1(e_{x,k}(t), e_{y,k}(t)) = (e_{x,k}(t) + e_{y,k}(t))^2$,

$V_2(e_{x,k}(t), e_{y,k}(t)) = (e_{x,k}(t) - e_{y,k}(t))^2$, and satisfies the conditions of Corollary 3 when $V_1(e_{x,k}(t), e_{y,k}(t))$

$= \alpha e_{x,k}(t) + \beta e_{y,k}(t), V_2(e_{x,k}(t), e_{y,k}(t)) = \beta e_{x,k}(t) + \alpha e_{y,k}(t)$. In following Figure I and Figure II, the output errors $e_{x,k}(t), e_{y,k}(t)$ are exhibited at iteration $k=4, k=5$, respectively.

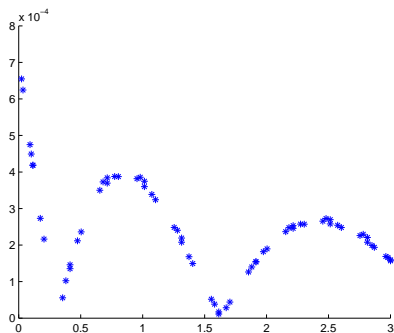


FIGURE I. ERROR $e_{x,k}(t)$ AFTER ITERATION 4

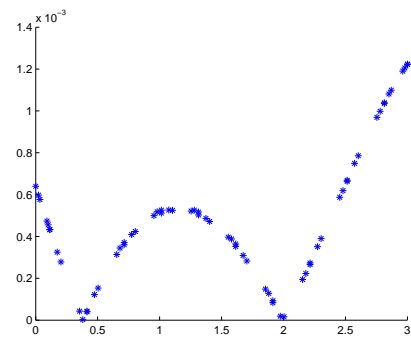


FIGURE II. ERROR $e_{y,k}(t)$ AFTER ITERATION 4

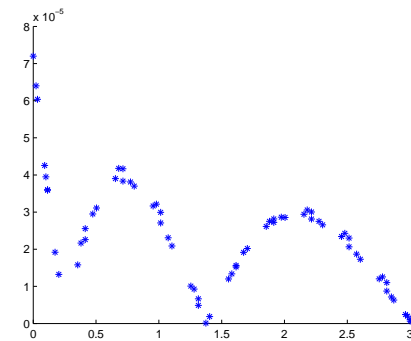


FIGURE III. ERROR $e_{x,k}(t)$ AFTER ITERATION 5

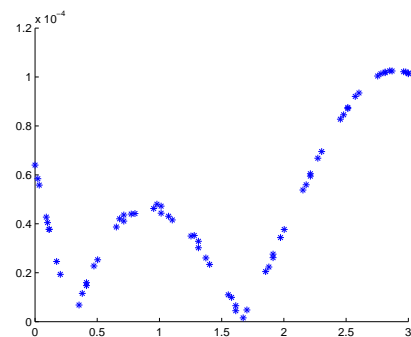


FIGURE IV. ERROR $e_{y,k}(t)$ AFTER ITERATION 5

V CONCLUSION

In this paper, considering the iterative learning control problem for a class of systems, and combining with vector Lyapunov function, the novel controllers, which can guarantee the robust convergence of the tracking error, are designed. From Figs.1 and 2 of the given example, we find that the output errors $e_{x,k}(t), e_{y,k}(t)$ downsize almost 10 times from iteration 4 to iteration 5. So it is made known that the proposed method is effective.

ACKNOWLEDGMENTS

This work is supported by the National Natural Science Foundation of China (11371221), the Natural Science Foundation of Shandong Province of China (ZR2014AM032), and the Project of Shandong Province Higher Educational Science and Technology Program (J16LI15).

REFERENCE

- [1] S. Arimoto, S. Kawamura, and F. Miyazaki. Bettering operation of robots by learning, *Journal of Robotic Systems*, 1(2), pp.123-140, 1984.
- [2] H.-S. Lee and Z. Bien, A note on convergence property of iterative learning controller with respect to sup norm, *Automatica*, vol.33, no.8, pp.1591–1593, 1997.
- [3] Y. Chen, Z. Gong, and C. Wen. Analysis of a high-order iterative learning control algorithm for uncertain nonlinear systems with state delays, *Automatica*, vol.34, no.3, pp.345–353, 1998.
- [4] J.-X. Xu and Y. Tan. A composite energy function-based learning control approach for nonlinear systems with time-varying parametric uncertainties, *IEEE Transactions on Auto-matic Control*, vol. 47, no. 11, pp. 1940–1945, 2002.
- [5] Tayebi. Adaptive iterative learning control for robot manip-ulators, *Automatica*, vol.40, no.7, pp.1195–1203, 2004.
- [6] R. H. Chi, Z. S. Hou, and J. X. Xu. AdaptiveILCforaclass of discrete-time systems with iteration-varying trajectory and random initial condition, *Automatica*, vol.44, no.8, pp.2207–2213, 2008.
- [7] C.-J. Chien. A combined adaptive law for fuzzy iterative learning control of nonlinear systems with varying control tasks, *IEEE Transactions on Fuzzy Systems*, vol.16, no.1, pp.40–51, 2008.
- [8] Y.-C. Wang and C.-J. Chien. Decentralized adaptive fuzzy neural iterative learning control for nonaiae nonlinear inter-connected systems, *Asian Journal of Control*, vol.13, no.1, pp.94–106, 2011.
- [9] J.-X. Xu, D. Huang, V. Venkataraman, and T. C. T. Huynh. Extreme precise motion tracking of piezoelectric positioning stage using sampled-data iterative learning control, *IEEE Transactions on Control Systems Technology*, vol.21, no.4, pp.1432–1439, 2013.
- [10] Q. Lv, Y.-C. Fang, and X. Ren. Iterative learning control for accelerated inhibition effect of initial state random error, *Acta Automatica Sinica*, vol.40, no.7, pp.1295–1302, 2014.
- [11] J.-M. Wei, Y.-A. Hu, and M.-M. Sun. Observer-based adaptive iterative learning control for a class of nonlinear time delay systems with input saturation, *Mathematical Problems in Engineering*, vol. 2015, Article ID 645161, 19 pages, 2015.
- [12] J. Li and J. Li, Iterative learning control approach for a kind of heterogeneous multi-agent systems with distributed initial state learning, *Applied Mathematics and Computation*, vol.265, pp.1044–1057, 2015.
- [13] L. Yan and J. Wei. Fractional order nonlinear systems with delay in iterative learning control, *Applied Mathematics and Computation*, vol.257, pp.546–552, 2015.
- [14] H. Cai, Y. Huang, J. Du, T. Tang, D. Zuo, and J. Li. Iterative learning control with extended state observer for telescope sys-tem, *Mathematical Problems in Engineering*, vol.2015, Article ID 701510, 8 pages, 2015.
- [15] Zhang Qunli. The effect of initial state error for nonlinear systems with delay via iterative learning control, *Advances in Mathematical Physics*, Volume 2016, Article ID 461950, 6pages, 2016.
- [16] D. D. Bainov and P. S. Simeonov. Stability with respect to part of the variables in systems with impulse effect, *Journal of Mathematical Analysis and Applications*, 124(2), 547-560, 1987.
- [17] G.K. Kulev and D. D. Bainov. Second method of Lyapunov and comparison principle for systems with impulse effect, *Journal of Computation and Applied Mathematics*, 23(3), 305-321, 1988.
- [18] D. D. Bainov and P. S. Simeonov. Systems with Impulsive Effect: Stability Theory and Applied, Ellis Horwood, Chichester, UK, 1989.
- [19] D. D. Bainov and P. S. Simeonov. Theory of Impulsive Differential Equations: Periodic Solution and Applications, Longman, Harlow, UK, 1993.
- [20] I. M. Stamova. Vector Lyapunov functions for practical stability of nonlinear impulsive functional differential equations, *Journal of Mathematical Analysis and Applications*, 325(1), 612-623, 2007.
- [21] S. Xinyu, G. Hongjian, and S. Xiangyun. Theory and Application of Impulsive Differential Equations, Science Press, Beijing, China, 2011.
- [22] Q. Zhang, A class of vector Lyapunov functions for stability analysis of nonlinear impulsive differential systems, *Mathematical Problems in Engineering*, vol. 2014, Article ID 649012, 2014, 9 pages.
- [23] M. X. Sun and B. J. Huang. Iterative learning control, National Defence Industry Press, Beijing, China, 1999.

Dynamic Data Modeling of SCR Denitration System Based on Mutual Information

Wenjie Zhao* and Luyao Zhang

Department of Automation, North China Electric Power University, Baoding, Hebei Province, China

*Corresponding author

Abstract—The establishment of accurate models is vital in parametric optimization of control systems, and the choice of input variables can directly affect the accuracy and complexity of the model. Therefore, this paper proposed a modeling method based on mutual information (MI) and least squares support vector machine (LSSVM). On the basis of MI, the problem of delay, the correlation and redundancy among variables were considered synthetically. The optimal ones were screened through field measured variables by MI, and chosen as the input of LSSVM for predictions of output NOx concentration. The results proved the method can decrease complexity, improve approximation and generalization capability.

Keywords—coal-fired unit; SCR de-NOx system; mutual information; least squares support vector machine

I. INTRODUCTION

SCR denitrification (de-NOx) technology has been essential due to growth of demand for environmental protection. A model of SCR de-NOx system with good precision can be very important to optimize the control strategy of de-NOx system and improve the field control effect.

Numerous studies have developed models to predict the output NOx concentration. They are divided into two main groups: mechanism modeling and experimental modeling. Mechanism modeling methods expounded well, since they adopted partial differential equations to describe the SCR denitrification process of mass and energy, and the mechanism of Eley-Rideal was generally considered suitable for the process of SCR de-NOx [1]. However, these methods were accused to be not suitable for every model, furthermore, analysis and formula deductions were considered to be quite intricate. Among experimental modeling methods, Artificial Neural Networks (ANN) and Support Vector Machine (SVM) have come into wide use in this area. They had strong nonlinear modeling capabilities, and were applicable to the case of complex systems and processes. Reference [2] combined ANN and genetic algorithm (GA) to model the characteristics of NOx emission and carbon combustion. References [3,4] used support vector machine (SVM) and least square support vector machine (LSSVM) respectively to establish the boiler combustion models and predict emissions of NOx. The major problems encountered above were adjusting parameters and selecting comprehensive data, since these parameters can affect modeling accuracy, and if input variables were unable to excite the entire internal state of the system, a high-precision model can not be obtained.

In addition, these models ignored time delay and the importance of interdependency between variables, and were only applied to steady-state models, which had some limitations and were difficult to use in the design of control strategies.

In view of the shortcomings above, a dynamic modeling method of LSSVM based on MI was proposed. MI had good performances in correlation analysis and feature selection [5,6]. LSSVM had strong generalization and approximation abilities, including reducing the risk of overfitting in modeling and generating models for the small number of records as well [4,7].

In the model, MI was used through field measured variables to detect interactions, select appropriate delay and eliminate redundancy. The optimal ones were chosen as the input of LSSVM for predictions of output NOx concentration. The results showed that the method proposed in this paper was of high prediction accuracy.

II. SCR DENITRIFICATION SYSTEM

The system adopted the fly-ash-rich arrangement (the SCR de-NOx reactor in the middle of economizer and air preheater). The flue gas from the economizer was reacted with diluted ammonia in the SCR denitrification reactor, and redoxed to H₂O and N₂ in the presence of catalysts. And the schematic illustration is shown in Figure 1. As most of the NOx in the boiler flue gas exists in the form of NO, the main reactions are as follows:

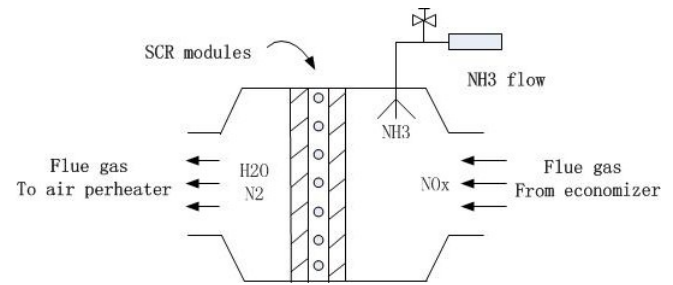
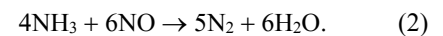
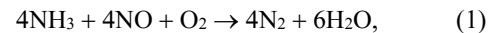


FIGURE I. SCHEMATIC ILLUSTRATION



III. VARIABLE SELECTION

A. Mutual Information

Mutual information is used to evaluate the amount of information that a event contributes to another, and is widely used in feature selection. MI is a nonnegative number ($I(x, y) \geq 0$), and a value of zero denotes irrelevance.

The MI between x and y is defined by the following formula:

$$I(x, y) = \int_y \int_x p(x, y) \log \frac{p(x, y)}{p(x)p(y)}. \quad (3)$$

If x and y are random variables, $p(x)$ and $p(y)$ are probability density functions, and $p(x, y)$ represents the joint probability of a given stimulus.

Conditional mutual information (CMI) adds the selection of redundant variables on the basis of variable correlation. On the premise of S , the importance of x is determined by interdependency between x and y . In other words, a higher value of CMI shows more new information x can provide conditioned on S .

The CMI between x and y conditioned on S is defined by the following equation:

$$I(x, y | S) = \int_S \int_y \int_x p(x, y | S) \log \frac{p(x, y | S)}{p(x | S)p(y | S)} dx dy dS. \quad (4)$$

If x , y and S are random variables, $p(x, y | S)$ is probability density function, $p(x | S)$, $p(y | S)$ are conditional probability distribution function.

B. Selection of Variables for SCR Denitrification System

This paper took the SCR de-NOx system of coal-fired units as research object. The SCR reaction mechanism of coal-fired units was complex, and the influential factors of denitrification efficiency could be quite a lot. This paper selected generator power (x_1), total air volume (x_2), total coal volume (x_3), input NOx concentration (x_4), NH₃ flow (x_5), NH₃ valve position (x_6), oxygen concentration in flue gas (x_7) and flue gas temperature (x_8) as original input variables, and output NOx concentration as the output variable (y).

According to the process analysis of SCR de-NOx system, gas flow and chemical reaction could give rise to the time lag, in addition, the correlation and redundancy should be fully considered. Therefore, this paper proposed the following method:

1) Selection of optimal time delay:

a) Suppose 16 types of time delay for each of the 8 input variables (As a matter of experience, initial time delay is in the range of 0 to 150 s. Sampling time is 10 s, so $\tau \in [0, 15]$).

b) Calculate the MI between 120 (8×15) types of input sequences and the output variable, as is shown in (3). When

every input variable and the output variable have the maximum MI, the delay is the optimal delay of corresponding input variable.

2) Selection of input variables:

a) Set threshold value $\delta = 0.15$ ($\delta I(y, y) = 0.7$), and use the following equation

$$I(x_i(t - \tau), y) > \delta I(y, y), \quad (5)$$

to eliminate weakly correlated variables: oxygen concentration in flue gas. The result is as shown in the Figure 2.

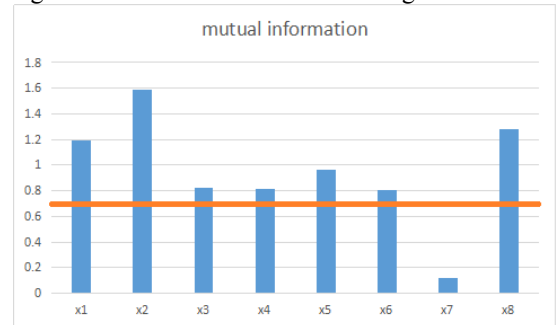


FIGURE II. PRELIMINARY SELECTION BASED ON MI

b) Initialize S as a null set. Select the input sequence of the maximum MI and put it in S .

c) On the premise of S , calculate the CMI (shown in (4)) between every input variable and the output variable, and the input variable with the largest CMI is selected and put into S .

d) Repeat the step c) until the observed value is zero, or the number of input variables meets the qualification. And the final selected input variables are the optimal ones. The experimental conditions and their results were summarized in Table 1.

TABLE I. THE OPTIMAL INPUT VARIABLES

No	Selected input variables	
	Name	Time delay (10s)
1	total air volume	-9
2	input NOx concentration	-2
3	NH ₃ flow	-8
4	flue gas temperature	-7

The MI between the optimal input variables and the output in different delay time are shown in Figure 3.

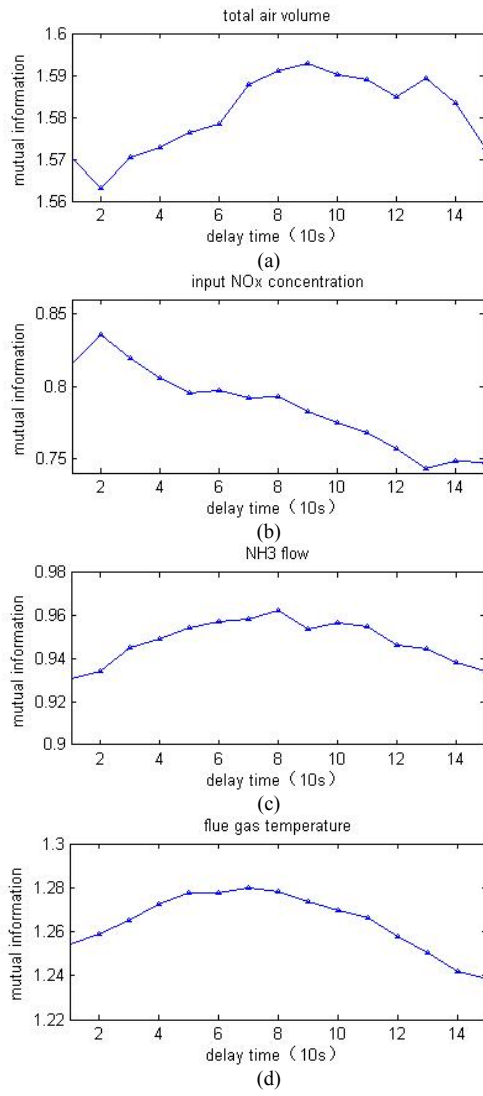


FIGURE III. TIME DELAY ESTIMATION BASED ON MI

The total air volume, input NOx concentration and NH₃ flow are selected, and they directly participate in chemical reactions, Temperature determines the speed of chemical reactions, therefore the results fit chemical principle well. Generator power and total coal volume are eliminated because of the small value of the CMI, and they are highly redundant with total air volume in reality. Likewise, NH₃ valve position is eliminated, as it is used to control NH₃ flow. The method screens out variables of low interdependency and high redundancy well, and simplify subsequent modeling.

IV. DYNAMIC DATA MODELING

A. Least Squares Support Vector Machine

As an intelligent soft computing method, LSSVM develops a comprehensive model with minimum structural risk to predict targets by using nonlinear kernel regression, and the regression function of LSSVM can be defined as follows:

$$\begin{cases} \min \frac{1}{2} \omega^T \omega + \frac{1}{2} \gamma \sum_{i=1}^n (\xi_i^2), \\ s.t. \quad y = \omega^T \varphi(x_i) + b + \xi_i, \quad i = 1, 2, \dots, n \end{cases} \quad (6)$$

where ω is weight vector, $\varphi(\cdot)$ is map function, γ is penalty function, ξ is slack variable.

The model of LSSVM is obtained by lagrange multiplier and KKT condition, and defined as follows :

$$y(x) = \sum_{i=1}^n \alpha_i K(x, x_i) + b, \quad (7)$$

where α_i is the lagrange multiplier, $K(x, x_i)$ is kernel function. This paper uses Radial basis Function (RBF) as kernel function:

$$K(x, x_i) = \exp(-\|x - x_i\|^2 / \sigma^2), \quad (8)$$

B. Prediction of Output NOx Concentration

Based on the result of MI and LSSVM modeling, this paper selected total air volume, input NOx concentration, NH₃ flow, flue gas temperature and the first order feedback from output NOx concentration as the input variables to predict. The structure of the model is shown in Figure 4.

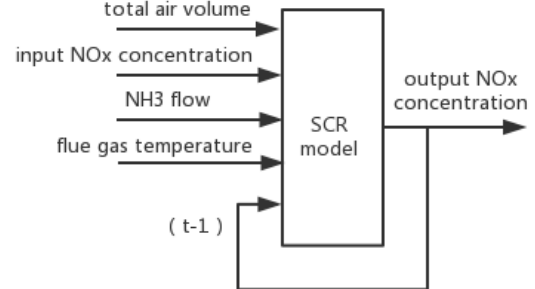


FIGURE IV. THE STRUCTURE OF THE MODEL

This paper selected 8000 groups of the historical data in dynamic as samples, among which 6000 groups were used as the training samples while the rest were test ones. As for parameter optimization, particle swarm optimization (PSO) were used to search optimal parameters γ and σ^2 for LSSVM. RMSE and MAE were used to evaluate the accuracy of the model. The formulas are as follows:

$$RMSE = \sqrt{\sum_{i=1}^n (y_i - \hat{y}_i)^2 / n}, \quad (9)$$

$$MAE = \frac{1}{n} \sum_{i=1}^n |y_i - \hat{y}_i|. \quad (10)$$

Training, test curves and their errors are shown in Figure 5. As for RMSE and MAE, the training set: RMSE=0.3685, MAE=0.1758; test set: RMSE=1.0472, MAE=0.7908. These outcomes suggest that the model can be compatibly used for the modeling of SCR de-NOx system, which exists complex relationships between variables.

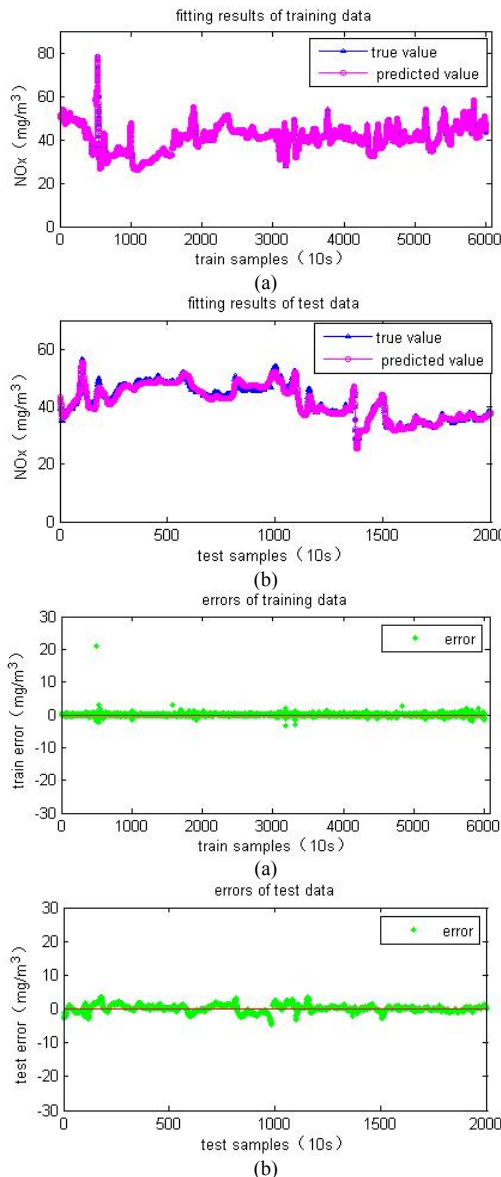


FIGURE V. FITTED CURVE AND ERRORS

V. CONCLUSION

In view of the complex mechanism of SCR de-NOx system and the strong coupling between variables, this paper presents a dynamic data modeling method based on least squares support vector machine (LSSVM) and mutual information (MI) based

on the SCR de-NOx data of a power plant. This method evaluated the importance of every input variable and chose the ones of high correlation and low redundancy as the inputs of LSSVM to calculate output NOx concentration. The results revealed that combination of LSSVM and MI can be successfully used in estimating the dynamic characteristics of output NOx concentration.

ACKNOWLEDGMENT

This project was funded by the National Key R&D of China (Grant No: 2016YFB0600701) and the Hebei Province Natural Science Foundation of China (No. F2014502059). The authors would like to thank Engineer Geng B. of JingLong power plant for his assistance to collect the operation data.

REFERENCES

- [1] N. Y. Topsøe, "Mechanism of the Selective Catalytic Reduction of Nitric Oxide by Ammonia Elucidated by in Situ On-Line Fourier Transform Infrared Spectroscopy," *Science*, vol. 265, pp. 1217-1219, August 1994.
- [2] H. Zhou, K. Cen, and J. Fan, "Modeling and optimization of the NOx emission characteristics of a tangentially fired boiler with artificial neural networks," *Energy*, vol. 29, pp. 167-183, January 2004.
- [3] F. Si, et al. "Optimization of coal-fired boiler SCRs based on modified support vector machine models and genetic algorithms." *Fuel*, vol. 88, pp. 806-816, May 2009.
- [4] T. Yang, C. Cui, Y. Lv, and J. Li, "Modeling on SCR process of a coal-fired boiler using LSSVM method," *IEEE Control and Decision Conference*, 2015, pp. 4025-4028.
- [5] S. Chehreh Chelgan, B. Shahbazi, and E. Hadavandi, "Support vector regression modeling of coal flotation based on variable importance measurements by mutual information method," *Measurement*, vol. 114, pp. 102-108, January 2018.
- [6] M. Han, W. Ren, and X. Liu, "Joint mutual information-based input variable selection for multivariate time series modeling," *Engineering Applications of Artificial Intelligence*, vol. 37, pp. 250-257, January 2015.
- [7] F. Kaytez, M. C. Taplamacioglu, E. Cam, and F. Hardalac, "Forecasting electricity consumption: A comparison of regression analysis, neural networks and least squares support vector machines," *International Journal of Electrical Power & Energy Systems*, vol. 67, pp. 431-438, May 2015.
- [8] G. Brown, A. Pocock, M. Zhao, and M. Luján, "Conditional Likelihood Maximisation: A Unifying Framework for Information Theoretic Feature Selection," *Journal of Machine Learning Research*, vol. 13, pp. 27-66, January 2012.

Research on Hierarchical Interactive Teaching Model Based on Naive Bayesian Classification

Dongyan Fan

Information faculty, Business College of Shanxi University, Taiyuan 030031, China

Abstract—The purpose of this research is improving the current inject classroom teaching mode that ignores individual differences and inefficiency of students. By studying classification algorithm in data mining and applying the classification method based on Naive Bayes algorithm, we designed and implemented scientific classification of students, and draw lessons from stratified and interactive teaching mode, so as to build a new effective teaching mode. The results show that through scientific classification of students, real-time hierarchical interaction teaching effectively stimulate students' interest in learning, improve cooperation ability, and improve classroom teaching efficiency.

Keywords—*Naive Bayesian; student classification; hierarchical interactive; teaching model*

I. INTRODUCTION

Under the background of big data era, the current teaching mode is not adapt to the cultivation of innovative talents, there are many problems, such as low efficiency of classroom, teachers' manipulation of teaching process, ignore the individual differences of students in knowledge transfer ability. Therefore, this study aimed at these problems, by studying classification algorithm in data mining and applying the classification method based on Naive Bayes algorithm, we design and implement scientific classification of students, and draw lessons from stratified and interactive teaching mode, so as to build a new effective teaching mode. The mode enable students to learn efficiently, so as to adapt to the trend of rapid development of new technology and cultivate innovative talents.

II. RESEARCH METHOD

The research and practice of the hierarchical interactive teaching model based on the Naive Bayesian classification is based on the classification of students' differences. So there are two major tasks need to do: the approaches to the students' difference measurement and grouping and the design of hierarchical interactive teaching framework. Its method flow is shown in Figure I.

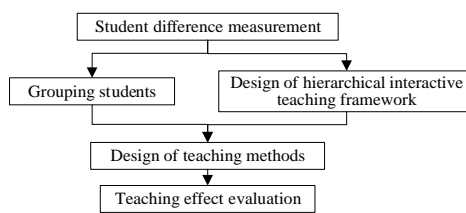


FIGURE I. RESEARCH METHOD FLOW

First of all, based on the samples, the naive Bayes algorithm according to the student's attribute value is used to test the students' differences. Then, according to the results to make a scientific difference classification to achieve effective grouping for students. At the same time, the design of the hierarchical interactive teaching framework is carried out by the two subjects (the student is the main body, the teacher is the leading part). Finally, the teaching effect is evaluated and analyzed.

III. STUDENT CLASSIFICATION DESIGN BASED ON NAIVE BAYESIAN

A. Naive Bayesian Theoretical Principle

At present, there are many kinds of algorithms in data mining, such as based on Bayes algorithm, decision tree algorithm, neural network algorithm, rough set algorithm, genetic algorithm, support vector machine algorithm and so on. In the practical application of many classification algorithms, the most widely used algorithm is Naive Bayesian algorithm model. Naive Bayes is a simple and effective classification model. From Bayes' theorem recall that:

$$P(B|A) = \frac{P(A|B)P(B)}{P(A)} \quad (1)$$

Equation (1): $P(A)$ and $P(B)$ separate representation the probability of occurrence of events A and events B .

$P(A|B)$ indicates the probability of occurrence of event A under the premise that event B occurs. $P(A|B)$ is a priori probability, and its value is often easily obtained.

$P(B|A)$ indicates the probability of occurrence of event B under the premise that event A occurs. $P(B|A)$ is a posteriori probability, and its value is the result of the solution of the Bayesian formula.

The classifier structure diagram based on the naive Bayes algorithm is shown in Figure II. It's leaf node A_m represents the m attribute, and the root node C represents the category. Suppose $D = \{C, A, S\}$ are training samples, it includes the student category $C = \{C_1, C_2, \dots, C_i\}$ and the student attribute $A = \{A_1, A_2, \dots, A_m\}$. Suppose $S = \{S_1, S_2, \dots, S_n\}$ represents a collection of classified students, in which S_n represents n th student. Suppose $X_k = \{a_1, a_2, \dots, a_m\}$ is a student to be classified,

in which each a_m represents an attribute eigenvalue of the pending item X_k .

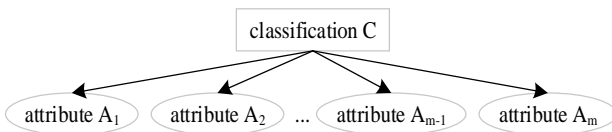


FIGURE II. THE CLASSIFIER STRUCTURE DIAGRAM

B. Design the Individualized Attributes of Students

The student classification method based on the naive Bayes algorithm is used the information of the past students as the sample set , which is used to construct the naive Bayes classifier.

Students are classified according to the information of the students' attributes. The students divided into the same category are not simply using the score as criterion of evaluation. Its are classified by comprehensive evaluation after combination of other attributes.

The difference classification based on the naive Bayes algorithm is select the individual attributes of the students as shown in Figure III. The students which 8 attribute values similar in the two dimensions (character and learning style) are put into one category, while the 12 attributes values of the three dimensions of personal basic situation, learning interest and cognitive ability are different. The purpose of the classification is to carry out differential teaching to implicit dynamic stratification and heterogeneous cooperation for students' cognitive ability, learning interest and basic information.

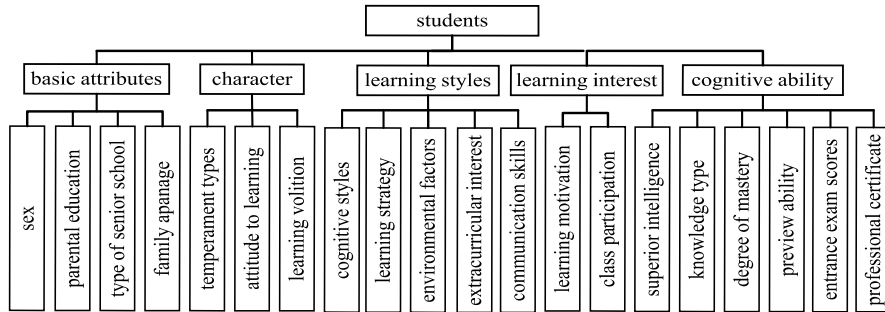


FIGURE III. INDIVIDUALIZED ATTRIBUTES OF STUDENTS

C. Student Classification Design Based on Naive Bayesian

The process based on the naive Bayes classification is shown in Figure IV.

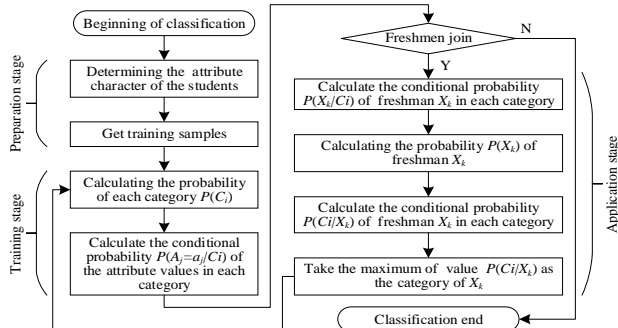


FIGURE IV. STUDENT CLASSIFICATION CYCLE FLOW CHART BASED ON NAIVE BAYES ALGORITHM

1) $P(C_i)$ is set to indicate the frequency of the occurrence of the student category C_i in the training sample concentration, that is the category probability. For sample data sets, there are different levels of students in each category, which avoids the discrimination of students.

$$P(C_i) = \frac{\text{Count}(C_i)}{n} \quad (2)$$

The function $\text{Count}(C_i)$ represents the number of students belonging to category i which is in the entire student sample collection of S . n represents the total number of the entire student sample collection of S .

2) $P(A_j = a_j | C_i)$ is set to represent the conditional probability of each characteristic attribute value of the student in the category.

$$P(A_j = a_j | C_i) = \frac{\text{Count}_{C_i}(A_j = a_j)}{\text{Count}(C_i)} \quad (3)$$

$A_j = a_j$ indicates that the value of the j attribute is a_j .The function $\text{Count}_{C_i}(A_j = a_j)$ represents the number of students which the attribute name is A_j and attribute value is a_j in the i student category.

3) $P(X_k | C_i)$ is set to represent the conditional probability of the students X_k to be classified in the student category C_i , m represents the number of attributes that describe student differences.

$$P(X_k | C_i) = \prod_{j=1}^m P(A_j = a_j | C_i) \quad (4)$$

4) $P(A_j = a_j)$ is set to represent the probability of the student's attribute A_j when the value is a_j .

$$P(A_j = a_j) = \frac{\text{Count}(A_j = a_j)}{n} \quad (5)$$

The function $\text{Count}(A_j = a_j)$ indicates the number when the value of attribute j is a_j .

5) $P(X_k)$ is set to indicate the probability that the student X_k should be classified in the training sample concentration.

$$P(X_k) = \prod_{j=1}^m P(A_j = a_j) \quad (6)$$

6) $P(C_i | X_k)$ is set to represent the conditional probability that the student X_k should be classified to category i .

$$P(C_i | X_k) = \frac{P(X_k | C_i) P(C_i)}{P(X_k)} \quad (7)$$

7) $P(C_{\max} | X_k)$ is set to represent the maximum category probability of the student X_k which should be classified to the student category.

$$P(C_{\max} | X_k) = \max \{P(C_1 | X_k), P(C_2 | X_k), \dots, P(C_i | X_k)\} \quad (8)$$

C_{\max} indicates the maximum category of conditional probability which is obtained by (8).

Finally, (8) is used to calculate the maximum category probability of the students to be classified in the students' category. That is the category of the students to be classified. At this point, one classification ends.

IV. THE DESIGN OF THE HIERARCHICAL INTERACTIVE TEACHING FRAMEWORK

The hierarchical interactive teaching model is an independent, inquiring and cooperative teaching model based on the classification of the naive Bayes algorithm. This model breaks the original classroom structure, and takes the interaction of teachers and students as the carrier, and also group autonomy, and let the students as the subject of the class. This model is guided by the task of the problem, and it is based on the students' self-study, and it aims at the completion of the task of the group. This model creates an ecological chain class based on group mutual learning to solve problems. It pays attention to the state of learning and the quality of life for every student. The design of the hierarchical interactive teaching model framework is shown in Figure V.

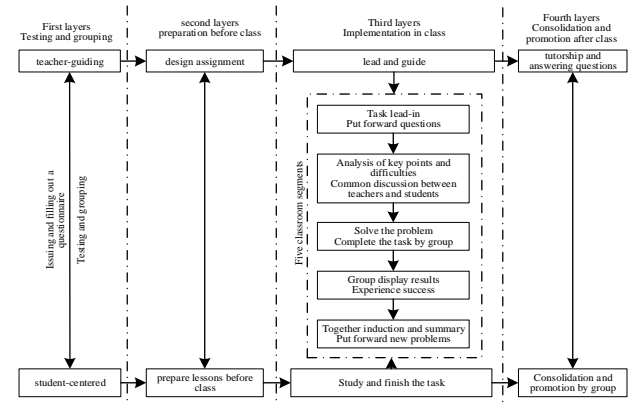


FIGURE V. THE HIERARCHICAL INTERACTIVE TEACHING MODEL FRAMEWORK

The four layers of the hierarchical interactive teaching model are closely related to each other, and support each other dynamically with the spiral. The five segments drive each other to form a whole, interlace and connect with each other. This teaching mode makes the classroom an active area for teachers and students to resonate with their ideology and to show their personality together.

V. ANALYSIS OF TEACHING EFFECT

In this paper, the teaching effect is analyzed from two aspects by using the method of questionnaire and comparative experiment. First, the experimental class's comparative analysis before and after the experiment is carried out. Then, a comparative analysis between the experimental class and the contrast class is carried out.

The comparative data of the experimental class before and after the experiment are shown in Figure VI. From Figure VI, it can be seen that 85.72% of the students have an attitude of approval towards the application of the hierarchical interactive teaching model based on the naive Bayes algorithm in the teaching. There are 70.13% of the students satisfied with the improved teaching effect. At the same time, it can be seen that the students' interest in learning and the ability to communicate and cooperate have improved obviously.

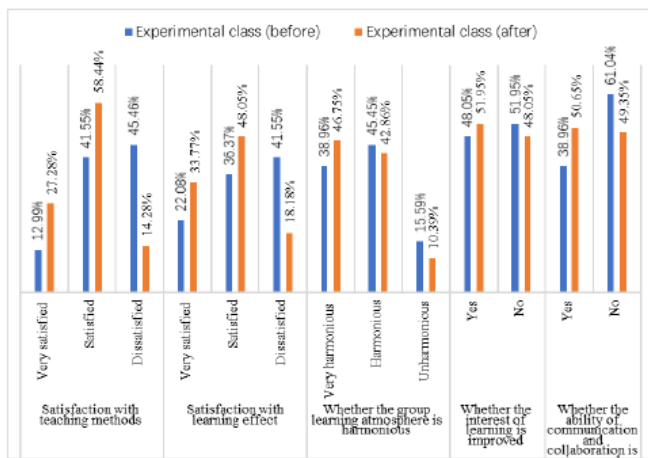


FIGURE VI. THE COMPARATIVE DATA OF THE EXPERIMENTAL CLASS BEFORE AND AFTER THE EXPERIMENT

The comparison between the experimental class and the contrast class is shown in Figure VII. From Figure VII, we can see that students' satisfaction degree, teaching effect satisfaction and group learning atmosphere based on Naive Bayes algorithm classification are higher than those of the contrast class. At the same time, it can be seen that the students' interest in learning and the ability to communicate and cooperate have also been improved.

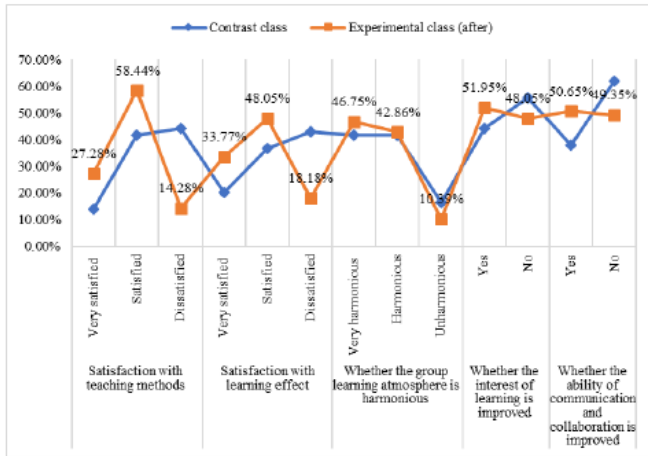


FIGURE VII. THE COMPARISON BETWEEN THE EXPERIMENTAL CLASS AND THE CONTRAST CLASS

VI. CONCLUSION

The comprehensive analysis shows that, in the implementation of the hierarchical interactive teaching model based on the naive Bayes algorithm, the new teaching mode was accepted by the students, it was welcomed by the students. The new teaching mode can improve the ability of learning interest and collaboration of students. It has a very good teaching effect. Experiments show that the classification algorithm based on Naive Bayes has better feasibility and effectiveness in solving student classification problem.

However, due to the limited personal time and ability, there are still some shortcomings in the study. In order to better achieve hierarchical interaction teaching mode based on Naive

Bayes algorithm and improve teaching effect, we still need to further improve the limitation of applying naive Bayes algorithm, that is, suppose the attributes of students are independent.

ACKNOWLEDGMENT

This work was supported by “Research and construction of the practice teaching system of information specialty(J2016138, The major project of teaching reform research in Shanxi Education Department)” and “The optimization and the platform construction of the practice teaching system of information specialty (SYJ201509, The major project of the research on teaching reform Business College of Shanxi University)”. Our special thanks are due to Prof. Ma Shangcui, for his helpful discussion with preparing the manuscript.

REFERENCES

- [1] Jonathan Rauh. Problems in Identifying Public and Private Organizations: A Demonstration Using a Simple Naive Bayesian Classification[J]. *Public Organization Review*,2015,15(1).
- [2] SangitaB, P., Deshmukh, S.R.. Use of Support Vector Machine, decision tree and Naive Bayesian techniques for wind speed classification[P]. Power and Energy Systems (ICPS), 2011 International Conference on,2011.
- [3] Yan Dong. Hierarchical interactive teaching mode and its practice and exploration of mathematics teaching in Senior High School [D]. Southwest University,2016.
- [4] Chen Zhiqiang. Hierarchical interactive teaching mode and its practice and exploration of mathematics teaching in Senior High School [D]. Henan University,2016.
- [5] S. Mukherjee and N. Sharma. Intrusion detection using naïve Bayes classifier with feature reduction[J].*Procedia Technology*,vol. 4, pp. 119–128, 2012.
- [6] L. Jiang, Z. Cai, D. Wang, and H. Zhang. Improving tree augmented naive Bayes for class probability estimation[J]. *Knowledge-Based Systems*, vol. 26, pp. 239–245, 2012.
- [7] Sharma RK, Sugumaran V, Kumar H, Amarnath M. A comparative study of naïve Bayes classifier and Bayes net classifier for fault diagnosis of roller bearing using sound signal[J].*International Journal of Decision Support Systems*. 2015 Jan 1; 1(1):115–29.
- [8] Hamse Y Mussa, John BO Mitchell, Robert C Glen. Full “Laplacianised” posterior naïve Bayesian algorithm[J]. *Journal of Cheminformatics*. 2013 5:37.
- [9] K. Magesh Kumar, P. Valarmathie. Domain and Intelligence Based Multimedia Question Answering System[J]. *International Journal of Evaluation and Research in Education*, Vol. 5, No. 3, September 2016 : 227 – 234.
- [10] [11]Zhipun Wang1, Li Chen, Terry Anderson. A Framework for Interaction and Cognitive Engagement in Connectivist Learning Contexts[J]. *International Review of Research in Open and Distance Learning*, Vol. 15, No.2, Apr 2014:121-141.

A Probability Model of Calculating L2 Cache Misses

 Kecheng Ji¹, Ming Ling^{1,*} and Li Liu²
¹National ASIC System Engineering Technology Research Center, Southeast University, Nanjing, China

²Institute of Integrated Circuits Technology, Southeast University, Wuxi, China

^{*}Corresponding author

Abstract—Stack or reuse distances have been widely adopted in studying memory localities and cache behaviors. However, the memory references, normally profiled by a binary instrumentation tool, only reflect the accessing sequence of instruction fetching and load or store executions. That is why the stack or the reuse distances obtained from these memory references cannot be used to predict the L2 or lower cache misses. This paper proposes a probability model to calculate the L2 reuse distance histogram from the L1 stack distance histograms without any extra simulations. The L2 cache misses or memory localities can be predicted fast and accurately based on the result of our model. We use 13 benchmarks chosen from *Mobybench 2.0* and *SPEC 2006* to evaluate the accuracy of our model. With the support of *StatCache* and *StatStack*, the average absolute error of modeling the L2 cache misses is about 8%. Meanwhile, contrast to *gem5* fast simulations, the process of predicting L2 cache misses can be sped up by 50 times on average.

Keywords—probability model; stack distance; reuse distance; L2 cache misses

I. INTRODUCTION

For studying cache behaviors, the analytical models are normally fed with statistical memory characteristics, such as reuse or stack distance histograms [1]. However, these statistical characteristics are frequently obtained by profiling memory traces or emulating application executions [2], which only reflect memory behaviors in L1 caches. Therefore, lots of prior studies choose to use trace-driven simulations to predict L2 or lower level cache misses [3]. Although trace-driven simulations perform faster than detailed ones, the time overhead is still considerably larger than that of analytical models. Furthermore, the growing length of application traces and the non-unified simulator interfaces often bring storage and flexibility problems. Unfortunately, according to the study by [4], these problems have been more serious in recent years. On the other hand, the flexibility problem still remains as a big challenge and lots of frustrating coding as well as debugging works are needed. Last but not least, because they mainly focus on proposal evaluations rather than providing a guidance in architecture designs, simulation-based methods normally have rare architecture insights.

Therefore, this paper proposes a probability model to estimate the L2 reuse distance histogram from L1 stack distance histograms directly without any simulations. To our best knowledge, this model is the first analytical method to predict the L2 reuse distance histogram directly from the L1 stack distance histograms. The calculated L2 reuse distance histogram can be applied to predict L2 cache misses in single-core processors. Meanwhile, the study of contention behaviors in the

multi-core shared cache can also take the advantage of fast modeling with the predicted results from our model.

The rest of the paper is organized as follows: Section II introduces how to calculate the L2 reuse distance while the model constructing is given in Section III. Section IV shows the experiment setup and studies the evaluation results. Finally, Section V concludes this paper.

II. CALCULATING THE L2 REUSE DISTANCE

A. Classical Stack Distance Theory

For studying cache behaviors, the stack distance is defined as the number of unique cache lines that accessed by the memory references during a reuse epoch, where a reuse epoch refers to the time interval between two successive memory references to the same cache line [5]. To collect the stack distance, prior studies usually construct the LRU stack history [6] that records latest references to different cache lines within each reuse epoch. In this way, the stack distance of current memory request can be easily calculated by counting the number of these latest references. Figure I shows a sequence of memory references to the L1 cache. X_i represents the i_{th} serviced reference while the accessed cache lines are labeled with the letters A, B, C and D. Although the cache line B has been accessed by 4 references X_4 , X_7 , X_9 and X_{10} within the reuse epoch of X_{11} , only X_{10} is recorded in the LRU stack history. Thus, the stack distance of X_{11} is 3 because there are 3 latest references X_5 , X_8 and X_{10} in the reuse epoch of X_{11} . We define the accessed order of different cache lines within a reuse epoch as the LRU stack history of that epoch.

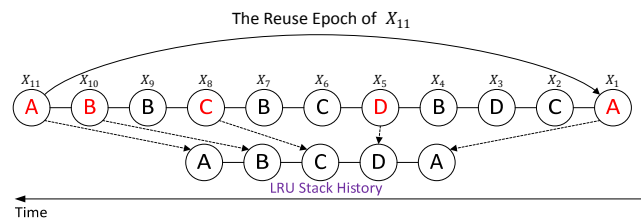


FIGURE I. LRU STACK HISTORY OF THE TWO MEMORY REFERENCES TO THE CACHE LINE A

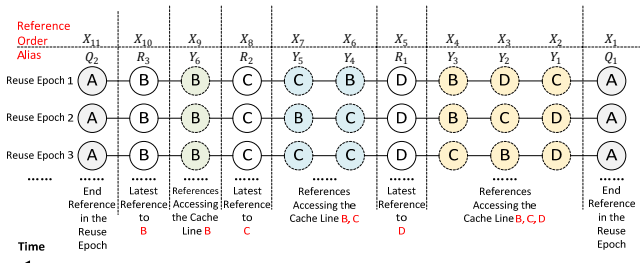


FIGURE II. SOME OTHER POSSIBLE REUSE EPOCH WITH THE SAME LRU STACK HISTORY IN FIGURE I

Normally, the collected stack distances of each reference are used to construct the so-called stack distance histogram for estimating LRU cache misses [5]. When the L1 cache has l cache lines, the number of cache misses can be calculated as (1) where $H_{S,L1}(k)$ is defined as the L1 stack distance histogram.

$$\text{Cache Misses} = \sum_{k=l}^{\infty} H_{S,L1}(k) \quad (1)$$

B. L2 Reuse Distance

Generally, memory references to the L2 cache are caused by L1 cache misses. Therefore, the L2 reuse distance of X_{11} in Figure I can be calculated by counting the number of L1 cache misses in the L1 reuse epoch of X_{11} . We define $P_{k \rightarrow r}$ to describe the ratio of how many L1 reuse epochs with stack distance k will generate r misses, or in other words, the L2 reuse distance r . In this case, the L2 reuse distance histogram $H_{r,L2}(r)$ can be calculated by (2).

$$H_{r,L2}(r) = \sum_{k=l}^{\infty} P_{k \rightarrow r} * H_{S,L1}(k) \quad (2)$$

Typically, the references within each L1 reuse epoch can be classified into 2 groups. As shown in Figure I, the references of the first group, which is named as the set $\{NE\}$, do not generate reuse behaviors within the reuse epoch of X_{11} , such as X_2 , X_3 and X_4 . On the other hand, the references in the second group, which is named as the set $\{E\}$, have reuse epochs embedded in the X_{11} epoch, like X_5 , X_6 etc. In this paper, we name these nested reuse epochs as “embedded epochs”.

Across the whole program, there may be more than one possible reuse epochs that have the same LRU stack history. Figure II shows some other possible reuse epochs of X_{11} , which have the same LRU stack history shown in Figure I. For the given LRU stack history ($B \leftarrow C \leftarrow D$) within the epoch between X_1 and X_{11} , X_{10} must access the cache line B to guarantee the last accessed cache line is B. Meanwhile, according to the definition of LRU stack history, X_9 also must be a reference to the cache line B. In the same manner, the cache lines accessed by X_7 and X_6 are limited to B and C, while the references before X_5 can access anyone of the cache lines B, C and D. To classify above patterns, we give aliases for different references in the reuse epoch of X_{11} . The set $\{R_i\}$ represents the references that recorded as latest references in the LRU stack history. For example, X_5 has the alias of R_1 in Figure II. The end references in the target reuse epoch are denoted with the set $\{Q_i\}$. Lastly, other references in the epoch are named as the set $\{Y_i\}$.

1) *L1 Cache Misses in the Set $\{NE\}$* : Figure III simplifies the cases in Figure II to explain how to calculate $P_{k \rightarrow r}$ in this paper, where there is only one reference Y_1 and one embedded epoch that named as y' . Meanwhile, the L1 cache is always configured with 2 cache lines in the following discussions.

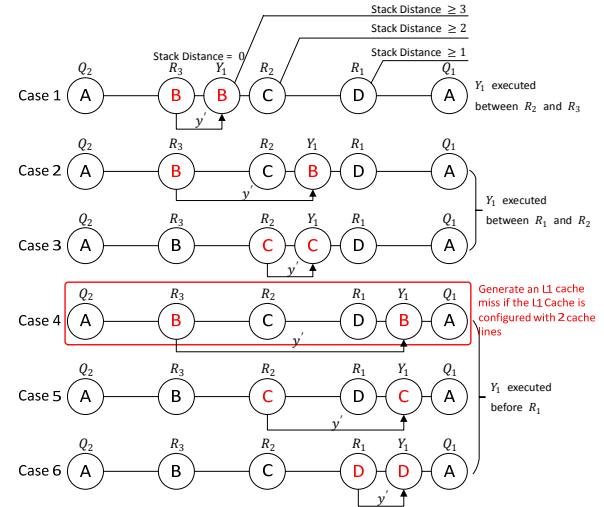


FIGURE III. ONLY ONE REFERENCE Y_1 IN THE REUSE EPOCH OF Q_2

As shown in the case 1 of Figure III, R_3 belongs to the set $\{E\}$ because it generates an embedded epoch y' with Y_1 (for the given LRU stack history shown in Figure I, the only possible cache line that accessed by Y_1 is B). The L1 stack distance of R_3 is 0. On the other hand, Y_1 , R_1 and R_2 are the members of the set $\{NE\}$. The L1 stack distance of Y_1 is larger than or equal to 3 because 3 different cache lines (C, D, A) have been accessed before Y_1 . Similarly, the L1 stack distances of R_1 and R_2 are larger than or equal to 1 and 2, respectively. There will be two possible cases, shown as case 2 and case 3, when Y_1 is serviced between R_1 and R_2 (Y_1 either accesses the cache line B or C). Meanwhile, there are 3 possible cases when Y_1 is executed before R_1 , which are sketched as case 4 to case 6 (the cache line accessed by Y_1 can be anyone of B, C or D).

Although the references in the set $\{NE\}$ do not generate reuse epochs in the epoch of Q_2 , their minimum L1 stack distances are determined, which have been analyzed before. For these references, the probabilities of generating L1 cache misses can be calculated using the L1 stack distance histogram. For each memory reference, we define P_m as the probability of generating an L1 cache miss given its L1 stack distance is larger than or equal to m . By generalizing the case of R_1 , P_m can be calculated as (3) when the L1 cache has l cache lines. If l is smaller than or equal to m , the reference is certain to trigger an L1 cache miss. In this case, P_m should equal 1.

$$P_m = \begin{cases} \frac{\sum_{k=m}^{\infty} H_{S,L1}(k)}{\sum_{k=l}^{\infty} H_{S,L1}(k)}, & (l > m) \\ 1, & (l \leq m) \end{cases} \quad (3)$$

To make the expression of $P_{k \rightarrow r}$ more concise and easier to calculate, we introduce one unified, weighted average probability $P_{m,avg}$ to replace the usage of a group of different

P_m . According to (3), $\sum_{k=m}^{\infty} H_{S,L1}(k) * P_m$ represents the number of L1 cache misses that generated by the references whose L1 stack distances are larger than or equal to m . By exploring all possible m , P_{m_avg} could be calculated as (4).

$$P_{m_avg} = \frac{[\sum_{m=1}^{\infty} P_m * (\sum_{k=m}^{\infty} H_{S,L1}(k))]}{\sum_{m=1}^{\infty} \sum_{k=m}^{\infty} H_{S,L1}(k)} \quad (4)$$

2) *L1 Cache Misses in the Set {E}*: As shown in Figure III, there is only one case (case 4) that the embedded epoch y' generates an L1 cache miss (as we assumed before, the L1 cache has only 2 cache lines). In this paper, we assume that all possible cases of y' share the same probability to appear within the reuse epoch of Q_2 . Therefore, the probability of y' to cause an L1 cache miss can be described as 1/6 because there are 6 possible cases of y' in Figure III.

3) *Generalization*: P_y is defined as the probability of having an L1 cache misses in the set {E}. Based on the discussion in Figure III, P_y could be calculated as (5). The L1 cache has l cache lines while the L1 stack distance of Q_2 is k .

$$P_y \approx \frac{\sum_{m=0}^{k-l} \sum_{i=1}^{k-l-m} i}{\sum_{i=1}^k i}, \quad (k \geq l) \quad (5)$$

Actually, there may be more than one members in {E}. We observe that P_y could be calculated as (6) (represented as $P_y(n)$) approximatively while there are n references in the set {E}.

$$P_y \approx \frac{\sum_{m=0}^{k-l} \sum_{i=1}^{k-l-m} i}{\sum_{i=1}^k (i*n)}, \quad (k \geq l) \quad (6)$$

III. MODEL GENERALIZATION

A. The Probability of Multiple y'

As we mentioned above, there will be more y' epochs generated when more references Y_i are executed in the reuse epoch of Q_2 . To describe the appearance ratios of different numbers of y' , we use $P_e(k, n)$ to represent the probability of having n embedded epochs within the epoch of Q_2 , given the L1 stack distance of Q_2 is k .

Given a reuse epoch q with stack distance s ($s \leq k$), the epoch q could be embedded in the reuse epoch Q_2 or not. Meanwhile, the epoch q can merely appear within the references whose L1 stack distances are larger than or equal to s , while the number of these references is $\sum_{a=s}^{\infty} H_{S,L1}(a)$, in which $H_{S,L1}(a)$ represents the L1 stack distance histogram. Thus, for Q_2 with L1 stack distance k , the probability of having one embedded epoch with the L1 stack distance s can be calculated as $H_{S,L1}(k) / \sum_{a=s}^{\infty} H_{S,L1}(a)$. Considering all possible s , $P_e(k, 1)$ can be estimated as (7).

$$P_e(k, 1) = \sum_{s=1}^{k-1} \left(\frac{H_{S,L1}(k)}{\sum_{a=s}^{\infty} H_{S,L1}(a)} \right) \quad (7)$$

Furthermore, assuming each embedded epoch is independent with each other, $P_e(k, n)$ can be calculated as (8).

$$P_e(k, n) = [\sum_{s=1}^{k-1} \left(\frac{H_{S,L1}(k)}{\sum_{a=s}^{\infty} H_{S,L1}(a)} \right)]^n \quad (8)$$

B. The Calculation of $P_{k \rightarrow r}$

Ultimately, the probability $P_{k \rightarrow r}$ can be obtained using (9) when the L1 stack distance equals k and the L2 reuse distance is r . For each reuse epoch, $P_e(k, n)$ represents the probability of having n reuse epochs y' (equals the members of set {E}). $C_n^x (P_y(n))^x * (1 - P_y(n))^{n-x}$ denotes the probability of generating x L1 cache misses when there are n reuse epoch y' within the current epoch. For example, in Figure III, x is either 1 or 0 while n is 1 (because there is one and only one reuse epoch y' within the epoch of Q_2). Lastly, $C_k^{r-x} (P_{m_avg})^{r-x} (1 - P_{m_avg})^{k-r+x}$ gives the probability of causing $r - x$ L1 cache misses from the set {NE}.

$$P_{k \rightarrow r} = \sum_{n=1}^{\infty} [P_e(k, n) * C_n^x (P_y(n))^x * (1 - P_y(n))^{n-x} * C_k^{r-x} (P_{m_avg})^{r-x} (1 - P_{m_avg})^{k-r+x}] \quad (9)$$

IV. EVALUATIONS

The cache architecture used for evaluations in this paper has two levels. From the CPU side to the memory side, the independent instruction and data caches are connected to the L2 shared cache through a crossbar. To simplify the discussion, all caches are fully-associative. However, it will be not difficult to extend our work to set-associative architectures. The replacement policy of L1 caches is set with the Least Recently Used (LRU) while that of the L2 cache could be configured as the Random or the LRU. The evaluating platform is implemented with gem5 *AtomicSimpleCPU* full-system simulator (containing two-level caches and DRAMs).

A. Evaluations of Predicting L2 Cache Misses

1) *StatCache and L2 Cache Misses with the Random Replacement Policy*: Figure IV shows the absolute errors of predicting L2 cache misses using the *StatCache* [7]. Briefly, the average absolute error of the tested benchmarks is around 8%. However, for some benchmarks, such as *BaiduMap* and *BBench*, the prediction errors increase significantly, up to 11.9%. The *StatCache* assumes that the memory references share the same L1 cache miss rate during a small execution slot. However, the correctness of this assumption depends on the length of profiling interval. The memory references of *BaiduMap* and *BBench* may not satisfy the assumption of *StatCache* when the profiling interval contains one million memory references in this paper.

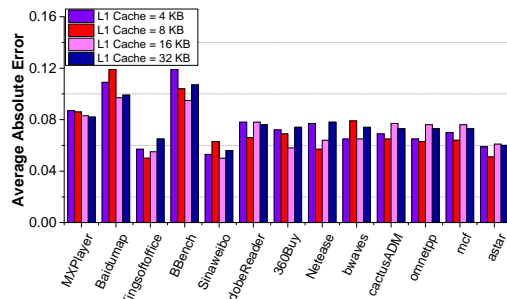


FIGURE IV. ABSOLUTE ERRORS OF PREDICTING L2 RANDOM CACHE MISSES

2) *StatStack and L2 Cache Misses with the LRU Replacement Policy:* *StatStack* [5] has provided an efficient method to calculate the stack distance histogram using the reuse distance histogram, which is accepted in this paper. Figure V shows the absolute errors of predicting L2 LRU cache misses. Most absolute errors are below 7%, which are lower than the errors in L2 Random cache miss predictions. This error reduction, we believe, could be caused by the error masking effects. For example, the reuse epoch, whose stack distance should be predicted as 8, is predicted with stack distance 9 using our model and *StatStack*. However, this reuse epoch will be regarded as a cache hit when the L2 cache is set with 16 cache lines, regardless the predicted stack distance is 8 or 9.

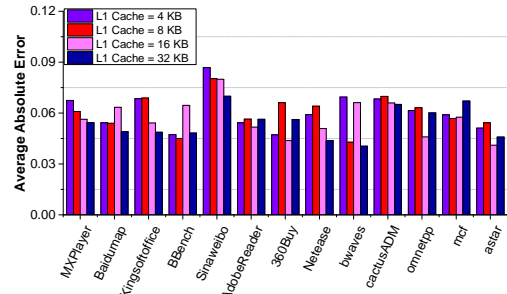


FIGURE V. ABSOLUTE ERRORS OF PREDICTING L2 LRU CACHE MISSES

B. Time Overhead

Figure VI shows the time overhead comparisons between gem5 *AtomicSimpleCPU* simulations and implementations of our model. The Y-axis gives the consumed minutes for predictions, which are shown in a log scalar. The X-axis represents all tested benchmarks. Briefly, the prediction can be sped by more than 50 times on average by using our model. Meanwhile, we can see that the time consumed in the L2 histogram calculation gives the half contribution to the total overhead of our model implementations approximately.

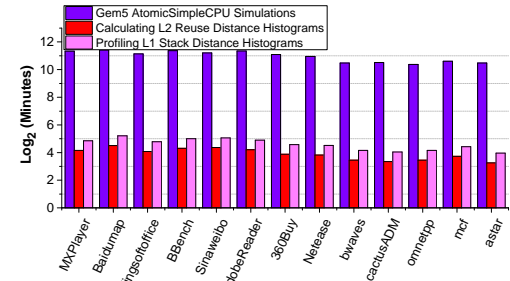


FIGURE VI. TIME OVERHEAD COMPARISONS BETWEEN GEM5 ATOMICSIMPLECPU SIMULATIONS AND OUR MODEL

V. CONCLUSION

This paper proposes a probability model to predict the L2 reuse distance histogram without any extra simulations. With the support of *StatCache* and *StatStack*, the calculated L2 histogram can be adopted for modeling L2 Random and LRU cache misses with the average errors of 8% and 6.8%, respectively. Our future works will extend the model application to multi-core architectures and consider the influences of the set-associative organization as well.

ACKNOWLEDGMENT

This work was supported under the Chinese National Mega Project of Science Research under Grant no.2014ZX01030101.

REFERENCES

- [1] Tao Tang, Xuejun Yang, and Yisong Lin. Cache miss analysis for gpu programs based on stack distance profile. In *Distributed Computing Systems (ICDCS)*, 2011 31st International Conference on, pages 623–634. IEEE, 2011.
- [2] George Alm’si, Clin Cas, caval, and David A Padua. Calculating stack distances efficiently. In *ACM Sigplan Notices*, volume 38, pages 37–43. ACM, 2002.
- [3] Richard A Uhlig and Trevor N Mudge. Trace-driven memory simulation: A survey. *ACM Computing Surveys (CSUR)*, 29(2):128–170, 1997.
- [4] Anastasiia Butko, Rafael Garibotti, Luciano Ost, Vianney Lapotre, Abdoulaye Gamat  , Gilles Sassatelli, and Chris Adeniyi-Jones. A tracedriven approach for fast and accurate simulation of manycore architectures. In *Design Automation Conference (ASP-DAC)*, 2015 20th Asia and South Pacific, pages 707–712. IEEE, 2015.
- [5] David Eklov and Erik Hagersten. Statstack: Efficient modeling of lru caches. In *Performance Analysis of Systems & Software (ISPASS)*, 2010 IEEE International Symposium on, pages 55–65. IEEE, 2010.
- [6] Bryan T Bennett and Vincent J. Kruskal. Lru stack processing. *IBM Journal of Research and Development*, 19(4):353–357, 1975.
- [7] Erik Berg and Erik Hagersten. Statcache: a probabilistic approach to efficient and accurate data locality analysis. In *Performance Analysis of Systems and Software*, 2004 IEEE International Symposium on-ISPASS, pages 20–27. IEEE, 2004.

Deflection Analysis and Iterative Solution Method of Slender Telescopic Booms

Xuyang Cao, Zhenhua Gu* and Haojie Yu

School of Mechanical Engineering, Dalian University of Technology, 116024 Dalian, China

*Corresponding author

Abstract—In order to analyze accurately the deformation of the telescopic boom in the case of large deformation, an initial deflection curve can be get according to the nonlinear bending differential equation and calculation method. The retraction amount in initial axial direction of the boom and the second-order bending moment can be get after counting process with the initial deflection curve. Then these data can be used to amend the bending moment in the nonlinear bending differential equation and so a more accurate deflection curve can be get. The deflection curves of a typical telescopic boom were calculated and the results were compared with the results obtained by the approximate calculation method. The results show that the calculation method proposed in this paper can obtain the deflection curve of the telescopic boom accurately under large deformation condition. The results obtained by using the traditional approximation of the calculation method are too large.

Keywords—telescopic boom; deflection curve; nonlinearity; numerical calculation

I INTRODUCTION

Most of the large construction machinery (such as cranes and aerial vehicles) have many box-type telescopic boom structures. Telescopic arms are the main load-bearing parts of such machines. The structure with large slenderness ratio leads to obvious non-linear characteristics and its performance has an important impact on the safe operation of the whole machine^[1]. As the result, bending analysis is an important part of its performance evaluation.

At present, the researches on flexing lines of telescopic arms are in the approximate equation of flexure of beam sections. Huiming Xie^[2] deduced the curve expression using the boundary condition of the beam; Wenjing Wang et al^[3] combined the elastic stability theory to analyze the boom system non-linearly. Casafont M et al^[4] used the finite element model based on the uncoupled buckling mode constraint to derive the constraint applied to the finite element model from the generalized beam theory.

Based on the analysis of related literatures, at present, the non-linear factors are not accurately considered in the solution of flexural curves. This paper draws on and improves the research methods of predecessors, considering all the nonlinear factors and solving the more accurate deflection curve of the telescopic arm.

II TELESCOPIC BOOM DEFLECTION EQUATION ESTABLISHED

A. Flexure Equation of Variable Cross Section Extension Beam

Telescopic boom in the luffing plane can be regarded as a simply supported outrigger. Its flexural analysis is carried out in the luffing plane^[5]. In this paper, a typical five-arms telescopic boom is taken as the research object, as Figure I shows. The hinge point at the bottom of the telescopic boom is set as the origin of the coordinate system, and the axis direction of the telescopic arm before deformation is the x-axis, and the x-axis square along the arm end. The y-axis is in the luffing plane and is perpendicular to the x-axis.

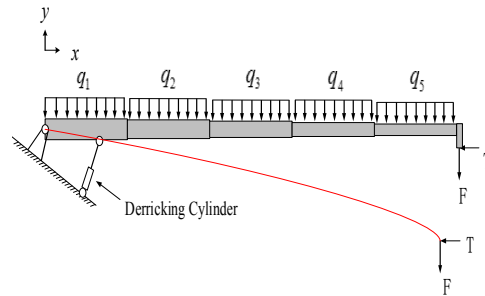


FIGURE I. MODEL OF THE TELESCOPIC BOOM

In the pure bending problem, the approximate differential equation of the flexure curve is^[6,7]:

$$\frac{d^2w}{dx^2} = \frac{M}{EI} \quad (1)$$

Formula (1) is suitable for small deformation. For large deformation, using formula (1) will make larger error in calculation, which requires a more accurate formula, as shown in equation (2):

$$\frac{\frac{d^2w}{dx^2}}{\left[1 + \left(\frac{dw}{dx}\right)^2\right]^{\frac{3}{2}}} = \frac{M}{EI} \quad (2)$$

Applying Eq. (2) to solve the bending deformation of

telescopic boom, the corresponding deflection curve equation is obtained [6]:

$$\frac{d^2w}{dx^2} = \frac{M(x, F, T, q_i)}{EI_i} \quad (i=1,2,3,4,5) \quad (3)$$

In the formula:

$M(x, F, T, q_i)$ —bending moment at a certain position on the arm, it is a function;

q_i —each section of the arm to withstand the horizontal uniform load line density, which is the weight of the arm in the horizontal component of the force generated;

E —metal elastic modulus;

I_i —the moment of inertia.

B. Calculation of First-order Flexing Curve

If we consider only the impact of lateral force, which means calculating the first-order deflection curve, the simplified model of telescopic boom at this time is shown in Figure II.

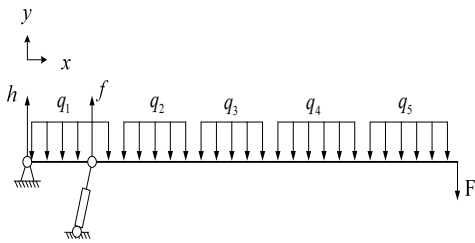


FIGURE II. FORCE DIAGRAM EXCLUDE AXIAL FORCE

The h and f are reaction forces. Its calculation formula can be derived as follows:

$$\left\{ \begin{array}{l} f = \frac{1}{d_0} \mathbf{d} \cdot \mathbf{d}^T \begin{bmatrix} \frac{1}{2} & 1 & 1 & 1 & 1 \\ & \frac{1}{2} & 1 & 1 & 1 \\ & & \frac{1}{2} & 1 & 1 \\ & & & \frac{1}{2} & 1 \\ & & & & \frac{1}{2} \end{bmatrix} \cdot \mathbf{q} + \frac{l}{d_0} F \\ h = \mathbf{d}^T \cdot \mathbf{q} - f - \frac{l-d_0}{d_0} F \end{array} \right. \quad (4)$$

In the formula:

d_0 —the distance between two hinges;

$\mathbf{d} = [d_1 \ d_2 \ d_3 \ d_4 \ d_5]^T$ — the extension of each arm from bottom to top;

$\mathbf{q} = [q_1 \ q_2 \ q_3 \ q_4 \ q_5]^T$ —uniform load density generated by arm self weight;

l —telescopic total length.

Regardless of arm weight, the first-order moment is calculated as follows:

$$M(x) = \begin{cases} \frac{l-d_0}{d_0} F \cdot x, & x < d \\ (l-x)F, & d \leq x \leq l \end{cases} \quad (5)$$

Considering the effect of uniform load generated by arm weight, a complete formula of first-order bending moment is obtained:

$$M_1(x) = \begin{cases} \frac{l-d_0}{d_0} F \cdot x + hx - U_0, & 0 < x < d_0 \\ F \cdot (l-x) - U_1, & d_0 \leq x < d_1 \\ F \cdot (l-x) - U_2, & d_1 \leq x < (d_1 + d_2) \\ F \cdot (l-x) - U_3, & (d_1 + d_2) \leq x < (d_1 + d_2 + d_3) \\ F \cdot (l-x) - U_4, & (d_1 + d_2 + d_3) \leq x < (d_1 + d_2 + d_3 + d_4) \\ F \cdot (l-x) - U_5, & (d_1 + d_2 + d_3 + d_4) \leq x < l \end{cases} \quad (6)$$

In the formula:

$U_0, U_1, U_2, U_3, U_4, U_5$ —the correction value of the bending moments of each section of the telescopic boom, which can be calculated as follows:

$$\left\{ \begin{array}{l} U_0 = q_1 \cdot d_1 \cdot (l-x-\frac{d_1}{2}) + q_2 \cdot d_2 \cdot (l-x-d_1-\frac{d_2}{2}) + q_3 \cdot d_3 \cdot (l-x-d_1-d_2-\frac{d_3}{2}) + \frac{1}{2} q_4 \cdot (l-x-d_1-d_2-d_3)^2 \\ U_1 = q_1 \cdot d_1 \cdot (l-x-\frac{d_1}{2}) + q_2 \cdot d_2 \cdot (l-x-d_1-\frac{d_2}{2}) + q_3 \cdot d_3 \cdot (l-x-d_1-d_2-\frac{d_3}{2}) + \frac{1}{2} q_4 \cdot (l-x-d_1-d_2)^2 \\ U_2 = q_1 \cdot d_1 \cdot (l-x-\frac{d_1}{2}) + q_2 \cdot d_2 \cdot (l-x-d_1-\frac{d_2}{2}) + q_3 \cdot d_3 \cdot (l-x-d_1-d_2-\frac{d_3}{2}) + \frac{1}{2} q_4 \cdot (l-x-d_1)^2 \\ U_3 = q_1 \cdot d_1 \cdot (l-x-\frac{d_1}{2}) + \frac{1}{2} q_2 \cdot (l-x-d_1)^2 \\ U_4 = \frac{1}{2} q_3 \cdot (l-x)^2 \\ U_5 = \frac{1}{2} q_4 \cdot (l-x)^2 \end{array} \right. \quad (7)$$

Substituting Eq.(4) and (7) into Eq. (6), the formula for calculating the first moment on the telescopic boom can be obtained. Substituting equation (6) into equation (3) gives the solution of the deflection equation given the values of E and I_i , where the deflection curve obtained is the first-order deflection curve.

C. The Length Contraction in Original Axis

As shown in Figure III, when the arm is not deformed, the position of the arm end is at the point a , and the final equilibrium position of the arm end after the deformation is at the point b . Point a and point b in the original axis direction (x axis direction) there is deviation, as Δl shown in Figure III.

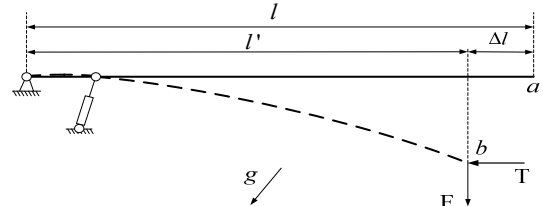


FIGURE III. DIAGRAM THAT SHOWS THE LENGTH CHANGE OF AN OVERHANGING BEAM IN AXIAL DIRECTION

The amount of l' in Figure III is the length of the arm in

the x direction after deformation, which satisfies the relation:

$$l' + \Delta l = l \quad (8)$$

The length of the deformed flexure curve can be obtained by integral formula, while the length of the telescopic arm does not change before and after the deformation, so that the formula (9) can be deduced:

$$\int_0^{l'} \sqrt{1+w'^2} dx = l \quad (9)$$

Not only the total length of the arm, but also the extension length of each arm is also retracted in the x direction. The calculation method is also similar to equation (9), which is as Eq. (10):

$$\int_0^{l_i'} \sqrt{1+w'^2} dx = l_i \quad (10)$$

In the formula:

$$l_i = \sum_1^i d_i, (i=1,2,3,4) \quad (11)$$

From Eq. (9) and (10), we can calculate the updated length of each arm and whole arm in the original axial direction after deformation.

D. Deflection Calculation Considering Second Order Effect

When the outrigger is subjected to axial force, the axial force tends to generate bending moment, that is, the second-order bending moment. So the deformation of the outrigger becomes larger. The calculation of second-order bending moment is related to the post-deformation equilibrium position and therefore can not be calculated before the deformation, which makes it difficult to obtain the bending line considering the second-order effect.

Now given the initial arm end coordinates as (l, δ) , then the arm at any point of the moment can be calculated according to equation (12).

$$M = T(\delta - y) + F(l - x) \quad (12)$$

Shown in Figure IV, take a small section of the telescopic arm. Its bending moment can be calculated by equation (12).

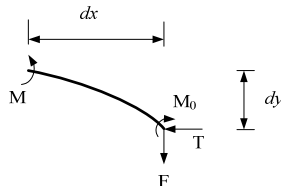


FIGURE IV. FORCE DIAGRAM OF A PUNY SEGMENT OF BOOM

According to the balance of forces, Eq.(13) is available:

$$M = Fdx + Tdy + M_0 + M_1(x) = Fdx + Tdy + T(\delta - y) + F(l - x) + M_1(x) \quad (13)$$

For the micro-segment arm, its deflection in line with the small deformation assumption, the deflection curve can take Eq. (1) to calculate. The formula (1) seeking a derivative of x, combined with equation (13), the micro-segment deflection of the differential equation can be deduced:

$$\frac{d^3 y}{dx^3} + \frac{T}{EI} \frac{dy}{dx} + \frac{F}{EI} = 0 \quad (14)$$

This is a constant coefficient of non-homogeneous linear differential equations. Its general solution can be obtained as follows:

$$p = C_1 \sin \sqrt{\frac{T}{EI}} \cdot x + C_2 \cos \sqrt{\frac{T}{EI}} \cdot x - \frac{1}{\tan \theta} \quad (15)$$

Assume the equation of $k = \sqrt{T/EI}$, then the above formula will become the formula as follows:

$$y = -\frac{1}{k} \cdot C_1 \cos k \cdot x + \frac{1}{k} \cdot C_2 \sin k \cdot x - \frac{1}{\tan \theta} x + C_3 \quad (16)$$

The boundary conditions expressed by the positions of two hinges are:

$$\begin{cases} y(0) = 0 \\ y(d) = 0 \end{cases} \quad (17)$$

Take the initial arm position of the second derivative as the last boundary conditions, which can be expressed as follows:

$$y''(l) = 0 \quad (18)$$

Substituting Eq.(17) and (18) into (16), Eq.(19) can be get:

$$\begin{cases} -\frac{1}{k} C_1 + C_3 = 0 \\ -\frac{1}{k} C_1 \cdot \cos kd + \frac{1}{k} C_2 \cdot \sin kd - \frac{d}{\tan \theta} + C_3 = 0 \\ kC_1 \cdot \cos kl - kC_2 \cdot \sin kl = 0 \end{cases} \quad (19)$$

Solve the above equations, and the following results can be obtained.

$$\left\{ \begin{array}{l} C_1 = \frac{kd \sin kl}{\tan \theta \cdot (\sin kl + \sin kd \cos kl - \sin kl \cos kd)} \\ C_2 = \frac{kd \cos kl}{\tan \theta \cdot (\sin kl + \sin kd \cos kl - \sin kl \cos kd)} \\ C_3 = \frac{d \sin kl}{\tan \theta \cdot (\sin kl + \sin kd \cos kl - \sin kl \cos kd)} \end{array} \right. . \quad (20)$$

To sum up, considering the second-order effect, the telescopic arm flexural equation is as equation (16). The undetermined coefficient can be obtained using Eq. (20).

III SIMULINK SIMULATION MODEL ESTABLISHMENT AND NUMERICAL SOLUTION

This chapter will use Simulink as a supporting tool, programming corresponding procedures for numerical solution. This study uses the QY25H5 telescopic crane for the data prototype. Its basic parameters are shown in Table I.

TABLE I.BASIC DATA OF THE TELESCOPIC BOOM IN CRANE QY25H5

Items	Value	Items	Value
Total length of beam (l)	24293.5 [mm]	The density (ρ)	7.85×10^6 [kg/mm ³]
Distance between hinge points (d)	5270 [mm]	Acceleration of gravity (g)	9.8 [m/s ²]
Length of first arm (l_1)	9172.5 [mm]	Moment of inertia of first arm (I_1)	100230730 [mm ⁴]
Length of second arm (l_2)	9088 [mm]	Moment of inertia of second arm (I_2)	82214974 [mm ⁴]
Length of third arm (l_3)	8920 [mm]	Moment of inertia of third arm (I_3)	604812697 [mm ⁴]
Length of fourth arm (l_4)	8720 [mm]	Moment of inertia of fourth arm (I_4)	399694165 [mm ⁴]
Length of fifth arm (l_5)	8670 [mm]	Moment of inertia of fifth arm (I_5)	214359536 [mm ⁴]

One typical condition is chosen to be simulated in this paper. It sets the load as 25t and telescopic boom elevation as 30°. The Simulink model is compiling according to the calculation method in the first chapter and the data provided in the previous case of this chapter is taken into the program. Then, the curve data can be get and the graph can be drawn, as shown in Figure V.

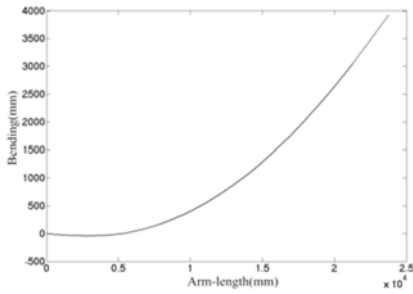


FIGURE V. DEFLECTION CURVE

In addition, the study also obtained an approximate curve of deflection for comparison based on the commonly used

method of solving approximation curves. The approximate calculation method is completely based on the linear differential equation (1), ignoring the discussion in Section 1.3, which means only one process before the output results. The resulting deflection curve is shown in Figure VI.

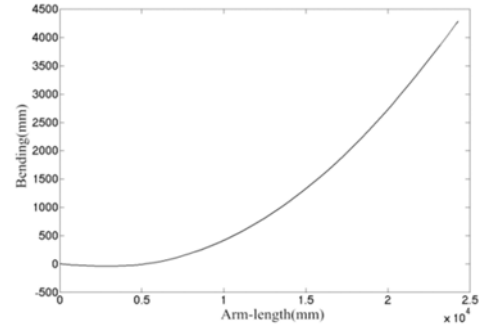


FIGURE VI. APPROXIMATE DEFLECTION CURVE

The results show that the deflection curve of the telescopic arm obtained by the calculation method proposed in this study is smaller than that of the conventional approximate calculation method, and the difference is more significant when the arm length of the telescopic arm is larger.

IV CONCLUSION

The method described in this paper for calculating the flexing line of the telescopic boom fully considers all the nonlinear factors that may exist under actual conditions. The nonlinear deflection differential equations used in this paper can greatly improve the accuracy of the calculation compared with the commonly used linear equations, as well as the consideration of the length retraction in original axis and the second-order bending moment. Compared with the general calculation method, the proposed method can solve the flexure curve of the telescopic arm more accurately, and can greatly improve the accuracy of the calculation of the flexible curve of the telescopic arm with large deformation.

ACKNOWLEDGEMENTS

This research was financially supported by National Natural Science Foundation of China (Grant No.51475068).

REFERENCES

- [1] Lin HUANG. Optimization research of structure for crane telescopic boom [D]. Dalian University of Technology, 2007.
- [2] Hui-ming XIE. The recurrence calculation of the deflection curve [J]. Mechanics and Engineering, 2009, 31 (6):74-75.
- [3] Wen-jing WANG, Qi-qing YI, Wei HUANG, et al. Deflection curve analysis on cable booms [J]. Chinese Journal of Construction Machinery, 2013, (1):46-50.
- [4] Casafont Miquel, Marimon Frederic, Pastor, Maria Magdalena. Calculation of pure distortional elastic buckling loads of members subjected to compression via Calculation of pure distortional elastic buckling loads of members subjected to compression via the finite element method [J]. Thin-Walled Structures, 2009, 47(6-7):701-729.
- [5] Cheng QI. Telescopic boom optimization research based on the nonlinear bending [D]. Dalian University of Technology, 2010.
- [6] Hong-wen LIU. Mechanics of materials I [M]. Beijing: Higher Education Press, 2011.
- [7] Hong-wen LIU. Mechanics of materials II [M]. Beijing: Higher Education Press, 2011.

The Reciprocal Sums of the Pell Numbers

Fuling Zhang*

School of Mathematics and Physics, Weinan Normal University, Weinan, Shaanxi, 714099, P.R.China

*Corresponding author

Abstract—In this paper, we consider the reciprocal sums of the Pell numbers by elementary methods. First, we investigate the reciprocals sums of two products of Pell numbers. Then, we study the alternating reciprocals sums of two products of Pell numbers. Last, we consider the reciprocal sums of even and odd terms in the Pell sequence. We obtain some interesting identities involving the Pell numbers.

Keywords—pell numbers; reciprocal sum; identity

I. INTRODUCTION

Fnis defined by the second-order linear recurrence sequences

$$F_{n+2}=F_n+F_{n-1}, F_0=0, F_1=1, \quad (1.1)$$

The Fibonacci numbers can be defined by Binet's formulae $F_n=\alpha n-\beta n\alpha-\beta$, where $\alpha=1+52, \beta=1-52$, (1.2)

There are many interesting results on the properties of Fibonacci sequences; see [1–6]. Ohtsuka and Nakamura [1] studied the properties of the Fibonacci numbers and proved the following two interesting identities:

$$k=n\infty 1F_{k-1}=F_{n-2}, \quad \text{if } n \text{ is even and } n \geq 2, F_{n-2}-1, \text{ if } n \text{ is odd and } n \geq 1. \quad (1.3)$$

$$k=n\infty 1F_{k-1}=F_nF_{n-1}-1, \quad \text{if } n \text{ is even and } n \geq 2, F_nF_{n-1}, \quad \text{if } n \text{ is odd and } n \geq 1. \quad (1.4)$$

x is the floor function; that is, it denotes the greatest integer less than or equal to x.

Wang AYZ, Zhang F. [3] researched the properties of the Fibonacci numbers and proved the following four interesting identities:

$$k=nmn1F_{2k-1}=F_{2n-1}, \quad \text{if } m=2 \text{ and } n \geq 3, F_{2n-1}-1, \text{if } m \geq 3 \text{ and } n \geq 1. \quad (1.5)$$

$$k=nmn1F_{2k-1}-1=F_{2n-2}, \quad \text{For all } n \geq 1 \text{ and } m \geq 2. \quad (1.6)$$

$$k=nmn1F_{2k-1}=F_{4n-2}, \quad \text{For all } n \geq 1 \text{ and } m \geq 2. \quad (1.7)$$

$$k=nmn1F_{2k-12}-1=F_{4n-4}, \quad \text{For all } n \geq 1 \text{ and } m \geq 2. \quad (1.8)$$

Wang AYZ, Liu RN [4] demonstrated the following identities for the Fibonacci numbers

$$k=nmn1F_kF_{k-1}-1=F_{n2}, \quad \text{if } n \text{ is even, } F_{n2}-1, \quad \text{if } n \text{ is odd.} \quad (1.9)$$

$$k=nmn1F_{2k-1}-1=F_{4n-3}, \quad \text{For all } n \geq 2 \text{ and } m \geq 2. \quad (1.10)$$

Pn is also defined by the second-order are

$$P_{n+2}=2P_{n+1}+P_n, P_0=0, P_1=1. \quad (1.11)$$

The Pell numbers also provide boundless opportunities to experiment, explore, and conjecture, they are a lot of fun for inquisitive amateurs and professionals alike. The authors [7] and [8] studied the infinite sums derived from the Pell numbers and proved the following identities:

$$k=n\infty 1P_{k-1}=P_{n-1}+P_{n-2}, \quad \text{if } n \text{ is even and } n \geq 2, P_{n-1}+P_{n-2}-1, \quad \text{if } n \text{ is odd and } n \geq 1. \quad (1.12)$$

$$k=n\infty 1P_{k-2}=2P_{n-1}+P_{n-1}, \quad \text{if } n \text{ is even and } n \geq 2, 2P_{n-1}+P_n, \quad \text{if } n \text{ is odd and } n \geq 1. \quad (1.13)$$

Xu and Wang [9] proofed the following interesting identities for the Pell numbers:

$$k=n\infty 1P_{k-3}=P_{n-2}P_{n-1}+3P_nP_{n-12}+\dots+6182P_n-9182P_{n-1}, \quad \text{if } n \text{ is even and } n \geq 2, P_{n-2}P_{n-1}+3P_nP_{n-12}+\dots+6182P_n-9182P_{n-1}, \quad \text{if } n \text{ is odd and } n \geq 1. \quad (1.14)$$

Applying elementary methods, we investigate the partial finite sums of the Pell numbers in this paper, and obtain some interesting families of identities. In section 2, we consider the sums of products of two reciprocals. In section 3, we study the alternating sums of products of two reciprocals. In section 4, we consider the reciprocal sums of even and odd terms in the Pell sequence.

II. RESULTS I: THE RECIPROCAL SUMS

$x^2-2x-1=0$, the Pell numbers can be defined by Binet-like formulae:

$$P_n=\gamma n-\delta n-\delta, \quad \text{where } \gamma=1+2, \delta=1-2.$$

Using the Binet-like formulae, we can obtain properties of Pell numbers:

Lemma 2.1 Let m, n, s, t be positive integers

$$P_m P_n - P_s P_t = (-1)^{m+1} P_{n-s} P_{n-t}, \quad (n > \max\{s, t\}, m+n=s+t) \quad (2.1)$$

Lemma 2.2

$$P_m P_n + P_{m+1} P_{n+1} = P_{m+n+1}. \quad (2.2)$$

As consequence of (2.2), we have the following result:

Corollary 2.3

$$P_n^2 + P_{n+1}^2 = P_{2n+1}. \quad (2.3)$$

Corollary 2.4

$$P_{n-1}P_{n+1} + P_nP_{n+2} = P_{2n+1}. \quad (2.4)$$

Lemma 2.5

$$P_{n+1}P_{n+2} - P_{n-1}P_n = 2P_{2n+1}. \quad (2.5)$$

Proof Applying (2.4) and recursion formula of Pell numbers

$$\begin{aligned} 2P_{2n+1} &= 2P_{n-1}P_{n+1} + 2P_nP_{n+2} \\ &= (P_{n+2} - P_n)P_{n-1} + (P_{n+1} - P_{n-1})P_{n+2} \\ &= P_{n+1}P_{n+2} - P_nP_{n-1} \end{aligned}$$

Lemma 2.6

$$P_{n+2}^2 - P_n^2 = 2P_{2n+2}. \quad (2.6)$$

Proof Applying (2.3)

$$\begin{aligned} P_{n+2}^2 - P_n^2 &= P_{2n+3}^2 - P_{n+1}^2 - P_n^2 \\ &= P_{2n+3}^2 - (P_{n+1}^2 + P_n^2) \\ &= P_{2n+3}^2 - P_{2n+1}^2 \\ &= 2P_{2n+2} \end{aligned}$$

A. Reciprocal Sum of $P_k P_{k+1}$

Lemma 2.7 If $n \geq 1$,

$$2P_{2n+1}^2 + 1 > 2(P_{n+1}^2 + 1)^2 > P_nP_{n+1}(2P_{n+1}^2 + 1) \quad (2.7)$$

Proof applying (2.3)

$$2P_{2n+1}^2 + 1 = 2(P_n^2 + P_{n+1}^2)^2 + 1 > 2P_{n+1}^4 + 4P_{n+1}^2 + 2 = 2(P_{n+1}^2 + 1)^2,$$

Therefore

$$2P_{2n+1}^2 + 1 > 2(P_{n+1}^2 + 1)^2 > 2(P_{n+1}^2 + 1)P_nP_{n+1} > P_nP_{n+1}(2P_{n+1}^2 + 1).$$

Then

$$\left[\left(\sum_{k=n}^{mn} \frac{1}{P_k P_{k+1}} \right)^{-1} \right] = \begin{cases} 2P_n^2, & \text{if } n \text{ is even} \\ 2P_n^2 - 1, & \text{if } n \text{ is odd} \end{cases}$$

Proof applying (2.1)

$$\frac{1}{2P_k^2} - \frac{1}{P_k P_{k+1}} - \frac{1}{2P_{k+1}^2} = \frac{P_{k+1}^2 - 2P_k P_{k+1} - P_k^2}{2P_k^2 P_{k+1}^2} = \frac{P_{k-1} P_{k+1} - P_k^2}{2P_k^2 P_{k+1}^2} = \frac{(-1)^k}{2P_k^2 P_{k+1}^2}, \quad (2.8)$$

Therefore

$$\frac{1}{P_k P_{k+1}} = \frac{1}{2P_k^2} - \frac{1}{2P_{k+1}^2} + \frac{(-1)^{k-1}}{2P_k^2 P_{k+1}^2}, \quad (2.9)$$

Now we have

$$\sum_{k=n}^{mn} \frac{1}{P_k P_{k+1}} = \frac{1}{2P_n^2} - \frac{1}{2P_{mn+1}^2} + \sum_{k=n}^{mn} \frac{(-1)^{k-1}}{2P_k^2 P_{k+1}^2}, \quad (2.10)$$

If n is even, it is easy to see that

$$\sum_{k=n}^{mn} \frac{(-1)^{k-1}}{2P_k^2 P_{k+1}^2} < 0$$

By the above equation (2.10)

$$\sum_{k=n}^{mn} \frac{1}{P_k P_{k+1}} < \frac{1}{2P_n^2}. \quad (2.11)$$

For any $k \geq 1$

$$\begin{aligned} \frac{1}{2P_k^2 + 1} - \frac{1}{P_k P_{k+1}} - \frac{1}{2P_{k+1}^2 + 1} &= \frac{(2P_{k+1}^2 + 1)P_k P_{k+1} - (2P_k^2 + 1)(2P_{k+1}^2 + 1) - (2P_k^2 + 1)P_k P_{k+1}}{(2P_k^2 + 1)P_k P_{k+1}(2P_{k+1}^2 + 1)} \\ &= \frac{(2P_{k+1}^2 - 2P_k^2)P_k P_{k+1} - (2P_k^2 + 1)(2P_{k+1}^2 + 1)}{(2P_k^2 + 1)P_k P_{k+1}(2P_{k+1}^2 + 1)} \\ &= \frac{(-1)^k 2P_k P_{k+1} - 2P_k^2 - 2P_{k+1}^2 - 1}{(2P_k^2 + 1)P_k P_{k+1}(2P_{k+1}^2 + 1)} < 0. \end{aligned} \quad (2.12)$$

Then

$$\frac{1}{P_k P_{k+1}} = \frac{1}{2P_k^2 + 1} - \frac{1}{2P_{k+1}^2 + 1} + \frac{(-1)^{k-1} 2P_k P_{k+1} + 2P_k^2 + 2P_{k+1}^2 + 1}{(2P_k^2 + 1)P_k P_{k+1}(2P_{k+1}^2 + 1)},$$

So

$$\begin{aligned} \sum_{k=n}^{mn} \frac{1}{P_k P_{k+1}} &= \frac{1}{2P_n^2 + 1} - \frac{1}{2P_{mn+1}^2 + 1} + \sum_{k=n}^{mn} \frac{(-1)^{k-1} 2P_k P_{k+1} + 2P_k^2 + 2P_{k+1}^2 + 1}{(2P_k^2 + 1) P_k P_{k+1} (2P_{k+1}^2 + 1)} \\ &> \frac{1}{2P_n^2 + 1} - \frac{1}{2P_{2n+1}^2 + 1} + \frac{(-1)^{n-1} 2P_n P_{n+1} + 2P_n^2 + 2P_{n+1}^2 + 1}{(2P_n^2 + 1) P_n P_{n+1} (2P_{n+1}^2 + 1)} \\ &> \frac{1}{2P_n^2 + 1} - \frac{1}{2P_{2n+1}^2 + 1} + \frac{1}{P_n P_{n+1} (2P_{n+1}^2 + 1)}, \end{aligned}$$

Using (2.7)

$$\sum_{k=n}^{mn} \frac{1}{P_k P_{k+1}} > \frac{1}{2P_n^2 + 1}, \quad (2.13)$$

Combining (2.11) and (2.13), we have

$$\frac{1}{2P_n^2 + 1} < \sum_{k=n}^{mn} \frac{1}{P_k P_{k+1}} < \frac{1}{2P_n^2},$$

which means that the statement is true when n is even

$$\left\lfloor \left(\sum_{k=n}^{mn} \frac{1}{P_k P_{k+1}} \right)^{-1} \right\rfloor = 2P_n^2. \quad (2.14)$$

If n is odd, a similar calculation show that, for $k \geq 1$

$$\begin{aligned} \frac{1}{2P_k^2 - 1} - \frac{1}{2P_{k+1}^2 - 1} &= \frac{(2P_{k+1}^2 - 1) P_k P_{k+1} - (2P_k^2 - 1)(2P_{k+1}^2 - 1) - (2P_k^2 - 1) P_k P_{k+1}}{(2P_k^2 - 1) P_k P_{k+1} (2P_{k+1}^2 - 1)} \\ &= \frac{(2P_{k+1}^2 - 2P_k^2) P_k P_{k+1} - (2P_k^2 - 1)(2P_{k+1}^2 - 1)}{(2P_k^2 - 1) P_k P_{k+1} (2P_{k+1}^2 - 1)} \\ &= \frac{(-1)^k 2P_k P_{k+1} + 2P_k^2 + 2P_{k+1}^2 - 1}{(2P_k^2 - 1) P_k P_{k+1} (2P_{k+1}^2 - 1)} > 0, \end{aligned} \quad (2.15)$$

So

$$\frac{1}{P_k P_{k+1}} = \frac{1}{2P_k^2 - 1} - \frac{1}{2P_{k+1}^2 - 1} - \frac{(-1)^k 2P_k P_{k+1} + 2P_k^2 + 2P_{k+1}^2 - 1}{(2P_k^2 - 1) P_k P_{k+1} (2P_{k+1}^2 - 1)},$$

From which we get

$$\sum_{k=n}^{mn} \frac{1}{P_k P_{k+1}} = \frac{1}{2P_n^2 - 1} - \frac{1}{2P_{mn+1}^2 - 1} - \sum_{k=n}^{mn} \frac{(-1)^k 2P_k P_{k+1} + 2P_k^2 + 2P_{k+1}^2 - 1}{(2P_k^2 - 1) P_k P_{k+1} (2P_{k+1}^2 - 1)},$$

Hence

$$\sum_{k=n}^{mn} \frac{1}{P_k P_{k+1}} < \frac{1}{2P_n^2 - 1}. \quad (2.16)$$

With (2.10) and (2.6),

$$\begin{aligned} \sum_{k=n}^{mn} \frac{1}{P_k P_{k+1}} &= \frac{1}{2P_n^2} - \frac{1}{2P_{mn+1}^2} + \sum_{k=n}^{mn} \frac{(-1)^{k-1}}{2P_k^2 P_{k+1}^2} \\ &> \frac{1}{2P_n^2} - \frac{1}{2P_{2n+1}^2} + \frac{1}{2P_n^2 P_{n+1}^2} - \frac{1}{2P_{mn+1}^2 P_{n+2}^2} = \frac{1}{2P_n^2} + \frac{2P_{2n+2}}{2P_n^2 P_{n+1}^2 P_{n+2}^2} - \frac{2P_{2n+2}}{2P_{2n+1}^2 P_{2n+2}^2}. \end{aligned}$$

According to (2.2) and (2.3)

$$P_{2n+1} = P_{n-1} P_{n+1} + P_n P_{n+2} = P_n^2 + P_{n+1}^2,$$

So

$$P_{2n+1} > P_n P_{n+2}, \text{ and } P_{2n+2} > P_{2n+1} > P_{n+1}^2,$$

Hence

$$2^2 P_{2n+2} P_{2n+1}^2 > 2P_n^2 P_{n+1}^2 P_{n+2}^2,$$

As a result

$$\sum_{k=n}^{mn} \frac{1}{P_k P_{k+1}} > \frac{1}{2P_n^2}, \quad (2.17)$$

Combining (2.11) and (2.13),

$$\frac{1}{2P_n^2} < \sum_{k=n}^{mn} \frac{1}{P_k P_{k+1}} < \frac{1}{2P_n^2 - 1},$$

When n is odd, that the statement is true

$$\left\lfloor \left(\sum_{k=n}^{mn} \frac{1}{P_k P_{k+1}} \right)^{-1} \right\rfloor = 2P_n^2 - 1. \quad (2.18)$$

On the basis of (2.14) and (2.18), we have the theorem 2.8.

Corollary 2.9

$$\left\lfloor \left(\sum_{k=n}^{\infty} \frac{1}{P_k P_{k+1}} \right)^{-1} \right\rfloor = \begin{cases} 2P_n^2, & \text{if } n \text{ is even} \\ 2P_n^2 - 1, & \text{if } n \text{ is odd} \end{cases}.$$

Proof applying (2.8), if n is even

$$\frac{1}{2P_k^2} - \frac{1}{P_k P_{k+1}} - \frac{1}{2P_{k+1}^2} = \frac{(-1)^k}{2P_k^2 P_{k+1}^2} > 0,$$

Hence

$$\frac{1}{2P_k^2} > \frac{1}{P_k P_{k+1}} + \frac{1}{2P_{k+1}^2} > \frac{1}{P_k P_{k+1}} + \frac{1}{P_{k+1} P_{k+2}} + \frac{1}{2P_{k+2}^2} > \dots,$$

So

$$\sum_{k=n}^{\infty} \frac{1}{P_k P_{k+1}} < \frac{1}{2P_n^2}; \quad (2.19)$$

In line with (2.12)

$$\frac{1}{2P_k^2 + 1} - \frac{1}{P_k P_{k+1}} - \frac{1}{2P_{k+1}^2 + 1} < 0,$$

Therefore

$$\frac{1}{2P_k^2 + 1} < \frac{1}{P_k P_{k+1}} + \frac{1}{2P_{k+1}^2 + 1} < \frac{1}{P_k P_{k+1}} + \frac{1}{P_{k+1} P_{k+2}} + \frac{1}{2P_{k+2}^2 + 1} < \dots,$$

As a result

$$\frac{1}{2P_n^2 + 1} < \sum_{k=n}^{\infty} \frac{1}{P_k P_{k+1}}, \quad (2.20)$$

Combining (2.19) and (2.20), when n is even, the statement is true

$$\frac{1}{2P_n^2 + 1} < \sum_{k=n}^{\infty} \frac{1}{P_k P_{k+1}} < \frac{1}{2P_n^2}. \quad (2.21)$$

With (2.8), when n is odd,

$$\frac{1}{2P_k^2} - \frac{1}{P_k P_{k+1}} - \frac{1}{2P_{k+1}^2} = \frac{(-1)^k}{2P_k^2 P_{k+1}^2} < 0,$$

So

$$\frac{1}{2P_k^2} < \frac{1}{P_k P_{k+1}} + \frac{1}{2P_{k+1}^2} < \frac{1}{P_k P_{k+1}} + \frac{1}{P_{k+1} P_{k+2}} + \frac{1}{2P_{k+2}^2} < \dots,$$

Hence

$$\frac{1}{2P_n^2} < \sum_{k=n}^{\infty} \frac{1}{P_k P_{k+1}}, \quad (2.22)$$

On the basis of (2.15)

$$\frac{1}{2P_k^2 - 1} - \frac{1}{P_k P_{k+1}} - \frac{1}{2P_{k+1}^2 - 1} > 0,$$

Therefore

$$\frac{1}{2P_k^2 - 1} > \frac{1}{G_k G_{k+1}} + \frac{1}{2P_{k+1}^2 - 1} > \frac{1}{P_k P_{k+1}} + \frac{1}{P_{k+1} P_{k+2}} + \frac{1}{2P_{k+2}^2 - 1} > \dots,$$

So

$$\sum_{k=n}^{\infty} \frac{1}{P_k P_{k+1}} < \frac{1}{2P_n^2 - 1}, \quad (2.23)$$

Combining (2.22) and (2.23), when n is odd, the statement is true

$$\frac{1}{2P_n^2} < \sum_{k=n}^{\infty} \frac{1}{P_k P_{k+1}} < \frac{1}{2P_n^2 - 1}. \quad (2.24)$$

Accordance with (2.21) and (2.24), we have the Corollary 2.9.

III. MAIN RESULTS II: ALTERNATING RECIPROCAL SUMS

Lemma 3.1

$$\frac{P_{2n+2}}{P_{2n+1}} - \frac{P_{mn+2}}{P_{mn+1}} < 0 \quad . \quad (3.1)$$

Proof applying (2.1),

$$\frac{P_{2n+2}}{P_{2n+1}} - \frac{P_{mn+2}}{P_{mn+1}} = \frac{P_{2n+2} P_{mn+1} - P_{2n+1} P_{mn+2}}{P_{2n+1} P_{mn+1}} = (-1)^{2n+1} \frac{P_{(m-2)n+1}}{P_{2n+1} P_{mn+1}} < 0.$$

As a similar way, we have

Lemma 3.2

$$\frac{P_{2n+1}}{P_{2n}} - \frac{P_{mn+2}}{P_{mn+1}} < 0 \quad . \quad (3.2)$$

Lemma 3.3

$$\frac{1}{P_{2n}-1} - \frac{P_{n+1}}{P_n P_{2n+1}} = \frac{(-1)^{n+1} P_n + P_{n+1}}{(P_{2n}-1) P_n P_{2n+1}} > 0 \quad . \quad (3.3)$$

Lemma 3.4

$$\frac{1}{P_{2n}+1} - \frac{P_{n+1}}{P_n P_{2n+1}} = \frac{(-1)^{n+1} P_n - P_{n+1}}{(P_{2n}-1) P_n P_{2n+1}} < 0 \quad . \quad (3.4)$$

Lemma 3.5

$$\frac{P_{n+1}}{P_n} - \frac{1}{P_{2n}} = \frac{P_{2n+1} + (-1)^{n+1} - 1}{P_{2n}} \quad . \quad (3.5)$$

Proof combining (2.1), (2.2) and (2.3),

$$\begin{aligned} \frac{P_{n+1}}{P_n} - \frac{1}{P_{2n}} &= \frac{P_{2n} P_{n+1} - P_n}{P_n P_{2n}} = \frac{(P_{n-1} P_n + P_n P_{n+1}) P_{n+1} - P_n}{P_n P_{2n}} = \frac{P_{n-1} P_{n+1} + P_{n+1}^2 - 1}{P_{2n}} \\ &= \frac{(P_{n-1} P_{n+1} - P_n^2) + (P_n^2 + P_{n+1}^2) - 1}{P_{2n}} = \frac{P_{2n+1} + (-1)^n - 1}{P_{2n}}. \end{aligned}$$

Use the same way, we have

Lemma 3.6

$$\frac{P_{n+1}}{P_n} + \frac{1}{P_{2n}} = \frac{P_{2n+1} + (-1)^n + 1}{P_{2n}} \quad . \quad (3.6)$$

Theorem

$$\left[\left(\sum_{k=n}^{mn} \frac{(-1)^k}{P_k P_{k+1}} \right)^{-1} \right] = \begin{cases} P_{2n} - 1, & \text{if } n \text{ is even} \\ -P_{2n} - 1, & \text{if } n \text{ is odd} \end{cases} \quad . \quad (3.7)$$

Proof applying (2.1),

$$\frac{(-1)^k}{P_k P_{k+1}} = \frac{P_{k+1}^2 - P_k P_{k+2}}{P_k P_{k+1}} = \frac{P_{k+1}}{P_k} - \frac{P_{k+2}}{P_{k+1}},$$

So

$$\sum_{k=n}^{mn} \frac{(-1)^k}{P_k P_{k+1}} = \sum_{k=n}^{mn} \left(\frac{P_{k+1}}{P_k} - \frac{P_{k+2}}{P_{k+1}} \right) = \frac{P_{n+1}}{P_n} - \frac{P_{mn+2}}{P_{mn+1}}, \quad (3.7)$$

If n is even, with (3.1) and (2.1)

$$\frac{P_{n+1}}{P_n} - \frac{P_{mn+2}}{P_{mn+1}} < \frac{P_{n+1}}{P_n} - \frac{P_{2n+2}}{P_{2n+1}} = \frac{P_{2n+1} P_{n+1} - P_{2n+2} P_n}{P_n P_{2n+1}} = \frac{(-1)^n P_{n+1}}{P_n P_{2n+1}} = \frac{P_{n+1}}{P_n P_{2n+1}},$$

On the basis of (3.3)

$$\frac{P_{n+1}}{P_n} - \frac{P_{mn+2}}{P_{mn+1}} < \frac{P_{n+1}}{P_n P_{2n+1}} < \frac{1}{P_{2n} - 1}; \quad (3.8)$$

According to (3.5) and (3.2)

$$\begin{aligned} \frac{P_{n+1}}{P_n} - \frac{1}{P_{2n}} - \frac{P_{mn+2}}{P_{mn+1}} &= \frac{P_{2n+1}}{P_{2n}} - \frac{P_{mn+2}}{P_{mn+1}} + \frac{(-1)^{n+1} - 1}{P_{2n}} = \frac{P_{2n+1}}{P_{2n}} - \frac{P_{mn+2}}{P_{mn+1}}; \\ \frac{P_{n+1}}{P_n} - \frac{P_{mn+2}}{P_{mn+1}} &> \frac{1}{P_{2n}}, \end{aligned} \quad (3.9)$$

Combining (3.7), (3.8) and (3.9), when n is even, the statement is true

$$\left[\left(\sum_{k=n}^{mn} \frac{(-1)^k}{P_k P_{k+1}} \right)^{-1} \right] = P_{2n} - 1 \quad . \quad (3.10)$$

If n is even, with (3.1) and (2.1)

$$\frac{P_{n+1}}{P_n} - \frac{P_{mn+2}}{P_{mn+1}} < \frac{P_{n+1}}{P_n} - \frac{P_{2n+2}}{P_{2n+1}} = \frac{P_{2n+1} P_{n+1} - P_{2n+2} P_n}{P_n P_{2n+1}} = \frac{(-1)^n P_{n+1}}{P_n P_{2n+1}} = -\frac{P_{n+1}}{P_n P_{2n+1}},$$

Applying (3.4)

$$\frac{P_{n+1}}{P_n} - \frac{P_{mn+2}}{P_{mn+1}} < -\frac{1}{P_{2n} + 1}, \quad (3.11)$$

Using (3.6) and (3.2)

$$\frac{P_{n+1}}{P_n} + \frac{1}{P_{2n}} = \frac{P_{2n+1} + (-1)^{n+1} + 1}{P_{2n}} = \frac{P_{2n+1}}{P_{2n}},$$

$$\frac{P_{n+1}}{P_n} + \frac{1}{P_{2n}} - \frac{P_{mn+2}}{P_{mn+1}} = \frac{P_{2n+1}}{P_{2n}} - \frac{P_{mn+2}}{P_{mn+1}} > 0,$$

Hence

$$\frac{P_{n+1}}{P_n} - \frac{P_{mn+2}}{P_{mn+1}} > -\frac{1}{P_{2n}}, \quad (3.12)$$

Combining (3.7), (3.11) and (3.12), when n is odd, the statement is true

$$-\frac{1}{P_{2n}} < \sum_{k=n}^{mn} \frac{(-1)^k}{P_k P_{k+1}} = \frac{P_{n+1}}{P_n} - \frac{P_{mn+2}}{P_{mn+1}} < -\frac{1}{P_{2n} + 1},$$

Therefore

$$\left\lfloor \left(\sum_{k=n}^{mn} \frac{(-1)^k}{P_k P_{k+1}} \right)^{-1} \right\rfloor = -P_{2n} - 1 \quad (3.13)$$

According to (3.10) and (3.13), we established the theorem 3.7.

IV. MAIN RESULTS III: THE RECIPROCAL SUMS OF EVEN AND ODD TERMS

Theorem 4.1 If $m \geq 3$ and $n \geq 1$,

$$\left\lfloor \left(\sum_{k=n}^{mn} \frac{1}{P_{2k}} \right)^{-1} \right\rfloor = 2P_{2n-1} - 1$$

Proof applying (2.1), or $k \geq 2$

$$\frac{1}{2P_{2k-1}-1} - \frac{1}{P_{2k}} - \frac{1}{2P_{2k+1}-1} = \frac{2(P_{2k+1} - P_{2k-1})P_{2k} - (2P_{2k-1} - 1)(2P_{2k+1} - 1)}{(2P_{2k-1} - 1)P_{2k}(2P_{2k+1} - 1)} = \frac{2P_{2k-1} + 2P_{2k+1} - 5}{(2P_{2k-1} - 1)P_{2k}(2P_{2k+1} - 1)} > 0$$

$$\frac{1}{2P_{2k-1}-1} - \frac{1}{P_{2k}} - \frac{1}{2P_{2k+1}-1} = \frac{2P_{2k-1} + 2P_{2k+1} - 5}{(2P_{2k-1} - 1)P_{2k}(2P_{2k+1} - 1)} > 0 \quad (4.1)$$

Which implies that

$$\frac{1}{P_{2k}} = \frac{1}{2P_{2k-1}-1} - \frac{1}{2P_{2k+1}-1} - \frac{2P_{2k-1} + 2P_{2k+1} - 5}{(2P_{2k-1} - 1)P_{2k}(2P_{2k+1} - 1)} < \frac{1}{2P_{2k-1}-1} - \frac{1}{2P_{2k+1}-1},$$

So

$$\sum_{k=n}^{mn} \frac{1}{P_{2k}} < \frac{1}{2P_{2n-1}-1} - \frac{1}{2P_{2mn+1}-1} < \frac{1}{2P_{2n-1}-1} \quad (4.2)$$

From (2.1) we obtain

$$\frac{1}{2P_{2k-1}} - \frac{1}{P_{2k}} - \frac{1}{2P_{2k+1}} = \frac{P_{2k+1}P_{2k} - 2P_{2k-1}P_{2k+1} - P_{2k-1}P_{2k}}{2P_{2k-1}P_{2k}P_{2k+1}} = \frac{-1}{P_{2k-1}P_{2k}P_{2k+1}} \quad (4.3)$$

Hence

$$\frac{1}{P_{2k}} = \frac{1}{2P_{2k-1}} - \frac{1}{2P_{2k+1}} + \frac{1}{P_{2k-1}P_{2k}P_{2k+1}},$$

Therefore

$$\sum_{k=n}^{mn} \frac{1}{P_{2k}} = \frac{1}{2P_{2n-1}} - \frac{1}{2P_{2mn+1}} + \sum_{k=n}^{mn} \frac{1}{P_{2k-1}P_{2k}P_{2k+1}} > \frac{1}{2P_{2n-1}} - \frac{1}{2P_{2mn+1}} + \frac{1}{P_{2n-1}P_{2n}P_{2n+1}} \quad (4.4)$$

For all $n \geq 1, m \geq 3$, with (2.2)

$$P_{m-1}P_n + P_mP_{n+1} = P_{m+n}, \quad P_{m+n} > P_mP_{n+1} > P_mP_n,$$

Which implies that

$$P_{2n-1}P_{2n}P_{2n+1} < P_{6n+1} < P_{2mn+1},$$

With (4.4)

$$\sum_{k=n}^{mn} \frac{1}{P_{2k}} > \frac{1}{2P_{2n-1}} - \frac{1}{2P_{2mn+1}} + \frac{1}{P_{2n-1}P_{2n}P_{2n+1}} > \frac{1}{2P_{2n-1}} \quad (4.5)$$

According to (4.2) and (4.5), we established the theorem 4.1.

Corollary 4.2

$$\left\lfloor \left(\sum_{k=n}^{\infty} \frac{1}{P_{2k}} \right)^{-1} \right\rfloor = 2P_{2n-1} - 1.$$

Theorem 4.3 If $m \geq 2$ and $n \geq 1$,

$$\left\lfloor \left(\sum_{k=n}^{mn} \frac{1}{P_{2k-1}} \right)^{-1} \right\rfloor = 2P_{2n-2}.$$

Proof applying (2.1), or $k \geq 2$

$$\frac{1}{2P_{2k-2}} - \frac{1}{P_{2k-1}} - \frac{1}{2P_{2k}} = \frac{P_{2k-1}P_{2k} - 2P_{2k-2}P_{2k} - P_{2k-2}P_{2k-1}}{2P_{2k-2}P_{2k-1}P_{2k}} = \frac{1}{P_{2k-1}P_{2k}P_{2k+1}} > 0, \quad (4.6)$$

$$\frac{1}{P_{2k-1}} = \frac{1}{2P_{2k-2}} - \frac{1}{2P_{2k}} - \frac{1}{P_{2k-2}P_{2k-1}P_{2k}} < \frac{1}{2P_{2k-2}} - \frac{1}{2P_{2k}},$$

$$\sum_{k=n}^{mn} \frac{1}{P_{2k-1}} < \frac{1}{2P_{2n-2}} - \frac{1}{2P_{2mn}} < \frac{1}{2P_{2n-2}} \quad (4.7)$$

$$\frac{1}{2P_{2k-2}+1} - \frac{1}{P_{2k-1}} - \frac{1}{2P_{2k}+1} = \frac{2(P_{2k} - P_{2k-2})P_{2k-1} - (2P_{2k-2} + 1)(2P_{2k} + 1)}{(2P_{2k-2} + 1)P_{2k-1}(2P_{2k} + 1)} = \frac{2^2 - 2P_{2k-2} - 2P_{2k} - 1}{(2P_{2k-2} + 1)P_{2k-1}(2P_{2k} + 1)} < 0$$

$$\sum_{k=n}^{mn} \frac{1}{P_{2k-1}} = \frac{1}{2P_{2n-2}+1} - \frac{1}{2P_{2mn}+1} + \sum_{k=n}^{mn} \frac{2P_{2k-2} + 2P_{2k} + 1 - 2^2}{(2P_{2k-2} + 1)P_{2k-1}(2P_{2k} + 1)},$$

$$\sum_{k=n}^{mn} \frac{1}{P_{2k-1}} > \frac{1}{2P_{2n-2}+1} - \frac{1}{2P_{2mn}+1} + \frac{2P_{2n-2} + 2P_{2n} + 1 - 2^2}{(2P_{2n-2} + 1)P_{2n-1}(2P_{2n} + 1)},$$

By reason of

$$\frac{2P_{2n-2}+2P_{2n}+1-2^2}{(2P_{2n-2}+1)P_{2n-1}(2P_{2n}+1)} > \frac{2P_n+1}{(2P_{2n-2}+1)P_{2n-1}(2P_n+1)} > \frac{1}{(2P_{2n-2}+1)P_{2n-1}} > \frac{1}{2P_{4n}+1} > \frac{1}{2P_{2mn}+1},$$

Hence

$$\sum_{k=n}^{mn} \frac{1}{P_{2k-1}} > \frac{1}{2P_{2n-2}+1} \quad (4.8)$$

According to (4.7) and (4.8), the theorem 4.3 is true.

$$\text{Corollary 4.4} \quad \left\lfloor \left(\sum_{k=n}^{\infty} \frac{1}{P_{2k-1}} \right)^{-1} \right\rfloor = 2P_{2n-2}.$$

Theorem 4.5 If $m \geq 2$ and $n \geq 1$,

$$\left\lfloor \left(\sum_{k=n}^{\infty} \frac{1}{P_{2k}^2} \right)^{-1} \right\rfloor = 2P_{4n-2} - 1.$$

Proof applying (2.1) and (2.4)

$$P_{2k}^2 - P_{2k-2}^2 = 2P_{4k-2}, \quad (4.9)$$

$$P_{2k+2}^2 - P_{2k}^2 = 2P_{4k+2}, \quad (4.10)$$

$$P_{2k-1}^2 P_{2k+1}^2 - P_{2k-2}^2 P_{2k+2}^2 = 5(P_{2k}^2 + P_{2k-1} P_{2k+1} - 4), \quad (4.11)$$

According to (4.9), (4.10) and (4.11)

$$\frac{1}{2P_{2k-2}} - \frac{1}{P_{2k-1}} - \frac{1}{2P_{2k}} = \frac{P_{2k-1}P_{2k} - 2P_{2k-2}P_{2k} - P_{2k-2}P_{2k-1}}{2P_{2k-2}P_{2k-1}P_{2k}} = \frac{1}{P_{2k-1}P_{2k}P_{2k+1}} > 0$$

Hence

$$\frac{1}{2P_{4k-2}-1} - \frac{1}{P_{2k}^2} - \frac{1}{2P_{4k+2}-1} > 0, \quad (4.12)$$

Therefore

$$\sum_{k=n}^{mn} \frac{1}{P_{2k}^2} < \frac{1}{2P_{4n-2}-1} - \frac{1}{2P_{4mn+2}-1} < \frac{1}{2P_{4n-2}-1} \quad (4.13)$$

For all $k \geq 2$,

$$\begin{aligned} \frac{1}{2P_{4k-2}} - \frac{1}{P_{2k}^2} - \frac{1}{2P_{4k+2}} &= \frac{P_{2k}^2(P_{4k+2} - P_{4k-2}) - 2P_{4k-2}P_{4k+2}}{2G_{4k-2}G_{2k}^2G_{4k+2}} \\ &= \frac{-(4P_{2k}^2 - 4P_{2k-1}P_{2k+1})}{P_{4k-2}P_{2k}^2P_{4k+2}} < \frac{-1}{P_{4k-2}P_{4k+2}} < 0 \end{aligned} \quad (4.14)$$

From which we obtain

$$\sum_{k=n}^{mn} \frac{1}{P_{2k}^2} > \frac{1}{2P_{4n-2}} - \frac{1}{2P_{4mn+2}} + \sum_{k=n}^{mn} \frac{1}{P_{4k-2}P_{4k+2}} > \frac{1}{2P_{4n-2}} - \frac{1}{2P_{4mn+2}} + \frac{1}{P_{4n-2}P_{4n+2}}$$

Applying (2.4)

$$2P_{8n+2} = P_{4n+2}^2 - P_{4n}^2 = 2P_{4n+1}(P_{4n+2} + P_{4n}) > 2P_{4n+1}P_{4n+2} > 2P_{4n+2}P_{4n-2}$$

So

$$\sum_{k=n}^{mn} \frac{1}{P_{2k}^2} > \frac{1}{2P_{4n-2}} \quad (4.15)$$

Combining (4.13) and (4.15), we have theorem 4.5

$$\text{Corollary 4.6} \quad \left\lfloor \left(\sum_{k=n}^{\infty} \frac{1}{P_{2k}^2} \right)^{-1} \right\rfloor = 2P_{4n-2} - 1.$$

Theorem 4.7 If $m \geq 2$ and $n \geq 1$,

$$\left\lfloor \left(\sum_{k=n}^{mn} \frac{1}{P_{2k-1}^2} \right)^{-1} \right\rfloor = 2P_{4n-4}.$$

Proof by the calculation of (2.4), we obtain, $k \geq 2$

$$P_{2k+1}^2 - P_{2k-1}^2 = 2P_{4k} \quad (4.16)$$

$$P_{2k-1}^2 - P_{2k-3}^2 = 2P_{4k-4} \quad (4.17)$$

From (4.16) and (4.17)

$$\begin{aligned} &P_{2k-1}^2(P_{4k} - P_{4k-4}) - 2P_{4k}P_{4k-4} \\ &= \frac{1}{2}P_{2k-1}^2(P_{2k+1}^2 - 2P_{2k-1}^2 + P_{2k-3}^2) - \frac{1}{2}(P_{2k+1}^2 - P_{2k-1}^2)(P_{2k-1}^2 - P_{2k-3}^2) \\ &= \frac{1}{2}(P_{2k+1}P_{2k-3} - P_{2k-1}^2)(P_{2k+1}P_{2k-3} + P_{2k-1}^2) \\ &= 2(P_{2k+1}P_{2k-3} + P_{2k-1}^2) \end{aligned} \quad (4.18)$$

By (4.16), (4.17) and (4.18)

$$\frac{1}{2P_{4k-4}} - \frac{1}{P_{2k-1}^2} - \frac{1}{2P_{4k}} = \frac{P_{2k-1}^2(P_{4k} - P_{4k-4}) - 2P_{4k}P_{4k-4}}{2P_{4k-4}P_{2k-1}^2P_{4k}} = \frac{P_{2k+1}P_{2k-3} + P_{2k-1}^2}{P_{4k-4}P_{2k-1}^2P_{4k}} > 0,$$

Which implies

$$\frac{1}{P_{2k-1}^2} < \frac{1}{2P_{4k-4}} - \frac{1}{2P_{4k}}$$

Hence

$$\sum_{k=n}^{mn} \frac{1}{P_{2k-1}^2} < \frac{1}{2P_{4n-4}} - \frac{1}{2P_{4mn}} < \frac{1}{2P_{4n-4}}, \quad (4.19)$$

$$\begin{aligned} \frac{1}{2P_{4k-4}+1} - \frac{1}{P_{2k-1}^2} - \frac{1}{2P_{4k}+1} &= \frac{2(P_{4k}-P_{4k-4})P_{2k-1}^2 - (2P_{4k-4}+1)2(aP_{4k}+1)}{(2P_{4k-4}+1)P_{2k-1}^2 2(aP_{4k}+1)} \\ &= \frac{2^2(P_{2k+1}P_{2k-3} + P_{2k-1}^2) - (P_{2k+1}^2 - P_{2k-3}^2) - 1}{(2P_{4k-4}+1)P_{2k-1}^2 (2P_{4k}+1)} \end{aligned}$$

By reason of

$$P_{2k+1}P_{2k-3} + P_{2k-1}^2 = (2P_{2k} - P_{2k-1})(P_{2k-1} - 2P_{2k-2}) + P_{2k-1}^2 = 5P_{2k-1}^2 + 4,$$

$$P_{2k+1}^2 - P_{2k-3}^2 = 12P_{2k-1}(P_{2k} + P_{2k-2}) > 24P_{2k-1}^2 + 16,$$

Therefore

$$2^2(P_{2k+1}P_{2k-3} + P_{2k-1}^2) - (P_{2k+1}^2 - P_{2k-3}^2) - 1 < -P_{2k-1}^2.$$

So

$$\frac{1}{2P_{4k-4}+1} - \frac{1}{P_{2k-1}^2} - \frac{1}{2P_{4k}+1} < \frac{-1}{(2P_{4k-4}+1)(2P_{4k}+1)} < 0 \quad (4.20)$$

$$\frac{1}{P_{2k-1}^2} > \frac{1}{2P_{4k-4}+1} - \frac{1}{2P_{4k}+1} + \frac{1}{(2P_{4k-4}+1)(2P_{4k}+1)},$$

$$\begin{aligned} \sum_{k=n}^{mn} \frac{1}{P_{2k-1}^2} &> \frac{1}{2P_{4n-4}+1} - \frac{1}{2P_{4mn}+1} + \sum_{k=n}^{mn} \frac{1}{(2P_{4k-4}+1)(2P_{4k}+1)} \\ &> \frac{1}{2P_{4n-4}+1} - \frac{1}{2P_{4mn}+1} + \frac{1}{(2P_{4n-4}+1)(2P_{4n}+1)}, \end{aligned}$$

Also because

$$(2P_{4n-4}+1)(2P_{4n}+1) = 2^2 P_{4n-4} P_{4n} + 2P_{4n-4} + 2P_{4n} + 1 < P_{8n} + 1$$

So

$$\sum_{k=n}^{mn} \frac{1}{P_{2k-1}^2} > \frac{1}{2P_{4n-4}+1} \quad (4.21)$$

Combining (4.19) and (4.21), the statement is true

$$\left\lfloor \left(\sum_{k=n}^{mn} \frac{1}{P_{2k-1}^2} \right)^{-1} \right\rfloor = 2P_{4n-4}$$

$$\text{Corollary 4.8 } \left\lfloor \left(\sum_{k=n}^{\infty} \frac{1}{P_{2k-1}^2} \right)^{-1} \right\rfloor = 2P_{4n-4}.$$

ACKNOWLEDGEMENT

This research was financially supported by the Special projects of scientific research of education department of Shaanxi Provincial (15JK1262).

REFERENCES

- [1] Ohtsuka H, Nakamura S. On the sum of reciprocal Fibonacci numbers[J]. Fibonacci Quart.46/47(2008/2009),153-159.
- [2] Wang AYZ, Wen PB. On the partial finite sums of the reciprocals of the Fibonacci numbers[J]. Inequal.Appl.2015, (1),1-13. DOI:10.1186/s13660-015-0595-6.
- [3] Wang AYZ, Zhang F. The reciprocal sums of even and odd terms in the Fibonacci sequence[J]. Inequal.Appl.2015 (1),1-13.DOI:10.1186/s13660-015-0902-2.
- [4] Wang AYZ, Liu RN. Sums of products of two reciprocal Fibonacci numbers[J]. Adv.Differ.Equ.2016, 2016(1),1-26. DOI:10.1186/s13662-016-0860-0.
- [5] Wang,AYZ,Zhang,F.The reciprocal sums of the Fibonacci3-subsequences[J].Adv.Differ.Equ.2016-2016(1),1-15. DOI:10.1186/s13662-016-0761-2.
- [6] SarahH. Holliday, Takao. Komatsu. On the Sum of Reciprocal Generalized Fibonacci Numbers[J].Integers.2011,11(4),441-455.
- [7] Z. Wenpeng and W.Tingting.The infinite sum of reciprocal Pell numbers[J]. Applied Mathematics and Computation, vol. 218, no. 10, pp. 6164-6167, 2012.
- [8] W. Zhang and T. Wang.The infinite sum of reciprocal of the square of the Pell numbers[J]. Journal of Weinan Teacher's University, vol. 26, pp. 39-42, 2011.
- [9] Z. Xu and T. Wang. The infinite sum of the cubes of reciprocal Pell numbers, [J]. Advances in Difference Equations, vol. 2013, article 184, 2013.

Tests for Spatial Correlation of Dependent Variables in Spatial Dynamic Panel Data Models

Rong Sun*

Dept of Math and statistics, Chongqing University of Technology and Business, Chongqing, 400067, China

*Corresponding author

Abstract—This paper considers a spatial dynamic panel data regression model with fixed effects, spatial correlation of dependent variables and error serial among cross sectional units. When the number of individuals n , the number of time periods T are large, and T is asymptotically large relative to n , the paper derives various Lagrange multiplier tests and likelihood ratio test statistics for this panel data regression model including tests for spatial correlation of dependent variables in jointly, marginally or conditionally (one-dimensional and two-dimensional). Limiting null distributions of the tests are derived.

Keywords—dynamic spatial panel data; spatial correlation; lagrange multiplier tests; likelihood ratio tests

I INTRODUCTION

Spatial panel models are becoming popular in econometric applications. To capture correlation among cross-sectional units, the spatial autoregressive (SAR) model by Cliff and Ord (1973) has received the most attention in economics. The testing for SAR models, Baltagi and Li (1995) addressed the problem of jointly testing for error serials correlation and individual effects for the panel data model with no spatial effects; Anselin (1988, 2001) and Anselin and Bera (1998), have studied the problem of testing for spatial dependence; Baltagi et al. (2003) considered the problem of jointly testing for random region effects in the panel as well as spatial correlation of error serials across these regions. however, the study did not consider the added problem of serial correlation in the remainder error term. Baltagi et al. (2007) consider the testing of spatial and serial dependence in an extended model, where serial correlation on each spatial unit over time, in addition to spatial dependence across spatial units are allowed in the disturbances; Myoung Jin Jang and Dong Wan Shin(2014) consider the testing for time effects and spatial effects by Lagrange multiplier and likelihood ratio texts about panel model with spatial autocorrelation and heterogeneity of error serials across time, they derived the limiting null distributions of test statistics jointly, marginally or conditionally. These panel models do not incorporate time lagged dependent variables as dynamic structures in the regression equation, this paper shall generalizes the previous studies by deriving joint, conditional and marginal tests of LM and LR, that consider the testing of the lag effects on dependent variables, spatial and serial dependence in the extended dynamic panel model with spatial correlation of dependent variables and error serial among cross sectional units, and studies their small sample properties using Monte Carlo experiments, our Monte Carlo evidence shows their good size properties and power properties except for a few

cases where there is significant size distortion and the lower power.

The remainder of the paper is organized as follows. Section 2 presents a spatial dynamic panel data regression model with fixed effects and spatial correlation of dependent variables cross sectional units. Section 3 provides the LM and LR test statistics as well as their limiting null distributions.

II THE MODEL AND THE LIKELIHOOD FUNCTION

A. The Model

The regression model Considered in this paper is

$$\begin{aligned} Y_{nt} &= \lambda_0 W_n Y_{nt} + \gamma_0 Y_{n,t-1} + X_{nt} \beta_0 + C_{n0} + U_{nt} \\ U_{nt} &= \rho_0 M_n U_{nt} + V_{nt} \\ t &= 1, 2, \dots, T \end{aligned} \quad (1)$$

where $Y_{nt} = (y_{1t}, y_{2t}, \dots, y_{nt})$ and

$V_{nt} = (v_{1t}, v_{2t}, \dots, v_{nt})$ are $n \times 1$ column vector and v_{it} is i.i.d across i and d with zero mean and variance σ_0^2 . W_n is an $n \times n$ nonstochastic spatial weights matrix that generates the spatial dependence on y_{it} between cross sectional units, X_{it} is the p -dimensional vector of covariates, and C_{n0} is an $n \times 1$ column vector of fixed effect. M_n is an $n \times n$ nonstochastic spatial weights matrix for the disturbance.

Therefore, the parameters in this model is $(\lambda, \gamma, \beta, \rho, \sigma^2)$. if unnecessary, will make the inference complicated and even inefficient when T or N is fixed.

Define $S(\lambda) = I_n - \lambda W_n$ and $R(\rho) = I_n - \rho M_n$ for any λ and ρ . at the true parameter Assuming the infinite sums are well-defined, by continuous substitution,

$$Y_{nt} = \sum_{h=1}^{\infty} (S_n^{-1})^h \gamma^{h-1} (C_{n0} + X_{n,t-h} \beta_0 + (R_n^{-1})^{h-1} V_{n,t-h})$$

$$= A_n + X_{nt} \beta_0 + E_n$$

Where

$$\begin{aligned} A_n &= \sum_{h=1}^{\infty} (S_n^{-1})^h \gamma^{h-1} C_{n0}, & X_{nt} &= \sum_{h=1}^{\infty} (S_n^{-1})^h \gamma^{h-1} X_{n,t-h}, \\ E_n &= \sum_{h=1}^{\infty} (S_n^{-1})^h (\gamma R_n^{-1})^{h-1} V_{n,t-h}. \end{aligned} \quad (2)$$

B. The Concentrated Likelihood Function

Denote $\theta = (\lambda, \gamma, \rho, \sigma^2)$, θ_0 indicates the true value of parameters. For notational purpose, we define

$$\begin{aligned} \tilde{Y}_{nt} &= Y_{nt} - \frac{1}{T} \sum_{t=1}^T Y_{nt}, & \bar{Y}_{nT,-1} &= \frac{1}{T} \sum_{t=1}^T Y_{n,t-1}, & S &= S_n(\lambda), \\ \hat{S} &= S_n(\hat{\lambda}), & \dot{S} &= S_n(\dot{\lambda}), & \tilde{Y} &= (\tilde{Y}'_{n1}, \dots, \tilde{Y}'_{nT})', \\ \tilde{Y}_{-1} &= (\tilde{Y}'_{n0}, \dots, \tilde{Y}'_{nT-1})'. \end{aligned}$$

Where $\hat{\lambda}$ is unrestricted QMLES, $\dot{\lambda}$ is restricted QMLES, Similarry, we define $\tilde{X}_{nt}, \tilde{V}_{nt}, \tilde{R}, \hat{\tilde{R}}, \tilde{X}, \tilde{X}_{-1}, \tilde{X}, \tilde{X}_{-1}$.

By the transformation approach we get the likelihood function is

$$L_{nT}(\theta) = -\frac{n(T-1)}{2} \ln 2\pi - \frac{n(T-1)}{2} \ln \sigma^2 + (T-1)(\ln |S| + \ln |R|) - \frac{1}{2\sigma^2} \sum_{t=1}^T \tilde{V}'_{nt} \tilde{V}_{nt} \quad (3)$$

$$\text{Where } \tilde{V}_{nt} = R[S \tilde{Y}_{nt} - \gamma \tilde{Y}_{n,t-1} - \tilde{X}_{nt} \beta] \quad (4)$$

III TEST STATISTICS

In this section, we derive *LM* tests and *LR* tests as well as their limiting null distributions. The LM statistic for testing a specific null hypothesis H_0 against H_1 is given by

$$LM = \left(\frac{\partial L_{nT}}{\partial \theta_*} \Bigg|_{\theta_*=\tilde{\theta}_*} \right)' \left[E \left(\frac{\partial^2 L_{nT}}{\partial \theta_* \partial \theta_*'} \Bigg|_{\theta_*=\tilde{\theta}_*} \right) \right]^{-1} \left(\frac{\partial L_{nT}}{\partial \theta_*} \Bigg|_{\theta_*=\tilde{\theta}_*} \right) \quad (5)$$

Where $\theta_* = (\lambda, \gamma, \rho)'$, $\tilde{\theta}_*$ is the restricted QMLES under H_0 , and $\frac{\partial L_{nT}}{\partial \theta_*} \Bigg|_{\theta_*=\tilde{\theta}}$ and

$\frac{\partial^2 L_{nT}}{\partial \theta_* \partial \theta_*'} \Bigg|_{\theta_*=\tilde{\theta}}$ are the partial derivatives with respect to

θ , evaluated at $\tilde{\theta}$. The *LR* statistic is given by $LR = L(\hat{\theta}) - L(\tilde{\theta})$, where $\hat{\theta}$ is the unrestricted MLE. For simplicity of notation, let

$$I(\theta) = E \left(\frac{\partial^2 L_{nT}}{\partial \theta \partial \theta'} \Bigg|_{\theta=\theta} \right), \quad L_v = L(\hat{\theta}) \text{ and}$$

$$L_R = L(\tilde{\theta})$$

IV TESTS FOR SPATIAL CORRELATION ON y_{it} BETWEEN CROSS SECTIONAL UNITS H_0 : $\lambda = 0$

We derive marginal and conditional tests for s for spatial correlation on y_{it} between cross sectional units.

A. One-dimensional Conditional Tests for Spatial

Correlation $H_0: \lambda = 0$ Assuming Admitting Non-zero γ and ρ

Under H_0

$$\begin{aligned} \tilde{Y}_{nt} &= \sum_{h=0}^{\infty} \gamma^h (\tilde{X}_{n,t-h} \beta_0 + R_n^{-1} \tilde{V}_{n,t-h}) \\ &= \tilde{X}_{nt} \beta + R_n^{-1} E_{nt} \end{aligned}$$

$$\text{Where, } \tilde{X}_{nt} = \sum_{h=0}^{\infty} \gamma^h \tilde{X}_{n,t-h}, \quad E_{nt} = \sum_{h=0}^{\infty} \gamma^h \tilde{V}_{n,t-h}$$

Under H_0 , we have

$$\left. \frac{\partial L_{nT}}{\partial \theta_*} \right|_{\theta_*=\tilde{\theta}}^c = \begin{pmatrix} D(\tilde{\lambda}) \\ 0 \\ 0 \end{pmatrix} = \begin{pmatrix} \frac{1}{\sigma^2} \sum_{t=1}^T (\tilde{R} \tilde{W} \tilde{Y}_{nt})' \tilde{V}_{nt} \\ 0 \\ 0 \end{pmatrix} \quad (14)$$

the elements of the information matrix $I(\tilde{\theta}_*) \Big|_{H_0}^c = E \left(\frac{\partial^2 L_{nT}}{\partial \theta_* \partial \theta_*'} \Bigg|_{\theta_*=\tilde{\theta}} \right)$ are given by

$$I_{11} \Big|_{H_0}^d = (T-1) tr W^2 + \hat{A}_r tr (\hat{R}^{-1} W' \hat{R} \hat{R} W \hat{R}^{-1}) + \frac{1}{\sigma^2} \hat{\beta}' \sum_{t=1}^T \tilde{X}'_{nt} W' \hat{R} \hat{R} W \tilde{X}_{nt} \hat{\beta}$$

$$I_{12} \Big|_{H_0}^d = \frac{1}{\sigma^2} \hat{\beta}' \sum_{t=1}^T \tilde{X}'_{nt} W' \hat{R} \hat{R} W \tilde{X}_{nt-1} \hat{\beta}$$

$$I_{13} \Big|_{H_0}^d = \hat{B}_\lambda [T - 1 - \frac{(\hat{\gamma} - \hat{\gamma}^T)}{(1-\hat{\gamma})(1-\hat{\gamma}^2)} + \frac{\sum_{i=1}^{T-1} i \hat{\gamma}^i}{(1-\hat{\gamma}^2)T}]$$

$$I_{22} \Big|_{H_0}^d = \frac{1}{\sigma^2} \hat{\beta} \sum_{t=1}^T \hat{X}'_{nt-1} \hat{R}' \hat{R} \hat{X}_{nt-1} \hat{\beta} + A_\lambda n$$

$$I_{23} \Big|_{H_0}^d = -2[\frac{(T-1)-(T-1)(\gamma - \gamma^{T-1})}{T(1-\gamma)} - \frac{\sum_{i=1}^{T-2} i \gamma^i}{T}] tr(M \hat{R}^{-1})$$

$$I_{33} \Big|_{H_0}^c = (T-1) tr[\hat{H}_n' \hat{H}_n + \hat{H}_n^2]$$

Where $\hat{A}_\lambda = [\frac{T-1}{(1-\gamma^2)} - \frac{2(1-\gamma^T)}{(1-\gamma)(1-\gamma^2)} + \frac{2\sum_{i=1}^{T-1} i \gamma^i}{T(1-\gamma^2)}]$

$$\hat{B}_\lambda = tr[\hat{R}^{-1} W M + (\hat{R}^{-1})^2 W \hat{R} M]$$

$$\hat{\beta} = (\hat{X}_n' \hat{R}' \hat{R} \hat{X}_n)^{-1} \hat{X}_n' \hat{R}' \hat{R} (\hat{Y}_{nt} - \gamma \hat{Y}_{nt-1}),$$

$$\hat{V}_{nt} = \hat{R}(\hat{Y}_{nt} - \gamma \hat{Y}_{nt-1} - \hat{X}_{nt} \hat{\beta}), \hat{\sigma}^2 = \sum_{t=1}^T \hat{V}_{nt}' \hat{V}_{nt} / n(T-1) \quad (15)$$

So, by equation (5) the resulting conditional LM statistic is given

$$(16) \quad LM_\lambda = D(\hat{\lambda})^2 / \left\{ (T-1) tr W^2 + A_\lambda tr(\hat{R}^{-1} W \hat{R}' \hat{R} W \hat{R}^{-1}) + \frac{1}{\sigma^2} \hat{\beta} \sum_{t=1}^T \hat{X}_{nt-1}' W' \hat{R}' \hat{R} W \hat{X}_{nt-1} \hat{\beta} \right\}$$

The derivation of this LM test statistic is given in Appendix A.3. This LM statistic should be asymptotically distributed as χ^2_1 under H_0 as $T, N \rightarrow \infty$ which will be formally proved in Theorem 3 in Section 3.6.

The conditional LR test for $H_0 : \lambda = 0$ vs $H_1 : \lambda \neq 0$ admitting non-zero λ and ρ is given by $LR_\lambda = 2(L_U - L_R)$

Where

$$L_U = -\frac{n(T-1)}{2} (\ln 2\pi \hat{\sigma}^2 + 1) + (T-1) (\ln |\hat{S}| + \ln |\hat{R}|),$$

$$L_R = -\frac{n(T-1)}{2} (\ln 2\pi \hat{\sigma}^2 + 1) + (T-1) \ln |\hat{R}|$$

Where the unrestricted MLEs are same as equation (9).

Under H_0 the LR_λ statistic is asymptotically distributed as χ^2_1

B. One-dimensional Marginal Tests for Spatial Error Correlation $H_0 : \lambda = 0$ Assuming $\gamma = \rho = 0$

This is a one-dimensional marginal test for spatial dependence on y_{it} no ignoring the presence of lag effect and spatial error correlation cross sectional units. when $\gamma = \rho = 0$, R reduce to unit matrix , under the null hypothesis,

$$\hat{\beta} = (\hat{X}_n' \hat{X}_n)^{-1} \hat{X}_n' \hat{Y}_n, \quad \hat{V}_{nt} = \hat{Y}_{nt} - \hat{X}_{nt} \hat{\beta}, \quad \hat{\sigma}^2 = \sum_{t=1}^T \hat{V}_{nt}' \hat{V}_{nt} / n(T-1)$$

$$D(\hat{\lambda}) = \frac{1}{\hat{\sigma}^2} \sum_{t=1}^T (\hat{W} \hat{Y}_{nt})' \hat{V}_{nt}, \quad I_{11} \Big|_{H_0}^c 2(T-1) tr W^2 + \frac{1}{\hat{\sigma}^2} \hat{\beta} \sum_{t=1}^T \hat{X}_{nt}' W' W \hat{X}_{nt} \hat{\beta}$$

the LM test statistic for testing H_0 , call it $LM_{\lambda/\rho}$

$$LM_{\lambda/\rho} = D(\hat{\gamma})^2 / (2(T-1) tr W^2 + \frac{1}{\hat{\sigma}^2} \hat{\beta} \sum_{t=1}^T \hat{X}_n' W' W \hat{X}_{nt} \hat{\beta}) \hat{W}_{nt} / n(T-1) \quad (17)$$

This LM statistic should be asymptotically distributed as χ^2_1 under H_0 as as $T, n \rightarrow \infty$ which will be formally proved in Theorem 2 in Section 3.5.

The Marginal LR test for $H_0 : \gamma = 0$ vs $H_1 : \gamma \neq 0$ assuming $\lambda = \rho = 0$ is given by $LR_{\lambda/\rho} = 2(L_U - L_R)$

$$L_U = -\frac{n(T-1)}{2} (\ln 2\pi \hat{\sigma}^2 + 1), \quad L_R = -\frac{n(T-1)}{2} (\ln 2\pi \hat{\sigma}^2 + 1)$$

Where $\hat{\beta} = (\hat{X}_n' \hat{X}_n)^{-1} \hat{X}_n' (\hat{Y}_{nt} - \gamma \hat{Y}_{nt-1})$,

$$\hat{V}_{nt} = \hat{Y}_{nt} - \gamma \hat{Y}_{nt-1} - \hat{X}_{nt-1} \hat{\beta}, \quad \hat{\sigma}^2 = \sum_{t=1}^T \hat{V}_{nt}' \hat{V}_{nt} / n(T-1),$$

Under H_0 the $LR_{\lambda/\rho}$ statistic is asymptotically distributed as χ^2_1

V SUMMARY

This paper generalized the model in Baltagi and Li (1995) paper, Baltagi et al. (2003) paper and Baltagi et al. (2007) paper, and considers a spatial dynamic panel data regression model with fixed effects, spatial correlation of dependent variables and error serial among cross sectional units. When the number of individuals n , the number of time periods T are large, and T is asymptotically large relative to n , the paper derives various Lagrange multiplier tests and likelihood ratio test statistics for this panel data regression model including tests for spatial correlation of dependent variables. Limiting null distributions of the tests are derived.

ACKNOWLEDGEMENT

This research was financially supported by Statistical science research project of China National Bureau of Statistics (2016LY28) and Social science planning project of Chongqing Social Science Association (2016YBJJ022). We would like thank anonymous referees for their helpful comments and suggestions.

REFERENCES

- [1] Cliff, A.D., Ord, J.K., 1973. Spatial Autocorrelation. Pion Ltd., London.
- [2] Baltagi, B.H., Li, Q., 1995. Testing AR (1) against MA (1) disturbances in an error component model. *Journal of Econometrics* 68, 133–151.
- [3] Anselin, L., Bera, A.K., 1998. Spatial dependence in linear regression models with an introduction to spatial econometrics. In: Ullah, A., Giles, D.E.A. (Eds.), *Handbook of Applied Economic Statistics*. Marcel Dekker, New York.
- [4] Anselin, L., 2001. Rao's score tests in spatial econometrics. *Journal of Statistical Planning and Inference* 97, 113–139.
- [5] B.H. Ba Itagi, S.H. Song, and W. Koh, Testing panel data regression models with spatial error correlation, *J. Econometrics* 117 (2003), 123–150.
- [6] Baltagi, B., Song, S.H., Jung, B.C., Kon, W., 2007. Testing for serial correlation, spatial autocorrelation and random effects using panel data. *Journal of Econometrics* 140, 5–51.
- [7] Myoung Jin Jang and DongWan Shin, Tests for random time effects and spatial error correlation in panel regression models. *Statistics*, 48(2014), No. 1, 101–120.
- [8] Jihai Yua, Robert de Jong, Lung-fei Lee, Quasi-maximum likelihood estimators for spatial dynamic panel data with fixed effects when both n and T are large, *Journal of Econometrics* 146 (2008), 118–134.
- [9] Lee, L.F., and J. Yu, Estimation of Spatial Autoregressive Panel Data Models with Fixed Effects. *Journal of Econometrics*. *Journal of Econometrics* 154(2010), 165–185.
- [10] Su L, Yang Z, Su L, et al. QML estimation of dynamic panel data models with spatial errors. *Working Paper [J]. Journal of Econometrics*, 2007, 185(1):230–258.

MOOC Course Evaluation Based on Big Data Analysis

Yong Luo^{1,2,*}, Jianping Li¹, Zheng Xie¹, Guochang Zhou¹ and Xiao Xiao³

¹College of Science, National University Of Defense Technology, Changsha, China

²Hunan Provincial Key Laboratory of Network Investigational Technology, China

³Higher Education Press, Beijing, China

*Corresponding author

Abstract—The rapid development of MOOC, more and more same courses appear on the MOOC platform. For learners without the guidance of course selection, a lot of time wasted in the course to browse and try to learn. At the same time, lack of evaluation led to a decline in the quality of the course. In this paper, MOOC learning behavior data is used to construct a evaluation algorithm based on data distribution. Through theoretical analysis and data experiment, a standard model based on normal distribution is constructed. The evaluation algorithm is based entirely on learning data. Objective and dynamic real-time gives the standard points for each course. Not only help learner select the right courses, but also be able to promote the builders improve the lesson.

Keywords—MOOC; big data analysis; course evaluation; normal distribution

I INTRODUCTION

The term MOOC (Massive Open Online Course) proposed by Dave Cormier and Brian Alexander. The earliest MOOC course was Artificial Intelligence by Stanford University professor Sebastian in 2011. The number of learners reached 160,000, and eventually 23,000 people completed the course. In 2012, Professor Schlumberger founded Udacity, a for-profit MOOC platform. Udacity, Coursera and Edx are the three most influential MOOC platforms in the world. MOOC brings a whole new paradigm to the sharing of higher education and resources. More and more universities participate in course construction. The number of courses offered is also rapidly increasing. Take the Chinese University MOOC as an example. By December 2017, the platform has 148 cooperative universities. A total of 1042 courses were opened. The number of similar or related courses is also on the rise. There are 325 courses related to higher mathematics in Chinese University MOOC.

After the learner comes into contact with MOOC, how to choose the course is the first step, and it is also the most crucial step. Because many same courses are held on the same platform, learners often do not know which course to choose. But, the depth of these courses and teaching characteristics are different. In fact, students find it hard to find a course that suits their needs. They can only see the course profile. But these are not enough. MOOC course learners waste a great deal of time browsing and experimenting with the lessons. We found that a

large number of students did not insist on learning, due not to choose the right courses. On the other hand, if the course does not have an objective and fair evaluation system, the builders did not promote it.

Therefore, how to recommend corresponding courses accurately and how to evaluate the courses objectively is a very important issue for MOOC. Today with big data support, we can use data processing techniques to analyze and evaluate lessons. Through the analysis of learning behavior data, to describe the characteristics and level of the course. This will improve the accuracy of student electives, improve student learning efficiency.

Currently all platforms are lack of a scientific course evaluation system. This article will establish a rating system based on big data statistical analysis. Through this, to provide learners with a comprehensive course information, as well as curriculum level indicators. Provide a reference for learners, and also promote builders to continuously improve the level of lessons. In summary, the evaluation system has a high application prospect. But also has some academic research value.

At present, the research on MOOC evaluation at home and abroad has just started. The National Center for Higher Education initiated the MOOC research project in 2017. Research and evaluate the courses in Chinese University MOOC. Expect to be able to make a scientific and reasonable evaluation of the course. To achieve the goal of raising MOOC level.

The United States, Britain, Japan and other economically developed countries have accumulated a great deal of experience in practice. In MOOC learning behavior data analysis, Anderson [3] found through data mining technology some of the factors that affect the learning effect of MOOC course. Adamopoulos [4] studied the factors that affect the retention rate of MOOC students. Gillani [5] analyzed "Business Strategy Fundamentals" course 87,000 trainees in the course forums and the relationship with grades. Guo [6] studied the relationship between MOOC video mode and learning effect through data analysis, and proposed a scientific and reasonable course video recording mode. Domestic MOOC teaching and research focused on MOOC in teaching practice and quality control. Jiang [7] classify learners according to the Chinese MOOC learning behavior characteristics. He studied in

depth the relationship between learning behavior and outcomes. Deng [8] paid attention to MOOC's problems in quality assurance and evaluation mechanism.

In summary, MOOC research has made a lot of achievements in both theory and application. But existing research rarely involves the assessment of MOOC course quality. In particular, there is a lack of quantitative evaluation of MOOC course quality.

II LEARNING BEHAVIOR DATA DISTRIBUTION

All set up similar courses MOOC behavior data for the overall ξ . Overall ξ follows a normal distribution. Each MOOC course learning behavior data as a sub-sample $\xi_1, \xi_2, \dots, \xi_n$. By the sampling distribution theorem:

Let the overall ξ obey the normal distribution $N(a, \sigma)$, $\xi_1, \xi_2, \dots, \xi_n$ is its sub sample, The mean and variance of the subsamples are denoted as $\bar{\xi}$ and S^2 respectively.

Then $\bar{\xi}$ obeys normal distribution $N(a, \frac{\sigma}{\sqrt{n}})$, $\frac{nS^2}{\sigma^2}$ obeys the

χ^2 distribution with degree of freedom $n-1$. Briefly written as: $\frac{nS^2}{\sigma^2} : \chi_{(n-1)}^2$, $\bar{\xi}$ and S^2 are independent of each other.

Orthogonal linear transformation of the sample is as follows:

$$\left\{ \begin{array}{l} \eta_1 = \frac{1}{\sqrt{1 \cdot 2}} [\xi_1 - \bar{\xi}] \\ \eta_2 = \frac{1}{\sqrt{2 \cdot 3}} [\xi_1 + \xi_2 - 2\bar{\xi}] \\ \vdots \\ \eta_{n-1} = \frac{1}{\sqrt{(n-1) \cdot n}} [\xi_1 + \xi_2 + \dots + \xi_{n-1} - (n-1)\bar{\xi}] \\ \eta_n = \frac{1}{\sqrt{n}} [\xi_1 + \xi_2 + \dots + \xi_{n-1} + \xi_n] \end{array} \right.$$

The following shows that η_1, \dots, η_n is independent of each other and has the same normal distribution $N(a, \sigma)$. Due to orthogonal transform to maintain the same length, so

$$\sum_{i=1}^n \eta_i^2 = \sum_{i=1}^n \xi_i^2$$

Notice that $(\xi_1, \xi_2, \dots, \xi_n)$ is a joint distributed n -dimensional normal. Its joint density function is

$$f(x_1, \dots, x_n) = \left(\frac{1}{\sigma\sqrt{2\pi}}\right)^n \prod_{i=1}^n e^{-\frac{x_i^2}{2\sigma^2}}$$

$$= \left(\frac{1}{\sigma\sqrt{2\pi}}\right)^n e^{-\frac{1}{2\sigma^2} \sum_{i=1}^n x_i^2}$$

Since the absolute value of the determinant is equal to 1, the union density function of (η_1, \dots, η_n) is

$$g(y_1, \dots, y_n) = \left(\frac{1}{\sigma\sqrt{2\pi}}\right)^n e^{-\frac{1}{2\sigma^2} \sum_{i=1}^n y_i^2}$$

Then the joint distribution of (η_1, \dots, η_n) is an n -dimensional normal distribution. And in the normal case, irrelevance and independence are equivalent. Thus η_1, \dots, η_n is independent of each other and has the same normal $N(0, \sigma)$ random variables.

When $\eta_n = \sqrt{n}\bar{\xi}$, $\eta_n^2 = n\bar{\xi}^2$, that is

$$\begin{aligned} nS^2 &= \sum_{i=1}^n (\xi_i - \bar{\xi})^2 = \sum_{i=1}^n \xi_i^2 - n\bar{\xi}^2 \\ &= \sum_{i=1}^n \eta_i^2 - \eta_n^2 = \sum_{i=1}^{n-1} \eta_i^2 \end{aligned}$$

Then

$$nS^2 = \frac{1}{\sigma^2} \sum_{i=1}^{n-1} \eta_i^2 \sim \chi_{(n-1)}^2$$

And nS^2 and η_n are independent of each other. That is, nS^2 and $\bar{\xi}$ are independent of each other.

From the above analysis, when there are more courses to join the MOOC platform, new courses can be regarded as a sub-sample $\xi_1, \xi_2, \dots, \xi_n$ of all MOOC courses ξ . Because of the overall MOOC learning behavior data is subject to normal, the data of new course also obey the normal distribution. Thus, according to the sampling distribution theorem, when the number of similar MOOC courses is small, its learning behavior data also obeys normal distribution.

III COURSE SCORE MATHEMATICAL MODELING

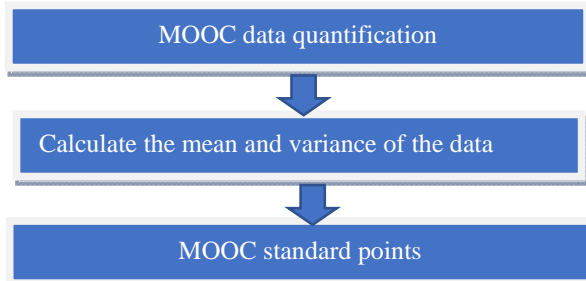


FIGURE I. DATA PROCESSING FLOW CHART

Data processing as shown above. First, quantify learning behaviors and course data. Calculate the mean and variance of the data for the same course. Get the normal distribution of parameters. Finally calculate the standard points.

There is an objective difference between each type of course and each type of learning behavior. And as the annual course joins, the size of the data is constantly changing. Affected by these factors, the same behavior data, at different times and different types of grading results are different. This reflects the objective and dynamic score. The algorithm can achieve real-time data calculation. And realize the equivalent calculation between different data. Based on the data approximation to normal distribution conditions, the following standard algorithm is proposed.

Convert each quantized MOOC data score to a standard normal distribution. Then use the same method to expand and translate to complete the equivalence of different learning behaviors. The specific method is described as follows:

There are n identical courses, choose a behavior data X . It obeys normal distribution. That is $X : N(a, \sigma^2)$.

$$a = \frac{\sum_{i=1}^n X_i}{n} \quad n \text{ is the average of all courses data.}$$

$$\sigma = \sqrt{\frac{\sum_{i=1}^n (X_i - a)^2}{n}} \quad n \text{ is the standard deviation. If the data for this course is } X. \text{ The standard formula is:}$$

$$T = 100 \cdot \frac{X - a}{\sigma} + 500$$

To improve the resolution of the data, the data is magnified and panned. 100 here to enlarge parameters, 500 for the translation parameters. Through this formula can be seen, equivalent points can be decimal, such a score more accurate.

In addition, if $T > 900$, referred to as $T = 900$; if $T < 100$, referred to as $T = 100$;

Therefore $T \in [100, 900]$. This equivalent process is actually based on a certain approximation. In fact, the standard normal distribution of the density function is:

$$p(x) = \frac{1}{\sqrt{2\pi}\sigma} e^{-\frac{(x-a)^2}{2\sigma^2}}$$

Due to $X : N(a, \sigma^2)$, $\frac{X - a}{\sigma} : N(0, 1)$. And $T \in [100, 900]$, then $\frac{X - a}{\sigma} \in [-4, 4]$.

$$P = \int_{-4}^4 p(x)dx = 0.9999$$

This shows that $\frac{X - a}{\sigma}$ falls in the interval $[-4, 4]$ probability of 99.99%. Therefore, the above approximation is reasonable.

IV DATA EXPERIMENT AND ANALYSIS

We will test the distribution of MOOC learning behavior data. We choose the Chinese University of MOOC platform learning behavior data to conduct research. The data type is Advanced Mathematics learning behavior and course data. A total of four types of data were studied. Respectively, the number of elective courses, video traffic, the number of forum posting and the number of people who obtained the certificate. We normalize the data to $[0, 900]$ this data interval. Then calculate the mathematical expectation and standard deviation for each class of data for all classes. As shown in Table I:

TABLE I. EXPECTATIONS AND STANDARD DEVIATIONS OF LEARNING BEHAVIOR DATA

Data category	Mathematical Expectation	Standard Deviation
Elective number	407.1587	104.7397
Video traffic	406.0047	106.9768
Forum posting	398.6446	114.2184
Certificate number	396.3465	105.4982

The data in the above table is the parameter for calculating standard points. In order to analyze the distribution of data, it is necessary to draw a distribution image of the behavior data. This article is achieved by grouping the data. Calculate the frequency of each group of data. Describe the distribution of MOOC learning behavior data. In the experiment, our segmentation interval is the standard score of 20. The frequency is the number of courses falling within this range of scores.

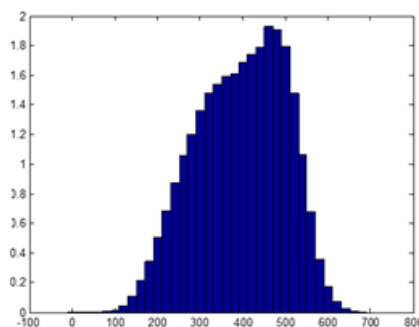


FIGURE II. MOOC FORUM POST DATA DISTRIBUTION

The figure is the equivalent distribution of MOOC behavioral data. From the learning behavior data image, the distribution image is very close to the normal distribution. It shows that MOOC behavior data is normally distributed. Our standard method of division is scientific and rational.

V SUMMARY

In this paper, we build a dynamic assessment system. The entire evaluation system is not subject to man-made subjective factors. Through the theoretical analysis and experimental research, the law of MOOC learning behavior data was obtained. These rules promote the construction of MOOC curriculum. Evaluation can motivate builders of MOOC courses to improve the quality of the course. The ultimate realization of the healthy development of MOOC.

REFERENCES

- [1] Guidelines on the Quality Assurance of Distance Learning. Quality Assurance Agency for Higher Education.1999:88-101
- [2] Phipps & Merisotis. Quality on the Line:Benchmarks for success In Internet –Based Distance Education. Research report of The Institute for Higher Education Policy. 2000.46-53.
- [3] Anderson, D. Huttenlocher, J. Kleinberg, et al. Engaging with massive online courses, 2014:687-698.
- [4] P. Adamopoulos, What makes a great MOOC? An interdisciplinary analysis of student retention in online courses. In Proceedings of the 34th International Conference on Information Systems, 2013, ICIS'13.
- [5] N. Gillani. Learner communications in massively open online course. OxCHEPS Occasional Paper, 2013:53.
- [6] P. J. Guo, J. Kim, R. Rubin. How video production affects student engagement: an empirical study of MOOC videos ACM Conference on Learning @ Scale Conference. ACM, 2014:41-50.
- [7] Z. X. Jiang, Y. Zhang, X. M. Li, Learning Behavior Analysis and Prediction Based on MOOC Data, Journal of Computer Research and Development, 2015, 52(3):614-628. (In Chinese)
- [8] H. Deng, M. Li, Y. Chi. Courses and knowledge system network modeling in MOOC. Course Education Research, 2013 (7), 5-7. (In Chinese)

The Application of Data Mining Techniques in College Students Information System

Yang Liu¹, Jingwei Chen^{2*}, Jun Liu¹, Wei He¹ and Tingting Li³

¹Institute of information science and engineering, Chongqing Jiaotong University, China

²Chongqing Key Laboratory of Automated Reasoning and Cognition, Chongqing Institute of Green and Intelligent Technology, Chinese Academy of Sciences, Chongqing, China

³School of Mathematics and Statistics, Southwest University, China

*Corresponding author

Abstract—Nowadays, with the expanding of database application, every fields have accumulated huge amounts of data including the College students' activities records. These records are very meticulously reflecting the status of the students' learning and life by analysis their relationships using data mining techniques. The traditional methods of choosing Excellent students and Outstanding Class Leader and Postgraduate Recommendation and Poor students is manual manipulation. But, in this paper, we develop a system which brings in data mining techniques with decision tree algorithm and association rules mining algorithm. Through analyzing the data from college student library records and consumption records and student score and psychological test done by the students, this information system can automatically show the results under data mining algorithm.

Keywords—date mining; decision tree algorithm; association rules mining algorithm; database application

I. INTRODUCTION

Data mining is one of the most important areas in Database. The current situation of higher education represents the development of the country. It's a good way to manage college students with data mining technology instead of traditional mining manipulation [1-5]. At present, the campus almost all use electronic management by campus card system. This system records all the students' activities including shopping on campus and dining in university students' dining halls and the time when they are in and out of the library. Of course, it also records the student score of every course.

Presently, some of researchers have studied parts of the relationship between the data [6-8], but, they don't analyze it from different aspects of college students which are the special community. The function modules are dispersive. In other words, the date in the college management system database is existence, but, we pay no attention to the relationships during them. So, when we want to select excellent students or outstanding class leader or postgraduate recommendation or poor student, we are accustomed to manual analysis. Furthermore, because of the academic stress, parts of college students get psychological problems. Unfortunately, the advisers can't find it timely. They always know the students who has psychological problems until it's very serious. As it

often happens, this leads to that the student gets mentally ill or suicide.

According to this situation, this paper provides a view to help management the students' life and study. We use decision tree algorithm and association rules mining algorithm to analyzing the huge amounts of data in the system database. By analyzing the relationship between the data, we can more and more conveniently manage the students.

A. Decision Tree Algorithm

Decision tree algorithm is a kind of methods approximating discrete function value. C4.5 algorithm [9-10] is an important kind of classification decision tree algorithm in machine learning and it's an improved algorithm of the ID3 algorithm [11-13]. In this system, we use C4.5 algorithm to analyze the scores and psychological states and consumption of the college students and build the decision tree of students' comprehensive evaluation.

The standard is based on the average score. It divides into five grades that greater than 90 and 80~90 and 70~80 and 60~70 and less than 60. At first, we compute the information entropy $H(X)$ [14] of students' score sample based on formula(1) and the conditional entropy $H(X|Y)$ [15] based on formula(2).

$$H(X) = -\sum_{i=1}^n P(C_i) \log_2 P(C_i) \quad (1)$$

X represents the sample data set;

n represents all the possible symbolic number of X;

C_i represents the different possible value of the i kind sample;

$P(C_i)$ represents the probability of the sample data belonging to i;

The information entropy is used to compute the expectation of information. And the conditional entropy is used to compute the uncertainty for the random variable X when received the random variable Y.

$$H(X | Y) = -\sum_{j=1}^m \sum_{i=1}^n P(C_i, T_j) \log_2 P(C_i | T_j) \quad (2)$$

C_i represents the signal source from X;

T_j represents the signal source from Y;

$P(C_i | T_j)$ represents the probability when Y is T_j and X is C_i ;

The difference of the $H(X)$ and $H(X|Y)$ is the information gain[15] based on formula(3).

$$Gain(X/Y) = H(X) - H(X|Y) \quad (3)$$

B. Association Rules Mining Algorithm

In this system, the association rules mining algorithm used by us mainly learn the Apriori algorithm[16-17] through the degree of support and the confidence. The evaluation result in this comprehensive evaluation system is given by this two standard.

The degree of support computed by formula(4).

$$Support(X) = occur(X)/count(D) = P(X) \quad (4)$$

$P(X)$ shows the probability of X appearing in D.

The degree of confidence computed by formula(5).

$$Confidence(X \rightarrow Y) = Support(X \cup Y) / Support(X) = P(Y/X) \quad (5)$$

$P(Y/X)$ reflects some relations between X and Y.

II. RELATED WORK

In our view, we divide the system into four functional models. The first one is the score analysis model. And the second one is the consumption analysis model. Then the third one is the psychological status testing model. The last one is the comprehensive analysis model as Figure 1.

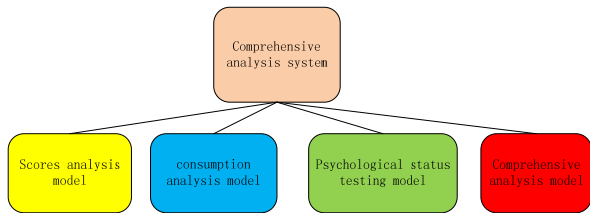


FIGURE I.

THE FRAME OF THE COMPREHENSIVE ANALYSIS SYSTEM

Using decision tree algorithm, we classify the attributes of students' score and consumption and psychological status into different degrees. The different degrees of the attributes influence the results of the evaluation.

A. Decision Tree Algorithm Applying in the System

The first function model is the score analysis as figure 2. It has included every course score of every student in different class. We can use decision tree algorithm to get some regularities during different courses for one student. For example, if one student is good at Operating System, it also is good at Database Theory. If one student does well in fresh year and second year and third year, it also does well in the last year and Graduation Design. From the database, we can get an information entropy $H(X)$ for each student X. At the same time, conditional entropy $H(X|Y)$ can be computed. So, the information gain can be calculated.

The algorithm of building the decision tree is followed.

The tree begins with the single node which represents the samples.

1. If the samples have existed in the same category, then, this node is a leaf node marked with this category.

2. Or else, it will automatically generate node which choose the one occupying most of the attributes.

3. After analysis and conclusion, the information from the samples are divided into many sets. Every branch node can get the value of its sub-set. Every sub-set corresponds a branch. For every sub-set from the last step, it repeats the procedure. Then, it will produce a decision tree for every samples.

4. Once a kind of attribute appears in one node, it doesn't need to consider its descendant.

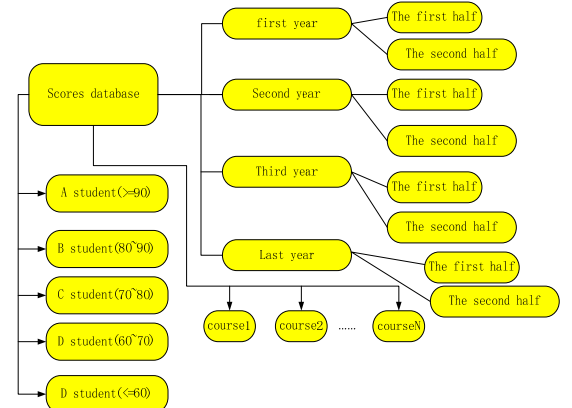


FIGURE II.

THE SCORE ANALYSIS MODEL WITH DATABASE

This algorithm will stop when satisfy these conditions as follow:

1. All the samples of the nodes belong to the same category.

2. There is no left attributes used to divide. In this condition, the nodes of the tree will update after analysis and conclusion, and it can automatically generate the leaf nodes marked with the category which has the most elements.

3. If one branch doesn't have sample which satisfies this existed category, it will build a leaf node with the sample which has majority classes.

B. Association Rules Algorithm Applying in the System

Using association rules algorithm, we take support degree and confidence degree standard to support the results given by the system when we select excellent students or outstanding class leader or postgraduate recommendation or poor student. Based on Apriori[8] algorithm, our method is followed:

1. Build the initializing collections of students' scores and consumptions and psychology testing status from the database.
2. Give the association rules which we build in rule base.
3. If the confidence degree of the student meets the threshold value we need, then the student will be the candidate.

The holistic concept is as the figure 3.

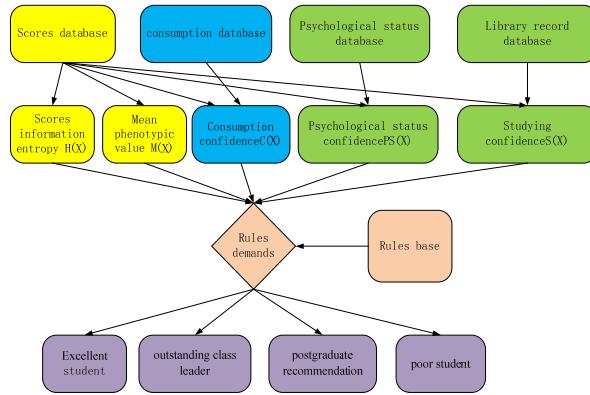


FIGURE III. THE HOLISTIC CONCEPT OF COMPREHENSIVE ANALYSIS MODEL

III. THE FUSION OF THESE TWO ALGORITHMS

Both of these two algorithms have advantages in solving specific problems. Using their respective advantage, we bring them in our system as figure 3. When we analyze students score, we use decision tree algorithm which the whole frame is as figure 4. We analyze their consumption and psychological status with association rules algorithm.

A. The Mean Phenotypic Value Analysis of Student

$$M(X) = \frac{\sum_{i=1}^n i.score(X)}{n} \quad (6)$$

$$M(X) = \frac{\sum_{i=1}^n i.score(X)}{n} \times 0.3 + \frac{\sum_{j=1}^m j.score(X)}{m} \times 0.7 \quad (7)$$

$$M(X) = \frac{\sum_{i=1}^n i.score(X)}{n} \times 0.2 + \frac{\sum_{j=1}^m j.score(X)}{m} \times 0.3 + \frac{\sum_{k=1}^t k.score(X)}{t} \times 0.5 \quad (8)$$

$$M(X) = \frac{\sum_{i=1}^n i.score(X)}{n} \times 0.1 + \frac{\sum_{j=1}^m j.score(X)}{m} \times 0.2 + \frac{\sum_{k=1}^t k.score(X)}{t} \times 0.3 + \frac{\sum_{l=1}^s l.score(X)}{s} \times 0.4 \quad (9)$$

Where $i.score(X)$ represents the score of the course i of the student X . $H(X)$ can reflect the stability of the student X . $M(X)$ represents phenotypic value. If the student is just a freshman, then we consider mean phenotypic value $M(X)$ as the first one in formula (6). If he is a second year student, then we take formula (7) into account. In the similar way, if he is a third year student, formula (8) will be used. Formula (9) will be taken, only when it is the last year student.

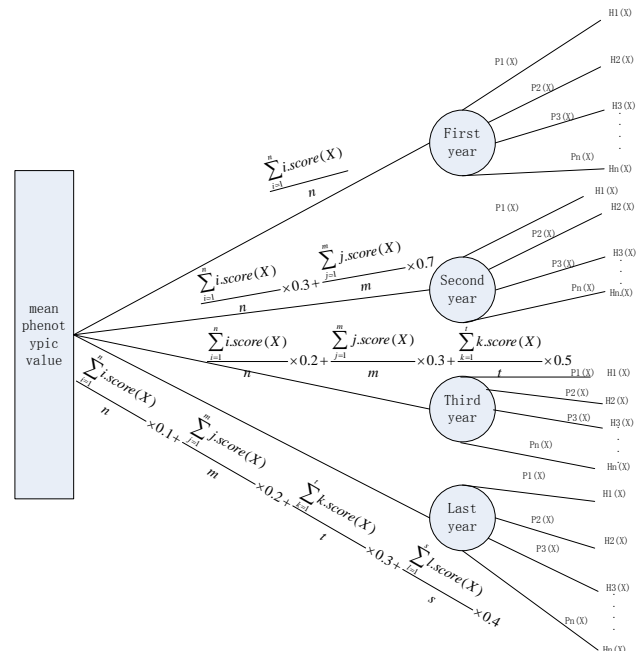


FIGURE IV. THE SKETCH FRAME DECISION TREE OF STUDENTS SCORE ANALYSIS

So, from $H(X)$ of the student X , we can get hold of the studying status of the student X . If the $H(X)$ becomes lower, we can use the second core model-psychological status testing model. Through testing, we can know the reason why the student gets a poor mark.

B. The Psychological Status Testing Model Analysis Methods

This model includes eight parts as figure 5. Every part has lots of testing subjects which are automatically generated by system from the question database. Of course, this question database is from authority health psychological questions updated timely [9]. Here, we choose highcharts [10] to show the results which are from students' testing. Based on the relation setting, it will appear amazing effect. Difference

weighted method brings in counting the total values as formula (10).

$$ZX = W_1Z_1 + W_2Z_2 + W_3Z_3 + W_4Z_4 + W_5Z_5 + W_6Z_6 + W_7Z_7 + W_8Z_8 \quad (10)$$

Where W_i represents the number of the subject from one of the eight parts, and Z_i represents the proportion in the subject. Through doing the test, we can master the dynamic psychological of the student. So, if the student appears some serious psychological crazy disease like depressive disorder, we can help him in time.

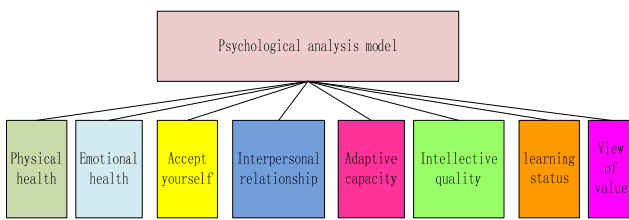


FIGURE V. THE COMPOSITION OF THE PSYCHOLOGICAL ANALYSIS MODEL

If the student's psychological status is right, we should check his record in and out of the library. The consumption records should be checked too if necessary.

C. The Comprehensive Selection System

TABLE I. PART OF EACH INDEX DATA OF THE STUDENT

Student NO.	Score information entropy $H(X)$	Mean phenotypic value	Consumption value	Psychological health value
060123	2.17	91	20	85
060102	4.76	65	25	74
060219	1.67	62	22	80
...
060114	1.13	47	46	57

This model includes selecting excellent students and outstanding class leader and postgraduate recommendation students and poor students.

At first, we must set up the standard value which we need and get the mean phenotypic value from the score database and consumption value and psychological health value. Then, we built the data source as table 1.

Each functional model of this part in comprehensive selection system has its own rules. So, different rules algorithms should be used.

IV. THE ALGORITHMS IN ANALYZING

When selecting excellent students, we should take two factors into refer, the mean phenotypic value and score information entropy of one student. The extra factor will be considered when we select outstanding class leader is that whether he or she is a class leader. the algorithm is as followed.

This algorithm is also suitable to selecting the postgraduate recommendation. But, when we award the poor students scholarship, the consumption value and psychological health value and library status confidence value are referenced. The algorithm is as followed next.

The Algorithm of Selecting Excellent Students

Input: $H_i(X)$ and $M_i(X)$ of each student, $i=1$ to n

Output: the students set Z_1

1: filter the data, screening the $H_i(X)$ and $M_i(X)$ of each student in the same class;

2: sorting the $M(X)$ set of all the students from big to small ;

3: if more than one student has the same value equal $M_i(X)$

Then these students who have the same value $M_i(X)$

belong to one set $S(X)$;

Sorting $H_i(X)$ of all students in $S(X)$ from small to large;

The top of the queue belongs to Z_1 .

Else

The top of the $M(X)$ queue belongs to Z_1 .

The algorithm of selecting poor students

Input: $H_i(X)$, $M_i(X)$, $PS(X)$, $C(X)$ and $S(X)$

Output: the students set Z_3

1: setting a threshold value T for $M_i(X)$ like 75, filter the students based on T ;

2: through the above algorithm based on $H_i(X)$ and $M_i(X)$, we get the queue Z_1' ;

3: sorting the data $C(X)$ of all students in Z_1' , then storing in queue R_1 as order from small to large;

4: setting a threshold value C for $C(X)$, filter the students based on Z_1' , the students who is less than C divide into Z_2' ;

5: sorting the data $PS(X)$ of all students in Z_2' , then storing in queue R_2 as order from big to small;

6: sorting the data $S(X)$ of all students in Z_2' , then storing in queue R_3 as order from big to small;

7: sorting the data $H((PS(X), S(X)) | (C(X), M(X), H(X)))$ of all students in Z_2' , then storing in Z_3 as order from small to large;

V. CONCLUSIONS

In this paper, we proposed a feature selection method for high education management when choosing special students each semester. In our proposal, the data is preprocessed firstly by the decision tree algorithm and association rules algorithm. Then, based on the previous step, we extract the data for further processing. The implement show that this method is a great improvement in college student management and study life. We can master the dynamic state of each student. If his study is declined, we can get his library record and information entropy to know whether he becomes slacker, or the consumption record to know whether he is too fun, or the psychology health test to know whether he is in a bad mood during this period. So, it's greatly effectively in students' study and life by this way.

ACKNOWLEDGMENT

This work was supported by the Science and Technology Research Project of Chongqing Education Commission (under grant KJ1705121), and the Basic and Frontier Research Projects of Chongqing (under grant cstc2016jcyJA0285 and

estc2016jcyjA0510). Also, the present work was partially supported by NSFC11501540.

REFERENCES

- [1] L. Ming-Jiang, L. Yu, Y. Tang, et al. An Applied Research on Data Mining in Management of College Students with Financial Difficulties. Journal of Qiannan Normal College for Nationalities, 2014.
- [2] B. Shannaq, Y. Rafael, V. Alexandro. Student Relationship in Higher Education Using Data Mining Techniques. Global Journal of Computer Science & Technology, 2010, 10(2010):45-59.
- [3] X. J. Cai, Y. R.Jiang. Application of Fuzzy Data Mining in College Students Management. Journal of South China Agricultural University, 2006.
- [4] H. R. Wang. Research on the application of data mining in teaching management. Electronic Design Engineering, 2013.
- [5] Y. He, S. Zhang. Application of Data Mining on Students' Quality Evaluation// Intelligent Systems and Applications (ISA), 2011 3rd International Workshop on. IEEE, 2011:1-4.
- [6] N. C. Pradeep, Planning I P, Customer S. Data Mining in Management, and Practice. LAP LAMBERT Academic Publishing, 2012.
- [7] N. B. Peyman, E. Vahab. Introduction to quantitative researches in management (case study: applications of data-mining in management). 2011.
- [8] D. F. Cao, Y. H. Wang. Application of data mining in management information system of comprehensive evaluation of employees. Hebei Journal of Industrial Science & Technology, 2012.
- [9] J. R. Quinlan. C4.5: programs for machine learning. Morgan Kaufmann Publishers Inc. 2014.
- [10] J. R. Quinlan. Improved use of continuous attributes in C4.5. Journal of Artificial Intelligence Research, 1996, 4(1):77-90.
- [11] S. Hong, S. Ratté, S. A. Prescott, et al. Building A Smart Academic Advising System Using Association Rule Mining. Computer Science, 2014, 32(4):1413-1428.
- [12] S. H. Park, S. Y. Jang, H. Kim, et al. An association rule mining-based framework for understanding lifestyle risk behaviors. Plos One, 2014, 9(2):e88859-e88859.
- [13] N. Dang, L. T. Nguyen, B. Vo, et al. A novel method for constrained class association rule mining. Information Sciences, 2015, 320:107-125.
- [14] J. Liang, Z. Shi, D. Li, et al. Information entropy, rough entropy and knowledge granulation in incomplete information systems. International Journal of General Systems, 2006, 35(6):641-654.
- [15] Q. S. Zhang, S. Y. Jiang. A note on information entropy measures for vague sets and its applications. Information Sciences, 2008, 178(21):4184-4191.
- [16] A. Inokuchi and T. Washio and H. Motoda, "An Apriori-Based Algorithm for Mining Frequent Substructures from Graph Data", Proceedings of the 4th European Conference on Principles of Data Mining and Knowledge Discovery, Springer-Verlag, (1970):13—23.
- [17] H. Sakai and M. Wu, M. Nakata, "Apriori-Based Rule Generation in Incomplete Information Databases and Non-Deterministic Information Systems", Health Management Technology, 2014, 130(3):343-376.

Design and Implementation of Database Centralized Access Control and Audit System

Ying Zheng¹ and Qinghai Bai^{2,3}

¹Journal Editorial Department, Inner Mongolia University for Nationalities, Tongliao, 028000, China

²College of Computer Science and Technology, Inner Mongolia University for Nationalities, Tongliao, 028000, China

³Institute of Computer Application Technology, Inner Mongolia University for Nationalities, Tongliao, 028000, China

Abstract—This paper explores the Oracle database security access control's implementation strategies, including: realize the centralized access control to the distributed Oracle database and audit through centralized policy configuration; realize the security access control to the Oracle database through encapsulating PL/Sql Developer database management tools, without changing PL/Sql Developer tools' database DBA operating practices; the system can configure the database management strategy based on different DBA roles or database users so that different DBA role can access to different database schema or a combination of database schema, realizing the SQL script review and audit.

Keywords—oracle database; security access control; audit

I. INTRODUCTION

The Oracle database is one of popular databases used by large enterprises^[1, 2]. This paper explores the Oracle database security access control's implementation strategies. Its main functions are as follows.

(1) Realize the centralized access control to the distributed Oracle database and audit through centralized policy configuration;

(2)realize the security access control to the Oracle database through encapsulating PL/Sql Developer database management tools, without changing PL/Sql Developer tools' database DBA operating practices;

(3)the system can configure the database management strategy based on different DBA roles or database users so that different DBA role can access to different database schema or a combination of database schema, realizing the SQL script review and audit.

After the system implementation, all the passwords, including the database servers', the application server operating systems', and the database systems', are under the unified administration of the system and specialized operating maintenance department.

If the scrip needs approval to perform, then submit the approval first. If the script requires audit, then perform the audit. It can set a period of time when no operations of database are permitted.

The database operation and maintenance team, under the administration of the database manager of the operation and

maintenance department, is in charge of all the operation and maintenance of the database system.

II. THE TYPICAL OPERATION AND MAINTENANCE PROCESS ANALYSIS

As an IT service company engaging in database operation and maintenance for many years, a typical outsourcing database operation and maintenance client has a similar organization structure^[3, 4]. However, this organization structure has the following drawbacks. First of all, the client DBA cannot manage all production databases by artificial means, since even the routine maintenance also requires a lot of effort (for example, change passwords and backup scrips for all databases). Secondly, the client DBA does not know what operations have been performed on the production database. Thirdly, the Operation & Maintenance Company's professional DBA and the Development Company's engineer do not develop a good combination. If the operation and maintenance DBA can assist the development engineer to review all executed SQL statements or scripts, it is able to reduce a lot of potential problems^[5].

Implementing this system can effectively solve the above problems.

In a production environment, all production databases will be recorded into the system as data source. Client, Operation & Maintenance Company, and Development Company, as different roles, will be given various permissions (DDL, DML, DCL, etc.), corresponding to the actual situation and the individual data sources. Mapping the roles and the data sources can effectively mask the actual accounts and passwords of the production database, preventing the leakage of passwords. When the Operation & Maintenance Company or the Development Company's staffs execute the SQL statements, these statements will be sent to the end for the audit of client DBA. Only through passing the audit, can the SQL statements and scripts be executed in production environment. At the same time, the client DBA can assign a trusted Operation & Maintenance DBA to help complete the audit.

After a series of system implementation above, it in nature represents a reform of operation and maintenance management.

III. THE PROCESS OF USING THE SYSTEM

A. The Running Process

Through the massive open-source database audit, the database management and data source management can add the production database as well as its users and passwords that need to be managed to the massive open-source database audit software.

Through user management and role management, it can add the company and its employees that need to be managed to the massive open-source database audit software.

Through the role data source function of the system, it can establish the mapping of database users and database accounts.

After completing the above work, the system can be put into operation.

B. Log in the System

Open the IE browser and enter the address in the address bar to log in the page. Enter the username / password and log in the system homepage.

C. Database Management

In the database management tab, add all the production databases to the system.

Click the “Add” button and fill in the relevant information. For example, enter the database name A1_ODS, URL (THIN mode) jdbcOracle:thin:@192.168.1.60:1521:al_ods.

Instructions as follows:

The string format of URL (THIN) mode is: fixed string (jdbc: Oracle: thin:) @ database IP address: Port: Service name.

RUL (connection string) is the DESCRIPTION part of tnsnames.ora file, such as:

```
(DESCRIPTION=(ADDRESS_LIST=(ADDRESS=(PROT
OCOL=TCP)(HOST=192.168.1.60)(PORT=1521)))(CONNEC
T_DATA=(SERVER=DEDICATED)(SERVICE_NAME=ods
)) )
```

It will return to the list page after a successful registration of production database.

D. Data Source Management

Data source management is to achieve the function of allocating and managing the operation rights of all database accounts and passwords.

Click the “Add” button to add the database user information.

The suggested naming rules for data source name field are as follows: example name_username_utility (company name). For example, ods is the example name, scott is the database user name, and dev refers to development. It can easily be classified and managed through standardized naming.

Database fields can be automatically selected, without manual entry.

The username and password fields are the sys system administrator's account and password.

The purpose field is a descriptive field and can be filled according to the actual situation.

The access time field needs to be filled out similarly to the UNIX system's cron tab command. It can limit user's access time to the database by setting time limits.

The database user permission level field can be used to configure the system whether it records users' operations, whether audit the statements containing the keyword (for example, update, insert.....), whether open some functions of PLSQL DEV.

When the database information is incorrect or fill out the wrong password, the system will alarm errors.

After adding the sys users, we can repeat the steps above and add other users to the massive open-source audit software.

Note: The sys users should be added first.

E. Role Management

In the customer's organizational structure, each company is responsible for different task, including development, maintenance, and monitoring. Therefore, different company may play a different role.

Click the “Add” button and add the privilege information of the role.

Fields explanations are as follows: the user's role name should be filled by following the “example name_role type” format. Select the appropriate privileges for roles based on actual conditions.

F. Role Data Source

The role data source is to carry out the roles and corresponding database accounts. After establishing the role data source mapping, all operators who belong to certain role can only use the corresponding database account to operate the database. Meanwhile, the privileges of the operator are limited by the privileges the role and the database account. His or her operations will be recorded and audited by the system.

Click the “Add” button and add the role management data source information page.

Fields explanations are as follows: the role field is the established role; the data source field is the established data source user. The two fields are not required manual entry. You can select them from the list.

Click the “Submit” button and return to the role data source list page.

G. User Management

User management is to register and record the specific operator according to his or her role (or company).

Fields explanations are as follows: the user name refers to the English code of the operator; the full name can fill out the

real name of the operator; the user group is the operator's company; the professional status is the operator's specific job position; the user's role is the operator's database account; the log-in password is the password of operator using pl/sql dev.

Click the "Submit" button and return to the user list.

H. Approval Management

The approval management includes pending PL/SQL, approval implementation records, approval return records, approval implementation records (30 days ago), approval return records (30 days ago), and other functional modules.

The system will execute the SQL statement in three statuses: the status of submission, the status of approval, the status of approval return.

When an operator executes a SQL statement, if the statement has the key word of "approved", the operator could not execute the statement in the production system. The statement needs to be approved by customers. Its status should be "submission".

When a client DBA believes that the submitted SQL statement can be executed, he or she will give approval and the statement will be executed by the operator. Otherwise, the operator cannot execute the statement.

Click the hyperlink column in the "Title" list and enter the approval page.

Under normal conditions, only the client DBA can carry out the approval. The operation and maintenance DBA can review operations. "Approval" means all approved SQL statements can be executed. The reviewed SQL statement still needs approval before implementation. By means of this arrangement, the operation and maintenance DBA can take advantage of their professional skills and provide a reference for client DBA decisions.

The client DBA can also give full authorization to the operation and maintenance DBA for approval. Thus, it can reduce the workload of client DBA. The client DBA can concentrate on the more important production system.

After the approval, you can check the approval records.

Click the hyperlink column in the "Title" list and enter the details page.

After the operator executes the statement, it can be found in the approval execution record page.

The approval return records save the SQL statements that the client DBA did not give approval of execution. These records indicate that the returned SQL statements may make mistakes or potential risks in execution.

I. Audit Management

The audit management module is the system audit logs, including the following three aspects: database audit logs, system operations logs, and system log-in logs.

The database audit logs record the execution of SQL statements, including the executor, database, database account, application time, status of SQL statement and result.

Click the "Notes" hyperlink and view the detailed process of the application, approval, and execution of the statement.

The system operations logs record the history of user using the massive open-source database audit software. The massive open-source database audit software can automatically save the user name, IP address, operating contents, operating results, date, and so on.

The system log-in logs record the history of user logging in the massive open-source database audit software. The massive open-source database audit software can automatically save the user name, IP address, date, and so on.

ACKNOWLEDGMENT

This paper Supported by Inner Mongolia Colleges and Universities Scientific Research Projects (NJZC16191) and Dr. Scientific Research Fund of Inner Mongolia University for Nationalities (BS323).

REFERENCES

- [1] Chen jing,Fan naiji,Yuan xiaodong,Jiang yilan.Oracle database access technology under Matlab environment [J](in Chinese). Journal of Computer Applications, 2015,S1:78-82+97.
- [2] Ni jiaming,Han qiang.The design of power Information System data recovery system Based on Oracle Database [J] (in Chinese). Electrical Applications,2016,12:74-76+81.
- [3] Guang baohua,Jia fengwei,Wang tianjing.The database access control policy based on the properties for Cloud storage platform [J] (in Chinese). Computer Science,2016,03:167-173.
- [4] Zhu yi,Zhu hong,Xie meiyi,Feng yucai.Mandatory Access Control formal analysis and proof for Database Management System [J] (in Chinese). Computer Systems,2015,03:401-407.
- [5] Wang zhenhui,Wang zhenduo,Xie yingbai,Zhi kanmai.Web Database Security Middleware Research and Design Based on XML [J] (in Chinese). Journal of Computer Applications and Software,2015,08:38-42+179.

A Simple Fusion Method for Trajectory Data of Aircraft

Dingxin Yang*, Peng Du and Jinwei Sun

China Satellite Measure and Track Centre, China Jiangyin

*Corresponding author

Abstract—Propose a fusion arithmetic for trajectory data of aircraft in flight. The method uses a variety of trajectory data which we can get for fusion calculation, then we can reduce a composite trajectory data for digital-guided, and as the basis of judging the aircraft flight state. Through the past, an active phase of the aircraft tracking data playback, testified the practicability and effectiveness.

Keywords—trajectory; fusion; support

I. INTRODUCTION

In the process of aircraft in flight, the measured data of aircraft trajectory is adopted for the digital guiding of measuring devices, and it is also a major basis for estimating the trajectory of aircrafts. With the ever increasing developments of aeronautics measuring techniques, there are a variety of external trajectory procedures which make various trajectory measuring sources available. Thus we have more choices of trajectory data utilization. Aircraft launching tasks are short in time and demands real-time property of data measuring. It requires stable and precise delivery of digital guiding data, together with reliable estimation of trajectory data. Existing methods are mainly based on human jobs including comparing the target trajectory and the theoretical trajectory, and observing the curves of trajectory speed and height is also necessary. Since human jobs are involved, this process takes long time and becomes unreliable. Once errors occur, the digital guiding data will be quite unstable and the secure of measuring devices are influenced. This paper proposes a integration method for trajectory data, and it computes a systematic trajectory dataset based on integration of the retrieved trajectory data. Our method improves the reliability of trajectory significantly.

II. DATA INTEGRATION ALGORITHM

After measuring devices obtain m measuring values denoted x_i ($i=1,2,\dots,n$), the integration method utilizes these values in a synthetical manner [1]. Here x_i does not follow the normal distribution due to the computation error, noises, measuring conditions, precision of measuring devices and certain factors of the measured objects. So data processing methods based on the normal distribution model will suffer from systematic error [2]. In reality, the quality of measured data is decided by facticity of x_1, x_2, \dots, x_n . The better the facticity of x_i is, the more support it gets from the other data. The support provided by x_j to x_i can be considered as the confidence of x_i judged by x_j . Here we denote the support

between different data items as a relative distance. The definition of the relative distance d_{ij} is given as in (1):

$$d_{ij} = |x_i - x_j| \quad (1)$$

As shown in equation (1), the larger d_{ij} is, the more differences exist between x_j and x_i , and the less support we get. The relative distance adopt available measured data, and requires no priori information. Then we define a supporting function r_{ij} :

$$r_{ij} = -\frac{d_{ij}}{\max\{d_{ij}\}} + 1 \quad (2)$$

Here $\max\{d_{ij}\}$ is the maximal value among all the relative distances, and the larger a relative distance is, the less the support provided. As depicted in equation (2), the support value is zero when the maximal relative distance is reached, and here we say there is no support between data items. In opposite, a data item provides a support value as 1 to itself, since the relative distance is valued 0.

This function provides two properties:

- 1) The function value is opposite to the relative distances;
- 2) Since the function value is in $[0, 1]$, the advantages of membership function in the fuzzy set theory can be used in the data processing phase, and absolution of support between different data items can be avoided. This improves the precision and reliability of data integration result.

Given the problem of data integration, we conduct a supporting matrix R as in (3):

$$R = \begin{bmatrix} r_{11} & r_{12} & \cdots & r_{1n} \\ r_{21} & r_{22} & \cdots & r_{2n} \\ \vdots & \vdots & \ddots & \vdots \\ r_{n1} & r_{n2} & \cdots & r_{nn} \end{bmatrix} \quad (3)$$

The value r_{ij} is the supporting value of x_i and x_j , so R is a symmetric matrix, and it can not express the total support from

a measured data item. Thus we define weight coefficient $\bar{\omega}_i$

$$\sum_{i=1}^n \bar{\omega}_i = 1$$

($\bar{\omega}_i \geq 0$), where $i=1, 2, \dots, n$. Take $\bar{\omega}_i$, r_{i1} , r_{i2} , \dots , r_{in} into consideration together, then we define a group of none negative parameters v_1, v_2, \dots, v_n so that

$$\bar{\omega}_i = v_1 r_{i1} + v_2 r_{i2} + \dots + v_n r_{in} \quad (4)$$

In the form of matrix, we have

$$W = RV \quad (5)$$

Here we have $W = [\bar{\omega}_1, \bar{\omega}_2, \dots, \bar{\omega}_n]^T$ and $V = [v_1, v_2, \dots, v_n]^T$. Since $r_{ij} \geq 0$, the matrix R is a none negative matrix so it has a maximal eigenvalue $\lambda \geq 0$, and $\lambda V = RV$. Then we can get the corresponding feature vector $V = [v_1, v_2, \dots, v_n]^T$. Suppose that

$$\bar{\omega}_i = \frac{v_i}{v_1 + v_2 + \dots + v_n} \quad (6)$$

Then $\bar{\omega}_i$ is the i th weight coefficient of the measured data item x_i , and integration result of the n measured data items is given as in (7):

$$x = \bar{\omega}_1 x_1 + \bar{\omega}_2 x_2 + \dots + \bar{\omega}_n x_n \quad (7)$$

This method is suitable to integrate more than three types of measured data, and it provides advantages as below:

- 1) Real-time property and feasible computation;
- 2) Only measured data is required and no priori information is necessary, where existing methods demand priori information of measuring devices [5][6];
- 3) The more types of measured data, the better quality of integration results.

III. IMPLEMENTATION AND APPLICATION

A. Implementation

The trajectory of aircraft consists of seven elements as denoted by $r = \{t, x, y, z, vx, vy, vz\}$. Here t is the time, and x, y, z are the axis values in 3-d space [3]. At the same time, vx, vy, vz are the speed values along 3-d axis directions. We get a group of trajectory data with the measured trajectory data integration algorithm introduced in the last section. And the result is used for digital guiding, monitor display and state judgement.

The detailed workflow is shown in figure 1.

1) Receive different types of trajectory data in a real-time manner;

2) Align all the measured trajectory data in terms of time and space, and interpolation algorithms are adopted. In this process, all the trajectory data are transformed into a single coordinate system.

3) If we have more than three types of trajectory data, utilize data integration algorithm to obtain a group of systematic trajectory output. More details are referred to [4].

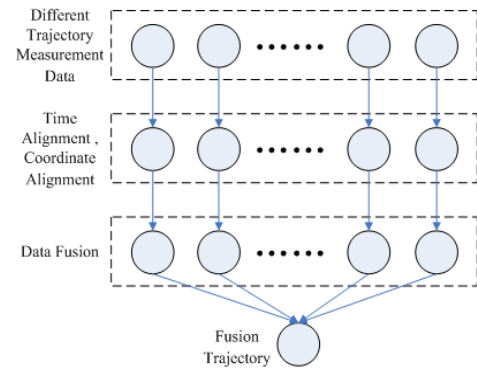
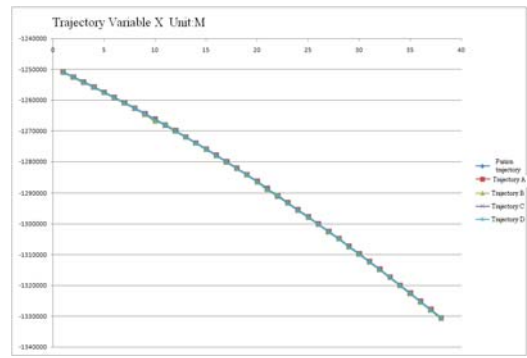


FIGURE I. THE FRAMEWORK OF IMPLEMENTATION.

B. Application

We implement our method using VC++6.0, and a project for integration computation of aircraft launch trajectory data is conducted. The algorithm details are referred to [4]. We simulate the aircraft launch task with historical record data, and get four types of measured trajectory data denoted by A, B, C and D. We only list six axis values of a trajectory as (x, y, z, v_x, v_y, v_z) due to the limit of space, and Some of the result is shown in figure 2.



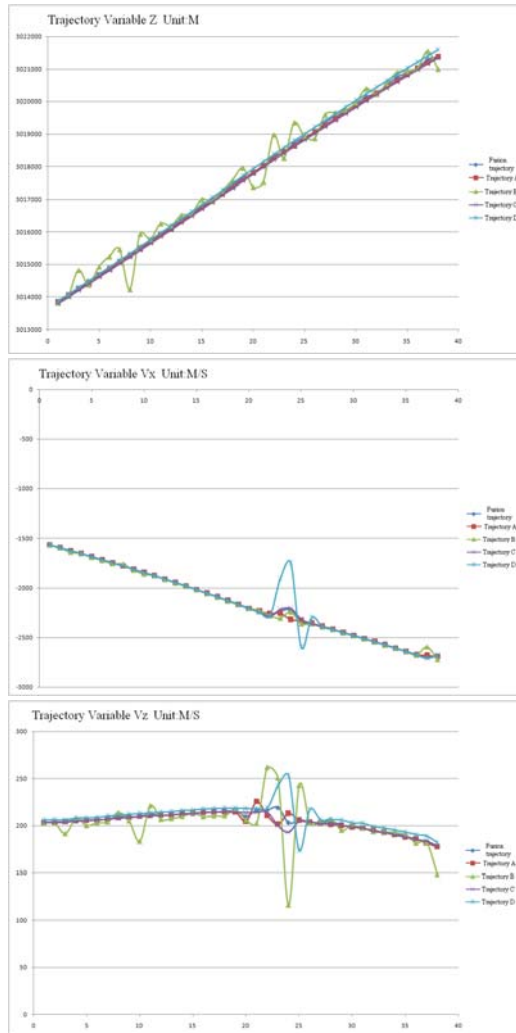


FIGURE II. THE INTEGRATION RESULTS OF A AEROGRAPH TRAJECTORY.

As shown in the measured results, the algorithms are able to integrate all the measured data, and the variables are suitable. This method provides precision, and it gives smooth result when certain types of data are shaking. So we conclude that our method has reasonable effectiveness and efficiency, and it improves the reliability of trajectory data utilization.

IV. CONCLUSION

We repeat with task record data, and it is shown that our method is able to integrate trajectory data while providing real-time property. This method still needs further verification in more complex environments, since the aircraft launching process is complex and of unknown factors. What is more, our method can be used in other applications which are in demand of data integration.

REFERENCES

- [1] Dai YP. Multi sensor data fusion theory and Application[M]. Beijing Institute of Technology press, Beijing, China. 2004: 37-61.
- [2] Sha DG. Evaluation of uncertainty in measurement and analysis of error[M]. China metrology press, Beijing, China. 2003: 47-66.
- [3] Hu SL. Pulse radar tracking measurement data processing technology[M]. National Defence Industry Press, Beijing, China. 2007:20-34.
- [4] Xu SL. Common algorithms for assembly (C++ language description) (Fourth Edition)[M]. Tsinghua University press, Beijing, China. 2008: 95-114.
- [5] Xiang SL. Application of the technology of tracking real-time fusion[J]. Chinese radar. 2008(4): 1-3.
- [6] Wang Zhaogang , Wu Yinlin. Data Fusion to Ballistic Trajectory Estimation Based on The Least Square Estimate for Multi photo electric Cinetheodolite Intersection [J]. Journal of Projectiles, Rockets, Missiles and Guidance. 2011:31(3): 172-176.

Empirical Test of Arbitrage Pricing Model for the SSE 50 Index Stocks

Mingyue Ding¹, Yumei Pan² and Yanqiang Ding^{3,*}

¹Ji'nan Center for Marketing via Phones, China Ping'an Life Insurance Corp., Ji'nan, China

²Accounting Department, Shandong University, Ji'nan, China

³School of Economics, Shandong University, Ji'nan, China

*Corresponding author

Abstract—The objective of this paper is to test the applicability of arbitrage pricing theory specifically for the performance of the SSE 50 Index composite stocks listed on China's Shanghai Stock Market. Two groups of the SSE 50 Index stocks have been selected and tested. Principal component analysis is used to extract the common factors that influence the daily mean rate of return without dividends of the selected stocks for the period from January 2, 2014 to July 21, 2017. Two-pass regression method is employed to test the significance of the common factors in arbitrage pricing model. The main findings in this analysis are that for the first group of 15 persistently included stocks in the SSE 50 index there could not be found out significant common factors, and for the second of 11 in-and-out stocks of the SSE 50 index there could be found out two significant common factors. The results of this study suggest that we should investigate separately into specific blocks of capital markets when we are checking the applicability of arbitrage pricing theory and designing optimal quantitative investment strategies based on arbitrage pricing model.

Keywords—arbitrage pricing model; principal components analysis; SSE 50 index composite stocks

I INTRODUCTION

SSE 50 index was launched on January 2, 2004 by China's Shanghai Stock Exchange (SSE). The index is computed using the 50 most representative stocks listed on the Shanghai Stock Exchange. These composite stocks are of large scale and actively traded with sound liquidity. Arguably, these blue chip stocks are the most important potential targets of investment. However, specific analysis on these stocks is rare and outdated.

The purpose of this paper is to make a specific and in-depth analysis of the performance of the stocks in the SSE 50 index and the common factors influencing them based on the arbitrage pricing theory, using the most recent data available. This paper will examine whether the arbitrage pricing model and quantitative methods can apply to China's market of pillar blue chips. This analysis will be helpful for us to understand the core part of China's capital markets and the nature of the ballast stone stocks, and let us know whether optimal quantitative investment strategies can be designed based on arbitrage pricing model.

The research scope of this paper will be limited to two groups of the stocks that have been included in the SSE 50 index as its composite stocks. The first group includes the stocks that are persistently included in the index not only during the period

from as late as July 1, 2013 to July 21, 2017, most of the selected stocks were also in the index before July 1, 2013, and even since the inception of the index on January 1, 2004. The second group is composed of the stocks that entered and then left the SSE 50 index during the period from December 16, 2013 to July 21, 2017. The data to be analyzed will be limited to the daily **mean rate of return** (MRR) without dividends of the chosen stocks during the recent three and a half years from January 1, 2014 to July 21, 2017, when the data was downloaded from CSMAR® database.

There will be two stages in this research. Principal component analysis will be first used to discover whether there are and to extract common factors that influence the rate of return to investment in the stocks, and then the two-pass regression procedure will be employed to test the significance of the common factors and decide whether arbitrage pricing models will apply to the pricing of these stocks. Microsoft Excel will be used to clean and organize the daily trading data of the selected stocks, IBM SPSS for principal component analysis, and MathWorks' MATLAB for the two-pass regression procedure to test the significance of the common factors.

The paper is structured as follows. The following section will provide a brief review of the theoretical and empirical studies on asset pricing and China's stock markets. The third section will introduce the arbitrage pricing theory and models, and relevant analytical methodology. Data description will be supplied in the fourth section, and principal component analysis and testing for arbitrage pricing model are done in section five and six respectively. The thesis concludes in section seven with main findings of the research and suggestion for future investigation.

The major contribution of this paper to the arbitrage pricing theory literature and practical investment and risk management is its ad hoc examination on the applicability of arbitrage pricing model to the SSE 50 index stocks which are the blue chips on China's capital markets.

II REVIEW OF THEORETICAL AND EMPIRICAL LITERATURES

Ross [1] developed the arbitrage pricing theory that derives the gains of stocks from the characteristics of the gain producing process of stocks, providing a broader point of view on the market equilibrium process and the risk-return relation.

Chamberlin and Rothschild [2] first proved that extracting the eigenvectors, i.e. principal component analysis, is a good way to find the approximate factor structures. Connor and Korajczyk [3, 4] extended the asymptotic principal components analysis to identify statistically the approximate common factors and compute the risk premium to overcome the shortcomings of the factors analysis methodology to empirically specify and test arbitrage pricing models.

Ravi Shukla [5] pointed out that the assumptions of the arbitrage pricing theory may not be satisfied when the random process of rate of return of stocks is not linear, or the random variance is not totally diversified, or there might exist arbitrage opportunities.

Zhu [6] introduced arbitrage pricing theory to Chinese readers. Later on Chinese scholars have used Chinese market data to test empirically the general applicability of arbitrage pricing theory in China's stock markets and relationship between macroeconomic forces and the market performance (rate of return and its risk) of stocks. Most of the empirical analysis on China's stock markets are positive and confirm the fitness of arbitrage pricing theory, while some other disagreed. Some authors have also tried to make investment recommendations based on their research results.

Ji and Hu [7] analyzed the daily rates of return of the 50 composite stocks during the first half year after the launching of the index from January 2, 2004 to May 27, 2004. The authors drew out nine common factors that had impacts on the daily rates of return of the composite stocks included in the index. The first common factor contributed 38.56% of the variance in the daily rates of return, and the nine factors together contributed 68.4% of the variance in the daily rates of return.

Ji and Hu [7] recommended investors to choose the representative stock of each risk factor, and to create a portfolio by the correspondent weight contributed to the variance in the rate of return by each risk factor, thus to simulate the risk-return structure of the investment in SSE 50 index to get the market rate of return to investment.

Su Ping [8] used the trading data of 16 selected stocks from the 88 stocks which were in the SZSE 100 index to investigate a multi-factor arbitrage pricing model for China's Shenzhen Stock Market under the conditions of permitted and forbidden short sales respectively. The author showed that the multi-factor arbitrage pricing model can give investors reliable investment suggestions, and calculated the optimal quantitative strategies for investing in the selected stocks.

Yin and Chen [9] made empirical analysis on single factor, five-factor, and ten-factor arbitrage pricing model by means of asymptotic principal component analysis, using 463 prices of 35 stocks on China's Shanghai Stock Market and Shenzhen Stock Market. The authors found out that arbitrage pricing models with one, five, and ten factors are all better than capital assets pricing model (CAPM) in explaining the variance in the rates of return of the stocks.

III BRIEF REVIEW OF ARBITRAGE PRICING MODEL AND ANALYTICAL METHODS

A. Arbitrage Pricing Model

According to Reinganum [10], there are three assumptions in arbitrage pricing theory: capital market are perfectly competitive; investors always avoid the risk and prefer more wealth than less with certainty; a multi-factor model could represent the stochastic process of the generating asset return. Focusing on a strict factor structure, the arbitrage pricing theory holds that the expected return is linearly related to its covariance with the factors when there is no arbitrage. That is to say the factor loadings or betas are proportional to the returns' covariance with the factors. Huberman [11] expounded the mathematics of arbitrage pricing theory.

A multi-factor arbitrage pricing model can be specified as following:

$$P_i = E(P_i) + \beta_{i1}\Phi_1 + \beta_{i2}\Phi_2 + \dots + \beta_{ik}\Phi_k + \varepsilon_i \quad (1)$$

Where R_i is the return rate of company i 's stock; $E(R_i)$ is the expected return rate of company i 's stock; Φ_j is the deviation from the expected value of the j^{th} factor, and its expected value is zero; β_{ij} is the sensitivity of the stock of company i to the j^{th} factor; ε_i is the influence of company's own characteristic on return, and its expected value is zero and totally independent with the factors and other companies' characteristics.

In this way, the return behavior of different risk assets are linked with multi factors, and any part of change of asset return that could not be explained by the change of multi-factors just belongs to the asset.

In a large portfolio, zero-investment's return with zero-systematic-risk portfolio is zero only if the idiosyncratic effects vanish. United the theory of linear algebra and the rationales of economics, we can express the expected return on any asset i :

$$E_i = \lambda_0 + \lambda_1\beta_{i1} + \dots + \lambda_k\beta_{ik} \quad (2)$$

Where λ_0 could be regarded as the expected return rate on an asset with the risk which is zero-systematic (i.e., $b_{01} = b_{02} = \dots = b_{0k}$). $\lambda_1, \dots, \lambda_k$ are the weight of factor, and could be explicated as factor risk premium. And the relationship between the price or return of asset i and the risk premium is shown by b_i .

B. Principal Components Analysis

Principal component analysis (PCA) is a statistical process invented by Karl Pearson in 1901 that converts observation values of a set of possibly correlated variables into values of linearly irrelevant variables called principal components (or sometimes the main variation pattern) using orthogonal transformations. Principal components analysis is mostly used as a tool in exploratory data analysis and for making predictive models. Using the principal components analysis we could get the number of main components that is less than or equal to the number of original variables, the first principal component causes the greatest share of variance, and the variance caused by the following components decreases.

According to Chamberlain and Rothschild [2], when asset returns have a factor structure with a small number of factors, the covariance matrix of asset returns may be written as the sum of a diagonal matrix and a matrix of short rank. That is, in a strict k-factor asset market arbitrage pricing model, the return on the i^{th} asset is generated by

$$\rho_i = E(\rho_i) + \beta_{i1}\Phi_1 + \dots + \beta_{ik}\Phi_k + \varepsilon_i, \quad (3)$$

Where the factors F_k are uncorrelated with the idiosyncratic disturbances ε_i , which are in turn uncorrelated with each other. This implies that the covariance matrix may be decomposed into a matrix of rank k and a diagonal matrix. That is, for any N , $\Sigma_N = B_N B_N' + D_N$, where B_N is the $N \times k$ matrix of factor loadings and D_N is a diagonal matrix.

Chamberlain and Rothschild [2] defined an approximate k -factor markets structure when there is a sequence $\{\beta_{i1}, \dots, \beta_{ik}\}$, $i \in (1, \infty)$, such that for any N , $\Sigma_N = B_N B_N' + R_N$, where the i, j element of the $N \times k$ matrix B_N is β_{ij} and R_N is a sequence matrices with uniformly bounded eigenvalues, and showed that extracting the eigenvectors of Σ_N is a good way of finding approximate factor structures. That is to say, principal component analysis is an appropriate technique for finding an approximate factor structure.

The procedures of asymptotic principal component analysis is composed of five steps according to Yin and Chen [9]. In general circumstances, the sample is sufficiently large, steps 4 and 5 can be skipped. The advantage of asymptotic principal component method is that it is not necessary to select factors ex ante, and the extracted common factors are linearly independent with each other and with the residual terms.

C. Two-pass Regression Method for the Test of Arbitrage Pricing Model

For the test of arbitrage pricing model, the two-pass regression method is often to use [8]. In accordance with principal components analysis, the first pass is to ensure the structure of arbitrage pricing model, and get the estimated values of the sensitivity to the factors through the multiple linear regression, and the second pass, using the estimated values of the sensitivity to the factors as explanatory variables, to check whether arbitrage pricing theory is established using cross section regression.

$$\rho_{it} = \alpha_i + \beta_{i1}\Phi_{1t} + \beta_{i2}\Phi_{2t} + \dots + \beta_{ik}\Phi_{kt} + \varepsilon_{it} \quad (4)$$

$$\rho_i = L_0 + L_1\beta_{i1} + L_2\beta_{i2} + \dots + L_k\beta_{ik} + \varepsilon_i \quad (5)$$

r_i is the mean return rate of the stock i , that is the sum of daily return rate divided by the number of days. $\beta_{i1}, \beta_{i2}, \dots, \beta_{ik}$ are the loading values obtained by principal components analysis, that is, the sensitivities. In generally, we do the regression with all the principal components which were extracted. However, there has another method to do the regression, which is stepwise regression. Stepwise regression is a method of fitting regression models in which predictive variables are selected by automated procedures. It is basically repeated several times, each time removing the weakest relevant variables, then the best variables to explain the distribution are left.

IV DESCRIPTION OF DATA AND ITS SOURCES

SSE 50 index takes December 31, 2003 as its base day, and its base point is 1000. Its 50 composite stocks are adjusted half a year according to the principles of sample stability and dynamic tracking, and every time of adjusting at most 10% of the composite stocks can be changed. Tentative adjustment can be made under some special cases such as when some stocks emerge to be among the top stocks or acquisition and merging occurred.

As of July 21, 2017, the composite stocks of SSE 50 index have been adjusted normally for twenty-seven times and tentatively for fourteen times. There are a total of 163 stocks that have been selected as composite stocks of the index for a total of 196 inclusions into the index and a total of 146 exclusions from the index. Thirty stocks have been remained in the index during this research period. These stocks are presented in Table 1. The data in the rightmost three columns can be found in Fact Book 2016 [12].

* 600887 was excluded from it on January 5, 2009; * 601766 was excluded on January 4, 2011; * 601688 was excluded on January 4, 2012; ** Included in the index 10 trading days after their initial public offer; † Used for principal components analysis later on because they had data on all the trading days. Sources: CSMAR® database provided by Shenzhen GTA (GuoTaiAn) Information Technology Corporation; Shanghai Stock Exchange [12].

TABLE I. PERSISTENT COMPOSITE STOCKS OF SSE 50 INDEX FROM 2014 TO 2017

Stock Code	Short Name of the stocks	Date of Inclusion	Date of IPO	Number of Tradable Shares [10,000 shares]	Closing Price [RMB yuan]	Weight in SSE 50 Index [%]
600000	Pudong Development Bank	2004/1/2	1999/11/10	1865347	18.27	4.20
600016†	Minsheng Bank	2004/1/2	2000/12/19	2955177	9.64	6.75
600028†	China Petroleum & Chemicals	2004/1/2	2001/8/8	9555777	4.96	1.27
600030†	CITIC Securities	2004/1/2	2003/01/06	981466	19.35	3.76
600036	China Merchants Bank	2004/1/2	2002/4/9	2062894	17.99	4.56
600050†	China Unicom	2004/1/2	2002/10/9	2119660	6.18	1.30
600104	Shanghai Automobile Industry Group	2004/1/2	1997/11/25	1102557	21.22	1.71
600887*	Yili Group	2004/1/2; 2012/7/2	1996/3/12	601565	16.43	2.43
600519†	Kweichow Moutai	2005/7/1	2001/8/27	125620	218.19	2.66
601006***†	Daqin Railway	2006/8/15	2006-08-01	1486679	8.62	1.26
601398**	Industrial and Commercial Bank	2006/11/10	2006/10/27	26961221	4.58	2.41
600048	Poly Real Estate	2007/1/4	2006/7/31	1075525	10.64	1.70
601628***†	China Life	2007/1/23	2007/1/9	2082353	28.31	1.15
601166**	Industrial Bank	2007/2/19	2007/2/5	1617962	17.07	5.57
601318**	China Ping An Insurance	2007/3/15	2007/3/1	1083266	36.00	9.39
601328***†	Bank of Communications	2007/5/29	2007/5/15	3925086	6.44	3.69
601088***†	China Shenhua	2007/10/23	2007/10/9	1649104	14.97	0.72
601857***†	Petro China	2007/11/19	2007/11/5	16192208	8.35	0.99
601601†	China Pacific Insurance	2008/7/1	2007/12/25	628670	28.86	2.20
600837**	Haitong Securities	2009/1/5	1994/2/24	809213	15.82	3.16
601169	Bank of Beijing	2009/1/5	2007/9/19	1267223	10.53	2.61
601766*	CRRC	2009/7/1; 2011/7/1	2008/8/18	2291769	12.85	2.88
601668†	China State Construction	2010/1/4	2009/7/29	2990056	6.34	2.34
601288***†	Agricultural Bank of China	2010/7/29	2010/7/15	29405529	3.23	2.99
601818**	Everbright Bank of China	2011/1/4	2010/8/18	3981036	4.24	1.64
601688*	Huatai Securities	2011/1/4; 2013/1/4	2010/2/26	544372	19.72	1.59
600111†	Northern Rare-Earth	2011/1/4	1997/9/24	221920	14.02	0.75
601989†	China Shipbuilding Industry	2011/7/1	2009/12/16	1795786	9.40	2.11
600518	Kangmei Pharmaceutical	2013/07/01	2001/3/19	439743	16.95	1.26
600999	China Merchants Securities	2013/07/01	2009/11/17	480310	21.70	1.54

During the period from December 16, 2013 to July 21, 2017, there are eight normal adjustments and one times tentative adjustment of the composite stocks. There are forty-one stocks being included into and forty-one stocks excluded from the SSE

50 index at the same time. Among the newly included stocks, twenty-one stocks were excluded from the index later on during the same period. These stocks are presented in Table 2.

TABLE II. IN-THEN-OUT COMPOSITE STOCKS OF SSE 50 INDEX FROM 2014 TO 2017

Stock Code	Short Name of the stocks	Date of Inclusion	Date of exclusion	Date of IPO	Number of Tradable Shares [10,000 shares]	Closing Price, 2005 [RMB yuan]
600018	Shanghai International Port Group	2013/12/16	2016/06/13	2000/07/19	2275518	6.48
600637	BesTV (Shanghai Oriental Pearl Media)	2013/12/16	2017/06/12	1993/03/16	215844	37.89
600406	NARI Technology Development	2013/12/16	2015/12/14	2003/10/16	220575	16.68
600332	Guangzhou Baiyunshan	2013/12/16	2015/06/15	2001/02/06	103634	30.27
601117†	China National Chemical	2013/12/16	2014/12/15	2010/01/07	493300	6.89
600089†	TBEA	2014/06/16	2015/12/14	1997/06/18	317812	11.77
600196†	Fosun Pharmaceutical	2014/06/16	2015/06/15	1998/08/07	190561	23.49
600703	San'an Optoelectronics	2014/06/16	2015/06/15	1996/05/28	237038	24.28
601118†	China Hainan Rubber Industry Group	2014/06/16	2015/06/15	2011/01/07	393117	7.56
600832	Shanghai Oriental Pearl Group/Old	2014/06/16	2015-05-20 delisted	1994/02/24	n.a.	n.a.
600690	Qingdao Haier	2014/12/15	2015/12/14	1993/11/19	550947	9.92
601998†	China CITIC Bank Corp	2014/12/15	2017/06/12	2007/04/27	3190516	7.22
600109†	Sinolink Securities	2014/12/15	2017/06/12	1997/08/07	283686	16.12
600150†	China State Shipbuilding	2014/12/15	2016/06/13	1998/05/20	137812	34.83
600372†	Aviation Electronics	2014/12/15	2015/06/15	2001/07/06	175916	24.63
600893	Aero-engine	2015/05/20	2017/06/12	1996/04/08	136514	45.03
600583†	Offshore Oil Engineering	2015/05/20	2015/12/14	2002/02/05	404901	8.95
600795†	GD Power Development	2015/12/14	2016/12/12	1997/03/18	1781554	3.93
601669	Power Construction Corporation of China	2015/12/14	2016/12/12	2011/10/18	330000	8.03
601377†	Industrial Securities	2016/06/13	2017/06/12	2010/10/13	520000	11.00
601919	COSCO SHIPPING Holdings	2016/06/13	2016/12/12	2007/06/26	763567	9.02
601727	Shanghai Electric Group	2016/06/13	2016/12/12	2008/12/05	985100	11.54

† Used for principal components analysis later on because they had data on all the trading days. Sources: CSMAR® database provided by Shenzhen GTA (GuoTaiAn) Information Technology Corporation; Shanghai Stock Exchange [12].

We can observe from Table 1 that among the 30 stocks which are remained inclusion in the SSE 50 index there are eight stocks which were originally included in the index when the index was initiated on January 2, 2004; there are nine stocks which were included tentatively in the index 10 trading days after their IPO in 2006, 2007, and 2010; there are seven stocks that were included in the index within half a year or around a year from 2006 to 2010; there are only two stocks which were lately included in July, 2013.

There are nine stocks in the banking sector, four in the security sector, three in the insurance sector, taking weights of 32.78%, 10.05%, and 12.74% in the SSE 50 index respectively; thus the financial sector takes a weight of 55.57% in the SSE 50 index. There are two stocks in the petroleum and chemicals sector, one in the coal and electricity sector (601088), one in the telecommunication sector (60050), two in the railway and locomotive sector (601006 and 601766), together the energy and infrastructure sectors take a weight of 8.42% in the index; the rest eight stocks are in the sectors of manufacturing, construction (601668), mineral (600111), and real estate (600048), taking a weight of 14.96% in the index. In total, the persistent composite stocks of the SSE 50 index take a weight of 78.95% in the index in 2015 [12].

The daily trading data of the thirty persistent stocks of the SSE 50 index and that of the twenty-one in-then-out stocks from January 1, 2014 to July 21, 2017 is retrieved from CSMAR® database provided by Shenzhen GTA (GuoTaiAn) Information Technology Corporation at the website of the library of China's Shandong University. Because of missing trading data for some of the chosen stocks, later on in this paper fifteen of the thirty persistent stocks and eleven of the in-then-out stocks with full trading data (as indicated in Table 1 and Table 2 by a † symbol) will be selected to do principal components analysis and test the applicability of arbitrage pricing theory.

V ANALYSIS OF THE DATA USING PRINCIPAL COMPONENT ANALYSIS

In this paper, IMB SPSS 23 was used to do the principal component analysis for both the fifteen persistent stocks (first data set) and eleven in-then-out stocks (second data set) with full trading data. The result is shown in Figure I and Figure II.

Component	Initial Eigenvalues			Extraction Sums of Squared Loadings		
	Total	% of Variance	Cumulative %	Total	% of Variance	Cumulative %
1	8.860	59.064	59.064	8.860	59.064	59.064
2	1.333	8.887	67.952	1.333	8.887	67.952
3	.802	5.348	73.299			
4	.690	4.601	77.901			
5	.632	4.214	82.115			
6	.497	3.312	85.427			
7	.397	2.644	88.071			
8	.368	2.455	90.526			
9	.308	2.054	92.580			
10	.274	1.830	94.410			
11	.262	1.748	96.158			
12	.200	1.333	97.491			
13	.151	1.008	98.499			
14	.122	.811	99.310			
15	.103	.690	100.000			

Extraction Method: Principal Component Analysis.

FIGURE I. TOTAL VARIANCE EXPLAINED FOR THE 15 PERSISTENT STOCKS

Component	Initial Eigenvalues			Extraction Sums of Squared Loadings		
	Total	% of Variance	Cumulative %	Total	% of Variance	Cumulative %
1	6.361	57.830	57.830	6.361	57.830	57.830
2	1.390	12.640	70.470	1.390	12.640	70.470
3	.640	5.820	76.290			
4	.543	4.939	81.229			
5	.475	4.314	85.543			
6	.368	3.350	88.893			
7	.327	2.975	91.868			
8	.316	2.871	94.739			
9	.243	2.213	96.952			
10	.203	1.842	98.795			
11	.133	1.205	100.000			

Extraction Method: Principal Component Analysis.

FIGURE II. TOTAL VARIANCE EXPLAINED FOR THE 11 IN-THEN-OUT STOCKS

In Figure I, there are 15 factors influencing the rate of return. According to the principle that the eigenvalues is greater than one to extract factors, percentage of variance and the cumulative percentage explained by the factors is as shown. Two principal components were extracted, they can explain 67.95% of the variance in the set of data. Figure II shows that there are 11 factors influencing the rate of return, and also two principal components were extracted, they can explain 70.47% of the variance in the set of data.

Figure III shows the loading value matrix of the two principal components for the first and second data set. There lists the loading values of the two components, which are sensitivity of the rate of return to the common factors. The loading values are the basis for regression analysis next.

Component Matrix^a

	Component	
	1	2
S600016	.776	-.384
S600028	.829	.015
S600030	.749	.199
S600050	.728	.341
S600111	.604	.565
S600519	.582	.142
S601006	.741	.285
S601088	.834	.171
S601288	.831	-.395
S601328	.840	-.312
S601398	.794	-.445
S601601	.836	-.071
S601628	.804	-.079
S601668	.732	.332
S601857	.788	-.084

Extraction Method: Principal Component Analysis.

a. 2 components extracted.

Component Matrix^a

	Component	
	1	2
S601998	.697	-.530
S600089	.742	.096
S600109	.832	-.266
S600150	.823	.228
S600196	.811	-.292
S600372	.589	.610
S600583	.712	.364
S600795	.864	-.200
S601117	.746	.238
S601118	.647	.396
S601377	.849	-.366

Extraction Method: Principal Component Analysis.

a. 2 components extracted.

FIGURE III. LOADING VALUE MATRIX OF COMPONENTS FOR THE 15 PERSISTENT STOCKS (LEFT PART) AND THE 11 IN-THEN-OUT STOCKS (RIGHT PART)

There is no significant difference in the coefficients of the original variables in each factor, and the coefficients of the individual variables in the factor can be differentiated to the maximum and minimum poles by rotation. We use the mean orthogonal rotation, so that the number of variables with a high loading value on a factor and the number of factors in the variable are minimized. After the rotation, the loading value matrix is as Figure IV.

Rotated Component Matrix^a

	Component	
	1	2
S600016	.830	.245
S600028	.598	.574
S600030	.415	.654
S600050	.303	.745
S600111	.060	.825
S600519	.331	.499
S601006	.351	.712
S601088	.496	.692
S601288	.879	.274
S601328	.828	.341
S601398	.885	.212
S601601	.663	.515
S601628	.644	.488
S601668	.312	.741
S601857	.636	.474

Extraction Method: Principal Component Analysis.

Rotation Method: Varimax with Kaiser Normalization.

a. Rotation converged in 3 iterations.

Rotated Component Matrix^a

	Component	
	1	2
S601998	.873	.065
S600089	.492	.564
S600109	.799	.352
S600150	.466	.716
S600196	.801	.319
S600372	.036	.847
S600583	.292	.744
S600795	.780	.423
S601117	.401	.673
S601118	.222	.726
S601377	.878	.289

Extraction Method: Principal Component Analysis.

Rotation Method: Varimax with Kaiser Normalization.

a. Rotation converged in 3 iterations.

FIGURE IV. LOADING VALUE MATRIX OF COMPONENTS FOR THE 15 PERSISTENT STOCKS (LEFT PART) AND THE 11 IN-THEN-OUT STOCKS (RIGHT PART) AFTER ROTATED

VI TEST OF ARBITRAGE PRICING MODEL BY TWO-PASS REGRESSION METHOD

A. Regression for the First Data Set

For the first data set, regress the mean rate of return to the coefficients of two principal components (loading values) based on the Eq. 5, and the result is shown as Fig. 5. Beta_1 is β_{11} and Beta_2 is β_{12} . $R^2 = 0.12$ means the coefficients of the two principal components can explain 12% of the variance in the

mean rate of return. So, the mean rate of return might not have linear relationship with the coefficients of the two principal components. Besides, the coefficients (λ_0 's) of the β_0 's are not significant, and β_{11} is more significant than β_{12} . T-test shows that λ_1 could be zero with 32.9% possibility, and λ_2 could be zero with 98% possibility. So, the two principal components are not significant.

Considering that loading value of the two principal components may affect each other, we regress the mean rate of return to β_{11} and β_{12} respectively. The results are shown as Fig. 6 and Fig. 7. As we can see, the significant level of both two λ 's are increased. There is 79.4% possibility that λ_1 could not be zero, and 54.7% possibility that λ_2 could not be zero. However, they didn't achieve the 90% significant level. In addition, using the stepwise regression method to do regression, no variables entered into the equation.

Rotated Component Matrix ^a		
	Component	
	1	2
S6000016	.830	.245
S600028	.598	.574
S600030	.415	.654
S600050	.303	.745
S600111	.060	.825
S600519	.331	.499
S601006	.351	.712
S601088	.496	.692
S601208	.879	.274
S601328	.829	.341
S601398	.885	.212
S601601	.663	.515
S601628	.644	.488
S601668	.312	.741
S601867	.636	.474

Rotated Component Matrix ^a		
	Component	
	1	2
S601998	.873	.065
S600089	.492	.564
S600109	.799	.352
S600150	.466	.716
S600196	.801	.319
S600372	.036	.847
S600583	.292	.744
S600795	.780	.423
S601117	.401	.673
S601118	.222	.726
S601377	.878	.289

Extraction Method: Principal Component Analysis.
 Rotation Method: Varimax with Kaiser Normalization.
 a. Rotation converged in 3 iterations.

Model Summary

Model	R	R Square	Adjusted R Square	Std. Error of the Estimate
1	.347 ^a	.120	-.027	.000555713

a. Predictors: (Constant), Beta_2, Beta_1

ANOVA^a

Model	Sum of Squares	df	Mean Square	F	Sig.
1 Regression	.000	2	.000	.819	.464 ^b
Residual	.000	12	.000		
Total	.000	14			

a. Dependent Variable: MRR

b. Predictors: (Constant), Beta_2, Beta_1

Coefficients^a

Model	Unstandardized Coefficients		Standardized Coefficients	t	Sig.
	B	Std. Error	Beta		
1 (Constant)	.003	.002	.000	1.439	.176
Beta_1	-.002	.002	-.352	-1.018	.329
Beta_2	-1.560E-5	.001	-.009	-.025	.980

a. Dependent Variable: MRR

FIGURE V. REGRESSION TO THE COEFFICIENTS OF THE TWO PRINCIPAL COMPONENTS
Model Summary

Model	R	R Square	Adjusted R Square	Std. Error of the Estimate
1	.346 ^a	.120	.052	.000533926

a. Predictors: (Constant), Beta_1

ANOVA^a

Model	Sum of Squares	df	Mean Square	F	Sig.
1 Regression	.000	1	.000	1.773	.206 ^b
Residual	.000	13	.000		
Total	.000	14			

a. Dependent Variable: MRR

b. Predictors: (Constant), Beta_1

Coefficients^a

Model	Unstandardized Coefficients		Standardized Coefficients	t	Sig.
	B	Std. Error	Beta		
1 (Constant)	.003	.001	.000	1.894	.081
Beta_1	-.002	.002	-.346	-1.332	.206

a. Dependent Variable: MRR

FIGURE VI. REGRESSION TO THE COEFFICIENT OF THE FIRST PRINCIPAL COMPONENT
Model Summary

Model	R	R Square	Adjusted R Square	Std. Error of the Estimate
1	.210 ^a	.044	-.030	.000556510

a. Predictors: (Constant), Beta_2

ANOVA^a

Model	Sum of Squares	df	Mean Square	F	Sig.
1 Regression	.000	1	.000	.599	.453 ^b
Residual	.000	13	.000		
Total	.000	14			

a. Dependent Variable: MRR

b. Predictors: (Constant), Beta_2

Coefficients^a

Model	Unstandardized Coefficients		Standardized Coefficients	t	Sig.
	B	Std. Error	Beta		
1 (Constant)	.001	.000	.000	5.369	.000
Beta_2	.000	.000	.210	.774	.453

a. Dependent Variable: MRR

FIGURE VII. REGRESSION TO THE COEFFICIENT OF THE FIRST PRINCIPAL COMPONENT

B. Regression for the Second Data Set

For the second data set, there has 11 stocks, and two principal components. As well as the first data set, regress the mean rate of return to the coefficients of the two principal components (loading values) based on the Eq. 5. This time, use the stepwise regression method directly.

Model Summary				
Model	R	R Square	Adjusted R Square	Std. Error of the Estimate
1	.945 ^a	.893	.881	.000130746
2	.968 ^b	.937	.921	.000106470

a. Predictors: (Constant), Beta_2

b. Predictors: (Constant), Beta_2, Beta_1

ANOVA ^a						
Model	Sum of Squares	df	Mean Square	F	Sig.	
1	Regression	.000	1	.000	75.130	.000 ^b
	Residual	.000	9	.000		
	Total	.000	10			
2	Regression	.000	2	.000	59.434	.000 ^c
	Residual	.000	8	.000		
	Total	.000	10			

a. Dependent Variable: MMR

b. Predictors: (Constant), Beta_2

c. Predictors: (Constant), Beta_2, Beta_1

FIGURE VIII. MODEL SUMMARY FOR THE SECOND DATA SET WITH STEPWISE REGRESSION

Figure VIII illustrates the order of the factors which are introduced. According to the results of the variance analysis, the factor which has the greatest contribution to the return rate variance is introduced first. The first model introduces the factor β_{i2} and the second model introduces the factor β_{i1} . R^2 of the first model is 0.893, meaning that the first model can explain 89.3% of the variance in the mean rate of return. When the factor β_{i1} is added, R^2 increases to 0.937. In F-test, $F = 59.434$ is high as well, that means factors β_{i1} and β_{i2} could explain the variance in the mean rate of return significantly, and the mean rate of the return has a linear relationship with the factors β_{i1} and β_{i2} .

Coefficients ^a					
Model	Unstandardized Coefficients		Standardized Coefficients	t	Sig.
	B	Std. Error	Beta		
1	(Constant)	.001	.000	14.549	.000
	Beta_2	-.001	.000	-8.668	.000
2	(Constant)	.000	.000	-.810	.442
	Beta_2	-.001	.000	-6.725	.000
	Beta_1	.001	.000	.271	.046

a. Dependent Variable: MMR

FIGURE IX. COEFFICIENT OF THE STEPWISE REGRESSION

Figure IX lists the unstandardized coefficients, standardized coefficients, hypothesis test of regression coefficient (t-test) and the P-value. According to t-test, the P-value for factors β_{i1} and β_{i2} are 0.046 and 0.000, respectively. At 95% significance level, the coefficient of factors β_{i1} and β_{i2} are significant. So, this data set is suitable for analysis by arbitrage pricing model.

VII SUMMARY AND FURTHER WORK

The main findings in this paper is that the first data set of the 15 persistently included stocks in the SSE 50 index is not consistent with the arbitrage pricing theory, that is, there could not be found out significant common factors for this group of stocks, and the 11 in-then-out stocks of the SSE 50 index is

consistent with the APT, that is, there could be found out two significant common factors for this group of stocks. This is different from the much more general outcomes in the academic literatures about the applicability of arbitrage pricing theory to China's stock markets.

This study suggests that we should investigate separately into specific blocks of capital markets when we are checking the applicability of arbitrage pricing theory and designing optimal quantitative investment strategies accordingly. Future studies must further examine the reasons why the markets of stocks which are included in the SSE 50 index performed differently in terms of characteristics of the industries and governance, long term variance in their rates of return, and trading dynamics. In a separate paper we are going to calculate the optimal quantitative investment strategies for the 11 in-then-out stocks of the SSE 50 index. We should further check the applicability of arbitrage pricing model to other groups of the SSE 50 Index stocks in earlier and later periods than that in this paper.

ACKNOWLEDGEMENT

This paper is part of the first author's dissertation - Quantitative Portfolio Strategy: An Empirical Analysis of SSE 50 Index Stocks Based on APT Model, submitted in partial fulfilment of the degree of MSc in Financial Engineering (2016|2017), University of Birmingham, The United Kingdom. The author (Mingyue Ding, ID: 1727011) gratefully appreciates the pertinent and patient supervision by her tutor Tatiana Gaydaenko.

REFERENCES

- [1] S. Ross, The arbitrage Theory of Capital Asset Pricing, *Journal of Economic Theory*, 23 (1976) 341-360.
- [2] Chamberlain, Gary, Michael Rothschild, Arbitrage, Factor Structure, and Mean Variance Analysis on Large Asset Markets, *Econometrica*, 51 (1983) 1281-1304.
- [3] Connor, Gregory, Robert A. Korajczyk, Performance measurement with the arbitrage pricing theory: A new framework for analysis, *Journal of Financial Economics*, 15 (1986) 373-394.
- [4] Connor, Gregory, Robert A. Korajczyk, Risk and return in an equilibrium APT: application of a new test methodology, *Journal of Financial Economics*, 21 (1988) 255-290.
- [5] Ravi Shukla, An Empiricist's Guide to the Arbitrage Pricing Theory, Working Paper of the 10th Conference of America's Financial Management Association, Florida (1999).
- [6] Zhu Jing, the 9th Lecture on the Theories and Practices of Security Markets: Portfolio Choice Theory, *World Economic Papers*, 1993, pp.55-60, 79.
- [7] Ji Jun, Hu Qinglin, A Study on the Arbitrage Pricing of the SSE 50 Index, *Statistics and Decision*, 12 (2004) 32-33.
- [8] Su Ping, A Case Study of Multi-factor APT Model Used in Shenzhen Stock Market, *Journal of Zhejiang Business Technology Institute*, 1 (2007) 12-17.
- [9] Yin Xiangfei, Chen Liuqin, An Empirical Study of Arbitrage Pricing Theory on China's Stock Markets: Based on the Asymptotic Principal Components Methodology, *Journal of the Henan Institute of Financial Management*, 1 (2008) 90-95.
- [10] M. Reinganum, The Arbitrage Pricing Theory: Some Empirical Results, *The Journal of Finance*, 2 (1981) 313-321.
- [11] G. Huberman, A simple approach to arbitrage pricing, *Journal of Economic Theory*, 28 (1982) 183-91.
- [12] Shanghai Stock Exchange, Fact Book 2016, pp.35-42.

The Results of the General Traffic Measurements Analysis on the Example of Łódź Voivodeship (in Poland)

Elżbieta Macioszek*, Grzegorz Sierpiński, Marcin Staniek and Damian Lach

Transport Systems and Traffic Engineering Department, Faculty of Transport, Silesian University of Technology, Poland

*Corresponding author

Abstract—The article presents the results of a detailed analysis of data from the General Traffic Measurements carried out in the years 2000 - 2015 on voivodeship roads. The analysis was carried out on the results from the Łódź Voivodeship in Poland.

Keywords—traffic engineering; road traffic measurements

I. INTRODUCTION

es in AADT values in the years 2000c measurements and surveys are the basic source of data for conducting further various types of analyzes (f.ex. [1-8]). The article presents the results of a detailed analysis of data from the General Traffic Measurements (GTM) carried out in the years 2000 - 2015 on voivodeship roads. The analysis was carried out on the results from the Łódź Voivodeship in Poland. The analysis included such features as:

- annual average daily traffic (AADT) in voivodeship;
- annual avarage daily traffic divided into particular generic groups, such as: motorcycles, passenger cars, light trucks, lorries without trailers, lorries with trailers, buses and agricultural tractors;
- Load of voivodeship roads with annual avarage daily traffic;
- Load of voivodeship roads with annual avarage daily traffic divided into particular generic groups.

In addition, AADT changes were analyzed on the three most-intensive voivodship roads.

II. CHARACTERISTICS OF THE VOIVODESHIP ROADS NETWORK IN THE ŁÓDŹ VOIVODSHIP (IN POLAND)

The Łódź Voivodeship is located in the central part of the country. Its capital and main administrative center is Łódź. According to data published by the Central Statistical Office (GUS), in 2017 [9], about 2.5 million inhabitants live in the aforementioned region, which with not the largest area (18200 km²) gives a population density of about 137 people/km² (fifth result in the country). The Łódź Voivodeship has a very extensive network of roads, in particular when it comes to national roads. The A1 and A2 motorways as well as the S8 and S14 expressways pass through its areas. In addition, this area is

characterized by a dense network of provincial roads, whose total length is 1152.4 km, of which 125.4 km are located in urban areas. The list of roads in the Łódź Voivodeship is shown in Table 1.

TABLE I. THE LIST OF ROADS IN ŁÓDŹ VOIVODESHIP (IN POLAND).
SOURCE: OWN RESEARCH ON THE BASIS OF [10-13]

Number of road	The route of the road
449	Syców - Ostrzeszów - Błaszki
450	Kalisz - Grabów nad Prosną - Wyszanów - Wieruszów - Opatów
469	Uniejów - Gostków - Wróblew
473	Koło - Dąbie - Uniejów - Balin - Szadek - Łask
478	Rzymosko - Księża Wólka - Krępa
479	Dąbrówka - Sieradz
480	Łask - Widawa - Szczerców
481	Łask - Widawa - Widoradz Górnny
483	Łask - Szczerców - Nowa Brzeźnica - Częstochowa
484	Buczek - Zelów - Bełchatów - Kamieńsk
485	Pabianice - Wadlew - Bełchatów
486	Wieluń - Droga 43 - Działoszyń
491	Działoszyń - Droga 42 - Łobodno - Częstochowa
492	Waźne Młyny - Łobodno - Kolbuck - Wręczyca Wielka - Błachownia
573	Nowy Duninów - Gostynin - Żychlin
581	Gostynin - Łanięta - Krośniewice
583	Bedlno - Żychlin - Sanniki
584	Sanniki - Kiernozja - Łowicz
702	Kutno - Piątek - Zgierz
703	Porczyń - Podłębie - Gostków - Łęczyca - Piątek - Łowicz
704	Jamno - Kołacín - Brzeziny
705	Śladów - Sochaczew - Skierkiewice - Jeżów
707	Skierkiewice - Rawa Mazowiecka - Nowe Miasto nad Pilicą
708	Ozorków - Warszyce - Stryków - Brzeziny
710	Łódź - Konstantynów Ł. - Szadek - Warta - Błaszki
713	Łódź - Andrychów - Kurowice - Ujazd - Tomaszów Mazowiecki - Januszewice
714	Rzgów - Kurowice
715	Brzeziny - Koluszki - Budziszewice - Ujazd
716	Koluszki - Rokiciny - Piotrków Trybunalski
725	Rawa Mazowiecka - Biała Rawska - Bielski Duży
726	Rawa Mazowiecka - Inowlódz - Opoczno - Żarnów
728	Grójec - Nowe Miasto Nad Pilicą - Końskie - Lopuszno
742	Przygłów - Łęczno - Ręczno - Włoszczowa - Nagłowice
746	Żarnów - Końskie
784	Radomsko - Cięzkowice - Święta Anna
785	Cięzkowice - Żytno - Maluszyn - Włoszczowa

III. ANALYSIS OF THE RESULTS OF GENERAL TRAFFIC MEASUREMENTS IN THE YEARS 2000-2015 IN THE ŁÓDŹ VOIVODESHIP (IN POLAND)

The AADT is the basic parameter calculated for all road sections of provincial road network and the method of its calculation depends on type of measuring point. For basic road sections and for road sections passing through towns where traffic measurements are performed on full-time the AADT value is calculated from equation [14]:

$$AADT = \frac{A_1 \cdot N_1 + 0.85 \cdot A_2 \cdot N_2 + A_3 \cdot N_3 + ANT}{N} \left(\frac{\text{veh}}{24\text{hours}} \right) \quad (1)$$

Where:

AADT- annual average daily traffic,

A_1 - average daily traffic on weekdays from Monday to Friday, from 6.00 pm. to 22:00 am,

$0.85 \cdot A_2$ - average daily traffic on Saturdays and pre-holiday days, from 6.00 pm. to 22:00 am,

A_3 - average daily traffic on Sundays and holidays, from 6.00 pm. to 22:00 am,

ANT- average night traffic, from 22:00 am. to 6:00 pm,

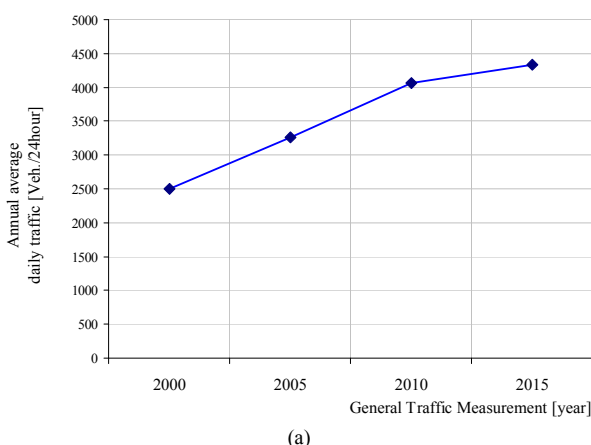
N_1 - number of working days in a year,

N_2 - number of Saturdays and pre-holiday days in the year,

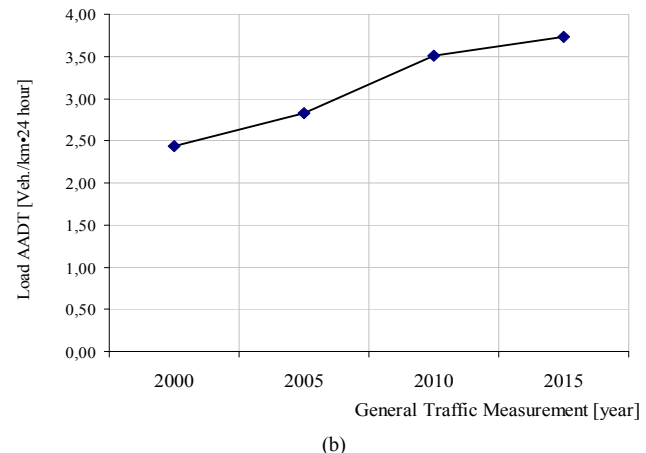
N_3 - number of Sundays and holiday days in a year,

N - number of all days in the year.

On the Fig. 1a shows changes in the value of the annual average daily traffic on provincial roads in the Łódź Voivodeship in the years 2000-2015. On the basis of Fig. 1a, an increase in the AADT value in the discussed region can be seen. This increase, similarly to the entire country, can be described as almost systematic. In 2015, there was a very small increase in AADT in comparison to the previous measurement made in 2010. The largest change in AADT was recorded in 2010, when the rate was 4056 vehicles/day, which gives an increase of 25% compared to the previous measurement made in 2005.



(a)



(b)

FIGURE I. A) CHANGES IN THE AADT VALUE ON VOIVODESHIP ROADS B) THE LOAD OF AADT ON VOIVODESHIP ROADS IN THE ŁÓDŹ VOIVODESHIP IN THE YEARS 2000-2015

In turn, Fig. 2a presents changes in the AADT value divided into particular generic groups of vehicles. On the basis of Fig. 2a, it can be stated that passenger cars traffic in 2000-2010 on voivodeship roads in the region undergoes a systematic increase. In 2015, the increase in AADT was lower than in previous years and amounted to 8%. In the years 2000-2015, the value of AADT of passenger cars increased by 82% in total.

The largest increase in AADT value of motorcycles was recorded in GTM 2010. In relation to the previous measurement, this index increased by 27 vehicles/day, i.e. by as much as 225%. In the years 2000-2005, there was a slight decrease in the value of AADT (by 8%). However, in GTM 2015, a small increase in the value of this indicator was found in relation to the measurement made in 2010 by 3%.

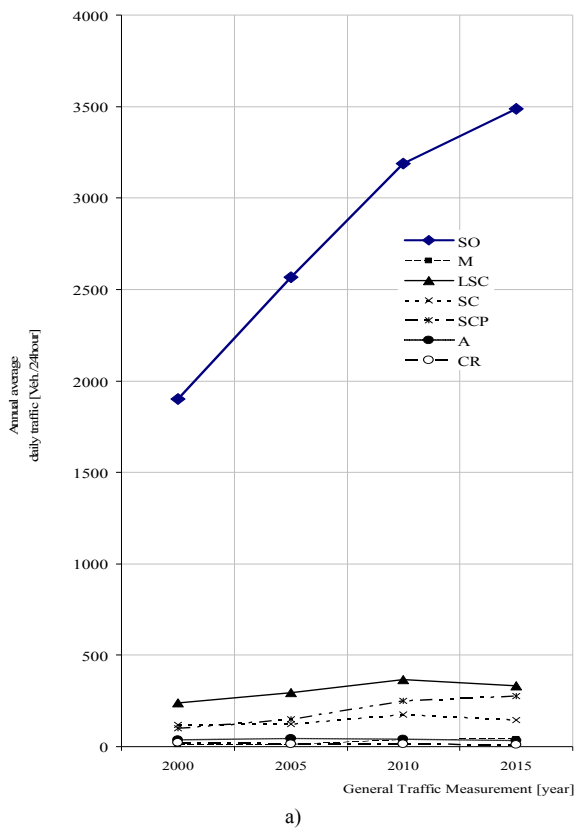
The intensity of light truck traffic on voivodeship roads in the years 2000-2010 has been systematically increasing. This trend has changed in GTM 2015, in which there was a drop in the AADT value of light goods vehicles. In relation to the measurement made in 2010, the value of AADT decreased by 12%.

The largest increase in the value of AADT for trucks without trailers was recorded in 2010. In comparison to the previous measurement, this indicator has changed by 47 vehicles/day (i.e. an increase of 37%). The GTM 2005 also recorded an increase in the AADT value in relation to the previous measurement, however, it was not as significant as in the above-mentioned GTM 2010 and amounted to only 8%. The upward trend has changed in 2015, when the AADT value of lorries without trailers has decreased by 15% compared to the previous measurement.

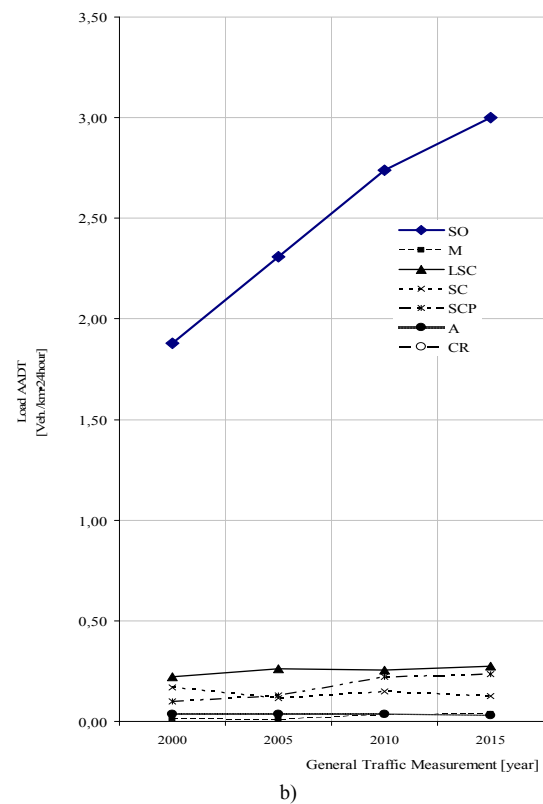
AADT values of trucks with trailers in the years 2000-2015 were growing. This increase can be described as irregular. The highest increase in the value of this indicator was recorded in 2010, when the movement of trucks with trailers changed by 102 vehicles/day (i.e. an increase of 70%). In the remaining measurements, the increase was 41% in 2005 and 11% in 2015, respectively.

Changes in the AADT value of buses in the years 2000-2015 were very irregular. In 2005, the discussed indicator increased by 19%. In all subsequent measurements this movement was in a downward trend. However, in 2010, the drop in the bus AADT was very small and amounted to 2%. In the GTM 2015, a 24% reduction in the value of the discussed indicator was recorded compared to the GTM 2010.

In the years 2000-2005 and 2010-2015, there was a decrease in the value of AADT of agricultural tractors. Changes in the value of this indicator were similar in both periods and amounted to 27% in 2005 and 29 % in 2015, respectively. In GTM 2010 there was a minimal increase in the AADT value of agricultural tractors in relation to the previous measurement. The increase was 6 %.



a)



(Where: SO - passenger cars and vans, M - motorcycles, LSC - light trucks, SC - lorries, SCP - lorries with trailers, A - buses, CR - agricultural tractors)

FIGURE II. A) CHANGES IN THE AADT VALUE DIVIDED INTO INDIVIDUAL GENERIC GROUPS, B) CHANGES IN THE LOAD OF THE VOIVODSHIP ROADS NETWORK OF THE ŁÓDŹ VOIVODESHIP AADT DIVIDED INTO INDIVIDUAL GENERIC GROUPS IN THE YEARS 2000-2015

On the Fig. 1b shows changes in the load of the voivodeship road network in the Łódź Voivodeship AADT in the years 2000-2015. On the basis of Fig. 1b, it can be stated that the load of voivodeship roads over the entire AADT analysis period has increased. The highest value of AADT was recorded in GTM 2015 and it amounted to 3.69 vehicles/km·day. The lowest value of the AADT road load was obtained in GTM 2000 and it amounted to 2.38 vehicles/km·day. In the years 2000-2015, the value of this indicator increased by a total of 55%.

On the Fig. 2b shows changes in the load of voivodeship roads in the Łódź Voivodeship AADT divided into individual generic groups in the years 2000-2015. The load values of AADT road network increased. The minimum value was recorded in GTM 2000 and it amounted to 1.81 vehicles/km·day. The maximum value was obtained in the study, which was carried out in 2015 and it amounted to 2.96 vehicles/km·day. Throughout the analysis period, the value of the load on the road network AADT of passenger cars increased by 64%.

As can be seen on Fig. 2b, at the beginning of the analyzed period, i.e. in GTM 2005, there was a minimal decrease in the road load AADT of motorcycles by about 12% in relation to the measurement made in 2010. The largest escalation of the

discussed indicator took place in the GTM 2010. There was a very large increase in road load of AADT motorcycles (0,035 vehicles/km·day). In the years 2000-2015, the load on the AADT of motorcycles increased by as much as 216%.

In the case of a generic group of light trucks, it can be stated that in the years 2000-2015 the increase in the value of the AADT road network load was dominating. Only in the GTM 2010 there was a slight decrease in this indicator (by almost 1%). The minimum value of the load on AADT road network for light trucks was obtained in GTM 2000, which was then 0,221 vehicles/km·day. The maximum value was recorded in GTM 2015 and amounted to 0,281 vehicles/km·day. Throughout the analysis period, the load value of AADT road network for light trucks increased by 27%.

Changes in the load on the AADT road network for lorries without trailers were irregular. At the beginning of the analyzed period, i.e. in the GTM 2005, there was a slight decrease in the value of the said ratio in relation to GTM 2000 by 2%. Also in this study, a minimum value was obtained in the entire analyzed period, which was 0,110 vehicles/km·day. The largest increase in the road load of AADT trucks without trailers was recorded in GTM 2010 (increase by 37%). In this study, the maximum value of the indicator was also obtained, which was 0,150 vehicles/km·day.

The value of the load on the AADT road network for lorries with trailers increased throughout the analyzed period. The largest increase - by as much as 70% - was recorded in the GTM 2010. The maximum value of this indicator was recorded in GTM 2015 and amounted to 0,239 vehicles/km·day. However, the minimum value was recorded in 2000 and it amounted to 0,100 vehicles/km·day. Throughout the analysis period, the load on the AADT road network for lorries with trailers increased by almost 140%.

In turn, the load values of the bus AADT road network did not change significantly. It was not until the GTM 2015 that a clear decrease of this indicator by 24% was noted. In the same study, the minimum value of bus load AADT for buses was obtained, which was 0,029 vehicles/km·day.

In the years 2000-2015, the decrease of the load value of AADT road network of farm tractors was dominating. Only in the GTM 2010 there was a slight increase of the mentioned indicator by 7%. Throughout the analysis period, the load on the AADT road network of agricultural tractors decreased by 51%.

In the next stage of the work, voivodeship roads with the largest AADT in the Łódź Voivodeship in 2015 were analyzed in detail. These are roads DW 485, DW 713 and DW 714. On the Fig. 3 shows changes in AADT values in the years 2000-2015 on these three roads. On the basis on Fig. 3 can be stated that AADT values on voivodeship road No. 485 increased in each subsequent GTM. In 2015, the result was 7969 vehicles/day. It was the largest AADT value among all surveyed voivodeship roads. In GTM 2000, the obtained value of this indicator was also the highest in the voivodeship. On the other hand, in the subsequent measurements, the received SDRR values were respectively the second in 2005 and the

third in 2010, the result of the largest of all voivodeship roads in the discussed region. In the years 2000-2015, the AADT value on the voivodeship road No. 485 increased by 51%.

On the other hand, the AADT value on voivodeship road No. 713 increased in 2000-2005 and in 2010-2015. In GTM 2010 there was a minimal decrease in this indicator. In the research carried out in 2015, the value of AADT was 7,859 vehicles/day. It was the second largest result among all voivodeship roads in the discussed region. In previous measurements, the values recorded were respectively the second in 2000, the first in 2005 and the fifth in 2010 as the largest result among all voivodeship roads in the discussed region. Throughout the analysis period, the value of AADT on the voivodeship road No. 713 increased by 59%.

The values of AADT on provincial road No. 714 increased in each subsequent measurement. In GTM 2015, the AADT value was 7,542 vehicles/day. It was the third largest result among all voivodeship roads in the discussed region. In previous measurements, the values recorded were respectively the fourth in 2000 and 2010 and the third in 2005 as the largest result among all voivodeship roads in the discussed region. Throughout the analysis period, the value of AADT on the voivodeship road No. 714 increased by 81%.

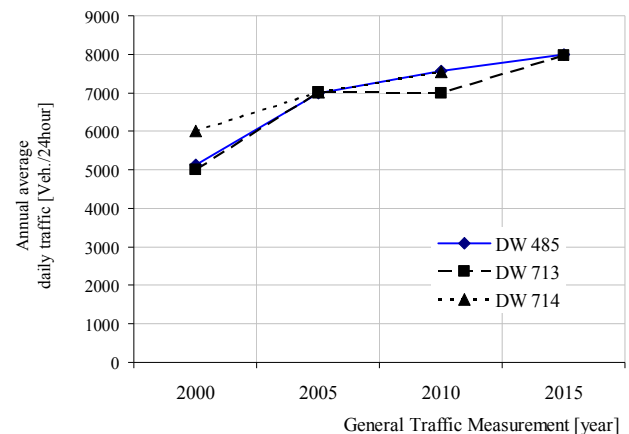


FIGURE III. CHANGES IN THE VALUE OF AADT OF DW 485, DW 713 AND DW 714 IN THE YEARS 2005-2015 IN THE ŁÓDŹ VOIVODESHIP

IV. SUMMARY

Based on results of the analyses addressing the general traffic measurements in Łódź Voivodeship over the years 2000 - 2015 one could formulate the following conclusions:

- Passenger car traffic on voivodeship roads has been systematically growing. In 2015, the increase in the value of AADT was lower than in previous years and amounted to 8%. Throughout the analysis, the value of AADT for passenger cars increased by 82%,

- The highest increase in AADT value of motorcycles on voivodeship roads was recorded in GTM 2010. In comparison to the previous measurement, this index increased by 27 vehicles/day (i.e. an increase of 225%). Throughout the

analysis period, the AADT value of motorcycles increased by 222%,

- The light trucks traffic has been systematically increasing. This trend has changed in GTM 2015, in which the decline in the AADT value of light goods vehicles was recorded for the first time in the discussed period. In relation to the measurement made in 2010, the value of AADT decreased by 12%,

- The largest increase in the value of AADT for trucks without trailers was recorded in 2010. In comparison to the previous measurement, this indicator has changed by 47 vehicles/day (i.e. an increase of 37%). The upward trend changed in 2015, when the value of AADT of trucks without trailers compared to the previous measurement decreased by 15%,

- AADT values for trucks with trailers have increased. This increase can be described as irregular. The largest increase in the value of this indicator was recorded in 2010. The increase was then 70%,

- Changes in bus AADT values were very irregular. In 2005, the discussed indicator increased by 19% in relation to the results from the previous measurement. In subsequent measurements, this movement was declining, while in 2010 the drop in the value of AADT for buses was very small and amounted to less than 2%. In GTM 2015, a larger reduction in the value of the indicator was noted (by about 24%),

- During the entire analysis period, the AADT values of agricultural tractors dropped. The decreases in the value of the indicator in question were respectively 27% in 2005 and 29% in 2015. The exception is the GTM 2010, in which there was a minimal increase in the value of AADT of agricultural tractors (by 6%) in relation to the previous measurement,

- In the entire analysis period, the value of the voivodeship roads load of AADT increased by almost 55%;

- For voivodeship roads where the highest AADT values were recorded in 2015 include roads: DW 485, DW 713 and DW 714,

- In the years 2000-2015, the AADT values on each of these three roads increased by 51% respectively to DW 485, by 59% at DW 713 and by as much as 81% at DW 714.

ACKNOWLEDGEMENT

This research was supported by the Transport Systems and Traffic Engineering Department, Faculty of Transport, Silesian University of Technology.

REFERENCES

- [1] T. Szczuraszek, E. Macioszek, Proportion of vehicles moving freely depending on traffic volume and proportion of trucks and buses, *The Baltic Journal of Road and Bridge Engineering* 8, no 2 (2013) 133–141.
- [2] E. Macioszek, Relationship between vehicle stream in the circular roadway of a one-lane roundabout and traffic volume on the roundabout at peak hour, in: J. Mikulski (Ed.), *Telematics - Support for Transport*. CCIS, Springer, Heidelberg 2014, vol. 471, pp. 110–119.
- [3] E. Macioszek, The influence of motorcycling and cycling on small one-lane roundabouts capacity, in: J. Mikulski (Ed.), *Modern Transport Telematics*. CCIS, Springer, Heidelberg 2011, vol. 239, pp. 291–298.
- [4] E. Macioszek, D. Lach, Analysis of the results of general traffic measurements in West Pomeranian Voivodeship over the years 2005-2015, *Scientific Journal of Silesian University of Technology. Series Transport*. 97 (2017) 95–104 (in press).
- [5] E. Macioszek, M. Czerniakowski, Road traffic safety-related changes introduced on T. Kościuszki and Królowej Jadwigi Streets in Dąbrowa Górska between 2006 and 2015. *Scientific Journal of Silesian University of Technology. Series Transport*. 96 (2017) 95–104.
- [6] E. Macioszek, Geometrical determinants of car equivalents for heavy vehicles crossing circular intersections, in: J. Mikulski (Ed.), *Telematics in the Transport Environment*. CCIS, Springer, Heidelberg 2012, vol. 329, pp. 221–228.
- [7] [7] E. Macioszek, Analysis of significance of differences between psychotechnical parameters for drivers at the entries to one-lane and turbo roundabouts in Poland, in: G. Sierpiński (Ed.), *Intelligent Transport Systems and Travel Behaviour*. AISC, Springer, Switzerland 2017, vol. 505, pp. 149–161.
- [8] E. Macioszek, Analysis of the effect of congestion in the lanes at the inlet to the two-lane roundabout on traffic capacity of the inlet, in: J. Mikulski (Ed.), *Activities of Transport Telematics*. CCIS, Springer, Heidelberg 2013, vol. 395, pp. 97–104.
- [9] Central Statistical Office. Area and population in territorial cross section in 2017, <http://stat.gov.pl/>
- [10] General Director of National Roads and Motorways. Order No 74 of the General Director of National Roads and Motorways of 2 December 2008 on Numbering Voivodship Roads, https://www.gddkia.gov.pl/userfiles/articles/z/zarzadzenia-generalnego-dyrektor_6335/documents/32_2004.pdf
- [11] General Director of National Roads and Motorways. Order No 78 of the General Director of National Roads and Motorways of 11 December 2009 Amending the Ordinance on the Numbering of Voivodeship Roads, https://www.gddkia.gov.pl/userfiles/articles/z/zarzadzenia-generalnego-dyrektor_3184/documents/scan2080.pdf
- [12] General Director of National Roads and Motorways. Order No. 45 of the General Director of National Roads and Motorways of 17 December 2012 Amending the Ordinance on the Numbering of Voivodeship Roads, https://www.gddkia.gov.pl/userfiles/articles/z/zarzadzenia-generalnego-dyrektor_10385/zarzadzenie%2045.pdf
- [13] General Director of National Roads and Motorways. Order No 61 of the General Director of National Roads and Motorways of 20 December 2013 Amending the Ordinance on the Numbering of Voivodeship Roads, https://www.gddkia.gov.pl/userfiles/articles/z/zarzadzenia-generalnego-dyrektor_11943/zarzadzenie%2061.pdf
- [14] General Traffic Measurements Guidelines on Provincial Roads in 2015, https://www.gddkia.gov.pl/userfiles/articles/g/generalny-pomiar-ruchu-w-2015_15598/Wytyczne%20GPR%20na%20dr%20woj%20w%202015%20r_zakceptowane_ok.pdf

Estimation of the Average Treatment Effect with Missing Outcome Data

Feng Han

Teachers' College of Beijing Union University, Beijing, 100011, China

Abstract—Missing outcome data occurs often in the causal inference of observational studies. For example, in observational study on the safety of a Traditional Chinese Medicine (TCM) injection in market, some patients are missing safety outcome variables. In this paper we proposed a consistent estimator for the average treatment effect (ATE) with partially missing outcome data and derived the asymptotic variance of the proposed ATE estimator under the condition that the missing-data mechanism is missing at random (MAR). We then proceeded to assess the performance of the asymptotic variance estimator via a simulation study. The simulation study showed that the asymptotic variance estimator had good performance in finite sample sizes. This asymptotic variance could then be used to construct a confidence interval for the average treatment effect. We also compared the bias and mean squared error (MSE) of the ATE estimators based on the proposed method-dealing with the missing outcomes with that of the complete-data method, which means that directly deleting the samples with the missing data through a simulation study. The simulation study showed that the MSE and Bias of our method were smaller than the complete-data method under MAR. In addition, we also found that coverage of the confidence interval constructed on the ATE and its asymptotic variance from our method are better than those based on the traditional method.

Keywords—average treatment effects (ATE); asymptotic variance; delta-method; missing data

I. INTRODUCTION

Recently, there has been a surge in theoretical work focusing on estimating ATE without missing outcome data. For estimation of the ATE, various semi-parametric estimation methods have been proposed, including the regression methods (Heckman et al., 1997; Hahn, 1998; Imbens et al., 2003) methods using the propensity score such as weighting (Hirano et al., 2003), matching on covariates (Rosenbaum, 1995; Abadie and Imbens, 2002), blocking (Rosenbaum and Rubin, 1984), and combinations of those approaches(Graf, 1997).

The propensity score methodology is the most commonly used method among the aforementioned approaches. Hirano et al. (2003) gave the most complete theory on the use of the propensity score methodology when the propensity score is estimated. Montes-Rojas (2009) derived the asymptotic variance of the ATE estimator with the propensity score is estimated by the M-estimator using the Delta method (Wooldridge, 2002). In practice, this asymptotic variance can be used to measure the accuracy of the ATE estimators and to construct confidence interval for the ATE.

There can be a large amount of missing data in observational studies of medicine, however. For example, in the observational study on the safety of a Traditional Chinese Medicine (TCM) injection, some patients are missing safety outcome variables.

In cases where some subject outcomes are missing, the most commonly used technique to estimate the ATE and its associated variance is to exclude subjects with missing outcomes, then perform analysis of the remaining data. This approach is called a complete-case analysis.

When subjects with any missing outcomes are excluded, it is well known that a complete-case analysis can give highly inefficient estimators and potentially biased results. Thus, the method of directly deleting missing data will result in a significant loss of information.

Among various kinds of method for dealing with missing data, one common method is the inverse probability weighting method (IPW). Since Horvitz and Thompson (1952) first proposed to use this method to estimate population mean with nonrandomized missing data mechanisms in 1952, in effect, this approach did not get widely used for a very long time.

It was not until the end of the twentieth Century that this approach has become popular when Robins and Rotnitzky (1995) proved that the inverse probability weighting estimator is a consistent and asymptotically normal estimator in a multivariate regression model and proposed a modified IPW estimator (Little, 1995). Wooldridge (2002) proposed the inverse probability weighted minimization estimator in order to analyze no-response questions in the investigation of a period or multi period (Little and Rubin, 1987). Carpenter et al. (2005) proved that the IPW estimator with double robustness through the empirical analysis (Ralph, 2000). These results make IPW method has received more and more attention.

To increase efficiency and reduce the bias, it is necessary to develop methods that incorporate the partially missing outcome data into the analysis. In this paper, we propose a method by providing formulas that can estimate ATE and its associated variance with missing outcome data. The proposed method is under the missing at random (MAR) assumption, which implies that the missing-data process can depend only on the observed covariates, but not on the missing outcome (Little, 1995; Little and Rubin, 1987; Ralph, 2000; Rubin, 1976). We propose a new ATE estimator under the MAR condition and prove that the new estimator was consistent. We also extend the asymptotic variance formula of the ATE

estimator on complete data by Montes-Rojas (2009) and derived the asymptotic variance formula of the ATE estimator on non-complete data with missing outcomes.

Our simulation study demonstrates the high accuracy of the proposed method in estimating the ATE and its asymptotic variance. In this paper, we also apply the proposed method to a post-surveillance TCM study. The paper is organized as follows. Section 2 provides notation and derives the ATE estimators with partially missing outcome data. Section 3 derives the asymptotic variance of the ATE estimators under the condition that missing-data mechanism is MAR. Section 4 evaluates the accuracy of the resulting asymptotic variance formula by comparing the empirically estimated variance with the variance estimate derived using the asymptotic formula in a simulation study and compares the MSE of the ATE estimators between the proposed method that addresses the missing outcomes and the conventional method that deletes the samples with the missing data. Then, we also compare the confidence interval coverage constructed by two different methods. We give some remarks and conclusion in Section 5.

II. AVERAGE TREATMENT EFFECT ESTIMATORS WITH MISSING OUTCOME DATA

In this section we derive the ATE estimators with partially missing outcome data. We follow the standard notation in Imbens (2004) and Montes-Rojas (2009). Consider N individuals indexed by $i = 1, K, N$, who may receive a certain “treatment”, indicated by the binary variable $W_i = 0, 1$. Each individual has a pair of potential outcomes (Y_{0i}, Y_{1i}) that corresponds to the outcomes that the individual would have been observed with and without the receipt of the treatment, respectively.

The fundamental problem of causal inference is the inability to observe at the same time the outcomes of the same individual both with and without the receipt of treatment effects. That is, we can only observe $Y_i = W_i Y_{1i} + (1 - W_i) Y_{0i}$ and a set of exogenous covariates X_i . We define the propensity score as $p(X_i) = p(W_i = 1 | X_i = x_i)$. We are interested in estimating the ATE, defined as $\delta = E(Y_{1i} - Y_{0i})$. In addition, we let R_i denote a dummy variable such that $R_i = 0$ when the outcome of the i th individual is missing; and $R_i = 1$ otherwise. We extend the idea in Montes-Rojas (2009) and derive the ATE estimators under the condition that the missing-data mechanism is MAR. To derive our estimators, we need to make the following assumptions.

Assumption 1 $0 < p(X_i) < 1$.

This assumption means that each individual in the population has a positive probability of receiving either treatment. In the study, the propensity score is usually obtained from logistic regression. As long as we focus on the

distribution of the propensity score, we may assess that whether the assumption 1 is feasible.

Assumption 2 $R_i \perp W_i \perp (Y_{0i}, Y_{1i}) | X_i$.

This assumption says that Y_{1i} and Y_{0i} are independent of W_i, R_i given X_i . This assumption ensures that we can stratified according to known covariates, and the causal effect of each layer is identifiable, similar to the negligible assumption for a complete data (Rosenbaum and Rubin 1983). For the actual data, how do we verify that it meets this assumption? This depends on the background of the actual data. We generally based on the background of the data to determine the missing mechanism. As the examples in this article shows, we can consider the missing mechanism as missing at random. Thus, the missing indicator variables are independent with missing outcome variable, given the value of the covariates. This can be expressed as $R_i \perp Y_i | X_i$. Since $Y_i = W_i Y_{1i} + (1 - W_i) Y_{0i}$, so apparently we can get $R_i \perp W_i | X_i$ and $R_i \perp (Y_{0i}, Y_{1i}) | X_i$.

Next, as long as we can verify $W_i \perp (Y_{0i}, Y_{1i}) | X_i$, we can determine that whether the assumption 2 is satisfied. The verification for this assumption is similar to the negligible assumption for a complete data. The difference between the two is that the data we are concerned is a data with missing outcome variable. The approach used in this paper is the inverse probability weighting method.

Proposition 1. Under Assumptions 1 and 2 and the condition that the missing-data mechanism is MAR, we can write δ as the expected value of a weighted equation.

The average treatment effect in the presence of missing outcome data can be written as follows:

$$\delta = E\left(\frac{R_i W_i Y_i}{p(X_i) p(R_i = 1 | X_i)} - \frac{R_i (1 - W_i) Y_i}{(1 - p(X_i)) p(R_i = 1 | X_i)}\right).$$

The proof of this proposition is given in Appendix.

Based on the result in Proposition 1, we propose the following consistent estimator for δ , when the missing outcome data mechanism is MAR:

$$\hat{\delta} = N^{-1} \sum_{i=1}^N \left[\frac{R_i W_i Y_i}{p(X_i) p(R_i = 1 | X_i)} - \frac{R_i (1 - W_i) Y_i}{(1 - p(X_i)) p(R_i = 1 | X_i)} \right] \quad (1)$$

When propensity score and missing-data mechanism are known, we can prove that the estimator from equation (1) is an unbiased estimator for the ATE by the property of an identically independent sample.

It is noteworthy that in equation (1) the propensity score and missing-data mechanisms are usually unknown, and they

need to be estimated by means of a parameter model (such as logit or probit). It can be easily shown that the proposed estimator in equation (1) is a consistent estimator of ATE when the parameters in the propensity score are estimated by an M-estimator and the parameters in the missing-data mechanisms are also estimated by an M-estimator.

III. THE ASYMPTOTIC VARIANCE OF AVERAGE TREATMENT EFFECT ESTIMATORS WITH MISSING OUTCOME DATA

In practice, the propensity score $p(X_i)$ is usually unknown and need to be estimated based on data. Here we assume that $p(X_i) = \Phi(X_i; \gamma^*)$,

where γ^* denotes the true value of the parameters γ , in the propensity score.

Here we let $\hat{\delta}$ denote a two-step estimator of δ . This means that the parameters γ in the propensity score are estimated using the M-estimator $\hat{\gamma}$. Generally, the M-estimator can be defined to be a zero of an estimating function (Van de Geer, 2000). This estimating function is the derivative of another statistical function. For example, a maximum-likelihood estimate is often defined to be a zero of the derivative of the likelihood function with respect to the parameter. Thus, a maximum-likelihood estimator is often a critical point of the score function (Ferguson, 1982).

Here δ is estimated via equation (1) with $p(X_i)$ being replaced by $\Phi(X_i; \hat{\gamma})$. We also let δ^* denote the true value of δ .

Next, we deal with the situation where the missing-data mechanism is MAR. In this case, we also need to model the missing data mechanism, $p(R_i = 1 | X_i)$.

We assume that $p(R_i = 1 | X_i) = \pi(X_i; \beta^*)$, where β^* represents the true value of β , and β denotes parameters to be estimated in the missing-data mechanism. Let $\hat{\beta}$ be the M-estimator of β , based on the above parametric model for $p(R_i = 1 | X_i)$.

Let $\hat{\hat{\delta}}$ denote a three-step ATE estimator of δ^* that is given by formula (1) with both γ and β being replaced by the M-estimators $\hat{\gamma}$ and $\hat{\beta}$, respectively.

A. Theorem 1

When the missing-data mechanism is MAR, under the conditions that $p(X_i)$ can be estimated via a parameter model, we can derive the asymptotic variance of ATE estimator as follows:

$$\begin{aligned} & \lim_{N \rightarrow \infty} \text{VAR} \left[\sqrt{N} \left(\hat{\hat{\delta}} - \delta^* \right) \right] \\ &= \lim_{N \rightarrow \infty} \text{VAR} \left[\xi(Y_i, W_i, R_i, X_i; \theta^*, \delta^*) + T(\theta^*, \delta^*) D(W_i, R_i, X_i; \theta^*) \right] \end{aligned}$$

Where

$$\theta^* = \begin{pmatrix} \gamma^* \\ \beta^* \end{pmatrix},$$

$$\begin{aligned} & \xi(Y_i, W_i, R_i, X_i; \theta^*, \delta^*) \\ &= \frac{R_i W_i Y_i}{p(X_i) p(R_i = 1 | X_i)} - \frac{R_i (1 - W_i) Y_i}{(1 - p(X_i)) p(R_i = 1 | X_i)} - \delta^* \\ &= \frac{R_i W_i Y_i}{\Phi(X_i; \gamma^*) \pi(X_i; \beta^*)} - \frac{R_i (1 - W_i) Y_i}{(1 - \Phi(X_i; \gamma^*)) \pi(X_i; \beta^*)} - \delta^* \\ & T(\theta^*, \delta^*) = E \left[\nabla_{\theta} \xi(Y_i, W_i, R_i, X_i; \theta^*, \delta^*) \right] \end{aligned}$$

And $D(W_i, R_i, X_i; \theta^*)$ is the influence function of an M-estimator for the parameters θ when θ is equal to the true value θ^* .

The proof of this theorem is given in the Appendix.

In practice, a consistent estimator of this asymptotic variance can be obtained by the sample version:

$$\begin{aligned} & \text{Est.VAR} \left[\sqrt{N} \left(\hat{\hat{\delta}} - \delta^* \right) \right] \\ &= N^{-1} \sum_{i=1}^N \left[\xi \left(Y_i, W_i, R_i, X_i; \hat{\theta}, \hat{\hat{\delta}} \right) + T \left(\hat{\theta}, \hat{\hat{\delta}} \right) D(W_i, R_i, X_i; \hat{\theta}) \right]^2 \quad (2) \end{aligned}$$

In the actual analysis, if the propensity score is estimated by the logistic regression, the estimated value of the propensity score can be expressed as $p(X) = \frac{e^{\gamma X}}{1 + e^{\gamma X}}$; the missing mechanism can also be estimated by the logistic regression that can be expressed as $p(R = 1 | X) = \frac{e^{\beta X}}{1 + e^{\beta X}}$. Then, we can get that

$$\begin{aligned} & \xi\left(Y_i, W_i, R_i, X_i; \hat{\theta}, \hat{\delta}\right) \\ &= \frac{R_i W_i Y_i}{p(X_i) p(R_i = 1|X_i)} - \frac{R_i (1-W_i) Y_i}{(1-p(X_i)) p(R_i = 1|X_i)} - \hat{\delta} \\ &= \frac{R_i W_i Y_i}{\frac{e^{\gamma X_i}}{1+e^{\gamma X_i}} \frac{e^{\beta X_i}}{1+e^{\beta X_i}}} - \frac{R_i (1-W_i) Y_i}{\left(1 - \frac{e^{\gamma X_i}}{1+e^{\gamma X_i}}\right) \frac{e^{\beta X_i}}{1+e^{\beta X_i}}} - \hat{\delta} \\ & T(\theta, \delta) = E[Y_i | W_i, R_i, X_i; \theta, \delta]. \end{aligned}$$

Here putting

$$\hat{\theta} = \begin{pmatrix} \hat{\gamma} \\ \hat{\beta} \end{pmatrix}$$

$$\begin{aligned} & D(W_i, R_i, X_i; \hat{\theta}) \\ &= \begin{cases} \nabla_{\gamma} \left[W_i \ln \frac{e^{\gamma X_i}}{1+e^{\gamma X_i}} + (1-W_i) \ln \left(1 - \frac{e^{\gamma X_i}}{1+e^{\gamma X_i}} \right) \right] \Big|_{\gamma=\hat{\gamma}} \\ \nabla_{\beta} \left[W_i \ln \frac{e^{\beta X_i}}{1+e^{\beta X_i}} + (1-W_i) \ln \left(1 - \frac{e^{\beta X_i}}{1+e^{\beta X_i}} \right) \right] \Big|_{\beta=\hat{\beta}} \end{cases} \end{aligned}$$

And into the equation (2), we can get the asymptotic variance of the ATE estimation constructed by the formula (1). With estimator and its asymptotic variance, we can construct confidence intervals. The confidence interval of the real value of the ATE for the nominal level of $100 \times \alpha\%$ confidence

can be expressed as $\hat{\delta} \pm Z_{\frac{\alpha}{2}} \frac{\sigma}{\sqrt{N}}$, where σ represents the estimated standard deviation for ATE estimation.

IV. SIMULATION STUDY

A. Simulation Setup

We conducted a simulation study to assess the performance of the proposed ATE estimator, called Method I, and its asymptotic variance formula in finite sample sizes.

We also compared the performance of Method I with the complete-data method, which deleted subjects with the missing data and then applied the methods of Hirano et al. (2003) and Montes-Rojas (2009) with the remaining complete data to estimate the ATE and computed the associated variance estimate. We call the conventional method Method II.

The simulation study used six covariates and 1000 randomly generated data sets for each of the three parameter configurations to be given in Table 1 below. The sample size for each simulated data set was set to be 1000, 2000 and 5000,

respectively. All statistical analyses were conducted using SAS software, version 9.2.

The parameters were set up as follows:

First, we generated the six covariates

$X_1, X_2, X_3, X_4, X_5, X_6$. The covariate X_1 and X_2 were drawn from the normal distribution with the mean and variance, (μ_1, σ_1^2) and (μ_2, σ_2^2) , respectively. The covariates X_3, X_4, X_5, X_6 were drawn from a Bernoulli distribution with P_3, P_4, P_5, P_6 , respectively.

We chose three different parameter settings for the parameters, $\mu_1, \sigma_1^2, \mu_2, \sigma_2^2, P_3, P_4, P_5, P_6$,

And those values are listed in Table I.

TABLE I. PARAMETER SETTINGS FOR SIMULATION

Settings	μ_1	σ_1^2	μ_2	σ_2^2	P_3	P_4	P_5	P_6
1	0.600	1	0.010	0.600	0.040	0.200	0.800	0.300
		0.600						
2	0.400	1	0.010	0.600	0.040	0.200	0.600	0.250
		0.400						

Second, we generated two potential outcomes Y_1 and Y_0 for each subject in the sample according to the following model:

$$Y_j = \alpha_{0(j)} + \alpha_{1(j)} X_1 + \alpha_{2(j)} X_2 + \alpha_{3(j)} X_3 + \alpha_{4(j)} X_4 + \alpha_{5(j)} X_5 + \alpha_{6(j)} X_6 + \varepsilon_j, j = 0, 1,$$

Where

$$\begin{aligned} [\alpha_{0(0)}, \alpha_{1(0)}] &= [0, 0]; [\alpha_{0(1)}, \alpha_{1(1)}] = [0.02, 0.03]; [\alpha_{2(0)}, \alpha_{3(0)}] = [0.1, 0.1]; [\alpha_{3(0)}, \alpha_{4(0)}] = \\ & [0.01, 0.02]; [\alpha_{4(0)}, \alpha_{5(0)}] = [0.2, 0.2]; [\alpha_{5(0)}, \alpha_{6(0)}] = [0.02, 0.02] \end{aligned}$$

And ε_j was drawn from the normal distribution with $\mu = 0$ and $\sigma^2 = 1$

Third, the treatment assignment W for each subject was generated by the following model:

$$p(W = 1|X) = \frac{e^{\gamma_0 + \gamma_1 X_1 + \gamma_2 X_2 + \gamma_3 X_3 + \gamma_4 X_4 + \gamma_5 X_5 + \gamma_6 X_6}}{1 + e^{\gamma_0 + \gamma_1 X_1 + \gamma_2 X_2 + \gamma_3 X_3 + \gamma_4 X_4 + \gamma_5 X_5 + \gamma_6 X_6}},$$

Where

$$\gamma_0 = 0, \gamma_1 = 0.2, \gamma_2 = 0.2, \gamma_3 = 3, \gamma_4 = 0.4, \gamma_5 = 0.2, \gamma_6 = 0.3$$

The value of the generated W for a subject determines which of the two potential outcomes, Y_1 and Y_0 , is observed for this subject. If $W=1$, Y_1 is observed, and if $W=0$, Y_0 is observed.

Up to this point, we have randomly generated complete data sets under the three different parameter configurations.

Fourth, we generated the missing outcomes, according to the MAR missing data. Under the MAR missing data mechanism, we generated a missing-data indicator for each subject, R , from a Bernoulli distribution with the following event probability with covariates $X_1, X_2, X_3, X_4, X_5, X_6$:

$$p(R = 1|X) = \frac{e^{\eta_0 + \eta_1 X_1 + \eta_2 X_2 + \eta_3 X_3 + \eta_4 X_4 + \eta_5 X_5 + \eta_6 X_6}}{1 + e^{\eta_0 + \eta_1 X_1 + \eta_2 X_2 + \eta_3 X_3 + \eta_4 X_4 + \eta_5 X_5 + \eta_6 X_6}}$$

Where
 $\eta_0 = 0, \eta_1 = 0.02, \eta_2 = 0.6, \eta_3 = 1, \eta_4 = 0.05, \eta_5 = 0.2, \eta_6 = 0.1$.

For each of the three parameter configurations, we repeated the above process 1000 times. Then, we got 1000 randomly generated data sets under each of the three parameter settings.

To evaluate the effect of the sample size on the accuracy of the estimated variance of the ATE estimator, we further considered four different sample sizes, 1000, 2000 and 5000, for each of the three parameter settings in Table I.

B. Performance Measures

For comparison of point estimators for the ATE, we used bias and mean squared error (MSE). We define these quantities below.

Let $\hat{\delta}_m$ and $\hat{\delta}_{Z_m}$ be the estimates for the ATE, δ^* , derived using the proposed method and the complete case method, respectively, using the m th simulated data set. Then, the biases of these ATE estimators are given, respectively, as follows:

$$\text{Bias} = \frac{1}{1000} \sum_{m=1}^{1000} (\hat{\delta}_m - \delta^*) \quad \text{Bias} = \frac{1}{1000} \sum_{m=1}^{1000} (\hat{\delta}_{Z_m} - \delta^*).$$

The MSE of the ATE estimators are given, respectively, as follows:

$$\text{MSE} = \frac{1}{1000} \sum_{m=1}^{1000} (\hat{\delta}_m - \delta^*)^2,$$

$$\text{MSE} = \frac{1}{1000} \sum_{m=1}^{1000} (\hat{\delta}_{Z_m} - \delta^*)^2.$$

We assessed the performance of the asymptotic variance estimator of the ATE, by comparing it with the empirical variances estimators.

For the estimator for the ATE proposed in this paper, the empirical variance is defined as follows:

$$S^2 = \frac{1}{999} \sum_{m=1}^{1000} (\hat{\delta}_m - \bar{\delta})^2.$$

The derived asymptotic variance formula in this article is as follows:

$$\begin{aligned} \text{Est. VAR}(\hat{\delta}) &= \frac{1}{1000} \sum_{m=1}^{1000} \text{VAR}(\hat{\delta}_m) \\ &= \frac{1}{1000} \sum_{m=1}^{1000} \left\{ N^{-2} \sum_{i=1}^N \left[E(Y_i | W_i, R_i, X_i; \theta, \hat{\delta}_m) + T(\theta, \hat{\delta}_m) D(W_i, R_i, X_i; \theta) \right]^2 \right\} \end{aligned}$$

C. Simulation Results

The simulation results are summarized in Table II and Table III.

TABLE II. SIMULATION RESULTS: EMPIRICAL VARIANCE VS. VARIANCE USING THE FORMULA

Parameter setting	Sample Size	Empirical variance(S2)	Variance formula	using the
1	1000	0.025297	0.027354	
	2000	0.011545	0.011372	
	5000	0.004210	0.004283	
	1000	0.021957	0.022679	
2	2000	0.009939	0.009979	
	5000	0.003447	0.003763	

TABLE III. SIMULATION RESULTS: BIAS AND MSE OF ATE ESTIMATOR

Parameter setting	Sample Size	Method	Bias	MSE
1	1000	I	-0.006010	0.025308
		II	-0.008010	0.033745
		I	0.002377	0.011539
		II	0.003405	0.015930
		I	0.000463	0.004206
	2000	II	0.000545	0.005628
		I	-0.000850	0.021935
		II	-0.002990	0.031240
		I	0.002734	0.009936
		II	0.004447	0.013400
2	5000	I	0.000445	0.003443
		II	0.000990	0.004453

TABLE IV. COVERAGE PROBABILITIES OF THE 95% CONFIDENCE INTERVALS

Parameter setting	Sample Size	Method	Coverage probabilities
1	1000	I	0.946
		II	0.893
		I	0.948
		II	0.904
		I	0.954
	2000	II	0.904
		I	0.951
		II	0.890
		I	0.955
		II	0.885
2	5000	I	0.960
		II	0.897

Note: *Method I, calculated with the formula constructed in this paper;

#Method II, calculated by the method of directly deleting samples with missing outcomes.

By comparing the empirical variance with the variances obtained with the formula in Table II, we can conclude that the asymptotic variance formula of the proposed ATE

estimator under MAR missing data provides an accurate variance estimation of the estimated ATE.

In addition, from the bias and MSE results of the ATE estimators in Table III, we can conclude that the proposed method in this paper (Method I) outperforms the complete case method (the method of directly deleting patients with missing outcomes). We can also see from Table IV that coverage of the confidence interval constructed on the ATE and its asymptotic variance from method I with 95% confidence level is greater than that based on the traditional method. Moreover, the explicit variance estimator for the proposed ATE estimator also performs well in the sample sizes considered in the simulation study.

V. CONCLUSION AND DISCUSSION

For the analysis of observational data with a partially missing outcome variable, in this article we proposed an estimator for the ATE when the missing outcome is MAR, and also derived the associated variance formula. Furthermore, we verified the accuracy of the variance formula via the simulation study. The advantage of having a variance formula, such as this, is simple to calculate the variance estimate in practice. We compared the proposed method with the commonly used complete-case method and showed our method outperforms the commonly used method.

In this paper, we used a parametric model to estimate the propensity score and the missing-data mechanism. The disadvantages of using the parametric model are that modeling needs to be based on certain assumptions. A further research idea might be to relax these parametric model assumptions by using non-parametric models for the propensity score with the missing-data outcome data.

In other words, we first estimated propensity score with missing outcome data, and then get the estimator of ATE by inverse probability weighting. Furthermore, we can also use variance formula given in this paper to estimate the variance estimators of the ATE. So that we can make a reasonable statistical inference and this inference has very important reference value in practical research. It is worth mentioning that the assumption required by using the method of this article is relatively relaxed. From the practical examples given in this paper, we know that in the observational data analysis, assumption 1 generally can be met and assumption 2 is also possible to meet depends on the missing data mechanism. We can also say that whether the missing data mechanism satisfies MAR is important for assumption 2. Of course, we need to make a judgment based on a medical background in the actual study. In short, the method presented in this paper has a certain value.

ACKNOWLEDGEMENT

This paper has been funded by the Beijing Union University Project Management Fund. (No. 32207531102).

REFERENCES

- [1] Abadie, A. and Imbens, G. (2002).Simple and Bias-Corrected Matching Estimators for Average Treatment Effects. NBER technical working paper, No.283.
- [2] D'Agostino, R. B. and Rubin, D. B. (2000).Estimating and Using Propensity Scores with Partially Missing Data. *Journal of the American Statistical Association* 95(451), 749-759.
- [3] Ferguson, T. S. (1982).An inconsistent maximum likelihood estimate. *Journal of the American Statistical Association* 77 (380), 831-834.
- [4] Graf, E. (1997).The Propensity Score in the Analysis of Therapeutic Studies. *Biometrical Journal* 39(3), 297-307.
- [5] Hahn, J. (1998).On the Role of the Propensity Score in Efficient Semiparametric Estimation of Average Treatment Effects. *Econometrica* 66,315-331.
- [6] Heckman, J., Ichimura, H. and Todd, P. (1997).Matching as an Econometric Evaluation Estimator: Evidence from Evaluating a Job Training Program. *Review of Economic Studies* 64,605-654.
- [7] Hirano, K., Imbens G. and Ridder G. (2003).Efficient Estimation of Average Treatment Effects Using the Estimated Propensity Score. *Econometrica* 71, 1161-1189.
- [8] Horvitz, D. and Thompson, D. (1952).A Generalization of Sampling without Replacement from a Finite Population. *Journal of the American Statistical Association* 47,663 - 685.
- [9] Imbens, G. W. (2004).Nonparametric estimation of average treatment effects under exogeneity: a review. *Review of Economics and Statistics* 86(1), 4-29.
- [10] Imbens, G. W., Newey, W. and Ridder, G. (2003). Mean-Squared-Error Calculations for Average Treatment Effects. Department of Economics, UC Berkeley, unpublished manuscript.
- [11] Little, R. J. (1995).Modeling the dropout mechanism in repeated-measures studies. *Journal of the American Statistical Association* 90, 1112-1121.
- [12] Little, R. J. and Rubin, D. B. (1987).Statistical Analysis with Missing Data. J. Wiley & Sons, New York.
- [13] Montes-Rojas, G. (2009).A note on the variance of average treatment effects estimators. *Economics Bulletin* 29(4), 2937-2943.
- [14] Robins, J. M. and Rotnitzky, A. (1995).Semiparametric Efficiency in Multivariate Regression Models with Missing Data. *Journal of the American Statistical Association* 90,122-129.
- [15] Rosenbaum, P. (1995).Observational studies. New York: Springer-Verlag.
- [16] Rosenbaum, P. and Rubin, D. (1984).Reducing the Bias in Observational Studies Using Sub-classification on the Propensity Score. *Journal of the American Statistical Association* 79,516-524.
- [17] Rubin, D. B. (1976).Inference and missing data (with discussion).*Biometrika* 63,581-592.
- [18] Van de Geer, S.A. (2000).Empirical Processes in M-estimation: Applications of empirical process theory, volume 6 of Cambridge Series in Statistical and Probabilistic Mathematics. Cambridge University Press, Cambridge.
- [19] Wooldridge, J. M. (2002).Econometric analysis of cross section and panel data. The MIT Press, Cambridge, Massachusetts.

Parametric Design on Stubble-cutting Disc with Oblique Ripples Based on Reverse Engineering Methods

Ping Zhao, Xuewei Bai, Yongkui Li*, Yue Tian and Changyi Lv

Engineering College, Shenyang Agricultural University, Shenyang, 110866, China

*Corresponding author

Abstract—Aiming at the design and manufacture difficulty of stubble-cutting disc with oblique ripples, taking one made by America as research object, a kind of computer aided design method was proposed, which was fulfilled in the basis of the structural parameters that were obtained through reverse engineering technology. The point cloud data were obtained by using a Digital Structure Light 3D scanner and a binocular stereoscopic vision system, then the structural equation and parameters was acquired by fitting the data of feature points extracted from the point clouds through boundary detected and curvature calculation. On this basis, 3D parametric model of the stubble-cutting disc with oblique ripples was created in a computer aided design system of Solidworks, which will provide a foundation for its engineering analysis, parameter optimization and mould manufacture. At the same time, this work broadens the range of application of reversing engineering, and also will provide references for researching the application of reverse engineering in the design and manufacture of agricultural machinery.

Keywords—computer vision; parametric design; reverse engineering; reverse solution of structural parameter; stubble-cutting disc

I INTRODUCTION

Stubble-cutting sword is the key component of no-tillage seeding, which is required to have better performances of cutting stubble and preventing block. The researches[1-3] shown Stubble-cutting disc with oblique ripples has the advantages of less resistance, strongly block-preventing property, bigger ditching width, smaller disturbance to the soil, etc. But its design and manufacture are extremely difficult in China, nowadays, which is studied through drawing lessons from foreign technology, designers' experience and the tests [2].

Reverse Engineering (RE) is a hot topic in modern design and manufacturing field at present, and it has been widely used in aerospace, aviation, automotive, bio-medicine, archaeological relics copy, bionic engineering, etc. Reverse engineering technology commonly starts with a measurement of the solid model; then reconstructs a geometric model based on coordinate data derived from the measurement system; in the end fulfills rapid prototyping, mold manufacture or redesign. In this process, reconstructing curved surface and 3D model using the coordinate data is one of the important aspects. There are two

approaches generally to construct curved surface by point cloud data: (1) constructing curved surface directly by the point cloud, (2) fitting curve by the points, and then constructing the surface by the fitted curve. For a long time, the focus of the RE has been these aspects, occasionally, been used in other respect, such as Kamran Mohaghegh etc [4], proposed a new method of reversing engineering that incorporate construction geometry and design intent. However, as to a part whose shape is complex, frequently curvature variation and relatively regular, the two methods of constructing curved surface by point cloud data will generate bigger error or even impossible. So authors introduce a different viewpoint which focuses on the part's geometry. Namely, a new approach in reverse engineering of such a complex and regular part (Stubble-cutting sword) was proposed, in which a combined reverse engineering technology was used to acquire the part's structural parameters and equations, then to construct 3D model through parameters, which is much more valid.

This study fulfilled reverse solution of parametric equation of the stubble-cutting disc with oblique ripples made in America by using reverse engineering technology, and then the three-dimensional (3D) model was reconstructed according to obtained parameters, which will provide a new method for its design, and pave the way for its redesign and mould manufacture.

II DIGITAL MEASUREMENT OF THE STUBBLE-CUTTING DISC WITH OBLIQUE RIPPLE



FIGURE I. THE MAIN PART OF 3D SCANNER

In this study, the point cloud data were obtained through a Digital Structure Light (DSL) 3D(three dimensional) scanner based on binocular vision system; it is composed of a computer,

a projector for projecting a beam of structured light, two CCD cameras, 1394 video capture card, some cables and software system. The main parts of 3D scanner are shown in Figure I, its scan scope and time are $400 \times 300 \sim 200 \times 150\text{mm}^2$ and 5s respectively.

A. The Scheme Design and Planning

The stubble-cutting disc with oblique ripples is shown in Figure II (a). In order to avoid the influence of surface reflection, the differences of color and curvature, and other factors on image quality, the developer was evenly sprayed on its surface, and the labels were stuck on it before measuring, as shown in Figure II (b). The labels serve two purposes: (1) as identification points while scanning; (2) as datum points while jointing point cloud data obtained through scanning twice.

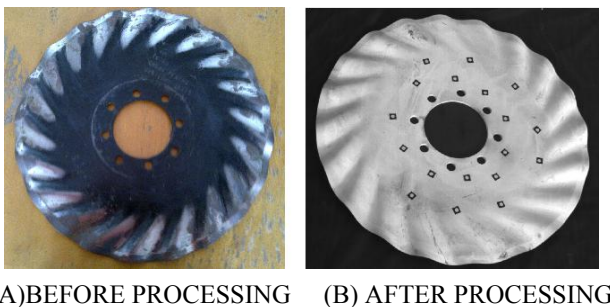


FIGURE II. THE STUBBLE-CUTTING DISC WITH OBLIQUE RIPPLES BEFORE AND AFTER PROCESSING

B. The Measurement of Boundary Curve Points

Obtaining the boundary points aims at acquiring its structure and parameters. The measuring method based on binocular stereovision was used to obtain 3D coordinates of boundary curve.

1) Image acquisition

The left and right images were taken through binocular vision system of 3D scanner that has been calibrated by using the method of reference [5]. At this point, the 3D scanner neither launched grating nor scanned surface.

2) Image processing

In order to obtain better edge of the stubble-cutting disc with oblique ripples, acquired images were processed in Matlab software by image processing techniques before detecting edge, including binarization, de-noising.

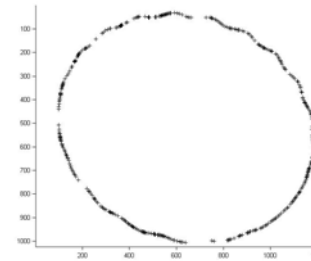
Binariization means that the whole image is only black and white. According to the difference between target and background in gray characteristics, we may regard the image as the combination of target and background with different grayscale. The key is to select optimal threshold. When the gray value of a pixel is greater than the threshold, the pixel belongs to interested target, and its color is white. Conversely, the pixel belongs to background, and its color is black. In this study, the optimal threshold is obtained by function `graythresh()` in MATLAB. It analyzes automatically grayscale histogram, and then determines the optimal threshold according to histogram.

The aim of image de-noising is to reduce random noise that will worsen image quality. There are a lot of de-noising methods that can be divided into two kinds, one kind is the method based on time domain, and another is the method based on frequency domain. The main methods of time-domain de-noising are the weighed smoothing, median filtering, and mathematical morphology. The main methods of frequency-domain de-noising are classic digital filtering, homomorphism filtering and wavelet analysis. In this paper, we adopt median filtering. This method can restrain disturbing pulses and pointlike noise and keep image edge better. Median filtering is finished by function `medfilt2()` in MATLAB in this study.

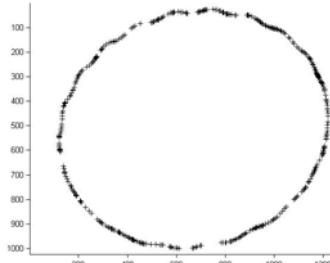
3) Edge detection

At present, the approaches of edge detection mainly are based on differential operation. Differential operation includes first differential calculus and second differential calculus; the edge detection operators based on first differential calculus include Roberts operator[6], Sobel operator, Prewitt operator and Canny operator[7], etc. the edge detection operators based on second differential calculus include Laplacian operator and LOG(Laplacian of Gaussian) operator. A lot of experiments were finished according to all kinds of operators, but, the results weren't favorable. In this study, considering the specific object, we used mathematical morphological method to finish edge detection, which could be finished by function `bwmorph(*,'remove')` in MATLAB.

4) Edge corner detection and stereo matching



(A) CORNER POINTS IN LEFT IMAGE



(B) CORNER POINTS IN RIGHT IMAGE

FIGURE III. DETECTED EDGE CORNER POINTS OF THE STUBBLE-CUTTING DISC WITH OBLIQUE RIPPLES

In order to improve matching speed, the corner points of edge in two images were extracted by using Harris operator[8], on this basis, stereo matching was realized with the combination

of feature matching and area matching under epipolar constraint, namely, take the corner points of edge as matching objects, epipolar constraint[9] and regional correlation were used to finish the edge matching of left and right image. Epipolar constraint can reduces the search space to one dimension (along the epipolar lines)[10]. Regional correlation was resolved by NCC(Normalized Cross Correlation) [11]. According to proposed method, extracted corner points are shown in Figure III.

5) 3D coordinates calculation in binocular vision

In binocular stereo vision, (X_{cL}, Y_{cL}, Z_{cL}) and (X_{cR}, Y_{cR}, Z_{cR}) are the coordinates of a given point in space in left and right camera coordinate system respectively; (x_L, y_L) and (x_R, y_R) are the coordinates of left and right image points in left and right image coordinate system respectively. The effective focal lengths of left and right camera are f_L and f_R respectively. The equations as follows are obtained according to pinhole imaging and perspective transformation model.

$$\begin{bmatrix} x_L \\ y_L \\ 1 \end{bmatrix} = \begin{bmatrix} f_L & 0 & 0 \\ 0 & f_L & 0 \\ 0 & 0 & 1 \end{bmatrix} \begin{bmatrix} X_{cL} \\ Y_{cL} \\ Z_{cL} \end{bmatrix} \quad (1)$$

$$\begin{bmatrix} x_R \\ y_R \\ 1 \end{bmatrix} = \begin{bmatrix} f_R & 0 & 0 \\ 0 & f_R & 0 \\ 0 & 0 & 1 \end{bmatrix} \begin{bmatrix} X_{cR} \\ Y_{cR} \\ Z_{cR} \end{bmatrix} \quad (2)$$

The relative positions between left and right cameras can be expressed by rotation matrix R_c and translation vectors T_c as follows.

$$\begin{bmatrix} X_{cR} \\ Y_{cR} \\ Z_{cR} \end{bmatrix} = [R_c \quad T_c] \begin{bmatrix} X_{cL} \\ Y_{cL} \\ Z_{cL} \\ 1 \end{bmatrix} \quad (3)$$

The follow Eq.4 can be obtained by Eq. 1 ~ Eq.3.

$$\begin{bmatrix} x_R \\ y_R \\ 1 \end{bmatrix} = \begin{bmatrix} f_R & 0 & 0 \\ 0 & f_R & 0 \\ 0 & 0 & 1 \end{bmatrix} [R_c \quad T_c] \begin{bmatrix} \frac{x_L}{f_L} Z_{cL} \\ \frac{y_L}{f_L} Z_{cL} \\ Z_{cL} \\ 1 \end{bmatrix} \quad (4)$$

According to Eq.1, Eq.2 and Eq.4, the 3D coordinates (X_{cL}, Y_{cL}, Z_{cL}) and (X_{cR}, Y_{cR}, Z_{cR}) in left and right cameras coordinate systems can be obtained when (x_L, y_L) , (x_R, y_R) , f_L , f_R , R_c and T_c are known. Then, calculating the 3D coordinates in world coordinate system using the left and right camera external parameters, namely, the relative positions parameters between cameras and world coordinates, which could be obtained by camera calibration.

The edge points of the stubble-cutting disc with oblique ripples were obtained according to matching results and the principle of binocular vision, as shown in Figure IV. We can see that the edge points are smooth as a whole.

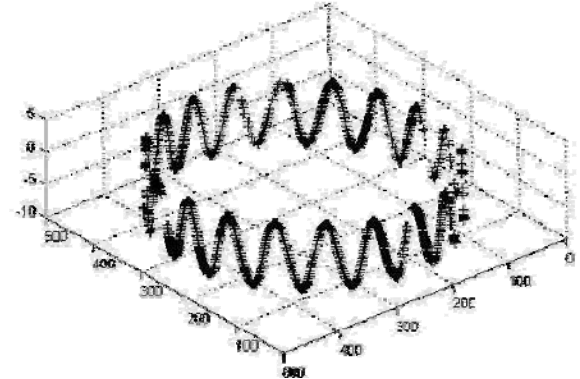


FIGURE IV. ACHIEVED 3D COORDINATES OF THE BOUNDARY CURVE OF THE STUBBLE-CUTTING DISC WITH OBLIQUE RIPPLES

C. The Measurement of 3D Data Points in Inner Part

The size of stubble-cutting is beyond single measurement scope of the 3D scanner, so, the whole surface data were obtained through the method that two-time measurement data were automatic registered to combine a uniform model. The point clouds are shown in Figure V.

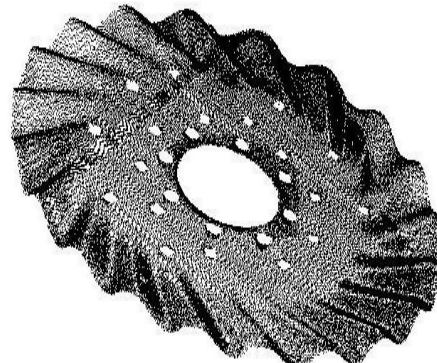


FIGURE V. SURFACE POINT DATA OF THE STUBBLE-CUTTING DISC WITH OBLIQUE RIPPLES

III REVERSE SOLUTIONS OF STRUCTURAL PARAMETERS AND EQUATIONS

A. Structural Parameters of Stubble-cutting Disc with Oblique Ripples

The gaufers of disk sword with ripples are defined as sword ridge. The sword whose ridge lines pass through the center is defined as centripetal stubble-cutting disc, whereas the sword whose ridge lines don't pass through the center is defined as oblique stubble-cutting disc. As shown in Figure VI, OC is the ridge line of centripetal stubble-cutting disc; BC is the ridge line of stubble-cutting disc with oblique ripples. The main structural parameters are outer radius of ripples (R), inner radius of ripples (r), ripple angle (α), the number of ripples (Z), the thickness of sword (h), the curve of outer profile and its amplitudes (A).

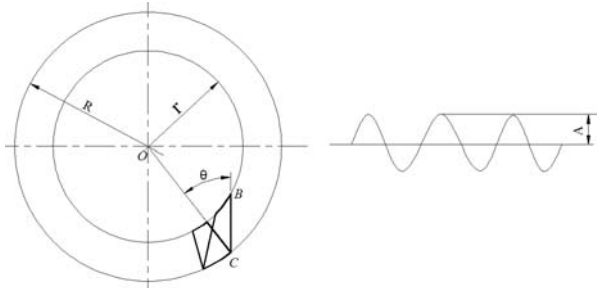


FIGURE VI. STRUCTURAL PARAMETERS OF THE STUBBLE-CUTTING DISC WITH OBLIQUE RIPPLES

B. Reverse Solutions of Structural Parameters and Equations

1) The curve equation of outer profile and outer radius of the ripples

The curve equation of outer profile and outer radius of the ripples were acquired through the boundary data of outer profile [Figure IV], the methods and steps are as follows:

(1) Obtain the outer radius and center through fitting into a circle using x and y coordinates of boundary points; R was 213.87mm, and center coordinates were (212.58, 283.06);

(2) Make the center of fitted circle coincide with the origin of coordinate system by using coordinate translation;

(3) Convert the 3D coordinate system(x, y, z) into cylinder coordinate system (r, θ, z), and solve the corresponding θ values of boundary data;

(4) Solve the functional relation between z and θ through data fitting method. The sine curve fitting algorithm was selected after contrasts of several fitting methods. Given sine function: $z = A \sin(b\theta + c)$, the fitting results with a 98% confidence are shown in Table I.

TABLE I. DATA FITTING RESULTS OBTAINED BY SINE CURVES

Fitting parameters	Fitting results	Confidence interval	Root mean square error	Correlative coefficient
A	5.082	5.014-5.131	0.5082	0.9708
b	19.26	19.24-19.28		
c	2.15	2.103-2.196		

The contrast relation between measured data points and fitting curve is shown in Figure VII. The fitting results indicate the profile curve of ripples really is a sine curve. Outer profile curve of ripples in 3D coordinate system, which was obtained by its structural parameters, is shown in Figure VIII.

2) Reverse solution of inner radius of ripples (r) and ripple angle (α)

Equations The position at inner radius of ripples is a transition from curved surface to plane, so its curvature is strongly variational, which is the same pattern as the position of ridge line. Those make curvature calculation available to extract the data of inner radius and ridge line.

Inner boundary data of ripples was extracted through only single scanning data in order to avoid errors caused by data integrating. The single scanning data is shown in Figure IX, and obtained points of ripples' profile through curvature calculation are shown in Figure X, in which the "+" are the inner boundary points of ripples.

The inner boundary points were fitted into a circle, with the radius being 149.16mm, namely, $r=149.16$ mm.

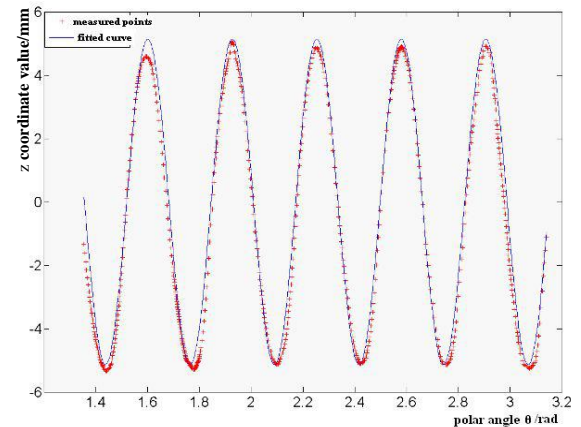


FIGURE VII. COMPARISON DIAGRAM BETWEEN MEASURED BOUNDARY DATA POINTS AND THEIR FITTING CURVE

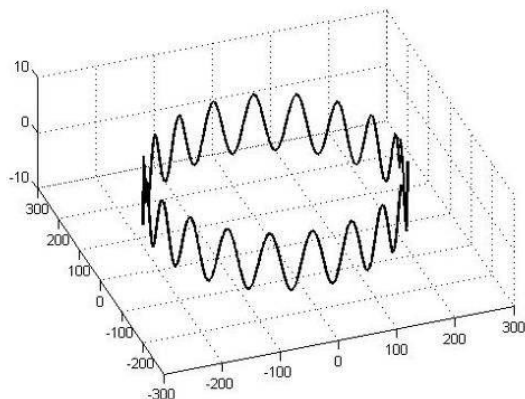


FIGURE VIII. OUTER PROFILE CURVE OF RIPPLES OBTAINED BY ITS STRUCTURAL PARAMETERS IN 3D COORDINATE SYSTEM

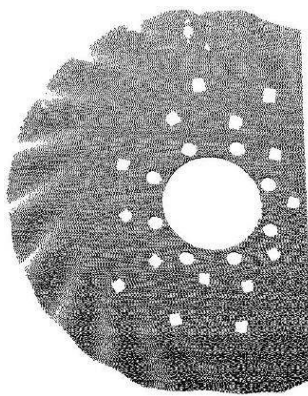


FIGURE IX. SINGLE SCANNING DATA

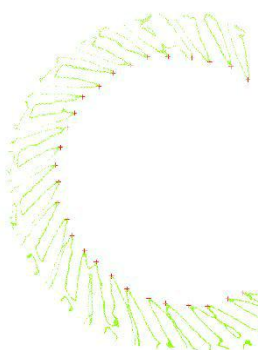


FIGURE X. EXTRACTED INNER BOUNDARY POINTS OF RIPPLES

The reverse solution of ripple angle(α) was obtained by extracting sword ridge line that could be got from the curvature calculation result of ripple profile based on color feature. As shown in Figure XI, the continuous line is ridge line acquired through a ripple profile. One ridge line could be obtained a ripple angle, the final ripple angle (α) was the average value of those, and it was 29.702° .

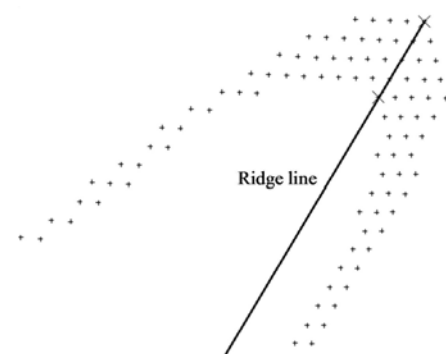


FIGURE XI. THE PROFILE POINTS OF A RIPPLE AND OBTAINED RIDGE LINE

IV THE CREATING OF 3D MODEL

The 3D model was created through using obtained the structural parameters in a computer aided design system of Solidworks, and the results are shown in Figure XII, which will provide the basis for subsequent engineering analysis, parameter optimization and mould manufacture. Compared with 3D model reconstruction based on point cloud data, the advantage of model reconstruction based on structural parameters is that it fulfills the parametric design, and in this instance the model structure can vary with its parameters, fulfills authentic parametric design.

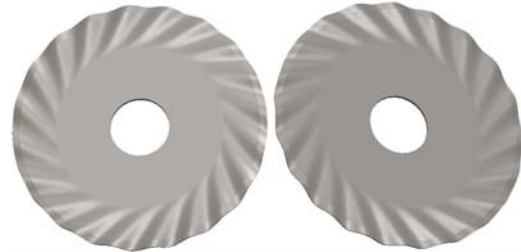


FIGURE XII. 3D MODEL OF STUBBLE-CUTTING DISC CREATED THROUGH OBTAINED STRUCTURAL PARAMETERS

V CONCLUSIONS AND RESULTS

(1) The reverse solution of structural parameters and equation of stubble-cutting disc with oblique ripples were well fulfilled through reverse engineering technology. The results show that the outer profile of ripples is sine curve, as for the given stubble-cutting disc with oblique ripples made by America, the equation is $z = 5.082 \sin(19.26^\circ \cdot 2.15)$, and its ripple angle(α) is 29.702° , outer radius of ripples(R) is 213.87mm , inner radius of ripples(r) is 149.16mm .

(2) The reconstruction of the 3D parametric model of stubble-cutting disc with oblique ripples provides the foundation for its parameter optimization and mould manufacture, and the research results provide a new method for its design and manufacture. At the same time, this research also provides a reference for the application of reverse engineering technology in the design and manufacture of agricultural machine.

(3) The research results also illustrate that RE can be used to obtain the parameters and equations of the regular structures.

ACKNOWLEDGEMENT

The digital measurement method in this research was supported by the National Science Foundation of China (51505305) and Doctoral Fund of Ministry of Education of China (20132103120016).

REFERENCES

- [1] Zhao Xu, Zhang Zuli, Tang Ping, Zhang Guoliang, Zhang Weizheng, Behavior of Passive Stubble-cutting Disc with Oblique Ripples, Transactions of the Chinese Society for Agricultural Machinery, 42(2011)64-67.
- [2] Zhang Zuli, Zhao Xu, Bai Xiaohu, Zhang Xudong, Kinematics Analysis and Simulation of Disc Coulter with Oblique Ripple, JOURNAL OF AGRICULTURAL MECHANIZATION RESEARCH, 31(2009) 27 -30.
- [3] Zhao Xu, Zhang Zuli, Bai Hongchun, Zhang Guoliang, Zhang Xudong, The New Type Residues Cutting and Anti-blocking Device, JOURNAL OF AGRICULTURAL MECHANIZATION RESEARCH, 31(2009) 58-61.
- [4] Kamran Mohaghegh, Mohammad H. Sadeghi, Amir Abdullah, Reza, Improvement of reverse-engineered turbine blades using construction geometry, The International Journal of Advanced Manufacturing Technology, 49(2010) 675-687.
- [5] Ping Zhao, Yong-kui Li, Li-jun Chen, Xue-wei Bai, Camera calibration technology based on circular points for binocular stereovision system, Communications in Computer and Information Science,158(2011) 356-363.
- [6] Roberts L G, Machine Perception of Three-Dimensional Solids, In Proceedings of Optical and Electro-optical Information Processing, 1965, pp.159-197.
- [7] JOHN CANNY, A Computational Approach to Edge Detection, IEEE Transactions on Pattern Analysis and Machine Intelligence,1986, pp.679-698.
- [8] Chris Harris, Mike Stephens, A COMBINED CORNER AND EDGE DETECTOR, In Proceedings of the 4th Alvey vision conference, 1988, pp.189-192.
- [9] Larry S.Shapiro, Andrew Zisserman, Michael Brady, Motion From Point Matches Using Affine Epipolar Geometry, Lecture Notes in Computer Science, 801(1994)73-84.
- [10] Ingemar J.Cox, Sunita L.Hingorani, Satish B.Rao, A Maximum Likelihood Stereo Algorithm, Computer Vision and Image Understanding, 63(1996)542-567.
- [11] Kai Briechle, Uwe D.Hanebeck, Template Matching Using Fast Normalized Cross Correlation, In Proceedings of SPIE, V.4387, Optical Pattern Recognition XII, Orlando, FL. 2001, pp.95-102.

The Mathematical Model of the Natural Evolution Law of Cosmic Material Organisms

Sai Chuen Hui

Frontier Science Research Institute of Hong Kong Limited

Abstract—The "Goldbach conjecture" is proved by "simultaneous screening of positive and negative sides". And the computational values of "modeling" in various scientific fields coincide with reality, theory, experiment and astronomical observation. The universe is superimposed by the energy of equal positive and negative universe into a coupling strength explosion. After decoupling, the 4% energy is transformed into "matter" and "biological evolution", and it can justify itself. It is pointed out that the natural evolution of the universe exists in the eternal "law of the universe".

Keywords—goldbach's conjecture; positive and negative screening; quantum biology; quantitative change to qualitative change; energy / material world; universal rules

I. A UNIVERSE OF MATHEMATICS

Without understanding its language, no one can read the great book of the universe, its language is mathematics – Galileo

A. "Goldbach's Conjecture"

(a) Every Even Number Is The Sum Of Two Odd Prime Numbers.

(b) Each Odd Number Is The Sum Of Three Odd Prime Numbers.

The narrative is concise and difficult to prove. It is known as the Pearl on the crown of mathematics.

B. Positive and Negative one Screening Conclusion

[Theorem 1] the exact solution formula of Goldbach's conjecture:

$$Z_w(w) = Z_{p,q}(w) + 2Z_a(w) \dots \dots (2.2)$$

$$Z_{p,q}(w) = w+1 + \sum_{\substack{l+m \leq n \\ l,m \geq 0}} (-1)^{l+m} \sum_{\substack{1 \leq j_1 < \dots < j_l \leq n \\ 1 \leq j_1 < \dots < j_m \leq n \\ \{j_1 \dots j_l\} \cap \{j_1 \dots j_m\} = \emptyset}} \left[\frac{w - r_{j_1 \dots j_m}^{j_1 \dots j_l}}{p_{j_1} \dots p_{j_l} p_{j_1} \dots p_{j_m}} + 1 \right] - 2A_{w-1} \dots \dots (1.3)$$

[Theorem 2] any even number as the sum of two odd primes of the odd prime number, the limit value is the total number of odd primes after prescribing and constant not less than 1.

$$Z_w^*(w) \geq [\pi(\sqrt{w}) - 1] + A_{w-1}$$

$$A_{w-1} = \begin{cases} 1 & w-1 \text{(Prime number)} \\ 0 & w-1 \text{(Is the number of)} \end{cases} \binom{1}{w-1} \begin{cases} (\text{Not sifted}) \\ (\text{Have been sifted}) \end{cases}$$

Checking calculation: Taking the minimum value =6 of the even number, the limit value

$$Z_w^*(w) = [\pi(\sqrt{6}) - 1] + \binom{1}{0} = [1 - 1] + \binom{1}{0} \geq 1$$

Goldbach's conjecture

[Theorem 1-2] confirmed by the United States Intellectual Property Office and 2012.4.4 to the certificate of authorization.

Xiamen University mathematician Li Wenqing (Chen Jingrun teacher) guide the audit results. Opening an equation to solve the two unknowns is an alternative mathematics and is in the ascendant. If we use the formula (1.3) to calculate the "heavy prime number" table, we call it "double key lock cryptography", "biological DNA sequence", "atomic energy meter", "universe 4% substance" and so on. Can be accurate look up! Implementation of einstein"..... How to set up an aesthetic system that can be expressed strictly by formula "to describe the lifetime wish of the universe with a mathematical formula!"

C. Six Hexadecimal

1. "1" is the "concept" of numbers. "1" is not the prime number, is the original minimum unit of things, atomic clock half period cannot show time! Clear concept! Otherwise, a mathematical crisis is inevitable

2. Prime number is the most basic, stable and irreplaceable primitive number of primitive mathematical elements of a thing.

3. Natural integers are divided into even and odd numbers According to the nature of the number, Goldbach conjectures that the mathematical theory is divided into: Each even number is the sum of two odd prime numbers B) every odd number is the sum of three odd prime numbers The minimum common divisor between 2 and 3 is: 2 multiplied by 3 = 6 And is the universe matter mathematical "six-ary"; "Six hexadecimal" can prove "twin prime conjectures" and "Liang Dingxiang's conjecture".

4. The ratio of material and cosmic energy to the total mass of 4% is an example of six calculation.

See the table below

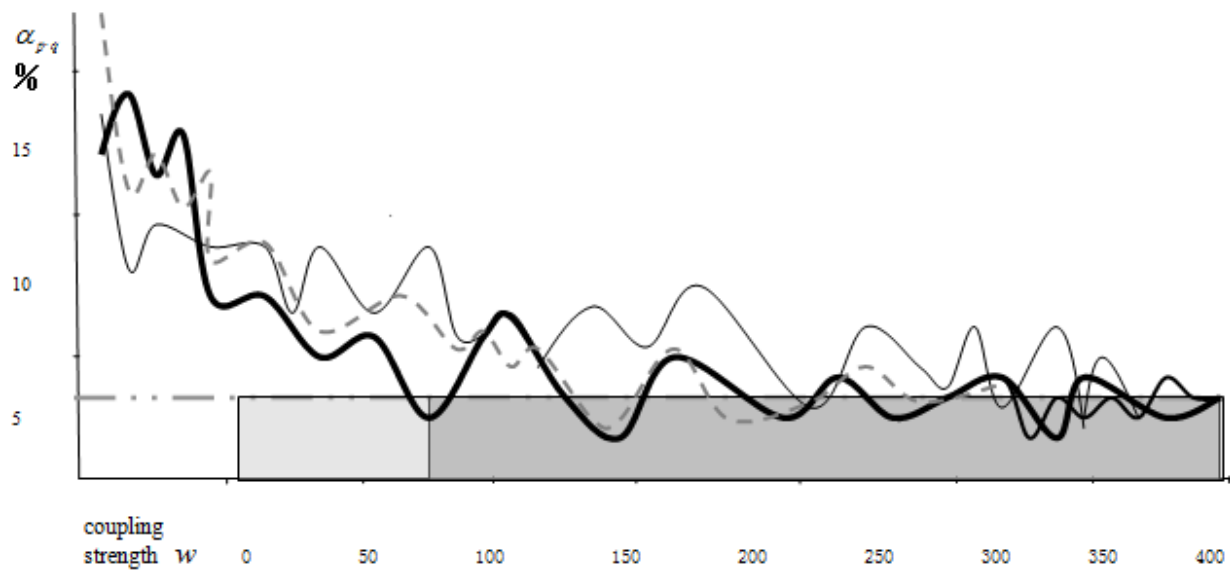


FIGURE I. DIAGRAM OF THE CALCULATED RATIO OF ORDINARY MATTER TO GROSS COSMIC ENERGY

D. Figure Out

1. Material atom $\binom{p}{q}$ The total number of heavy prime numbers accounts for the coupling strength w Ratio: Fine black is the coupling strength $w = 6n$ $n=1, 2, 3, \dots$ The curve of the number of atoms (heavy prime)

Green black is the coupling strength $w = 6n+2$ The curve of the number of atoms (heavy prime)

Virtual black is the coupling strength $w = 6n-2$ The curve of the number of atoms (heavy prime)

2. When large even number $w > 50$ At a time (yellow region), there are three odd prime numbers of 3.5.7 and the ratio of the substance to the cosmic energy of three quarks 4.6 %;

3. When deep black zone is the coupling strength $w \geq 122$, The ratio of average ordinary matter to cosmic energy is coincidental.; 4 %On-line.

(Eight) Six is the most accurate and quickest way to solve dark matter dark energy values

II. WHAT IS THE UNIVERSE

The predecessor of the universe is only the equal positive and negative energy, the algebra and the zero, and the no dimension is the empty state.

A. What is the "Singularity" of the Big Bang?

There is no matter, no time or space. There are only equal positive and negative energy or the philosophical realm of "unity of opposites" in the universe.

The truth of the "singularity" of the B. Big Bang is

(1) There is no material particle. Where is the volume space of the particle?

(2) There is no big explosion in the universe. What is the energy that makes "the temperature infinitely high"?

(3) There is no physical and material movement. Where is time and space?

Is that the reason? Unbelievable assumptions!

B. The Coupling Explosion Between the Positive and Negative "Cosmic Energy". Decoupling Transmutation into the Material Universe

C. Coupling Strength $w = \pm\sqrt{2E}$ E Energy

D. Combinatorial Mathematics

Odd number combination—3 A quark composed of particles: an even number of combinations - producing an atom

The gauge field makes the particles transform each other. Now, the new material particles can be accurately calculated by (1.3).

E. Energy Transmutation into Matter

All things in the universe have the basic law of unity of opposites, and the corresponding mathematics is [positive and negative sifting]: its combination 2^n It's just the combination of cosmic matter:

a) A combination of positive and negative 3 different quantities $n = 3$ $2^n = 2^3 = 8$ (hexagram) is the eight state of the particle and the protein eight polymer.

b) The number of 6 combinations of positive and negative $n = 6$ $2^n = 2^6 = 4^3 = 64$ (hexagram) the 64 codons of a creature; 64 basic particles.

$\binom{p}{q}$ An atom consists of a proton p (UUD positive energy) and a neutron q (UDD—negative energy). The neutron is an electron and an inverse neutrino, which is an odd prime number. There is no prime factor and can not be decomposed. It is the reason that the hadron can not get out of the quark, but it can only decay.

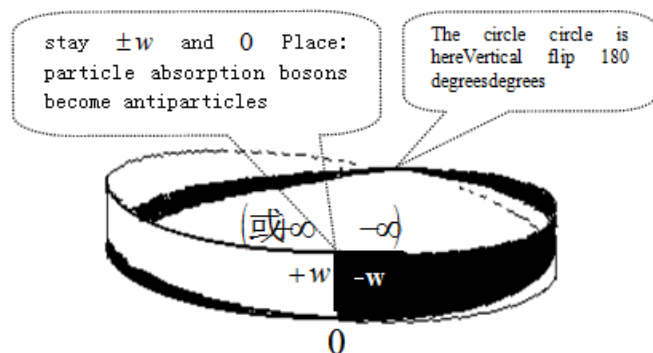


FIGURE II. INVERSE SYMMETRIC ROTATIONAL CYCLE DIAGRAM OF POSITIVE AND NEGATIVE ENERGY UNDER THE CONTROL OF COUPLING STRENGTH EXPLODING UNDER THE TRIGGER OF ANTIMATTER (COSMIC GENE) AND TRANSMUTATION INTO THE MATERIAL UNIVERSE. WITHOUT CHANGING THE MOTION AND ROTATION OF PARTICLES UNDER THE CHARGE CONJUGATION TRANSFORMATION THE COLLISION OF THE TWO PROTONS BECOMES A COLLISION OF TWO ANTI-PROTONS. THE COLLISION OF THE TWO PROTONS BECOMES A COLLISI

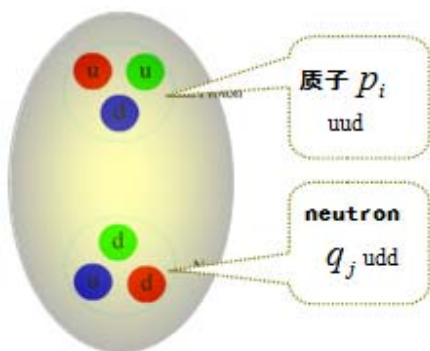


FIGURE III. OTH THE POSITIVE AND THE ANTI ATOMS ARE MADE UP OF PROTONS AND NEUTRONS. THE ELECTRONS IN THE PERIPHERY OF THE ATOM ARE PROVIDED BY NEUTRONS. (NOTE: U QUARKS; D QUARKS)

Material Generation and Evolution

"So far, scientists do not yet know where the particle mass comes from," Goldbach conjectured: quarks in particles are matter, while wandering quarks are energy. The quark state determines the quality or energy.

A. The Conversion of Energy into the Production of Material Particles and Atoms

The energy is accelerated in the current accelerator, so that the coupling strength is high enough to decouple the energy of the new particles. Artificial elements such as: 104-111 Rf-Rg

Natural number K × 108	927.333	930.886	945.098	937.992
984.181	952.204	998.393	966.416	

Atomic number	104	105	106	107
108	109	110	111	
Material element name	钅卢* Rf	钅杜* Db	钅喜* Sg	钅波* Bh
钅黑* Hs	钅麦* Mt	钅鑑* Ds	钅鑰* Rg	
Relative atomic value	[261]	[262]	[266]	[264]
[277]	[268]	[281]	[272]	

(Note: “*” It's an artificial element)

This is an empirical study of energy transmutation into matter. In other words, "matter is the crystallizer of energy"

Energy is an invisible thing. We can only measure the voltage and quantity of the energy by modern science and technology; who has no ability or ability to measure the three-dimensional volume and age of the energy? Positive and negative energy is equal or not in contact with (Mathematics expressed as 0), only the positive and negative energy superposition coupling strength explosion, decoupling into matter!

B. The Evolution of the Energy Decoupling of the Big Bang into the Material Process

(1) Under the early weak interaction of the big bang, 3 quarks were gathered and converted into basic particles. mathematical "quality and energy cycle theory": the coupling strength under be concentrated to a proton and neutron in the nucleus (see Figure 8). Mass and energy combinations: divided into so-called odd combinations (particles), even combinations (into atoms) Is the "two wave particle dualism", the fundamental reason of material and energy equivalent.

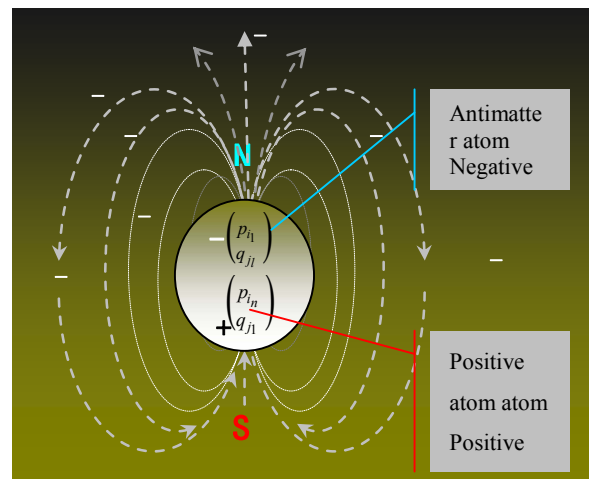


FIGURE IV. THE POLARITY AND MAGNETIC LINE OF FORCE OF ATOMS

Is Schrodinger in the quantum superposition state a paradox of living and giant cats?

C. Atom - Made up of Positive and Negative Atoms

Both the positive and the counter atoms are made up of protons and neutrons (see Figure 8) The antimatter atom is the left in (4.3) $\binom{p_{i1}}{q_{j1}}$ $p - q < 0$; Positive atom atom $\binom{p_{in}}{q_{jn}}$ $p - q > 0$ [$\binom{p_{i1}}{q_{j1}} + \binom{p_{in}}{q_{jn}}$] This is the so-called "atom". What is the difference between a proton and a neutron energy?

It is the number of peripheral electrons provided by the anti atom. The magnetic field produced by the electronically negative energy is the cause of Universal gravitation (see Figure 9).

*D. Qualitative Change Caused by "Quantitative Change"
(See Figure 9-10)*

In the physical universe, antimatter 23%, positive and negative energy account for 73%, and "positive matter" accounts for only 4%. Antimatter is a category of energy that cannot be decoupled, and antimatter (atom) is the shadow of a positive matter, and is a future cosmological gene. It is the N pole negative pressure of the magnetic field. So it's hard for us to get in touch with them.

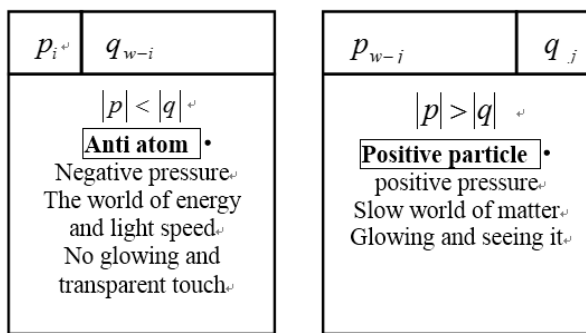


FIGURE V. DIAGRAM OF POSITIVE AND ANTIMATTER DIFFERENCE
 NOTE: p POSITIVE PARTICLE q ANTI PARTICLE
 ANTI PARTICLE

E. Qualitative Change Caused by "Quantitative Change" (See Figure 9)

F. The Mechanism of Universal Gravitation (See Figure 11)

The explosion is controlled by strong coupling strength. The anti matter atom decoupling community produced by the atoms of a double material, with the energy of the positive particles and the negative particles, can not counteract each

Positive energy of upper set

$$S = \left\{ \binom{0}{w}, \binom{1}{w-1}, \dots, \binom{n_x}{q_{j_x}}, \dots, \binom{p_{i_1}}{q_{j_1}}, \dots, \binom{p_i}{q_j}, \dots, \binom{p_{i_2}}{q_{j_2}}, \dots, \binom{p_{ix}}{n_x}, \dots, \binom{w-1}{1}, \binom{w}{0} \right\} \dots \dots \dots \quad (4.3)$$

Antimatter atom $p - q < 0$ ←----- Lower set negative energy

(4.3) Type: $\binom{p}{q}$ It's a material atom -- one of them $\binom{p}{q}$
 Proton positive energy, $\binom{q}{q}$ Negative energy of neutron

H. Symmetry Breaking

It refers to the reduction of variability or symmetry in a certain transformation. That is, a certain characteristic of an object is no longer a constant in a certain transformation, and its symmetry is destroyed, so it is called symmetry breaking.

In coupling strength w Under control, the strong force is in (4.3). $\binom{n_x}{q_{jx}}$ Dark antimatter atom and $\binom{p_{ix}}{n_x}$ Binding of dark positive matter atoms $[\binom{n_x}{q_{jx}} + \binom{p_{ix}}{n_x}]$ When the "atom": It

other.

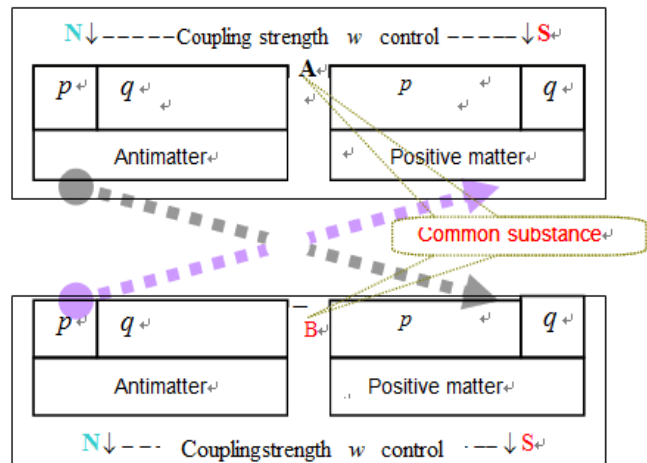


FIGURE VI. UNIVERSAL GRAVITATIONAL INTERACTION MECHANISM

It is the magnetic strength B of the material itself, the external gravity strength, and the field of the magnetic field (induction).

The Big Bang is in a state of symmetry and antimatter. But astronomical observations show that today's universe is mainly material! Where did the antimatter go? Mathematics shows that the so-called "atom" is the twin community of positive and negative atoms! This section explains the trend of antimatter.

G. Symmetry and Breaking and Mathematical Mathematics

(1) symmetry is the twin coexistence of a negative atom and a positive atom $\left[\begin{pmatrix} p_{ij} \\ q_{j_2} \end{pmatrix} + \begin{pmatrix} p_{i2} \\ n_{j_1} \end{pmatrix} \right]$. Look up (in 4.3).

is negative energy (dark matter). $\{ \binom{n_x}{n_x} \text{ Positive energy, } \binom{n_x}{n_x} \text{ Negative energy} \}$ Is the category of energy, only "symmetry breaking"! $\binom{p_{ix}}{p_{ix}}$ Show only positive particles!

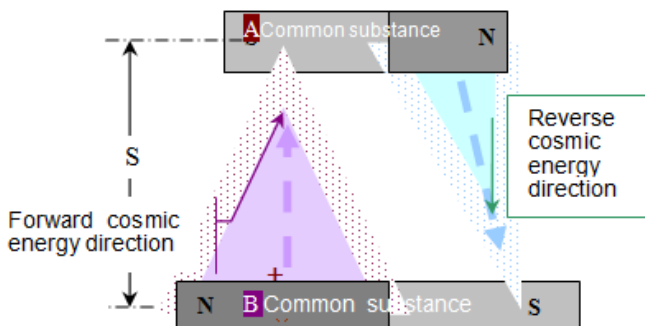


FIGURE VII. THE GRAVITY OF THE MAGNETIC FORCE LINE OF A TWO OBJECT PRODUCES A TWO-WAY COUPLING FORCE

III. ORIGIN AND EVOLUTION OF LIFE

A "gene" evolved with biological evolution. The genetic information contained in DNA metabolic evolution is the basis of all modern life functions. In the paleontological world, nucleic acids have a catalytic and genetic function that evolved into a genetic code consisting of four nucleotides. Finally, the optimum number of four bases is obtained.

The formation of organic small molecules, organic macromolecules, amino acids, purines, organic macromolecular proteoglycan, nucleic acids, polysaccharides and polysaccharides are the main components of cytoskeleton. All cell walls and nucleic acids are genetic material.

Through polymerization, the formation of biological macromolecules, self replicating and self selection. Calculation shows that the combination of the material particles and the 64 codons of the biological state of yin and Yang is eight Batu self-organization, replication and mutation. The mathematical correspondence between the DNA double chain complementary sequence and the positive and negative sieves confirms the existence of "natural biologic program software". As long as a person's oligonucleotide primers are primed, that

$r_{j_1 \dots j_m}^{h \dots i_l}$ is the initial value, according to (2.3), the DNA sequence of each chromosome can be calculated, which is consistent with the real biological gene encoding rule.

A. Goldbach's Conjecture is Embodied in the Chain of Biological Genes

An even number w . It is the sum of two odd prime numbers $w = p + q$ (the unity of opposites and the combination of yin and Yang) see the picture 13, 14

B. The Basic Combination of All Things in the Universe: 2^n

1. $2^n = 2^3 = 8$ It is the eight polymer of the protein (the eight state of the particle).

2. $2^n = 2^6 = 64$ It's the codons 64

Along as we figure out the primer value of Figure 14 (each person is fixed value), we can calculate all kinds of DNA sequences according to [theorem 1] Goldbach guess's exact solution formula (2.3). (Note: "double key lock password" Chinese and American patent is the live DNA password!)

This is using mathematics to describe biology at a quantum level. Known as "quantum biology".

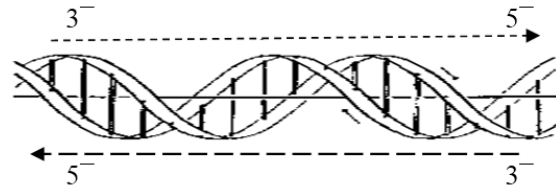
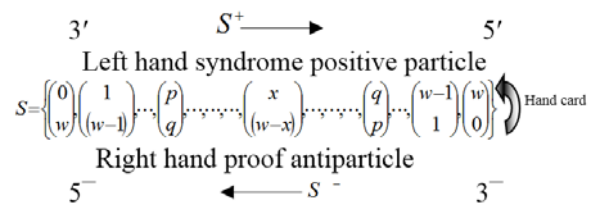


FIGURE VIII. TWO REVERSE PARALLEL POLYNUCLEOTIDE CHAINS AROUND. THE DOUBLE HELIX STRUCTURE WITH A CENTER SHAFT MADE OF THE WINDING



The mathematical formula of weak interaction of (1.3) positive and antimatter

C. The Number of Odd Prime Pairs (Base Pairs) $Z_w(w)$

The sequence length is the square root of the number of oligonucleotides and S the number of elements of a set $n = \pm \pi(\sqrt{w})$ Corresponding.

If there are "eight polymer" oligonucleotides (a total of 65536) on the chip, the longest sequence length that can be measured is 256bp (base pair).

even number. The number of all the odd prime number pairs (base pairs) — Exact solution to 1 pages (1.3)

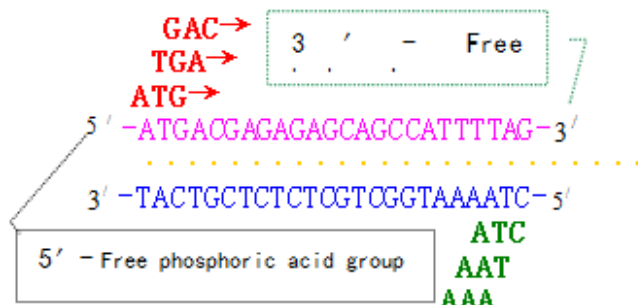


FIGURE IX. CORRESPONDING TO THE THREE YIN SANYANG FIGUE 14 THREE READING FRAME AND TRI GOSSIP. NOTE: GOLDBACH CONJECTURE THAT EACH ODD NUMBER OF [2] IS THE SUM OF 3 PRIME NUMBERS

D. Each Odd Number is Equal to the Sum of 3 Primes, Corresponding to Each Codon Consisting of 3 Nucleotides

The gene of the encoded protein contains the readable frame (ORF), and the analysis complexity is that each DNA sequence has 6 reading frames averaging each. Average $4^3 =$

64 bpOne time. This combination of Yin Yang and Yin and Yang (positive and negative) entity 2^6 Complete anastomosis. For the 64 codons that correspond to the genetic code. DNA can be seen as a character set of four characters: $\Sigma = \{A, G, C, T\}$ Four decimal code. Base pairing principle detailed: [simple DNA code] patent number: 200810067374.X

The human DNA password is fixed. It is from one person. "Primer value" is the initial value Calculate it by (1.3)!

E. Variation

In the mathematical formula of Quantum Biology (1.3): the coupling strength of biological DNA code is different from that of 2 units. The difference of Hatching Temperature determines the sex, such as the crocodile, the appearance and personality of children, and the reasons for their differences with their parents.

Only female and male heterosexual combinations will mutate, and cloning will not mutate or decline! The sum of algebra is produced under the condition of "unity of opposites".

IV. COSMIC LAW

What is the two eternal explanation of the law of Physics

Time is the product of matter plus movement; only mathematics can fully clarify the understanding: "mass energy" is eternal; 2, movement is eternal; it is the intrinsic nature of matter and energy. If the speed of light is the intrinsic property of the photon, the "photon" has only energy and no mass.

A. The Mathematical Conclusion Of Goldbach's Conjecture

The first unity of opposites in the law of the universe: the combination of yin and Yang

Even conjecture: every even number $w \geq 6$ It is the sum of two odd prime numbers

1. Superposition of positive and negative energy into coupling strength explosion 4% energy transmutation into material universe

$$2. \text{ Material atoms} \left[\begin{pmatrix} p_{i_1} \\ q_{j_2} \end{pmatrix} + \begin{pmatrix} p_{i_2} \\ n_{j_1} \end{pmatrix} \right]. \text{ Anti atom} \begin{pmatrix} p_{i_1} \\ q_{j_2} \end{pmatrix}$$

Positive atom $\begin{pmatrix} p_{i_2} \\ n_{j_1} \end{pmatrix}$ It is the result of opposites and unity The twin community. (Twin community)

3. The breeding inheritance of animals and plants is the positive and anti complementary products of the DNA two chain (see Figure 13).

B. The Basic Particles of the Second Rules - Three Ones

Odd number conjecture: every odd number $N \geq 9$ It is the sum of three odd prime numbers

1. Material particles - the combination of 3 quarks: p proton (uud); q neutron (udd).

2. The biological codons are composed of three nucleotides: each DNA sequence is composed of three forward and three reverse combinations

C. The Third Rules of the Universe 2"

All things in the universe are the transformation of energy! It depends on the coupling strength $w = \pm \sqrt{2E}$ and the combined elements $n = \pm \pi(\sqrt{w})$. The odd prime number of the "anti matter" (1.3) negative energy of the "antimatter" (anti matter) type is a complete sequence that satisfies 2^n the need for the conversion of energy into a material double atom. universal gravitation is necessary. All things in the universe are the transformation of energy! It depends on the coupling strength $w = \pm \sqrt{2E}$ and the combined elements $n = \pm \pi(\sqrt{w})$. The odd prime number of the "anti matter" (1.3) negative energy of the "antimatter" (anti matter) type is a complete sequence that satisfies 2^n the need for the conversion of energy into a material double atom. $\left[\begin{pmatrix} p_{i_1} \\ q_{j_2} \end{pmatrix} + \begin{pmatrix} p_{i_2} \\ n_{j_1} \end{pmatrix} \right]$ universal gravitation is necessary.

1. The universe is $n=1$; $2^1=2$ Two combinations of positive and negative energy.

2. Matter is $n=3$; $2^3=8$ matter is the eight heavy state of the particle (protein eight polymer).

3. Biology is $n=6$; $2^6=64$ 64 codons (64 basic particles).

D. The Upper Class Base of the Fifth Rule [Index] Growing at the Bottom

(1) The material universe is both positive and negative energy 2 as the bottom n product, 3 square "eight heavy material particles", and 6 is the biological 64 codon.

(2) In the field of biology, "big fish eat small fish eat shrimp", "law of the jungle" and "biological food chain";

The history of human society: nomadic hunting, fishing, and grain surplus produced a slave society. The stability of agriculture and more grain, the emergence of feudal society; the industrialization of capitalism. Small is the individual, the country, the resources, the interests of the regional war... Will the United States and Russia have a nuclear war? Human beings are living and dying at the crossroads?

E. The Law Of The Fifth Universe -- Cycle And Infinity

1. The physical universe is running at 0 and infinity (reality is carried out under limited coupling strength), and they are the reciprocal. 180 degrees of particle flipping: charge conjugate transformation... "Antimatter" is a mirror of "positive matter". The mass is exactly the same, and its antiparticle and charge are opposite.

2. Energy converts to material circulation: (1) opposites and unity (2) qualitative change

3. When the substance annihilated, the life body died; the function of the brain disappeared - no soul!

4. Circulatory immortality - the mating and reproduction of animals, the growth cycle of plants and males and females, the change of social system, and the cycle of quality and energy.

5. The birth and death of the universe

1) Decide on the big bang / black hole struggle, the ultimate black hole to eat out the material

2) The material mass can be 4% to the line ratio, the material universe is just a moment.

F. *The First Driving Force*

The annihilation of a black hole, including light matter, is annihilated into positive and negative energy from both sides. The explosive force that causes the superimposed coupling of the random positive and negative cosmic energy is—I want to use an animal's instinct to live a good day I dream more about why the natural evolution of the universe is like this

The law of nature is also a two-sided sword.

REFERENCES

- [1] The key to the mysteries of the universe The application of Goldbach's Goldbach conjecture Published by the Hongkong Academy of scientific research.

Research on Filter Rod Loose Quality of Double Channel Forming Machine Based on Apriori Algorithm of Interestingness

Min Zhang, Liming Zhu* and Yumin Wang

China Tobacco Zhejiang Industrial Co. LTD., Hangzhou, China

*Corresponding author

Abstract—Double channel forming machine opening quality data by sampling and conversion into the mining of association rules based on Apriori algorithm, correctness verification and quality deviation setting parameters, makes the equipment in adjusting the parameters set to drive the delivery index get reliable performance.

Keywords—interest degree; APRIORI; double channel; filter rod forming machine

I. INTRODUCTION

Double channel forming machine is the production equipment of filter rod, is a kind of high speed and super high speed rolling equipment for molding equipment, which loosening raw materials of filter rod--two cellulose acetate tow, on the loose quality correlation can be found between equipment and production quality, contribute to the optimization and stability of the equipment. The loosening machine is mainly composed of tow guiding device and independent opener which stretching and fluffing of two acetate fiber tow. Degree of loosening will not only affect the quality of the direct filter rod, but also affect the sensory quality and product stability of cigarettes. The loosening of the filter rod consists mainly of three steps.

1. Tow input: make the tow out of the package smoothly.
2. Prestretch of the silk bundle: make the tow stretch out in a number of positions, and the fiber bundles are separated so that the fiber tow can be supplied and processed evenly;
3. Tow stretch and relaxation: the tow is extracted from the tow package and transmitted through the machine, and the tow is loosened and relaxed through the different load ratio and speed of the roller set.

In the process of equipment loosening and solidification, the research of the degree of loose and the quality of filter rod can be very important in the process of equipment commissioning and production. The research on the parameter setting process and the quality of filter rod is an important topic at present.

II. APRIORI ALGORITHM

Apriori algorithm is one of the most basic idea of mining association rules of frequent itemsets algorithm, the algorithm effect is[1]: using the recursive method to find all frequent sets, and then generate strong association rules by the frequency set, these rules must satisfy the minimum support degree and confidence degree. Once these rules are generated, only those

rules that are larger than the given minimum credibility are left behind.

The Apriori algorithm is composed of two steps: connection and pruning.

Connection: in order to find L_k , a collection of candidate K item sets is generated through L_{k-1} connection with itself, and the candidate K item set is recorded as C_k .

The two elements in L_{k-1} , L_1 and L_2 , can perform connection operations:

C_k is a superset of L_k namely, its members may not be frequent, but all k- frequent sets in C_k . So can get L_k by scanning the database by calculating the support of each k- item set.

Pruning: if a subset (k-1) of a candidate K itemset C_k is not in L_{k-1} , then the candidate is not likely to be frequent, so it can be deleted from C_k and get the compressed C_k .

Pseudo-code of Apriori algorithm:

The D: object database;

The Min_sup: minimum support threshold.

Output: frequent itemsets in L:D.

Method:

```

L1=find_frequent_1-itemsets(D);
for(k=2;Lk-1 != ∅ ; k++){
    Ck=apriori_gen(Lk-1);
    For each transaction t ∈ D {//
        Scanning D for counting
        Ct=subset(Ck,t); // Get a
        subset of T, they are
        candidates
        for each candidate c ∈ C;
            C.count++;
    }
    Lk={c ∈ C|c.count>=min_stp}
}
return L=UkLk;

```

III. PROBLEMS OF THE APRIORI ALGORITHM

Interest degree and confidence level set to mine meaningful association rules from massive data. However, the algorithm has the following problems in practical application.

(1) to excavate the strong association rules that have a gap with the reality. For example, in the application of electronic medical record data analysis [2]

(2) the database scan level is huge. In many studies, it has been concerned about this. Various improvement methods and measures have been put forward to improve its executability and reduce expenses.

Therefore, many scholars have proposed the Apriori algorithm based on the degree of interest, and the basic principles are as follows:

Association Rules: the formulae of association rules are described as: set up $I = \{i_1, i_2, \dots, i_m\}$ is a collection of m different items, and D is a set of transactions for I , where each transaction T contains a number of items I_1, I_2, \dots, I_K , each transaction item is recorded as TID.

Support [3]: defined as $\text{Support}(X) = \text{occur}(X) / \text{count}(D) = P(X)$.

Confidence[3]: is defined as $\text{conf}(X \rightarrow Y) = \text{supp}(X, Y) / \text{supp}(X) = P(Y|X)$.

The interestingness of association rules is described in rule sets of items such as X are set to another degree of correlation between Y , denoted as $X \Rightarrow Y$, if the $X \Rightarrow Y$ rule interestingness value is greater, the greater the tightness is $X \Rightarrow Y$;

The specific description of the algorithm is [2]:

If $P(XY) = P(X)P(Y)$ means that the item set X is independent of the item set Y ; if $P(XY) > P(X)P(Y)$ means that the event X and Y is related events, the two are not independent to each other. The association rules $X \Rightarrow Y$ excavated, set X and Y set interest degree:

$$RI(XY) = P(XY) / (P(X)P(Y))$$

$$P(X)P(Y)$$

When $RI > 1$, it is shown that the item set X is positively related to the item set Y , and the occurrence of X will increase the probability of the occurrence of Y .

When $RI < 1$, it is shown that the item set X is negatively correlated with the item set Y , and the occurrence of X will reduce the probability of the occurrence of Y .

When $RI=1$, it is shown that the item set X is independent of the item set XY , and there is no correlation between X and Y .

IV. LOOSING QUALITY VERIFICATION MODEL OF FILTER BAR APRIORI ALGORITHM BASED ON INTEREST DEGREE

Research purpose: The research is mainly about the relationship between the set value of the equipment and the quality of the final production, especially on the weight, draw resistance and hardness of the filter rod, by analyzing and mining data association, the information excavated is of great reference value in the decision-making process of small to big parameter setting, whether the equipment debugging is qualified or not.

Work flow module: data collection, data preprocessing, association rules mining, judgment module, equipment adjustment;

Equipment sampling: sampling through the front and rear channels. The sample can be taken in many groups, and each group can take more than one.

Filter bar inspection: through the inspection of the sample product, the results of the detection into the form;

The data transformation and elimination, the obtained data are converted to the algorithm model to calculate the value, and the special data are eliminated.

From the interest based Apriori algorithm calculation model, the concrete conclusions are obtained. After verifying the conclusion of module validation, the conclusions are fed back to the equipment, and the parameters are adjusted. All the processes are referred to figure 1.

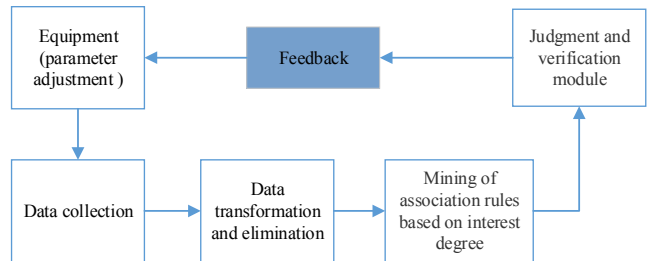


FIGURE I. PARAMETER ADJUSTMENT MODEL OF APRIORI ALGORITHM BASED ON INTEREST DEGREE

In the process of loosening and forming, there are four values of indicators represent the key indicators in the quality test, Save in the database as Table 1.

TABLE I. KEY INDEX PARAMETER

Field name	Data type	length
Expansion degree	Char	10
draw resistance average value	float	4
Weight average	Float	4
Hardness average	float	4

The effect of loosening is mainly on the absorption and filling of the tow. The channel of filter rod is sampled, and the front and rear channels are taken 15 groups, each group is 20, and the resistance and weight are detected. The test results of 100m and 150mm for two stages of air loosening in the front and back channels are shown in Table 2.

TABLE II. TEST RESULTS OF 100M AND 150MM FOR TWO STAGES OF AIR LOOSENING IN THE FRONT AND BACK

	sample name		ITEM average	ITEM average
	Loose width (mm)		100	150
The Front Channel	Draw resistance average value(mmH ₂ O)		262.8	262.09
	Weight	average(g)	0.71	0.71
	Hardness	average(%)	86.2	86.19
The Rear Channel	raw resistance average value(mmH ₂ O)		255.5	260.7
	Weight	average(g)	0.71	0.708
	Hardness	Average(%)	86.18	87.08

Data transformation: transform the specific data detection value into the system measurable and the specific value that the model can use, so we transform the data of Table II into machine operation language. Such as table 3, set up the resistance average 262.1 positive and negative 1 to A, more than 259.1 and less than 260.1, or the value more than 262.1 and less than 263.1 is set to B, the value more than 263.1 or less than 259.1 is set to C; set up weight average 0.7 positive and negative 0.05 to D, the value more than 0.69 and less than 0.695, or more than 0.705 and less than 0.71 is set to E, the value more than 0.71 or less than 0.69 is set to F; set up hardness average 86.2 positive and negative 0.1 to G, the value more than 86.0 and less than 86.1, or the value more than 86.3 and less than 86.4 is set to H, or more than 86.4 and less than 86.0 is set to I. So put the data of table 2 into table 3.

TABLE III. CONVERSION DATA OF TABLE 2.

Sample	ITEM	ITEM
A	0	1
B	1	0
C	0	0
D	1	1
E	0	0
F	0	0
G	1	1
H	0	0
I	0	0
A	0	1
B	0	0
C	1	0
D	1	1
E	0	0
F	0	0
G	1	0
H	0	0
I	0	1

Through the Apriori algorithm based on the interest degree, the experimental data from the test data are used as the source data, and the verification test model is verified.

Through the preliminary statistics of the data collection samples and the threshold used in the experiment, the minimum support degree (min_support) is 10%, the minimum confidence level (min_confident) is 50% and the interest threshold (RI) is 0.8. In the opening width 100MM and 150MM test. The loosen width is defined as T100, T150, draw resistance value as R, weight as W, and hardness as Y. When the association rule of the loosen channel quality is the same as the association rule of the posterior track, we can see that the Apriori algorithm based on interest is used to mine the relevant rules.

TABLE IV. THE APRIORI ALGORITHM USING THE INTEREST THRESHOLD

Associati on rules	T100->R	T100->W	T100->Y	T150->R	T150->W	T150->Y
Support degree	0.53	0.13	0.25	0.62	0.12	0.24
Confiden t degree	89.12%	52.13%	50.65%	92.03%	56.00%	60.65%
Interest degree	1.04	0.3	0.2	0.99	0.3	0.2
Actual conform ation of the front channel	conform ance					
Actual conform ation of the rear channel	conform ance					

It can be seen from table 4, after the mining of the above association rules, the production was sampled at 100mm and 150mm in open pine. As a precaution, a double sample T test for the sample material is also carried out. The results show that the two sample T test, when there is no significant difference between the weight and the circumference of the rear channel products, $P=0.00$, because of $P \leq 0.05$, it is believed that there is a significant difference in the drag resistance of the rear road products when the width of the two stage is 100mm and 150mm, there is no significant difference between the results of the sampling in the front, and the results based on the mining of the interest association rules are consistent.

V. SUMMARY

In this paper, association rules mining is done through data transformation and sorting through Apriori algorithm through interest data association rules, so that equipment adjustment and parameter settings are verified, and the decision support degree of poor performance is given.

REFERENCE:

- [1] MA Yong, ZHAO Xue-ming, SUN Bo. The Analysis Method of Web Log based on Apriori Algorithm.[A]. Computer security Specialized Committee of China Computer Society. Twenty-seventh National Symposium on computer security academic exchange [C].2012:3.
- [2] Liu Li-gang, Zhong Rui,Yang Juan.Application of Apriori algorithm based on interest measure in data analysis of electronic medical records. Journal of Jiangxi University of Science and Technology,2013,34(5):73-76
- [3] ZHOU Xin, SHA Chao-Feng, ZHU Yang-Yong, Another threshold of interest degree-association rules[J]. Computer research and development.2000, 37(5):627-633.
- [4] Li-ming ZHU, Min ZHANG, Jin XU, Qiang ZHU and Shuai YANG, A process tracking system of quality parameters for dual channel forming machine, International Conference on Computer Mechatronics and Electronic Engineering,2016:39-43.

Research on Process -Resources Dynamic Configuration Model of Digital Inspection Management System

Jian Yao and Guijiang Duan

School of Mechanical Engineering and Automation, Beihang University, Beijing 100191, China

Abstract—Dynamic matching between inspect resources and business processes in digital inspect and MBD (Model Based Definition) environments is a challenging problem. This paper present an approach of building a digital inspection management model based on process-resource dynamic configuration system. Furthermore, the paper described the model from two parts: one was data interaction among inspection, plan and manufacture, the other was process-resource dynamic coupling. It implemented data exchange by the data interaction technology based REST. Then it achieved through the dynamic configuration technology of the process-resource configuration based on the workflow engine. The digital inspection management system was developed to matching process and resource on the basis of the model. Finally, an example of the measurement business management module was provided to validate this model.

Keywords—inspect resource; dynamic configuration; workflow engine; digital inspection management system

I. INTRODUCTION

Today, digital measurement technology has been increasingly applications in the field of modern manufacturing with the rapid development of design and manufacturing technology. Compared with the conventional analog-based and manual measurement mode, a large number of digital inspection equipment such as CMM (Coordinate Measuring Machine) and laser tracker are in the application of the digital detection technology to achieve the automatic acquisition of inspection data, information storage and efficient transmission. Paradoxically, diverse equipment and huge amount of data collected leaded the complexity of the association between inspection resources, such as different types of equipment use different measurement procedures, measurement methods and theoretical data. The above characteristics are not available in the detection technique based manual. It was based on manually collect data, matched inspect resources semi-automatically, determine inspect results to a single criterion. This make detection management system correspondingly not adapt to the transmission mode of the MBD (Model Based Definition) dataset in the collaborative manufacturing system and not solve the problem that feedback digital model defects and configure inspect resources flexibly.

Establish a resource dynamic configuration system with flexible workflow as the center was tried to by many scholars to realize the dynamic coupling between the resources and the business process and to solve the information silos among

design, manufacture and detection. There are many attempts to use models or algorithm to fulfill the flexible of the workflow. The multi-autonomic objects flexible workflow based on autonomic computing technology realized the intelligent flexibility of the workflow through the collaborative work of the multi-autonomic objects embedded in each workflow activity [1]. Furthermore, workflow had to adapt to constantly changing business conditions. Establishing a criterion that ensure compliance of in-progress workflow instances with a modified workflow schema can make it true that such changes can be propagated to already running WF instances, but without causing inconsistencies and errors [2]. And leveraged ideas from the Open-Water approach into 3-tier architecture and achieved a workflow support combined with adaptive workflow management to create a flexible workflow support and management system was proposed in [3]. In terms of algorithms, two examples are the component adjustment algorithm based on reconfigurable process model and componentization achieving the separation of process logic and business logic [4], the approach based on SWN(Stochastic Well-Formed Nets) models for formal Modelling of a dynamic reconfiguration on CBS(Component-Based Systems) that allow quantitative analysis [5]. Unfortunately, those attempts only limited to the process itself, however, ignore the significant part that realizing the dynamic configuration of data linking to the process.

The above research results achieved the flexibility of the workflow itself, adapt to the needs of real-time changes in the process of data and achieved dynamic correlation between data and process. However, the scope of the study is limited to a single-system data and processes dynamic configuration, which cannot achieve information exchange among multiple systems. Besides, the dynamic configuration algorithm was highly correlated with the process. And the algorithm logic was quite complicated and was difficult to update for the complex detect resource relationship configuration, which lead to the decrease of flexibility. So it was a good strategy to build a inspect business management system that was suitable for multi-system data interaction and low resource allocation.

II. INSPECTION DATA AND DESIGN DATA, MANUFACTURING DATA INTERACTION MODE

According to the forms and functions of existence, manufacturing enterprise data management model can be divided into physical layer, management layer and data layer.

Inspection data and design data, manufacturing data interaction model was shown in Figure I.

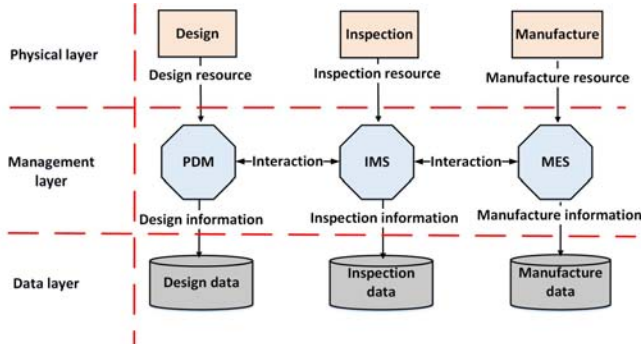


FIGURE I. INSPECTION DATA AND DESIGN DATA, MANUFACTURING DATA INTERACTION MODEL

The physical layer represents the physical department, the management layer represents the information management system corresponding to the physical layer, and the data layer represents the data storage system corresponding to the management system. Design resources produced by design department of the physical layer were transformed into the information resources by management PDM (Product Data Management) data and stored in the data layer as design data; the manufacturing resources generated by the physical layer manufacturing process were transformed into manufacturing information resources and stored in the data layer as manufacturing data through the MES (Manufacturing Execution System); the inspection resources generated by the physical layer inspection process were transformed into the manufacturing data and stored in the data layer by the management layer's IMS (Inspect Management System), so as to realize the longitudinal data transfer among the design, manufacture, production. At the management layer, real-time information exchange between inspection and design and production was achieved through data exchange between IMS and PDM system, MES system. The detail realization method is as follows: digital design resources such as model data and product data was transmitted through the PDM system to IMS system achieving data exchange between design and inspection; production resources transmission to the IMS system through MES to achieve data interoperability between production and inspection; IMS collected and analyzed the measurement data in the form of XML, TXT, and pictures in inspection resource automatically, and fed back the analysis results and existing problems into the PDM and MES systems to form a complete resource interaction closed loop for design, production and inspection.

III. DATA EXCHANGE BETWEEN DIGITAL INSPECTION SYSTEM AND DESIGN, PRODUCTION

In the enterprise, MBD data was transmitted along the path of design → production → inspection. The key to achieving data transmission completely and rapidly lie in that the data interaction between different systems was Seamless convergence. The data set in MBD was structured in the PDM system. That is to say, the characteristic information such as shape and material of a single part was stored in the database in

a form of single data element. In the aspect of data exchange between design and production, we adopt the REST (Representational State Transfer) service architecture based on Resource Oriented Architecture (ROA) to publish the process resources and business entity resources as services to the rest service layer. In REST [6] service, any resource is an entity that can be identified by a unique Uniform Resource Locator (URL), which can be accessed via HTTP (Hyper Text Transfer Protocol) [7]. The service layer assigned a unique URI (Universal Resource Identifier) to each resource. When data interaction was required, the service client send HTTP method information including POST, GET, PUT and DELETE to the target system at the Web layer. Then it requested service to the rest service layer via the Resource Request Handler and get the requested resource based on the URI. Resources will be converted resources into making the browser available through Browser Requester Handler by the server and fed back to the client. The data type of the resource can be JSON (JavaScript Object Notation), XML (Extensible Markup Language) or RSS (Really Simple Syndication). JSON is a lightweight data exchange format. RSS is a format for describing and synchronizing website content. REST operating mechanism was shown in Figure II. The realization process of the data interaction between the digital inspection system and the design and production is that the inspection and management system obtains the MBD model information of the product object in the PDM through the Get service according to the URI and stores the information in its own database. Meanwhile, the MES in the task allocation information were get according to the URI through the Get service and loaded into the task panel. Finally, the inspection management system assigned the measurement results and the data set defect information to a specific URI, so that the PDM and the MES can obtain the corresponding information through the Get service to achieve the complete loop of the data interaction.

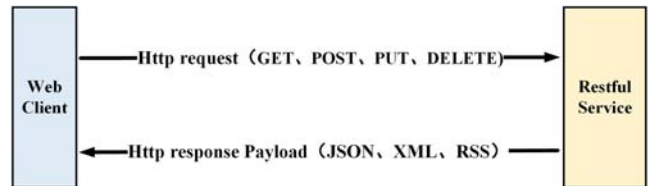


FIGURE II. REST OPERATING MECHANISM

IV. DYNAMIC CORRELATION BETWEEN INSPECTION RESOURCES AND PROCESSES

Inspection resources can be divided into inspection business resources and inspection data resources. Inspection business resources included the inspection object, inspectors, inspection equipment and other related resources. Inspection data resources were consists of forms, data and other related resources. Each resource in the inspection business resource and the inspection data resource was given a unique identifier that make it unique in the resource-process relationship mapping table. Process - resource unique identifier assignment rules was as shown in Table I.

TABLE I. PROCESS - RESOURCE UNIQUE IDENTIFIER ASSIGNMENT RULES

Name	Basic Element	Unique Identifier
Inspection business resources	Inspection object	inspection object number
	Inspectors	Inspectors' ID
	Inspection task	Task's ID
	Inspection equipment	Inspection equipment's number
	Others	URI
Inspection data resources	Form	URL(Uniform Resource Locator)
	Data	Data's number
	Measure programmer	Measure programmer's number
	Measure method	Measure method's number
	Others	URI
Flow	Business flow	Business flow's ID
	Flow node	Flow node's ID

The description of the process-resource dynamic configuration process was as follows:

- 1) Obtaining inspection data from PDM and MES through REST service and converting it into the resources in the system as basic data for inspection;
- 2) Assign the inspection data resources and inspection business resources with a unique identifier and store them into the corresponding resource mapping table;
- 3) Concrete the inspection business resource mapping table and the inspection data resource mapping table into a dynamic business configuration table and a business service dynamic configuration table in the database, and associating the resources with the process node through the process configuration engine in the process designer;
- 4) The data resources processed in the system were fed back to the PDM and MES system through the REST service.

V. APPLICATIONS

The application of part measurement business management module of digital inspection management system in the measurement department of a manufacturing enterprise is used to illustrate the realization process of the process - resource dynamic allocation mechanism. This department undertook the

whole company's digital inspection tasks, which had a larger of the daily average measuring volume and a wide range of inspection objects. Besides, highly requirements about analysis and feedback was required and the types of measurement equipment selected and types of the same kind of inspection data acquisition equipment were very different in the same process. And at the same time, due to the fact that it is in the process of digital inspection technology being promoted in an all-round way, the business process changes frequently and the inspection resource type has a short update cycle. It is urgent to solve the problem of data transmission in the MBD data model. Therefore, the digital inspection management system based on flexible configuration of resources become the best solution to solve the above problems.

Part measurement business management instance model was illustrated in Figure 3. Delegated measurement information and inspection device information were passed from the PDM and MES systems to the part measurement business management module through the REST service. The measurement data in the part measurement business management module is transmitted to the SPC module for data analysis, and the exception information is fed back to the PDM and the MES in real time. At last, the measurement results were delivered to the MES system through REST services, forming a closed loop of data exchange between inspection and design, production. The workflow engine generates the first version of the part inspection business process according to the requirements, and then couples and associates the process nodes with the corresponding inspection business resources and inspection data resources. This module supports both the process of submitting scan code and the batch operation of process nodes in order to adapt to the requirement of making the testing business digitally and intelligently. The application of this system realized the real-time dynamic configuration of business processes under the condition of business processes and inspection resources' constantly updating and solved the problem of how to achieve the barrier-free transmission and rapid feedback of datasets in MBD environment.

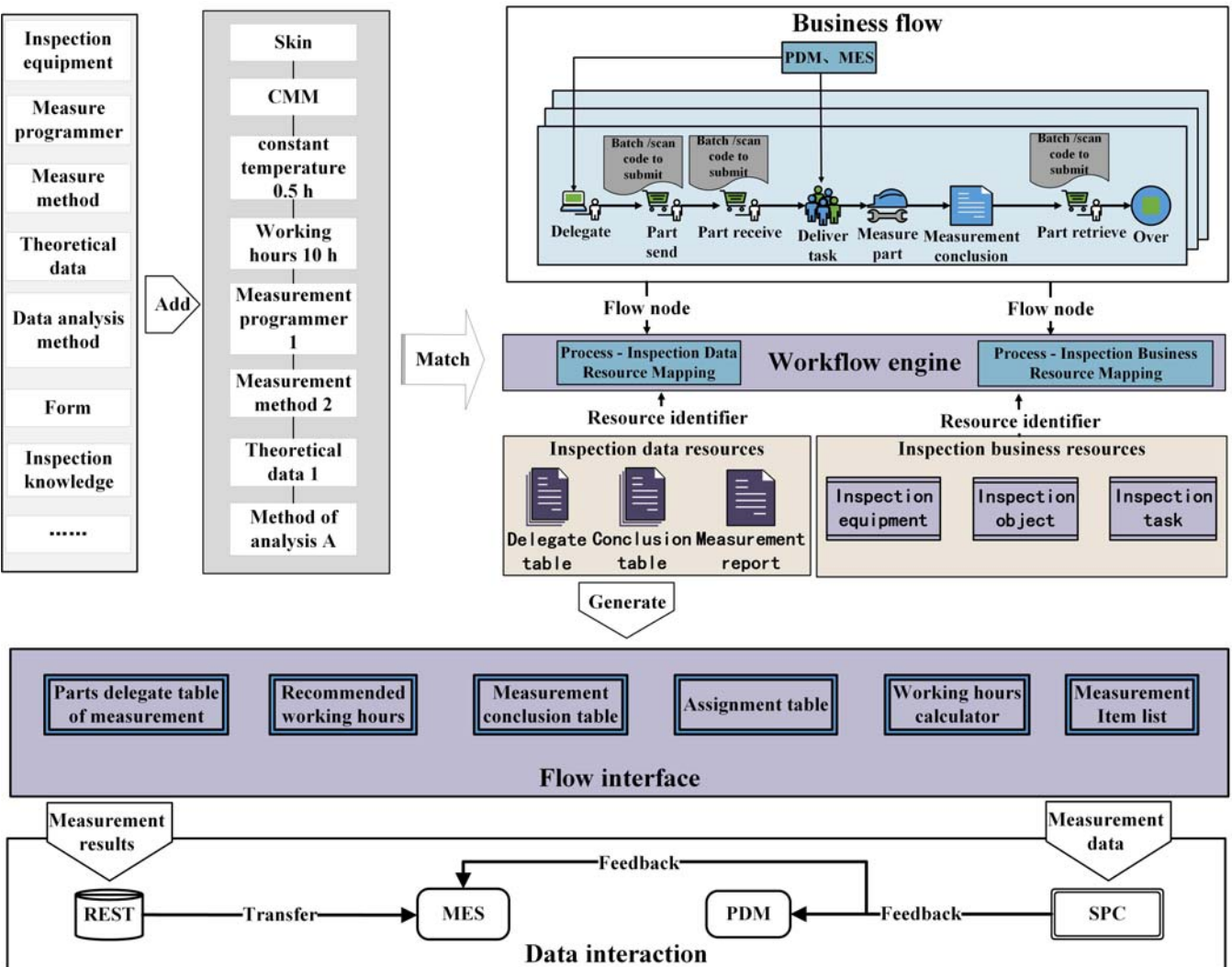


FIGURE III. PART MEASUREMENT BUSINESS MANAGEMENT INSTANCE MODEL.

VI. CONCLUSION

This paper presented a digital inspection management model based on process-resource dynamic configuration, elaborated the operating mechanism of the model, the representation of the model and examples of system application. The model realized the real-time interaction of data between inspection and design, production, and achieved the dynamic coupling of resources and processes in order to adapt to the development of digital detection technology and the continuous advancement of intelligent manufacturing in manufacturing enterprises. Based on the model, we developed a digital inspection management system and achieved good results in the enterprise application.

REFERENCES

- [1] W. Dongbo, Y. Xutian, L. Weifang and S. Yi Xiao, "Research on agile supply chain based on multi-autonomic objects flexible workflow," Application Research of Computer, pp. 541–543, February 2010.

- [2] S. Rinderle, M. Reichert and P. Dadam, Flexible Support of Team Processes by Adaptive Workflow Systems, Distributed and Parallel Databases, pp.91–116, 2004.
- [3] N. C. Narendra, "Flexible Support and Management of Adaptive Workflow Processes," Information Systems Frontiers, pp. 247–262, July 2004.
- [4] L. Yajie, H. Weiping, C. Jinliang, D. Rong and H. Yanli, "MES Process Evolution Method based on Reconfigurable Process Model and Componentization," Computer Integrated Manufacturing Systems, pp:735-744., March 2014.
- [5] H. Zerguine, N. Salmi and M. Ioualalen, "Accompanying Component Based Systems Dynamic Reconfiguration with formal modelling and analysis," 2nd International Conference on Future Internet of Things and Cloud (FiCloud), Barcelona SPAIN,2014,pp:513–520.
- [6] [6] P. Federica, T. Stefano, and G. Dino, "A Web of Things Framework for RESTful Applications and Its Experimentation in a Smart City," IEEE SYSTEMS JOURNAL, pp. 1412–1423, October 2016.
- [7] F. L. DAMARIS, S. Luis and C. Antonio, "A RESTful and semantic framework for data integration," SOFTWARE-PRACTICE & EXPERIENCE, 2015, pp:1161–1188.

Two-step Gaussian Process Regression Improving Performance of Training and Prediction

Wei Wang*, Santong Zhang, Wei Yang and Xiangbin Liu

School of Electronic and Information Engineering, Beijing Jiaotong University, China

*Corresponding author

Abstract—Since Gaussian process regression (GPR) cannot feasibly be applied to big and growing data sets, this paper introduces an integration algorithm called Two-step Gaussian Process Regression (TGPR) which speeds up both training and prediction to solve the problem. First, analyze the basics behind regular GPR. Then, introduce TGPR by using the inducing inputs to optimize the regular GPR algorithm. Last, apply TGPR to a three-dimension model, the experimental results compared with regular GPR show that TGPR is faster and more accurate.

Keywords—gaussian process; regression; inducing inputs; hyperparameter

I INTRODUCTION

Gaussian Process Regression is a newly developed method for machine learning based on Bayesian theory and statistical learning theory. It is first applied to machine learning by Rasmussen and Williams [1]. The prediction result of GPR has a clear probabilistic meaning compared with Artificial Neural Networks (ANN) [2] and Support Vector Machine (SVM) [3].

Although GPR has many advantages, its computational complexity increases sharply as the size of the measurements expands. Many sparse algorithms have been proposed to reduce computation. Williams presents the Nyström method for efficient GPR [4]. Snelson presents Sparse Pseudo-inputs Gaussian Process (SPGP) model whose covariance is parameterized by the locations of pseudo-input [5]. Tresp presents BCM (Bayesian Committee Machine) method to combine estimators that are trained on different data sets [6].

This paper is organized as follows. After providing the necessary background on GPR, the prediction and training of regular GPR is introduced in Section 2. In Section 3, a novel sparse algorithm TGPR which uses the inducing inputs is introduced. Section 4 presents the simulation on three-dimension model. The conclusions of TGPR algorithm is in Section 5.

II GAUSSIAN PROCESS REGRESSION

A. Prediction

A Gaussian Process (GP) is a collection of random variables, any finite numbers of which have joint Gaussian distributions. It can be expressed as follows:

$$\mathbf{f} \sim N(\mathbf{f} | \mathbf{m}, K) \quad (1)$$

Where, \mathbf{m} is mean function and $K = k(x, x)$ is covariance function, they are both called kernel function which describe the probabilistic meaning of GPR [7].

Regression is that, first get the function relation between measurement inputs X_m and measurement outputs \mathbf{f}_m , being $\mathbf{f}_m = f(X_m)$. Then predict the unknown test outputs \mathbf{f}_* given test inputs X_* . The first step is called training while the second step is called prediction.

Considering the measurement input set $X_m = \{x_{m_1}, x_{m_2}, \dots, x_{m_{n_m}}\}$ that consists of n_m points, and the test input set $X_* = \{x_{*_1}, x_{*_2}, \dots, x_{*_n_*}\}$ that consists of n_* points. The prior distribution of \mathbf{f}_m and \mathbf{f}_* is given by:

$$\begin{bmatrix} \mathbf{f}_m \\ \mathbf{f}_* \end{bmatrix} \sim N \left(\begin{bmatrix} \mathbf{m}_m \\ \mathbf{m}_* \end{bmatrix}, \begin{bmatrix} K_{mm} & K_{m*} \\ K_{*m} & K_{**} \end{bmatrix} \right) \quad (2)$$

The measurement outputs are generally affected by Gaussian white noise $\mathbf{v} \sim N(0, \hat{\Sigma}_{f_m})$ where $\hat{\Sigma}_{f_m} = diag(\hat{\sigma}_{f_{m1}}^2, \hat{\sigma}_{f_{m2}}^2, \dots, \hat{\sigma}_{f_{m_{n_m}}}^2)$. As a result, the measurement output becomes $\hat{\mathbf{f}}_m = \mathbf{f}_m + \mathbf{v}$. The posterior distribution of \mathbf{f}_* can be calculated from the conditional probability formula:

$$\mathbf{f}_* \sim N \left(\mathbf{m}_* + K_{*m} K_{mm}^{-1} (\hat{\mathbf{f}}_m - \mathbf{m}_m), K_{**} - K_{*m} (K_{mm} + \hat{\Sigma}_{f_m})^{-1} K_{m*} \right) \quad (3)$$

B. Training

In the training step, the mean function generally is initialized to zero mean function, and covariance function is chosen as the well-known Squared Exponential covariance function (SE):

$$k(\mathbf{x}, \mathbf{x}') = \lambda_f^2 \exp\left(-\frac{1}{2}(\mathbf{x} - \mathbf{x}')^T \Lambda_x^{-1} (\mathbf{x} - \mathbf{x}')\right). \quad (4)$$

Where, $\lambda_f^2 = k(\mathbf{x}, \mathbf{x})$,
 $\Lambda_x = \lambda_x^2 = \text{diag}(\lambda_{x_1}^2, \lambda_{x_2}^2, \dots, \lambda_{x_m}^2)$ while
 $\lambda_{x_1}^2, \lambda_{x_2}^2, \dots, \lambda_{x_m}^2$ is length scale for each input.

Then there is a set $\theta = \{\lambda_x, \lambda_f, \hat{\sigma}_{f_m}\}$, in which all parameters are called hyperparameters [8]. Only with the truest set of hyperparameters called the most likely hyperparameters, the model can be explained exactly by the function relation between X_m and f_m . The most likely hyperparameters can be chosen using Maximum Likelihood method. According to Bayesian theory, the posterior hyperparameter distribution is found as follows:

$$p(\theta | \hat{f}_m, X_m) = \frac{p(\hat{f}_m | \theta, X_m) p(\theta | X_m)}{p(\hat{f}_m | X_m)}. \quad (5)$$

The key now is to find the maximum of (5). Remember that the covariance function is SE, now take the logarithm of (5), and then consider the derivative with respect to the hyperparameters:

$$\frac{\partial \log(p)}{\partial \theta} = -\frac{1}{2} \text{tr}\left(P^{-1} \frac{\partial P}{\partial \theta}\right) + \frac{1}{2} \text{tr}\left(\alpha^T \frac{\partial P}{\partial \theta} \alpha\right) = \frac{1}{2} \text{tr}\left((\alpha \alpha^T - P^{-1}) \frac{\partial P}{\partial \theta}\right). \quad (6)$$

Where $P = (K_{mm} + \hat{\Sigma}_{f_m})$, $\alpha = P^{-1}(\hat{f}_m - \mathbf{m}_m)$. Note

that $\theta = \{\lambda_x, \lambda_f, \hat{\sigma}_{f_m}\}$, it means there will be three derivatives. Applying gradient ascent algorithm to all these derivatives, the most likely hyperparameters can be found [9].

C. Downsides of GPR

In the training step of GPR, the main computation focus on inverting the matrix $K_{mm} + \hat{\Sigma}_{f_m}$, resulting $O(n_m^3)$ runtime requirement. In the prediction step of GPR, it takes $O(n_m^2 n_*)$ time to calculate f_* . When the number of measurements n_m grows big, GPR runs into computational problems, requiring amounts of time.

III TWO-STEP GAUSSIAN PROCESS REGRESSION

A. Speeding up Prediction: Using Inducing Inputs

The inducing inputs set $X_u = \{x_{u_1}, x_{u_2}, \dots, x_{u_{n_u}}\}$ that consists of n_u inducing inputs [10] is introduced to speed up prediction.

STEP 1. Calculating the posterior distribution of the inducing outputs f_u given measurements (X_m, f_m) .

Assuming that f_m and f_* are conditionally independent given f_u . The prior distribution of f_m and f_u is given by:

$$\begin{bmatrix} f_m \\ f_u \end{bmatrix} \sim N\left(\begin{bmatrix} \mathbf{m}_m \\ \mathbf{m}_u \end{bmatrix}, \begin{bmatrix} K_{mm} & K_{mu} \\ K_{um} & K_{uu} \end{bmatrix}\right). \quad (7)$$

The outputs f_m are still affected by Gaussian white noise $\mathbf{v} \sim N(0, \hat{\Sigma}_{f_m})$ and can be written as:

$$f_m = \hat{f}_m + \mathbf{v} \sim N(\hat{f}_m, \hat{\Sigma}_{f_m}) \quad (8)$$

There are two distributions for f_m , (7) and (8). Here the idea is to combine these two distributions. The operation called “combine” is introduced as follows:

Assuming that, for n independent measurements, the random variable \mathbf{x} can be explained by n distributions, being $N(\mathbf{m}_1, K_1), \dots, N(\mathbf{m}_n, K_n)$. Then the posterior distribution for \mathbf{x} can be calculated by combining these n distributions. Here use the operator \oplus as “combine”, the posterior distribution for \mathbf{x} is now given by:

$$f_x(\mathbf{x}) \sim N(\boldsymbol{\mu}_x, \Sigma_x) = N(\mathbf{m}_1, K_1) \oplus \dots \oplus N(\mathbf{m}_n, K_n) \quad (9)$$

$$\boldsymbol{\mu}_x = \Sigma_x (K_1^{-1} \mathbf{m}_1 + K_2^{-1} \mathbf{m}_2 + \dots + K_n^{-1} \mathbf{m}_n). \quad (10)$$

$$\Sigma_x = (K_1^{-1} + K_2^{-1} + \dots + K_n^{-1})^{-1}. \quad (11)$$

Then the posterior distribution of f_m and f_u can be calculated by combining (7) and (8):

$$\begin{bmatrix} f_m \\ f_u \end{bmatrix} \sim N\left(\begin{bmatrix} \boldsymbol{\mu}_m \\ \boldsymbol{\mu}_u \end{bmatrix}, \begin{bmatrix} \Sigma_{mm} & \Sigma_{mu} \\ \Sigma_{um} & \Sigma_{uu} \end{bmatrix}\right). \quad (12)$$

$$\begin{bmatrix} \boldsymbol{\mu}_m \\ \boldsymbol{\mu}_u \end{bmatrix} = \begin{bmatrix} \Sigma_{mm} (K_{mm}^{-1} \mathbf{m}_m + \hat{\Sigma}_{f_m}^{-1} \hat{f}_m) \\ \mathbf{m}_u + K_{um} (K_{mm} + \hat{\Sigma}_{f_m})^{-1} (\hat{f}_m - \mathbf{m}_m) \end{bmatrix}. \quad (13)$$

$$\begin{bmatrix} \Sigma_{mm} & \Sigma_{mu} \\ \Sigma_{um} & \Sigma_{uu} \end{bmatrix} = \begin{bmatrix} K_{mm} (K_{mm} + \hat{\Sigma}_{f_m})^{-1} \hat{\Sigma}_{f_m} & \hat{\Sigma}_{f_m} (K_{mm} + \hat{\Sigma}_{f_m})^{-1} K_{mu} \\ K_{sm} (K_{mm} + \hat{\Sigma}_{f_m})^{-1} \hat{\Sigma}_{f_m} & K_{uu} - K_{um} (K_{mm} + \hat{\Sigma}_{f_m})^{-1} K_{mu} \end{bmatrix}. \quad (14)$$

From (12), not only the posterior distribution of inducing outputs \mathbf{f}_u is found, but also that of the measurement outputs \mathbf{f}_m which are noiseless. It is one of the advantages of TGPR algorithm.

STEP 2. Just using the posterior distribution of \mathbf{f}_u to predict the test outputs \mathbf{f}_* .

The prior distribution of \mathbf{f}_u and \mathbf{f}_* is given by:

$$\begin{bmatrix} \mathbf{f}_u \\ \mathbf{f}_* \end{bmatrix} \sim N\left(\begin{bmatrix} \mathbf{m}_u \\ \mathbf{m}_* \end{bmatrix}, \begin{bmatrix} K_{uu} & K_{u*} \\ K_{*u} & K_{**} \end{bmatrix}\right) \quad (15)$$

Another distribution of \mathbf{f}_u is from (12), it is:

$$\mathbf{f}_u \sim N(\boldsymbol{\mu}_u, \Sigma_{uu}) \quad (16)$$

The idea is still to combine (15) and (16). But note that, the prior knowledge of \mathbf{f}_u , being $\mathbf{f}_u \sim N(\mathbf{m}_u, K_{uu})$, has been used in both of these two distribution of \mathbf{f}_u . Combining (15) and (16) will use the prior knowledge twice, which is unacceptable, it is necessary to separate that prior for one time. Here use the operator $!$ as “separate”, so the operation called “separate” is introduced as follows:

$$N(\boldsymbol{\mu}_x, \Sigma_x)! N(\mathbf{m}_u, K_{uu}) = N(\boldsymbol{\mu}_x, \Sigma_x) \oplus N(\mathbf{m}_u, -K_{uu}). \quad (17)$$

Then the posterior distribution of \mathbf{f}_u and \mathbf{f}_* can be calculated by combining (15) and (16), and separating $N(\mathbf{m}_u, K_{uu})$ from the result for one time:

$$\begin{bmatrix} \mathbf{f}_u \\ \mathbf{f}_* \end{bmatrix} \sim N\left(\begin{bmatrix} \boldsymbol{\mu}_u \\ \boldsymbol{\mu}_* \end{bmatrix}, \begin{bmatrix} \Sigma_{uu} & \Sigma_{u*} \\ \Sigma_{*u} & \Sigma_{**} \end{bmatrix}\right) \quad (18)$$

$$\begin{bmatrix} \boldsymbol{\mu}_u \\ \boldsymbol{\mu}_* \end{bmatrix} = \begin{bmatrix} \boldsymbol{\mu}_u \\ \mathbf{m}_* + K_{*u} K_{uu}^{-1} (\boldsymbol{\mu}_u - \mathbf{m}_u) \end{bmatrix} \quad (19)$$

$$\begin{bmatrix} \Sigma_{uu} & \Sigma_{u*} \\ \Sigma_{*u} & \Sigma_{**} \end{bmatrix} = \begin{bmatrix} \Sigma_{uu} & \Sigma_{uu} K_{uu}^{-1} K_{u*} \\ K_{*u} K_{uu}^{-1} \Sigma_{uu} & K_{**} - K_{*u} K_{uu}^{-1} (K_{uu} - \Sigma_{uu}) K_{uu}^{-1} K_{u*} \end{bmatrix} \quad (20)$$

Performance of TGPR.

Assuming K_{uu}^{-1} has been calculated in STEP 1., calculating the posterior distribution of \mathbf{f}_* only takes

$O(n_u n_*^2)$ time. Compared with $O(n_m^2 n_*)$ time regular GPR takes, TGPR algorithm has speeded up prediction.

B. Speeding up Training: Train n_m Times Individually

STEP 1. Calculating \mathbf{f}_u individually using each of n_m measurements.

Assuming that each test output $f_{m_1}, \dots, f_{m_{n_m}}$ is fully independent given \mathbf{f}_u . Firstly use the first measurement $(\mathbf{x}_{m_1}, \hat{f}_{m_1})$ to calculate the distribution of \mathbf{f}_u , resulting in $\mathbf{f}_u^1 \sim N(\boldsymbol{\mu}_u^1, \Sigma_{uu}^1)$. Then use the second measurement $(\mathbf{x}_{m_2}, \hat{f}_{m_2})$ to find $\mathbf{f}_u^2 \sim N(\boldsymbol{\mu}_u^2, \Sigma_{uu}^2)$, and so on. At last n_m distributions of \mathbf{f}_u are calculated.

STEP 2. Combining n_m distributions of \mathbf{f}_u .

The next thing to do is to combine all these n_m distributions together. Note that, each of these distributions contains the prior knowledge of \mathbf{f}_u . Combining n_m distributions will use the prior knowledge n_m times, so separating that prior distribution for n_m times is indispensable:

$$\mathbf{f}_u \sim N(\boldsymbol{\mu}_u, \Sigma_{uu}) = N(\boldsymbol{\mu}_u^1, \Sigma_{uu}^1) \oplus N(\boldsymbol{\mu}_u^2, \Sigma_{uu}^2) \oplus \dots \oplus N(\boldsymbol{\mu}_u^{n_m}, \Sigma_{uu}^{n_m})! \underbrace{N(\mathbf{m}_u, K_{uu})}_{(n_m-1)\text{times}} \quad (21)$$

Then the posterior distribution of \mathbf{f}_m and \mathbf{f}_u becomes:

$$\begin{bmatrix} \mathbf{f}_m \\ \mathbf{f}_u \end{bmatrix} \sim N\left(\begin{bmatrix} \boldsymbol{\mu}_m \\ \boldsymbol{\mu}_u \end{bmatrix}, \begin{bmatrix} \Sigma_{mm} & \Sigma_{mu} \\ \Sigma_{um} & \Sigma_{uu} \end{bmatrix}\right) \quad (22)$$

$$\begin{bmatrix} \boldsymbol{\mu}_m \\ \boldsymbol{\mu}_u \end{bmatrix} = \begin{bmatrix} \mathbf{m}_m + \Sigma_{mm} \hat{\Sigma}_{f_m}^{-1} (\hat{f}_m - \mathbf{m}_m) \\ \mathbf{m}_u + \Sigma_{um} \hat{\Sigma}_{f_m}^{-1} (\hat{f}_m - \mathbf{m}_m) \end{bmatrix} \quad (23)$$

$$\begin{bmatrix} \Sigma_{mm} & \Sigma_{mu} \\ \Sigma_{um} & \Sigma_{uu} \end{bmatrix} = \begin{bmatrix} \Sigma_{mm} & \hat{\Sigma}_{f_m} (\Lambda_{mm} + \hat{\Sigma}_{f_m})^{-1} K_{mu} \Delta_{uu}^{-1} K_{uu} \\ K_{uu} \Delta_{uu}^{-1} K_{um} (\Lambda_{mm} + \hat{\Sigma}_{f_m})^{-1} \hat{\Sigma}_{f_m} & K_{uu} \Delta_{uu}^{-1} K_{uu} \end{bmatrix} \quad (24)$$

$$\Sigma_{mm} = (\Lambda_{mm}^{-1} + \hat{\Sigma}_{f_m}^{-1})^{-1} + \hat{\Sigma}_{f_m} (\Lambda_{mm} + \hat{\Sigma}_{f_m})^{-1} K_{mu} \Delta_{uu}^{-1} K_{um} (\Lambda_{mm} + \hat{\Sigma}_{f_m})^{-1} \hat{\Sigma}_{f_m} \quad (25)$$

$$\text{Where } \Lambda_{mm} = \text{diag}(K_{mm} - K_{mu} K_{uu}^{-1} K_{um}), \\ \Delta_{uu} = K_{uu} + K_{um} (\Lambda_{mm} + \hat{\Sigma}_{f_m})^{-1} K_{mu}.$$

Performance of TGPR

The combined posterior distribution of \mathbf{f}_u can be obtained from (22), by which the training only takes $O(n_m n_u^2)$ time. Compared with $O(n_m^3)$ time regular GPR takes, TGPR algorithm has speeded up training.

C. Choosing the Inducing Inputs

The assumptions of TGPR algorithm cause K_{mm} to become:

$$K_{mm} = K_{mu} K_{uu}^{-1} K_{um} + \text{diag}(K_{mm} - K_{mu} K_{uu}^{-1} K_{um}) = K_{mu} K_{uu}^{-1} K_{um} + \Lambda_{mm}. \quad (26)$$

This means that K_{mm} now depends on K_{uu} . The idea to choose inducing inputs is to treat inducing inputs set X_u as another hyperparameter. That is, maximize the posterior hyperparameter distribution $p(\theta | \hat{\mathbf{f}}_m, X_m)$ with respect to K_{uu} . $p(\hat{\mathbf{f}}_m | X_m, X_u)$ in (5) now becomes:

$$p(\hat{\mathbf{f}}_m | X_m, X_u) = N(\hat{\mathbf{f}}_m | \mathbf{m}_m, K_{mm} + \hat{\Sigma}_{f_m}). \quad (27)$$

Then by applying the Maximum Likelihood method in Section 2.2 to (26) and (27), the most likely inducing inputs will be found.

IV SIMULATION

The simulations are performed on a personal computer. And the Gaussian function used in the simulation is the semi-randomly chosen function as follows:

$$f(x_1, x_2) = \left(\frac{x_1}{4} \right)^2 + \left(\frac{x_2}{4} \right)^2 - \sin\left(2\pi \frac{x_1}{5}\right) \left[1 - \frac{1}{2} \cos\left(2\pi \frac{x_2}{4}\right) \right] + \sin\left(2\pi \frac{x_2}{5}\right) - 1. \quad (28)$$

The three-dimension model of (28), which lies on the interval $x_1, x_2 \in [-2, 2]$, is shown in Figure I.

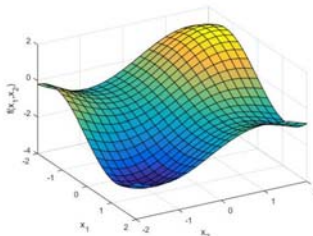


FIGURE I. THE THREE-DIMENSION MODEL

In simulations, the mean is zero mean function, while the covariance is SE with $\lambda_f = \lambda_{x_1} = \lambda_{x_2} = 1$. The function is affected by Gaussian white noise with $\hat{\sigma}_{f_m} = 0.5$.

One of the prediction results for above model using TGPR with $n_m = 500$ is shown in Figure II(a), while the error is shown in Figure II(b). The red dots are measurements; the blue plane is the exact function while the green plane is the prediction result; the translucent gray planes indicate 95% confidence intervals (CIs); the purple plane indicates error, being the prediction result minus the exact function.

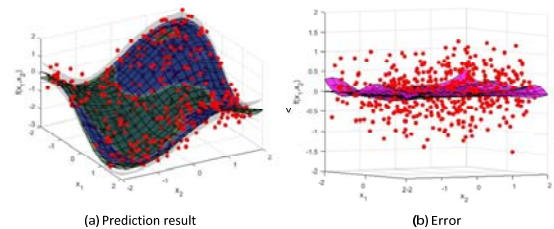


FIGURE II. THE PREDICTION RESULT AND ERROR

Five simulations for further analyses and comparisons are performed in the case of $n_u = 25$ and $n_u = 100$ respectively. The results are the averages of 100 simulation runs and are shown in Table I. The root mean square error (RMSE) is calculated over inputs to analyze the accuracy of the algorithms. A lower RMSE means a better accuracy.

TABLE I. SIMULATION RESULTS

Simulation	$n_u = 25$			$n_u = 100$		
	n_m	Run time	RMS E	n_m	Run time	RM SE
1. Regular GPR with $n_m = 5000$	5000	2.09s	0.048	5000	2.01s	0.049
2. Regular GPR with $n_m = 10000$	10000	10.11s	0.038	10000	9.95s	0.038
3. TGPR with $n_m = 5000$	5000	0.028s	0.056	5000	0.065s	0.050
4. TGPR with $n_m = 10000$	10000	0.046s	0.047	10000	0.109s	0.038
5. TGPR with the same runtime as 1	100000	2.09s	0.042	250000	2.01s	0.0086

The analyses for Table I are as follows:

(1) No matter which GPR algorithm is applied, the more measurements used in training step, the more accurate the prediction becomes, and more time the prediction will take.

(2) In TGPR algorithm, the more inducing inputs used, the more accurate the prediction becomes, and more time the prediction will take.

(3) In regular GPR, as the number of measurements grows big, there is a significant increase of runtime (Simulation 1 and 2).

(4) Given the same number of measurements, compared with regular GPR, TGPR reduces the regression time with a slight decrease in accuracy (Simulation 1 and 3).

(5) As the number of measurements grows from 5000 to 10000, the improvement of regression performance that gains from TGPR algorithm is more significant. TGPR reduces the regression time without any decrease in accuracy (Simulation 2 and 4).

(6) Given the same amount of runtime, compared with regular GPR, TGPR algorithm noticeably improves the accuracy of prediction because it can incorporate more measurements (Simulation 1 and 5).

V CONCLUSION

For reducing the computational complexity in regular GPR, Two-step Gaussian Process Regression algorithm is proposed in this paper. By using the inducing inputs, TGPR reduces the

prediction time from $O(n_m^2 n_*)$ to $O(n_u n_*^2)$. By training n_m times individually, TGPR reduces the training time from $O(n_m^3)$ to $O(n_m n_u^2)$. The performance of TGPR algorithm and regular GPR are compared based on several simulations. The results show that, when working on a large number of measurements, TGPR algorithm significantly speeds up training and prediction. And due to that more measurements can be incorporated in less time, TGPR algorithm also provides a more accurate prediction.

ACKNOWLEDGEMENTS

This research is supported by Key Projects in the National Science & Technology Support Program under No. 2013BAK06B03 and the Natural Science Foundation of China (61673050).

REFERENCE

- [1] Rasmussen, Carl Edward, and Christopher KI Williams. Gaussian processes for machine learning. Vol. 1. Cambridge: MIT press, 2006.
- [2] Zhang, Guoqiang, B. Eddy Patuwo, and Michael Y. Hu. Forecasting with artificial neural networks: The state of the art. International journal of forecasting 14.1 (1998): 35-62.
- [3] Cristianini, Nello, and John Shawe-Taylor. An introduction to support vector machines and other kernel-based learning methods. Cambridge university press, 2000.
- [4] Williams, Christopher KI, and Matthias Seeger. Using the Nyström method to speed up kernel machines. Advances in neural information processing systems. 2001.
- [5] Snelson, Edward, and Zoubin Ghahramani. Sparse Gaussian processes using pseudo-inputs. Advances in neural information processing systems. 2006.
- [6] Tresp, Volker. A Bayesian committee machine. Neural computation 12.11 (2000): 2719-2741.
- [7] Titsias, Michalis K., and Neil D. Lawrence. Bayesian Gaussian process latent variable model. International Conference on Artificial Intelligence and Statistics. 2010.
- [8] Blum, Manuel, and Martin A. Riedmiller. Optimization of Gaussian process hyperparameters using Rprop. ESANN. 2013.
- [9] Bottou, Léon. Large-scale machine learning with stochastic gradient descent. Proceedings of COMPSTAT2010. Physica-Verlag HD, 2010. 177-186.
- [10] Quiñonero-Candela, Joaquín, and Carl Edward Rasmussen. A unifying view of sparse approximate Gaussian process regression. Journal of Machine Learning Research 6.Dec (2005): 1939-1959.

Research on Configuration Optimization of Multi-echelon Inventory Based on Component Commonality

Lijun Qiu¹, Linyu Fu², Qi Dong², Chongyi Liu^{2,*}, Kun Xian³ and Xinhua Weng⁴

¹Naval Aeronautical and Astronautical University, Yantai 264001 Shandong, China

²Naval Aeronautical and Astronautical University, Coast Defense Troop Institute, Yantai 264001 Shandong, China

³91183 PLA, Qingdao 266000 Shandong, China

⁴91515 PLA, Sanya 572061 Hainan, China

*Corresponding author

Abstract—In view of the repairable spare parts, considering the actual situation that component commonality exists in warship equipment, the requirements of spare parts and sites in all levels are modified. A multi-echelon configuration model of common parts based on METRIC theory is established. The marginal optimization algorithm is used to obtain spare parts. The optimal supply support schemes prove that this model improves the model evaluation accuracy and reduces the total configuration cost under the premise of meeting the requirements of support index, which provides a theoretical basis and decision support for the current equipment to promote the use of component commonality.

Keywords—spare part; component commonality; multi-echelon configuration strategy

I. INTRODUCTION

Failure modes and fault characteristics are not single because of various types of spare parts, so it is difficult to achieve the best effect through relying on single maintenance mode or maintenance strategy. Therefore, according to the actual situation that different types of spare parts adopt different maintenance strategies, it is of great value and significance to study spare parts allocation optimization and inventory control models under different maintenance strategies. With the continuous installation of new equipment, the generalization degree of components of various devices is improving too. It is necessary to study the influence of the commonality of spare parts on its configuration optimization programs. Corrective maintenance is a widely adopted strategy for spare parts maintenance. It is also an important object to study configuration optimization of spare parts multi-echelon. The research foundation is derived from the METRIC model proposed by Sherbrooke, and the theoretical basis is static Palm theorem[1]. Although multi-echelon configuration optimization research based on the theory is very extensive, the literatures [2-5] study demand fitting distribution, constructing objective function optimization algorithm, and other aspects deeply, according to the problem of the spare parts allocation of high dimension, nonlinear, multi-objective and so on. However, few scholars have studied the configuration optimization of general spare parts. The literature[6] has established the purchasing

decision model of component commonality by introducing the important degree of spare parts, but does not consider the multi-echelon inventory problem. In the actual process of equipment support, the proportion of commonality is gradually increasing. In the study of spare parts allocation, the factors must be included in the model. The improved multi-echelon configuration model is presented, which based on component commonality in this paper. And marginal optimization algorithm is used to solve the model to get the optimal configuration program.

II. MULTI-ECHELON INVENTORY MODEL FOR COMPONENT COMMONALITY

A. Spare Parts Demand Rate Model

The demand rate of spare parts LRU_j in one site is $\lambda_{j(n,m)}$, m ($m=1,2,\dots,M$) is the protection of site number, $j=1,2,\dots,J$ is the number of spare parts, n ($n=1,2,3$) is the protection of the level number, $n=1$ is depot level site, $n=2$ is intermediate level site, $n=3$ is the crew level site; fault isolation rate of SRU_{jk} is $q_{jk(n,m)}$, $\lambda_{jk(n,m)}$ is the demand rate on the crew level site m of SRU_{jk} ($m \in Echelon(N)$).

$$\lambda_{jk(n,m)} = \begin{cases} \sum_{j=1}^J \lambda_{j(n,m)} (1 - NRTS_{j(n,m)}) q_{jk(n,m)} & 1 \leq k \leq z \\ \lambda_{j(n,m)} (1 - NRTS_{j(n,m)}) q_{jk(n,m)} & z+1 < k \leq K \end{cases} \quad (1)$$

$NRTS_{j(n,m)}$ is the probability that a failure of LRU_j can not be repaired at the site m . For m , ($m \notin Echelon(N)$)

$$\lambda_{j(n,m)} = \sum_{l \in Unit(m)} \lambda_{j(l,m)} \cdot NRTS_{j(l,m)} \quad (2)$$

$$\lambda_{jk(n,m)} = \begin{cases} \sum_{l \in Unit(m)} \lambda_{jk(l,m)} \cdot NRTS_{jk(l,m)} + \sum_{j=1}^J \lambda_{j(n,m)} (1 - NRTS_{j(n,m)}) q_{jk(n,m)} & 1 \leq k \leq z \\ \sum_{l \in Unit(m)} \lambda_{jk(l,m)} \cdot NRTS_{jk(l,m)} + \lambda_{j(n,m)} (1 - NRTS_{mj}) q_{jk(n,m)} & z+1 < k \leq K \end{cases} \quad (3)$$

$NRTS_{jk(l,m)}$ is the probability that failure SRU_{jk} cannot be repaired at the lower level site m; $Unit(m)$ is the lower level site of the site.

B. Correction of the Mean and Variance of Supply Channels for Spare Parts

The availability of warship equipment is mainly affected by the shortage of spare parts, and the shortage number of spare parts is closely related to maintenance. Therefore, the key of modeling is to determine the mean and variance of spare parts supply channels. Through the survey, it has been found that the channels include the number of repairs, the number of recharge and the number of maintenance delays [7].

(1) the number of failure parts in repair

At any time in the steady state, the number of fault LRU_j and SRU_{jk} repairs at a site m are respectively

$$E[X_{j(n,m)}^R] = \lambda_{j(n,m)} (1 - NRTS_{j(n,m)}) T_{j(n,m)} \quad (4)$$

$$E[X_{jk(n,m)}^R] = \lambda_{jk(n,m)} (1 - NRTS_{jk(n,m)}) T_{jk(n,m)} \quad (5)$$

$T_{j(n,m)}$ and $T_{jk(n,m)}$ are the average repair time for the failure LRU_j and SRU_{jk} at the site m respectively:

$$T_{j(n,m)} = \frac{\sum_{k=1}^K \lambda_{jk(n,m)} T_{jk(n,m)}}{\sum_{k=1}^K \lambda_{jk(n,m)}} \quad (6)$$

(2) the amount of recharge

The amount of recharge are the supply number of spare parts from the superior site to the site m and the number of spare parts in the transportation process, and the quantity of the delayed supply which is not enough for the superior site's existing stock.

$$E[X_{j(n,m)}^S] = \lambda_{j(n,m)} NRTS_{j(n,m)} O_{j(n,m)} + f_{j(n,m)} EBO_{j(n-1,m)} \quad (7)$$

Then we have

$$f_{j(n,m)} = \frac{\lambda_{j(n,m)} NRTS_{j(n,m)}}{\sum_{m=1}^M \lambda_{j(n,m)}} \quad (8)$$

(3) the number of maintenance delays caused by maintenance

This value is equal to the sum of SRU_{jk} and its shortage number EBO_{jk(n,m)}, that is,

$$E[X_{j(n,m)}^D] = \sum_{k=1}^K h_{jk(n,m)} EBO_{jk(n,m)} \quad (9)$$

$$h_{jk(n,m)} = \frac{\lambda_{j(n,m)} (1 - NRTS_{j(n,m)}) q_{jk(n,m)}}{\lambda_{jk(n,m)}} \quad (10)$$

In summary, the mean of supply channels $E[X_{j(n,m)}]$ for spare parts LRU_j at the site m is as follows:

$$\begin{aligned} E[X_{j(n,m)}] &= E[X_{j(n,m)}^R] + E[X_{j(n,m)}^S] + E[X_{j(n,m)}^D] \\ &= \lambda_{j(n,m)} (1 - NRTS_{j(n,m)}) T_{j(n,m)} + \lambda_{j(n,m)} NRTS_{j(n,m)} O_{j(n,m)} \\ &\quad + f_{j(n,m)} EBO_{j(n-1,m)} + \sum_{k=1}^K h_{jk(n,m)} EBO_{jk(n,m)} \end{aligned} \quad (11)$$

When a site m applies for a spare part to a higher level site, the probability of a delay by a higher level site supplying to the site m is subject to binomial distribution. Therefore, the variance $\text{Var}[X_{j(n,m)}]$ of the supply channel for the spare parts LRU_j of the site m is as follows

$$\begin{aligned} \text{Var}[X_{j(n,m)}] &= \lambda_{j(n,m)} (1 - NRTS_{j(n,m)}) T_{j(n,m)} + \lambda_{j(n,m)} NRTS_{j(n,m)} O_{j(n,m)} \\ &\quad + f_{j(n,m)} (1 - f_{j(n,m)}) EBO_{j(n-1,m)} + f_{j(n,m)}^2 VBO_{j(n,m)} \\ &\quad + \sum_{k=1}^K h_{jk(n,m)} (1 - h_{jk(n,m)}) EBO_{jk(n,m)} + \sum_{k=1}^K h_{jk(n,m)}^2 VBO_{jk(n,m)} \end{aligned} \quad (12)$$

$VBO_{jk(n,m)}$ is the variance of the shortage spare parts, the specific calculation method can be referred in paper[8].

III. OPTIMIZATION MODEL OF SPARE PARTS

Effectiveness parameters of ship equipment support commonly include availability, satisfaction rate, utilization rate, delay time, and so on [9].

The availability of equipment is obtained by [1], which combined with the structure of the equipment and the multilevel inventory system.

$$A = \frac{\sum_{m=1}^M N_{(3,m)} A_{(3,m)}}{\sum_{m=1}^M N_{(3,m)}} = \frac{\sum_{m=1}^M N_{(3,m)} \prod_{j=1}^J \left(1 - EBO_{j(3,m)} / \left(N_{(3,m)} Z_j\right)\right)^{Z_j}}{\sum_{m=1}^M N_{(3,m)}} \quad (13)$$

Z_j is single number of LRU_j, $N_{(3,m)}$ is the equipment number of crew level site m.

The satisfaction rate of the spare parts system is

$$FR = \frac{\sum_{m=1}^M N_{(3,m)} FR_{(3,m)}}{\sum_{m=1}^M N_{(3,m)}} \quad (14)$$

$FR_{(3,m)}$ is satisfaction rate of spare parts at the crew level site m, and can be obtained by the following formula,

$$FR_{(3,m)} = \frac{\sum_{j=1}^J \sum_{X_{j(3,m)}=0}^{S_{j(3,m)}-1} \lambda_{j(3,m)} p(X_{j(3,m)})}{\sum_{j=1}^J \lambda_{j(3,m)}} \quad (15)$$

The utilization ratio of spare parts system is

$$UR = \frac{\sum_{m=1}^M N_{(3,m)} UR_{(3,m)}}{\sum_{m=1}^M N_{(3,m)}} \quad (16)$$

The delay time of spare parts support system is

$$MLDT = 365 \times 24 \times \frac{\sum_{m=1}^M N_{(3,m)} MLDT_{(3,m)}}{\sum_{m=1}^M N_{(3,m)}} \quad (17)$$

$$MLDT_{(3,m)} = \frac{\sum_{j=1}^J EBO_{j(3,m)}}{\sum_{j=1}^J \lambda_{j(3,m)}} \quad (18)$$

Therefore, an optimization model based on component commonality is established, that is, the cost is the optimization goal and the effectiveness is constrained.

$$\begin{cases} \min C = \sum_{m \in Echelon(N)} \sum_{j=1}^J c_j s_{j(n,m)} \\ \text{s.t. } A > A_0 \quad FR > FR_0 \quad MLDT < MLDT_0 \quad UR > UR_0 \end{cases} \quad (19)$$

IV. ALGORITHM OF OPTIMIZATION MODEL

Marginal optimization algorithm is one of the most common and effective algorithms for spare parts allocation model. The principle of the algorithm is to compare spare parts marginal allocation benefits of sites, and determine spare parts location, then iterate until the model constraint condition is satisfied. Because the availability model of ship equipment is a sum function of the shortage spare parts at the crew level sites, the objective function is separable, so the objective function is convex, the marginal optimization algorithm can determine the optimal solution of every iteration[7-11]. Considering the relationship between the availability and the number of spare parts shortage, the marginal benefit for the availability of the ship equipment value is converted to marginal benefit value of the number of spare parts shortage on the crew level, which can improve the efficiency of algorithm. The concrete steps are as follows:

Step1: initialization, the initial spare parts configuration scheme s is 0.

Step2: the marginal benefit value $\delta_{j(n,m)}$ of the spare parts allocation at all levels sites is increased by 1 respectively through formula (20):

$$\delta_{j(n,m)} = \frac{EBO(s) - EBO(s + \Delta_{j(n,m)})}{C_j} \quad (20)$$

$EBO(s)$ is sum of the expected spare parts shortage at crew level site under the allocation scheme s, $EBO(s + \Delta_{j(n,m)})$ is the expected spare parts shortage at crew level site, based on the allocation scheme s, it equals to number of spare parts j in allocation site (n,m) plus 1.

Step3: according to the results of the Step2, the site $\delta_{j(n,m)}$ corresponding to the maximum value is selected and the configuration amount adds 1.

Step4: the configuration plan is updated, and the availability, spare parts support probability and other parameters are calculated, the result are determined whether achieve the constraint requirements. If not, then goes to Step2, continue to iterate; if the result meets the constraints, then goes to Step5.

Step5: spare parts configuration program is outputted.

V. EXAMPLE ANALYSIS

Compass is the main platform of ship navigation equipment, its supply support system structure as shown in Figure I. The

device is equipped with three crew level site, and the number are (12,10,8) respectively. The purchase delay time at middle level sites are 8 days and 6 days, the purchase delay time at crew level site are 4 days, 3 days and 4 days. The configuration program of spare parts is optimized, which the system availability is 0.95.

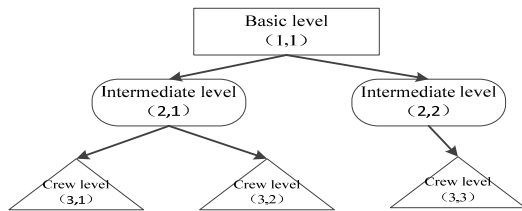


FIGURE I. SCHEMATIC DIAGRAM OF WARSHIP EQUIPMENT STRUCTURE SYSTEM

The solution process of the configuration optimization plan is analyzed, and the cost efficiency curve for the marginal optimization algorithm is shown in Figure II.

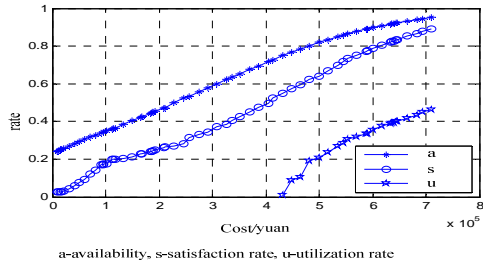


FIGURE II. CURVE OF EFFECTIVENESS VS. COST FOR COMPONENT COMMONALITY

From the above chart, availability, satisfaction rate and utilization rate are increasing nonlinearly with the increase of the cost, and the availability curve has the characteristics of convexity, which reflects the marginal value is strictly monotonically decreasing with the increase of iteration, the initial value of 0.0002 is declined to , as shown in Figure III; the expected shortage value is reduced to 1.4622 from 34.7857, but this is not strictly monotone, as shown in figure IV.

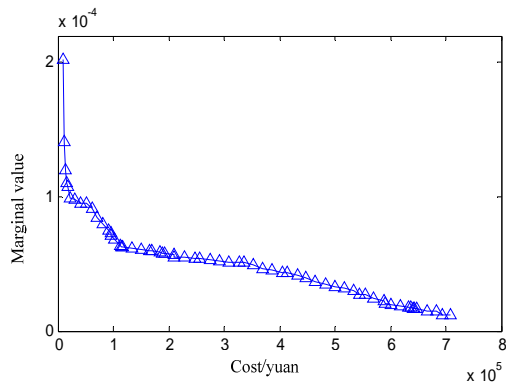


FIGURE III. THE CURVE OF MARGIN VALUE

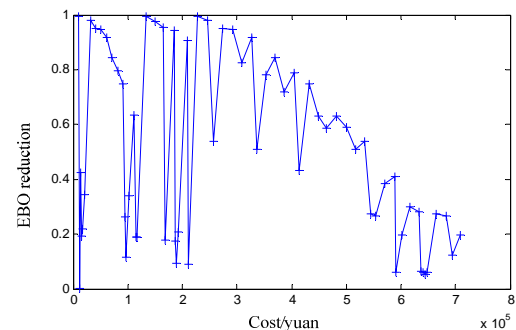


FIGURE IV. THE CURVE OF EBO REDUCTION

Figure V shows a marginal optimization algorithm for solving the relationship between delay time and cost.

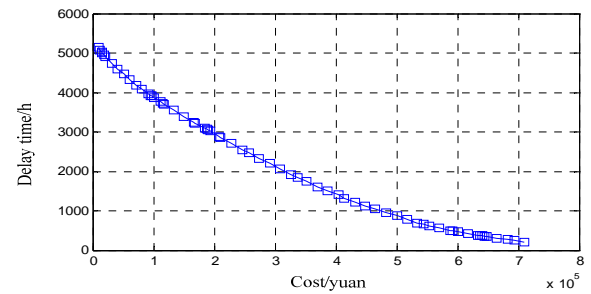


FIGURE V. THE CURVE OF EFFECTIVENESS VS. COST FOR MLDT

From the above chart, with the cost increases, the number of spare parts is also increased, and the delay time is strictly monotonically decreased, that is from 5134h to 214h.

VI. CONCLUSION

In spare parts supply, the problem of component commonality exists in most equipment, and the optimization model of spare parts allocation based on component commonality is established. The result in the case shows that the problem of deviations in availability is solved by the model in the paper, which save the inventory of supply system. The evaluation precision is improved by the model in paper in case that requirement of support indexes are needed, and the total cost is reduced. Therefore, the result can provides a theoretical basis and decision support for the use of component commonality.

REFERENCES

- [1] Sherbrooke Craig C. Optimal Inventory Modeling of Systems: Multi-Echelon Techniques [M]. Second Edition. New York ; Springer Science Business Media, 2004
- [2] Zhang Lin, Zhao Jie, Tang Chao, etc. Research on the Echelon Inventory Model of the Repairable Spares [J]. Acta ArmamentarII, 2009, 30(11): 90-94.
- [3] Wang Yabin, Zhao Jianmin, Cheng Zhonghua, etc. Optimization for spare parts allocation in multi-echelon support system based on improved MOPSO [J]. System Engineering and Electronics, 2015, 37(7): 1581-1586.

- [4] Jayaraman V, Pirkul H. Planning and coordination of production and distribution facilities for multiple commodities [J]. European Journal of Operational Research, 2001, 133(2): 394-40.
- [5] Wong H, Cattrysse D, Oudheusden D V. Stocking decision for repairable spares pooling in a multi-hub system [J]. International Journal of Production Economics, 2005(93): 309-317.
- [6] Mao Shihong. Decision research on purchase quantity allocation for general spare parts base on importance degree [J]. Science and Technology Management Research, 2012, 13: 242-244.
- [7] Ruan Minzhi, Li Qingmin, Li Cheng, etc. Improved-Layered-Marginal Algorithm to Optimize Initial Spare Part Configuration Project [J]. ACTA Armamentaria, 2012, 33(10): 1251-1256.
- [8] Sherbrooke C C, Optimal inventory modeling of system: Multi-Echelon Techniques [M]. Springer. 2004.
- [9] Francesco Costantino, Giulio Di Gravio, Massimo Tronci, Multi-echelon, multi-indenture spare parts inventory control subject to system availability and budget constraints [J]. Reliability Engineering & System Safety, 2013, 119(0): 95-101.
- [10] Dong Qi, Xu Tingxue, Zhao Jianzhong, etc. Multi-objective optimization configuration for special equipment materials on warship [J]. Science & Technology Review, 2015, 33(19): 96-101.
- [11] Wong H., Van Houtum G.J., Cattrysse D., Van Oudheusden D., Stocking decisions for repairable spare parts pooling in a multi-hub system [J]. International Journal of Production Economics, 2005, 93: 309-317.

Theoretical Research on Concentric Circular Selection of Sample Points for Flatness Error Measurement of Revolving Body End-face

Lei Zhang*, Wenying Wang, Peng Guan and Jun Cheng

Mechanical Engineering and Automation School, Northeastern University, Shenyang 110004, P. R. China

*Corresponding author

Abstract—According to flatness error measurement of revolving body end-face, selection of sample points for flatness error measurement and flatness error evaluation method are mainly researched, the influencing factors are analyzed. Former concentric circular selection of sample points gets many restrictions, the measurement point arranges normally on the straight line that diffused. In this paper, a new concentric circular selection of sample points for flatness error measurement is presented and described by mathematical formulas in detail. The new method of arranging sample points can install quantity and the location of sample points wantonly on circumference direction and diameter direction, and satisfies the needs of the measure of flatness error. Based on using the research methods of relative subjects of other countries for reference, the simulation method for flatness error evaluation of concentric circular selection of sample points is presented, the mathematical model is simulated, and the simulation results are compared and analyzed. Since concentric circular selection of sample points is arranged the central symmetry of sample points, the orthogonal least-square mathematical models of flatness error evaluation for revolving body end-face are built, not only calculation is simple, and can raise the precision of calculation.

Keywords—flatness error of revolving body end-face; concentric circular selection of sample points; mathematical description; least-square method

I. INTRODUCTION

To a great extent, the method of arranging sample points for flatness error measurement is affected by the method of measurement, evaluation method, the geometric shape of measured workpieces and other factors^[1-4]. For flatness error measurement of revolving body end-face, using concentric circular to arrange sample points has been narrated in related books. But this method which is still based on gradienter and autocollimation make use of pitch to the measure. Data obtained by the use of indirect measurement estimate flatness error. In the process of arranging sample points, these points that consist of concentric circles cover linear according to radiation patterns. Not only that, this method, which comes from practice and does not do the theoretical research, can't be combined with subsequent flatness error evaluation method well. So, we will make an accurate mathematical description of concentric circles in this paper, moreover, considering factors that affect the follow-up methods of evaluation and arranging

sample points, we optimize the method of concentric circles to better adapt to our needs to assess the method of error measurement.

II. ESTABLISHING CONCENTRIC CIRCULAR SELECTION OF SAMPLE POINTS

A. The Mathematical Description of Concentric Circular Selection of Sample Points

The method of arranging sample points is discontinuous in the mathematical description, as a result, the parameters are independent of each other. The main parameters of the method are the step of head and circular motion speed of benchmark, we set that the step of head is r , the circular speed of benchmark is ω , when the head reaches one position of a step, the benchmark rotate a cycle to take some measure. Because the radius and the number of points may be independently in each circle what concentric circles are composed of, and we can make that the radius of $i+1^{th}$ circle is more one step r of the head than former. The concentric circular selection of sample points is described as follows in the polar.

$$L_i = i \times \frac{R}{M} \quad i = 1, 2, \dots, M ; j = 1, 2, \dots, N \quad (1)$$

$$\theta_j = j \times \frac{2\pi}{N} \quad i = 1, 2, \dots, M ; j = 1, 2, \dots, N \quad (2)$$

Where, L_i is the diameter of j^{th} point of the i^{th} circle in the polar, θ_j is the angle of j^{th} point of the i^{th} circle in the polar, R is the radius of benchmark, M is scores of radius, N is scores of circle. The concentric circular selection of sample points can be described as follows in the rectangular coordinates system.

$$x_i = i \times \frac{R}{M} \times \cos \frac{2\pi j}{N} \quad i = 1, 2, \dots, M ; j = 1, 2, \dots, N \quad (3)$$

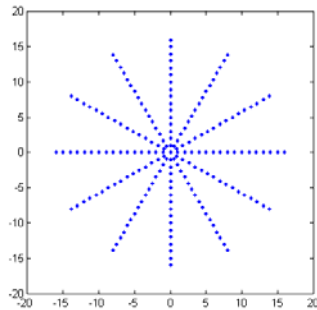
$$y_j = i \times \frac{R}{M} \times \sin \frac{2\pi j}{N} \quad i=1,2,\dots,M; \quad j=1,2,\dots,N \quad (4)$$

Among, x_i —X-coordinate of j^{th} point of the i^{th} circle, y_j —Y-coordinate of j^{th} point of the i^{th} circle, R —the radius of benchmark, M —scores of the radius, N —scores of the circle.

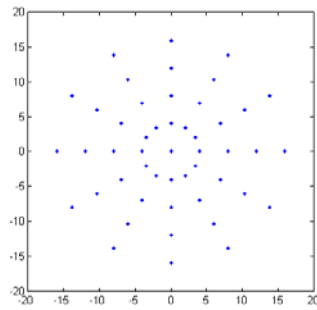
B. The Explanation of Parameters and the Influence on the Method of Arranging Sample Points in Mathematical Expression

From the formula (3), (4) we can see, we need to determine three parameters R , M and N in the mathematical description. R is measured parameters of revolving body end-face determined by the radius of measured plane, and It depends on the distance between the maximum radius concentric circle and the actual measuring work-piece according to the measurement standards. The bigger M is, the smaller radial distance of the concentric circles of each round is, and the more dense points cover in the radial, as is shown in Figure I.

N has influence on both the position and the distribution of sample points. The bigger N is, the larger the number of points, and the more dense they cover on the circumference, as is shown in Fig.II.

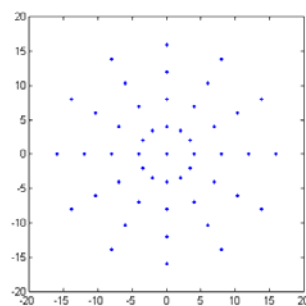


(a) $M = 16$, the figure of concentric circular selection of sample points

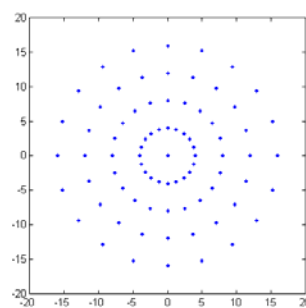


(b) $M = 4$, the figure of concentric circular selection of sample points

FIGURE I. THE INFLUENCE OF THE RADIUS EQUAL NUMBER M ON BOTH THE LOCATION AND DISTRIBUTION OF THE POINTS



(a) $N = 12$, the figure of concentric circular selection of sample points



(b) $N = 20$, the figure of concentric circular selection of sample points

FIGURE II. THE INFLUENCE OF CIRCUMFERENTIAL EQUAL NUMBER N ON BOTH THE LOCATION AND DISTRIBUTION OF THE POINTS

III. THE OPTIMIZATION OF CONCENTRIC CIRCULAR SELECTION OF SAMPLE POINTS

Because M and N are two independent parameters, and M has made the radius take the average, so optimizing parameters of concentric circular is mainly to optimize N . We can adjust N , or give a certain discipline of N to make the location of points change.

From Figure I to Figure II, we can make a conclusion that these points present radially and in a straight line. The points are dense at the beginning, however, with the concentric circles of gradually increasing radius, they become fragmented. This does not guarantee an equal distribution of the points, which has negative effect on assessment for least-square method in later. We can design parameters of the method through self-developed algorithm, and regulate N to achieve the desired effect of points by the condition of algorithm. Thus, we can not only make the arbitrariness of arranging sample points to be stronger, but also makes them more average. Figure III is the figure of points generated when N with 2π cycle adds 2 as $R = 36$, $M = 6$, We can see from the graph, although this figure is also concentric circular selection of sample points, but doesn't have very strong regularity of the method, and points appear more uniform.

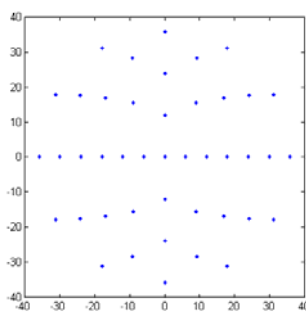


FIGURE III. THE FIGURE OF OPTIMIZED CONCENTRIC CIRCULAR SELECTION OF SAMPLE POINTS

IV. ESTABLISHING THE MATHEMATICAL MODEL OF LEAST-SQUARE METHOD OF CONCENTRIC CIRCULAR SELECTION OF SAMPLE POINTS

If N is always the even number in the process of arranging sample points, then the x and y coordinate system of every discrete sampling point have a symmetrical center. What's more, if the origin o of the space rectangular coordinates system $oxyz$ established in the actual plane is coincident with benchmarks set of symmetrical center, we can undertake Boolean manipulation. At the moment, we can establish mathematical model for the measure of flatness error by using the orthogonal least square method. And the algorithm of concentric circles is greatly simplified than spiral, so as to increase the flatness error evaluation efficiency.

In the space rectangular coordinates system $oxyz$, the general equation for plane is

$$Ax + By + Cz + D = 0 \quad (5)$$

If $a = -A/C$, $b = -B/C$, $d = -D/C$, then the general equation for plane can be written as

$$z = ax + by + d \quad (6)$$

In the case of discrete sampling, the least squares plane equation is

$$\begin{aligned} & z_j = ax_i + by_j + d, \\ & i = 1, 2, \dots, m; j = 1, 2, \dots, n \end{aligned} \quad (7)$$

Type (7), d is the least square plane and Z axis intersection point of z coordinate; a is the least squares plane and xoz coordinate plane intersection slope; b is the least squares plane and yoz coordinate plane intersection slope.

The distance between each sampling point $Q_{ij}(x_i, y_j, z_{ij})$ ($i = 1, 2, \dots, m$; $j = 1, 2, \dots, n$) and corresponding point in the least squares plane is

$$\varepsilon_{ij} = \frac{z_{ij} - z'_j}{\sqrt{1+a^2+b^2}} = \frac{z_{ij} - ax_i - by_j - d}{\sqrt{1+a^2+b^2}}, \quad i = 1, 2, \dots, m; \\ j = 1, 2, \dots, n \quad (8)$$

But, a and b are small, so there are:

$$\varepsilon_{ij} = z_{ij} - z'_j = z_{ij} - ax_i - by_j - d, \quad i = 1, 2, \dots, m; j = 1, 2, \dots, n \quad (9)$$

Where, z_{ij} is each discrete sampling points of z coordinate. According to the least square method, there is

$$\left\{ \begin{array}{l} d = \sum_{i=1}^m \sum_{j=1}^n z_{ij} / mn \\ a = \sum_{i=1}^m \sum_{j=1}^n x_i z_{ij} / n \sum_{i=1}^m x_i^2 \\ b = \sum_{i=1}^m \sum_{j=1}^n y_j z_{ij} / m \sum_{j=1}^n y_j^2 \end{array} \right. \quad (10)$$

From each sampling point $Q_{ij}(x_i, y_j, z_{ij})$ ($i = 1, 2, \dots, m$; $j = 1, 2, \dots, n$) to corresponding point in the least squares plane, the deviation of z coordinate is

$$\varepsilon_{ij} = z_{ij} - ax_i - by_j - d, \quad i = 1, 2, \dots, m; j = 1, 2, \dots, n \quad (11)$$

So, the flatness error from orthogonal least square method

$$\begin{aligned} f &= \max \{ \varepsilon_{ij} \} - \min \{ \varepsilon_{ij} \} \\ &= \max \{ z_{ij} - ax_i - by_j \} - \min \{ z_{ij} - ax_i - by_j \}, \quad (12) \\ & i = 1, 2, \dots, m; j = 1, 2, \dots, n \end{aligned}$$

V. THE SIMULATION OF FLATNESS ERROR MEASUREMENT

A. The Method of Acquiring Simulated Data in Computer

If want to verify the feasibility of a mathematical model, or is the characteristic of mathematical model itself, then we need to import the corresponding data for the calculation. As far as the mathematics model of concentric circular for flatness error measurement is concerned in the paper, it mainly studies the feasibility of mathematical model itself, and gives the

corresponding results with different parameters of the model. The data used in this paper, is from the thesis published in the high level journal, and is what author M.Affan Badar, Shivakumar Raman obtain through the experiment. The concrete experimental conditions are as follows [3, 4].

We process a $100 \times 100\text{mm}$ plane with the method of grinding, and measure the plane by Brown & Sharpe Reflex 343 series of three coordinates measuring instrument. The article makes the method of arranging sample points to use grids, by the least square method for flatness error measurement, the results of measurement are as follows: The three geometric parameters in ideal plane are $a = -0.00091, b = -0.00067, d = 85.0528$, relative to the plane of ideal the highest point error is $e_{\max(+)} = 0.06793$, the lowest point error is $e_{\max(-)} = 0.06796$, flatness error is $F_e = 0.13589$.

Considering the method of in the paper is different from above, we should think whether those points can be availed directly. Because the established mathematical model is to apply the least square method, as well as literature[3, 4], so changing the method of arranging sample points has little impact on the least square method to assess, when the length unit of the points is same, and the area is similar.

B. To Determine Concentric Circular Selection of Sample Points and Analyze the Simulation Result

We put experimental data into the mathematical model to achieve three main parameters in the least square ideal plane equation, $a = 0.1544 \times 10^{-3}, b = -0.6148 \times 10^{-4}, d = -84.8742$, then invoke Pingding function to get the results of flatness error measurement $e_{\max(+)} = 0.0536, e_{\max(-)} = -0.0835, F_e = 0.1371$, the highest point is 84th sample point, the lowest point is 13th sample point.

Through the simulation analysis we can see: in the case of concentric circular selection of sample points, flatness error by the least square method differ the traditional pitch method whose results are 0.95%. But we should notice a bit, the simulation is in different method, so we cannot expect that results are completely consistent. While the difference of 0.95 of the results corresponds with the basic conclusion which we mentioned above in error prediction, which can explain that the mathematical model built in the paper can be applied to flatness error measurement.

As we know, both grids and concentric circular selection of sample points for flatness error measurement measure data Z. When evaluate concentric circular selection of sample points for flatness error in the paper, we use the orthogonal least square method which is also used by grids. So the coefficient matrix A, which the orthogonal least square method assess in the method and the original, is the same in form. Therefore, the main difference is coordinates data produced by the method of arranging sample points between two methods

VI. CONCLUSION

The paper establish mathematical model of concentric circular selection of sample points for flatness error measurement, it is different from the previous has many restrictions, whose points must spread in the straight line. The points may be set on any position with any quantity in the circumference and radial, which meets the need of flatness error measurement. Because of the central symmetry of concentric circular selection of sample points, we choose the orthogonal least square method, and the calculation of the method and the matrix is simple, which increases the calculation precision.

ACKNOWLEDGEMENT

This project was supported by National Natural Science Foundation of China in 2015 (No. 51575096).

REFERENCES

- [1] Bi Fei, Yujian Fan, Wenxiong Xu Adaptive Sampling Method: A New Sampling Method for the Measurement of Geometric Forms. *Journal of Applied Sciences*, 1994, 12 (4): 1423-430
- [2] Taicang Zhang. Research of Arrange Measuring Line and Point in Pitch Measurement of Flatness. *Journal of Astronautic Metrology and Measurement*, 1993, 12(6): 33-38
- [3] M.Affan Badar, Shivakumar Raman, Pakize S.Pulat. Intelligent Search-Based Selection of Sample Points for Straightness and Flatness Estimation [J], *Journal of Manufacturing Science and Engineering*, 2003, 125: 263-270
- [4] M.Affan Badar, Shivakumar Raman, Pakize S.Pulat. Experimental Analysis of Search-Based Selection of Sample points for Straightness and Flatness Estimation [J], *Journal of Manufacturing Science and Engineering*, 2005, 127: 97-101

An Improved Differential Evolution for Constrained Optimization Problems

Liechao Zhang and Lin Shang*

Wuhan Technical College of Communications, Wuhan 430065, China

*Corresponding author

Abstract—A fast and robust differential evolution based on orthogonal design (ODE) is proposed, and then it is used to solve constrained optimization problems. The ODE combines the conventional DE (CDE), which is simple and efficient, with the orthogonal design, which can exploit the optimum offspring. The ODE has some features. 1) It uses a robust crossover based on orthogonal design and an optimal offspring is generated with the constrained statistical optimal method. 2) To decrease the number of the orthogonal design and make the algorithm converge faster, decision variable fraction strategy is applied here. 3) It uses simple diversity rules to handle the constraints and maintain the diversity of the population; 4) A multi-parent hybrid adaptive-crossover-mutation operator based on the non-convex theory is proposed, which can enhance the non-convex search ability. 5) The ODE simplifies the scaling factor F of the CDE, which can reduce the parameters of the algorithm and make it easy to use for engineers. We execute the proposed algorithm to solve 13 benchmark functions with linear or/and nonlinear constraints. Through comparison with some state-of-the-art evolutionary algorithms, the experimental results demonstrate that the performance of the ODE outperforms other evolutionary algorithms in terms of the quality of the final solution and the stability; and its computational cost (measured by the average number of fitness function evaluations) is lower than the cost required by the other techniques compared.

Keywords—differential evolution; orthogonal design; simple diversity rules; hybrid adaptive-crossover-mutation; function optimization

I. INTRODUCTION

Evolutionary algorithm is an adaptive, self-organizing and implicitly parallel algorithm based on groups of heuristic searching algorithm, which utilizes individuals from groups to search in the solution domain. In the process of evolution, individuals in groups produce new individuals by genetic operators, maintain the diversity of the population and search in the new space to get the optimization. For now, there has been a many branches of EA, including genetic algorithm, evolutionary programming, evolution strategies, genetic programming and so on.

In real engineering design, some complex function optimization problems are often met, which are always nonlinear, incontinuous, indifferentiable, multimodal, multi-extremum, no-convex and numerical algorithms(such as simplex method, conjugate gradient method) to get ideal optimization. In recent years, many scholars apply evolution algorithms to complex function optimization and get ideal

results. In function optimization^[2,3,5,6], the objective function often comes with a lot of equation and inequality constraints, which bring challenges to optimization method. In constrained global optimization problems, penalty functions are usually used to deal with constrained functions .That is, punish the constrained function with a penalty factor, and then add the penalty term to the objective function, which convert the problem to a global optimization without constraints. Although the method has been widely used, its drawbacks is that it's difficult to set and regulate the penalty factor, which means too large or too small penalties will make it simple feasibility rules to deal with the constrained functions and get good results^[8].Recently, some scholars have the feasibility of using a few simple rules to deal with constraint function^[8,10,11], good results have been achieved.

Differentia evolution^[2] is a fast evolutionary algorithm, which uses differential information between individuals to direct search. DE performed well on the International Contest on Evolutionary Computation and get widely used. Compared with other evolutionary algorithm its different characteristics, K.Price and R.Storm designed ten different strategies of DE for users to choose. However, CDE converges slowly in evolution of the late when dealing with the global optimal solution approaches the boundary of feasible and infeasible region. it will be difficult to get the optimal solution or slowing down of convergence will appear.

In this paper, an improved version of the differential evolution based on the orthogonal design(ODE) is presented. Its feature is: a new hybrid adaptive crossover operator is presented to enhance the global searching ability of the algorithm and non-convex search; in the meantime, to ensure better individuals will come out in the evolution, orthogonal crossover operator and constraint statistical optimal method are adopted, combined with decision variable fraction strategy in order to decrease the number of the orthogonal crossover operator and constraint statistical optimal method are adopted, combined with decision variable fraction strategy in order to decrease the number of the orthogonal design and make the algorithm converge faster; It uses simple diversity rules to handle the constraint. This algorithm is called CDE for short. To make it simple to use, the ODE simplifies the scaling factor, and take consistent random numbers in the interval $(0,1]$.Though 13 standard functions, the superior performance of ODE is verified.

II. PROBLEM DEFINITION

Without loss of generality, take the constrained minimization function optimization for example, which can be described as follows:

$$\text{Minimize } f(X), \quad X = (x_1, x_2, \dots, x_N) \in R^N \quad (1)$$

to satisfy:

$$\begin{cases} g_i(X) \leq 0, & i = 1, 2, \dots, p \\ h_j(X) = 0, & j = 1, 2, \dots, q \end{cases} \quad (2)$$

among which $X \in S \cap \Gamma$. $S \subseteq R^N$ is called search space, Γ is feasible region, $f(X)$ is objective function, X is a N -dimensional decision vector, $X = [x_1, x_2, \dots, x_N]^T$, each independent variable x_i to satisfy certain constraint:

$$l_i \leq x_i \leq u_i, \quad i = 1, 2, \dots, N \quad (3)$$

p is the number of Inequality constraints, and q is the number of inequity constraints. The constraints can be linear or nonlinear.

III. ORTHOGONAL DESIGN

In industry, agriculture and scientific research, multi-factor influence on products is often taken into consideration. If arrange comprehensive experiments with each factors of different level of mutual collocation, it will be difficult or even impossible to realize. Orthogonal design can get optimization, determine the effect of index factors and levels first, then select the appropriate orthogonal array, according to which the experiment can be arranged. At the end, Analysis of the test results and get a good level.

The orthogonal array has the following properties:

1. For the factor in any column, every level occurs equal times.
2. For the two factors in any two columns, every combination of two levels occurs equal times to represent the experiments.
3. Any two experiments are not the same, so their results cannot be compared directly.
4. If any two columns of an orthogonal array are swapped, the resulting array is still an orthogonal array.
5. If some columns are taken away from an orthogonal array, the result is still an orthogonal array with a smaller number of factors.

IV. ODE: ORTHOGONAL DE

In order to get rapid convergence as the region of global minimum, make it easy to manipulate and get better solutions, we modify the CDE. The enhancements of ODE are as follows:

A. Orthogonal Crossover Operator

1. Design of the orthogonal array

To design a minimal orthogonal array, in the research, we use the two level orthogonal array $L_{2^J}(2^{2^J-1})$, $R = 2^J$ denotes the number of the rows of orthogonal array, and $C = 2^J - 1$ denotes the number of the columns. The orthogonal array needs to find a proper J to satisfy

$$\begin{aligned} \text{Minimize : } R &= 2^J \\ \text{St : } C &= 2^J - 1 \geq N \end{aligned} \quad (4)$$

Where N is the number of the variables. In this study, we adopt the algorithm described in Ref.^[5] to construct an orthogonal array. In particular we use $L(R, C)$ to indicate the orthogonal array; and $L(i, j)$ denotes the level of the j th factor in the i th combination in $L(i, j)$.

2. Generation of the orthogonal sub-population

After construction a proper orthogonal array, we select two parents randomly, $X_1 = (x_{11}, x_{12}, \dots, x_{1N})$ and $X_2 = (x_{21}, x_{22}, \dots, x_{2N})$, to generate the orthogonal sub-population $O(R, N)$ for two level orthogonal crossovers.

3. Direct statistical optimal method with constraints

In order to choose a better individual as offspring from the orthogonal group, Ref.^[5] chooses the offspring according to the fitness value. However, we know that any two experimental results cannot be compared directly from the third property of orthogonal array. As a result, in order to generate the best offspring from the orthogonal array, the algorithm presents a direct statistical optimal method with constraints based on traditional statistics to satisfy the constraint conditions, which is similar to Taguchi method in Ref.^[6] and statistical optimal method in Ref.^[7], where constraint conditions are added based on intuitive method to verify the diversity of the population.

Calculation of the value of the k th level of j th factor $E(j, k)$ is

$$\begin{cases} E(j, k) = \sum_{L(i, j)=k} X_{i \cdot} f \\ CE(j, k) = \sum_{L(i, j)=k} X_{i \cdot} cf \end{cases} \quad (5)$$

where $X_{i \cdot}$ f is the fitness value of the i th combination's constrained function. In this way, generate the best offspring to each factors in Algorithm 2.

B. Decision Variable Fraction Strategy

If the dimension of the variable is higher, it needs to design a larger orthogonal array with more rows. For example, if N=30,R=32;N=10,R=128. When we use Algorithm 2 to generate an offspring, it may evaluate too many times, leaving the efficiency low. Therefore, ODE uses decision variable fraction strategy to divide the variable into groups(fractions can be equal or not equal). For simple calculation, fractions are equally spaced) to reduce the number of factors. For example, divide 30-dimensional variable into 2 groups, in the way the orthogonal array(R=4) can satisfy the requirements.

C. Simple Diversity Rules

To maintain the diversity of population, 2 rules are put forward to compare 2 individuals when handling constrained optimization. Formula(6) calculates the target fitness value of individuals; formula(7) calculates the sum of constrained functions; formula(8) compares two individuals

$$X.f = f(X) \quad (6)$$

$$X.cf = \sum_{i=1}^q \max\{0, g_i(X)\} + \sum_{j=1}^p \max\{0, |h_j(X)| - \eta\} \quad (7)$$

$$\text{Better}(X_1, X_2) = \begin{cases} X_1.cf < X_2.cf, & 1 \\ X_1.cf > X_2.cf, & 0 \\ (X_1.cf == X_2.cf) \cap (X_1.f < X_2.f), & 1 \\ (X_1.cf == X_2.cf) \cap (X_1.f == X_2.f), & 2 \\ (X_1.cf == X_2.cf) \cap (X_1.f > X_2.f), & 0 \end{cases} \quad (8)$$

where $|h(X)| - \eta$ denotes transforming equality constraint into inequality by deducting a small positive(namely equation tolerance). In formula (8), if return values is 1, individual X1 precedes X2, X1 will be accepted in evolution; if return values is 0, individual X2 precedes X1, X2 will be accepted; if return values is 2, X2 and X1 have the same performance , the 2 individual will be accepted with the same probability in the evolution. In this way, it can be ensured that some infeasible individuals are in the population and thus pressure is relieved and population's diversity is kept.

D. Hybrid Adaptive Crossover Mutation Operators

To enhance the algorithm's no-convex search ability, ODE designs multil-parent non convex crossover operators, as the formula (9) show:

$$P_1 = \sum_{i=1}^p a_i * X_i \quad (9)$$

where $a_i \in [-0.5, 1.5]$ is a random number, and $\sum_{i=1}^p a_i = 1$, p denotes the number of chosen parents. formula (9) is mentioned in

Ref.[3],and a_i choosing random number from [-0.5,1.5] can enhance the algorithm's no-convex search ability.

ODE generated individuals respectively by formula (9) and DE/rand/1/bin strategy, then choose a better one as offspring to compare with the parent individual. If the offspring precedes the parent, it will replace the parent; otherwise the offspring will be abandoned.

E. Simplifying the Scaling Factor

The scaling factor F is generated uniform randomly from $F \in (0, 1]$ in the proposed ODE to make is simple and easy to use without inaccuracy caused manual set.

V. LABORATORY FINDING

A. Experimental Environment And Parameter Setting

For all experiments in ODE, we used the following parameters:

Population size: M=100;probability of crossover: CR=0.9; DE strategy: DE/rand/1/bin; largest number of fitness evaluation: NFFE=240 000; number of parent : P=6; Halting precision: $\epsilon = 1e^{-30}$; decision variable fraction: if dimension of variable N>8,F=2,otherwise F=N; equality constraint tolerance: $\eta = 0.0001$.

B. Benchmark Functions

In order to test the performance of ODE, 13 benchmark function Ref.^[9] were used,11 of which are first proposed in Ref ^[12],2 of which are added by ^[9]. All of the 13 are benchmark functions for constrained optimization problems and are widely used in may Refs. Functions g02, g03, g08, g12 are for the max of objective functions and the other are for the min. Properties of the functions have been described in Ref ^[9].

C. Experimental Results

Every function operates independently 30 times, the results are shown as follows: 1)best function results Best; 2) medium results Media; 3) mean best results Mean Best; 4) worst results Worst; 5) standard deviation Std. Dev; 6) mean function fitness evaluation MFFE; 7) success rate Sr(if $|f(X^*) - f(X_{best})| \leq 1e^{-4}$ or best results precede global optimal solution, the operation will be successful); 8) mean time of operating time T. Table 1 shows the results of ODE experiments. In order to test the performance of ODE, the author compare its results with other evolution, which are HM^[12], SR^[9], ASCHEA^[13], CHDE^[11] and SMES^[8]. Table 2 is comparison of best results between ODE and HM, SR, ASCHEA, CHDE, SMES; Table 3 is comparison of mean results between ODE and HM, SR, ASCHEA, CHDE, SMES; Table 4 is comparison of worst results between ODE and HM, SR, ASCHEA, CHDE and SMES.

TABLE I. STATISTICAL RESULTS OF ODE(RESULTS IN BOLD DENOTES BEST RESULTS PRECEDE GLOBAL OPTIMAL SOLUTION)

Problem	Optimal	Best	Media	Mean Best	Worst	Std. Dev.	MFFE	Sr	T (s)
g01	-15	-15	-15	-15	-15	0	41,752	100%	1.265
g02	0.803619	0.803619	0.801252	0.801981	0.792609	0.003518	108,678	80%	4.906
g03	1	1.0005	1.0005	1.0005	1.0005	0	209,260	100%	6.359
g04	-30665.539	-30665.539	-30665.539	-30665.539	-30665.539	0	33,999	100%	0.953
g05	5126.498	5126.4967	5126.4967	5126.902	5127.896	0.4786	102,230	56.67%	3.359
g06	-6961.814	-6961.814	-6961.814	-6961.814	-6961.814	0	12,385	100%	0.344
g07	24.306	24.306	24.306	24.306	24.306	0	71,710	100%	2.593
g08	0.095825	0.095825	0.095825	0.095825	0.095825	0	2,515	100%	0.078
g09	680.63	680.63	680.63	680.63	680.63	0	21,028	100%	0.687
g10	7049.25	7049.248	7049.248	7049.248	7049.24802	2.945×10^{-16}	125,890	100%	3.031
g11	0.75	0.7499	0.7499	0.7499	0.7499	0	32,965	100%	0.921
g12	1	1	1	1	1	0	1,998	100%	0.984
g13	0.05395	0.05387	0.4384	0.3230	0.4384	0.1762	212,169	33.33%	6.906

VI. DISCUSSIONS AND ANALYSIS

We can see from table 1 that ODE can find all global optimal solutions to benchmark functions. And the best results of g03, g05, g10, g11 and g13 are better than the global optimal solutions, which depends on the magnitude of the equation tolerance η when transforming the equality constraint into inequality constraint. MFFE of all functions is smaller than largest number of evolution, ten of which are smaller than 100000. Success rate is 100% except for g02, g05 and g13, which denotes the absolute values of difference between final result and optimal solution are smaller or equal compared with 1e-4 or optimal solutions during the 30 ODE operations.

Moreover, all the functions give small standard deviation, nine(g01, g03, g04, g06, g07, g08, g09, g11 and g12) of which analyses are zero. Analyses above indicate that ODE has outstanding performance when handle constrained optimization problems, which can give high accuracy, more stable solution quality and faster convergence speed. However, ODE doesn't perform well handling g13 with the success rate of 33.33%, and other 20 operations get the local optimal solution 0.4383652659. Thus the algorithm doesn't work well with the equality constraint and needs to be improved, which doesn't go against the "No-Free-Lunch" theory proposed in Ref [14].

TABLE II. COMPARISON OF BEST RESULTS BETWEEN ODE AND HM,SR,ASCHEA,CHDE SEMS (RESULTS IN BOLD ARE BETTER OR GLOBAL OPTIMAL SOLUTION)

Problem	Optimal						
		HM	SR	ASCHEA	CHDE	SMES	ODE
g01	-15	-14.7886	-15	-15	-15	-15	-15
g02	0.803619	0.79953	0.803515	0.785	0.803619	0.803601	0.803619
g03	1	0.9997	1	1	1	1	1.0005
g04	-30665.539	-30664.5	-30665.539	-30665.5	-30668.539	-30665.539	-30665.539
g05	5126.498	--	5126.497	5126.5	5126.497	5126.599	5126.4967
g06	-6961.814	-6952.1	-6961.814	-6961.81	-6961.814	-6961.814	-6961.814
g07	24.306	24.620	24.307	24.3327	24.306	24.327	24.306
g08	0.095825	0.095825	0.095825	0.095825	0.095825	0.095825	0.095825
g09	680.63	680.91	680.630	680.632	680.630	680.632	680.63
g10	7049.25	7147.9	7054.316	70561.13	7049.24802	7051.903	7049.248
g11	0.75	0.75	0.75	0.75	0.749	0.75	0.7499
g12	1	0.99999	1	A. NA	1	1	1
g13	0.05395	NA	0.053957	B. NA	0.053866	0.053986	0.05387

1.Comparison Between ODE and HM

ODE get better best results than HM in 11 functions (g01, g02, g03, g04, g05, g06, g07, g09, g10, g11 and g12). In g08, the two best results are global optimal solution. In the

meantime, mean and worst results of ODE are better than HM's in 12 functions(g01,g02, g03, g04, g05, g06, g07, g08, g09, g10, g11 and g12), HM doesn't test function g13, so it doesn't need any comparisons.

2.Comparison Between ODE and SR

Comparison with SR, ODE gets better best result in g02, g03, g05, g07, g10, g11 and g13. For other 6 functions, both algorithm get best results equal to optimal solution. For g02, g03, g05, g06, g07, g09, g10 and g11, ODE gets better mean results and worst results. But mean results and worst results of SR are better than ODE for g13. For other functions, mean results and worst results of both algorithm are optimal solution.

3.Comparison Between ODE and ASCHEA

Comparison with ASCHEA, ODE gets best results in nine functions, except that the two 2 algorithms get the same best results. And ODE get bets better mean results than ASCHEA, except for the same mean results in functions g01 and g08. ASCHEA doesn't test function g12 and g13, doesn't get worst results, so it doesn't need comparison.

TABLE III. COMPARISON OF MEAN RESULTS BETWEEN ODE AND HM,SR,ASCHEA,CHDE SEMS (RESULTS IN BOLD ARE BETTER OR GLOBAL OPTIMAL SOLUTION)

Problem	Optimal						
		HM	SR	ASCHEA	CHDE	SMES	ODE
g01	-15	-14.7082	-15	-14.84	-14.792134	-15	-15
g02	0.803619	0.79671	0.781975	0.59	0.746236	0.785238	0.801981
g03	1	0.9989	1	0.99989	0.640326	1	1.0005
g04	-30665.539	-30665.5	-30665.539	-30665.5	-30592.154435	-30665.539	-30665.539
g05	5126.498	--	5128.881	5141.65	5218.729114	5174.492	5126.902
g06	-6961.814	-6342.6	-6875.940	-6961.81	-6367.575424	-6961.284	-6961.814
g07	24.306	24.826	24.374	24.66	104.599221	24.475	24.306
g08	0.095825	0.0891568	0.095825	0.095825	0.091292	0.095825	0.095825
g09	680.63	681.16	680.656	680.641	692.472322	680.643	680.63
g10	7049.25	8163.6	7559.192	7193.11	8442.656946	7253.047	7049.248
g11	0.75	0.75	0.75	0.75	0.761823	0.75	0.7499
g12	1	0.99913	1	C. NA	1	1	1
g13	0.05395	D. NA	0.057006	E. NA	0.747227	0.166385	0.3230

TABLE IV. COMPARISON OF WORST RESULTS BETWEEN ODE AND HM,SR,ASCHEA,CHDE SEMS (RESULTS IN BOLD ARE BETTER OR GLOBAL OPTIMAL SOLUTION)

Problem	Optimal						
		HM	SR	ASCHEA	CHDE	SMES	ODE
g01	-15	-14.6154	-15	NA	-12.743044	-15	-15
g02	0.803619	0.79119	0.726288	NA	0.302179	0.751322	0.792609
g03	1	0.9978	1.00	NA	0.029601	1	1.0005
g04	-30665.539	-30645.9	-30665.539	NA	-29986.2144	-30665.539	-30665.539
g05	5126.498	--	5142.472	NA	5502.410392	5304.167	5127.896
g06	-6961.814	-5473.9	-6350.262	NA	-2236.950336	-6952.482	-6961.814
g07	24.306	25.069	24.642	NA	1120.541494	24.843	24.306
g08	0.095825	0.0291438	0.095825	NA	0.027188	0.095825	0.095825
g09	680.63	683.18	680.763	NA	839.782911	680.719	680.63
g10	7049.25	9659.3	8835.655	NA	15580.370333	7638.366	7049.24802
g11	0.75	0.75	0.75	NA	0.870984	0.75	0.7499
g12	1	0.99195	1	NA	1	1	1
g13	0.05395	F. NA	0.216915	NA	2.259875	0.468294	0.4384

4.Comparison Between ODE and CHDE

Comparison with CHDE, ODE gets better best results for function g03, g05 and g10. But for function g13, best results of CHDE are slightly better ODE's. The 2 algorithms get the same best results for other functions. Except for the same

results for function g12, ODE gets better mean and worst results for other 12 functions.

5. Comparison Between ODE and SEMS

Best results of ODE are better than SEMS for 8 functions(and). And the 2 algorithms get the same best results

equal to optimal solutions for the other 5 functions. Mean and worst results of ODE are better than SEMS for 8 functions (and). Only worst results of SMES for function are better than ODE's . The 2 algorithms get the same mean and worst results for the other 3 functions.

Judging from the evaluations, ODE can converge fast for all functions with less evaluation times. In all algorithms compared above, the evaluation times of HM, SR, ASCHEA, CHDE and SMES are 1 400 000, 35 000, 1 500 000, 348 000 and 240 000. As has been shown in Table 1, MFFE of ODE is less than other 5 algorithms. That denotes fast convergence, which is of great significance in practical engineering optimization.

VII. CONCLUSION AND FUTURE WORK

For faster speed and stronger speed, this paper has improved CDE and applied orthogonal design to the algorithm, which generates offspring by 2 levels crossover operators and statistical optimal method. In the meantime, ODE utilizes hybrid adaptive crossover operators with non-convex search ability to enhance the non-convex search ability. Through decision variable fraction strategy, it can decrease the number of orthogonal design factors. In that way it will be possible to design a smaller orthogonal array to decrease fitness evaluation is used to handle to constrained functions. Tested by 13 benchmark functions of different kinds and compared with other algorithms, ODE doesn't only speed up convergence on the basis of CDE, but also have improvement on the accuracy and stability of solutions. Moreover, ODE performs better than other 5 algorithms. However, ODE has the drawback of local convergence when handling multi-function optimization with equality constraint, which we will improve in the future. Besides, applying the algorithm to other optimization problems(such as dynamic function optimization, noise function and multi-objective optimization) will be another research area.

ACKNOWLEDGMENT

This work was supported by the key project of "12th Five-Year" planning of Education Science in Hubei province under Grant No.2013A052 and Wuhan Technical College Of Communications Scientific Research and Innovation Team Grant No. CX2018A02 ,No.CX2018B02.

REFERENCES

- [1] T. Bäck, H.-P. Schwefel, An overview of evolutionary algorithms for parameter optimization [J]. *Evolutionary Computation*, 1 (1): 1-23, 1993.
- [2] R. Storn, K. Price, Differential evolution—A simple and efficient heuristic for global optimization over continuous spaces [J]. *Journal of Global Optimization*, 11: 341–359, 1997.
- [3] Guo Tao, Kang Li-shan. A new Evolutionary Algorithm for Function Optimization [J]. *Wuhan University Journal of Nature Sciences*, 4(4): 409-414, 1999.
- [4] KaiTai Fang, ChangXin Ma. Orthogonal And Uniform Experimental Design [M]. Science Press, 2001.
- [5] Y. W. Leung, Y. Wang. An Orthogonal Genetic Algorithm with Quantization for Global Numerical Optimization [J]. *IEEE Transactions on Evolutionary Computation*, 5(1), 41-53, 2001.
- [6] J. T. Tsai, T. K. Liu and J. H. Chou. Hybrid Taguchi-Genetic Algorithm for Global Numerical Optimization [J]. *IEEE Transactions on Evolutionary Computation*, 8(4), 365-377, 2004.
- [7] SanYou Zeng, Wei Wei, LiSan Kang ect. Multi-objective Evolution Algorithm Based On Orthogonal Design [J]. *Chinese Journal of Computers*, 28(7): 1153-1162, 2005.
- [8] Mezura-Montes, E., Coello Coello, C.A. A Simple Evolution Strategy to Solve Constrained Optimization Problems [J]. *IEEE Transactions on Evolutionary Computation*, 9(1): 1-17, 2005.
- [9] Runarsson, T.P., Yao, X. Stochastic Ranking for Constrained Evolutionary Optimization [J]. *IEEE Transactions on Evolutionary Computation*, 4: 284–294, 2000.
- [10] Deb, K. An Efficient Constraint Handling Method for Genetic Algorithms [J]. *Computer Methods in Applied Mechanics and Engineering*, 186: 311–338, 2000.
- [11] E. Mezura-Montes, A. Coello Coello, and I. Tun-Morales. Simple Feasibility Rules and Differential Evolution for Constrained Optimization [J]. *Proceedings of the 3rd Mexican International Conference on Artificial Intelligence*, pages 707-716, 2004.
- [12] Koziel, S., Michalewicz, Z. Evolutionary Algorithms, Homomorphous Mappings, and Constrained Parameter Optimization [J]. *Evolutionary Computation* 7: 19–44, 1999.
- [13] S. B. Hamida and M. Schoenauer, ASCHEA: New results using adaptive segregational constraint handling [J]. In Proc. Congress on Evolutionary Computation, vol. 1, May 2002, pp. 884–889.
- [14] David H. Wolpert, William G. Macready. No Free Lunch Theorems for Optimization [J]. *IEEE Transactions on Evolutionary Computation*, 1(1): 67-82, 1997.
- [15] K. Price and R. Storn, Home Page of Differential Evolution, Available Online at: <http://www.ICSI.Berkeley.edu/storn/code.html>, 2008.

Effect of Workload Characteristics on Similarity Analysis

Jiang Sha^{1,*} and Wenjuan Xu²

¹National ASIC System Engineering Technology Research Center, Southeast University, Nanjing, China

²Institute of Integrated Circuits Technology, Southeast University, Wuxi, China

*Corresponding author

Abstract—Workload characterization is the basis for similarity analysis, which is the core idea behind benchmark subsetting to pick up the most representative programs or program slices. The set of characteristics is crucial to the result of similarity analysis. Current studies typically use microarchitecture-independent characteristics (MICs) which reveal the inherent program behaviors to evaluate the similarities. In this paper, we propose a novel MICs: serializing instruction distance (SID). SID can describe the serializing instructions behavior that causes a significant performance loss of system-intensive mobile applications. The distribution of critical path length is also used as a MICs because it can reflect the inherent instruction level parallelism (ILP). Furthermore, we employ the comprehensive set of MICs to pick a representative set of program slices for each program of a mobile benchmark suites: Moby. The instructions per cycle (IPC) of each program slice is used to predict the whole program performance. The coefficient of variation of IPCs is under 6% and weighted average IPC prediction error is only 7%.

Keywords—microarchitecture-independent characteristics; similarity analysis; mobile applications; serializing instruction

I. INTRODUCTION

Benchmarking is the foundation of processor performance evaluation and prediction [1] [2]. However, due to quantities of dynamic instructions of running benchmarks and the low speed of cycle-accurate simulator, the tedious simulation cost too much time to estimate performance. So it is necessary to subset benchmarks by reducing the total number of dynamic instructions. The current methodology for this purpose mainly involves sampling simulation, statistical simulation and workload synthesis. The core idea behind these techniques is to pick up the most representative programs or program slices through similarity analysis.

Workload characterization is the basis for similarity analysis of program behaviors. There are two approaches to extract workload characteristics. One is microarchitecture-dependent characteristics (MDCs) and the other is microarchitecture-independent characteristics (MICs). MDCs define a set of metrics dependent on microarchitecture, mainly including instructions per cycle (IPC), cache miss rate and branch misprediction rate. Unfortunately, MDCs are often inconsistent on various platforms with different microarchitectures, the conclusions drawn from MDCs are only applicable for the specific microarchitecture. In some cases, even applications have the same performance on the same platform, their inherent behaviors are still different [3] [4]. Inherent behavior is the behavior of program itself, not affected by the platform.

Consequently, due to independency on microarchitectures, MICs are widely regarded as workload characteristics to represent program inherent behaviors. Traditionally, MICs are categorized into several groups consisting of instruction mix, inherent instruction level parallelism (ILP), register dependency distance, memory access locality, instruction locality and branch behaviors [5] [6] [7] [8] [9] [10].

MICs are essential to workload characterization based on inherent behaviors. For example, clustering based on shape or color of the boxes in Figure I., we will get two different results (subset A and subset B). Thinking of these boxes as benchmarks, MICs directly decide that the subsetting framework will export to different results of subsets, which have different representativeness. So the definition of MICs is crucial. The workload characteristics should cover all important program behaviors which influence the performance to the maximum extent. However, mobile applications express some different behaviors from traditional benchmarks due to frequent system calls and libraries invocations [11] [12] [13].

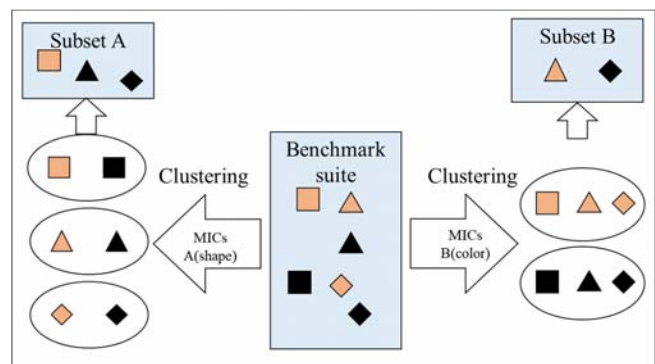


FIGURE I. EFFECT OF MICs ON BENCHMARK SUBSETTING.

Therefore, the purpose of this paper is to find the inherent program behaviors of Android applications and research on the effect of new characteristics on similarity analysis. In a summary, our contributions are as the followings:

- We propose serializing instruction distance (SID) as a new MIC to represent the serializing instruction behavior.
- We firstly employ the critical path length distribution as the corresponding MICs of inherent ILP.

- We firstly use coefficient of variation to validate the representativeness of the set of program slices.

II. METHODOLOGY

A. Microarchitecture-independent Workload Characterization

1) Serializing instruction distance:

As an important behavior of Android applications, the serializing instructions (SIs) have a significant impact on performance of system-intensive workloads. SIs can cause a 3–17% overall performance loss in some benchmarks running on Linux OS [14]. In our cases of three Android applications and three SPEC benchmarks, we measure the amount of SIs and stalled cycles due to SIs on a full-system simulator (details are mentioned in section III).

As shown in Figure II., SIs of the most left three Android applications occupy only 1-2% of total dynamic instructions but contribute 16-22% of total cycles. While there is almost no SIs executed in the three SPEC benchmarks on the right. Frequent SIs have a significant impact on performance. Therefore, we propose a new MIC, SID to represent the serializing instruction intensity statistically. SID is defined as the number of instructions between two adjacent serializing instructions. There is a large amount of serializing instructions to generate too many SID. Hence, to distinguish the differences of variable SI behaviors, we statistically calculate the distribution of SID (P_{SID}) ranging from 2^{i-1} to 2^i-1 (i is in $\{0, 1, \dots, 10\}$). Equation (1) gives its definition.

$$P_{SID} = \begin{cases} \frac{T_i}{Inst_{SI}}, & (i = 0) \\ \sum_{d=2^{i-1}}^{2^i-1} \frac{T_d}{Inst_{SI}}, & (0 < i \leq 10) \end{cases} \quad (1)$$

Where, T_d is the times of SID equal to d , $Inst_{SI}$ is the total numbers of SI.



FIGURE II. INSTRUCTION MIX AND % CYCLES SPENT STALLED DUE TO SIS.

2) Critical path length:

A serial of instructions with strong dependence cannot be out-of-order execution, especially for long dependency chains, which will limit the ILP. Critical path length is defined as the number of instructions in the longest dependent chain. We use the distribution of critical path length to reflect the dependence between instructions. For the convenience of measurement, we

actually collect the critical paths in the range of every fixed amount of instructions (refer to instruction window size, we use 40 in this paper). So we statistically calculate these characteristics to get a probability distribution from 1 to 40.

Besides, we measure spatial and temporal locality of memory and instruction. Because they are particularly important with respect to cache behaviors. We also use the proportion of register read and write and register dependency distance. To express the complexity of control flow behavior, we measure basic block size, branch direction (forward or backward), average branch taken rate, average branch transition rate and branch spatial locality. All the MICs employed in this paper are shown in TABLE I.

TABLE I. MICROARCHITECTURE-INDEPENDENT CHARACTERISTICS

Group	No.	Characteristic/Metric
Instruction mix	1-6	integer, floating-point, branch, read, write and serializing instruction
Critical path length	7-46	cpath1~40
Register traffic	47-48	register read, register write
	49-68	register_dependent_distance1~20
Instruction locality	69-89	instAddr0~20
	90-100	instReuse0~10
Memory locality	101-112	loadGlobalAddr0~11
	113-124	loadLocalAddr0~11
	125-136	storeGlobalAddr0~11
	137-148	storeLocalAddr0~11
	149-159	loadGlobalReuse0~10
	160-170	loadLocalReuse0~10
	171-181	storeGlobalReuse0~10
	182-192	storeLocalReuse0~10
Control flow complexity	193-201	basicBlockSize0~8
	202-205	fwBranch, bwBranch, takenBranch, transitionRate
	206-216	branchAddr0~11
Serializing instruction distance	217-227	serialInstDist0~10

B. Verification Standard

We group program slices into clusters according to their MICs and choose the most representative slice in each group using K-means.

Usually, weighted average IPC is used to evaluate the representativeness of those selected slices in a result that each slice's contribution to the cluster is ignored. So we exploit coefficient of variation (CV) and weighted average IPC to achieve more accurate similarity analysis. The verification algorithm is as follows:

- 1) Calculating the average CV of IPCs of all slices in each cluster.
- 2) Calculating the prediction error of weighted average IPC of representative slices for each cluster.

The CV is a well-known statistical metric to consider the uncertainty of a random variable. CV is generally defined as the standard deviation (square root of variance) divided by the mean [15]. The smaller CV is better. Therefore, we use the CV to evaluate the uniformity of IPC.

Furthermore, the slices closest to the centers of the clusters are chosen to be the representatives, and the proportions of dynamic instructions in the clusters become their weights (w_r). Then we use the weighted average IPC of representative slices (IPC_r) to predict the program's IPC as shown in (2).

$$IPC_{Predicted} = \sum_{r=1}^K w_r \cdot IPC_r \quad (2)$$

III. RESULTS

A. Experiment Setup

1) Platforms and tools

We modify the gem5 simulator [16] to collect MICs and MDCs of program slices for each program. Gem5 is a cycle-accuracy architecture simulator. It supports ARM ISA which is a prevalent mobile platform and other ISAs. We conduct our experiments on *arm_detailed* mode of gem5 by setting default configuration which similar to ARM Cortex-A15.

2) Benchmarks

Moby is a mobile benchmark suite which contains a diverse set of Android applications [13]. It also includes another benchmark named BBench [11]. They are all real-world Android applications and have been ported to gem5 simulator. We use five of them and also choose three benchmarks from SPEC CPU 2006 [20] as a comparison. The benchmarks used in this paper are listed in TABLE II.

TABLE II. BENCHMARKS

Suite	Program	Operation/Input
Moby	BaiduMap	Load an area's map
	BBench	Load web pages
	JingDong	Load information
	K9Mail	Load>Show emails
	KingsoftOffice	Open a doc file
SPEC CPU 2006	bzip2	Train inputs
	gcc	
	mcf	

B. Validation of Representativeness of Program Slices

We separate the five Android applications into 97,824 slices by context switches. Putting all the program slices into the same workload space, we use our proposed methods to extract 227 dimensions of MICs, and group them into K distinct clusters by K-means to pick a representative set of program slices. Based on the achieved representative program slices, we carry out the effect of SID and critical path length on similar analysis.

1) CV of IPCs inside clusters:

It is necessary to validate whether the IPC of slices in the same cluster are basically consistent. Figure III. gives average CVs of IPCs at different reduction ratios in cases of all MICs, MICs except SID and MICs except SID and critical path length respectively. The reduction ratio refers to the total number of program slices divided by K. In a general way, we hope to use as few slices as possible to represent the entire program.

It is obvious that CV is the smallest when SID and critical path length are included in MICs. And with the increase in reduction ratio, this advantage is more obvious, which is clearly beneficial to performance evaluation.

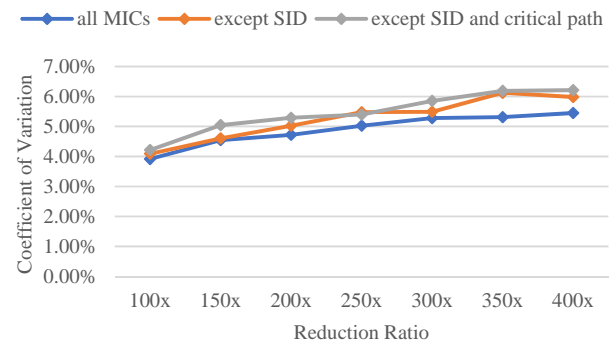


FIGURE III. COEFFICIENT OF VARIATION OF IPCS.

2) Weighted average IPC:

Using the representative slices' IPCs along with their weights referenced in equation (2), we can predict the IPCs of the programs respectively. Figure IV. shows when reduction ratio equals to 400, the IPC prediction errors of the five Android applications range from 0.5% to 15%. The average error can reach only 7%. As a comparison, we give the IPCs predicted based on all MICs and MICs except SID and critical path length. Overall, the differences between the two results are very small, but the former results slightly better than the latter in some programs.

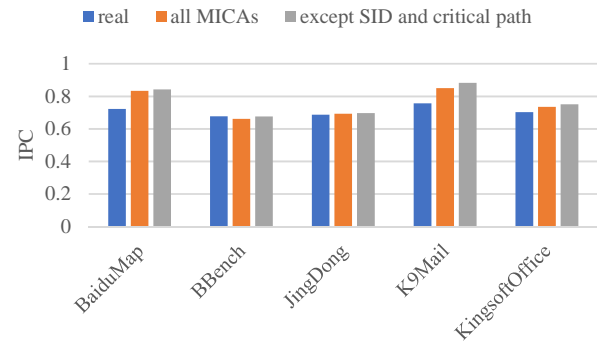


FIGURE IV. PREDICTION ERROR OF IPC (400X REDUCTION RATIO).

IV. RELATED WORK

The researches on program similarity analysis using MICs have fruitful achievements [3] [4] [5] [6] [7] [8]. Eeckhout et al. [5] found similarities of samples in SPEC2000 using 47 MICs and then selected 148 simulation points of 32,964 ones in SPEC2000. The error could be 1.11% by comparing the CPI between the selected simulation points and the completed benchmark simulation. Joshi et al. [6] selected a representative subset of 5 programs from 22 benchmarks in SPEC2000 using 29 MICs to further reduce the number of benchmarks need to be simulated. Hoste et al. [8] extended this methodology from general purpose applications to domain specific applications: BioPerf (bioinformatics) [17], BioMetricsWorkload (biometrics) [18] and MediaBench II (multimedia) [19].

However, the above benchmark suites are all traditional benchmark suites. Like the most widely used general purpose

benchmarks SPEC CPU [20], by design, stress primarily the CPU and are meant to be portable, avoiding extensive use of system calls and shared libraries. While real-world smartphone applications, in contrast, suffer more performance penalties incurred due to use of these [11]. Huang et al. [13] presented a mobile benchmark suite including 10 popular Android applications, named Moby, and captured some MICs: instruction mix, working sets, reuse distance distributions and instruction execution flow. Besides, Wells and Sohi [14] illustrated that frequent SIs have a significant impact on performance of system-intensive workloads. SIs can cause a 3–17% overall performance loss in some benchmarks running on Linux OS.

Obviously, considering the characteristics of mobile applications on Android OS, it is necessary to find new MICs that can extract program SI behavior features. Furthermore, previous set of MICs [4] define inherent ILP as IPC of an idealized out-of-order processor (with perfect caches and branch predictor). From the measurability point of view, the prime necessity is to build an ideal CPU, which is a very difficult task. So it is also necessary to define new metrics of inherent ILP in a better way. And then achieve a more comprehensive set of MICs for representative program slices choice during workload characterization.

V. CONCLUSION

In this paper, we propose the serializing instruction distance as a novel MIC and involve the critical path length to make similarity analysis. Using the comprehensive set of MICs, we pick a representative set of program slices and validate their representativeness. We find that the CV of IPCs inside clusters decreases when SID and critical path length are included in the set of MICs. And the average IPC prediction error of Android applications in Moby is 7% with the reduction ratio of 400.

ACKNOWLEDGMENT

This research was supported by the National Science and Technology Major Project (Grant No. 2014ZX01030-101).

REFERENCES

- [1] L. Eeckhout, "Computer Architecture Performance Evaluation Methods," Synthesis Lectures on Computer Architecture, vol. 5. pp. 1–145, 2010.
- [2] J. L. Hennessy and D. A. Patterson, Computer architecture: a quantitative approach. 2012.
- [3] K. Hoste and L. Eeckhout, "Comparing Benchmarks Using Key Microarchitecture-Independent Characteristics," 2006 IEEE International Symposium on Workload Characterization, San Jose, CA, 2006, pp. 83-92.
- [4] K. Hoste and L. Eeckhout, "Microarchitecture-Independent Workload Characterization," in IEEE Micro, vol. 27, no. 3, pp. 63-72, May-June 2007.
- [5] L. Eeckhout, J. Sampson and B. Calder, "Exploiting program microarchitecture independent characteristics and phase behavior for reduced benchmark suite simulation," IEEE International. 2005 Proceedings of the IEEE Workload Characterization Symposium, 2005., 2005, pp. 2-12.
- [6] Ajay Joshi, Aashish Phansalkar, L. Eeckhout and L. K. John, "Measuring benchmark similarity using inherent program characteristics," in IEEE Transactions on Computers, vol. 55, no. 6, pp. 769-782, June 2006.
- [7] A. Phansalkar, A. Joshi, L. Eeckhout and L. K. John, "Measuring Program Similarity: Experiments with SPEC CPU Benchmark Suites," IEEE International Symposium on Performance Analysis of Systems and Software, 2005. ISPASS 2005., Austin, TX, 2005, pp. 10-20.
- [8] K. Hoste and L. Eeckhout, "Characterizing the Unique and Diverse Behaviors in Existing and Emerging General-Purpose and Domain-Specific Benchmark Suites," ISPASS 2008 - IEEE International Symposium on Performance Analysis of Systems and software, Austin, TX, 2008, pp. 157-168.
- [9] W. Alkohlani, J. Cook, and N. Siddique, "Insight into Application Performance Using Application-Dependent Characteristics," in Performance Modeling, Benchmarking and Simulation of High Performance Computer Systems - PMBS '14, vol. 8966, S. A. Jarvis, S. A. Wright, and S. D. Hammond, Eds. Cham: Springer International Publishing, 2015, pp. 107–128.
- [10] W. Alkohlani and J. Cook, "Towards Performance Predictive Application-Dependent Workload Characterization," 2012 SC Companion: High Performance Computing, Networking Storage and Analysis, Salt Lake City, UT, 2012, pp. 426-436.
- [11] A. Gutierrez et al., "Full-system analysis and characterization of interactive smartphone applications," 2011 IEEE International Symposium on Workload Characterization (IISWC), Austin, TX, 2011, pp. 81-90.
- [12] D. Pandiyan, S. Y. Lee and C. J. Wu, "Performance, energy characterizations and architectural implications of an emerging mobile platform benchmark suite - MobileBench," 2013 IEEE International Symposium on Workload Characterization (IISWC), Portland, OR, 2013, pp. 133-142.
- [13] Y. Huang, Z. Zha, M. Chen and L. Zhang, "Moby: A mobile benchmark suite for architectural simulators," 2014 IEEE International Symposium on Performance Analysis of Systems and Software (ISPASS), Monterey, CA, 2014, pp. 45-54.
- [14] P. M. Wells and G. S. Sohi, "Serializing instructions in system-intensive workloads: Amdahl's Law strikes again," 2008 IEEE 14th International Symposium on High Performance Computer Architecture, Salt Lake City, UT, 2008, pp. 264-275.
- [15] Wenczeko, E., and P. Wijekoon. "Improved estimation of the mean in one-parameter exponential families with known coefficient of variation." Statistical Papers 46.1 (2005): 101-115.
- [16] N. Binkert, S. Sardashti, R. Sen, K. Sewell, M. Shoaib, N. Vaish, M. D. Hill, D. A. Wood, B. Beckmann, G. Black, S. K. Reinhardt, A. Saidi, A. Basu, J. Hestness, D. R. Hower, and T. Krishna, "The gem5 simulator," ACM SIGARCH Comput. Archit. News, vol. 39, no. 2, p. 1, 2011.
- [17] D. A. Bader, Yue Li, Tao Li and V. Sachdeva, "BioPerf: a benchmark suite to evaluate high-performance computer architecture on bioinformatics applications," IEEE International. 2005 Proceedings of the IEEE Workload Characterization Symposium, 2005., 2005, pp. 163-173.
- [18] Chang-Burn Cho, A. V. Chande, Yue Li and Tao Li, "Workload characterization of biometric applications on Pentium 4 microarchitecture," IEEE International. 2005 Proceedings of the IEEE Workload Characterization Symposium, 2005., 2005, pp. 76-86.
- [19] Chunho Lee, M. Potkonjak, and W. H. Mangione-Smith, "MediaBench: a tool for evaluating and synthesizing multimedia and communications systems," in Proceedings of 30th Annual International Symposium on Microarchitecture, 1997, pp. 330–335.
- [20] SPEC CPU2006 benchmark suite. <http://www.spec.org/cpu2006/>

Markov-Based Forecasting Model for Enterprise Human Resources Internal Supply

Pu Li¹, Fengming Liu^{1,*} and Chengcheng Li¹

School of Management Science and Engineering, Shandong Normal University, Ji'nan 250014, China

*Corresponding author

Abstract—With the enhanced competition of enterprises on the talent, the rational manpower planning in enterprises to protect the human resources needs of enterprises becomes an important driving force to promote the development of enterprises. Human resources forecast is the premise and basis of manpower planning, which is of great significance to the sustainable development of enterprises. This paper focuses on the human resource internal supply forecast and establishes the forecasting model based on Markov chain. Firstly, this paper analyzes the factors that affect the internal human resource supply and compare the methods of human resources internal supply forecast. Then, this paper provides the steps of the human resource internal supply forecast in enterprises, determines the construction method of the forecasting model, and establishes the Markov forecast model. Finally, this paper uses the proposed model to predict the human resources within the M enterprise and gives suggestions for the internal supply of the M enterprise which have certain practical significance.

Keywords—human resource supply; markov chain; forecasting

I INTRODUCTION

Human resources forecast is mainly to predict the supply and demand of employees. In terms of human resources supply forecast, the external supply is affected by various environmental and market factors in most enterprises, which is difficult to forecast. And the supply of employees is mainly from the internal supply. Therefore, the forecast of internal supply in the enterprise has become the main aspect of human resources supply forecast. Shanshi Liu and Lingquan Wen [1] used Delphi method to forecast human resources. Zhiqiang Li et al. [2] introduced and reviewed the characteristics and applicable conditions of the four quantitative forecasting methods, such as, nonlinear regression forecasting, gray system prediction, Markov model and neural network prediction. Songyuan Li, Dechong Wang et al. [3] further explored the methods of supply and forecast, and these methods were more detailed classification and comparison. Through the study of these literatures, we can find that the Markov method becomes the main research method of human resources supply forecast with the advantages of non-aftereffect property, accessible data, simple and scientific method and wide application range.

In the application of human resources forecast research, Markov method has a wide range of applications and taken on good effect. Lagarde and Cairns [4] have modeled the movements of medical workers to solve the problems of human resources policies. Saad and Adnan et al. [5] used the Markov

chain to forecast the flow of university lecturers in order to advise on the recruitment and budget of university lecturers. Feyter [6], Dimitriou and Georgiou et al. [7] divided the staff into several groups, taking into account the flow of staff within and between departments. Raghavendra, Sankaran and Nilakantan [8], Nilakantan [9] extended the model to the organization of labor outsourcing, among which Nilakantan [9] also evaluated the different HR policies. In domestic, Hongli Sun and Yonggui He et al. [10] took the power plant as an example to validate the Markov model in practical application. Ying Yan and Juan Li [11], Siping Fang [12], Lu Zhang and Liyun Liu [13] and others also use the Markov model to study Human resource forecast.

In the view of human resource internal supply forecast, this paper uses the Markov chain to establish the forecasting model. And it also provides detailed steps and formulas which enable enterprises to more effectively predict the internal supply. The reasonable internal supply is of positive significance to the flow of the internal staff, the construction of the staff echelon, the development of the employee's career and the control of the labor cost.

II THE MARKOV FORECAST MODEL OF HUMAN RESOURCES INTERNAL SUPPLY

A. Modeling Idea

The Markov chain is a method of modeling the human resource internal supply using statistical principles. The basic idea is to calculate the transition probability of all types of employees through statistical analysis of historical data, and thus forecasts the future trend of employee turnover. The greatest feature of the application of Markov chain is the non-aftereffect property of Markov chain, that is, in a random process, the future state of the system is independent of the past state and is only related to the present state. Meanwhile, the application model of Markov chain also requires the smoothness of the transition trend, that is, the factors that affect the current state of the enterprise don't change greatly, and the flow of the staff has certain regularity, otherwise it needs to be recalculated [19].

III MARKOV CHAIN

If the state of the stochastic process is known at a particular time t_0 , the conditional probability distribution of the state at

time $t > t_0$ is independent of the state before time t_0 and only with the time t_0 . The process is called Markov process.

The Markov process is defined as follows:

Assuming that $\{X(t), t \in T\}$ is a stochastic process, I is state space, and for any positive integer $n \geq 3$, any time $t_1 < t_2 < \dots < t_n \in T$, and any state $x_1, x_2, \dots, x_n \in I$, when $P\{X(t_1) = x_1, X(t_2) = x_2, \dots, X(t_n) = x_n\} > 0$,

$$\begin{aligned} P\{X(t_n) = x_n | X(t_1) = x_1, X(t_2) = x_2, \dots, X(t_{n-1}) = x_{n-1}\} \\ = P\{X(t_n) = x_n | X(t_{n-1}) = x_{n-1}\} \end{aligned}$$

It is said that the stochastic process $\{X(t), t \in T\}$ has Markov property, and the process is called the Markov process [20].

Assuming that the random sequence $\{X_n, n \in T\}$ has the parameter set $T = \{0, 1, 2, \dots\}$ and the discrete state space I. If for any integer $n \in T$ and any state $i_0, i_1, \dots, i_{n+1} \in I$,

$$\begin{aligned} P\{X_{n+1} = i_{n+1} | X_0 = i_0, X_1 = i_1, \dots, X_n = i_n\} \\ = P\{X_{n+1} = i_{n+1} | X_n = i_n\} \end{aligned}$$

The random sequence $\{X_n, n \in T\}$ is called Markov chain [15].

The conditional probability $p_{ij}(n) = P\{X_{n+1} = j | X_n = i\}$ is called the one-step transition probability of the Markov chain $\{X_n, n \in T\}$ at time n , referred to as the transition probability. The conditional probability $p_{ij}^{(k)}(n) = P\{X_{n+k} = j | X_n = i\}$ is called the k -step transition probability of the Markov chain $\{X_n, n \in T\}$ at time n [16].

One-step transition probability makes up the matrix P

$$P = (p_{ij}) = \begin{bmatrix} p_{11} & p_{12} & \cdots & p_{1j} & \cdots \\ p_{21} & p_{22} & \cdots & p_{2j} & \cdots \\ \vdots & \vdots & \ddots & \vdots & \vdots \\ p_{ii} & p_{ii} & \cdots & p_{ij} & \cdots \\ \vdots & \vdots & \ddots & \vdots & \cdots \end{bmatrix}$$

It is called one-step transition probability matrix. The one-step transition probability p_{ij} has the following basic properties:

$$(1) p_{ii} \geq 0, i, j \in I$$

$$(2) \sum_{i \in I} p_{ij} = 1, i \in I \quad [20-21]$$

If the transition probability $p_{ij}(n)$ of the Markov chain $\{X_n, n \in T\}$ is independent of the time n for any $i, j \in I$, the Markov chain is the homogeneous Markov chain and $p_{ij}(n)$ as p_{ij} [20].

The transition probability of the homogeneous Markov chain is independent of the time n , that is, the transition probability is independent of the starting point of the transfer, which means that the transition probability is stationary. In this paper, the study of the internal supply forecast of human resources is based on the premise that human resources management policy remains unchanged, which is consistent with the requirements of Homogeneous Markov chain.

The construction of this model is as follows:

Supposed that x_n is the time t_n , usually in years as a unit;

Assuming that there are $n+1$ position categories in the enterprise, where the $n+1$ th category is the separation, the position state of each category is $A_i (i = 1, 2, 3, \dots, n)$. Each category has r position levels, so the position state of a certain level of category can be expressed as $A_{ir} (r = 1, 2, 3, \dots, n)$.

The transition probability $p_{A_{ir} A_{js}}$ represents the probability that the employees who are in the r th level of the i th category at time t_n are transferred to the s th level of the j th category in time t_{n+1} . The formula is $p_{A_{ir} A_{js}} = P\{x_{n+1} = A_{js} | x_n = A_{ir}\}$.

The construction of human resources internal supply forecasting model based on Markov chain is as follows:

(1) On the basis of thorough understanding of the enterprise, the positions are divided into different categories and levels to get the initial distribution matrix, i.e. $(p_{A_{11}}, \dots, p_{A_{1n}}, p_{A_{21}}, \dots, p_{A_{2n}}, p_{A_{31}}, \dots, p_{A_{3n}}, \dots, p_{A_{m1}}, \dots, p_{A_{mn}})$. Generally, there are three categories of positions within the enterprise, i.e. managers, technicians and ordinary staff, and the level is divided into grassroots staff, middle staff and senior staff.

(2) Collect and analyze the historical data of personnel changes in the enterprise, estimate the frequency and mode of the position transfer, and pay attention to the position category and the level of each position category to be consistent in each cycle. If the frequency and mode of transfer are definite and stable, the annual transition probability can be calculated, and

then the average transition probability can be calculated, such as Eq. (1). In Eq. (1), we assume that each year has the same weight.

$$P_{A_{ir}A_{js}} = \frac{1}{T} \sum_{t=0}^T \frac{n_{A_{ir}A_{js}}(t+1)}{n_{A_{ir}}(t)} \quad (1)$$

$$i=1,2,3,\dots,n \quad j=1,2,3,\dots,n \quad r=1,2,3,\dots,n \quad s=1,2,3,\dots,n$$

And $0 < p_{A_{ir}A_{js}} < 1$. T is the time range of the historical data, generally in years as a unit. $n_{A_{ir}A_{js}}(t+1)$ is the number of employees who moves from the r th level of i th category to the s th level of j th category during the period $(t, t+1)$. $n_{A_{ir}}(t)$ is the initial number of employees in the r th level of i th category at time t .

(3) Based on the average probability, the employee flow table and employee transfer matrix P are established. In the table employee flow, taking into account the situation of employee turnover, there is $p_{A_rA_{r+1}}$ in Table II.

$$P = \begin{pmatrix} P_{A_1A_1} & P_{A_1A_2} & \cdots & P_{A_1A_n} & \cdots & P_{A_1A_1} & P_{A_1A_2} & \cdots & P_{A_1A_m} & P_{A_1A_{m+1}} \\ P_{A_2A_1} & P_{A_2A_2} & \cdots & P_{A_2A_n} & \cdots & P_{A_2A_1} & P_{A_2A_2} & \cdots & P_{A_2A_m} & P_{A_2A_{m+1}} \\ \vdots & \vdots & \cdots & \vdots & \cdots & \vdots & \vdots & \cdots & \vdots & \vdots \\ P_{A_mA_1} & P_{A_mA_2} & \cdots & P_{A_mA_n} & \cdots & P_{A_mA_1} & P_{A_mA_2} & \cdots & P_{A_mA_m} & P_{A_mA_{m+1}} \\ \vdots & \vdots & \cdots & \vdots & \cdots & \vdots & \vdots & \cdots & \vdots & \vdots \\ P_{A_mA_1} & P_{A_mA_2} & \cdots & P_{A_mA_n} & \cdots & P_{A_mA_1} & P_{A_mA_2} & \cdots & P_{A_mA_m} & P_{A_mA_{m+1}} \\ P_{A_{m+1}A_1} & P_{A_{m+1}A_2} & \cdots & P_{A_{m+1}A_n} & \cdots & P_{A_{m+1}A_1} & P_{A_{m+1}A_2} & \cdots & P_{A_{m+1}A_m} & P_{A_{m+1}A_{m+1}} \\ P_{A_{m+2}A_1} & P_{A_{m+2}A_2} & \cdots & P_{A_{m+2}A_n} & \cdots & P_{A_{m+2}A_1} & P_{A_{m+2}A_2} & \cdots & P_{A_{m+2}A_m} & P_{A_{m+2}A_{m+1}} \\ \vdots & \vdots & \cdots & \vdots & \cdots & \vdots & \vdots & \cdots & \vdots & \vdots \\ P_{A_mA_1} & P_{A_mA_2} & \cdots & P_{A_mA_n} & \cdots & P_{A_mA_1} & P_{A_mA_2} & \cdots & P_{A_mA_m} & P_{A_mA_{m+1}} \end{pmatrix}$$

The matrix is a one-step transition probability matrix. P_n is a n-step transition probability matrix, which can forecast the flow of employees from the initial year to the nth year.

(4) Establish the forecasting model. According to the number of employees in the end of the year and the transition probability matrix, the number of employees of internal supply can be predicted. Assuming that the nth distribution matrix of employees

$$(p_{A_1}(n), \dots, p_{A_n}(n), p_{A_1}(n), \dots, p_{A_n}(n), p_{A_1}(n), \dots, p_{A_n}(n), \dots, p_{A_1}(n), \dots, p_{A_n}(n))$$

The formula is shown in Eq.(2).

$$\begin{aligned} & (p_{A_1}(n), \dots, p_{A_n}(n), p_{A_1}(n), \dots, p_{A_n}(n), p_{A_1}(n), \dots, p_{A_n}(n), \dots, p_{A_1}(n), \dots, p_{A_n}(n)) \quad (2) \\ & = (p_{A_1}, \dots, p_{A_n}, p_{A_1}, \dots, p_{A_n}, p_{A_1}, \dots, p_{A_n}, \dots, p_{A_1}, \dots, p_{A_n}) \bullet P_n \end{aligned}$$

IV CASE ANALYSIS

A. Total Amount of Human Resources

Although the growth rate of M enterprise has fluctuated, but it is greater than zero, which shows that the M enterprise were in the period of development and the total staff steadily increased in 2011-2016 (Figure 1). With the continuous expansion of the scale of production and operation, managers should pay more attention to the internal flow of employees, do a good job of internal supply of human resources, prevent the fault phenomena of supply, meanwhile attract outstanding talent to join, and the form a good flow of the talent.

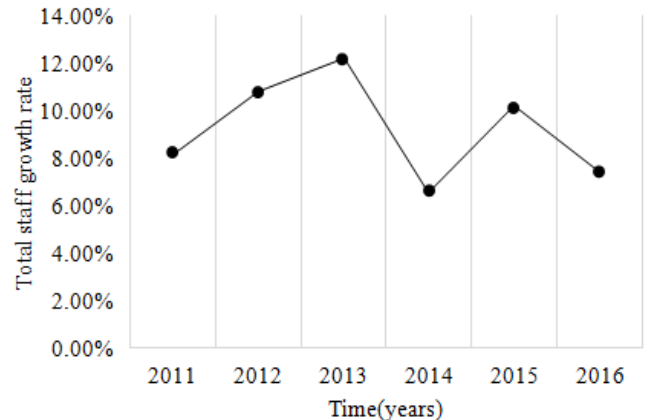


FIGURE I. TOTAL STAFF GROWTH RATE IN 2011-2016

According to the historical data in 2015 and the employee transition matrix, the number of human resource supply in 2016-2018 can be forecasted by the Eq. (2). The results are shown in Table I:

TABLE I. FORECASTING RESULTS IN 2016-2018

Time(years)\Category	M			T		G	Total amount
	M ₁	M ₂	M ₃	T ₁	T ₂	G	
2016	1	3	7	5	7	25	48
2017	1	3	7	4	6	21	42
2018	1	3	7	4	5	17	37

V ANALYSIS OF RESULTS AND SUGGESTIONS

Comparing the actual quantity of the various categories of the M enterprise in 2016 with the amount the model predicted, it can be seen that the error of the forecasting results of managers and technicians is small and the accuracy of the model is high. It can also be seen from the overall prediction that the number of supply forecast of managers shows a steady trend, which is related to the stability of organizational structure of the M enterprise and the vertical promotion mechanism. Therefore, in the practical application of the M enterprise, we can only use this model to predict the key to managers. Therefore, in the practical application of the M enterprise, we can only use this model to emphatically predict the category of managers, and the managers are also an important part of the enterprise. Other categories can refer to the results of this model.

and in combination with other forecasting methods to further improve the accuracy of the forecast.

The results of this paper show that it is feasible to apply the model to human resources planning in the enterprises. The flexibility of this model allows enterprises to predict only one category or level of positions, such as management category, etc. These categories are usually an important part of the enterprise and have stability and potential laws in terms of the flow of employees. The forecast of these categories is not only accurate, but also saves the forecasting cost of enterprises. At the same time, flexibility also means that this model can be combined with other forecasting methods to jointly forecast the human resources supply, which can provide reference and support for manpower planning. In addition, the model can also provide the structural distribution of the forecast quantity of the human resource internal supply, which can potentially sort out the internal positions, clarify the position level, and find gaps in talent. The prediction results of this model not only reflect the vertical promotion channel, but also reflect the possibility of horizontal flow of employees, which plays a good guiding role in the establishment of the development channels of employees and also play an important reference role in the construction of enterprise talent echelon.

VI CONCLUSIONS

The results of this paper show that it is feasible to apply this model to the human resources supply forecast. This model can provide information on the quantity and structure of human resources internal supply in enterprises, and provide support and reference for manpower planning. In addition, the model also can only forecast a certain category of positions in the enterprise, not only can forecast the different levels of positions within the category, but also can be used in conjunction with other methods to improve the accuracy of prediction, which reflects the flexibility of the model. The results of the model also reflect the number and channels of the horizontal and vertical flow of the staff in enterprises, which provides a reference and guidance for enterprises to develop the construction of staff echelon and establish a reserve talent pool. However, due to the limit of my knowledge level and the practice level, there are still shortcomings in the paper to be improved. Subject to time constraints, survey access to information is limited. At the same time, in the calculation of the transition probability is used on the average probability, which not according to the actual situation of enterprises to distinguish between different years and sets a different weight, resulting in a discrepancy between predicted results and actual data.

ACKNOWLEDGEMENT

This work was supported in part by the National Natural Science Foundation of China (No. 61170038, 61472231, 71701115), the National Social Science Foundation of China (No. 14BTQ049), the Shandong Natural Science Foundation(ZR2017MF058), and Special project for Internet development of social science planning special program of Shandong province(17CHLJ23).

REFERENCES

- [1] Liu S, Ling W. The Application of Delphi Method in Enterprise Human Resource Forecast. *Enterprise Economy*, 2003, (2):116-117.
- [2] Li Z, Wang Y. Quantitative Forecasting Method and Review of Four Kinds of Human Resources. *Statistics & Decision*, 2008, (7):30-32.
- [3] Li S, Wang D. Analysis on the Demand and Supply Forecast Method in Human Resource Planning. *Journal of Huanghe S&T University*, 2011, 13(1):79-81.
- [4] Lagarde M, Cairns J. Modelling human resources policies with Markov models: an illustration with the South African nursing labour market. *Health Care Management Science*, 2012, 15(3):270-282.
- [5] Saad S A, Adnan F A, Ibrahim H, et al. Manpower planning using Markov Chain model. 2014, 1605(1):1123-1127.
- [6] De Feyer T. Modelling heterogeneity in manpower planning: dividing the personnel system into more homogeneous subgroups: Research Articles. *Applied Stochastic Models in Business & Industry*, 2006, 22(4):321-334.
- [7] Dimitriou V A, Georgiou A C, Tsantas N. The multivariate non-homogeneous Markov manpower system in a departmental mobility framework. *European Journal of Operational Research*, 2013, 228(1):112-121.
- [8] Raghavendra B G, Sankaran J K, Nilakantan K. A proportionality model of Markov manpower systems. *Journal of Modelling in Management*, 2011, 6(1):100-122.
- [9] Nilakantan K. Evaluation of staffing policies in Markov manpower systems and their extension to organizations with outsource personnel. *Journal of the Operational Research Society*, 2015, 66(8):1324-1340.
- [10] Sun H, He Y, Zhang W, Han Y. Application of Markov model in human resource supply forecasting in enterprises. *Journal of North China Electric Power University (Natural Science Edition)*, 2004, 31(5):56-58.
- [11] Yan Y, Li J. Application of Markov Transfer Matrix in Human Resource Supply Forecasting. *Market Forum*, 2011, 2011, (9):46-47.
- [12] Fang S. Forecast of Business Internal Human Resources Supply Based on Markov Chain. *Journal of Beijing Polytechnic College*, 2004, 3(4):101-103.
- [13] Zhang L, Liu L. Application of Markov Chain Model in Human Resource Forecasting [J]. *Modern Business Trade Industry*, 2013, (2):97-98.
- [14] Ding Y S, Liu F M, Tang B Y, Context-Sensitive Trust Computing in Distributed Environments", *Knowledge-Based Systems*, 2012(28) 105-114.
- [15] Liu F M, Li X, Ding Y S, Zhao H F, Liu X Y, Ma Y H, Tang B Y, A Social Network-Based Trust-Aware Propagation Model for P2P Systems, *Knowledge-Based Systems*, 2013(41), 8-15.
- [16] Liu F M, Wang L, Gao L, Li H X, Zhao H F, Sok Khim Men. A Web Service Trust Evaluation Model Based on Small-World Networks, *Knowledge-Based Systems*, 2014(57) 161-167.
- [17] Liu F M, Wang L, Henric Johnson, Zhao H F, Analysis of Network Trust Dynamics Based on Evolutionary Game, *Scientia Iranica, Transaction E: Industrial Engineering*, 2015(22.6): 2548-2557.
- [18] Liu F M, Zhu X Q, Hu Y X, Ren L H, Henric Johnson, A Cloud Theory-Based Trust Computing Model in Social Networks. *Entropy* 2017, 19(1), 11.
- [19] Huo Y. The Construction and Application of Company Human Resources Planning Model Base Take F Mine as the Example. *Taiyuan: Taiyuan University of Technology*, 2012
- [20] Wang L. Probability Theory and Stochastic Process: Theory History and Application. *Beijing: Tsinghua University Press*, 2012.
- [21] Sun Q, Sun H. Random process: content, methods and techniques. *Wuhan: Huazhong University of Science & Technology Press*, 2004.

The Coordinated Replenishment Policy in a decentralized Assembly System

Jianhong Yu^{1,*}

School of Business, Jianghan University, Wuhan, China

Abstract—The synchronization and coordination of material flows in the assembly system is much more important and complex. To analyze how to coordinate the material flows for the assembly supply chain, we consider an assembly system with two component-suppliers and one manufacturer, under stochastic finished product demand. Two replenishment policies are proposed and analyzed. One is the decentralized replenishment policy without horizontal coordination, and the other is the coordinated replenishment policy with horizontal coordination. Results show that there is a unique optimal solution to minimize the supply chain cost, and coordination replenishment policy can efficiently deduce supply chain cost due to the horizontal coordination.

Keywords—coordinated replenishment; assembly system; horizontal coordination

I. INTRODUCTION

The coordination of components is a key issue in assembly system [1]. In an assembly system, the finished product is assembled with hundreds or thousands components. Due to the complexity and difficulty of coordination, in practice, most manufacturers only consider the vertical coordination between suppliers and the manufacturer, but don't consider the horizontal coordination between suppliers. However, in assembly system, the quantity of final products is decided by the least quantity of components. The discoordination between suppliers not only reduces the service level, but also increases the components' inventory cost. Therefore, how to realize the coordination between suppliers is very important.

Nowadays, some researchers have done some relative research. Khouja and Goyal [2] conduct a comprehensive review of coordinated replenishment literature from 1989 to 2005, which addresses constrained, stochastic, and dynamic demands. De Boeck and Vandaele [3] analyze the problem of synchronizing material flows, and find synchronization can reduce the overall pipeline inventory. Ma and Gong [4] set a production-distribution model, and propose to order parts replenishments proportionally between various suppliers. De Boeck and Vandaele [5] study a generic first-come first-serve assembly system, and find that parts supply has to be synchronized and needs a cap in order to shut down the input streams. Limère [6] analyzes a multi-component assembly system, and finds that hybrid materials feeding policies is preferred. Li et al. [7] propose a holding-cost subsidy contract to coordinate the decentralized assembly system. Most recently, Li et al. [8] investigated collaborative scheduling in the assembly system, and show that the performance of supply-hub

coordinated schedule is superior to that of decision made independently by the manufacturer and the supplier.

From the above literatures, most researchers only discuss the collaboration of upstream materials in centralized decision model. Though some literatures discusses how to collaborate upstream materials of assembly system, there are still issues that need to be addressed. As we all know, the bill of material (BOM) is very important to the assembly system. A bad decision on one component's replenishment in a BOM will invalidate other components' optimal replenishment decisions, thus leading to low SC efficiency [9]. In this paper, we consider the horizontal coordination between suppliers and propose a simple and practical replenishment policy based on (Q, r) policy, which is popular used by many manufacturers in practice.

II. PROBLEM DESCRIPTION AND NOTATIONS

We consider a two-key-suppliers and one-manufacturer system, where in each supplier provides a different component. The manufacturer needs the two key parts to produce a final product. It is an assemble-to-order (ATO) system. The components are replenished according to the (Q, r) policy. Without loss of generality, the time for assembling the components is assumed to be negligible, which is appropriate when the suppliers are far from the manufacturer. In addition, we don't consider the residual value of surplus products and the assembly cost. Therefore, products are only assembled to order and no parts are sent to the manufacturer without orders from customers. The unmet demand is fully backordered.

We assume the demand of the finished product is stochastic, and the per unit time demand during lead time follows a normal distribution with mean μ and standard deviation σ . The two suppliers are reliable. Without loss of generality, we assume the lead time of component 1 is longer than that of component 2, and both suppliers have the same internal service level.

The inventory control policy is CVMI (Consignment Vendor Management Inventory), that is suppliers are in charge of the replenishment policy of components, and suppliers are only paid for the components used by the manufacturer. The manufacturer adopts a multi-period rolling plan and information sharing to coordinate material flows, that is, the vertical coordination between suppliers and manufacturer is realized. However, according to the bill of materials (BOM), to improve the performance of the whole system, not only the vertical coordination is needed, but also the horizontal coordination between suppliers is very necessary. The horizontal coordination can efficiently deduce the mismatching probability of

components, and can lower the probability of backorders and increase customer service level.

In our model, suppliers bear the inventory holding cost, which consist of the average regular and safety inventory

holding cost and backlogging inventory cost. In addition, the backlogging inventory cost is the inventory cost that caused by the stockout of other parts.

The notations are summarized in table 1.

TABLE I. THE DEFINITION OF NOTATIONS

notation	definition	notation	definition
i	the number of component, $i = 1, 2$	$f_i(x_i)$	the density function of x_i
L_i	replenishment lead time of component i	$F_i(x_i)$	the cumulative probability function of x_i ,
h_i	the inventory cost per unit per time of component i	μ_i	the mean of demand for component i during lead time L_i , where $\mu_i = \mu L_i$
F_i	the fixed replenishment cost of components i per replenishment cycle	σ_i	the standard deviation of demand for component i during lead time L_i , where $\sigma_i = \sigma\sqrt{L_i}$
D	the expected value of annual demand	z	the safety factor, $z > 0$
π	the penalty cost per unit backorder	$\Phi(z)$	the internal service level of component i
x_i	the lead time demand of component i	P	the customer service level for the manufacturer
Q_i	the replenishment quantity of part i	P^0	the lowest limited service level, that is $P^0 < P$
r_i	the reorder point of component i	z^0	the value of safety factor when $P = P^0$

III. THE DECENTRALIZED REPLENISHMENT POLICY WITHOUT HORIZONTAL COORDINATION

In this replenishment policy, according to manufacturer's demand planning and service level requirement, the suppliers make decisions on component replenishment plans to minimize its cost. The horizontal coordination between suppliers is not considered, which may result in excess inventory of one part type, while the other component is out of stock.

The probability of component i out of stock during the lead time is $P\{x_i > r_i\} = \int_{r_i}^{+\infty} f_i(x_i)dx_i = 1 - \Phi(z)$, where $\Phi(z)$ is the internal service level of component i . When $\Phi(z)$ is high, such as $\Phi(z) \in (0.90, 0.99)$, the probability of having both components shortages simultaneously is very small and negligible [10]. The expected backorder per cycle can be expressed as $B_i(r_i) = \int_{r_i}^{\infty} (x_i - r_i)f_i(x_i)dx_i$. So, the expected cost of supplier i per unit time can be expressed as:

$$E[TC_{si}] = \frac{D}{Q_i} F_i + h_i \left(\frac{Q_i}{2} + z\sigma\sqrt{L_i} \right) + h_i \frac{D}{Q_j} \int_{r_j}^{+\infty} (x_j - r_j) f_j(x_j) dx_j \quad (1)$$

Where the first term is the fixed replenishment cost per unit time of supplier i ; the second term is the regular and safety inventory cost per unit time of supplier i ; while the third term is the backlogging inventory cost per unit time of supplier i due to lack of component j , ($j = 1, 2, j \neq i$). Note that backlogging is caused by the shortage of the components.

Management requires customer service level satisfies $P = \Phi(z)^2 \geq P^0 = \Phi(z^0)^2$, that is $\Phi(z) \geq \Phi(z^0)$.

The expected cost of the manufacturer per unit time can be expressed as:

$$E[TC_m] = \pi \sum_{i=1}^2 \frac{D}{Q_i} \int_{r_i}^{\infty} (x_i - r_i) f_i(x_i) dx_i \quad (2)$$

The expected cost of the whole supply chain per unit time $E[TC_{sc}] = E[TC_{si}] + E[TC_m]$.

A. Proposition 1

In the decentralized replenishment policy without horizontal coordination, the expected cost per unit time of supplier i is convex in Q_i , and there is a unique optimal quantity Q_i^* that minimizes $E[TC_{si}]$ and $z = z^0$. Therefore, the optimal quantity can be characterized as:

$$Q_i^* = \sqrt{2DF_i/h_i} \quad (3)$$

Proof: Due to lacking of horizontal coordination, the expect cost of supplier i is strictly increasing in z , so there is $z = z^0$. Obviously, the expect cost of supplier i is strictly convex in Q , and we get the optimal value from the first order condition.

IV. THE COORDINATED REPLENISHMENT POLICY WITH HORIZONTAL COORDINATION

In this paper, we use the common replenishment cycle to coordinate different components' replenishment, in order to optimize the total cost and improve service level. To simplify, a base replenishment quantity is used to instead of the common replenishment cycle. Let Q be the base replenishment quantity. Without loss of generality, let Q be the smaller quantity of component, and let kQ be the replenishment quantity of supplier 2, where k is an integer.

The customer service level under The coordinated replenishment policy with horizontal coordination is limited to the lowest internal service level, so P satisfies $P = \Phi(z) \geq \Phi(z^0)$.

The expected supply chain cost per unit time can thus be expressed as:

$$\begin{aligned}
E[TC_{sc}] = & \frac{D}{Q}F_1 + h_1\left(\frac{Q}{2} + z\sigma\sqrt{L_1}\right) + \frac{D}{kQ}h_1\left[\int_{\mu L_1+z\sigma\sqrt{L_2}}^{r_1}(x_1 - \mu L_1 - z\sigma\sqrt{L_2})f_1(x_1)dx_1\right. \\
& + \int_{r_1}^{\infty}(z\sigma(\sqrt{L_1} - \sqrt{L_2})f_1(x_1)dx_1)] + \frac{D}{kQ}F_2 + h_2\left(\frac{kQ}{2} + z\sigma\sqrt{L_2}\right) \\
& + h_2\frac{D}{kQ}(k-1)\int_{r_1}^{\infty}(x_1 - r_1)f_1(x_1)dx_1 + \pi\frac{D}{kQ}[(k-1)\int_{r_1}^{\infty}(x_1 - r_1)f_1(x_1)dx_1 \\
& \left. + \int_{\mu L_1+z\sigma\sqrt{L_2}}^{\infty}[x_1 - (\mu L_1 + z\sigma\sqrt{L_2})]f_1(x_1)dx_1]\right]
\end{aligned} \tag{5}$$

Where the first three terms are respectively the replenishment cost, the regular and safety inventory cost, and the backlogging inventory cost of component 1; while the 4-6 terms are those of component 2, the 7th term is the backorder cost per unit time. To simplify the above function, let

$$\begin{aligned}
B = & F_2 - (h_2 + \pi)\int_{r_1}^{\infty}(x_1 - r_1)f_1(x_1)dx_1 + \pi\int_{\mu L_1+z\sigma\sqrt{L_2}}^{\infty}[x_1 - (\mu L_1 + z\sigma\sqrt{L_2})]f_1(x_1)dx_1 \\
& + h_1\left[\int_{\mu L_1+z\sigma\sqrt{L_2}}^{r_1}(x_1 - \mu L_1 - z\sigma\sqrt{L_2})f_1(x_1)dx_1 + \int_{r_1}^{\infty}(z\sigma(\sqrt{L_1} - \sqrt{L_2})f_1(x_1)dx_1)\right], \\
\text{and } A = & F_1 + (h_2 + \pi)\int_{r_1}^{\infty}(x_1 - r_1)f_1(x_1)dx_1.
\end{aligned}$$

The expected supply chain cost can be reformed as,

$$E[TC_{sc}] = \frac{D}{Q}A + \frac{h_1}{2}Q + \frac{D}{kQ}B + \frac{h_2}{2}kQ + (h_1\sqrt{L_1} + h_2\sqrt{L_2})z\sigma$$

To obtain the following Proposition, we need to relax the integral constraint of k .

A. Proposition 2

There exists a unique optimal solution that minimizes the expected supply chain cost, when $B > 0$. For any given z , $E[TC_{sc}]$ is a joint convex function of Q and k , and the optimal value can be denoted as

$$Q^* = \sqrt{\frac{2DA}{h_1}} \quad \text{and} \quad k^* = \sqrt{\frac{Bh_1}{Ah_2}} \tag{6}$$

Proof: Relaxing the integral constraint of k , we can get the derivative of $E[TC_{sc}]$ with respect to z , Q and k ,

$$\begin{aligned}
\frac{\partial E[TC_{sc}]}{\partial z} = & \sigma(h_1\sqrt{L_1} + h_2\sqrt{L_2}) - \frac{(k-1)D}{kQ}(h_2 + \pi)\sigma\sqrt{L_1}\int_{r_1}^{\infty}f_1(x_1)dx_1 \\
& - \frac{D}{kQ}\pi\sigma\sqrt{L_2}\int_{\mu L_1+z\sigma\sqrt{L_2}}^{\infty}f_1(x_1)dx_1
\end{aligned}$$

$$\frac{\partial^2 E[TC_{sc}]}{\partial z^2} = \frac{(k-1)D}{kQ}(h_2 + \pi)\sigma^2L_1f_1(r_1) + \frac{D}{kQ}\pi\sigma^2L_2f_1(\mu L_1 + z\sigma\sqrt{L_2}) > 0$$

$$\frac{\partial E[TC_{sc}]}{\partial Q} = -\frac{D}{Q^2}(A + \frac{B}{k}) + \frac{h_1 + kh_2}{2}$$

$$\frac{\partial^2 E[TC_{sc}]}{\partial Q^2} = \frac{2D}{Q^3}(A + \frac{B}{k}) > 0; \quad \frac{\partial E[TC_{sc}]}{\partial k} = -\frac{DB}{k^2Q} + \frac{h_2Q}{2}$$

$$\frac{\partial^2 E[TC_{sc}]}{\partial k^2} = \frac{2DB}{k^3Q} > 0$$

It is obviously that $\lim_{z \rightarrow \infty} \frac{\partial E[TC_{sc}]}{\partial z} = \sigma(h_1\sqrt{L_1} + h_2\sqrt{L_2}) > 0$ and $z > 0$. Therefore, there is a unique optimal solution (Q, k, z) to minimize the supply chain cost per unit time.

For any giving z , it is easy to know that $E[TC_{sc}]$ is strictly convex in Q for any giving $k > 0$, and it is also strictly convex in k for any giving $Q > 0$. To prove $E[TC_{sc}]$ is joint strictly in Q and k , we get the optimal value $Q = \sqrt{\frac{2D(A + \frac{B}{k})}{h_1 + kh_2}}$ and $k = \sqrt{\frac{2DB}{h_2Q^2}}$. Submit them into the Hessian matrix about Q and k of $E[TC_{sc}]$, which satisfies the equation $H = \frac{4D^2}{k^4Q^4}(kAB + B^2) - (\frac{DB}{k^2Q^2} + \frac{h_2}{2}) = \frac{kA}{B}h_2^2 > 0$. Therefore, $E[TC_{sc}]$ is joint convex in Q and k , and the optimal values satisfy the first order condition.

Substituting (2) and (3) into (1), we can obtain the optimal supply chain cost,

$$E[TC_{sc}] = \sqrt{2DAh_1} + \sqrt{2DBh_2} + (h_1\sqrt{L_1} + h_2\sqrt{L_2})z\sigma \tag{7}$$

V. NUMERICAL ANALYSIS

To further analyze the coordinated replenishment policy with horizontal coordination and the effect parameters, let $D = 5500$, $\mu = 15$, $\sigma = 10$, $L_1 = 25$ days, $L_2 = 20$ days, $h_1 = 35$, $h_2 = 25$, $F_1 = 100$, $F_2 = 350$, $\pi = 80$, and $\Phi(z^0) \geq 95\%$. Let superscript d and c respectively denote the decentralized replenishment policy without horizontal coordination and the coordinated replenishment policy with horizontal coordination.

The results of effect of service level are shown in Figure 2. The left picture of Figure 2 analyzes the effect of internal service level $\Phi(z)$ on the supply chain cost. Let $\Phi(z)$ range from 90% to 99.99%, and find that supply chain costs of both strategies first decrease with $\Phi(z)$ and then increase. However, the inflection points of the two cost curves are different, and that of the coordinated replenishment policy is much lower than that of the decentralized replenishment policy. The right picture of Figure 2 shows the impacts of P^0 are different from $\Phi(z)$. It shows that a low P^0 has not any effect on the supply chain cost of the coordinated replenishment policy. However, when P^0 is higher enough, the cost curves will significantly go up. The effect of P^0 on the decentralized replenishment policy is similar to that of $\Phi(z)$, due to $\Phi(z)^2 = P$. Obviously that the coordinated replenishment policy always dominates the other policy, regardless of the service level.

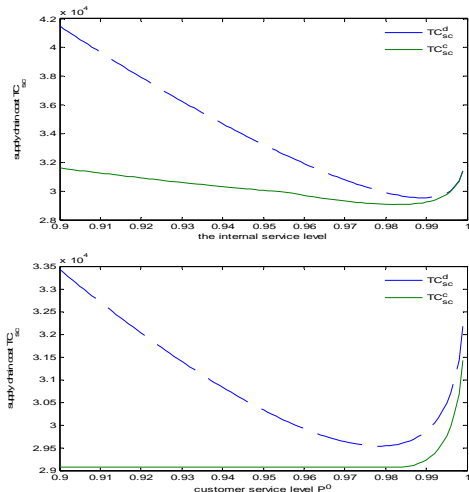


FIGURE I. THE EFFECT OF SERVICE LEVEL

The results of parameters' effects are shown in Table 2, where the base data means the results are calculated based on the data in the above section, and $\Delta TC_{sc} = \frac{TC_{sc}^d - TC_{sc}^c}{TC_{sc}^d} * 100\%$. Obviously, the customer service level under the decentralized policy always satisfies $P = \Phi(z^0)^2 = 90.25\%$.

TABLE II. THE IMPACTS OF PARAMETERS ON BOTH POLICIES

parameters	P^c	TC_s^d	TC_s^c	ΔTC	parameters	P^c	TC_s^d	TC_s^c	ΔTC	
Base data	98.2	332	290	12.5	Base data	98.2	332	290	12.5	
8%	46	68	75	7%	8%	46	68	77	2%	
45	98.0	352	314	10.7	75	97.9	296	262	11.4	
0	4%	35	55	3%	D	00	6%	65	77	
35	98.2	339	298	11.8	50	97.3	254	229	9.89	
F ₂	0	0%	32	96	9%	00	9%	18	03	
20	98.4	318	272	14.2	30	98.2	332	290	12.5	
0	5%	14	93	1%	μ	8%	46	68	7%	
10	98.1	305	245	19.6	20	98.2	332	290	12.5	
0	3%	01	15	3%	8%	46	68	7%		
35	96.9	404	349	13.4	25	98.1	426	356	16.4	
0%	15	77	6%		7%	90	57	7%		
h ₂	25	98.2	357	313	12.4	20	98.2	379	323	14.7
8%	76	35	1%		2%	68	69	5%		
15	98.2	304	267	12.4	70	98.5	341	292	14.3	
6%	99	00	6%		0%	66	80	0%		
5	98.5	236	209	11.7	50	97.9	323	288	10.8	
6%	80	03	3%		4%	26	18	5%		

Table 2 shows that when the parameters decrease, the expected supply chain cost of both policies will decrease. Customer service levels of coordinated policy increases with D and π , and decrease with σ . The cost advantage of coordinated policy increases with h_2 and σ , and decreases with h_2 and π , meanwhile there is no clear relationship between cost and D . However, coordinated policy still outperforms the decentralized policy, even when π is much larger. Results also show that component parameters have different effects on customer service level. P^c increases as F_2 and h_2 decrease, but only when they vary within a certain range.

VI. CONCLUSION

In assembly systems, shortage of one or several components may discontinue the whole production process and result in huge loss. Coordination and synchronization of material flows is very important for improving supply chain efficiency. This paper studies the coordination replenishment policies in a decentralized assembly system. We propose and compare two different policies, which are the decentralized replenishment policy without horizontal coordination and the coordination replenishment policy with horizontal coordination. The results show that, (1) There is a unique optimal solution in the both replenishment policies. (2) Based on the parameters analysis, the coordination replenishment policy with horizontal coordination has obviously cost advantage than the decentralized replenishment policy without horizontal coordination. (3) The customer service level P^0 can affect the supply chain cost of the decentralized replenishment policy, but it has no impact on that of the coordinated replenishment policy when it is lower than a certain value.

ACKNOWLEDGEMENT

This research was financially supported by Hubei Provincial Department of Education Humanities and social sciences research project (17G058), the Natural Sciences Foundation of China under Grants NSFC71471084, the key open-ended program of Wuhan Research Institute of Jianghan University (IWHS2016104), and the Funding under the Project of "Superiority Characteristic Disciplines Group of Hubei Provincial Higher Universities-Urban Circle Economy and Industrial Integration Management".

REFERENCES

- [1] J. S. Song, P. Zipkin. Supply chain operations: assemble-to-order systems. Handbooks in Operation Research and Management Science, 11. Supply Chain Management. Elsevier, Amsterdam, The Netherlands. (2003)
- [2] M. Khouja, S. Goyal. A review of the joint replenishment problem literature: 1989-2005. Eur. J. Oper. Res. 186(2008) 1-16.
- [3] L. D. Boeck, N. Vandaele.. Coordination and synchronization of material flows in supply chains: an analytical approach. Int. J. Prod. Econ. 116(2008) 119-207.
- [4] S. H. Ma, F. M. Gong. Collaborative decision of distribution lot-sizing among suppliers based on supply-hub. Industrial Engineering and Management, 14(2009) 1-9.
- [5] L. D. Boeck, N. Vandaele. Analytical analysis of a generic assembly system. Int. J. Prod. Econ. 131(2011) 107-114.
- [6] V. Limère. To kit or not to kit: optimizing part feeding in the automotive assembly industry. 4OR-Q. J. Oper. Res. 11(2013) 97-98.
- [7] S. Y. Li, D. Z. Zhang, F. P. Jin. Base inventory cooperation strategy of multi-parts with supply-hub. International Journal of Business and Management, 8(2013) 96-104.
- [8] G. Li, F. Lv, X. Guan. Collaborative scheduling model for supply-hub with multiple suppliers and multiple manufacturers. The Scientific World Journal, <http://dx.doi.org/10.1155/2014/894573>, (2014).
- [9] O. Fujiwara, D. Swdarage. An optimal (Q, r) policy for a multipart assembly system under stochastic part procurement lead times[J]. Eur. J. Oper. Res. 100(1997) 550-556.
- [10] H. Gurnani, R. Akella, J. Lehoczky. Supply management in assembly systems with random yield and random demand[J]. IIE Transaction, 32(2000) 701-714.

Hardware Design of SUAV Flight Control System Based on STM32F427

Tao Yang*, Liren Chai and Gang Wang

China Academy of Aerospace Aerodynamics, Beijing, 100074, China

*Corresponding author

Abstract—As an emerging high-tech device, the SUAV plays a more and more significant role in military and civilian fields because of its advantages such as low cost, high safety, flexible usability and easy maintenance. The flight control system is the core of the SUAV, which exerts a big influence on SUAV performance to a large extent. In order to meet the requirement of low power consumption, simple structure and high performance, this paper designs the hardware of SUAV flight control system based on STM32F427. The modular hardware design is introduced in detail, including the digital control circuit, the power circuit, the sensor circuit and the interface circuit. The flight control system designed in this paper is feasible, effective and reliable, fulfilling the design demand and improving the control and operation performance of the SUAV.

Keywords—SUAV; flight control; hardware design; STM32F427

I INTRODUCTION

In recent times, study of the small unmanned aerial vehicle (SUAV) is attracting more and more attention as a result of its simple structure, easy maintenance, flexible take-off and landing, high cost-benefit ratio and great maneuvering performance[1,2]. SUAV is widely applied in different fields, accomplishing different tasks, to name a few, aerial photography, geographical mapping, remote sensing and telemetry, power line inspection, forest fire fighting, atmosphere monitoring, environmental protection, resource exploration, pesticide spraying and plant protection [3,4]. The glorious prospect arouses a large amount of manpower and financial investment in the study of all kinds of advanced SUAV technologies among various countries all over the world. With the utilization of new technologies, SUAV is becoming increasingly indispensable. The air-rang, flight height, flight duration, flight speed, ceiling, loading capacity, reliability and maintainability are the main performance indicators of SUAV, which depend largely on performance of the flight control system [5].

The flight control system is the top priority in the SUAV. The control system accepts the command from the ground station and acquires sensors output for data fusion. And then it sends the control command to different actuators according to the corresponding control laws. The flight control system conducts navigation, control, communication and other core missions during the SUAV flight [6]. It is of big research value when it comes to autonomous flight, route planning, airborne equipment management, cooperative control of multiple vehicles, and security administration of prohibited area. For

higher flight quality, the flight control system has to respond rapidly and work efficiently, while low power consumption, small size and light weight is also required. Stable and effective hardware design of the flight control system is the basis of all these. Under this background, the hardware is designed with two STM32F427 as its core. One STM32F427 executes the control algorithm and digital communication, captures PWM input signals, and outputs PWM driving signals. In the meantime, the other one communicates with all kinds of sensors.

II WORKING PRINCIPLES OF THE UAV FLIGHT CONTROL SYSTEM

During the SUAV flight missions, the flight control system downloads waypoint information and instructions of the ground station via data radio at first. And then the flight parameters are obtained according output of different sensors, thus calculating the current SUAV attitude and position. According to the waypoints set in advance, the flight control system figures out the actuator control value, with it the control surface rotating correspondingly [7]. As shown in Figure I, the data communication system conducts data communication between the ground station and the flight control system, ensuring correct transmission of the command and waypoints information. After analysis of the sensor data, the flight control system sends the position command to the actuator, thereby changing the flight attitude. What's more, with the help of data radio, the flight control system sends back the flight status and the airborne equipment status to the ground station for display and control, in order to inform the manipulator of the real-time flight attitude and position, thus ensuring the flight security and stability in case of emergency with the stringent control exerted in time by the manipulator. To summarize, function of the flight control system can be divided into two parts. On one hand, the flight control system keeps the SUAV flight safe and stable with preset rules, and changes the attitude and waypoints after receiving new instructions from the ground station. One the other hand, it manages airborne equipment, including flight parameters acquisition and status parameters storage as well as control and monitoring of the airborne equipment.

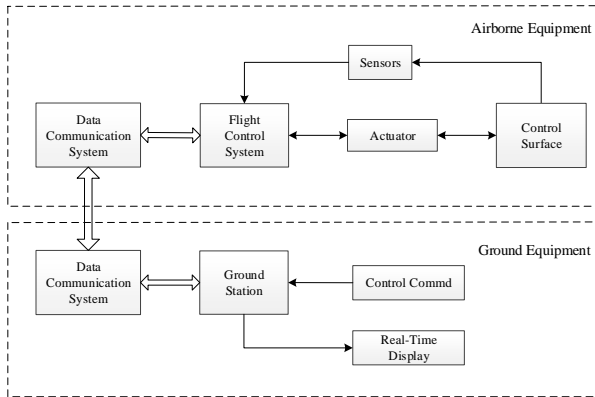


FIGURE I. BLOCK DIAGRAM OF THE FLIGHT CONTROL SYSTEM

III THE HARDWARE DESIGN

Due to the complex hardware design of the flight control system. It is introduced in the form of modular design with the following 4 sections: the digital control circuit, the power circuit, the sensor circuit and the interface circuit. There are two control chips STM32F427 in the digital control circuit. One cooperates with the other one to conduct digital control. The power circuit offers power supply for the whole hardware. The sensor circuit is made of various sensors which provides the attitude and position reference. The interface circuit contains the communication interface and the PWM and capture interface.

A. The Digital Control Circuit

The digital control circuit contains two control chips STM32F427. The STM32F427 device is based on the high-performance ARM Cortex-M4 32-bit RISC core operating at a frequency of up to 180 MHz. The Cortex-M4 core features a floating point unit, and it implements a memory protection unit. It incorporates high-speed embedded memories with Flash memory up to 2 Mbyte, SRAM up to 256 Kbytes, and backup SRAM up to 4 Kbytes. There are various enhanced I/Os and peripherals as well as standard and advanced communication interfaces. Thanks to its high computing speed, large Flash and SRAM memory, powerful peripherals, and rich communication interfaces, STM32F427 is one of the perfect choices for SUAV flight control.

As shown in Figure II, the STM32F427 in the left is the control core of the flight system with the control algorithm performed in it. It captures the PWM input signals to obtain the actuator throttle command, and it generates the corresponding PWM driving signals for the actuator. It reserves the UART, CAN and SBUS communication interfaces. As for data uploading and downloading, a FRAM chip with memory up to 256KB stores the control parameters and preset waypoints information; a 8GB EMMC chip records the airborne flight data online in real time; all the data mentioned above can be downloaded from the flight control system by a USB interface for offline data analysis and flight replay. A UART interface links the left STM32F427 and the right one together. The STM32F427 in the right acquires information from all kinds of sensors, calculates the flight attitude and position, and reports back to the left control chip simultaneously. The 3-Axis digital

compass module combines 3-axis magneto-resistive sensors and 3-axis MEMS accelerometers; The 3D AHRS/VRU/IMU module outputs 3D orientation, 3D rate of turn, 3D accelerations, and 3D magnetic field; The altimeter provides a precise digital 24 bit pressure and temperature value; The GNSS module can receive up to three GNSS systems (GPS/Galileo) together with BeiDou or GLONASS) concurrently. Also there is a FRAM chip recording the configuration parameters of the various sensors.

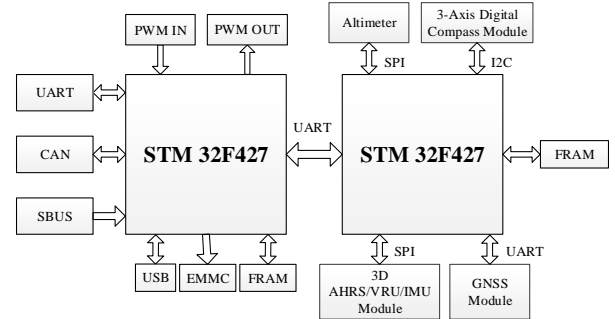


FIGURE II. BLOCK DIAGRAM OF THE DIGITAL CONTROL CIRCUIT

B. The Power Circuit

The system power input can be from batteries or the DC power supply, with a wide range input from 9V to 36V. As shown in Figure III, the complete 8A switch mode DC/DC power supply LTM4613 transforms the power input into +6V with ultralow noise as the power source of actuator PWM driving output. At the same time, the electromagnetic compatible (EMC) DC/DC buck converter LTM8033 transforms the power input into +5V, with output current up to 3A. +5V is the power source of USB interface. The low-dropout linear regulator TPS74091 transforms +5V into +3.3V, a multiple power source for the control core STM32F427, the altimeter, the GNSS module, the 3D AHRS/VRU/IMU module, the 3-Axis digital compass module, the UART and CAN communication circuit, and the FRAM and EMMC chip.

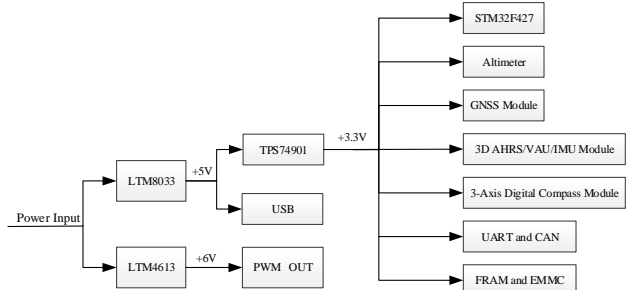


FIGURE III. SYSTEM POWER SUPPLY

C. The Sensor Circuit

1) The 3D AHRS/VRU/IMU module

As shown in Figure IV, the 3D AHRS/VRU/IMU module selected is MTi-3-AHRS-8A7G6. It is available as an inertial measurement unit (IMU), vertical reference unit (VRU) or attitude and heading reference system (AHRS). This module is fully functional with different self-contained components,

rendering it easy to design. And only a few hardware components are needed. Signals are fully processed onboard, requiring very little resources from the control chip STM32F427 over SPI interface. The host can read out the data by customized frequency and output format. Its roll/pitch accuracy is 1.0° RMS, and its yaw accuracy is 2° RMS under dynamic conditions, which is excellent for control and navigation of SUAV.

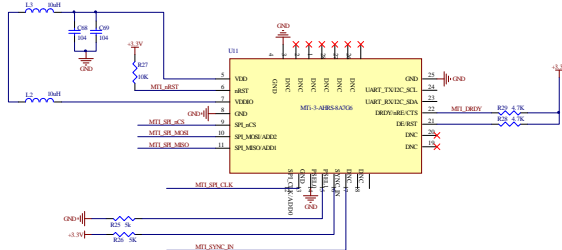


FIGURE IV. THE 3D AHRS/VRU/IMU MODULE CIRCUIT

2) The altimeter

As shown in Figure V, the altimeter sensor selected is MS5803. It is a high-resolution 24 bit altimeter sensor, communicating with STM32F427 via SPI interface. Its altitude resolution can be up to 20 cm. There are different operation modes, allowing the user to optimize for conversion speed and current consumption. The communication protocol is simple, without the need of programming internal registers in the device.

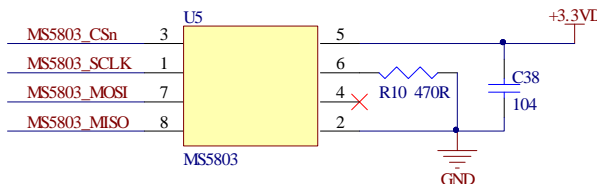


FIGURE V. THE ALTIMETER CIRCUIT

3) The GNSS module

As shown in Figure VI, the GNSS module sensor selected is MAX-M8. MAX-M8 communicates with the flight control system via UART interface. It recognizes multiple constellations simultaneously and provides outstanding positioning accuracy in scenarios with urban canyon or weak signals. It offers high performance even at low power consumption levels. It provides best performance for passive and active antennas designs of the SUAV.

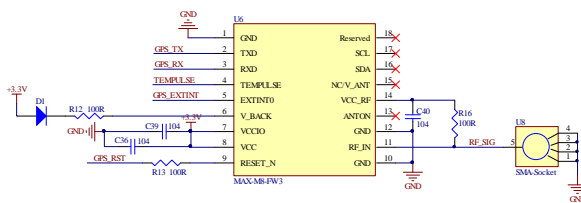


FIGURE VI. THE GNSS MODULE CIRCUIT

4) The 3-Axis digital compass module

As shown in Figure VII, the 3-Axis digital compass selected is HMC6343. Through I2C interface, MC6343, a fully integrated compass module combining 3-axis magneto-resistive

sensors and 3-axis MEMS accelerometers with required analog and digital support circuits, transmits the heading computation results to the flight control system. The sensor features precision sensitivity and linearity, as well as solid-state construction with very low cross-axis sensitivity designed to measure both direction and magnitude of Earth's magnetic fields.

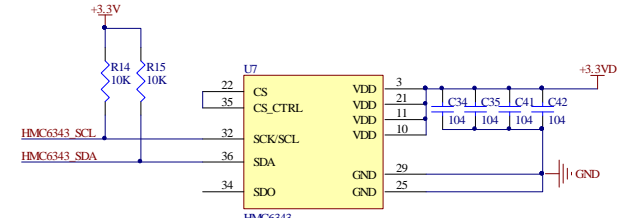


FIGURE VII. THE 3-AXIS DIGITAL COMPASS MODULE CIRCUIT

D. The Interface Circuit

The interface circuit is made up of two kinds of interfaces, namely, communication interface and the PWM and capture interface. The communication interfaces are UART, CAN and SBUS interfaces. The UART conducts the communication between the flight control system and the data radio as well as the data and parameter transmission between the two control chips STM32F427. The SBUS interface connects with a SBUS receiver, exclusive for Futaba SBUS protocol. The rest communication interfaces are backups for future extension. The control system captures 6 channels of PWM input signals and outputs 16 channels of PWM driving signals. The electric level of PWM input signals is +5V, which has to be transformed into +3.3V to meet the requirement of STM32F427 I/O level. For more powerful driving ability, the PWM output signal has the electric level of +6V.

IV CONCLUSION

As the advance of science and technology, the SUAV is playing a more and more significant role in modern world, no matter whether it comes to the military field or the civilian fields. As the brain of SUAV, the flight control system must perform properly and stably without any mistakes. The hardware of the flight control system based on STM32F427 is designed in this paper, with advantages of small size and light weight. After several ground tests in our research group, this flight control hardware proves to be feasible and reliable, and it works efficiently while the power consumption low, thus fulfilling the design demand and improving the control and operation performance of the SUAV.

REFERENCES

- [1] Yang Lei, The Design of Small UAV Flight Control System Based on STM32, Harbin: Northeast Forestry University, 2016.
- [2] Zhou Wenxia, Research on UAV Flight Control Computer Platform Based on ARM, Nanjing: Nanjing University of Aeronautics and Astronautics, 2008.
- [3] Hu Yong, Ding Wanshan, Design of the Hardware Platform for a UAV Flight Control System Based on DSP, Metrology and Measurement Technology. 5 (2004) 35-38.

- [4] Wang Wei, Design of UAV Flight Control Computer Based on DSP, Nanjing: Nanjing University of Aeronautics and Astronautics, 2009.
- [5] Yu Xiaozhou, Zhou Fengqi, Huanghe, Hardware Platform for the UAVs based on the SOPC Technology, Fire Control and Command Control. 12 (2006) 48-50.
- [6] Wang Bin, Design of a UAV Flight Control Computer System, Nanjing: Nanjing University of Aeronautics and Astronautics, 2007.
- [7] Liang Shuang, Design and Implement of Hardware and Attitude Reference System for the Flight Control System of Small UAV, Chongqing: Chongqing University, 2016.

The Current Status of Informatization and Information Literacy in Advanced Medical Institutions

Na Wang¹ and Jinguo Wang^{2,*}

¹Department of Anesthesiology, The First Hospital of Jilin University, China

²Department of Urology, The First Hospital of Jilin University, China

*Corresponding author

Abstract—This paper analyzes the main problems and causes in the practice of information quality education in higher medical institutions. The paper puts forward the effective way to cultivate and improve the information quality of medical students by the education curriculum and teaching. Mainly Through the build scientific and rational curriculum system of medical students information literacy, the integration of information quality education and the medical professional courses and quality evaluation standard system, teachers' and students' information literacy are improved. The role of libraries of the advanced medical colleges and universities must be given full play. The cooperation of librarians and medical professional teachers must be reasonably strengthened to create a good environment for campus informatization to promote development of the information quality education and improve the information literacy of medical students and teachers.

Keywords—informatization; information literacy; medical science

I. INTRODUCTION

The medical science is the fastest field of development. The progress of medical technology, medical information and medical knowledge update at a amazing speed. The cycle of advancement speeds up unceasingly. The information technology is widely used in medicine. The information-based degree of clinical medical work is more and more high. In the future, doctors' work faces a growing and increasing complex area of the clinical diagnosis and treatment work. It endows with higher demand and more responsibility. The importance of information quality will become the clinical medical work conditions and the necessary quality in the future. [1]

Training qualified information talents of advanced medical education for the society is facing the severe challenges in the information age. The advanced medical colleges and universities which cultivate medical graduates have concrete medical professional knowledge and good clinical skills. At the same time, they should also cultivate their good information literacy. Information quality education is an important issue in advanced medical colleges and universities.

II. CONCEPT OF INFORMATION LITERACY

A. Information Awareness Quality

Information consciousness refers to the information in people's minds which reflect the qualification of the career. People have sensibility and sustained attention to information and they have judgment and insight of information value. [2]

B. Information Ability Quality

Information ability refers to the ability of people to obtain, process and use information. It has become a problem that everyone must face how to extract useful information from the vast information resources. Information ability is one of the skills that people must possess in a new age. [3]

C. Information Moral Quality

Information ethics refers to the moral norms that people should follow in the information activities, such as protecting intellectual property rights, respecting privacy and resisting bad information. The network has a great negative effect, as well as an endless benefit of our life.

The network space is a mixture. The infringement of copyright behavior is increasingly rampant and the information environment is being seriously polluted, so training the correct information channel is becoming more and more important. [4]

III. HISTORY OF THE CULTIVATION OF INFORMATION LITERACY

The research on domestic information capacity was originated in the early 1980s. As our country began to clean up the far-left thoughts influence in the fields of social economy, science and culture, academic research is broken gradually, inspired by the situation of many scholars, starting from the perspective of science and technology. The economic and cultural development actively brings up their respective discipline. [5]

Some scholars have proposed to develop the scientific capacity of our country. When they deal with the basic content of social science, the efficiency of the digital intelligence system is also an important aspect. Some scholars in the book

intelligence community have been enlightened and began to discuss the problem of information ability in China.

Domestic scholars generally use intelligence to characterize the information we use today. Accordingly, researchers generally use intelligence with a little information capability. After many years unavoidably in the blind state of information, researchers noticed that the intelligence ability of student learning, scientific research and enterprise management are important. Emphasis on intelligence ability is one of the most basic professional skills or creativity structure elements. Emphasis of the library organization to carry out information education improves the ability of users' information. [6]

The primary index of the evaluation index system is usually the index of sub-index or criterion property, which is the refinement of the total target. Generally, the primary index cannot be judged directly, but it should be evaluated according to the standard of the underlying index.

Though the information ability is a dynamic concept, in different stages it has different connotation and denotation. Both at home and abroad, it has not yet been a unified definition and it includes the study of individual and the whole society. This article refers to information ability, which refers to the individual user information ability.

A person with information ability, information knowledge should be followed by the ability to use computer to collect information. The information ability is the ability of processing, analyzing and identifying information.

IV. OVERVIEW OF FOREIGN INFORMATION CAPABILITY RESEARCH

In the United States, information capabilities have long been incorporated into the national education goals. The training of information capabilities has been incorporated into the curriculum. Researchers from all disciplines and in various social production departments have begun to study the information capabilities of their respective disciplines of their departments. More and more scholars are concerned about the performance of information ability in various work stations, the mechanism of function and the way of cultivation.

There are numerous articles on case studies and theoretical studies of information capability. Governments are also actively trying to improve the information capabilities of countries and citizens. The current research areas include several aspects, including how to calibrate the level of information ability and the degree of progress, how to measure information ability training program to improve individual quality effect, how for information to play a role in different working environments and how to improve labor productivity. [7]

V. DOMESTIC INFORMATION CAPABILITY RESEARCH

Most of the domestic researchers take information ability as information retrieval, information processing ability, information analysis ability, as well as library using ability. However, in the 1980s, the researchers emphasized the cultivation and improvement of information ability. Especially

for the librarians and college students' information ability training method of the research is very active. They emphasized the significance of the literature retrieval course in colleges and universities. The various units of its own opinions are on the specific situation. [8] They not only carried out all kinds of specialized subjects, such as science and technology workers, farmers, businessmen, journal editors, the composition of the graduate students and teachers' information ability cultivation approaches of research, but also carried out subject information users on a general sense. Libraries and achievement improve the way of research.

Domestic information research ability on the content of a distinctive feature is the introduction of foreign literature achievements and progress and the basic way is to compile or review on foreign related research literature. The current research focuses on the definition, main content, main evaluation methods and teaching practice of some schools. Also some scholars pay attention to the research content of localization, the analysis of the similar foreign research under the background of theoretical framework and practical experience. Quality education activities of domestic college students information has been carried out. The research and research fields are still hot.

VI. CHINESE EVALUATION STANDARD RESEARCH

It is not difficult to find that it is based on the definition of information quality of the American library association. From the formation of information database, the required information acquisition, assessment of obtained information, the use of information and related economic, legal and social responsibility, etc., this paper also expounds the essential skills in the process of information collection and utilization.

It focuses on the assessment of information ability and information ethics. At present, domestic scholars have formed a unified understanding of the content system of information literacy. That includes three parts, information awareness, information ability and information ethics. Therefore, it is not enough to evaluate Chinese information quality education with American standard.

The evaluation indexes of information awareness and other aspects need to be supplemented. It has been a long time since Chinese colleges and universities carried out information quality education. Most of the papers remain on the technical aspects of how literature retrieval courses to be opened and taught. There are not many papers on the information quality education.

The evaluation standard of education of information quality in China reflects the advantages of network, database, multimedia and other information technologies for users to collect and utilize information. The content of information ability, information awareness and information morality are evaluated. [9]

The specific content includes the content and scope of the specific information needs, the efficient access to the required information, the information evaluation and information sources to assess its value and effectiveness. It integrates the acquired information into your own knowledge system and use

information to accomplish specific tasks. The economic, political, legal and social norms associated with information use.

VII. TRAINING OBJECTIVES OF INFORMATION LITERACY

The training objectives of information literacy include several aspects. How to choose and judge information sources is an important aspect. The advantages and disadvantages of the alternative information must be judged. How to master the ability to use various information from different counties is necessary. How to use the relevant information caves to improve the project review and evaluation is needed. Information is a resource and has value of wealth.

Because the database has great storage capacity and low price, simple and convenient method of use, it can solve the printed retrieval tool and has the advantages such as aging. It makes the disc play a more and more important role in information retrieval. It can be used both on single disk and on line. [10]

Many university libraries have to purchase the database for information retrieval, so they want to introduce students to the databases which can let them know what they will need to check, what kind of information in the database, how to check questions and so on. For databases abroad, because of its instruction, methods are used when retrieving methods similar to those of international online retrieval systems, it introduced the online retrieval. The key is to introduce the domestic several databases.

VIII. SETTING UP A FULL-TIME TEACHING STAFF

The teaching of information quality is mainly for the teacher and the library staff or information management department. This kind of staff teaching structure has its unreasonable aspect. It should build a group that combines the professional teacher with the quality teacher troop to apply their respective specialty.

Online information scattered disorderly, but its distribution has a general rule with timeliness. It has four types of information including electronic journals, electronic newspapers, dynamic information and bibliographic database. If it is divided by form, it also includes text information and non-text information. If it is divided according to the processing degree, it can include the original information and index guide. [11]

Its original sources of information are similar. But due to the particularity of the network transmission, there are specially applicable to the distribution of the information network. It should include the following categories, including Book information, meeting information, patent information, government publications information, information provided by universities, information provided by commercial companies, research institutions and academic groups. Information contains in the newsgroup and communication discussion groups, information provided by libraries on the Internet, online information provided by the commercial online retrieval system. There is also information provided by professional information service providers.

It's not just about the types of information you need to introduce, but also about what information services are available in each type and which sites can get the information you need most in.

IX. SUMMARY

The determination of information literacy of college students requires a relative standard or accepted definition of information literacy. The concept of information literacy is not unified without international standard definition, so we used the foreign reference extensively. Relevant authorities or organizations would agree with the definition of information literacy made by the American library association. It is namely that the information literacy is to realize that when you need information, you have the ability to find, evaluate and effectively use the information needed.

In a fundamental sense, people with information literacy are those who know how to learn. They know how to learn, because they know how to organize the knowledge, how to find information and how to use information, so that others can learn from them, and they have been ready for lifelong learning.

REFERENCES

- [1] Bimber. Three aces of Technological Determinism. Does Technology Drive History?: The Dilemma of Technological determinism. 1994
- [2] Burrows S. Developing an "evidence-based medicine and use of the biomedical literature" component as a longitudinal theme of an outcomes-based medical school curriculum: year 1. *J Med LibrAssoc*. 2003
- [3] John Weckert. What is so bad about Internet content regulation?[J]. *Ethics and Information Technology*. 2000 (2)
- [4] Tomas A. Lipinski, Johannes Britz. Rethinking the ownership of information in the 21st century: Ethical implications[J]. *Ethics and Information Technology*. 2000 (1)
- [5] Joseph D Bronzino. Health Care and Information Ethics:Protecting Fundamental Human Rights. *Health Progress*. 1999
- [6] Herman T. Tavani. The state of computer ethics as a philosophical field of inquiry: Some contemporary perspectives, future projections, and current resources[J]. *Ethics and Information Technology*. 2001 (2)
- [7] Alison Adam,Jacqueline Ofori-Amanfo. Does gender matter in computer ethics?[J]. *Ethics and Information Technology* . 2000 (1)
- [8] Tavani. H.T. The State of Computer Ethics As A Philo-sophical Field of Inquiry:So me Contemporary Perspec-tives,Future Projections, and Current Resources. *Ethics and Information Technology*. 2001
- [9] Lipsld T A, Britz J. Rethinking the Ownership of Information in the 21stCentury: EthicalImplications. *Ethics and Inform ation Technology*. 2000
- [10] Tim Jordan. Cyberpower—the culture politics of cyberspace and the internet. 1999
- [11] Thompson P.B. Privacy, Secrecy and Security. *Ethics and Information Technology*. 2001

Research and Realization for Information System of Shenhua Ningxia Coal Integration Based on XML

Xiaoyan Zhang¹, Huan Li¹ and Shiheng Liu²

¹Xi'an University of Science and Technology, China

²Shenhua Ningxia coal industry group company, China

Abstract—Shenhua Ningxia Coal Group as a modern large-scale coal enterprises, attaches great importance to information management, and promote the development of the coal industry. There are many information management systems within the group, playing an important role, but the various systems are independent, the system can not be shared between the data, which led to the emergence of "information silos". In response to this problem, The data relation between several systems of the group adopts the way of XML technology and middleware to establish the heterogeneous data fusion model, and uses the similarity algorithm to match the attribute columns to break the heterogeneity among the databases and realize the data integration among the systems.

Keywords—information silos; XML technology; middleware; data integration

I. INTRODUCTION

In recent years, the coal industry information construction has been rapidly developed, and the information management system has been established in various departments of the enterprise. With the development of information and network era, more and more enterprises need to realize the integrated management and realize the data sharing among various information systems within the enterprise. However, since each independent system uses different databases and data models, it is difficult to synchronize data and thus form an information island. Therefore, it is an urgent issue to realize data synchronization and data sharing in heterogeneous databases.

Shenhua Ningxia Coal Group Company has taken the forefront of the coal industry in information construction. At present, 23 sets of management information systems of Shenhua Ning Coal Group Company are put into operation. However, due to the fact that the management of various system data of the Group is not truly unified, The data of each system can not be shared. Aiming at this problem, Ningxia coal Group proposed to achieve group information integration by the end of 2016. In this paper, the unified integration of coal quality information of Ningxia coal group is analyzed and studied, and the coal information sharing between five coal-related systems is realized.

II. ANALYSIS OF THE CURRENT SITUATION OF SHENHUA NINGXIA COAL INFORMATION SYSTEM.

Shenhua Ningxia Coal Group attaches great importance to information construction and information management .Currently 23 sets of management information systems within the group to facilitate the user's operation, and play a good role in

their respective application scenarios. However, due to the independence of each system, different system developers use different databases and system environments, resulting in the system can not be shared between the data, so that the system can not be unified management of information, the lack of connectivity between systems, making the system Between the "information island" phenomenon. A large number of data and information are scattered to different systems(1), data sharing and data integration can not be carried out, and there is data interaction between independent information systems. Therefore, data integration is needed to achieve data sharing between systems.

The systems involved in the management of coal quality information include the coal quality management information system, the Shenhua Ningxia ERP management system, the transportation and marketing management information system, the coal metering information system and the coal washing plant information system. Each system is independent of others and each has different emphasis. Therefore, we can not see all the data inside the group from a macro perspective. And there is data exchange among all systems. Users are required to repeat input for the amount of the system, which increases the work load. In addition, multiple management systems are run in the group at the same time. For information department managers, they need to learn a different system of operating and maintenance methods , the task is arduous, so the system need to be solved between heterogeneous, as this can lighten the user's workload and can realize the group information integrated management.

A. Analysis of Heterogeneous Data of Shenhua Ningxia Coal

Shenhua Ningxia Coal Group involved in coal quality information system has five independent subsystems: coal quality management information system, Shenhua Ningxia ERP management system, transportation management information system, coal measurement information system and coal washing plant information system, the use of subsystems Database and system architecture vary, and each system's database table naming format, constraints and table structure is inconsistent, so to achieve heterogeneous database system information integration needs to break the heterogeneity between the database to achieve each Data conversion between databases and transparent access between heterogeneous databases. There are data exchange among these systems in the group, and each system is independent and connected with each other. In order to ensure the consistency of data among the systems and prevent users from doing duplicate entry work, the quality management system of the coal quality system is overlapped with several other systems to realize data sharing.

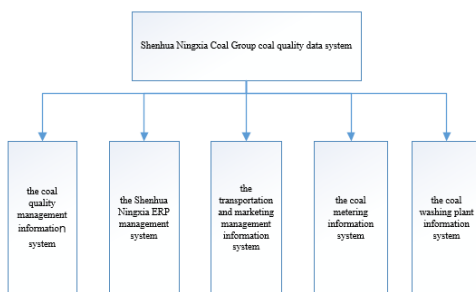


FIGURE I. SHENHUA NINGXIA COAL QUALITY DATA SYSTEM

As shown in Figure 1, this paper mainly focuses on the data integration of the above five systems. The five systems have different emphases. Many of the information between the systems is duplicated. Because of the independent existence of each other, the staff need to repeatedly input data. Shenhua Ningxia ERP Management System in order to settle the coal quality data in the coal quality management information system and the sales volume of the railway and highway in the transportation system, the coal quality management system needs to obtain the "quantity" of coal from the measurement system, And some data are obtained from transportation management information system. There is data exchange between the five systems. In order to facilitate the operation and use of the users, it is necessary to realize the integration among several systems.

B. The Key Technology of Coal Quality Data Integration

Data integration is to integrate data from different systems and different storage media into the same data environment and present it as a unified data view(2). Data integration of multiple data sources that is, to break the heterogeneity between the database, make full use of the scattered data resources in various systems, and truly achieve data sharing.

At present, the way to solve heterogeneous databases is federation, data warehousing and middleware(3). The federated database system consists of a set of local databases that work in coordination with each other but maintain their autonomy. There is no unified mode between systems, which is suitable for data volume Relatively small heterogeneous database; data warehouse is the heterogeneous database data extracted, filtered and stored in a data warehouse, so as to facilitate data query, only for small changes in the data and a small amount of data in the database; and The Mediator method is by far the most popular way to create an integrated database. The middleware gets the user's request and feeds it back to the data layer, which parses the data layer's query results into an XML format and returns it to the client.

Database intermediate technology to provide users with access to heterogeneous data sources unified interface, so users do not need to know how to communicate between the various databases, how to connect, data extraction, data synthesis and data query transparency, the user only need to operate the query . The use of middleware to eliminate the heterogeneity between the database, the general relational database consists of many sheets of data tables, and each table contains a different record, each record will be composed of many data columns, so the smallest of the relational database Data that is a column, and the data ta-

ble is the database entity, the table by the primary key and foreign key association, so the system integration in order to make heterogeneous database data unification, the need to transform the table in the database into xml Document form, convenient data reading and transmission between tables.

XML language is a cross-platform language, has a good data storage format, and flexibility is good, scalability, ease of network transmission. Data can be exchanged between different databases through xml language, and the middleware method based on XML language can be used to integrate the data of heterogeneous databases, which can solve the problem of "information isolated islands" between independent heterogeneous databases.

III. IMPLEMENTATION OF COAL DATA INTEGRATION

A. Mapping between XML Documents and Databases

Xml document data model can be seen as a "tree" shape, by the parent node and child nodes, for each database information table corresponds to an XML document, the data table name as the XML document's parent node, each attribute column Is a child node, the information in the table traverses until the end of the last line, you can map all the information in the data table into xml form. As follow.

TABLE I. PERSON INFO

Name	Age	Position	Sex	Worktime	Firdegree
wang	26	operator	female	2011-09	undergraduate
li	25	technican	male	2010-10	undergraduate

```

<?xml version="1.0" standalone="yes"?>
< PersonInfo >
  <Name> wang</Name>
  <Age>26</Age>
  <Position> operator </Position>
  <Sex>female</Sex>
  <Worktime>2011-09 </Worktime>
  <Firdegree> undergraduate</Firdegree>
</ PersonInfo >
< PersonInfo >
  <Name> li </Name>
  <Age>25</Age>
  <Position> technican </Position>
  <Sex> male </Sex>
  <Worktime>2010-10 </Worktime>
  <Firdegree> undergraduate</Firdegree>
</ PersonInfo >
  
```

B. Heterogeneous Database Data Integration Process

Middleware technology is used to realize the information sharing of heterogeneous databases. By adding middleware layer to the database layer and presentation layer, the data between each database is processed. First, the user requests data from the presentation layer, and the request is received by the middleware. The middleware analyzes and decomposes the query request, and finally publishes this function to each database. After the database receives the query data and returns the query result to the corresponding wrapper, the wrapper converts the result of the query into xml documents, and data mapping,

synonymous data and synonymous data matching mapping, and finally these results are integrated into a global view file, returned to the user.

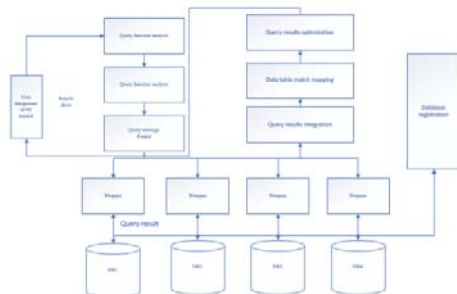


FIGURE II. COAL QUALITY DATA INTEGRATION ARCHITECTURE DIAGRAM

C. System Integration and Results

System integration using middleware way to achieve heterogeneous database data communication, xml technology to achieve heterogeneous database table data conversion, matching the mapping of data results using common matching algorithm for attribute matching and will be similar to the meaning of The words are unified named to facilitate the user's query, and finally all the results will be displayed as a virtual global view, the final results will be displayed in the client interface. In the process of data integration for the same meaning but naming a few different forms of matching mapping algorithm used to achieve. Data integration between two systems, need to match the attribute column between database tables, can we truly achieve the data sharing between two systems, property is obtained by using the edit distance algorithm into the column of similarity, the higher the similarity value of property, the closer the relationship between can match(4). For example, the two systems of coal quality management information system and coal industry transportation and marketing group enterprise management system have data interaction. The coal quality management system needs to obtain the information such as the highway, railway, coal mass and pricing standard of commercial coal, System of mine name, mine point, brand and customer name and marketing system to establish the corresponding relationship in order to pull the data in the distribution of coal quality information system.

TABLE II. TWO TABLE NAMES AND ATTRIBUTES

num	The transportation mine.	The name of the coal mine.	NULL	Default
1	Jinfeng Coal Mine	Jinfeng mine	Y	NULL
2	Baijigou Coal Mine	Baijigou mine	Y	NULL
3	Hongliu Coal Mine	Hongliu mine	Y	NULL
4	Golden company		Y	NULL

TABLE III. SIMILARITY CALCULATION

num	The transportation mine.	The name of the coal mine.	Similarity value
1	Jinfeng Coal Mine	Jinfeng mine	0.75
2	Baijigou Coal Mine	Baijigou mine	0.75
3	Hongliu Coal Mine	Hongliu mine	0.75
4	Golden company		0

IV. CONCLUSION

With the development of informatization, the integrated management of information in coal enterprises is also gradually taking shape. In order to meet the actual demand, coal enterprises may use different systems, but these systems exist independently and cause some data to be unavailable and effective Use, you need to integrate the data between the various systems, this paper uses middleware to achieve information fusion between heterogeneous databases, using xml document data mapping between database tables to achieve data sharing within the group system, user-friendly The use of truly integrated information management group.

ACKNOWLEDGMENT

Supported by Industrial Project of Science and Technology Department of Shaanxi Province (2014K05-37)

Supported by the Serving Local Project of Education Department of Shaanxi Province (14JF016)

REFERENCES

- [1] Liu xingzhi. The Present Situation and Promotion Measures of Shendong Information Construction. *information Technology*.2015
- [2] Jianjiang Zhang.Research on Heterogeneous Database Integration Middleware Based on xml. [D].2010
- [3] Yidan Zhou.Research on query rewrite in heterogeneous data integration system.[D].2017
- [4] Ke wei.Design and implementation of similarity query system in heterogeneous database.[D].2016

Designing of IoT Platform Based on Functional Reactive Pattern

Haidong Lv, Xiaolong Ge, Hongzhi Zhu, Zhiwei Yuan, Zhen Wang and Yongkang Zhu
City Institute of Dalian University of Technology, Dalian China

Abstract—To meet the real-time requirement and data fast processing has become a significant challenge in the Internet of Things platform. In an attempt to design and implement new reactive paradigm , this paper presents an innovative functional reactive programming model to design and implement IoT platform using Node.js, Kafka, MQTT, Angular and RxJS etc technologies to process high speed device collecting data. In this IoT platform system the functional reactive approach has been pushing both on the back-end and the front-end to simplified IoT platform system designing and programming and reduce the development time and effort. Future research will focus on the practice validation of this work by implementing this IoT platform into a big data system and artificial intelligence application.

Keywords—internet of thing; functional reactive programming; MQTT; kafka

I. INTRODUCTION

At present the IoT connected devices are turning up everywhere, according to IoT analysts, the number of networked electronics is projected to exceed 20-50 billion devices by 2020. The Internet of Things is giving rise to a new era of networked computing where business applications intelligently monitor and control remote sensors, mobile devices, and smart machines and where devices such as actuators, valves and switches are connected and communicating.

Almost every major IT companies are offering their own IoT platform to manage these IoT devices. And hundreds of technology companies are offering capabilities for IoT use case implementation.

Normally most IoT application platforms[1] are developed by using the monolith architecture and synchronizing working model, due to it mainly uses thread technique to process multiple concurrent IoT devices connection, so it can not suit to manage vast devices and meet the high performance requirement.

To overcome those monolith system shortcoming, the new trend technique functional reactive architecture which based on micro-services and non-blocking design patterns appeared and developed for resolving these problem, this innovative solutions that intelligently monitor and control remote sensors and devices are revolutionizing enterprise computing.

Reactive programming is an important concept that provides a lot of advantages: it naturally handles asynchrony and provides a model for dealing with complex data and time

flow while also lessening the need to resort to shared mutable state.

Reactive programming is specific to suit for design and implement applications such as interactive UIs and animation, client-server communication, robotics, IoT, sensor networks, etc.

Reactive Programming raises the level of abstraction of all kind of system code so developer can then focus on the interdependence of events that define the business logic, rather than having to constantly fiddle with a large amount of implementation details.

Reactive streams is suited to manage time-related complexity well, it makes reasoning about asynchronous events, controlling their timing, and combining them simpler. It is much simpler than using callbacks, and even simpler than using Promises. Since the server logic naturally deals with multiple identical request events, a stream where the events can flow and be processed is a better mental model compared to single-execution Promise abstraction.

Reactive programming main purpose is moving of everything that is outside of our control to inputs or outputs, leaving the system main logic inside a pure function.

Functional reactive programming (FRP) is a programming paradigm for reactive programming, specifically asynchronous data flow programming using the building blocks of functional programming such as map, reduce, filter etc.

This paper main focus on how to design non-blocking, highly responsive, resilient, elastic, and message-driven IoT management platform application.

In order to make FRP programming more easily and high productivity, a lot of new technology and languages has been invented.

In the server side development the Node.js and Vert.x are mainly used to develop reactive event-base application, The micro service framework Seneca, SocketCluster which based on Node.js can develop reactive micro service simply and efficiently. Another framework Zetta is an open source platform built on Node.js for creating Internet of Things servers that run across geographical distributed computers and the cloud, it combines REST APIs, WebSockets and reactive programming and is perfect for assembling many devices into data-intensive, real-time applications.

In the front side the famous framework Angular, React and Vue.js are all mainly used to develop reactive UI application,

this paper uses the Google Angular as the IoT platform front end UI development technology to simplified complex front-end designing and programming.

With these latest technologies and functional reactive programming, the advanced IoT platform was designed and implemented in the real industry field, this Innovative solutions that intelligently monitor and control remote sensors and devices are revolutionizing enterprise computing.

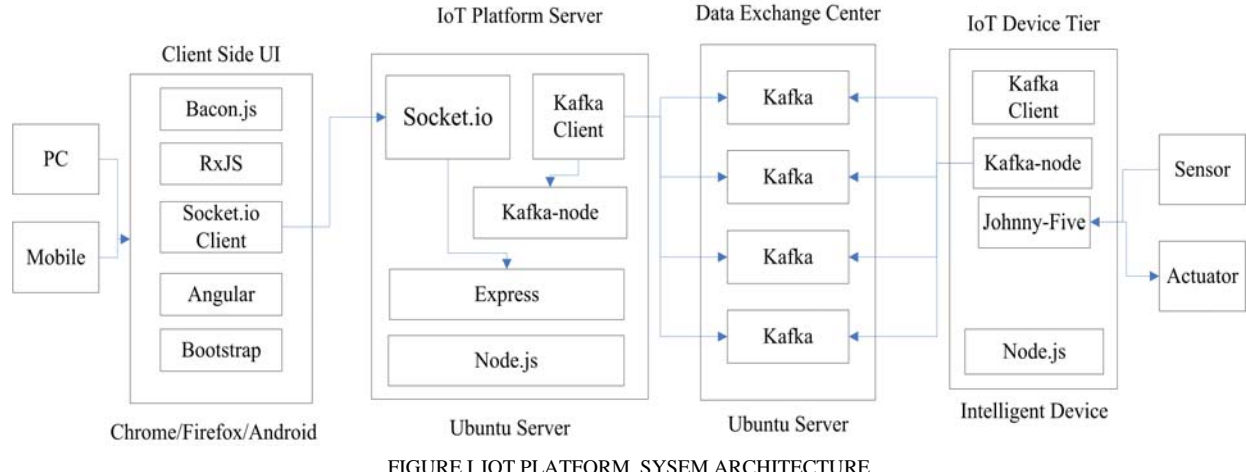


FIGURE I.IOT PLATFORM SYSTEM ARCHITECTURE

The whole platform is built based on Ubuntu server 16.04 and Node.js 8.9.4. Due to Node.js uses an event-driven, non-blocking I/O model that makes it lightweight and efficient[2], it is perfect programming platform to develop real time application such as automatically control system and IoT system.

The figure.1 above shows reactions among the different parts inside the platform. It is mainly based on NodeJS. The NodeJS platform has a variety of modules that are perfect for the Internet of Things. This platform be mainly built upon event driven, reactive steam, MQTT[3] and Kafka[4][5], it works in asynchronous non-blocking development model, which does not mean to be multiple threading, but the non-blocking I/O for handling network, file system and others, it uses the callbacks system, so it can possible to handle a huge number of events per second using a single thread. This feature is exactly what this IoT system needs.

The key for implementing the IoT platform[6] is the reactive stream[7]. At device tier the data detected by the sensor is transformed into stream and send with Kafka-Node platform to Kafka cluster center in the reactive mode. The platform server side receives the data by subscribing the topic of Kafka in asynchronous reactive mechanism and then send to other data processing and analysis component by send emit with Node's socket.io or event. Finally the user interface with web or mobile at the client site receives the data though Angular and Sokcet.io client in the event stream way[8].

III. REACTIVE MESSAGE EXCHANGE CENTER DESIGN

In large companies and industry, the IoT platform need to manage vast numbers of IoT device endpoints and to collect and act upon massive volumes of raw business data generated

II. IoT PLATFORM ARCHITECTURE DESIGN

The IoT platform architecture from a high-level perspective is showed in Figure 1, the whole platform is consist of four subsystem: backed end server, data exchange center, sensor side and client UI side.

by the devices. With the traditional architecture system, it can not transform and process so vast data in the real time, result in the data which can be stored in time has been lost.

In order to meet the requirement, the platform use Apache Kafka framework as device message exchange center. Apache Kafka is a streaming platform for collecting, storing, and processing high volumes of data in real time. Before Apache Kafka, there was not a solution that perfectly met the IoT vast data processing in real time. Traditional messaging systems are real-time, but were not designed to handle data at scale. Kafka typically serves as a central data hub in which all data within an enterprise is collected.

The data can then be used for continuous processing or fed into other systems and applications in real time[9].

A Kafka cluster was built in the IoT platform to meet the vast data processing requirement. All the distributed IoT devices data was collected and transformed with MQTT protocol to Kafka Pub/Sub queue.

In the platform when use setup a new IoT device, the platform will automatically create a specific topic in Kafka with using its stream API, there after all the data which is collected from this device will be send to the topic to store. The platform can acted as Kafka consumer to subscribe this topic and can get the data with streaming API automatically in real time. Each IoT device will have a corresponding topic in Kafka cluster.

The platform use Kafka-node framework which is a Node.js client with Zookeeper integration for Apache Kafka. In the platform the following snippet code is illustrated how to use Kafka-node within Node.js to connect Kafka as its client as

producer to send data to Kafka or as consumer to receive data of device[10].

```
var kafka = require('kafka-node');
var KeyedMessage = kafka.KeyedMessage;
var Producer = kafka.Producer;
var client = new kafka.Client('210.30.108.30:12001,
210.30.108.31:12001, 210.30.108.32:12001');

var producer = new Producer(client);
producer.send(payloads, function (err, data) {
  cb(data);
});
```

For transforming data, the JSON has been the standard data format in nearly all kind of applications and systems, in this IoT platform all the data from or to devices need to convert to JSON format, the following snippet code shows how to implement the task.

```
var express = require('express');
var app = express();
var kafka = require('./Kafka.js');
var bodyParser = require('body-parser');
// create application/x-www-form-urlencoded encoding
var urlencodedParser = bodyParser.urlencoded({ extended:
false });

app.post('/toKafka', urlencodedParser, function (req, res) {
  // convert to JSON format
  kafka.produce(req.body.key, req.body.message,  function
(result) {
    res.send(result)
  });
});
```

IV. IoT DEVICES TIER DATA COLLECTION AND TRANSFORMATION DESIGN

The device tier encompasses a wide variety of intelligent endpoints, including mobile computing devices, wearable technology, remote sensors and controls, and autonomous machines and appliances. Normally the IoT platform might manage hundreds of thousands or even millions of devices, so the processing capability is very important, only the functional reactive paradigm can meet this requirement.

Under the functional reactive programming pattern the whole IoT system needs to work as stream event driven and synchronized model which about collecting streams of measurement values, storing them for later use and visualization as well as transforming and combining data into message streams that can then be fed to actuators, such as pumps and valves.

This platform uses the MQTT protocol for transferring device's data between platform server and IoT devices. MQTT is special with super lightweight architecture and is ideal for scenarios where bandwidth is not optimal.

This platform supports two kinds of IoT devices, one is worked as MQTT broker, the other is worked as MQTT client. When the device is MQTT broker, the platform can configure the management device as client to subscribe the specific.

The platform server uses the MQTT broker framework Mosca, it is a node.js MQTT broker, which can be used as standalone or embedded in another Node.js application. The IoT device can be acted as MQTT client endpoint to publish or subscribe data to and from MQTT broker.

The following snippet code shows how an IoT device which acted as MQTT client to measure data from sensor with Johnny-Five framework which can be used in Node.js platform using JavaScript programming language and then send to server side with MQTT technology. Johnny-Five has grown from a passion project into a tool for inspiring learning and creativity from all across the world.

```
var mqtt = require('mqtt');
var five = require("johnny-five");
var board = new five.Board();
var mqttclient=mqtt.connect('mqtt://210.30.108.30',{
  username:'iotplatform',
  password:'xxxxxx',
  clientId:'device#1'
});
mqttclient.on('connect', function () {
  board.on("ready", function() {
    var DeviceSensor = new five.Thermometer({
      controller: "BMP085"
    });
    //event for temperature change
    DeviceSensor.on("change", function() {
      var sendData={deviceNo:1201, data:this.celsius};
      mqttclient.publish('device#1', sendData); //send data to
server broker
    });
  });
});
```

V. IoT DEVICE MANAGEMENT CENTER DESIGN

The IoT platform provides web and mobile UI for customers to manage their IoT devices. By comparing the most popular framework products on the market: Angular, React and Vue.js. The Google Angular is selected to be used in platform client side, due to its reusing one code and abilities to build apps for any deployment target such as web, mobile web, native mobile and

native desktop. Further more the Angular main works in functional reactive pattern, it puts IoT platform in control over scalability and meet huge data requirements by building data models on RxJS, Immutable.js or another reactive push-model. So the platform both server, client and device tier all work in the same reactive work model.

Angular is reactive (non-blocking) by using observable or promises programming paradigm, the result in the front end of IoT platform is in reactive also.

At current time, Kafka does not have any JavaScript web client support, a middle tier has to implement between Kafka message center and Angular client, the socket.io framework is the best choice for this purposes.

In server side the platform use Kafka-Node as client to connect to Kafka and then send the device data through socket.io to Angular client, include web and mobile.

With Node.js, Kafka and socket.io in server side, Angular gets are a reactive partner, the front end UI use the same and familiar syntax with a functional programming model in the server side.

VI. CONCLUSIONS

In the paper a advanced and innovated IoT platform system which combined functional reactive programming and event-based, no-blocking architecture has been designed and implemented. Compared with the traditional platform, the new kind of system has short development time and high development efficiency. Further it also keep the IoT platform more maintainable and extensible due to its micro-service architecture. With FRP the IoT application system can be easy designed and implemented with all the benefits of a mature and vibrant both back-end and front-end framework ecosystem.

In the future the reactive paradigm will influence and shape the world of IoT application for many years to come, and it will be the future direction of IoT platform designing and developing.

ACKNOWLEDGMENT

This project was supported by the innovative and entrepreneurial training program for national college students in local colleges and universities in 2017 published by Ministry of education of China (No:201713198003).

REFERENCES

- [1] Muhammad Suryanegara; Ajib Setyo Arifin; Muhamad Asvial; Gunawan Wibisono: A system engineering approach to the implementation of the Internet of Things (IoT) in a country. 2017 4th International Conference on Information Technology, Computer, and Electrical Engineering (ICITACEE), Year: 2017;Pages:20-23.)
- [2] Martin K. Mwila: Design and implementation of a Node.js based communication framework for an unmanned autonomous ground vehicle.2017 Pattern Recognition Association of South Africa and Robotics and Mechatronics (PRASA-RobMech),Year:2017,Pages:74-79.
- [3] Manel Houimli; Laid Kahloul; Sihem Benabou: Formal specification, verification and evaluation of the MQTT protocol in the Internet of Things. 2017 International Conference on Mathematics and Information Technology (ICMIT). Year:2017, Pages:214-221, IEEE Conferences.
- [4] Godson Michael D'silva; Azharuddin Khan; Gaurav; Siddhesh Bari, in: Real-time processing of IoT events with historic data using Apache Kafka and Apache Spark with dashing framework, 2017 2nd IEEE International Conference on Recent Trends in Electronics, Information & Communication Technology (RTEICT),Year:2017,Pages:1804-1809.IEEE Conference.
- [5] Zhenghe Wang; Wei Dai; Feng Wang; Hui Deng; Shoulin Wei; Xiaoli Zhang; Bo Liang: Kafka and Its Using in High-throughput and Reliable Message Distribution, 2015 8th International Conference on Intelligent Networks and Intelligent Systems (ICINIS), Year:2015,Pages:117-120.IEEE Conferences.
- [6] Alireza Kahrobaeian; Yasser Abdel-Rady I. Mohamed: Interactive Distributed Generation Interface for Flexible Micro-Grid Operation in Smart Distribution Systems, IEEE Transactions on Sustainable Energy,Year: 2012, Volume: 3, Issue: 2,Pages: 295 - 305,Cited by: Papers (38).
- [7] M Abdul Salam; S. Sethulakshmi: Control for grid connected and intentional islanded operation of distributed generation, 2017 Innovations in Power and Advanced Computing Technologies (i-PACT),Year: 2017,Pages:1-6. IEEE Conferences.
- [8] Ashwini Raut: Real time monitoring of substation by using cloud computing, 2017 Third International Conference on Sensing, Signal Processing and Security (ICSSS),Year: 2017,Pages:138-147,IEEE Conferences.
- [9] Washington Velásquez Vargas; Andres Munoz-Arcentales; Joaquín Salvachúa Rodríguez: A distributed system model for managing data ingestion in a wireless sensor network, 2017 IEEE 7th Annual Computing and Communication Workshop and Conference (CCWC),Year: 2017,Pages:1 - 5,IEEE Conferences.
- [10] Evgeny L. Romanov; Galina V. Troschina, The IoT-architecture on the principles of reactive programming. 2017 International Multi-Conference on Engineering, Computer and Information Sciences (SIBIRCON),Year:2017,Pages:317-322.

Networking Mechanism of Fire Monitoring System Based on Internet of Things

Fangwen Xu¹, Jianjun Yi^{1,*}, Liang He^{2,3}, Xiaomin Zhu¹ and Zhuoran Wang¹

¹Department of Mechanical Engineering, East China University of Science and Technology, Shanghai 200237, China;

²Shanghai Aerospace Control Technology Institute, Shanghai 201109, P. R. China

³Shanghai Key Laboratory of Aerospace Intelligent Control Technology, Shanghai 201109, P. R. China

*Corresponding author

Abstract—Nowadays, there are some problems exist in remote monitoring of IoT fire control system, such as bad real-time performance, difficulty access of massive nodes, the security problems arisen due to the lack of standardized authentication and registration mechanism. In view of the problems above, this paper proposes a networking mechanism of fire monitoring system based on IoT. This mechanism uses public IoT cloud hosting service to meet the needs of mass nodes access. System architecture is Publish/subscribe mode based on lightweight MQTT protocol, so it can meet the real-time data transmission. We add the node certification mechanisms in the process of node registration and encrypt the message in the process of transmission. This standardized network-access mechanism improves the security of the whole system. Through short-term testing, this network mechanism can well solve the above problems in the current fire monitoring system. Due to its scalability and high stability, this network mechanism can be widely used in online monitoring of large-scale public places and buildings.

Keywords—Network Mechanism; MQTT; registration; authentication

I. INTRODUCTION

With the rapid economic development in our country and the continuous expansion of urban construction, the number of high-rise, super-tall buildings and large-scale buildings in cities has been increasing. However, due to the high floors, complicated functions, numerous facilities and staff, the hidden danger of causing fires also increases greatly. Therefore, fire prevention work which relates to the safety of people's life and property becomes increasingly important. It is necessary to develop the fire Internet of Things technology platform[1].

This paper focuses on networking mechanism based on the Internet of Things fire monitoring system. It can meet the flexible access of massive nodes and give access to alarm of fire facilities, flow and pressure parameters, temperature and equipment voltage parameters. We collect, process, analyze the real-time useful information during the reliable transmission and realize the effective perception of fire safety management information. [2].

Nowadays, the fire monitoring system based on IoT in the market is still in infancy. Most of the system applies the request/reply mode, which is synchronous. The publish/subscribe mode with the advanced IoT protocol is rarely used. However, this mode decouples the relationship between

the customer (publisher) who post the message and the customer (subscriber) who subscribe to the message. In addition, most of the fire monitoring systems at this stage merely realize the data transmission and seldom consider the cyber security of the system. They do not have a standard registration and authentication mechanism, which makes the node management of the system nonstandard and it is the very easy to eavesdrop the transmitted data. And the system can be also easily broken paralyzed by hackers' disguised nodes through the information bomb and denial of service means. So it is particularly important to consider of the system safety and standardized management in firefighting field, which is an important public utility involving the life and property of the masses. Therefore, this paper presents a networking mechanism of fire monitoring system based on the Internet of Things from the perspective of cyber security, management standardization, remote monitoring and maintenance of firefighting facilities[3].

This article is divided into four chapters. The second chapter describes the Internet of Things fire monitoring information system overall framework. The third chapter introduces the main technical realization of IOT fire monitoring information system in detail, including the IoT protocol selection, the process of node authentication registration and the design and implementation of the edge node. The fourth chapter summarizes this article.

II. THE OVERALL FRAMEWORK OF THE FIRE MONITORING SYSTEM BASED ON THE INTERNET OF THINGS

The architecture of the fire monitoring system based on the Internet of Things includes the perception layer, transport layer, storage layer and application layer.

The perception layer is mainly used for information collection for various types of fire equipment and environmental parameters. The data collected will be transmitted according to pre-defined protocol including the node number and time stamping. At the same time, combined with RFID technology, fire extinguishers, fire hydrants and otherfirefighting facilities can be located and position information of them will be real-time transmitted in order to achieve the intelligent monitoring and maintenance of the fire service facilities.

The transport layer applies the SSL protocol in the way of digital certificate and key encrypt to complete node and cloud two-side authentication and data encryption. The authenticated node will successfully register into the fire monitoring system,

and encrypt and package the data collected from the sensing layer, and publish it to the cloud through WIFI or Ethernet network via the MQTT protocol so that the cloud information can be collected and shared. Considering that there are some environments without WiFi or Ethernet networks, we construct the WSN network using Zigbee's ad hoc networking technology in this scenario. The information from the sensing layer is transmitted to the gateway via the MQTT-SN application layer protocol which is transplanted to the Zigbee protocol stack. In the gateway side, we achieve the protocol conversion between MQTT-SN and MQTT, and then transmit the data to the cloud via MQTT[4].

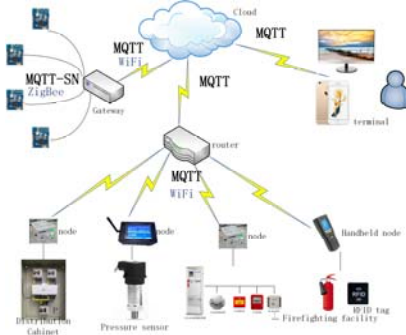


FIGURE I. THE ARCHITECTURE OF THE SYSTEM

The storage layer uses cloud hosting services so that we just focus on the IoT business. The system will realize the cloud-based MQTT hosting services by using the public cloud IoT HUB service. And the application layer mainly realizes the interaction between the monitoring system and the user. The management staff or other staff members use the MQTT protocol in the terminal to obtain the real time or the historical information of the fire system.

III. THE MAIN TECHNICAL IMPLEMENTATION OF THE NETWORKING MECHANISM

The innovation of this system lies in the use of lightweight MQTT protocol, which supports publish/subscribe message push mode and ensures the real-time transmission of system data. At the same time, The node registration and authentication mechanism is introduced in this mechanism in order to ensure the security and reliability of the system. We will separately introduce the use of the MQTT protocol, node certification registration mechanism and the design and implementation of the Internet of Things edge below.

A. MQTT-based Publish/Subscribe Message Push Mode

MQTT (Message Queuing Telemetry Transport) is an instant messaging protocol developed by IBM that promises to be an important part of the Internet of Things. It can complete instant messaging in case of less occupied resources than other protocols[5].Compared with HTTP, CoAP, XMPP and other protocols, MQTT protocol has the following advantages:

- MQTT is based on TCP and is more reliable
- MQTT realizes Publish / Subscribe mode in an asynchronous way.

- MQTT provides many thoughtful designs for Internet of Things, such as Quality of service and "last will."
- MQTT is a binary format which is lighter than XMPP.

Instead of requesting/answering such a synchronization mode, the publish/subscribe model decouples the relationship between the client (publisher) who posts the message and the client (subscriber) who subscribes to the message. So there is no need for publisher and subscriber to establish contact directly[6].

MQTT categorize messages by a UTF-8 string topic, which can represent multiple levels of relationships through backslashes. Topics can be filtered by wildcards. Among them, '+' can filter one level, while '#' can only appear at the end of the topic to filter any level [5].According to the fire monitoring situation, we customize some topics like below:

- building-b / floor-5: Representing the devices on the fifth floor in Building B.
- + / floor-5: Representing the devices on the fifth floor in any building.
- building-b / #: Representing all the devices in building B.

B. The Edge Node's Authentication Registration Process

The heart of the IoT is to make life more comfortable and convenient by exchanging and analyzing data from connected everything. However, unpredictable adverse consequences result from the disclosure of sensitive data and the unlawful control of devices. For the utility like fire protection, which is related to people's life and property safety, the consideration of IoT security is particularly important. The cyber security in this system is ensured by two ways. One is to realize the data encryption communication between the nodes and the cloud. The other is the authentication of edge node's identity and the cloud's identity. The following is the flow of device registration process to the cloud.

The system in our paper takes advantage of the MQTT security features at the transport and application layers. Using SSL, a very sophisticated security protocol to create a secure connection when nodes are handshaking, so that it can prevent hackers from eavesdropping or tampering with the messages. Ensuring the identity of each node (authentication) will be an extremely important consideration for IoT network security. The security of the IoT edge nodes includes confidentiality and integrity. The common way is the use of public keys or private keys as a unique part of the authentication and identification process.An authenticated node helps the system designers ensure that these devices meet all of the required standards without risking the entire network ecosystem.

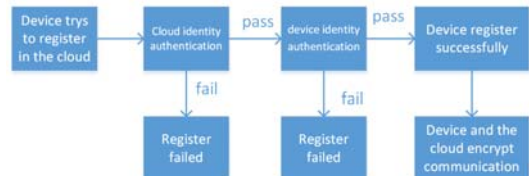


FIGURE II. THE NODE'S REGISTRATION PROCESS

Cyber security is the foundation for a successful deployment of the Internet of Things. At present, the edge node is the weakest part of the network to ensure IoT security, while the protection of encryption key can help ensure the edge node identity. The best way to achieve this is to use the protected hardware. According to the research on the reliability and the cost of the security IC in the market, our edge node uses Atmel ATECC508 to implement encryption function. Atmel ATECC508A is the first IC to integrate the ECDH (Elliptic Curve Diffie-Hellman) security protocol and provides reliable security for the Internet of Things (IoT) market such as home automation, industrial networking, accessories and supplies verification. ATECC508 integrated with ECDH and ECDSA which can effectively provide superior confidentiality, data integrity and authentication capabilities for the MCU or MPU which runs encryption/decryption algorithms such as AES in the software. [7].

Each ATECC508 chip has a pair of unique public and private keys in the factory time. And each edge node in the system is assigned with a unique UUID. Therefore, during the production of the edge node, the UUID, the public key and private key of the node are one-to-one and unique. Based on this feature, the UUID is used as the starting point to implement the process of the register and authentication of the edge node later[8].

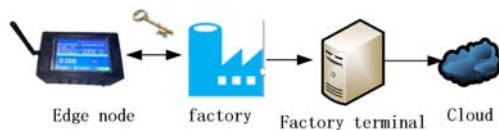


FIGURE III. THE PUBLIC KEYS STORAGE FLOW IN THE FACTORY TIME

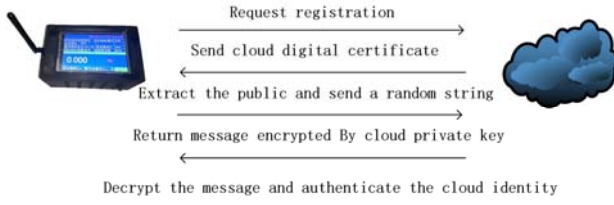


FIGURE IV. THE AUTHENTICATION PROCESS OF THE CLOUD IDENTITY

The workflow of the edge node in the production time is shown in the figure. After the edge node has been uploaded the factory time code, the ATECC508 chip of the node will generate a pair of public key and private key. The MCU reads the public key of the ATECC508 chip via the IIC interface and sends the public key and the corresponding UUID of the edge node to the receiving terminal of the factory. The receiving terminal is used to process the public key and the UUID information of all nodes from the factory and then pack all of the information and upload them to the cloud platform database for storage. These data will be used in the later authentication.

When the nodes finish the factory process, they should be re-burned the application stage code before they are put into formal use. In the application process of the edge node, the authentication and registration process of the node mainly

includes the cloud identity authentication and the node identity authentication.

When the edge node connects to the network and tries to link the cloud for the first time, the cloud will send its own certificate information through the SSL protocol. After the node receives it, it will decrypt the cloud certificate according

to the CA public key storage in the firmware of the node in order to get the cloud Public key. The node then will send a random string to the cloud to encrypt using the cloud private key. The cloud will return the encrypted message to the node.

And the cloud public key decrypted before will be used by the node to decrypt the returned message. If the decrypted message is the same as the random string generated before, the owner of the private key is really the cloud that certifies the certificate. After the authentication confirms the identity of the cloud, the identity of the node which is attempting to register will be certified next.

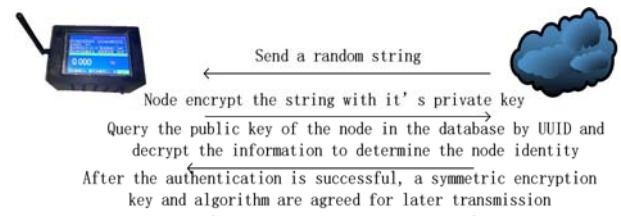


FIGURE V. THE AUTHENTICATION PROCESS OF THE NODE IDENTITY

The cloud sends a random string to the node. The node encrypts it with its own private key and returns it to the cloud. The cloud uses the node's UUID to query the public key stored in the cloud database and use this public key to decrypt the message. If the decrypted string is the same as the previous one sent before. The identity of the node is confirmed and the handshake process finishes successfully, allowing the edge node's registration in the cloud. After the registration process finishes successfully, the node will generate a random symmetric key. Then the node will encrypt the symmetric key and its corresponding algorithm using its own private key and sends the encrypted messages to the cloud. The cloud decrypts the encrypted messages using the node's public key and gets the symmetric encryption key and algorithm agreed by both parties. So, only the node and the cloud these two parts know the agreed symmetric key and algorithm. In this way, the messages encrypted by this symmetric key and algorithm will be protected from being eavesdropped and lost.

C. The Design and Implementation of the Edge Node

In order to adapt to different environments, we may use WIFI or Ethernet these two ways to communicate. Therefore, in the design of the edge node, we should consider both WIFI and Ethernet communication module integration.

The main chip is the stm32F4 chip of Cortex M4 core. We use the ESP32WIFI module as the wireless communication module and realize Ethernet transmission by using the W5500 chip to complete SPI to Ethernet protocol conversion. The main chip connects the encryption chip ATECC508A by IIC to realize the generation of key pairs and private key storage. An external flash chip is used to store the CA public key information used to

check the cloud certificate, the cloud connecting URL address, and the configuration information of the WiFi and Ethernet modules, and so on. The physical appearance of the external node is shown below.



FIGURE VI. THE PHYSICAL APPEARANCE OF THE NODE



FIGURE VII. THE NODE'S LOG FROM THE UART

The implementation of the nodes' MQTT transplantation in software is mainly in two aspects: One is ESP8266 IDE 2.0 MQTT protocol development for ESP8266 module and the other is the development of the application layer MQTT protocol based on Ethernet transmitting in stm32 IDE.

I use the public MQTT broker CloudMQTT to test the network access function of this node. The configuration information like router name, password, broker URL, port and user name and password registered in the broker are set in the program. After uploading the compiled file into the module, the node successfully run as shown. We can see the Log information from the output of the node serial port. The node successfully connect to the MQTT cloud broker. and the node and the node successfully subscribed and released three topics. And the same time, the cloud could receive the message posted by the node in real time.

IV. SUMMARY

In this paper, we propose a networking mechanism of fire monitoring system based on IoT according to the problems exist in remote monitoring of IoT fire control system. The hardware and software development of the edge node have been implemented. The feasibility of this networking mechanism is verified through the test between the edge node and MQTT broker. Because of the scalability, high stability of the network mechanism, it can be widely used in large-scale public places and buildings online monitoring.

Due to the time constraints, there is still room for improvement. For the scenario that does not cover the WiFi network, this article just proposes a feasible scheme framework but does not realize and demonstrate some specific details in the scheme. In the follow-up research, I will conduct an in-depth

research on network mechanism of massive heterogeneous nodes.

ACKNOWLEDGMENTS

This paper was supported by the Research Foundation of Science and Technology Commission of Shanghai under Grant No. 10DZ1500200, the Natural Science Fund of China (NSFC) under Grant Nos. 51575186, 51275173, and 50975088, the Fundamental Research Funds for the Central Universities under Grant No. WH0913009, Shanghai Pujiang Program under Grant No. PJ201000353, and Shanghai Software and IC industry Development Special Fund under Grant No. 120493.

REFERENCES

- [1]. A. Foster, "Messaging technologies for the industrial internet and the internet of things whitepaper," PrismTech, 2015, 23 (1): 5-8
 - [2]. B.-C. Chifor, I. Bica, V.-V. Patriciu, F. Pop, A security authorization scheme for smart home Internet, 2015, 57 (1): 5-8
 - [3]. Internet Of things devices, Future Gener. [J]Computer.Syst. 2017, 57 (2): 7-10
 - [4]. Daniel Barata, Andreia Carreirob. System of acquisition, transmission, storage and visualization of Pulse Oximeter and ECG data using Android and MQTT [J]. Procedia Technology 9 (2013) 1265–1272
 - [5]. Komkrit Chooruang, Pongpat Mangkalakeeree.Wireless Heart Rate Monitoring System using MQTT [J]. Procedia Technology 86 (2016) 160 -163
 - [6]. Rui-xiang Chen,Xiao-qiang Zhang,Chao-yang Peng,Hong-yong Zhang(2013). A Study on Design and Implementation of Remote Fire Monitoring System for Buildings[J].Procedia Engineering, 52,56 – 59.
 - [7]. Ke Yin, JunCheng Jiang(2014). an Application of Internet of Things in the Field of Urban Building Fire Safety[C].International Journal of Safety and Security Engineering,4(2),135-142.
 - [8]. B. B Prahладa Rao, Cloud computing for Internet of Things & sensing based applications .Sensing Technology (ICST), 2012 Sixth International Conference on 18-21 Dec. 2012, Kolk

Developing a Smart Energy Monitoring Terminal Based on Internet of Things

Shaoru Zhang¹, Jianjun Yi^{2,*}, Liang He^{2,3} and Fangwen Xu¹

¹Department of Mechanical Engineering, East China University of Science and Technology, Shanghai 200237, China;

²Shanghai Aerospace Control Technology Institute, Shanghai 201109, P. R. China

³Shanghai Key Laboratory of Aerospace Intelligent Control Technology, Shanghai 201109, P. R. China

*Corresponding author

Abstract—With the widespread application of power electronics technology, power pollution is becoming more and more serious. Based on the research of existing energy monitoring terminal, an energy monitoring terminal for monitoring and analyzing the power quality based on Internet of Things (IoT) technology is proposed in this paper, the terminal architecture, software flow chart is also provided, and the core circuit is described. Through validation, the terminal, presented in this paper, has some superiority of fully function, simple structure, easy to use and high accuracy, and has a broad market prospect.

Keywords—energy monitoring; IoT; data acquisition; wireless communication

I INTRODUCTION

In recent years, with the increasing level of industrial automation in our country, more and more large-scale non-linear loads have been used, seriously affect the power quality of public power grids and the negative influences have also become serious[1]. For example, the extensive use of rectifiers, electric arc furnaces and electric locomotives has brought a series of technical and economic benefits as well as greatly increased the harmonic content of power grids. Harmonic in the power grid will make the transmission and distribution equipment such as rotating electrical machines, transmission lines, transformers and other devices overheat. At present, most domestic power quality monitoring equipment has fewer functions. Foreign companies such as Fluke has a single product category and the product is usually expensive.

IoT is an extension of internet applications, the internet of things and things connected to achieve information management, remote management control and intelligent monitoring[2].The characteristics of information monitoring, automation and interaction of electric energy monitoring determine that the current traditional electric energy monitoring needs to be integrated with IoT technology. As for the electricity monitoring, the energy monitoring device with a single function isn't suitable for power quality monitoring requirement. It is important to develop an energy monitoring terminal with IoT function, which integrates the functions of measurement, communication and analysis to monitor the power quality.

The overall structure of power monitoring terminal is proposed in Section 2. The power data acquisition and process principles, harmonic detection based on Fast Fourier Transform and LoRa wireless communication network are introduced

respectively in Section 3. Validation of this terminal is given in Section 4. Summary is drawn in final Section.

II DEVELOPMENT OF ENERGY MONITORING TERMINAL

Aimed at the problems such as high price, fewer interfaces and lacks of flexibility and extensibility of the existing monitoring terminal, the energy monitoring terminal proposed in this paper has the following functions:

(1)Power Quality Monitoring Function: The monitoring terminal measures the basic power indicators and detects voltage deviation, frequency deviation, three-phase unbalance and harmonic content.

(2)Display Function: The monitoring terminal displays the electrical monitoring data and the alarm information on-site.

(3)Communication Function: The power quality monitoring terminal sends the parameters to the remote server through wired or wireless communication.

III POWER MONITORING TERMINAL OVERALL STRUCTURE

Based on the current research on energy monitoring technology, the monitoring terminal utilizes dedicated measurement chip and ARM architecture. Dedicated metering chip is responsible for collecting and processing electrical parameters. The main controller is responsible for reading the data in the dedicated metering chip register. Then the main controller displays and sends the data through the wired or wireless communication. Based on the above design concept, the overall structure of the energy monitoring terminal shown in Figure I.

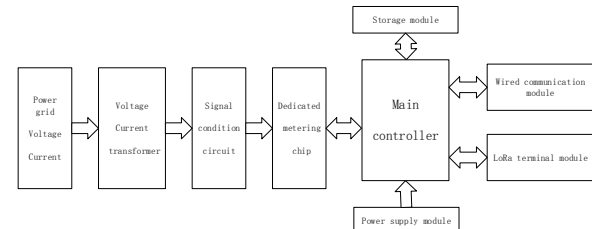


FIGURE I. THE OVERALL STRUCTURE OF THE ENERGY MONITORING TERMINAL

In Figure I, three-phase voltage and current signal of electric equipment input signal conditioning circuit through voltage and current transformers. The signal conditioning circuit is to filter, shape, amplify and impedance matching the signals transmitted

by transformers, so that the signal range is suitable for dedicated metering chips. The purpose of the dedicated measurement chip is to deal with the signal that output by the signal conditioning circuit. Then the dedicated measurement chip calculates, analyzes the signal, and gets the required energy parameters and indicators. The main controller function is to read the power data in the dedicated metering chip register and it's also responsible for the storage, alarm and communication.

A. Power Data Acquisition and Processing

The monitoring terminal uses RN7302 as the dedicated measuring chip for data acquisition. The chip is a multi-function and high-precision three-phase energy metering chip, which is suitable for three-phase three-wire and three-phase four-wire applications.

Data acquisition and processing circuit includes voltage signal acquisition, conditioning circuits, current signal acquisition, conditioning circuits, as showed in Figure II, Figure III.

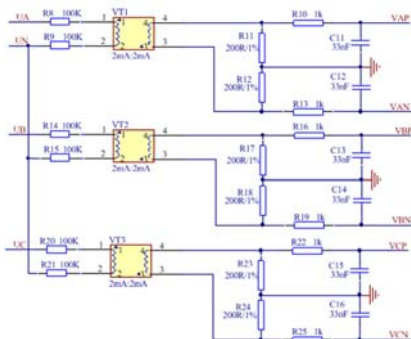


FIGURE II. COLLECTION CIRCUIT OF VOLTAGE SIGNAL

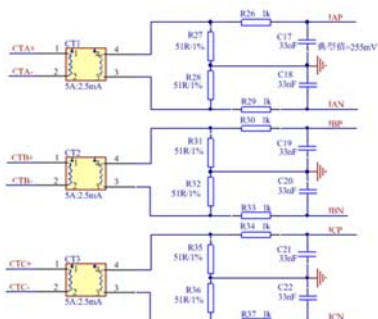


FIGURE III. COLLECTION CIRCUIT OF CURRENT SIGNAL

Figure II is a collection and conditioning circuit of the voltage signal. The DL-PT202H1 voltage transformer is to collect the voltage signal. The transformer is a current type voltage transformer, so add a resistor at its input to convert the measured voltage into current. Through the sampling resistor the current signal will be converted to the voltage signal then the voltage signal inputs the dedicated measuring chip.

The collection and conditioning circuit of the current signal is similar to the circuit of voltage signal. The DL-CT21C2.0 voltage transformer is to collect the current signal. Through sampling resistor, the current signal that output by the transformer will be converted to voltage signal. The voltage

signal passes through the filter and inputs the dedicated measuring chip.

The basic parameters of power quality contain RMS voltage, RMS current, active power, reactive power, apparent power and power factor and other parameters, the paper focuses on the description of above parameters. Based on circuit theory, this paper lists the electricity parameter calculation method. The effective values of voltage and current and the formula of active power are shown in equations 1,2,3:

$$U_{rms} = \sqrt{\frac{1}{T} \int_0^T U^2(t) dt} \quad (1)$$

$$I_{rms} = \sqrt{\frac{1}{T} \int_0^T i^2(t) dt} \quad (2)$$

$$P = \frac{1}{T} \int_0^T u(t)i(t)dt \quad (3)$$

$u(t)$, $i(t)$ in the formula represent the analog voltage and current signals. U_{rms} , I_{rms} respectively represent voltage and current RMS. P represents the active power. This paper discretizes the voltage and current signals, and introduced the voltage and current RMS and active power in discrete domain, respectively, as shown in equations 4,5,6:

$$U_{rms} = \sqrt{\frac{1}{N} \sum_{n=1}^N u(n)^2} \quad (4)$$

$$I_{rms} = \sqrt{\frac{1}{N} \sum_{n=1}^N i(n)^2} \quad (5)$$

$$P = \frac{1}{N} \sum_{n=1}^N u(n)i(n) \quad (6)$$

Energy monitoring terminal applies the dedicated energy metering chip to process the power data, the data acquisition software just reads the data in register. When the monitoring terminal receives the instruction to read the data, it firstly initializes the SPI communication with the metering chip, and then the main controller sends the correspond command to the dedicated measurement chip and waits for the response. The dedicated measurement sends the energy data monitoring data to the main controller.

B. Harmonic Detection Based on Fast Fourier Transform

Fast Fourier Transform is widely used in the field of signal processing, which samples in one cycle and acquires a series of discrete-time signals. After the analog and digital conversion, these data are sent to the microprocessor for processing [3]. The amplitude and phase of harmonics contained in the voltage and current signal will be calculated by multiplying the conversion factor.

Take a series of discrete time $\{f_k\}$ assuming that the sequence is evenly distributed on the axis, the corresponding

time coordinates time coordinates $t=kT/N$, the value of each time point is $f(kT/N)$.

$$nw_1t = n \frac{2\pi}{T} \times k \frac{T}{N} = \frac{2\pi}{N} kn \quad (7)$$

According to the discrete time series $\{f_k\}$, the formula for calculating the coefficients a_n and b_n of the n -th harmonic can be obtained:

$$a_n = \frac{2}{T} \sum_{k=0}^{N-1} f_k \cos \frac{2\pi}{N} kn \times \frac{T}{N} = \frac{2}{N} \sum_{k=0}^{N-1} f_k \cos \frac{2\pi}{N} kn, n = 0, 1, \dots, N-1 \quad (8)$$

$$b_n = \frac{2}{T} \sum_{k=0}^{N-1} f_k \sin \frac{2\pi}{N} kn \times \frac{T}{N} = \frac{2}{N} \sum_{k=0}^{N-1} f_k \sin \frac{2\pi}{N} kn, n = 0, 1, \dots, N-1 \quad (9)$$

The main controller adapts 128-point Fast Fourier Transform algorithm to extract 0-50 harmonics from the six-channel synchronous sampling data which are obtained from the dedicated measuring chip voltage and current waveform buffer registers. For example, the main controller sets the dedicated measuring chip to collect the instantaneous value of 128 points in one cycle, the sampling frequency is 6.4 KHz. Via low-pass filter dedicated measuring chip suppress high-frequency noise.

C. LoRa Wireless Communication Network Structure

The monitoring terminal utilizes the latest IoT wireless communication technology (LoRa) to set up a wireless sensor network for data transmission. LoRa terminal module utilizes microprocessor based on 32-bit Cortex-M3 architecture as the core, equipped with SX1278 based RF module [4]. The module utilizes an efficient cyclic error correction coding algorithm, which has high coding efficiency and strong error correction capability. Under the condition of sudden interference, the module can correct the interfered data packet proactively [5]. The software flow chart is shown in Figure IV.

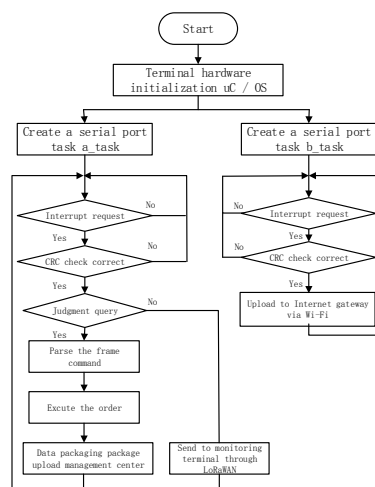


FIGURE IV. LORA TERMINAL MODULE SOFTWARE FLOW CHART

The LoRa wireless network utilizes a star self-organizing network and socket communication based on the TCP / IP protocol to upload the power data to the Internet gateway

through the public network, and is also responsible for receiving instructions from the electric energy data center. When the Lora terminal module receives the packet from the energy data center or the packet uploaded from the monitoring terminal, the Lora terminal module performs CRC check on the packet data to ensure that the data is accurate.

IV VALIDATION OF THE TERMINAL

Table I - Table III is the monitoring power data.

TABLE I. PHASE A MONITORING DATA

N O	Fre que ncy (Hz)	Volt age (V)	Cur re nt (A)	Three- phase unbal ance Factor (%)	Act ive po wer (W)	React ive power (VAr)	Insp ectin g pow er(V A)	Po wer fact or
1	50. 01	231. .8	1.2 1	0.27	188. .7	-16.8	282. 8	0.6 67
2	49. 98	231. .5	1.2 2	0.20	188. .4	-16.0	282. 7	0.6 61
3	50. 16	231. .7	1.2 2	0.25	188. .2	-16.5	282. 6	0.6 65

TABLE II. PHASE B MONITORING DATA

N O	Fre que ncy (Hz)	Volt age (V)	Cur ren t(A)	Three- phase unbal ance Factor(%)	Act ive po wer (W)	React ive power (VAr)	Insp ectin g pow er(VA)	Po wer fact or
1	49.9 9	231. 4	1.21	0.24	188. .5	-16.7	282.7	0.66 7
2	49.9 8	231. 7	1.22	0.25	188. .7	-16.1	282.6	0.66 1
3	50.0 1	231. .7	1.22	0.27	188. .3	-16.6	282.7	0.66 6

TABLE III. PHASE C MONITORING DATA

N O	Fre que ncy (Hz)	Volt age (V)	Cur rent (A)	Three- phase unbal ance Factor(%)	Act ive po wer (W)	React ive power (VAr)	Insp ectin g pow er(VA)	Po wer fact or
1	50.0 1	231. .7	1.21	0.22	188. .3	-16.7	282.8	0.66 5
2	49.9 7	231. .5	1.22	0.25	188. .7	-16.4	282.6	0.66 6
3	50.0 2	231. .6	1.22	0.25	188. .4	-16.6	282.7	0.66 5

The left picture in Figure V shows the real-time waveform of the A-phase voltage of the measurement chip. The right picture shows the 1-10th harmonic values after the Fast Fourier Transform.

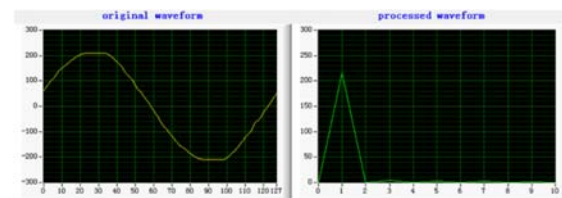


FIGURE V. MEASUREMENT CHIP REAL-TIME WAVEFORM AND HARMONIC VALUES

The test results show that the power monitoring terminal meets the design requirements. In the dynamic range of 5000:1, the nonlinear error of measuring chip is less than 0.1% and the accuracy of monitoring terminal reaches 0.2S level.

V SUMMARY

The power quality monitoring terminal based on embedded and Internet of Things (LoRa) technology is discussed in this paper. Energy monitoring terminal is not only conducive to the energy sector to strengthen the regulation of energy system and improve regulation of energy grid but also provide decision-making basis for the management of power quality.

ACKNOWLEDGMENTS

This paper was supported by the Military and civilian integration project(Shanghai economic and information commission) under Grant No.201720, the Natural Science Fund of China (NSFC) under Grant Nos. 51575186, 51275173, and 50975088, the Fundamental Research Funds for the Central Universities under Grant No. WH0913009, Shanghai Pujiang Program under Grant No. PJ201000353, and Shanghai Software and IC industry Development Special Fund under Grant No. 120493.

REFERENCES

- [1] Bollen M H J. Understanding Power Quality Problems – Voltage Sags and Interruptions J.IEEE Press Series on Power Engineering,2000,15(9):112-117
- [2] Rafiei, M. Elmi, S & Zare, A. (2012). Wireless communication protocols for smart metering applications in power distribution networks. In: Electrical Power Distribution Networks (EPDC), 2012 Proceedings of 17th Conference on.
- [3] Andria G, Savin M, Trotta A. Windows and interpolation algorithms to improve electrical measurement accuracy J. IEEE Trans on Instrumentation and Measurement.38(4): 856-863.
- [4] Malasani R. Long-distance wireless-LAN directional antenna alignment: US, US8462066 P.2013.
- [5] Mohamed Aref, Axel Sikora, Free Space Range Measurements with Semtech LoRaTM Technology A.2014 2nd International Symposium on Technology and Applications(IDAACS-SWS).Oefenbourg,2014,19-23.

A Cloud Platform for Smart Firefighting Facilities Maintenance Based Internet of Things

Wenchao Guan¹, Jianjun Yi^{1,*}, Liang He^{2,3}, Yajun Zhang¹ and Pengfei Liu^{2,3}

¹Department of Mechanical Engineering, East China University of Science and Technology, Shanghai 200237, China;

²Shanghai Aerospace Control Technology Institute, Shanghai 201109, P. R. China;

³Shanghai Key Laboratory of Aerospace Intelligent Control Technology, Shanghai 201109, P. R. China

*Corresponding author

Abstract—The traditional form of maintenance and management of fire facilities has shortcomings such as low efficiency, inadequate supervision, inaccurate updating and inconvenient query of information, causing huge security risks. Therefore, this paper proposes and designs an intelligent maintenance cloud platform for fire facilities based on Internet of things (IoT) and cloud computing, to realize the centralization and transparency of maintenance and management of fire facilities. The platform mainly consists of three subsystems, task management system, facilities file management system and information query system, which archives those functions like the generation, dispatching and management of maintenance task, fire-fighting facilities management and online statistic query. Moreover, it provides users with SaaS services in the form of web and app, which reduces the user's investment in the construction of data center and the development of software. After deployment and operation in a construction unit, the result shows that this platform greatly facilitates the maintenance management of firefighting facilities, improves maintenance efficiency and reduces maintenance cost.

Keywords—IoT; fire-fighting maintenance; SaaS; cloud computing

I INTRODUCTION

The traditional firefighting facilities maintenance is mainly in the form of manual inspection, manual records, paper-based archives, resulting in inefficient supervision, facilities monitoring oversight, the information update delay, inconvenience query of the fire information and many other issues. As a result, the inspection for firefighting facilities is frequently missing and the available firefighting equipment cannot be found in the event of a disaster, which leads to a huge security risk [1]. In addition, single, scattered maintenance system is not conducive to the supervision of fire management. Therefore, it is imperative to study a centralized and platform-based system to achieve fire maintenance management.

Internet of things technology expands the Internet application to the real object and realizes the identification, location, monitoring and management of everything through the collection, transmission, exchange, processing and other processes of physical information. Therefore, by using Internet of things technology, it's possible to identify every fire facility, collect the level, water pressure, voltage and switch volume of

fire facilities, and realize the real-time perception of fire facilities [2]. However, in the face of the storage processing of massive data and the problem of rapid deployment and iteration of the system, the traditional system architecture is not enough to deal with. Thus, it's necessary to introduce cloud-computing technology, processing massive data collected by Internet of things, and carrying Internet of things system, to provide users with platform services.

At present, the firefighting maintenance systems at home and abroad are being developed and in operation, but most of these are independent systems. They cannot provide platform services and easily lead to forming information islands. Therefore, based on Internet of Things and cloud computing technology, this paper designs and develops a cloud platform for smart firefighting facilities maintenance, to provide platform services for the maintenance and avoid shortcomings of current systems. The main contents are as follows: the first part mainly introduces design of this cloud platform architecture, including basic IoT layer and platform layer, the second part focuses on the design and implementation of main functions of intelligent maintenance system operating in this cloud platform. Finally, this paper introduces the verification of this platform and makes a conclusion.

II ARCHITECTURE OF THE PLATFORM

To achieve intelligent maintenance of firefighting facilities, it needs to identify every facility and record the data including basic information and maintenance records so that we can obtain real-time operating status of fire-fighting facilities, to find out the problems in the operation of fire-fighting facilities in time and eliminate the hidden danger in the bud. Therefore, the cloud platform for smart fire facilities maintenance designed by this paper consists of IoT infrastructure layer and cloud platform layer. Figure I shows the architecture diagram.

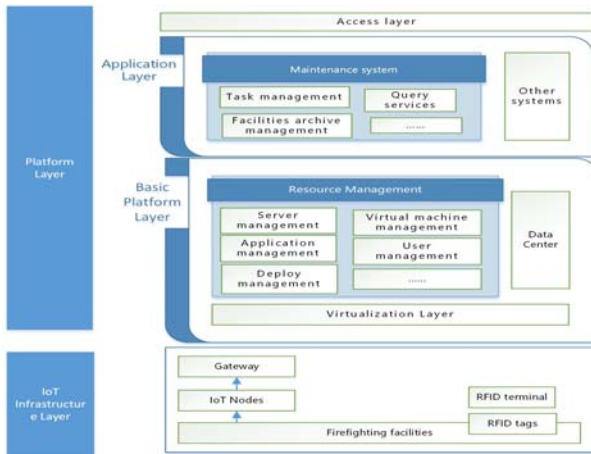


FIGURE I. THE PLATFORM ARCHITECTURE

In the IoT infrastructure layer, real-time on-line monitoring of firefighting facilities can be accomplished by deploying self-developed IoT monitoring nodes to collect firefighting facilities data such as water pressure and power supply in real time, and then forwarding the data to the cloud platform, so that abnormal situation can be found and processed in time. RFID tags are used to identify firefighting facilities, and the RFID terminal can upload the real-time data like the data of facilities maintenance so as to achieve accurate and timely collection and tracking of facilities data.

In the platform layer, the support layer provides the basic environment for the application layer and is divided into three layers, virtualization layer, resource management layer and data center. The virtualization layer virtualizes physical resources including server clusters, storage devices and network devices and so on to form a virtualization pool [3,4]. The resource management layer is responsible for all virtual resource management, including resource allocation, virtual machine resource management, application deployment, user management and so on. And the data center is responsible for storing and processing data related to the platform and cloud applications [5]. The application layer carries the system of smart firefighting facilities maintenance designed by this paper and provides firefighting maintenance services in SaaS for users.

III DESIGN AND IMPLEMENTATION OF THE PLATFORM

The cloud platform for smart firefighting facilities maintenance designed by this paper mainly provides users with SaaS form of maintenance service. Therefore, public cloud is used for providing cloud platform operation environment for application platform layer. And in the application platform layer, services are mainly provided by the smart firefighting maintenance system, which constructed by J2EE technology [6]. The architecture diagram of this system is shown in Figure II.

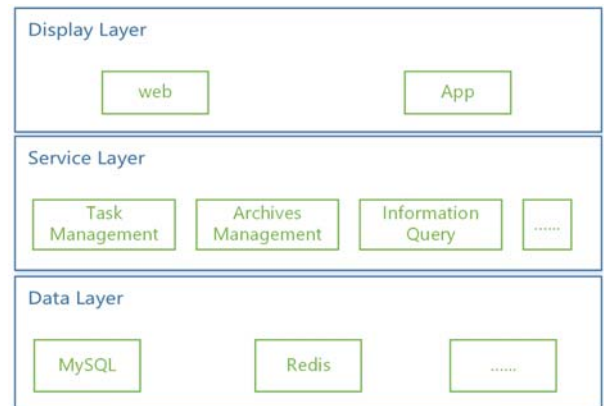


FIGURE II. SMART MAINTENANCE SYSTEM ARCHITECTURE

A. Task Management Subsystem

The task management subsystem is mainly responsible for the configuration, generation, scheduling and management of tasks such as the maintenance task and the inspection task. This system consists of four parts: application service for maintenance, task configuration service, task scheduling service and task management service. Figure III shows data stream between above four parts.

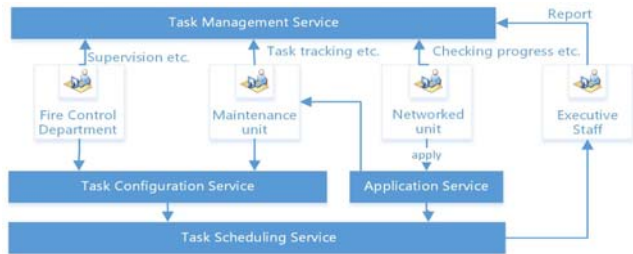


FIGURE III. THE RELATIONSHIP DIAGRAM OF FOUR PARTS OF TASK MANAGEMENT SUBSYSTEM

The task configuration service provides configuration service for different types of task, including periodic task, task from application form, random task and so on. The firefighting maintenance unit can configure periodic maintenance tasks, inspection tasks through the service, including 2-hours inspection, 8-hours inspection, daily inspection, weekly inspection and custom inspection and so on. And the fire management unit can create random inspection task to complete the fire safety inspection work for the jurisdiction units through the service. After the configuration completed, the system automatically generates the task book and sends it to the scheduling system for unified task scheduling.

The task scheduling service part mainly achieves the function of dispatching tasks to the corresponding personnel, including maintenance application, periodic tasks, tasks that need to be manually scheduled, and tasks that are temporarily scheduled. When the user's application for maintenance service is approved, the dispatching service will select the appropriate maintenance personnel to receive the task according to the priority of the task and the location of the service client and the location of the service personnel on the map, and send the task to

the selected maintenance personnel. Figure IV shows the workflow of this service.

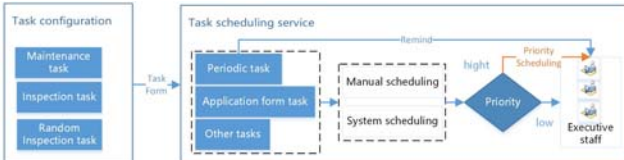


FIGURE IV. THE WORKFLOW OF TASK SCHEDULING SERVICE

The task management service provides services with users like tracking position and status of workers during the task, checking task progress, reviewing task reports and evaluating maintenance service and so on. During task execution, the system tracks the real-time geographic location of the workers corresponding to the task and records the real-time trajectories and the task logs. After the task completed, the system automatically generates the task report according to the task records uploaded by the operator for the relevant personnel to review. The networked unit users can make evaluation for the maintenance service, which will be included in the task report and checked by the audit staff. Figure V shows the service workflow.

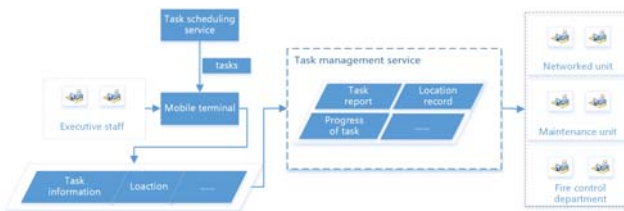


FIGURE V. THE WORKFLOW OF TASK MANAGEMENT SERVICE

B. Management Subsystem of Facilities Archives

The management subsystem of facilities archives is responsible for the management of electronic archives of firefighting facilities. First of all, by sticking or packaging RFID tags on fire-fighting facilities they can get the unique identification mark. These tags can only be read or written by the RFID terminals that have been registered in the platform, which solves the problem of difficult identification of fire-fighting facilities. Then, users can use those terminals to record and upload the usage of firefighting equipment or the data of maintenance or inspection of firefighting facilities by reading or writing the tags on them [2,7,8]. These data will be uploaded into this subsystem. When there are abnormal information such as abnormal report, expiration of firefighting equipment, the system will automatically notify the manager to process, ensuring that all the equipment is in the available state. In this way, the system can record and track all the data in firefighting facilities service cycle.

C. Information Query Subsystem

This paper builds query engine for the information query subsystem based on Elastic Search, which provides query services to user information, statistical information, and historical record and so on:

- User information query: This service provides user account detail and basic information of all networking units. These information will be different for different roles.

- Statistical query: The statistics query service provides diversified data statistics service and displays the query results graphically. And different users can get different query result according to their authorities. For example, networking units can just make statistical inquiries on the operation of their own firefighting facilities and keep abreast of the operation of fire-fighting facilities. The fire control departments can make statistical query on all the data in the area under their jurisdiction.

- History query: The history query service provides querying of the history of maintenance tasks, the inspection tasks and other historical records, including the application form of maintenance service, service job records of service personnel, job reports, and the history of job scheduling records and so on.

IV VERIFICATION OF THE PLATFORM

This paper takes the firefighting facilities maintenance in a certain unit's building as a pilot to verify the function and stability of the system. Take fire extinguisher maintenance in this unit as an example. The management of the unit fire extinguisher is chaotic before access to the system. The problems like lack of information records, lack of maintenance, fire extinguishers missing, expired issues not found in time etc. existed for a long time. After access to the system, the fire extinguishers in all places are identified through RFID tags and their electronic records are stored into the data center of the platform. By scanning these tags through mobile RFID terminals, the user can query detail information of a fire extinguisher, record and upload the abnormal information or data of fire extinguishers inspection or maintenance, which ensures in-time update of relevant information of the fire extinguisher. By summarizing all these information, the system feedback problems such as fire extinguishers missing or expiring to the responsible person in time to guarantee that they can identify and solve these problems in time. After online configuration of periodic inspection of fire extinguisher and maintenance tasks, the system automatically sends these tasks to designated personnel and reminds them when the time of next execution of the task is up. It ensures the effective implementation of fire extinguisher maintenance system, avoiding the problem of missing even disorderly, giving to the unit a great convenience of fire extinguisher maintenance management work. Figure VI shows a pc webpage screenshot of the system.

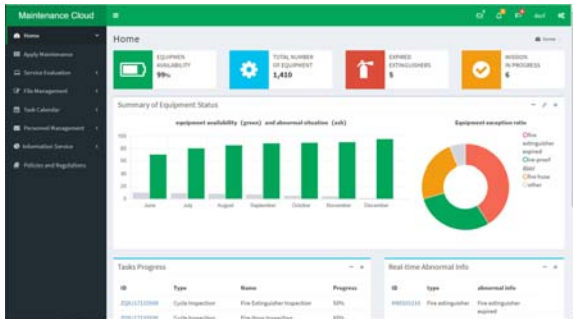


FIGURE VI. HOMEPAGE SCREENSHOT OF SYSTEM UNDER THE AUTHORITY OF NETWORKED UNIT

Through the pilot verification in this unit, it shows that this cloud platform designed by this paper can provide users with platform-based maintenance services, greatly improving the maintenance efficiency of fire facilities and reducing costs, achieving the anticipated goals.

V CONCLUSION

This paper, by combining Internet of things and cloud computing technology, designs and develops a cloud platform for smart firefighting facilities maintenance, which provides platform services for the maintenance and management. By using this platform, users of networked units can conveniently apply, track and evaluate maintenance services, and the maintenance units can promptly conduct the acceptance, arrangement and management of maintenance services. In addition, fire control departments can conveniently conduct relevant inspections, issue announcements. It greatly improves the efficiency of fire maintenance and management and reduces costs. Moreover, the design of this platform fully takes into account the versatility and scalability so that the platform can be applied to not only the fire facilities maintenance, but also other facilities maintenance field.

ACKNOWLEDGMENTS

This paper was supported by the Military and civilian integration project(Shanghai economic and information commission) under Grant No.201720, the Natural Science Fund of China (NSFC) under Grant Nos. 51575186, 51275173, and 50975088, the Fundamental Research Funds for the Central Universities under Grant No. WH0913009, Shanghai Pujiang Program under Grant No. PJ201000353, and Shanghai Software and IC industry Development Special Fund under Grant No. 120493.

REFERENCES

- [1] Tian-yi Shen, Xing-yuan Wang, Nan Xu, Qian Cao. The design of firefighter maintenance supervision system by information technology, J. Electronic Technology & Software Engineering. 12 (2017) 228.
- [2] Lei Xu. Research on Smart Grid Equipment Management System based on RFID Internet of things Technology, D. North China Electric Power University. (2016).
- [3] Fu-yong Kang. Environmental Private Cloud Platform Design and its SaaS Model Zongliang Jianpai Business System Implementation, D. University of Electronic Science and Technology of China. (2013).
- [4] Jin-Mook Kim, Jeong-Kyung Moon, Bong-Hwa Hong. Research of Virtualization Services Valuation for Cloud Computing Environment, J. Embedded and Multimedia Computing Technology and Service. 181 (2012) 631-620.
- [5] Harrabi M A, Sofiene C, Wafa M. Deploying an internet of things cloud platform on openstack, J. Information Technology and Computer Applications Congress. (2015).
- [6] Cheng-gang Yang. Fire Management System Design and Implementation Based on Internet of Things, D. Jilin University. (2015).
- [7] Zhong-quanYang. Design and Realization of Firefighting Facilities Monitoring Platform Based on RFID Technology, J. Technology and Economic Guide. 20 (2016) 18-19.
- [8] Na Li, Ai-nan Wang. Intelligent Fire Storage System Based on Internet of Things, J. Internet of things technologies. 11 (2017) 42-44.

K-out-of-n Model to Calculate the Availability of a Business System

Huan Xu¹, Ruihong Yan^{2,*} and Xiaoling Wang³

¹Information Department, China Southern Power Grid Guangzhou, Guangdong, China

²Department of Computer Science and Engineering, Shanghai Jiao Tong University, Shanghai, China

*Corresponding author

Abstract—This paper shows a model to calculate the availability of a business system. K - out - of - n model is a system consists of n parts. When there are at least k parts during normal work, the system can work normally. Also, the paper gives a MTBF usability testing method to test the availability.

Keywords—availability; k out of n model; MTBF

I INTRODUCTION

Because of the informatization, all kinds of network infrastructure, application system constantly improve and upgrade. There is a growing dependence on information grid system. With the deepening of the process of informatization, informatization gradually entered a period of application and network integration development from the basic network construction, application system construction. The traditional information management can no longer meet the needs of the automation and standardization of information management. There is an urgent need for effective means of scientific management to realize the operation maintenance function, and realize the maximization of interests [1].

In environment of the smart grid, the establishment of an information system for operational monitoring actively monitoring platform is very important, which can realize the management of the information system of the safety equipment and security protection, information filtering of the smart grid environment, active operations of the various controlled equipment monitoring management.

Smart grid business involved in power grid dispatching automation, relay protection and safety equipment, power plant control automation, substation automation, distribution network automation, electric power load control, power market, power user information collection, intelligent electricity and other fields. The smart grid system contains many hardware and software technology, involves many manufacturers products. The complex environment of application system integrated use, the different structure and the infrastructure make it difficult to get a unified management. Branches widely distributed in the system and complex equipment take the challenges for unified management. Parallel network and the present situation of the large users bring difficulties to smart grid operations management standardization work. Mass of network devices, the host server, without a unified platform, application system can't formulate unified management strategy, troubleshooting

rate is low, the core business is run normally without effective detection means, unpredictable and take measures in advance. And with the continuous development of information construction, the complex huge infrastructure also in unceasingly thorough, in products, network structure, business relationships continually changing [2].

In the information system of power grid enterprise, even if they deploy with a variety of operational monitoring system, but also often have a business system problem how to find the point of failure. Investigate its reason, mainly is the most current operational monitoring system is separated to monitor the working state of the business system component, such as network, server, database, etc., and the operational monitoring level is low. Especially in the network environment, if only know presented according to a switch port throughput or grouping, it is difficult to find cause of abnormal operation [3].

To solve this problem, an effective way is the construction of an integrated operational monitoring management platform: it is able to run with the organization's current environment matching effectively, help the managers to master the complex information system running state, at the same time, provide management personnel with concise and effective operation monitoring system, help the organization to enhance operational monitoring efficiency. Ensure the effective use of information resources and business operation with high availability, continuity and security [1].

II RELATED WORK

The operational monitoring management information system in early stage focus on individual equipment more such as hardware and network management, mainly take the infrastructure network, then the operational management is through the management of the network devices and monitor and ensure the normal operation of the network. When malfunction come down, system response in time and locate equipment failure. But this kind of system for business system can only carry on the simple management operations. With the mature of enterprise information system, enterprise's focus shifting from the single point of equipment management monitoring to the whole integrated management system [1].

But because the rapid development of technology, IP technology gradually become the key infrastructure of the business for carrying all kinds of data, workflow, the application

of interactive, multimedia information. On the one hand, all service in the information system of organization's core business, must depend on IP technology to realize the connectivity, on the other hand, IP technology for access to these complex information system and management provides a good consistency, real-time performance management channel. Based on the IP based network, various network, computing, storage, and application of integrated management become possible.

In the early 1980's, the British government commerce (OGC) in order to improve the efficiency of information equipment and systems, to guarantee the healthy operation of information system of effective service outsourcing management, computer and communications agency is designated to research a kind of method, which is used to guide the efficient and economic operation of the national government department information equipment and systems. And Library of information Infrastructure (IT Infrastructure Library, ITIL) comes out. It brings together the best practices of IT service industry. ITIL is to guide how to define in operations management personnel, process, service, activities and the relationship between guiding framework mouth [4].

ITIL has experienced more than 30 years of development. In 2005, the international organization for standardization based on ITIL made the IS02000 international standards of IT service management. According to the demand of government departments, business groups and the energy industry enterprise development, ITIL can ensure the effect of the IT resources and low cost. Large IT companies and relevant government departments make ITIL get continuous growth and rich. ITIL eventually becomes internationally recognized best practices [5]. And now, ITIL standard is widely used in companies such as Microsoft, HP, IBM, CA, and is put into practice. On the basis of practice, ITIL forme the respective ITSM (information technology service management, IT service management) method theory and products, and become their IT services market brand. Based on ITIL processes and philosophy, user can establish a reasonable working process, reasonable arrangement of personnel, clear responsibilities, avoid fault mutual shuffle. It can help the relevant person in charge of business find and solve the problem, quickly resume business. With the unified monitoring platform, the various monitoring resources are centralized to display and alarm for unified management, overall comprehensive, fast, understand the running status of the current system help operations staff to quickly locate the fault, shortening the time of screening [6].

III K - OUT - OF - N SYSTEM MODELING

K - out - of - n model is a system consists of n parts. When there are at least k parts during normal work, the system can work normally. If there are n - k parts malfunctioned, it will enter a state fault system. K - out - of - n models are common descriptions and fault-tolerant computing research and engineering design model of the redundant system, which can be widely used in fault-tolerant technology of information system. For a given k - out - of - n system, the system will run to the system failure. There is a sequence of failure parts. Every failure of components effect the remaining parts of survival. When the first n - k + 1 components fail, while the rest of the k - 1 parts or

normal, the whole system has failed. If we ignore the possible correlation between target system components, it is possible to underestimate the failure rate of the whole system, and to overestimate the analysis of the system availability indicator.

For the normal work of the k - out - of - n system, assumed to satisfy the following conditions:

1) k - out - of - n system, which all the parts are in good condition in the beginning, when the work parts number is less than k or failure parts number is greater than n - k + 1, will enter a state of failure;

2) n component failure events are independent of each other. Assuming failure can immediately be detected, multiple component failure probability is zero at the same time;

3) r maintenance personnel can only repair one part at the same time a part. The events that $1 \leq r \leq n-k+1$ parts can be repaired are independent of each other. And repair time obey exponential distribution parameter for μ ;

4) the system state depends on the number of components in the system failure, such as the system is in state i said i have a component failure;

5) during the system running, all load borne by the current live parts evenly, for example if the system is in state i, which means there are i components in failure state, then the full system load will be split by residual n - i the parts.

6) when system is in i state, the single component obeys exponential distribution parameter λ_i , α_i indicates the failure rate of system in the state i, μ_i says the system is the repair rate in state i.

When the system is in state 0, the failure rate of each parts is λ_0 . There are n possible components failed at this time, so the probability of state 0 to state 1 is $\alpha_0 = n\lambda_0$; When the system is in state 1, the failure rate for each component is λ_1 . The component failure may occur n - 1 conditions, so the probability of state 1 to state 2 is $\alpha_1 = (n-1)\lambda_1$, and the rest of n - 1 parts divide all load. The transition probability of state 0 to the state 1 is $\mu_1 = \mu$; When the system is in state i, component failure has n - i conditions, failure rate for live parts is λ_i , the system will have probability of $\alpha_i = (n-i)\lambda_i$ into the i+1 state, and n - i live parts divide all loads.

Given a random variable N (s) stands for the number of failure parts in the interval (0, s), and $N(0) = 0$. Apparently random process $\{N(s), s \geq 0\}$ independent increment, and does not occur at the same time two component failure, therefore $\{N(s), s \geq 0\}$ is an independent increment, and it won't happen that there are two failed parts at a same time.

Given T_i which stand for the time staying in each state. It is a set of random variables of two parameter weibull distribution. The correlation of the time T_i of system in state i-1 with the time after system state i, is the affect of the ith failed part to the rest parts. Given S_i stand for the time point of ith part failed, and

there are $S_t = \sum_{j=1}^t T_j$. The Copula function of multidimensional random variables ($T_1, T_2, \dots, T_n - k$) which are composed with the above a set of random vector, is a marginal distribution function $F_1(t_1), F_2(t_2), \dots, F_{n-k}(t_{n-k})$ of the multivariate distribution function, and has the Gumbel copulas connect functional form.

Given a sequence of failure parts, the correlation coefficients between the part i and part j in failure sequence can use r_{ij} to measure, correlation coefficients between all the parts can be said as a correlation matrix $R = (r_{ij})$, one of them

$$r_{ij} = \begin{cases} \tau_{ij}, & 1 \leq i < j \leq n - k + 1 \\ 1, & i = j \\ 0, & i > j \end{cases} \quad (1)$$

K - out - of - n system component failure sequence correlation matrix calculation algorithm is as follows

K - out - of - n system component failure sequence correlation matrix calculation algorithm

Input: n, k, the system state set $\{0, 1, \dots, n - k\}$, component failure time sequence $T_1, T_2, \dots, T_{n-k+1}$, output: related to the matrix $R = (r_{ij})$

steps:

1. Calculate single component failure rate in system 0 condition
2. Calculate the failure rate system in each state
3. The timing of the system state transition sequences

$$S_m = \sum_{1 \leq m} T_m, m \in \{1, 2, \dots, n - k + 1\}$$

4. Uses $\alpha_m = \lambda_0 S_m^{Y-1}$ to calculate Y

5. Use λ_0 and Y to get the distribution function T_i

$$u_i = e^{\lambda_0 S_{i-1}^Y - \lambda_0 (S_{i-1} + t)^Y}, i = 1, 2, \dots, n - k$$

6. The correlation coefficient calculation

for $i = 1 : n - k$

for $j = i + 1 : n - k + 1$

Kendall rank correlation coefficient calculation

end

end

7. Return $R = (r_{ij})$, in

which $r_{ij} = \begin{cases} \tau_{ij}, & 1 \leq i < j \leq n - k + 1 \\ 1, & i = j \\ 0, & i > j \end{cases}$

IV OUR EXPERIMENT

We put forward a project based on the threshold of MTBF usability testing method, it can be in a shorter test period and make full use of a small amount of the system under test, test verification system can reach purchase demand for usability metrics

For a given repairable k - out - of - n system, if the system steady-state availability for a given value is a , then you can always find a minimal positive integer min_b , when work than B min_b or maintenance time, meet

$$(k-1)! \left(\frac{B^{n-k+1}}{n!} + \frac{B^{n-k}}{(n-1)!} + \frac{B^{n-k-1}}{(n-2)!} + \dots + \frac{B^1}{k!} + \frac{B^0}{(k-1)!} \right) \geq \frac{1}{1-a} \quad (2)$$

MTBF

In which $B = \frac{MTBF}{MTTR}$

Average trouble-free operation index MTBF (mean time between failure) refers to the repairable k for a given threshold k - out - of - n system, if a single redundant component in the mean times to repair MTTR (mean time to recover) index can be obtained by measuring, the MTBF of the redundant parts of threshold value is defined as $\min B * MTTR$.

And MTBF mean for a given threshold value theorem can repair k - out - of - n system, if a single redundant component in the mean times to repair can be obtained by measuring the MTTR indicators, for a given system steady-state availability forecasts a , we can always find $\min * MTBF$ redundant components, as long as the average trouble-free operation time redundant components index $MTBF > \min * MTBF$, there will be established system availability $A > a$.

It can be seen from the MTBF threshold value theorem, that for a k - out - of - n redundant system, if the MTTR of the redundant components are measurable, we do not need to measure the whole system by using the method of online test for a long time availability index, just in a relatively short period of time of redundant components MTTR and MTBF testing. As long as you can verify its component index MTBF is greater than its MTBF threshold, can explain the given k - out - of - n redundant systems to achieve a given level of usability.

V CONCLUSION

This paper designed and implemented a K - out - of - n system modeling to get the data of a system. In addition, we design a MTBF threshold value theorem to test the system. By using such evaluation model, system can be analyzed, and it can help system manager to evaluate the availability. We hope these works be a theoretical and practical guide for future research.

ACKNOWLEDGEMENT

This research was financially supported by the National Science Foundation.

REFERENCES

- [1] Liu Yawei. IT operational monitoring management system based on SOA architecture design and implementation [D]. Tianjin university of technology, (2014).
- [2] Lee. The smart grid environment information active safety control system design and implementation [D]. Xiamen university, (2014).
- [3] Wu Shun Xu Dawei, Wei Zheng, Hu Chengchen to Wan Gong, guo, Tang Yazhe. Information system based on user experience active operations platform [J]. Electric power information column, (2014).
- [4] Huangyan, Canal. ITIL practices: operations management system design and implementation of [J]. South China financial computer, 2009 (8): 16 to 18.
- [5] Xu Weizhong, Xu Hao, and Gao Donghuai. The campus network integrated service management system based on ITIL study [J]. Information technology, 2012, (2): 114-117.
- [6] Jan van Bon. IT Service Management And Introduction, VanHarenVanHaren Publishing, (2002): 20-58.

Research on Implementation of Knowledge Convergence Based on Apache Jena3

Xiabai Yang^{1,*}, Ming Yang¹, Deqiang Yang² and Yu Huang³

¹Yunnan College of Finance and Economics, Kunming 650222, China

²College of Computer Science and Information Technology, Yunnan Normal University, Kunming 650092, China

³Kunming Railway Vocational Technical College, Kunming 650208, China

*Corresponding author

Abstract—With the development of Internet and Semantic Web technology, a huge amount of information appears on the network. Meanwhile, more and more knowledge was described based on XML (eXtensible Markup Language) and RDF(Resource Description Framework)format. It is a worthy study on problem of Knowledge Convergence on “how to make the computer automatically to extract useful knowledge from the existing knowledge through the Set Operation and reasoning”. This paper mainly studies on the architecture of Apache Jena3, operations of Union, Intersection and Difference. And these operations are Knowledge Convergence implemented by Java programming based on Apache Jena3 system. The results have been validated by online Parser “W3C RDF Validator”, which proves that the programming design implementing Knowledge Convergence based on Apache Jena3 is correct.

Keywords—apache jena3; semantic Web; RDF; RDFS;OWL; knowledge convergence; union operation; intersection operation; difference operation; triple

I. INTRODUCTION

In February 1998, XML1.0 became the standard recommended by the W3C(WWW Consortium). RDF was adopted as a W3C recommendation in 1999. The RDF1.0 specification was published in 2004, the RDF1.1 specification in 2014. RDFS(Resource Description Framework Schema Specification) is an extension of the symbol and syntax of the XML language, which can be said of RDF data and grammar Specification.

With the development of the semantic WEB, the Internet knowledge based on XML format and RDF format is increasing, and it is a worthy study on problem of Knowledge Convergence on “how to make the computer automatically to extract useful knowledge from the existing knowledge through the Set Operation and reasoning”. Since 2003, my team has studied the semantic WEB architecture, Jena2 architecture, RDF API of Jena2 system, Triple (subject, predicate, object) and Triple Store, based on Jena2 system using the Java programming to realize the Union, Intersection and Difference Operation of Knowledge Convergence, and the relevant papers have been published. This paper mainly studies on the architecture of Apache Jena3 system, operation of Union, Intersection and Difference. The operations are Knowledge Convergence achieved by Java programming based on Apache Jena3 system, and the program results have been validated by online Parser “W3C RDF Validator”, which proves that the

programming design achieving Knowledge Convergence based on Apache Jena3 is correct.

II. SEMANTIC WEB ARCHITECTURE

In 2001, Tim Berners-Lee, the founder of WWW proposed the semantic Web architecture is made up of seven layer[1], as shown in figure I, from down to up in turn to Unicode+ URI, XML+NS+XMLS, RDF+RDFS, Ontology Vocabulary, Logic, Proof and Trust, which lays the foundation for the development of the semantic Web.

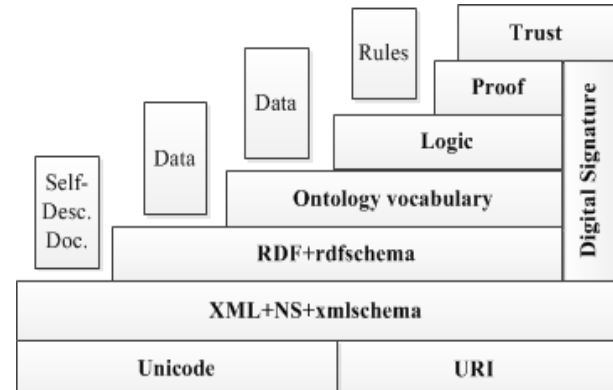


FIGURE I. SEMANTIC WEB ARCHITECTURE

III. APACHE JENA3 ARCHITECTURE OVERVIEW

Jena1 was the first version released in 2000, Jena2 in 2003, Apache Jena3(Jena3) in 2015.

Jena3 is a free and open source Java framework for building Semantic Web and Linked Data applications. It is a toolkit for processing semantic WEB written in the Java language[2]. Jena3 is a major version release for Jena - it is not binary compatible with Jena2. The migration consists of package renaming and database reloading. Packages with a base name of com.hp.hpl.jena become org.apache.jena.

At Jena3's core, it stores information as RDF triples in directed graphs, and allows programming to remove, add, store, manipulate and publish that information. Jena3 consists of several subsystem such as Store API, Inference API, Parsers and writers, RDF API, Ontology API, SPARQL API and Fuseki, etc. As shown in figure II.

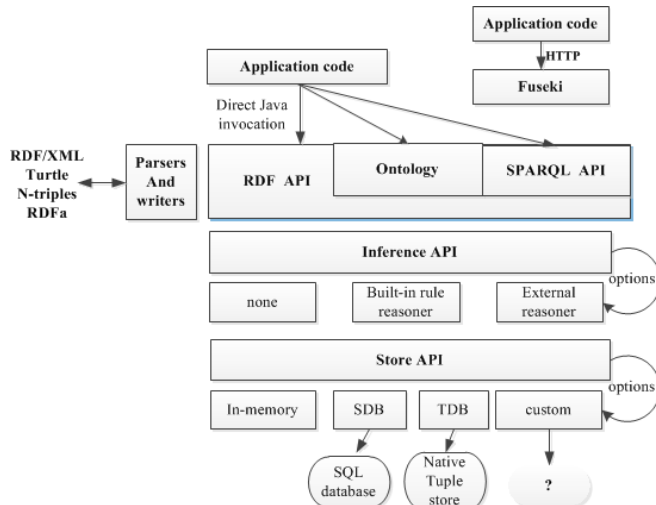


FIGURE II. THE APACHE JENA3 ARCHITECTURE

A. RDF API

The RDF API provides Java application interfaces for users that create and read RDF graphs, and support for RDF/XML or Turtle formats. SPARQL (Simple Protocol and RDF Query Language) is an engine for querying RDF data, which is a Query Language and data acquisition Protocol for RDF development and connects web3.0 and Semantic web, supporting remote federated queries and free text search.

B. Store API

Store API mainly provides TDB and SDB applications, TDB is the data saved in a Triple format, which supports the full range of Jena APIs. SDB is data saved in SQL database format.

C. Ontology API

Ontology API usage models, RDFS and the Web Ontology Language (OWL) add extra semantics for RDF data. RDF has two ontology languages: RDFS and OWL. OWL is much more expressive, and Jena3 supports both languages through the Ontology API.

D. Inference API

Inference API provides an application interface for reasoning, which can work based on the rules of inference or using built-in OWL and RDFS reasoners.

The main features of semantic web applications: the semantic rules of RDF, RDFS and OWL can be used to infer unknown information that is contained in RDF direct graph. For example, if C is the biological father of B, and B is the biological father of A, then by implication C is the grandfather of A, and A is the grandson of C.

E. Fuseki

Fuseki provides interaction with your server-side RDF data over HTTP. That is to say: Fuseki is a server, and it can access RDF models data over the web using SPARQL and HTTP.

IV. DESIGN AND IMPLEMENTATION OF KNOWLEDGE CONVERGENCE BASED ON APACHE JENA3

The website of Apache Jena (<http://jena.apache.org>) is an open source web site which studies and researches the Jena system. Apache Jena provides common Apache-jena and Apache-jena-fuseki for semantic WEB users.

Apache-jena contains API, SPARQL engine, TDB (native RDF database) and command-line tools. Apache-jena-fuseki is the Jena SPARQL server. In 2017, the new version released by Apache Jena is Apache-jena-3.6.0.Zip and Apache-jena-fuseki-3.6.0.Zip. Jena3 requires Java8 (from Jena version 3.0 onwards).

Development environment set up: Windows 7 operating system, install Java 1.8.0_121,Eclipse4.7.0, download Apache-jena-3.6.0. Zip, set up the Eclipse environment, import the Jena system and call the RDF API programming provided by the Jena system to implement Knowledge Convergence by the operations of Union, Intersection and Difference (source code omitted). The interface design is showed in figure III.

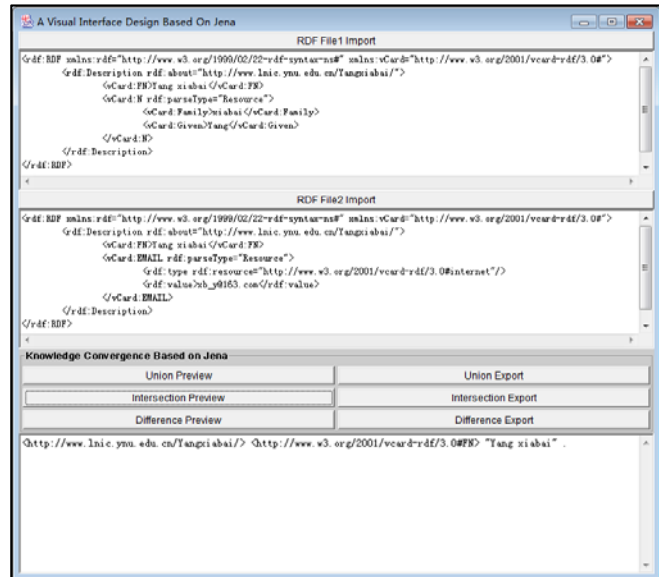


FIGURE III. A VISUAL INTERFACE DESIGN AND INTERSECTION PREVIEW (WITH THE OUTPUT FORMAT "N-TRIPLE")

Figure 3 shows the interface design of the Knowledge Convergence and the results of the Intersection Operation (N-TRIPLE parameter display). The command button "RDF File1 Import" and "RDF File2 Import" respectively implements the import of first RDF file and the second RDF file from the storage medium. The contents of the two RDF files are shown in Textbox1 and Textbox2 respectively. The "Union Preview", "Intersection Preview" and "Difference Preview" command button respectively implement the Union, Intersection and Difference Operation between RDF file1 with RDF file2 and show the results in the Textbox3. The "Union Export", "Intersection Export" and "Difference Export" command buttons respectively implement the Union, Intersection and Difference Operation between RDF file1 with RDF file2, and export the results to the storage medium.

V. PARSERS AND VALIDATION RESULTS

"The W3C RDF Validator" is an RDF Validator provided by the website (<https://www.w3.org/RDF/Validator/>). The two original files (file1.rdf, file2.rdf) and the three RDF files (Union.rdf, Intersection.rdf, Difference.rdf) which were generated from the program in figure 3 are uploaded to the web site for parsing and validation respectively. As the results shown from figure IV to figure VIII, each figure shows the corresponding Triple and Graph of the RDF file.

Figure IV is the original File1.rdf document. Figure V is the original file2.rdf document. Figure VI is the result of Union Operation between fine1.rdf with fine2.rdf. Figure VII is the result of Intersection Operation between fine1.rdf with fine2.rdf. Figure VIII is the result of Difference Operation between fine1.rdf with fine2.rdf.

The validation shows that the results obtained from the Union, Intersection and Difference Operation of Knowledge Convergence between RDF file1.rdf with RDF file2.rdf are correct.

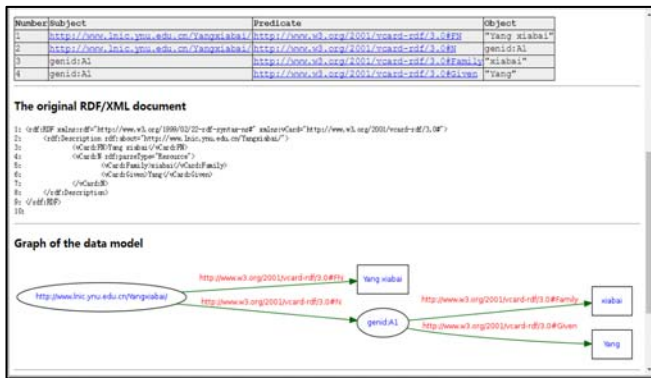


FIGURE IV. THE ORIGINAL FILE1.RDF DOCUMENT

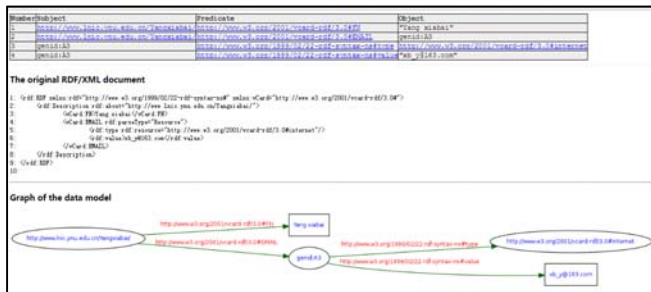


FIGURE V. THE ORIGINAL FILE2.RDF DOCUMENT

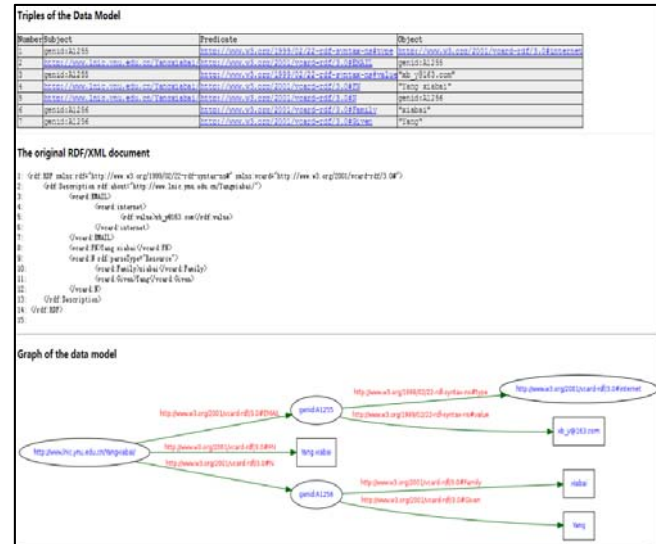


FIGURE VI. THE UNION OPERATION RESULT

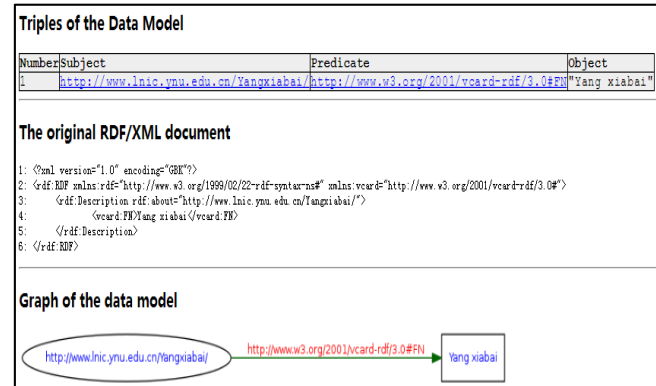


FIGURE VII. THE INTERSECTION OPERATION RESULT

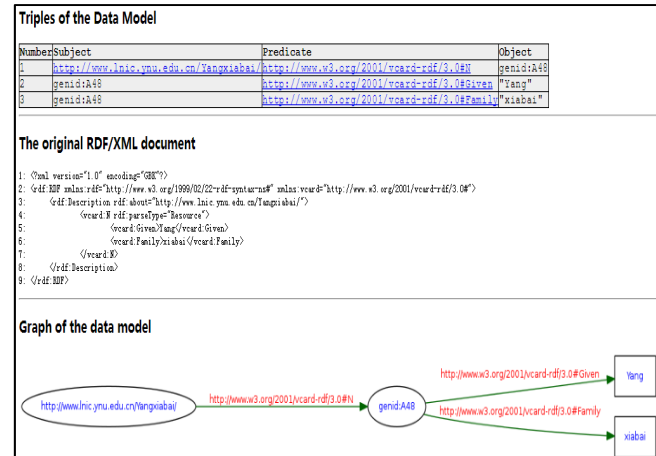


FIGURE VIII. THE DIFFERENCE OPERATION RESULT

REFERENCES

- [1] Berners-Lee, T.; Hendler, J.; Lassila O., "The Semantic Web", Scientific American, May 2001.
- [2] http://jena.apache.org/about_jena/architecture.html, "Jena architecture overview", January 2018.

The Semantic Retrieval System for Learning Resources Based on Subject Knowledge Ontology

Bei Wu

College of mechanical and Electronic Information, Wuhan University of Engineering Science, Hubei, 430200, Wuhan, P. R. China

Abstract—There are many kinds of learning resources in the online education platform, but there are still many problems, such as learning resources are difficult to retrieve, search results are redundant, and can only be retrieved by keywords, but lack of semantic support. This paper integrated semantic web into the retrieval of learning resources, and designed the subject knowledge ontology as the knowledge description of learning resources semantic retrieval system, and implemented the semantic retrieval of learning resources through ontology concept similarity analysis, ontology reasoning and ontology in computing and other sectors, to reduce the redundancy of information retrieval results and realize the display of high related resources.

Keywords—knowledge retrieval; knowledge navigation; learning resources

I. INTRODUCTION

Digital learning resources have massive, distributed, heterogeneous, multi-level features, and there are different standards, high cost, personalized, low level intelligent services, resulting in a large number of digital learning resources can not be shared. One hand, digital educational resources can be shared and poor, on the other hand, digital educational resources is redundant.

Serious waste retrieval of educational resources caused great distress to the learner. How to integrate these various types of the public the mass education resources for learners to provide a unified retrieval services, and the field of digital learning problems to be solved.

Existing solutions such as search engine technology, and other applications in the field of network resource retrieval, the far-reaching social implications. Information retrieval technology is currently mainly solve the massive resources of the indexing and retrieval can not solve digitized learning the knowledge organization and meta-data semantic description such as, therefore general-purpose search engine technology in the field of digital education resources integrated retrieval also can not completely meet the digitized learning in a areas learners personalized needs.

There are two reasons: the description of learning resources is different and lack of a unified educational resources metadata standard description system, no fixed metadata mapping mechanism; Second, the distribution of educational resources is too wide, the various disciplines are not formed unified body of discipline, lack of effective methods and means of the educational resources of knowledge organization. Search engine using traditional principle, there is no strict norms of scientific terminology entry, and use key words to search for related information,

and show the advantages of rapid positioning precision appeared to be inadequate.

In response to these problems, the paper proposed the digital learning resources knowledge organization model which is applied to retrieve digital learning resources. Based knowledge organization model of digital educational resources, it can effectively solve the semantic gap problem of digital educational resources metadata, semantic mapping mechanism is formed between the metadata descriptions, and to lay the basis of resource integration for integrated retrieval of digital educational resources. Therefore, this paper will apply knowledge organization model of educational resources to the organization, navigation and retrieval of digital learning resources, to build knowledge-based organizational model of digital learning resources navigation prototype system. The paper uses knowledge organization model of learning resources to knowledge organization for Educational Technology website navigation on the classification of the network of educational resources.

II. THE APPROACH OF THE CONSTRUCTION FOR KNOWLEDGE RETRIEVED AND NAVIGATION SYSTEM

An easy way to comply with the journal paper formatting requirements is to use this document as a template and simply type your text into it.

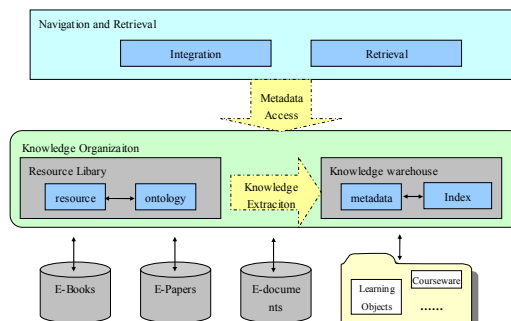


FIGURE I. THE APPROACH OF THE NAVIGATION AND INTEGRATED RETRIEVAL FOR LEARNING RESOURCES

Ontology-based knowledge organization model is applied to the integrated retrieval. The approach of the navigation and integrated retrieval for learning resources is shown in Figure I.

The navigation and integrated retrieval for learning resources includes the following modules:

The resource layer: the main data file of digital learning resource library includes the following resources: teaching

cases, teaching materials, and digital learning courseware; e-paper and e-books.

The layer of knowledge organization: knowledge organization model of digital learning resources with the proposed organization and management of a centralized digital education resources, the formation of a resource library, disciplinary ontology library, metadata extraction and automatic classification on the basis of formation by learning resources metadata warehouse of knowledge and education resource classification index.

The layer of Integrated retrieval: mainly includes integrated metadata access and integration and sharing of digital educational resources, when the user access to the knowledge warehouse integrated search portal through digital educational resources through metadata access interface knowledge warehouse metadata unified access.

III. THE KNOWLEDGE RETRIEVED AND NAVIGATION SYSTEM FOR WEB BASED LEARNING RESOURCES

The function modules of knowledge retrieved and navigation System for web based learning Resources is shown in Figure II. The system embodied knowledge organization model associated learning resources both inside and outside the organization, to achieve the educational resources the pretreatment and knowledge organization and navigation, and is reflected in the formation of a database of educational resources, including indexing library, professional word library and abstract database.

The function of the system is divided into four modules: resource module, pretreatment module, database module and knowledge organization and navigation module, which is as follows:

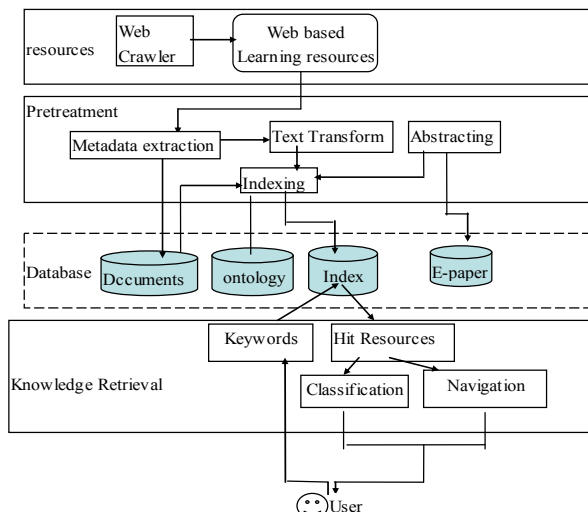


FIGURE II. KNOWLEDGE RETRIEVED AND NAVIGATION SYSTEM FOR WEB BASED LEARNING RESOURCES

A. The Module of Knowledge Retrieved and Navigation System

The resources module: This module consists mainly collected from the Internet to the various types of educational resources on the same topic, these different resource formats, such as. Html Doc, ppt, pdf, etc. It Collect the resources using a Web crawler. In this system, it mainly use Heritrix web crawler, the reptiles by secondary

development on the basis of its source code, open source web crawler using java language development, to meet the needs of the project. Filter which independent web pages little relationship with the subject, such as advertising, too many hyperlinks page.

The pretreatment module: pretreatment layer search to educational resources for processing, its main features include: metadata extraction and mapping, document conversion, automatic abstracting and indexing. Metadata extraction and mapping for conversion extraction of metadata and metadata standards of educational resources, which identify classes extracted identifier in HTML description metadata extraction, the semantic content of the class meta-data extraction Chapter keyword extraction method. The main function is to convert the document to varying resource file format converted to txt format, in order to facilitate the extraction of resources, the resources stored in the document library after document conversion. The automatic summarization module is mainly used resources generated abstracts which can help users quickly understand the main content of the resource, and thus determine the need for further view the entire contents of the resource. It will improve the speed of retrieval of resources.

The database module: mainly during system operation needs to access a variety of data resources and knowledge resources entities document library, the document describes ontology database indexing library, abstract database. And provide a mechanism for access to knowledge resources entity, body and other data resources, For example, the entity of resources, unified resource access interface; JDBC (Java Database Connectivity) will provide access interface for the database; OWL file Education Resource Description constituted body, will provide access to the Jena API and other standards-based interface.

Knowledge organization and navigation module: It is mainly used to retrieve the results of the second organization, and navigation resources generated automatically. First through the conversion of metadata heterogeneous metadata are mapped to the same standard, to achieve heterogeneous metadata reorganization. It is a resource secondary tissue by classifying the retrieval result, which will provide to the users to more clearly understand the results.

B. The Assessment to Web Based Learning Resources

Access to web based learning resource is through the web crawler, which is a program or script a according to certain rules, automatically crawl the World Wide Web information. Some infrequently used name there are ants, automatic indexing, a simulation program or worms. We primarily use an open source crawler software heritrix. On the basis of the heritrix secondary development interface localization, it is to adapt to the needs of the application.

Heritrix the runs as follows:

Through the command heritrix - admin = admin: admin start Web crawler.

C. Metadata Mapping

Metadata Mapping is of mutual conversion the information loss minimum between different metadata standards, and its essence is a meta-data standard elements and qualifiers converted to another metadata standard

elements and qualifiers. OAI-PMH data providers generally provide metadata to the Dublin core set of DC metadata form not represented by DC standards metadata must first be converted, and then stored in the DP for SP harvest. This article, we are funded by the JISC (Joint Information Systems Committee) Fund RELOAD (<http://www.reload.ac.uk/new/editor.html>), according to the need for a secondary development from standardized platform.

D. Knowledge Retrieved and Navigation Process of Web Based Learning Resources

The process of Web based learning resources retrieval application is as follows based on the knowledge organization prototype system. All web content within a certain range of the network on a theme first Web crawler crawling to the local, and then document the pretreatment and document format conversion, html, pdf, ppt, doc format convert txt format in order to extract the contents of the resource. The third step is the help of the professional lexicon the resources extracted content indexing and generate automatic summarization formation of the resource index libraries and abstract database. When users retrieve resources, first search keywords are submitted to the system resources by indexing library to find out all the hits keywords, all hit the resources to organize knowledge organization model and automatically generates navigate back to the user.

Specified for the new job crawling seed URL (South China Normal University the modern education technology boutique Courses: <http://jpkc.gdou.com/Jyjs/Home/>), for example, will start the New Task reptiles that automatically search the network crawling the specified web content. Crawling is completed, all of the content crawled all stored locally. By the the knowledge organization after local HTML pages form simply file. Then it is passed to the index file retrieval system of educational resources. Complete knowledge organization and retrieval of educational resources on the Web.

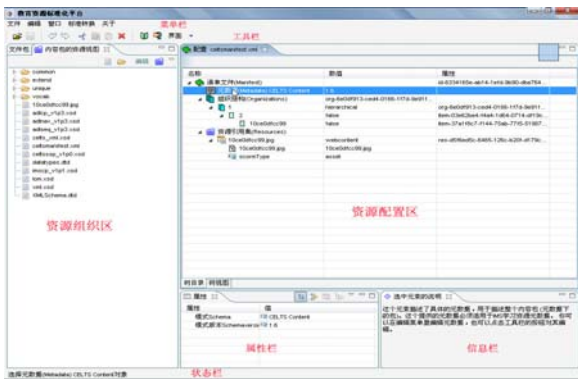


FIGURE III. METADATA MAPPING AND TRANSFORMING

resource integration for integrated retrieval of digital educational resources. Therefore the paper use the knowledge organization model Knowledge Organization for Educational website navigation on the classification of the web based learning resources.

REFERENCES

- [1] Lu X N , Kahle B. Automatic Metadata Generation for Scanned Scientific Volumes[C] . Proceeding of the 2008 ACM Workshop on Research Advances in large Digital book Repositories , New York ,NY,USA :ACM ,2008 (10):57 – 58.
- [2] Liu Fang, Zhu sha. Description System of DC Metadata in Digital Library Based on/RDF. Journal of Academic Library and Information Science, 2005, 23(3):25~27.
- [3] Wang Y, Yang JM, Lai W. Exploring traversal strategy for Web forum crawling. In: Myaeng S, Oard D, Sebastiani F, Chua T, Leong M, eds. Proc. of the ACM Conf. on Research and Development in Information Retrieval (SIGIR 2008). Singapore: ACM Press, 2008. 459~466.
- [4] Cai R, Yang JM, Lai W. iRobot: An intelligent crawler for Web forums. In: Huai J, Chen R, Hon H, Liu Y, Ma W, Tomkins A, Zhang X, eds. Proc. of the Int'l Conf. on World Wide Web (WWW 2008). Beijing: ACM Press, 2008. 447~456.
- [5] Guo Hao College of Computer and Software Taiyuan University of Technology Taiyuan, ChinaChen Junjie College of Computer and Software Taiyuan University of Technology Taiyuan,ChinaGuo Tao Network Center Taiyuan University of Technology Taiyuan, China. Web-Oriented Book Domain Metadata Description Research[A]. Mingmin Gong.IEEE Computer Society[C].IEEE Computer Society,2010.
- [6] Chang CH, Kayed M, Girgis MR, Shaalan KF. A survey of Web information extraction systems. IEEE Trans. on Knowledge and Data Engineering, 2006,18(10):1411~1428.
- [7] Freitag D, McCallum A. Information Extraction with HMM Structures Learned by Stochastic Optimization [C]//Proceedings of the 18th Conference on Artificial Intelligence. 2000: 584~589.

IV. THE CONCLUSION

The paper proposed the digital learning resources knowledge organization model which is applied to retrieve digital learning resources. Based knowledge organization model of digital educational resources, it can effectively solve the semantic gap problem of digital educational resources metadata, semantic mapping mechanism is formed between the metadata descriptions, and to lay the basis of

A QoS-based User Reputation Measurement Method for Web Services

Jianlong Xu^{1,2,3,*}, Yindong Chen¹ and Changsheng Zhu¹

¹Shantou University, Shantou 515063, P.R. China

²Hanshan Normal University, Chaozhou 521041, P.R. China

³Guangdong Key Laboratory of Big Data Analysis and Processing, Guangzhou 510006, P.R. China

*Corresponding author

Abstract—In Web services environment, high-quality services discovery and selection depend on reliable users with high reputations. However, user reputation is hard to accurately obtain directly. To evaluate the reliability of users, we present user reputation measurement method, named URMM. Based on the historical Quality of Service (QoS) values of users, we calculate user reputation value by the median and iteration operation. Based on real world public datasets, we conduct extensive experiments and demonstrate our proposed approach is more simple and effective than traditional approach.

Keywords—Web services; quality of service; reputation

I. INTRODUCTION

As a kind of distributed applications, Web services have played an important role in industry and academia [1], [2]. In Web services environment, users can invoke large amounts of Web services with equivalent similar functionalities. As the number of Web services increases on the Internet, it is necessary to select the best Web service that provides the best performance. To address this issue, many researchers have already carried out a great amount of work by employing personalized QoS properties (e.g., response time, invocation failure rate) which are observed by users [3], [4]. However, the most research work assumes that the QoS properties provided by users are reliable when making service selections. In fact, in the complex network environment, users may provide unreliable QoS values because: 1) The users are irresponsible and may provide arbitrary QoS values, they may submit random or maximal / minimal values as their service QoS evaluation data. 2) Some users may be the service providers simultaneously, so they may give good QoS values for their own services and bad QoS values for their competitors' services. Therefore, unreliable users have a strong impact on the services selection. If users select services according to the QoS data given by unreliable users, they may select the unsuitable or bad services. User reputation needs to be considered when making selection and accurate reputation measure of Web services is crucial.

To address this problem above, in this paper, we present user reputation calculation model, named URMM. In our approach, reputation measurement model is based on the historical QoS values. Our major contributions are summarized as follows: 1) We present URMM to calculate the reputation of each user. Based on the historical QoS values, our model can

provide reasonable reputation value for each user. 2) Both theoretical analysis and extensive experiments are conducted to demonstrate that our model is more simple and effective in contrast to traditional approach.

The rest of our paper is organized as follows. We review the related work in Section 2 and propose our reputation model in Section 3. Section 4 presents experimental results and Section 5 concludes the paper.

II. RELATED WORK

User reputation indicates the reliability and creditability of a user. Since the variability and uncertainty of user behavior, user reputation is hard to accurately obtain directly. Therefore reputation calculation models have been attracted a great deal of attention by many researchers. Generally, reputation calculation methods can be divided into two categories: content-driven and user-driven. For content-driven, reputation value is obtained according to the quality and quantity of user-generated contents and the survival time of these contents, such as Wikipedia entry [5] and the location edit of the Google map system [6]. For user-driven, the user reputation calculation and analysis are based on user feedback ratings. Obviously, the user reputation calculation of Web services belongs to user-driven. In the related researches, Mizzaro et al. [7] proposed Mizz model which was applied in assessment of scholarly papers. But this model cannot guarantee the convergence of reputation calculation. De et al. [8] proposed an iterative filtering method from an optimization perspective, but the convergence of the algorithm is affected by the parameter settings. To address the convergence issue, Rong-Hua Li et al. [9] put forward six convergence algorithms for reputation calculation, there are L1AVG, L2AVG, L1MAX, L2MAX, L1MIN and L2M1N, respectively. Based on the work of Rong-Hua Li, Baichuan Li et al. [10] propose a topic-biased model (TBM) to estimate user reputation which is applied in rating systems. However, these two models are also affected by the parameter settings, such as the damping factor.

Our work is inspired by [9] and [10], which focuses on the convergence of the algorithm. Different from the related work, our algorithm provides more simple and direct way to obtain the user reputation which does not adjust the parameter in the calculative process. In addition, experiment on real data shows that our model is more effective.

III. MODEL

A. Problem Description

In Web services environment, service invocations can produce a user-service QoS matrix with respect to each QoS attribute. In this matrix, each row and column denotes a service user and a candidate service, respectively, and each entry in the matrix denotes the QoS value observed by a user when invoking a service. However, in contrary to the rating values in rating systems, the QoS values are not limited in a certain range. Therefore, traditional reputation calculation models may not be applicable.

We assume a service computing environment with m users $U=\{u_1, u_2, \dots, u_m\}$ and n services $S=\{s_1, s_2, \dots, s_n\}$. The user-service matrix is an $m \times n$ matrix $Q \in \mathbb{R}^{m \times n}$, each entry in this matrix q_{ij} ($i \leq m, j \leq n$) denotes the value of QoS property (e.g., response time, throughput) of Web service j observed by service user i . If user i did not invoke Web service j before, then $q_{ij}=\text{null}$. Our goal of reputation calculation is to excavate the information from the QoS data of each user.

B. User Reputation Calculation Model

Literature [9] had proposed L2-AVG method to calculate reputation which can be express as:

$$\begin{cases} A_j^{k+1} = \frac{1}{|H_j|} \sum_{u_i \in H_j} q_{ij} r_i^k \\ r_i^{k+1} = 1 - \frac{d}{|O_i|} \sum_{s_j \in O_i} (q_{ij} - A_j^{k+1})^2 \end{cases} \quad (1)$$

where A_j is the average QoS value for service j , k indicates the k^{th} iteration, A_j^{k+1} is A_j in the $k+1^{\text{th}}$ iteration, r_i^k is the reputation r_i in the k^{th} iteration, H_j is the set of users which invokes service j , $|H_j|$ denotes the quantity of users who have invoked service j , O_i is the set of services invoked by user i , $|O_i|$ denotes the number of services which have been invoked by user i , d is a decay constant in $(0,1)$.

The main idea of L2-AVG algorithm is to find out the degree of user QoS value deviates from the population mean. However, it is suitable for rating system that the rating values are limited in a certain range. In real-world, since the distributions of QoS data are highly skewed with large variances, this method may suffer when users give unreliable ratings. For example, an unreliable user gives a negative date or very big date may have a negative impact on the mean and the reputation calculation results. To address this problem, we propose our new user reputation evaluation approach based on medium value analysis, which named URMM.

We assume the reputation of users can be represented as $R=\{r_1, r_2, \dots, r_m\}$ ($0 \leq r_i \leq 1$). The most reliable user's reputation value is 1 while the least reliable user's reputation value is 0. We have:

$$\begin{cases} M_j^{k+1} = \underset{u_i \in H_j}{\text{med}}(q_{ij} r_i^k) \\ r_i^{k+1} = 1 - \frac{1}{|O_i|} \sum_{s_j \in O_i} \left(\frac{(q_{ij} - M_j^{k+1})^2}{\max_{s_j \in O_i} (q_{ij} - M_j^{k+1})^2} \right) \end{cases} \quad (2)$$

where M_j is the medium QoS value for service j , M_j^{k+1} is M_j in the $k+1^{\text{th}}$ iteration, the meaning of other parameters r_i^k , H_j , O_i , $|O_i|$ are the same with Eq.(1).

The calculation method of Eq.(2) can be explained that a certain user reputation depends on the gap between QoS values observed by this user and the medium of QoS values observed by other users. If a user provides a Web service QoS values which are quite difference with medium of other users' QoS values, then the user is likely to be unreliable. In Eq.(2), r_i is determined by q_{ij} and M_j^{k+1} . In our model, in the initialization step, $k=0$ and $r_i^0=1$. Then the medium QoS value for service j and the reputation of the user i are calculated according to Eq.(2) by an iterative method. When k is more than RMaxI (the maximum number of iterations) or the absolute of $r_i^{k+1} - r_i^k$ satisfies the required accuracy (less than threshold), the algorithm will be terminated and outputs the user reputation.

IV. EXPERIMENT

In this section, we conduct experiments to validate our URMM approach. We use the real-world datasets released by Zheng et al. [11] in our experiments. This dataset includes a 339×5825 matrix containing 339 service users and 5825 real Web services. The entries in the matrix include response time property and throughput. In our experiments, we adopt a part of the response time dataset and add unreliable user to the dataset. The response time values of the unreliable users are randomly generated and these values are unreliable. We use a 5×6 user-service matrix where data of user 1 to 4 are reliable and user 5 is unreliable. The goal of our experiment is to calculate each user's reputation value and identify the unreliable user by our approach. In the following experiments, we set RMaxI as 10 and set threshold as 0.001. Table 1 show the user-service matrix.

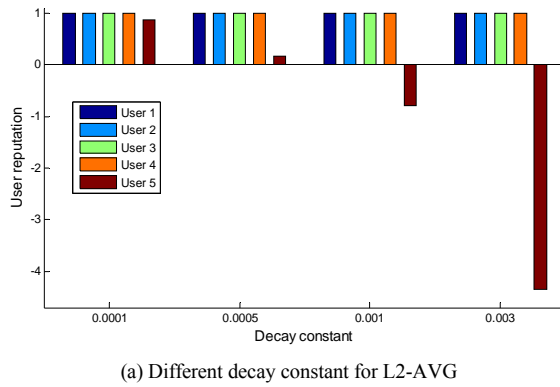
TABLE I. 5×6 USER-SERVICE RESPONSE TIME MATRIX

	Service 1	Service 2	Service 3	Service 4	Service 5	Service 6
User 1	5.9820	0.2280	0.2370	0.2210	0.2220	0.5270
User 2	2.1300	0.2620	0.2730	0.2510	0.2540	0.4270
User 3	0.8540	0.3660	0.3760	0.3570	0.3580	0.1150
User 4	0.6930	0.2260	0.2330	0.2200	0.2190	0.3440
User 5	40.2633	43.6892	41.3455	42.1141	42.7393	44.7136

To prove the effectiveness of our method, we ran extensive experiments and compare our method with L2-AVG [9]. We vary decay constant d with different value for L2-AVG. The experimental results of users reputation calculation iteration process based on L2-AVG is illustrated in Figure 1.

From Figure 1, when $d=0.0001$, the reputations of user 1 to 5 are 0.9957, 0.9953, 0.9950, 0.9950, 0.8793, respectively.

When $d=0.001$, the reputations of user 1 to 5 are 0.9979, 1.0000, 0.9998, 0.9998, -0.7853, respectively. The reputation values are different with different decay constant. When $d=0.001$, the reputations value of user 5 is negative, which contradicts the range of reputation. The reason is that: in the process of iterative, if the decay constant d is inappropriate, the value of multiplying $(q_{ij} - A_j^{k+1})^2$ and d will be increased by the QoS date of user 5 in Eq.(1), and the result of dividing $|O_i|$ by this value is bigger than 1. Therefore, it needs to adjust d to obtain satisfactory results when L2-AVG algorithm is employed.



(a) Different decay constant for L2-AVG

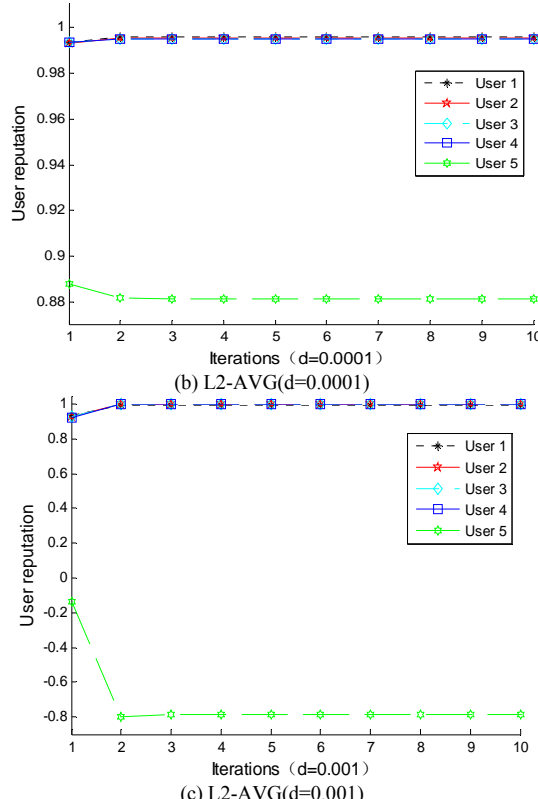


FIGURE I. USER REPUTATION CALCULATION ITERATION PROCESS BASED ON L2-AVG

The experimental results of our approach are illustrated in Figure 2. Figure 2 (b) is the enlarged view of user 1 to user 4 in

Figure 2 (a). From Figure 2, the reputations of user 1 to 5 are 0.9999, 1.0000, 1.0000, 0, respectively. Comparing with the L2-AVG algorithm, our approach is more simple and efficient. Firstly, it needs no decay constant to adjust the calculation result. Second, for L2-AVG algorithm, the average value is tremendously impacted by the specific abnormal data (e.g. the data of user 5) while our approach can avoid being impacted by the specific abnormal data. When suffering from an unreliable user (the QoS data q_{ij} is very big or very small relative to other data of reliable user), since $(q_{ij} - M_j^{k+1})^2$ is close to or equal to $\max(q_{ij} - M_j^{k+1})^2$, the reputation of unreliable user is very small in our approach. Third, our model is faster than L2-AVG ($d=0.0001$), the reputations can be obtained after two iterations in our algorithm while three iterations in L2-AVG when $d=0.0001$.

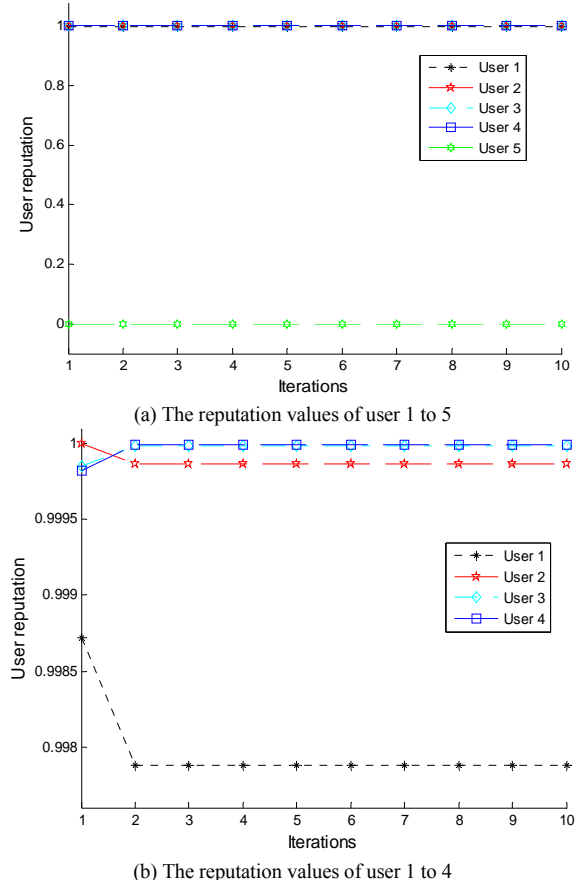


FIGURE II. USER REPUTATION CALCULATION ITERATION PROCESS BASED ON URMM

V. CONCLUSION AND FUTURE WORK

It is essential to obtain user reputation value before Web services selection and recommendation. In this paper, we present a user reputation calculation approach, namely URMM, which is based on the median and iteration operation. Extensive experiments are conducted on a real-world dataset and the experimental results show that our proposed approach is more simple and effective in contrast to traditional approach. In the future work, we aim to investigate better user reputation

calculation approaches, for example, we will try to optimize the reputation calculating method by taking the online environment into consideration, do more experiments to test the performance of our model and compare with more other algorithms.

ACKNOWLEDGMENT

This research was financially supported by the National Natural Science Foundation of China (No. 61702318), the Guangdong High-Level University Project “Green Technologies for Marine Industries”, Guangdong Common Colleges Young Innovative Talents Project (No. 2016KQNCX056), and Shantou University National Fund breeding project (No.NFC16001), Guangdong Natural Science Foundation (2015A030313433), Characteristic Innovation project in Higher Education of Guangdong (2015KTSCX036).

REFERENCES

- [1] Martin Garriga, Andres Flores, Alejandra Cechich, Alejandro Zunino, “Web Services Composition Mechanisms: A Review,” IETE Technical Review, vol.32, 2015, pp. 376-383.
- [2] Jianlong Xu, Zibin Zheng, and Michael R. Lyu. “Web Service Personalized QoS Prediction via Reputation-based Matrix Factorization”. IEEE Transactions on Reliability. vol.65, 2016, pp.28-37.
- [3] Bernard O, Paul S, Beat W, “Modeling Services and Web Services: Application of ModelBus,” In Proceedings of the International Conference on Software Engineering Research and Practice, Las Vegas, 2017, pp. 557-563
- [4] Jianxun Liu , Mingdong Tang , Zibin Zheng. “Location-Aware and Personalized Collaborative Filtering for Web Service Recommendation,” IEEE Transactions on Services Computing, vol.9, 2016, pp. 686-699.
- [5] B. Thomas Adler, Luca de Alfaro, “A content-driven reputation system for the Wikipedia,” In Proceedings of the 16th ACM International Conference on World Wide Web, Banff, Canada, 2007, pp. 261-270.
- [6] Adler, B. T., De, A. L., Kulshreshtha, A., and Pye, I, “Reputation systems for open collaboration,” Communications of the ACM, vol. 54, 2011, pp. 81-87.
- [7] Mizzaro S. “Quality control in scholarly publishing: A new proposal,” Journal of the American Society for Information Science and Technology, vol.54, 2003, pp. 989-1005.
- [8] De Kerchove C, Van Dooren P. “Iterative filtering in reputation systems,” SIAM Journal on Matrix Analysis and Applications, vol.31, 2010, pp. 1812-1834.
- [9] Rong-Hua Li, Jerry Yu Xu, Huang Xin, Hong Cheng. “Robust Reputation-Based Ranking on Bipartite Rating Networks,” In Proceedings of the 2012 SIAM International Conference on Data Mining, 2012, pp.612-623.
- [10] Baichuan Li, Rong-Hua Li, Irwin King, M.R. Lyu, and Jeffrey Xu Yu. “A Topic-Biased User Reputation Model in Rating Systems,” Knowledge and Information Systems (KAIS), vol.44, 2015, pp. 581-607.
- [11] Zibin. Zheng, Yilei. Zhang, and Michael. R. Lyu, “Distributed QoS evaluationsfor real-world web services,” in Proceedings of the 17th IEEE International Conference on Web Services (ICWS), Miami, Florida, 2010, pp. 83–90.

Prolong Lifespan of Wireless Sensor Network with Optimized Information Compression Algorithm and Magnetic Resonant Concept

Manish Bhardwaj^{1*} and Anil Ahlawat²

¹SRM IST, Computer Science and Engineering, Modinagar, Ghaziabad, India

²KIET, Computer Science and Engineering, Muradnagar, Ghaziabad, India

*Corresponding author

Abstract—Remote sensor systems maintain numerous applications in various fields. Sparing vitality in such systems is continuously a basic issue that should be considered to delay the network lifespan. Bunching in the systems is additionally considered as a vitality sparing directing strategy. This manuscript, propose the two technique by which the vitality problem of a remote sensor can be resolved. In first Strategy, with the help of wireless power transfer recharge all the node of the network and in the second strategy a new information gathering strategy, called firmness technique, keeping in mind the end goal to altogether diminish information transmitting among grouped systems for vitality sparing reason. In the strategy, Wavelet essential is utilized in each group to pack information to be sent to the base-station (BS). At the BS, all the detecting information can be remade in light of the compacted tests gathered from groups. We additionally investigate what's more, plan the aggregate vitality utilization for information transmitting between sensors in the systems and from the systems to the BS. Reproduction comes about are given to illuminate our examination and to propose ideal cases for the system to expend the slightest control. In this manuscript, new proposed technique shows the results with various performance parameters like, power consumption, network lifespan in Inter and Intra transmissions.

Keywords—power consumption; LEACH; base Station; vitality

I. INTRODUCTION

Late years, much research contemplates in remote sensor systems take a great deal of consideration since the systems have numerous applications. Following articles or identifying occasions are exceptionally normal applications in various fields. Sensors are sent haphazardly in a backwoods to recognize fire. They can be sent in a detecting field to save individuals or on the other hand to distinguish oil spill. In different cases, sensors are additionally sent to assemble scalar maps for information examination purposes. The maps are manufactured in light of crude information gathered from all sensors in the detecting fields. WSNs are inserted with distinctive topologies. They could be dynamic or settled structures contingent upon the reasons for such systems. Group based, tree-based, babble based, arbitrary walk, and so forth are extremely regular information accumulation techniques applying in the systems. Every technique has unmistakable focuses to be used for particular applications. Remote

associations have a few alternatives including Bluetooth, Wi-Fi, RF in which they are appropriate in applications.

Grouping calculations are considered as a vitality sparing information accumulation strategies in the systems. K-implies, Drain is regular a technique to separate the system into bunches. K-implies enhances the transmitting separations between bunch heads (CHs) and non-CH sensors to diminish vitality utilization for sensors. Filter picks CHs based on stochastic hypothesis to adjust vitality in the system since the greatest work stack dependably falls on CHs. Numerous other grouping calculations have demonstrated their vitality effective focuses for WSNs. Groups could be orchestrated unequally with a specific end goal to adjust the devoured vitality between bunches since the ones near the BS dependably spend more vitality than the one more remote.

In this paper, we apply Wavelet change hypothesis for bunching in WSNs to pack detecting information in each group. In a bunched arrange, each group has one bunch head (CH) also, the rest are non-CH sensors. All non-CH sensors send their own particular information to the CH they have a place with. This CH increases the gathered information including its own particular information to Wavelet coefficients also, just sends the huge changed coefficients to the base station (BS) or the information handling focus. The BS gathers the extensive coefficients from all groups following that way and recreates all information from the groups to have the capacity to assemble a scalar guide. We additionally propose distinctive approaches to forward the changed coefficients from CHs to the BS; the coefficients are sent straightforwardly to the BS or transferred between other CHs to at long last achieve the BS. Vitality utilization for information transmission in the systems is detailed.

The rest of this paper is sorted out as takes after. Issue Formulation and Energy Consumption Analysis are tended to in Section II and III, separately. Reproduction comes about are given in Section IV. At last, Conclusions and future work are in Section V.

II. RELATED WORK

Xiaoqin Chen et al [1] Add knowledge transfer of data, which was hired to use the data rate and delay gloves hobby wait queue with a given weak low electrical current to make

better use of its channels are also offered awareness of traffic protocol for a particular mobile network (CARM). CARM implemented method for data transmission lines, propagation speed in order to prevent data transfer speed road links that do not match. CARM It was discussed and developed a network of only IEEE 802.11b. However, it is applied to the rates of multi-network Ad Hoc.

J. M. Kim et al. [2] this paper improves the LEACH protocol with the help of cluster head election method. In this paper fuzzy logic technique is used and with the help of this technique, network chooses the cluster head so that lifetime of the network gets increased.

Manish et al. [3] describe the concept of reduction of power consumption in communication process. This manuscript describes the RECAODV algorithm which minimizes the energy consumption in the network and increase the lifetime of network. It also explain the concept of wireless power transfer between the nodes of the network.

Manish et al. [4] this paper apply a wireless power transfer and Backpressure Technique to reduce the power problem of the network nodes. This paper shows the simulation results by using the energy conservation algorithm. This paper increased the significant lifetime of the network. Link utilization, route maintenance and reduce overhead is the main objective of this paper.

Manish et al. [5] this paper brief the cooperative communication in different nodes which communicate with same data at a single instant of time. This paper uses the optimum relay nodes selection technique in CC network and with the help of this technique, it reduces the power consumption of the network.

Sotiris Nikoletseas et al. [6] this paper focus on wireless charging of the portable de-vices for this it is work on two different types of protocols one perform wireless charging, evaluate the charging efficiency, and second maintain the balances of the chargers. This paper evaluates the results in real time environment.

Bernard Mumo Makaa et al. [7] this paper simply demonstrates the application of solid state tesla coils. According to the results, this paper shows that tesla coils are highly capable of generating high voltage, high-frequency waveforms. It also shows that tesla coils are designed for wireless power transfer.

Xiao Lu et al. [8] this paper discussed the issues related to wireless power charging and development of a commercial product that using this concept of wireless charging. It shows the wireless charging standards and latest network applications which are used in the market. It also discusses the challenges to implementing the wireless charging concept.

III. WIRELESS POWER GENERATION AND TRANSMISSION TECHNIQUE

Family unit gadgets create generally little magnetic fields. Therefore, chargers hold gadgets at the separation important to initiate a present, which can just happen if the curls are near one another. Since an attractive field spreads every way,

making a bigger one would squander a considerable measure of vitality [9]. An effective approach to exchange control between loops isolated by a couple of meters is that we could expand the separation between the curls by adding resonance to the condition. A decent approach to comprehend resonance is to consider it as far as sound. A question's physical structure - like the size and state of a trumpet - decides the recurrence at which it normally vibrates. This is its resonant recurrence. It's anything but difficult to motivate articles to vibrate at their full recurrence and hard to inspire them to vibrate at different frequencies. This is the reason playing a trumpet can make an adjacent trumpet start to vibrate [10]. The two trumpets have the same resounding recurrence. Enlistment can occur little distinctively if the electromagnetic fields around the loops resound at a similar recurrence. The hypothesis utilizes a bended curl of wire as an inductor. A capacitance plate, which can hold a charge, joins to each finish of the loop as appeared in Figure 1. As power goes through this curl, the loop starts to reverberate. Its thunderous recurrence is a result of the inductance of the curl and the capacitance of the plates [11].

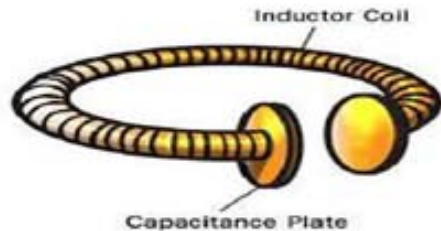


FIGURE I. CAPACITANCE PLATES WITH CURL

Power, going along an electromagnetic wave, can burrow from one loop to alternate as long as they both have the same resonant recurrence [12]. In a short hypothetical investigation they exhibit that by sending electromagnetic waves around in an exceedingly precise waveguide, transitory waves are created which convey no vitality. A transient wave is close field standing wave showing exponential rot with separate. On the off chance that a legitimate full waveguide is brought close to the transmitter, the evanescent waves can enable the vitality to burrow (particularly transient wave coupling, what might as well be called burrowing to the power drawing waveguide, where they can be corrected into DC control. Since the electromagnetic waves would burrow, they would not proliferate through the air to be ingested or scattered, and would not disturb electronic gadgets. For whatever length of time that the two loops are out of scope of each other, nothing will happen, since the fields around the curls aren't sufficiently solid to influence much around them. So also, if the two curls reverberate at various frequencies, nothing will happen [13]. Be that as it may, if two resounding loops with a similar recurrence get inside a couple of meters of each other, surges of vitality move from the transmitting curl to the accepting loop. As per the hypothesis, one loop can even send power to a few getting curls, as long as they all resound at an indistinguishable recurrence from appeared in Figure 2. The specialists have named this non-radiative vitality exchange since it includes stationary fields around the curls as opposed to fields that spread every way [14].



FIGURE II. POWER TRANSMISSION TO MULTIPLE CURLS

As indicated by the hypothesis, one loop can energize any gadget that is in go, as long as the curls have the same full recurrence. "Full inductive coupling" has enter suggestions in taking care of the two principle issues related with non resonant inductive coupling and electromagnetic radiation, one of which is caused by the other; separation and productivity [15]. Electromagnetic enlistment chips away at the rule of an essential curl producing a transcendently attractive field and an optional loop being inside that field so a current is actuated inside its loops. This causes the moderately short range because of the measure of energy required to create an electromagnetic field. Over more noteworthy separations the non-resonant enlistment strategy is wasteful and squanders a great part of the transmitted vitality just to expand [16]. This is the place the resonance comes in and helps productivity significantly by "burrowing" the magnetic field to a collector loop that resounds at a similar recurrence. Not at all like the different layer optional of a non-resonant transformer, such accepting loops are single layer solenoids with firmly divided capacitor plates on each end, which in mix enable the curl to be tuned to the transmitter recurrence in this manner dispensing with the wide vitality squandering "wave issue" and permitting the vitality used to concentrate in on a particular recurrence expanding the range.

IV. PROBLEM DESCRIPTION

We accept N sensors arbitrarily appropriated with an equivalent likelihood in a detecting region. N_c groups are pre-decided for the system. Along these lines, N_c CHs are haphazardly looked over all the sensors in light of a likelihood N_c/N . This can share the weight of workload of being CHs for each sensor. At that point, the rest as non-CH sensors pick one CH which is nearest to shape bunches. By and large, each bunch has (N/N_c) sensors. What's more, each CH has $(N/N_c - 1)$ non-CH sensors. As appeared in

Figure 3, non-CH sensors send specifically information to their own CHs. Each CH forms the gathered information inside its group also, sends a specific number of tests to the BS for information recreation following the Wavelet-based information pressure calculation.

As said the past areas, the system is isolated into N_c group. Figure 1 demonstrates the bunched arrange in general with the BS outside the detecting zone. For the most part, all non-CH sensors send their information to the CHs. All the CHs forward all the got information including their own to the BS.

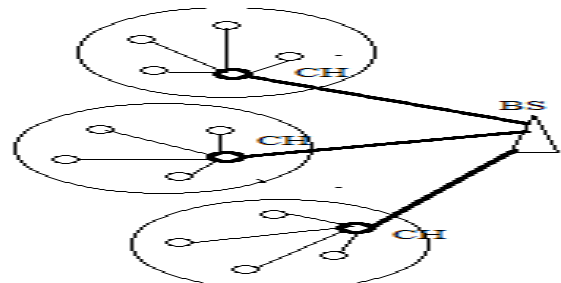


FIGURE III. CLUSTER HEAD WITH BASE STATION

In the proposed calculation, each CH makes one Wavelet sub-framework ϕ_j with measurement $(m_j \times m_j)$, where m_j is the number of sensors in the j th bunch. Information gathered at each bunch is increased to a sub-lattice in which, every one of the passages are made by the Matlab charge haarmtx(m_j). A huge extent of the flag vitality is centered on the principal huge coefficients, given as K coefficients. Just these coefficients are sent to the BS from all the CHs. The rest of the changed coefficients can be considered as zeros. At the transmission time only $K = \sum_{j=1}^{N_c}$ large coefficient will sent so that it save lot of power in transmission sense.

Transformed coefficient is shows in the form of z_j , and it is represented as $z_j = \sum_{i=1}^{m_j} x_i$. In this method number of sensors is propositional to the number of Major coefficient $(k_j/K) = (m_j/N)$. After transmitting the data to base station it can calculate the received data into original form like $x' = \sum_{j=1}^{N_c} T_j z_j$

The proposed calculation can likewise function admirably with adaptation to non-critical failure in the system since all sensors alternate to wind up CHs. Breakdown hubs are not picked after each round of picking CHs or non-CH sensor hubs. The flaws of the system or on the other hand sensor hubs could be recognized and recuperated by blame tolerant calculations for grouped systems or for tree based systems. Broke down hubs are detached yet could be utilized for transferring information in the system if conceivable. This could be an open work for our future research.

A. Optimizrd Information Compression Algorithm

1. In this algorithm the network is divided into various clusters name as N_c
2. Every cluster head work is to collect data from the all other node of the cluster including its own data.
3. After collecting all the data it multiplies it into certain function.
4. Certain Sample of that function called as major coefficient is sent to the base station as transmitting data.
5. The transmission of the data to base station can be perform into two ways like either the data is directly sent to the base station or it is sent with the help of intermediate nodes.
6. At the receiver point the receiver collect the data from N_c clusters and then wrap out the data with the help of reverse method and get the original data.

7. With the help of the method less data is transmitted through the channel and it save the lot of power of the nodes and cluster head and ultimately the power of network.

B. Power Consumption Analysis

Network uses the power for transmitting and receiving the data and these are denoted by P_{T1} and P_{T2} respectively.

$$P_{T1} = P_T + P_a(d) \quad (1)$$

$$P_{T2} = P_R \quad (2)$$

P_T and P_R are the power used for the part of non transmission and non receiving processes. P_a is the actual power consumed and it is the function of distance. This manuscript calculate the two type of power consumption first used in transmission between sensors and cluster head and second which is used in transmission from cluster head to base station.

A) P_{Sc} power consumption calculation

According to the network distribution in clusters N_c . The network consist of one cluster head and $(N/N_c - 1)$ sensors nodes.

$$P_{Sc} = N_c(N/N_c - 1)E[r\alpha] \quad (3)$$

In the above equation r is behave like a random value of distance between the Cluster head to sensor nodes and α denotes the pathway loss exponent.

According to the paper the value of the $E[r\alpha]$ can be calculated as

$$L^2/2\pi N_c \quad (4)$$

so that the power consumption of P_{Sc} is as

$$P_{Sc} = (N/N_c - 1) L^2/2\pi \quad (5)$$

B) P_{Cb} power consumption calculation

Major coefficient of the network is calculated as

$$K = N_c k_j \quad (6)$$

The Power consumed by the transmission for cluster head to base station is as

$$P_{Cb} = K E[d^2] \quad (7)$$

According to paper the total power is calculated as

$$P_{total} = (N/N_c - 1) L^2/2\pi + K L^2/6 \quad (8)$$

V. SIMULATIONS AND RESULTS

We think about both regular sorts of systems, square detecting territory with measurement 150×150 . In this system, there are 1500 sensors arbitrarily sent. K-implies and LEACH are likewise conveyed to gather information and to contrast and our examination comes about. Genuine sensor readings gathered from Sensor scope are utilized for recreating. We assess the aggregate vitality utilization for the systems and give the execution of the proposed calculation with the information.

Figure 4 represents the line graph between power consumption in Intra cluster Communication and number of clusters in the network. As graph shown the three different curve for LEACH, K-means and Proposed Optimized Information Compression algorithm. Power consumption in LEACH is higher than the K-Means and OICA algorithms. When we look for the K-Means and OICA curves it is look similar that means proposed algorithm give slightly better results than K-means algorithm.

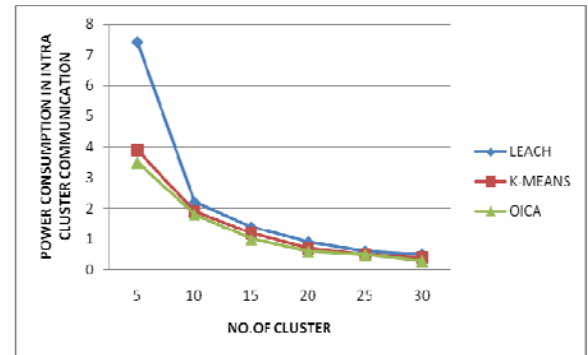


FIGURE IV. POWER CONSUMPTION IN INTRA CLUSTER COMMUNICATION VS NO. OF CLUSTERS

Figure 5 represents the line graph between power consumption in communication to base station and number of clusters. This line graph shows the variation of power consumption between the LEACH, k-means and proposed algorithm as the number of clusters increases. According to the graph proposed algorithm behave better than other to algorithm in respect of power consumption in communication to base station.

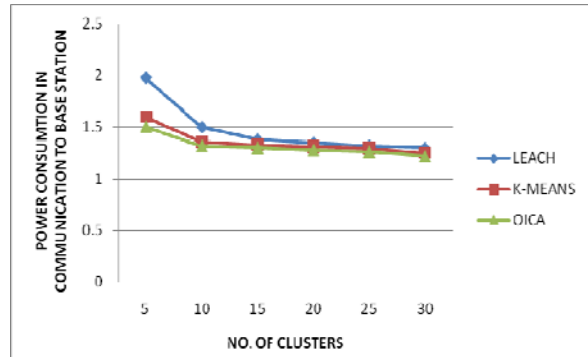


FIGURE V. POWER CONSUMPTION IN COMMUNICATION TO BASE STATION VS NO. OF CLUSTERS

Figure 6 shows the graph in which different temperature reading are displayed. Each and every sensor gives the recorded reading to the cluster head of the each cluster. This step is the basic or traditional step which is followed by every sensor node in the network.

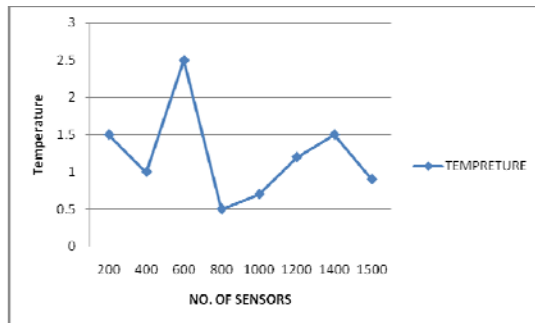


FIGURE VI. TEMPERATURE VS NO. OF SENSORS

Figure 7 represent the line graph of optimized transformed coefficient which is transfer to the base station instead of all the readings will be transfer to base station. That is the job of cluster head to create the coefficient and then transformed to base station so that lot of power would be saved.

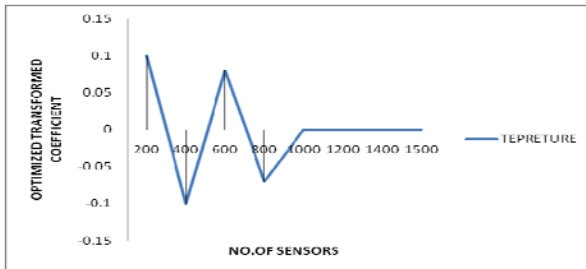


FIGURE VII. OPTIMIZED TRANSFORMED COEFFICIENT VS NO. OF SENSORS

VI. CONCLUSION

This manuscript proposed optimized information compression algorithm (OICA) for bunched WSNs to decrease vitality utilization in gathering tangible information. In light of the way that all information vitality centered in moderately little quantities of vast coefficients in the changed vector, we just send the vast coefficients to the BS for the flag recuperation process. These coefficients are mapped at the BS to recoup all tactile readings from the system. We examined and planned either the intra-bunch vitality utilization or the aggregate devoured vitality for the system to transmit information. Reenactment comes about are accommodated both expended estimation and the optimized information compression technique. We recommend an ideal case for the systems to utilize multi-bounce if many groups are connected. Second proposed method to resolve the power problem of wireless sensor network is also give significant results with the help of this concept sensor are free with power problem. In future work, we will ponder the limit for the quantity of bunches in both commotion and silent situations.

REFERENCES

- [1] T. Arampatzis, J. Lygeros, and S. Manesis, "A survey of applications of wireless sensors and wireless sensor networks," in Intelligent Control, Proceedings of the 2005 IEEE International Symposium on, Mediterranean Conference on Control and Automation, pp. 719–724, IEEE, 2005.
- [2] M. J. Kim, "CHEF: Cluster Head Election mechanism using Fuzzy logic in Wireless Sensor Networks", *Proc. of ICACT*, pp. 654- 659, 2008.
- [3] M. Bhardwaj and A. Ahlawat, "Reduce Energy Consumption in Ad hoc Network with Wireless Power Transfer Concept ", *International Journal of Control Theory and Applications*, vol. 10, issue 13, 2017.
- [4] M. Bhardwaj, "Enhance life Time of Mobile Ad hoc Network using WiTriCity and Backpressure Technique", 1877-0509 © 2015 The Authors. Published by Elsevier B.V. This is an open access article under the CC BY-NC-ND license, doi: 10.1016/j.procs.2015.07.447.
- [5] M. Bhardwaj, "Selection of Efficient Relay for Energy-Efficient Cooperative Ad Hoc Networks" *American Journal of Networks and Communications. Special Issue: Ad Hoc Networks*, vol. 4, no. 3-1, pp. 5-11, 2015.
- [6] S. Nikoletseas, "An experimental evaluation of wireless power transfer protocols in mobile ad hoc networks", *IEEE Wireless Power Transfer Conference (WPTC)*, pp.1- 3, 2015.
- [7] M. B. Makaa, "Analysis of WPT system using rearranged indirect-fed method for mobile applications", *IEEE Wireless Power Transfer Conference (WPTC)*, pp.1- 4, 2015.
- [8] Z. Han, "Wireless Charging Technologies: Fundamentals Standards and Network Applications", *Communications Surveys & Tutorials IEEE*, vol. 18, pp. 1413-1452, ISSN 1553-877X.
- [9] M. Bhardwaj and A. Bansal,"Energy Conservation in Mobile Ad Hoc Network Using Energy Efficient Scheme and Magnetic Resonance", *Advances in Networks. Special Issue: Secure Networks and Communications*, vol. 3, no. 3-1, pp. 34-39, 2015.
- [10] J. Kim, J. Jang, "AODV based EnergyEfficient Routing Protocol for Maximum Lifetime in MANET", *IEEE Conference on Telecommunications*, pp. 1-212, 2006.
- [11] L. Guo, Y. Liu, T. Jiang, "Energy Efficient on-demand MultipathRouting Protocol for Multi-hop AdHoc Networks", *IEEE Symposium on Spread Spectrum Techniques and Applications*, pp. 1-820, 2009.
- [12] G. Ferrari, S.A. Malvassori, "Physical Layer-ConstrainedRouting in Ad-hoc Wireless Networks: A Modified AODV Protocol with Power Control" *IEEE International Workshop on Wireless Ad hoc Network*, pp23-27, 2005.
- [13] R. C. Shah, J. M. Rabaey, "Energy awarerouting for low energy ad hoc sensor networks", *IEEE Wireless Communications and Networking*, pp. 1-931, 2002.
- [14] M. Bhardwaj, A. Singh, "Power Management of Ad Hoc Routing Protocols Using Mobility Impact and Magnetic Resonance", *Advances in Networks. Special Issue: Secure Networks and Communications*, vol. 3, no. 3-1, pp. 27-33, 2015.
- [15] S. Nikoletseas, P. T. Raptis, "Interactive Wireless Charging for Energy Balance", *IEEE Distributed Computing Systems (ICDCS)*, pp. 262-270, ISSN 1063-6927, 2016.
- [16] M. Bhardwaj, A. Pathak, "Optimum Experimental Results of AODV, DSDV & DSR Routing Protocol in Grid Environment", *Procedia computer science, 3rd International Conference on Recent Trends in Computing*, vol 57, pp. 1342–1350, 2015.

Analysis of Topic Influence and Post Features of Sina-Weibo

Borong Lyu, Xinhui Shao*, Yinbo Huang and Yuyang Xie

Department of Mathematics, Northeastern University, Shenyang 110819, P.R.China

*Corresponding author

Abstract—Microblog serves as an outlet for expressing ideas of events and plays a significant role in propagating news. This paper focused on the most popular microblog in China - Sina-Weibo and discussed topic influences. Firstly, this paper decomposed topic structure into Average Fundamental Popularity and Information Tipping Points. This paper classified topics into three patterns. Next, we collected 10455 available Information Tipping Points and obtained all the posts on each one by Python. We processed these posts and got 20 features, including features within the social network and features in the whole network, such as Ratio of Original Posts and Forward Hierarchy. Furthermore, K-means and EM algorithm were applied to cluster subtopics. Statistical methods such as Spearman Rank Correlation Coefficient Method, the Levene Homogeneity of Variance Test, and One-way Analysis of Variance were used to analyze the relationship among some features. We find that eight of all the features have strong relationships with the Number of Weibo Posts. Furthermore, the total number of posts on one topic (the Number of Weibo Posts) can represent topic impact. This paper established a predictive model via the regression method to predict the Number of Weibo Posts. We also find that whether a topic can become influential can be predicted by its features in the whole network. Finally, this paper applied SVM algorithm to determine which subtopic can become a trending issue.

Keywords—Sina-Weibo; social network; features; information tipping points; predictive model

I. INTRODUCTION

Social networks are becoming major sources of commentaries on a wide range of topics [1]. When a user posts something on the social network, his followers can leave a comment, give a like, or even forward it. Some posts are reposted by millions of users in the social network, changing public opinions significantly. Thus, predictive analysis of the social network is of great value. Since some trending topics are caused by exclusive links which cannot be described or predicted by information diffusion models but can be analyzed by data analysis methods [2, 3], data analyzing of social networks is a prospective field with wide implications.

Studies focus on predicting popular posts based on post features in the social network from a data analyzing perspective have just begun. In [4, 5, 6], a number of features that might affect retweetability of tweets were examined. Cao, Wu, Shi, Liu, Zheng, & Luo. (2014). base on a large number of online data from Sina-Weibo [7], analyzed a variety of possible factors that can affect users' retweeting behavior. A

dataset of Twitter conversations was used in [8] and found that users could entertain a maximum of 100-200 stable relationships. In [9], celebrity and ordinary users' behaviors on Sina-Weibo were investigated and compared. Hong, Dan, & Davison (2011) predicted the popularity of message according to a number of features, such as temporal information, users, as well as structural properties of users' social graph on a large scale dataset [10]. In [11], researchers purposed an algorithm to predict the number of retweets according to a set of features. Researchers in [12] took Sina-Weibo as a case to study whether structural features of contents can be used to predict the popularity of short messages. Researchers in [13] investigated the attributes and relative influence of 1.6M Twitter users by tracking 74 million diffusion events.

However, most of the predictive works focus on features of a single blog or a whole topic. Very few researchers have analyzed the topic structure deeply and classified the topic patterns before applying data analyzing algorithms. Gruhl, Guha, Liben-Nowell & Tomkins. (2004). formalized the notion of long-running "chatter" topics consisting recursively of "spike" topics [14]. In [15], Topical Affinity Propagation (TAP) model was proposed to describe the social impact of topic hierarchy on large networks.

This paper takes Sina-Weibo, a microblog which enjoys a great popularity in China as a case and focuses on the structure of topics as well as analyzes the topic patterns by decomposing topic structures into average fundamental popularity and information tipping points. Furthermore, this paper clears out features about information tipping points to analyze topic popularity thoroughly through data mining algorithms and statistical methods.

The remainder of this article is arranged as follows: In section 2, this paper decomposes topic components and classifies topic patterns into three categories. Data background is contained in section 3. The relationship among posts features is put forward in section 4. In the end of the paper, conclusions are drawn in Section 5.

II. TOPIC STRUCTURE ANALYSIS

A. Topic Components Analysis

This section discusses basic components of a topic. Up to now, only researchers in [9] have broken down the topic structure. They formed the notion of *chatter* and *spike*: There is a possibility that bloggers express their new thoughts on any

given day about any topic which might have nothing to do with currently trending topics. This constitutes the *chatter* on that topic. Occasionally, an event occurring in the real world raises a great deal of dissension. This constitutes the *spike* on that topic. According to the data analysis result in [9], spikes do not typically propagate through Blogspace. Thus, a basic topic composed of *chatter* and recursively of *spikes*. This paper adapts the idea in [9] and improves it.

Some topics in the social network include a basic numbers of blogs, such as *Presidential Election*, *Microsoft*, and *Smart Phone*. On any given day, some bloggers express their thoughts on the topic or response to other postings. These constitute the basic popularity of that topic. The variations of these topics are apparently relevant to their social background. For example, the presidential election in 2016 facilitates *#Trump* to be the most popular topic in the past few years. The basic popularity is assumed to remain fixed during a short period. This paper now renames it appropriately as *average fundamental popularity*. For instance, topic “South China Sea” has an average fundamental popularity.

Occasionally, an event occurring in the real world leads to a heated discussion. Information thrives suddenly like a virus, such as “South China Sea arbitration” and “Establish San-Sha City in the South China Sea”. These subtopics constitute variation. This paper now renames it as *Information tipping point*[16].

To the best of our knowledge, there has not been any model describing wax and wane of a topic yet. A Model which aims to analyze and predict the variation of *average fundamental popularity (social background)* of a long-term should take sociology factors into consideration, such as news from mass media, government policies, GDP, and economic crisis, etc. This paper leaves it as an open problem. This paper devotes attention to short-term topics, where its *average fundamental popularity* is assumed to remain fixed and unchanged.

B. Topic Pattern Classification

Topics are classified into three patterns in this section according to the 10900 trending news we choose. First, we write a Python web crawler to obtain 10900 trending news events from 00:00:00 May 31st, 2016 to 23:59:59 December 31st, 2016 from a famous news website in China-Tencent News [12]. Next, for each news event, we obtain the number of posts of this topic per day. The detail about how the dataset is obtained is stated in Section 3.

We manually find that topic can be classified into three patterns. Most topics have several tipping points. Moreover, each tipping point obviously has a reason. Some of these tipping points are related to news events, others exist because of their content reach *resonance*. They have three patterns according to the number of *information tipping points* and their *average fundamental popularity*, which is familiar to that the researcher in [9] found on Blogspace.

- Topics with no much talk during common time with only few tipping points. These topics have only few posts before and after their tipping points. Such as

“Alipay + withdraw + charging”. There are 42387 blogs about this topic, and the most frequent posting is 27277 posts on September 12th. As is shown in fig. 1. The red line represents posts that are original and the green line represents reposts. Posts posted by news media are represented by yellow. Blogs about this topic first appeared in the social network on September 12th. Sina-Weibo reacted fast and calmed down fast too. On September 20th, the number of posts decreased to 209. Indeed, Alipay announced their withdraw charge policy on September 12th. The second information tipping point exists on October 12th mainly because it is the day when the withdraw policy became effective. The posts before September 12th exists because Wechat carried out new withdraw charge policy in March, and users on microblog compared these two applications. Furthermore, it is obvious that this tipping point is caused by exclusive links.

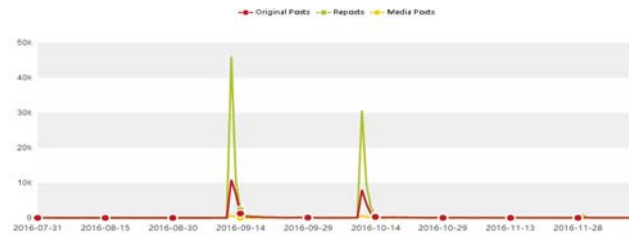


FIGURE I. THE NUMBER OF WEIBO POSTS ABOUT “ALIPAY WITHDRAW CHARGE” PER DAY

- Topics which their posts per day fluctuate within a narrow range with no obvious tipping point, such as “*Chinese and Vietnam strategic cooperate*”. We use keywords “(*China+ Vietnam*) + *strategic+ cooperate*”, and obtain the number of posts which mention these words per day. As is shown in Figure 2, there are 621 posts in total and 24 posts maximum. Although there is a fluctuating profile, the total number is low. Moreover, the topic has no tipping point and its’ number of posts per day is fluctuating in a narrow range. The average fundamental popularity remains the same. From the viewpoint of news events, there is no striking news about this topic.

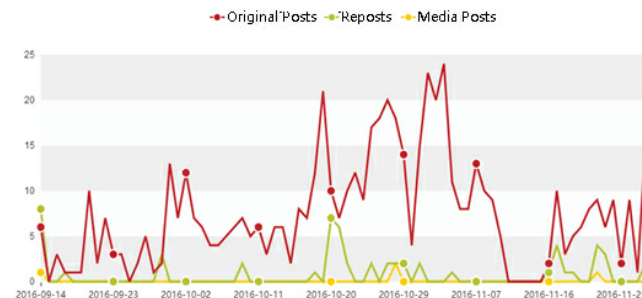


FIGURE II. THE NUMBER OF WEIBO POSTS ABOUT “CHINA AND VIETNAM STRATEGIC COOPERATE” PER DAY

- Topics which have a significant *Average fundamental popularity* level and quite sensitive to external world events. They have many *Information Tipping Points*. Such as the topic *Brexit vote*. The Brexit vote

happened on June 24th. As is shown in Figure 3(a), the tipping point on the left represents the striking news-Brexit vote. However, because of its high popularity, there are small tipping points even after one month as is shown in Figure 3(b). One of the tipping points in October appears because some influential users compared this vote with the presidential election in America, pointing out how democracy and voting system sucks. A striking news like this is always accompanied by a few tipping points and any little item can result in a tipping point.

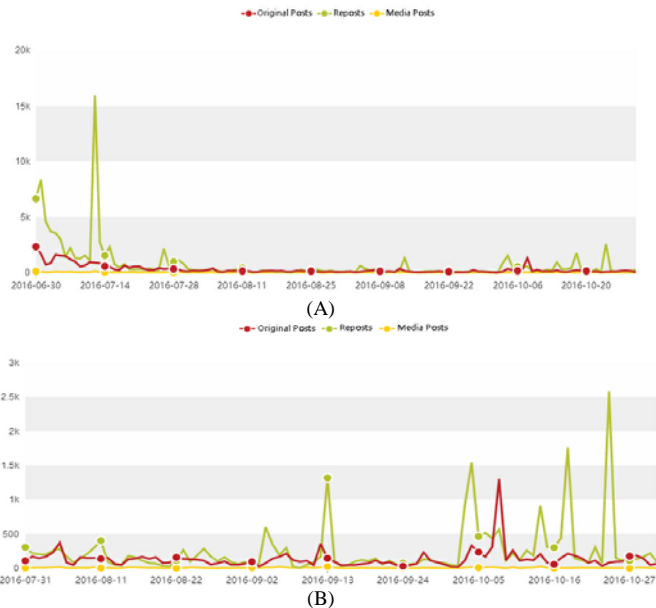


FIGURE III. (A). THE NUMBER OF WEIBO POSTS ABOUT “BREXIT VOTE” PER DAY FROM JUNE 30TH TO OCTOBER 31TH. (B). THE NUMBER OF WEIBO POSTS ABOUT “BREXIT VOTE” PER DAY FROM JULY 31ST TO OCTOBER 31TH

III. DATA BACKGROUND

This section illustrates how this paper clears out information tipping points.

It is interesting to figure out problems such as: Whether more media accounts along with hot discussions; whether hot discussions along with more original posts or reposts; and whether hot discussions have a correlation with certified accounts. This paper focuses on information tipping points of topics of type 1 and type 3 and discusses these problems

In order to focus on information tipping points, unknown social effect have to be eliminated. We focus on topics in a short-term so that social effect is assumed to remain fixed. Indeed, each tipping point is connected to a news event. Firstly, we choose 10900 trending news events between 00:00:00 May 31st, 2016 and 23:59:59 December 31st, 2016 from a famous news website- China Tencent News [17].

Next, for each news event, we obtain the number of posts on this topic per day.

Then, we need to clear out keywords connected to different news events. On each news event, to make sure the keywords

we obtain are about this news event and all the blogs related to the news event are included, we have to check repetitively. Indeed, only keywords are not enough, sometimes more exclusive words are needed.

If the profile of the number of posts per day has more than one peak, we would manually add exclusive words to this news event. If it has more than 3 peaks, we would delete this news in our database. Up to now, we have 10565 news events. Meanwhile, the date when each event happens and the date when each event comes to an end can also be determined (Usually a few days).

Moreover, we judge whether it has more than 100 relevant posts maximum. If it does, this news is regarded as a tipping point. Finally, we obtain 10507 news events.

The whole process is shown in Figure 4.

In the end, for each tipping point, this paper obtains The Number of Weibo Posts (total relevant posts) (denoted as F); 17 features within the social network: see Table 1, and (b) 3 features in the whole network as is shown in Table 2.

TABLE I. FEATURES WITHIN THE SOCIAL NETWORK

Symbol	Meaning
A	Median of Opinion Leaders’ Fan Number (opinion leaders here means blog users of top 10 forwards)
X_1	Median of Forwarded Number of Core Communication Agencies (Core communication agencies means agency accounts of top 10 forwards, so as follows)
X_2	Median of Forwarded Number of Enthusiastic Media
X_3	Median of Forwarded Number of Enthusiastic Media People
X_4	Median of Forwarded Number of Core Internet Users
B	Forwarded Number of Popular Original Posts
C	Forwarded Number of Popular Forwards
D	Ratio of Original Posts
E	Forward Hierarchy (including Initial Forward, Second Forward, Third Forward, Fourth Forward)
G	Certified Account

Among these features, Original Posts refer to posts that are originally created by blog user. A post which is not originally created but forwarded is called repost. Enthusiastic Media refer to media accounts of top 10 forwards. Enthusiastic media people refer to media people’s accounts of top 10 forwards. Core Internet Users means common users’ accounts (which have no correlation with mass media) of top 10 forwards. When calculating Median of Forwarded Number, this paper refers to the forwarded number of popular original posts only.

Certified account: Including Common User, Orange V, Talent, and Blue V. When a user is certified by Sina-Weibo, a

logo will appear next to this users' pseudonym (a colored V for orange V and blue V; a red star for talent). Blue V means the same as Orange V but is designed for agencies, medium, and enterprises. Having an Orange V or a Blue V certification needs to: follow more than 30 accounts; possess more than 100 followers; and have more than two mutual fans with an Orange/Blue V mark. Talent mark is acquired by accumulating scores, which are obtained by login, posting.etc. Since the certified logo is obvious and it represents influential people, this might affect users' behavior on the social network.

TABLE II. FEATURES IN THE WHOLE NETWORK

Symbol	Meaning
H	The Number of Reports in the Whole Network.
I	Ratio of Blogs to Reports in the Whole Network
J	Median of Forwarded Number of Popular Reports in the Whole Network

When confronted with impossible observations in the data collected, relevant news event is deleted. In the end, there are 10455 news events left.

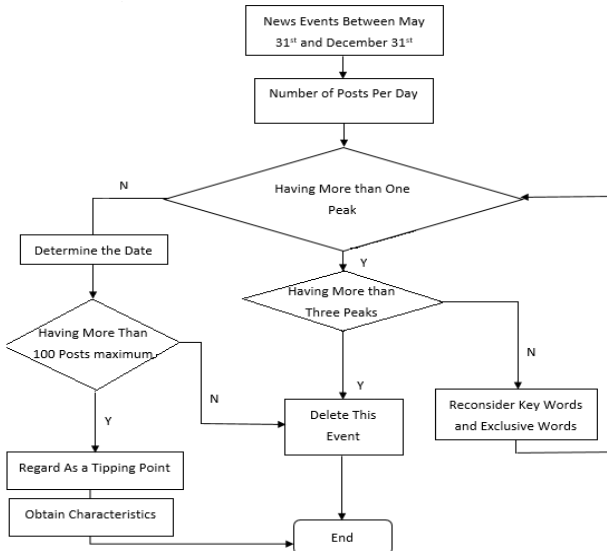


FIGURE IV. FEATURES IN THE WHOLE NETWORK

IV. FEATURES CORRELATED WITH INFORMATION TIPPING POINTS

A. Features Within the Social Network

The factors correlated with information tipping points are discussed in this section

1) Clusters

K-means Cluster algorithm is applied to classify all these tipping points into 2 clusters according to their features. It is obvious that one *tipping point* cluster is made up of news events which received little attention (Cluster 1) and the other

one is made up of news events with lively discussions (Cluster 2) [18].

Then Expectation-maximization algorithm is applied to cluster the Number of Weibo Posts. The number of categories increases to 4, but still can be manually classified into two clusters, which is the same as K-means Cluster algorithm. Therefore, they can be classified into 2 categories according to only one variable-The Number of Weibo Posts, which can represent topic's influence in the social network.

2) Ratio of Original Posts

The relationship between clusters and Ratio of Original Posts is analyzed in this section. As is shown in the box plot in Figure 5.

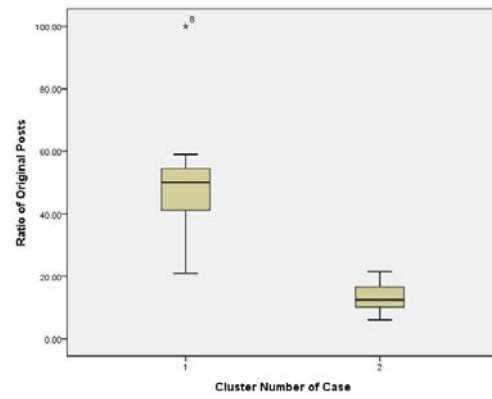


FIGURE V. RELATIONSHIP BETWEEN CLUSTERS AND RATIO OF ORIGINAL POSTS

It is obvious that most posts about lively discussed news events are reposts. In a word, more posts in total, more reposts in ratio.

3) Forwarded Number of Popular Original Posts, Forwarded Number of Popular Forwards.

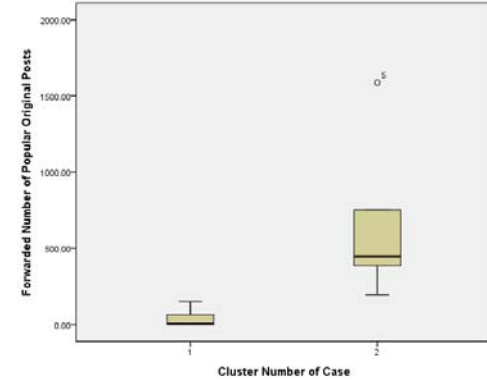


FIGURE VI. RELATIONSHIP BETWEEN FORWARDED NUMBER OF POPULAR ORIGINAL POSTS AND CLUSTERS

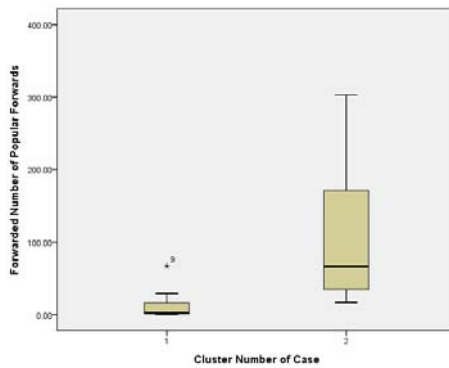


FIGURE VII. RELATIONSHIP BETWEEN FORWARDED NUMBER OF POPULAR FORWARDS AND CLUSTERS

As is shown in Figure 6 and 7, it is obvious that with more intense discussions, higher the Forwarded Number of Popular Original Posts and Forwarded Number of Popular Forwards will be.

4) Median of Opinion Leader's Fan Number

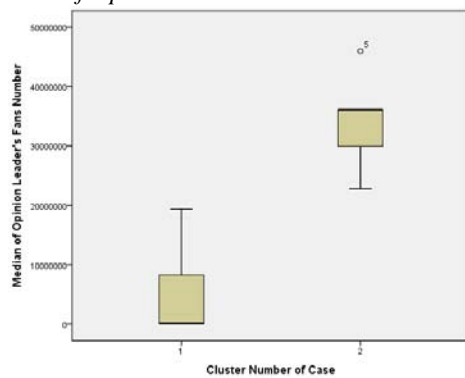


FIGURE VIII. RELATIONSHIP BETWEEN MEDIAN OF OPINION LEADER'S FAN NUMBER AND CLUSTERS.

Lively discussed topics are always related to influential users.

5) Median of Forwarded Number of Core Communication Agencies/Enthusiastic Media/Enthusiastic Media People/Core Internet Users

According to the data we have, hot topics usually have more Median of Forwarded Number of Communication Agencies/Media/Media People/ Internet Users. Moreover, Forwarded Number of Enthusiastic Media \geq Enthusiastic Media People \geq Core Internet Users \geq Core Communication Agencies under most of the circumstances.

Here we discuss the relationship between these four accounts.

This paper calculates their spearman correlation coefficient, the result is shown in Table 3.

TABLE III. SPEARMAN CORRELATION COEFFICIENT AMONG MEDIAN OF FORWARDED NUMBER OF CORE COMMUNICATION AGENCIES/ENTHUSIASTIC MEDIA/ENTHUSIASTIC MEDIA PEOPLE/CORE INTERNET USERS

	x_1	x_2	x_3	x_4	
x_1	Correlation Coefficient Sig. (2-tailed) N	1.000 0 13	0.749** 0.003 13	0.736** 0.004 13	0.742** 0.004 13
x_2	Correlation Coefficient Sig. (2-tailed) N	0.749** 0.003 13	1.000 0 13	0.782** 0.002 13	0.823** 0.001 13
x_3	Correlation Coefficient Sig. (2-tailed) N	0.736** 0.004 13	0.782** 0.002 13	1.000 0 13	0.956** 0 13
x_4	Correlation Coefficient Sig. (2-tailed) N	0.742** 0.004 13	0.823** 0.001 13	0.956** 0 13	1.000 0 13

**. Correlation is significant at the 0.01 level (2-tailed).

P-Value is less than significant level 0.05, thus, we reject the original hypothesis. These four variables have a strong linear correlation. Therefore, a linear regression analysis model can be set.

For example, we can use any three of these four variations to predict the other one.

The linear regression analysis result applying enters regression method is stated as follows:

$$x_4 = -8.722 + 0.094x_2 - 0.395x_1 + 0.978x_3$$

Then its' residual normal P-P plot is drawn in Figure 9.

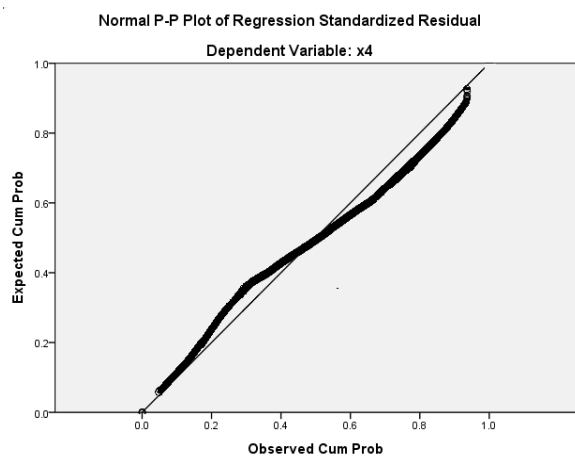


FIGURE IX. NORMAL P-P PLOT OF REGRESSION STANDARDIZED RESIDUAL

In light of our data set is impossible to be large, the linear regression model can be regarded as a satisfying result.

6) Common Account, Certified Account.

Before one-way analysis of variance, Homogeneity of variance test is needed. The P-value of Levene homogeneity of variance test is 0.135. This P-value is bigger than the significance level, so the original hypothesis should be accepted. Thus, one-way analysis of variance can be preceded. As is shown in Table 4.

TABLE IV. ANOVA COMMON ACCOUNT

	Sum of Squares	df	Mean Square	F	Sig.
Between Groups	13.882	5235	13.882	0.128	0.727
Within Groups	1188.604	5220	108.055		
Total	1202.486	10455			

Since the P-value of one way analysis of variance is 0.727, the original hypothesis should be accepted. As a result, Common Users and topic classification are irrelevant. If we ignore a few extreme points in case1, Common Users change in the same range, and so is Certified Accounts.

Here we conclude that Certified Accounts have nothing to do with users' behavior. This is to say, no matter what kind of account this user possesses, the possibility of getting involved in an issue is the same. Moreover, a few extreme points were removed and we calculated their average: Common Users take up 82.55%, Orange V takes up 4.16%, Talent takes up 9.05%, and Blue V takes up 4.25%. Unfortunately, the official number is not available in concern of information disclosure, we cannot validate this assumption.

7) Forward Hierarchy

The analyzing process is the same as Certified Account, and so is the conclusion. For Initial Forward, Homogeneity of Variance Test is preceded first. The P-value of Levene Homogeneity of variance test is 0.112, which is bigger than the significance level, so the original hypothesis should be accepted. Thus, one-way analysis of variance can be preceded. The result is shown in Table 5.

TABLE V. ANOVA INITIAL FORWARD

	Sum of Squares	df	Mean Square	F	Sig.
Between Groups	1723.331	5235	1723.331	3.963	0.072
Within Groups	4783.107	5220	434.828		
Total	6506.438	10455			

Because the P-value of one way analysis of variance is 0.072, the original hypothesis should be accepted. As a result, Initial Forward and topic classification is irrelevant. For the Second/Third/Fourth Forward, the result is the same. Here we conclude that Forward Hierarchy has nothing to do with users' behavior, no matter how many times a post being forwarded, so the possibility of being forwarded again still remains the same.

8) Predictive Model

Up to now, 8 relevant features have been recognized, and their linear relationship between The Number of Weibo Posts is obvious. Thus, we proceed linear regression analysis applying enter regression method.

The result is as follows:

$$F=174.905X_1 + 7.762X_2 - 1041.811X_3 - 340.076X_4 - 114.523B \\ + 1755.961C + 78.950D - 6135.466$$

Its residual normal P-P plot is shown in Figure 10.

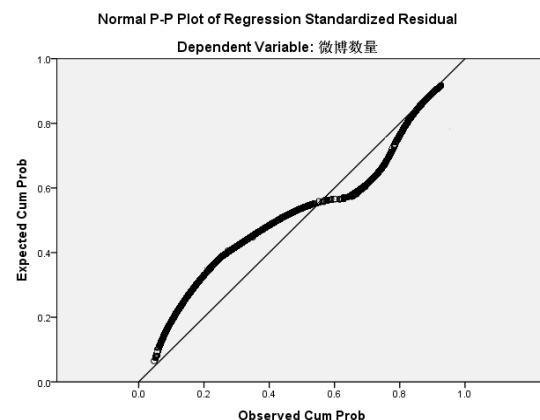


FIGURE X. NORMAL P-P PLOT OF REGRESSION STANDARDIZED RESIDUAL

In light of our dataset is not large, the standardized residual is considered to comply normal distribution, this result is reliable. This linear model can be used to predict The Number of Weibo Posts. Furthermore, this linear model can be used to predict how influential this news event can be.

B. Features of the Whole Network

In this section, we discuss the relationship between features in the whole network and its popularity in Sina-Weibo, this section continues to use the clustering result in section 4.1.1.

Reports Number in the whole network. The Ratio of Blogs to Reports and Median of Forwarded Number of Popular Reports in the Whole Network cannot determine clusters alone.

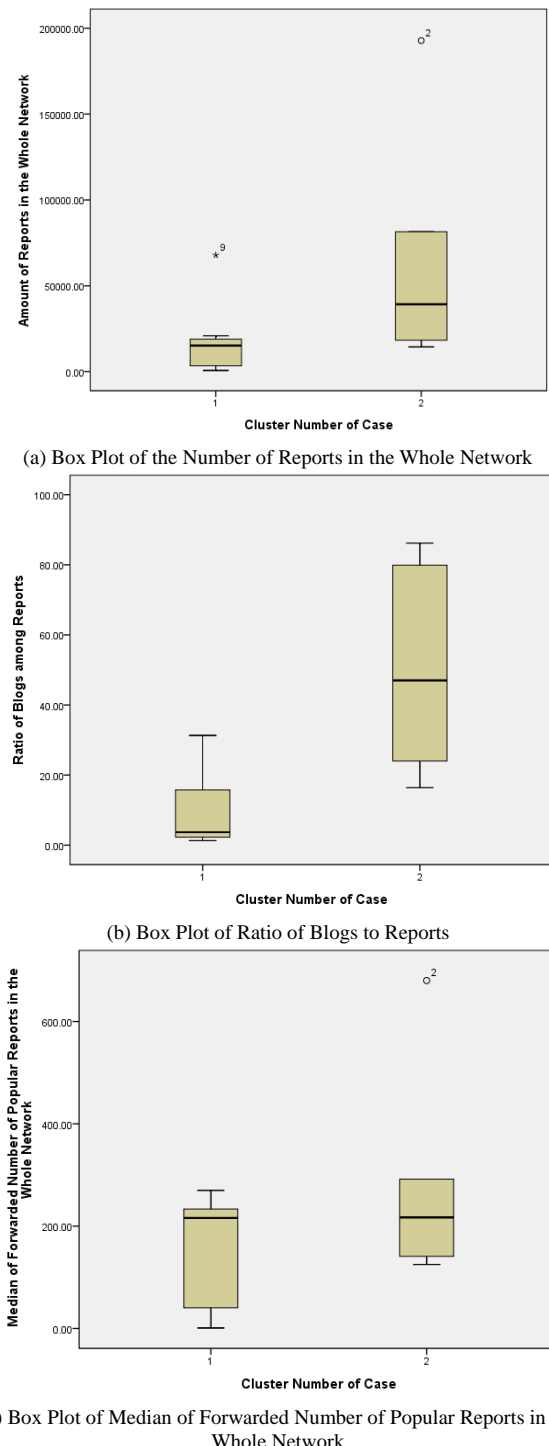


FIGURE XI. BOX PLOT OF FEATURES IN THE WHOLE NETWORK

None of these features can determine subtopics clusters alone. However, as is analyzed in section 4, the Number of Reports in the Whole Network multiple The Ratio of Blogs to Reports represents the Number of Weibo Posts. Furthermore, these two features can represent clusters. Moreover, the Number of Reports in the Whole Network and Median of Forwarded Number of Popular Reports in the Whole Network

can be used to predict the subtopics' cluster. Here Support Vector Machine algorithm (SVM) is applied [13].

This paper implemented this algorithm with MATLAB. The discriminant function is as follows:

$$c(\tilde{x}) = \sum_i \beta_i K(b_i, \tilde{x}) + b = 0.3484K(b_1, \tilde{x}) + 0.1200K(b_{205}, \tilde{x}) + 0.0703K(b_{478}, \tilde{x}) - 0.0130K(b_{521}, \tilde{x}) - 0.5256K(b_{10036}, \tilde{x}) + 0.0772$$

The error rate is 0. Thus, the Number of Reports in the Whole Network and Median of Forwarded Number of Popular Reports in the Whole Network can be used to predict whether a subtopic can become a hot topic.

V. CONCLUSIONS

This paper first divided *information tipping points* into two clusters by using the K-means algorithm and found out that one cluster is composed of news events of few attentions; the other one is made up of news events with lively discussions. Moreover, with MATLAB, implementation of the Expectation-Maximization algorithm to cluster the Number of Weibo Posts was discussed and found that it can totally represent topic influence.

This paper, with SPSS, concluded that more posts in total, more reposts in ratio. Higher the forwarded number of popular original posts is, higher the forwarded number of popular forwards will be and more influential users are involved in. Furthermore, Median of Forwarded Number of Core Communication Agencies/Enthusiastic Media/Enthusiastic Media People/Core Internet Users has strong correlation relation with each other.

Next, one-way analysis of variance revealed that common account, certified account, and forward hierarchy have nothing to do with the popularity of subtopics. Also, we could deduce that the average ratio of certified account in our database equals the ratio of certified account to all blog users in the social network. Finally, we established a predictive model to predict The Number of Weibo Posts using 8 relevant features.

For features in the whole network, this paper applied Support Vector Machine algorithm to obtain a discriminant function to determine whether this topic can become a trending issue.

The main contributions of this paper are:

- Discussed topic structure more thoroughly. Topic components were decomposed into *Average fundamental popularity* and *information tipping points*.
- This paper focused on topic level and analyzed features of *information tipping points* from a data mining perspective.
- This paper is the first to take features in the whole network into consideration. Since social network is now interrelated with the whole network closely, our research is deep and profound.

ACKNOWLEDGMENT

This paper acknowledges Sina WYQ for the data they provide [19]. Sina WYQ is an official public opinion analysis website; it can provide data on Website, Microblog, WeChat, News Media, and Newspapers to analysis public sentiment. We also acknowledge National Natural Science Foundation of China (No. 11371081) for their support.

REFERENCES

- [1] Wikipedia: Microblogging in China. Retrieved on February 20, 2017, from https://en.wikipedia.org/wiki/Microblogging_in_China.
- [2] Cha, M., Mislove, A., Adams, B., & Gummadi, K. P. (2008). Characterizing social cascades in flickr. ACM. The Workshop on Online Social Networks. (pp. 13-18). Seattle, Washington, USA.
- [3] Liben-Nowell, D., & Kleinberg, J. (2008).Tracing information flow on a global scale using internet chain-letter data. In Proceedings of the National Academy of Sciences of the United States of America (pp. 4633-4638). USA.
- [4] Suh, B., Hong, L., Pirolli, P., & Chi, E. H. (2010). Want to be retweeted? Large scale analytics on factors impacting retweet in Twitter network. In Proceedings of the IEEE International Conference on Social Computing. (pp. 177-184). Pala Alto. USA.
- [5] Zaman, T. R., Herbrich, R., van, Gael, J., & Stern, D. (2010). Predicting information spreading in Twitter. In Proceedings of the Neural Information Processing Systems. (pp. 598-601) Vancouver, Canada.
- [6] Zarrella, D., Science of Retweets. Retrieved on February 15, 2017, from <http://danzarrella.com/the-science-of-retweets-report.html>.
- [7] Cao, J., Wu, J., Shi, W., Liu, B., Zheng, X., & Luo, J. (2014). Sina Microblog information diffusion analysis and prediction. Chinese Journal of Computers. 37(4), 779-790.
- [8] Zhang, B., Guan, X., Khan, M. J., & Zhou, Y. (2012). A Time-Varying Propagation Model of Hot Topic on BBS Sites and Blog Networks. Information Science. 187(1), 15-32.
- [9] Liu, X., Wang, W., & Wu, J. (2015). Celebrity and ordinary users: A Comparative Study of Microblog User Behaviors on Sina-Weibo.Journal of Data and Information Science. 32(9), 83-95.
- [10] Hong, L.J., Dan, O., Davison, BD. (2011). Predicting Popular Messages in Twitter. Proceedings of the 20th international conference companion on World Wide Web. (pp. 57-58). New York, USA.
- [11] Kupavskii, A., Ostroumova, L., Umnov, A., Usachev, S., Serdyukov, P., Gusev, G., Kustarev, A. (2012). Prediction of Retweet Cascade Size over Time. In Proceedings of the 21st ACM International Conference on Information and Knowledge Management. (pp. 2335-2338). Maui, Hawaii, USA.
- [12] Bao, P., Shen, H., Huang, J., Cheng, X. (2013). Popularity Prediction in Microblogging Network: A Case Study on Sina Weibo. In Proceedings of the 22nd International Conference on World Wide Web. (pp. 177-178). New York, USA.
- [13] Bakshy, E., Hofman, JM., Mason, WA., Watts, DJ. (2011). Everyone's an influencer: Quantifying influence on Twitter. Proceedings of the Fourth ACM International Conference on Web Search and Data Mining. (pp. 65-74). New York, USA.
- [14] Gruhl, D., Guha, R., Liben-Nowell, D., & Tomkins, A. (2004). Information Diffusion through Blogspace. International Conference on World Wide Web (pp.491-501). New York, USA.
- [15] Tang, J., Sun, J., Wang, C., & Yang, Z. (2009). Social Influence Analysis in Large-scale Networks. ACM SIGKDD International Conference on Knowledge Discovery and Data Mining (pp. 807-816). Paris, France.
- [16] Gladwell, M. (2000). *The Tipping Point: How Little Things Can Make a Big Difference*. Little Brown.
- [17] Tencent News. Retrieved on December 1, 2016, from http://news.qq.com/china_index.shtml.
- [18] Wu, X., & Kumar, V. (2013). *The Top Ten Algorithm in Data Mining*. Tsinghua University Press.
- [19] Sina-WYQ. Retrieved on December 16, 2016, from <http://wyq.sina.com>.

Sentiment Analysis of Emergencies Based on Microblogging

Changjin Liu^{1,2}, Xin Ye^{1,*}, Hongxia Dai¹, Fan Chen³ and Luan Dong¹

¹Faculty of Management and Economics, Dalian University of Technology, No.2 Linggong Road, Dalian 116024, China

²Tsinghua-Berkeley Shenzhen Institute, University Town of Shenzhen, Nanshan District, Shenzhen, 518055, China

³Transportation Management College, Dalian Maritime University, NO.1 LingHai Road, Dalian 116026, China

*Corresponding author

Abstract—With wide use of microblogging, the sentiment analysis of emergencies based on microblogging is helpful to analyze the trend of public opinion, and is beneficial to monitor and guide the public opinion correctly for government. Firstly, word2vec is used to transform microblogging text into the feature vector with high-dimensional space. Then, a classification algorithm based on random forest optimized by genetic algorithm is proposed. Finally, an experiment is performed. The result shows that the accuracy of microblogging sentiment classification based on proposed classification algorithm is improved greatly compared with classical single classifiers.

Keywords—emergencies; sentiment analysis; Word2vec; random forest; genetic algorithm

I. INTRODUCTION

With the rapid development of Web technology, people use Internet forums, blogs, microblogging and other ways to express their views and feelings about social emergency. However, when the public opinions pose a threat to social order and have a bad influence on people's life, Internet emergency happens [1]. The platform like microblogging contains a large amount of opinion-rich data, which reflects the viewpoint of people targeting various types of Internet emergencies in real-time [2]. The emotion of people often affects the development of the whole event. Therefore, it is of great value to do research on public opinion of emergencies network, especially the sentiment analysis of emergencies based on microblogging. And it is helpful to monitor and guide the public opinion correctly for government.

In recent years, sentiment analysis in the field of emergencies has attracted a large number of researchers to study. In this part, we give a brief introduction to the previous work on the methods for sentiment analysis in the field of emergencies. Tong LI proposed a sentiment analysis and prediction model based on multiple model integration, and use this model to achieve the purpose of sentiment classification and trend prediction of public opinion [3]. Jing WANG considered the difference of evaluation objects, used a variety of feature selection methods and machine learning method to analyze the sentiment [4]. Guolan CHEN proposed a sentiment analysis method based on the combination of sentiment lexicon and semantic rules, and calculated the sentiment tendencies of the whole topic based on the influence of microblogging users [5]. Yuanyuan LI proposed a multi-feature combination method based on emotion dictionary and CRF model to analyze the

sentiment [6]. Shihai TIAN proposed to improve the potential semantic analysis and support vector machine algorithm for sentiment classification, based on mining public opinion information through meta-search technology, and increasing the baseline offset value to optimize the emotional feature orientation weight [7].

At present, scholars put forward a variety of methods in the study of sentiment analysis of emergencies [8-10]. The commonly methods are based on the traditional lexicon [11-13] or based on machine learning such as SVM [14-16], and random forest algorithm is rarely used. Random forest algorithm is the integration of multiple single decision tree classifiers, which can improve the generalization ability of classifiers [17]. Furthermore, the combination of random forest and genetic algorithm can greatly improve the accuracy of the sentiment classification [18]. Therefore, aiming at the sentiment analysis of emergencies, the classification algorithm based on random forest optimized by genetic algorithm(GA-RF) is proposed in this paper.

The rest of this paper is organized as follows. Section 1 details our techniques and proposes the classification algorithm based on random forest optimized by genetic algorithm(GA-RF). Then, Section 2 performs an experiment and analyzes the results. Finally, Section 3 concludes this paper.

II. PROPOSED METHOD

A. Overview

The general framework of this paper is displayed in Figure 1. Firstly, the comments data are extracted from microblogging. Secondly, these data are preprocessed. And next, the comments data are transformed into vectors based on word2vec model. Finally the classification algorithm based on random forest optimized by genetic algorithm (GA-RF) is used to classify comments data into two sentiment polarities (positive or negative).

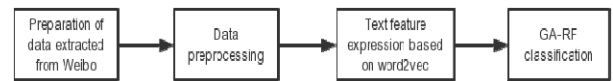


FIGURE I. THE GENERAL FRAMEWORK OF PAPER

B. Preprocessing

1) *Data collection*: There are more than 5000 comments data are extracted from the search API of SinaWeibo.

2) *Data preprocessing*: This step mainly consists of noise reducing, text segmenting, and stopwords deleting three parts.

a) *Noise reducing*: Regular expressions are used to remove URL links, microblogging topic tags, location information, microblogging forward signs, and microblogging emoticons.

b) *Text segmenting*: Jieba word segment tool is adopted to segment the comments text into words and text.

c) *Stopwords deleting*: The natural language processing stopwords provided on CSDN is used to remove useless words.

C. Vector Representation Based on Word2vec

Word2vec is a tool released by Google in 2013. This tool can find the semantic relationships between words in the document and vectorize text [19-20]. Word2vec adopts two

main model architectures, continuous bag-of-words(CBOW) model and continuous skip-gram model [19].

In this paper, skip-gram model is used to train the training file. Firstly, Chinese Wikipedia corpus are trained to get the word2vec model. Then, the trained model is applied to represent the comments data as 400 dimensional vectors, which are marked with sentiment polarities.

D. Classification algorithm based on GA-RF

Integrated learning is a methodology that combines multiple classifiers, and can achieve better performance than a single classifier. In order to improve the accuracy of microblogging sentiment classification, a new integrated learning algorithm based on random forest is proposed. This algorithm use genetic algorithm to optimize random forest for selecting the best performing decision tree.

The process of classification algorithm based on random forest optimized by genetic algorithm is represented in Figure 2.

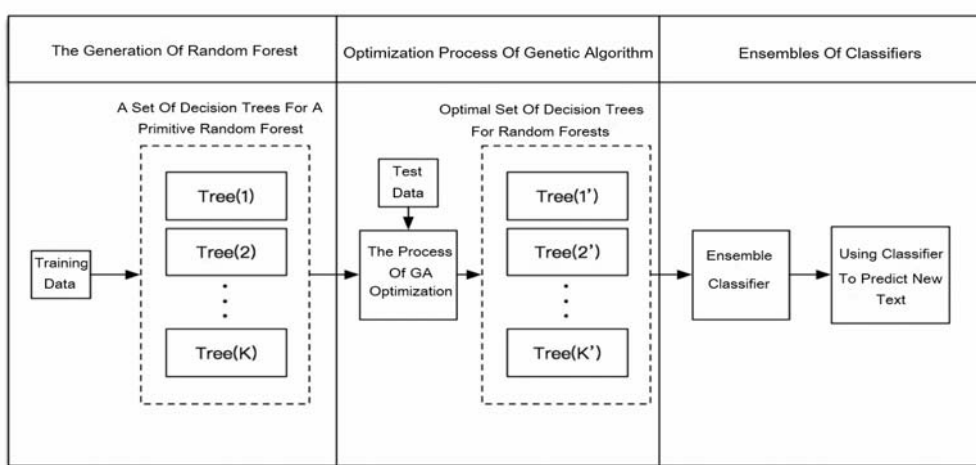


FIGURE II. THE PROCESS OF CLASSIFICATION ALGORITHM BASED ON GENETIC ALGORITHM FOR RANDOM FOREST OPTIMIZATION

Where, K is the total number of decision trees in trained random forest, and K' is the number of new decision trees after the selection of genetic algorithm, and $K' < K$.

In genetic algorithm, fitness function directly reflects the target optimization function of algorithm. In this paper, fitness function is defined as the accuracy of classifiers. In order to make the crossover and mutation directly affect the independent variables of the objective function, 0 and 1 are used to indicate whether the N -th tree of a trained random forest is selected. For example, there is a random forest that has been trained with 10 decision trees, 0 indicates that the N -th tree is not selected, while 1 is selected. Assuming that the initial selection is 2-th, 3-th, 5-th and 8-th trees. Table 1 gives an example of chromosome coding.

TABLE I. THE EXAMPLE OF CHROMOSOME CODING

Tree number	1	2	3	4	5	6	7	8	9	10
Binary coding	0	1	1	0	1	0	0	1	0	0

In genetic algorithm, there are three kinds of operators that control the genetic and replication process of chromosomes. In this paper, binary tournament selection is selected as the selection operator, and single-point crossover is selected as the crossover operator. A variation gene is selected randomly in a chromosome, and the value is transformed between 0 and 1.

III. EXPERIMENT AND DISCUSSION

A. Data Sets

The comments data of four hot topics in 2016 are selected. And then, the AHP method is used to label 3000 comments data manually. A brief summary of data sets is represented in Table 2. To conduct experiments, data sets is divided into two parts, one part with 1350 positive comments and 1350 negative, is used as train data. The other part is used as test data.

TABLE II. A BRIEF SUMMARY OF DATA SETS

Data Set	Positive	Negative	Total
Train Data	1350	1350	2700
Test Data	150	150	300

B. Experimental Parameters

In this section, the value of experimental parameters for three classic classification algorithms and GA-RF are set. The value of parameters are mainly depended on the best results of some experiments and the experience. The value of specific parameters are listed in Table 3.

TABLE III. THE VALUE OF PARAMETERS

Method	Parameters set
SVM	SVM: C-SVC; Kernel function: RBF;
Random Forest	Random forest scale: 100;
KNN	Number of neighbours: 5
Genetic Algorithm	Population number: 260; Crossover and Mutation rate: 0.8; Gene mutation rate: 0.1; Number of reproduction: 500;

Results of experiments are evaluated with accuracy, precision and recall. The accuracy is used as the core evaluation index, and the precision and recall is used as the secondary evaluation index.

TABLE IV. THE PERFORMANCE OF THREE CLASSIFICATION ALGORITHM (SVM, RANDOM FOREST AND KNN)

	SVM			Random Forest			KNN		
	Accuracy	Precision	Recall	Accuracy	Precision	Recall	Accuracy	Precision	Recall
1	0.6367	0.3985	0.6647	0.6133	0.4060	0.6367	0.5567	0.3008	0.4431
2	0.59	0.4311	0.6165	0.6067	0.4251	0.6466	0.5867	0.2994	0.4436
3	0.59	0.4236	0.6603	0.6267	0.4091	0.6644	0.6167	0.2597	0.4863
4	0.62	0.4236	0.6603	0.6367	0.3611	0.6346	0.5367	0.3333	0.4167
5	0.6367	0.3958	0.6667	0.5833	0.4792	0.6410	0.5967	0.2778	0.4808
6	0.65	0.3846	0.6815	0.6033	0.4266	0.6306	0.5867	0.3217	0.5032
7	0.6667	0.3241	0.6581	0.6333	0.3793	0.6452	0.57	0.2897	0.4387
8	0.6267	0.4028	0.6538	0.6167	0.3889	0.6218	0.56	0.2708	0.4038
9	0.5933	0.4765	0.6846	0.5833	0.5	0.6923	0.5933	0.3059	0.4615
10	0.6333	0.4286	0.6928	0.6133	0.4014	0.6275	0.5667	0.3537	0.4902
AVG	0.6243	0.4089	0.6639	0.6133	0.4177	0.6433	0.5667	0.3013	0.4568

TABLE V. THE EXPERIMENTAL RESULT OF GA-RF

Fold	1	2	3	4	5	6	7	8	9	10	AVG
Accuracy	0.7667	0.7612	0.7600	0.7846	0.7652	0.7824	0.7935	0.7658	0.7846	0.7741	0.7738

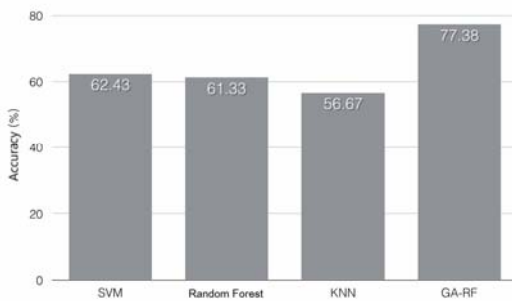


FIGURE III. THE COMPARISONS OF LASSIFICATION AVERAGE ACCURACY

C. Performance of Sentiment Classification

The performance of three classification algorithm (SVM, random forest and KNN) is listed in Table 4. A comparative analysis based on three classification algorithm is given below. Firstly, the precision of SVM is very low, while the recall rate is high. This performance indicates that the classification accuracy of the samples, which divided into positive emotions by the SVM algorithm is very high, but not all positive emotion samples are correctly classified. On the contrary, the SVM algorithm is very likely to ignore the positive emotion samples. Secondly, compared with SVM, the precision of random forest is higher and recall is lower. This shows that random forest performs better for text marked as positive emotion. Thirdly, KNN shows the worst performance among three classification algorithm, indicating that KNN is unsuitable for emotion classification in this particular issue.

Then, the algorithm based on random forest optimized by genetic algorithm model is adopted. Similarly, 10-fold cross is used and calculate the average of accuracy. The experimental results are listed in Table 5. As expected, GA-RF is significantly better than other algorithms.

Figure 3 shows the comparisons of average accuracy from different classification algorithm. The classification accuracy of GA-RF is the highest, and is 23.9%, 26.2% and 36.5% higher than SVM, random forest and KNN respectively. SVM has a second high accuracy, which is 1.8% and 10.2% higher than the random forest and KNN.

IV. CONCLUSION

In this paper, the sentiment analysis of emergencies based on microblogging is studied. After word2vec is used to transform text into the feature vector, the classification algorithm based on random forest optimized by genetic algorithm is proposed. The experimental results show that the

method gives better results than single classifiers. However, compared with other studies, the accuracy is still need to be improved.

In the future, there is a need to apply the same method to explore the change of public opinion during the life cycle of emergency. Try to find the changing characteristics of public opinion during the evolution of events, and find the impact of government measures on public opinions.

ACKNOWLEDGMENT

This work was supported in part by the National Natural Science Foundation of China under Grant 71533001 and in part by the Liaoning province economic and social development project of Liaoning Provincial Federation Social Science Circles of China under Grant 2017lslktyb-044.

REFERENCES

- [1] Dehai LIU, Weiguo WANG, Hongyi LI. Evolutionary Mechanism and Information Supervision of Public Opinions in Internet Emergency [J]. Procedia Computer Science, 2013, 17:973-980.
- [2] Faliang HUAN, Shichao ZHANG, Jilian ZHANG, Ge YU. Multimodal Learning for Topic Sentiment Analysis in Microblogging[J]. Neurocomputing, 2017, 253(C):144-153.
- [3] Tong LI, Zhijie SONG. Public sentiment of emergent events based on model integration and its trend prediction[J]. Systems Engineering — Theory & Practice, 2015, 35(10):2582-2587.
- [4] Jing WANG. Analysis on Sentiment Orientation and Its Evolution of Emergency Network Public Opinion, 2012.
- [5] Guolan CHEN. Monitoring Based on The Micro-blog Burst Incidents Word And Sentiment Analysis [J]. Nanjing University Of Posts And Telecommunications, 2015.
- [6] Yuanyuan LI. Research on Hot Event Sentiment Analysis for Topic Microblog [J]. Anhui University, 2016.
- [7] Shihai TIAN, Deli LYU. An Early Warning Algorithm for Public Opinion of Safety Emergency[J]. Data Analysis and Knowledge Discovery, 2017, 1(2):11-18.
- [8] Huifeng TANG, Songbo TAN, Xueqi CHENG. A survey on sentiment detection of reviews[J]. Expert Systems with Applications, 2009, 36(7):10760-10773.
- [9] Bing LIU. Sentiment Analysis and Opinion Mining[M]. Morgan & Claypool Publishers, 2012.
- [10] Tsitsarau M, Palpanas T. Survey on mining subjective data on the web[M]. Kluwer Academic Publishers, 2012.
- [11] Minqing HU, Bing LIU. Mining and summarizing customer reviews[C]//Proceedings of the tenth ACM SIGKDD international conference on Knowledge discovery and data mining. ACM, 2004: 168-177.
- [12] Kim S M, Hovy E. Identifying and analyzing judgment opinions[C]//Proceedings of the main conference on Human Language Technology Conference of the North American Chapter of the Association of Computational Linguistics. Association for Computational Linguistics, 2006: 200-207.
- [13] Augustyniak L, Kajdanowicz T, Szymanski P, et al. Simpler is better? Lexicon-based ensemble sentiment classification beats supervised methods[C]//Advances in Social Networks Analysis and Mining (ASONAM), 2014 IEEE/ACM International Conference on. IEEE, 2014: 924-929.
- [14] Shoushan LI, Zhongqing WANG, Guodong ZHOU, Sophia Yat Mei Lee. Semi-Supervised Learning for Imbalanced Sentiment Classification.[C]// Pacific-Asia Conference on Advances in Knowledge Discovery and Data Mining. Springer-Verlag, 2009:588-595.
- [15] Rui XIA, Tao WANG, Xuelei HU, Chengqing ZONG. Dual Training and Dual Prediction for Polarity Classification[C]// Meeting of the Association for Computational Linguistics. 2013:521-525.
- [16] Hongwei WANG, Lijuan ZHENG. Sentiment classification of Chinese online reviews: a comparison of factors influencing performances[J]. Enterprise Information Systems, 2016, 10(2):228-244..
- [17] Abellán J, Mantas C J, Castellano J G. A Random Forest approach using imprecise probabilities[J]. Knowledge-Based Systems, 2017.
- [18] Dao S D, Abhary K, Marian R. An innovative framework for designing genetic algorithm structures[J]. Expert Systems with Applications, 2017, 90:196-208.
- [19] Tomas Mikolov, Kai CHEN, Greg Corrado, Jeffrey Dean. Efficient Estimation of Word Representations in Vector Space[J]. Computer Science, 2013.
- [20] Tomas Mikolov, Ilya Sutskever, Kai CHEN, Greg Corrado, Jeffrey Dean. Distributed Representations of Words and Phrases and their Compositionality[J]. Advances in Neural Information Processing Systems, 2013, 26:3111-3119.

Research on the Similarity of Microblog Rumors Based on Bayesian Network

Chengcheng Li, Fengming Liu* and Pu Li

School of Management Science and Engineering, Shandong Normal University, Ji'nan 250014, China

*Corresponding author

Abstract—The research of text similarity, especially for rumors texts, which constructed the calculation model on the basis of known rumors and calculated its similarity. From which, people can recognize the rumors in advance, and improve their vigilance to effectively block and control rumors dissemination. Based on Bayesian network, the similarity calculation model of microblog rumors texts was built. At the same time, taking into account not only the rumors texts have similar characters, but also the rumors producers have similar characters, and therefore the similarity calculation model of rumors texts makers was constructed. Then, the similarity between the text and the user was integrated, and the microblog similarity calculation model was established. Finally, also experimentally studied the performance of the proposed model on the microblog rumors text and the user data set. The experimental results indicated that the similarity algorithm proposed in this paper can be used to identify the rumors of texts and predict the characters of users more accurately and effectively.

Keywords—*microblog rumors; similarity; bayesian network*

I. INTRODUCTION

Microblog is a new media platform based on the social network of user interaction to share, disseminate and exchange the short and real-time data. Its features of originality, interaction, convenience and fragmentation will mainly focus on future development of microblog on the aspect of information construction, business model promotion, and other aspects [1-4]. In the microblog, users are not only foundation, but also main part that constitutes microblog framework combined with microblog text. The unique interaction of microblog among users build a complex and large social network, and its multi-level fission can make microblog content that is forwarded, continued to spread and amplified quickly by a lot of fans [5]. Among these, the typical example is the spread of microblog rumors [6-7] that causes a very bad impact not only on the microblog cyberspace, but also on people's daily life. So microblog rumors are widely explored and studied.

In order to scientifically and effectively manage massive amounts of data and user information, and refine microblog network space, researchers conduct a large number of analysis and experiment in the prediction of microblog rumors similarity [8-10]. We take into account not only the rumors texts have similar characters, but also rumors producers have similar features. Therefore, on the one hand, in the study of microblog text content, because microblog is short text with the features of short length and sparse feature words in its text, it results the

previous calculation method of text similarity that cannot be directly applied in the detection of microblog text similarity. Thus, scholars begin to study the similarity of short text. On the other hand, in the exploration of microblog users, the number of users has been risen with the gradual growth and generalization of social networks. Therefore, here are many scholars begin to analyze behavior similarity of microblog users [11] so that better achieve users' forecast in some aspects [12-13].

For the calculation of the microblog content similarity, the traditional method is to transform the data and return the unified calculation to research based on extracted keyword and short text classification [14]. At present, the automatic extraction method based on semantic and conceptual terms is widely used. This method mainly uses the semantic dictionary to obtain the semantic knowledge among vocabularies and further to extract the text keywords. At the same time, for the calculation of users behavior similarity [15], researchers found that it has been widely used in enterprises microblog about customer service, and analyzed spending habits of potential customers who have similar behaviors through data mining; and search interests and hobbies information of users that further satisfy users' demands, which can increase the interaction between two parties [16-21]. However, in recent years, for the analysis and exploration of the text content of microblog rumors and the calculation of users behavior similarity is still in infant stage, and its related methods, indicators and verification are not enough integrity that needs to be further improved.

This paper adds the unique feature vector of microblog. In the study of text similarity, we consider the rhetorical devices, sentence features and sensitive words use. In the study of user similarity, we take into account the user's commenting behavior, forwarding behavior, @ behavior and other interactive behaviors. So from which we can get more comprehensive and targeted information of microblog text and user and improve the accuracy of the calculation method.

II. SIMILARITY MODELING AND CALCULATION METHOD OF MICROBLOG RUMORS BASED ON BAYESIAN NETWORK

A. Microblog Text Similarity Modeling Based on Bayesian Network

Due to the short length of microblog text, the characteristic words of composition text are less, the correlation between keywords is weaker and so on, and the processing of short text is becoming the mainstream of text processing. Through the

microblog rumors of the massive data study found that in the language of microblog rumors more popular, spoken language heavier, mostly using exaggeration, irony, citation and other rhetoric, rendering tension, rapid atmosphere; Phrases, sentences, affirmative sentences, exclamatory sentences, and syntactic style strong; in the use of words, the use of easy to stir up the group of emotional sensitive words [22]. Based on this, this paper constructs the Bayesian network model based on the similarity calculation method of short text keyword, and analyzes the characteristics of microblog rumor itself, adding text rhetorical devices, sentence features and sensitive words, then given the different weight coefficients, it can distinguish the importance degree of the various contribution degrees of eigenvectors in short text similarity calculations.

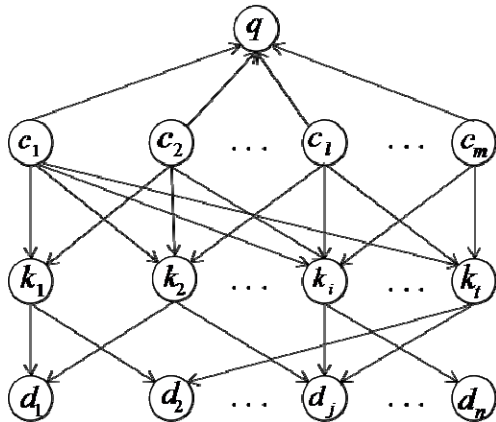


FIGURE I. MICROBLOG TEXT MODELING BASED ON BAYESIAN NETWORK

III. MICROBLOG USER SIMILARITY MODELING BASED ON BAYESIAN NETWORK

Bayesian network is through the directed acyclic graph to describe the probability of the relationship between the definition of microblog user set for the network node set. Each node represents a microblog user, between the node between the arc on behalf of the user similarity relationship. In order to form a directed acyclic graph between the user nodes, this paper establishes the query propagation tree by constructing the query propagation tree, and the query user node is the parent node of the tree. When the query user sends a query message, it will query its similar users, if the similar user spread the rumor, record the information, and then query the next similar user, if the user did not propagate the rumor, The similar user as a starting point, the downward expansion of the query, and so on, you can create a query rumor diffusion tree. It should be noted that when the number of layers of the query reaches the pre-specified value, the query is no longer extended downward. In addition, the query users can only receive a query, cannot be multiple inquiries, otherwise it will form a query storm.

The Bayesian network is constructed according to the query propagation tree, then the prior probability distribution of the nodes to be calculated and the conditional probability distribution among the nodes are calculated. And according to the original path return probability distribution information to the query user, query user according to the return information

and Bayesian formula to predict the probability that the user publish or reprint rumors. Finally, this probability is compared with a given probability threshold, and if it is greater than the threshold, then the user will propagate the rumor. The query extension tree is shown in Fig. 2.

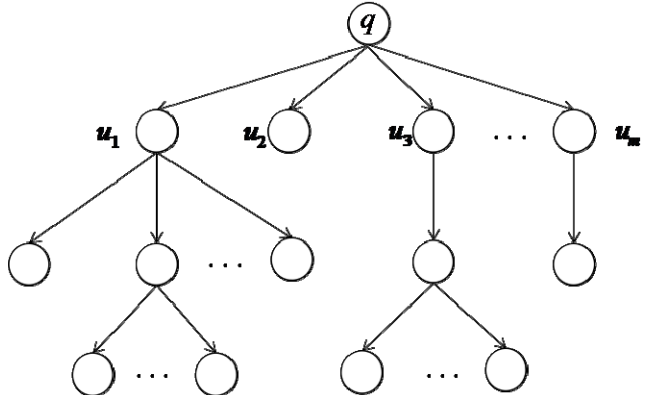


FIGURE II. MICROBLOG USER MODELING BASED ON BAYESIAN NETWORK

IV. MICROBLOG RUMORS SIMILARITY ALGORITHM BASED ON BAYESIAN NETWORK

In the first two sections, we focus on modeling the microblog text and the user, in microblog social network through constructing Bayesian network, we can predict the similarity between text and rumors sample (i.e. the probability that the detected text is the rumor) and the probability that the user of the detected text is the rumor producer. Now we propose an integrated model. That is, we take two models of the text and the user into one model, so that microblog text and its user information can be effectively embedded in the network to improve the accuracy and stability of the forecast. To achieve this goal, we have to define the two networks in the microblog social network, respectively, on behalf of the text space network and user space network. The integrated model is shown in Fig. 3.

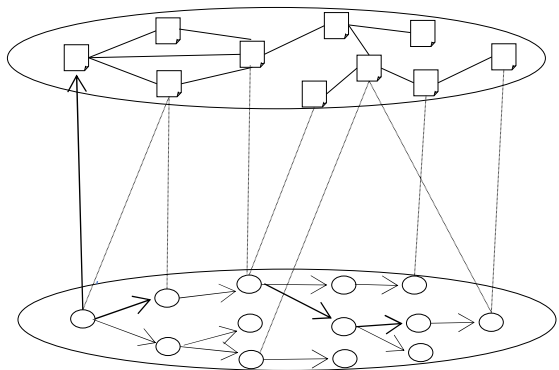


FIGURE III. THE MICROBLOG INTEGRATED MODEL

V. EXPERIMENTS

This paper chooses the data sets from Sina Weibo to start the experiment and verify the feasibility of this model. In the

process of collecting the experimental data, we refer to the data of "Statistical and Semantic Analysis of Rumors in Chinese Social Media"[23], which divides microblog rumors into several different categories, namely politics, economy, fraud, social life, common sense and other categories. In the analysis we delete too short text content or microblog picture.

In order to test and verify this model, we choose microblog rumors that are relatively more class - fraud class to verify. After that, in the fraudulent microblog rumors we extract a text to take pre-operation in a random way. Based on the analysis of the text similarity, we extract microblog's characteristic vector in the content, rhetorical devices, sentence features and sensitive words. Based on the analysis of user similarity, we find the user of the query text and study the publisher's attention to the number of users, fans, praise behavior, commenting behavior, reproduced behavior, etc., so that it's similar users in-depth study. In the process of verification, we have simplified the specific algorithm. The main purpose of simplification is to ensure the stability of the model, then we try to avoid the data to do too much of the changes. But the final test results are no substantive impact, so we see them as the experimental results of this study are credible.

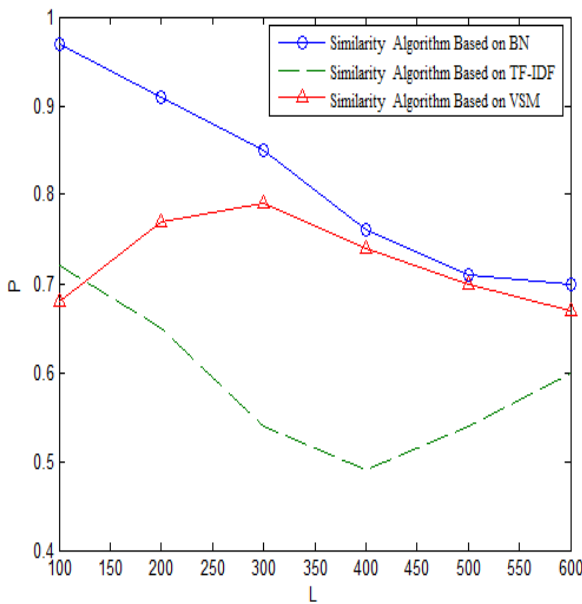


FIGURE IV. COMPARISON OF THE ACCURACY OF THE THREE ALGORITHMS

VI. CONCLUSION

This paper starts from the analysis of microblog rumors' similarity and uses Bayesian network to construct the model. First, in order to calculate the similarity of microblog social network rumors, we generate two models of the text and user into a unified model, so that we can improve the research accuracy of the microblog rumors similarity. Based on the study of the microblog rumor text's model, we calculate text similarity by extracting the eigenvector of the query microblog text. Based on the microblog user's model, we establish

Bayesian network by using the probability information and the similarity relation between the users. Then by using Bayesian formula and the calculation, we can judge the probability that the rumor spreads. Finally, the experiment and analysis are carried out on the microblog rumor text and the user data set. The experimental results show that the similarity algorithm proposed in this paper can be used to identify the rumors of text and predict the characters of users more accurately and effectively.

ACKNOWLEDGEMENT

This work was supported in part by the National Natural Science Foundation of China (No. 61170038, 61472231, 71701115), the National Social Science Foundation of China (No. 14BTQ049), the Shandong Natural Science Foundation(ZR2017MF058), and Special project for Internet development of social science planning special program of Shandong province(17CHLJ23).

REFERENCES

- [1] Ding Z Y, Jia Y, Zhou B. Survey of Data Mining for Microblogs. *Journal of Computer Research and Development*, 2014, 51(4):691-706.
- [2] Liao Y, Moshtaghi M, Han B. Mining Micro-Blogs : Opportunities and Challenges, *Proceedings of Social Networks: Computational Aspects and Mining*, Springer, 2011:1-28.
- [3] Lei C C, Zhang A, Qi Q W, Su H M. Grid-based Location Microblog Data Fetching and Human Information Extraction. *Science of Surveying and Mapping*, 2017, (02):125-129.
- [4] Cui J D, Du W Q, Guan Y, Luo W D. Research on the Evolution of Micro-blog User Information Personalized Recommendation Model Based on LDA. *Information Science*, 2017, (08):3-10.
- [5] B D Davison, L Hong, D Yin. Structural Link Analysis and Prediction in Microblogs. *Acm Conference on Information and Knowledge Management (CIKM2011)*. Glasgow, Scotland, UK, 2011(10):1163-1168.
- [6] Lei H Z, Zhang J, Lan J L. The Diffusion Effect of "Weibo Community" Negative Information Based on the Rumor Spreading Model and Case Studies. *Modern Information*, 2015, 35(5):30-34.
- [7] Li Y, Wang X Y, Zhang X G. Predicting Trending Messages and Diffusion Participants Based on Multi-types of Influences in Microblogs. *Application Research of Computers*, 2016, (10):2910-2913+2918.
- [8] Sun Y F, Li S. Similarity-Based Community Detection in Social Network of Microblog. *Journal of Computer Research and Development*, 2014, 51(12):2797-2807.
- [9] Yao B X, Ni J C, Yu P P, Li L L, Cao B. Micro blog user recommendation algorithm based on similarity of multi-source information. *Journal of Computer Applications*, 2017, (05):1382-1386.
- [10] Zheng Z Y, Jia C Y, Wang Z F, Li D. Computing Research of User Similarity Based on Micro-blog. *Computer Science*, 2017, (02):262-266.
- [11] Mepherson M, Smith-Lovin L, Cook J M. Birds of a feather: Homophily in Social Networks. *Annual Review of Sociology*, 2001: 415-444.
- [12] Resnick P, Iacovou N, Suchak M. GroupLens: An Open Architecture for Collaborative Filtering of Netnews. Chapel Hill, North Carolina, United States: ACM, 1994.
- [13] Lawrence R D, Almasi G S, Kotlyar V. Personalization of Supermarket Product Recommendations. Berlin Springer, 2001.
- [14] Zhang B, Zhang Y, Gao K N. Combining Relation and Content Analysis for Social Tagging Recommendation. *Journal of Software*, 2012, 23 (3):476-488.
- [15] Zhu X Q, Liu F M, Research on Behavior Model of Rumor Maker Based on System Dynamics, Complexity, Hindawi, Volume 2017, Article ID 5094218, 9 pages. <https://doi.org/10.1155/2017/5094218>.

- [16] Li Q Q, Gu J F. Activity Driven Modelling of Online Social Network. *Journal of Systems Engineering*, 2015, 30 (1):9-15.
- [17] Ding Y S, Liu F M, Tang B Y, Context-Sensitive Trust Computing in Distributed Environments”, *Knowledge-Based Systems*, 2012(28) 105-114.
- [18] Liu F M, Li X, Ding Y S, Zhao H F, Liu X Y, Ma Y H, Tang B Y, A Social Network-Based Trust-Aware Propagation Model for P2P Systems, *Knowledge-Based Systems*, 2013(41), 8–15.
- [19] Liu F M, Wang L, Gao L, Li H X, Zhao H F, Sok Khim Men. A Web Service Trust Evaluation Model Based on Small-World Networks, *Knowledge-Based Systems*, 2014(57) 161-167.
- [20] Liu F M, Wang L, Henric Johnson, Zhao H F, Analysis of Network Trust Dynamics Based on Evolutionary Game, *Scientia Iranica, Transaction E: Industrial Engineering*, 2015(22.6): 2548-2557.
- [21] Liu F M, Zhu X Q, Hu Y X, Ren L H, Henric Johnson, A Cloud Theory-Based Trust Computing Model in Social Networks. *Entropy* 2017, 19(1), 11.
- [22] Cheng A X, Xia C Q. On the Linguistic Features of Microblog Rumor. *Southeast Communication*, 2014, (11):98-100.
- [23] Liu Z Y, Zhang L, Tu C C, Sun M S. Statistical and Semantic Analysis of Rumors in Chinese Social Media. *Scientia Sinica (Informationis)*, 2015, (12):1536-1546.

Attention-based ResNet for Chinese Text Sentiment Classification

Hu Han*, Xuxu Bai and Jin Liu

School of Electronic & Information Engineering, Lanzhou Jiaotong University, Lanzhou, Gansu ,730070,China

*Corresponding author

Abstract—Identifying sentiment polarity of a document is a building block of sentiment classification and natural language processing tasks, it aims to automate the prediction of sentiment orientation in a document. In general, recently fast-growing Deep Neural Networks(DNN) method has been extensively used as a sentiment learning approach. But the dominant approach for sentiment classification tasks are recurrent neural networks, in particular LSTM, and convolutional neural networks. However, these architectures are rather shallow in comparison to the Residual Neural Networks(ResNet) which have pushed in computer vision. We present a model using ResNet for high-level document representation, and attention mechanism to capture the crucial components for document. The experimental results show that using up to 2 ResNet block and attention mechanism achieve state-of-the-art performance on three public sentiment classification datasets.

Keywords—sentiment classification; attention mechanism; ResNet

I. INTRODUCTION

Opinions are key influencers to almost all of our activities, since whenever we need to make a decision, e.g., when we purchase products, we want to know others' opinions. From the industry point of view, grasping know the feelings of customers about products may support strategic market decisions. Moreover, individuals may want to know others' opinions about political candidates before making a voting decision in a political election. Nowadays, many people present their opinions on the Internet, which benefits the researchers devising automatic procedures to identify these textual reviews/opinions to be positive or negative [1,2]. Mining opinions from these texts is known as sentiment classification, which is a special task of text classification whose objective is to automatically classify a document according to the sentiment polarities of opinions it contains, e.g., positive or negative, like or dislike.

Most existing methods for document sentiment classification consists of two parts: (a) designing text features such as bag-of-words [2] and (b) training some machine learning models using text features and annotated sentiment polarities. Since the performance of the classifiers relies heavily on the effectiveness of feature engineering, these methods usually focus on extracting features from texts and sentiment lexicons [3].

Motivated by the success of deep learning's application in computer vision, speech recognition [4] and natural language

processing [5], neural networks have been employed in sentiment classification and exhibited powerful ability of learning text features without feature engineering. In the canonical neural sentiment classification models [5,6], a sentence or a document is simply vectorized and then taken as input of the models which generate the semantic representations of the text. By embedding additional information e.g. user's preference and product's characteristics into input, several models [6,7] have proved the improvement of the accuracy of sentiment classification.

Convolutional neural networks, in Residual Neural Networks(ResNets), are very successful in computer vision. This fundamental idea of ResNets is to answering a question notorious problem of vanishing/exploding gradients. The best networks are using more than 150 layers as in [8]. Nowadays, [9] using ResNet to generate the semantic representations of document, this is the first time very deep Convolutional nets have been applied to text processing. Attention has become an effective mechanism to obtain superior results, as demonstrated in image recognition [10], machine translation [11] and text summarization [12]. Even more, attention can improve the ability to question answer.

In this work we propose a new neural sentiment classifier which combines Residual Neural Networks and Attention mechanism. We compare our model with neural sentiment classifiers PCNN and PCNN+Dropout [13]. Experimental results show that, our method outperforms most of the baseline methods and the state-of-the art approaches. The main contribution of this work are as follows:

- We present a new neural network model by combining ResNet and Attention for document-level sentiment classification.
- We validate the influences of the number of ResNet blocks for sentiment classification.
- We report empirical results on three datasets and show that our proposed model outperforms state-of -the-art models for sentiment classification.

II. RELATED WORK

With the huge success of deep learning in computer vision, speech recognition and natural language processing, in NLP field, neural network due to its ability of text representation has introduced into sentiment classification. Existing neural network methods can be divided into two groups: word

embedding and semantic composition. For learning word embeddings, [14] use local and global contexts, [7,15-18] further incorporate sentiment of texts. [5] adopt convolution neural network (CNN) to learn sentence representations and achieve outstanding performance in sentiment classification.

[13] adopt piecewise CNN(PCNN) to combine the structural features, in which the feature vector of a sentence is divided into three segments and does the max-pooling for each of them achieve higher than all of the baseline performance of Chinese hotel datasets and Stanford Sentiment TreeBank.

Recurrent neural network (RNN) also benefits sentiment classification because it is capable of capturing the sequential information. There are also some hierarchical models proposed to deal with document-level sentiment classification [17,19] which generate different levels (e.g., phrase, sentence or document) of semantic representations within a document. Moreover, attention mechanism is also introduced into sentiment classification, which aims to select important words from a sentence or sentences from a document [20,21] proposed user product attention based(UPA-NSC) method improve performance of sentiment classification.

[22] use convolutional layer capturing the character local connectivity of scene text recognition tasks and use RNN to learn sequential information. [9] propose using very deep convolutional network(VDCNN) for text classification, which using 2 ResNet block and k-max pooling to detect the k most important features in a sentence. Inspired by this, we feed word embedding vector to ResNet block which learning word context feature and using attention mechanism to compute words contribute from input sentence.

III. METHODS

In this section, we will introduce our Attention-based Residual Network(ARN) model in detail. First, we give the formalizations of document-level sentiment classification. Afterwards, we discuss how to obtain document semantic representation via the Attention-based ResNet, which incorporates the forward and backward information. The enhanced sentence representation is used as input for document representation. An overall illustration of Attention-based ResNet model is shown in Fig.I, which consist of four modules: embedding module, ResNet Block, attention module and dropout module.

A. Formalization

We represent the review as a document d with n words $\{w_1, w_2, \dots, w_n\}$. Document-level sentiment classification aims to inferring the numeric rating(1-5 or 1-10 stars) or sentiment polarity(positive, negative) of these reviews according to their text information.

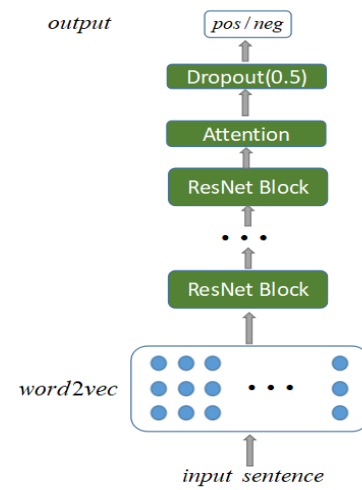


FIGURE I. THE ARCHITECTURE OF OUR ATTENTION-BASED RESNET SENTIMENT CLASSIFICATION MODEL

B. Embedding Module

We use ***word2vec*** embed each word into a low dimension semantic space. Let W be an word embedding generated by an unsupervised method such Glove or SkipGram, where d is the dimension of word vectors and $|V|$ is the vocabulary size. Word embedding may be fine tuned in the training of our framework because of corpus limited for training word embedding.

C. ResNet Block

The role of the ResNet Block is to read the embedding vectors for input sentence and construct the high-level representation. Formally, in this paper we consider a building block defined as:

$$y = F(x, w_i) \cdot x \quad (1)$$

Here x , and y are the input and output vectors of the ResNet block. An detail illustration of ResNet Block is given Fig.II. ResNet block is a sequence of three convolutional layers, each one followed by a BatchNormalization layer and an ReLU activation. The kernel size and filters of all the convolution is 5 and 200, respectively.

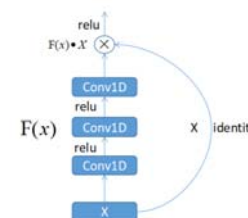


FIGURE II. THE ARCHITECTURE OF OUR RESNET BLOCK DETAIL.

D. Attention

While the ResNet Block has richer capacity, however, not all words contribute equally to the sentiment classification. Attention mechanism has huge success to capture the crucial components over high-level semantic.

Formally, the enhanced sentence representation is a weighted sum of hidden states as:

$$s_i = \sum_{j=1}^{l_i} \alpha_j^i h_j^i \quad (2)$$

where α_j^i measures the importance of the j -th word or sentence for current sentence. Thus, the attention weight α_j^i for each hidden state can be defined as :

$$\alpha_j^i = \frac{\exp(e(h_j^i))}{\sum_{k=1}^{l_i} \exp(e(h_k^i))} \quad (3)$$

where e is a score function which scores the importance of words for composing document representation. The score function e is defined as :

$$e(h_j^i) = v^t \tanh(W_H h_j^i + b) \quad (4)$$

where W_H, v^t are weight matrices for hidden state.

E. Sentiment Classification

We apply our model to document level sentiment classification under supervised learning framework. Document representation d is extracted from the words in the documents, it is a high level representation of the document. The sentiment classifier is built from documents with gold standard sentiment labels.

We use sigmoid to build the classifier because its outputs can be interpreted as conditional probabilities. Softmax is calculated as given in Equation 5, where C is the category number(e.g. positive or negative):

$$p_c = \frac{\exp(d_c)}{\sum_{k=1}^C \exp(d_k)} \quad (5)$$

Where p_c is the predicted probability of sentiment class c . In our model, cross-entropy error between gold sentiment distribution and our model's sentiment distribution is defined as loss function for optimization when training:

$$L = - \sum_{d \in D} \sum_{c=1}^C p_d^g(d) \cdot \log(p_c(d)) \quad (6)$$

IV. EXPERIMENTS

We evaluate the effectiveness of our model on Chinese hotel sentiment classification datasets, which are built by Songbo Tan, and Stanford Sentiment TreeBank(SST). SST use real number for [0,1] to represent document sentiment score. We split real number to binary and five classification problem which binary classification problem(SST-2) means [0, 0.5] is negative and [0.5, 1] means positive, five classification problem(SST-5) is [0, 0.2], [0.2, 0.4], [0.4, 0.6], [0.6, 0.8], [0.8, 1]. We split each corpus into training, validation and testing sets in the proportion of 8:1:1. We use metrics Accuracy which measures the overall sentiment classification performance.

$$\text{accuracy} = \frac{T}{N} \quad (7)$$

where T is the numbers of predicted sentiment rating that are identical with gold sentiment ratings, N is the numbers of documents. We use pre-trained the 100-dimensional word embeddings on each corpus separately with SkipGram [14]. We set the widths of convolutional filters as 5, number of filters set to 200. We tune the hyper parameters on the validation sets and use ADAM to update parameters when training. We select the best configuration based on performance on the validation set, and evaluate the configuration on the test set.

A. Baseline Methods

We compare our neural network model with several baseline methods for Chinese hotel and Stanford Sentiment TreeBank(SST) document sentiment Classification:

a) *PCNN* [13]: implement the piecewise convolution neural networks(PCNN) for document sentiment classification.

b) *PCNN+Dropout* [13]: implement the PCNN and use the Dropout to enhance the performance.

For all baseline methods above, we report the results in [13] since we use the same data sets.

B. Experimental Results

TABLE I. EXPERIMENTAL RESULTS

Model	Data Sets		
	Hotel	SST-2	SST-5
CNN	0.885	0.819	0.455
PCNN	0.897	0.833	0.456
PCNN+Dropout	0.910	0.854	0.459
our model	0.930	0.872	0.470

Experimental results are given in Table 1. We obtain state-of-the-are results for all three data sets. Overall, compared to previous PCNN+Dropout model, our best architecture with 2 ResNet block and attention mechanism has growth almost 1.1% and 1.6% in the Stanford Sentiment TreeBank dataset. To be specific, Chinese Hotel dataset has a test accuracy of 0.93 compared to 0.91. This represents a gain of 2% absolute

accuracy. The significant improvements which we obtain on Chinese Hotel dataset compared to PCNN+Dropout models do not include any data oversampling technique or re-weight technique, even though this is imbalance data sets, which means the number of negative is the double of positive.

C. Model Analysis: Number of ResNet Block

To investigate the performance of our model with various number of ResNet block. Table 2 shows the performance of various number of ResNet block and Figure III shows the convergence process of different number of ResNet block. From the table, we can observe that various number of ResNet block has different ability to capture document semantic. In this work, we have explored five different depths for our networks: 1, 2, 3, 4 and 5, which we define as being the number of ResNet block.

As we increase the number from 1 to 2 of block, the predicting accuracy increase can be improved from 91.8% to 93.0%. As we continue to increase number of block, from 2 blocks to 5 blocks, the convergence time and algorithms performance both decreased.

TABLE II. MODEL ANALYSIS: NUMBER OF RESNET BLOCK

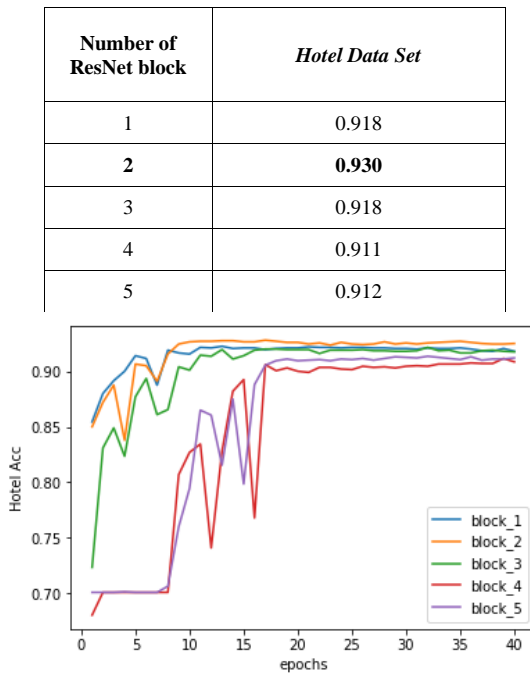


FIGURE III. MODEL ANALYSIS WITH DIFFERENT NUMBER OF RESNET BLOCK.

V. CONCLUSION

In this paper, we propose an Attention-based ResNet network which incorporates ResNet block and attention with document level. Our model can take account of document information with ResNet block. In experiments, we evaluate our model on three sentiment classification task. The experimental results show that our model achieves significant and consistent improvements compared to other state-of-the-

art methods. Our model are much deeper than previously published neural network in sentiment classification field. This result make us believe future research should invest into making text processing models deeper to capture semantic information.

We will explore more in future as follows:

(1) In this paper, we only consideration CNN to capture semantic representation, we will explore why our model is so powerful and why very deep neural network can capture so much high-level semantic.

(2) We will explore the effectiveness of our model on aspect level sentiment classification.

VI. ACKNOWLEDGMENT

This work was supported by the National Social Science Foundation of China(No.17BXW071) , National Natural Science Foundation of China(No.71461017) and the Technology Program of Lanzhou Science and Technology Bureau(No.2014-1-168).

REFERENCES

- [1] Bo Pang and Lillian Lee, Opinion Mining and Sentiment Analysis, 2008.
- [2] Bo Pang, Lillian Lee and Shivakumar Vaithyanathan, Thumbs up? Sentiment Classification using Machine Learning Techniques, EMNLP, 2002, pp.79-86.
- [3] I. S. Jacobs and C. P. Bean, Lexicon-Based Methods for Lexicon-Based Methods for Sentiment Analysis in Magnetism, ACL, 2011, pp. 271-350.
- [4] Amodei, Dario and Anubhai, Rishita and Battenberg, Eric and Case, Carl and Casper, Jared and Catanzaro, Bryan and Chen, Jingdong and Chrzanowski, Mike and Coates, Adam and Diamos, Greg, Deep Speech 2: End-to-End Speech Recognition in English and Mandarin. 2015.
- [5] Yoon Kim, Convolutional neural networks for sentence classification. EMNLP. 2014.
- [6] Richard Socher, Jeffrey Pennington, Eric H Huang, Andrew Ng, and Christopher D Manning. Semi-supervised recursive autoencoders for predicting sentiment distributions. EMNLP, 2011, pp. 151-161.
- [7] Duyu Tang, Bing Qin and Ting Liu. Learning Semantic Representations of Users and Products for Document Level Sentiment Classification. ACL, 2015.
- [8] Kaiming He, Xiangyu Zhang, Shaoqing Ren and Jian Sun, Deep residual learning for image recognition. In proceedings of the IEEE Conference on Computer Vision and Pattern Recognition, 2016, pp. 770-778.
- [9] Alexis Conneau, Holger Schwenk, Yann Le Cun, Loic Barrau, Very Deep Convolutional Networks for Text Classification, arXiv preprint arXiv:1606.01781v2.
- [10] Volodymyr Mnih, Nicolas Heess and Alex Graves, Recurrent models of visual attention. Neural Information Processing Systems, 2014, pp. 2204-2212.
- [11] Dzmitry Bahdanau, Kyunghyun Cho and Yoshua Bengio, Neural machine translation by jointly learning to align and translate. arXiv preprint arXiv:1409.0473.
- [12] Jiwei Tan, Xiaojun Wan and Jianguo Xiao, Abstractive Document Summarization with a Graph-Based Attentional Neural model, ACL, 2017, pp. 1171-1181.
- [13] Du Chang-shun, Huang Lei, Sentiment analysis with piece convolution neural network, 2017.
- [14] Tomas Mikolov, Kai Chen, Greg Corrado and Jeffrey Dean, Efficient estimation of word representations in vector space, arXiv preprint arXiv:1301.3781.

- [15] Andrew L Maas, Raymond E Daly, Peter T Pham, Dan Huang, Andrew Y Ng, and Christopher Potts., Learning word vectors for sentiment analysis, ACL, 2015, pp. 142-150
- [16] Igor Labutov and Hod Lipson, Re-embedding words. ACL, 2013.
- [17] Duyu Tang, Bing Qin and Ting Liu, Document modeling with gated recurrent neural network for sentiment classification, EMNLP, 2015, pp. 1422-1432.
- [18] Duyu Tang, Furu Wei, Nan Yang, Ming Zhou, Ting Liu, and Bing Qin, Learning sentiment-specific word embedding for twitter sentiment classification, ACL, 2014, pp. 1555-1565.
- [19] Parminder Bhatia, Yangfeng Ji, and Jacob Eisenstein, Better document-level sentiment analysis from rst discourse parsing, EMNLP, 2015.
- [20] Zichao Yang, Diyi Yang, Chris Dyer, Xiaodong He, Alex Smola and Eduard Hovy. Hierarchical attention networks for document classification, NAACL, 2016.
- [21] Huimin Chen, Maosong Sun, Cunchao Tu, Yankai Lin and Zhiyuan Liu., Neural Sentiment Classification with User and Product Attention, EMNLP, 2016.
- [22] Baoguang Shi, Xiang Bai and Cong Yao, An End-to-End Trainable Neural Network for Image-based Sequence Recognition and Its Application to Scene Text Recognition, IEEE Transactions on Pattern Analysis and Machine Intelligence, 2015.

Speech Enhancement Based on Sparse Representation Using Joint Dictionary

Ming Wei¹, Zheng Liu^{1,2}, Xueqin Chen^{1,*} and Heming Zhao¹

¹School of Electronic and Information Engineering, Soochow University, China

²Suzhou Industrial Park Institute of Services Outsourcing, China

*Corresponding author

Abstract—A new speech denoising method that aims for processing corrupted speech signal which is based on the sparse representation theory of speech signal. In this paper, we train a composite dictionary consisting of the concatenation of the speech dictionary and the noise dictionary by using the K-SVD algorithm. Noise is divided into structured and unstructured noise in this paper. For structured noise, we train speech and noise dictionary firstly, and then according to the different coherence between speech and noise, we use LARC algorithm with a suitably chosen residual coherence threshold to realize the separation of the speech and the noise. For unstructured noise, we only need speech dictionary to extract the clean speech from corrupted speech. Experiments indicate that the proposed method gives better enhancement results in terms of quality measures of speech. The proposed method outperforms the universal dictionary speech enhancement algorithm.

Keywords—speech denoising; composite dictionary; K-SVD algorithm; speech enhancement; LARC algorithm

I. INTRODUCTION

Speech is important information carrier of language communication. It narrows the communication gap between people and speeds up the exchange of information [1]. However, there are many different kinds of noise in the real world, which tends to reduce speech clarity and intelligibility [1]. Therefore, the research of speech enhancement technology is particularly important. Speech enhancement technology has been applied in many areas, such as mobile communications, hearing aids and pre-treatment of speech recognition system [2]. The purpose of speech enhancement is to extract the clean speech signal from the noisy speech signal as much as possible, so as to improve the clarity and intelligibility of the speech signal. At present, there are many ways to implement speech enhancement. The traditional methods including spectral subtraction, wiener filtering and subspace methods [1].

In recent years, with the development of sparse representation theory, sparse representation and dictionary learning techniques have been widely used in the field of signal processing [3]. The signal sparse representation refers to the over-complete atomic dictionary select a few atoms for linear combination to approximate the signal [4]. The purpose of dictionary learning is to find the optimal set of atoms which can capture the characteristics of these signals well [4]. Sparse representation in speech signal processing applications are mainly focus on Voice Activity Detection (VAD), pitch estimation, speaker recognition and speech recognition [4]. At present, speech enhancement algorithms based on sparse

representation are also discussed in some literature. For example, in the literature [2], a speech enhancement algorithm for sparse representation in the time domain is proposed. In this algorithm, a dictionary is obtained by using the K-singular value decomposition (K-SVD) algorithm and the clean speech is reconstructed by the Orthogonal Matching Pursuit (OMP) [2].

The traditional speech enhancement algorithm based on sparse representation is a universal dictionary denoising algorithm [1]. It trains a universal dictionary and separates the speech and the noise by controlling the sparsity of the signal decomposition on the dictionary according to the sparsity of speech and noise [2]. This method has some obvious effects on denoising of unstructured noise (such as Gaussian white noise). However, in real life, there are many structured noises, which have the same sparsity as the speech [5]. Therefore, it is very difficult to achieve the separation of speech and noise by this method. This paper uses a speech enhancement algorithm based on the joint dictionary learning, which is implemented in the short-time Fourier transform (STFT) magnitude domain [5]. First, assuming that the magnitude of the noisy speech is a linear additivity of the noise magnitude and the speech magnitude [6], ignoring the influence of the phase [7]. Then, we use the training samples of speech signal and noise signal to learn the speech dictionary and the noise dictionary respectively, then concatenate these two dictionaries. In the enhancement part, we use the least angle regression (LARS) with a coherence criterion (LARC) algorithm [2], the noisy signal is sparsely represented on this composite dictionary. According to the coherence between the signal and the dictionary, the speech and the noise can be respectively represented by the corresponding dictionary. Finally, we extract the clean speech from the corrupted speech signal.

II. METHOD

Consider the following model for noisy speech:

$$y = s + i \quad (1)$$

where y , s and i denote noisy speech, clean speech and noise, respectively. The purpose of speech enhancement is to estimate the speech components \hat{s} from the noisy signal and reconstruct the original clean speech. The proposed method in this paper is divided into two parts: dictionary learning part and speech enhancement part [8]. The specific process is as follows.

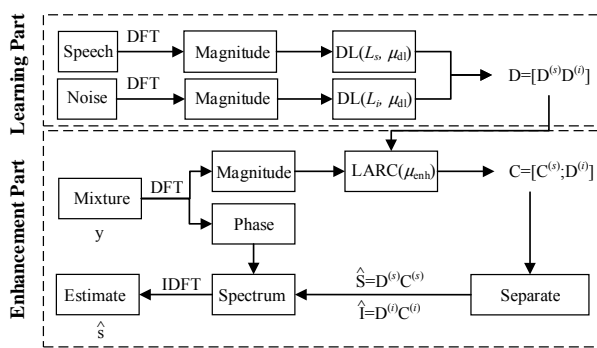


FIGURE I. SPEECH ENHANCEMENT BLOCK DIAGRAM BASED ON JOINT DICTIONARY

A. Dictionary Learning Part

We consider a signal x and an over-complete dictionary $D = [d_{(1)} d_{(2)} d_{(3)} \dots d_{(L)}] \in \mathbb{R}^{D \times L}$ consisting of L unit-norm atoms. We slide a window to divide the signal into N frames and make short-time Fourier transform with this signal, and then we obtain a signal matrix $X = [x_{(1)} x_{(2)} \dots x_{(N)}] \in \mathbb{R}^{D \times N}$. Signal matrix X can be decomposed into a dictionary D and a coding $C = [c_{(1)} c_{(2)} \dots c_{(N)}] \in \mathbb{R}^{L \times N}$. The target function of dictionary learning is given by

$$\arg \min_{D, C} \|X - DC\|_F^2 \quad (2)$$

subject to a sparsity constraint on C . $\|\cdot\|_F$ denotes the Frobenius norm.

In this paper, we choose the K-SVD algorithm for dictionary learning [9]. The redundant dictionary training based on K-SVD learning algorithm includes three steps: dictionary initializing, sparse coding and dictionary atoms updating [9]. When considering this available scheme, sparse coding and dictionary updating should be alternately performed, thus the redundant dictionary and the sparse matrix can be updated synchronously [3]. General steps are as follows:

1) Dictionary initializing

The selection of the initial dictionary is random [8], but the proper initial dictionary can effectively reduce the number of the dictionary learning iterations and increase the rate of learning [11]. In this paper, we select the over-complete cosine basis as the initial dictionary [8].

2) Sparse coding

The initial dictionary must be assumed as fixed firstly in this step. Aligning with this, the signal matrix X should be decomposed over this initial dictionary by using the least angle regression (LARS) with a coherence criterion algorithm (LARC). Since the iterative termination condition is decided by the coherence between decomposition residual and the current atom of dictionary [10]. In a word, the sparse matrix can be got by solving the following formula.

$$\min_{D, C} \|c_i\|_0 \text{ s.t. } \|X - DC\|_F^2 \leq \epsilon. \quad (3)$$

3) Dictionary updating

This step is aiming to update the redundant dictionary [11]. It is important to fix the sparse matrix which has been trained at the last step. It is updated atom-by-atom and this is an iterative process. The residual norm that separates the contribution of k , $k \in [1, L]$ th atom which is being updated can be formulated as

$$\begin{aligned} \|X - DC\|_F^2 &= \left\| X - \sum_{j=1}^L d_{(j)} c^{[j]} \right\|_F^2 \\ &= \left\| \left(X - \sum_{j \neq k} d_{(j)} c^{[j]} \right) - d_{(k)} c^{[k]} \right\|_F^2 \\ &= \|E_k - d_{(k)} c^{[k]}\|_F^2 \end{aligned} \quad (4)$$

The residual norm is minimized by seeking for a rank-one approximation [12]. The approximation is based on computing the singular value decomposition (SVD) [13].

Let ω be the set of indices of columns that correspond to the signals that use the atoms.

$$\omega_k = \{ i \mid 1 \leq i \leq N, c^{[k]}(i) \neq 0 \} \quad (5)$$

Define E_R^k as the set of columns in E_k indexed by ω_k . Compute the SVD of E_R^k ,

$$E_R^k = U \Lambda V^T \quad (6)$$

We update $d_{(k)}$ as the first column of U , and $c^{[k]}$ as $\Delta_{1,1}$ times the first row of V^T [14].

B. Speech Enhancement Part

In this part, our purpose is to obtain an estimate \hat{s} of clean speech and an estimate \hat{i} of the noise, given noisy speech y , a speech dictionary $D^{(s)} \in \mathbb{R}^{D \times L_s}$ and a noise dictionary $D^{(i)} \in \mathbb{R}^{D \times L_i}$. For the formal analysis, noise can be divided into unstructured and structured noise [5]. Due to the structure of the noise magnitude, structured noise can be sparsely coded in a suitable dictionary and unstructured noise cannot be sparsely coded in any fixed dictionary [5], in particular not in speech dictionary. Therefore, we can make use of the characteristic of the structural noise and enhance noisy speech in different ways.

1) Unstructured noise

Due to the non-sparsity of unstructured noise, we cannot train dictionary for noise. For the suppression of this noise, in the enhancement step, the noisy speech y is only sparsely coded in the speech dictionary using LARC with a suitably chosen residual coherence threshold μ_{enh} . LARC coding captures the structured speech signal components which have a coherence to the speech dictionary that is above the threshold, while discarding the noise components, as they fall below the residual coherence threshold [2]. The vector of coding coefficient matrix $C^{(s)} \in \mathbb{R}^{L_s}$ is obtained as follows.

$$\mathbf{C}^{(s)} \leftarrow \text{LARC}(\mathbf{D}^{(s)}, \mathbf{y}, \mu_{\text{enh}}) \quad (7)$$

An estimate of the clean speech is obtained as $\hat{\mathbf{S}} = \mathbf{D}^{(s)} \mathbf{C}^{(s)}$.

2) Structured noise

A structured noise can be sparsely represented with low approximation error in a suitably trained noise dictionary [2]. In order to enhance speech degraded by structured noise which are partially coherent to the speech dictionary, the noisy speech is sparsely coded in the composite dictionary consisting of the concatenation of the speech and the noise dictionary [5]. Noisy speech \mathbf{y} is sparsely coded in the composite dictionary $\mathbf{D} = [\mathbf{D}^{(s)} \mathbf{D}^{(i)}]$ using LARC with a suitably chosen residual coherence threshold μ_{enh} . The vector of coding coefficient matrix \mathbf{C} is obtained as follows.

$$\mathbf{C} \leftarrow \text{LARC}([\mathbf{D}^{(s)} \mathbf{D}^{(i)}], \mathbf{y}, \mu_{\text{enh}}) \quad (8)$$

The matrix $\mathbf{C} = [\mathbf{C}^{(s)}; \mathbf{C}^{(i)}]$ consists of weights $\mathbf{C}^{(s)}$ corresponding to the speech dictionary $\mathbf{D}^{(s)}$, as well as weights $\mathbf{C}^{(i)} \in \mathbf{R}^{L_i}$ corresponding to the noise dictionary $\mathbf{D}^{(i)}$. An estimate of the clean speech is obtained as $\hat{\mathbf{S}} = \mathbf{D}^{(s)} \mathbf{C}^{(s)}$.

III. EXPERIMENT AND PERFORMANCE EVALUATION

A. Experimental Settings

In this paper, speech data is obtained from the GRID audio-visual corpus [2]. This large multi-talker corpus has been provided for studies in speech perception with a recording of 1000 sentences. The corpus involves speech recording of 34 speakers of both genders with sentences of about 1.1-2.2s. We have used 30 sentences of different male speakers as speech dictionary learning samples in our experiments. We chose 4 different kinds of noise (white, babble, volvo and leopard) from the NOISEX-92 corpus as noise dictionary learning samples [14]. The samples are resampled at 16kHz. The time-domain signals are transformed into STFT domain and the frame length is set to 512 point with 50% overlap. Noisy speech is synthetically generated by adding clean speech and noise at various SNRs, since objective measures require access to the clean speech signal.

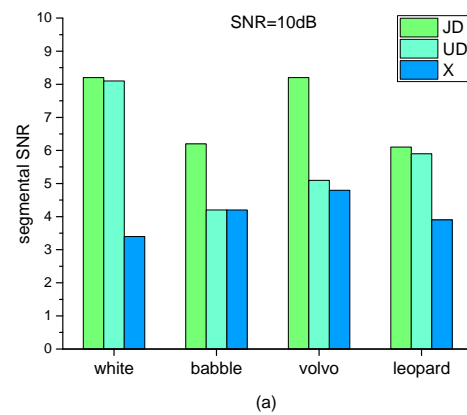
Dictionaries are trained using K-SVD algorithm, initialized with cosine basis. Each dictionary contains 800 atoms and the number of iterations are 30. For dictionary learning, the residual coherence threshold μ_{dl} was set to 0.2 for all dictionaries. μ_{enh} during enhancement was set to 0.15.

B. Performance Evaluation

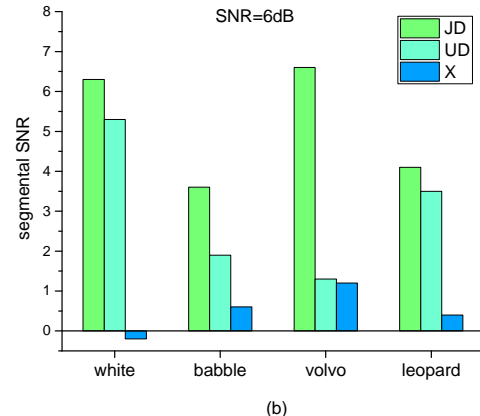
The performance of a speech enhancement algorithm can be measured both subjectively and objectively [2]. Subjective measurements are based on the judgment of human listeners, and are important because in many applications (such as hearing aids) the output of the enhancement algorithm has to appeal to the human ear. However, subjective evaluation takes time, is expensive, and usually requires trained listeners. As an alternative, objective measures provide mathematical models of some perceptual aspects of the human auditory system [2].

We evaluate our proposed method in the segmental SNR (SegSNR). SegSNR is a simple objective measure, computed on individual signal frames, and the per-frame SNRs are averaged over time. The larger the value of the SegSNR, the better the denoising performance.

In order to evaluate the performance, we compare our proposed method with universal dictionary learning algorithm[1]. The universal dictionary learning algorithm is also based on sparse representation, which uses K-SVD algorithm to train a universal dictionary and reconstruct the clean speech with OMP algorithm.



(a)



(b)

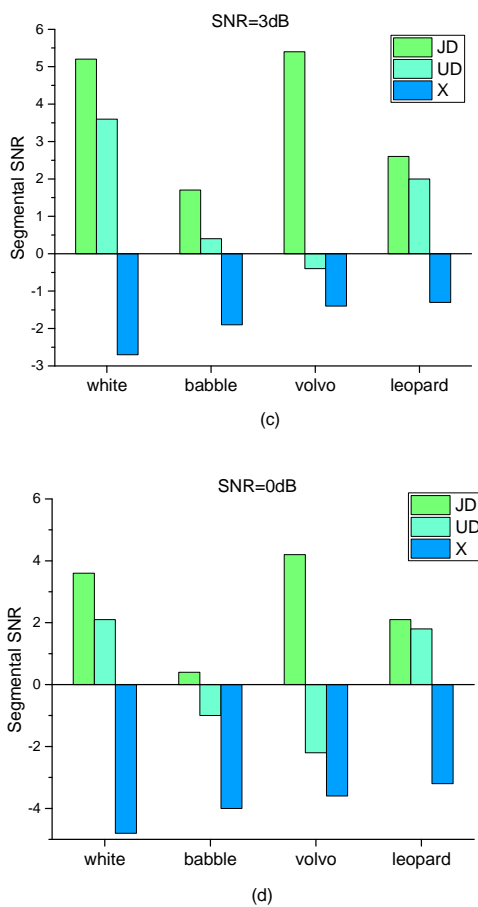


FIGURE II. (a), (b), (c) AND (d) DENOTE THE DENOISING PERFORMANCE OF “JD” AND “UD” AT DIFFERENT SNR.

FIGURE II shows the results of segmental SNR for the proposed and universal dictionary learning method. “JD” denotes joint dictionary learning method (proposed method). “UD” denotes universal dictionary learning method. “X” denotes the objective measurement before any enhancement. The results consistently indicate that the proposed method works better than the “UD” and “X”, which means proposed method outperforms better than universal dictionary learning method.

IV. CONCLUSION

In this paper, we adopt a novel method based on sparse representation theory to enhance the degraded speech. The method has trained composite dictionary consisting of the concatenation of the speech dictionary and the noise dictionary by using the KSVD algorithm, then takes advantage of the different coherence between the speech and the noise and uses LARC with a suitably chosen residual coherence threshold to realize the separation of the speech and the noise. In experimental results, we have showed that our method is outperform than the universal dictionary speech enhancement algorithm. Although this method has effectively improved the speech signal quality to a certain extent, but there is a large research space that do not be explored in this work. For example, the research of the optimization algorithm for greed algorithm

when training the dictionary, the research of a redundant dictionary and more. In a word, all of these are the research direction.

ACKNOWLEDGMENT

This work is supported by the national natural science foundation of China under grant No.61340004 and by Jiangsu higher vocational college teachers professional leader advanced research project under grant No.2017GRGDYX058.

REFERENCES

- [1] L. Huang, L. Li and S. He, "Speech Enhancement Based on Sparse Representation Using Universal Dictionary", International Conference on Anti-Counterfeiting Security and Identification, pp. 1-4, 2013.
- [2] C. D. Sigg, T. Dikk and J. M. Buhmann, "Speech enhancement using generative dictionary learning", IEEE Trans. on Audio Speech Lang. Process., vol. 20, no. 6, pp. 1698-1712, 2012.
- [3] Y. Zhou, H. Zhao, X. Chen, T. Liu, D. Wu and L. Shang, "Speech denoising based on sparse representation algorithm", 12th International Conference on Intelligent Computing Theories and Application, pp. 202-211, 2016.
- [4] Tak W. Shen and Daniel P. K. Lun, "A speech enhancement method based on sparse reconstruction on log-spectra", HKIE Transactions Hong Kong Institution of Engineers, vol. 224, no. 1, pp. 24-34, 2017.
- [5] C. Sigg, T. Dikk, and J. Buhmann, "Speech enhancement with sparse coding in learned dictionaries", Proc. IEEE Int. Conf. Acoust. Speech Signal Process., pp. 4758-4761, 2010.
- [6] G. Bao, Y. Xu, and Z. Ye, "Learning a discriminative dictionary for single-channel speech separation", IEEE Trans. on Audio Speech and Lang. Process., vol. 22, no. 7, pp. 1130-1138, 2014.
- [7] Y. Zhao, X. Zhao and B. Wang, "A speech enhancement method employing sparse representation of power spectral density", Journal of Information and Computational Science, vol. 10, no. 6, pp. 1705-1714, April 2013.
- [8] N. Zhao, X. Xin and Y. Yang, "Sparse representations for speech enhancement", Chinese Journal of Electronics, vol. 20, no. 2, pp. 268-272, April 2011.
- [9] M. Aharon, M. Elad, A. Bruckstein and Y. Katz, "K-SVD: An algorithm for designing of overcomplete dictionaries for sparse representation", IEEE Trans. Signal Process., vol. 54, no. 11, pp. 4311-4322, Nov. 2006.
- [10] M. Yang, L. Zhang, J. Yang and D. Zhang, "Metaface learning for sparse representation based face recognition", IEEE International Conference on Image Processing, pp. 1601-1604, 2010.
- [11] Y. Hao and C. Bao, "An Improved Dictionary Learning Method for Speech Enhancement", Asia-Pacific Signal and Information Processing Association Annual Summit and Conference, pp. 144-147, 2015.
- [12] S. Mavaddaty, S. M. Ahadi and S. Seyedin, "Modified coherence-based dictionary learning method for speech enhancement", IET Signal Processing, vol. 9, no. 7, pp. 537-545, 2015.
- [13] M. Sun; Y. Li, J. F. Gemmeke and X. Zhang, "Speech Enhancement Under Low SNR Conditions Via Noise Estimation Using Sparse and Low-Rank NMF with Kullback–Leibler Divergence", IEEE Trans. on Audio Speech and Lang. Process., vol. 23, no. 7, pp. 1233 - 1242, 2015.
- [14] Y. He, J. Han, S. Deng, T. Zheng and G. Zheng, "A solution to residual noise in speech denoising with sparse representation", Proc. IEEE Int. Conf. Acoust. Speech Signal Process., pp. 4653-4656, 2012.

Research on Estimation Method of Mileage Power Consumption for Electric Vehicles

Yang Xu and Kaiyu Wang*

Automotive Electronics and Embedded System Research Center, Chongqing University of Posts and Telecommunications,
Chongqing 400065, P. R. China

*Corresponding author

Abstract—Accurate estimation of the power consumption of electric vehicles in the future driving route will help to reduce the user's range anxiety, which results from short all electric range of electric vehicles and the lack of charging facilities. The existing research methods mainly focus on three aspects: vehicle energy consumption, driving cycle identification and driving cycle prediction. In this paper, a method of estimating mileage power consumption based on driving cycle identification and prediction is proposed. Firstly, driving cycle categories and energy consumption of each category are obtained through conducting screening, sectioning, principal component analysis and fuzzy C clustering to the vehicle's historical operation data. Then, the future vehicle speed curve is predicted based on historical data, elevation information and real-time road congestion information, and the mileage consumption estimation model is established based on the identification and prediction of the driving cycle. Finally, 10 groups of real vehicle tests were carried out on the experimental vehicle. And the results showed that the average error between the estimated value of the mileage power consumption and the test value is 4.15%, which met the requirements of the daily use of electric vehicles.

Keywords—electric vehicles; mileage power consumption estimation; driving cycle identification; driving cycle prediction

I. INTRODUCTION

Electric vehicle has attracted more and more attention due to its advantages of environmental protection, energy saving and intelligence. However, the majority of electric vehicle have short all electric range and fast charging facilities have not been widely popularized. Users will be worried that the existing electricity cannot guarantee the arrival of vehicles, and there is no timely charging facilities on the way, resulting in "mileage anxiety". Therefore, the accurate estimation of the power consumption between the destination and the destination is conducive to enhancing the user's confidence in the use of electric vehicles.

At present, most of the research focuses on the electric vehicle's remaining mileage, that is, how far the electric vehicle can run, and less about the estimation of the power consumption between the beginning and the destination specified by the user. There are three main aspects of the estimation of the remaining driving mileage: vehicle's energy consumption [1-3], driving cycle identification [4-7] and driving cycle prediction [8-10]. The method from the perspective of vehicle energy consumption focuses on the influence of vehicle driving parameters on the mileage. According to the principle of equal output energy and vehicle energy consumption, the vehicle's mileage is estimated.

In the estimation method of driving cycle recognition, the fragments of vehicle speed curve are divided into several types. And it is considered that the future energy consumption of vehicle is equal to the average energy consumption in the past period. The estimation method of driving cycle prediction is based on the driving cycle identification method and combines with the prediction of the driving cycle in the future, making a more accurate estimation. In this paper, a method of estimating mileage power consumption based on driving cycle identification and prediction is proposed. It aims at the actual demand for predicting power consumption (SOC changes) between the location and destination given by users. The diagram in Figure 1 represents the overall objective of this research.

The remaining of this paper is organized as follows. The cluster analysis of the driving cycle will be carried out in section II. In the section III, a vehicle speed curve prediction model will be discussed. In section IV, a estimation method of mileage power consumption will be discussed and validated following by some simulation results in section II and section III. Finally a conclusion will be made in section V.

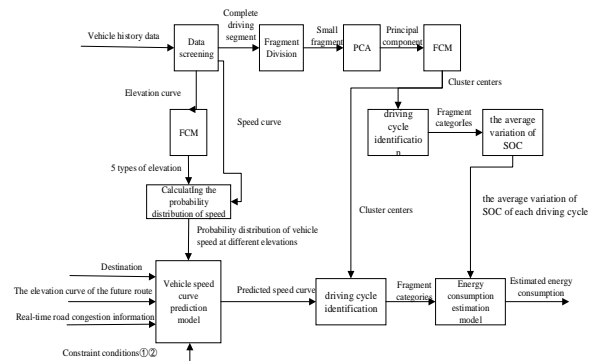


FIGURE I. BLOCK DIAGRAM OF THE ESTIMATION METHOD OF MILEAGE POWER CONSUMPTION FOR ELECTRIC VEHICLES

II. CLUSTER ANALYSIS OF DRIVING CYCLE

A. Characteristic Parameters of the Driving Cycle Fragment

Generally speaking, vehicle driving cycles is described by vehicle speed time curve. Typical driving cycles include UDDS operation in America, NEDC operation in Europe, and 10-15 working conditions in Japan. For extracting and analyzing the characteristic parameters of vehicle driving cycles, typical ECE15 driving cycle is used in [6]. In [7], the real driving data

of the vehicle is used and divided according to the unit SOC in order to improving the accuracy. In this paper, not only the influence of vehicle speed and congestion on the vehicle energy consumption but also the influence of the change of lane's altitude on the vehicle energy consumption is considered. The speed curve and the GPS information is obtained in vehicle network monitoring platform. In the vehicle historical driving data, 30 complete driving processes were selected, which were divided into 718 driving cycle segments based on 120s. The data range covers the running data of the vehicle from June to December, 2016, and the running time was 8:00-22:00.

In order to accurately describe the characteristic information of vehicle speed curve, 12 characteristic parameters were identified in [6] and [7] to describe vehicle speed time curve in driving cycle segments which were also used in this paper as listed in Table 1.

TABLE I. THE CHARACTERISTIC PARAMETERS OF THE SPEED CURVE OF THE DRIVING CYCLE SEGMENT

Parameter	Meaning	Parameter	Meaning
v_{max}	The highest speed	v_{sd}	Standard deviation of speed
v_m	Average speed	A_{max}	Maximum acceleration
P_i	Parking ratio	A_{min}	Maximum deceleration
v_{mr}	Running average speed	P_a	Acceleration ratio
A_a	Average acceleration of acceleration section	P_d	Deceleration ratio
A_d	Average acceleration of deceleration section	P_c	Uniform speed ratio

For reducing the amount of calculation, the principal component analysis (PCA) of 12 parameters extracted from the vehicle running data was carried out in [6] and [7]. According to the principle of PCA [11], if the cumulative contribution rate of the former k principal components is above 80%, the k principal components can be used to represent the original variables. After analyzing, 4 parameters which are highly correlated with the principal components are selected: the highest speed, average speed, parking ratio and average acceleration, as the characteristic parameters of fuzzy c-means (FCM) clustering algorithm.

B. The FCM Analysis of the Driving Cycle Fragments

The FCM algorithm [12] is an important branch of fuzzy pattern recognition. Its essence is to iterate and modify the cluster center and membership matrix to minimize the objective function value. Each element in K-means can only belongs to one category, while an element in the FCM belongs to each category with a different probability. Similar to K-means, the target function of FCM is as follows:

$$J_m = \sum_{i=1}^N \sum_{j=1}^C u_{ij}^m \|x_i - c_j\|^2, \quad 1 \leq m \leq \infty \quad (1)$$

Where m is a weighted index, $\|x_i - c_j\|^2$ is the distance between the ith data points and the cluster center of class jth and u_{ij} is the degree of membership of the ith data point belonging to class jth, which is limited by: $0 \leq u_{ij} \leq 1$, $\sum_{i=1}^C u_{ij} = 1$. The FCM aims at calculating the membership degree matrix U and the cluster center matrix C to minimizing the object function J_m .

When the number of clusters $c = 4$, the cluster centers are shown in Table 2. And parameters from left to right are: the highest speed, average speed, parking ratio and average acceleration.

TABLE II. CLUSTER CENTER OF 4 TYPES OF DRIVING CYCLES

Categories	Cluster centers after 300 iterations	Driving cycle characteristics
C_1	(12.618, 5.287, 0.446, -0.005)	High parking ratio, low speed
C_2	(74.443, 62.231, 0.004, -0.014)	Smooth road, high speed
C_3	(42.815, 26.201, 0.069, 0.003)	Medium parking ratio and speed
C_4	(59.385, 48.532, 0.004, 0.003)	A small number of parking, medium speed

Consider the change in altitude alone and divide it into 5 classes. When the number of clusters $c = 5$, the cluster centers are shown in Table 3.

TABLE III. FIVE KINDS OF CLUSTER CENTERS FOR ALTITUDE CHANGE

Categories	Cluster centers after 300 iterations	Elevation characteristics
C_1	-101.445	Middle elevation change, little steep downhill
C_2	45.463	Small elevation change, flat road
C_3	-277.397	Large elevation change, steep downhill
C_4	199.818	Middle elevation change, little steep uphill
C_5	410.465	Large elevation change, steep uphill

There will have 20 categories of driving cycles on the overall consideration of maximum speed, average speed, parking ratio, average acceleration and altitude change. The average variation of SOC in the 20 categories of driving cycles can be obtained by the formula (2):

$$\overline{\Delta SOC}_i = \frac{\sum_{k=1}^{n_i} \Delta SOC_k}{n_i}; \quad i = 1, 2, \dots, 20 \quad (2)$$

Where $\overline{\Delta SOC}_i$ is the SOC average variation of class ith, n_i is the number of driving cycles in class ith and ΔSOC_k is the SOC variation of kth fragment in class ith.

According to formula (2), the average variation of SOC in the 20 categories of driving cycles are list in Table 4.

TABLE IV. VERAGE CHANGE OF SOC UNDER 20 TYPES OF DRIVING CYCLES

categories	the average variation of SOC	categories	the average variation of SOC
C_1	1.42131054	C_{11}	1.20294766
C_2	1.52115799	C_{12}	1.0206714
C_3	1.40876679	C_{13}	0.66156447
C_4	1.3240051	C_{14}	1.23478949
C_5	1.63209656	C_{15}	1.23449078
C_6	1.3485119	C_{16}	1.00145896
C_7	1.2146521	C_{17}	1.46666667
C_8	1.06038662	C_{18}	1.18666667
C_9	0.36728395	C_{19}	0.95892833
C_{10}	1.47922074	C_{20}	1.1

III. PREDICTION OF SPEED CURVE BETWEEN ORIGIN AND DESTINATION

A. Prediction Method of Speed Curve between Two Place

In this paper, vehicle's history driving data and future driving path information were used to forecasting the speed curve. From history driving data, vehicle's speed probability distribution in different elevation were extracted, and future driving path information includes elevation curve and real time traffic jam level. Figure 3 shows the framework of the predication method, and the specific procedure is explained as follows:

- According to the destination set by user, the future driving path between origin and destination is acquired from Omni range system like google maps. Based on this, information including elevation curve and real time traffic jam can be extracted in the same time.
- Splitting the total driving path into path segments per 50 meters, and computing the elevation change level of every segment. according to speed distribution of different elevation change level and the constrain condition proposed later, the speed cure could be generated randomly in every path segment.
- Finally, total future driving path's speed curve can be acquired by combing the path segments' speed curve.

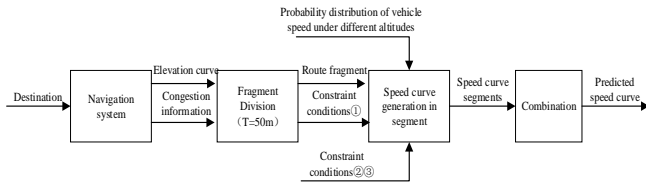


FIGURE II. VEHICLE SPEED CURVE PREDICTION MODEL

B. Constrain Condition

As indicated above, there are three constrain condition in the vehicle speed curve prediction model, they are explained in follow:

- Real time traffic jam constrains. According to *Evaluation Index System of Urban Road Traffic Management* announced by Chinese ministry of public security in 2002, the average speed is used to determinate traffic jam level. In [13], average speed is chosen as traffic jam level evaluation index preferentially. If it is absence, the amount and density of vehicle will be alternative. According to China and some other country's index, the speed thresholds for different traffic jam level are determined and the result is shown in Table 5. Accordingly, the speed range of every segment, which can be obtained after getting real-time road congestion information, can be as one of the constrain conditions for generating speed curve.

TABLE V. DETERMINATION OF TRAFFIC CONGESTION LEVEL IN ACTUAL ROAD CONDITIONS

Congestion level	speed /km·h ⁻¹)	Vehicle flow/(car·min ⁻¹)	traffic density /(car·m ⁻¹)
Smooth	v ≥ 30	q ≤ 60	k ≤ 0.5
amble	20 ≤ v < 30	60 < q ≤ 90	0.5 < k ≤ 0.75
congestion	10 ≤ v < 20	40 ≤ q < 60	0.75 < k ≤ 0.9
severe congestion	v < 10	q < 40	q > 0.9

- Integral on generated speed curve's must equals to actual mileage of segment. as what mentioned before, path segment's mileage is 50 meters, so the equation (3) must be satisfied on every segment.

$$S = \sum_{k=0}^{t_i} v(k) \cdot T = 50 \quad (3)$$

Where S is driving mileage and t_i is driving time of the i th path segment. T is the time serial's step value which is 1 second, $v(k)$ indicates speed of k th moment.

- The rate of speed change should under a constrain level. It is a basic fact that the speed change of vehicle in a determined step value should under a threshold which is make sense, and the threshold is extracted from history data:

$$0 \leq \Delta \leq 2.8 \quad (4)$$

Where Δ indicates the threshold.

IV. EVALUATION METHOD OF ENERGY CONSUMPTION BETWEEN ORIGIN AND DESTINATION AND VERIFICATION

A. Evaluation Method of Energy Consumption between Origin and Destination

The proposed evaluation method's procedures is shown at Figure IV, there are mainly 4 steps in this method:

- Splitting the predicated speed curve of future driving path into n segments by invariable time interval, which is 120 seconds in this paper. Then the 4 feature parameter can be computed.
- Elevation change curve between two places should be acquired by GPS, then the absolute change value can be extracted from the curve.
- Computing the distances of target segment to 20 clustered centers. Base on nearest neighbor principle determine which category the target segment is belong to. The distance's calculation formula is (5):

$$d_i = \sqrt{\sum_{k=1}^5 (x_k - c_{ik})^2}; i = 1, 2, \dots, 20 \quad (5)$$

Where d_i is the distance between target segment and the i th segment, x_k is k th feature parameter value of target segment, c_{ik} is value of k th feature parameter of i th driving cycle center.

- After identifying the category of the fragment, the energy consumption between the destination and the destination is calculated by the formula (6):

$$SOC_{cos} = \sum_{i=1}^n \Delta SOC_i \quad (6)$$

Where SOC_{cos} is the estimated energy consumption and ΔSOC_i is the SOC variation of each fragment.

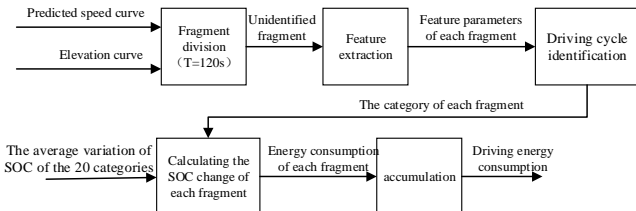


FIGURE III. ESTIMATION METHOD OF VEHICLE ENERGY CONSUMPTION BETWEEN STARTING AND DESTINATION

B. 4.2 Verification of the Method

In order to verify the accuracy and universality of the estimation method of vehicle energy consumption, 10 groups of tests were carried out for different elevation changes, number of corners and road congestion. The evaluation index is the absolute error between the estimated value and the actual value.

$$SOC_{dev} = |SOC_{ev} - SOC_{rel}| \quad (7)$$

The 10 sets of test results and errors are shown in Table 6.

TABLE VI. THE TEST RESULTS

Order	The proportion of smooth, amble, congestion, severe congestion(%)	Elevation, bend	The estimated value (%)	The actual value (%)	The absolute error (%)
1	(85,7,4,4)	flat	35.20	35.33	0.13
2	(88,3,2,7)	a bit flat	78.84	78.32	0.52
3	(100,0,0,0)	Small change in elevation	37.81	38.90	1.09
4	(80,13,7,0)	Small change in elevation	55.32	52.68	2.64
5	(86,7,3,4)	Small change in elevation and less bends	37.32	34.53	2.79
6	(86,2,10,2)	Middle change in elevation	54.54	58.6	4.06
7	(92,0,0,8)	Large change in elevation	78.91	83.83	4.92
8	(55,22,16,7)	Small change in elevation	34.7	26.72	7.98
9	(70,21,6,3)	Middle change in elevation, more bends	36.75	28.76	7.99
10	(87,2,4,6)	Large change in elevation, a lot of bends	51.3	41.88	9.42

According to Table 6, when the road is flat or the elevation changes little, the algorithm's errors are less than 5%. When road congestion is serious (the 8th group) or elevation (the 9th group), the error increases slightly. Due to the lack of consideration on the impact of bends to speed and energy consumption, due to no consideration of the impact of the curve on the speed and energy consumption, the error will also increase in the bend road.

V. CONCLUSIONS

In this paper, a method of estimating mileage power consumption based on driving cycle identification and prediction is proposed. It aims at the actual demand for predicting power consumption (SOC changes) between the location and destination given by users. In the driving cycle identification, the PCA and FCM are used to analyze the vehicle history data and then classify the driving cycle. In the driving cycle prediction, combining with the probability distribution of speed at different altitudes under the historical data, real-time traffic congestion information and other two constraints, the future route speed curve is predicted, achieving the prediction of future driving cycles. Finally, the feasibility of the estimation method of electric vehicle mileage consumption based on driving cycle identification and prediction is verified by 10 groups of tests.

ACKNOWLEDGMENT

The authors would like to thank Automotive Electronics and Embedded System Research center for all fruitful group discussions and feedbacks. This project is financially supported by the Doctoral Scientific Research Foundation of Chongqing University of Posts and Telecommunications, and the project number is A2017-134.

REFERENCES

- [1] C. H. Lee and C. H. Wu, "A novel big data modeling method for improving driving range estimation of EVs," in IEEE Access, vol. 3, pp. 1980-1993, 2015.
- [2] N. Chang, D. Baek and J. Hong, "Power consumption characterization, modeling and estimation of electric vehicles," 2014 IEEE/ACM International Conference on Computer-Aided Design (ICCAD), San Jose, CA, 2014, pp. 175-182.
- [3] J. Hong, S. Park and N. Chang, "Accurate remaining range estimation for Electric vehicles," 2016 21st Asia and South Pacific Design Automation Conference (ASP-DAC), Macau, 2016, pp. 781-786.
- [4] H. Yu, F. Tseng and R. McGee, "Driving pattern identification for EV range estimation," 2012 IEEE International Electric Vehicle Conference, Greenville, SC, 2012, pp. 1-7.
- [5] Q. Gong, S. Midlam-Mohler, V. Marano, G. Rizzoni and Y. Guezenneec, "Statistical analysis of PHEV fleet data," 2010 IEEE Vehicle Power and Propulsion Conference, Lille, 2010, pp. 1-6.
- [6] A. D. Yin, H. Zhao, B. Zhou, "Driving range estimation for battery electric vehicles based on driving cycle identification," in Automotive Engineering, vol. 11, pp. 1310-1315, 2014.
- [7] J. Lian, A. N. Zheng, Y. F. Zhou, "Driving range estimation for electric vehicles based on battery state of charge and driving cycle identification," in Science Technology & Engineering, vol. 16, no. 16, pp. 113-117, 2016.
- [8] G. M. Liu, M. G. Ouyang, L. G. Lu, "Driving range estimation for electric vehicles based on battery energy state estimation and vehicle energy consumption prediction," in Automotive Engineering, vol. 11, pp. 1302-1309, 2014.
- [9] J. A. Oliva, C. Weihrauch and T. Bertram, "Model-based remaining driving range prediction in electric vehicles by using particle filtering and

- Markov chains," 2013 World Electric Vehicle Symposium and Exhibition (EVS27), Barcelona, 2013, pp. 1-10.
- [10] F. A. Bender, M. Kaszynski and O. Sawodny, "Drive Cycle Prediction and Energy Management Optimization for Hybrid Hydraulic Vehicles," in IEEE Transactions on Vehicular Technology, vol. 62, no. 8, pp. 3581-3592, Oct. 2013.
- [11] J. W. Han, K. Micheline, P. Jian, Data mining concepts and techniques, 3rd ed., Singapore: Elsevier, 2012, pp. 67.
- [12] X. Q. He, Multivariate statistical analysis multivariate statistical analysis 2nd ed., Beijing: China Renmin University Press, 2008, pp.189.
- [13] T. T. Yang, X. Li, "Accuracy assessment of real-time road status system based on multi-original data," in Journal of Jiangsu Normal University: Natural Science ed., vol.3, no. 34, pp. 65-69, 2016.

Coordinated Electric Vehicle Charging Based on Real-Time Pricing

Xinshu Wan^{1,*}, Wangcheng Zhu¹, Ning Su² and Jiahong Wu³

¹Electric Power Research Institute of Hainan Power Grid Co., Ltd., Haikou 570125, China

²Qionghai Power Supply Company of Hainan Power Grid Co., Ltd., Qionghai 571400, China

³Nanjing Sifang E-power Automation Co., Ltd., Nanjing 211111, China

*Corresponding author

Abstract—Based on the existing time-of-use electricity price pricing scheme of Beijing, a real-time pricing scheme for electric vehicle charging is proposed in this paper to perform load shifting by adjusting the hourly-changed charging price. A two-stage model of determining electric vehicle charging price is proposed. In the first stage, the charging load of the next day is predicted according to statistical probabilities. Together with the prediction of the base load pattern, the charging price of each hour is then optimized accordingly as a reference for the next day. In the second stage, the exact charging price is set ahead of each hour based on the power demand in previous hours and the desired load curve. The model is first built and then solved using the CPLEX software and MATLAB programming. The simulation result shows that the peak load as well as the peak-valley load difference is reduced. The charging cost of customers is also expected to be diminished.

Keywords—electric vehicle; real-time pricing; price prediction; charging schedule

I. INTRODUCTION

Climate change has raised worldwide concern over the greenhouse gas emitted by internal combustion engines. Electric vehicles can help improve air quality and reduce pollution. Up till now, many countries have announced regulations to promote electric vehicles and restrict the use of traditional vehicles. For example, France and Britain will ban the sale of cars burning gasoline from 2040. Car manufacturers like Volvo have announced plans to produce pure electric vehicles or vehicles using clean energy in the future. It is evident that electric vehicles will be purchased and used by more and more household in the future.

However, as pointed out by many literatures, uncoordinated charging of electric vehicles will bring serious problems to the power grid [1-3]. For instance, the charging demand of electric vehicles will coincide with the existing peak of load curve, creating a higher power consumption. The problem has two aspects. Firstly, the peak of base load and the popular hours of uncoordinated charging load appear at nearly the same time. Secondly, under the uncoordinated charging scheme, electric vehicle users tend to charge their cars simultaneously at certain hours after they have parked their vehicles. In order to alleviate the problem, the charging of electric vehicles should be coordinated.

Under the uncoordinated charging scenario, the increase of charging load will bring more uncertainties to the operation of power grid. In order to shift the charging load, two methods can be adopted: direct load control or price signal. According to economic principles, introducing lower charging prices in the valley period can encourage more power consumption and reduce peak-valley difference. Commonly used pricing schemes include time-of-use (TOU) tariff, real-time pricing (RTP) and critical period pricing (CPP). Among them, RTP is considered to be the most effective scheme [4].

The objective functions selected by existing literatures include minimization of peak-load difference [5-6], minimization of charging cost [4], maximization of power grid companies, maximization of users' satisfaction, etc. Some authors combine several of the above-mentioned objectives to create a multi-objective optimization model.

RTP is a typical method of demand side response. Many scholars have researched on this topic and have come up with several pricing models. The authors in [7] propose a RTP scheme using the power output of PV sources as input, together with the users' response to changes in price, leading the users to transfer their power demand and use the consume the output of photovoltaic energy as much as possible. In [8], the authors study the consumers' price elasticity under the RTP scheme, including self- and cross-elasticity, to realize the users' reaction to varying prices. Reference [9] come up with an iterable optimization model of determining RTP. By using the least square method, the relationship between users' demand and price of electricity is fitted. According to the price elasticity of demand, the load response model is constructed and solved to maximize the users' interest. A robust optimization model aiming at decreasing the total operational cost of charging service supplier is set up in [10]. Since the uncertainty of electricity price is considered, as long as the predicted price deviates from the prediction within a certain extent, the charging schedule can still be optimized.

The method raised in this paper differs from [11] in that the fixed reference charging curve is updated every hour, so that a more precise target curve is generated. A rolling optimization model over the next 24 hours is developed in [12] by calculating the best charging scheme every 30 minutes based on the latest charging load information. Based on this method, this paper takes the latest prediction of load into consideration.

Moreover, the minimization of peak-valley is selected as the objective, along with the reduction of charging cost.

The coordinated charging strategy raised in this paper features: (1) a two-stage charging scheme which optimizes the charging behavior with the next 24 hours, aiming at minimizing the peak-load difference of the daily load curve; (2) generation of the electricity price of charging and prediction of EV charging load of the next day in the first stage, considering the users' demand and safety of the grid; (3) determination of the final charging price based on the latest prediction of charging load and the deviations generated in previous time slots.

The rest of the paper is formulated as follows: the two-stage RTP scheme is constructed in Section II; Section III illustrates the simulation results; the analysis and conclusion are presented in Sections IV and V respectively.

II. MODEL CONSTRUCTION

A. Stage One

Although many load prediction methods have been developed, still the real load will deviate from the predicted value. The factors affecting electric vehicle drivers' behavior include bad weather condition, traffic control, etc. Since the daily travelling mileage is not affected by the start time of charging, the charging demand is the same before and after optimization. Meanwhile, the price of electricity within a time slot should exceed the cost of energy generation and transmission. In order to protect the interest of electric vehicle drivers, an upper boundary should be set.

Because the charging process can only start before the end of travelling, the optimized start time of charging can only be postponed. In order to alleviate the impact on vehicle users, the delay should be made as short as possible.

Price elasticity is effective in terms of analyzing customers' response to changes in price [6]. The demand of electricity changes with the variation of price, as described by

$$\varepsilon = \Delta D / \Delta \pi \cdot \pi_0 / D_0, \quad (1)$$

where ΔD and $\Delta \pi$ represent the change in load and price, π_0 and D_0 are the initial values of load and price, and ε is the price elasticity matrix. The price elasticity matrix is consisted of two parts: self-elasticity and cross-elasticity. The self-elasticity is situated at the diagonal of the matrix, while off-diagonal elements are cross-elasticities. Because the daily charging demand must be satisfied, the shift of charging load caused by self-elasticity is not considered. The change of load at time slot t_i caused by change of price at time slot t_j is denoted by ε_{ij} . This paper adopts the electricity price elasticity proposed by [13]. As the RTP changes every hour, the size of the price elasticity matrix is 24×24 . The total change of load in hour i caused by changes of price in all the other hours is

$$\Delta D(t_i) = \sum_{j=1}^{24} \varepsilon_{ij} \Delta \pi_j D_0(t_i) / \pi_0, \quad (2)$$

where $\Delta \pi_j = \pi_j - \pi_{j0}$; π_j and π_{j0} represent the proposed real-time price and the original TOU price respectively. The changed demand of charging power at hour i becomes

$$D(t_i) = D_0(t_i) + \Delta D(t_i). \quad (3)$$

The optimization model is constructed as follows:

$$\text{minimize} \quad [\max D_T(t_i) - \min D_T(t_i)] \quad (4)$$

$$\text{subject to} \quad \sum_{i=1}^{24} D(t_i) = \sum_{i=1}^{24} D_0(t_i) \quad (5)$$

$$D(t_i) \leq P_{\max}(t_i) \quad (6)$$

$$\sum_{i=1}^{24} \pi(t_i) = \sum_{i=1}^{24} \pi_0(t_i) \quad (7)$$

$$\sum_{i=1}^{24} D(t_i) \times \pi(t_i) \leq \sum_{i=1}^{24} D_0(t_i) \times \pi_0(t_i) \quad (8)$$

Equation (5) means that the total charging power demand is not changed before and after optimization. $P_{\max}(t_i)$ in (6) denotes the maximum charging power restricted by the ratings of lines and transformers. Eq.(7) represents the mean price of electricity before and after the optimization is constant. (8) means that the total cost after the optimization should be lower than before.

B. Stage Two

By solving the optimization model in stage one, the predicted charging power is obtained and used as the reference of the second stage. The objective of the second stage is to make the actual charging curve as close to the day-ahead predicted value as possible. The reference curve generated in stage one is idealized in that charging load in several hours are set to be zero. In reality, drivers will charge their vehicles in day time due to urgent charging need. The model assumes that the total charging power within a day in the studied region is nearly constant, which is evident that drivers tend to charge their batteries full at the end of the day. Therefore, the total charging demand of the remaining hours of a day can be predicted by the existing charging data of each of the past time slots. When the latest prediction deviates from the day-ahead reference value, actions should be taken to reduce the difference. The self-elasticity of electricity is utilized to alter the electricity price and charge the charging demand.

The reference is updated every hour to maintain its precision. The time step of one hour is selected to accommodate the hourly changed RTP. When updating the prediction, the actual charging load and other load are added into the model to generate a new reference curve. When the

above-mentioned data are unavailable, the previous obtained prediction is used.

The revision of the reference load curve is as follows:

Firstly, the accumulated deviance of the actual curve and the day-ahead predicted values are calculated and evenly distributed to all the remaining hours of that day. Namely, for the accumulated charging demand not served, certain amount of predicted will be added to the prediction curve to be the new reference curve of future hours. As for the exceedingly used charging demand, some load will be diminished from the old curve. Since even distributions is adopted, even the latest data cannot be obtained, the daily charging reference can still be kept until the end of the day.

Secondly, the base load curve may deviate from predicted. However, methods with high precision has been developed and can be used to accurately predict the total load of the next few hours. The prediction method of the base load curve exceeds the scope of this paper. It is assumed that the base load demand of the next few hours can be predicted with high accuracy. This paper focuses on the adjustment of reference charging curve according to changes of base load.

The reference charging load is updated using the following equation:

$$D_p(h) = D_{p0}(h) + [\sum_{i=1}^{h-1} D_{p0}(t_i) - \sum_{i=1}^{h-1} D_a(t_i)] / (25 - h), \quad (9)$$

where $D_{p0}(t_i)$ denotes the original reference charging load for the i^{th} hour, and $D_p(t_i)$ is the actual charging power of the i^{th} hour.

In order to calculate the change of charging price, the shifted value of charging load should be obtained. The available charging power that can be supplied of each hour consists of two parts. One is brought by the deviation of predicted and actual values of the base load. The other is determined by the accumulated deviation of the actual and predicted charging load. The charging load of each hour is obtained by

$$\Delta D(h) = \Delta D_p(h) + \Delta L_p(h). \quad (10)$$

Considering the reduction of load during peak hours, when the actual charging power is less than predicted, the abundant power will not be added to the available charging power. According to the load consumption pattern, 17.00 to 21.00 are selected as peak hours. The effect on the available charging power is given by

$$\Delta D(h) = \begin{cases} D_p(h) - D_{p0}(h) + L_p(h) - L_{p0}(h) & h \notin [17, 21] \\ D_p(h) - D_{p0}(h) & h \in [17, 21] \end{cases}, \quad (11)$$

where $L_p(t_i)$ denotes the latest prediction of base load in the i^{th} hour, and $L_{p0}(t_i)$ is the original prediction of base load in the i^{th} hour used in stage one.

The change of charging price can be calculated using

$$\Delta\pi(h) = \pi_0(h) \cdot \Delta D(h) / [\varepsilon(h) \cdot D_0(h)], \quad (12)$$

where $\varepsilon(h)$ represents the self-elasticity of electricity in the hour of h .

III. SIMULATION RESULTS

A. Uncoordinated Charging

Because fast charging is usually used when in urgent scenarios, its demand is not affected by price. In order to study the optimal RTP, this paper focuses on the normal charging behavior of electric vehicles, which is commonly used by consumer vehicles. Since the power is relatively small, its demand is sensitive to changes in price.

According to the national household travel survey conducted by the US Department of Transportation, although the daily travel behavior of a single vehicle is hard to predict, the travelling of a flock of vehicles has some regular patterns. It is found that the ending time of the last journey of a day coincides with normal distribution [14], namely

$$T_{\text{return}}(V_i) \sim N(\mu_T, \sigma_T^2). \quad (13)$$

Meanwhile, the daily travelling mileage can be approximated by log-normal distribution, namely

$$\text{distance}(V_i) \sim \text{lognormal}(\mu_d, \sigma_d^2). \quad (14)$$

Moreover, this paper further assumes that the normal charging power is evenly distributed between the lower and higher boundary

$$D_{\text{vehicle}}(V_i) \sim U[P_{\min}, P_{\max}], \quad (15)$$

where P_{\min} and P_{\max} represent the minimum and maximum charging power.

Assume that the total number of electric vehicles in a certain region is 50,000. The daily travelling distance distribution has a mean value of 20km and a variance of 8.8km. The start time of charging follows the normal distribution whose mean value equals 17.6h and variance equal 3.4h. The lower and upper boundaries of normal charging power are 2kW and 5 kW respectively.

The typical base load data of an area is shown in Table I. The total load curve can be obtained by combining the base load and charging load. According to equations (13)-(15), the daily charging load can be obtained using Monte-Carlo Simulation method. The result is shown in Figure I.

TABLE I. BASE LOAD OF EACH HOUR

Hour	Load/MW	Hour	Load/MW
1	511	13	682.5
2	532.5	14	692.5
3	520	15	688
4	491	16	686
5	543.5	17	729
6	566	18	735
7	596	19	778
8	643.5	20	775
9	717.5	21	729
10	734	22	681
11	752.5	23	581.5
12	670	24	553.5

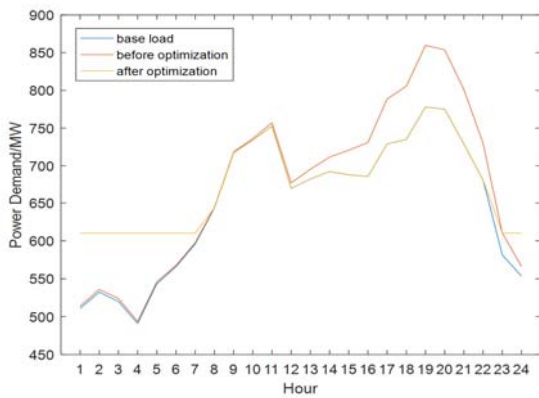


FIGURE I. BASE LOAD AND CHARGING LOAD.

B. Coordinated Charging

After implementing the optimization model proposed in stage one, the resulting load curve can be obtained. The new total load curve is illustrated by the yellow line in Figure I. The corresponding RTP of each hour is presented in Figure II.

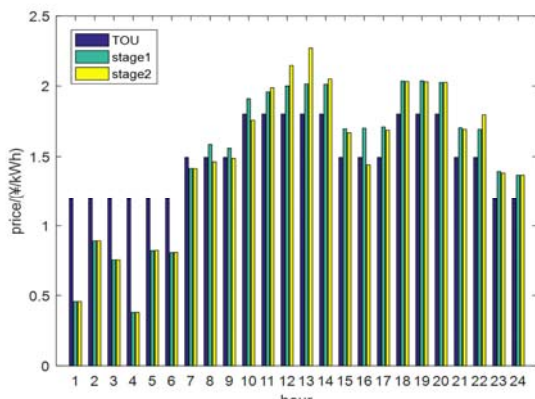


FIGURE II. PRICE OF DIFFERENT STAGES

IV. ANALYSIS

As can be seen clearly from the red line in Figure I, because the peak charging demand of electric vehicles appears at the same time with the maximum of load demand, the peak increases from 778MW to 830.9MW, rising by 6.8%.

After optimization, a large amount of charging power is shifted to the time period when base load is low and electricity is cheap. The minimum total power usage rises to 610.22MW. Meanwhile, the ideal charging demand during peak hours is decreased to zero, avoiding the increase of maximum load demand. In order to encourage drivers to perform load-shedding and valley-filling, the charging price is modified accordingly. Since the base load during evening are varied between hours, the optimized prices of electricity also differ from each other to flatten the total load curve and avoid a new peak load in the evening. As is restricted by the time order, the start time of charging can only be postponed. Consequently, the charging load are shifted to time slots when base load is low, namely midnight and early morning. The maximum decrease of charging price is 68% and the price drops to 0.3837 yuan/kWh, which creates enough stimulation for customers to delay their charging behavior. In order to balance the price, the price of electricity of charging increases in day time. The maximum price appears at 19.00 when the price increases from 1.8044 yuan/kWh to 2.0364 yuan/kWh. The peak-valley difference drops from 405.9MW to 309.0MW, fulfilling the objective of load-flattening.

Under the uncoordinated scenario, the total cost of charging is 960,518.5 yuan. After stage one, the cost becomes 331694.6 yuan, which results from the large amount of load shifted from peak hours to valley hours. Because of the drop of charging cost, customers of electric vehicles gain more benefit. At the same time, since the amount of energy purchased from power grid during peak hours are reduced, the cost of charging service providers also decreases. However, their profit is influenced by the price users pay for charging. Under the pricing regulations, these service providers can gently increase charging prices of several hours to keep their balance. As for grid companies, with the drop of peak load and decrease in peak-valley difference, the reliability of service is boosted, along with an increase in the utilization rate of generators. As the load changed in stage two, the economic performance cannot be evaluated. However, the second stage takes the latest load prediction into account, creating a more accurate reflection of the actual load on the charging price.

V. CONCLUSIONS

The results show that the proposed real-time pricing mechanism has a positive influence on electric vehicle users and power grid. Charging service providers can also keep their financial balancing by setting a higher price during peak hours. Using price signals to control the charging demand is a simple, flexible and effective method. It has a potential of implementation in the future. The two-stage pricing model takes advantage of both the day-advance and hour-advance mechanisms, announcing the relatively accurate price ahead of time and making small variations according to the precise predictions.

ACKNOWLEDGEMENT

This research is supported by China Southern Power Grid Corporation (Research and Application of Key Technologies of Intelligent Cloud Service in Hainan Power Grid).

REFERENCES

- [1] ZHANG Cong. The Related Study on Impacts And Utilization of Large-scale Electric Vehicles Integration into Power Grid[D]. Wuhan: Huazhong University of Science and Technology, 2015.
- [2] HU Zechun, SONG Yonghua, XU Zhiwei, et al. Impacts and Utilization of Electric Vehicles Integration Into Power Systems[J]. Proceedings of the CSEE, 2012, 32(04):1-10.
- [3] GAO Ciwei, ZHANG Liang. A Survey of Influence of Electrics Vehicle Charging on Power Grid[J]. Power System Technology, 2011, 35(02):127-131.
- [4] Vagropoulos S, Balaskas G, Bakirtzis A. An investigation of plug-in electric vehicle charging impact on power systems scheduling and energy costs[J]. IEEE Transactions on Power Systems, 2017, 32(3):1902-1912.
- [5] Singh M, Thirugnanam K, Kumar P, et al. Real-Time Coordination of Electric Vehicles to Support the Grid at the Distribution Substation Level[J]. IEEE Systems Journal, 2015, 9(3):1000-1010.
- [6] Kim S J, Giannakis G B. Real-time electricity pricing for demand response using online convex optimization[C]// Innovative Smart Grid Technologies Conference. IEEE, 2014:1-5.
- [7] SHI Leilei, HU Jianzhao, HAN Shengfeng. An electricity price excited load transfer strategy for improving PV penetration ability to power systems[J]. Power System Protection and Control, 2016, 44(23): 153-157.
- [8] HUANG Haixin, DENG Li, WEN Feng. Customer Response Behavior Based on Real-Time Pricing[J]. Electric Power Construction, 2016, 37(2):63-68.
- [9] MENG Xiang, MA Xiaojun, YU Chao, et al. Real-Time Electricity Price Optimizaion Model Based on User Response[J]. Electrician Abstracts, 2014(03):58-60.
- [10] Soroudi A, Keane A. Robust optimization based EV charging[C]// Electric Vehicle Conference. IEEE, 2015:1-6.
- [11] Sundstrom O, Binding C. Flexible Charging Optimization for Electric Vehicles Considering Distribution Grid Constraints[J]. IEEE Transactions on Smart Grid, 2012, 3(1):26-37.
- [12] O'Connell A, Flynn D, Keane A. Rolling Multi-Period Optimization to Control Electric Vehicle Charging in Distribution Networks[J]. IEEE Transactions on Power Systems, 2014, 29(1): 340-348.
- [13] Taylor T N, Schwarz P M, Cochell J E. 24/7 Hourly Response to Electricity Real-Time Pricing with up to Eight Summers of Experience[J]. Journal of Regulatory Economics, 2005, 27(3): 235-262.
- [14] Zhang W, Zhang D, Mu B, et al. Decentralized Electric Vehicle Charging Strategies for Reduced Load Variation and Guaranteed Charge Completion in Regional Distribution Grids[J]. Energies, 2017, 10(2): 147.

Analysis and Research on the Task Pricing of “Making Photos and Making Money”

Leyuan Zhao¹, Bo Zhang¹, Juntian Bo¹ and Wenfei Zhao^{2,*}

¹Students' Brigade, Naval Aviation University, Yantai Shandong, 264001, China

²School of Basic Sciences for Aviation, Naval Aviation University, Yantai Shandong, 264001, China

*Corresponding author

Abstract—We research the operation of an APP, which collects the data of related products through the members' photographs. We organize the information collected and make a regression model. We use MATLAB to make a scatter plot to understand the task in the APP in longitude - latitude - price distribution in three-dimensional coordinates, and the relationship between task pricing and membership information. The task pricing is also related to the task location. The study find that the original program has many unreasonable places. We analyze the main influencing factors and formulated the task package model, and then re-determine the task pricing scheme based on the order of magnitude. The model and scheme are properly amended by using the member's position and the position of the task. The revised pricing plan is more reasonable and more practical.

Keywords—linear regression; package distribution; sub-regional model

I. INTRODUCTION

"Photo Earning Money" is a new self-service model that runs on the mobile Internet. It allows users to download APPs, register as a member, and then take a photo-taking task (such as going to the supermarket to check the availability of a product). Members earn APP for the task of the nominal reward. APP has become the core of the platform to run, and APP is the core element of the task pricing. If the pricing is not reasonable, some tasks will no one cares that lead to the failure of commodity inspection. Based on the collected data, we analyze its pricing rules and study the impact of various major factors on pricing through scatter plot. We find that the tasks in this APP can be packaged together in two-dimensional coordinates, and to re-establish a more reasonable pricing. In this study, we perform parametric analysis and testing using a binary regression equation.

II. PACKAGING PRICING BASED ON REGRESSION EQUATION

Based on the collected data, we perform the least-squares regression analysis of the task position and the task price, and find out the regression equation. Then, we test the linearity of the regression model and the significance of regression coefficients. If the relationship between the two is not a simple linear relationship, you can change the relationship according to the scatter plot, substituting the data of the relevant data and other factors, and check whether the accuracy is improved. Then according to the improvement of the law of setting the task price to be amended and compared with the original plan.

Set up a model of task force w and task position (x, y) linear regression analysis, and we get n independent observation data for [1]. E_n is the n unit matrix.

$$\begin{cases} w_i = \beta_0 + \beta_1 x_i + \beta_2 y_i + \varepsilon_i, \\ \varepsilon_i \sim N(0, \sigma^2), i = 1, \dots, n, \end{cases} \quad (1)$$

$$\begin{cases} w = X\beta + \varepsilon, \\ \varepsilon \sim N(0, \sigma^2 E_n), \end{cases} \quad (2)$$

A. Principle of Order of Magnitude

At a certain point, the distance between all other points is calculated. We select the shortest distance from the distance, and select points that are at the same order of magnitude as the other points. We consider these points to be the closest point to the center point. We find a way to package the tasks. Pack two tasks. Here we use the order of magnitude of the most recent principle to set up a collection of points that can be packaged. We coordinate all task position coordinates on the plane of longitude and latitude, and set each point as $P_i (i = 1, 2, \dots, n)$. Take the P_1 as an example, calculate the distance $D_i (i = 2, 3, \dots, n)$ between all other points $P_i (i = 2, 3, \dots, n)$ and P_1 .

$$D_i = |P_i - P_1| (i = 2, 3, \dots, n)$$

$$\xi_i = \frac{D_i}{D_j} (i = 2, 3, \dots, n)$$

The shortest distance between P_j and P_1 distances is D_j . The order of magnitude of ξ_i is calculated as $\xi_i (i = 2, 3, \dots, n)$. All the points $\xi_i < 10$ are selected, and some of these points is the distance from P_1 recent points. If you

find P_1 to be in the same algorithm of its recent focus point nearest points, these points can be packaged with P_1 together.

B. Formulation of Packaging Methods and Pricing Models

The more the number of tasks packaged, the greater you conduct the remuneration. Here the problem translates to the setting of the suppression factor $\varepsilon(n)$. It can be seen that the coefficient of inhibition varies with the number of tasks in the package, and the problem is similar to the issue of payroll tax. The commonly used method is "sub-deduction", that is, different salary sections to pay the tax ratio is different [2].

III. APPLICATION

The number of task breakpoints n_1 、 n_2 、 n_3 should be adapted to the nearest number of points at each point under the recent order of magnitude. The distribution of points obeys normal distribution $n \sim N(\mu, \delta^2)$, in which $\mu=6.3$, $\delta=0.732$. Therefore, we set the maximum number of tasks in the package as 10, the number of tasks breakpoint $n_1=1$ 、 $n_2=3$ 、 $n_3=6$ 、 $n_4=9$, the size of the increase in proportion of $\varepsilon_i(n)$ ($i=1, 2, 3, 4$) is to:

$$\varepsilon_i(n) = \begin{cases} 0, & i=1, \\ 2.5, & i=2, \\ 5, & i=3, \\ 7.5, & i=4. \end{cases}$$

By researching task price W , we let t be the gratuity growth value based on the membership credit value, and use $t = \beta_0 + \beta_1 z + \gamma$, obtained by MATLAB $\hat{\beta}_0 = 3.4411$, $\hat{\beta}_1 = 0.1850$, the correlation coefficient $r = 0.0062$. So the final packaging task to provide remuneration for

$$W = \begin{cases} y_1 + \dots + y_n + t, & n=1, \\ y_1 + \dots + y_n - (n-1) \times 2.5 + t, & 1 < n \leq 3, \\ y_1 + \dots + y_n - 5 - (n-3) \times 5 + t, & 3 < n \leq 6, \\ y_1 + \dots + y_n - 20 - (n-6) \times 7.5 + t, & 6 < n < 10. \end{cases} \quad (3)$$

A. Sub-regional Research

We merge or remove a few tasks that are independent from dense areas and far apart from each other, and are not suitable

for packaging. In the range of longitude $112.8^\circ \sim 114.4^\circ$ and latitude $22.4^\circ \sim 23.8^\circ$, it divides 20 areas with concentrated task positions and calculates the number of tasks in each area. In the same way, the member distribution is divided as shown in Figure 1 and Figure 2:

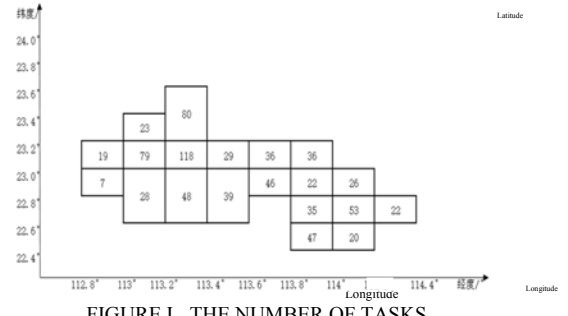


FIGURE I. THE NUMBER OF TASKS

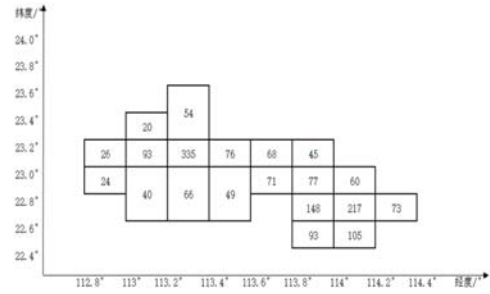


FIGURE II. THE NUMBER OF MEMBERS

The intensity of the task point and the degree of aggregation of members is basically consistent. The introduction of variables a , said the number of a region can be packaged, the number of tasks set in a region is u , the number of members is m , then the number of a package can be calculated as

$$\alpha = \begin{cases} \frac{u \times m}{2 \times (u+m)}, & 500 < u, \\ \frac{u \times m}{3 \times (u+m)}, & 500 > u > 100, \\ \frac{u \times m}{4 \times (u+m)}, & u < 100. \end{cases} \quad (4)$$

α is rounded to the number of packages for the end of a regional plan for. [3] Calculated by MATLAB, $\hat{\beta}_0 = -19.437497$, $\hat{\beta}_1 = 0.278544$, $\hat{\beta}_2 = 2.476796$. However, the R^2 is too small, so the two are not simple linear relationships.

Therefore, we observe the relationship between the task price and the distribution of mission locations through a scatter graph, as shown in Figure 3.

The picture shows that there is a different price stage for the same location, and it is calculated that the two are not simply linear. From this we can conclude that when a business sets a price for a task, and it does not mainly consider the distribution of locations. Obviously, the task position is to affect the task pricing. [4]

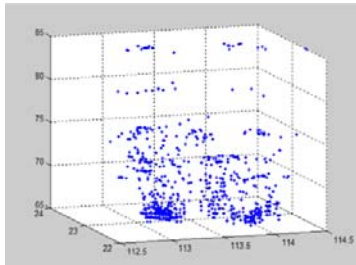


FIGURE III. TASK LIST PRICE AND TASK LOCATION DIAGRAM

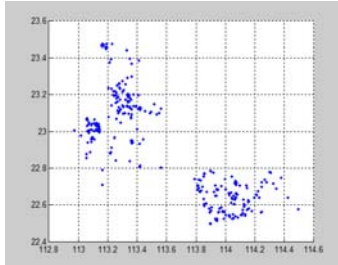


FIGURE IV. FAILED TASK DISTRIBUTIO

Figure 4 shows that the failed tasks are mainly distributed in two relatively concentrated areas, longitude $113^{\circ} \sim 113.6^{\circ}$ latitude $22.8^{\circ} \sim 23.2^{\circ}$ and longitude $113.8^{\circ} \sim 114.3^{\circ}$ latitude $22.5^{\circ} \sim 22.8^{\circ}$.

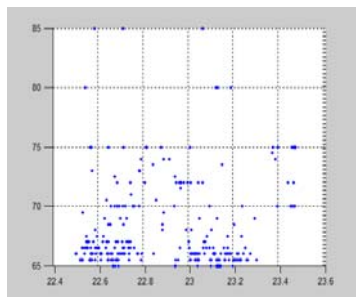


FIGURE V. FAILURE TASK LATITUDE-PRICE CHART

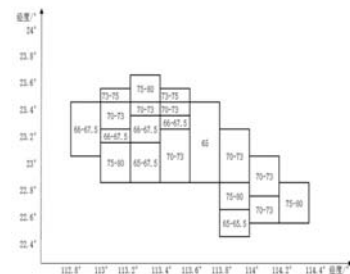


FIGURE VI. SUB-REGIONAL PLAN PRICING RANGE CHART

As can be seen from Figure 6, the prices of failed tasks are generally low except for a few. From Figure 4 and Figure 5, we know that the prices of failed tasks are low and concentrated in the longitude $112.8^{\circ} \sim 114.6^{\circ}$ and latitude $22.4^{\circ} \sim 23.6^{\circ}$ regions. We take a uniform distribution of 15 points. In the success of the task we randomly found with each point and the price difference is less than 3 Yuan each of the five points. We let the 75 points longitude, latitude, task value into the MATLAB to calculate the value of stats and substituted several times. When the resulting stats $>= 0.8$ (stats = 0.861 in a trial), we think such arrangement meeting the needs, which will greatly improve the success of the task rate.

We take into account the location of members and the location of characters and price relationship, according to the region to develop price plans, price should be within the scope of the plan. Plan as shown in Figure 6. In the completed tasks, the few independent of the dense outer area should be merged or eliminated. Count different regions and price of the task, the success rate reached 72.9%. The new mission location point is plotted in MATLAB, as shown in Figure 7:

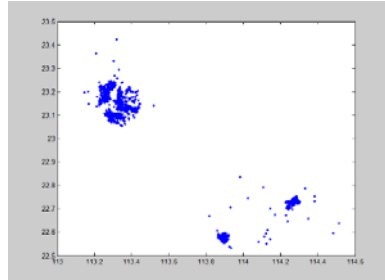


FIGURE VII. NEW MISSION DISTRIBUTION

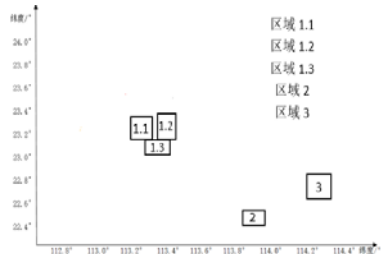


FIGURE VIII. NEW TASK AREA DIVISION DIAGRAM

Seen from the figure, mainly concentrated in three regions:

- Longitude $113.1^{\circ} \sim 113.5^{\circ}$ and latitude

$23^\circ \sim 23.3^\circ$ lines surround the area.

- Longitude $113.8^\circ \sim 114.0^\circ$ and latitude $22.5^\circ \sim 22.6^\circ$ lines surround the area.

- Longitude $114.2^\circ \sim 114.4^\circ$ and latitude $22.7^\circ \sim 22.8^\circ$ lines surround the area.

A. Develop A Package Plan

According to the recent order of magnitude, the task point in the area 1,2and3 are relatively far from each other. So we do not consider cross-regional packaging. The distribution of task points in area 1 can be further divided into 3 areas, and we have to arrange packing schemes separately in these 5 areas. Regional distribution shown in Figure 8:

Without affecting the regularity of statistics, the number of tasks in each region was calculated after merging the task points close to each region and removing the task points without considering packing. The number of tasks is 1.1: 509 in the area, 1.2: 712 in the area, 1.3: 208, Zone 2: 253, Zone 3: 292.

In the same way, the number of members in each region is 1.1: 195 in the region, 1.2: 194 in the region, 1.3: 168 in the region, 2:93 in the region, and 3:73 in the region.

Using formula (4), the planned number of planned packages in each region is 1.1: 74, 1.2: 76, 1.3: 27, 2: 23, and 3: 20.

B. Develop A Unit Price

Taking into account the membership and the intensity of the task, set the number of tasks in a region, the number of members, to develop the unit price of E:

$$E = 60 + \frac{5 \times u}{m}$$

Set the unit price for the region 1.1: 72 Yuan, the region 1.2: 73 Yuan, the region 1.3: 65 Yuan, the region 2:74 Yuan, the region 3:80 Yuan.

C. Set A Package Price

Amending regression equation coefficients to construct a model of single factor linear regression of packaging task price W and membership credit value

$$W = \beta_0 + \beta_1 z + \varepsilon$$

β_0 , β_1 is regression coefficients , calculated by MATLAB $\beta_0=5.741$, $\beta_1=0.835$.

Each region finally formulates the specific price according to the formula (3) combining the member's specific credit value and the specific task.

REFERENCES

- [1] Sijin An and Jian Zhai. Analysis and prediction model of the influence factors of software crowdsourcing engagement [N]. Computer system application, volume 24, volume 10, 2015.
- [2] Shoukui Si and Xijing Sun. Mathematical modeling algorithm and application [M]. Defense industry press, 2011.
- [3] Huiwen Wang. The least squares regression method and its application [M]. Beijing: national defense industry press, 2000.
- [4] Zhuolin Li. The graphical method of statistical data and its application [D]. Chongqing: Chongqing University, 2015.

Research on Task Pricing of Crowdsourcing Platform

Senrong Ma¹, Lei Wang¹, Jiae Guo¹ and Gang Zhou^{2,*}

¹Students' Brigade, Naval Aviation University, Yantai Shandong, 264001, China

²School of Basic Sciences for Aviation, Naval Aviation University, Yantai Shandong, 264001, China

*Corresponding author

Abstract—With the development of the science and technology, a new business model for publishing tasks over the internet has emerged. This paper mainly focuses on the task completion of crowdsourcing platform and pricing scheme. By packaging tasks centrally, we establish a task pricing model based on partial least square regression and partial binary tree support vector machine. Traditional pricing schemes only consider the benefits of the platform but neglect the benefits of the users. Thus, it has the problem of low completion rate and dispersion of tasks. Comparing with the traditional pricing scheme, this model can not only improve the task completion rate but also maximize the benefits of both the task platform and the user. Besides, the model can avoid the problem of user congestion and make the model more secure and reliable.

Keywords—partial binary tree support vector machine; genetic algorithm; crowdsourcing platform

I. INTRODUCTION

With the rapid development of mobile internet technology, more and more enterprises choose to collect a wide range of data offline confirmation and collection work through the internet self-help platform. Through the platform, users receive and release the task to earn a reward. Different from the common pricing project, the task pricing of the internet crowdsourcing platform not only involves a large amount of data, covers a wide range of areas, and also has complex influence factors. Besides, it also needs to consider the problem of maximizing the interests of both task arranger and user. However, most of the traditional pricing model use profit optimization model and establish the correlation function to solve the problem. These models only take the maximizing profits of the merchant into account, but they neglect the users' idea. Therefore, the traditional model can't solve the bidirectional benefit maximization pricing demand based on big data platform. In order to adapt to the change of the task pricing, combining with the specific task needs, we present a pricing scheme based on partial least square regression and partial binary tree support vector machine model.

II. THE RULE OF TASK PRICING

A. Setting up Partial Least Square Regression Model

We consider the modeling of dependent variable is y_1 and x_1, x_2, \dots, x_m are individual independent variables, and finally establish the partial least square regression model $y_1 = b_1x_1 + b_2x_2 + \dots + b_mx_m$.

According to the reality of the subject, the setting of the independent variable is as follows:

TABLE I. INDEPENDENT VARIABLE DESCRIPTION

x_1	Mission location latitude
x_2	Mission location longitude
x_3	Member location latitude
x_4	Longitude of member location
x_5	Member credit value

Note that F_0 is a standardized variable for variable task pricing y and E_0 is the normalized matrix of the set of independent variables X .

$$F_{0i} = \frac{y_i - \bar{y}}{s_y}, i = 1, 2, \dots, n \quad (1)$$

$$E_{ij} = \frac{X_{ij} - \bar{X}_j}{s_j}, j = 1, 2, \dots, p \quad (2)$$

First, a component u_1 extracted from $u_1 = F_0 c_1, \|c_1\| = 1$, is the first spindle of F_0 , extract t_1 from F_0 , w_1 is the first spindle of E_0 , with the constraints of $\|w_1\| = 1, \|c_1\| = 1$ to find the maximum value of $w_1^T E_0^T F_0 c_1$, using the Lagrange algorithm to remember:

$$\text{Cov}(t_1, u_1) = \sqrt{\text{Var}(t_1) \text{Var}(u_1)} r(t_1, u_1) \rightarrow \max \quad (3)$$

$$s = w_1^T E_0^T F_0 c_1 - \lambda_1(w_1^T w_1 - 1) - \lambda_2(c_1^T c_1 - 1) \rightarrow \max \quad (4)$$

s is the partial respectively derivative of $w_1, c_1, \lambda_1, \lambda_2$, and then we make it zero, through derivation, it is possible to:

$$\left. \begin{array}{l} E_0^T F_0 F_0^T E_0 w_1 = \theta_1^2 w_1 \\ F_0^T E_0 E_0^T F_0 c_1 = \theta_1^2 c_1 \end{array} \right\} \quad \theta_1 = 2\lambda_1 = 2\lambda_2 = w_1^T E_0^T F_0 c_1 \quad (5)$$

w_1 is a unit eigenvector corresponding to the eigenvalue matrix $E_0^T F_0 F_0^T E_0$. On the other hand, c_1 is the unit eigenvector of θ_1^2 . θ_1^2 is the maximum value of the matrix of $E_0^T F_0 F_0^T E_0$. Then we get spindle w_1 and c_1 ,

Then we obtain the two regression equations of E_0 and F_0 for t_1 and then the regression coefficient vector is:

$$F_0 = t_1 r_1^T + F_1, \quad E_0 = t_1 p_1^T + E_1, \quad (6)$$

$$p_1 = \frac{E_0^T t_1}{\|t_1\|^2}, \quad r_1 = \frac{F_0^T t_1}{\|t_1\|^2}. \quad (7)$$

E_1 and F_1 are the residual matrices of the two regression equations, using the residuals matrix E_1 and F_1 instead of E_0 or F_0 . The same method is used to calculate the second axes w_2 , c_2 and the second principal components. If the m operation is performed, there will be:

$$E_0 = t_1 p_1^T + t_2 p_2^T + L + t_m p_m^T + E_m, \quad (8)$$

$$F_0 = t_1 r_1^T + t_2 r_2^T + L + t_m r_m^T + F_m. \quad (9)$$

III. APPLICATION OF MODEL

According to the thought steps of partial least square regression algorithm, we obtain the regression equation of task pricing:

$$y_1 = -0.0034x_1 - 0.0606x_2 - 0.0169x_3 + 0.0245x_4 - 0.0760x_5. \quad (10)$$

TABLE II. VARIABLE CORRELATION COEFFICIENT MATRIX

	x_1	x_2	x_3	x_4	x_5	y_1
x_1	1.0000	-0.9795	-0.0862	0.0764	-0.2262	0.0694
x_2	-0.9795	1.0000	0.0862	-0.0815	0.2528	-0.0975
x_3	-0.0862	0.0862	1.0000	-0.7378	0.0903	-0.0474
x_4	0.0764	-0.0815	-0.7378	1.0000	-0.1909	0.0539
x_5	-0.2262	0.2528	0.0903	-0.1909	1.0000	-0.0838
y_1	0.0694	-0.0975	-0.0474	0.0539	-0.0838	1.0000

According to the algorithm step, we obtain the final result of the task pricing through the classification of classifier. Set up scatter diagram for the post pricing task, and the distribution of the pricing results as shown in figure 1 and figure 2.



FIGURE I. COMPLETION OF TASKS



FIGURE II. TASK COMPLETION QUANTIZING

From the above picture, we can also get the analysis of the reasons for the unfinished task: from the distribution of scatter points, the correlation between the completion of the task and the bid price is relatively large, and the correlation with the member distribution is relatively weak.

IV. ESTABLISHMENT OF PARTIAL BINARY TREE SUPPORT VECTOR MACHINE

The idea of this method is to use partial two tree structure, a class of samples is extracted as the first classification at every time, thus, the classification of k problem is transformed into the classification of $k-1$ problem, after that, we use the double

support vector machine to implement classification for each node. The algorithm is divided into four steps:

1. Initialize the data.
2. Generate binary tree structure.
3. TVSM training.
4. Test pricing results.

V. APPLICATION OF MODEL

For the specific pricing items, we use the partial binary tree support vector machine to make scheme. The specific member information and the task position are shown in the attachment.

Set the distance standard value between the task point and the member position as r_0 , the distance between the task point and the member position is r , set a target function $F(n)$ which is the ratio of the distance between the task point and the member position and the standard distance:

$$F(n) = \frac{r}{r_0} \quad (11)$$

Use $F(n)$ to represent the fitness value between each task and the members who can accept the task. $T(n)$ is the maximum value used to store the tasks accepted by each member.

The specific steps of implementing the algorithm are as follows:

1. Generate the first member who accept the task, and calculate the fitness of each task to the member and the maximum limit value of the task.

2. Set the probability of each task selected by a member to be P_i ,

$$P_i = \frac{F(i)}{\sum_{i=1}^n F(i)} \quad (12)$$

3. Use the roulette method to make members choose tasks randomly.

4. Randomly select a pair of tasks and members to cross the operation to calculate the value of the fitness value and the number of tasks for the members.

5. Update the task information. Mark the completed tasks as 0, meanwhile the uncompleted tasks are set to 1, after that carryout the cross operation between the tasks and the members.

6. Select the largest fitness value and compare it with the fitness of the current optimal solution. If the fitness value of the optimal solution is greater than the optimal solution, replace the

current optimal solution, and update the membership information and the number of accumulated.

7. Loop iteration, when the number of times reaches the setting maximum, jump out of the loop, outputs the optimal solution.

The block diagram of the specific procedure is as follows:

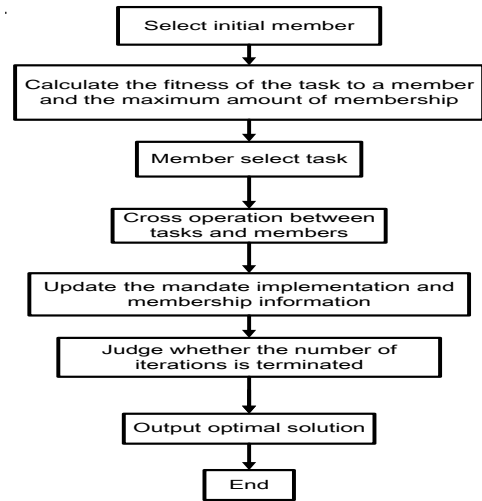


FIGURE III. BLOCK DIAGRAM

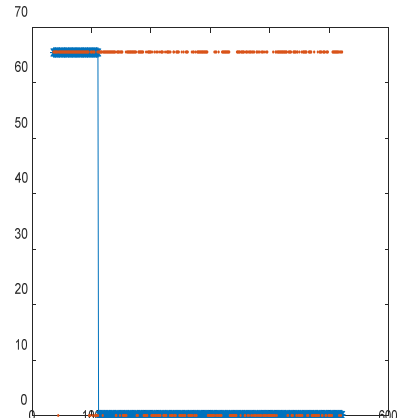


FIGURE IV. TEST RESULT

A. Test Classification Results

As 4 shown in the figure, the test graph intuitively gives the pricing results after the first SVM classifier. The upper blue dot set represents the priced task, the orange dot set represents the task pricing situation after being classified by the SVM classifier, and the horizontal coordinates represent the numerical code of the task label.

According to the algorithm step, we obtain the final result of the task pricing through the classification of classifier. Set up scatter diagram for the post pricing task, and the distribution of the pricing results as shown in figure 5. By calling the function of the SVM toolbox in MATLAB, the sample is classified according to appendix. After the classification, the tasks of

different pricing are distinguished by different colors, and the scatter diagram is drawn in figure 6.

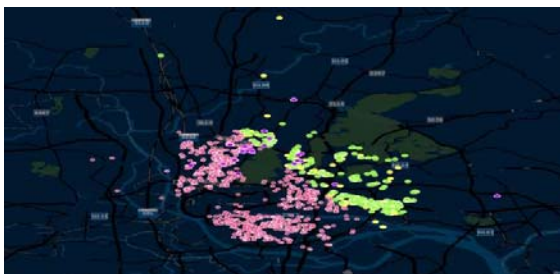


FIGURE V. TASK PRICING SCATTER PLOT



FIGURE VI. PRICING RESULTS SCATTER PLOT

B. SPSS Correlation Test

Correlate the obtained pricing scheme with the argument set consisting of all arguments to obtain the correlation test results as shown in Table 3.

TABLE III. CORRELATION TEST

		argument	
		price	
price	Pearson correlation	1	.823
	Significant (bilateral)		.796
	N	2067	2067
argument	Pearson correlation	.823	1
	Significant (bilateral)	.796	
	N	2067	2067

The test results show that the final pricing is significantly correlated with the set of independent variables at 0. 05 level, and the Pearson correlation coefficient is 0. 823, and result verifies the feasibility of the scheme.

VI. CONCLUSION

By using the partial least square regression and partial binary tree support vector machine model, this paper presents a new secure and reliable pricing scheme based on the service crowdsourcing business model on the internet, which can better adapt to the complexity of crowdsourcing business data and the complexity of the region. Meanwhile, this model can improve the task completion rate and make platform and user reach profit

maximization. Besides, the model has good practicability and generalization. Through the adjustment and expansion of project parameters, the model can also complete the pricing of other crowdsourcing projects. We hope that the model can be used more in the future research.

REFERENCES

- [1] Shoukui Si. Mathematical modeling algorithm and application [M]. Beijing: national defense industry press, 2011:39-63.
- [2] Bei lei Qin, Application of partial least squares regression in hydrological analysis [J]. Journal of Sichuan University (Engineering Science Edition). 2003:116-117.
- [3] Juan ying Xie, Zhang Bingquan, Wang Wan-z, Multiclass classification algorithm based on double support vector machine. Journal of Nanjing University (Natural Science) 2011:355-360.

An Approach Assessing Software Trustworthiness

Xinglong Xie* and Weixian Xue
Xi'an University of Technology, 710048, China
*Corresponding author

Abstract—This paper is aimed at presenting a technique appraising software trustworthiness grounded on Grey correlation analysis, which performs calculating of the weight for each index by virtue of trapezoidal fuzzy number. This paper initially works out at positive and negative ideal values for trustworthiness indicators, whereby to figure out the Grey correlation degree concerning the index value and the ideal value whereof. Grounded on this, the paper estimates the value for software trustworthiness and the empirical evidence reveals that the specified methodology is of validity and accuracy. Hence, this technique can be applied into more studies on software trustworthiness.

Keywords—trustworthiness measure; trustworthiness indicator; positive (negative) ideal value; trapezoidal fuzzy number; grey correlation analysis

I INTRODUCTION

Software trustworthiness, developed on the footing of correctness, dependability, security and real-time, drives at the totality of all features and peculiarities relevant to the capability of a software system satisfying expectations and its implied demand. With the advent of an ever-expanding software scale, this topic presently concerns a great deal, including market demand, modeling, testing, maintaining and run-time supporting for software, and has aroused extensive attention and witnessed a growth in related-studies. And has shifted into comprehensive consideration of multiple attributes such as accountability, security and practicality from focusing on the analyzing, testing and verifying of a single attribute amid the early studies [1, 2, 3, 4, 5, 6]. Especially, Immonen and Palviainen claimed that software worthiness needs to be gauged from three tiers:software component, architecture and system [7]. Ding, Lu and Yang designed a demand-driven model [8], and Zhao and Sun explored techniques concerning trustworthiness assessment [9]. Cai, Zou and Shao came up with a framework appraising the credibility of a supporting software [10]. Li et al. proposed a software trustworthiness model, integrating risk management and cost control [11]. D. Lizcano et al. put forward an automatic framework of software trustworthiness to support verification and validation, which has been demonstrated valid [12].

In general, existing methods are mainly divided into two classes: model-based, which focus on software framework modeling and perform the evaluating assignment prior to software delivery, and, application-based, which seek to make judgment of trustworthiness on evidence attained following software operations. The latter approaches think over multiple properties regarding evidence of trustworthiness during each

stage of the software life cycle yet most of property values suffer from poor information and expert judgment is inevitably subjective, this having triggered a departure from reality. Thus, notwithstanding orthodox theorems, which have set up considerable quantities of trustworthiness-evaluating frameworks amid efficiency-orientation, they are subjected to inadequacy in the number of trustworthiness attributes and draw certain static conclusions in spite of quantifying software trustworthiness. Concerning software trustworthiness assessment, quantitative and qualitative analysis should be employed as well as multiple properties. This would enhance translation of findings stemming from trustworthiness research into actual productivity, diminishing the costs for software failure.

The purpose of this paper is to contribute to a growing body of literature on software trustworthiness assessment through regarding software trustworthiness as a decision-making of multiple fuzzy Grey attributes. We design a framework by means of considering six first-grade indicators in the criteria tier and thirteen second-grade indicators in the sub-criteria tier, which gives our study superior in comparison with traditional methods. Furthermore, we solves the model by resorting to Grey correlation methodology, characterized by both trapezoidal fuzzy number deciding weights and comparison with ideal values. All this allows us to address issues set out in existing software trustworthiness studies.

The reminder of this paper is organized as follows. Section II contains the theoretic basis and modeling of software trustworthiness. Methodology is presented in section III. IV contains empirical analysis. We concluded in section V.

II THEORETIC BASIS AND MODELING

Software trustworthiness appraising is viewed as a systematic engineering, including evidence gleaning, indicator designing, trustworthy attribute measuring, methodology estimating trustworthiness, expert comments and user feedback (see Figure I). Testimony collection runs through the whole life cycle of software, during which any figure, document or information, which mirrors a certain credibility property, can be treated as evidence. Thus, data concerning norms of all classes, reviews and tests in the course of software development, figures arising from entity analysis and testing, user satisfaction degree and remarks of a third party, all fall into the category of valid reliable proofs, marked by objectiveness, relevancy and availability.

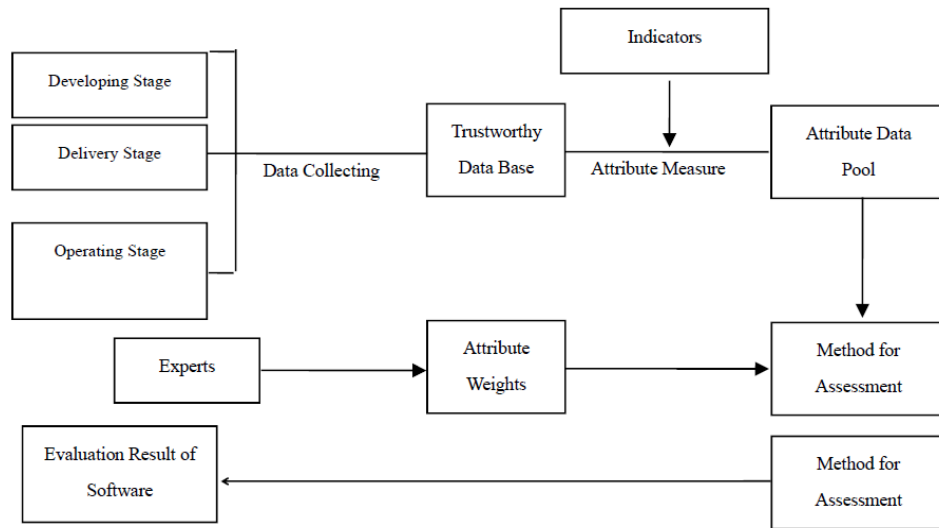


FIGURE I. RESEARCHING STRUCTURE OF SOFTWARE TRUSTWORTHINESS ESTIMATION

Worthiness attribute is understood to be direct information describing and appraising the reliability of a software system, gauged by utilizing indicators, heterogeneous in the relative importance. So, it is vital how to ascertain the weight of an index. This is generally left to experts and consumers, who can give the value of each indicator, whereby weights to be calculated. The core in software trustworthiness assessment lies in the algorithm, employed for the sake of calculating software system behavior, user-expected behavior, and actual results.

Index framework concerning software trustworthiness evaluation refers to an organism consisting of interrelated reliability attributes and metric values whereof. This has

aroused attention from scholars and registered an increase in the number of studies. Zhao et al. proposed a technique for confidence level gauging of software by virtue of Pi calculation [13]. Yang et al. brought forward a software-behavior-based dynamic structure of indexes, which is able to assess a behavior locus and examine the deviation degree regarding a point scene by performing calculation of context values invoked by the system and establishing the constraint rules regarding system-calling parameters [14]. In view of software attribute measurement and operability, this paper prefer to opt for usability, reliability, security, real-time and maintainability as indicators at the first rank, under which there are a certain number of sub-indicators (Figure II).

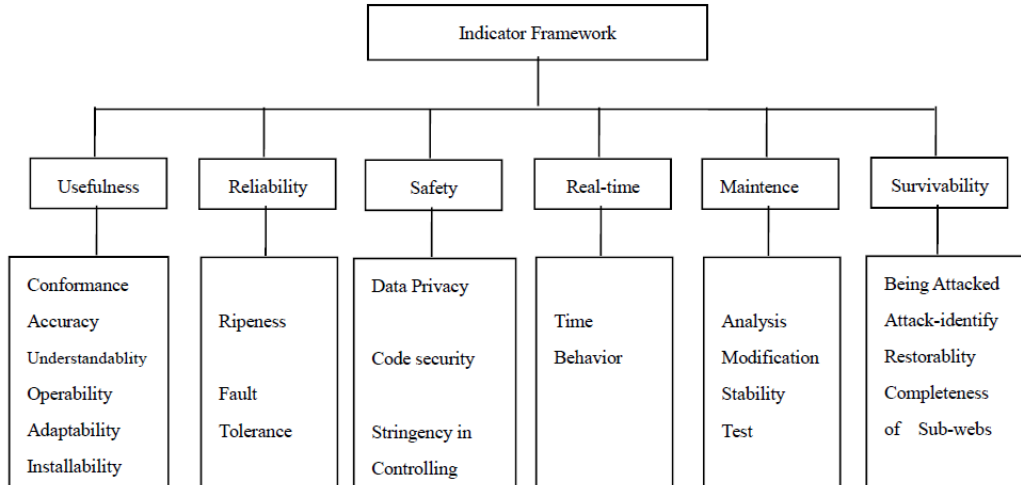


FIGURE II. FRAMEWORK REGARDING APPRAISING SOFTWARE TRUSTWORTHINESS

III FUZZY GREY RELATIONAL METHOD

A. Indicator Framework and Ideal Point

The framework evaluating software trustworthiness can be referred as a system characterized by uncertainties, small

samples and information insufficiency attributable to difficulties in the acquisition of indicator values. In this article, $G_j \in G (j=1,2,\dots,n)$ denotes the attributes concerning software trustworthiness, $A_i (i=1,2,\dots,m)$ a software remaining to be appraised. $S=(S_{ij})_{m \times n}$, in which the larger some indexes, the better they will be while other indicators are on the contrary:

the smaller, the better. Normalization is employed to process these indexes for eliminating consequences exerted on results to be estimated,

this yielding matrix $R=(r_{ij})_{m \times n}$:

$$r_{ij} = \frac{s_{ij}}{\max\{s_{ij}\}} \quad (1 \leq i \leq m) \quad \text{for efficiency indexes} \quad (1a)$$

$$r_{ij} = \frac{\min\{s_{ij}\}}{s_{ij}} \quad (1 \leq i \leq m) \quad \text{for cost indexes} \quad (1b)$$

Utilizing ideal points can give rise to reference indicator series, for which, the maximum for an indicator acting as the ideal point while the minimum the negative counterpart.

$$r^+ = \max_i \{r_{ij}\} \quad (j=1, 2, \dots, n) = (r_1^+, r_2^+, \dots, r_n^+) \quad (2a)$$

And

$$r^- = \min_i \{r_{ij}\} \quad (j=1, 2, \dots, n) = (r_1^-, r_2^-, \dots, r_n^-) \quad (2b)$$

B. Attribute Weight Calculation

For fuzzy set F in the real number field, there exists $a < b < c < d$, if the membership function is:

$$\mu_F(x) = \frac{x-a}{b-a} \quad (a < x < b) \quad (3a)$$

$$\mu_F(x) = 1 \quad (b \leq x \leq c) \quad (3b)$$

$$\mu_F(x) = \frac{x-c}{d-c} \quad (c < x < d) \quad (3c)$$

$$\mu_F(x) = 0 \quad (\text{else}) \quad (3d)$$

Then this subjection function is viewed as the fuzzy number of trapezoid, signed by (a, b, c, d) . It is employed to compute the weight of a trustworthiness property by taking following steps: let $W_k = w_j(k)$ be the weight for G_j given by the expert panel, this leading to formation of trustworthiness attribute weight matrix $W_k = (w_j)$. $E_k \in [0, 1] \quad (k=1, 2, \dots, p)$ indicates the decision-making weight of experts or users, satisfying $\sum E_k = 1$. Table I reveals the principle concerning evaluation.

In conformity with the membership function of ladder-shaped vague numbers, we can find a fuzzy judgment of indicator G_j in the relative importance by specialist k :

$$w'_{jk} = (a_{jk}, b_{jk}, c_{jk}, d_{jk})$$

Whereby to secure the comprehensive weight for G_j by the expert team:

$$w'_j = (a_j, b_j, c_j, d_j) = \left(\sum_{k=1}^p E_k a_{jk}, \sum_{k=1}^p E_k b_{jk}, \sum_{k=1}^p E_k c_{jk}, \sum_{k=1}^p E_k d_{jk} \right) \quad (4)$$

Let the optimistic co-efficient of experts be 0.5, then there exists the following:

$$d(w'_j) = \frac{(a_j + b_j + c_j + d_j)}{4} \quad (5)$$

Weight is formalized by adopting the following specification to generate a weight vector:

$$w_j = \frac{d(w'_j)}{\sum_{j=1}^n d(w'_j)} \quad (6)$$

Thus, the weight vector for index G_j can be expressed in the following form: $w = (w_1, \dots, w_j, \dots, w_n)$ where $\sum_{j=1}^n w_j = 1$

C. Trustworthiness Grade

Formula 1 and 2, coupled with 7, can conclude distance V_j^+ between real and positively-ideal values and V_j^- between real and adversely-ideal values:

$$V_j^+ = |r_j - r_j^+| \quad (7a)$$

And

$$V_j^- = |r_j - r_j^-| \quad (7b)$$

Next, to attain the correlation coefficient between trustworthiness attributes and the ideal set through following specifications:

$$\beta_j^+ = \frac{\min_j V_j^+ + \rho \max_j V_j^+}{\sum_j V_j^+ + \rho \max_j V_j^+} \quad (8a)$$

And

$$\beta_j^- = \frac{\min V_j^- + \rho \max V_j^-}{\sum_{j=1}^n w_j} \quad (8b)$$

Where β_j^+ refers the coefficient, which associates the trustworthiness property with and the positively ideal property, and, β_j^- means one, which connects the trustworthiness property to the negatively ideal property, and ρ is termed as distinguishing coefficient, falling into $[0,1]$, generally being fixed at 0.5. This, plus using formula (6), can contribute to production of relevancy degree between the scheme for the attribute set concerning software reliability and the positively (adversely) ideal attribute set:

$$\beta^+ = \frac{\sum_{j=1}^n w_j \times \beta_j^+}{\sum_{j=1}^n w_j} \quad (9a)$$

And

$$\beta^- = \frac{\sum_{j=1}^n w_j \times \beta_j^-}{\sum_{j=1}^n w_j} \quad (9b)$$

Synthesizing β^+ and β^- can give rise to generating of estimated numerical value for software trustworthiness:

$$\beta = \frac{\beta^+}{\beta^+ + \beta^-} \quad (10)$$

Comparing β with the criteria can find out at which level a software being gauged is positioned in the case of trustworthiness.

IV EMPIRICAL ANALYSIS

This paper would aim to measure the self-adapting temperature software at the machine room of a telecommunication firm, which places high requirements on software properties such as reliability and just-in-time. To achieve this end, the project team develops three sets of embedded software systems by virtue of resorting to compiling C and Java language. On the footing of software trustworthiness features, this paper designs an indicator framework via having some of indexes stemming from Figure II as references (see Table II).

TABLE II. FRAMEWORK

Goal	Software		Trustworthiness Value			
	Usability/I ₁		Reliability/I ₂		Security/I ₃	
Sub-criteria	Function Accuracy/I ₁₁	Operability/I ₁₂	Easy Installation/I ₁₃	Error-making Frequency/I ₂₁	Fault Tolerance/I ₂₂	Confidentiality/I ₃₁
Criteria	Real-time/I ₄	Maintainability/I ₅			Survivalability/I ₆	
Sub-criteria	Timeliness/I ₄	Diagnosability/I ₅₁	Modifiability/I ₅₂	Stability/I ₅₃	Reversibility/I ₆₁	Self-improvement/I ₆₂

Three experts are invited to assign each sub-criterion a weight by fuzzy words described on the Table I. For this specialist group, each is viewed as having the same position in the weight decision-making, namely, E1= E2= E3=1/3, and all first-grade indicator are equally treated in the weight distribution, coming at 1/6.

TABLE I. EVALUATION OF BLUR WORDS AND EXPRESSIONS

Vague words	Unimportant	Less important	Important	More important	Extremely important
(a,b,c,d)	(0,0,0,3)	(0.3,3,3,5)	(3,5,5,7)	(5,7,7,9)	(7,9,9,10)

With regard to the initial procedure, it is dedicated to estimating the indicator vector. Take three sub-criteria under I1 for example. The weights concluded by three specialists and listed on table 3, the comprehensive weights of specialists generated by formula (4), the blur weights attained by (5), and post-formalized values stemming from (6) can lead to production of the final weight vector W1=(w11, w12, w13)=(0.42,0.31,0.27). In the same token, weight vectors for other second-level indicators can be available. This, in couple with the weights concerning first grade indicators, can bring about engendering of comprehensive weight vectors for second grade indexes, denoted by W=(W1, W2,...,Wn).

The next step is to find a matrix of assessing trustworthiness S_{3×13} through gauging each attribute value for software A1(i=1,2,3) to derive Grey number vector G_j (j=1,2,...,n):

$$S_{3\times 13} = \begin{bmatrix} 0.91 & 0.93 & 0.92 & 0.95 & 0.84 & 5 & 5 & 0.99 & 0.94 & 0.90 & 4 & 0.93 & 0.84 \\ 0.87 & 0.91 & 0.96 & 0.97 & 0.83 & 3 & 5 & 0.90 & 0.95 & 0.93 & 3 & 0.98 & 0.91 \\ 0.96 & 0.94 & 0.95 & 0.97 & 0.95 & 4 & 4 & 0.94 & 0.95 & 0.85 & 4 & 0.95 & 0.90 \end{bmatrix},$$

normalizing which can generate:

$$R_{3\times 13} = \begin{bmatrix} 0.95 & 0.98 & 0.94 & 1 & 0.89 & 1 & 1 & 0.91 & 1 & 0.96 & 1 & 0.95 & 0.92 \\ 0.91 & 0.96 & 1 & 0.98 & 0.88 & 0.6 & 1 & 1 & 0.98 & 1 & 0.75 & 1 & 1 \\ 1 & 1 & 0.97 & 0.98 & 1 & 0.8 & 0.8 & 0.95 & 0.99 & 0.91 & 1 & 0.97 & 0.99 \end{bmatrix}.$$

Third, the positively ideal point and negatively are ascertained based on (2):

$$\begin{aligned} r+ &= (1,1,1,1,1,1,1,1,1,1,1,1,1), \\ r- &= (0.91,0.96,0.94,0.98,0.88,0.6,0.8,0.91,0.98, \\ &91,0.75,0.95,0.92). \end{aligned} \quad 0.$$

Finally, we, recurring to these formularies from (7) to (10), figure out the composite correlative degree between A_i and the ideal scheme: $\beta = (\beta_1, \beta_2, \beta_3) = (0.92, 0.94, 0.93)$. Evidently, software A_2 enjoys the highest trustworthiness, confirmed by $\beta_2 = 0.94$, closest to 1, in conformity with the argument from some current literature.

V CONCLUSIONS AND PROPOSALS

The contribution of this paper is to provide an evaluation of software trustworthiness. We extend the current analysis by employing Grey correlation methodology as most current literature on software trustworthiness assessment, suffers from incompleteness in the estimation of trustworthiness values. This allows the study to improve accuracy through trapezoidal fuzzy number, lessening negative effects of expert subjectivity on indicator weight estimation. The proposed methodology is proved to be of validity, rationality and appropriate amount of calculation and worthwhile to be applied into more studies on software trustworthiness.

However, a number of issues should be addressed in software trustworthiness evaluation. Among these are critical technology development and research for modern methods such as meta model, data processing and quantification. Also of interest would be designing a set of decision-making rules, which need to be refined and optimized. With regard to a certain specific software, index framework should be established on the footing of demand for reliability as disparities in the selection of indicator frameworks may induce the degree of correlation to be variable, exerting impacts on final results. At last, more research can be done to better capture attributes' own interactions and mechanisms whereof.

ACKNOWLEDGMENT

The authors are thankful to the national social science foundation of China under grant No.17BJL005.

REFERENCES

- [1] B.Steffen, H.Wilhelm, P. Alexandra, Trustworthy software systems:a discussion of basic concepts and terminology, ACM SIGSOFT Software Engineering Notes Archive. 31(2006) 1-18.
- [2] T.Bao, S.F.Liu, X.Y.Wang, Research on trustworthiness evaluation method for domain software based on actual evidence, Chinese Journal Of Electronics. 20(2011) 824-851.
- [3] V. Basiliv, P. Donzelli, S.Asgari, A unified model of dependability: capture dependability in context, IEEE Software. 21(2004) 19-25.
- [4] B.Whitworth, J Fjermestad, D.Mahinda, The web of system performance, Communications of the ACM.49(2006) 93-99.
- [5] G.Water, Software dependability evaluation based on markov usage models, Performance Evaluation.40(2000) 199-222.
- [6] Y. Zhang, B.Fang, C.Y. Xu, Trustworthy Metrics Models for Internet Ware, Wuhan University Journal of Natural Sciences. 13(2008) pp. 547-552.
- [7] A. Immonen,M. Palviaine, Trustworthiness evaluation and testing of open source components, in: QSIC 07Proceedings of the Seventh International Conference on Quality Software, IEEE Computer Society ,Washington,2007, pp316-321.
- [8] Sh. Ding, F.J. Lu, Sh. L.Yang, A Requirement-driven software trustworthiness evaluation and evolution model, Journal of Computer Research and Development. 48(2011) 647-655.
- [9] H.Q.Zhao, J. Sun, A methodological study of evaluating dependability of SOA software system,Chinese Journal of Computers.33(2010) 2202-2210.
- [10] S.B.Cai, Y. Zh. Zou, L. S. Shao, Framework supporting software assets evaluation on trustworthiness, Journal of Software. 2(2010) 359-372.
- [11] J.P. Li, M.L. Li, D.S.Wu, H.Song, An integrated risk management and optimization model for trustworthy software process management, The Journal of Systems and Software. 89(2014) 63-75.
- [12] D. Lizcano, J.Soriano, G.Lopez, J.J.Gutierrez, Automatic verification and validation wizard in web-centered end user software engineering, The Journal of Systems and Software.125(2017) 47-67.
- [13] Q. Zhao, H. Q.Wang, G.Sh. Feng, Measuring method of software dependability based on Pi calculus, Journal of Jilin University: Engineering and Technology Edition.41(2011) 1685-1689.
- [14] X.H.Yang, Zhou X.H. Zhou, J.F. Tian, Novel dynamic trusted evaluation model of software behavior, Journal of Chinese Computer Systems.31(2010) 2113-2120.

Study on Scientific Location Level Classification and Optimization Methods of Military Equipment Maintenance Support Sites Network

Gong-da Yan, Peng Dong, Wei Lu and Peng Yu

Dept. of Management Engineering and Equipment Economic, Naval Univ. of Engineering, Wuhan 430033, China

Abstract—The scientific location of military equipment maintenance support sites problems are concerned by scholars. We study how to solve the location level classify without participation of experts, by setting up Hopfield neural network module, designing concrete computational procedures, and finally illustrating though an application case. The study can provide simple and practical theories and methods' reference for our military equipment maintenance support sites activities.

Keywords—Military equipment; Maintenance support sites; Location level classify

I. INTRODUCTION

The level of military equipment maintenance support sites are influenced by many aspects of the indicators [1], because these indicators are both qualitative and quantitative, and in different time, the dominant positions are also different for the imparity of military situation, so the relation of maintenance support sites' level and indicators are nonlinear in a certain time period. The study on military equipment maintenance support location based on neural network provides a new scientific ideas for location selection problems, and solves the problems about how to carry out the location selection without experts. In the absence of experts evaluation of maintenance support sites of the practical work level to select location can take use of historical data, through Hopfield neural network training, stimulating experts thinking, evaluating level of military maintenance support sites, and finally providing the basis for choosing the good maintenance support sites.

II. ANALYSIS OF THE SCIENTIFIC LOCATION LEVEL CLASSIFICATION BASED ON HOPFIELD NEURAL NETWORK

A. The Basis Theory Analysis of Hopfield Neural Network

Neural networks have been applied in many areas and location problems is a typical kind of decision problem [2, 3]. Hopfield network is a fully connected model of neural network, using structure features and method of study different from stratum neural network, stimulating memory mechanism of the biological neural network, and obtain satisfactory results [4]. The network and the learning algorithm was first put forward by American physicist in 1982, so it's called Hopfield neural network.

Network structure. Binary Neural Network was first proposed by Hopfield, the output of the neuron only take value of 1 and -1, so it was also called Discrete Hopfield Neural Network, DHNN is a feedback network which is a single layer

and the output is binary. For binary neurons, it's computation formula is as follows:

$$u_j = \sum w_{ij} y_i + x_i \quad (1)$$

x_i means external output, and there also have:

$$\begin{cases} y_j = 1, u_j \geq \theta_j \\ y_j = -1, u_j < \theta_j \end{cases} \quad (2)$$

A DHNN network state is the collection of information about output neural network, it's n neurons network for an output layer, which the status is a n-dimensional vector when it's time t.

$$Y(t) = [y_1(t), y_2(t), \dots, y_n(t)]^T \quad (3)$$

Because $y_i(t)$ ($i = 1, 2, \dots, n$) can take value of 1 or -1, n-dimensional vector $Y(t)$ has 2^n kinds of state, namely the network has 2^n kinds of states. Using $y_i(t)$ to represent the first j neurons, namely node j is in the time t state, thus the node's next time t+1 state can pray:

$$y_i(t+1) = f[u_j(t)] = \begin{cases} 1, u_j(t) \geq 0 \\ -1, u_j(t) < 0 \end{cases} \quad (4)$$

$$u_j(t) = \sum_{i=1}^n w_{ij} y_i(t) + x_j - \theta_j \quad (5)$$

If w_{ij} equals to 0 when $i=j$, it's means that the output of a neuron will not feed back to its input, then DHNN is called no-feedback neural network. If w_{ij} is not equal to when $i=j$, it means that the output of a neural will feed back to its input, then DHNN is called self-feedback neural network.

Network workings. Hopfield network operates according to dynamics methods, it's working process is the evolution of the state of the neurons, that is, evaluating according to the direction of the "energy" (Lyapunov function) reduction from the initial state, until reach to a steady state, this state is the output of the network. There have two mainly forms of Hopfield network' workings:

a) Serial (asynchronous) working. At any time t, only a certain neuron i changes in accordance with formula (4) and formula (5), and other neurons' states are not changed.

b) Parallel (synchronous) working. At any time t , the state of part of neurons or whole neurons will change in the meantime.

Network stability. Network stability is defined as: if the network is stable at some point, the state will no longer change, says that the network is in steady state.

$$v(t + \Delta t) = v(t) \quad \Delta t > 0 \quad (6)$$

Can be seen from the structure of DHNN: it is a kind of multiple input and contains Kan value of binary nonlinear dynamic systems. In the dynamic system, balanced steady state can be understood as a system's some kind of energy function in the process of system movement, it's energy declining and at last in a minimum value. Coben and Crossberg have given the sufficient conditions about Hopfield network' stability, pointed out that if Hopfield network' weight matrix W is a symmetric matrix, and the diagonal element is 0, the network is stable. That is, in the weight matrix W , if:

$$\begin{cases} w_{ij} = 0, i = j \\ w_{ij} = w_{ji}, i \neq j \end{cases} \quad (7)$$

B. The Applicability Analysis of Hopfield Neural Network

Military equipment maintenance support sites level are divided into base level maintenance support sites, relay level maintenance support sites and grass roots level maintenance support sites. In the location task, generally, only base level maintenance support sites and the more important relay level maintenance support sites have the condition of experts' participating and assisting decision-making. In other conditions, maintenance support sites' location only can be got by authority leadership and supervisor through experience.

But it will give us great convenience and scientific basis if using neural network to assist decision-making [5,6]. Using neural network to solve location problems, assuming that there has a complex function relation between the conditions of maintenance support sites and the decision-making of maintenance support sites, it can be got through on-the-spot investigation and research by experts. Then, through neural network, using experts' successful location history as the training data, then the function relation can be fitted. The training is actually through the theory formula of the neural network, carrying on the function' multiple fitting one by one, closing to the experts' location function obtained by calculation. As a result of the function fitting of the neural network can be trained for many times to get close to the primitive function, considering the progress of computer technology and computational speed, thus through the computer to design neural network, the error between the function we fit and the function of experts can be infinitely narrow. Therefore, neural network can help us to make decisions.

C. The Location Requirement Analysis of Military Equipment Maintenance Support Sites

All kinds of construction requirements generally include the following aspects:

Invisibility. Avoiding foreign investigation at ordinary times is to prevent leaks in the enemy spy operations; avoiding enemy attack in wartime is to ensure our military equipment to be repaired and got "regeneration", thus can be put into battle again.

Defense. It should have a certain capability of defense for more important military equipment maintenance support sites, in order to reduce the damage of enemy attack and our military casualties, ensure support sites have a certain capability of maintenance support.

Land prices. With the development of economy, it has to take cost into account. Today, even the military land also appears the difficulties of land requisition, and our military spending is limited after all, it can't be squandered at will. Therefore, land prices should be taken into account when we site.

Environment. Military equipment maintenance support sites location should be avoided setting up in high temperature, damp or other bad environment as far as possible, so as not to speed up the equipment wear and tear. It should be avoided setting up in busy streets or poor folk custom villages and towns, lest appearing leaks or dispute of military and civilian.

Hydrology. Military equipment maintenance support sites should be set up in coastal, along the river or around the terminal for large equipment or imported equipment in need of water.

Transportation. Good transportation is the need of carriage at ordinary times, but good transportation is necessary for operational security or dangerous evacuation in wartime. Transportation should be taken into consideration when locating support sites.

Area. According to the requirement put forward by equipment support management and user department, organizing related experts to determine after system demonstration, ensuring the area of military equipment maintenance support sites can meet the function of maintenance support sites, and adequate facilities can be equipped with for military equipment maintenance support.

Energy. Military equipment maintenance support sites should be set up in the place with enough energy supply, especially for higher degree support sites, on account of some large maintenance support equipments have huge consumption, therefore, energy has to be taken into account.

III. THE ANALYSIS OF MODEL BUILDING BASED ON HOPFIELD NEURAL NETWORK

Based on the analysis above, equipment maintenance center location mainly considers eight factors: hidden, defense, land prices, environment, hydrology, transportation, area and energy. Under the condition of hypothesis above indicators, designing calculation steps as shown in figure 1.

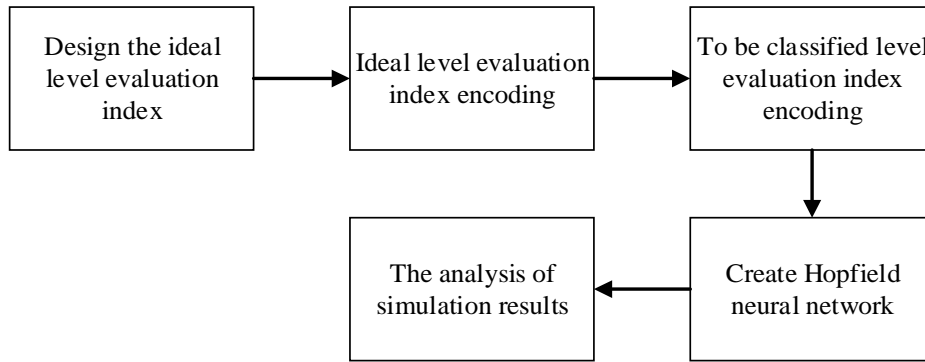


FIGURE I. THE FLOW CHART OF ESTABLISHED MODEL BASED ON HOPFIELD NEURAL NETWORK

Design the ideal level evaluation index. Assuming that there have ten historical schemes, fuzzy evaluation matrix is obtained by expert scoring method, if the scoring is on percentage system, to be normalized for table 1.

Ideal level evaluation index encoding. The states of discrete Hopfield neural network neurons are only 1 or -1, so it needs to be encoded when mapping evaluation index for the state of neurons. Coding rule is: when it is greater than or equal to the level of respect, the corresponding neurons state set to "1", otherwise set to "-1".

Assuming that there have four evaluation schemes, history scheme is divided into four grades. Put each evaluation index average of each sample as the ideal evaluation index of each level. Namely, the balance of Hopfield neural network, such as the table 2. Corresponding four level evaluation indexes encoding of grade A, B, C, D.

To be classified level evaluation index encoding. Four scheme indexes to be evaluated shown as table3. The data of the scheme can be obtained by previous record query, can be obtained by professional field, and can also be obtained by the experience of authority department and supervisor, if the score is not between 0 and 1, the data can be normalized between 0 and 1, and code in the end, the coding result is shown in figure 3.

Create a network. After designing five ideal level evaluation indexes and encoding, using neural network toolbox built in MATLAB to create three type Hopfield neural network [7,8].

Using the function `newhop()` of MATLAB neural network toolbox, the weight correction method the function using is the orthogonalization:

Step 1: input N input modes $t = \{t^2, t^2, \dots, t^N\}$ and parameters τ, h .

Step 2: calculate $A = \{t^2 - t^N, t^2 - t^N, \dots, t^{N-1} - t^N\}$.

Step 3: do singular value decomposition for A, and calculate the rank of $AK = \text{rank}(A)$.

Step 4: calculate $T^P = \sum_{i=1}^K u^i(u^i)^T$ and $T^m = \sum_{i=K+1}^N u^i(u^i)^T$ by respectively using formula $U^P = \{U^1, U^2, \dots, U^K\}$ and $U^m = \{U^{K+1}, U^{K+2}, \dots, U^N\}$.

Step 5: calculate $W^n = T^P - \tau \times T^m$ and $b^t = t^N - W^n \times t^N$.

Step 6: calculate $W = \exp(h \times W^t)$.

Step 7: calculate $b = U \times \begin{bmatrix} C_1 \times I(K) & 0(K, N-K) \\ 0(N-K, K) & C_2 \times I(N-K) \end{bmatrix} \times U^T \times b^t$, in which $C_1 = \exp(h) - 1$ and $C_2 = -[\exp(-\tau \times h) - 1]/\tau$.

Simulation and analysis. After creating a network, put the four to be classified scheme evaluation indexes as the input of Hopfield neural network, through the study of the agreed number, the policy results can be obtained. The simulation structure is as follows in figure 4. From the results, plan 1 belongs to class A, plan 2 belongs to class B, plan 3 and plan 4 both belong to class C. Thus the choice is plan 1.

TABLE I. GRADE EVALUATION INDEXES OF EACH SCHEME

Index Scheme \	Hidden	Defense	Land prices	Environment	Hydrology	Transportation	Area	Energy	Conclusion
Scheme 1	1.00	1.00	1.00	1.00	1.00	1.00	1.00	1.00	1.00
Scheme 2	0.80	0.87	0.89	0.82	0.78	0.80	0.75	0.33	0.79
Scheme 3	0.67	0.93	0.22	0.75	1.00	0.80	0.49	0.66	0.74
Scheme 4	0.92	0.72	0.67	0.66	0.56	0.80	0.75	0.69	0.91
Scheme 5	0.87	0.93	1.00	1.00	1.00	1.00	1.00	1.00	0.96
Scheme 6	0.80	0.72	0.89	0.82	0.89	0.80	0.75	1.00	0.83
Scheme 7	0.67	0.72	0.67	0.66	0.67	0.60	0.49	0.66	0.69
Scheme 8	0.72	0.80	0.78	0.75	0.78	0.80	0.75	0.66	0.75
Scheme 9	0.60	0.60	0.56	0.58	0.56	0.60	0.49	0.66	0.58
Scheme10	0.47	0.47	0.44	0.41	0.44	0.40	0.49	0.35	0.51

TABLE II. IDEAL FOUR LEVEL EVALUATION INDEXES

Index Level \	Hidden	Defense	Land prices	Environment	Hydrology	Transportation	Area	Energy
A	0.8780	0.8480	0.8900	0.8600	0.8460	0.8800	0.8040	0.8500
B	0.5480	0.7960	0.5580	0.7320	0.7800	0.6800	0.5940	0.4920
C	0.2820	0.2940	0.2860	0.2440	0.2380	0.2640	0.2660	0.2940
D	<0.2820	<0.2940	<0.2860	<0.2440	<0.2380	<0.2640	<0.2660	<0.2940

TABLE III. FOUR SCHEMES TO BE CLASSIFIED LEVEL EVALUATION INDEXES

Index Scheme \	Hidden	Defense	Land prices	Environment	Hydrology	Transportation	Area	Energy	conclusion
Scheme1	0.9200	0.8000	0.8900	0.9200	0.8900	0.8000	1.0000	1.0000	\
Scheme 2	0.5200	0.8000	0.6700	0.8200	0.7800	0.6000	0.4900	0.7200	\
Scheme 3	0.6700	0.5200	0.4900	0.3200	0.4900	0.4000	0.1900	0.2900	\
Scheme 4	0.0800	0.2300	0.4600	0.3200	0.2900	0.3000	0.5400	0.3300	\



FIGURE II. IDEAL FOUR LEVEL EVALUATION INDEXES ENCODING

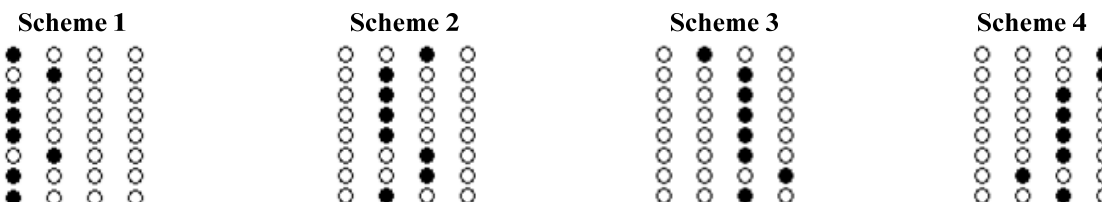


FIGURE III. FOUR SCHEMES TO BE CLASSIFIED LEVEL EVALUATION INDEXES ENCODING

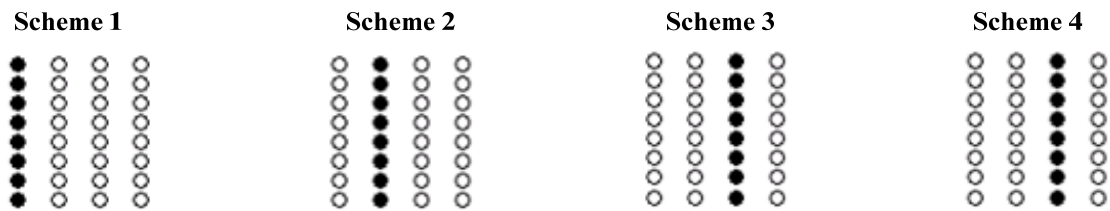


FIGURE IV. FOUR SCHEMES TO BE CLASSIFIED LEVEL EVALUATION INDEXES ENCODING SIMULATION RESULTS

IV. CONCLUSION

This paper has mainly studied level classification problems of military equipment maintenance support sites. The location model aims to combine neural network with military maintenance support sites, so that the location task can be completed better and more quickly, especially at the basic level of equipment maintenance support sites in the absence of experts. Therefore, it has great important realistic significance and economic interests of the military for accelerating the formation of weapons and equipment's fighting effectiveness and security capabilities.

ACKNOWLEDGEMENT

This work is supported by Naval Engineering University Research Funding Project under Grant 20161613 and 20161614.

REFERANCES

- [1] HUANG Yi-jia. A few questions need to be focused on our military equipment maintenance support power constriction under the condition of informatization. *J. Equipment*, 2007, 1(3): 2-3.
- [2] HE Yu-bing, LI Xin-zhong. Neural network control technology and application. M. Science Press, 2000.
- [3] WANG Xu, WANG Hong, WANG Wen-hui. Artificial neural network theory and application. M. Shenyang: Northeastern University Press, 2000.
- [4] LI Guo-hui. The enterprise competitiveness evaluation model based on Hopfield neural network. *J. Computer Science*, 2011, 38(10): 1-2.
- [5] WANG Wei. Artificial neural network theory—introduction and application. M. Beijing: Beijing University of Aeronautics and Astronautics Press, 1995.
- [6] F. Fnaiech, D. Bastard, V. Buzenac, R. Settineri, and M. Najim. A fast Kalman filter based new algorithm for training feedforward neural networks. *J. Proc. EUSIPCO 94*, Edinburg, U.K, 1994, 9: 13-16.
- [7] GE Zhe-xue. Neural network theory and MATLAB R2007 implementation. M. Beijing: Electronic Industry Press, 2007.
- [8] SHI Feng, WANG Xiao-chuan, YU Lei. Thirty cases analysis of MATLAB neural network. M. Beijing: Beijing University of Aeronautics and Astronautics Press, 2002.

The Application of Circular Collision Detection and Target Tracking to Improve the Collision Accuracy in 2D Games

Jungyoon Kim¹, Jiyong Ge², Zhixiao Wang² and Wonhyung Lee^{2,*}

¹Graduate School of Game, Gachon University, 1342 Seongnam Daero, Sujeong-Gu, Seongnam-Si, Gyeonggi-Do, South Korea.

²Graduate School of Advanced Imaging Science, Multimedia and Film, Chung-Ang University, 84 Heukseok-ro, Heukseok-dong, Dongjak-gu, Seoul, South Korea.

*Corresponding author

Abstract—Interaction design, as the language between game and player, plays an important role in the whole game design. This paper introduces a 2D flying shooting game which is a combination of Arduino integrated circuit equipment and Processing programming software, and players can control the game by the PS2 joystick or computer keyboard. The application of circular collision detection technology and target tracking algorithm greatly improves the collision accuracy.

Keywords—collision accuracy; circular collision detection; target tracking

I. INTRODUCTION

At present, playing video games is a popular way for people to reduce the pressure of their lives. And there are two categories of game products in current market: software game and hardware game. However, game development in the future must be a combination of hardware and software. The interactivity of modern game design will determine the fate of the game.

In addition, how to detect collision is a technical problem that most competitive games need solving. To solve the problem, a variety of algorithms and techniques have been developed to improve the accuracy and efficiency of collision detection in related research fields.

This paper presents a 2D shooting game based on hardware and software development platform. Two techniques are employed in the game: circular collision detection and target tracking. Compared with the rectangular collision detection and pixel collision detection method, circular collision detection is easy to find a balance between speed and accuracy. The target tracking algorithm gives boss monster sprites the function of tracking the master sprite in the game.

II. RELATED WORKS

Shooting game is a very popular game type and is also a kind of action game [1]. There are many ways to realize shooting game, such as FPS shooting game based on Unity3D, 2D shooting game based on iOS, flight shooting game based on Android. Moreover, there are many popular development

languages in game development, including C/C++ language, C# language, Java language, assembler language and so on [2].

In this paper, the proposed shooting game uses software platform and hardware platform for serial communication. The hardware platform is composed of Arduino UNO integrated circuit board and PS2 joystick module, and the software platform mainly uses the Processing (programming language) which is based on the Java programming language.

III. THE RESEARCH RELATED TO ARDUINO PROGRAMMING

Arduino is an open source electronic prototype platform with resource expansion and artistic experience. It mainly includes Arduino board and Arduino IDE software programming platform [3]. The Arduino platform, developed by a European development team in the winter of 2005, has the features of simplicity, rapid development. In addition, it can drive motors, LEDs, sensors and other components. Therefore, the Arduino microcontroller is often used as an open source programmable tool to create interactive work [4]. As shown in Fig. 1, The Monet painting in the canvas accepts the photosensitive resistance of the Arduino controller, and the stronger the light is detected, the brighter the oil painting will be. On the contrary, the darker it becomes. This is a classic example of Arduino programming.

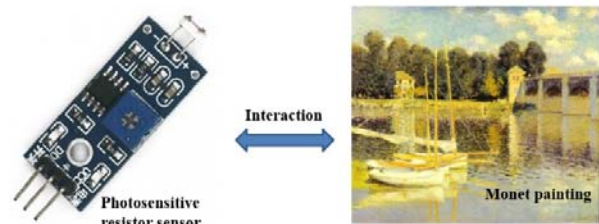


FIGURE I. THE TRANSFORMATION OF LIGHT IN MONET'S OIL PAINTING

Arduino is often used as a microcontroller in game development. This game uses Arduino board and PS2 joystick module to make a game microcontroller as Fig. 2.

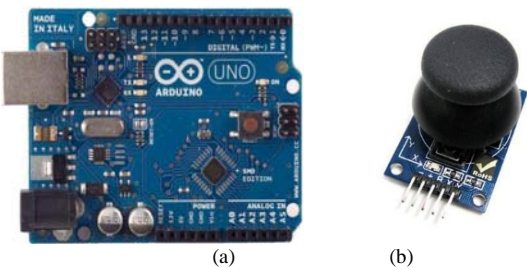


FIGURE II. (A) ARDUINO CIRCUIT BOARD (B) PS2 JOYSTICK MODULE

The Arduino hardware module connects to the computer through the USB data line, and it can realize and communicate with the Arduino IDE software platform. In the game, players can choose to use joystick or keyboard to control the direction of movement of the master sprite. The master sprite represents the role of the player in this game.

IV. APPLYING PROCESSING IN GAME DESIGN

Processing is an interactive graphical programming language used in the electronic art, media art and visual interaction design [5]. Compared with some other high-level languages, Processing is more specialized and easier to use. At present, although Processing has not been widely used in large-scale game development, with superior image processing and modeling capabilities, it can create exquisite game characters and improve the comfort of the game screen. This makes it have great potential in the field of game development.

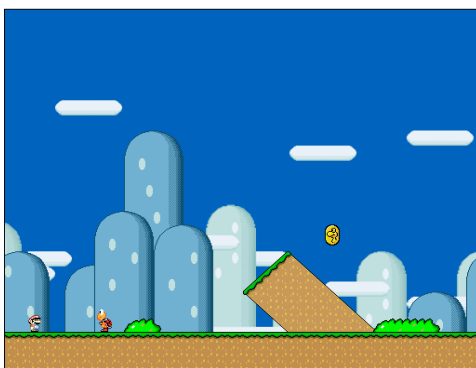


FIGURE III. MARIO GAME

It can design many interactive games through using Processing. As follows, Fig. 3 is a Mario game. The flight shooting game designed in this paper uses Processing to load the master sprite and a variety of different monster sprite models, design the corresponding game scene, add the appropriate background sound, and simulate the impact explosion effect.

Arduino programming and Processing programming can be well applied into video games. The following content will analyze how to improve the game interaction through the platform of Arduino and Processing.

V. OBJECT COLLISION AND DETECTION METHOD

Collision detection is a question that needs to be solved in many fields, including robot motion, animation simulation, computational geometry, virtual reality games [6]. Collision detection typically refers to the computational problem of detecting the intersection of two or more objects [7]. The traditional collision detection algorithm, which is the most basic collision detection algorithm, needs to traverse all the basic set elements. Therefore, the disadvantage is the low-efficiency of the operation.

The effect of video game must conform to the physical laws of the world. Therefore, collision detection is an unavoidable problem in game creation. This paper focuses on the collision detection problem in 2D games. There are many kinds of collision detection methods in the 2D games, such as rectangular detection, circular detection, pixel detection and so on.

The collision detection of general rules can be processed into rectangular collision. The principle is to determine whether the two rectangular regions overlap [8]. And the diagrammatic sketch is illustrated in Fig. 4. If the side rectangle intersects with the center, it will be considered as a collision.

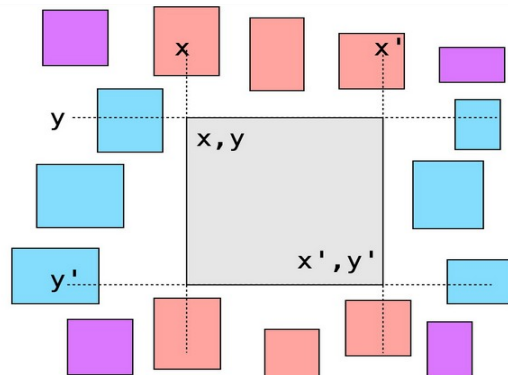


FIGURE IV. RECTANGULAR COLLISION DETECTION

Rectangular collision detection algorithm is a rough collision detection method, which is not suitable for collision detection among irregular objects. Compared with rectangular collision detection, choosing circular collision detection is much better. Its detection principle is to determine whether the distance between two circle's centers is greater than the sum of two different radii [9], as shown in Fig. 5.

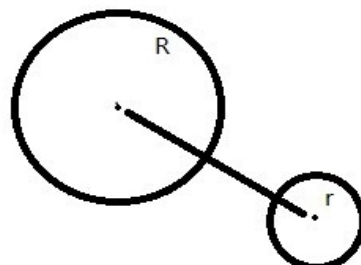


FIGURE V. CIRCULAR COLLISION DETECTION

Pixel detection is one of the most accurate detection methods. The test method is to check and compare each pixel of the two graphs. Although the precision of pixel collision detection is high, the operation efficiency is very low. As the range and type of each algorithm are different, it is necessary to choose the appropriate collision detection algorithm. After testing and analysis, the circular collision detection is the most suitable algorithm for 2D games.

VI. THE APPLICATION OF CIRCULAR COLLISION DETECTION AND TARGET TRACKING IN GAME DESIGN

Compared with other algorithms, the circular collision detection algorithm is simple to calculate. In addition, it not only ensures the detection accuracy, but also improves the detection speed. The result is shown in Fig. 6.

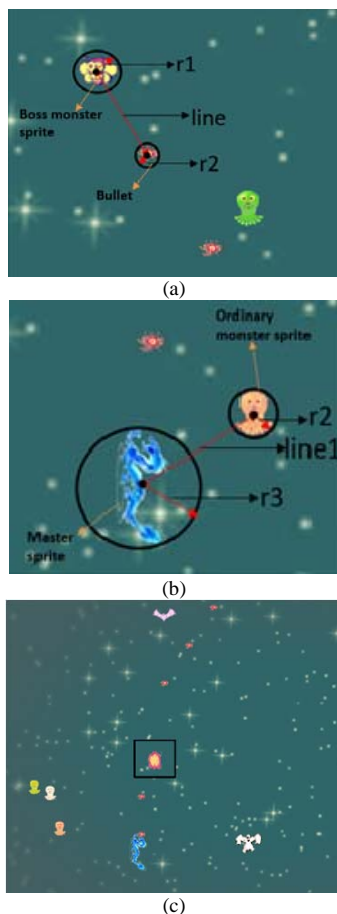


FIGURE VI. CIRCULAR COLLISION DETECTION: (A) MONSTER SPRITE AND BULLET (B) MONSTER SPRITE AND MASTER SPRITE (C) COLLISION EXPLOSION

From the Fig. 6 (a), an explosion can't be seen when the sum of radius r_1 and radius r_2 is less than the line which is the distance between monster sprite and bullet. Otherwise, the players can see that. Fig. 6(b) is similar with Fig. 6(a). Fig. 6(c) is the explosion effect during the collision.

Moreover, the target tracking algorithm is also used in this game. When the boss monster sprite appears, it will judge the

coordinate of the master sprite firstly, and then move close to it until boss monster sprite was destroyed or collision happened. The tracking demo has been shown in Fig.7.

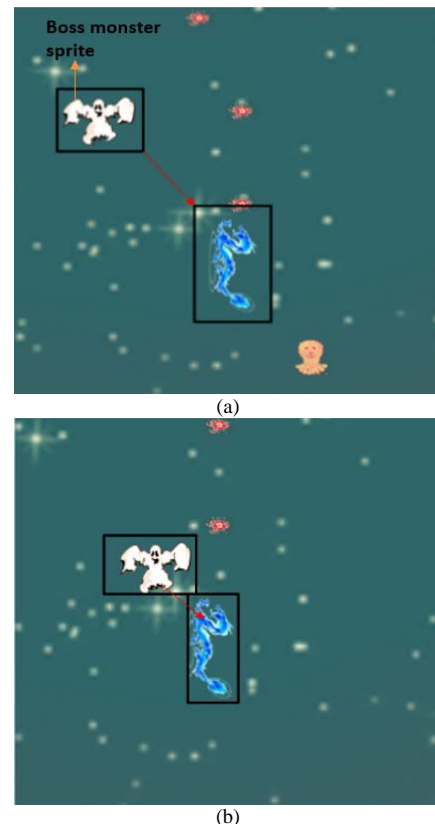


FIGURE VII. TARGET TRACKING

Moving object detection and tracking is a process that combines the image pattern recognition and image tracking method to detect the target in the image sequence, and it is a hot topic in the field of computer vision. It mainly involves digital image processing, statistics, cognitive science, computer science and many other fields [10]. Therefore, it has a strong theoretical and practical value. This technology is fully applied to the game design in this paper.

VII. SUMMARY

This paper proposes a method to realize 2D flying shooting game based on the Arduino hardware platform and Processing software platform. Through the serial port, the game fully integrates the electronic technology, SCM technology and graphics programming technology.

Meanwhile, the application of circular collision detection and object tracking algorithm enriches the game plot and enhances the collision accuracy. Furthermore, the game player can interact with the game to enjoy the fun and ease the pressure.

ACKNOWLEDGEMENT

This research is supported by Ministry of Culture, Sports and Tourism (MCST) and Korea Creative Content Agency (KOCCA) in the Culture Technology (CT) Research & Development Program 2017 (R2017030062_00000001) and Industry-Academic Cooperation Foundation of Chung-Ang University.

REFERENCES

- [1] Information on https://en.wikipedia.org/wiki/Shooter_game/
- [2] Information on https://en.wikipedia.org/wiki/Game_programming
- [3] Yusuf Abdullahi Badamasi, The working principle of an Arduino, IEEE, 11th International Conference on Electronics, Computer and Computation, 2014.
- [4] A. M. Gibb, NEW MEDIA ART, DESIGN, AND THE ARDUINO MICROCONTROLLER: A MALLEABLE TOOL, Master's thesis, Pratt Institute, Feb.2010, pp. 1-6.
- [5] Information on [https://en.wikipedia.org/wiki/Processing_\(programming_language\)/](https://en.wikipedia.org/wiki/Processing_(programming_language))
- [6] R. Boulle, A. Luciani, Collision detection algorithm, a handbook of terms, Enactive Systems Books, 2007, pp. 44-45.
- [7] Information on [https://en.wikipedia.org/wiki/Collision_detection/](https://en.wikipedia.org/wiki/Collision_detection)
- [8] Information on <http://compsci.ca/v3/viewtopic.php?t=13661>
- [9] Kaiqiang Guo, Jiewu Xia, An Improved Algorithm of Collision Detection in 2D Grapple Games, Third International Symposium on Intelligent Information Technology and Security Informatics, 2010, pp. 328-331.
- [10] Xiao-Feng Tong, Han-Qing Lu, Qing-Shan Liu, An effective and fast soccer ball detection and tracking method, Proceedings of the 17th International Conference on Pattern Recognition, 2004. ICPR 2004.

Research on the Protection and Reconstruction of the Landscape Heritage Based on Digital Reduction Technology

—Taking AD1837 as an Example of the Huangci Bridge in Qing Dynasty in Nanning, Guangxi

Chongen Wang and Shaojie Wang

The Main Building of Forestry Cadre School, No. 23, No. 63 South District, South inner ring, Yingze District, Taiyuan City, Shanxi, 030012

Abstract—This paper is based on digital reduction technology and from the perspective of ancient bridge protection and the surrounding environment landscape reconstruction, putting forward to the methods of landscape heritage protection and reconstruction. And the second through the field investigation, this paper analyzes current situation of the Huangci Bridge ontology and the surrounding environment, the problems can roughly be divided into three categories, and then summarize and put forward the corresponding solutions. The article finally through the establishment of the model to the emperor gave bridge garden heritage. Lastly, through the establishment of the model, the paper presents the reconstruction design of the heritage and the surrounding environment of the Huangci Bridge Landscape and summarizes the methods of reconstruction for the same type's protection and reconstruction reference.

Keywords—Huangci Bridge; landscape heritage; reconstruction

I. FOREWORD

“A river spawned a flourishing street.” This is how the local people praised the Xinjiang market street. More than 170 years ago, in the riverfront of today’s Xinjiang county, Yongning district, Nanning, Guangxi province, businessmen clustered, formed the thriving Xinjiang market. The bridge, the quay, the salt shops, the hotels and the stables, all together, painted the Huangci bridge a splendid picture. To promote its traditional culture and national spirit, the local government developed an unique historical and landscape heritage, radiates from the Huangci Bridge and the Xinjiang Grand Quay, that is rife of special features of its own. This article, through a systematic analysis of the Huangci Bridge, the Xinjiang Grand Quay and their peripheral buildings and environment, attempt to revive the prosperity of the Huangci Bridge historical and landscape heritage.

Huangci Bridge historicalal landscape heritage is located in the north of Xinjiang Street, Xinjiang county, 32 kilometers southeast of downtown of Nanning City. The bridge was built in 1837, the 17th year of the reign of Daoguang Emperor, Qing Dynasty. It was then reconstructed in 1987 by the local

government. In 1989, the local government of Yongning county pronounced the Huangci Bridge as Protected Cultural Relic Unit of Yongning county. The government later decided to rebuild the historical quay of an ancient salt route and rename it Xinjiang Grand Quay. In 2009, the bridge was announced to be a Protected Cultural Relic Unit of Nanning city. Its Protected Area extends outwards 20 meters of the bridge’s perimeters, and the Development Control Area extends outwards 100 meters of the bridge’s perimeters. Huangci bridge is 60 meters long, 8 meters wide and 14 meters high. It is a typical official style stone arch bridge of Qing dynasty. The value of Huangci Bridge have high value of historical, artistic, scientific and social.

II. ANALYSIS OF THE STATUS QUO

The Huangci historical landscape heritage includes material entities, material space, surrounding area and the overall layout within the protected zone and the development control area. Nevertheless, the Huangci Bridge and Xinjiang Grand Quay suffer from some problems, which can be categorized under three types, namely, structural safety, integrity, and historical continuity.

III. STRUCTURAL SAFETY

A. The Structural Issues of the Huangci Bridge

The bridge was reconstructed from curved arch bridge to flat arch bridge in 1987. Ostensibly, brackets (beam) and beams were added to the bridge to enforce its structural integrity, but these actually damaged the structure of original design. Furthermore, the new bridge’s design did not incorporate a scientific drainage system, caused the bridge to be eroded by rainwater as it sits in a rainy area. Year after year, the bridge deck became rough, the bridge body is covered with moss, and the load-bearing wall of the west arch even has a 1 cm wide, 800 cm high crack, which seriously affects the integrity and durability of the structure (Figure 1).

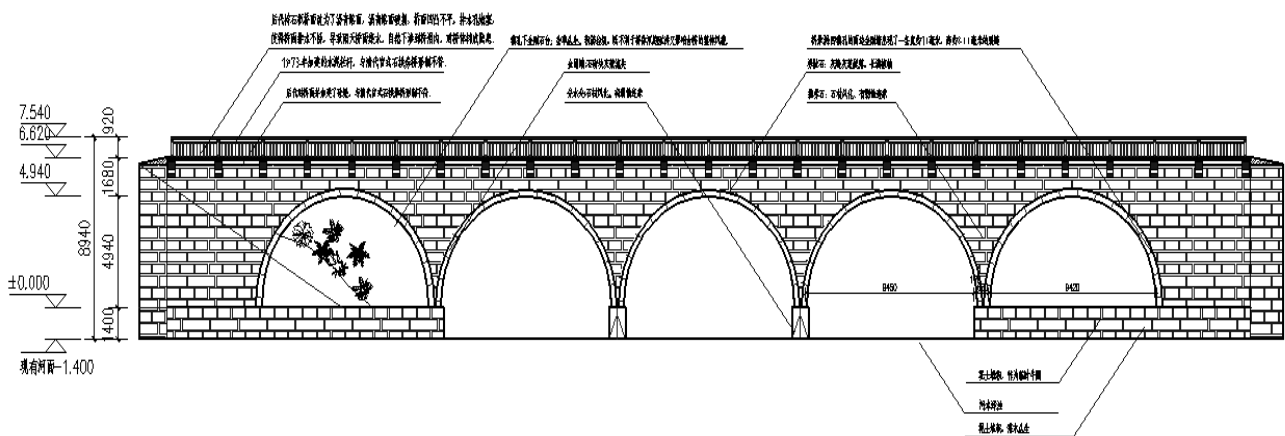


FIGURE I. THE PRESENT SITUATION SURVEY MAP OF THE HUANGCI BRIDGE

B. The Structural Issues of Xinjiang Grand Quay

The Xinjiang Grand Quay was renovated in 1995, over 30 steps of cascading brick stairs stretches from the road to the river. This design made the part of the quay which is in the same section with the opening of the east arch of the bridge higher than the (water) level under that arch, which in turn affected the flood discharging capacity of the east arch opening during the wet season.

C. Problems with the Surrounding Area

The banks of the river are made of soil. Mud and vegetation are flooded into the river during wet seasons. This elevated river bed and silt up the stream, and thus water level rises and river flow becomes impeded. In addition, there is no mound between the road. These factors all cause potential safety hazards to the Huangci Bridge historical and landscape heritage.

D. Integrity

It is learnt by referring relevant documents and interviewing local elderly residents, in building the original bridge, the original bridge railings (now reconstructed as cement railings) and the gazebo for the stele (now reconstructed as a terrace and the plaque with inscription attached to a short all) were not built in accordance to the original design, due to funding shortage and social instability. In addition, the detention/retention basin was overgrown with weeds and piled with garbage, which spoiled the view of the bridge and damages its flood discharge capacity, especially during wet seasons. The natural banks of the river are made of soil, with no revetments built. During wet seasons, mud, garbage and vegetation are flooded into the river, causing river bed to elevate and silting up the river. All of these negatively affect the Huangci Bridge historical and landscape heritage's coordinated integrity.

IV. RESTORATION METHODS

A. Structural Safety

The structural safety of the Huangci Bridge and the Xinjiang Grand Quay should be first made sure before it is attempted to revive the landscape.

The Huangci bridge itself could be, by structural analyses based on information gleaned from investigations and surveys, restored with the curvy horizontal design. The original design ensures a combination of scientific overall structure and elegant curves. Meanwhile, consolidate the foundations, mend the cracks and fissures. For small cracks, the unique local pointing technique to fill with mortar; apply epoxy on wider cracks, and therefore ensures the principle of "restoring the old as the old" (Figure2).

Regarding the Grand Quay, choose local stones, rebuild the stairs on the east opening, to enhance the flood discharge capacity of the east opening and make it parallel to the river bank, which makes the middle platform of the quay as high as the water level of the east opening.

On top of that, build revetments in line with local terrain, clean away garbage in the openings and surrounding area and silt mud on river bed. Plant vegetation by the traditional Chinese garden design, and renovate the drainage ditch with local stone material. Add traffic barriers between the bridge and roads. Fundamentally solve drainage, consolidate the structure, and enable all basic functions.

The restoration of structural safety is the foundation for achieving the coordinated integration and inheritance and continuation. Its restoration has its own uniqueness, as different measures are applied to different objects.

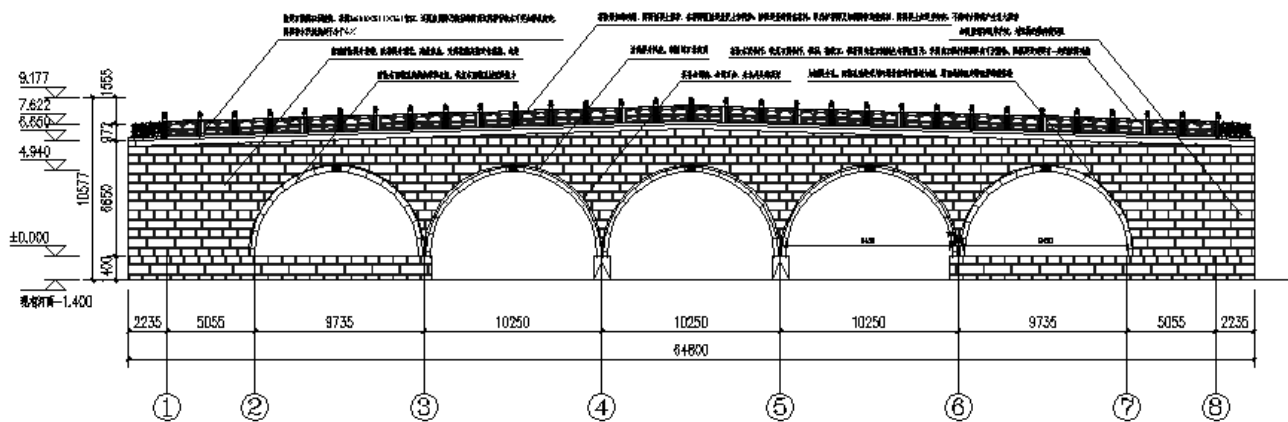


FIGURE II. THE FACADE REAPPEAR DESIGN OF THE HUANGCI BRIDGE

B. Integrity

About the restoration of overall coordination, firstly each material element should be perfected. Next, it is essential to control every step from the philosophy of design to construction technique. Based on extraction of original philosophy of design and historical information, the railing and stele pavilion need to be completed. Since there is no record of the original design, the design of the pattern of the railing should accord with the pattern of traditional official bridges and at the same time apply local elements and decoration technique to represent its historical locality. The stele gazebo can be built on its old location on the terrace with a hexagonal tented roof, which unifies practicality with aesthetics.

Secondly, the creation of building space and surrounding environment should be based on the actual buildings. The Xinjiang Grand Quay is an indispensable part to the whole landscape, a newly designed and constructed quay. After the reformation, the quay would be made more spatially comfortable, and the river would also appear to be more intimate to viewers. The bridge, the quay, the stele gazebo, the revetments, the houses and surrounding vegetation would conform into an integrated landscape.

C. Continuity

The restoration of the continuity is based on analysis of value, to transcend structural safety and integrity. It is the excavation, restructuring and sensible presentation of the material entities, material space and surrounding areas.

As shown in figure 2, the Huangci bridge spans over the river and extends to the villages on its two ends. The houses on both sides of the bridge serve as finishes to the landscape. The Xinjiang Grand Quay connects the horizon to the surface of the water. The stele gazebo links the aforementioned two spaces. Vegetation on the two banks is like a thread run through the bridge, the quay, the stele gazebo and residential houses along

the river. The finishing touches to this restoration plan are in the stele gazebo, it will attract people to stop in here and read the stele to the history of the Landscap while enjoying the intoxicating view.

D. Summary of Restoration Methods

The restoration of the historical cultural landscape has its own complexity and uniqueness. There are four parts of the material system of the landscape: 1) artificial elements – actual buildings; 2) the space—the empty place; 3) the natural elements – the surrounding environment; 4) the overall pattern, which is the entity that unifies artificial and natural elements. Through survey of historical documentations and analysis and comparison, this article used a concrete example to discuss and summarize the restoration of urban historical and cultural landscapes.

First, we have analyzed the material buildings of the landscape. A historical and cultural landscape is a landscape, it should comprise several material elements, such as terrain, landform, buildings, the water body, vegetation and etc. And “historical” and “cultural” means the landscape carries historical and cultural information. The restoration of these landscapes should start with protecting these elements, and at the same time innovatively utilize them, not just simply making the landscape to appear again.

Secondly, on top of protecting the material buildings of the landscape, the material space, the surrounding environment and the overall pattern need to be preserved and revived too.

In addition, the value analysis of the constituent components is also crucial (table 3). Only deeply analyze the value of the historical and cultural landscape can combine the constituent elements.

TABLE I. ANALYSIS OF CONSTITUENT ELEMENTS OF THE HISTORICAL AND CULTURAL LANDSCAPE

Macro Elements	Micro Elements	Analysis of Value	Restoration Method
Material Substance	Material subjects' elements: terrain and landform, water body, buildings, vegetation	historical Value: historical events, historical figures, local building traditions	Restore its authenticity, identifiability, continuity, integrity and etc.
	Spatial elements Surrounded and defined by material objects such as space form, Space composition and etc.	Artistic value: artistic creation, aesthetic taste, artistic styles, specific eras, typical styles, religious faiths	Restoration of space texture and loci features and etc.
Material Space		Scientific value: creation achievements (achievements during the process and after the creation process), technological achievements	Methods including preservation, transformation, renovation, restoration, reconstruction, and rebuilding.
	Natural environment and artificial elements such as mountains and rivers, views and vegetation.	Cultural value: ethnic culture, local cultures and customs, ethos, religious culture, intangible culture	Methods include preserving the relations between natural and artificial elements. For example, typical buildings, special space (to respect the spatial layout, preserve the overall pattern, style and structural relations)
Surroundings	Human activities and natural environment interact under certain geographical and historical conditions, to form an overall pattern and order, such as spatial structure and landscape structure.		
Overall pattern			

Based on the analysis of the constitution and value of the landscape, it can be drawn that a historical and cultural landscape is virtually an intersection between relic buildings and surrounding environment. The restoration of the historical and Cultural Landscape is the combination between the protection of relic buildings and the reformation and utilization of surrounding environment. The method of the restoration of the historical and Cultural Landscape should also comply with the methods of relic building protection and the reformation of surrounding environment.

V. CONCLUSION

Given the fast progress of urbanization, we should tend to historical and cultural landscapes and value their protection and restoration, as they are not only the necessary part of the development of a city, but also a prerequisite for the continuity of the unique texture of a city(Figure3、4). Hopefully, the methods summarized in this article may offer some theoretical assistance to research on regional historical and cultural landscapes. Meanwhile, it can provide some restoration methods for other historical and cultural landscapes of the same type.

We are greatly grateful to the great amount of support from the Nanning Administration of Press and Television and the Government of Xinjiang County that we have received. The methods presented in this article are merely the viewpoints of the authors and are in need of further improvements. However, hopefully some lessons can be drawn from it for other researchers.



FIGURE III. THE REAPPEAR DESIGN OF THE BUILDING LANDSCAPE AND ENVIRONMENT



FIGURE IV. THE REAPPEAR DESIGN OF THE BUILDING LANDSCAPE AND ENVIRONMENT No.2

REFERENCES

- [1] Xuezhang Jia On the Status Quo and Solution to China's Ancient Bridges' Preservation [J] Shanxi Architecture 2011.35-37
- [2] Beijing Research Institute of Ancient Architecture. Beijing Ancient Architecture Culture Series -Bridges and Pagodas [M]. Beijing: Beijing Art and Photography Publishing House, 2014.
- [3] Dake Liu.The Ancient Architecture of China with Stones and Tiles [M]. China Architecture & Building Press, 2008.
- [4] Heping Li, Jing Xiao. The protection and utilization of urban historical and cultural resources [M]. Science Press, 2014.
- [5] Nanning Evening News, 2013.
- [6] CHUN Qing, TANG Ye-zheng, PAN Jian-wu,Dong Yun-hong. Research on conservation of Jin Hu Bridge, a Stone arch bridge built in the Ming Dynasty [J] . Sci ConservArchaeol, 2016, 28(3): 65-72.

- [7] XIANG Yi-qiang, LI Qiu-ping, LUO Guan-zhou. Series of histori-cal stone arch bridge structures in shaoxing and protection strategy [J]. J Jiangnan Univ (Nat Sci Ed). 2010, 9(5): 563-566.
- [8] LI Guang, TANG Li, SONG Hai-bo. Research on the protection and repair of main structure for Hehe bridge [J]. Ind Construct, 2011, (Suppl): 809-812, 844.

Research on the Developing Approach of Digital Humanities in the Field of Library Science in China

Panpan He* and Ya Chen

Dept. of Information Management, Nanjing University ,China

*Corresponding author

Abstract—Under the tide of digital humanities, the Library actively participates in the research and practice. It has made considerable achievements. Based on the research documents collected by the CNKI and WOS database, this research reviews digital humanities in the field of Library Science. This article attempts to analyze the hot spots and development trends in order to gain a deeper understanding of research results and forecast the future research direction. The basic issues of digital humanities, library resources construction, library services and scientific research support. According to the analysis and discussion of the research and practice, the key points can be concluded to three parts, they are collaborative communication during country and domain, create good digital humanities atmosphere, carry out the research in an innovative way.

Keywords—library; digital humanities; developing approach; hotspot analysis

I. INTRODUCTION

Since the concept of "Digital Humanities" was proposed in 2001, it has attracted much attention from humanities researchers. Statistics showed that over 180 research institutes, technology centers named are running. Many humanities scholars also carry out the project^[1]. With the rapid development of information technology, Digital Humanities, with the characteristics of its cross - disciplinary and cross - field, which has break through its barriers and boundaries of subject, profoundly influenced literature, archaeology and other fields. Now it has became a powerful complement and strong power of traditional humanities research. For its academic and application value, it can be summarized into 4 parts: save the time and energy of traditional humanities scholars in text processing, find information, calculation; the introduction of new methods and tools to solve the problem of traditional humanities; use digital tools or way of thinking to put forward new questions in humanities; use digital thinking to creatively destroy and build the traditional humanities field^[2].

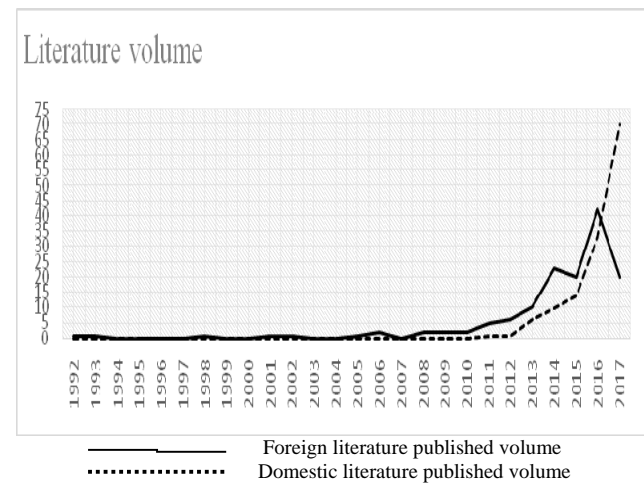
Under the background of "Digital Humanities", it naturally touches upon the field of library science and brings it with new opportunities. Digital humanities in the field of Library Science, which is that the Library attempts to explore the question of digital humanities from its perspective, and attempts to promote, participate in and dominate the research and practice. Since the 1990s, compared with China, the study of digital humanities in the field of libraries has been mainly focused on countries like Europe and the United States^[3]. How to participate in research and practice has become a topic that

scholars urgently need to solve. In recent years, the research topic are the introduction of digital humanities, the role orientation, the relationship between digital humanities and libraries. However, there is still a lack of in-depth discussion on the research and practice of from the perspective of metrology^[4]. This article attempts to sort out the way of development of Digital Humanities, analyze the hot spots and development trends in order to gain a deeper understanding of their research results and forecast the future research direction.

II. THE DATA SOURCE

Based on the words *digital humanities*, and *humanities computing*, *digital humanities*, *humanities computing* as the subject, it retrieves the relevant literature from the Chinese Science citation database and CNKI, which limited field of Information Science and Library Science, until November 13, 2017, it has got about 140 foreign documents and 116 Chinese literature. About the research method, this article mainly choose the literature analysis method to analyze the various aspects of the digital humanities research literature.

TABLE I. THE AGE OF LITERATURE PUBLISHED IN THE LIBRARY OF DIGITAL HUMANITIES AT HOME AND ABROAD



III. ANALYSIS ON THE APPROACH OF THE DEVELOPMENT OF DIGITAL HUMANITIES IN THE FIELD OF LIBRARY

Since the 1990s, the research has been mainly focused on countries like Europe and the United States, while China has generally started in 2011. Therefore, in order to analyze the

research literature comparatively and explore its research process, the article lists foreign literature accordingly. As an emerging field, from research papers and topics, we can analyze the development path of digital humanities.

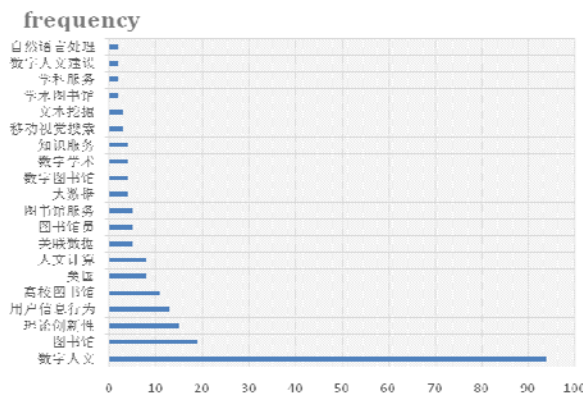
In Library Science, the literatures have fluctuated over 20 years, but it was still on the rise in the whole. The 2010s was an important turning point. The number was in a slow growth trend before 2010s, but it began to grow rapidly after 2010s. Comparatively, its research is at the initial stage at 2011s, it began to grow rapidly after 2012s. Thus, after 2012, the academic community began to try to support and participate in research and practice in various forms.

The development trend can be divided into 3 stages: the early embryonic stage (2011-2012 years), the attention of this stage is not high. It was not until 2011s that the literature appeared. In the initial stage (2013-2015 years), the research literature has been growing slowly and the annual literature amount has been kept in 5-15. The high-speed development stage (after 2016), In 2016, Peking University library launched the series of Digital Humanities activities and invited Digital Humanities Scholars to give special lectures, so the 2016 academic paper "blowout" appeared.

A. Research Topic Word Frequency Distribution

Through the analysis of key words and word frequency, the theme distribution of research in China can be grasps. A total of 351 key words are obtained in this study. In high-frequency keyword, user information behavior, related data, librarians, digital humanities construction, big data, digital library, subject service, text mining, knowledge service and other key words appear. Among them, the digital library reflects the research object of Digital Humanities and the keywords about related data, text mining and Natural Language Processing describe the research technology and methods of Digital Humanities.

TABLE II. DOMESTIC LIBRARY DIGITAL HUMANITIES RESEARCH HIGH FREQUENCY KEYWORDS (FREQUENCY>2)



Through the Co-occurrence of time zone images by high-frequency keywords, we can understand the change and development of theme. The key high-frequency words that appeared were digital humanities, librarians, natural language processing, knowledge services and resource construction. The

digitization shows that our libraries focus on problem-based research. In the subsequent start-up period (2013-2015), research emerged with keywords such as text mining, academic libraries, open access, big data, data management, data warehousing and more, which pay more attention on data organization and processing. In recent years (after 2016s), the key words are user information behavior, library service, research support and subject service in this field, which indicates that our country begins to pay attention to the application and influence of research.

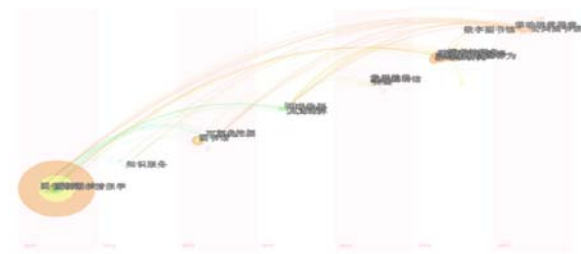


FIGURE I. DIGITAL HUMANITIES LITERATURE HIGH FREQUENCY KEYWORDS CO-OCCURRENCE TIME ZONE VIEW

IV. DIGITAL HUMANITIES RESEARCH HOT SPOT AND CORRELATION ANALYSIS

The analysis of keyword clustering can reflect the hot issues in the field of Digital Humanities. Using CitespaceV to draw the key word common map of the Digital Humanities and select the clustering function, 30 key words co-occurrence clustering are generated, which can reflect the research direction of Library's Digital Humanities field in label 3. We can classify these keywords into 3 themes: Digital Humanities foundation research, library resources construction, library service and research support.



FIGURE II. LIBRARY DIGITAL HUMANITIES LITERATURE CO-OCCURRENCE CLUSTERING MAP

A. Research on Basic Problems

The Digital Humanities originated from the practice and basic problems were naturally in open discussion . In order to grasp the relationship between the digital technology and the humanities and social sciences [5], Guang Yang explored the

ontology of the object of ,it involves the mining, organization, development and analysis of resources. In order to understand it deeply, we must understand the basic theory about technology and standard, technology foundation^[6]. Wei Liu and Ying Ye thought that the way of technology system and theoretical structure showing the interdisciplinary and cross-border integration, which mainly including digital technology, visualization technology and theoretical results related to structured data, humanities, or computing the visual image or humanities, intelligence or extended applications covering knowledge reconstruction and enhancement technology etc^[7]. Xuefang Zhu put forward the concept of digital human storage, which is the technological basis for the realization of projects and the way of application. The framework of human entity definition, domain ontology modeling, humanities entity digitalization acquisition and multi-dimensional aggregation service are constructed^[8]. Lijun Ma thought that the future development is influenced by the Digital Humanities and the library service is changing to the 3 modes of embedded subject service, integrated knowledge service and data analysis service^[9].

B. The Construction of Library Resources

I) the construction of resources : As a document resource management center, library can make use of its own resources and technical advantages to actively invest in the practice of Digital Humanities. Guang Yang thinks that library resources are becoming digitalized, but traditional resources rarely touch deep level applications. In order to guarantee the application of resources exploration, organization and development, we must integrate resources^[10].

II) infrastructure construction :A good infrastructure, that is, an internal and external balanced human digital ecosystem, played an important role in the sustainable development of technical and humanistic research. Wei Liu and Rong Xie thought that the infrastructure construction based on support activities should have all the documents, data, related software tools, academic exchanges and public facilities and related services in the world. They advocated to work at the national macro level and followed certain technical standards, norms and agreements^[11].

III) Librarian construction: The digital humanistic practice has put forward new requirements for librarians. Jie Li put forward that in order to realize the role transformation of librarians, we need to learn and explore from 5 aspects: data manager, resource discovery and integrator, interdisciplinary knowledge transmitter, content disseminator and promoter, and infrastructure builder^[12].Huan Ling believed that librarians should have the ability to guide readers to read humanities books, interact with readers fully and analyze information according to readers' requirements^[13].

C. Library Service and Scientific Research Support

I) Digital Humanities is an interdisciplinary scientific research and practice activity which is intersected by digital technology and humanistic exploration. Xiaoying Ceng pointed out that The library have the functions of achievement dissemination and knowledge popularization, project support

and auxiliary functions, provide embedded subject services, data analysis services, results operation and application functions", she appeal for new growth points of their services^[14].Yongzhong Lai believed that the research and practice of Digital Humanities and the feasibility of logical unity and realistic logic, its research support mainly includes 8 aspects: Digital Humanities, scientific research and guidance services, resource acquisition and push, research data management, research support tools, research space, academic communication and publication, scientific research influence evaluation and scientific research personnel education^[15]. Digital Humanities is the inevitable trend after the construction of digital library to a certain scale. the function and methods of related data technology in Digital Humanities Research are presented in detail, and the digital humanistic service for knowledge discovery^[16].

II) It can be seen that the humanities research under the background of "Digital Humanities" presents the characteristics of digitalized research objects, multidisciplinary research teams, intelligent research methods and diversified research paradigms. It is necessary to construct the new connotation of library knowledge service and to inject new research connotation into the work of Library and information and provide a new opportunity for the library's knowledge service^[17]. In addition, the library has the function of communication in the field of Digital Humanities. In order to strengthen the library culture function and influence, we can introduce the concept and technology of Digital Humanities from three aspects, they are introducing the concept and technology of Digital Humanities, expanding the dissemination service of Digital Humanities, providing data management services, deepening the level of information services, carrying forward the humanities reading and innovating the classic reading promotion service mode^[18].

V. REAEARCH AND PRACTICE ANALYSIS OF DIGITAL HUMANITIES

A. Development Stage Analysis

For the new field of Digital Humanities, the domestic library circles are still in the exploration stage in theory and practice, but the results are considerable. From the content of this paper, the related theoretical research has discussed the role of Library in Digital Humanities^[19], Digital Humanities technology and theoretical structure, service mode and other issues, which provided theoretical and method support for its research and practice. At the same time, it explored the way of The Library to participate in Digital Humanities in practice, including the establishment of Digital Humanities Center, recruitment of Digital Humanities librarians, infrastructure construction, research support services and project support^[20].

B. Characteristics Analysis of Research

From the view of the research practice, the following characteristics are mainly presented. The first characteristic is extensive research topics, which covers the history and the ancient discipline service, mining, culture, Huizhou studies, Genealogy Research etc. It involves not only traditional humanities materials, but also Digital Humanities materials.

The original digital data is also included in the research area, and the introduction of digital technology is also emphasized. The second characteristic is intelligence research process, using the latest digital and data related technologies to intelligently process, collect and retrieve data, help quickly sort out, locate and grasp the theme and spy the core meaning of the discipline context, save time and cost of research. The second characteristic is the synergy of research methods, which focuses on the combination of humanistic research and computational tools, makes the textual research appear in the form of data. Interdisciplinary collaboration and innovation enable humanities scholars to understand and value digital technologies and methodological tools, and promote natural science scholars familiar with the humanities research objects and ideas^[21].

C. Research Defect Analysis

The digital humanities research in The Library started relatively later, and the study atmosphere is not strong. The research depth and level only stay at the simple level of service and support. Most scholars have not enough understanding of digital humanities. The corresponding concepts, connotation and denotation and other basic theoretical issues have not yet reached an agreement. At the same time, the lack of more professional digital technologies and methods to support research that the foundation of later research is not strong. Libraries regularly handle structured resources such as textual historical materials, lack of research on unstructured data^[22]. In addition to technical and literacy training, some humanities researchers lack of digital thinking, less contact with some research methods and skills such as analysis and interpretation of relevant data, and have certain deviations from the overall study. In addition, domestic scholars may encounter issues like resource fragmentation, data access and limited openness in the research process. To a certain extent, it blocked the exchange of resources and academic cooperation in the field of interaction. Thus, we should break through the limitations of the supportive service model and structured resources. Facing with the full integration of humanities research process, it use digital technology to participate in digital humanities practice with interdisciplinary thinking and perspective in order to effectively promote effectively promote the humanities research and development^[23].

D. The Key Points of Digital Humanities Development in Chinese Library

I) *Cross-border Transnational Exchange and Collaborative Research* : Chinese scholars should actively participate in digital humanities projects, alliances and conferences of international libraries, communicate effectively and share experiences. As far as possible to participate in the construction of foreign projects, and invited foreign experts to help skills and project management experience training. The Library introduced foreign cases of achievement for analysis and research, combined with the actual situation of China to form best practices. For example, they can cooperate with blogs and online publishing platforms to introduce specialized equipment, tools and software, provide digital publishing

services for digital humanities and enhance their usability by extending services. The Library should realize open strategy. and actively cooperate with universities, research centers, national digital infrastructure and other organizations and institutions, and customize personalized digital humanities services according to the needs of service objects. With the subjects of computer linguistics, history and geography, social sciences, publishing to build digital humanities collaborative research center. After reaching a certain scale, the Digital Humanities Center Alliance can be formed. From the standpoint of its own subject, the Library have to break through the limitations of natural social sciences, humanities and application projects. Comprehensively combine research methods and approaches in other disciplines to research and realize the maximization of resources at the research level, the maximum generalization of analytical methods and the maximum knowledge contents^[24].

II) *Good digital humanistic atmosphere to create*: It can create good digital humanistic atmosphere from the national policies, libraries and other parts. The country formulate a development plan, set up a digital humanistic fund, encourage the establishment of library-centered exchange and share platform to attract humanities scholars in various fields. And the country can also build learning communities to encourage teachers and scholars to conduct academic exchanges and mutual assistance. In order to consolidate the data foundation of digital humanities research and realize the data acquisition and opening up, the Library need to improve its own reserve of resources, construct a collection resource system and open up the existing database and corpus resources with low utilization rate. Set up digital humanities exchange platform and alliance to share the cost of purchasing resources or to exchange views on the process and achievements of open project construction. The library should nurture digital humanities librarians and actively popularize digital humanities and provide consulting services based on their own properties of intermediary and academic. It provides digital humanities researchers with professional knowledge and techniques Training, improve digital humanities. Establish and improve the guarantee mechanism and promote the guiding and normative system and mechanism, the synergistic relationship mechanism of exchange and cooperation, the management mechanism of scientific planning and efficient governance, the marketing mechanism to enhance the recognition and brand value, the evaluation mechanism of quality and benefit and other aspects of innovation. The library can collect and sort out the humanities research database, tool software or platform information from around the world, and discuss the release of relevant news and information to facilitate more users' attention.

III) *Digital Humanities research in an innovative way*: Encourage, advocate and mobilize the participation of the whole society, widely absorb social funds, popularize digital humanities knowledge and achievements, and promote digital humanities research and practice. Drawing on the experience of foreign foundations, establishing a digital humane project funding system can attract privately funded digital humanities projects. In addition to being funded by the National Natural Science Fund. The Humanities and Social Science Fund can

be included Encourage universities and research institutes, private enterprises and enterprises to join the research team, including those with market prospects related to economic and social development, also encourage enterprises and private parties to participate in and promote the development toward the market and industrialization. In cooperation with publishers, media companies, etc, they may entrust part of the publicity, dissemination and promotion of digital humanities and research results. Collaborate with bookstores and business organizations to create a digital laboratory that integrates learning, creative products, shared bookstores, cinemas, galleries, music, photography and other creative digital spaces to create amateurs and humanities scholars to draw the public's understanding. Pay attention to and participate in the practice, carry out projects in a multi-dimensional way of thinking. In cooperation with data providers, outsourced data vendors are commissioned to carry out data analysis. However, in the outsourcing cooperation, The library need to be involved in the supervision of data management and project processes to gradually accumulate and summarize project implementation and management experience. Draw on the experience of big data processing, refer to the editing and publishing departments or data analysis companies for processing results of non-written materials, digging and developing interdisciplinary thinking and perspectives, and processing unstructured data.

VI. CONCLUSION

Although the development of digital humanities has brought opportunities to the library, it has even brought challenges. Although the current digital library humanities research is still in the exploratory stage, as long as preparations are made and its advantages are taken advantage of, breakthroughs in auxiliary supportive services Restrictions, to take the leading position in innovative digital art research and practice, to promote cross-border exchanges and cooperation, to create a good digital humanistic atmosphere, the library can continue to promote its digital humanities to further and further development.

ACKNOWLEDGMENT

The preferred spelling of the word “acknowledgment” in America is without an “e” after the “g”. Avoid the stilted expression, “One of us (R. B. G.) thanks . . .” Instead, try “R. B. G. thanks”. Put sponsor acknowledgments in the unnumbered footnote on the first page.

REFERENCES

- [1] Benjun Zhu,Hua Nie. Digital Humanities: The New Direction of Library Practice[J]. Journal of University Library,2017,35(04):23-29
- [2] Guang Yang. Research on the Strategy and Application of Library Resources Integration under the Background of Digital Humanities [J]. Journal of hebei Library,2015,35(10):7-9.
- [3] Xiao Guan. Digital Humanities: Concept, Current Situation and Thinking[R/OL].[2014-11-07]. <http://meeting.lib.szu.edu.cn/conference/zh-hans/information?v=07000003>.
- [4] Wei LIU,Discussion on the Technical System and Theoretical Structure of Digital Humanities [J]. Journal of China Library,2017,43(05):32-41.
- [5] Jie Li. Library Conversion under the Background of Digital Humanities [J]. Library Research and Work,2017,(10):26-30+37
- [6] Huan Ling. Discussion on Library Reader Service under the Backgrund of Digital Humanities[J].Office Bussiness,2017,(17):159-160
- [7] Rong Xie,Lei Zhanag,Yongjuan Liu. The Construction of National Data Base for Digital Humanities [J]. Journal of China Library,2016,42(05):29-39
- [8] Xiaoying Ceng. Library on the Background of Digital Humanities :Role and Service[J]. Books and Intelligence,2014,(04):111-113
- [9] Benjun Zhu,Hua Nie. Cross-border and integration: Digital Humanities from a Global Perspective—Summary of the First Digital Humanities Forum[J]. Journal of University Library,2016,34(05):16-21
- [10] Cuijuan Xai, Lie Zhang. Application of Relevance Data in Genealogical Digital Humanities [J]. Library Magazine,2016,35(10):26-34
- [11] Ernesto Priani Saiso. Finding support for disruption: developinga digital humanities project in Mexico [J]. Aslib Proceedings, 2012, 64 (1): 97-103
- [12] Buddenbohm S, Matoni M, Schmunk S, Thiel Carsten .Quality Assessment for the Sustainable Provision of Software Components and Digital Research Infrastructures for the Arts and Humanities[J].bibliothek forschung und praxis,2017(41):231-241
- [13] SoringS.Techincal and Infrastructural Solutions for Digital Scholarly Editions: DARIAH-DE and TextGrid[J] bibliothek forschung und paraxis.2016(40)207-212
- [14] <https://luc.edu/ctsdh/researchprojects/jesuitlibrariesproject/>
- [15] <https://er.educause.edu/articles/2014/6/linked-jazz-building-with-linked-open-data>
- [16] Leydesdorff L, Salah AAA. Maps on the basis of the Arts & Humanities Citation Index: The journals Leonardo and Art Journal versus “digital humanities” as a topic[J] journal of the American society for information science and technology,2010(61) :787-801
- [17] Toms EG, O'Brien HL. Understanding the Information and Communication Technology Needs of the e-Humanist [J] journal of documentation,2008(64)102-103
- [18] Xiaoxi Zhang.American College Students set up Digital Humanities Major.Chinese Journal of Social Science, 2016-01-15
- [19] PooleAH.The conceptual ecology of digital humanities[J]journal of documentation,2017(73):91-122
- [20] Yaoran Zhang,Shaozhen Zhang. Digital Humanities Suevey in American Universities[J].Library Forum,2017,37(03):26-34
- [21] Ping Ke,Ping Gong. The Evolution of Digital Humanities and Its Hotspot Analysis[J].Journal of China Library,2016,42(06):13-30
- [22] Liheng XU. Why We need Digital Humanities [N]. Social Science Journal,2017-08-24(005)
- [23] G. Eason, B. Noble, and I. N. Sneddon, “On certain integrals of Lipschitz-Hankel type involving products of Bessel functions,” Phil. Trans. Roy. Soc. London, vol. A247, pp. 529–551, April 1955
- [24] Liheng,Xu:Why we need Digital Humanities[J] Society proceedings,2017-08-24(005)

Total Quality Management (TQM) or Continuous Improvement System (CIS) in Education Sector and Its Implementation Framework towards Sustainable International Development

Vijayan Gurumurthy Iyer

Professor and Dean (R & D), Narasaraopeta Engineering College, Affiliated to Jawaharlal Nehru Technological University Kakinad, A-2/31, Kendiraya Vihar-II , Paruthipattu, Avadi, Chennai-600 071,India

Abstract—Sustainable international development (SIND) is a kind of international development that meets the needs of the present without compromising the ability and efficacy of future generations to meet their own needs [@25,26,27 Vijayan Gurumurthy Iyer, World Engineers' Convention(WEC) 2004, Shanghai, China]. Total quality management (TQM) or continuous improvement system (CIS) can be defined as a set of systematic activities carried by an institution to efficiently achieve institutional objectives that satisfies beneficiaries at the appropriate time and price. TQM is a comprehensive and structured approach to sustainable educational management that seeks to improve the educational services through refinements in response to continuous feedback. Educational quality is defined as the degree of excellence with respect to totality of features and characteristics of educational services that bear on its ability and efficiency in terms of knowledge and character to satisfy a given or implied need while training the human mind. CIS of an education sector that shall achieve academic and research excellence and thus lead to SIND. International Organizational for Standardization (ISO)'s 9000 standards focus on quality management (TQM) of all sorts of organizations. It defines the features on quality management system (QMS) that need to be in place to ensure that institutions identify and focus on improving areas where they have significant deficiencies. The objectives of the study are (i) to conduct action-based and field research on TQM to present QM ideas on education, (ii) to identify quality compliance requirements (QCRs) for an educational sector adherence to established standards based on an educational research conducted on quality circles (QCs) duly launched in twelve educational institutions in south India and (iii) to promote sustainable policy recommendation to strengthen quality and quantity educational services. Education coupled with entrepreneurial process is an intricate SIND process which is a targeted area of research to alleviate poverty from the emerging enterprising spirit. Output of the process is an international and national educational service to the beneficiaries concerning to both educational quality and quantity management. TQM processes are divided into four sequential categories such as plan, do, check, and act (PDCA cycle) for continuous process improvement. In the *planning* phase, educationalists define the problem to be addressed, collect relevant data, and ascertain the root cause of the academic problem; in the *doing* phase, educationalists develop and implement a comprehensive solution, and decide upon a measurement to gauge its and efficiency ; in the *checking* phase, educationalists confirm the result through

before-and-after data comparison; in the *acting* phase, educationalists document their results , inform others about process changes, and make recommendations for the problem to be addressed in the next PDCA cycle. It is concluded that TQM as a management approach of an educational institution centered on quality, based on the participation of all its members and aiming at long term success through learner satisfaction and benefits to all members of the institution and society. TQM in an educational sector is based on quality management from the student's point of view. Based on this action-based and field research conducted on TQM, sustainable policy recommendation may be taken to strengthen both quality and quantity educational services concerned to both knowledge and character in educational sector. In the present article, importance of possible inclusion of TQM and steps involved for an implementation of framework in education sector are discussed. Educational Enterprise Resource Planning(ERP) software effectively and efficiently integrates the islands of information within the educational institution through, internet of things-sustainable architecture.

Keywords—character; education, internet of things-sustainable architecture; knowledge; management; policy; process; product; quality; quantity; research; strength; sustainable international development; teaching; training the human mind

I. INTRODUCTION

Higher level educational institutions (HLEs) need to implement the educational values and quality improvement for the truth and pursue knowledge [1]. There must be specific focus given on the educational innovations, vision, mission and goals, guiding principles, environmental assessment, quality policies and principles, total quality management, technical knowledge, character, master plans for institutional growth, supply of value added knowledge based trained human power, obtaining feedback from stakeholders and for continual improvement, quality innovations in management and green information communication technologies (GICT).

About 88% economic growth is created by innovation [2]. To achieve this level, literacy rate should be high. It is necessary to take considerable steps to achieve socio-economic development by tapping educational and entrepreneurial resources. To ensure efficient and effective

socio-economic transformation, the input resources that are innovation in quality and quantity of education coupled with entrepreneurship, sustainable international development, educational research and total quality management methods. It has been found that there are considerable lags in academic performance index (API) and continuous improvement system (CIS) right from the school education to teacher education and higher educational institutions that are important dependent parameter concerning to increase the literacy level [3]. This research paper discusses such fulfilment of lags highlighting an importance of TQM in an education sector and its implementation framework towards SIND. Sustainable national development (SIND) is a kind of national development that meets the needs of the present without compromising the ability and efficacy of future generations to meet their own needs.

The A.K economic model for output level of sustainable economic growth is the product of sustainable engineering or technical factor level (A) and the capital (K) [3]. Therefore, the solution is the creation of new sustainable enterprises by innovation. As per the standard production function discussed in the paper, the development of new knowledge is a crucial factor for economic growth as certain educational innovation level is required in engineering or technical systems. The sustainable economic growth is hereby explained by three factors as given below:-

1. The natural increase in the accumulation of labour potential [4],
2. Capital accumulation or money with which a business is being started and run,
and
3. Sustainable technological momentum (also called as total factor productivity (TFP) or efficiency) in industrial processes.

The increase of labour and the capital accumulation be account for 12 percent of the economic growth, but the knowledge emerged that is coming from outside economy is described as technological change that is approximately account for about 88 percent [4]. The fundamental entrepreneurial momentum keeps the capital development dynamic which comes from the new enterprise creation process, new goods or service requirement from customers, the new methods of production and processes, new transportation, and new markets and new forms of an industrial organization.

Standard Production Function (SPF) is expressed as

$$Y = f(C, L)$$

where Y=Output, C=Capital, and L=Labour
As knowledge is an important factor for the economic growth, Process Production function, (PPF)

$$Y = f(X_1, X_2, X_3 \dots X_n)$$

Standard Production Function (SPF) is modified as

$$Y = A(C, L) f(C, L)$$

'A' represents Knowledge and character on sustainable engineering or technical system,

$Y =$ Output ,
 $C =$ Capital
 $L =$ Labour
 $f =$ Standard production function

Hence the development of new knowledge is a crucial factor for the sustainable economic growth. As per the given standard production function, knowledge and character are decisive production variations [5].

A. Objectives of This Research

The objectives of the study are (i) to conduct action-based and field research on TQM to present QM ideas on education, (ii) to identify quality compliance requirements (QCRs) for an educational sector adherence to QM standards based on an educational research conducted on quality circles (QCs) duly launched in twelve educational institutions in south India , (iii) To set up Academic performance index (API) based appraisal system (APIBAS) and continuous improvement system (CIS) including faculty performance assessment and evaluation regime and (iv) to promote sustainable policy recommendation to strengthen quality and quantity educational services.

B. Associated Objectives

1. To identify and evaluate present educational problems in educational sector;
2. To provide solution for the various problems encountered with reference to :-
 - (i) conduction of quality improvement (QI) programs for faculty to enrich techno-pedagogue skills, professional and research training requirements, the conduction of innovative add-on courses (QIPs) and research-oriented courses, and workshop,
 - (ii) Setting up of Academic performance index (API) based appraisal system (APIBAS) and continuous improvement system (CIS) including faculty performance assessment and evaluation regime ,
 - (iii) defining workload norms for faculty employed in lower and Higher Learning Institutions,
 - (iv) updating comprehensive profile for the Science, Humanity, Engineering and Technological faculty.
 - (v) to incorporate industrial oriented courses in Curriculum,
 - (vi) to formulate and appraise innovative in-service and pre-service and post-service faculty development programs (FDPs) .
 - (vii) to improve the research productivity of faculty and quality of lectures in educational institutions,
 - (viii) to promote conduction of feasible experiments in education sector by investigation devises.
3. To implement Total Quality Management (TQM) concepts in an educational sector,

4. To inculcate innovation in educational sector through research publications and citations;
5. To promote the concept of sustainable entrepreneurship education in education sector;
6. To promote environmental education in an education sector as environmental science, solid and hazardous waste management, sustainable entrepreneurship, sustainable development and total quality management are the basis of environmental education in this century.

7. To fulfil the following academic missions [5]:

- (i) Problem focused education
- (ii) Research oriented programmes
- (iii) Interdisciplinary approach;
- (iv) Experiential learning and training approach

8. To implement ERP that effectively and efficiently integrates the islands of information within the educational institution through, internet of things- sustainable architecture.

II. MATERIALS AND METHODS

The author has conducted action-based and field research trials on TQM to present QM ideas for education and quality compliance requirements (QCRs) for an educational sector adherence to established ISO standards based on an educational research conducted on quality circles (QCs) duly launched in twelve educational institutions in south India. As per educational statistics study revealed that a person receives one-fourth of education from teacher, another fourth by own intellectual efforts, another fourth from fellow people and the rest during time through life experience [6]. An entrepreneur learns from life experience of education. The subtle relationship between education and entrepreneurship is an intricate process that need to be inculcated in our educational system to benefit more from the emerging sustainable enterprises spirit [7]. Entrepreneurial process is set of entrepreneurial activities that are interacting and inter-relating each other [8]. That is quality in terms of relevance and degree of academic excellence and quantity in terms of number of elements access to these activities.

A. Total Quality Management (TQM)/CIS in an Education Sector

Total Quality Management (TQM) concepts consisting of institution -wide efforts to establish permanent a climate for continuously improving its ability, efficiency and values to deliver high-quality educational services to the beneficiaries [9].

TQM requirements for an educational sector adherence to established standards such as International Organization for Standardization's ISO 9000 series as given in figure mentioning the process approach in an educational system. It defines that TQM as a management approach of an educational institution centered on quality, based on the participation of all its members and aiming at long term success through customer satisfaction and benefits to all

members of the institution and society. Hence, TQM is a process or activity which is based on quality management from the beneficiaries' point of view as shown in figure 1.

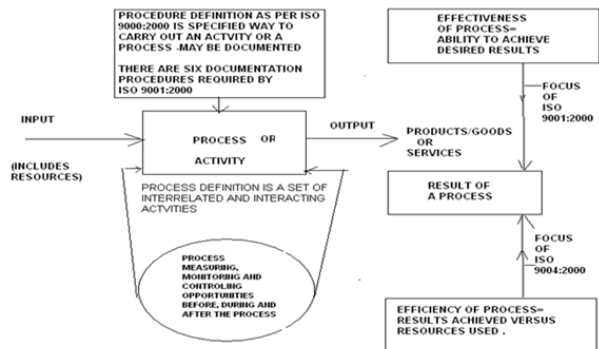


FIGURE I. SCHEMATIC REPRESENTATION OF A PROCESS

ISO 9000 series focus on quality management and defines the features of quality management system (QMS) that need to be established to ensure that educational sectors identify and focus on improving the areas where they have significant educational deficiencies. TQM techniques and various process analysis tools include statistical process control, zero defect process, lean manufacturing system and six sigma belt and international organization for standardization (ISO) standards such as ISO 9000 , ISO 14000 , ISO 18000 and ISO 50000 standards. Educational institutions must be able to implement TQM by following QM standards for sustainable educational development [10].

B. Quality Circles in Educational Institutions

Quality circles (QCs) have been launched in Prince Dr. Vasudevan College of Engineering & Technology (Affiliated to Anna University) at Chennai. QCs facilitate educational sectors to identify and solve the academic and research related problems. There is scope enhancement for the group-based solution of academic and research related problems.

QC employs the following quality improvement (QI) tools:

1. Cause –and –Effect diagrams (Fishbone diagrams)
2. Pareto Charts
3. Data Collection through Check Sheets (Process Maps, Data gathering tools), Stratification of data.
4. Graphical tools such as Histograms , Frequency diagrams and Pie charts
5. Statistical Quality Control(SQC) and Statistical Process Control Charts (SPC) Charts
6. Scatter Diagrams and Plots and Correlation Analysis
7. Operation and Process Flow Charts

QCs have been adopted to prepare 'Total Quality People(TQP)' so as to promote SPC and SQC in academics and research for improvement of students' academic performance and personality development , teaching and learning process that include steps to improve results[11] .

The class committee serves as a' QC' for the class. The course committee serves as QC for the course. University and college class committee consists of the concerned teacher,

student representatives and a chairperson who is not teaching the class be formed for each class. QC's meet on a regular basis normally at two-week intervals of time for one or two hour's durations. Four or five meetings per semester have been conducted. The functions of the class committees are to identify academic and research problem faced by the students which must be taken up on priority. Problems are solved by basic problem-solving methods. Solutions for the problems are identified and evaluated. This creates and generates number of viable alternative solutions.

Hence, the class committees function towards addressing students' problem and solution, including assignment of weightage for various course modules of evaluation, identification of weak students and improving their performance, failure mode effect analysis (FMEA) and recommending necessary corrective action and preventive action by the faculty.

The students' absenteeism is the most widespread problem existing in the institution for a long time. By discussion in the QC and class room using brainstorming and other TQM tools, various causes and effects are evaluated. Late coming is a problem in educational institution. An attempt has been made to solve students' late coming problem by studying causes and effects. Steps to improve academic and research performance have been evaluated.

Iyer, Vijayan Gurumurthy has discussed an integrative approach in the paper entitled "Education Coupled with Entrepreneurial Process Approach Towards Sustainable Development" which has been included in Abstracts & Proceedings Book of the Global Conference on Contemporary Issues in Education (ISSN: 18770428) organized by the Academic World Education and Research Center, www.awer-center.org, at Las Vegas, USA during 12-14, July 2014 duly published by Elsevier B.V. Ltd., <http://www.globalcenter.info/globe-edu/wp-content/uploads/2013/06/GLOBE-EDU-2014-Abstracts-Book.pdf>, pp.17 , 32-33. Sustainable entrepreneurship is an integrative approach based on entrepreneurship and innovation management. It focuses in depth understanding aspects as idea generation, science, engineering and technology-based entrepreneurship, marketing and markets, organization and project management, new sustainable product and process development, entrepreneurial finance, human resource development and operations [12]. This is called special education which will be encouraged to combine and apply students' creativity and innovation to design and develop science, engineering or technology and environment-based idea. The objective of an educations sector is to introduce the concept, issue, and theme related to business planning, strategy, and entrepreneurship as well as the functional activities in a sustainable business venture such as guidelines to set up an entrepreneur and become a successful entrepreneur. It is necessary to explore such business planning and strategic management issues of engineering or technology driven enterprises in the initial stages of development. Business analysis and planning skills are developed in this course.

The beneficiaries will be encouraged to assess and evaluate their potential for entrepreneurial careers and develop attitudes and skills that will be useful in engineering or technological new ventures.

1. Learn and understand market identification and assessment techniques
2. Guidance on how to develop new business idea and successful business plan preparation.
3. Fundamental of finance and marketing
4. Intellectual property protection
5. Soliciting funds
6. Successful business partnership
7. Preparation of Detailed Project Reports (DPRs)
8. Project implementation schedule.

"Sustainable entrepreneurship" is a kind of entrepreneurship that meets the needs the present without compromising the effectiveness, efficiency and values of future generations to meet their own needs [12]. A person who sets up and runs successfully a small, medium or large-scale enterprise or business at considerable risk is an entrepreneur. The entrepreneur combines efficiently six kinds of input resources, viz., capital, man power, market, machineries, raw materials and method so as to transform manufacture of output goods, products or provide services. An entrepreneur is thus who organizes, manages, assumes risks and enjoys profits of enterprise or business successfully. A sustainable entrepreneur propels entrepreneurial growth through innovation. Environmental entrepreneur considers the environment in organizational planning and decision making and to arrive at actions which are more environmentally and socially compatible. The concept of sustainability is highlighted when one works in a manner that resources do not get depleted due to business endeavors. Hence, implementation of this concept enables final year undergraduate course students to become successful new entrepreneurs [12].

C. Educational Resource Planning (ERP)- A Software for Computer Based Education through, Internet of Things-sustainable Architecture

Enterprise Resource Planning (ERP) is a software that helps to integrate nearly all the functions of an educational institution enabling to plan, track and see its resources in the best viable way to receive its customers [13]. The resources are (1) faculty and staff that is man power, (2) Infra structure facilities that is machine power, (3) sustainable educational methods, (4) educational materials, (5) capital budgeting and financial resources and (6) market to meet supply and demand of value added trained human power .

ERP effectively and efficiently integrates the islands of information within the educational institution through, internet of things-sustainable architecture.

The sustainable methods and educational materials including self-learning entrepreneurial materials (SLEM) have been employed. Since there is considerable educational growth

in terms of quantity in Schools, Universities and Colleges, there is an unsustainable growth of infrastructures. As per an educational survey, only, about 66% of the faculty members possess master's degree in their respective disciplines. More than 90% of them do not have sufficient industrial and field experience in teaching and research. Hence it is required for them to improve their standard of education to master's and doctorate degree as well research level [13].

To develop faculty various innovative methods such as quality improvements (QI) programs, flexible QI programmes, faculty development programmes , in-house QI programmes, distance-cum-contact courses, summer and winter schools, and part-time programs must be conduct in teacher educator institutions in regular intervals of time. It has been observed that participants in such programmes are very less. Faculty must be provided with sufficient career opportunities to improve upon their qualifications through the quality improvement (QI) programs to get them imparted technoscientific pedagogical skills and professional training requirement including research expertise. Under the quality improvement programs (QIP), a variety of short term courses need to be imparted to meet the sustainable training needs for all levels of faculty.

The educational sector should incorporate three methods, viz., [1] Total Quality Management, [2] Peer Review and Evaluation, and [3] Sustainable Assessment and Accreditation by a competent educationalist or peer organization.

Sustainable research provides efficient methods and educational innovations to improve the research and teaching productivity of faculty and quality of lectures at par with the international academic excellence in an educational sector [14]. The quality and quantity management system standards including internal academic audits may be practiced in schools, teacher education and higher educational institutions. TQM/CIS elements are given below:

1. Requirements of scientifically trained human power
2. Quality circles in educational institutions
3. To specify faculty workload norms and workload distribution per week;
4. Preparation of lecture plans (yearly/semester wise, weekly & daily), lesson action plans for Theory, and laboratory practice;
5. Self-assessment Report by the faculty for each day's progress (work diary) provided in Table. Reporting weekly summary report by the teacher given in Table
6. Requirements for the structure of the classroom lecture and quality of lectures.
7. Methods for preparation of the lecture notes and research methods for preparation of lecture notes supplement. Updated research information from internet. Video lecture programmes.
8. Computer oriented e-based education.

9. Setting up of comprehensive performance based appraisal system for the faculty called academic and research performance indicator

10. Training and development of teacher-educator

11. ACADIS (Academic Information System), teaching slots and faculty credit log concepts.

12. Sustainable entrepreneurial education.

13. Importance of environmental education in an education sector as Environmental Science and the Sustainable Development and total quality management are the basis of environmental education of this century for the quality of life.

D. Values Driven Quality Management (VDQM) System Approach

Culture must be realized for quality and productivity within an educational sector [15]. Quality management (QM) is defined as a set of systematic activities carried out by the entire institution to effectively and efficiently achieve institutional objectives to provide educational services with a level of quality that satisfies customers at the appropriate time and cost. QM is the culture of an institution committed to customer satisfaction through continuous improvement. By supplementing the QM with the culture which continuously incorporate educational values into the management of quality in an educational sector. That is by superimposing the culture cycle on the QM cycle shall create and generate the values driven QM (VDQM) cycle as shown in figure 2.

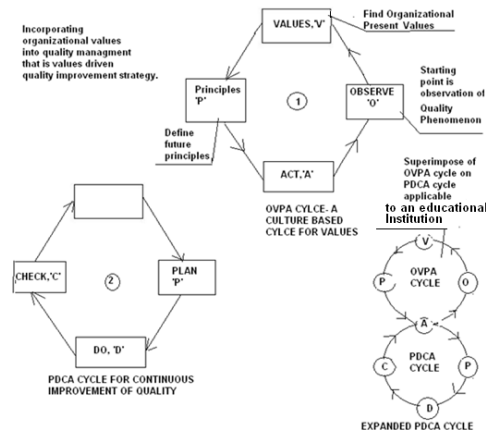


FIGURE II. CULTURE BASED TOTAL QUALITY MANAGEMENT (OVPA CYCLE) OBSERVE, VALUES, PRINCIPLES, AND ACT CYCLE BY INCORPORATING THE EXPANDED PDCA CYCLE FOR AN EDUCATION SECTOR FOR SUSTAINABLE INTERNATIONAL DEVELOPMENT

VDQM system is a culture based comprehensive and structured approach to an educational management that seeks to improve the values and quality of educational services through ongoing refinements and incorporating educational values in response to continuous feedback. By implementing VDQM in an educational sector shall succeed sustainable development. Sustainable development can be defined as a kind of development that meets the needs of the present without compromising the ability, efficiency and values of future generations to meet their own needs. VDQM is defined

as values driven quality management system approach of an educational institution centered on quality and values based on the participation of all its members and aiming at long term success through customer satisfaction and benefits to all members of the institution and society. The approach is based on values driven quality management from the stakeholder's point of view. VDQM processes are divided into eight sequential categories: plan, do, check, act, observe, values, principles, and act . VDQM will be based on the integration of PDCA (plan, do, check, act, observe) cycle and OVPA (observe, values, principles, and act) cycle . This combined cycle is also called the expanded Deming's cycle for deriving culture oriented continuous process improvement. In the *planning* phase, educationalists define the problem to be addressed, collect relevant data, and ascertain the problem's root cause; in the *doing* phase, educationalists develop and implement a solution , and decide upon a measurement to gauge its values, effectiveness and efficiency ; in the *checking* phase , educationalists confirm the result through before-and-after data comparison; in the *acting* phase, educationalists document their results , inform others about process changes, and make recommendations for the problem to be addressed in the next OVPA cycle or *culture's* cycle for incorporating values. Culture processes are divided into four sequential categories: observe, values, principles, and act. In the *observation* phase, educationalists observe present quality related phenomena of educational services; in the *values* phase, educationalists find present values of the educational services ; in the *principles* phase , educationalists define future principles and in the *acting* phase, educationalists document their overall results , inform others about process changes, and make recommendations for the problem to be addressed in the PDCA cycle. ISO 9000 series focus on quality management for all sorts of manufacturing and service organizations. The features of quality management system (QMS) standards are established to ensure our educational sector identifies and focuses on improving the areas where they have significant educational deficiencies. In the present article, importance of VDQM in an educational sector has been discussed .VDQMS standards and their compliance requirement (CR) with respect to higher and lower learning institutions (HLIs and LLIs) have been discussed such as International Organization for Standardization's ISO 9000 series, ISO 14000 series, ISO 50000 series, ISO 18000 series and by continuously working with culture based quality policies our educational institutions automatically becomes part of the quality management (QM) process[16].

III. RESULTS

Given below results and discussions provided which were based on the conduction of action-based and field research on TQM conducted in twelve educational institutions in south India .

A. Result of Comprehensive Academic and Research Performance Appraisal System

A performance-based appraisal system for teachers should be setup in educational institution well integrated with institutional functioning and this should lead to the

identification of individual training and research and development needs [17]. This should also enable the identification of teachers whose performance is outstanding. Such performances and excellence should be well recognized and rewarded. All teacher educational institutions should introduce a system for performance appraisal. The performance report should comprise the data such as publication of refereed research papers of faculty, paper reading in seminars / refereed conference, publication of books, research citations, citation indexed database(CID), research contributions, biographical reference books, patents, innovations, inventions and refereed discoveries. This system should be followed by the management for career advancement of faculty in their institutions.

IV. DISCUSSIONS

A. Educational Resources Planning (ERP) Software

Why is ERP Required?

- (1) Speed of the teaching-learning process,
- (2) Monitoring, measurement and control opportunities in educational environment,
- (3) Innovation in education and entrepreneurship.

Approach to ERP Implementation - A Road Map

Road Map for successful implementation of ERP

1. Clear Management Commitments
2. Top class ERP leadership
3. ERP only after process improvement
4. Training to implementation task force and user group
5. Right choice of ERP packages

Four options for developing ERP Packages

1. Developing an own ERP package (in-house development)
2. Modifying and enhancing the capabilities of the existing system
3. Buying readymade package
4. Engaging a software company

ERP effectively and efficiently integrates the islands of information within the educational institution through, internet of things-sustainable architecture.

4.7 Correct approach to ERP software

The options are dependent upon strategic planning and decision-making process and need a substantial capital investment. Right option must be selected only after evaluating the cost-benefit analysis [18].

4.8 Discussions on Quality Circles in Educational Institutions

Quality circles (QCs) have been launched in Prince Dr. Vasudevan College of Engineering & Technology (Affiliated

to Anna University) at Chennai during investigation period. QC facilitate educational sectors to identify and solve the academic and research related problems. There is scope for the group-based solution of academic related problems.

QC employs the following quality improvement (QI) tools:

1. Cause –and –Effect diagrams (Fishbone diagrams)
2. Pareto Charts
3. Data Collection through Check Sheets (Process Maps, Data gathering tools), Stratification of data.
4. Graphical tools such as Histograms, Frequency diagrams and Pie charts
5. Statistical Quality Control(SQC) and Statistical Process Control Charts (SPC) Charts
6. Scatter Diagrams and Plots and Correlation Analysis
7. Flow Charts

QCs have been adopted to prepare ‘Total Quality People(TQP)’ so as to promote SPC and SQC in academics and research for improvement of students’ academic performance and students’ personality development , teaching and learning process which include steps to improve results .

B. Discussions on Computer Based E.education Process

There are timetabling, scheduling software have been designed to use the available teaching resources effectively. Each faculty must maintain a course page descriptive and notify web URL address to the students. Lesson plans for theory, tutorial and practice shall be prepared and uploaded in website including lesson plans, lecture notes, supplements. These locations or pages can also display students’ attendance, test marks, and assignments. There shall be a class group or course group for each subject and these e-group members having mail ID communicated though e-mail compulsory.

ERP effectively and efficiently integrates the islands of information within the educational institution through, internet of things-sustainable architecture.

Given below concept of Academic Information System (ACADIS), Teaching Slot Concept (TSC) and Faculty Credit Log Concept (FCLC) to efficiently manage academic courses conducted for the various classes at all levels [19].

ACADIS, Teaching Slot and Faculty Credit Log Concept

Step-1 : Preparation of academic information system ;-

Details of Academic courses are prepared which is called Academic Information system (ACADIS) during trimester / semester.

1. One lecture hour per week is rated as one credit hour.
2. Two tutorials or two practical hours per week are rated as one credit.

Example: - How to prepare the ACADIS

Step II: Preparation of teaching slots: -

This is the one page information which shows the teaching slots of the faculty and free time slots (FTS).

1. The teaching workload is calculated as in terms of credit based contact hours.
2. One lecture hour per week is rated as one credit hour.
3. Two tutorial or two practical hours per week are rated as one credit.
4. The conduct hour is sum of theory tutorial and practical hours.
5. The conduct hour is interpreted as “One hour of practical / tutorial classes is treated as one hour of lecture”.
6. The departmental codes are identified in three letters.
7. The number of teaching slots is prepared as one line statement.

For example a teaching slot statement mentioned below is interpreted as (Provided in Table-1)

ECE4A- EC402-T1-3.5-ECE-SLT

ECE4A is the Branch code / semester / Sub-section

EC402 is the Subject code entitled

“ Transmission lines and Wave guides”

T1 is the main teacher / T2 is second assisting teacher / T3 is Third assisting teacher.

D1TI is Day 1 main teacher / D1T3 is Day I third assisting teacher.

3.5 is the credit hours of the individual teacher

ECE is the handling department

SLT is the mnemonic of handling teacher.

Example: - How to prepare the Teaching Slots

TABLE I. EXAMPLE OF TEACHING SLOTS CONCEPT ERP

Teaching Slots	S. No	Teaching Slots
ECE4A-EC402-T1-3.5-ECE-SLT	35	ECE6-6E1-D2T1-2.25-ECE-ASL
ECE4A-EC403-T1-3.5-ECE-DKS	36	ECE6-6E1-D2T2-1.5-ECE-AKT

Step- III : Faculty credits log concept:

The teacher individual Teaching Workload and Projects Workload are given in credits.

C. Environmental Science and Sustainable Development are the Basis of Environmental Education and Research (EER) towards Sustainable National Development

Environmental education and research is a new multidisciplinary aspect with implemented ecological philosophy and ecological ethics, establishing New Civilization Sustainable Development through a new subject Environmental Science [20]. This signifies a new education. New civilization requires innovative approaches to education that will be educated in “Modern Research Universities and Colleges and Schools which have a unique and key role. This means information, knowledge and understanding of the

following significant fields: a) in the concept of sustainable development- knowledge of the basic principles: precaution, risk prediction, prevention of causes, new assessment of the environment, changed behavior, changed methods of consumption and the establishment of the necessary demographic institutions and processes, b) in ecology, main principles , laws, definitions and terminology, c) basic factors of the environment , air , water, soil , solid waste , bio-diversity, the circles of matter, d) sources and methods of risk introduction to the environment e) Impact of old technologies and fundamental knowledge in the new technologies and other solutions in different fields outside the profession. New education is necessary which will be carried out from two aspects, (i) interwoven through all professional subjects and (ii) synthetic multidisciplinary by the integrating subject- Environmental Science and Sustainable Development [21]. Based on experience in transferring the knowledge in the field of (i) Environmental Science and (ii) Sustainable Development to the students at several faculties, that the last two semesters of University education in all disciplines of science, engineering and technology should include the course "Environmental Science", Environmental Impact Assessment, Total Quality Management, and "Sustainable Development" [22,23]. The last year of studies is most suitable because till that time the student has acquired knowledge in different domains of his profession, so with the study of Environmental science and sustainable development, the student synthesize knowledge [24]. The course should cover approximately two lessons per week and two lessons for the discussion on the preparation of the essay and individual seminar paper [25,26,27] @Vijayan Gurumurthy Iyer, World Engineers' Convention(WEC) 2004 , Shanghai, China].

V. CONCLUSION

Sustainable international development (SIND) is a kind of development that meets the needs of the present without compromising the ability and efficacy of future generations to meet their own needs. Total quality management (TQM) is defined as a set of systematic activities carried by an institution to efficiently achieve institutional objectives that satisfies beneficiaries at the appropriate time and price.

The objectives of the study were (i) to conduct action-based and field research on TQM to present QM ideas on education, (ii) to identify quality compliance requirements (QCRs) for an educational sector adherence to established standards based on an sustainable educational research conducted on quality circles (QCs) duly launched in twelve educational institutions in south India (iii) To set up Academic performance index (API) based appraisal system (APIBAS) and continuous improvement system (CIS) including faculty performance assessment and evaluation regime and (iv) to promote sustainable policy recommendation to strengthen quality and quantity educational services. ERP effectively and efficiently integrates the islands of information within the educational institution through, internet of things-sustainable architecture.

As per educational statistics study revealed that a person receives one-fourth of education from teacher, another fourth by own intellectual efforts, another fourth from fellow people

and the rest during time through life experience. An entrepreneur learns from life experience of education. The subtle relationship between education and entrepreneurship is an intricate process that needs to be established in educational sector to benefit more from the emerging sustainable enterprises spirit to alleviate poverty and sustainable development.

Entrepreneurial process is set of entrepreneurial activities interacting and inter-relating each other. That is quality in terms of relevance and degree of academic and research excellence and quantity in terms of number of elements accessing to these activities. The development of new knowledge is a crucial factor for the sustainable economic growth. As per the given standard production function, knowledge and character is a decisive production variation. The educational sector should incorporate three systematic methods, viz., [1] Total Quality Management, [2] Peer Review and Evaluation, and [3] Sustainable Assessment and Accreditation (SAA) by a competent educationalist or peer organization.

VDQM system is a culture based comprehensive and structured approach to an educational research management that seeks to improve the values and quality of educational services through ongoing refinements and incorporating educational values in response to continuous feedback. By implementing VDQM in an educational sector shall succeed sustainable development.

Academic Performance Index (API) based appraisal system and Continuous Improvement System (CIS) for faculty and the institutions should be setup integrated with institutional functioning and this should lead to the identification of individual training and research and development needs.

Based on this action-based and field research conducted on TQM, sustainable policy recommendation may be taken to strengthen both quality and quantity educational services concerned to both knowledge and character in educational sector. It is need of the hour to promote environmental education and research in education sector as Environmental science and sustainable development are the basis of sustainable education in this 21 st Century.

ACKNOWLEDGMENT

The author is thankful to Prof. Dr. Chemedu Fininsa, Vice President for Academic Affairs of Haramaya University for encouragement and permission to participate in International Conference on Quality Education. The author expresses his gratitude to the management, faculty and staff of Haramaya University (HU), College of Education and Behavioral Sciences (CEBS) and Higher Education Relevance and Quality Agency (HERQA) and the organizers of International Conference on Quality Education for accepting his paper in conference theme entitled " Strengthening Quality and Relevance of Education for Sustainable National Development" and for giving an opportunity to present this research paper during April, 4-5, 2014 at Haramaya, East Africa and inclusion in abstract book PP 44-45. The author is thankful to Scientific Committee of GLOBE-EDU 2014 for

publishing the research paper entitled “Education Coupled with Entrepreneurial Process Approach Towards Sustainable Development” in the abstracts book and proceedings of Global Conference on Contemporary Issues in Education at Las Vegas, USA(ISSN: 18770428) duly organized by the Academic World Education and Research Center, www.awer-center.org during 12-14, July 2014 and duly published by Elsevier Limited, URL : <http://www.globalcenter.info/globe-edu/wp-content/uploads/2013/06/GLOBE-EDU-2014-Abstracts-Book.pdf>, pp.17 , 32-33. The author expresses his thanks to All India Council for Technical Education (AICTE) as Expert Visiting Committee (EVC) member for arranging academic expert visits to more than ten numbers of educational institutions. The author expresses his gratitude to Mr.M.V.Koteshwara Rao , The Chairman of Narasaraopet Engineering College (Autonomous), Affiliated to JNTU-K , Guntur District, Andhra Pradesh for encouragement to publish this research work. The author extends his due acknowledgements to the organizers of 32nd Indian Engineering Congress for publishing this research paper in a Technical Volume of The Institution of Engineering (India).

The author extends his gratitude to the Organizers of 2018 International Conference on Computer Science, Electronics and Communication Engineering (CSECE2018) held during February 7-8, 2018 at Wuhan , China and for TPC service acceptance as well as General Chairs of the Committees of CSECE2018 of course publication of this research manuscript.

REFERENCES

- [1] Gail M.Gallitnt et., (2009), “The Content and Format of a Professional Development Program and its Attitudinal Effect on Teachers of Mathematics in WSEAS Proceedings of the *International Journal of Education and Information Technologies Issue 3 , Volume 5*, 2011, pp. 336-343.
- [2] Vijayan G. Iyer , et al ,(2012),“ Environmental Process Based Education and Research for Better Life and Enactment of International Environmental Impact Laws-2012 , “Models and Methods in Applied Sciences”, In Proceedings of the 2nd International Conference on Environment , Economics, Energy, Devices, Systems, Communications, Computers, Mathematics (EDSCM'12) (ISBN: 978-1-61804-082-4).International Authority for the Advancement of Science and Applications of Technology (IAASAT) , April 2-4, 2012 at Saint Malo& Mont Saint-Michel, France, pp.44-56.
- [3] Vijayan G. Iyer, (2011), “ Environmental Process Based Education and Research for Better Life and Enactment of International Policy Act on Environment 2011 . Book of Proceedings of the World Forum International Congress, “Natural Cataclysms and Global Problems of the Modern Civilization” , GEOCATACLYSM-2011 (ISBN 978-9952-451-14-6),19-21, publishers SWB-International Publishing House 2012, London, September 19-21, 2011, Istanbul, Turkey, SWB London, 2012, 621 p. , *International Committee on Global Geological Change and Environmental Changes Geo Change* , pp. 565-566.
- [4] Vijayan G. Iyer, (2011)Recent Research Results and Activities of Vijayan Gurumurthy Iyer”, Sub Title: “Environmental Education and Research for Better Life”, Abstracts of Selected papers and Bibliography By Vijayan G Iyer”, (ISBN-10: 3845405740 , ISBN-13: 978-3-8454-0574-2) Edited By Tatiana Melnic LAP LAMBERT Academic Publishing GmbH DudweilerLandstraße 99 66123 Saarbrücken, Germany,116 p, Release Date 30 June 2011.
- [5] Vijayan G.Iyer, (2007)“*Environmental Science and Sustainable Development are The Basis of Environmental Education for the 21 St Century*”, Abstracts Book of the IV National Teacher's Science Conference 2007 (NTSC-2007), Theme entitled” Environmental Education for Better Life” ID number 1/Tamilnadu/17 organized by NCSTC-Network , New Delhi , Hosted by Pahal, Uttanchal , Rajeev Gandhi NavodayaVidyalaya , Dehradun, www.ncstc-network.org, 22-25 September 2007,pp.69-70.
- [6] Vijayan G.Iyer, (2009)*“Environmental Science and Sustainable Development are The Basis of Environmental Education in the 21 St Century ”*, Proceedings of the VII th International Conference on Challenges in Higher Education and Research in the 21 st Century, CD-ROM, English Language Faculty of Engineering , Technical University of Sofia , Recreation Hotel, Sozopol, Bulgaria, 2-5 June, 2009 , http://elfe.tu-sofia.bg/cher21/program_2009.doc.
- [7] Vijayan G.Iyer, (2009)*“Some Innovative Practices on Quantity and Quality of Engineering Education and Research”*, Proceedings of the VII th International conference on Challenges in Higher Education and Research in the 21 st Century, CD-ROM, English Language Faculty of Engineering, Technical University of Sofia , Recreation Hotel, Sozopol, Bulgaria, 2-5 June, 2009, http://elfe.tu-sofia.bg/cher21/program_2009/doc.
- [8] Vijayan G.Iyer, et al.(2009), “Some Innovative Practices on Quantity and Quality of Engineering Education and Research” , *Proceedings of the 6 th WSEAS International Conference on Engineering Education* (EE '09). (ISBN:978-960-474-100-7, ISSN: 1790-2769), pp.97-107, Recent Advances in Engineering Education, Reference Book and Text Book of Mathematics and Computer Science in Engineering, Rodos Island, Greece, July, 22-24, 2009.
- [9] Vijayan G.Iyer, et al.(2006), “Quantity and Quality in Engineering Education and Research”. Book of the Proceedings of the 3rd *WSEAS International Conference on Engineering Education* (ISSN:1790-5117, ISBN:960-8457-47-5), (EE'06), CD-ROM, WSEAS ID number 535-414, July 11-13, 2006, Vouliagmeni, Athens, Greece, pp. 97-107.
- [10] Vijayan G.Iyer, et al.,(2006) “Efficient Methods to Improve the Productivity of a Teacher and Quality of Lectures in Teacher Educational Institutions”, Book of the *Proceedings of the 3rd WSEAS International Conference on Engineering Education* (ISSN:1790-5117, ISBN:960-8457-47-5), CD-ROM, ID : 535-413, July 11-13, 2006, Athens, Gr, pp. 73-96.
- [11] Vijayan G.Iyer, et al.,(2009) ““Some Innovative Practices on Quantity and Quality of Engineering Education and Research” , (AEBD'09), (ISSN:1790-5109, ISBN:978-960-474-091-8), pp. 237-252, WSEAS ID No. 617-121 , La Laguna, Tenerife, Canary Islands, Spain , 1-3, July 2009, <http://www.wseas.us/conferences/2009/lalaguna/wwai> .
- [12] Vijayan G.Iyer,(2003) “*Efficient Methods to Improve the Productivity of a Teacher and Quality of Lectures in Teacher Educational Institutions*”, Proceedings of the National Seminar on Innovative Practices and Experiments in School Education and Teacher Education and All India Competition on Innovative Experiments and Practices, April , 14-17, 2003, Department of Teacher Education & Extension(DTEE), National Institute of Education (NIE), National Council of Educational Research & Training, New Delhi , Ref. ETE-2 .
- [13] Vijayan G.Iyer,(2006)“Plenary lecture-III, Quantity and Quality in Engineering Education and Research”. Book of the Proceedings of the 3rd WSEAS International Conference on Engineering Education (ISSN:1790-5117, ISBN:960-8457-47-5), (EE'06), CD-ROM, WSEAS ID number 535-414 , July 11-13, 2006, Vouliagmeni, Athens, Greece, pp. 97-107.
- [14] Vijayan G.Iyer,(2006)“*Quantity and Quality in Engineering Education and Research*”, Program Book of the Seventh WFEO World Congress on Engineering Education: Mobility of Engineers, CD-ROM, Budapest in Hungary, World Federation of Engineering Organizations (WFEO), 4-8 March 2006, pp.14.
- [15] Vijayan G.Iyer,(2007)“*Environmental Science and Sustainable Development are The Basis of Environmental Education for the 21 St Century*”, Abstracts Book of the IV National Teacher's Science Conference 2007 (NTSC-2007), Theme entitled” Environmental Education for Better Life” ID number 1/Tamilnadu/17 organized by NCSTC-Network , New Delhi , Hosted by Pahal, Uttanchal , Rajeev Gandhi NavodayaVidyalaya , Dehradun, www.ncstc-network.org, 22-25 September 2007,pp.69-70.
- [16] Vijayan G.Iyer,(2013) “Some Practical Hints on Sustainable Entrepreneurial Process”, In Proceedings of Second FEIAP Convention and International Conference entitled “Engineering Initiatives for Sustainable Development Integrating Innovation and Ethics”, Federation of Engineering Institutions of Asia and Pacific (FEIAP) organized by The Institution of Engineers (India) and hosted by Andhra Pradesh State Centre , May , 8 -11, 2013, pp.177-185.

- [17] Vijayan G.Iyer,(2013) "Some Practical Hints on Occupational Safety and Health Compliance Requirements in Industries", In Proceedings of Safety Conference 2013 , Safety in Infrastructure Sector, 19-20 July 2013 Venue IE(I) Auditorium, Organized by the Institution of Engineers (India), Tamilnadu State Centre , 19 Swami Sivanadanda Salai, Chepauk, Chennai-5 , pp.46.
- [18] Vijayan G.Iyer,(2013) "The Sustainable Entrepreneurial Process to Starting an Enterprise from Scratch - Guidelines to Set up a Sustainable Enterprise", In Abstract book of the 28 th Indian Engineering Congress (IEC), 2013 , Technical Paper Session/Colloquium of Interdisciplinary Engineering on 22.12.2013) of Theme: "Engineering Advancements and Accelerated Nation Building Organized by the Institution of Engineers (India) Hosted by Tamilnadu State Centre at Hotel The Leela Palace, Chennai during December 20-22 , 2013, pp. 189.
- [19] Vijayan G.Iyer,(2013), "Sustainable Entrepreneurship Education is A New Dimension in Higher Technical Education for Sustainability", In Proceedings of 43 rd ISTE National Annual Convention 2013 Theme: "Empowering Technical Education to Address Sustainability and Global Competitiveness", Sub theme: New Dimensions in Higher Technical Education for Sustainability (ISBN: 978-93-5142-315-7) Organized by Indian Society for Technical Education-T.K. Institute of Engineering &Technology, Warananagar, Tal: Panhala, Dist. Kolhapur-416 113 on 19-21 st December 2013.
- [20] Iyer, Vijayan Gurumurthy, "Study of Sustainable Enterprise Creation Process towards Economic Development", In Abstract Book of Ingenieria 2014 Latin America and Caribbean Congress and Exhibition, Argentina for the Subject Area: 1-1 , Developing Economies (ECO's), Job No. 429 Poster Presentation on 3 rd November 2014 at 8:00-9:00 hrs held during 3-6, November 2014 at Centro Costo Salguero, Buenos Aires, Argentina, <http://www.ingenieria2014.org/programa>, Included in Congress Book of Proceedings for Engineering2014 at Argentina titled 'Building a Sustainable Regional Future'.
- [21] Iyer, Vijayan Gurumurthy, "Policy Study of Education Coupled with Entrepreneurial Process for Sustainable Development " , In Abstract Book of Ingenieria 2014 Latin America and Caribbean Congress and Exhibition -Argentina for the Subject Area: 3.3, Educational and Professional Regional Integration(EPRI), Job No. 432 Poster presentation on 3 rd November 2014 at 09:00-10:00 hrs during 3-6, November 2014 at Centro Costo Salguero Buenos Aires, Argentina, <http://www.ingenieria2014.org/programa>, Full Paper Included in Congress Book of Proceedings for Engineering2014 at Argentina titled 'Building A Sustainable Regional Future'.
- [22] Iyer Vijayan Gurumurthy (2017)."*Strategic Environmental Assessment (SEA) Process for the Higher Education Institutions (HEIs) to Achieve Research and Academic Excellence* ", Journal of Modern Education Review , ISSN 2155-7993,USA, December 2016, Volume 6, Number 12, PP. 958-970 (13 pages) @Academic Star Publishing Company , New York, USA, <http://www.academicstar.us>
- [23] Iyer Vijayan Gurumurthy (2016)."Environmental and Quality Management for the Higher Education Institutions to Achieve Research and Academic Excellence ", Journal of Modern Education Review (JMER), ISSN 2155-7993,USA, February 2016, Volume 6, Number 2 , PP. 135-146 (12 pages) @Academic Star Publishing Company , New York, USA, <http://www.academicstar.us>.
- [24] Iyer, Vijayan Gurumurthy."Education Coupled with Entrepreneurial Process Approach Towards Sustainable Development", Journal titled Procedia- Social and Behavioral Sciences (ISSN: 1877-0428) Published by ScienceDirect , Elsevier Ltd., Oxford, UK, www.sciencedirect.com, 177 (2015) 147-161, PP 147-161.
- [25] Iyer, Vijayan Gurumurthy (2017)."*Self- Bibliographical References of Prof.(DL)Dr.Vijayan Gurumurthy Iyer, Sub title: "Sustainable Self-Bibliographical References About Sustainable Literature by Prof.(D.SC.,LL.D.,DL) Dr. Vijayan Gurumurthy Iyer* ", (ISBN-13: 978-3-330-06124-8) ISBN-10: 3330061243 EAN: 9783330061248) Edited By Natalia Cojocar Acquisition Editor and published by LAP LAMBERT Academic Publishing of OmniScriptum GmbH & Co. KG Bahnhofstraße 28, D-66111 Saarbrücken , Germany ; 64.90 € Euro. Number of Pages 196. Published on 24.03.2017.
- [26] Iyer, Vijayan Gurumurthy (2017). "Total Quality Management (TQM) in Education Sector and Its Implementation Framework Towards Sustainable National Development". In the Technical Volume Proceedings of the 32 nd Indian Engineering Congress, Theme entitled "Innovation in Engineering: Competitive Strategy Perspective" (ISBN: 978-93-86724-29-8) held during 21 st-23 rd December 2017 at Chennai Organized by The Institution of Engineers (India) Published by Excel India Publishers, New Delhi, Proceedings page number 412-421.
- [27] Iyer, Vijayan Gurumurthy. "*Eco-Friendly Rubberized Cotton Fabric Roller Development for Cotton Roller Gins*", "Proceedings of the World Engineers Convention (ISBN: 7-5046-3929-X), Volume 'E' 'Agricultural Engineering and Food Security (ISBN 7-89995-986-1)' , theme entitled "Engineers Shape the Sustainable Future", CD-ROM, 2-6 November 2004, Shanghai in China, China Association for Science and Technology (CAST) and World Federation of Engineering Organizations, China Science & Technology Press", pp. 105-114.

Author Index

A

- Ahlawat, Anil 474
Arao, Ayako 31

B

- Bai, Xuewei 383
Bai, Qinghai 358
Bai, Xuxu 495
Bhardwaj, Manish 474
Bo, Juntian 514

C

- Cai, Siji 282
Cao, Li 295
Cao, Yuyin 147
Cao, Xuyang 333
Chai, Zidong 131
Chai, Liren 139, 435
Chen, Ya 541
Chen, Xueqin 500
Chen, Xiaoming 179
Chen, Yijie 279
Chen, Yufeng 142
Chen, Wei 204
Chen, Yu 204
Chen, Jingwei 353
Chen, Yindong 470
Chen, Fan 487
Cheng, Jun 413
Cui, Guoqin 100

D

- Dai, Wei 59
Dai, Hongxia 487
Deng, Xiaoguang 170
Deng, Yalin 166
Ding, Mingyue 364
Ding, Yanqiang 364
Dong, Zaopeng 147
Dong, Qi 408
Dong, Luan 487
Dong, Peng 527
Du, Fu 279
Du, Wenfeng 302
Du, Xuehui 50
Du, Ruizhong 83
Du, Shengwu 253
Du, Wenfeng 265, 302
Du, Xuehui 50
Du, Ruizhong 83
Du, Shengwu 253
Du, Peng 361
Duan, Guijiang 399
Duan, Lijuan 100

F

- Fan, Dongyan 325

- Fan, Chunming 124
Fu, Linyu 408
Fu, Xiangheng 274
Fu, Yu 88

G

- Gao, Jun 179
Gao, Feng 21
Ge, Xiaolong 445
Ge, Jiyong 532
Gong, Kecheng 69
Gu, Zhenhua 333
Guan, Xuchen 54
Guan, Peng 413
Guan, Wenchao 457
Gui, Peng 279
Guo, Zhichao 40
Guo, Yingqing 54
Guo, Lili 291
Guo, Jiaen 518
Guo, Wei 242
Guo, Yong 291

H

- Han, Feng 377
Han, Jun 1
Han, Hu 495
Hayashi, Masayoshi 105
He, Minghao 1
He, Jian 74
He, Liang 157, 449, 453, 457
He, Shun 204
He, Wei 353
He, Panpan 541
He, Tianting 200
He, Pengfei 265
Higaki, Hiroaki 31, 105
Hong, Ruxia 196
Hu, Hao 36
Hu, Jinchun 253
Hu, Yi 170
Hu, Chenglong 26
Hu, Tao 113
Huang, Zhangqin 74
Huang, Zechun 200
Huang, Xinghuai 54
Huang, Yu 464
Huang, Yinbo 479
Hui, Sai Chuen 308, 389

I

- Iyer, Vijayan Gurumurthy 546

J

- Jabbar, Saba Qasim 191
Ji, Kecheng 329
Jia, Tianyi 64

Jiang, Yanmei	174
Jin, Yanhua	5
Jing, Haixia	64
K	
Kadhim, Dheyaa Jasim	191
Kang, Kai	10
Kim, Jungyoon	532
L	
Lach, Damian	372
Lan, Wenjiao	124
Lee, Wonhyung	532
Li, Wanchun	45
Li, Yongzhen	26,162
Li, Hongke	237
Li, Yongkui	383
Li, Yingxiang	45
Li, Jiehong	282
Li, Nan	79
Li, Yue	88
Li, Junshan	170
Li, Yu	191
Li, Tingting	353
Li, Pu	427,491
Li, Yapeng	109
Li, Chao	166
Li, Yunqian	210
Li, Zhi	249
Li, Xiaodong	282
Li, Mengyuan	298
Li, Jianping	349
Li, Chengcheng	427,491
Li, Shufang	179
Li, Yiping	287
Li, Huan	442
Lin, Taobei	224
Lin, Daohong	142,210,216,230
Ling, Lie	21
Ling, Ming	329
Liu, Zhengguo	64
Liu, Yujing	79
Liu, Pengfei	157,457
Liu, Dong	170
Liu, Xue	174
Liu, Xu	187
Liu, Jun	353
Liu, Fanming	83
Liu, Xiaobo	131
Liu, Qi	302
Liu, Chongyi	408
Liu, Junliang	187
Liu, Zipu	200
Liu, Shiheng	442
Liu, Zheng	500
Liu, Yun	224
Liu, Xiangbin	403
Liu, Fengming	427,491
Liu, Chong	83
Liu, Fangyuan	249
Liu, Li	329
Liu, Yang	353
Liu, Changjin	487
Liu, Jin	495
Lu, Xiaofei	1
Lu, Wenxiu	242
Lu, Yingmao	157
Lu, Wei	527
Luo, Wanlu	207
Luo, Yong	349
Lv, Changyi	383
Lv, Haidong	445
Lyu, Borong	479
M	
Ma, Haoran	5
Ma, Ning	166
Ma, Jiyuan	302
Ma, Senrong	518
Ma, Youwei	204
Ma, Jianwu	207
Ma, Kai	269
Macioszek, Elżbieta	372
P	
Pan, Yumei	364
Peng, Yuanxi	69
Q	
Qian, Guobin	45
Qian, Yongyou	200
Qiu, Lijun	408
Qiu, Weigen	183
Quinn, Wagner	249
R	
Ren, Zhengying	237
S	
Sha, Jiang	423
Shan, Dibin	50
Shang, Enyao	253
Shang, Lin	417
Shao, Lei	210
Shao, Xinhui	479
Shen, Xiaohong	64
Shen, Chengfang	59
Shi, Ying	174
Shu, Leizhi	69
Sierpiński, Grzegorz	372
Staniek, Marcin	372
Su, Ning	509
Sun, Rong	345
Sun, Jinwei	361
Sun, Xueguang	183
Sun, Limin	295
Sun, Ping	245
T	
Tang, Qiu	45
Tang, Xiaojie	1
Tian, Yue	383
W	
Wan, Xinshu	14,142,210,224,509
Wang, Hongguang	21

Wang, Zhilin	79
Wang, Yumin	396
Wang, Jinguo	439
Wang, Zhen	445
Wang, Wenjuan	50
Wang, Jun	134
Wang, Na	439
Wang, Zhuoran	449
Wang, Xiaoling	461
Wang, Jing	196
Wang, Zeqi	261
Wang, Zhixiao	532
Wang, Haiyan	64
Wang, Ning	88
Wang, Di	118
Wang, Baosen	118,124
Wang, Wei	403
Wang, Lei	518
Wang, Chongen	536
Wang, Shaojie	536
Wang, Nan	50
Wang, Gang	139,435
Wang, Yujun	242
Wang, Longxuan	265
Wang, Wenyi	413
Wang, Kaiyu	504
Wei, Ming	500
Wei, Wei	174
Wen, Haolin	113
Weng, Xinhua	408
Wu, Jun	109
Wu, Bei	467
Wu, Ruoyu	59
Wu, Guodong	134
Wu, Yu	96
Wu, Qiang	210
Wu, Jiahong	509
X	
Xian, Kun	408
Xiao, Min	200
Xiao, Wenlei	258
Xiao, Feng	162
Xiao, Litian	298
Xiao, Nan	298
Xiao, Xiao	349
Xie, Zhenchao	14,142,216,230
Xie, Yuyang	479
Xie, Caiyun	196
Xie, Xinglong	522
Xie, Zheng	349
Xie, Shuai	134
Xie, Longhan	282
Xu, Fan	100
Xu, Mengyan	279
Xu, Wenjuan	423
Xu, Fangwen	449,453
Xu, Yang	504
Xu, Guanghui	134
Xu, Weiming	269
Xu, Huan	461

Xu, Kunyuan	5
Xu, Zhu	200
Xu, Jianlong	470
Xue, Weixian	522

Y

Yan, Yongsuo	147
Yan, Gongda	113,527
Yan, Ruihong	461
Yang, Tao	139,435
Yang, Deqiang	464
Yang, Xiabai	464
Yang, Xiumin	261
Yang, Ming	464
Yang, Yifeng	242
Yang, Guoyong	21
Yang, Dingxin	361
Yang, Wei	403
Yao, Jian	399
Ye, Xin	487
Yi, Jianjun	157,449,453,457
Yi, Xingyu	258
Yin, Yang	237
Yu, Haojie	333
Yu, Jianhong	431
Yu, Peng	527
Yu, Hong	196,
Yuan, Zhiwei	445
Yuan, Kang	302

Z

Zeng, Chonghan	88
Zhang, Qianning	200
Zhang, Song	261
Zhang, Yafeng	279
Zhang, Qunli	315
Zhang, Luyao	321
Zhang, Lei	147,261,413
Zhang, Liechao	417
Zhang, Xiaoyan	10,442
Zhang, Yanbo	131
Zhang, Yue	162
Zhang, Shuailiang	265
Zhang, Fuling	337
Zhang, Min	396
Zhang, Yajun	457
Zhang, Fei	162
Zhang, Zhijun	179
Zhang, Bo	514
Zhang, Dongkui	100
Zhang, Xinyu	131
Zhang, Longyan	291
Zhang, Shaoru	453
Zhang, Xiangjin	59
Zhang, Zhongyu	154
Zhang, Shixiang	204
Zhang, Santong	403
Zhao, Xiaolin	88
Zhao, Gang	258
Zhao, Heming	500
Zhao, Leyuan	514

Zhao, Wenfei	514
Zhao, Fangyuan	5
Zhao, Wenjie	321
Zhao, Daozhi	118
Zhao, Dangli	187
Zhao, Ping	383
Zheng, Ying	358
Zhong, Liqiong	36
Zhou, Shijie	69
Zhou, Gang	518
Zhou, Hao	74
Zhou, Xiao	204
Zhou, Guochang	349
Zhou, Hongjun	210
Zhu, Xiaomin	157,449
Zhu, Zijiang	170
Zhu, Wangcheng	14,216,224,230,509
Zhu, Liming	396
Zhu, Hongzhi	445
Zhu, Tongyu	40
Zhu, Changsheng	470
Zhu, Yongkang	445